

Finn B. Jensen  
William A. Kuperman  
Michael B. Porter  
Henrik Schmidt

# Computational Ocean Acoustics

*Second Edition*



Modern Acoustics and Signal Processing

 Springer

# **Modern Acoustics and Signal Processing**

## **Editor-in-Chief**

WILLIAM M. HARTMANN

Michigan State University, East Lansing, Michigan

## **Editorial Board**

YOICHI ANDO, Kobe University, Kobe, Japan

WHITLOW W. L. AU, Hawaii Institute of Marine Biology, Kane'ohe, Hawaii

ARTHUR B. BAGGEROER, Massachusetts Institute of Technology, Cambridge,  
Massachusetts

NEVILLE H. FLETCHER, Australian National University, Canberra, Australia

CHRISTOPHER R. FULLER, Virginia Polytechnic Institute and State University,  
Blacksburg, Virginia

WILLIAM A. KUPERMAN, University of California San Diego, La Jolla, California

JOANNE L. MILLER, Northeastern University, Boston, Massachusetts

MANFRED R. SCHROEDER, University of Göttingen, Göttingen, Germany

ALEXANDRA I. TOLSTOY, A. Tolstoy Sciences, McLean, Virginia

For further volumes:

<http://www.springer.com/series/3754>



Finn B. Jensen • William A. Kuperman  
Michael B. Porter • Henrik Schmidt

# Computational Ocean Acoustics

Second Edition



Springer

Finn B. Jensen  
NATO Undersea Research Centre  
Viale San Bartolomeo 400  
La Spezia, 19126, Italy  
[Jensen@nurc.nato.int](mailto:Jensen@nurc.nato.int)

William A. Kuperman  
Marine Physical Lab., Mail Code 0205  
Scripps Institution of Oceanography  
Gilman Dr. 9500  
La Jolla, CA 92093-0238, USA  
[wkuperman@ucsd.edu](mailto:wkuperman@ucsd.edu)

Michael B. Porter  
Heat, Light, and Sound Research, Inc.  
3366 North Torrey Pines Court, Suite 310  
La Jolla, CA 92037, USA

Henrik Schmidt  
Massachusetts Institute of Technology (MIT)  
Massachusetts Avenue 77  
Cambridge, MA 02139, USA

ISBN 978-1-4419-8677-1      e-ISBN 978-1-4419-8678-8  
DOI 10.1007/978-1-4419-8678-8  
Springer New York Dordrecht Heidelberg London

Library of Congress Control Number: 2011927154

© Springer Science+Business Media, LLC 2011  
All rights reserved. This work may not be translated or copied in whole or in part without the written permission of the publisher (Springer Science+Business Media, LLC, 233 Spring Street, New York, NY 10013, USA), except for brief excerpts in connection with reviews or scholarly analysis. Use in connection with any form of information storage and retrieval, electronic adaptation, computer software, or by similar or dissimilar methodology now known or hereafter developed is forbidden.  
The use in this publication of trade names, trademarks, service marks, and similar terms, even if they are not identified as such, is not to be taken as an expression of opinion as to whether or not they are subject to proprietary rights.

Printed on acid-free paper

Springer is part of Springer Science+Business Media ([www.springer.com](http://www.springer.com))

# Series Preface

“...Soun is noght but air y-broke”

— Geoffrey Chaucer  
end of the 14th century

Traditionally, acoustics has formed one of the fundamental branches of physics. In the twentieth century, the field has broadened considerably and become increasingly interdisciplinary. At the present time, specialists in modern acoustics can be encountered not only in Physics Departments, but also in Electrical and Mechanical Engineering Departments, as well as in Departments of Mathematics, Oceanography, and even Psychology. They work in areas spanning from musical instruments to architecture to problems related to speech perception. Today, six hundred years after Chaucer made his brilliant remark, we recognize that sound and acoustics is a discipline extremely broad in scope, literally covering waves and vibrations in all media at all frequencies and at all intensities.

The series of scientific literature, entitled *Modern Acoustics and Signal Processing (MASP)*, covers all areas of today's acoustics as an interdisciplinary field. It offers scientific monographs, graduate level textbooks, and reference materials in such areas as architectural acoustics, structural sound and vibration, musical acoustics, noise, bioacoustics, physiological and psychological acoustics, speech, ocean acoustics; underwater sound; and acoustical signal processing.

Acoustics is primarily a matter of communication. Whether it be speech or music, listening spaces or hearing, signaling in sonar or in ultrasonography, we seek to maximize our ability to convey information, and at the same time, to minimize the effects of noise. Signaling has itself given birth to the field of signal processing, the analysis of all received acoustic information or, indeed, all information in any electronic form. With the extreme importance of acoustics for both modern science and industry in mind, AIP Press is initiating this series as a new and promising publishing venture. We hope that this venture will be beneficial to the entire international acoustical community, as represented by the *Acoustical Society of America*, a founding member of the American Institute of Physics, and other related societies and professional interest groups.

It is our hope that scientists and graduate students will find the books in this series useful in their research, teaching, and studies.

James Russell Lowell once wrote: "In creating, the only hard thing's to begin." This is such a beginning.

*Robert T. Beyer  
Series Editor-in-Chief*

# Preface to the Second Edition

This is the second edition of our book *Computational Ocean Acoustics*, revised and supplemented, including much new material reflecting the progress in computational acoustics and related signal processing issues over the past 17 years. New material appears throughout the book, but we should like to draw attention to the following topics: the basic theory of waveguide invariants in Chap. 2, with a generalization of the concept to realistic, range-dependent waveguides in Chap. 5. The presentation of ray methods in Chap. 3 has been significantly modified to provide a more intuitive development of the fundamental ray concepts. Some intricate issues (aliasing, etc.) related to discrete wavenumber integration in Chap. 4 have been explained in detail, including several illustrative examples. Also, the extension of the wavenumber-integration technique to 3-D scattering and reverberation scenarios in horizontally-stratified waveguides has been included in Chap. 4, together with several illustrative numerical examples. Within the framework of normal-mode theory (Chap. 5), there is new material on mode identification, as well as on normal modes in elastic media. In addition, a section on scattering from objects in a waveguide has been added, together with a 3-D example of mode coupling around seamounts. Chap. 6 has been updated with recent developments in parabolic-equation modeling, notably improvements in dealing with elastic media, and 4-D code implementations for pulse propagation in general 3-D environments. In Chap. 7, we have added a description of the virtual-source concept (VSC) for target scattering, and also expanded on the finite-element (FE) section to address the use of this technique for target scattering in ocean waveguides. Several numerical examples illustrate current capabilities in FE/VSC modeling. Chapter 8 contains new material on Doppler shift in a waveguide, based both on wavenumber-integration and normal-mode theory. Chapter 9 has a new section dedicated to the extraction of time-domain Green's functions from noise correlation functions. Finally, recent developments in signal processing for sonar applications have been added to Chap. 10, specifically on time-domain processing, vector-sensor beamforming, synthetic signal and sensor stimulation, and phase conjugation and time reversal. Finally, extensive use of color illustrations throughout has improved the appearance of this book significantly.

The authors wish to thank the many colleagues who provided material for the book or reviewed parts of the manuscript. These include Michael Ainslie, Michael Collins, Kevin Cockrell, Lee Culver, Gerald D'Spain, Stephanie Fried,

Peter Gerstoft, Oleg Godin, Paul Hursky, Kevin LePage, Wenyu Luo, Ed McDonald, Peter Nielsen, Philippe Roux, Hee-Chun Song, Frédéric Sturm, and Shane Walker. Special thanks go to Mario Zampolli for helping out with the section on finite-element applications. Three of the authors' research reported here has been supported by the U.S. Office of Naval Research, Ocean Acoustics Program, while one author (FBJ) has been supported for 35 years by the NATO Undersea Research Centre. This support is gratefully acknowledged.

Since this book represents a major milestone in the authors' research careers, we wish to acknowledge the unwavering support from our wives, *Patrizia, Gaby, Laurel, and Satu*, to whom this new edition is dedicated.

*Finn B. Jensen*

*William A. Kuperman*

*Michael B. Porter*

*Henrik Schmidt*

# Preface to the First Edition

The importance of computers in scientific research today is universally recognized. Several new journals dedicated to the fields of Computer Science and Computational Physics have appeared over the past decade, and it is evident that computers have already changed our approach to doing science, both experimentally and theoretically.

A statement by Prof. Norman Zabusky in the October 1987 issue of *Physics Today* clearly points to the crux of the matter: “We are in the midst of a computational revolution that will change science and society as dramatically as the agricultural and industrial revolutions did. The discipline of computational science is already significantly affecting the way we do hard and soft science. Computers with fast, interactive visualization peripherals have come of age and provide a mode of working that is coequal with laboratory experiments and observations and with theory and analysis. We can now grapple with nonlinear and complexly intercoupled phenomena in a relatively short time and provide insight for quantitative understanding and better prediction.”

The above comments on the impact of computers on research in virtually all disciplines of science certainly also apply to the field of ocean acoustics, where we have observed an explosive growth in the development and use of numerical models since the mid-1970s. Numerical models have become standard research tools in acoustic laboratories, and computational acoustics is becoming an ever more important branch of the ocean acoustic science. Only the numerical approach allows us to include the full complexity of the acoustic problem, and moreover, a *numerical* experiment is both faster and cheaper than an actual ocean experiment.

Since ocean acoustic modeling has now reached a mature state of development, we feel that the timing is right for a textbook on computational acoustics. The book is intended to present the state-of-the-art of numerical techniques as applied to solving the wave equation in heterogeneous fluid–solid media. Emphasis is on developing the theoretical foundation which directly leads to numerical implementations for real ocean environments. Various computational schemes are discussed in detail, and, in contrast to standard textbooks where acoustic effects are demonstrated through analytical expressions, fundamental propagation features are here illustrated graphically, often in color.

It is anticipated that the text will be useful to both universities and government laboratories. In universities, such material is covered in various departments including Applied Mathematics, Geology and Geophysics, and Ocean Engineering, or in special programs on Acoustics. The text would be appropriate either as a course directly in computational ocean acoustics or as a principal reference in a more general course on computational techniques for problems in wave propagation. The level of the text is suitable for either graduate students or undergraduates at the senior level.

The other important audience for this text is in government (especially Navy) and industry laboratories, which are involved in either the development or use of propagation models. For users, a principal problem is that of understanding both the mathematical and numerical limitations of the various modeling techniques.

The authors all have many years of experience in the field. By involving four authors, each one being an expert on one or more of the topics listed in the table of contents, it was hoped to provide an in-depth treatment of all aspects of computational ocean acoustics, ranging from the fundamentals of wave propagation theory, over particular solution techniques (rays, wavenumber integration, normal modes, parabolic equations), to the detection of signals in the presence of noise.

Much of the research which forms the basis for this book was carried out at the SACLANT Undersea Research Centre, La Spezia, Italy. This institution has had a consistent effort in acoustic modeling since the mid-1970s, and all four authors have spent varying lengths of time at SACLANTCEN since then. It is the inspiring and fertile research environment at this Centre together with its excellent computing and graphics facilities which is the real reason for this book becoming a reality. The authors also wish to express their gratitude to the members of the SACLANTCEN Environmental Modeling Group, Giancarlo Dreini, Carlo Ferla, Cinzia Isoppi and Giovanna Martinelli, for their assistance in the development and maintenance of the various acoustic models. We are also grateful to Alvaro Carrara for helping with the illustrations for the book.

Finally, we wish to thank the many colleagues who performed a critical review of parts of the manuscript at various stages of preparation. Among those are Dale Ellis, Richard Evans, Joo-Thiam Goh, Frank Ingenito, Ed McDonald, John Perkins, Richard Pitre, George Rolt, and Alex Tolstoy. Special thanks go to Mike Collins for helping us keep abreast of the most recent parabolic equation developments, and to Ken Rolt for doing a thorough and detailed editing of the entire manuscript.

*Finn B. Jensen  
William A. Kuperman  
Michael B. Porter  
Henrik Schmidt*

# Contents

<b>1 Fundamentals of Ocean Acoustics .....</b>	<b>1</b>
1.1 Introduction .....	1
1.2 The Ocean-Acoustic Environment .....	3
1.3 Some Acoustic Preliminaries .....	10
1.3.1 Sources and Receivers .....	10
1.3.2 Energy, Power and Intensity .....	11
1.3.3 Relevant Units .....	13
1.3.4 Transmission Loss .....	14
1.4 Sound Propagation in the Ocean .....	15
1.4.1 Characteristic Propagation Paths .....	15
1.4.2 Deep Water .....	17
1.4.3 Shallow Water .....	28
1.4.4 Range-Dependent Environments .....	32
1.5 Volume Attenuation .....	35
1.5.1 Attenuation of Plane Waves .....	35
1.5.2 Attenuation in Seawater .....	36
1.6 Bottom Loss .....	38
1.6.1 Fluid–Fluid Interface .....	40
1.6.2 Fluid–Solid Interface .....	43
1.6.3 Layered Fluid Halfspace .....	45
1.6.4 Arbitrary Layering .....	50
1.7 Boundary and Volume Scattering .....	51
1.7.1 Surface Scattering .....	52
1.7.2 Bottom Scattering .....	54
1.7.3 Volume Scattering .....	54
1.8 Ambient Noise .....	57
1.9 Sound Propagation Models .....	60
Problems .....	61
References .....	62
<b>2 Wave Propagation Theory .....</b>	<b>65</b>
2.1 The Wave Equation .....	65
2.1.1 The Nonlinear Wave Equation .....	66
2.1.2 The Linear Wave Equation .....	67

2.2	The Helmholtz Equation.....	71
2.3	Homogeneous Media .....	73
2.3.1	Coordinate Systems.....	73
2.3.2	Source in Unbounded Medium.....	75
2.3.3	Source in Bounded Medium.....	77
2.3.4	Point Source in Fluid Halfspace.....	80
2.3.5	Transmission Loss .....	81
2.4	Layered Media and Waveguides .....	83
2.4.1	Integral Transform Techniques .....	84
2.4.2	Source in Fluid Halfspace .....	87
2.4.3	Reflection and Transmission .....	93
2.4.4	Ideal Fluid Waveguide .....	102
2.4.5	The Pekeris Waveguide .....	118
2.4.6	Waveguide Invariants .....	133
2.5	Deep-Ocean Waveguides .....	139
2.5.1	Exact Solutions .....	140
2.5.2	WKB Solutions .....	143
	Appendix 1: Principle of Reciprocity .....	147
	Problems .....	149
	References.....	152
<b>3</b>	<b>Ray Methods .....</b>	<b>155</b>
3.1	Introduction .....	155
3.2	Ray Bending .....	156
3.3	Mathematical Derivation .....	158
3.3.1	Solving the Eikonal Equation .....	160
3.3.2	Solving the Transport Equation .....	163
3.3.3	Ray Amplitudes and Jacobians.....	166
3.3.4	Initial Conditions .....	167
3.3.5	Intensity Calculations.....	168
3.4	Ray Anomalies .....	175
3.4.1	Caustics and Shadow Zones .....	175
3.4.2	Region of Validity of the Ray Solution .....	178
3.5	Gaussian Beams.....	180
3.5.1	Gaussian Beams in Free Space .....	180
3.5.2	Gaussian Beam Tracing .....	181
3.6	Additional Mathematical Properties .....	185
3.6.1	Alternate Forms of the Ray Equations .....	185
3.6.2	Treatment of Attenuation .....	187
3.6.3	Interfaces and Boundaries .....	188
3.6.4	Weak Interfaces and Ocean Sound-Speed Discontinuities .....	194
3.6.5	Fermat's Principle.....	195
3.6.6	Simplifications for Stratified Media.....	196

3.6.7	Snell's Law .....	198
3.6.8	Reciprocity .....	199
3.7	Numerical Solution .....	200
3.7.1	Direct Integration .....	201
3.7.2	Cell Methods: $n^2$ Linear .....	206
3.7.3	Cell Methods: $c$ Linear .....	208
3.7.4	False Caustics and Profile Interpolation .....	211
3.7.5	Finding Eigenrays.....	213
3.8	Extensions and Related Techniques .....	216
3.8.1	The WKB Method .....	216
3.8.2	Ray Theory via the WKB Approximation .....	219
3.8.3	The Ray Invariant and the Waveguide Invariant.....	220
3.8.4	Hamiltonian Formulation of Ray Acoustics .....	223
3.8.5	Three-Dimensional Ray Tracing .....	225
Appendix 1:	Recipe for Simple Ray Code.....	226
Appendix 2:	A Useful Property of the Jacobian .....	227
Problems .....	.....	228
References .....	.....	230
<b>4</b>	<b>Wavenumber Integration Techniques .....</b>	<b>233</b>
4.1	Introduction .....	233
4.2	Mathematical Derivation .....	235
4.2.1	Integral Transform Solution .....	235
4.2.2	Homogeneous Fluid Layers .....	237
4.2.3	$n^2$ -Linear Fluid Layers .....	238
4.2.4	Homogeneous Elastic Layers .....	240
4.2.5	Boundary Conditions .....	242
4.2.6	Attenuation .....	243
4.3	Numerical Solution of the Depth Equation .....	244
4.3.1	Direct Global Matrix Approach .....	245
4.3.2	Propagator Matrix Approach .....	251
4.3.3	Invariant Embedding Approach .....	255
4.4	Reflection Coefficients.....	257
4.5	Wavenumber Integration.....	258
4.5.1	Fast Field Approximation .....	260
4.5.2	Truncation of Integration Interval .....	261
4.5.3	Wavenumber Discretization: Aliasing .....	262
4.5.4	FFP: Fast Field Program.....	265
4.5.5	Complex Contour Integration .....	268
4.5.6	Fast Hankel Transforms .....	272
4.5.7	Trapezoidal Rule Integration .....	276
4.5.8	Filon Integration .....	278
4.5.9	Adaptive Integration .....	279
4.6	Frequency Integration.....	280
4.7	Range-Dependent Propagation .....	281
4.8	3-D Wavenumber Integration.....	282

4.9	Scattering and Reverberation in a Stratified Ocean .....	284
4.9.1	Target Scattering .....	285
4.9.2	Rough Interface Reverberation .....	287
4.9.3	Scattering from Volume Inhomogeneities .....	292
4.10	Numerical Examples .....	297
4.10.1	Waveguide with an Elastic Bottom .....	297
4.10.2	The Bucker Waveguide .....	300
4.10.3	Beam Reflection and Transmission .....	302
4.10.4	Arctic Propagation .....	305
4.10.5	Seabed Target Scattering and Reverberation .....	309
4.10.6	Reverberation from Seabed Volume Inhomogeneities ..	314
Appendix 1:	Recipe for Simple WI/FFP Code.....	320
Appendix 2:	Roughness Perturbation Operators .....	324
Problems .....	328	
References .....	332	
<b>5</b>	<b>Normal Modes .....</b>	<b>337</b>
5.1	Introduction .....	337
5.2	Mathematical Derivation .....	338
5.2.1	Point Source in Cylindrical Geometry .....	338
5.2.2	Line Source in Plane Geometry .....	341
5.3	Modal Expansion of the Green's Function .....	343
5.4	The Isovelocity Problem.....	344
5.5	A Generalized Derivation .....	349
5.6	A Deep Water Problem: The Munk Profile .....	356
5.7	Numerical Approaches .....	360
5.7.1	Finite-Difference Methods .....	362
5.7.2	Layer Methods .....	372
5.7.3	Shooting Methods .....	373
5.7.4	Root Finders .....	375
5.7.5	Choice of Numerical Algorithm .....	379
5.8	Prüfer Transformations and Mode Counting .....	380
5.8.1	Top Halfspaces .....	382
5.8.2	Bottom Halfspaces .....	384
5.9	Modal Perturbation Theory .....	385
5.9.1	Modal Propagation Loss .....	385
5.9.2	Modal Group Velocity .....	390
5.10	Elastic Media .....	391
5.10.1	Governing Equations .....	391
5.10.2	Numerical Discretization .....	394
5.10.3	Shooting Methods and Compound Matrices .....	395
5.10.4	Boundary and Interface Conditions .....	397
5.10.5	Numerical Example.....	400
5.11	Normal Modes for Range-Dependent Environments.....	402
5.11.1	Coupled Modes .....	403
5.11.2	One-Way Coupled Modes .....	407

5.11.3	The Adiabatic Approximation.....	408
5.11.4	Example: A Warm-Core Eddy .....	411
5.12	Scattering from Objects in a Waveguide .....	413
5.12.1	Scattering Geometry .....	413
5.12.2	The Plane-Wave Scattering Function .....	414
5.12.3	Scattering from Spherical Objects in a Waveguide.....	417
5.12.4	Scattering from Non-Spherical Objects.....	421
5.13	Normal Modes for 3-D Varying Environments .....	423
5.13.1	Horizontal Refraction Equations .....	423
5.13.2	Global Propagation .....	426
5.13.3	3-D Mode Coupling Around Seamounts .....	429
5.14	Waveguide Invariant and Dispersion for Realistic Environments ..	438
5.14.1	The Waveguide Invariant Is Variable!.....	440
5.14.2	Range-Dependent Group Speed and Adiabatic Mode Theory .....	441
5.14.3	Waveguide Invariant for Range-Dependent Environments .....	443
Appendix 1:	Recipe for Simple Mode Code.....	445
Appendix 2:	Evaluation of the Normalization Term .....	447
Problems .....	449	
References.....	452	
<b>6</b>	<b>Parabolic Equations .....</b>	<b>457</b>
6.1	Introduction .....	457
6.2	Derivation of Parabolic Equations .....	458
6.2.1	Standard PE Derivation.....	458
6.2.2	Generalized PE Derivation .....	460
6.2.3	Expansion of the Square-Root Operator .....	461
6.2.4	Phase Errors and Angular Limitations .....	466
6.3	The Elastic PE.....	470
6.4	Starting Fields .....	472
6.4.1	Numerical Starters .....	473
6.4.2	Analytical Starters .....	476
6.4.3	Spectral Properties of Sources .....	482
6.5	Solutions by FFTs .....	486
6.5.1	The Split-Step Fourier Algorithm .....	487
6.5.2	Error Analysis.....	490
6.5.3	Numerical Implementation .....	493
6.5.4	Variable Density .....	495
6.5.5	Attenuation .....	496
6.6	Solutions by FDs and FEs .....	497
6.6.1	Field Equations on Horizontal Interfaces .....	498
6.6.2	IFD Formulation .....	500
6.6.3	Error Analysis .....	503
6.6.4	Numerical Implementation .....	505

6.7	The Problem of Energy Conservation in PEs .....	506
6.8	Three-Dimensional PEs .....	509
6.8.1	Expansion of the Square-Root Operator .....	509
6.9	Numerical Examples .....	512
6.9.1	Beam Propagation .....	512
6.9.2	Propagation in a 2-D Wedge .....	515
6.9.3	Propagation Over a Seamount .....	516
6.9.4	Propagation Over a Sloping Elastic Bottom .....	517
6.9.5	Propagation in a 3-D Wedge .....	517
	Appendix 1: Recipe for Simple PE Code .....	523
	Problems .....	526
	References .....	527
<b>7</b>	<b>Finite Differences and Finite Elements .....</b>	<b>531</b>
7.1	Introduction .....	531
7.2	Differential Equations .....	532
7.3	Finite-Difference Methods .....	534
7.3.1	Introduction .....	534
7.3.2	Difference Approximations .....	534
7.3.3	Convergence and Stability .....	537
7.3.4	The Wave Equation .....	538
7.4	Finite-Element Methods .....	545
7.4.1	Introduction .....	545
7.4.2	Mathematical Derivation .....	547
7.4.3	The Acoustic Wave Equation .....	551
7.4.4	The Elastic Wave Equation .....	562
7.4.5	Coupled Fluid–Elastic Domains .....	565
7.4.6	Steady-State Solutions .....	566
7.4.7	Perfectly Matched Layers .....	566
7.4.8	Time Recurrence .....	569
7.5	Boundary-Element Methods .....	570
7.5.1	Introduction .....	570
7.5.2	The Boundary-Integral Equation .....	571
7.5.3	Boundary-Element Equations .....	573
7.5.4	Coupled Domains .....	576
7.5.5	Virtual Source Concept .....	580
7.6	Numerical Examples .....	584
7.6.1	Scattering by Arctic Ice Features .....	584
7.6.2	Scattering from Objects Near Interfaces .....	590
	Appendix 1: Variational Formulation for Fluid–Elastic Interaction .....	598
	Appendix 2: Farfield Computations .....	604
	Problems .....	605
	References .....	607

<b>8 Broadband Modeling</b> .....	611
8.1 Introduction .....	611
8.2 Fourier Synthesis of Frequency-Domain Solutions .....	612
8.2.1 Evaluation by FFT .....	613
8.2.2 Complex Frequency Integration.....	616
8.3 Time-Domain Solutions .....	617
8.3.1 Ray Methods .....	617
8.3.2 Spectral Integral Techniques .....	619
8.3.3 Parabolic Equations.....	621
8.4 Doppler Shift in a Waveguide .....	623
8.4.1 Wavenumber Integral Representation.....	625
8.4.2 Normal Mode Representation .....	628
8.4.3 Doppler Shift for Active Sonar.....	630
8.5 Numerical Examples.....	633
8.5.1 The Head-Wave Problem .....	633
8.5.2 Mode Dispersion in a Waveguide .....	636
8.5.3 3-D Wedge Propagation .....	640
8.5.4 Seismic Interface Waves .....	643
8.5.5 Deep-Water Propagation.....	647
8.5.6 Surface-Duct Propagation with Leakage .....	652
8.5.7 Acoustic Emission from Ice Fractures .....	654
Problems .....	657
References.....	659
<b>9 Ambient Noise</b> .....	661
9.1 Introduction .....	661
9.2 Surface Noise in a Stratified Ocean .....	662
9.2.1 Mathematical Derivation .....	663
9.2.2 Spatial Distribution of Noise Sources.....	665
9.2.3 Wavenumber Integral Representation.....	666
9.2.4 Normal Mode Representation .....	667
9.2.5 Noise in a Homogeneous Halfspace .....	669
9.2.6 Noise in Stratified Media .....	671
9.3 Extracting Time-Domain Green's Functions from Noise Correlation Functions.....	678
9.3.1 The Time-Domain Green's Function .....	680
9.3.2 Emergence of Coherent Wavefronts from Noise .....	681
9.3.3 Data Examples of Extracting Wavefronts from Noise .....	682
9.4 Surface Noise in a Three-Dimensional Ocean.....	686
9.4.1 Noise Modeling by Adiabatic Modes.....	687
9.4.2 Simulated Noise Fields in 3-D Environments .....	691
9.4.3 Noise Modeling by PE.....	694
9.4.4 Downslope and Deep-Ocean-Basin Noise Field .....	696
Appendix 1: Evaluation of the Cross-Spectral Density .....	697
Problems .....	702
References.....	703

<b>10 Signals in Noise .....</b>	705
10.1 Introduction .....	705
10.2 The Energetics of Signals in Noise .....	706
10.2.1 Array Gain .....	706
10.2.2 Sonar Equation .....	708
10.3 Plane-Wave Beamforming .....	714
10.3.1 Linear Beamforming .....	714
10.3.2 Adaptive Beamforming .....	716
10.3.3 Multiple-Constraints Beamforming .....	722
10.3.4 White-Noise Constraint Processor .....	723
10.4 Time-Domain Processing .....	724
10.4.1 Isovelocity Time-Delay Beamforming .....	725
10.4.2 Non-Isovelocity Time-Delay Beamforming: The Turning Point Filter .....	725
10.4.3 Example: Passive Fathometer .....	726
10.5 Performance Prediction: Modeling, Beamforming and the Sonar Equation .....	728
10.6 Matched-Field Processing .....	730
10.7 Simulating Matched-Field Processing .....	733
10.7.1 Depth-Range Matched Field Processing .....	734
10.7.2 Three-Dimensional Matched Field Processing .....	741
10.8 Vector-Sensor Beamforming .....	750
10.9 Synthetic Signals and Sensor Stimulation .....	754
10.9.1 Stochastic Signal and Noise Model .....	755
10.9.2 Snapshot Synthesis .....	755
10.9.3 Signal Variability .....	756
10.9.4 Noise Realizations .....	757
10.10 Phase Conjugation and Time Reversal .....	758
10.10.1 Theory and Simulation for Phase Conjugation/TRM in the Ocean .....	759
10.11 Summary .....	767
Problems .....	767
References .....	769
<b>About the Authors .....</b>	773
<b>Name Index .....</b>	775
<b>Subject Index .....</b>	783

# Chapter 1

## Fundamentals of Ocean Acoustics

### 1.1 Introduction

The origin of computational and *numerical* acoustics coincides with the emergence of theoretical physics [1] as an intellectual endeavor. Pythagoras developed the theory of the (Western) musical scale in terms of a device called a monochord in which adjacent consonant notes of the musical scale were obtained by plucking two string segments whose relative lengths were ratios of the small integers 1, 2, and 3. He recognized that the lengths of these strings were inversely proportional to the frequency of sound generated when plucked. Since that time, computational methods in acoustics have expanded to use more numbers than these first three integers. Mersenne [2] in the seventeenth century added the irrationals as a numerical tool when he determined that the frequency of a vibrating string was proportional to the square root of its cross-sectional area. He further added to the quantitative tradition of acoustics with conclusions such as: “The velocity of sound is greater than the velocity of cannon balls and equals 230 six-foot intervals per second.” Although the former statement is also probably true for sound propagating in water, Mersenne’s contributions to the understanding of underwater acoustics are suspect judging from his speculation that sound travels more slowly in water than air because the density of water is greater than air.

An impressive list of physicists and mathematicians from Galileo, Newton to Rayleigh, and beyond have made major contributions to the theory of acoustics in gases, liquids, and solids. In that sense, the history of acoustics reads like a Who’s Who of Physics and Mathematics. The disputes of those days involved the giants of science and were not for the intellectually meek. For example, Euler’s and Lagrange’s ideas on sound propagation were attacked rather energetically by d’Alembert. The latter was not exactly an amateur acoustician. He was the first to write down the partial differential equation describing the motion of a vibrating string which we now refer to as the wave equation. Without present day computers and associated numerical methods, he developed a method to solve this type of equation: separation of variables.

Newton is normally credited with the first theoretical attempt to describe sound propagation in a fluid. Ocean acoustics, the subject of this book, is the science of

sound in the sea and encompasses not only the study of sound propagation, but also the masking of sound by interfering acoustic phenomena. Its origins also date back centuries; for example, both of these aspects were recognized by Leonardo da Vinci who noted that sound travels to great distances in the sea and referred to interfering phenomena (in this case, self noise) by suggesting the listener "...cause your ship to stop..." [3] before deploying a listening tube through the air–water interface. This listening tube was improved upon by Colladen and Sturm [4] who, on Lake Geneva in 1826, employed a trumpet-like device to receive sound emitted by a submerged bell 15 km away. By essentially a time-of-flight measurement, they measured the speed of sound to an accuracy of about two tenths of 1%. In addition, "Colladen marveled that so little energy at the source could be transmitted so great a distance through the water medium and could still be detected by the trumpet receiver." It is still believed that sound is the only practical way to propagate signals to great distances in the sea.

The development of acoustics theory has followed a different historical path than optics and electromagnetic theory [5]. While there has been a long-running battle in optics between ray and wave theory, acoustics originally developed with wave and vibration concepts as far back as ancient Greek times. For example, musical sound is the result of air motion generated by a vibrating musical instrument. This sound is propagated in an analogous manner to water surface waves which propagate disturbances (signals), but does not propagate matter to long distances. The bending of sound around corners is then easily understood in the context of diffraction in the water surface wave analogy. In acoustics, the ray picture evolved as a mathematical approximation to wave theory. In underwater acoustics, in which the medium is inhomogeneous and bounded by complicated interfaces, ray theory has historically proved to be an indispensable tool for understanding and studying sound propagation. However, with the advent of computers and the recent developments of numerical physics, sound propagation in the ocean can now be studied and quantitatively described in greater detail with the more exact wave theory. This trend is particularly important to the study of extracting signals from complex interfering fields in which a quantitative understanding of the amplitude, phase, and higher order moments of all the relevant fields is necessary.

Research in the field of experimental ocean acoustics requires extensive equipment, with typically at least one ship and often an assortment of at-sea platforms equipped with sound projectors, receiving arrays, and sensors to measure the ocean environment. The requirements to measure the latter arise because the ocean is the medium which defines the acoustic index of refraction and the ocean surface and bottom (and layers below) are the interfaces that define the boundary conditions of the partial differential equations descriptive of sound propagation in the ocean. Very often, the oceanographic and ocean geology measurements associated with an acoustic experiment rival or exceed the complexity of the acoustic measurements.

In this chapter, the ocean environment will be introduced and described prior to the acoustics. Then, we present underwater acoustics with minimum mathematics in a detailed, though, descriptive manner, associating various acoustic topics with the details of the previously discussed ocean environment.

## 1.2 The Ocean-Acoustic Environment

The ocean is an acoustic waveguide limited above by the sea surface and below by the seafloor. The speed of sound in the waveguide plays the same role as the index of refraction does in optics. Sound speed is normally related to density and compressibility. In the ocean, density is related to static pressure, salinity, and temperature. The sound speed in the ocean is an increasing function of temperature, salinity, and pressure, the latter being a function of depth. It is customary to express sound speed ( $c$ ) as an empirical function of three independent variables: temperature ( $T$ ) in degrees centigrade, salinity ( $S$ ) in parts per thousand, and depth ( $z$ ) in meters. A simplified expression for this dependence is [6]

$$\begin{aligned} c = & 1449.2 + 4.6 T - 0.055 T^2 + 0.00029 T^3 \\ & + (1.34 - 0.01 T)(S - 35) + 0.016 z. \end{aligned} \quad (1.1)$$

For most cases, the above equation is sufficiently accurate; however, when propagation distances are derived from time-of-flight measurements, more accurate sound-speed formulas may be required [7–9].

Seasonal and diurnal changes affect the oceanographic parameters in the upper ocean. In addition, all of these parameters are a function of geography. Figure 1.1 shows a typical set of sound-speed profiles indicating greatest variability near the surface as function of season and time of day. In a warmer season (or warmer part of the day), the temperature increases near the surface and hence the sound speed increases toward the sea surface. This near-surface heating (and subsequent cooling) has a profound effect on surface-ship sonars. Thus, the diurnal heating causes poorer sonar performance in the afternoon—a phenomenon known as the *afternoon effect* [3]. The seasonal variability, however, is much greater and therefore more important acoustically.

In non-polar regions, the oceanographic properties of the water near the surface result from mixing due to wind and wave activity at the air-sea interface. This near-surface *mixed layer* has a constant temperature (except in calm, warm surface conditions as described above). Hence, in this isothermal mixed layer we have a sound-speed profile which increases with depth because of the pressure gradient effect, the last term in (1.1). This is the *surface duct* region, and its existence depends on the near-surface oceanographic conditions. Note that the more agitated the upper layer is, the deeper the mixed layer and the less likely will there be any departure from the mixed-layer part of the profile depicted in Fig. 1.1. Hence, an atmospheric storm passing over a region mixes the near-surface waters so that a surface duct is created or an existing one deepened or enhanced.

Below the mixed layer is the thermocline where the temperature decreases with depth and therefore the sound speed also decreases with depth. Below the thermocline, the temperature is constant (about 2°C—a thermodynamic property of salt water at high pressure) and the sound speed increases because of increasing pressure. Therefore, between the deep isothermal region and the mixed layer, we must

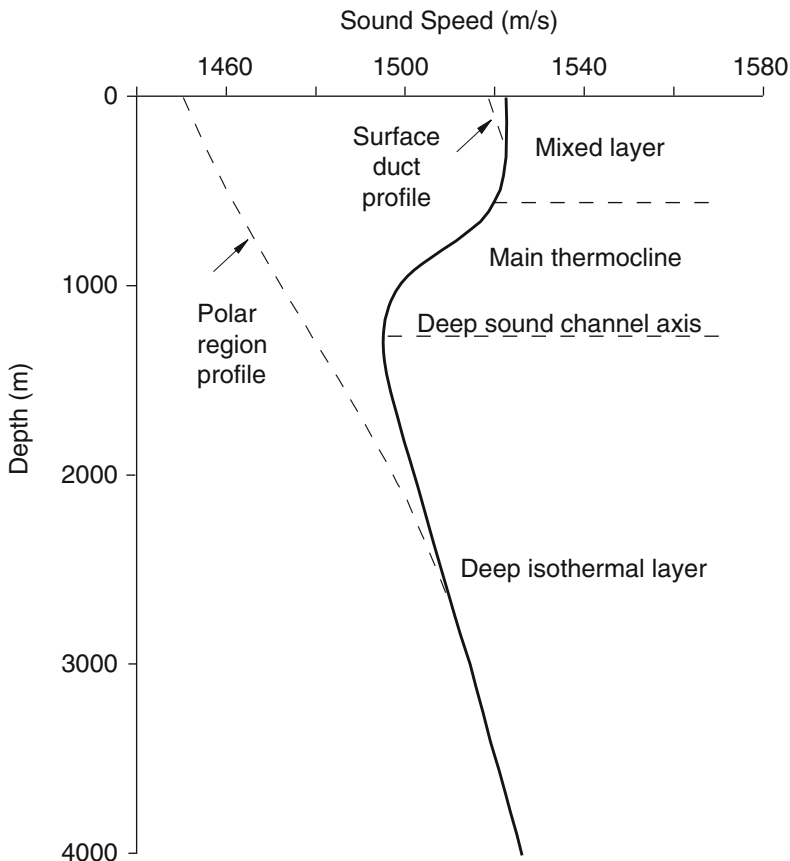


**Fig. 1.1** Generic sound-speed profiles

have a minimum sound speed which is often referred to as the axis of the *deep sound channel*. However, in polar regions, the water is coldest near the surface and hence the minimum sound speed is at the ocean-air (or ice) interface as indicated in Fig. 1.1. In continental shelf regions (shallow water) with water depth of the order of a few hundred meters, only the upper part of the sound-speed profile in Fig. 1.1 is relevant. This upper region is dependent on season and time of day, which, in turn, affects sound propagation in the water column.

Figure 1.2 is a contour display of the sound speed structure of the North and South Atlantic [10] with the deep sound channel indicated by the heavy dashed line. Note the geographic (and climatic) variability of the upper-ocean sound-speed structure and the stability of this structure in the deep isothermal layer. As explained above, the axis of the deep sound channel becomes shallower toward both poles, and eventually reaches the surface.

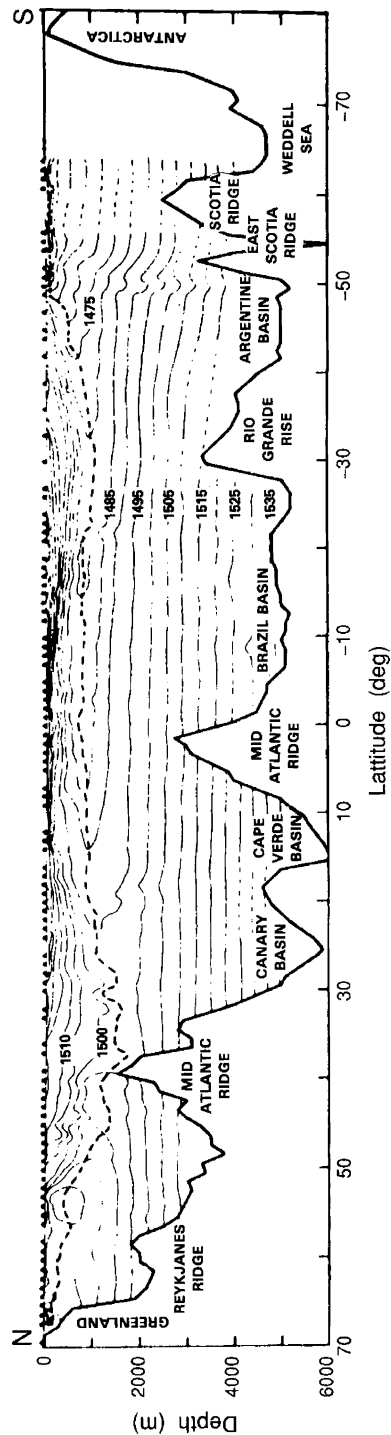
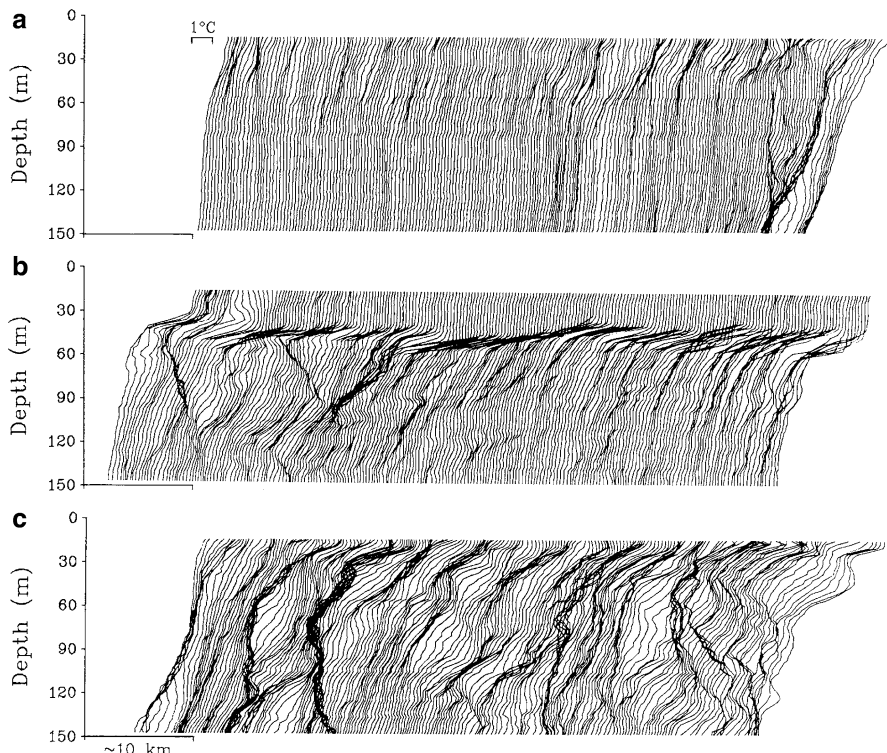


Fig. 1.2 Sound speed contours taken from the North and South Atlantic along  $30.50^{\circ}\text{W}$ . Dashed line indicates axis of deep sound channel (from Northrup and Colborn [10])

Of course, the ocean sound-speed structure is not frozen in time nor space. On the contrary, the ocean has its own weather system — mesoscale phenomena which, it is estimated, contain more than 90% of the oceans' kinetic energy. Time and distance scales associated with such phenomena are of the order of months and hundreds of kilometers, respectively. In addition, there are slow-moving currents like the Gulf Stream, internal waves with horizontal scales up to 10 km, vertical scales one tenth of that, times scale of minutes to hours, and quite a bit of microstructure on the order of centimeters.

Figure 1.3 illustrates the microstructure variability along three tracks in the Norwegian Sea [11]. The data were recorded on a towed thermistor chain, covering ranges of approximately 50 km per track and depths between 15 and 150 m. Even though the data were all collected in the same area within a period of 2 weeks in June 1987, we notice strong differences in lateral variability along the three tracks. Thus, Fig. 1.3a displays a stable water column well suited for a deterministic modeling approach at all frequencies of practical importance in ocean acoustics. Figure 1.3b, on the other hand, shows a section with a stable surface layer, but with



**Fig. 1.3** Temperature profile sections from the Norwegian Sea. (a) Laterally stable ocean. (b) Stable surface layer with some lateral variability below the thermocline. (c) Strong lateral variability in the upper 150 m (figure adapted from Sellschopp [11])

some microstructure variability below the thermocline which would cause scattering of high-frequency sound. Finally, the situation shown in Fig. 1.3c with strong lateral variability at all depths definitely requires a stochastic modeling approach, except at very low frequencies.

In general, all of the oceanographic structure described above has an effect on sound propagation, both as a source of attenuation and of acoustic fluctuations [12]. Mesoscale and Gulf-Stream-like phenomena can be treated deterministically by range-dependent or three-dimensional acoustic models whereas internal wave and microstructure phenomena are presently best treated by stochastic models.

Turning to the upper and lower boundaries of the ocean waveguide, the sea surface is a simple horizontal boundary and a nearly perfect reflector. The seafloor, on the other hand, is a lossy boundary with strongly varying topography across ocean basins (Fig. 1.2). Both boundaries have small-scale roughness associated with them, e.g. surface gravity waves, which causes scattering and attenuation of sound. In terms of acoustic modeling, the seafloor is definitely the most complex boundary, exhibiting vastly different reflectivity characteristics in different geographical locations.

Although the sea surface in most cases is treated as a simple, perfectly reflecting boundary, there are cases where it has more profound implications on the propagation of sound. One is the Arctic, where the ice cover is an elastic medium supporting a complex seismic wavefield, which couples with and affects the underwater acoustic propagation. This will be discussed in Chaps. 4 and 7. Another case is high sea states, where in addition to large waves, the upper ocean will have a significant infusion of air bubbles [13]. Although the volume concentration of air is relatively small, usually a small fraction of 1%, the effect on the acoustic field may be significant, because of the dramatic effect of even small air concentrations on the speed of sound.

As will be discussed in Chap. 2, the speed of sound depends on the fluid bulk modulus  $K$  and density  $\rho$ ,

$$c^2 = \frac{K}{\rho}. \quad (1.2)$$

Assume a water volume  $V$  has a suspension of small air bubbles of volume fraction  $\phi$ . With the specific density of water and air being  $\rho_w$  and  $\rho_a$ , respectively, the effective density  $\rho_e$  of the volume is simply the weighted average of the two densities,

$$\rho_e = \phi\rho_a + (1 - \phi)\rho_w. \quad (1.3)$$

Now assume the volume is exposed to a change in hydrostatic pressure  $\Delta p$ . This pressure will compress both the air bubbles and the water, with equilibrium requiring the air and water pressure to both increase by  $\Delta p$ . With the specific bulk moduli for air and water being  $K_a$  and  $K_w$ , respectively, the total volume change due to the hydrostatic pressure increase is

$$\Delta V = \Delta V_e + \Delta V_w = \phi \frac{\Delta p}{K_a} + (1 - \phi) \frac{\Delta p}{K_w} \quad (1.4)$$

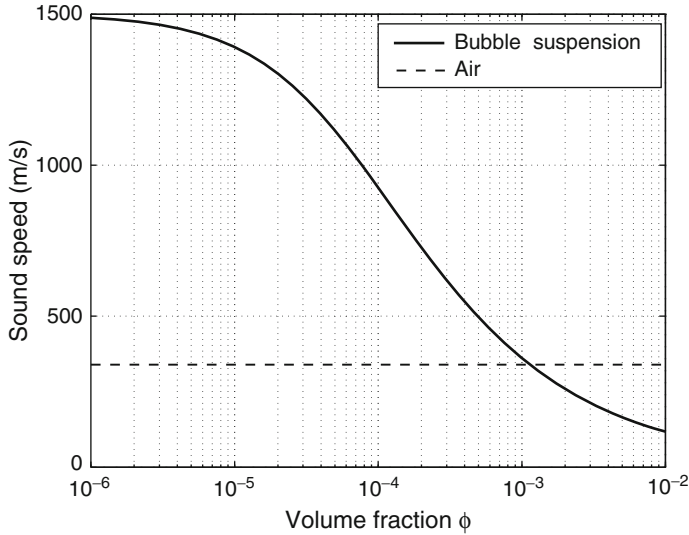


**Fig. 1.4** Effective sound speed for water with suspended air bubbles, as function of volume fraction

yielding the effective bulk modulus

$$K_e = \frac{\Delta p}{\Delta V} = \left[ \frac{\phi}{K_a} + \frac{1-\phi}{K_w} \right]^{-1}. \quad (1.5)$$

Thus, the densities combine as two resistors in series, while the bulk moduli combine as two resistors in parallel. The effect on the effective sound speed is surprisingly dramatic, with even small bubble concentrations significantly lowering the sound speed, as illustrated in Fig. 1.4. Note that for volume fractions in excess of 0.1%, the effective sound speed is less than the speed of sound in air. It should be pointed out that, in addition to near the surface, gas bubbles may also play an effect in the seabed, where gas may be produced by biological decay processes.

The structure of the ocean bottom depends on the local geology, but in general it consists of a thin stratification of sediments overlying the oceanic crust in the deep ocean and relatively thick stratification over continental crust on the continental shelves. The nature of the stratification is dependent on many factors, including geological age and local geological activity. Thus, relatively recent sedimentations will be characterized by plane stratification parallel to the seabed, whereas older sediments and sediments close to the crustal plate boundaries may have undergone significant deformation. Other geological features introducing deformation of the sediment stratifications are *salt diapirs* and *faults*. An example of a complicated bottom layering is given in Fig. 1.5, which displays a seismic section from the Mediterranean. Note that while the upper stratification is almost parallel to the seafloor, deeper layers are strongly inclined.

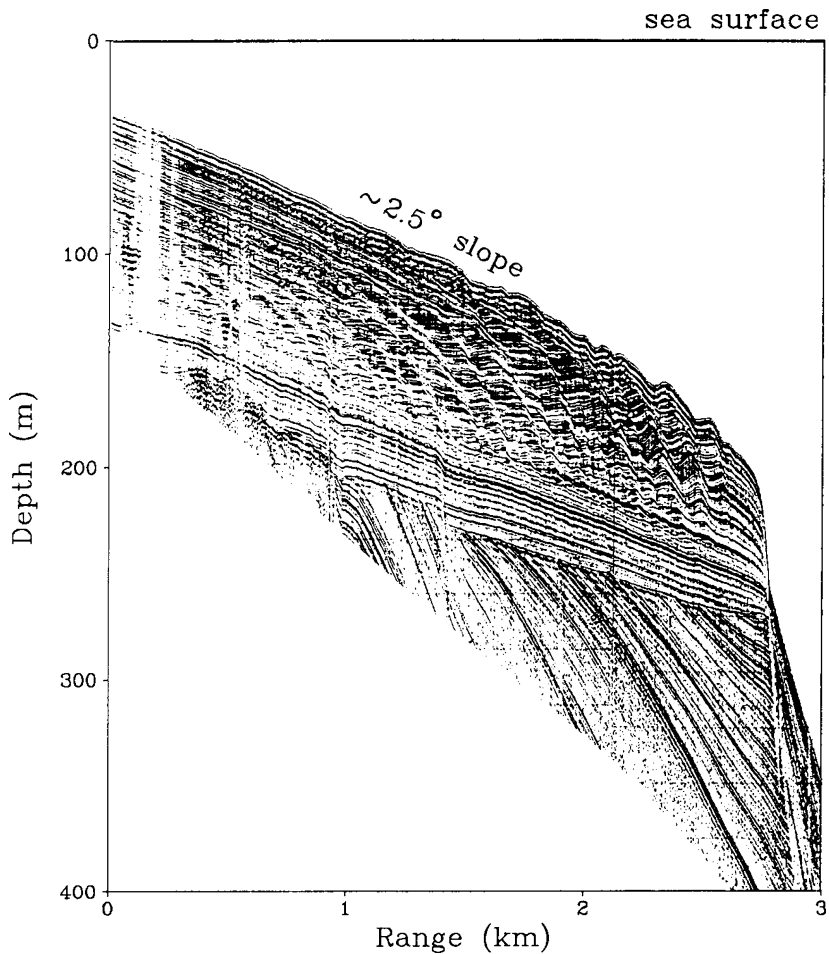


**Fig. 1.5** Seismic profile section from coastal-water area in the Mediterranean Sea. (Courtesy T. Akal)

The seabed is in general quite flat, even close to seamounts, ridges, and the continental slopes, with a slope seldomly exceeding  $10^\circ$ . The importance of treating the ocean bottom accurately in the numerical models depends on factors such as source-receiver separation, source frequency, and ocean depth. Thus, the bottom interaction is in general unimportant for large ranges, high frequencies, and deep water due to the upward refracting sound-speed profile. On the other hand a correct treatment of the bottom as a (stratified) viscoelastic medium is crucial for short-range, low-frequency or shallow-water propagation.

## 1.3 Some Acoustic Preliminaries

### 1.3.1 Sources and Receivers

We are ultimately interested in modeling sound phenomena generated by a source and received by a hydrophone. While not concerned with the details of such devices, we briefly mention them in this section for reference and completeness.

A transducer converts some sort of energy to sound (source or projector) or converts sound to energy (receiver), usually electric [14, 15]. In underwater acoustics, piezoelectric and magnetostrictive transducers are commonly used. The piezoelectric effect is a result of the coupling between mechanical strain and electric field in certain crystals such as quartz, and certain composite materials such as lead zirconate titanate (PZT). Thus, such materials will exhibit a potential difference between the various faces of the crystal when undergoing mechanical strain, and vice versa. Note that there is also an electrostrictive effect which is common to all dielectrics but is much smaller than the piezoelectric effect: an electric field mechanically deforms the dielectric by inducing dipole moments. Magnetostriction is the change in dimensions of a ferromagnetic material when it is placed in a magnetic field and the change in magnetization when the material dimensions change due to an external force.

Some other transduction mechanisms employed are electrodynamic where, for example, sound pressure causes a coil to move through a magnetic field thereby generating an output voltage. This electromagnetic induction is the same principle used in electric generators. Electric motors and sound sources utilize the reverse effect.

Parametric or finite-amplitude sources [16–18] are sound projectors which are excited by two high-amplitude primary frequencies. The non-linearity of the medium results in the formation of sum and difference-frequency waves and their harmonics in the region in front of the projector. In practice the primary frequencies are high so that all but the difference-frequency wave is attenuated after a short distance (high-frequency attenuation is approximately proportional to frequency squared, see Sect. 1.5.2). Hence, the projector behaves like a low-frequency end-fire array with exponential shading. The main disadvantage of parametric sources is that they have low efficiency.

The parametric receiver also exists. It uses a high-frequency “pump” transmitter whose acoustic wave interacts with the signal to be detected. The output of the receiver is the sum and difference frequencies; the pump frequency is removed by a filter. The parametric receiver also behaves like an end-fire array.

Explosive and airgun sources are high-energy wideband types of sources. Actually, the technology is such that their signatures are fairly reproducible [3]. Electric discharge and laser sources are also being used.

Finally, we mention vector sensors. Recall that an acoustic wave in a fluid is a longitudinal wave. That is, the acoustical particle motion is aligned to the direction of propagation. Hence, a small transducer that measures a vector property such as velocity or acceleration will have frequency-independent directional properties as

opposed to a small pressure sensor that is omni-directional. Particle velocity, as will be shown in Chap. 2, is proportional to the pressure gradient so that pressure-gradient phones also have this directional property. In the literature, the term *vector sensor* often refers to a device that consists of two or three orthogonally aligned velocity (or other acoustic vector quantities) transducers and an omni-directional pressure transducer. Such a device has many advantages though one disadvantage is its susceptibility to flow noise (see, e.g., [19–21] and references therein). Some elementary signal processing used with vectors sensors is discussed in Chap. 10.

### 1.3.2 Energy, Power and Intensity

It takes *energy* to drive a source while acoustic propagation is often expressed in terms of transmission loss which is related to *intensity*. Here, we review some energy related properties as a prerequisite to the discussion on units and transmission loss which follow.

#### 1.3.2.1 Energy

Kinetic energy is the energy of motion of a particle with a certain mass. Since we are dealing with fluids, it is more convenient to ultimately express things in terms of the continuous variables of the system such as density. The kinetic energy of a mass  $m = \rho_0 V_0$  is then,

$$\text{KE} = \frac{1}{2}mv^2 = \frac{1}{2}\rho_0 V_0 v^2, \quad (1.6)$$

where  $v = \sqrt{v_x^2 + v_y^2 + v_z^2}$  is the magnitude of the acoustic particle velocity and the total density  $\rho$  is the sum of the ambient density  $\rho_0$  and the infinitesimal acoustic density disturbance  $\rho'$ . Note here that since a sound wave in a fluid is a longitudinal wave, the acoustic particle velocity is in the direction of propagation. For a simple harmonic oscillator, potential energy is imparted to the system by doing the work of moving the mass away from its equilibrium position. For the fluid, compression or decreasing the volume adds potential energy,

$$\text{PE} = - \int_{V_0}^V p' dV, \quad (1.7)$$

where  $p'$  is the acoustic pressure related to the total pressure  $p$  and ambient pressure  $p_0$  through the relation  $p = p_0 + p'$ . Since mass is conserved, we have, starting from the undisturbed volume  $V_0$ ,  $\rho_0 V_0 = \rho V \rightarrow dV = -\rho_0 V_0 (dp'/\rho_0^2)$ . Combining this with the linear equation of state of the fluid  $p' = \rho' c^2$ , see (2.12), we have for the volume element  $dV = -[V_0/(\rho_0 c^2)] dp'$  so that (1.7) can be rewritten as

$$\text{PE} = \int_{p'(V_0)=0}^{p'(V)} \frac{p' V_0}{\rho_0 c^2} dp' = \frac{1}{2} \frac{p'^2}{\rho_0 c^2} V_0. \quad (1.8)$$

Summing the kinetic and potential energy and dividing by  $V_0$  results in an expression for the total *instantaneous energy density*  $\mathcal{E}_i$  ( $p'$  and  $v$  are time-dependent quantities),

$$\mathcal{E}_i = \frac{1}{2}\rho_0 \left( v^2 + \frac{p'^2}{\rho_0 c^2} \right) = \rho_0 v^2 = \frac{p'^2}{\rho_0 c^2} = \frac{p'v}{c}, \quad (1.9)$$

where the last three expressions come from the *plane wave* impedance relation  $p'/v = \rho_0 c^2$ , see (2.20). If we take  $\mathcal{P}, \mathcal{V}$  as the amplitudes of the pressure and velocity, then the time-averaged (over one cycle) energy density is

$$\mathcal{E} = \frac{1}{T} \int_0^T \mathcal{E}_i dt = \frac{1}{2}\rho_0 \mathcal{V}^2 = \frac{\mathcal{P}^2}{2\rho_0 c^2} = \frac{\mathcal{P}\mathcal{V}}{2c}. \quad (1.10)$$

Finally, recall that the *rms* value of a sinusoidal process is  $1/\sqrt{2}$  of its amplitude:  $p_{\text{rms}}, v_{\text{rms}} = \mathcal{P}/\sqrt{2}, \mathcal{V}/\sqrt{2}$  so that the energy density in terms of *rms* quantities is

$$\mathcal{E} = \rho_0 v_{\text{rms}}^2 = \frac{p_{\text{rms}}^2}{\rho_0 c^2} = \frac{p_{\text{rms}} v_{\text{rms}}}{c}, \quad (1.11)$$

where we have dropped the prime notation since we are only dealing with acoustic quantities.

### 1.3.2.2 Power and Intensity

Intensity is the average rate of flow of energy through a unit area that is normal to the direction of propagation. Recall that energy rate is power. Intensity is, therefore, of the form  $c \times \mathcal{E} \times \text{area}$  where we use a unit area. Hence, from (1.11) we can expect the intensity to be of the form  $I_{\pm} = \pm p_{\text{rms}} v_{\text{rms}}$  where the  $\pm$  refers to waves traveling in either direction, i.e., intensity has a direction. Therefore, the magnitude of the intensity of a plane wave at a specified position is

$$I = \frac{\mathcal{P}\mathcal{V}}{2} = p_{\text{rms}} v_{\text{rms}} = \rho_0 c v_{\text{rms}}^2 = \frac{p_{\text{rms}}^2}{\rho_0 c}. \quad (1.12)$$

Note that there is a factor of two difference between amplitude and *rms* representations.

### 1.3.2.3 Complex Notation and Intensity

Let  $p$  and  $v$  be complex so we can, in general, write the pressure and velocity at some position as

$$p = \mathcal{P}e^{(i\omega t + \theta)}, \quad v = \mathcal{V}e^{(i\omega t + \phi)}. \quad (1.13)$$

The intensity, being a physical quantity, is the average over one period of the product of real pressure and real velocity,  $\text{Re}(p) \times \text{Re}(v)$ ,

$$\begin{aligned} I &= \langle \text{Re}\{p\} \times \text{Re}\{v\} \rangle_T \\ &= \frac{1}{T} \int_0^T \mathcal{P}\mathcal{V} \cos(\omega t + \theta) \cos(\omega t + \phi) dt \\ &= \frac{\mathcal{P}\mathcal{V}}{2} \cos(\theta - \phi) = \frac{1}{2} \text{Re}\{p^* v\}. \end{aligned} \quad (1.14)$$

### 1.3.3 Relevant Units

#### 1.3.3.1 Intensity and Decibels

The *decibel* (dB) is the dominant unit in underwater acoustics and denotes a ratio of intensities (not pressures) expressed in terms of a logarithmic (base 10) scale. Two intensities  $I_1$  and  $I_2$  have a ratio  $I_1/I_2$  in decibels of  $10 \log(I_1/I_2)$  dB. Absolute intensities can therefore be expressed by using a reference intensity. The presently accepted reference intensity is the intensity of a plane wave having a root-mean-squared (*rms*) pressure equal to  $10^{-6}$  pascals ( $\equiv \text{N/m}^2$ ) or a *micropascal* ( $\mu\text{Pa}$ ). Therefore, taking  $1 \mu\text{Pa}$  as the reference sound pressure level, a sound wave having an intensity of, say, one million times that of a plane wave of *rms* pressure  $1 \mu\text{Pa}$  has a level of  $10 \log(10^6) \equiv 60$  dB re  $1 \mu\text{Pa}$ . Pressure ( $p$ ) ratios are expressed in dB re  $1 \mu\text{Pa}$  by taking  $20 \log(p_1/p_2)$  where it is understood that the reference originates from the intensity of a plane wave of pressure equal to  $1 \mu\text{Pa}$ .

The average intensity  $I$  of a plane wave with *rms* pressure  $p$  in a medium of density  $\rho$  and sound speed  $c$  is  $I = p^2/Z$ , where  $Z = \rho c$  is called the *acoustic impedance*. In seawater,  $\rho c$  is  $1.5 \times 10^6 \text{ kg/(m}^2\text{s)}$  so that a plane wave of *rms* pressure  $1 \mu\text{Pa}$  has an intensity of  $0.67 \times 10^{-18} \text{ W/m}^2$  (i.e., 0 dB re  $1 \mu\text{Pa}$ ).

#### 1.3.3.2 Spectrum Level

The above discussion has direct application to both single frequency and continuous wave (CW) signals. However, very often we are concerned with broadband signals or noise. In this case, we must refer the acoustic intensity to a bandwidth and very often the reference bandwidth is 1 hertz (Hz). Hence, the spectrum level is expressed in units of decibels referenced to a micropascal in a 1.0 Hz band and sometimes written as dB// $\mu\text{Pa}^2/\text{Hz}$ . A source spectrum level must also have a reference distance so that an example of the unit of source spectrum level is dB// $\mu\text{Pa}^2/\text{Hz}$  @ 1 m. In the above cases, the spectral level is for a squared quantity such as intensity for which decibels are a natural unit. In the case of amplitude, we must still refer to a ratio of intensities so that the units of the corresponding spectral amplitude level would be dB// $\mu\text{Pa}/\sqrt{\text{Hz}}$ .

### 1.3.4 Transmission Loss

An acoustic signal traveling through the ocean becomes distorted due to multipath effects and weakened due to various loss mechanisms. The standard measure in underwater acoustics of the change in signal strength with range is *transmission loss* defined as the ratio in decibels between the acoustic intensity  $I(r, z)$  at a field point and the intensity  $I_0$  at 1-m distance from the source, i.e.,

$$\begin{aligned} \text{TL} &= -10 \log \frac{I(r, z)}{I_0} \\ &= -20 \log \frac{|p(r, z)|}{|p_0|} \quad (\text{dB re 1 m}). \end{aligned} \quad (1.15)$$

The last equation assumes that the acoustic impedance  $Z = \rho c$  at the field point is the same as that at the source. The intensity in a plane wave is then proportional to the square of the pressure amplitude. When plotting TL throughout the book, if the impedance of the field point is different than that at the source, for example, when the field point is in the ocean bottom, we omit the change in the impedance so as to maintain continuity of field quantities (pressure, displacement, etc.) across the bottom boundary in the plot.

Transmission loss may be considered to be the sum of a loss due to geometrical spreading and a loss due to attenuation. The spreading loss is simply a measure of the signal weakening as it propagates outward from the source. Figure 1.6 shows the two geometries of importance in underwater acoustics. First consider a point source in an unbounded homogeneous medium, Fig. 1.6a. For this simple case the power radiated by the source is equally distributed over the surface area of a sphere surrounding the source. If we assume the medium to be lossless, the intensity is inversely proportional to the surface of the sphere, i.e.,  $I \propto 1/(4\pi R^2)$ . From (1.15) we then find the *spherical spreading loss* to be given by

$$\text{TL} = 20 \log r \quad (\text{dB re 1 m}), \quad (1.16)$$

where  $r$  is the horizontal range in meters.

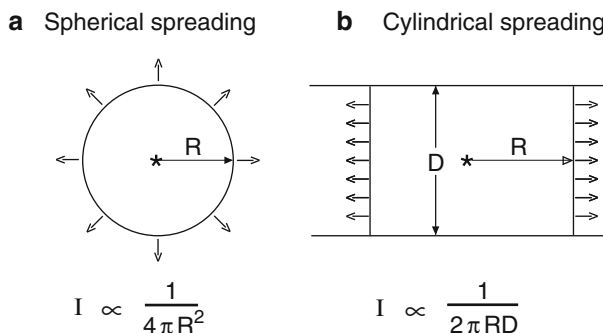


**Fig. 1.6** Geometrical spreading laws

When the medium has plane upper and lower boundaries as in the waveguide case in Fig. 1.6b, the farfield intensity change with horizontal range becomes inversely proportional to the surface of a cylinder of radius  $R$  and depth  $D$ , i.e.,  $I \propto 1/(2\pi RD)$ . The *cylindrical spreading loss* is therefore given by

$$\text{TL} = 10 \log r \quad (\text{dB re } 1 \text{ m}). \quad (1.17)$$

Note that for a point source in a waveguide, we have spherical spreading in the nearfield ( $r \leq D$ ) followed by a transition region toward cylindrical spreading which applies only at longer ranges ( $r \gg D$ ).

As an example consider propagation in a waveguide to a range of 100 km with spherical spreading applying on the first kilometer. The total propagation loss (neglecting attenuation) then becomes:  $60 \text{ dB} + 20 \text{ dB} = 80 \text{ dB}$ . This figure represents the minimum loss to be expected at 100 km. In practice, the total loss will be higher due both to the attenuation of sound in seawater, and to various reflection and scattering losses.

A quantitative understanding of acoustic loss mechanisms in the ocean is required for the modeling of sound propagation. These losses will be treated in detail in the subsequent sections. The most important loss mechanisms are volume attenuation (Sect. 1.5), bottom reflection loss (Sect. 1.6), and boundary and volume scattering loss (Sect. 1.7).

## 1.4 Sound Propagation in the Ocean

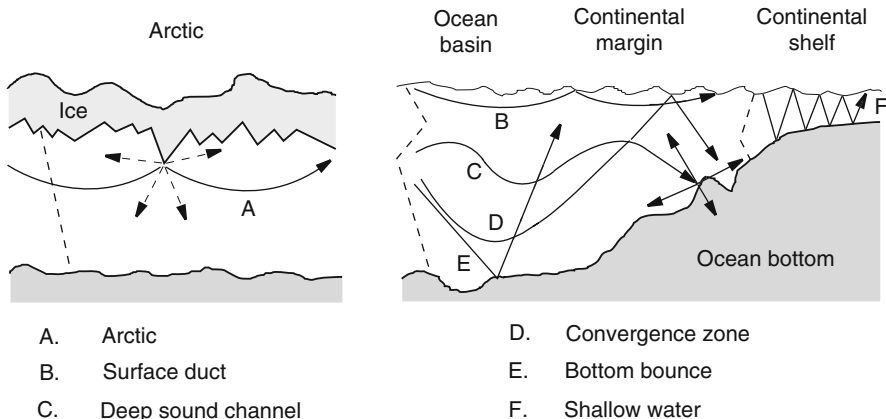
### 1.4.1 Characteristic Propagation Paths

Figure 1.7 is a schematic of the basic types of propagation in the ocean resulting from the sound-speed profiles (indicated by the dashed lines) discussed in Sect. 1.2. These sound paths can be understood from *Snell's law*,

$$\frac{\cos \theta}{c} = \text{const}, \quad (1.18)$$

which relates the ray angle, with respect to the horizontal, to the local sound speed. It is not difficult to see that the implication of this law is that sound bends locally toward regions of low sound speed (or sound is “trapped” in regions of low sound speed).

Simplest to explain are the paths about local sound speed minima: A, B, and C. Paths A and B correspond to surface duct propagation where the minimum sound speed is at the ocean surface (or beneath the ice cover for the Arctic case). Path C, depicted by a ray leaving a deeper source at a shallow horizontal angle, propagates in the *deep sound channel* whose axis is at the shown sound speed minimum. As shown in Fig. 1.2, this local minimum tends to become more shallow toward



**Fig. 1.7** Schematic representation of various types of sound-propagation paths in the ocean

polar latitudes converging to the Arctic surface minimum, path A. Hence, for mid-latitudes, sound in the deep channel can propagate long distances without interacting with lossy boundaries; low-frequency propagation via this path has been observed to distances of thousands of kilometers. Also, from the above description of the geographical variation of the acoustic environment combined with Snell's law, we can expect that shallow sources coupling into the water column at polar latitudes will tend to propagate more horizontally around an axis which becomes deeper toward the mid latitudes. Path D, which is at slightly steeper angles than those associated with path C, is *convergence zone* propagation, a spatially periodic ( $\sim 35\text{--}70\text{ km}$ ) refocusing phenomenon producing zones of high intensity near the surface because of the upward refracting nature of the deep sound-speed profile.

Referring back to Fig. 1.1, there may be a depth in the deep isothermal layer at which the sound speed is the same as it is at the surface. This depth is called the *critical depth* and, in effect, is the lower limit of the deep sound channel. A receiver below this depth will only receive sound from distant shallow sources via surface-interacting paths. A *positive* critical depth or *depth excess* specifies that the environment supports long-distance propagation without bottom interaction, whereas *negative* critical depth implies that the seafloor is the lower boundary of the deep sound channel. The bottom bounce path E is also a periodic phenomenon but with a shorter cycle distance and a shorter total propagation distance because of losses when sound is reflected from the ocean bottom. Finally, the right-hand-side of Fig. 1.7 depicts propagation in a shallow water region such as a continental shelf. Here, sound is channeled in a waveguide bounded above by the ocean surface and below by the ocean bottom. Because of the latter, negative critical depth environments exhibit much of the sound propagation physics descriptive of shallow-water environments.

There exists an alternative classification of ray paths in the ocean which is briefly introduced. This classification distinguishes between four types of rays: (1) rays

propagating via refracted path only and called *refracted refracted* (RR) rays (path C); (2) rays bouncing off the sea surface and called *refracted surface-reflected* (RSR) rays (paths A, B, and D); (3) rays bouncing off the seafloor and called *refracted bottom-reflected* (RBR) rays; and (4) rays reflected off both the sea surface and the seafloor and called *surface-reflected bottom-reflected* (SRBR) rays (path F). Clearly, the SRBR paths are the most lossy since they are subject to all of the loss mechanisms present in the ocean waveguide. On the other hand, the RR paths are only affected by attenuation and scattering within the water column (no boundary losses).

The modeling of sound propagation in the ocean is complicated because the environment varies laterally—is *range dependent*—and all environmental effects on sound propagation are dependent on acoustic frequency in a rather complicated way. As a result the ray-type schematic of Fig. 1.7 is misleading, particularly at low frequencies. We shall elaborate on the characteristic features of propagation in the ocean for selected environmental situations in both deep and shallow water, including two examples of propagation through range-varying environments.

## 1.4.2 Deep Water

The principal characteristic of deep-water propagation is the existence of an upward-refracting sound-speed profile which permits long-range propagation without significant bottom interaction. Hence, the important ray paths are either *refracted refracted* or *refracted surface-reflected*. Typical deep-water environments are found in all oceans at depths exceeding 2000 m.

### 1.4.2.1 Nearfield Lloyd-Mirror Pattern

We start the presentation of characteristic field patterns in deep water by considering the acoustic interference pattern created by a point source placed near a smooth, perfectly reflecting sea surface. The geometry is shown in Fig. 1.8 with S indicating

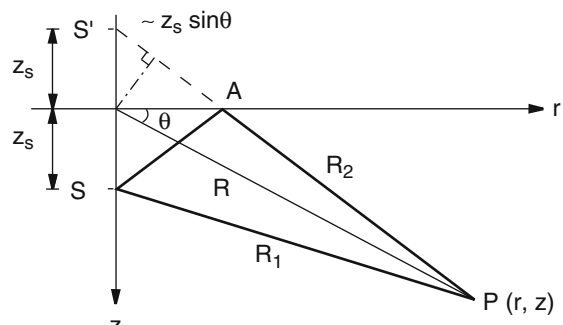


**Fig. 1.8** Geometry for surface image solution

the source position at a depth  $z_s$  below the sea surface ( $z = 0$ ). For any field point  $P(r, z)$ , there exist only two possible energy paths connecting source and receiver: the direct path SP and the surface-reflected path SAP. Assuming specular reflection at the sea surface, the reflected path appears to originate from the image source  $S'$ . Hence, the total field at  $P(r, z)$  can be written simply as the sum of two point-source contributions,

$$p(r, z) = \frac{e^{ikR_1}}{R_1} - \frac{e^{ikR_2}}{R_2}, \quad (1.19)$$

where  $k = 2\pi/\lambda$  is the acoustic wavenumber and

$$R_1 = \sqrt{r^2 + (z - z_s)^2}, \quad R_2 = \sqrt{r^2 + (z + z_s)^2}. \quad (1.20)$$

We have here suppressed the time dependence  $\exp(-i\omega t)$ . The minus sign in (1.19) is required to satisfy the pressure-release boundary condition ( $p = 0$ ) at the sea surface. Note that the source levels are normalized to give unit amplitude at 1-m distance from the source.

Equation (1.19) represents a quite complex interference pattern, for which we can derive a simplified expression by assuming the distance  $R$  from the origin to be much greater than the source depth  $z_s$ . Denoting the declination angle by  $\theta$ , we find that for  $R \gg z_s$ , the distances  $R_1$  and  $R_2$  can be approximated by

$$R_1 \simeq R - z_s \sin \theta, \quad (1.21)$$

$$R_2 \simeq R + z_s \sin \theta. \quad (1.22)$$

Assuming further that the ranges appearing in the denominators of both terms in (1.19) can be replaced simply by the slant range  $R$  (the amplitudes decay slowly with range), we obtain

$$\begin{aligned} p(r, z) &\simeq \frac{1}{R} \left[ e^{ik(R - z_s \sin \theta)} - e^{ik(R + z_s \sin \theta)} \right] \\ &= \frac{e^{ikR}}{R} \left[ e^{-ikz_s \sin \theta} - e^{ikz_s \sin \theta} \right]. \end{aligned} \quad (1.23)$$

We next replace the two exponentials by a trigonometric function to obtain

$$p(r, z) = -\frac{2i}{R} \sin(kz_s \sin \theta) e^{ikR}, \quad (1.24)$$

which means that the amplitude variation takes the simple form

$$|p| = \frac{2}{R} |\sin(kz_s \sin \theta)|. \quad (1.25)$$

For a point source in free space we would have a spherically expanding wave with  $|p| = 1/R$ . The reflecting sea surface is seen to generate a directional pattern with pressure maxima and minima given by

$$|p|_{\max} = \frac{2}{R} \quad \text{for} \quad \sin \theta = (2m - 1) \frac{\pi}{2kz_s}, \quad m = 1, 2, \dots \quad (1.26)$$

$$|p|_{\min} = 0 \quad \text{for} \quad \sin \theta = (m - 1) \frac{\pi}{kz_s}, \quad m = 1, 2, \dots \quad (1.27)$$

This is the classical surface-image or *Lloyd-mirror* interference pattern. Note that the pressure maximum is twice that of a single source (constructive interference) whereas the pressure minimum is zero (destructive interference). The number of Lloyd-mirror beams  $M$  is finite and can be determined from (1.26) to satisfy

$$(2M - 1) \frac{\pi}{2kz_s} \leq 1 \quad (1.28)$$

or

$$M = \text{int} \left\{ \frac{2z_s}{\lambda} + 0.5 \right\}, \quad (1.29)$$

where  $\lambda$  is the acoustic wavelength. Hence, the number of beams is directly proportional to the distance of the source from the surface in terms of wavelengths.

In underwater acoustics, the dependence of sound pressure on distance at a fixed depth  $z_r$  is of great importance. Introducing  $\sin \theta = z_r/R$  in (1.25) yields

$$|p| = \frac{2}{\sqrt{r^2 + z_r^2}} \left| \sin \frac{kz_s z_r}{\sqrt{r^2 + z_r^2}} \right|, \quad (1.30)$$

which again is an expression showing intermittent maxima and minima of the pressure amplitude with range. However, at large ranges ( $r \gg z_r$ ,  $\sin \theta \simeq \theta$ ) the above expression simplifies to

$$|p| \simeq \frac{2kz_s z_r}{r^2} \quad (1.31)$$

showing that the field decay eventually becomes monotonic. A pressure amplitude decay proportional to  $r^{-2}$  is equivalent to a transmission loss of

$$\text{TL} = 40 \log r, \quad (1.32)$$

which is seen to be twice the loss associated with spherical spreading. Note, however, that the strong field decay given by (1.32) is entirely an interference effect.

Let us consider a numerical example where a 150-Hz source is placed 25 m below the sea surface in a homogeneous water column of infinite extent and with a sound speed of 1500 m/s. Since the acoustic wavelength is 10 m, we find the number of Lloyd-mirror beams from (1.29) to be  $M = 5$ . The transmission loss versus range

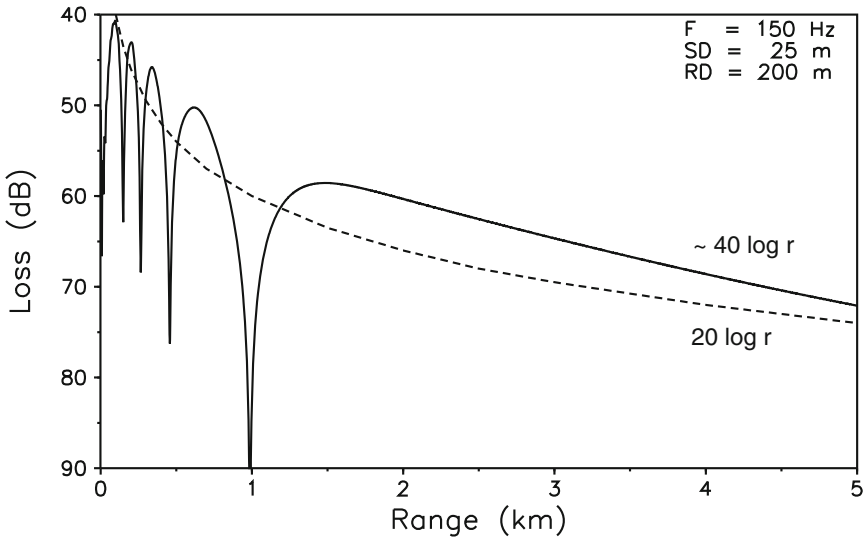


**Fig. 1.9** Nearfield surface-interference (Lloyd mirror) solution for point source in a homogeneous halfspace

for a 200-m deep receiver is shown in Fig. 1.9 as computed from the exact field solution given by (1.19). Note the oscillating field structure with five peaks and a farfield decay proportional to  $40 \log r$ .

The Lloyd-mirror interference pattern is a characteristic feature of deep-water propagation which shall be repeatedly referred to in this book. Moreover, the exact field solution for a homogeneous medium can be readily evaluated, making the image solution well-suited as a benchmark result for checking numerically implemented wave equation solutions.

#### 1.4.2.2 Convergence-Zone Propagation

The acoustic field pattern shown in Fig. 1.10 is definitely one of the most interesting features of propagation in the deep ocean. This pattern is referred to as *convergence zone* (CZ) propagation because the sound emitted from a near-surface source forms a downward-directed beam which, after following a deep refracted path in the ocean, reappears near the surface to create a zone of high sound intensity (convergence or focusing) at a distance of tens of kilometers from the source. The phenomenon is repetitive in range, with the distance between the high-intensity regions called the convergence-zone range.

The importance of convergence-zone (CZ) propagation stems from the fact that it allows for long-range transmission of acoustic signals of high intensity and low distortion. The first reference to CZ propagation in the open literature goes back to the early 1960s, when Hale [22] reported experimental data covering a range of almost

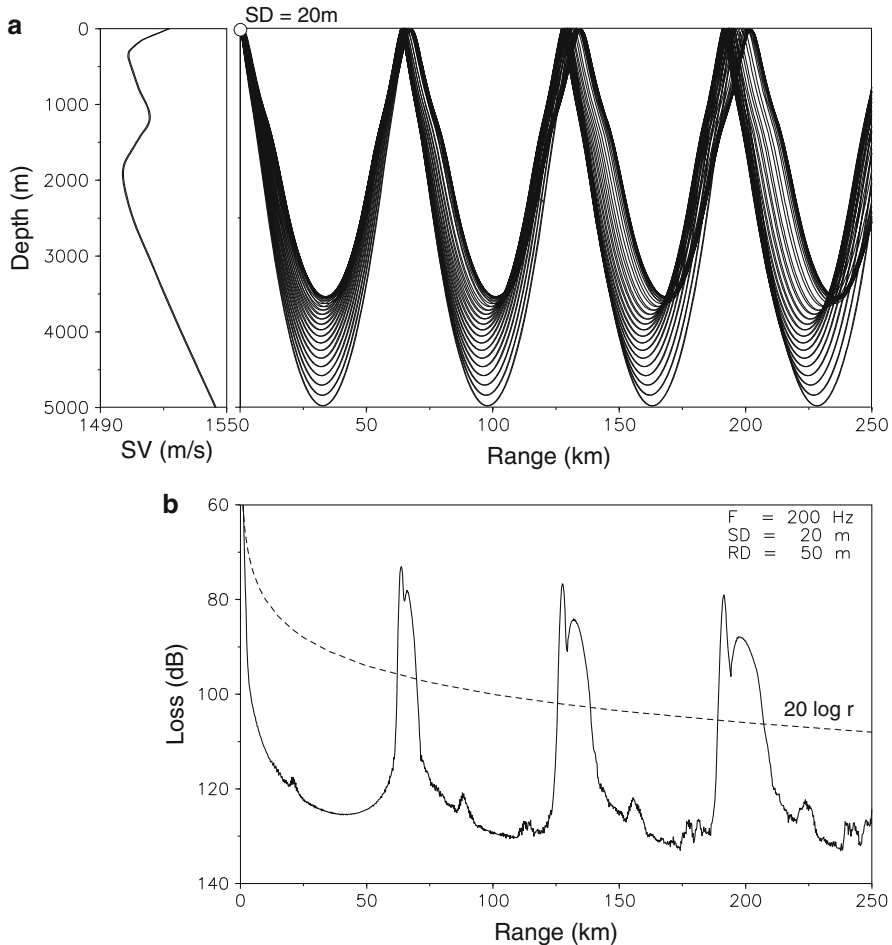


**Fig. 1.10** Convergence-zone propagation in the eastern North Atlantic. **(a)** Typical double-duct profile and associated ray diagram ( $|\theta_s| \leq 10^\circ$ ) showing that the deep-cycling paths refocus near the surface every 65 km. **(b)** Computed transmission loss at a frequency of 200 Hz

750 km and clearly showing 13 distinct convergence zones spaced approximately 55 km apart. Hale also addressed in some detail the environmental conditions for the existence of convergence zones and attempted a theoretical description of the convergence-zone structure using ray theory.

To illustrate some of the characteristics of CZ propagation, we turn to the example given in Fig. 1.10. The upper graph shows a typical double-duct profile from the eastern North Atlantic resulting from the mixing of resident Atlantic water with Mediterranean outflow through the Strait of Gibraltar. For a source at 20-m depth, we have traced the convergence-zone rays which emanate from the source within an aperture of  $\pm 10^\circ$  (steeper rays are reflected at the bottom). A necessary condition

for the existence of deep refracted paths in the ocean is that the sound speed near the bottom exceeds that at the source. This condition is easily verified from Snell's law, (1.18), which relates ray angles to local sound speeds. Thus, the launch angle for a ray grazing the bottom is given by  $\cos \theta_0 = c_0/c_b$ , where  $c_0$  is the sound speed at the source and  $c_b$  is the sound speed at the bottom of the ocean. Clearly, this ray only exists for  $c_b \geq c_0$ . The requirement of "depth excess" in the profile means that CZ propagation for shallow sources is possible only for water depth exceeding about 3500 m in the Atlantic and 2000 m in the Mediterranean.

Two additional conditions must be fulfilled to obtain a sharp, undisturbed convergence zone structure as shown in Fig. 1.10. First, the source must be near the surface so that the up and downgoing rays generate a well-collimated beam in the downward direction. Second, to avoid ducting near the surface (mixed modes of propagation) the source must be in a region of decreasing sound speed with depth. With these conditions fulfilled, we obtain the typical North Atlantic convergence-zone structure shown in Fig. 1.10b. The transmission-loss curve is a wave-theory solution (normal modes) for a frequency of 200 Hz and a receiver depth of 50 m. While ray theory predicts zero energy between the convergence zones, the wave solution indicates a finite sound level due to diffraction. In practical ocean experiments, these low-level regions will also be insonified by bottom-bounce energy.

The convergence zones in the North Atlantic are seen to be spaced approximately 65 km apart with a *convergence gain* of around 20 dB relative to spherical spreading [3]. Note also that the convergence-zone width increases with zone number; the second zone (near 130 km) is wider than the first, and so on, until eventually at several hundred kilometers the zones overlap and become indistinguishable.

The most important parameter for sonar applications is the convergence zone range, which is known to vary considerably with geographical location. Thus, the CZ spacing in the Mediterranean is only 35–40 km whereas it is 60–70 km in the Atlantic. It is convenient to be able to calculate the convergence-zone spacing from a simple formula without having to resort to a complete acoustic model. To this end we introduce a linearized version of the real sound-speed profile (Fig. 1.11), with the sound speeds at the layer interfaces denoted  $c_i$  and the sound-speed gradients denoted  $g_i$ . For simplicity, we take the source to be at the sea surface, which means that the CZ rays are limited by the  $0^\circ$ -ray and the ray grazing the bottom,  $\theta_c = \arccos(c_0/c_4)$ . Furthermore, we take the loop length of the  $0^\circ$ -ray as a measure of the convergence-zone spacing.

Knowing that the ray paths within linear profile segments are circular arcs, it is not difficult to show that the loop length ( $0^\circ$ -ray) for a simple bilinear profile is given by [23]

$$R_{CZ} = 2c_0 \sin \theta_1 \left( \frac{1}{|g_1|} + \frac{1}{|g_2|} \right), \quad (1.33)$$

where  $\theta_1 = \arccos(c_1/c_0)$  is the ray angle at the layer interface. This formula provides an accurate estimate of the convergence-zone range for single-duct profiles that can be approximated by two constant-gradient layers.

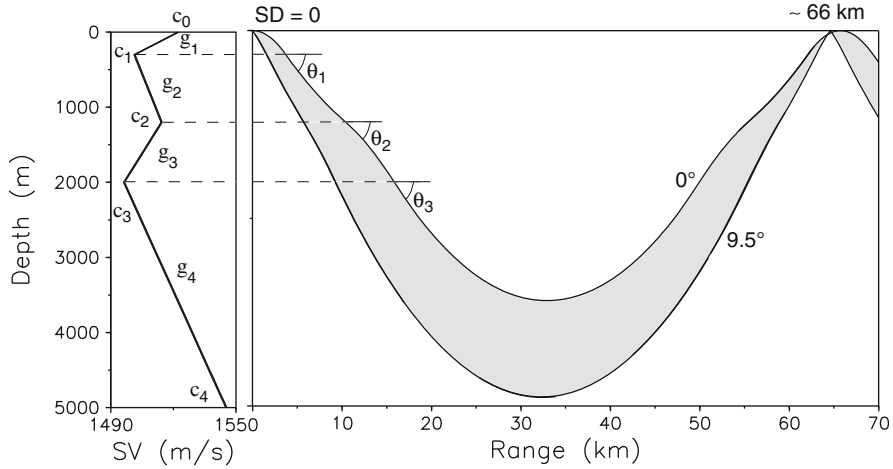


**Fig. 1.11** Convergence-zone paths for linearized version of the sound-speed profile given in Fig. 1.10. The calculated loop length of the  $0^\circ$ -ray emanating from a source at the surface is used for estimating the convergence-zone distance in the real North Atlantic environment

**Table 1.1** North Atlantic profile

Depth (m)	Sound speed (m/s)	Gradient (m/s/m)	$\sin \theta_i$
0	1522.0	–	–
300	1501.0	–0.0700	0.1655
1200	1514.0	0.0144	0.1024
2000	1496.0	–0.0225	0.1840
5000	1545.0	0.0163	–

In the case of the North Atlantic profile, we need to generalize the above formula to a four-layer system. Following the approach outlined by Tolstoy and Clay [23] we find

$$R_{CZ} = 2c_0 \left( \frac{\sin \theta_1}{|g_1|} + \frac{\sin \theta_1 - \sin \theta_2}{|g_2|} + \frac{\sin \theta_3 - \sin \theta_2}{|g_3|} + \frac{\sin \theta_3}{|g_4|} \right), \quad (1.34)$$

where the ray angles at the layer interfaces are given by

$$\theta_i = \arccos \left( \frac{c_i}{c_0} \right). \quad (1.35)$$

As an example let us consider the linearized North Atlantic profile given in Table 1.1. By inserting these values into (1.34) we find  $R_{CZ} = 65.9$  km, which is very close to the actual convergence-zone range of 65 km estimated from the transmission-loss result shown in Fig. 1.10b. For a typical Mediterranean summer

**Table 1.2** Mediterranean profile

Depth (m)	Sound speed (m/s)	Gradient (m/s/m)	$\sin \theta_i$
0	1540.0	–	–
100	1510.0	–0.3000	0.1964
2500	1550.0	0.0167	–

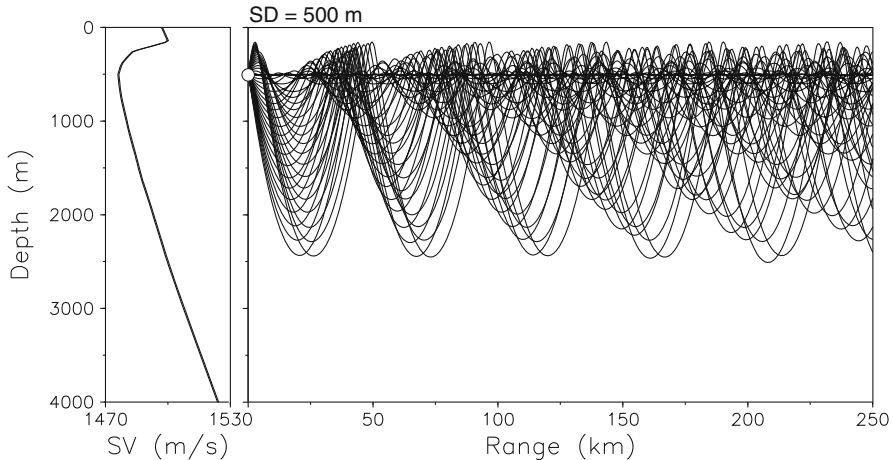


**Fig. 1.12** Deep-sound-channel propagation in the Norwegian Sea. For a source at the channel axis (500 m), the ray diagram shows that sound leaving the source within a  $\pm 10^\circ$  aperture propagates to long ranges without boundary interaction

profile with a sound channel axis at just 100-m depth (Table 1.2), we find the convergence-zone range from (1.33) to be 38.2 km, which is within 2 km of the range estimated from a full transmission-loss plot.

#### 1.4.2.3 Deep-Sound-Channel Propagation

Propagation in the deep sound channel, also referred to as the SOFAR channel, was originally investigated by Ewing and Worzel [24] during World War II. This internal sound channel allows for sound transmission entirely via refracted paths (Fig. 1.12), which means that a portion of the acoustic power radiated by a source in the channel propagates to long ranges without encountering reflection losses at the sea surface or the seafloor. Because of the low transmission loss, acoustic signals from small explosive charges in the deep sound channel have been recorded over distances of thousands of kilometers—in some cases even half way around the world.

The deep sound channel is not equally effective as a waveguide at all latitudes. As shown in Sect. 1.2, the sound-channel axis (minimum sound speed) varies in depth from around 1000 m at mid-latitudes to the ocean surface in polar regions.

A necessary condition for the existence of low-loss refracted paths is that the sound-speed axis is below the sea surface, since otherwise propagation becomes entirely surface-interacting and lossy (as in Arctic propagation). Moreover, the portion of the source power trapped in the waveguide is directly proportional to the aperture of ray angles propagating as internally refracted rays. For a source on the axis (Fig. 1.12) this aperture is straightforwardly determined from Snell's law as  $\theta_{\max} = \arccos(c_0/c_{\max})$ , where  $c_0$  is the sound speed at the channel axis (minimum speed) and  $c_{\max}$  is the maximum speed encountered between the channel axis and the sea surface (normally at the bottom of the mixed layer). For the Norwegian Sea profile shown in Fig. 1.12, the maximum source aperture is  $\pm 10^\circ$  (steeper rays will be surface-interacting). Generally, this source aperture is largest ( $\pm 15^\circ$ ) at mid-latitudes decreasing toward the poles. Consequently, the deep sound channel is most effective as a waveguide at mid to moderately high latitudes, where also the major part of the long-range transmission experiments have been performed [25].

#### 1.4.2.4 Surface-Duct Propagation

In temperate, windy regions of the world's oceans, the temperature profile regularly shows an isothermal layer just beneath the sea surface. This layer of isothermal water is maintained by turbulent wind mixing, extending deeper after a heavy storm, and becoming more shallow again during a period of light winds. There is also a seasonal dependence of the mixed-layer depth. Thus, the mean depth in the North Atlantic between  $40^\circ\text{N}$  and  $50^\circ\text{N}$  is smaller in summer ( $\sim 25\text{ m}$ ) than in winter ( $\sim 75\text{ m}$ ) [25]. Farther north, mixed-layer depths of 200–300 m are consistently observed in the winter period between December and April.

Acoustically, the isothermal mixed layer acts as a waveguide because of the slight increase in sound speed with depth ( $0.016\text{ m/s/m}$ ) caused by hydrostatic pressure. The result is that a portion of the acoustic energy emitted by a source placed in the mixed layer will be trapped in the surface duct. An illustrative example is given in Fig. 1.13, which displays the upper 500 m of the Norwegian Sea profile used previously (Fig. 1.12). The surface duct is 150 m deep with an increase in sound speed across the duct of just 3 m/s. For a source depth of 40 m, the ray diagram shows that energy emitted within a cone of  $\pm 3^\circ$  is trapped in the duct, whereas steeper rays leave the duct and propagate via deep refracted paths. The result is that a *shadow zone* is formed, limited above by the lower boundary of the surface duct ( $z = 150\text{ m}$ ) and to the left by the ray leaving the source at an angle slightly steeper than the critical angle (can be determined from Snell's law) for trapping within the duct. Of course, the shadow is not complete; insonification occurs due to wave effects such as diffraction and channel diffusion. Moreover, in real experimental situations the shadow zone is also insonified by sound scattered at the sea surface as well as by bottom-reflected energy.

Returning to the energy trapped in the surface duct (Fig. 1.13), we see that all paths interact with the sea surface and hence are subject to surface scattering loss.

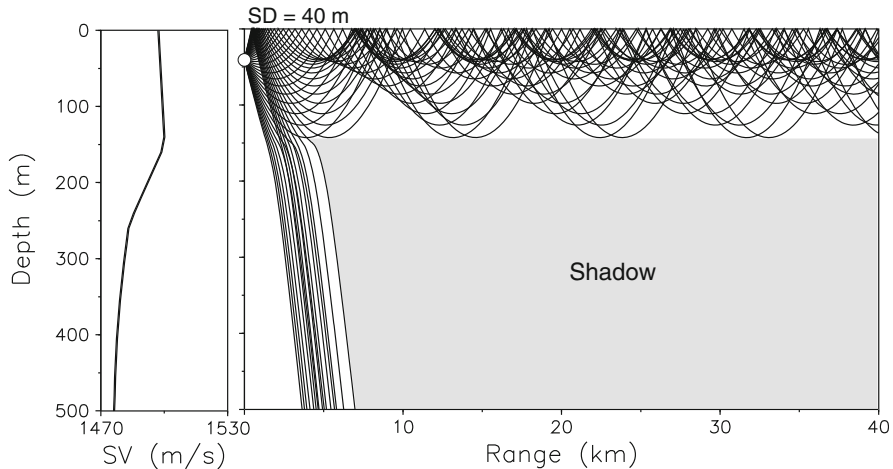


**Fig. 1.13** Surface-duct propagation in the Norwegian Sea. For a source at 40-m depth the ray diagram shows that only sound leaving the source within a  $\pm 3^\circ$  vertical aperture is trapped in the 150-m deep surface duct, repeatedly interacting with the sea surface. Steeper rays propagate via deep refracted or bottom-bounce paths

In general, the surface duct is an excellent waveguide in calm seas whereas the propagation conditions quickly deteriorate with increasing sea state. It is also clear that the surface duct is not a very stable feature since a heating of the upper layers by just  $1^\circ\text{C}$  increases the sound speed by  $\sim 3 \text{ m/s}$ , see (1.1), thus transforming the duct into a non-guiding isospeed surface layer.

Finally, it should be pointed out that the ray picture in Fig. 1.13 is entirely misleading at low frequencies. In fact, the surface duct ceases to trap energy when the acoustic wavelength becomes too large. This wave-theory cutoff phenomenon, common to all types of ducted propagation, shall be dealt with in detail in Chaps. 2 and 5 when discussing propagation in terms of normal modes. Here it suffices to give an approximate formula for the cutoff frequency below which no energy can propagate in the surface duct. For an isothermal surface layer of depth  $D$  in meters, the *cutoff frequency* in hertz is given by [3]

$$f_0 \simeq \frac{1500}{0.008 D^{3/2}}. \quad (1.36)$$

In our case of a 150-m deep surface duct, the cutoff frequency is around 100 Hz. Similarly, we find that a 50-m mixed layer acts as a sound channel only for frequencies above 530 Hz. In general, shallow ducts ( $D < 50 \text{ m}$ ) are most common, but they are effective waveguides only at higher frequencies where scattering losses become significant. The deeper ducts ( $D > 100 \text{ m}$ ), on the other hand, are effective waveguides down to much lower frequencies, but they occur less frequently.

### 1.4.2.5 Arctic Propagation

Propagation in the Arctic Ocean (Fig. 1.14) is characterized by an upward refracting profile over the entire water depth causing energy to undergo repeated reflections at the underside of the ice. The sound-speed profile can often be approximated by two linear segments with a steep gradient in the upper 200 m creating a strong surface duct followed by a standard hydrostatic pressure gradient ( $0.016 \text{ m/s/m}$ ) below. The steep gradient in the upper layer is caused both by the increase in temperature and in salinity with depth. The low salinity near the ice cover is due to freshwater contributions from melting.

The ray diagram in Fig. 1.14 shows that energy is partly channeled beneath the ice cover within the 200-m deep surface duct and partly follows deeper refracted paths. However, all rays within a cone of  $\pm 17^\circ$  propagate to long ranges without bottom interaction. The primary loss mechanism is clearly associated with surface scattering loss, and Arctic propagation is known to degrade rapidly with increasing frequency above 30 Hz. There is, however, also experimental evidence for propagation being poor at frequencies below 10 Hz. Hence, there seems to be a narrow band of frequencies, 10–30 Hz, for which we have optimum propagation in the Arctic environment [3].

While the high-frequency loss is easily explained in terms of scattering from the rough underside of the ice, the low-frequency loss is due to a completely different mechanism. In fact, at low frequencies, sound is not trapped effectively in the Arctic sound channel, with the result that bottom loss becomes significant. We can provide a simple estimate of the optimum frequency of propagation by recalling that the radiation pattern from a point source near a boundary is a series of Lloyd-mirror beams,

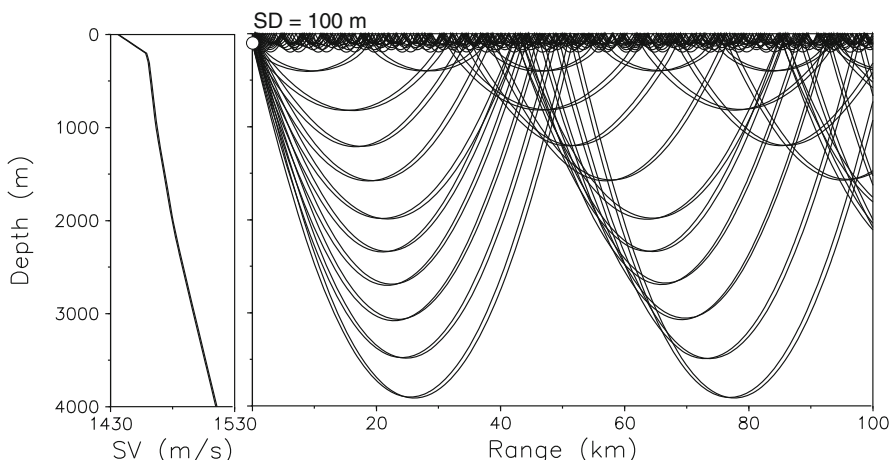


**Fig. 1.14** Arctic propagation for a 100-m deep source. The ray diagram shows that sound leaving the source within a  $\pm 17^\circ$  aperture interacts only with the sea surface. In case of ice cover, these propagation paths will all be subject to scattering loss at the rough underside of the ice

which, at higher frequencies, are refracted within the water column. However, at lower frequencies, these source beams become steeper and eventually bottom interacting. Assuming that the *optimum frequency* coincides with the situation where the lowermost Lloyd-mirror beam just grazes the seafloor, we find from (1.26) that

$$f_{\text{opt}} = \frac{c_0}{4z_s \sin \theta_c}, \quad (1.37)$$

where  $c_0$  is the sound speed at the source,  $z_s$  the source depth,  $\theta_c$  the critical grazing angle given by  $\theta_c = \arccos(c_0/c_{\max})$ , with  $c_{\max}$  being the sound speed at the seafloor.

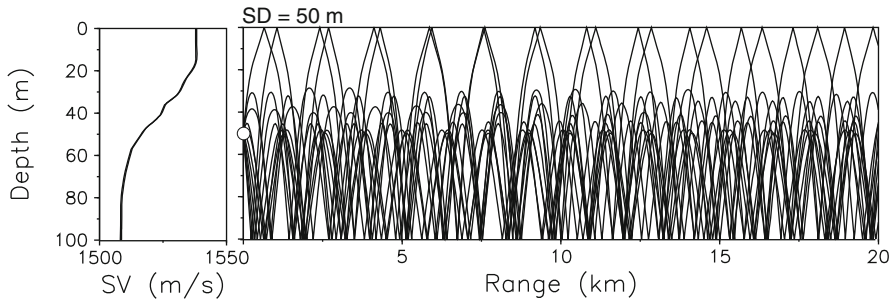
With this definition of the optimum frequency all energy paths for  $f < f_{\text{opt}}$  are bottom interacting and hence lossy. On the other hand, for  $f > f_{\text{opt}}$  the lowermost Lloyd-mirror beam just grazes the bottom, and, consequently, one low-loss refracted path exists. For the situation shown in Fig. 1.14 we find  $f_{\text{opt}} = 12$  Hz. Equation (1.37) shows that the optimum frequency is primarily dependent on the source depth and the water depth (through  $\theta_c$ ). Thus, a shallower source or smaller water depth both result in a higher optimum frequency.

### 1.4.3 Shallow Water

The principal characteristic of shallow-water propagation is that the sound-speed profile is downward refracting or nearly constant over depth, meaning that long-range propagation takes place exclusively via bottom-interacting paths. Hence the important ray paths are either *refracted bottom-reflected* or *surface-reflected bottom-reflected*. Typical shallow-water environments are found on the continental shelf for water depths down to 200 m.

The acoustics of shallow water has been thoroughly investigated both theoretically and experimentally. Yet, the accumulation of theory and measurements has failed to give us the quantitative understanding required for accurate prediction of long-range propagation in shallow water. The reason is the complexity of the problem. In shallow water, the surface, volume, and bottom properties are all important, are spatially varying – the oceanographic parameters are also temporally varying – and the parameters are generally not known in sufficient detail and with enough accuracy to permit long-range predictions in a satisfactory way.

A ray picture of propagation in a 100-m deep shallow water duct is shown in Fig. 1.15. The sound-speed profile is typical of the Mediterranean in the summer. There is a warm surface layer causing downward refraction and hence repeated bottom interaction for all ray paths. Since the seafloor is a lossy boundary, propagation in shallow water is dominated by bottom reflection loss at low and intermediate frequencies (<1 kHz) and scattering losses at high frequencies. The seasonal variation in sound-speed structure is significant with winter conditions being nearly isospeed. The result is that there is less bottom interaction in winter than in summer, which again means that propagation conditions are generally better in winter than in summer.



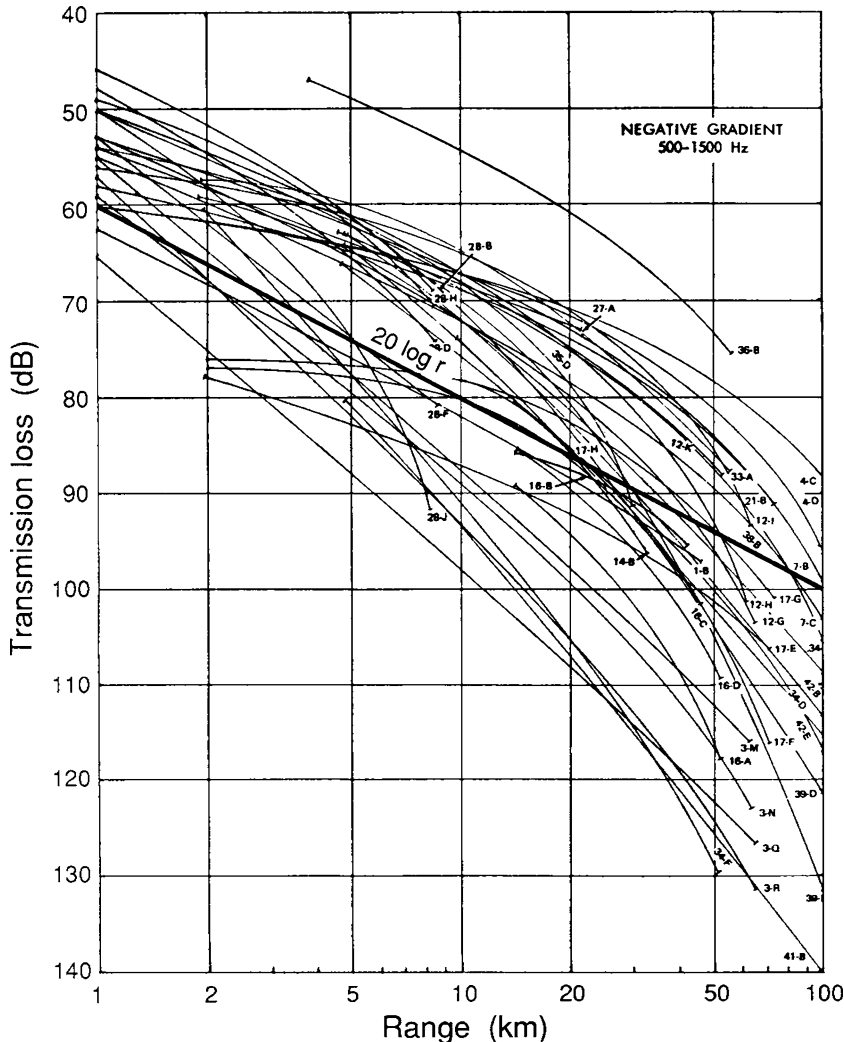
**Fig. 1.15** Shallow-water propagation in the Mediterranean in summer. For a source at mid-depth (50 m), the ray diagram shows that all propagation paths interact with the seafloor. Hence, long-range propagation is here dominated by bottom loss

Figure 1.16 gives an example of transmission-loss variability in shallow water [25]. The graph displays a collection of experimental data from different shallow-water areas (100–200 m deep) all over the world. The data refer to downward-refracting summer conditions in the frequency band 0.5–1.5 kHz. Two features are of immediate interest. One is the spread of the data amounting to around 50 dB at 100 km and caused primarily by the varying bottom-loss conditions in different areas of the world. The second feature is the fact that transmission is generally better than free-field propagation ( $20 \log r$ ) at short and intermediate ranges but worse at longer ranges. This peculiarity is due to the trapping of energy in the shallow-water duct, which improves transmission at shorter ranges (cylindrical versus spherical spreading), but, at the same time, causes increased boundary interaction, which degrades transmission at longer ranges.

A second example of transmission-loss variability in shallow-water is given in Fig. 1.17, where broadband data from two different geographical areas are compared. The upper data set, Fig. 1.17a, was collected in the Barents Sea in 60 m water depth. Note the high transmission losses recorded below 200 Hz, where energy levels fall off rapidly indicating that most of the acoustic energy emitted by the source is lost to the seabed. Jensen [26] showed that this excess attenuation is probably caused by the coupling of acoustic energy into shear waves in the seabed. In contrast to the high-loss environment in the Barents Sea, we show in Fig. 1.17b a data set from the English Channel in 90 m water depth. Here, propagation conditions are excellent over the entire frequency band. This second data set represents typical propagation conditions for thick sandy sediments with negligible shear-wave effects.

A common feature of all acoustic ducts is the existence of a low-frequency cutoff. Hence, there is a critical frequency below which the shallow-water channel ceases to act as a waveguide, causing energy radiated by the source to propagate directly into the bottom. This cutoff phenomenon shall be dealt with in detail in Chaps. 2 and 5, but we here provide a formula from which the *cutoff frequency* can be calculated,

$$f_0 = \frac{c_w}{4D \sqrt{1 - (c_w/c_b)^2}}. \quad (1.38)$$



**Fig. 1.16** Transmission-loss variability in shallow water (from Urick [25])

This expression is exact only for a homogeneous water column of depth  $D$  and sound speed  $c_w$  overlying a homogeneous bottom of sound speed  $c_b$ . Note that for a rigid bottom ( $c_b \rightarrow \infty$ ) the cutoff occurs when  $D = \lambda/4$ , where  $\lambda$  is the acoustic wavelength. For physically realistic bottom speeds, the cutoff frequency is somewhat higher than for the rigid bottom. As an example, let us take  $D = 100\text{ m}$ ,  $c_w = 1500\text{ m/s}$ , and  $c_b = 1600\text{ m/s}$  (sand–silt), which yields  $f_0 \simeq 11\text{ Hz}$  versus  $3.75\text{ Hz}$  for a rigid bottom.

Sound transmission in shallow water has the characteristic frequency dependent behavior shown in Fig. 1.17, i.e., there is an optimum frequency of propagation at

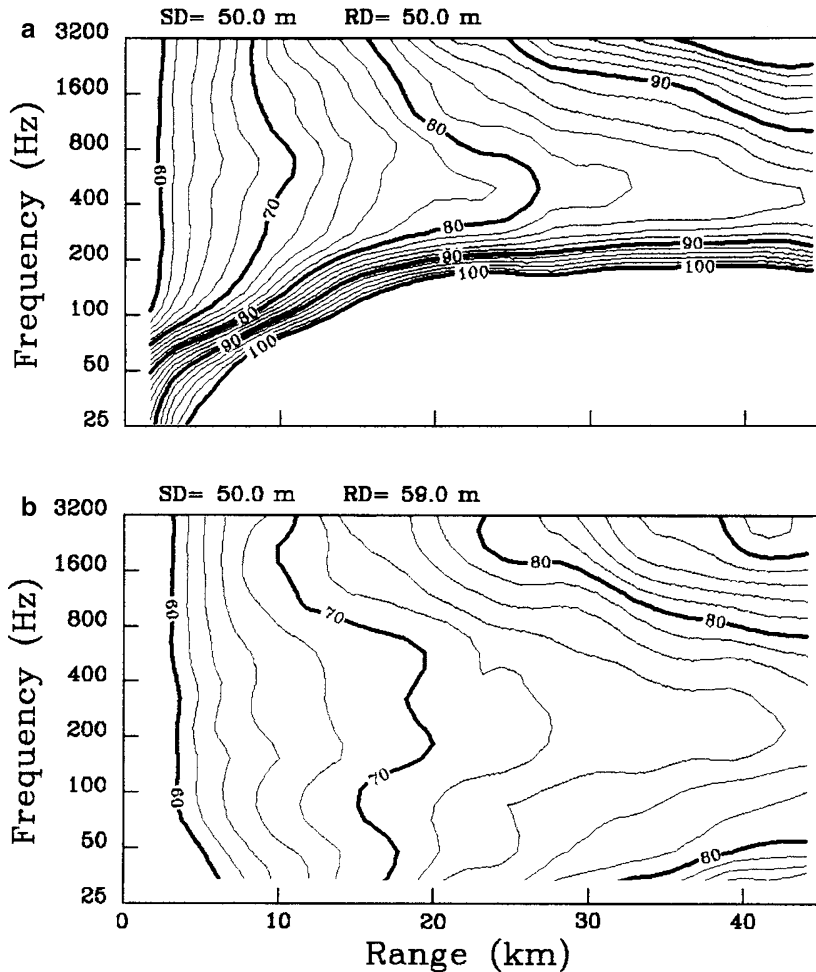


**Fig. 1.17** Contoured propagation losses versus frequency and range in two shallow-water areas. (a) Data from the Barents Sea in 60 m water depth exhibiting extreme losses at frequencies below 200 Hz. (b) Data from the English Channel in 90 m water depth showing a more typical low-frequency behavior. Note the characteristic feature of minimum loss in both data sets around 200–400 Hz at long ranges

longer ranges. Thus, we see that the 80-dB contour line extends farthest in range for frequencies around 400 Hz in Fig. 1.17a and around 200 Hz in Fig. 1.17b, implying that transmission is best at these frequencies—the *optimum frequencies* of propagation for the two sites.

Optimum frequency is a general feature of ducted propagation in the ocean. It occurs as a result of competing propagation and attenuation mechanisms at high and low frequencies. In the high-frequency regime, we have increasing volume

and scattering loss with increasing frequency (see Sects. 1.5 and 1.7). At lower frequencies the situation is more complicated. With increasing wavelength the efficiency of the duct to confine sound decreases (the cutoff phenomenon). Hence, propagation and attenuation mechanisms outside the duct (in the seabed) become important. In fact, the increased penetration of sound into a lossy seabed with decreasing frequency causes the overall attenuation of waterborne sound to increase with decreasing frequency. Thus we get high attenuation at both high and low frequencies, while intermediate frequencies have the lowest attenuation. It was shown by Jensen and Kuperman [27] that the optimum frequency for shallow-water propagation is strongly dependent on water depth ( $f_{\text{opt}} \propto D^{-1}$ ), has some dependence on the sound-speed profile, but is only weakly dependent on the bottom type. Typically, the optimum frequency is in the range 200–800 Hz for a water depth of 100 m.

#### 1.4.4 Range-Dependent Environments

It is often a good approximation to the real ocean-acoustic environment to consider it to be horizontally stratified, i.e., to assume that environmental parameters such as sound-speed profile, water depth, and bottom composition are invariant with range. This, however, is an approximation, since there is always some degree of lateral variability in the ocean. There are even situations where the lateral variability along the propagation path (*range dependence*) strongly influences the acoustic field pattern. We shall demonstrate this with two examples: one showing propagation through an ocean front in the Mediterranean, and the other showing propagation over a seamount in the North Pacific.

##### 1.4.4.1 An Ocean Front

Figure 1.18a shows a series of sound-speed profiles measured across the Maltese front in 1000 m of water. A broadband propagation experiment was performed with a source at 25 m and a receiver at 38 m. The ray diagram shows that a surface duct exists out to a range of around 12 km, where the profile gradient changes from being positive (which creates a duct) to being negative. The result is that almost all the acoustic energy leaks out of the duct at that range.

The effect of the horizontally varying profile structure on transmission loss is shown in Fig. 1.18b, where the measured loss at 250 Hz is compared with a theoretical result obtained with a parabolic equation (PE) model, see Chap. 6. Note the excellent agreement between theory and experiment for this complicated acoustic situation. Moreover, we see that the effect of the lateral change in sound-speed structure causes an increase in transmission loss of nearly 30 dB in the range interval 12–28 km. The high-intensity region near 30 km is due to a convergence-zone path.

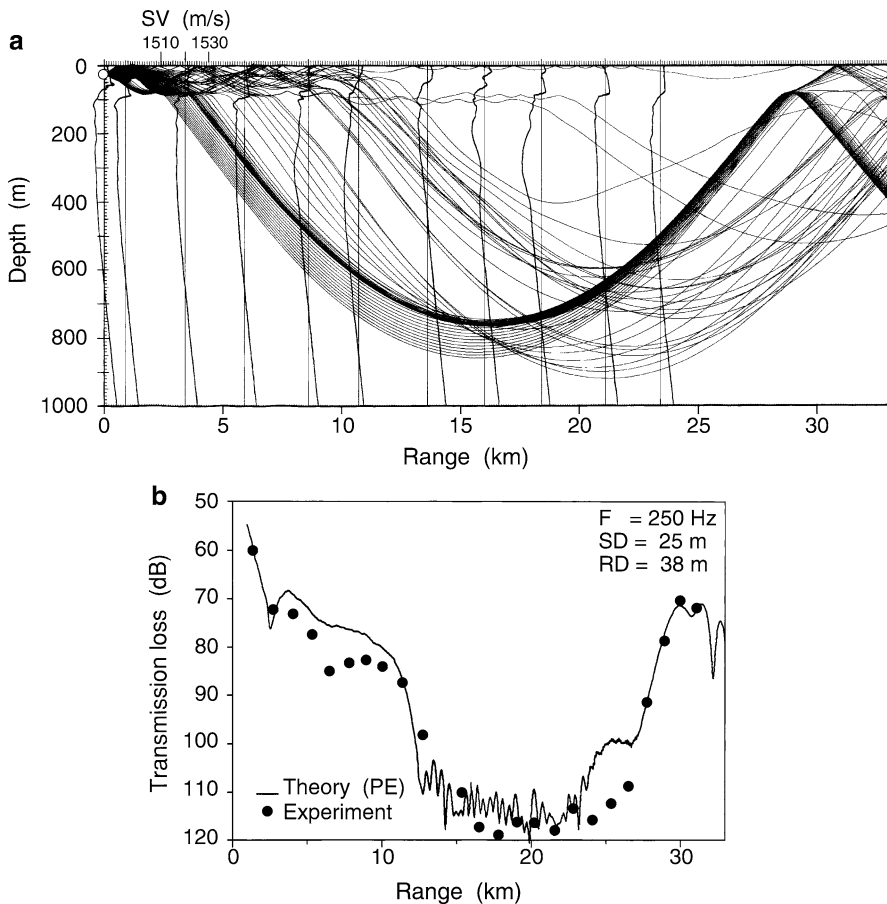


**Fig. 1.18** Sound propagation through an oceanic front in the Mediterranean. (a) Range-dependent sound speed structure and associated ray diagram showing trapping of sound in the surface duct out to a distance of 12 km from the source. (b) Comparison of theoretical and experimental transmission-loss data at 250 Hz for both source and receiver in the surface duct

#### 1.4.4.2 A Seamount

Some of the strongest range-dependent effects in ocean acoustics are observed in connection with varying bathymetry. As an example we consider propagation across a seamount in the Northeast Pacific [28]. Figure 1.19 depicts an environment characterized by two flat-bottom areas separated by a steep mount ( $14^\circ$  mean slope) that peaks approximately 420 m below the sea surface. The effect of the seamount on long-range propagation from a source at 363-m depth can be qualitatively assessed from the ray diagram. Only a narrow beam of rays close to the horizontal ( $\pm 5^\circ$ ) propagates undisturbed by the mount. Rays leaving the source at steeper angles all interact with the seamount and consequently suffer reflection loss. Moreover, ray

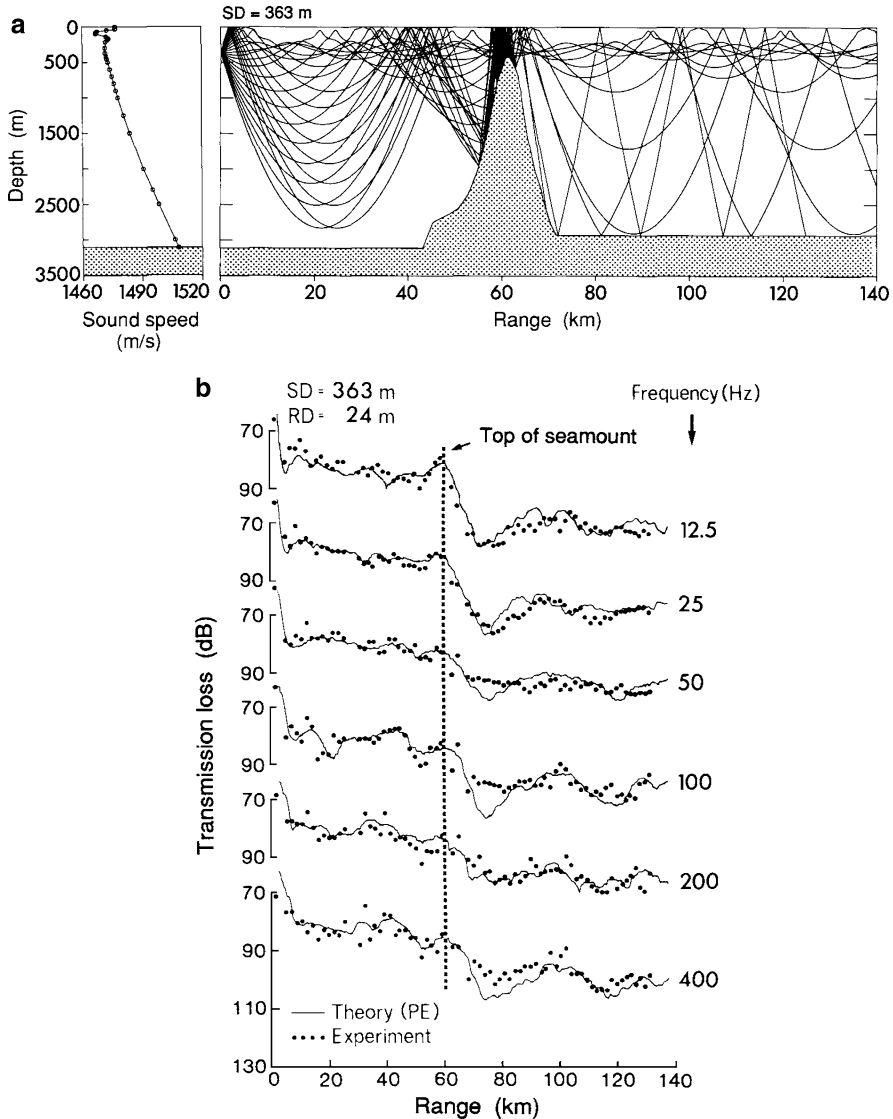


**Fig. 1.19** Propagation over a seamount in the eastern North Pacific. (a) Sound-speed profile, bathymetry, and associated ray diagram. (b) Comparison of theoretical predictions (*solid line*) with experimental transmission-loss data (*dots*) collected by Chapman and Ebbeson [28]

angles steepen by twice the bottom slope per bounce, i.e., around  $28^\circ$ , and hence can undergo a maximum of three upslope reflections before being redirected back toward the source. The result is that the seamount essentially blocks all rays with source angles greater than  $8\text{--}10^\circ$ .

A set of propagation-loss predictions (PE model) for a receiver at 24 m is compared with experimental data in Fig. 1.19b. The agreement between theory and experiment is seen to be excellent. Note, in particular, that the strong shadowing (20–30 dB) by the seamount at low frequencies is accurately predicted by the acoustic model. Clearly, the field structure in this deep-water environment would be quite different in the absence of the seamount, generally improving long-range propagation at the lower frequencies by 20–30 dB.

## 1.5 Volume Attenuation

### 1.5.1 Attenuation of Plane Waves

Plane-wave attenuation  $\alpha$ , which is the quantity used in the theoretical equations of acoustics, is defined from a decay-law-type differential equation, i.e.,

$$\frac{dA}{dx} = -\alpha A \implies A = A_0 \exp(-\alpha x), \quad (1.39)$$

where  $A_0$  is the *rms* amplitude at  $x = 0$ . The unit of  $\alpha$  is nepers/m if  $x$  is in meters. For example, a plane wave in free space with sound speed  $c$ , angular frequency  $\omega$ , and hence, wavenumber  $k \equiv \omega/c$ , that undergoes attenuation has the form

$$\exp(ikx - \alpha x) \equiv \exp[ikx(1 + i\delta)], \quad (1.40)$$

where  $\delta$  is called the *loss tangent*. The plane-wave attenuation  $\alpha'$  is often expressed as a loss in decibels per unit distance,

$$\text{Loss} \equiv -20 \log \frac{A}{A_0} \simeq 8.686 \alpha x \implies \alpha' \simeq 8.686 \alpha, \quad (1.41)$$

where  $\alpha'$  is in dB/m (if  $x$  is in meters) and should be multiplied by 1000 to be in units of dB/km.

Often, attenuation is included by adding an imaginary part to the sound speed so that  $c(z) = c_r(z) - i c_i(z)$ . In terms of the real and imaginary parts of the sound speed, the solution takes the form

$$\exp\left(\frac{i\omega x}{c}\right) = \exp\left[i\omega x \left(\frac{c_r + ic_i}{c_r^2 + c_i^2}\right)\right]. \quad (1.42)$$

By comparing (1.40) and (1.42) we see that for  $c_i^2 \ll c_r^2$ , the imaginary part of the sound speed is related to the attenuation in nepers/m as

$$c_i \simeq \frac{\alpha}{\omega} c_r^2 = \delta c_r. \quad (1.43)$$

Implicit in this treatment is that attenuation is linear with frequency (which is not always the case but can be appropriately addressed—see the discussion below on attenuation in seawater).

The attenuation can also be expressed as a function of frequency denoted here as  $\alpha^{(f)}$  in units dB/(m kHz). From (1.41), we immediately have

$$\alpha^{(f)} \simeq 8686 \frac{\alpha}{f}. \quad (1.44)$$

Alternatively, we can express attenuation as a function of wavelength denoted here as  $\alpha^{(\lambda)}$  in units dB/wavelength. For this quantity, we require that the ratio of the intensities in dB between points one wavelength  $\lambda$  apart be given by  $\alpha^{(\lambda)}$ . That is, we take

$$\alpha^{(\lambda)} = -10 \log \frac{I(x + \lambda)}{I(x)} = -20 \log \frac{e^{-\alpha(x+\lambda)}}{e^{-\alpha x}} = \alpha \lambda \cdot 20 \log e, \quad (1.45)$$

which implies

$$\alpha^{(\lambda)} \simeq 8.686 \alpha \lambda \simeq 54.58 \delta. \quad (1.46)$$

### 1.5.2 Attenuation in Seawater

When sound propagates in the ocean, part of the acoustic energy is continuously absorbed, i.e., the energy is transformed into heat. Moreover, sound is scattered by different kinds of inhomogeneities, also resulting in a decay of sound intensity with range. As a rule, it is not possible in real ocean experiments to distinguish between absorption and scattering effects; they both contribute to sound *attenuation* in seawater.

The frequency dependence of attenuation can be roughly divided into four regimes of different physical origin as displayed in Fig. 1.20 [25]. The lowest frequency regime, region I, is still not completely understood but it is conjectured that it is related to low-frequency propagation-duct cutoff, or in other words, leakage out of the deep sound channel. The main mechanisms associated with regions II and III are chemical relaxations of boric acid  $B(OH)_3$  and magnesium sulphate  $MgSO_4$ , respectively. Region IV is dominated by the shear and bulk viscosity associated with salt water (curve AA'). For reference, also the viscous loss associated with fresh water is shown as curve BB' in Fig. 1.20.

A simplified expression for the frequency dependence ( $f$  in kHz) of the attenuation is [25, 29, 30],

$$\alpha' \simeq 3.3 \times 10^{-3} + \frac{0.11 f^2}{1 + f^2} + \frac{44 f^2}{4100 + f^2} + 3.0 \times 10^{-4} f^2 \quad (\text{dB/km}) \quad (1.47)$$

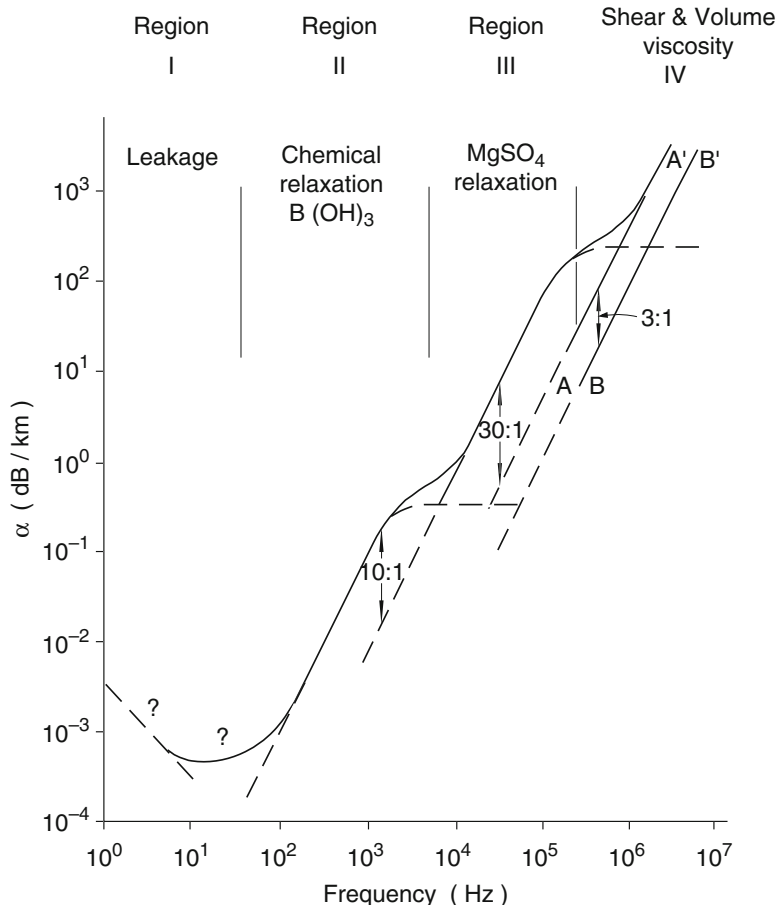


**Fig. 1.20** Regions of the different dominant processes of attenuation of sound in seawater (from Urick [25])

with the four terms sequentially associated with regions I–IV in Fig. 1.20. (See (1.41) for relating units to the plane-wave attenuation coefficient and (1.43) for conversion to a complex sound speed.) The above expression applies for a temperature of 4°C, a salinity of 35 ppt, a pH of 8.0, and a depth of about 1000 m, where most of the measurements on which it is based were made.

Even though the attenuation of sound in seawater has some dependence on temperature, pressure, salinity, and acidity (pH value), (1.47) is considered sufficiently accurate for most problems in ocean acoustics. However, better attenuation formulas are available, notably the rather complicated formula by Francois and Garrison [31], which is claimed to have an overall accuracy of 5%. From this formula we find that the dependence of attenuation on temperature and pressure is rather weak, while absorption due to boric acid relaxation has a marked geographical variation associated

with the difference in  $p\text{H}$  values throughout the oceans. Thus, the low-frequency ( $<1\text{ kHz}$ ) attenuation in the North Pacific ( $p\text{H} = 7.7$ ) is only about half that in the North Atlantic ( $p\text{H} = 8.0$ ). Clearly, a correction to (1.47) is required for even small changes in  $p\text{H}$  from the nominal value of 8.0. It may also be necessary to correct for salinity if it deviates much from 35 ppt. The salinity primarily affects the magnesium sulphate relaxation [31], and high-frequency ( $>1\text{ kHz}$ ) attenuation in, e.g., the Baltic ( $S = 8\text{ ppt}$ ) is less than half that in open oceans.

In summary, we see from (1.47) that the attenuation of low-frequency sound in seawater is very small. For instance, at 100 Hz a tenfold reduction in sound intensity ( $-10\text{ dB}$ ) occurs over a distance of around 2200 km. Even though attenuation increases with frequency ( $r_{-10\text{ dB}} \simeq 145\text{ km}$  at 1 kHz and  $\simeq 9\text{ km}$  at 10 kHz), no other kind of radiation can compete with sound waves for long-range propagation in the ocean. Electromagnetic waves, including those radiated by powerful lasers, are absorbed almost completely within distances of a few hundred meters.

## 1.6 Bottom Loss

When sound interacts with the seafloor, the structure of the ocean bottom becomes important. Ocean bottom sediments are often modeled as fluids which means that they support only one type of sound wave—a compressional wave. This is often a good approximation since the rigidity (and hence the shear speed) of the sediment is usually considerably less than that of a solid, such as rock. In the latter case, which applies to the *ocean basement* or the case where there is no sediment overlying the basement, the medium must be modeled as elastic, which means it supports both compressional and shear waves. In reality, the media are viscoelastic, meaning that they are also lossy.

A *geoacoustic model* is defined as a model of the real seafloor with emphasis on measured, extrapolated, and predicted values of those material properties important for the modeling of sound transmission. In general, a geoacoustic model details the true thicknesses and properties of sediment and rock layers within the seabed to a depth termed the *effective acoustic penetration depth*. Thus, at high frequencies, details of the bottom composition are required only in the upper few meters or tens of meters of sediment, whereas at very low frequencies ( $<10\text{ Hz}$ ) information must be provided on the whole sediment column and on properties of the underlying rocks.

The information required for a complete geoacoustic model should include the following depth-dependent material properties: The compressional wave speed  $c_p$ , the shear wave speed  $c_s$ , the compressional wave attenuation  $\alpha_p$ , the shear wave attenuation  $\alpha_s$ , and the density  $\rho$ . Moreover, information on the variation of all of these parameters with geographical position is required. Clearly, the construction of a detailed geoacoustic model for a particular ocean area is a tremendous task, and the amount of approximate (or inaccurate) information included is the primary limiting factor on the accurate modeling of bottom-interacting sound transmission in the ocean.

**Table 1.3** Geoacoustic properties of continental shelf and slope environments

Bottom type	$p$ (%)	$\rho_b/\rho_w$	$c_p/c_w$	$c_p$ (m/s)	$c_s$ (m/s)	$\alpha_p$ (dB/ $\lambda_p$ )	$\alpha_s$ (dB/ $\lambda_s$ )
Clay	70	1.5	1.00	1500	<100	0.2	1.0
Silt	55	1.7	1.05	1575	$c_s^{(1)}$	1.0	1.5
Sand	45	1.9	1.1	1650	$c_s^{(2)}$	0.8	2.5
Gravel	35	2.0	1.2	1800	$c_s^{(3)}$	0.6	1.5
Moraine	25	2.1	1.3	1950	600	0.4	1.0
Chalk	–	2.2	1.6	2400	1000	0.2	0.5
Limestone	–	2.4	2.0	3000	1500	0.1	0.2
Basalt	–	2.7	3.5	5250	2500	0.1	0.2

$$\begin{aligned} c_s^{(1)} &= 80 \tilde{z}^{0.3} & c_w &= 1500 \text{ m/s}, \quad \rho_w = 1000 \text{ kg/m}^3 \\ c_s^{(2)} &= 110 \tilde{z}^{0.3} \\ c_s^{(3)} &= 180 \tilde{z}^{0.3} \end{aligned}$$

The amount of literature dealing with acoustic properties of seafloor materials is vast. However, excellent summary papers have been published by Hamilton [32,33]. As an indication of the many different types of materials encountered just in continental shelf and slope environments, we list in Table 1.3 the geoacoustic properties of some typical seafloor materials, as compiled from [32,33]. A subsequent analysis of bottom sound speed and attenuation in shallow-water areas below 2 kHz is given in [34]. Higher frequency seafloor acoustics is reviewed in [35].

There are several interesting observations to be made here. First, we see that the porosity  $p$  relates in a simple fashion to the material density and the wave speeds, i.e., a lower porosity results in a higher density and higher wave speeds. Next, the shear speeds in unconsolidated sediments (clay, silt, sand, gravel, and moraine) are quite low but increase rapidly with depth  $\tilde{z}$  below the water-bottom interface. Hence, shear speeds in sediments are most appropriately given in terms of their depth dependence. Wave attenuations  $\alpha$  are generally given in units of dB per wavelength indicating that the attenuation increases linearly with frequency. Note that bottom materials are three-to-four orders of magnitude more lossy than seawater. Thus, at 100 Hz the attenuation in seawater is around 0.004 dB/km, whereas the compressional wave attenuation in bottom materials varies between 2 dB/km in basalt to around 63 dB/km in silt. Finally, it must be emphasized that the values given in Table 1.3 are merely indicative. The vastly different material compositions and stratifications encountered in the ocean seafloors essentially mean that a specific geoacoustic model must be established for any given (small or large) geographical area. With sufficient “ground truth” information incorporated in such a model, the acoustic prediction may actually become quite accurate even when propagation is dominated by bottom loss.

Reflectivity, the ratio of the amplitudes of a reflected plane wave to a plane wave incident on an interface separating two media, is an important measure of the effect of the bottom on sound propagation. For the purpose of discussing bottom loss mechanisms, we here derive reflection coefficients for a few simple cases, including homogeneous fluid and solid halfspaces and layered fluid halfspaces. Additional information on bottom reflectivity is given in Chap. 2.

### 1.6.1 Fluid–Fluid Interface

We consider reflection at an interface separating two homogeneous fluid media with density  $\rho_i$  and sound speed  $c_i$ ,  $i = 1, 2$ , as shown in Fig. 1.21. The pertinent grazing angles with the horizontal in the  $xz$ -plane are denoted by  $\theta_i$ . Assuming the incident plane wave to have unit amplitude and denoting the amplitudes of the reflected and transmitted waves by  $\mathcal{R}$  and  $\mathcal{T}$ , respectively, we can write the acoustic pressures as

$$p_i = \exp[ik_1(x \cos \theta_1 + z \sin \theta_1)], \quad k_1 \equiv \omega/c_1, \quad (1.48)$$

$$p_r = \mathcal{R} \exp[ik_1(x \cos \theta_1 - z \sin \theta_1)], \quad (1.49)$$

$$p_t = \mathcal{T} \exp[ik_2(x \cos \theta_2 + z \sin \theta_2)], \quad k_2 \equiv \omega/c_2. \quad (1.50)$$

where we have omitted a common time factor  $\exp(-i\omega t)$ .

The unknown quantities  $\mathcal{R}$ ,  $\mathcal{T}$ , and  $\theta_2$  are determined from the boundary conditions requiring continuity of pressure and vertical particle velocity across the interface at  $z = 0$ . With the total pressure in medium 1 given by  $p_1 = p_i + p_r$  and the pressure in medium 2 by  $p_2 = p_t$ , the boundary conditions can be mathematically stated as

$$p_1 = p_2, \quad \frac{1}{i\omega\rho_1} \frac{\partial p_1}{\partial z} = \frac{1}{i\omega\rho_2} \frac{\partial p_2}{\partial z}. \quad (1.51)$$

It is easily seen that the requirement of continuity of pressure at  $z = 0$  leads to

$$1 + \mathcal{R} = \mathcal{T} \exp[i(k_2 \cos \theta_2 - k_1 \cos \theta_1) x]. \quad (1.52)$$

Since the left side is independent of  $x$ , the right side must also be independent of  $x$ , which yields *Snell's law of refraction*,

$$k_1 \cos \theta_1 = k_2 \cos \theta_2. \quad (1.53)$$

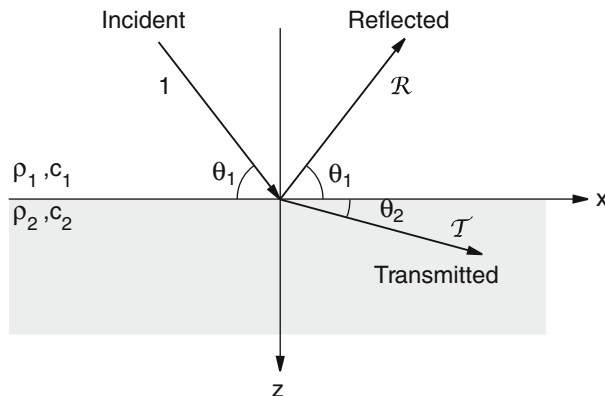


**Fig. 1.21** Reflection and transmission at a fluid–fluid interface

This law simply states the invariability of the horizontal component of the wave vector across the interface. We can now write (1.52) in the form

$$1 + \mathcal{R} = \mathcal{T}, \quad (1.54)$$

which together with the equation obtained from the second boundary condition,

$$1 - \mathcal{R} = \mathcal{T} \frac{\rho_1 c_1 / \sin \theta_1}{\rho_2 c_2 / \sin \theta_2}, \quad (1.55)$$

lead to the following expressions for the *reflection coefficient*  $\mathcal{R}$  and the *transmission coefficient*  $\mathcal{T}$ ,

$$\mathcal{R} = \frac{\rho_2 c_2 / \sin \theta_2 - \rho_1 c_1 / \sin \theta_1}{\rho_2 c_2 / \sin \theta_2 + \rho_1 c_1 / \sin \theta_1}, \quad (1.56)$$

$$\mathcal{T} = \frac{2 \rho_2 c_2 / \sin \theta_2}{\rho_2 c_2 / \sin \theta_2 + \rho_1 c_1 / \sin \theta_1}. \quad (1.57)$$

Finally, we can write the reflection and transmission coefficients in form of *effective impedances* as

$$\mathcal{R} = \frac{\mathcal{Z}_2 - \mathcal{Z}_1}{\mathcal{Z}_2 + \mathcal{Z}_1}, \quad \mathcal{T} = \frac{2\mathcal{Z}_2}{\mathcal{Z}_2 + \mathcal{Z}_1}, \quad (1.58)$$

where  $\mathcal{Z}_i \equiv \rho_i c_i / \sin \theta_i$  are the ratios of the pressure to the vertical particle velocity for a plane wave propagating in the positive  $z$ -direction in the  $i$ th medium [36]. Written in this form, more complicated reflection coefficients become intuitively plausible, as evidenced in the next section.

$\mathcal{R}$  is often referred to as the *Rayleigh reflection coefficient*. It has unit magnitude, meaning *perfect reflection*, when the numerator and denominator of (1.56) are complex conjugates. This can only occur when  $\sin \theta_2$  is purely imaginary, i.e., for  $\cos \theta_2 > 1$  (*total internal reflection*). From Snell's law, the *critical grazing angle* below which there is perfect reflection is found to be

$$\theta_c = \arccos \left( \frac{c_1}{c_2} \right). \quad (1.59)$$

Note that a critical angle only exists when the sound speed of the second medium is higher than that of the first.

A closer look at (1.56) shows that the reflection coefficient for lossless media is real for  $\theta_1 > \theta_c$ , which means that there is loss ( $|\mathcal{R}| < 1$ ) but no phase shift associated with the reflection process. On the other hand, for  $\theta_1 < \theta_c$  we have perfect reflection ( $|\mathcal{R}| = 1$ ) but with an angle-dependent phase shift. In the general case of lossy media ( $c_i$  complex), the reflection coefficient is complex, and, consequently, there is both a loss and a phase shift associated with each reflection.

Another special case of interest is when all energy is transmitted into the bottom, i.e.,  $|\mathcal{R}| = 0$ . From (1.56) and Snell's law we find that total transmission occurs at an angle  $\theta_0$  given by

$$\theta_0 = \arctan \sqrt{\frac{1 - (c_2/c_1)^2}{[(\rho_2 c_2)/(\rho_1 c_1)]^2 - 1}}. \quad (1.60)$$

This angle is called the *intromission angle*, and it clearly only exists when the fraction under the square root is positive. Hence there are two cases we need to consider:

1.  $c_2 < c_1$  with  $\rho_2 c_2 > \rho_1 c_1$ .
2.  $c_2 > c_1$  with  $\rho_2 c_2 < \rho_1 c_1$ .

While the first situation (low-speed, high-density sediment) is not uncommon for muddy bottoms, the second situation (high-speed, low-density sediment) never occurs in ocean acoustics.

The critical-angle concept outlined earlier is very important for understanding the waveguide nature of ocean acoustic propagation, particularly in shallow water. Consider a homogeneous water column with sound speed  $c_1$  overlying a homogeneous fluid bottom with speed  $c_2 > c_1$ , as shown in Fig. 1.22. Then there exists a critical angle of reflection given by  $\theta_c = \arccos(c_1/c_2)$ , with the result that energy propagating near the horizontal within an aperture of  $2\theta_c$  suffers no bottom loss and hence propagates to long distances ( $\theta_c$  is typically 10–30° for continental shelf sediments). Energy outside this cone (steeper angle energy) is partially transmitted into the seabed at each bounce, which results in a strong decay with range of the reflected component.

For the *lossy* (more realistic) bottom with complex sound speeds, we never get perfect reflection, as discussed earlier. However, the reflection loss for subcritical incidence is still much smaller than for supercritical incidence. With paths involving many bottom bounces such as in shallow-water propagation, bottom losses even as

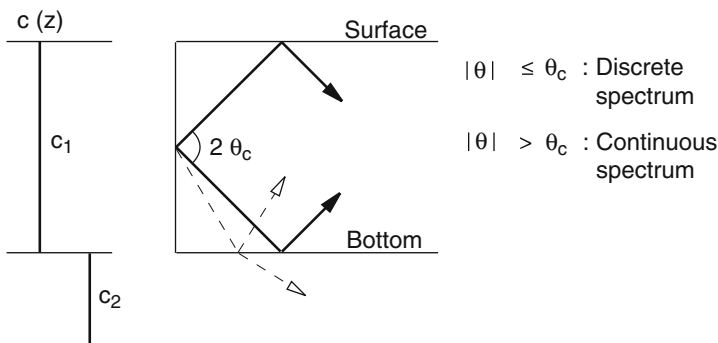


**Fig. 1.22** Long-distance propagation in ocean waveguides occurs within an aperture of  $2\theta_c$ . For angles greater than the critical angle  $\theta_c$ , acoustic energy is partially transmitted into the ocean bottom at each bounce resulting in severe decay of the acoustic field with range

small as a few tenths of a decibel per bounce accumulate to significant total losses since the propagation path may involve many tens or even hundreds of bounces.

The energy propagating near the horizontal within angles of  $2\theta_c$  is generally referred to as the normal-mode field (or *discrete spectrum*) because there will be a discrete set of angles that correspond to paths which constructively interfere, essentially making up the normal (natural) modes of the shallow water environment (Chap. 5). The modes are discrete since the near-perfect reflectivity permits the existence of a set of discrete vertical standing waves analogous to those of a vibrating string or an organ pipe. The steeper-angle energy outside  $2\theta_c$  is referred to as the nearfield (or *continuous spectrum*) and is rapidly lost into the bottom.

### 1.6.2 Fluid–Solid Interface

Consider the case in Fig. 1.21 where the second medium is a solid and thus supports shear as well as compressional waves with speeds  $c_s$  and  $c_p$ , respectively. The Rayleigh reflection coefficient is then given by an expression similar to that of (1.58) [36],

$$\mathcal{R} = \frac{\mathcal{Z}_{\text{tot}} - \mathcal{Z}_1}{\mathcal{Z}_{\text{tot}} + \mathcal{Z}_1} \quad (1.61)$$

with the total effective impedance of the second medium being

$$\mathcal{Z}_{\text{tot}} = \mathcal{Z}_p \cos^2 2\theta_s + \mathcal{Z}_s \sin^2 2\theta_s. \quad (1.62)$$

Snell's law for this case is

$$k_1 \cos \theta_1 = k_p \cos \theta_p = k_s \cos \theta_s. \quad (1.63)$$

It can be shown that the total impedance of the elastic medium is less than that of a liquid layer with the same compressional speed. Hence, the elastic interface appears to be “softer” than the equivalent liquid layer which can be thought to arise from the fact that the shear wave provides an additional degree of freedom for the acoustic wave to penetrate into the second medium. Actually, a good approximation (neglecting interface waves) for a second medium whose shear speed is greater than the compressional speed of the first medium is to replace the elastic reflection coefficient with the two-fluid reflection coefficient using the shear speed of the second medium as the compressional speed of an equivalent second *fluid* medium. For a more detailed discussion of reflectivity at fluid–solid interfaces, readers are referred to recent books by Brekhovskikh et al. [36, 37].

We now present a set of bottom-loss curves based on solutions of (1.61) for typical values of wave speeds, densities, and attenuations associated with ocean sediments. The displayed quantity is *bottom loss* in decibels defined as

$$\text{BL} = -10 \log |\mathcal{R}|^2. \quad (1.64)$$

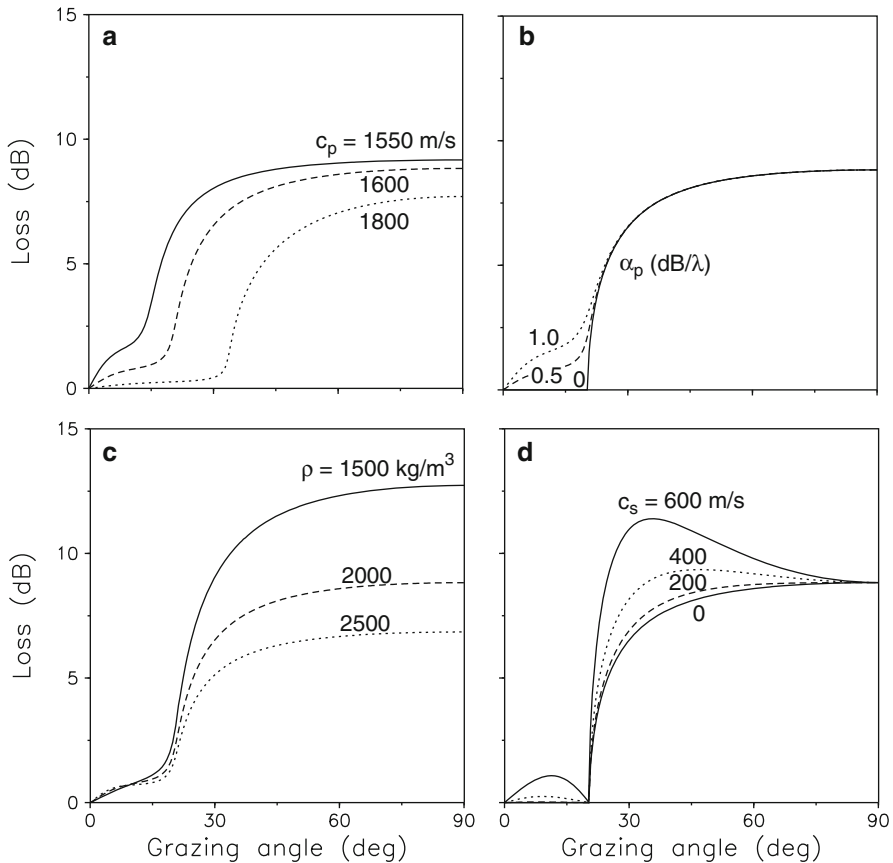


**Fig. 1.23** Bottom-loss curves for different values of (a) the  $p$ -wave speed, (b) the  $p$ -wave attenuation, (c) the density, and (d) the  $s$ -wave speed. The fixed parameters in each case are given in Table 1.4

**Table 1.4** Bottom parameters for reflection-loss calculations shown in Fig. 1.23

	$c_p$ (m/s)	$c_s$ (m/s)	$\alpha_p$ (dB/ $\lambda_p$ )	$\alpha_s$ (dB/ $\lambda_s$ )	$\rho$ (kg/m <sup>3</sup> )
Case (a)	—	0	0.5	0	2000
Case (b)	1600	0	—	0	2000
Case (c)	1600	0	0.5	0	—
Case (d)	1600	—	0.0	0	2000

$$c_w = 1500 \text{ m/s}, \rho_w = 1000 \text{ kg/m}^3$$

Figure 1.23 shows four sets of curves, with a single bottom parameter being varied in each graph. The water parameters are fixed to  $c_w = 1500$  m/s and  $\rho_w = 1000$  kg/m<sup>3</sup>. The fixed bottom parameters for each of the four cases are listed in Table 1.4.

It is clear from Fig. 1.23a that the compressional-wave speed in the bottom is an important parameter, which affects bottom loss at all grazing angles. In particular, it determines the *apparent* critical angle, which is around  $33.5^\circ$  for  $c_p = 1800$  m/s. A lower  $p$ -wave speed results in higher losses, particularly at lower grazing angles. Generally,  $c_p$  is the most important geoacoustic parameter.

Figure 1.23b displays the effect of  $p$ -wave attenuation on bottom loss. Note that for  $\alpha_p = 0$  we have a genuine critical angle effect, with perfect reflection for  $\theta \leq \theta_c$ . The  $p$ -wave attenuation only affects bottom loss below the critical angle, but it is the second most important geoacoustic parameter for modeling long-range shallow-water propagation.

In Fig. 1.23c, the effect of density on bottom loss is shown. While this parameter is seen to be very important near normal incidence, it has negligible effect below the critical angle. Hence, the bottom density is not important for modeling long-range propagation in the ocean.

The final result in Fig. 1.23d shows the effect of shear in the bottom. Note that shear waves are not excited at the critical angle nor at normal incidence. The effect of shear is small for  $c_s < 200$  m/s. However, higher shear speeds significantly affect bottom loss at both subcritical and intermediate grazing angles. Generally, the shear speed ranks as the third most important parameter in unconsolidated sediments. As mentioned earlier, in consolidated materials ( $c_s > c_w$ ) the shear speed takes on the role of the compressional speed in unconsolidated sediments and becomes the most important geoacoustic parameter.

The only one of the standard set of geoacoustic parameters not treated in this example is the attenuation parameter  $\alpha_s$  for shear waves. This parameter can be shown to have negligible effect on bottom loss for low-shear-speed sediments ( $c_s < c_w$ ). However, for shear speeds higher than the water speed, the shear attenuation again becomes an important parameter.

To illustrate the wide range of reflectivity conditions encountered for ocean bottoms, we have computed bottom loss for all the seafloor types listed in Table 1.3, see Fig 1.24. Note that the low-angle reflection loss varies from less than 1 dB per bounce for bottoms with good reflectivity (basalt, gravel, sand) to nearly 15 dB per bounce for bottoms with poor reflectivity (clay, chalk).

Finally, note that the reflection loss for a homogeneous bottom (Fig. 1.24) is *independent* of frequency. To demonstrate the kind of complication that arises in connection with layered bottoms, we next study reflectivity at a layered fluid structure composed of a thin top layer on a homogeneous halfspace.

### 1.6.3 Layered Fluid Halfspace

The geometry and notation for a three-layered fluid structure is given in Fig. 1.25. As before we assume the incident plane wave in medium 1 to have unit amplitude and denote the partial reflection and transmission coefficients by  $\mathcal{R}_{ij}$  and  $\mathcal{T}_{ij}$ , with the subscript sequence indicating the propagation direction relative to interface  $(i, j)$ .

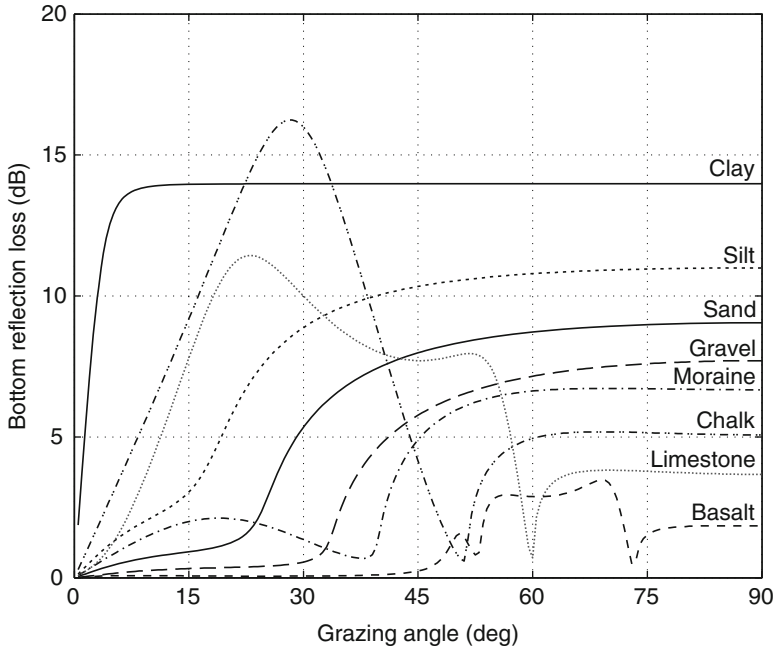


**Fig. 1.24** Computed bottom reflection loss vs. grazing angle for all bottom types listed in Table 1.3

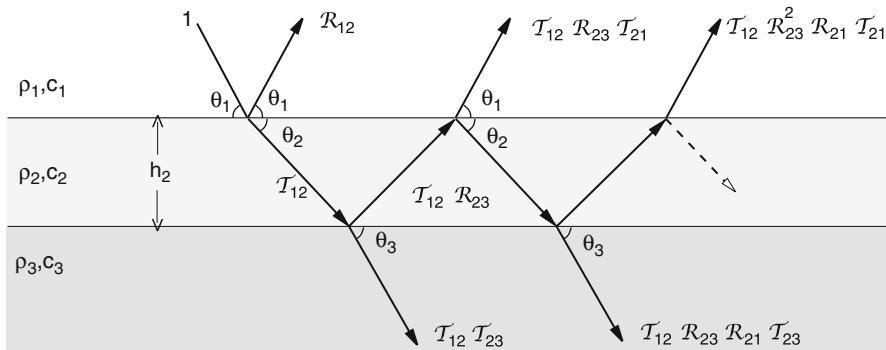


**Fig. 1.25** Reflection and transmission by a layered fluid structure

It is clear from Fig. 1.25 that the total up-traveling signal is the sum of an infinite number of partial transmissions and reflections. Thus, the secondary reflected wave is seen to have an amplitude of  $T_{12}\mathcal{R}_{23}T_{21}$  because this wave has been *transmitted* through interface (1,2), *reflected* at interface (2,3), and finally *transmitted* through interface (2,1). In addition to the amplitude changes at the interfaces, we also have to take account of the angle-dependent vertical phase delay for a path crossing the layer of thickness  $h_2$ ,

$$\phi_2 \equiv k_2 h_2 \sin \theta_2. \quad (1.65)$$

Noting that all reflected wave components have a double passage through the layer, the phase delays become integer multiples of  $2\phi_2$ . We can now write the total reflected field as

$$\begin{aligned}\mathcal{R} &= \mathcal{R}_{12} + \mathcal{T}_{12}\mathcal{R}_{23}\mathcal{T}_{21} \exp(2i\phi_2) + \mathcal{T}_{12}\mathcal{R}_{23}^2\mathcal{R}_{21}\mathcal{T}_{21} \exp(4i\phi_2) + \dots \\ &= \mathcal{R}_{12} + \mathcal{T}_{12}\mathcal{R}_{23}\mathcal{T}_{21} \exp(2i\phi_2) \sum_{n=0}^{\infty} [\mathcal{R}_{23}\mathcal{R}_{21} \exp(2i\phi_2)]^n.\end{aligned}\quad (1.66)$$

Using the sum for the infinite geometric series, we obtain

$$\mathcal{R} = \mathcal{R}_{12} + \mathcal{T}_{12}\mathcal{R}_{23}\mathcal{T}_{21} \exp(2i\phi_2) \frac{1}{1 - \mathcal{R}_{23}\mathcal{R}_{21} \exp(2i\phi_2)}. \quad (1.67)$$

This expression can be further reduced by using the identities  $\mathcal{R}_{21} = -\mathcal{R}_{12}$  and  $\mathcal{T}_{12}\mathcal{T}_{21} = 1 - \mathcal{R}_{12}^2$  [see (1.58) for verification],

$$\mathcal{R} = \frac{\mathcal{R}_{12} + \mathcal{R}_{23} \exp(2i\phi_2)}{1 + \mathcal{R}_{12}\mathcal{R}_{23} \exp(2i\phi_2)}. \quad (1.68)$$

Similarly, we find the total transmission coefficient to be given by

$$\mathcal{T} = \frac{\mathcal{T}_{12}\mathcal{T}_{23} \exp(2i\phi_2)}{1 + \mathcal{R}_{12}\mathcal{R}_{23} \exp(2i\phi_2)}. \quad (1.69)$$

Both the reflection and transmission coefficients are seen to be oscillatory functions of  $\phi_2 = 2\pi(h_2/\lambda_2) \sin \theta_2$ , i.e., they are functions of both frequency and angle. We shall shortly illustrate this dependency through a numerical example. However, for convenience we first express the reflection coefficient in terms of effective impedances.

By substituting (1.58) into (1.68) and making use of the standard definition of  $\tan \phi_2$  in terms of complex exponentials, we obtain

$$\mathcal{R} = \frac{\mathcal{Z}_2(\mathcal{Z}_3 - \mathcal{Z}_1) - i(\mathcal{Z}_2^2 - \mathcal{Z}_1\mathcal{Z}_3) \tan \phi_2}{\mathcal{Z}_2(\mathcal{Z}_3 + \mathcal{Z}_1) - i(\mathcal{Z}_2^2 + \mathcal{Z}_1\mathcal{Z}_3) \tan \phi_2}, \quad (1.70)$$

where

$$\mathcal{Z}_j = \frac{\rho_j c_j}{\sin \theta_j}, \quad j = 1, 2, 3. \quad (1.71)$$

The three angles are related through Snell's law,

$$k_1 \cos \theta_1 = k_2 \cos \theta_2 = k_3 \cos \theta_3. \quad (1.72)$$

We briefly illustrate the complications associated with reflections from layered systems by considering two special cases. For normal incidence ( $\theta_1 = \theta_2 = \theta_3 = \pi/2$ ), the vertical phase delay across the layer, (1.65), is simply given by

$$\phi_2 = 2\pi \left( \frac{h_2}{\lambda_2} \right). \quad (1.73)$$

The special cases arise when  $\tan \phi_2$  is either infinite or zero.

### 1.6.3.1 Quarter-Wavelength Layer

Let  $h_2 = (2m - 1)(\lambda_2/4)$ ,  $m = 1, 2, 3 \dots$ , which results in  $\tan \phi_2 = \infty$ . The reflection coefficient given by (1.70) then reduces to

$$\mathcal{R} = \frac{\mathcal{Z}_2^2 - \mathcal{Z}_1 \mathcal{Z}_3}{\mathcal{Z}_2^2 + \mathcal{Z}_1 \mathcal{Z}_3}, \quad (1.74)$$

which is seen to be zero for  $\mathcal{Z}_2 = \sqrt{\mathcal{Z}_1 \mathcal{Z}_3}$ . Hence, the reflection at the interface between two arbitrary fluid media can be completely eliminated by placing a quarter-wavelength layer between them with an impedance that is the geometric mean of the impedances of the two media. Layered systems have numerous applications in both acoustics and optics as filters, insulators, and antireflecting coatings.

### 1.6.3.2 Half-Wavelength Layer

Now let  $h_2 = m(\lambda_2/2)$ ,  $m = 1, 2, 3 \dots$ , which results in  $\tan \phi_2 = 0$ . The reflection coefficient given by (1.70) then reduces to

$$\mathcal{R} = \frac{\mathcal{Z}_3 - \mathcal{Z}_1}{\mathcal{Z}_3 + \mathcal{Z}_1}, \quad (1.75)$$

which is seen to be independent of  $\mathcal{Z}_2$ . Hence, a half-wavelength layer has no effect on the incident wave (as if the layer were absent), and reflection takes place as if media 1 and 3 were in direct contact with one another. This result can also be obtained by just assuming the layer to be thin compared to the acoustic wavelength ( $h_2 \ll \lambda_2$ ). The reflection coefficient is then found to be independent of  $\mathcal{Z}_2$  for all angles of incidence, i.e., we have derived the physically intuitive result that thin layers are acoustically transparent.

To illustrate the full complexity of reflection loss at a layered fluid bottom, we turn to a numerical example and solve (1.70) as a function of both angle and frequency for a specific set of layer parameters as given in Table 1.5. Note that both the sediment and the substrate are lossy media, which means that the impedances  $\mathcal{Z}_2$  and  $\mathcal{Z}_3$  are complex. The computed bottom loss in decibels, (1.64), is displayed

**Table 1.5** Layered fluid bottom

Layer	Thickness (m)	Sound speed (m/s)	Attenuation (dB/ $\lambda$ )	Density (kg/m <sup>3</sup> )
Water	$\infty$	1500	0.0	1000
Sediment	2.0	1550	0.2	1500
Substrate	$\infty$	1800	0.5	2000

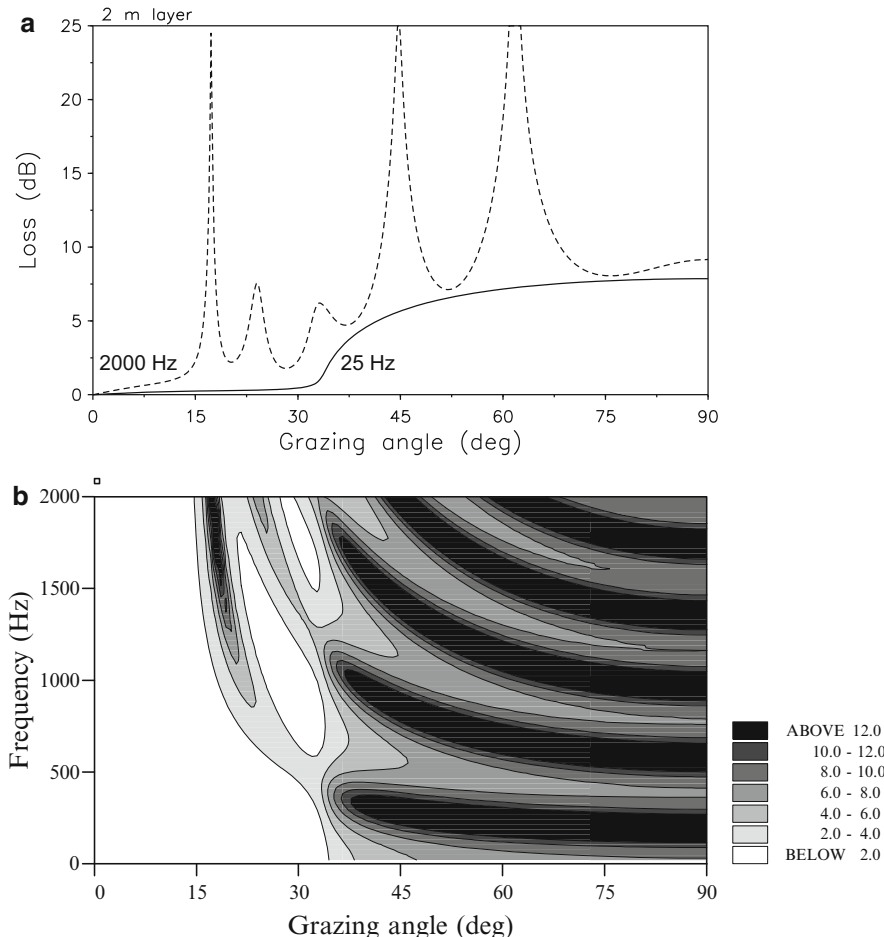


**Fig. 1.26** Reflection loss at layered fluid bottom with the parameters given in Table 1.5. (a) Loss vs. grazing angle. (b) Contoured loss vs. frequency and grazing angle

in Fig. 1.26. The upper graph shows loss versus angle at two specific frequencies (25 and 2000 Hz), whereas the lower graph shows contoured loss as a function of frequency and angle. Hence, the upper graph represents two horizontal cuts through the lower graph at frequencies 25 and 2000 Hz.

Note in Fig. 1.26a that the 25-Hz curve is very similar in shape to the curves shown in Fig. 1.23 for a halfspace. This is because the layer here is thin compared to the acoustic wavelength ( $h_2 = 2 \text{ m}$ ,  $\lambda_2 = 62 \text{ m}$ ), making the layer transparent to the incident wave. The apparent critical angle is given by  $\theta_c = \arccos(c_1/c_3) \simeq 33.6^\circ$ . At 2000 Hz we have a much lower critical angle of approximately  $14.6^\circ$  determined from the speeds in layers 1 and 2. Moreover, prominent resonance peaks are present in the loss curve at higher angles.

Figure 1.26b shows the full complexity of reflection loss at a layered fluid bottom. The apparent critical angle is seen to change smoothly from around  $33.6^\circ$  at low frequencies to  $14.6^\circ$  at high frequencies. The angle-dependent resonance pattern is also evident, with quarter and half-wavelength layer effects regularly interspersed at normal incidence.

#### 1.6.4 Arbitrary Layering

We finish our discussion of bottom loss by outlining the approach for treating arbitrarily layered fluid–solid structures [37]. Here the pressure reflection coefficient may be constructed by repeated application of the single-layer coefficient, (1.68). Let us consider an  $m$ -layered system consisting of halfspaces 1 and  $m$  separated by  $m - 2$  layers of different acoustic properties. The reflection coefficient for three lowest layers is then found from (1.68) to be

$$\mathcal{R}_{(m-2)m} = \frac{\mathcal{R}_{(m-2)(m-1)} + \mathcal{R}_{(m-1)m} \exp(2i\phi_{m-1})}{1 + \mathcal{R}_{(m-2)(m-1)} \mathcal{R}_{(m-1)m} \exp(2i\phi_{m-1})}. \quad (1.76)$$

Knowing  $\mathcal{R}_{(m-2)m}$ , we can move one layer up and compute the next reflection coefficient as

$$\mathcal{R}_{(m-3)m} = \frac{\mathcal{R}_{(m-3)(m-2)} + \mathcal{R}_{(m-2)m} \exp(2i\phi_{m-2})}{1 + \mathcal{R}_{(m-3)(m-2)} \mathcal{R}_{(m-2)m} \exp(2i\phi_{m-2})}. \quad (1.77)$$

Continuing this process toward the top layer, we finally arrive at the desired reflection coefficient  $\mathcal{R}_{1m}$  expressed in terms of the nested reflection coefficients as

$$\mathcal{R}_{1m} = \frac{\mathcal{R}_{12} + \mathcal{R}_{2m} \exp(2i\phi_2)}{1 + \mathcal{R}_{12} \mathcal{R}_{2m} \exp(2i\phi_2)}. \quad (1.78)$$

These recursive formulas require a numerical solution, which is precisely the task of the various sound propagation models described in Chaps. 3–7. While ray models typically use the plane-wave reflection coefficient as a descriptor of the bottom boundary conditions, wave models generally solve for the acoustic field in either a multilayered fluid or elastic structure.

## 1.7 Boundary and Volume Scattering

Scattering is a mechanism for loss, interference and fluctuation. A rough sea surface or seafloor causes attenuation of the mean acoustic field propagating in the ocean waveguide. The attenuation *increases* with increasing frequency. The field scattered away from the specular direction, and, in particular, the backscattered field (called reverberation) acts as interference for active sonar systems. Because the ocean surface moves, it will also generate acoustic fluctuations. Bottom roughness can also generate fluctuations when the sound source or receiver is moving. The importance of boundary roughness depends on the sound-speed profile which determines the degree of interaction of sound with the rough boundaries.

The scattering-theory literature is massive (see Ogilvy [38] for a review). Often the effect of scattering from a rough surface is thought of as simply an additional loss to the specularly reflected (coherent) component resulting from the scattering of energy away from the specular direction. If the ocean bottom or surface can be modeled as a randomly rough surface, and if the roughness is small with respect to the acoustic wavelength, the reflection loss can be considered to be modified in a simple fashion by the scattering process. A formula often used to describe reflectivity from a rough boundary is [36],

$$\mathcal{R}'(\theta) = \mathcal{R}(\theta) e^{-0.5 \Gamma^2}, \quad (1.79)$$

where  $\mathcal{R}'(\theta)$  is the new reflection coefficient, reduced because of scattering at the randomly rough interface.  $\Gamma$  is the Rayleigh roughness parameter defined as

$$\Gamma \equiv 2k\sigma \sin \theta, \quad (1.80)$$

where  $k = 2\pi/\lambda$  is the acoustic wavenumber and  $\sigma$  is the *rms* roughness. Note that the reflection coefficient for the smooth ocean surface is simply  $-1$  (the pressure-release condition is obtained from (1.56) by setting  $\rho_2 = 0$ ) so that the rough-sea-surface reflection coefficient for the coherent field is

$$\mathcal{R}'(\theta) = -e^{-0.5 \Gamma^2}. \quad (1.81)$$

For the ocean bottom, the appropriate geoacoustic parameters (see Table 1.3) are used for evaluating  $\mathcal{R}(\theta)$ , and the rough-bottom reflection coefficient is then obtained from (1.79).

As already mentioned, the coherent field is attenuated because of the generation of a scattered incoherent field, the latter often referred to as reverberation. This reverberant field is interference when one is concerned with receiving coherent waves for the purpose of processing signals.

The excitation of the scattered field is characterized by a *scattering cross section* which is defined as the ratio of the scattered power, referred to a unit distance, to the intensity incident on a unit area (or unit volume in the case of volume scattering).

Recall that power is the product of intensity and area so that a cross section is essentially an effective area which, when multiplied by the intensity of an incident field, gives the scattered power. In underwater acoustics, the surface (area) and volume scattering strength  $S_{s,v}$  has become the more conventional parameter of reverberation and it is defined as the ratio in decibels of the intensity of the sound scattered by a unit surface area or volume, referenced to a unit distance,  $I_{\text{scat}}$ , to the incident plane-wave intensity  $I_{\text{inc}}$ ,

$$S_{s,v} = 10 \log \frac{I_{\text{scat}}}{I_{\text{inc}}}. \quad (1.82)$$

Below we give empirical expressions for surface and bottom backscattering strengths, which have been employed with some success.

### 1.7.1 Surface Scattering

At the ocean surface, the Chapman–Harris curves [39] derived from measurements over the frequency range of 400–6400 Hz and wind speed up to 15 m/s, give the backscattering strength in decibels as

$$S_S = 3.3 \beta \log \frac{\theta}{30} - 42.4 \log \beta + 2.6 \quad \text{for} \quad \beta = 107 (wf^{1/3})^{-0.58}, \quad (1.83)$$

where  $\theta$  is the grazing angle in degrees,  $w$  the wind speed in m/s, and  $f$  the frequency in Hz.

More complete scattering models for the sea surface have been developed over recent years [40, 41]. These models include scattering due to surface roughness as well as a bubble layer when wave breaking takes place. The roughness contribution is composed of scattering from large-scale wave facets and scattering from small-scale roughness. The driving parameter is wind force, with bubble effects being dominant at low to moderate grazing angles and wind speeds above 3 m/s, and surface roughness being dominant at high grazing angles.

Representative results for monostatic scattering strength as a function of grazing angle and wind speed  $w$  are given in Fig. 1.27. The upper figure is based on the NRL model [40] and is computed for a frequency of 1.5 kHz. The lower figure is for a frequency of 25 kHz and is based on the APL–UW model [41]. With the proper choice of input parameters, both models have been shown to fit experimental data quite well. For comparison, the Chapman–Harris formula given by (1.83) has been plotted on both graphs for a wind speed  $w = 10$  m/s. This simplified formula performs well for grazing angles below 40–50°, but fails to account for the high-angle roughness effects. Note that the scattering strength generally increases with frequency, which is also apparent by comparing levels between Figs. 1.27a, b.

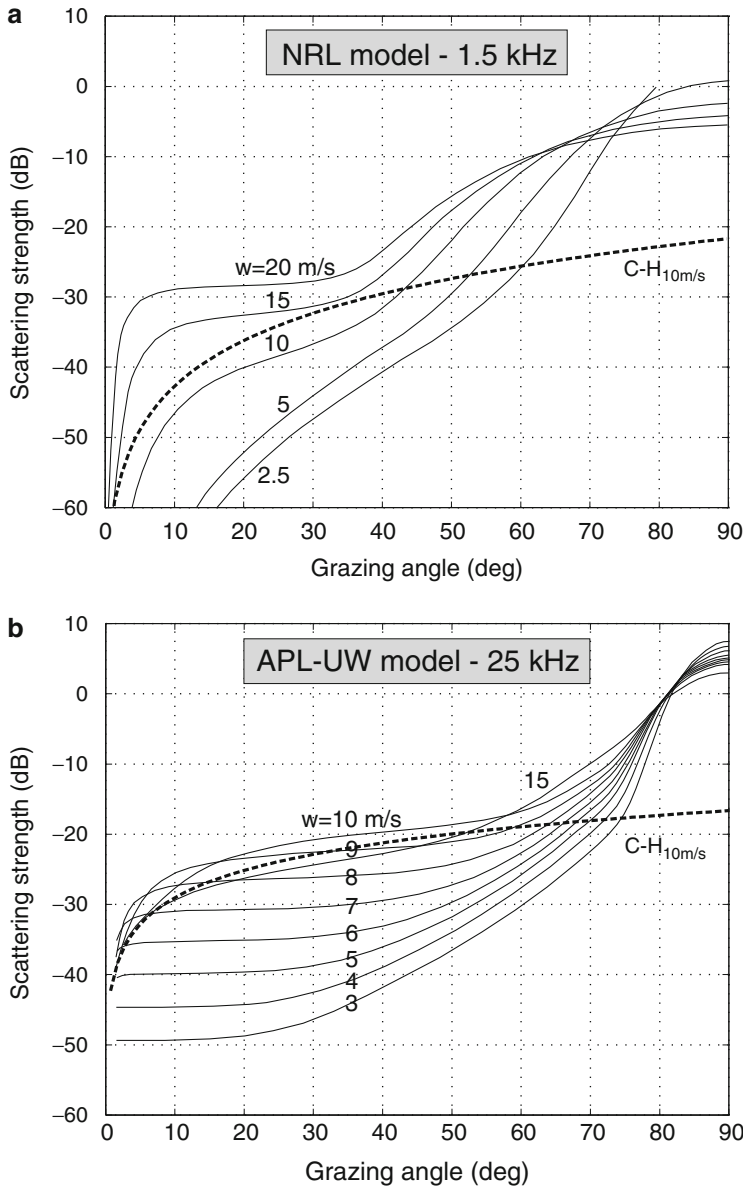


**Fig. 1.27** Monostatic backscattering strength at the sea surface as a function of wind speed.  
**(a)** The NRL model at 1.5 kHz. **(b)** The APL-UW model at 25 kHz

### 1.7.2 Bottom Scattering

At the ocean bottom, diffuse scattering described by *Lambert's law* together with an empirical scattering coefficient is used to estimate bottom scattering strengths from very rough ocean bottoms. Lambert's law states that the scattered power from a rough surface is proportional to  $\sin \phi$ , where  $\phi$  is the scattering angle. The incident power intercepted by the surface  $\delta A$  is proportional to the intensity  $I_{\text{inc}} \times \sin \theta \delta A$ . It then follows from Lambert's law that

$$I_{\text{scat}} \propto I_{\text{inc}} \sin \theta \sin \phi \delta A. \quad (1.84)$$

Next we apply (1.82) (per unit area) in the backscattered direction,  $\phi = \pi - \theta$ , to obtain the bottom backscattering strength,

$$S_B = -5 + 10 \log \sin^2 \theta, \quad (1.85)$$

where the first term,  $-5$  dB, is the proportionality constant arising from an assumption that all the incident energy is scattered and redistributed into the water column with no transmission into the bottom [3]. Often, the first term of (1.85) is empirically adjusted according to a measured scattering strength. For standard unconsolidated sediments ranging from silt to coarse sand, the first term in Lambert's law assumes values between  $-25$  and  $-35$  dB. An average value of  $-29$  dB is a popular first guess when estimating bottom backscattering with Lambert's law.

Physics-based models for scattering at a rough seabed have been developed both at NRL [40] and APL-UW [41]. These models assume that the surface roughness spectrum for a given bottom type is known together with the speeds ( $c_p$  and  $c_s$ ) and density of the bottom material. Moreover, the APL-UW model accounts for volume scattering within the sediments.

Representative results for monostatic scattering strength as a function of grazing angle and bottom type are given in Fig. 1.28. The upper figure is based on the NRL model [40] and is computed for a frequency of 3 kHz. The lower figure is for a frequency of 30 kHz and is based on the APL-UW model [41] which ignores shear in the bottom. With the proper choice of input parameters, both models have been shown to fit experimental data quite well. The geoacoustic parameters used for computing the bottom scattering curves are similar to those given in Table 1.3. In addition, representative roughness spectra must be associated with each bottom type.

For comparison, also Lambert's law with the first term equal to  $-29$  dB is shown in Fig. 1.28b. It is clear that this simple law provides a quite good fit to the high-frequency scattering strength curves for grazing angles up to  $60$ – $70$ °, with the proper choice of the proportionality constant.

### 1.7.3 Volume Scattering

In Sect. 1.5.2, we quantitatively summarized the frequency dependence of volume attenuation which is partly caused by scattering. This scattering also produces a

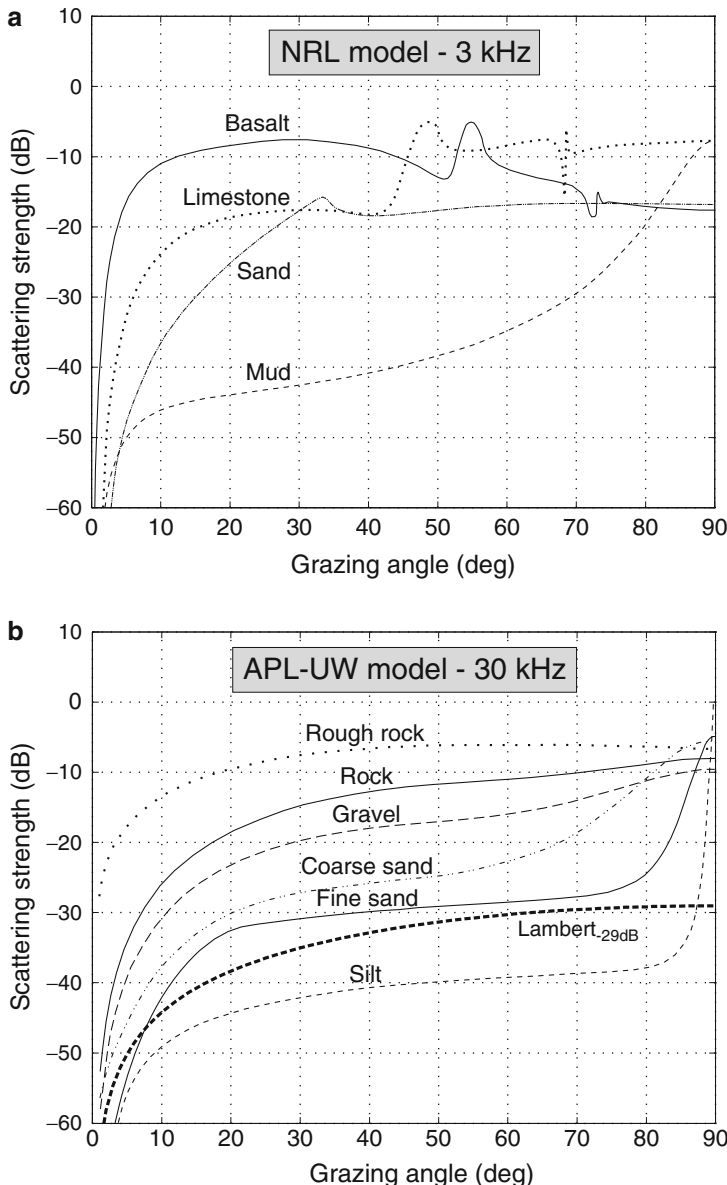


**Fig. 1.28** Monostatic backscattering strength at the bottom as a function of bottom type. **(a)** The NRL model at 3.0 kHz. **(b)** The APL–UW model at 30 kHz

backscattered or reverberant acoustic field. However, most volume reverberation is thought to arise from biological organisms. A quantity often used to describe volume backscattering is *column strength*. Returning to the discussion preceding (1.82),

a surface (area) scattering strength can be related to a local volume scattering strength  $s_v(z)$  at depth  $z$ ,

$$S_s = 10 \log \int_0^H s_v(z) dz = S_v + 10 \log H, \quad (1.86)$$

where  $S_v$  is an average volume backscattering strength and  $H$  is a layer thickness in consistent units. When  $H$  is made the size of a water column,  $S_s \equiv S_c$  is called the column, or integrated, scattering strength.

In general, volume scattering decreases with increasing depth (about 5 dB per 300 m) with the exception of the *deep scattering layer*. For lower frequencies (less than 10 kHz), fish with air-filled swim bladders are the main scatterers whereas above 20 kHz, zooplankton or smaller animals that feed upon the phytoplankton, and the associated biological chain, are the scatterers. The depth of the deep scattering layer varies throughout the day, being deeper in the day than at night and changing most rapidly during sunset and sunrise. This layer produces a strong scattering increase of 5–15 dB within 100 m of the surface at night, and virtually no scattering in the daytime at the surface since it can migrate down to a depth of about 200–900 m at mid-latitudes. Typical scattering results for the integral in (1.86) are shown Fig. 1.29. The difference in day and night spectra of column scattering strength is

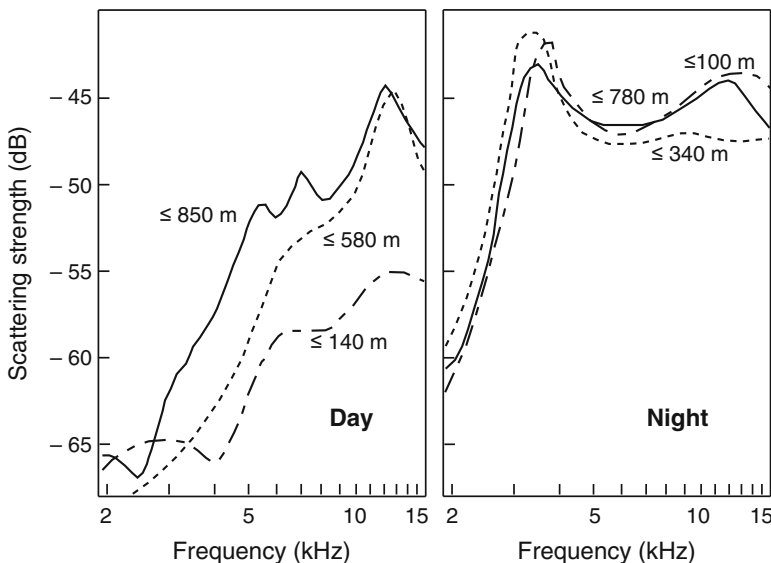


**Fig. 1.29** Day and night scattering strengths measurements using an explosive source (from Chapman and Marshall [42])

thought to arise from the lower hydrostatic pressure nearer the ocean surface which tends to reduce the resonance frequency of the swim bladders and, hence, move the spectral peak to lower frequencies at night.

Finally, scattering off bubbles near the surface is sometimes referred to as either a volume or surface scattering mechanism. These bubbles arise not only from sea surface action, but also from biological origins and from ship wakes. Furthermore, bubbles are not the only scattering mechanism, but bubble clouds may have significantly different sound speed than plain seawater thereby altering local refraction conditions. At the sea surface, the relative importance of roughness versus bubble effects is not yet resolved.

## 1.8 Ambient Noise

In underwater acoustics, ambient noise traditionally becomes an issue when it masks a signal of interest. Ocean acoustic signal processing (Chap. 10) is essentially a procedure for extracting a signal embedded in noise. The noise is irrelevant if the signal is very strong. However, the more interesting case is the marginal situation of low signal-to-noise ratio ( $S/N < 1$ ). Here, we would like to exploit the difference in the physical properties of the signal of interest and the noise to be rejected. For instance, omni-directional noise can be reduced by a directional receiver with narrow “look directions” (beams), while directional noise can be avoided by not looking in the direction of the noise. The more general case of achieving *noise gain*, i.e., enhancement of signal-to-noise ratio, is to somehow factor into the design of a receiving system knowledge of the general distribution of the ambient noise, including its coherence properties. In this section, we describe some of the properties of ocean ambient noise, with emphasis on its spectral character. In Chap. 9, we discuss the relevant acoustic theory which has application to modeling the spatial distribution of noise.

In addition to considering noise as a nuisance field, it has been recently recognized that noise also contains environmental information so that extracting this *environmental signal* from ambient noise has also become an interesting pursuit. Section 9.3 also discusses the nature of this embedded information in ambient noise while Sect. 10.4.3 describes one a specific application of extracting bathymetry information from noise.

There are two types of noise: man-made and natural, with the former increasing in level over the last few decades [43, 44]. The man-made noise primarily consists of shipping noise, though noise from offshore rigs is becoming more prevalent. In general, natural noise dominates at low frequencies ( $<10\text{ Hz}$ ) and at high frequencies ( $>300\text{ Hz}$ ) while shipping noise dominates in the intermediate region from 10 to 300 Hz. The field of ambient noise is reviewed rather extensively in [43, 45, 46], the latter being a series of reviews and research papers on natural mechanisms of sea noise. A summary of the spectrum of noise is shown in Fig. 1.30.

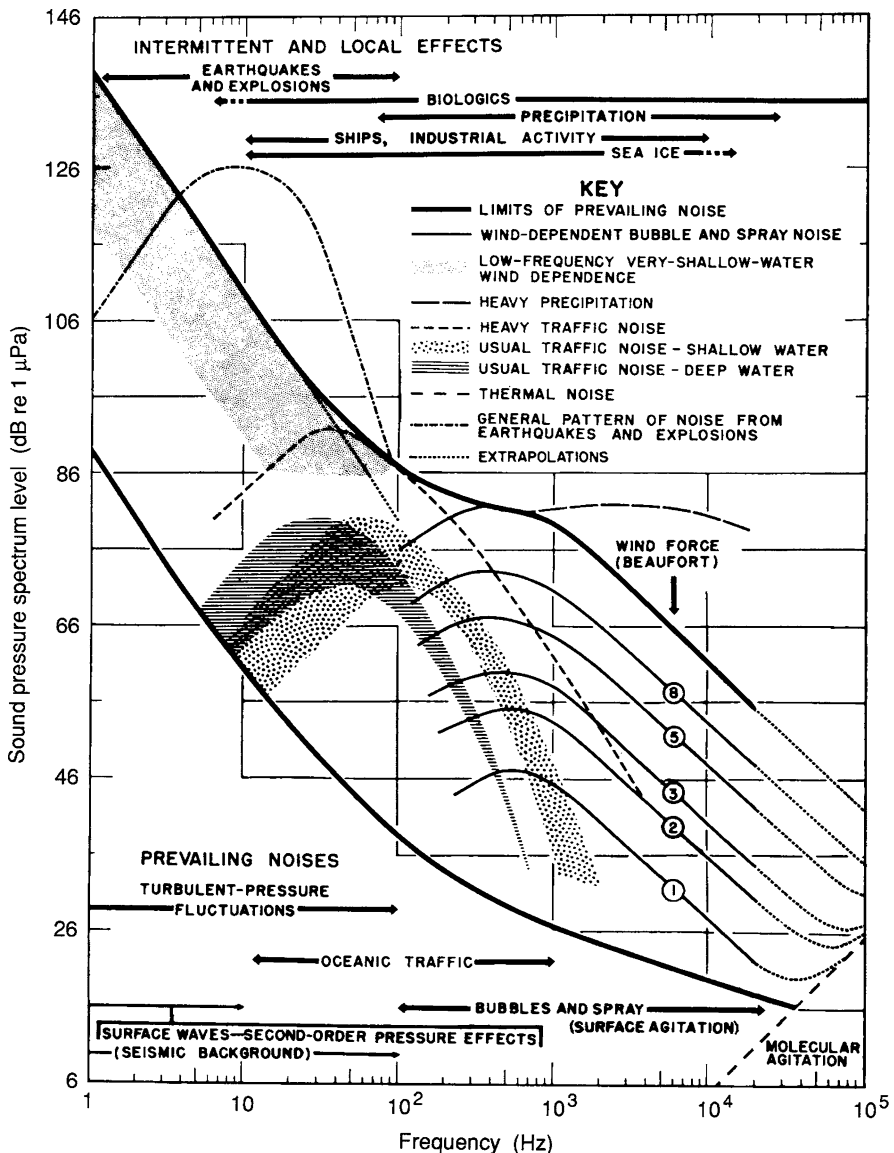


Fig. 1.30 Composite of ambient noise spectra (from Wenz [47])

The higher-frequency wind noise is usually parameterized according to sea state (also Beaufort Number) or wind force. The relationship between sea state, wind, and wave height is summarized in Table 1.6.

**Table 1.6** Descriptors of the ocean sea surface (from Wenz [47])

Sea criteria	Wind speed	12-h wind			Fully arisen sea			Sea-state scale
		Beaufort scale	Range knots (m/s)	Mean knots (m/s)	Wave height $t^{a,b}$ ft (m)	Duration $t^{a,c}$ (h)	Fetch $b^{c}$ naut. miles (km)	
Mirror-like	0	<1	(<0.5)	(1.1)	<1	<1	<10	0
Ripples	1	1–3	(0.5–1.7)	5	(<0.30)	<2.5	(<19)	$\frac{1}{2}$
Small wavelets	2	4–6	(1.8–3.3)	(2.5)	1–2	1–2	2.5–6.5	1
Large wavelets, scattered whitecaps	3	7–10	8 $\frac{1}{2}$	(4.4)	(0.30–0.61)	2–6	10–40	2
Small wavelets, frequent whitecaps	4	11–16	13 $\frac{1}{2}$	(5.5–8.4)	(0.61–1.5)	(0.61–1.8)	(19–74)	3
Moderate waves, many whitecaps	5	17–21	19	(8.5–11.1)	5–8	6–10	40–100	4
Large waves, whitecaps everywhere, spray	6	22–27	24 $\frac{1}{2}$	(11.2–14.1)	(12.6)	(1.5–2.4)	(74–185)	5
Heaped-up sea, blown spray streaks	7	28–33	30 $\frac{1}{2}$	(14.2–17.2)	(2.4–3.7)	8–12	10–17	11–18
Moderately high, long waves, spindrift	8	34–40	37	(17.3–20.8)	(15.7)	12–17	17–26	18–29
				(19.0)	(3.7–5.2)	(5.2–7.9)	(370–740)	200–400
					17–24	26–39	29–42	400–700
					(5.2–7.3)	(7.9–11.9)	(740–1300)	6
								7

<sup>a</sup>The average height of the highest one-third of the waves (significant wave height)<sup>b</sup>Estimated from data given in US Navy Hydrographic Office (Washington, DC) publication HO 604 (1951) and HO 603 (1955)<sup>c</sup>The minimum fetch and duration of the wind needed to generate a fully arisen sea

## 1.9 Sound Propagation Models

Much of this book is concerned with incorporating the phenomena described in this chapter into a theoretical and numerical formalism which will be quantitatively predictive for arbitrary ocean environments. Sound propagation in the ocean is mathematically described by the wave equation, whose parameters and boundary conditions are descriptive of the ocean environment. As schematically shown in Fig. 1.31, there are essentially five types of models (computer solutions to the wave equation) to describe sound propagation in the sea: Spectral or “fast field program” (FFP), normal mode (NM), ray, and parabolic equation (PE) models, and direct finite-difference (FD), or finite-element (FE) solutions of the full wave equation. All of these models permit the ocean environment to vary with depth. A model that also permits horizontal variations in the environment, i.e., sloping bottom or spatially variable oceanography, is termed *range dependent*.

As shown in Fig. 1.31, an a priori assumption about the environment being range independent, leads to solutions based on spectral techniques (FFP) or normal modes (NM); both of these techniques can, however, be extended to treat range dependence. While the coupled FFP solution is not dealt with in this book, extended modal solutions in terms of coupled or adiabatic modes are described in detail. Ray, PE, and FD/FE solutions are applied directly to range varying environments. For high frequencies (few kilohertz or above), ray theory, the infinite-frequency approximation, is still the most practical, whereas the other four model types become more and more applicable below, say, a kilohertz.

Acoustic modeling techniques in the frequency domain will be described in detail in Chaps. 3–7, whereas time-domain modeling will be addressed in Chap. 8. The last part of the book is dedicated to the application of these modeling techniques to the problems of ambient noise in the ocean (Chap. 9) and the extraction of signals from noise based on spatial processing (Chap. 10).

A final note: This book is not concerned with particular computer implementations of the various solution techniques listed above, but rather aims at presenting

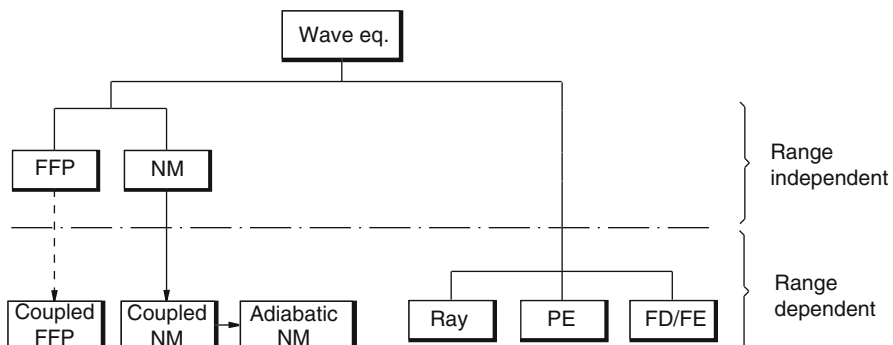


**Fig. 1.31** Hierarchy of underwater acoustic models

the theoretical basis for the various techniques in a consistent and interrelated fashion. An overview of the many computer models in use in the underwater acoustics community may be found in the book by Etter [48].

## Problems

**1.1.** In a deep ocean with constant salinity 3.5% the water temperature distribution is assumed to be exponential in depth,

$$T = T_0 \exp(-z/500),$$

where  $T$  and  $T_0$  are in degrees Celsius, and  $z$  is in meters.

- a. What is the minimum surface water temperature for which a deep sound channel (SOFAR) will exist?
- b. Determine the depth of the channel axis and the associated sound speed as function of the surface temperature.

**1.2.** Consider a 4000-m deep ocean with constant salinity 3.5%. The water temperature distribution is assumed to be exponential in depth,

$$T = 10 \exp(-z/500),$$

where  $T$  is in degrees Celsius, and  $z$  is in meters.

- a. At approximately which latitude would you expect to find such an environment?
- b. For a source at 100 m depth, discuss the existence of the various ray paths (RR, RSR, RBR and SRBR) in this environment.
- c. What is the surface temperature for which no pure RSR and RBR paths exist?

**1.3.** In air acoustics, the conventional reference for decibels is dB re 0.0002 dyn/cm<sup>2</sup> as opposed to dB re 1 μPa used in ocean acoustics.

- a. A human whisper and shout have acoustics powers of about  $10^{-10}$  and  $10^{-5}$  watts, respectively. Express their dB levels using both conventions. What would be the dB levels if the whole world shouted at once (in the same place)? Compare that to a jet or rocket in air or various types of ships in water.
- b. If a rock band played at the pain threshold, of about 140 dB, what is its power output in watts. What is its corresponding sound pressure level in water?
- c. For a 120-dB source in water (measured one meter from the source), what would its dB level be at ranges 1, 10, and 100 km assuming spherical spreading; cylindrical spreading? The loudest whales have source levels of about 190 dB. Compare this to a rock band.

**1.4.** An omni-directional source of frequency  $f$  is placed at a distance  $z_s$  from an infinitely rigid wall bounding a fluid halfspace with constant sound speed  $c$ .

- Describe the radiation pattern in the limit of  $z_s \rightarrow 0$ .
- Derive the expression for the number of *Lloyd-mirror* beams.
- Derive the asymptotic field decay parallel to the wall, and compare to the corresponding pressure-release surface result.

**1.5.** Estimate the convergence zone (CZ) separation for an Arctic environment with the sound speed profile given below. Assume linear sound speed variation between the profile depths.

Depth (m)	Sound speed (m/s)
0	1438.0
300	1460.0
4000	1519.2

**1.6.** Write a program for computing and displaying the magnitude and phase of the reflection and transmission coefficients for the interface separating two fluid halfspaces.

- Use your code to illustrate the concept of a *critical angle* by properly choosing the sound speeds and densities.
- For grazing angles of incidence smaller and larger than critical, discuss the depth-dependence (direction perpendicular to the interface) of the reflected and transmitted fields.
- Discuss the behavior of the phase of the reflection coefficient for incident grazing angles less than and larger than critical.
- Create an example illustrating the concept of an *intromission angle*.

**1.7.** Derive the expression for the reflection coefficient for a fluid layer overlying an infinitely rigid halfspace. Give a physical explanation for the frequency and grazing angle dependence of the magnitude and phase.

## References

1. G. Gamow, *The Great Physicists from Galileo to Einstein* (Harper and Brothers, New York, 1961)
2. R.B. Lindsay (ed.), *Acoustics: History and Philosophical Developments* (Dowden, Hutchinson and Ross, Inc., Stroudsburg, PA, 1972)
3. R.J. Urick, *Principles of Underwater Sound*, 3rd edn. (McGraw-Hill, New York, 1983)
4. M. Lasky, Review of undersea acoustics to 1950. J. Acoust. Soc. Am. **61**, 283–297 (1977)
5. A.D. Pierce, *Acoustics: An Introduction to Its Physical Principles and Applications* (American Institute of Physics, New York, 1989)
6. H. Medwin, C.S. Clay, *Fundamentals of Acoustical Oceanography* (Academic, San Diego, 1997)

7. V.A. Del Grosso, New equations for the speed of sound in natural waters (with comparisons to other equations). *J. Acoust. Soc. Am.* **56**, 1084–1091 (1974)
8. J.L. Spiesberger, K. Metzger, A new algorithm for sound speed in seawater. *J. Acoust. Soc. Am.* **89**, 2677–2688 (1991)
9. B.D. Dushaw, P.F. Worcester, B.D. Cornuelle, B.M. Howe, On equations for the speed of sound in seawater. *J. Acoust. Soc. Am.* **93**, 255–275 (1993)
10. J. Northrup, J.G. Colborn, Sofar channel axial sound speed and depth in the Atlantic Ocean. *J. Geophys. Res.* **79**, 5633–5641 (1974)
11. J. Sellschopp, Towed thermistor chain data collected during the cruise NORDMEER 87. Rep. FWG-87-4. (Forschungsanstalt der Bundeswehr für Wasserstraßen- und Geophysik, Kiel, Germany, 1987)
12. S.M. Flatté, Wave propagation through random media: Contributions from ocean acoustics. *Proc. IEEE* **71**, 1267–1294 (1983)
13. T.G. Leighton, *The Acoustic Bubble* (Academic, London, 1994)
14. O.B. Wilson, *Introduction to Theory and Design of Sonar Transducers* (Naval Sea Systems Command, Washington, DC, 1985)
15. H.G. Urban, *Handbook of Underwater Acoustic Engineering* (STN ATLAS Elektronik GmbH, Bremen, 2002)
16. P.J. Westervelt, Parametric acoustic arrays. *J. Acoust. Soc. Am.* **35**, 535–537 (1963)
17. B.K. Novikov, O.V. Rudenko, V.I. Timoshenko, *Nonlinear Underwater Acoustics* (American Institute of Physics, New York, 1987)
18. K. Naugolnykh, L. Ostrovsky, *Nonlinear Wave Processes in Acoustics* (Cambridge University Press, Cambridge, 1998)
19. A. Nehorai, E. Paldi, Acoustic vector sensor array processing. *IEEE Trans. Signal Proc.* **42**, 2481–2491 (1994)
20. M.J. Berliner, J.F. Lindberg, *Acoustic Particle Velocity Sensors: Design, Performance and Applications* (American Institute of Physics, New York, 1996)
21. G.L. D'Spain, J.C. Luby, G.R. Wilson, R.A. Gramann, Vector sensors and vector sensor line arrays: Comments on optimal array gain and detection. *J. Acoust. Soc. Am.* **120**, 171–185 (2006)
22. F.E. Hale, Long-range sound propagation in the deep ocean. *J. Acoust. Soc. Am.* **33**, 456–464 (1961)
23. I. Tolstoy, C.S. Clay, *Ocean Acoustics: Theory and Experiment in Underwater Sound* (American Institute of Physics, New York, 1987)
24. W.M. Ewing, J.L. Worzel, Long-range sound transmission. *Geol. Soc. Am. Mem.* **27** (1948)
25. R.J. Urick, *Sound Propagation in the Sea* (Defense Advanced Research Projects Agency, Washington, DC, 1979)
26. F.B. Jensen, Excess attenuation in low-frequency shallow-water acoustics: A shear wave effect? in *Shear Waves in Marine Sediments*, ed. by J.M. Hovem, M.D. Richardson, R.D. Stoll (Kluwer, Dordrecht, The Netherlands, 1991), pp. 421–430
27. F.B. Jensen, W.A. Kuperman, Optimum frequency of propagation in shallow water environments. *J. Acoust. Soc. Am.* **73**, 813–819 (1983)
28. N.R. Chapman, G.R. Ebbeson, Acoustic shadowing by an isolated seamount. *J. Acoust. Soc. Am.* **73**, 1979–1984 (1983)
29. W.H. Thorp, Analytic description of the low-frequency attenuation coefficient. *J. Acoust. Soc. Am.* **42**, 270 (1967)
30. F.H. Fisher, V.P. Simmons, Sound absorption in sea water. *J. Acoust. Soc. Am.* **62**, 558–564 (1977)
31. R.E. Francois, G.R. Garrison, Sound absorption based on ocean measurements. Part II: Boric acid contribution and equation for total absorption. *J. Acoust. Soc. Am.* **72**, 1879–1890 (1982)
32. E.L. Hamilton, Geoacoustic modeling of the sea floor. *J. Acoust. Soc. Am.* **68**, 1313–1340 (1980)
33. E.L. Hamilton, Acoustic properties of sediments. in *Acoustics and Ocean Bottom*, ed. by A. Lara-Sáenz, C. Ranz-Guerra, C. Carbó-Fitó (C.S.I.C, Madrid, Spain, 1987), pp. 3–58

34. J. Zhou, X. Zhang, Low-frequency geoacoustic model for the effective properties of sandy sea bottoms. *J. Acoust. Soc. Am.* **125**, 2847–2866 (2009)
35. D.R. Jackson, M.D. Richardson, *High-Frequency Seafloor Acoustics* (Springer, New York, 2007)
36. L.M. Brekhovskikh, Yu. Lysanov, *Fundamentals of Ocean Acoustics*, 2nd edn. (Springer, Berlin, Germany, 1991)
37. L.M. Brekhovskikh, O.A. Godin, *Acoustics of Layered Media I* (Springer, Berlin, Germany, 1990)
38. J.A. Ogilvy, Wave scattering from rough surfaces. *Rep. Prog. Phys.* **50**, 1553–1608 (1987)
39. R.P. Chapman, J.H. Harris, Surface backscattering strengths measured with explosive sound sources. *J. Acoust. Soc. Am.* **34**, 1592–1597 (1962)
40. R.C. Gauss, R.F. Gragg, D. Wurmser, J.M. Fialkowski, R.W. Nero, Broadband models for predicting bistatic bottom, surface and volume scattering strengths. *Rep. NRL/FR/7100-02-10042* (Naval Research Laboratory, Washington, DC, 2002)
41. APL-UW high-frequency ocean environmental acoustics model handbook. *Rep. APL-UW TR 9407* (Applied Physics Laboratory, University of Washington, Seattle, WA, 1994)
42. R.P. Chapman, J.R. Marshall, Reverberation from deep scattering layers in the western North Atlantic. *J. Acoust. Soc. Am.* **40**, 405–411 (1966)
43. D. Ross, *Mechanics of Underwater Noise* (Pergamon, New York, 1976)
44. R.K. Andrew, B.M. Howe, J.A. Mercer, M.A. Dzieciuch, Ocean ambient sound: Comparing the 1960s with the 1990s for a receiver off the California coast. *ARLO J. Acoust. Soc. Am.* **3**, 65–69 (2002)
45. R.J. Urick, *Ambient Sea Noise in the Ocean* (Naval Sea Systems Command, Washington, DC, 1984)
46. B.R. Kerman (ed.), *Sea Surface Sound: Natural Mechanisms of Surface Generated Noise in the Ocean* (Kluwer, Dordrecht, The Netherlands, 1988)
47. G.M. Wenz, Acoustic ambient noise in the ocean: Spectra and sources. *J. Acoust. Soc. Am.* **34**, 1936–1956 (1962)
48. P.C. Etter, *Underwater Acoustic Modeling and Simulation* (E & FN Spon, London, UK, 2003)

# Chapter 2

## Wave Propagation Theory

### 2.1 The Wave Equation

The wave equation in an ideal fluid can be derived from hydrodynamics and the adiabatic relation between pressure and density. The equation for conservation of mass, Euler's equation (Newton's second law), and the adiabatic equation of state are respectively

$$\frac{\partial \rho}{\partial t} = -\nabla \cdot \rho \mathbf{v}, \quad (2.1)$$

$$\frac{\partial \mathbf{v}}{\partial t} + (\mathbf{v} \cdot \nabla) \mathbf{v} = -\frac{1}{\rho} \nabla p(\rho), \quad (2.2)$$

$$p = p_0 + \rho' \left[ \frac{\partial p}{\partial \rho} \right]_S + \frac{1}{2} (\rho')^2 \left[ \frac{\partial^2 p}{\partial \rho^2} \right]_S + \dots \quad (2.3)$$

and for convenience we define the quantity

$$c^2 \equiv \left[ \frac{\partial p}{\partial \rho} \right]_S, \quad (2.4)$$

where  $c$  will turn out to be the speed of sound in an ideal fluid. In the above equations,  $\rho$  is the density,  $\mathbf{v}$  the particle velocity,  $p$  the pressure, and the subscript  $S$  denotes that the thermodynamic partial derivatives are taken at constant entropy. The ambient quantities of the quiescent (time independent) medium are identified by the subscript 0. We use small perturbations for the pressure and density,  $p = p_0 + p'$ ,  $\rho = \rho_0 + \rho'$ , and note that  $\mathbf{v}$  is also a small quantity; that is, the particle velocity which results from density and pressure perturbations is much smaller than the speed of sound.

### 2.1.1 The Nonlinear Wave Equation

Retaining higher-order terms in (2.1)–(2.3) yields a nonlinear wave equation. The nonlinear effects we include are contained in the quadratic density term in the equation of state, (2.3), and the quadratic velocity term (the convection term) in Euler's equation, (2.2). First multiply (2.2) by  $\rho$  and take its divergence; next, take the partial derivative of (2.1) with respect to time. Substituting one into the other yields

$$\frac{\partial^2 \rho}{\partial t^2} = \nabla^2 p + \partial_i \partial_j (\rho v_i v_j). \quad (2.5)$$

Here, the indices  $i, j = 1, 2, 3$  indicate  $x, y, z$ -components, respectively. Tensor notation is used; repeated indices signify a summation (e.g.,  $\partial_i v_i = \nabla \cdot \mathbf{v}$ ).

The first term on the right-hand side of (2.5) can be rewritten using (2.3) and (2.4) as

$$\nabla^2 p = \nabla^2 c^2 \left[ \rho' + \frac{1}{c} \frac{\partial c(\rho_0)}{\partial \rho} (\rho')^2 \right]. \quad (2.6)$$

The convection term on the right-hand side of (2.5) is more difficult to evaluate, but we can obtain an expression for it in the limit of small propagation angles  $\theta$  with respect to the main direction of propagation, e.g., the  $x$ -direction. (This is the same as the paraxial approximation for the parabolic wave equation discussed in Chap. 6.) Then we may estimate  $v_i$  using the linear impedance relation – to be later derived as (2.20) – together with the equation of state (2.3),

$$v_i = \frac{\rho' c}{\rho_0} [\delta_{i,x} + O(\theta)] + O(\rho'^2), \quad (2.7)$$

where  $\delta_{i,x}$  is the Kronecker delta symbol, so that

$$\partial_i \partial_j (\rho v_i v_j) \simeq \frac{1}{\rho_0} \nabla^2 c^2 (\rho')^2. \quad (2.8)$$

Substituting (2.6) and (2.8) into (2.5), we obtain the nonlinear wave equation

$$\frac{\partial^2 \chi}{\partial t^2} = \nabla^2 c^2 (\chi + \beta \chi^2) + O(\theta \chi^2, \chi^3) + \dots, \quad (2.9)$$

where  $\chi = \rho'/\rho_0$  is the density ratio and  $\beta = 1 + (\rho/c)[\partial c(\rho_0)/\partial \rho]$  the nonlinear parameter of the medium. We further discuss the nonlinear wave equation in Chap. 8, where we demonstrate its relationship to the parabolic equation and show how it can be used to solve problems directly in the time domain without resorting to Fourier synthesis.

## 2.1.2 The Linear Wave Equation

The linear approximations, which lead to the acoustic wave equation, involve retaining only first-order terms in the hydrodynamic equations [1, 2]. To lowest order, (2.1)–(2.4) become

$$\frac{\partial \rho'}{\partial t} = -\nabla \cdot (\rho_0 \mathbf{v}), \quad (2.10)$$

$$\frac{\partial \mathbf{v}}{\partial t} = -\frac{1}{\rho_0} \nabla p'(\rho), \quad (2.11)$$

$$\frac{\partial p'}{\partial t} = c^2 \left( \frac{\partial \rho'}{\partial t} + \mathbf{v} \cdot \nabla \rho_0 \right), \quad (2.12)$$

where we note that if  $\rho_0$  is constant, the last equation can also be written as

$$p' = \rho' c^2. \quad (2.13)$$

### 2.1.2.1 Wave Equation for Pressure

Considering that the time scale of oceanographic changes is much longer than the time scale of acoustic propagation, we will assume that the material properties  $\rho_0$  and  $c^2$  are independent of time. Then, take the partial derivative of (2.10) with respect to time and the divergence of (2.11); next, interchange the derivative operations and use (2.12) to obtain a wave equation for pressure,

$$\rho \nabla \cdot \left( \frac{1}{\rho} \nabla p \right) - \frac{1}{c^2} \frac{\partial^2 p}{\partial t^2} = 0, \quad (2.14)$$

where we have omitted the primes for pressure and density perturbations. If the density is constant in space, (2.14) can be replaced by the standard form of the wave equation,

$$\nabla^2 p - \frac{1}{c^2} \frac{\partial^2 p}{\partial t^2} = 0. \quad (2.15)$$

Using (2.12), the exact same equations for the density perturbation are obtained. Note that the appearance of  $c$  in the wave equation identifies it as the speed of sound, i.e., the speed of the propagating wave.

### 2.1.2.2 Wave Equation for Particle Velocity

Alternatively, we can take the divergence of (2.10) and the time derivative of (2.11), and combine the two using (2.12) to arrive at the wave equation for the particle velocity

$$\frac{1}{\rho} \nabla \left( \rho c^2 \nabla \cdot \mathbf{v} \right) - \frac{\partial^2 \mathbf{v}}{\partial t^2} = \mathbf{0}. \quad (2.16)$$

This form of the wave equation is a vector equation coupling the three spatial components of the particle velocity. It involves spatial derivatives of both density and sound speed, and is therefore rarely used, except for uni-axial propagation problems.

### 2.1.2.3 Wave Equation for Velocity Potential

If the density is constant or slowly varying, the vector equation (2.16) can be transformed into a simple scalar wave equation by introducing the velocity potential  $\phi$ , defined by

$$\mathbf{v} = \nabla\phi. \quad (2.17)$$

Substituting (2.17) together with the constant density condition  $\nabla\rho = \mathbf{0}$ , into (2.16), the latter takes the form

$$\nabla \left( c^2 \nabla^2 \phi - \frac{\partial^2 \phi}{\partial t^2} \right) = \mathbf{0}. \quad (2.18)$$

This equation is clearly satisfied if  $\phi$  satisfies the simple wave equation

$$\nabla^2 \phi - \frac{1}{c^2} \frac{\partial^2 \phi}{\partial t^2} = 0, \quad (2.19)$$

which is identical to the pressure wave equation, (2.15). Both equations are valid for varying sound speed, but for constant density only.

We note that there is a simple relationship between velocity and pressure for plane-wave solutions to the wave equation. This *impedance relation* is easily found using the velocity potential form of the wave equation with the solution  $\phi = f(x - ct)$ . From (2.17),  $v_x = \partial\phi/\partial x = f'(x - ct)$ , and from the linearized Euler equation (2.11),  $p = -\rho \partial\phi/\partial t = \rho_0 c f'(x - ct)$ , where  $f'$  denotes a derivative with respect to the argument of the function  $f$ . Comparing the pressure and velocity expressions yields the plane-wave impedance relation,

$$\frac{p}{v_x} = \rho_0 c. \quad (2.20)$$

### 2.1.2.4 Wave Equation for Displacement Potential

By using the kinematic relation between velocity and displacement  $\mathbf{v} = \partial\mathbf{u}/\partial t$ , it is easily shown that the displacement potential  $\psi$ , defined by

$$\mathbf{u} = \nabla\psi \quad (2.21)$$

is governed by a simple wave equation as well,

$$\nabla^2 \psi - \frac{1}{c^2} \frac{\partial^2 \psi}{\partial t^2} = 0. \quad (2.22)$$

As was the case for the other wave equations (2.15) and (2.19), also (2.22) is valid only for media with constant density. However, discrete changes in density can be handled through appropriate boundary conditions between regions of constant density. For such problems the boundary conditions require continuity of pressure and displacement (or velocity), and the potentials become discontinuous.

From the kinematic relations between displacements and velocities, (2.10), (2.12), and (2.21), we obtain the following expression for the acoustic pressure in terms of the displacement potential,

$$p = -K \nabla^2 \psi \quad (2.23)$$

with  $K$  being the *bulk modulus*,

$$K = \rho c^2. \quad (2.24)$$

Equation (2.23) is the constitutive equation for an ideal, linearly elastic fluid (*Hooke's law*). Combination of (2.22)–(2.24), yields the alternative expression for the acoustic pressure,

$$p = -\rho \frac{\partial^2 \psi}{\partial t^2}. \quad (2.25)$$

### 2.1.2.5 Source Representation

Underwater sound is produced by natural or artificial phenomena through forced mass injection. Such forcing terms were neglected in the mass conservation equation (2.10), and therefore also in the derived wave equations. However, such terms are easily included, leading to inhomogeneous wave equations, e.g., for the displacement potential

$$\nabla^2 \psi - c^{-2} \frac{\partial^2 \psi}{\partial t^2} = f(\mathbf{r}, t), \quad (2.26)$$

where  $f(\mathbf{r}, t)$  represents the volume injection as a function of space and time. Similar inhomogeneous forms of the wave equations for pressure or velocity are easily derived. In Sect. 2.3.2, we derive the expression for the forcing term corresponding to a simple point source.

### 2.1.2.6 Solution of the Wave Equation

The numerical methods described in Chaps. 3–7 all attempt to solve (2.26), or the equivalent pressure or velocity potential equations, with associated boundary and

radiation conditions. The major difference between the various techniques is the mathematical manipulation of (2.26) being applied before actual implementation of the solution. Another difference is the form of the wave equation used. Density changes in the stratified ocean are primarily of discrete nature, e.g., at the seabed and between layers in the bottom, whereas the density in the water column is virtually constant. Therefore, the simpler equations are usually used in numerical solutions which easily handle internal boundary conditions. On the other hand, some numerical methods treat internal discontinuities as smooth transitions, and such methods should clearly be based on (2.14).

The most direct approach is the *Finite Difference Method* (FDM), which directly discretizes (2.26) in space and time through approximations of the differential operators. This solution technique is described in Sect. 7.3.

The *Finite Element Method* (FEM) instead discretizes the medium and time into small blocks within which (2.26) can be solved analytically in terms of a selected set of degrees-of-freedom. The connectivity between the elements then leads to a linear system of equations in the degrees-of-freedom to be solved. Details on the FEM solution technique is given in Sect. 7.4.

In spite of the generality of direct, discrete methods such as FDM and FEM, their importance in ocean acoustics is rather limited due to excessive computational requirement. Thus, the FDM/FEM methods all require discretization of the acoustic field to a small fraction of a wavelength, and realistic propagation problems involve distances of hundreds to thousands of wavelengths.

The alternative numerical approaches described in Chaps. 3–6 are much more tractable in terms of numerical requirements and are therefore in more widespread use in the ocean acoustics community. However, the improved efficiency is obtained at the cost of generality. Thus, all these approaches are based on assumptions allowing for simplifying mathematical manipulations of the wave equation. These assumptions are identical to the ones applied in theoretical acoustics to obtain analytical solutions in one or more of the 4 dimensions (3 in space and 1 in time) of the total problem. All of the widespread numerical techniques could therefore, in fact, be considered hybrid analytical–numerical approaches, in contrast to the traditional terminology, where the two approaches are considered distinctly different. As an example, the Wavenumber Integration (WI) technique described in Chap. 4 only differs from analytical integral representations for propagation in a plane-parallel waveguide through the approach used to solve the system of linear equations in the unknown amplitudes, linked via the boundary conditions. The first uses a numerical equation solver, the latter pen and paper. In both cases, the final integral must be evaluated numerically.

In general, the numerical approaches applied in ocean acoustics today are based on important theoretical developments within the field of wave propagation over the past five decades, starting with the pioneering work on ocean waveguide theory by Pekeris [3]. Of particular importance are the various assumptions and approximations made in order to solve realistic propagation problems with the computer hardware at hand. For acousticians who consider applying one of the available numerical techniques, it is important to understand the limitations of the different techniques.

In the rest of this chapter, we therefore describe ocean-acoustic waveguide theory as it relates to the derivation of the numerical solution techniques. For a detailed description of the underlying theories, reference is made to the journal literature as well as the many textbooks devoted to the area of theoretical acoustics [2, 4–11].

## 2.2 The Helmholtz Equation

Since the coefficients to the two differential operators in (2.26) are independent of time, the dimension of the wave equation can be reduced to three by use of the frequency-time Fourier transform pair,

$$f(t) = \frac{1}{2\pi} \int_{-\infty}^{\infty} f(\omega) e^{-i\omega t} d\omega, \quad (2.27)$$

$$f(\omega) = \int_{-\infty}^{\infty} f(t) e^{i\omega t} dt \quad (2.28)$$

leading to the frequency-domain wave equation, or *Helmholtz equation*,

$$[\nabla^2 + k^2(\mathbf{r})] \psi(\mathbf{r}, \omega) = f(\mathbf{r}, \omega), \quad (2.29)$$

where  $k(\mathbf{r})$  is the medium wavenumber at radial frequency  $\omega$ ,

$$k(\mathbf{r}) = \frac{\omega}{c(\mathbf{r})}. \quad (2.30)$$

It should be pointed out that although the Helmholtz equation (2.29), due to the reduction in the dimension of this PDE, is simpler to solve than the full wave equation, (2.26), this simplification is achieved at the cost of having to evaluate the inverse Fourier transform, (2.27). However, many ocean acoustic applications are of narrow-band nature. The Helmholtz equation, rather than the wave equation, therefore forms the theoretical basis for the most important numerical methods, including the Wavenumber Integration (WI), Normal Mode (NM) and Parabolic Equation (PE) approaches, described in Chaps. 4, 5, and 6, respectively.

It is important to stress the difference between narrow-band processing in ocean acoustics and wide-band processing in seismics. The latter approach is viable because the length scale of the environmental features addressed in seismic experiments is of the same order of magnitude as the seismic wavelengths, and the time scales of the experiments are such that cross-spectral coherence can be assumed. In other words, seismic experiments are characterized by very few interactions with any single boundary, whereas a typical ocean acoustic experiment can have hundreds or thousands of interactions. This is basically the reason why time-domain approaches such as FDM and FEM have never gained widespread

popularity in ocean acoustics, whereas they are very important numerical analysis tools in the seismic community. There is, however, much virtue to time-domain solutions in terms of physical understanding, and time-domain solutions are produced routinely for exactly that purpose, both by Fourier synthesis and by direct time-domain solutions of the wave equation (see Chap. 8).

The environmental body forces such as gravity and magnetism are of no significance to acoustic propagation except for the effect of gravity on the sound speed variation in depth. The only body forces of importance are the acoustic sources, which include artificial sound generators as well as natural ones, e.g., noise generation at the sea surface and by marine animals. Since these sources are local in nature, most of the ocean environment is sourceless, with the wave field satisfying the homogeneous Helmholtz equation,

$$[\nabla^2 + k^2(\mathbf{r})] \psi(\mathbf{r}, \omega) = 0. \quad (2.31)$$

In spite of the relative simplicity of (2.31), there is no universal solution technique available. The actual solution technique that can be applied depends on the following factors:

- Dimensionality of the problem.
- Medium wavenumber variation  $k(\mathbf{r})$ , i.e., the sound speed variation  $c(\mathbf{r})$ .
- Boundary conditions.
- Source–receiver geometry.
- Frequency and bandwidth.

The Helmholtz equation (2.31) is a three-dimensional, elliptic partial differential equation, which can be solved either by analytical or numerical methods or by a combination of the two. The most convenient method is determined by the complexity of the *medium properties* and of the *boundary conditions* for the actual problem. Thus, for some problems the environment is so complex that only direct discrete methods such as FDM and FEM are applicable, whereas typical canonical problems are characterized by simple environmental models for which analytical methods are applicable. However, in general an optimum approach is a hybridization of analytical and numerical methods, and all the computational methods described in the following are of this category. Although these methods all have the Helmholtz equation as the starting point, they differ in the degree to which the analytical and numerical components are utilized in the solution scheme. Since the analytical methods are restricted to canonical problems with simple geometries, the computational methods with a large analytical component are therefore also restricted to problems where the actual environment is well represented by an idealized environmental model.

We here review the analytical approaches to the solution of the Helmholtz equation which, to various degrees, form the mathematical basis for the computational methods described in the next chapters. Further, we use these analytical methods to address the basic physics associated with propagation in the ocean waveguide.

## 2.3 Homogeneous Media

A very simple acoustic environment is that of a homogeneous medium with wavenumber  $k(\mathbf{r}) = k$ , occupying the volume  $V$  bounded by the surface  $S$ , shown in Fig. 2.1. In spite of the simplicity, this problem is well-suited to illustrate the basic principles of the solution of the Helmholtz equation.

### 2.3.1 Coordinate Systems

In a homogeneous medium, the homogeneous Helmholtz equation, (2.31), is easily solved, with a choice of coordinate system being imposed by the source and boundary geometry. Thus, if plane wave propagation is considered, a *Cartesian coordinate system*  $\mathbf{r} = (x, y, z)$  is the natural choice, with the Laplace operator,

$$\nabla^2 = \frac{\partial^2}{\partial x^2} + \frac{\partial^2}{\partial y^2} + \frac{\partial^2}{\partial z^2} \quad (2.32)$$

yielding plane wave solutions of the form

$$\psi(x, y, z) = \begin{cases} A e^{ik\mathbf{r}} \\ B e^{-ik\mathbf{r}}, \end{cases} \quad (2.33)$$

where  $\mathbf{k} = (k_x, k_y, k_z)$  is the wave vector and  $A$  and  $B$  are arbitrary amplitudes.

For a single plane-wave component, the coordinate system can be aligned with the propagation direction, e.g., with  $k_y, k_z = 0$ , yielding the simple solution

$$\psi(x) = \begin{cases} A e^{ikx} \\ B e^{-ikx}, \end{cases} \quad (2.34)$$

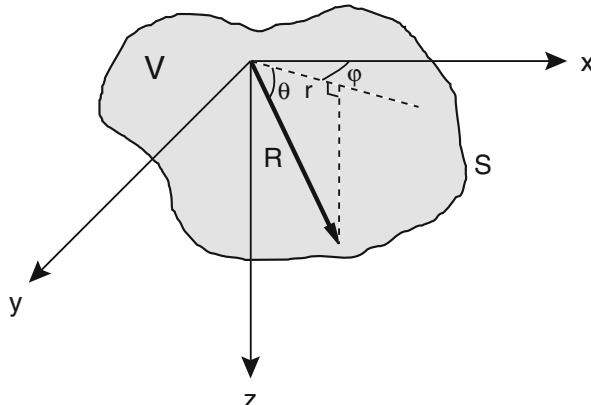


**Fig. 2.1** Homogeneous medium occupying the volume  $V$  bounded by the surface  $S$

which corresponds to a forward- and a backward-propagating plane wave solution with time dependence  $\exp(-i\omega t)$ .

Similarly, the field produced by an infinite, homogeneous line source is conveniently described in a *cylindrical coordinate system*  $\mathbf{r} = (r, \varphi, z)$ , with the  $z$ -axis coinciding with the source. Then, the field satisfies the homogeneous Helmholtz equation for  $r > 0$  with the Laplace operator,

$$\nabla^2 = \frac{1}{r} \frac{\partial}{\partial r} r \frac{\partial}{\partial r} + \frac{1}{r^2} \frac{\partial^2}{\partial \varphi^2} + \frac{\partial^2}{\partial z^2}. \quad (2.35)$$

For a uniform line source, the field only varies with range  $r$ , reducing the Helmholtz equation to the Bessel equation,

$$\left[ \frac{1}{r} \frac{\partial}{\partial r} r \frac{\partial}{\partial r} + k^2 \right] \psi(r) = 0 \quad (2.36)$$

with the solution

$$\psi(r) = \begin{cases} A J_0(kr) \\ B Y_0(kr) \end{cases} \quad (2.37)$$

or, in terms of Hankel functions,

$$\psi(r) = \begin{cases} C H_0^{(1)}(kr) = C [J_0(kr) + iY_0(kr)] \\ D H_0^{(2)}(kr) = D [J_0(kr) - iY_0(kr)]. \end{cases} \quad (2.38)$$

The latter form represents diverging and converging cylindrical waves for  $r \rightarrow \infty$ , as is clear from the asymptotic form of the Hankel functions for  $kr \rightarrow \infty$ ,

$$H_0^{(1)}(kr) \simeq \sqrt{\frac{2}{\pi kr}} e^{i(kr-\pi/4)}, \quad (2.39)$$

$$H_0^{(2)}(kr) \simeq \sqrt{\frac{2}{\pi kr}} e^{-i(kr-\pi/4)}. \quad (2.40)$$

These asymptotics also show that the cylindrically symmetric field produced by a line source decays in amplitude proportionally to  $r^{-1/2}$ . Approaching the source, the line source field exhibits a *logarithmic singularity*.

In the case of an omni-directional point source, the field only depends on the range from the source, and the solution is conveniently described in a *spherical coordinate system*, with the reduced Helmholtz equation being

$$\left[ \frac{1}{r^2} \frac{\partial}{\partial r} r^2 \frac{\partial}{\partial r} + k^2 \right] \psi(r) = 0, \quad (2.41)$$

which has the solutions

$$\psi(r) = \begin{cases} (A/r)e^{ikr} \\ (B/r)e^{-ikr}. \end{cases} \quad (2.42)$$

Again, these solutions correspond to diverging and converging spherical waves with the amplitude decaying proportional to  $r^{-1}$  in range.

The term *geometrical spreading loss* refers to these geometries. Thus, *cylindrical spreading loss* is proportional to  $r^{-1/2}$  and *spherical spreading loss* is proportional to  $r^{-1}$ .

### 2.3.2 Source in Unbounded Medium

The derivation of the field expression for an acoustic source in an unbounded medium is a simple example of how the solution of the homogeneous wave equation described above is combined with the boundary conditions to yield the solution to a particular problem.

Assume an acoustic field is produced in an infinite, homogeneous fluid by a small sphere of radius  $a$  (Fig. 2.2), with the surface displacement given as

$$u_r(t, a) = U(t). \quad (2.43)$$

In the homogeneous fluid, the field will be omni-directional, with the radial displacement

$$u_r = \frac{\partial \psi(r, t)}{\partial r}, \quad (2.44)$$

where the displacement potential  $\psi$  satisfies a homogeneous wave equation. By applying the Fourier transform to both the wave equation and the boundary condition at  $r = a$ , we obtain the Helmholtz equation (2.41) and the boundary condition,

$$u_r(a) = U(\omega). \quad (2.45)$$

The solution to the Helmholtz equation is a linear combination of the two independent solutions in (2.42), but since we assume the sphere is the only source in

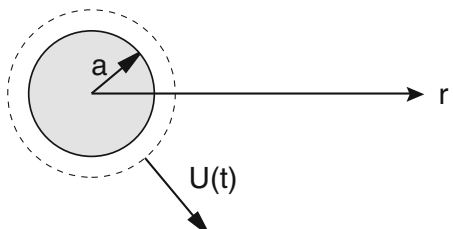


**Fig. 2.2** Vibrating sphere in an infinite fluid medium

the infinite medium, we can apply the *radiation condition* of no incoming waves at infinity to require that  $B = 0$ , i.e.,

$$\psi(r) = A \frac{e^{ikr}}{r} \quad (2.46)$$

with the corresponding displacement field given by (2.44) as

$$u_r(r) = A e^{ikr} \left( \frac{ik}{r} - \frac{1}{r^2} \right). \quad (2.47)$$

The amplitude  $A$  is now easily found from (2.45).

The *simple point source* corresponds to the case where the radius of the sphere is small compared to the acoustic wavelength, i.e.,  $ka \ll 1$ , in which case the expression for the surface displacement takes the form

$$u_r(\omega, a) = A e^{ika} \frac{ika - 1}{a^2} \simeq -\frac{A}{a^2} \quad (2.48)$$

yielding

$$A = -a^2 U(\omega). \quad (2.49)$$

Defining the *source strength*  $S_\omega = 4\pi a^2 U(\omega)$  as the volume-injection amplitude produced by the source at frequency  $\omega$ , we then obtain the solution for the field in the fluid,

$$\psi(r) = -S_\omega \frac{e^{ikr}}{4\pi r}. \quad (2.50)$$

The source strength  $S_\omega$  is of unit  $\text{m}^3$ , or volume. If we had based the derivation on velocity potentials, the source strength would be of unit  $\text{m}^3/\text{s}$ , representing volume rate.

The fraction in (2.50) is called the *Green's function*,

$$g_\omega(r, 0) = \frac{e^{ikr}}{4\pi r} \quad (2.51)$$

or, in general, for a source at  $\mathbf{r} = \mathbf{r}_0$ ,

$$g_\omega(\mathbf{r}, \mathbf{r}_0) = \frac{e^{ikR}}{4\pi R}, \quad R = |\mathbf{r} - \mathbf{r}_0|. \quad (2.52)$$

The Green's function satisfies the inhomogeneous Helmholtz equation,

$$[\nabla^2 + k^2] g_\omega(\mathbf{r}, \mathbf{r}_0) = -\delta(\mathbf{r} - \mathbf{r}_0), \quad (2.53)$$

which is easily verified by integrating (2.53) over a small volume containing the source point  $\mathbf{r}_0$ . The inhomogeneous Helmholtz equation for a simple point source of strength  $S_\omega$  at point  $\mathbf{r}_0$  is therefore,

$$[\nabla^2 + k^2] \psi(\omega, \mathbf{r}) = S_\omega \delta(\mathbf{r} - \mathbf{r}_0). \quad (2.54)$$

The Green's function of the time-domain wave equation is obtained by the Fourier transform of  $g_\omega$  as specified by (2.27),

$$g_t(\mathbf{r}, \mathbf{r}_0) = \frac{\delta(R/c - t)}{4\pi R} \quad (2.55)$$

and can be thought of as the impulse response in an unbounded medium. Note that the Green's function is symmetric in  $\mathbf{r}$  and  $\mathbf{r}_0$ ,

$$g_\omega(\mathbf{r}, \mathbf{r}_0) = g_\omega(\mathbf{r}_0, \mathbf{r}) \quad (2.56)$$

in accordance with the *principle of reciprocity* for the Green's function described in Appendix 1.

### 2.3.3 Source in Bounded Medium

Extending the analysis to a more realistic acoustic environment we next consider the problem illustrated in Fig. 2.3, where the medium occupies the volume  $V$  bounded by the surface  $S$ , with prescribed boundary conditions. An acoustic field is produced by a distribution of body forces  $f(\mathbf{r})$  within the volume  $V$ , and the displacement potential  $\psi(\mathbf{r})$  must, therefore, satisfy the inhomogeneous Helmholtz equation,

$$[\nabla^2 + k^2] \psi(\mathbf{r}) = f(\mathbf{r}). \quad (2.57)$$

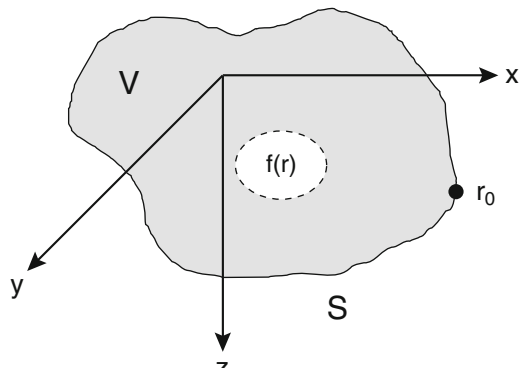


**Fig. 2.3** Sources in a volume  $V$  bounded by the surface  $S$

In the preceding section, we introduced the free-field Green's function  $g_\omega(\mathbf{r}, \mathbf{r}_0)$  satisfying (2.53). This was just a particular solution to (2.53) satisfying the radiation condition. In the case of a *boundary value problem*, we need the general solution of (2.53) which is a sum of a particular solution such as  $g_\omega(\mathbf{r}, \mathbf{r}_0)$  and a homogeneous solution  $H_\omega(\mathbf{r})$ , with the superposition of the two solutions satisfying the boundary conditions as well as the radiation conditions (for semi-infinite media).

We, therefore, introduce the *general Green's function* as

$$G_\omega(\mathbf{r}, \mathbf{r}_0) = g_\omega(\mathbf{r}, \mathbf{r}_0) + H_\omega(\mathbf{r}), \quad (2.58)$$

where  $H_\omega(\mathbf{r})$  is any function satisfying the homogeneous Helmholtz equation,

$$[\nabla^2 + k^2] H_\omega(\mathbf{r}) = 0. \quad (2.59)$$

The general Green's function then satisfies the same Helmholtz equation as  $g_\omega(\mathbf{r}, \mathbf{r}_0)$ ,

$$[\nabla^2 + k^2] G_\omega(\mathbf{r}, \mathbf{r}_0) = -\delta(\mathbf{r} - \mathbf{r}_0). \quad (2.60)$$

By multiplying (2.57) by  $G_\omega(\mathbf{r}, \mathbf{r}_0)$  and (2.60) by  $\psi(\mathbf{r})$  and subtracting the two, we obtain

$$G_\omega(\mathbf{r}, \mathbf{r}_0) \nabla^2 \psi(\mathbf{r}) - \psi(\mathbf{r}) \nabla^2 G_\omega(\mathbf{r}, \mathbf{r}_0) = \psi(\mathbf{r}) \delta(\mathbf{r} - \mathbf{r}_0) + G_\omega(\mathbf{r}, \mathbf{r}_0) f(\mathbf{r}). \quad (2.61)$$

Interchange of  $\mathbf{r}$  and  $\mathbf{r}_0$  followed by integration over the volume with respect to  $\mathbf{r}_0$  then yields

$$\begin{aligned} & \int_V [G_\omega(\mathbf{r}, \mathbf{r}_0) \nabla_0^2 \psi(\mathbf{r}_0) - \psi(\mathbf{r}_0) \nabla_0^2 G_\omega(\mathbf{r}, \mathbf{r}_0)] dV_0 \\ &= \int_V \psi(\mathbf{r}_0) \delta(\mathbf{r} - \mathbf{r}_0) dV_0 + \int_V f(\mathbf{r}_0) G_\omega(\mathbf{r}, \mathbf{r}_0) dV_0, \end{aligned} \quad (2.62)$$

where it has been assumed that the Green's function is symmetric, i.e.,  $G_\omega(\mathbf{r}, \mathbf{r}_0) = G_\omega(\mathbf{r}_0, \mathbf{r})$ . We will discuss this property in detail in Appendix 1. Using integration by parts (see Appendix 1), we now change the integration on the left-hand side to a surface integral and obtain,

$$\psi(\mathbf{r}) = \int_S \left[ G_\omega(\mathbf{r}, \mathbf{r}_0) \frac{\partial \psi(\mathbf{r}_0)}{\partial \mathbf{n}_0} - \psi(\mathbf{r}_0) \frac{\partial G_\omega(\mathbf{r}, \mathbf{r}_0)}{\partial \mathbf{n}_0} \right] dS_0 - \int_V f(\mathbf{r}_0) G_\omega(\mathbf{r}, \mathbf{r}_0) dV_0, \quad (2.63)$$

where  $\mathbf{n}_0$  is the outward-pointing normal on the surface. Equation (2.63) is *Green's theorem* for sources in a bounded medium. By letting the field points  $\mathbf{r}$  be on the boundary, (2.63) provides an integral equation, which should be solved for the field and its normal derivative at the boundary. Then (2.63) can be applied to provide the field at any point  $\mathbf{r}$  inside the volume  $V$ .

Green's theorem provides the most general formulation for acoustic boundary-value problems, but its use is highly dependent on the ability to solve the integral equation. Numerical solution can always be applied, but for some types of canonical problems, closed form analytical solutions are also possible. This is due to the fact that the general Green's function is arbitrary in the sense that the only requirements are that it must be symmetric and satisfy (2.60) everywhere within the volume  $V$ ; otherwise there are no requirements to the particular choice of the homogeneous solution  $H_\omega(\mathbf{r})$ . We can, therefore, choose a homogeneous solution which simplifies the solution of the integral equation. For example, choosing the homogeneous solution such that the Green's function vanishes on the boundary will remove half of the kernel of the surface integral in (2.63). For some problems, a Green's function can be found which satisfies the same boundary conditions as the field on parts of the boundary. In that case the two terms in the kernel of the surface integral are identical, eliminating the integral on that part of the boundary. Finally, it should be noted that the surface  $S$  does not have to coincide with the physical boundary; Green's theorem is valid for any volume containing the sources.

Green's theorem will be applied in Sect. 2.3.4 to solve a simple boundary value problem for which a well-known solution exists. However, we first apply it to derive a formal representation of the radiation condition which any field in an infinite medium must satisfy.

Let the surface  $S$  be a sphere centered at the receiver point  $\mathbf{r}$  and containing all areas of the medium where sources are present. Since the medium is infinite, the total field is obtained as an integral over all sources of the free-field Green's function, (2.52), times the source strengths, i.e., for general volume source distributions,

$$\psi(\mathbf{r}) = - \int_V f(\mathbf{r}_0) g_\omega(\mathbf{r}, \mathbf{r}_0) dV_0. \quad (2.64)$$

By comparing this expression with Green's theorem, (2.63), we find that the surface integral over the sphere must vanish,

$$\int_S \left[ g_\omega(\mathbf{r}, \mathbf{r}_0) \frac{\partial \psi(\mathbf{r}_0)}{\partial \mathbf{n}_0} - \psi(\mathbf{r}_0) \frac{\partial g_\omega(\mathbf{r}, \mathbf{r}_0)}{\partial \mathbf{n}_0} \right] dS_0 = 0. \quad (2.65)$$

With the radius of the sphere being  $R$ , we can then insert the free-field Green's function from (2.52) to yield for  $R \rightarrow \infty$

$$\int_S \frac{e^{ikR}}{4\pi R} \left[ \frac{\partial \psi(\mathbf{r}_0)}{\partial R} - ik \psi(\mathbf{r}_0) \right] dS_0 = 0. \quad (2.66)$$

Since the radius  $R$  of the circle is large but arbitrary, the integrand in (2.66) must decay more rapidly than  $R^{-2}$  to have the surface integral properly converge, which leads to the *radiation condition*,

$$R \left[ \frac{\partial}{\partial R} - ik \right] \psi(\mathbf{r}_0) \rightarrow 0, \quad R = |\mathbf{r} - \mathbf{r}_0| \rightarrow \infty. \quad (2.67)$$

### 2.3.4 Point Source in Fluid Halfspace

As an example of the use of Green's theorem to boundary value problems, we apply it to the simplest possible example of a bounded acoustic medium, which is the fluid halfspace shown in Fig. 2.4. The upper halfspace is assumed to be a vacuum, and the boundary condition to be satisfied by the field in the fluid halfspace therefore simply is that the pressure must vanish at the free surface ( $z = 0$ ). We have here introduced a Cartesian coordinate system with the origin on the surface and with the  $z$ -axis perpendicular to the surface. A simple point source is assumed to be placed at  $\mathbf{r}_s = (x_s, y_s, z_s)$ .

The pressure is derived from the displacement potential as

$$p(\mathbf{r}) = \rho \omega^2 \psi(\mathbf{r}) \quad (2.68)$$

and we can therefore replace the pressure-release boundary condition by the condition

$$\psi(\mathbf{r}_0) \equiv 0, \quad \mathbf{r}_0 = (x, y, 0). \quad (2.69)$$

The field in the fluid halfspace is determined by Green's theorem, (2.63), which upon insertion of the boundary conditions, (2.69), takes the form

$$\psi(\mathbf{r}) = \int_S G_\omega(\mathbf{r}, \mathbf{r}_0) \frac{\partial \psi(\mathbf{r}_0)}{\partial \mathbf{n}_0} dS_0 - \int_V f(\mathbf{r}_0) G_\omega(\mathbf{r}, \mathbf{r}_0) dV_0. \quad (2.70)$$

For a simple point source, (2.54) shows that the volume force term takes the form

$$f(\mathbf{r}_0) = S_\omega \delta(\mathbf{r}_0 - \mathbf{r}_s). \quad (2.71)$$

If, furthermore, we choose the general Green's function such that  $G_\omega(\mathbf{r}, \mathbf{r}_0) \equiv 0$  for  $\mathbf{r}_0 = (x, y, 0)$ , then (2.70) simply becomes

$$\psi(\mathbf{r}) = -S_\omega G_\omega(\mathbf{r}, \mathbf{r}_s). \quad (2.72)$$

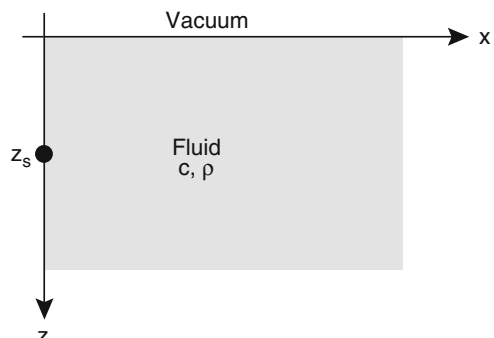


**Fig. 2.4** Point source in a fluid halfspace

For this simple case it is straightforward to choose a Green's function which vanishes on the free surface  $z = 0$ ,

$$\begin{aligned} G_\omega(\mathbf{r}, \mathbf{r}_0) &= g_\omega(\mathbf{r}, \mathbf{r}_0) + H_\omega(\mathbf{r}) \\ &= \frac{e^{ikR}}{4\pi R} - \frac{e^{ikR'}}{4\pi R'} \end{aligned} \quad (2.73)$$

with

$$R = \sqrt{(x - x_s)^2 + (y - y_s)^2 + (z - z_s)^2}, \quad (2.74)$$

$$R' = \sqrt{(x - x_s)^2 + (y - y_s)^2 + (z + z_s)^2}. \quad (2.75)$$

The solution for the displacement potential now takes the form

$$\psi(\mathbf{r}) = -S_\omega \left[ \frac{e^{ikR}}{4\pi R} - \frac{e^{ikR'}}{4\pi R'} \right], \quad (2.76)$$

which corresponds to the superposition of the free-space solutions for the source at depth  $z = z_s$  and an image source at  $z = -z_s$  in the vacuum halfspace. Thus, the solution obtained by Green's theorem is identical to the so-called *mirror* or *image method*, and the constructive and destructive interference of these two fields give rise to the well-known Lloyd-mirror pattern described in Sect. 1.4.2.

In general, an analytical solution is not easily obtained by Green's theorem. The critical issue is the determination of a Green's function which satisfies the same boundary conditions as the displacement potential on the boundary, thus eliminating the surface integral entirely. This is straightforward for problems with simple boundary geometry and homogeneous boundary conditions, as was the case in the halfspace problem. For heterogeneous media with simple boundary geometry but inhomogeneous boundary conditions, other approaches such as those described in the following sections are more feasible.

The generality of Green's theorem, on the other hand, makes it applicable to problems with complex boundary geometry, where it can be used to formulate an integral equation which can be solved numerically. Here, the numerical implementation via the Boundary Element Method (BEM) is extremely powerful for radiation and scattering problems, and it has become an increasingly popular numerical approach in structural acoustics, seismology, and recently, to some degree, also in ocean acoustics (Sect. 7.5).

### 2.3.5 Transmission Loss

In underwater acoustics, the field is traditionally expressed in terms of *transmission loss*, defined as

$$TL(\mathbf{r}, \mathbf{r}_s) = -10 \log \frac{I(\mathbf{r}, \mathbf{r}_s)}{I_0(\mathbf{r}_s)} = -10 \log \left( \frac{Z_0(\mathbf{r}_s)}{Z(\mathbf{r}, \mathbf{r}_s)} \left| \frac{p(\mathbf{r}, \mathbf{r}_s)}{p_0(\mathbf{r}_s)} \right|^2 \right), \quad (2.77)$$

where  $Z_0(\mathbf{r}_s)$ ,  $Z(\mathbf{r}, \mathbf{r}_s)$  are the acoustic impedances at the source and the field point, respectively, and  $p(\mathbf{r}, \mathbf{r}_s)$  is the acoustic pressure at point  $\mathbf{r}$  for a simple point source at point  $\mathbf{r}_s$ , and  $p_0(\mathbf{r}_s)$  is the pressure produced at a distance of 1 m from the same source in an *infinite, homogeneous medium* with impedance  $Z_0(\mathbf{r}_s)$ . For a bounded medium,  $p_0$  is generally different from the actual pressure due to the presence of the reverberant field from the boundaries. This particular normalization should be kept in mind when developing or comparing numerical algorithms. In what follows, we take the impedance at the source and field points to be the same.

With the pressure at range  $r$  from the source given in terms of the displacement potential as

$$p(r) = \rho\omega^2 \psi(\omega, r) \quad (2.78)$$

together with the expression for  $\psi(\omega, r)$  in (2.50), we can normalize the source to yield a pressure amplitude of unity for  $r = 1$ , by assuming the source strength,

$$S_\omega = -\frac{4\pi}{\rho\omega^2}. \quad (2.79)$$

This particular source strength is of unit  $\text{m}^3\text{s}^{-2}/\text{kg}$ , or  $\text{m}^2/\text{Pa}$ , and represents the volume injection amplitude necessary to produce a pressure amplitude of 1 Pa at 1 m distance from the source, at the radial frequency  $\omega$ . It is clear from this expression that a high-frequency source needs much less volume injection to produce a certain pressure than does a low-frequency source.

Using this source normalization, and defining the *transmission loss pressure* as the ratio,

$$P(\mathbf{r}, \mathbf{r}_s) = \frac{p(\mathbf{r}, \mathbf{r}_s)}{p_0(\mathbf{r}_s)} \quad (2.80)$$

the associated displacement potential  $\Psi = P/(\rho\omega^2)$ , is found by solving the inhomogeneous wave equation,

$$[\nabla^2 + k^2] \Psi(\mathbf{r}, \mathbf{r}_s) = -\frac{4\pi}{\rho\omega^2} \delta(\mathbf{r} - \mathbf{r}_s). \quad (2.81)$$

Alternatively, by inserting the relation between pressure and potential, we can formulate the wave equation directly for the transmission loss pressure,

$$[\nabla^2 + k^2] P(\mathbf{r}, \mathbf{r}_s) = -4\pi \delta(\mathbf{r} - \mathbf{r}_s). \quad (2.82)$$

Since the transmission loss definition refers to the field in an infinite medium, the same forcing term must be used in the inhomogeneous form of the wave equation (2.14) for media with density variation,

$$\rho \nabla \cdot [\rho^{-1} \nabla P(\mathbf{r}, \mathbf{r}_s)] + k^2 P(\mathbf{r}, \mathbf{r}_s) = -4\pi \delta(\mathbf{r} - \mathbf{r}_s). \quad (2.83)$$

In the following chapters, these equations will be used variably, with the actual choice being dependent on the nature of the numerical solution technique. However, in the remainder of this chapter we concentrate on the simple wave equation as applied to cases that allow for analytical solutions.

## 2.4 Layered Media and Waveguides

In heterogeneous media, the sound speed and density varies in one or more space coordinates. In cases where the variation occurs as discrete discontinuities in the medium properties, the derivation of the linear wave equation, (2.15), is not valid at the discontinuity itself, and the problem therefore has to be formulated as a boundary value problem. For continuously varying media, the space dependency is directly included in the wave equation.

In reality, the ocean environment is a combination of the two, with the medium properties changing abruptly at the seabed and at subbottom interfaces between different geological strata, but with the sound speed varying more or less continuously in the water column. However, since the analytical approach is different in the two cases, we will describe the solution of the wave equation in discretely and continuously varying media separately. The numerical approaches, in general, have to combine the treatment of these two types of medium heterogeneity.

A simple discrete model of the ocean environment is shown in Fig. 2.5. It consists of a layered waveguide with plane, parallel interfaces and with each layer assumed to be homogeneous. Although simplified, such a model is reasonable for modeling propagation in many ocean-acoustic scenarios. Further, the fact that solutions can be obtained in terms of basic physical components makes the horizontally stratified ocean model attractive in terms of physical understanding of the underlying propagation mechanisms.

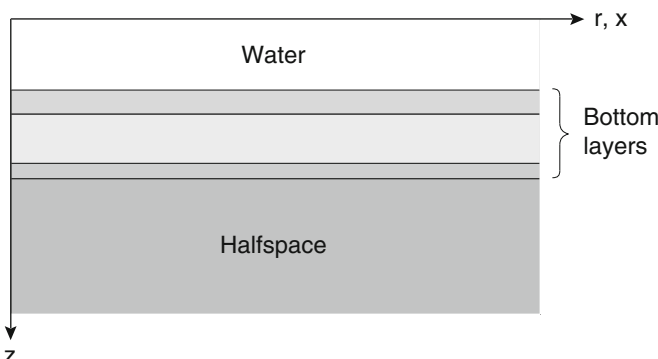


**Fig. 2.5** Horizontally stratified environment

### 2.4.1 Integral Transform Techniques

The *integral transform technique* is a classical approach to boundary value problems for environments where both the coefficients of the *Helmholtz equation* and the *boundary conditions* are independent of one or more space coordinates. In such cases, the dimension of the wave equation and the boundary conditions can be reduced through the use of integral transforms, which is equivalent to the technique of *separation of variables*.

There are several classes of canonical problems for which separation of variables can be applied, including spherically stratified Earth models, and laminated spherical and cylindrical shells. However, in underwater acoustics the most important canonical geometry for which this powerful analytical technique can be applied is the *horizontally stratified* or *range-independent* waveguide shown in Fig. 2.5.

The properties of the horizontally stratified waveguide only depend on the depth  $z$ ; all interfaces between the various media are plane and parallel. For this range-independent problem, the Helmholtz equation takes the form,

$$[\nabla^2 + k^2(z)] \psi(\mathbf{r}) = f(\mathbf{r}) \quad (2.84)$$

with the boundary conditions expressed in a general operator form as,

$$B [\psi(\mathbf{r})] |_{z=z_n} = 0, \quad n = 1 \dots N \quad (2.85)$$

with  $z_n$  being the depth of interface number  $n$ .

Before proceeding we have to choose a convenient coordinate system. The half-space problem treated in Sect. 2.3.4 is a very simple example of a range-independent problem. However, there the boundary conditions were homogeneous and simple, and we chose a spherical coordinate system for solving the Helmholtz equation because the source was a simple point source. In general, the boundary conditions are the complicating factor, and they therefore control the choice of coordinate system. Thus, to apply separation of variables to the range-independent problem, we must choose a coordinate system for which one of the axes is normal to the horizontal interface.

#### 2.4.1.1 Plane Propagation Problems

For plane problems such as those involving an infinite line source parallel to the stratification it is natural to choose a Cartesian coordinate system  $(x, y, z)$  with the  $z$ -axis perpendicular to the stratification and the  $y$ -axis parallel to the line source. The field then becomes independent of the  $y$ -coordinate, reducing the dimension of the Helmholtz equation to 2, the range  $x$  and the depth  $z$ , i.e., for a line source at  $(x, z) = (0, z_s)$ ,

$$\left[ \frac{\partial^2}{\partial x^2} + \frac{\partial^2}{\partial z^2} + k^2(z) \right] \psi(x, z) = S_\omega \delta(x) \delta(z - z_s). \quad (2.86)$$

We can now apply the Fourier transform pair,

$$f(x, z) = \int_{-\infty}^{\infty} f(k_x, z) e^{ik_x x} dk_x, \quad (2.87)$$

$$f(k_x, z) = \frac{1}{2\pi} \int_{-\infty}^{\infty} f(x, z) e^{-ik_x x} dx \quad (2.88)$$

to (2.86) to obtain the *depth-separated wave equation*,

$$\left[ \frac{d^2}{dz^2} + (k^2 - k_x^2) \right] \psi(k_x, z) = S_\omega \frac{\delta(z - z_s)}{2\pi}. \quad (2.89)$$

We next use the Fourier transform of Green's theorem in the form of (2.72) to obtain,

$$\psi(k_x, z) = -S_\omega G_\omega(k_x, z, z_s), \quad (2.90)$$

where  $G_\omega(k_x, z, z_s)$  is called the *depth-dependent Green's function*, which clearly must satisfy the same boundary conditions as  $\psi(k_x, z)$  for (2.90) to be valid.

Since the depth-dependent Green's function  $G_\omega(k_x, z, z_s)$  is the Fourier transform of the general Green's function, (2.58), it has the form,

$$G_\omega(k_x, z, z_s) = g_\omega(k_x, z, z_s) + H_\omega(k_x, z), \quad (2.91)$$

where  $g_\omega(k_x, z, z_s)$  is the Fourier transform of the free-field Green's function satisfying the equation,

$$\left[ \frac{d^2}{dz^2} + (k^2 - k_x^2) \right] g_\omega(k_x, z, z_s) = -\frac{\delta(z - z_s)}{2\pi}; \quad (2.92)$$

$H_\omega(k_x, z)$  satisfies the corresponding homogeneous differential equation.

Through (2.90) and (2.91), we have expressed the total solution as a *superposition* of the field produced by the source in an infinite medium and a homogeneous solution. The total field, of course, must satisfy the boundary conditions. Since the boundary conditions, (2.85), are independent of the horizontal coordinates, they can be Fourier transformed as well. The differential operators  $B[\psi(\mathbf{r})]$  now become algebraic operations, yielding the boundary conditions for the depth-separated wave equation in the form

$$B[\psi(k_x, z_n)] = 0. \quad (2.93)$$

The solution is now obtained by determining the homogeneous solution  $H_\omega(k_x, z)$  which, superimposed on the free-field Green's function  $g_\omega(k_x, z, z_s)$ , satisfies the boundary conditions in (2.93). The total spatial solution then follows by evaluating the inverse Fourier transform, (2.87).

### 2.4.1.2 Axisymmetric Propagation Problems

The more usual problem of a *simple point source* in a range-independent environment is treated in a similar way. Since the simple point source is omni-directional, the field only varies with depth and the horizontal range from the source. It is, therefore, natural to choose a *cylindrical coordinate system* for this problem, with the vertical  $z$ -axis passing through the source and the  $r$ -axis being parallel to the interfaces.

We can then integrate the Helmholtz equation, (2.84), with the Laplace operator given in (2.35), with respect to the azimuthal coordinate  $\varphi$  and apply the *Hankel transform* pair,

$$f(r, z) = \int_0^\infty f(k_r, z) J_0(k_r r) k_r dk_r, \quad (2.94)$$

$$f(k_r, z) = \int_0^\infty f(r, z) J_0(k_r r) r dr \quad (2.95)$$

to obtain the *depth-separated wave equation* for the cylindrical coordinate system,

$$\left[ \frac{d^2}{dz^2} + (k^2 - k_r^2) \right] \psi(k_r, z) = S_\omega \frac{\delta(z - z_s)}{2\pi}. \quad (2.96)$$

Equation (2.96) is identical to the depth-separated wave equation for the Cartesian coordinate system. The solution of the depth-separated wave equation, therefore, proceeds identically in the two cases. Further, the transforms of the boundary conditions are identical in the two cases, and we can therefore use the solution of (2.96) as the kernel for both of the inverse transforms, (2.87) and (2.94), for the line source and point source fields, respectively.

As was the case for the reduction of the wave equation to the frequency domain Helmholtz equation, the reduction of the three-dimensional Helmholtz equation to the one-dimensional, depth-separated wave equation is obtained at the cost of having to evaluate the infinite integrals of the inverse transforms. However, the asymptotic behavior of the integration kernels makes truncation of the integration interval possible, with small or insignificant error as a result, and numerical quadrature schemes are available for accurate evaluation of the truncated inverse transforms. This is described in detail in Chap. 4, where we discuss *wavenumber integration* methods. These methods directly implement the integral transform approach described here and therefore compute the “exact” solution for the range-independent problem. Alternative approximate methods are also available, including the *method of stationary phase* and the *normal mode* expansion. The basic principles of these techniques are described in this chapter, but much more detail on normal modes is given in Chap. 5.

Finally, there is much virtue to the integral transform solution in terms of physical interpretation. As is clear from the form of the inverse transform, (2.87), the integral transform represents a decomposition of the total field into plane waves propagating

with horizontal wavenumber  $k_x$ . Similarly, the Hankel transform, (2.94), represents a decomposition into conical waves as is clear from the relation

$$J_0(k_r r) = \frac{1}{2} [H_0^{(1)}(k_r r) + H_0^{(2)}(k_r r)] \quad (2.97)$$

together with the asymptotic form of the Hankel functions, (2.39) and (2.40).

The solution of the depth-separated wave equation therefore directly yields important interpretational results such as plane-wave reflection and transmission coefficients, with the wavenumber kernels providing information on the relative significance of the various plane-wave components in the total field. This will be illustrated both in this chapter and in Chap. 4 for increasingly complex range-independent environments.

### 2.4.2 Source in Fluid Halfspace

We will illustrate the basic principles of the integral transform solution by applying it to the case of a point source in a fluid halfspace, treated in Sect. 2.3.4 by means of Green's theorem. The environment, shown in Fig. 2.4, can be considered range-independent or horizontally stratified with just a single interface.

To apply the integral transform, we introduce a cylindrical coordinate system with the  $z$ -axis perpendicular to the surface and passing through the source. For the line-source problem, a Cartesian coordinate system should be used, yielding the exact same solution in the wavenumber domain. The field then only depends on the horizontal range and depth. The depth-separated wave equation for this case is, therefore, (2.96) with the medium wavenumber being constant,  $k(z) = k$ . The solution is given in terms of the depth-dependent Green's function in (2.90), where the Green's function, (2.91), is found as a superposition of the free-field solution to (2.92) and the two independent solutions to the corresponding homogeneous equation.

For a homogeneous medium, the solution to the homogeneous equation is of the form

$$H_\omega(k_r, z) = A^+(k_r) e^{ik_z z} + A^-(k_r) e^{-ik_z z} \quad (2.98)$$

with  $k_z$  being the vertical wavenumber,

$$k_z = \sqrt{k^2 - k_r^2}. \quad (2.99)$$

Since the inverse Hankel transform must be evaluated over a semi-infinite wavenumber domain, we have to choose a definition for the square root for  $k_r > k$ . We choose the definition

$$k_z = \begin{cases} \sqrt{k^2 - k_r^2}, & k_r \leq k \\ i\sqrt{k_r^2 - k^2}, & k_r > k. \end{cases} \quad (2.100)$$

With this definition, for  $z \rightarrow \infty$ , the first term in (2.98) corresponds to downward propagating waves for  $k_r < k$ , and exponentially decaying waves for  $k_r > k$ . Thus, this term can be eliminated for  $z \rightarrow -\infty$  due to the radiation condition for all values of  $k_r$ . Similarly, the second term can be eliminated for  $z \rightarrow +\infty$ . The radiation conditions at  $z \rightarrow \pm\infty$  therefore require the homogeneous solutions to be of the form

$$H_\omega(k_r, z) = \begin{cases} A^+(k_r) e^{ik_z z}, & z \rightarrow +\infty \\ A^-(k_r) e^{-ik_z z}, & z \rightarrow -\infty. \end{cases} \quad (2.101)$$

If we had defined the square root in (2.100) using  $-i$  for  $k_r > k$ , we would have to switch the terms when passing  $k_r = k$ . Although the present definition is chosen merely for convenience, it is absolutely essential to use the proper definition when we later introduce attenuation.

We next solve the inhomogeneous depth-separated wave equation for the free-field Green's function, (2.92). Except for the source depth  $z = z_s$ , the Green's function satisfies the homogeneous equation, with solutions of the form given in (2.101). Applying symmetry considerations for the field with respect to the plane  $z = z_s$ , we therefore have

$$\begin{aligned} g_\omega(k_r, z, z_s) &= A(k_r) \begin{cases} e^{ik_z(z-z_s)}, & z \geq z_s \\ e^{-ik_z(z-z_s)}, & z \leq z_s \end{cases} \\ &= A(k_r) e^{ik_z|z-z_s|}. \end{aligned} \quad (2.102)$$

We now integrate (2.96) from  $z_s - \epsilon$  to  $z_s + \epsilon$  to obtain

$$\left[ \frac{dg_\omega(k_r, z)}{dz} \right]_{z_s-\epsilon}^{z_s+\epsilon} + O(\epsilon) = -\frac{1}{2\pi}. \quad (2.103)$$

Inserting the derivative of (2.102) into (2.103) and letting  $\epsilon \rightarrow 0$ , we get,

$$A(k_r) = -\frac{1}{4\pi i k_z} \quad (2.104)$$

with the free-field depth-dependent Green's function following as

$$g_\omega(k_r, z, z_s) = -\frac{e^{ik_z|z-z_s|}}{4\pi i k_z}. \quad (2.105)$$

The point-source Green's function in an infinite medium is now obtained as the inverse Hankel transform of (2.105),

$$g_\omega(r, z, z_s) = \frac{i}{4\pi} \int_0^\infty \frac{e^{ik_z|z-z_s|}}{k_z} J_0(k_r r) k_r dk_r, \quad (2.106)$$

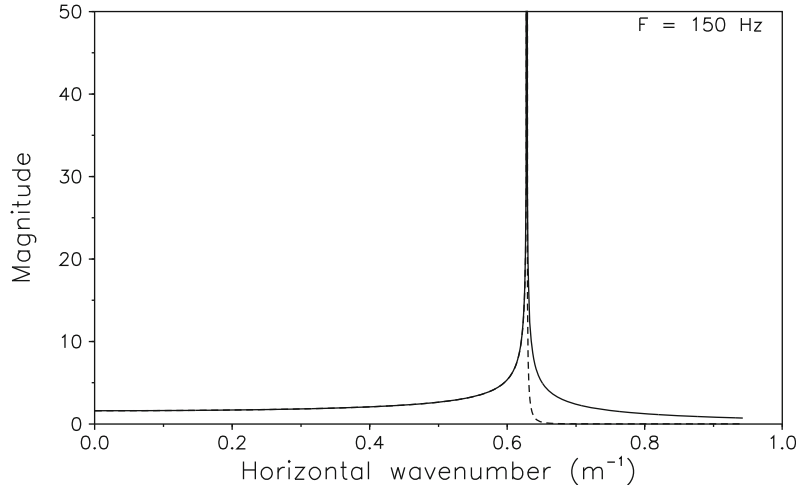


**Fig. 2.6** Magnitude of the depth-dependent Green's function for point source in an infinite medium, computed along a complex contour, offset from the real axis by the amount given in (4.115). *Solid curve:*  $z - z_s = \lambda/10$ . *Dashed curve:*  $z - z_s = 2\lambda$

which is the *Sommerfeld–Weyl integral*. This integral decomposes the point-source field into conical waves, propagating cylindrically in the horizontal direction, and propagating like plane waves in the vertical direction for  $k_r < k$ , and decaying exponentially in the vertical for  $k_r > k$ .

Before proceeding with the solution of the halfspace problem, we first discuss the basic physical significance of the depth-dependent Green's function for the point source in (2.105). Thus, Fig. 2.6 shows the magnitude of  $g_\omega(k_r, z, z_s)$  for receiver depths  $0.1 \lambda$  and  $2.0 \lambda$  below the source. At the medium wavenumber,  $k_r = k$ , the Green's function has a square root singularity, with the magnitude being independent of the receiver depth for  $k_r \leq k$ . To avoid this singularity, the kernel is computed along a contour displaced into the complex plane by an amount given by (4.115), usually applied to obtain a numerically stable integration, as will be discussed later in Sect. 4.5.5. This part of the wavenumber spectrum corresponds to waves propagating in the vertical direction due to the purely imaginary argument of the exponential function in (2.105); it is referred to as the *radiating spectrum*. However, for  $k_r > k$  the vertical wavenumber  $k_z$  is imaginary and the magnitude therefore becomes exponentially decaying with depth. This part of the wavenumber spectrum is called the *evanescent spectrum*.

It is important to stress that the representation of the depth-dependent Green's function in the wavenumber domain is a result of the rather arbitrary mathematical manipulation we have performed through the integral transformation of the Helmholtz equation. We can, therefore, not straightforwardly associate the features of Fig. 2.6 with specific physical wave phenomena. This is particularly evident for this simple problem of a point source in an infinite, homogeneous medium where the field is known to be a spherical wave propagating with the medium wavenumber.

This simple feature is not evident from the form of the depth-dependent Green's function in Fig. 2.6. However, after applying the inverse transform of (2.105) the resulting field will exhibit this behavior.

We can, however, analyze the significance of the two spectral domains by changing the integration variable for the radiating spectrum, which will dominate the solution for  $|z - z_s| \rightarrow \infty$ . As described above, the depth-dependent Green's functions for the point and line sources are identical, and for simplicity we will therefore do this for the line-source case. Introducing the *grazing angle*  $\theta$ , we have

$$k_x = k \cos \theta, \quad (2.107)$$

$$k_z = k \sin \theta, \quad (2.108)$$

$$\frac{dk_x}{d\theta} = -k_z. \quad (2.109)$$

The expression for the frequency-domain Green's function is obtained by applying the inverse Fourier transform, (2.87), to the depth-dependent Green's function. Assuming large depth separation of source and receiver, we include only the radiating spectrum in the integration, i.e.,

$$\begin{aligned} g_\omega(\mathbf{r}, \mathbf{r}') &\simeq \frac{i}{4\pi} \int_{-k}^k \frac{e^{ik_z|z-z_s|}}{k_z} e^{ik_x x} dk_x \\ &= \frac{i}{4\pi} \int_0^\pi e^{ik|z-z_s| \sin \theta + ikx \cos \theta} d\theta. \end{aligned} \quad (2.110)$$

In this form, the integral clearly represents the field as an integral of equal amplitude *plane waves* propagating at an angle  $\theta$  relative to the horizontal  $x$ -axis. Similarly, for the point source, the inverse Hankel transform represents the field as a superposition of *conical waves*. For small depth separations, the curvature of the cylindrically symmetric field produced by the line source cannot be represented by a superposition of plane waves alone. This curvature is therefore accounted for by the evanescent spectrum  $k_x > k$ , which is consistent with the exponential decay of this spectrum for increasing receiver depth as indicated in Fig. 2.6.

The evanescent spectrum is, in this case, a mathematical abstraction introduced by the choice of coordinate system, and it does not represent waves that can exist isolated in an infinite medium (for the radiating spectrum, the plane-wave components are real waves). However, this does not imply that the evanescent spectrum can be ignored, and the inverse transform must incorporate this spectrum to correctly represent the curvature of the wavefronts, in particular for small depth separations. Furthermore, for stratifications of media with different wave speeds, a certain value of the horizontal wavenumber  $k_x$  may be in the evanescent spectrum in one medium, but in the radiating spectrum in another. In this case, the evanescent spectrum gains physical significance and must be included in the analysis. Finally, for normal modes to exist in an ocean waveguide, the field must be evanescent in the lower halfspace representing the subbottom; otherwise energy would propagate

away from the waveguide. The same is the case for the seismic interface waves described in Chap. 4; they are evanescent both in the water and in the bottom. In conclusion, the *evanescent spectrum* is just as important for a correct representation of the field in stratified media as is the *radiating spectrum*.

Returning to the halfspace problem, we now seek the homogeneous solution, (2.98), which superimposed with the source Green's function, (2.105), satisfies the Fourier transform of the free-surface boundary condition, (2.69), i.e.,

$$\psi(k_r, 0) \equiv 0 \quad (2.111)$$

as well as the radiation condition for  $z \rightarrow \infty$ . The latter immediately removes the second term in (2.98), and we therefore have

$$\begin{aligned} \psi(k_r, 0) &= -S_\omega [g_\omega(k_r, 0, z_s) + H_\omega(k_r, 0)] \\ &= S_\omega \left[ \frac{e^{ik_z z_s}}{4\pi i k_z} - A^+(k_r) \right] = 0, \end{aligned} \quad (2.112)$$

which yields the solution for  $A^+(k_r)$ . The total field solution now becomes

$$\psi(k_r, z) = S_\omega \left[ \frac{e^{ik_z|z-z_s|}}{4\pi i k_z} - \frac{e^{ik_z(z+z_s)}}{4\pi i k_z} \right]. \quad (2.113)$$

The term in the bracket is the depth-dependent Green's function for the halfspace. Since it is a superposition of two free-field depth-dependent Green's functions, see (2.52), it is clear that its inverse transform is a superposition of two spherical wave-fields produced by the real source at  $z = z_s$  and a virtual source at  $z = -z_s$ , as obtained earlier in Sect. 2.3.4. The result is a Lloyd-mirror pattern in the field for  $z > z_s$  due to the interference of the two fields, and it is very illustrative of the versatility of the wavenumber representation to relate this physical behavior of the total field to the behavior of the depth-dependent Green's function. Thus, Fig. 2.7a shows the magnitude of the halfspace Green's function as a function of the horizontal wavenumber  $k_r$  (or  $k_x$  for the line source) for a source at depth  $z_s = 2.5 \lambda = 5\pi/k$ . The result for receiver depths  $z = z_s + 0.1 \lambda$  and  $z = z_s + 2 \lambda$  are indicated by a solid and a dashed line, respectively. Again the depth-dependence of the *evanescent spectrum* is evident, but the more interesting feature is the oscillating magnitude in the *radiating spectrum*. From (2.113) it is clear that the Green's function vanishes for

$$k_z = \frac{(m-1)\pi}{z_s}, \quad m = 1, 2, \dots \quad (2.114)$$

and has *maxima* for

$$k_z = \frac{(2m-1)\pi}{2z_s}. \quad m = 1, 2, \dots \quad (2.115)$$

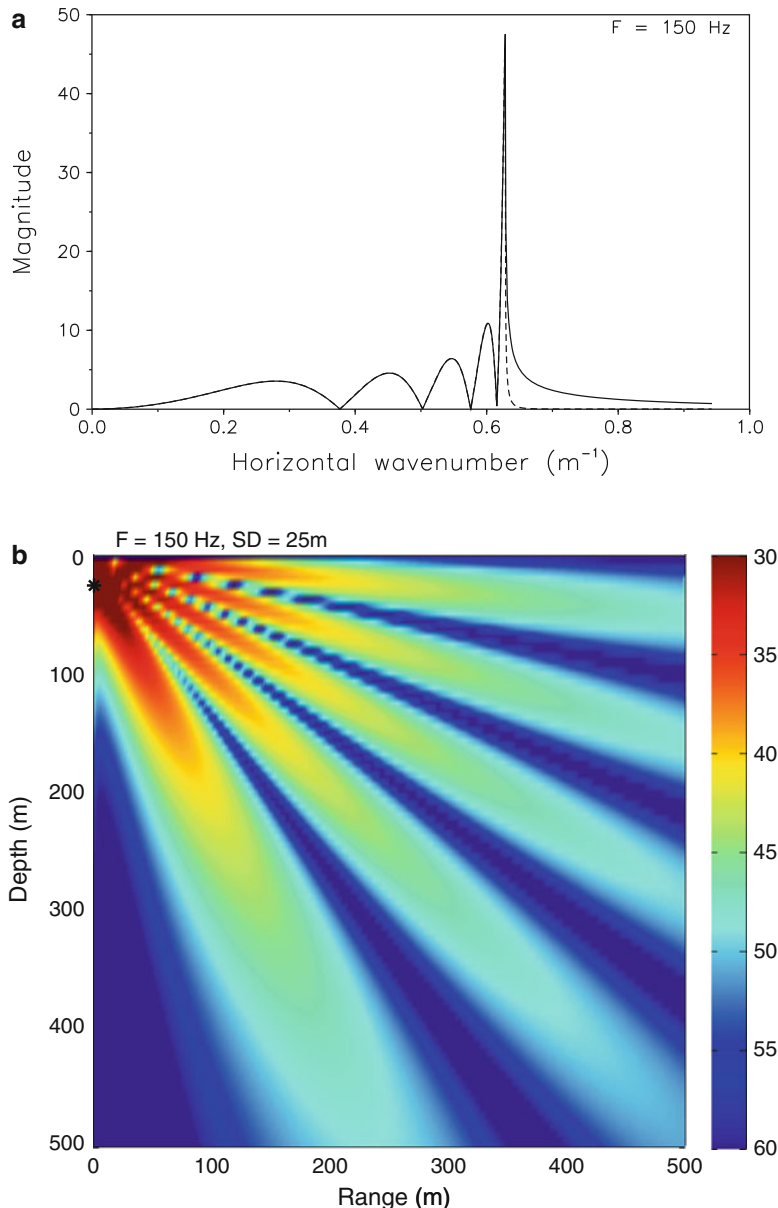


**Fig. 2.7** Source in a fluid halfspace. **(a)** Magnitude of the depth-dependent Green's function, computed along a complex contour, offset from the real axis by the amount given in (4.115). Solid curve:  $z - z_s = \lambda/10$ . Dashed curve:  $z - z_s = 2\lambda$ . **(b)** Pressure field contours

Introducing the relation between the wavenumbers and the grazing angle,  $k_z = k \sin \theta$ , these vertical wavenumbers correspond to the angles  $\theta_{\max}$  for the maxima and  $\theta_{\min}$  for the minima, where

$$\sin \theta_{\max} = \frac{(2m - 1)\pi}{2kz_s}, \quad (2.116)$$

$$\sin \theta_{\min} = \frac{(m - 1)\pi}{kz_s}. \quad (2.117)$$

These angles correspond to the angles for which the Lloyd-mirror pattern has respective maxima and minima, as is evident from Fig. 2.7b, which displays the transmission loss computed from the inverse Fourier transform, (2.87), of the Green's function in Fig. 2.7a. This feature of the field can be directly deduced from the wavenumber spectrum for the Green's function. Note that the amplitudes of the lobes in the Green's functions are inversely proportional to  $k_z$ . However, this is again a result of the transform, and if we change the integration variable to grazing angle in the radiating spectrum, the lobes will have equal amplitude – in agreement with the property of the Lloyd-mirror pattern that all lobes are of equal amplitude in the farfield, as can be seen in Fig. 2.7b.

Defining the *reflection coefficient* as the complex ratio between the reflected plane-wave amplitude and the incoming plane-wave amplitude at the surface  $z = 0$ , it is clear from the form of the solution, (2.113), together with the plane wave decomposition, (2.110), that for all wavenumbers or angles of incidence, the free-surface reflection coefficient is

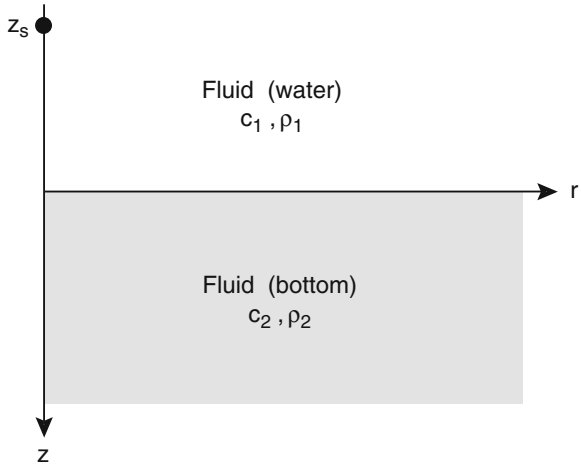
$$\mathcal{R} = -1. \quad (2.118)$$

### 2.4.3 Reflection and Transmission

The Lloyd-mirror effect described above is a characteristic feature of the interaction of an acoustic field with a smooth sea surface. However, the interaction with the bottom can be just as important, in particular in shallow water environments. Whereas the atmosphere is well represented by a vacuum, the seabed is an acoustic medium, and the bottom interaction problem has to be treated as a propagation problem in a heterogeneous medium.

The simplest bottom model consists of a fluid halfspace, and we will here analyze the isolated interaction with the bottom by assuming the upper halfspace to be a homogeneous fluid medium representing the water column, Fig. 2.8.

A simple point source of strength  $S_\omega$  is present in the upper halfspace at depth  $z = z_s$ . We have here introduced a cylindrical coordinate system with the  $r$ -axis along the interface and the  $z$ -axis passing through the source. Following the same procedure as in the preceding section, we express the wavenumber kernel for the field in terms of the Green's function satisfying the boundary conditions, (2.90), with  $G_\omega(k_r, z, z_s)$  given by (2.91) as a superposition of the free-field Green's function for the source and a homogeneous solution.

**Fig. 2.8** Two fluid halfspaces

Using the radiation condition, the homogeneous solution in the upper halfspace with wavenumber  $k_1 = \omega/c_1$  and density  $\rho_1$ , is

$$H_{\omega,1}(k_r, z) = A_1^-(k_r) e^{-ik_{z,1}z} \quad (2.119)$$

and similarly in the lower halfspace with wavenumber  $k_2 = \omega/c_2$  and density  $\rho_2$ ,

$$H_{\omega,2}(k_r, z) = A_2^+(k_r) e^{ik_{z,2}z}, \quad (2.120)$$

where  $k_{z,i}$ ,  $i = 1, 2$ , are the vertical wavenumbers for the two media. In the upper halfspace, the free-field Green's function, (2.52), must be added to yield the total Green's function.

The two unknown amplitudes for the homogeneous solutions are now determined from the boundary conditions. The first boundary condition expresses *continuity of vertical displacements*, i.e., in wavenumber space,

$$\frac{\partial \psi_1(k_r, z)}{\partial z} = \frac{\partial \psi_2(k_r, z)}{\partial z}, \quad z = 0. \quad (2.121)$$

Replacing  $\psi(k_r, z)$  by the Green's functions and inserting the two homogeneous solutions and the source Green's function from (2.105), we obtain for  $z = 0$ ,

$$k_{z,2} A_2^+(k_r) + k_{z,1} A_1^-(k_r) = k_{z,1} g_{\omega,1}(k_r, 0, z_s). \quad (2.122)$$

The second boundary condition expresses *continuity of pressure*,

$$\rho_1 \psi_1(k_r, z) = \rho_2 \psi_2(k_r, z), \quad z = 0. \quad (2.123)$$

Again, insertion of the Green's functions in the two media yields for  $z = 0$ ,

$$\rho_2 A_2^+ - \rho_1 A_1^- = \rho_1 g_{\omega,1}(k_r, 0, z_s). \quad (2.124)$$

The solution of (2.122) and (2.124) then leads to,

$$A_1^- = \frac{\rho_2 k_{z,1} - \rho_1 k_{z,2}}{\rho_2 k_{z,1} + \rho_1 k_{z,2}} g_{\omega,1}(k_r, 0, z_s), \quad (2.125)$$

$$A_2^+ = \frac{2\rho_1 k_{z,1}}{\rho_2 k_{z,1} + \rho_1 k_{z,2}} g_{\omega,1}(k_r, 0, z_s). \quad (2.126)$$

Since the wavenumber representation in a Cartesian coordinate system represents a decomposition into plane-wave solutions,  $g_{\omega}(k_r, 0, z)$  represents the complex amplitude at  $z = 0$  of plane waves incident from above, and  $A_1^-$  and  $A_2^+$  represent the amplitudes of the reflected and transmitted plane waves, respectively. Therefore, the fractions in (2.125) and (2.126) are directly the *reflection coefficient*  $\mathcal{R}$  and *transmission coefficient*  $\mathcal{T}$  for the displacement potential,

$$\mathcal{R} = \frac{\rho_2 k_{z,1} - \rho_1 k_{z,2}}{\rho_2 k_{z,1} + \rho_1 k_{z,2}}, \quad (2.127)$$

$$\mathcal{T} = \frac{2\rho_1 k_{z,1}}{\rho_2 k_{z,1} + \rho_1 k_{z,2}}. \quad (2.128)$$

By using (2.108), it is easily verified that these expressions are identical to those derived in Chap. 1 as (1.56) and (1.57).

We here briefly discuss the properties of the reflection and transmission coefficients. The trivial case of identical media, i.e.,  $k_1 = k_2$ ,  $\rho_1 = \rho_2$ , as expected yields  $\mathcal{R} \equiv 0$ ,  $\mathcal{T} \equiv 1$ . The case of the lower medium being vacuum should obviously yield the free surface reflection coefficient, which is easily verified by letting  $k_2 = \omega/c_2 \rightarrow \infty$  and  $\rho_2 = 0$ , yielding  $\mathcal{R} \equiv -1$  and  $\mathcal{T} \equiv 0$ . For other media we distinguish between a *hard bottom*,  $c_2 > c_1$  and a *soft bottom*,  $c_2 < c_1$ . Since the reflection and transmission properties are distinctly different in the two cases, we discuss them separately.

### 2.4.3.1 Hard Bottom

For the hard bottom, the medium wavenumber in the bottom is smaller than the wavenumber in the water,  $k_2 < k_1$ . We, therefore, have three different spectral regimes to consider in the horizontal wavenumber space, as shown in Fig. 2.9.

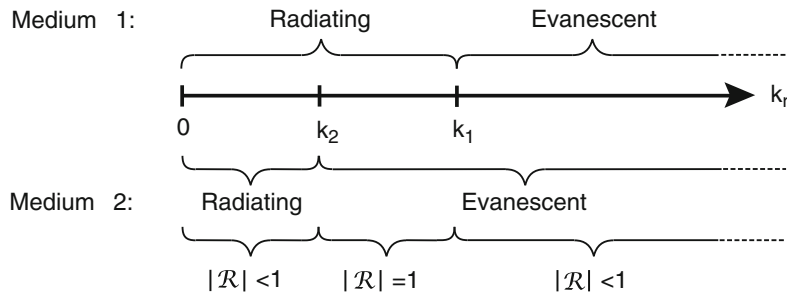


**Fig. 2.9** Spectral domains for a hard bottom,  $k_2 < k_1$

1.  $k_r < k_2$  : Waves are *propagating* vertically in both media and energy will be transmitted into the bottom:  $|\mathcal{R}| < 1$ .
2.  $k_2 < k_r < k_1$  : Waves are *propagating* in the upper halfspace (water) but are *evanescent* in the lower halfspace (bottom):  $|\mathcal{R}| = 1$ .
3.  $k_1 < k_r$  : Waves are *evanescent* in depth in both media:  $|\mathcal{R}| < 1$ .

This behavior of the reflection coefficient is easily verified by inserting the expressions for the vertical wavenumbers, (2.100), into (2.127). Note that in all three regimes the transmission coefficient will always be non-vanishing,  $\mathcal{T} > 0$ . This is due to the fact that even in the case of perfect reflection,  $k_2 < k_r < k_1$ , there will exist a non-vanishing evanescent field in the bottom, a feature which becomes significant for multilayered bottoms as described in Chap. 4. Note that for the simple halfspace problem, the reflection and transmission coefficients are independent of the frequency  $\omega$ .

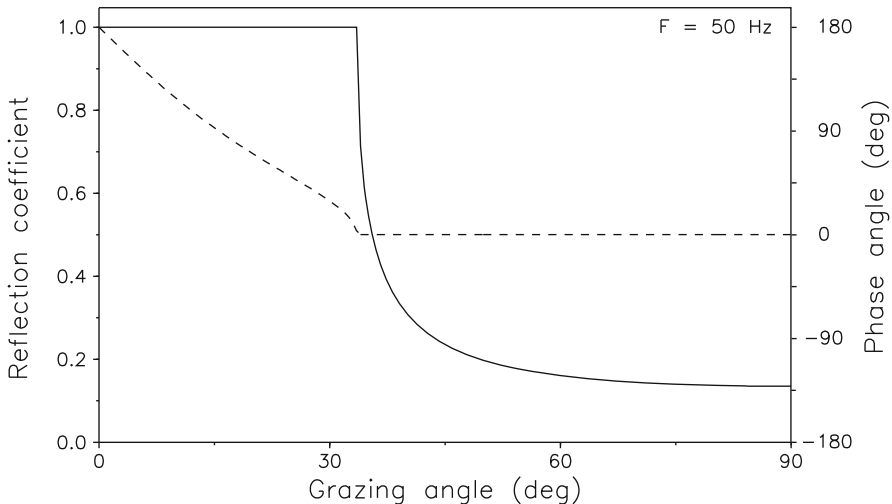
The reflection coefficient is often represented in terms of a magnitude and phase as,

$$\mathcal{R}(\theta) = |\mathcal{R}(\theta)| e^{-i\phi(\theta)}, \quad (2.129)$$

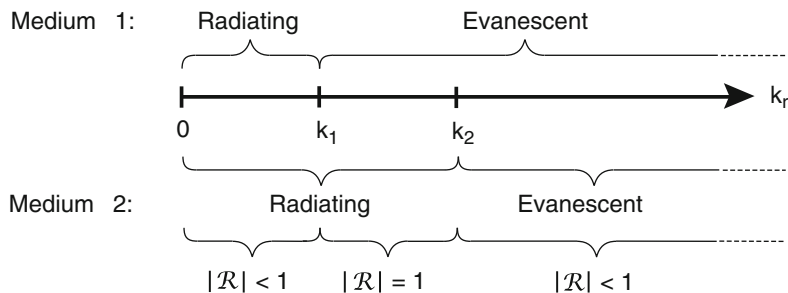
where  $\phi$  is a phase angle and  $\theta$  is the *grazing angle of incidence*, defined by  $\theta = \arccos(k_r/k_1)$ . This formulation, of course, only makes sense in the spectral regimes where the field is propagating vertically in the water, i.e., for  $k_{z,1}$  real.

Figure 2.10 shows the magnitude and phase of the plane-wave reflection coefficient for the following halfspace parameters:  $c_1 = 1500 \text{ m/s}$ ,  $\rho_1 = 1000 \text{ kg/m}^3$  in the water, and  $c_2 = 1800 \text{ m/s}$ ,  $\rho_2 = 1800 \text{ kg/m}^3$  in the bottom.

The *critical angle*  $\theta_c = \arccos(k_2/k_1) = 33.5^\circ$  is evident in both the magnitude and the phase, verifying the description of the behavior of the reflection coefficient given above, with perfect reflection ( $|\mathcal{R}| = 1$ ) for  $\theta < \theta_c$  and reflection loss ( $|\mathcal{R}| < 1$ ) for larger grazing angles. Note that in the region of perfect reflection, the phase angle changes from a  $180^\circ$  shift, i.e.,  $\mathcal{R} = -1$ , for  $\theta = 0^\circ$  to no phase shift at the critical angle. Above the critical angle there is no phase shift. In other words, for small grazing angles the reflection from a fluid–fluid interface is very similar to the reflection off a free surface, whereas for large grazing angles the reflection is more like the reflection from a rigid halfspace in terms of phase shift, but with reduced magnitude. We discuss these features further in relation to the determination of the acoustic field produced by the point source.



**Fig. 2.10** Reflection coefficient as a function of grazing angle for a hard-bottom halfspace. *Solid curve:* Magnitude. *Dashed curve:* Phase



**Fig. 2.11** Spectral domains for a soft bottom,  $k_1 < k_2$

### 2.4.3.2 Soft Bottom

A soft bottom is characterized by a speed of sound less than that of water, i.e.,  $c_2 < c_1$  or  $k_2 > k_1$ . Again, the wavenumber spectrum is divided into three different regimes, as shown in Fig. 2.11.

1.  $k_r < k_1$ : Waves are *propagating* vertically in both media and energy will be transmitted into the bottom:  $|\mathcal{R}| < 1$ .
2.  $k_1 < k_r < k_2$ : Waves are *evanescent* in the upper halfspace (water) but *propagating* in the lower halfspace (bottom):  $|\mathcal{R}| = 1$ .
3.  $k_2 < k_r$ : Waves are *evanescent* in depth in both media:  $|\mathcal{R}| < 1$ .

Since plane waves propagating in the water have horizontal wavenumbers that satisfy the relation  $k_r \leq k_1$ , only the first of the above spectral regimes is relevant for plane-wave reflection coefficients.

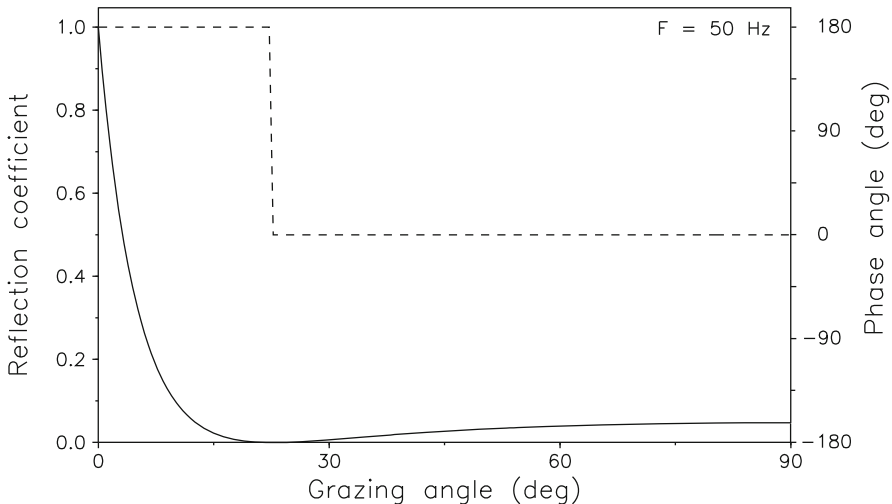


**Fig. 2.12** Reflection coefficient as a function of grazing angle for a soft-bottom halfspace. *Solid curve:* Magnitude. *Dashed curve:* Phase

Figure 2.12 shows the magnitude and phase of the plane-wave reflection coefficient for the following halfspace parameters:  $c_1 = 1500 \text{ m/s}$ ,  $\rho_1 = 1000 \text{ kg/m}^3$  in the water, and  $c_2 = 1300 \text{ m/s}$ ,  $\rho_2 = 1800 \text{ kg/m}^3$  in the bottom. In this case, there is no critical angle and perfect reflection only occurs in the trivial case of zero grazing angle. However, for the above set of parameters there exists an *intromission angle*  $\theta_0$  at which the reflection coefficient is zero and all energy is transmitted into the bottom. From (1.60) we find  $\theta_0 = 22.6^\circ$ , which is seen to coincide with the phase-angle shift of  $180^\circ$  in Fig. 2.12.

The practical application of plane-wave reflection coefficients is rather limited due to the fact that pure plane waves cannot be generated in reality. However, the concept of reflection coefficients is important for a physical understanding of the energy transport in and out of the ocean waveguide, and its application in numerical modeling of ocean acoustics is important for approaches based on plane-wave representations such as the ray approaches described in Chap. 3 and the wavenumber-integration approaches described in Chap. 4. In fact, for classical ray approaches the reflection and transmission coefficients provide the only means of incorporating boundaries into the ocean waveguide.

#### 2.4.3.3 The Point Source Field

To obtain the field produced by a point source at depth  $z = z_s$ , we use the Hankel transform of the wavenumber kernel,

$$\psi(k_r, z) = \begin{cases} -S_\omega [g_{\omega,1}(k_r, z, z_s) + H_{\omega,1}(k_r, z)], & z < 0 \\ -S_\omega H_{\omega,2}(k_r, z), & z > 0, \end{cases} \quad (2.130)$$

with the homogeneous solution  $H_{\omega,1}(k_r, z)$  given by (2.119) and (2.125), and with  $H_{\omega,2}(k_r, z)$  given by (2.120) and (2.126). The free-field Green's function  $g_{\omega,1}(k_r, z, z_s)$  is given by (2.105).

The total reflected field is now obtained by evaluating the wavenumber integral

$$\begin{aligned}\psi(r, z) &= \int_0^\infty A_1^-(k_r) e^{-ik_{z,1}z} J_0(k_r r) k_r dk_r \\ &= \frac{1}{2} \int_{-\infty}^\infty A_1^-(k_r) e^{-ik_{z,1}z} H_0^{(1)}(k_r r) k_r dk_r.\end{aligned}\quad (2.131)$$

In general, (2.131) must be evaluated numerically by one of the methods described in Chap. 4. However, an asymptotic evaluation can be obtained by the *method of stationary phase* for receivers in the farfield – see discussion associated with (2.161). Thus, for  $k_r r \gg 1$  the Hankel function in (2.131) can be replaced by its large argument asymptotic form, (2.39). Insertion of (2.125), (2.127), (2.129) and (2.105) into (2.131) then yields

$$\psi(r, z) = \frac{S_\omega e^{-i\pi/4}}{4\pi\sqrt{2\pi r}} \int_{-\infty}^\infty |\mathcal{R}(k_r)| \frac{\sqrt{k_r}}{ik_{z,1}} e^{-i[\phi(k_r) + k_{z,1}(z + z_s) - k_r r]} dk_r. \quad (2.132)$$

If the receiver is far away from the interface, i.e.,  $k_{z,1}(z + z_s) \gg 1$ , the integral is dominated by the contributions from points where the phase term in the kernel is stationary, i.e.,

$$\frac{\partial}{\partial k_r} [\phi(k_r) + k_{z,1}(z + z_s) - k_r r] = 0, \quad (2.133)$$

or

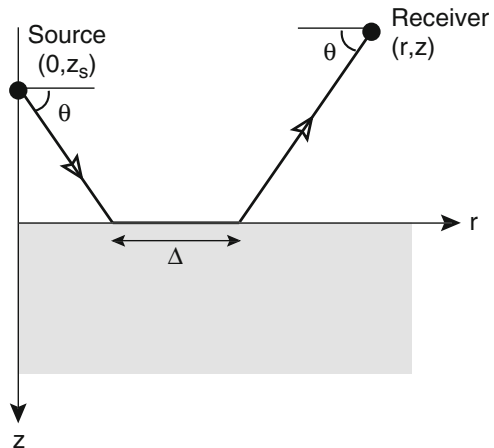
$$\frac{\partial\phi(k_r)}{\partial k_r} - \frac{k_r(z + z_s)}{k_{z,1}} - r = 0. \quad (2.134)$$

Thus, for a particular receiver position  $(r, z)$ , the solutions of (2.134) define the dominant plane-wave components of the field. A geometrical interpretation of this equation is obtained by introducing the grazing angle  $\theta$  defined by  $\cot\theta = k_r/k_{z,1}$ ,

$$r = \frac{\partial\phi(k_r)}{\partial k_r} - (z + z_s) \cot\theta. \quad (2.135)$$

As illustrated in Fig. 2.13, the solutions of (2.135) represent plane waves or *rays*, hitting the interface at grazing angle  $\theta$ , and propagating along the interface a distance  $\Delta = \partial\phi(k_r)/\partial k_r$  before being launched back toward the receiver, again at an angle  $\theta$  with respect to the horizontal. It should be noted that the grazing angle  $\theta$  is related to the horizontal wavenumber  $k_r$  through the relation  $\cos\theta = k_r/k_1$ , with the result that the *ray displacement*  $\Delta$  is a function of  $\theta$ . The ray displacement is therefore non-zero only for grazing angles where the phase of the reflection

**Fig. 2.13** Ray representation of reflection from a homogeneous halfspace



coefficient is varying. For the *hard-bottom* case shown in Fig. 2.10, there are two reflection regimes separated by the critical angle  $\theta_c$ :

1.  $\theta < \theta_c : \Delta = \partial\phi/\partial k_r > 0,$
2.  $\theta > \theta_c : \Delta = \partial\phi/\partial k_r = 0.$

Thus, for ranges larger than the *critical range*,  $r_c = -(z + z_s) \cot \theta_c$ , there will be a non-vanishing ray displacement. For shorter ranges, there is no displacement and rays are reflected specularly. It can be shown that a stationary phase point always exists at the critical angle where the phase curve in Fig. 2.10 has infinite curvature. For ranges larger than critical, a ray path with grazing angle  $\theta = \theta_c$  always exists, corresponding to the so-called *head wave*. Similar considerations for the *soft-bottom* case, Fig. 2.12, imply that here there is no ray displacement for any angle of incidence.

The physical explanation for the ray displacement is the existence of a evanescent field, propagating horizontally in the bottom for incident grazing angles smaller than critical, the so-called *lateral wave*. Although the evanescent spectrum is a mathematical abstraction for the infinite homogeneous medium, the ray displacement is an illustration of the fact that for propagation in inhomogeneous media, the evanescent spectrum has *physical significance* as well.

Since the phase of the reflection coefficient for the two-halfspace problem is frequency independent, the ray displacement is inversely proportional to frequency. Ray displacements are therefore usually ignored in high-frequency ray acoustics. However, for low and intermediate frequencies it is important to properly account for the ray displacement at the water–bottom interface. Even in cases where the bottom is ignored, a similar ray displacement must be accounted for at turning points in a refracting ocean. Thus, the  $\pi/2$  phase shift introduced at turning points in WKB ray theory (Chap. 3), should be accompanied by the corresponding horizontal ray displacement in order to obtain an accurate representation of the acoustic field. Again, the effect is less significant at high frequencies, where accumulated errors become important only at long ranges.

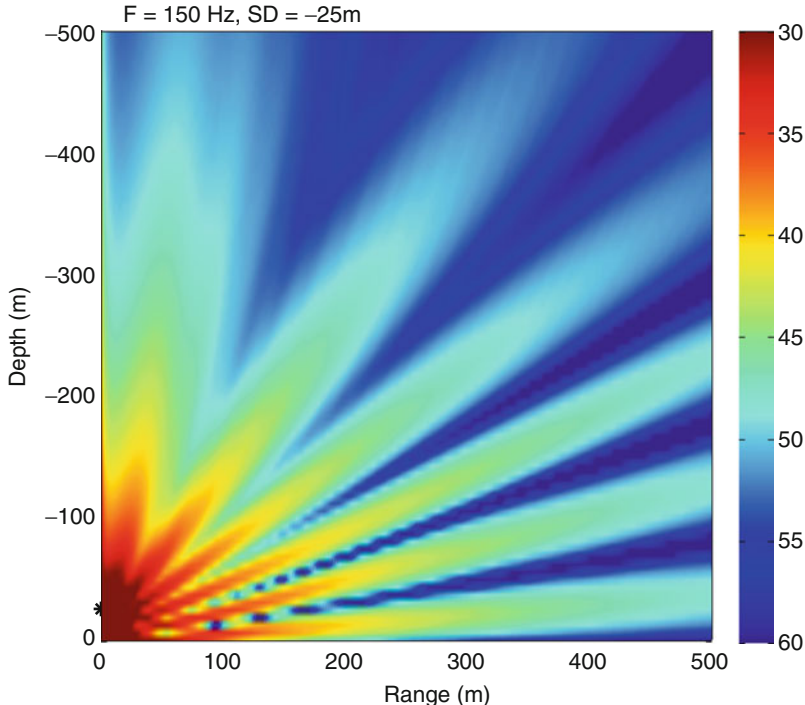


**Fig. 2.14** Pressure contours for reflection from a homogeneous halfspace

A numerical evaluation of the wavenumber integral representation for the total field yields the solution shown in Fig. 2.14 in the form of pressure contours in decibels. Comparing to the similar contour plot of the field in a fluid halfspace with a free surface, Fig. 2.7b, we note that for low grazing angles, the interference patterns are very similar, with a vanishing field for grazing angles approaching horizontal. This is because the phase of the reflection coefficient (see Fig. 2.10) approaches  $180^\circ$  for low grazing angles, which is the phase shift introduced also by the free surface. This clearly illustrates that the common assumption of a hard bottom reflecting similarly to an infinitely rigid bottom is a misconception. On the contrary, hard bottoms reflect as a free surface for small grazing angles.

The reflectivity behavior of various bottom types is more clearly illustrated by displaying the angular spectra of the total fields 50 m above the bottom, as shown in Fig. 2.15. As expected, the rigid bottom (dotted curve) has a maximum in the horizontal direction whereas the pressure-release bottom (dashed curve) has vanishing amplitude. The spectrum for the penetrable hard bottom (solid curve) is very similar to that of the pressure-release bottom for small grazing angles. On the other hand, for grazing angles larger than critical ( $33.5^\circ$ ), the reflectivity of the penetrable bottom is similar to that of the rigid bottom, except for the decrease in amplitude caused by the loss of energy to the transmitted wave.

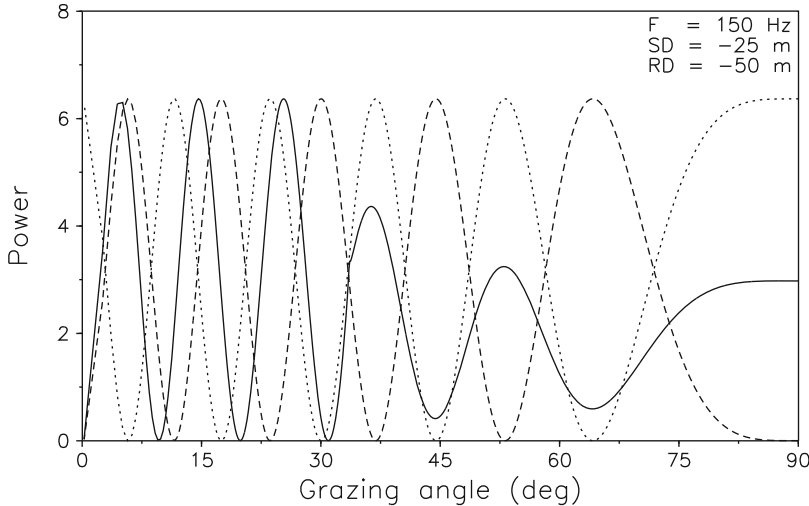


**Fig. 2.15** Angular spectrum for reflection from a homogeneous halfspace. *Solid curve:* Penetrable bottom. *Dashed curve:* Pressure release bottom. *Dotted curve:* Rigid bottom

#### 2.4.4 Ideal Fluid Waveguide

Up to this point we have dealt with the sea surface and sea bottom interactions as separate processes. However, the general ocean-acoustic propagation scenario involves interaction with both boundaries.

The simplest model of this ocean waveguide is a range-independent, isovelocitity water column with perfectly reflecting boundaries as shown in Fig. 2.16. Both the sea surface and the seafloor are taken to be pressure-release boundaries. As discussed in the previous section, this choice for the seafloor boundary condition is a reasonable approximation, since a penetrable seafloor at low grazing angles reflects similarly to a free surface. Moreover, long-range propagation is dominated by small propagation angles since high-angle energy is rapidly attenuated due to bottom loss.

Although the environmental model in Fig. 2.16 is a strongly over-simplified model of the real ocean, it is well-suited for illustrating some of the basic waveguide phenomena associated with ocean acoustic propagation.

As in the case of the simpler halfspace problems, we can obtain a solution to the waveguide problem using the superposition principle. The field produced by a point source at  $(0, z_s)$  in the absence of boundaries is given by

$$\psi(r, z) = -S_\omega \frac{e^{ikR}}{4\pi R} \quad (2.136)$$

Next, we need to add a solution to the homogeneous Helmholtz equation to satisfy the boundary conditions of vanishing pressure at the surface and bottom of the

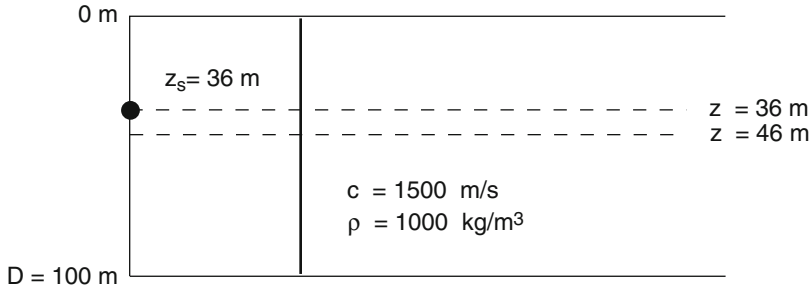


**Fig. 2.16** Idealized ocean waveguide model with pressure-release surface and bottom

waveguide. One method is to use the *image* or *mirror* method derived earlier from Green's theorem. However, this method is not easily generalized to more complex environments such as the Pekeris waveguide described in the next section. Alternatively, we use the integral transform technique, which is more general. The *image* method, however, has significant virtue in terms of physical understanding, and we shall therefore describe both solution approaches here.

#### 2.4.4.1 Image Method

As described in Sect. 2.4.2 for the homogeneous fluid halfspace, the image method superimposes the free-field solution with the fields produced by the image sources. In the halfspace case, only a single image source was necessary to satisfy the boundary conditions. In the waveguide problem, sound will be multiply reflected between the two boundaries, requiring an infinite number of image sources to be included. Figure 2.17 shows a schematic representation of the contributions from the physical source at depth  $z_s$  and the first three image sources, leading to the first 4 terms in the expression for the total field,

$$\psi(r, z) \simeq -\frac{S_\omega}{4\pi} \left[ \frac{e^{ikR_{01}}}{R_{01}} - \frac{e^{ikR_{02}}}{R_{02}} - \frac{e^{ikR_{03}}}{R_{03}} + \frac{e^{ikR_{04}}}{R_{04}} \right], \quad (2.137)$$

where the negative signs correspond to an odd number of reflections and the positive signs correspond to an even number of reflections. The remaining terms are obtained by successive imaging of these sources to yield the *ray expansion* for the total field,

$$\psi(r, z) = -\frac{S_\omega}{4\pi} \sum_{m=0}^{\infty} \left[ \frac{e^{ikR_{m1}}}{R_{m1}} - \frac{e^{ikR_{m2}}}{R_{m2}} - \frac{e^{ikR_{m3}}}{R_{m3}} + \frac{e^{ikR_{m4}}}{R_{m4}} \right] \quad (2.138)$$

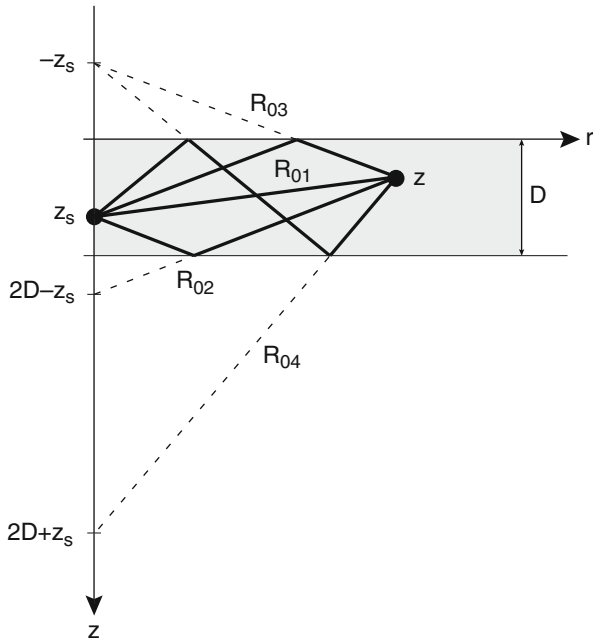


**Fig. 2.17** Superposition of free-field solution and first three image source solutions for an ideal waveguide

with

$$\begin{aligned}
 R_{mn} &= \sqrt{r^2 + z_{mn}^2}, \\
 z_{m1} &= 2Dm - z_s + z, \\
 z_{m2} &= 2D(m+1) - z_s - z, \\
 z_{m3} &= 2Dm + z_s + z, \\
 z_{m4} &= 2D(m+1) + z_s - z
 \end{aligned}$$

and  $D$  being the vertical depth of the duct.

The most important feature of the image approach is the direct association between individual terms in the ray expansion and a particular multiple arrival. However, it should be remembered that it is a steady-state solution, and the individual arrivals may only be identified in the time-domain solution, and here the frequency and bandwidth of the source signal plays an important role. Thus, only short, high frequency pulses can be individually identified as true images of the source signal.

To illustrate this important point, we substitute the time-domain Green's function of (2.55) into the above image solution to get the waveguide impulse response,

$$g_t(r, z) = \frac{1}{4\pi} \sum_{m=0}^{\infty} \left[ \frac{\delta(R_{m1}/c - t)}{R_{m1}} - \frac{\delta(R_{m2}/c - t)}{R_{m2}} \right. \\ \left. - \frac{\delta(R_{m3}/c - t)}{R_{m3}} + \frac{\delta(R_{m4}/c - t)}{R_{m4}} \right]. \quad (2.139)$$

The terms in the sum now represent a series of sharp impulses. For example, the first four terms, as per Fig. 2.17, represent direct, bottom bounce, surface bounce and bottom-surface bounce arrivals. One may convolve the results in (2.139) with a source function or filter these results within a specified bandwidth in order to obtain the pulse structure that indicates whether the arrivals are actually separated in time (see Sect. 8.3.1).

At lower frequencies the multiples will interfere in the time domain, and the received field will therefore be a distorted pulse. Here, an interpretation in terms of *normal modes* is more convenient. In general, the advantage of the source image approach and other ray approaches in terms of physical interpretation is most pronounced for high-frequency, transient propagation problems.

#### 2.4.4.2 Integral Transform Solution

Since the ideal waveguide is a simple example of a horizontally stratified medium, we can use the integral transform approach. The total field has the integral representation

$$\psi(r, z) = \int_0^\infty \psi(k_r, z) J_0(k_r r) k_r dk_r \quad (2.140)$$

with the kernel being a superposition of the depth-dependent Green's function and homogeneous solutions to the depth-separated wave equation,

$$\psi(k_r, z) = -S_\omega \left[ g_\omega(k_r, z, z_s) + H_\omega(k_r, z) \right]. \quad (2.141)$$

The free-field Green's function is given by (2.105) and the homogeneous solution by (2.98),

$$g_\omega(k_r, z, z_s) = -\frac{e^{ik_z|z-z_s|}}{4\pi ik_z}, \quad (2.142)$$

$$H_\omega(k_r, z) = A^+(k_r) e^{ik_z z} + A^-(k_r) e^{-ik_z z}. \quad (2.143)$$

The amplitudes of the homogeneous solutions are now determined from the boundary conditions. At both boundaries,  $z = 0$  and  $z = D$ , the pressure must vanish, requiring the displacement potential to vanish as well,

$$A^+(k_r) + A^-(k_r) = \frac{e^{ik_z z_s}}{4\pi ik_z}, \quad (2.144)$$

$$A^+(k_r) e^{ik_z D} + A^-(k_r) e^{-ik_z D} = \frac{e^{ik_z(D-z_s)}}{4\pi ik_z}. \quad (2.145)$$

These equations are now solved for the amplitudes  $A^\pm(k_r)$  of the homogeneous solution and superimposed onto the free-field solution to obtain,

$$\psi(k_r, z) = -\frac{S_\omega}{4\pi} \begin{cases} \frac{\sin k_z z \sin k_z(D - z_s)}{k_z \sin k_z D}, & z < z_s \\ \frac{\sin k_z z_s \sin k_z(D - z)}{k_z \sin k_z D}, & z > z_s. \end{cases} \quad (2.146)$$

This depth-dependent solution has poles for discrete values of the wavenumber given by

$$k_z D = m\pi, \quad m = 1, 2, \dots, \quad (2.147)$$

or, in terms of the horizontal wavenumber  $k_r = \sqrt{k^2 - k_z^2}$ ,

$$k_r = \sqrt{k^2 - \left(\frac{m\pi}{D}\right)^2}, \quad m = 1, 2, \dots \quad (2.148)$$

Equation (2.148) defines an infinite set of  $k_r$ -values, for which the solution has singularities, or poles, some of which may be real and the rest purely imaginary, as indicated in Fig. 2.18. The presence of the poles for real values of  $k_r$  is important for the evaluation of the wavenumber integral, (2.140), which by definition is performed along the real wavenumber axis. Using Cauchy's theorem we can deform the contour of integration into the complex plane to avoid the poles. Here, the *radiation condition* at  $r \rightarrow \infty$  determines whether the contour should pass above or below the poles on the real axis. We first use the relation between the Bessel and

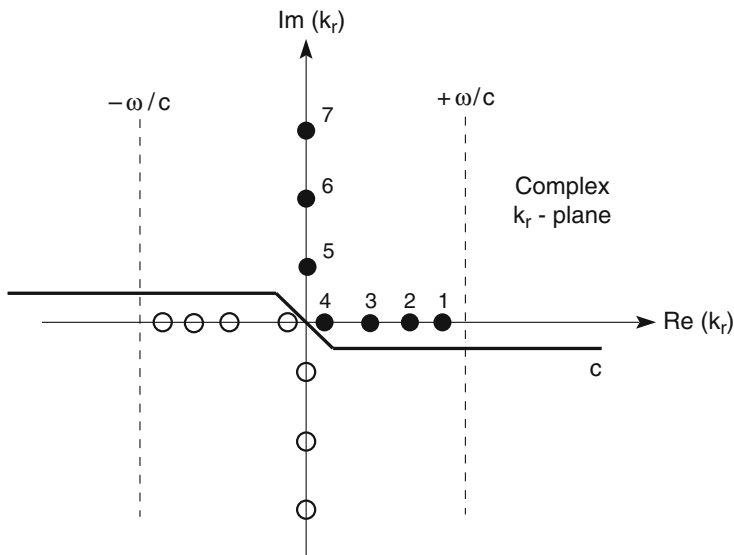


**Fig. 2.18** Singularities of the depth-dependent Green's function for an ideal waveguide

Hankel functions to change the integral into one containing only the Hankel function  $H_0^{(1)}(k_r r)$  representing outgoing waves at infinity,

$$\psi(r, z) = \frac{1}{2} \int_{-\infty}^{\infty} \psi(k_r, z) H_0^{(1)}(k_r r) k_r dk_r. \quad (2.149)$$

Due to the asymptotic behavior of the Hankel function, (2.39), we can close the integration contour in the upper imaginary halfplane, replacing the integral by the sum of the residues for the poles enclosed. To satisfy the radiation condition, only poles corresponding to outgoing and decaying waves should be enclosed by the contour. It is easily verified that the poles to be included are those on the positive real and imaginary axes, i.e., the filled circles in Fig. 2.18. Hence, the contour for evaluation of (2.149) should pass above the poles on the negative real axis and below the ones on the positive real axis as shown in Fig. 2.18. In principal, there are three different ways of evaluating the integral:

1. Asymptotic evaluation of the wavenumber integral by the method of stationary phase, which yields an expansion in terms of *eigenrays*, i.e., a series of rays connecting the source and receiver, including all reflected multiples. For the ideal waveguide, the terms in the stationary phase expansion are similar to the terms in (2.138) obtained by the *image method*. However, the stationary phase terms approximate the exact spherical wave representation by farfield plane waves. For horizontally stratified media, the stationary phase evaluation of the wavenumber integral is equivalent to the *ray tracing* approach described in Chap. 3.
2. Direct evaluation of the integral in (2.149) using numerical quadrature. This is the approach taken in the *wavenumber integration* techniques described in Chap. 4. This method is applicable to the present waveguide problem as well as to the earlier reflection and transmission problems.
3. Evaluation of the field as a sum of the residues for the poles enclosed by the integration contour described above. This is basically the approach taken in the *normal mode* methods described in Chap. 5. This method is applicable only to propagation problems which are dominated by the pole contributions.

#### 2.4.4.3 Normal Modes

The wavenumber integration approach is the most general since it is not dependent on the pole contributions being dominant. However, for the ideal waveguide an exact solution is obtained as an infinite sum of residues, and this solution is therefore the most convenient for this problem. In addition, each term in the sum has a distinct physical interpretation, as will be clear shortly. By simple algebra, the sum of the residues is obtained from (2.146) as,

$$\psi(r, z) = -\frac{iS_\omega}{2D} \sum_{m=1}^{\infty} \sin(k_{zm}z) \sin(k_{zm}z_s) H_0^{(1)}(k_{rm}r) \quad (2.150)$$

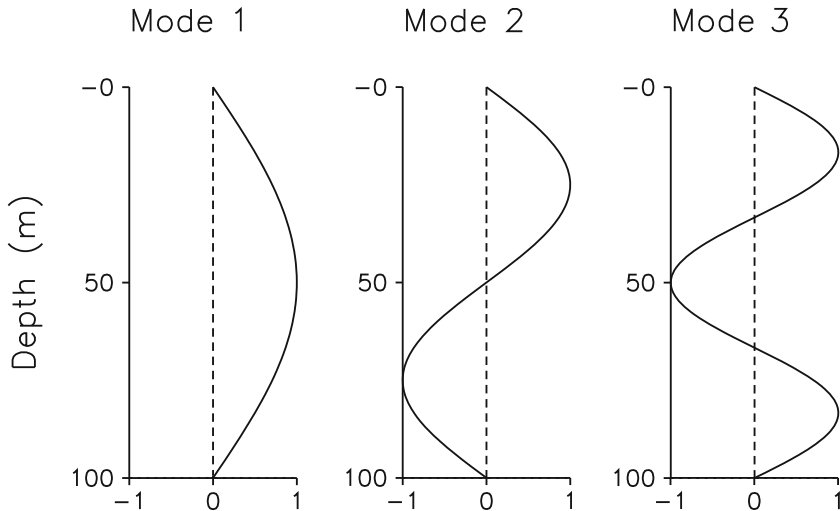


**Fig. 2.19** Depth dependence of the first 3 normal modes in ideal waveguide at 20 Hz

with the vertical and horizontal wavenumbers given by (2.147) and (2.148), respectively. Equation (2.150) is the *normal-mode expansion* of the field in the waveguide. Each term in the expansion has a simple trigonometric depth dependence of the form  $\sin(k_z m z)$ , as shown in Fig. 2.19.

In the normal-mode solution, the symmetry between source and receiver is evident. Therefore, if source and receiver are interchanged, the field remains the same, in accordance with the *reciprocity theorem* of linear acoustics. Further, it is clear that the magnitude of a particular mode, the *modal excitation*, is proportional to the amplitude of that particular mode at the source depth.

The horizontal dependence is determined by the horizontal wavenumber  $k_{rm}$ . There are naturally two groups of normal modes to be considered. The first group is the one for which  $k_{rm}$  is real. It is clear from the asymptotic form of the Hankel function, (2.39), that these modes are propagating horizontally away from the source. Similarly, it is easily verified from (2.39) that the modes with positive imaginary wavenumber are exponentially decaying in range, with a more rapid decay for larger absolute values of the wavenumber. The normal modes are therefore often categorized as follows:

$$\begin{aligned} \text{Propagating modes: } & k_{rm} \text{ real} & m < \frac{kD}{\pi}, \\ \text{Evanescent modes: } & k_{rm} \text{ imaginary} & m > \frac{kD}{\pi}. \end{aligned}$$

Here, it is important to emphasize the difference between the *evanescent modes* and the *evanescent spectrum* described earlier. The terms *radiating* and *evanescent spectra* refer to the *depth* behavior of the kernel in the spectral integral, the evaluation of which leads to the spatial representation of the field. In contrast, the modal sum is

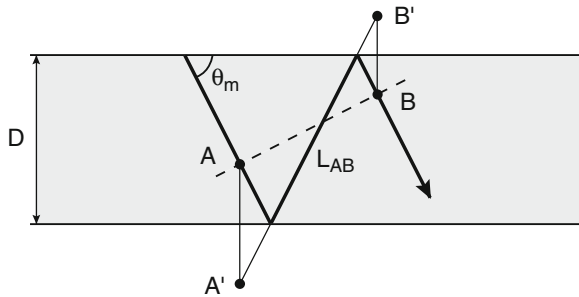


**Fig. 2.20** Geometrical interpretation of a normal mode

a result of the spectral integral being evaluated through contour integration, and the modal sum therefore directly represents the spatial distribution of the field, with the terms *propagating* and *evanescent* modes representing the field behavior in *range*. Consequently, there is no direct correspondence between the *evanescent* spectrum and the *evanescent* modes. In fact, since the spectral integral is evaluated along the real wavenumber axis, all the components in the kernel are *propagating* in range.

A normal mode is a superposition of up- and downgoing plane waves of equal amplitude and vertical wavenumber  $k_{zm}$ , as is clear from the relation

$$\sin(k_{zm}z) = \frac{e^{ik_{zm}z} - e^{-ik_{zm}z}}{2i}. \quad (2.151)$$

Both of these waves are propagating at grazing angles  $\theta_m = \arctan(k_{zm}/k_{rm})$ , where  $k_{rm}$  is the horizontal wavenumber. The ray path of such a plane wave in the waveguide is shown in Fig. 2.20. The dashed line shows the common wavefront for the wave passing through points A and B. The distance traveled between point A and B is

$$L_{AB} = \frac{2D}{\sin \theta_m} - \frac{2D}{\tan \theta_m} \cos \theta_m = 2D \sin \theta_m. \quad (2.152)$$

Insertion of the relation  $\sin \theta_m = k_{zm}/k$  together with (2.147) then yields,

$$L_{AB} = \frac{2\pi m}{k} = m\lambda, \quad (2.153)$$

where  $\lambda$  is the acoustic wavelength. Therefore, the discrete wavenumbers of the normal modes are those for which the multiple reflections of a plane wave are in phase at any point in the waveguide, which, in turn, gives rise to a resonance. It should be stressed that the ray equivalence of the modes illustrated in Fig. 2.20 is *different* from the ray representation of the *image method* in Fig. 2.17. Therefore, although both expansions in (2.138) and (2.150) provide exact solutions to the ideal waveguide problem, the physical significance of the individual terms is entirely

different. The *ray expansion* is a superposition of the field produced by all image sources, whereas the *modal expansion* is a sum of resonances or *eigenfunctions* for the waveguide.

We have here derived the modal expansion by complex contour integration of the Hankel transform solution. Alternatively, we could have derived the result directly as an eigenfunction expansion as is often done in the numerical models based on the normal mode approach (see Chap. 5). However, the present derivation clearly illustrates the close relationship between the *wavenumber integration* and *normal mode* approaches. Secondly, the present approach directly yields the individual modal amplitudes in (2.150), whereas the eigenfunction expansion approach must use the orthogonality relation of the modes to determine the modal amplitudes. Finally, since the wavenumber integral provides an exact solution, the derivation by contour integration directly provides an indication of the approximations made when applying normal mode approaches to non-perfect waveguides where the modal expansion is not exact. This will be demonstrated in the next section dealing with the classical Pekeris waveguide problem.

#### 2.4.4.4 Modal Dispersion

The number of propagating modes in a waveguide is dependent on frequency. Thus, it is clear from (2.148) that for  $kD < \pi$ , or  $\omega < \pi c/D$ , no propagating modes exist. On the other hand, at high frequencies there are many propagating modes. In addition, the modal wavenumbers relate to frequency in a nonlinear way, with the waveguide displaying strongly frequency-dependent propagation characteristics. The frequency dependence or *dispersion* of the normal modes is determined by inserting the definition of the medium wavenumber,  $k = \omega/c$ , into (2.148) and solving for  $\omega$ ,

$$\omega = c \sqrt{k_{rm}^2 + \left(\frac{m\pi}{D}\right)^2}. \quad (2.154)$$

This frequency–wavenumber relation for the modes is evident from Fig. 2.21, showing the so-called  $f - k$  diagram in the form of contours of the depth-dependent Green's function for source and receiver at depths 14 and 86 m, respectively, in a 100-m deep ideal waveguide. The hatched area indicates the spectral domain, bounded by the line  $f = \omega/2\pi = ck_r/2\pi$ , where the field is evanescent. Equation (2.154) shows that mode number  $m$  only has real horizontal wavenumbers for frequencies above the *cutoff frequency*  $f_{0m}$  given by

$$f_{0m} = \frac{\omega_{0m}}{2\pi} = \frac{mc}{2D}, \quad (2.155)$$

which for the present environmental model (Fig. 2.16) translates into  $f_{0m} = m \times 7.5$  Hz. These modal cutoff frequencies are evident also in Fig. 2.21 as regularly spaced high-intensity peaks along the frequency axis. At high frequencies, all modes asymptotically approach a propagation wavenumber which is equal to the medium wavenumber,  $k_{rm} \rightarrow k = \omega/c$ .

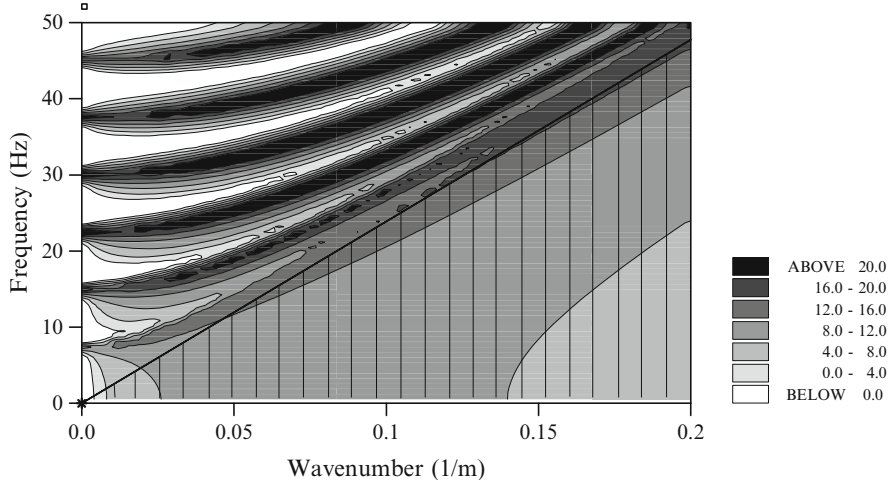


**Fig. 2.21**  $f - k$  diagram for a pressure-release waveguide of 100-m depth showing peaks corresponding to the first 6 propagating modes

The horizontal *phase velocity* of a mode is defined as

$$v_m = \frac{\omega}{k_{rm}}. \quad (2.156)$$

It is clear from Fig. 2.21 that the phase velocity is always larger than the medium velocity  $c$ , although it approaches  $c$  for increasing frequency. The phase velocity represents the horizontal velocity of a particular phase in the plane-wave representation of a mode, and it does not represent the speed of energy transport, which obviously must be less than or equal to the speed of sound. Thus, for steep propagation angles, the phase velocity approaches infinity, whereas horizontal propagation yields a phase velocity equal to the speed of sound. This, in turn, means that the plane waves interfering to produce a mode propagate nearly vertically when approaching the cutoff frequency, whereas the modal plane waves in the high-frequency limit propagate close to the horizontal.

To determine the energy transport velocity or *group velocity* of a particular mode, we need to transform the solution into the time domain since the concept of time has no meaning in the frequency domain. Assuming that we have a narrow-band source, the time dependence of the signal carried by mode number  $m$  is given by the inverse Fourier transform,

$$\psi(t) = \int_{\omega-\epsilon}^{\omega+\epsilon} \psi(\omega) e^{-i[\omega t - k_{rm}(\omega)r]} d\omega. \quad (2.157)$$

For a small time increment  $dt$  the signal will propagate horizontally a distance  $dr = u_m dt$ . The phase change of each component in the integral is therefore  $\omega$

$dt - k_{rm}(\omega) dr$ . For the signal to be unchanged over the time interval  $dt$  all components of the integral must stay in phase. This requires  $d\omega dt - dk_{rm}(\omega) dr = 0$ , or

$$u_m = \frac{dr}{dt} = \frac{d\omega}{dk_{rm}}. \quad (2.158)$$

Therefore, the signal carried by mode  $m$  will propagate with the horizontal speed  $u_m$ , which is the *group velocity*. It is found as the slope of the dispersion curves in Fig. 2.21.

Actually, for future reference, the group velocity can be obtained by the method of stationary phase analogous to the mathematical arguments used to introduce (2.134). Assuming the typical case that  $\psi(\omega)$  is a slowly changing function with respect to one oscillation of  $f(\omega) \equiv \omega t - k_{rm}(\omega)r$  in (2.157), most of the contributions to the integral will cancel out except in the non-oscillating neighborhood for those values of  $\omega$  for which  $f(\omega)$  is stationary. Then, for

$$\begin{aligned} \omega &= \omega_0 + \epsilon, \\ f'(\omega_0) &= 0 \quad \rightarrow \quad \frac{r}{t} = \frac{d\omega(k_{rm})}{dk_{rm}} \equiv u_{rm}, \end{aligned} \quad (2.159)$$

we can write the phase of the exponential as

$$f(\omega) = f(\omega_0) + \frac{\epsilon^2}{2} f''(\omega_0) + \dots \quad (2.160)$$

The limits of the integral in (2.157) can be extended to  $\pm\infty$  since the only contribution is from around  $\omega_0$ ; using (2.160), (2.157) becomes

$$\begin{aligned} \psi(t) &= \psi(\omega_0) e^{-i[\omega_0 t - k_{rm}(\omega_0)r]} \int_{-\infty}^{\infty} e^{-(i/2)\epsilon^2 f''(\omega_0)} d\epsilon \\ &= \frac{\sqrt{\pi}\psi(\omega_0)}{\left|\frac{1}{2}f''(\omega_0)\right|^{1/2}} e^{-i[\omega_0 t - k_{rm}(\omega_0)r \pm \pi/4]}, \end{aligned} \quad (2.161)$$

where  $f''(\omega_0)$  is evaluated from its definition and the  $\pm$  refers to whether  $f''(\omega_0)$  is negative or positive, respectively. The packet is now represented by a wave traveling at the group speed since the exponential above represents a wave satisfying the condition  $f'(\omega_0)$  as per (2.159). That is, since  $x/t = u_{rm}$ , a particular value of  $(\omega, k)$  found at  $(x_1, t_1)$  will be found at other space-time locations such that  $x_1/t_1 = x_2/t_2$ . Thus, we say that the energy associated with a particular frequency group will travel at the group speed  $u_{rm}$ .

The phase and group velocities versus frequency for the first 3 modes in the ideal waveguide are shown in Fig. 2.22. As required, the group velocity is always less than the speed of sound (1500 m/s), although approaching it at high frequencies. This is consistent with the above observation that at high frequencies the normal

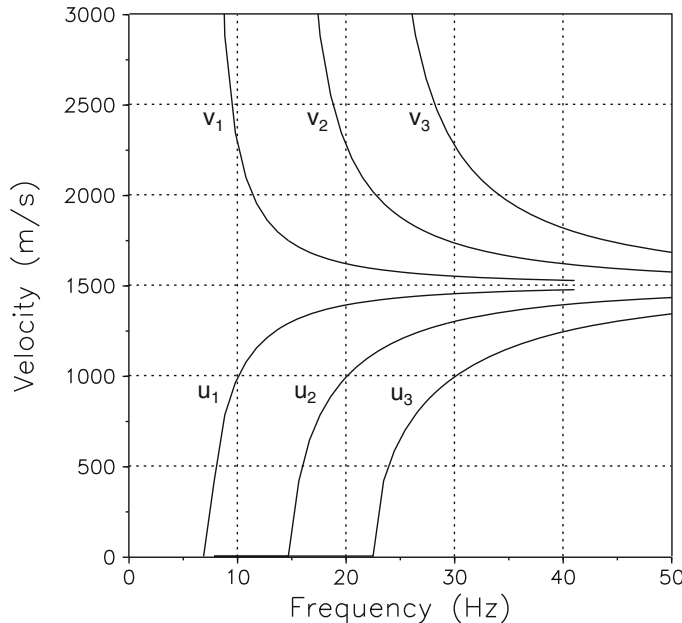


**Fig. 2.22** Frequency dependence of phase and group velocities for the first 3 propagating modes in an ideal waveguide

modes are produced by interference of plane waves propagating almost horizontally. Similarly, when approaching cutoff, the plane waves propagate more vertically, and consequently the group velocity approaches zero.

#### 2.4.4.5 The Waveguide Field

When two or more modes are propagating through the waveguide they will interfere. To illustrate this, consider two modes with horizontal wavenumbers  $k_{rm}$  and  $k_{rn}$  and amplitudes  $A_m(z)$  and  $A_n(z)$ , propagating far away from the source. Using (2.150) together with the asymptotic expression for the Hankel function, (2.39), the field of time dependence  $\exp(-i\omega t)$  is then found to have a range-dependent amplitude at depth  $z$  given by

$$\begin{aligned} |\psi(r, z)| &\simeq r^{-1/2} \left| A_m e^{ik_{rm}r} + A_n e^{ik_{rn}r} \right| \\ &= r^{-1/2} \sqrt{A_m^2 + A_n^2 + 2A_m A_n \cos[r(k_{rm} - k_{rn})]}. \end{aligned} \quad (2.162)$$

In addition to the cylindrical spreading loss  $r^{-1/2}$ , the amplitude will oscillate with the period

$$L = \frac{2\pi}{k_{rm} - k_{rn}}, \quad (2.163)$$

which is the *modal interference length*. The magnitude of the oscillations depends on the amplitudes of the two modes at depth  $z$ . Thus, if the two amplitudes are equal ( $A_m = A_n$ ), then the amplitude of the total field will vanish at ranges separated by the interference length  $L$ . If the amplitudes are different, the field never vanishes, but it shows an oscillatory pattern in range. Since the depth dependence is different for the two modes, also the modal interference pattern is depth dependent.

To illustrate the modal interference, we compute the field produced by a 20-Hz point source in a 100-m deep isospeed (1500 m/s) ocean environment with pressure-release surface and bottom. At 20 Hz, the number of propagating modes  $M$  is determined from the inequality

$$M < \frac{kD}{\pi} = \frac{2fD}{c} = 2.6667. \quad (2.164)$$

Therefore, two propagating modes will exist at 20 Hz, with the shapes given in Fig. 2.19. By placing the source at 36 m depth the two modes will be almost equally excited.

Figure 2.23a displays the magnitude of the depth-dependent solution, (2.146), versus horizontal wavenumber along a complex contour passing slightly below the real wavenumber axis as shown in Fig. 2.18. The solid curve shows the magnitude at depth 36 m, i.e., the same depth as the source, and the dashed curve shows the magnitude at 46 m depth. The two peaks correspond to the two modes of this problem, mode 1 with a wavenumber of  $0.076 \text{ m}^{-1}$ , and mode 2 with a wavenumber of  $0.055 \text{ m}^{-1}$ . At 36 m depth the modes are of almost equal amplitude, whereas mode 1 dominates at 46 m depths. The modal interference length is found from (2.163) to be  $L \simeq 300 \text{ m}$ , which is confirmed by the plot of the transmission loss versus range for the two depths, shown in Fig. 2.23b. Here, the change in interference strength with depth is evident as well.

Mode 1 is symmetric and mode 2 antisymmetric with respect to mid-depth as seen in Fig. 2.19. Therefore, the minima and maxima in the modal interference pattern will switch range position in the lower part of the waveguide. This is shown explicitly in Fig. 2.24, which displays transmission loss contours versus depth and range.

It should be emphasized that the solutions shown here are steady-state solutions of time dependence  $\exp(-i\omega t)$ , which means an unlimited duration of the source signal. For time-limited signals – even narrow-band CW signals – the different group velocities will separate the modes in the time domain at long ranges, as discussed in detail in Chap. 8. At a point in the waveguide where the steady-state solution predicts a vanishing field, the received field may consist of two identical CW pulses separated in time by  $\Delta t = \pi(1 + 2\ell)/\omega$ , with  $\ell$  being an integer, yielding a vanishing Fourier component at frequency  $\omega$ . This illustrates that care must be taken when analyzing experimental data of limited time duration with steady-state modeling techniques.

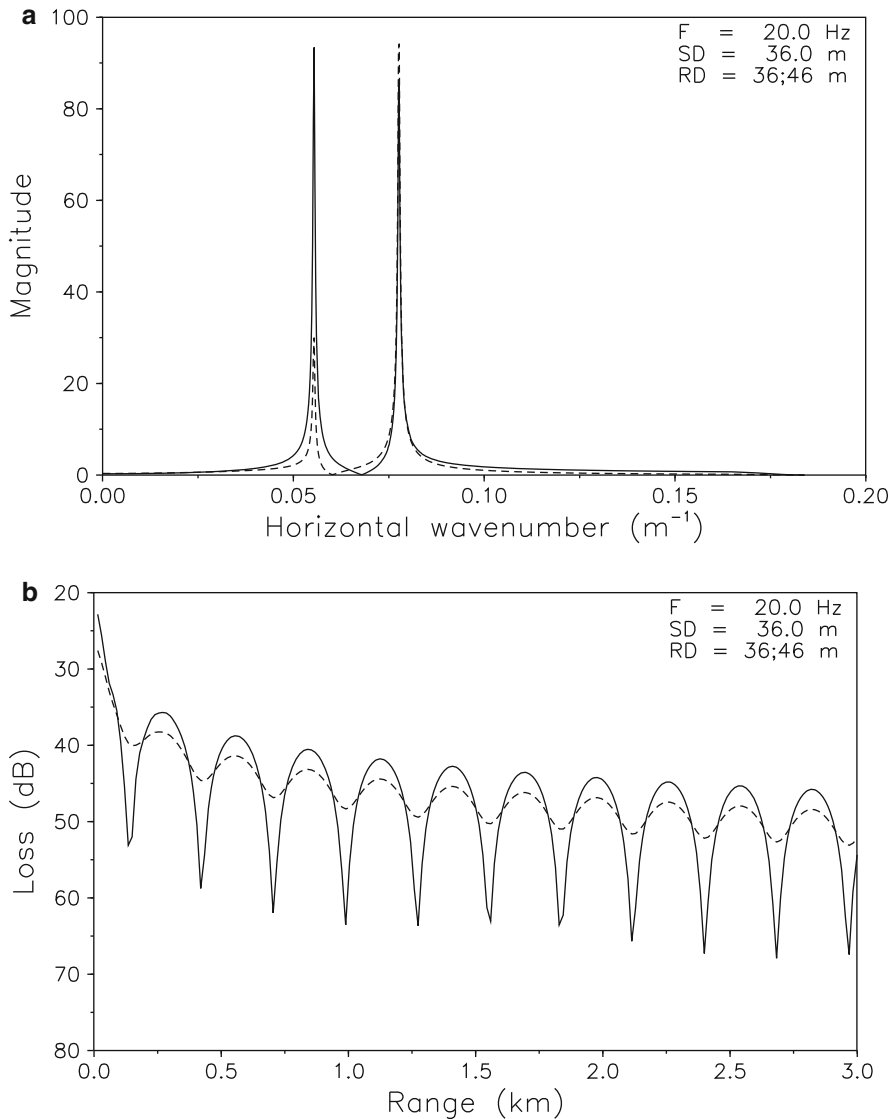


**Fig. 2.23** Acoustic field in an ideal waveguide of thickness 100 m for 20 Hz point source at 36 m depth. **(a)** Magnitude of the depth-dependent Green's function. **(b)** Transmission loss. *Solid curve:* Receiver depth 36 m. *Dashed curve:* Receiver depth 46 m

#### 2.4.4.6 Relationship Between Image and Modal Solutions

It is of interest to examine the relationship between the image solution and the modal solution [8]. Intuitively, it is clear, for example, that the Lloyd mirror field is easily described by using very few images whereas the field very far away from the

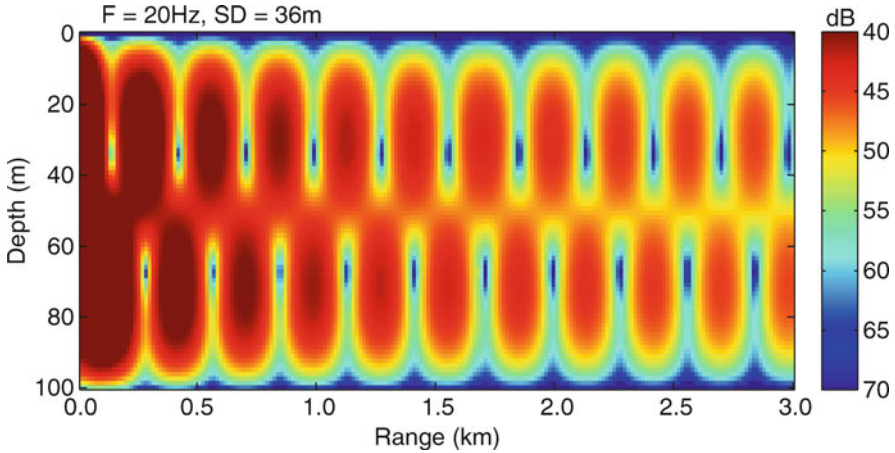


**Fig. 2.24** Contours of transmission loss vs. depth and range for 20 Hz point source at 36 m depth in an ideal waveguide of thickness 100 m

source in a waveguide would require a very large number of images as per (2.205). On the other hand, the description of the field near the source would require including the continuous spectrum, which, from Fig. 2.29a, we see involves a larger portion of the total wavenumber interval than the discrete part. This latter consideration implies that we must include a large sum of wavenumber components (that can be approximated by a large number of discrete modes of a much thicker waveguide). On the other hand, this near-field case can be treated by only a few images representing a direct path and a few bounces off either boundary with subsequent image contributions diminishing because higher angles have higher loss.

The above tradeoffs between images and modes leads us to the idea that the number of images and modal components have an inverse relationship similar to Fourier conjugate variables (e.g., the larger the relevant frequency interval, the shorter the pulse or time-domain interval). For simplicity, we seek the relationship between modal and image solutions of the ideal waveguide and therefore start with (2.150),

$$\psi = -\frac{iS_\omega}{4D} \sum_{n=1}^{\infty} \sin(k_{zn}z) \sin(k_{zn}z_s) H_0^{(1)}(k_{rn}r), \quad (2.165)$$

where  $k_{zn} = n\pi/D \equiv 2n\pi/d$  with the latter definition of  $d \equiv 2D$  being made for future convenience. Next, we employ the Poisson sum formula [12] (p. 483),

$$\sum_{m=-\infty}^{\infty} f(dm) = \frac{\sqrt{2\pi}}{d} \sum_{n=-\infty}^{\infty} F\left(\frac{2\pi}{d}n\right), \quad (2.166)$$

where we also use the Fourier transform convention in [12],

$$F(x) = \frac{1}{\sqrt{2\pi}} \int_{-\infty}^{\infty} f(y) e^{ixy} dy. \quad (2.167)$$

We, therefore, will be substituting (2.150) for  $F$ , which is even in  $n$  with the  $n = 0$  term vanishing, and where  $k_{rn}$  is given by (2.147) and (2.148). Therefore, each term is proportional to

$$\begin{aligned} F &= -\frac{iS_\omega}{4D} \sin(k_{zn}z) \sin(k_{zn}z_s) H_0^{(1)}(k_{rn}r) \\ &= -\frac{iS_\omega}{8D} \{\cos[k_{zn}(z - z_s)] - \cos[k_{zn}(z + z_s)]\} H_0^{(1)}(k_{rn}r). \end{aligned} \quad (2.168)$$

For the Poisson formula, these terms are all of the form

$$F_x = \pm \frac{iS_\omega}{8D} \cos[k_{zn}(z \pm z_s)] H_0^{(1)}(k_{rn}r) \equiv \pm \frac{iS_\omega}{4d} \cos(a_\pm x) H_0^{(1)}\left(r \sqrt{k^2 - x^2}\right), \quad (2.169)$$

where  $x \equiv 2n\pi/d$ ,  $d = 2D$ , and  $a_\pm = (z \pm z_s)$  and the  $\pm$ 's operations are realized together. The Poisson sum formula requires the Fourier transform over the even function  $F(x)$  and further, that it vanishes for  $n, x = 0$ . Therefore, we only require the cosine transform of  $F$  and the sum starting from  $n = 1$ . We can therefore rewrite the expression for the Poisson sum in the convenient form,

$$\frac{1}{2}f(0) + \sum_{m=1}^{\infty} f(dm) = \frac{\sqrt{2\pi}}{d} \sum_{n=1}^{\infty} \left[ \frac{-iS_\omega}{4\sqrt{2\pi}} \hat{F}\left(\frac{2\pi}{d}n\right) \right], \quad (2.170)$$

where we now can use cosine transforms and where,

$$\hat{F} = \cos(a_+x) H_0^{(1)}(r \sqrt{k^2 - x^2}) - \cos(a_-x) H_0^{(1)}\left(r \sqrt{k^2 - x^2}\right). \quad (2.171)$$

We then have for terms of the form  $f_\pm = f_+ - f_-$ ,

$$\begin{aligned} f_\pm(y) &= \pm \sqrt{\frac{2}{\pi}} \frac{iS_\omega}{4\sqrt{2\pi}} \int_0^\infty \cos(xy) \cos(a_\pm x) H_0^{(1)}\left(r \sqrt{k^2 - x^2}\right) dx \\ &= \frac{-iS_\omega}{4\pi} \int_0^\infty \{\cos[x(y + a_\pm)] + \cos[x(y - a_\pm)]\} H_0^{(1)}\left(r \sqrt{k^2 - x^2}\right) dx \\ &\equiv \pm \frac{S_\omega}{4\pi} [f(y + a_\pm) + f(y - a_\pm)], \end{aligned} \quad (2.172)$$

where  $y = dm = 2Dm$ . The integrals in all the terms can be evaluated using

$$\int_0^\infty \cos(xy) H_0^{(1)}(r \sqrt{k^2 - x^2}) dx = -\frac{ie^{ikR}}{R}, \quad R = \sqrt{r^2 + y^2}, \quad (2.173)$$

so that four terms are represented by,

$$f_{\pm}(y \pm a_{\pm}) = \pm \frac{-S_{\omega}}{4\pi} \frac{e^{ikR_{\pm a}}}{R_{\pm a}}, \quad R_{\pm a} = \sqrt{r^2 + (y \pm a_{\pm})^2}, \quad (2.174)$$

where we note that, for a given  $m$ , we have

$$R_{\pm a} = \begin{cases} \sqrt{r^2 + (2mD + z + z_s)^2}, \\ \sqrt{r^2 + (2mD + z - z_s)^2}, \\ \sqrt{r^2 + (2mD - z_s - z)^2}, \\ \sqrt{r^2 + (2mD - z + z_s)^2}. \end{cases} \quad (2.175)$$

We can rearrange the ordering of the *lhs* of (2.170) to be precisely equivalent to (2.138) since the quantities in the parentheses are a renumbered representation of the image depths listed below (2.138). For example, in (2.175) there are only two distinct terms for  $m = 0$  corresponding to  $\sqrt{r^2 + (z \pm z_s)^2}$ , which, by our convention are associated with  $\pm$  signs in front of each  $f_{\pm}$  term (note the factor  $\frac{1}{2}$  on the *lhs* of (2.170)). These two terms precisely correspond to the first and third terms of (2.138) for  $m = 0$ . The second and fourth terms of  $m = 0$  terms in (2.138) correspond to the third and fourth terms of  $m = 1$  in (2.175). Using all the  $m = 0$  and the third and fourth  $m = 1$  terms of (2.170) we therefore obtain the four  $m = 0$  terms in (2.138). Subsequent terms in this equation are obtained from the Poisson sum by similarly combining appropriate  $m, m + 1$  terms.

We have here shown that the modal sum is equivalent to the image sum and that they are Fourier transforms of each other in which the indices are the corresponding Fourier conjugate independent variables. It is important to note that in this isovelocity ideal waveguide, the image solution can be thought of as a ray representation of the total field that propagates from a point source. This is not at all the same as the geometrical interpretation or ray-mode analogy as depicted in Fig. 2.20. The latter refers to a homogeneous (source independent) solution of the waveguide whereas an image or mode solution corresponds to a particular solution for a specific source.

### 2.4.5 The Pekeris Waveguide

For the next level of complexity in modeling the ocean acoustic environment, we introduce the *Pekeris waveguide* shown in Fig. 2.25 [3]. Here, the bottom is more realistically represented by an infinite fluid halfspace, allowing for energy to be transmitted across the water-bottom interface and thereby introducing an additional loss mechanism to the waveguide propagation. As above, it is assumed that surface

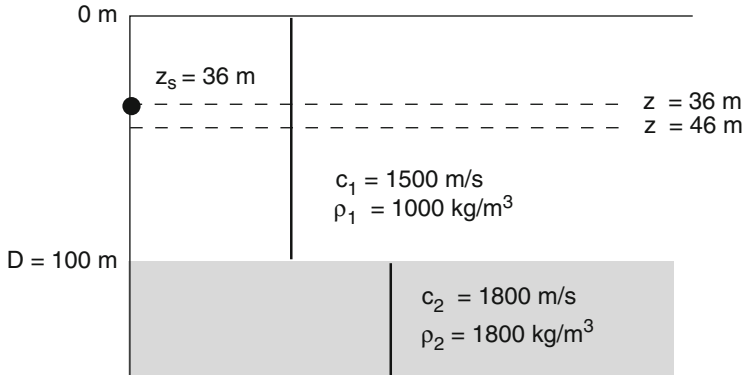


**Fig. 2.25** Pekeris waveguide with pressure-release surface and penetrable fluid bottom

and bottom are plane and parallel such that we can use the integral transform solution technique. The sound speeds are denoted  $c_1$  and  $c_2$  for the water and bottom, respectively, and the corresponding densities are  $\rho_1$  and  $\rho_2$ .

The source of strength  $S_\omega$  and time dependence  $\exp(-i\omega t)$  is assumed to be at depth  $z_s$  in the water column. Therefore, the kernel of the Hankel transform is,

$$\psi_1(k_r, z) = S_\omega \frac{e^{ik_{z,1}|z-z_s|}}{4\pi i k_{z,1}} + A_1^+(k_r) e^{ik_{z,1}z} + A_1^-(k_r) e^{-ik_{z,1}z} \quad (2.176)$$

with  $k_{z,1} = (k_1^2 - k_r^2)^{1/2}$ , where  $k_1 = \omega/c_1$  is the water wavenumber at frequency  $\omega$ . In the bottom the upward propagating component must vanish due to the boundary condition at infinity, yielding

$$\psi_2(k_r, z) = A_2^+(k_r) e^{ik_{z,2}(z-D)}, \quad (2.177)$$

where the vertical wavenumber must be defined as follows in order to satisfy the radiation condition for  $z \rightarrow \infty$ ,

$$k_{z,2} = \begin{cases} \sqrt{k_2^2 - k_r^2}, & |k_r| < k_2 \\ i \sqrt{k_r^2 - k_2^2}, & |k_r| > k_2, \end{cases} \quad (2.178)$$

with  $k_2 = \omega/c_2$ . We now have three unknown amplitudes of the homogeneous solutions to be determined from the boundary conditions.

The first boundary condition is that of *vanishing pressure* at the sea surface, requiring

$$A_1^+(k_r) + A_1^-(k_r) = S_\omega \frac{i e^{ik_{z,1}z_s}}{4\pi k_{z,1}}. \quad (2.179)$$

The remaining two boundary conditions are related to the field at the water–bottom interface. They are identical to the boundary conditions used to determine the plane-wave reflection coefficient, i.e., continuity of particle displacement, (2.122), and pressure, (2.124), across the interface. We obtain for continuity of *bottom particle displacement*,

$$k_{z,1} e^{ik_{z,1} D} A_1^+(k_r) - k_{z,1} e^{-ik_{z,1} D} A_1^-(k_r) - k_{z,2} A_2^+(k_r) = k_{z,1} S_\omega \frac{i e^{ik_{z,1}(D-z_s)}}{4\pi k_{z,1}} \quad (2.180)$$

and for continuity of *bottom pressure*,

$$\rho_1 e^{ik_{z,1} D} A_1^+(k_r) + \rho_1 e^{-ik_{z,1} D} A_1^-(k_r) - \rho_2 A_2^+(k_r) = \rho_1 S_\omega \frac{i e^{ik_{z,1}(D-z_s)}}{4\pi k_{z,1}}. \quad (2.181)$$

Equations (2.179), (2.180) and (2.181) combine into the following matrix equation for the amplitudes of the homogeneous solutions,

$$\begin{bmatrix} 1 & 1 & 0 \\ k_{z,1} e^{ik_{z,1} D} & -k_{z,1} e^{-ik_{z,1} D} & -k_{z,2} \\ \rho_1 e^{ik_{z,1} D} & \rho_1 e^{-ik_{z,1} D} & -\rho_2 \end{bmatrix} \begin{Bmatrix} A_1^+ \\ A_1^- \\ A_2^+ \end{Bmatrix} = \frac{i S_\omega}{4\pi k_{z,1}} \begin{Bmatrix} e^{ik_{z,1} z_s} \\ k_{z,1} e^{ik_{z,1}(D-z_s)} \\ \rho_1 e^{ik_{z,1}(D-z_s)} \end{Bmatrix}. \quad (2.182)$$

This system of equations with only three unknowns can obviously be solved analytically to yield a closed-form expression for the integration kernel in (2.176). However, in the general multi-layered case the number of equations scales approximately linearly with the number of layers, and the solution will have to be performed numerically, using one of the approaches described later in Chap. 4. On the other hand, the simplicity of the system of equations in (2.182) is convenient for demonstrating the non-triviality of obtaining stable numerical solutions.

Thus, if the coefficients in (2.182) are coded up directly, and the system is solved using a standard equation solver, numerical instability will occur in the evanescent regime  $|k_r| > k_1$  where the exponentials in the first and second column become exponentially growing and decaying, respectively. Once the difference in order of magnitude between the columns exceeds the arithmetic precision of the computer (15 digits in double precision), the system of equations becomes ill-conditioned because the two equations involving the exponentials become linearly dependent numerically. The solution to this numerical stability problem will be discussed extensively in Chap. 4, but is easily demonstrated for this simple example. Thus, unconditional stability is achieved by factoring out the growing exponential  $e^{ik_{z,1} D}$  from the first column, instead including it in the unknown complex amplitude  $A_1^+(k_r)$ . This is achieved simply by using the seabed instead of the sea surface

as arbitrary origin for the exponential function representing the “upgoing” wave in (2.176),

$$\psi_1(k_r, z) = S_\omega \frac{e^{ik_{z,1}|z-z_s|}}{4\pi i k_{z,1}} + A_1^+(k_r) e^{-ik_{z,1}(D-z)} + A_1^-(k_r) e^{-ik_{z,1}z}, \quad 0 \leq z \leq D. \quad (2.183)$$

Repeating the procedure above, the reader can easily verify that this kernel representation leads to a system of equation of the form

$$\begin{bmatrix} e^{-ik_{z,1}D} & 1 & 0 \\ k_{z,1} & -k_{z,1} e^{-ik_{z,1}D} & -k_{z,2} \\ \rho_1 & \rho_1 e^{-ik_{z,1}D} & -\rho_2 \end{bmatrix} \begin{Bmatrix} A_1^+ \\ A_1^- \\ A_2^+ \end{Bmatrix} = \frac{iS_\omega}{4\pi k_{z,1}} \begin{Bmatrix} e^{ik_{z,1}z_s} \\ k_{z,1} e^{ik_{z,1}(D-z_s)} \\ \rho_1 e^{ik_{z,1}(D-z_s)} \end{Bmatrix}, \quad (2.184)$$

where all terms with growing exponentials have been eliminated, resulting in a well-conditioned system which can be solved using a standard linear equation solver. It should be noted, though, that the solver, if based on Gaussian elimination, must apply pivoting to maintain stability if this system is applied directly in the above form (upper left coefficient will approach zero for large  $k_r$ ). As will be discussed in Chap. 4, even this tool can be avoided, simply by choosing a different ordering of the unknowns, here interchanging the up- and downgoing terms in (2.183). The use of proper origins for the exponentials, and a specific ordering of the unknowns are the basic ingredients of the Direct Global Matrix method described in Sect. 4.3.1. This procedure ensures unconditional stability at absolutely no computational cost, even in the general multilayered case.

#### 2.4.5.1 Normal Modes

The solution of (2.182) has poles for values of the horizontal wavenumber where the determinant of the coefficient matrix vanishes. The determinant is

$$\det(k_r) = -2i [\rho_1 k_{z,2} \sin(k_{z,1}D) + i\rho_2 k_{z,1} \cos(k_{z,1}D)] \quad (2.185)$$

leading to the following *characteristic equation* for the poles of the depth-dependent solution in the Pekeris waveguide,

$$\tan(k_{z,1}D) = -\frac{i\rho_2 k_{z,1}}{\rho_1 k_{z,2}}. \quad (2.186)$$

Like the case for the ideal waveguide, the solutions to (2.186) for which  $k_r$  is real correspond to *normal modes* propagating without loss (other than geometrical spreading loss). It is easily shown that (2.186) has solutions with real  $k_r$  only in the interval

$$|k_2| < |k_r| < |k_1|. \quad (2.187)$$

Therefore, no modes exist with real propagation wavenumbers less than  $k_2 = \omega/c_2$ . There is a simple physical explanation for this. For the small wavenumbers, the grazing angle of the plane waves constituting a mode would be above critical, with the field in the bottom being propagating in the vertical direction and therefore leaking energy out of the duct and into the bottom. A lossless mode can therefore not exist at these wavenumbers. Equation (2.186) may still have complex roots corresponding to modes decaying in amplitude with range. These solutions are called *leaky* or *virtual modes*.

As for the ideal waveguide, the inverse Hankel transform, (2.149), must be evaluated along the real wavenumber axis, passing below the poles on the positive axis and above the poles on the negative axis. Again, we can either evaluate the integral along such a contour, which is the *wavenumber integration* approach, or we can evaluate the integral by contour integration, closing the contour in the upper imaginary halfplane, the *normal mode* approach.

Here, however, the contour integration is not as simple as in the ideal waveguide case. This is due to the multi-valuedness of the square root function in the complex plane. Thus, for a complex variable  $z = \eta e^{i(\theta+2\pi n)}$  we have

$$\sqrt{z} = \sqrt{\eta} e^{i(\theta/2+n\pi)} = \pm \sqrt{\eta} e^{i\theta/2}, \quad 0 \leq \theta < 2\pi. \quad (2.188)$$

When choosing a particular definition – or *Riemann sheet* – for the square root as in (2.178), a discontinuity is introduced for the argument  $\theta = [0, 2\pi]$ , defining a *branch cut* for the square root. In (2.188) the branch cut was chosen to be along the real positive axis for the argument  $z$ , i.e.,  $\theta = [0, 2\pi]$ , but any value of  $\theta$  could be chosen for the branch cut. Depending on the form of the integration kernel, this discontinuity of the square root may introduce a discontinuity in the kernel. The closing of the integration contour requires that the integration kernel be analytic, and the contour must therefore not cross any discontinuities of the kernel. It is essential in the contour integration approach that the kernel discontinuities introduced by the branch cuts for the square root be properly defined.

The kernel for the total field is obtained by adding the free-field source contribution to the solutions of (2.182). Here, it turns out that the kernel is continuous at branch cuts for the vertical wavenumber  $k_{z,1}$ , but discontinuous at branch cuts for  $k_{z,2}$ . It is a general characteristic of integral transform solutions for layered problems that branch cuts exist for the upper and lower halfspaces, but never for the intermediate layers. This is clear from the form of the homogeneous solution, where a change of sign in the vertical wavenumber just switches the two terms, whereas a change of sign in the halfspace wavenumbers obviously affects the solution due to the fact that one term has been removed through the radiation condition.

The branch cuts for  $k_{z,2}$  must originate at the points  $k_r = \pm k_2$ , but can otherwise be chosen arbitrarily as long as they do not cross the real wavenumber axis along which the original integral is to be evaluated. A convenient choice is the EJP branch cut, named after Ewing, Jardetzky and Press [4], shown in Fig. 2.26. It is defined such that the vertical wavenumber  $k_{z,2} = (k_2^2 - k_r^2)^{1/2}$  is real along the branch cut, which covers the interval  $[-k_2, k_2]$  on the real  $k_r$  axis and the entire imaginary

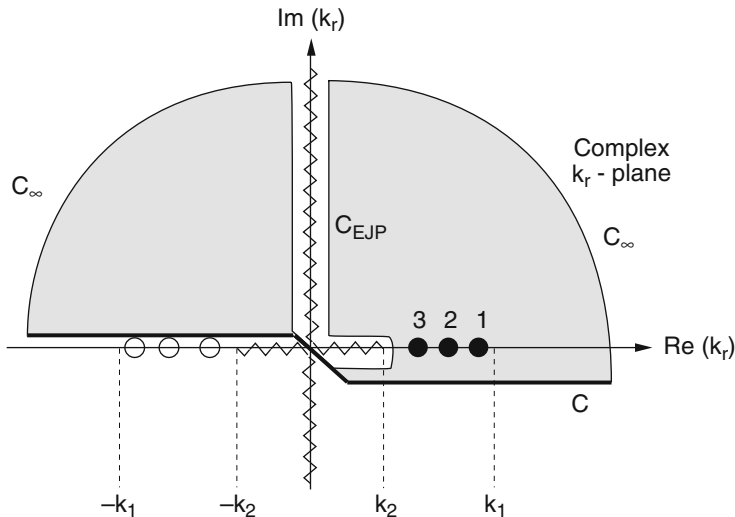


**Fig. 2.26** Complex wavenumber plane with EJP branch cut, poles and integration contour

axis. The EJP branch cut has the feature of yielding physically meaningful solutions in the bottom for all complex values of the wavenumber. Furthermore, it can be shown that no poles exist except for the ones on the real axis. With the choice of the vertical wavenumber definition given in (2.178), the Hankel transform, (2.149), must be evaluated along a contour passing below the branch cut on the positive real axis and above the branch cut on the negative real axis, as shown in Fig. 2.26.

We can now close the integration contour in the upper halfplane, replacing the original integral along the real axis with a sum of residues corresponding to the normal modes with real propagation wavenumbers, and a *branch line integral* along a contour  $C$  enclosing the *branch point*  $k_r = k_2$ . The branch line integral represents the contributions from spectral components radiating into the bottom ( $0 < k_r < k_2$ ), and from spectral components being evanescent in range. Therefore, the significance of the branch line integral diminishes with increasing range. The normal-mode approaches described in Chap. 5 often neglect the branch line contribution, thus yielding solutions which are not valid at short ranges.

The approximate modal solution for the Pekeris waveguide is similar in form to the modal sum for the ideal waveguide, (2.150), and given by

$$\psi(r, z) \simeq -\frac{iS_\omega}{2D} \sum_{m=1}^M a_m(k_{rm}) \sin(k_{zm}z) \sin(k_{zm}z_s) H_0^{(1)}(k_{rm}r), \quad (2.189)$$

where the modal wavenumbers  $k_{rm}$  are now solutions of the transcendental equation (2.186). The modal excitation is denoted  $a_m(k_{rm})$ , while  $k_{zm}$  is the vertical wavenumber in the water for mode  $m$ ,  $k_{zm} = k_{z,1} = (k_1^2 - k_{rm}^2)^{1/2}$ . As shown in Chap. 5, the modal excitation  $a_m(k_{rm})$  is a function of frequency.

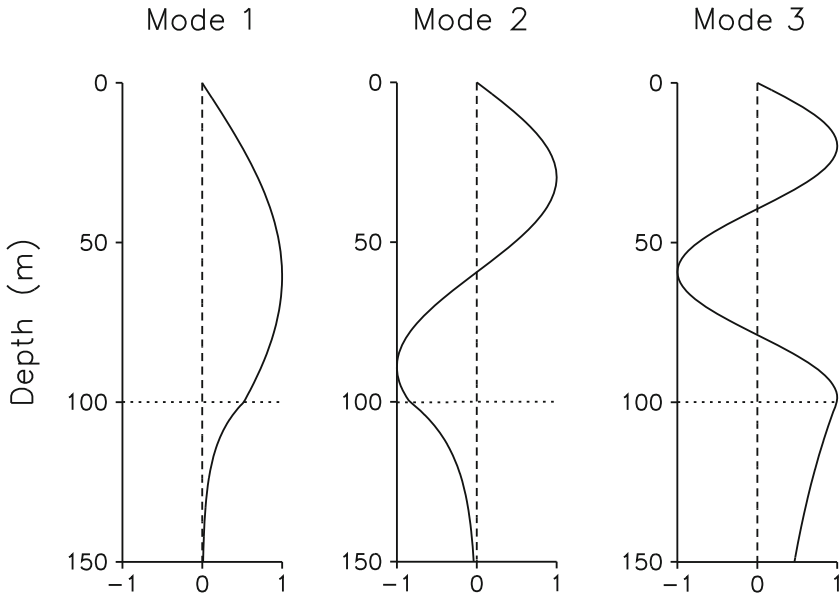


**Fig. 2.27** Depth dependence of acoustic pressure for the 3 normal modes in the Pekeris waveguide at 35 Hz

Each mode has a non-vanishing field in the bottom of the form given in (2.177), i.e., exponentially decaying in depth for  $k_{rm} > k_2$ . This is illustrated in Fig. 2.27 where the modal shapes at 35 Hz are shown in both the water column and the bottom for the environment given in Fig. 2.25. Note that the higher modes have smaller absolute values of the vertical wavenumber in the bottom and hence a longer evanescent tail. As explained earlier, the lower-order modes are very similar in shape to those of the ideal pressure-release waveguide, with a low amplitude near the bottom. On the other hand, the higher-order modes approach the shape expected for the ideal waveguide with a rigid bottom, for which the boundary condition is  $\partial\psi/\partial z = 0$ , leading to a high mode amplitude near the bottom.

#### 2.4.5.2 Modal Dispersion

The modal expansion in (2.189) is truncated to the  $M$  modes with real propagation wavenumbers. As was the case for the ideal waveguide,  $M$  increases with increasing frequency. When the frequency is lowered, the propagation wavenumber of a particular mode decreases according to the modal dispersion defined by the characteristic equation (2.186). When the modal wavenumber reaches the limit  $k_{rm} = k_2$ , the associated pole leaves the real axis, and although this complex mode still influences the field, it is said to be cut off. The radial cutoff frequency  $\omega_{0m}$  for mode

$m$  is determined from (2.186) by inserting  $k_{rm} = k_2 = \omega_{0m}/c_2$ , i.e.,  $k_{z,2} = 0$ , yielding

$$k_{zm}D = \omega_{0m}D \sqrt{c_1^{-2} - c_2^{-2}} = \frac{\pi}{2} + (m - 1)\pi, \quad m = 1, 2, \dots, \quad (2.190)$$

which leads to the following expression for the cutoff frequency for mode number  $m$ ,

$$f_{0m} = \frac{\omega_{0m}}{2\pi} = \frac{(m - 0.5)c_1c_2}{2D\sqrt{c_2^2 - c_1^2}}. \quad m = 1, 2, \dots \quad (2.191)$$

For increasing frequency, the wavenumber for a given mode approaches the water wavenumber  $k_1$  corresponding to horizontally propagating plane waves. The characteristic equation yields,

$$k_{zm}D \rightarrow m\pi \quad \text{for} \quad \omega \rightarrow \infty, \quad (2.192)$$

which is exactly the characteristic equation for the ideal waveguide. Therefore, as frequency increases, the modes of the Pekeris waveguide become more and more similar to those of the ideal waveguide described earlier. This asymptotic behavior of the modal dispersion is evident from Fig. 2.28a showing the  $f - k$  diagram in the form of contours of the depth-dependent Green's function for source and receiver at 14 and 86 m depth, respectively. The triangle in the lower right part of the figure bounded by the line  $f = \omega/2\pi = c_1k_r/2\pi$ , represents the spectral regime where the field is evanescent in the water column. On the other hand, the triangle in the upper left part bounded by the line  $f = \omega/2\pi = c_2k_r/2\pi$ , represents the *continuous spectrum* where the field is radiating into the bottom. Therefore, the relatively narrow, hatched part of the diagram represents the *discrete spectrum*. It is clear from Fig. 2.28a that for the Pekeris waveguide the cut off of the normal modes is a gradual process, with the modes having significant amplitudes well into the continuous spectrum. The continuous spectrum can, therefore, contribute significantly to the acoustic field as will be illustrated by an example in the next section.

Figure 2.28b displays the phase and group velocities for the first 3 modes versus frequency, as determined by the expressions  $v_m = \omega/k_{rm}$  and  $u_m = d\omega/dk_{rm}$ , respectively. At high frequencies the phase and group velocities both approach the water sound speed (1500 m/s), whereas at cutoff, both velocities approach the bottom sound speed (1800 m/s). While the phase velocity is monotonically decreasing with frequency, the group velocity has a minimum at a certain frequency, which in time-domain solutions give rise to the so-called *Airy phase* forming the tail of a transient modal arrival.

If, instead of the EJP branch cut, we choose the one used by Pekeris [3], poles will appear for complex wavenumbers close to the real and imaginary axes corresponding to *leaky* or *virtual modes*. Although this branch cut does not totally eliminate the branch line contribution, the inclusion of the virtual modes close to the real axis provides a better approximation to the full solution than that obtained by excluding the EJP branch line contribution. This will be discussed in more detail in Chap. 5.

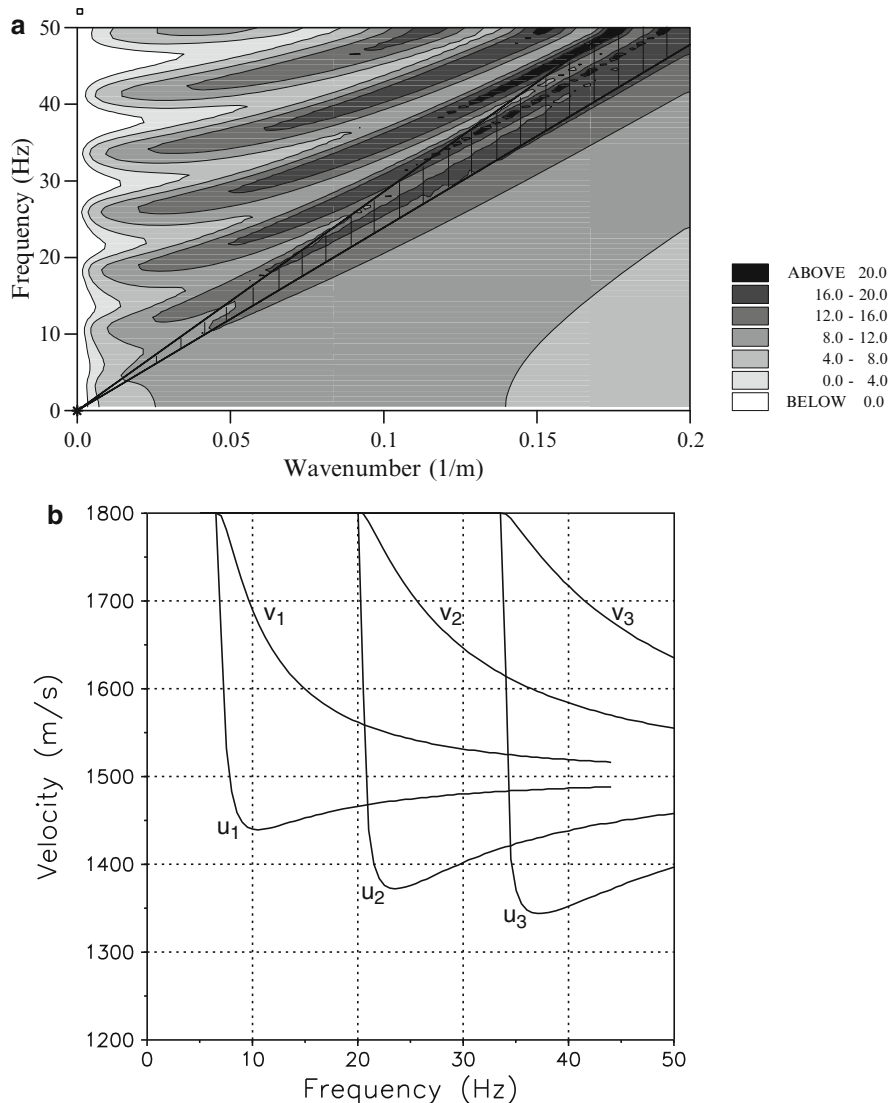


**Fig. 2.28** Dispersion of modes in the Pekeris waveguide. **(a)**  $f - k$  diagram in the form of contours of the depth-dependent Green's function. **(b)** Phase and group velocities vs. frequency for the first 3 modes

#### 2.4.5.3 The Waveguide Field

The presence of the branch line contribution makes the *modal* solution approximate, and we will therefore proceed with the *wavenumber integration* approach. It is

clear from Fig. 2.26 that the positive wavenumber axis is divided into three different spectral domains:

- $0 < k_r < k_2$  : The *continuous spectrum* where waves are radiating into the bottom, thus leaking energy away from the waveguide. Consequently, no lossless modes can exist in this spectral domain. On the other hand this part of the spectrum reflects the presence of leaky modes.
- $k_2 < k_r < k_1$  : The *discrete spectrum* where the field is propagating vertically in the water and is exponentially decaying in the bottom. This part of the spectrum contains the discrete poles corresponding to lossless modes.
- $k_1 < k_r$  : The *evanescent spectrum* where wave components in both water and bottom are exponentially decaying in the vertical. For the Pekeris waveguide no poles exist in this domain. However, for elastic bottoms the seismic interface waves pertain to this spectral domain.

To illustrate the significance of the different spectral domains, we consider a numerical example for the Pekeris waveguide given in Fig. 2.25. Except for the penetrable bottom with sound speed  $c_2 = 1800 \text{ m/s}$  and density  $\rho_2 = 1800 \text{ kg/m}^3$ , all other parameters are identical to those considered earlier for the ideal pressure-release waveguide.

Figure 2.29a shows the Hankel transform kernel along the same contour used in Fig. 2.23a for the ideal waveguide. The solid curve shows the kernel for a receiver depth of 36 m and the dashed curve for a receiver depth of 46 m. The different spectral regimes are separated by vertical dotted lines at  $k_r = k_1, k_2$ . There is one sharp peak in the discrete spectrum corresponding to the first propagating mode. The second peak at  $k_r = 0.068 \text{ m}^{-1}$  is part of the continuous spectrum, indicating the presence of a leaky mode close to the real axis. The width of the peak is related to the distance of the pole from the real axis, which is directly related to the modal damping versus range. In the present case, the leaky mode is very close to the real axis, and the associated modal damping is small. The modal wavenumbers are also affected by the presence of the bottom, with the second mode in particular moving to a higher horizontal wavenumber, and therefore lower vertical wavenumber compared to the ideal waveguide case. Therefore, the modal excitation is changed as well. The resultant transmission loss is shown in Fig. 2.29b. Since the propagating and the leaky modes are closer in terms of wavenumber, the modal interference length is longer than in the ideal waveguide case. The fact that one of the modes is attenuated with range due to leakage reduces the modal interference with range, and the field will ultimately be dominated by the lossless mode.

This example clearly illustrates the limitation of the traditional normal-mode approach. Thus, if the EJP branch line integral or the leaky modes for the Pekeris branch cut are ignored, only the propagating mode would be included, thus totally eliminating the modal interference, and providing accurate results only at very long ranges. The inclusion of the leaky modes in the solution is most important for cases with few propagating modes, e.g., in low-frequency shallow-water acoustics.

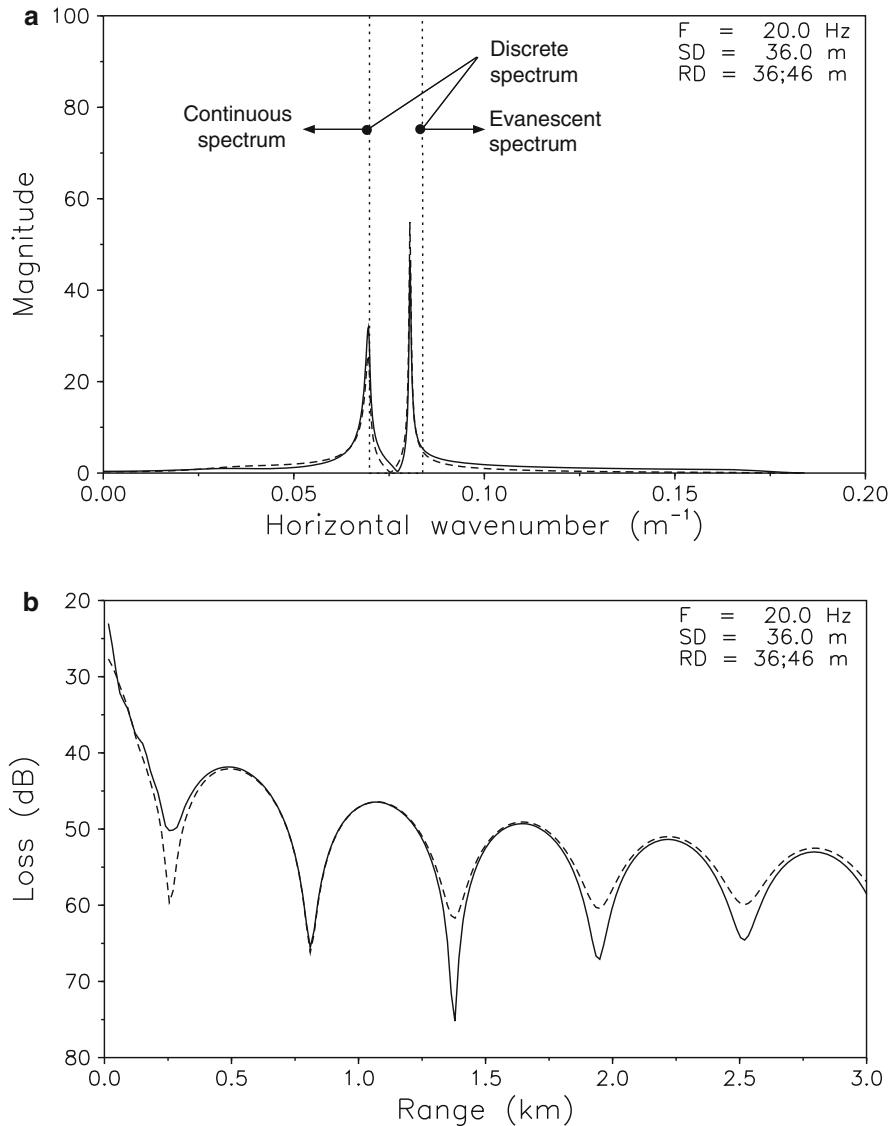


**Fig. 2.29** Acoustic field in a 100-m deep Pekeris waveguide for 20 Hz point source at 36 m. (a) Magnitude of depth-dependent Green's function. (b) Transmission loss. *Solid curve*: Receiver depth 36 m. *Dashed curve*: Receiver depth 46 m

#### 2.4.5.4 Reciprocity

The Pekeris waveguide and other stratified environmental models are characterized by discrete changes in density at the interfaces, with the displacement potential consequently being discontinuous. Therefore, the simple wave equation is not valid

at the interface itself, and the continuity of pressure and particle displacement across the interface is handled through the boundary conditions. As a consequence, the Green's function, although symmetric within each constant-density layer, is not symmetric across the interfaces. However, the acoustic field must still satisfy the *reciprocity principle* of linear acoustics, which is formally derived in Appendix 1. This is easily confirmed by modifying the discrete changes in density and sound speed at the interface to a gradual transition over a small region  $\epsilon$ . Then the transmission loss pressure for a source at  $\mathbf{r}_s$  is governed by the pressure wave equation (2.83), or for a field of time dependence  $\exp(-i\omega t)$ ,

$$\rho \nabla \cdot \left[ \frac{1}{\rho} \nabla P(\mathbf{r}, \mathbf{r}_s) \right] + k^2 P(\mathbf{r}, \mathbf{r}_s) = -4\pi \delta(\mathbf{r} - \mathbf{r}_s). \quad (2.193)$$

As described in Appendix 1, the solutions to (2.193) satisfy the reciprocity relation,

$$\rho(\mathbf{r}_s) P(\mathbf{r}, \mathbf{r}_s) = \rho(\mathbf{r}) P(\mathbf{r}_s, \mathbf{r}). \quad (2.194)$$

Now, by letting the transition region  $\epsilon$  approach zero, the solution will converge toward the solution for the original problem with discontinuous density and sound speed, and the transmission loss in the Pekeris waveguide and other stratified fluid media must therefore satisfy the reciprocity relation in (2.194) as well.

For the elastic stratifications treated in Chap. 4, the field must also satisfy certain reciprocity relations, specifically the *elastodynamic reciprocity theorem* ([13], Sect. 1.13). This classical reciprocity principle, which forms the basis for many engineering approaches such as the *principle of virtual work*, states that *for two independent forcing systems, the work carried out by the external forcing of one system on the response of the second system, is equal to the work carried out by the external forcing of the second one on the response of the first system*. We will here demonstrate that for fluid media this principle of reciprocity is consistent with (2.194).

For fluid media, the external forces are represented by the volume injection of the source, and the response is represented by the acoustic pressure [14]. Using the source definitions of Sect. 2.3.2, consider a simple point source of strength  $S_\omega$  at a point  $\mathbf{r}_1$  in an acoustic medium with density  $\rho_1$  and sound speed  $c_1$ . By definition this source creates a volume injection of  $S_\omega \delta(\mathbf{r} - \mathbf{r}_1)$ . At a receiver  $\mathbf{r}_2$  in a medium with density  $\rho_2$  and sound speed  $c_2$  this source will produce a displacement potential  $\psi(\mathbf{r}_2)$  with associated pressure,

$$p(\mathbf{r}_2) = \rho_2 \omega^2 \psi(\mathbf{r}_2). \quad (2.195)$$

A point source of strength  $S'_\omega$  placed at  $\mathbf{r}_2$  will similarly correspond to a forcing, or volume injection, of  $S'_\omega \delta(\mathbf{r} - \mathbf{r}_2)$ , and produce a pressure at  $\mathbf{r}_1$  given by

$$p'(\mathbf{r}_1) = \rho_1 \omega^2 \psi'(\mathbf{r}_1). \quad (2.196)$$

Now, the classical reciprocity principle states,

$$\int_V S_\omega \delta(\mathbf{r} - \mathbf{r}_1) p'(\mathbf{r}) dV = \int_V S'_\omega \delta(\mathbf{r} - \mathbf{r}_2) p(\mathbf{r}) dV, \quad (2.197)$$

or

$$S_\omega p'(\mathbf{r}_1) = S'_\omega p(\mathbf{r}_2). \quad (2.198)$$

This is the reciprocity principle for *pressure*. As described in Sect. 2.3.5, in order for the field solutions to directly represent transmission loss, the source strengths must be  $S_\omega = 4\pi/(\rho_1\omega^2)$  and  $S'_\omega = 4\pi/(\rho_2\omega^2)$ . Insertion of these into (2.198) directly yields the reciprocity relation for *transmission loss pressure* in (2.194).

By inserting the relations between potential and pressure into (2.198), we obtain the *reciprocity relation* for the *displacement potentials*,

$$\rho_1 S_\omega \psi'(\mathbf{r}_1) = \rho_2 S'_\omega \psi(\mathbf{r}_2). \quad (2.199)$$

#### 2.4.5.5 Attenuation

Up to this point, we have considered acoustic environments consisting of ideal fluid media. However, in the real ocean, sound waves are attenuated due to dissipation of energy into heat. The attenuation in sea water is very low at low and intermediate frequencies, and acoustic signals may propagate for thousands of kilometers without significant attenuation except for geometrical spreading loss. However, ocean sediments are characterized by high energy loss due to internal friction. Therefore, in environments with significant bottom interaction, such as shallow-water ducts similar to the Pekeris waveguide, bottom attenuation becomes a significant loss factor also for waterborne energy. Hence, in these cases it is crucial for a realistic modeling of the propagation characteristics that bottom attenuation be taken into account. The integral transform technique used for solving the Pekeris problem is easily modified to incorporate this effect.

Assume a plane harmonic wave of angular frequency  $\omega$  propagating in a homogeneous medium along the positive  $x$ -axis of a Cartesian coordinate system. In the absence of attenuation, such a wave has the form

$$\psi(x, t) = A e^{-i(\omega t - kx)}, \quad (2.200)$$

where  $k$  is the medium wavenumber and  $A$  is the amplitude. In the ideal fluid,  $k$  is real and the plane wave has constant amplitude for all ranges  $x$ . However, in reality the wave amplitude will decrease with range, and for media behaving in a linear fashion, e.g., linearly viscoelastic media, this attenuation must be exponential in range, and the plane-wave solution therefore takes the form

$$\psi(x, t) = A e^{-i(\omega t - kx) - \alpha x}, \quad \alpha > 0. \quad (2.201)$$

Defining  $\alpha = k\delta$ , (2.201) can be rewritten as

$$\psi(x, t) = A e^{-i[\omega t - k(1+i\delta)x]}, \quad (2.202)$$

which is a solution to the Helmholtz equation (2.31) with complex wavenumber,

$$\tilde{k} = k(1 + i\delta). \quad (2.203)$$

In isotropic media, the same will be the case for plane, attenuated waves in any spatial direction, and since the integral transform solution is based on a plane-wave decomposition, it is obvious that a viscoelastic attenuation can be accounted for by simply letting the medium wavenumbers be complex. All the waveguide solutions described above are, therefore, directly applicable to problems involving viscoelastic media.

The attenuation factor  $\delta$  is called the *loss tangent*. However, in underwater acoustics it is more common to express the attenuation in  $\text{dB}/\lambda$ , where  $\lambda$  is the wavelength,

$$\alpha = -20 \log \left| \frac{\psi(x + \lambda, t)}{\psi(x, t)} \right| = -20 \log [e^{-\delta k \lambda}] = 40\pi \delta \log e \simeq 54.58 \delta. \quad (2.204)$$

The attenuation in sediments is typically of the order 0.1–1.0  $\text{dB}/\lambda$  (see Sect. 1.6) with the corresponding loss tangents of order 0.002–0.02. Even with the imaginary part of the wavenumber being that small, the attenuation in range can be significant. Thus, Fig. 2.30 shows the transmission loss versus range at 46 m depth for

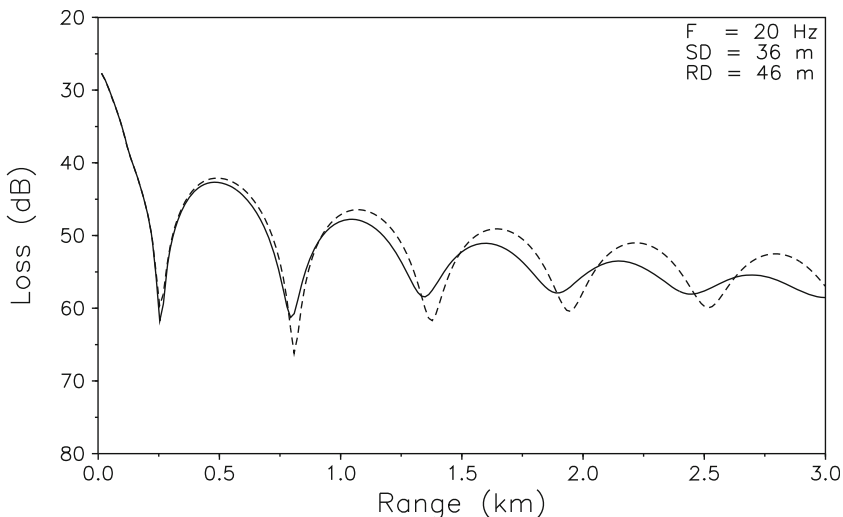


**Fig. 2.30** Transmission loss vs. range in a Pekeris waveguide with water depth 100 m. *Solid curve*:  $1.0 \text{ dB}/\lambda$  sediment attenuation. *Dashed curve*: lossless

the Pekeris waveguide example. The solid curve is for a bottom loss of  $1.0 \text{ dB}/\lambda$ , whereas the dashed curve is the lossless result, identical to the dashed curve in Fig. 2.29b.

There are three differences worth commenting on. Firstly, the transmission loss increases more rapidly with range for the lossy bottom. Secondly, the modal interference length is slightly different in the two cases, and finally the modal interference pattern is disappearing more rapidly with range for the lossy bottom.

Whereas the first difference is expected due to energy loss in the sediment, the two latter points are less obvious. However, they are quite easily explained by analyzing the behavior of the modal poles when attenuation is introduced. In that case, the branch point  $k_r = k_2$  in Fig. 2.26 moves slightly off the real axis and into the positive imaginary wavenumber plane. The same is the case for the solutions to the characteristic equation (2.186), with the imaginary part of the wavenumber representing the attenuation in range for the corresponding mode. Also, the real part of the modal wavenumber will change slightly. The effect is stronger the closer the modal wavenumber is to the branch point  $k_r = k_2$ . Therefore, both the imaginary and the real part of the propagation wavenumber will change more for the higher-order modes than for the lower-order modes. As a result the higher-order modes show more range attenuation than the lower-order modes. In physical terms, this is consistent with the observation that the higher-order modes have longer evanescent tails in the bottom and therefore are more sensitive to changes in bottom parameters.

In the present example, the second mode is leaky and therefore not in the discrete spectrum. However, it is very close to the branch point, thus undergoing bigger changes in terms of both propagation wavenumber and attenuation than the first, discrete mode. The result is a change in the modal interference length as well as a more rapid range decay of the field produced by the second mode, leading to a decaying interference pattern.

The field solutions shown in Fig. 2.30 are computed by wavenumber integration, for which the attenuation is actually an advantage due to the fact that the modal singularities are removed from the real integration axis. However, this example again stresses the care that must be exercised when devising approximate numerical schemes. Thus, as described in Chap. 5, most normal-mode approaches determine the real modal wavenumbers for the lossless case and add the modal attenuation in a perturbational sense. These methods will therefore not predict the change in interference pattern caused by changes in the real part of the propagation wavenumber. In propagation problems with small attenuation and many modes, the error is insignificant, but in extreme cases with high attenuation and few modes, such as the present example, the effect on the interference pattern may be important at long ranges.

#### 2.4.5.6 General Waveguide Image Solution

The Pekeris waveguide has a bottom whose reflection coefficient is given by (1.56). In general, if we let the reflection coefficient of the upper and lower boundaries of

the waveguide be given as  $\mathcal{R}_1$  and  $\mathcal{R}_2$  evaluated at the appropriate angle associated with each image term, respectively, then the generalized form of (2.138) (from [8]) is

$$\psi(r, z) = \frac{S_\omega}{4\pi} \sum_{m=0}^{\infty} (\mathcal{R}_1 \mathcal{R}_2)^m \left[ \frac{e^{ikR_{m1}}}{R_{m1}} + \mathcal{R}_1 \frac{e^{ikR_{m2}}}{R_{m2}} + \mathcal{R}_2 \frac{e^{ikR_{m3}}}{R_{m3}} + \mathcal{R}_1 \mathcal{R}_2 \frac{e^{ikR_{m4}}}{R_{m4}} \right], \quad (2.205)$$

where we note that  $\mathcal{R}_1 = -1$  for the pressure-release surface.

## 2.4.6 Waveguide Invariants

We have been mainly concerned with narrow-band or single-frequency propagation such as the two-mode case shown in Fig. 2.30. It turns out, as shown in Fig. 2.31, that the interference pattern at a slightly shifted frequency for the same propagation conditions has the same structure but with the maxima and minima slightly shifted as indicated by the lines through the maxima. This shift in the structure of the interference pattern as a function of frequency and range is a robust feature of waveguide propagation and is described by a scalar parameter referred to as the waveguide invariant [15, 16]. The same formalism associated with this invariant is also descriptive of the shift in the interference pattern with range and some environmental parameters instead of frequency [17–19]. The waveguide property of maintaining a robust interference pattern under an assortment of conditions is a consequence, as we show below, of an important invariant relationship between the change in group speed with respect to change in phase speed for a group of normal modes in the waveguide.

### 2.4.6.1 Frequency–Range Waveguide Invariant

We can obtain an expression for the trajectory in the frequency–range plane of the interference maxima (or minima) of the waveguide acoustic intensity  $I$  by simply differentiating the normal-mode expression for intensity  $I(r, z, \omega) = \text{const.}$  with respect to frequency and range and setting this expression equal to zero,

$$\frac{\delta\omega}{\delta r} = -\frac{\partial I}{\partial r} \Bigg/ \frac{\partial I}{\partial \omega}. \quad (2.206)$$

Intensity is proportional to the mean square pressure, as per (2.162), and can be written in the form

$$I(r, z; \omega) \propto \sum_n B_n^2 + 2 \sum_{m \neq n} B_m B_n \cos[\Delta k_{mn}(\omega) r], \quad (2.207)$$

where  $\Delta k_{mn} \equiv k_{rm} - k_{rn}$  are the interfering differences of pairs of horizontal modal wavenumbers and  $B_{m,n} = r^{-1/2} A_{m,n}$  are the mode amplitudes of (2.162)

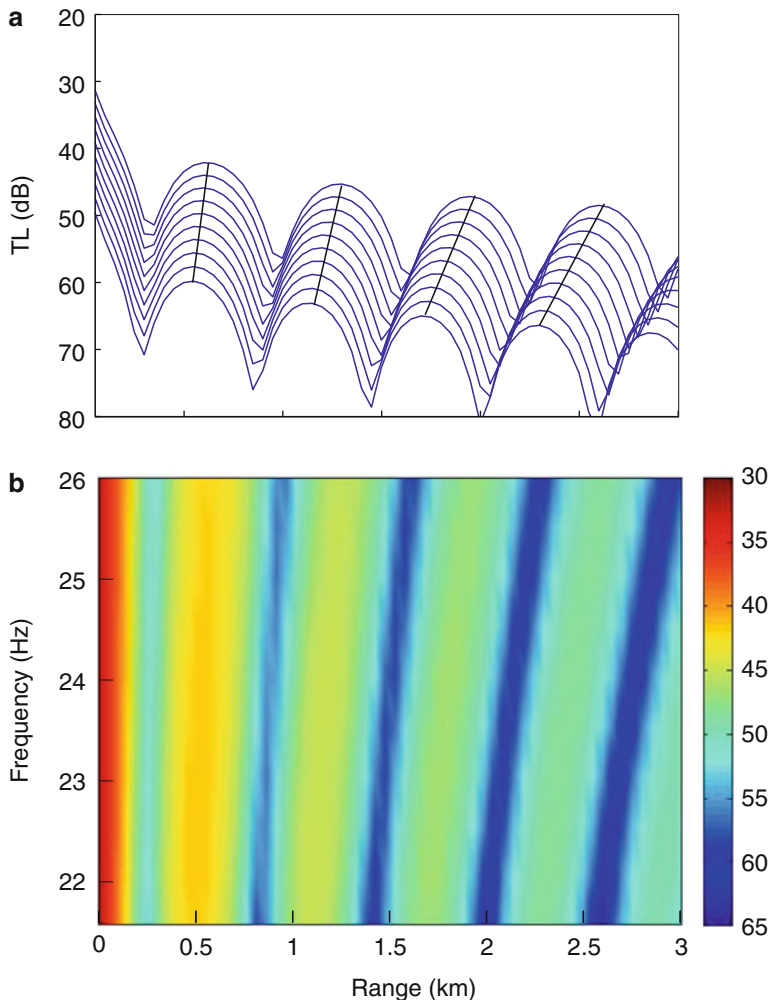


**Fig. 2.31** Acoustic field in an ideal waveguide of thickness 100 m for 20 Hz point source at 36 m depth. (a) Transmission loss from 21.5 to 26.0 Hz with 2 dB offset between curves. (b) Contour plot of (a) without offsets and with TL as the  $z$ -axis. These intensity bands are often referred to as striations

and are weakly dependent on range at specific ranges. Differentiating with respect to  $\omega$  and  $r$  and only retaining the dominant range terms, we obtain

$$\frac{\partial I}{\partial r} = - \sum_{m,n} B_n B_m (\Delta k_{mn}) \sin(\Delta k_{mn} r), \quad (2.208)$$

$$\frac{\partial I}{\partial \omega} = -r \sum_{m,n} B_n B_m \left( \frac{\partial \Delta k_{mn}}{\partial \omega} \right) \sin(\Delta k_{mn} r), \quad (2.209)$$

which we can immediately write as

$$\frac{\partial I}{\partial r} = -\omega \sum_{m,n} B_n B_m \left( \frac{1}{v_m} - \frac{1}{v_n} \right) \sin(\Delta k_{mn} r), \quad (2.210)$$

$$\frac{\partial I}{\partial \omega} = -r \sum_{m,n} B_n B_m \left( \frac{1}{u_m} - \frac{1}{u_n} \right) \sin(\Delta k_{mn} r), \quad (2.211)$$

where the phase and group velocities  $v_n$  and  $u_n$  are given by (2.156) and (2.158), respectively. Assuming a functional relationship between group and phase velocity, we can express individual phase and group velocities as a Taylor expansion around the average phase and group velocity  $v$  and  $u$  of a group of modes. Since (2.210) and (2.211) involve the inverse of phase and group velocity, which are defined as phase and group *slowness*, it is preferable to perform the expansion in terms of phase and group slowness ( $1/v$  and  $1/u$ ),

$$S_g^n = S_g + \frac{dS_g}{dS_p} (S_p^n - S_p), \quad (2.212)$$

where  $S_p^n$  and  $S_g^n$  are the phase and group slowness, respectively, of the  $n$ th mode. In addition,  $S$  without the superscript refers to the average phase and group slowness of the group of modes. Inserting the above expressions into (2.206) together with the definition of phase and group slowness (and taking  $S$  to be centered about the  $m$ th mode) gives

$$\frac{\delta r}{\delta \omega} = -\frac{r}{\omega} \frac{dS_g}{dS_p}. \quad (2.213)$$

We now define the “invariant”  $\beta$  such that,

$$\frac{1}{\beta} \equiv -\frac{dS_g}{dS_p} = -\left(\frac{v}{u}\right)^2 \frac{du}{dv}, \quad (2.214)$$

so that we can rewrite (2.213) as

$$\frac{\delta \omega}{\delta r} = \beta \frac{\omega}{r} \quad (2.215)$$

or

$$\frac{\omega}{\omega_0} = \left(\frac{r}{r_0}\right)^\beta. \quad (2.216)$$

We now demonstrate that  $\beta$  is approximately constant for a group of modes. Return to the ideal waveguide as described by the geometry of Fig. 2.20 and note that  $k_r \equiv \omega/v = k \cos \theta = (\omega/c) \cos \theta$ , where we have suppressed the modal index. Therefore, we have for the phase velocity,

$$v = \frac{\omega}{k_r} = \frac{c}{\cos \theta}. \quad (2.217)$$

Using (2.158), together with the assumption that the depth (or angle) dependence of the group of modes we are considering is approximately frequency independent (e.g.,  $k_{mz}$  for the ideal waveguide is not a function of frequency), the group velocity is given by  $u = c \cos \theta$ . We can then write the invariant for a simple waveguide as

$$\beta = \cos^2 \theta. \quad (2.218)$$

Since typical shallow-water environments have bottom critical angles of less than 20°, we have that for most bottom-reflecting shallow-water environments,  $\beta \approx 1$ . We will further discuss values of  $\beta$  for various profiles in Chap. 5.

#### 2.4.6.2 Generalized Waveguide Invariant

The previous procedure can be generalized [18] to include variations in environmental parameters instead of either range or frequency. For example, we may seek the constant intensity trajectory in the frequency–water depth plane, i.e., the change in the broadband frequency spectrum when the waveguide depth is changed. In that case, we would simply set the total intensity differential with respect to frequency and water depth equal to zero. Similarly, if we were interested in the spectral change with respect to some sound speed variation, we would set the total differential with respect to frequency and the parameter characterizing the sound speed (change) equal to zero. In both of the above cases, the partial of the intensity with respect to water depth or sound speed results in changing the cosine terms in (2.207) to a sine term. However, we now have to take derivatives of  $\Delta k_{mn}$  with respect to these parameters rather than the derivative with respect to range which just factored out the phase slowness terms.

To proceed with the generalization of the invariant formulation, we note from the derivation of (2.213), that the basic ingredient facilitating this derivation was that the coefficients of the  $\sin(\Delta k_{mn} r)$  are constant and could be factored out of the summation. We showed this to be true by a Taylor expansion around a group of modes. This is actually a stationary phase [ $\delta\Phi = \delta(\Delta k_{mn} r) = 0$ ] statement that the lines of constant intensity, which we refer to as striations, for a group of modes arise from the general condition of keeping the cosine term (and hence, its argument) in (2.207) constant. We can continue from (2.206) with the assumption that these terms are constant to obtain, after some straightforward algebra,

$$\frac{\delta r}{\delta \omega} = -\frac{r}{\omega} \left( \frac{\partial \Delta k_{mn}}{\partial \omega} \right) \left( \frac{\Delta k_{mn}}{\omega} \right), \quad (2.219)$$

which, given the definitions of group and phase speed (and slowness), is identical to (2.213) and therefore, in analogy to (2.216), we have

$$\frac{\Delta k_{mn}}{(\Delta k_{mn})_0} = \left( \frac{\omega}{\omega_0} \right)^{-\frac{1}{\beta}}. \quad (2.220)$$

Equation (2.220) states how a wavenumber difference changes with frequency starting from a given wavenumber difference. Recall from (2.163) that the wavenumber difference yields the modal interference length so that we can rewrite (2.220) in terms of how a modal interference length  $L_0$  evolves with frequency,

$$L = L_0 \left( \frac{\omega}{\omega_0} \right)^{\frac{1}{\beta}}. \quad (2.221)$$

Now, let  $\eta_q$  represent each of the waveguide parameters  $q = r, \omega, D, c$ , denoting range, frequency, water depth and sound speed, respectively, and define  $\Phi \equiv \Delta k_{mn}r$ . The general stationary phase condition is therefore

$$\delta\Phi = \sum_q \frac{\partial\Phi}{\partial\eta_q} \delta\eta_q. \quad (2.222)$$

Then, with  $r \equiv \eta_r$ ,  $\omega \equiv \eta_\omega$  and using the definition of  $\Phi$ , we have

$$\left( \frac{\partial\Delta k_{mn}}{\Delta k_{mn}} \middle/ \frac{\partial\eta_h}{\eta_h} \right) \frac{\delta\eta_h}{\eta_h} + \left( \frac{\partial\Delta k_{mn}}{\Delta k_{mn}} \middle/ \frac{\partial\eta_c}{\eta_c} \right) \frac{\delta\eta_c}{\eta_c} + \left( \frac{\partial\Delta k_{mn}}{\Delta k_{mn}} \middle/ \frac{\partial\omega}{\omega} \right) \frac{\delta\omega}{\omega} + \frac{\delta r}{r} = 0, \quad (2.223)$$

which, of course, reduces to (2.219) when there is no variation in water depth or sound speed.

Now consider the variation in frequency when the water depth is changed, i.e., the shift of the power spectrum interference maxima and minima as a function of waveguide depth. We already know from (2.206) and (2.219) that the expression in the parentheses of the third term is  $-1/\beta$ . The expression in the first parentheses can be obtained from (2.148) where we also note from (2.192) that the Pekeris waveguide wavenumbers approach the ideal waveguide wavenumbers for high frequency. As a matter of fact, the eigenvalues of this general class of *Sturm–Liouville* problems go to the ideal waveguide wavenumbers for large  $m$ .

Taking  $k_m = \sqrt{k^2 - m^2\pi^2/\eta_h^2}$ , and noting that  $k_m + k_n \approx 2k_m$ , we get

$$\frac{\partial\Delta k_{mn}}{\partial\eta_h} = -\frac{2\Delta k_{mn}}{\eta_h} \quad (2.224)$$

so that, taken alone, the first and third terms of (2.223) reduce to

$$\frac{\delta\omega}{\delta\eta_h} = -2\beta \frac{\omega}{\eta_h}. \quad (2.225)$$

This last expression is equivalent to an expression in Weston et al. [17] in which they studied time–frequency interference patterns resulting from a shallow-water

tidal cycle and where they also experimentally confirmed the above factor of 2. Similarly, consider the second term of (2.223), recalling that  $k = \omega/c$ , we obtain

$$\frac{\partial \Delta k_{mn}}{\partial \eta_c} = \left( \frac{k^2}{k_m k_n} \right) \frac{\Delta k_{mn}}{\eta_c} \approx \frac{\Delta k_{mn}}{\eta_c}, \quad (2.226)$$

where the last relation comes from the expression in parenthesis being approximately unity for a mode group such that  $m \approx n$  and for  $kh \gg 1$ . Considering variation in only the second and third terms of (2.223), we arrive at another invariant-like expression,

$$\frac{\delta \omega}{\delta \eta_c} = \beta \frac{\omega}{\eta_c}. \quad (2.227)$$

Hence, (2.215), (2.225), and (2.227) are “invariant” expressions for the ideal waveguide stating that the slope of the lines of constant intensity is an invariant for a specific mode group in a coordinate system of relative increments of  $\omega$  and  $\eta_q$ . Though our derivation was specific for ideal waveguides and/or Pekeris waveguides with high mode numbers, the result is more general; the invariants can be numerically calculated for a much broader class of waveguides and also approximated analytically for an assortment of waveguides [16]. The generalized invariant equations can therefore be written as

$$\frac{\delta \omega}{\delta \eta_q} = \gamma_{\omega:q} \frac{\omega}{\eta_q}, \quad (2.228)$$

where  $q$  is either range  $r$ , water depth  $D$  or sound speed  $c$  and we have shown above that for an ideal waveguide  $\gamma$  is given by

$$\gamma_{\omega:r,D,c} \approx 1, -2, 1, \quad (2.229)$$

where the notation indicates that we are considering variations in the interference structure in which one of the coordinates is always  $\omega$ . Therefore, (2.219), (2.224), and (2.226) can also be summarized as

$$\frac{\partial \Delta k_{mn}}{\partial \eta_q} = \frac{\gamma_{\omega:q}}{\beta} \frac{\Delta k_{mn}}{\eta_q}, \quad q = r, D, c. \quad (2.230)$$

These invariant expressions are particularly useful for studying a single hydrophone (and therefore at a single range) observable such as the shift in a spectral (frequency vs. intensity) broadband interference pattern with respect to the variation in one of the  $q$  parameters. In terms of invariants of the pairwise coordinate systems, i.e.,  $(r, \omega)$ ,  $(D, \omega)$ ,  $(c, \omega)$ , we can treat (2.223) as the result of a separation of variables yielding the three partial differential equations for  $\Delta k_{mn}(D, \omega)$ ,  $\Delta k_{mn}(c, \omega)$  and  $\Delta k_{mn}(r, \omega)$  as summarized by (2.230). After some algebra, the product of the three separation of variable solutions is

$$\Delta k_{mn} = \alpha_{mn} \eta_D^{\gamma_{\omega:D}/\beta} \eta_c^{\gamma_{\omega:c}/\beta} \omega^{-1/\beta}, \quad (2.231)$$

where  $\alpha_{mn}$  is a mode number dependent constant. Thus, for the ideal waveguide, we obtain

$$\Delta k_{mn} = \alpha_{mn} \frac{c}{\omega D^2} = \alpha_{mn} \frac{1}{k D^2}. \quad (2.232)$$

To check these results, we can just write out the expression for  $\Delta k_{mn}$  and take the limit of  $kh \gg 1$  to obtain

$$\Delta k_{mn} \approx \frac{(n^2 - m^2)\pi^2}{2} \frac{1}{k D^2}, \quad (2.233)$$

which agrees with (2.232).

The results presented in this section were mostly for an ideal waveguide. For more complicated environments, we must use numerical methods to compute the relevant modal quantities. This is discussed in some detail in Sect. 5.14.

## 2.5 Deep-Ocean Waveguides

In the previous section, we discussed propagation in waveguides composed of homogeneous fluid layers. Such environmental models are rather simplistic but they are useful for illustrating the fundamental characteristics of ocean acoustic propagation. Real sound-speed profiles have depth dependence and consequently need to be represented by a combination of layering and variable sound speed within the layers.

In general, the ocean environment varies in all spatial coordinates as well as time, with the latter giving rise to temporal fluctuations. Although the fluctuations will usually be characterized by temporal scales long compared to the acoustic time scales, they may have significant effect on advanced, high-resolution signal processing schemes based on ensemble averaging of the acoustic field. The development of ocean acoustic models for determining the stochastic properties of the field is still in its infancy, and the temporal variability is generally addressed through Monte Carlo simulations with deterministic models.

In terms of the spatial variability, the scales play an important role as well. Thus, the variability on scales smaller than the wavelength are best incorporated in a stochastic sense, and in recent years a significant effort has gone into the modeling of ocean environments with small-scale stochastic variability such as interface roughness and volume inhomogeneities—important mechanisms for scattering and reverberation. However, the propagation models in widespread use do not include stochastic variability but only large scale variability of deterministic nature.

The complexity of the acoustic modeling depends on the nature of the spatial variability. Thus, the real ocean has variation in sound speed with depth as well as in the horizontal. In general, the two- and three-dimensional variation requires the use of one of the numerical models described in later chapters, such as three-dimensional ray tracing, adiabatic or coupled modes, or parabolic equation

approaches. However, the basic physics of deep-ocean-waveguide propagation can be addressed by simpler methods due to the fact that the spatial scales of the horizontal variability in most cases are much larger than the scales of the vertical variability. Therefore, a range independent environmental model for the deep ocean can provide a realistic prediction of the acoustic propagation. This is particularly true at Arctic latitudes where the atmospheric influence on the underwater acoustic environment is limited by the ice cover and where the strongly upward refracting sound-speed profile eliminates effects of bottom bathymetry on long-range propagation.

Realistic range independent environmental models for the deep ocean are shown in Fig. 1.1. The deep ocean waveguide cannot, in general, be represented by a homogeneous fluid layer. However, if the range-independent ocean waveguide is represented by an increasing number of homogeneous layers, a numerical solution based on the field representation for homogeneous layers will converge toward the correct solution. It turns out, however, that a satisfactory convergence requires the layers to be less than one quarter of a wavelength thick. Such a technique is therefore only computationally convenient for low-frequency propagation in moderate water depths.

In general, it is much more convenient to divide the deep ocean into a relatively few number of layers with depth-varying properties in a form that allows for an analytic solution to the wave equation within each layer. We therefore seek solutions to the Helmholtz equation for the range-independent ocean environment,

$$[\nabla^2 + k^2(z)] \psi(r, z) = S_\omega \frac{\delta(r) \delta(z - z_s)}{2\pi r}, \quad (2.234)$$

where the medium wavenumber  $k(z)$  is now a function of depth. We can still solve this equation by separation of variables or by integral transforms to yield,

$$\psi(r, z) = \int_0^\infty \psi(k_r, z) J_0(k_r r) k_r dk_r \quad (2.235)$$

with  $\psi(k_r, z)$  satisfying the depth-separated wave equation,

$$\left[ 4 \frac{d^2}{dz^2} + (k^2(z) - k_r^2) \right] \psi(k_r, z) = S_\omega \frac{\delta(z - z_s)}{2\pi}. \quad (2.236)$$

The use of the integral transform approach is dependent on the availability of solutions to (2.236). For certain variations of the medium wavenumber  $k(z)$ , exact solutions can be obtained. Alternatively, approximate solutions may be obtained. In the following we describe such exact and approximate solutions to (2.236).

### 2.5.1 Exact Solutions

The deep-ocean waveguide is generally represented by a series of layers, within which the depth-dependence of the field has an analytic representation. A few examples of sound speed interpolation functions for which this is possible are given

in [20]. However, the actual choice of interpolation function is not very critical since the profile is usually measured at discrete depths with a finite uncertainty. We, here, describe the solution for a medium with the *pseudo-linear* sound speed variation

$$c(z) = \sqrt{\frac{1}{az + b}}. \quad (2.237)$$

Such a medium has a linear variation of the square of the index of refraction,  $n^2 = az + b$ , and is therefore also referred to an  $n^2$ -linear acoustic medium. The expression for the sound speed in (2.237) obviously only has physical meaning for depths satisfying the inequality  $az + b > 0$ . For this sound speed variation, the homogeneous, depth-separated wave equation becomes,

$$\left[ \frac{d^2}{dz^2} - [k_r^2 - \omega^2 (az + b)] \right] \psi(k_r, z) = 0. \quad (2.238)$$

By introducing the variable transformation,

$$\xi = (\omega^2 a)^{-2/3} [k_r^2 - \omega^2 (az + b)] \quad (2.239)$$

the following wave equation is obtained,

$$\left[ \frac{d^2}{d\xi^2} - \xi \right] \psi(\xi) = 0. \quad (2.240)$$

This is a special form of the Bessel differential equation, with two independent solutions given by the Airy functions  $\text{Ai}(\xi)$  and  $\text{Bi}(\xi)$  [21]. Independent homogeneous solutions to (2.238) are therefore

$$\psi^+(k_r, z) = \text{Ai}\left([\omega^2 a]^{-2/3} [k_r^2 - \omega^2 (az + b)]\right), \quad (2.241)$$

$$\psi^-(k_r, z) = \text{Bi}\left([\omega^2 a]^{-2/3} [k_r^2 - \omega^2 (az + b)]\right). \quad (2.242)$$

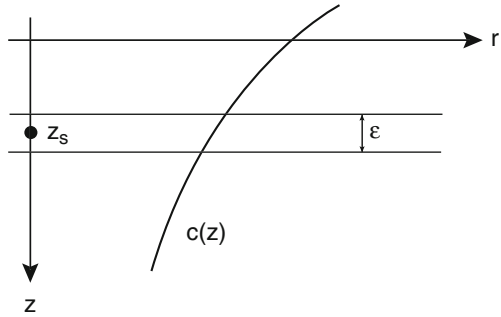
The field produced by a point source at depth  $z_s$  in such a medium is determined by introducing a thin homogeneous layer of sound speed  $c(z_s)$  and thickness  $\epsilon$  around the source, see Fig. 2.32. In the limit  $\epsilon \rightarrow 0$ , the solution of this layered problem converges to the solution of the original problem.

In Fig. 2.32, the sound speed variation is shown for the case in which  $a > 0$ , i.e.,  $\lim_{z \rightarrow \infty} c(z) = 0$  and  $\lim_{z \rightarrow -b/a} c(z) = \infty$ . The argument  $\xi$  of the Airy functions, (2.239), therefore has the limits,

$$\lim_{z \rightarrow \infty} \xi = -\infty, \quad (2.243)$$

$$\lim_{z \rightarrow -b/a} \xi = +\infty. \quad (2.244)$$

**Fig. 2.32** Point source in  $n^2$ -linear fluid medium



Since no sources are present in the two halfspaces, the field is given by (2.241) and (2.242), respectively. However, the field must satisfy the radiation condition for  $z \rightarrow \infty$  and the field must be limited for  $z \rightarrow -b/a$ . Since  $\lim_{\xi \rightarrow \infty} Bi(\xi) = \infty$  [21], the latter condition requires the depth dependence of the field in the upper halfspace to be of the form

$$\psi_1(k_r, z) = A_1^+ Ai(\xi). \quad (2.245)$$

Similarly, the radiation condition requires that only downgoing waves exist for  $z \rightarrow \infty$ . Because of the asymptotic behavior of the Airy functions for  $\xi \rightarrow -\infty$  [21], it is required that the field in the lower halfspace be of the form

$$\psi_3(k_r, z) = A_3^- [Ai(\xi) - iBi(\xi)]. \quad (2.246)$$

For the intermediate isovelocity layer, the depth-dependence of the field is directly given by (2.141), (2.142) and (2.143) as

$$\psi_2(k_r, z) = A_2^+ e^{ik_{z,2}z} + A_2^- e^{-ik_{z,2}z} + S_\omega \frac{e^{ik_{z,2}|z-z_s|}}{4\pi i k_{z,2}}. \quad (2.247)$$

The next step is to satisfy the boundary conditions of continuity of vertical displacement and pressure at the two interfaces at  $z = z_s \pm \epsilon/2$ . The expressions for the vertical displacement and pressure in terms of the displacement potential, (2.21) and (2.23), then leads to the following system of equations expressing the boundary conditions for  $\epsilon \rightarrow 0$ ,

$$A_1^+ \left[ -(\omega^2 a)^{1/3} Ai'(\xi_s) \right] - ik_{z,2} (A_2^+ - A_2^-) = -\frac{S_\omega}{4\pi}, \quad (2.248)$$

$$-A_1^+ Ai(\xi_s) + (A_2^+ + A_2^-) = -\frac{S_\omega}{4\pi i k_{z,2}}, \quad (2.249)$$

$$ik_{z,2} (A_2^+ - A_2^-) - A_3^- \left( -(\omega^2 a)^{1/3} [Ai'(\xi_s) - iBi'(\xi_s)] \right) = -\frac{S_\omega}{4\pi}, \quad (2.250)$$

$$-(A_2^+ + A_2^-) + A_3^- [Ai(\xi_s) - iBi(\xi_s)] = \frac{S_\omega}{4\pi i k_{z,2}}. \quad (2.251)$$

Here, the primes denote differentiation with respect to the argument. All terms involving the coefficients  $A_2^+$  and  $A_2^-$  are easily eliminated by pair-wise addition, and the resulting two equations give the following solutions,

$$A_1^+ = -\frac{S_\omega}{4\pi} \frac{2(\omega^2 a)^{-1/3} [\text{Ai}(\zeta_s) - i\text{Bi}(\zeta_s)]}{\text{Ai}'(\zeta_s) [\text{Ai}(\zeta_s) - i\text{Bi}(\zeta_s)] - \text{Ai}(\zeta_s) [\text{Ai}'(\zeta_s) - i\text{Bi}'(\zeta_s)]}, \quad (2.252)$$

$$A_3^- = -\frac{S_\omega}{4\pi} \frac{2(\omega^2 a)^{-1/3} \text{Ai}(\zeta_s)}{\text{Ai}'(\zeta_s) [\text{Ai}(\zeta_s) - i\text{Bi}(\zeta_s)] - \text{Ai}(\zeta_s) [\text{Ai}'(\zeta_s) - i\text{Bi}'(\zeta_s)]}. \quad (2.253)$$

The source field representations for the case where the sound speed increases with depth, i.e.,  $a < 0$ , is directly determined by symmetry considerations. The choice of depth axis  $z$  is arbitrary, and we can therefore perform the variable transformation  $z \rightarrow -z$ . This will change the sign of  $a$  in (2.237), and, as can be observed from (2.239),  $\zeta$  is then invariant to this transformation, and consequently the results above are still valid; they just have to be interchanged between the two halfspaces. The depth-dependent solution for a source in a  $n^2$ -linear fluid medium is therefore,

$$\begin{aligned} \psi(k_r, z) = & -\frac{S_\omega}{4\pi} \\ & \times \begin{cases} \frac{2(\omega^2 a)^{-1/3} [\text{Ai}(\zeta_s) - i\text{Bi}(\zeta_s)] \text{Ai}(\zeta)}{\text{Ai}'(\zeta_s) [\text{Ai}(\zeta_s) - i\text{Bi}(\zeta_s)] - \text{Ai}(\zeta_s) [\text{Ai}'(\zeta_s) - i\text{Bi}'(\zeta_s)]}, & a(z - z_s) \leq 0 \\ \frac{2(\omega^2 a)^{-1/3} \text{Ai}(\zeta_s) [\text{Ai}(\zeta) - i\text{Bi}(\zeta)]}{\text{Ai}'(\zeta_s) [\text{Ai}(\zeta_s) - i\text{Bi}(\zeta_s)] - \text{Ai}(\zeta_s) [\text{Ai}'(\zeta_s) - i\text{Bi}'(\zeta_s)]}, & a(z - z_s) \geq 0. \end{cases} \end{aligned} \quad (2.254)$$

In the next section, we use the approximate WKB ray solution to explain the physical significance of the solution in (2.254). Furthermore, in Chap. 4 we show how these solutions are applied to solve wave propagation problems in the deep ocean by dividing the environment into a set of discrete layers with an  $n^2$ -linear sound speed variation, (2.237), in each layer.

### 2.5.2 WKB Solutions

The depth-separated wave equation (2.236) is an ordinary differential equation which, without the source term, has the form

$$\frac{d^2\psi(z)}{dz^2} + k_z^2(z)\psi(z) = 0, \quad (2.255)$$

where  $k_z(z)$  is the depth-dependent vertical wavenumber. In the WKB approximation [7], we seek solutions to (2.255) in the form

$$\psi(z) = A(z)e^{i\phi(z)}, \quad (2.256)$$

where  $A(z)$  and  $\phi(z)$  are real functions of depth. For a homogeneous medium, solutions of this form are exact, with  $A(z) = A$  and  $\phi(z) = \pm k_z z$ . However, for general variations of the wavenumber, only approximate solutions of this form can be obtained, and the relative accuracy depends on the actual sound-speed profile. Inserting (2.256) into (2.255) yields

$$\left[ A''(z) + \left( k_z^2(z) - [\phi'(z)]^2 \right) A(z) \right] + i \left[ 2A'(z) \phi'(z) + A(z) \phi''(z) \right] = 0. \quad (2.257)$$

This equation requires that both the real and the imaginary term vanish. If we assume that the amplitude of the solution varies slowly in depth, such that

$$\left| \frac{A''(z)}{k_z^2(z) A(z)} \right| \ll 1, \quad (2.258)$$

then the equation for the real part of (2.257) takes the form

$$[\phi'(z)]^2 = k_z^2(z) \quad (2.259)$$

with the solution

$$\phi(z) = \pm \int_{z_0}^z k_z(z) dz, \quad (2.260)$$

where  $z_0$  is an arbitrary constant. Inserting  $\phi'(z) = \pm k_z(z)$  into the equation for the imaginary part then yields

$$2A'(z) k_z(z) + A(z) k_z'(z) = 0 \quad (2.261)$$

with the solution

$$A(z) = \frac{B}{\sqrt{k_z(z)}}, \quad (2.262)$$

where  $B$  is an arbitrary amplitude. Inserting these solutions into (2.256) then yields the *WKB approximation* to the depth-separated wave equation,

$$\psi(z) = \frac{B}{\sqrt{k_z(z)}} e^{\pm i \int_{z_0}^z k_z(z) dz}. \quad (2.263)$$

In terms of physical significance, the WKB approximation is a representation in terms of local plane-wave solutions, propagating horizontally with wavenumber  $k_r$  and vertically with wavenumber  $k_z(z)$ . It is, therefore, a solution in terms of *rays* propagating at grazing angle  $\theta(z) = \arctan [k_z(z)/k_r] = \arccos [k_r/k(z)]$ , i.e., plane waves satisfying Snell's law. The two solutions in (2.263) are propagating downward and upward for the positive and negative exponents, respectively. The individual solutions therefore do not contain internal reflections, as an exact solution

must do. The condition given by (2.258) represents the contribution from internal reflections. By inserting the amplitude solution, (2.262), into (2.258), the WKB condition can be rewritten as

$$\left| \frac{1}{k_z^2(z)} \left( \frac{d^2}{dz^2} \ln k_z^2(z) - \left[ \frac{d}{dz} \ln k_z(z) \right]^2 \right) \right| \ll 1. \quad (2.264)$$

If  $k_z(z)$  is assumed to be locally linear, then this condition is equivalent to

$$\frac{1}{k_z(z)} \left| \frac{d}{dz} \ln k_z(z) \right| \ll 1, \quad (2.265)$$

which shows that the WKB approximation is valid if the variation in the vertical wavenumber is small over a vertical wavelength. The WKB ray solution is therefore a *high-frequency approximation*. However, even at high frequencies the approximation will break down at points where the vertical wavenumber vanishes. In other words, the internal reflection cannot be neglected when the grazing angle of the WKB rays approach horizontal, i.e.,  $k_r = k(z)$ . The behavior of the WKB ray solution, therefore, needs special consideration for rays approaching such *turning points*.

In a downward refracting sound-speed profile (Fig. 2.33), we assume an upward propagating ray of horizontal wavenumber  $k_r$ , represented by the solution with the negative exponent in (2.263),

$$\psi^-(z) = \frac{B^-}{\sqrt{k_z(z)}} e^{-i \int_{z_-}^{z_-} k_z(z) dz}. \quad (2.266)$$

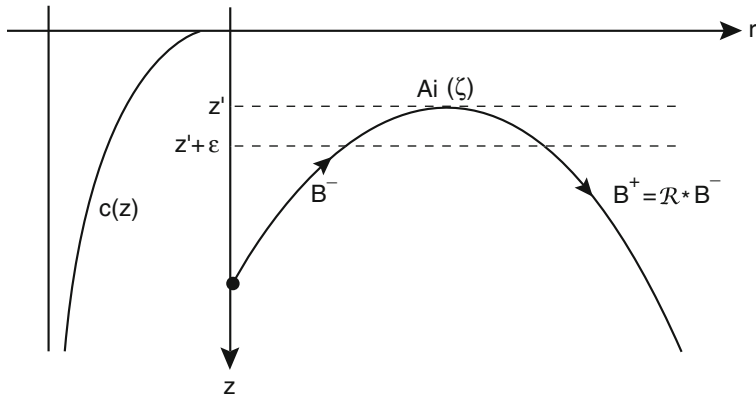


**Fig. 2.33** Reflection of a WKB ray at a turning point

After passing through the turning point at depth  $z'$  this ray will be downward refracted and must be represented by the solution with the positive exponent in (2.263),

$$\psi^+(z) = \frac{B^+}{\sqrt{k_z(z)}} e^{i \int_{z'}^z k_z(z) dz}. \quad (2.267)$$

To determine the arbitrary constants  $B^+$  and  $z^+$  we can introduce an interface just below the turning point at depth  $z' + \epsilon$ , and represent the solution at and above the turning point by the exact solution  $\text{Ai}(\xi)$ , assuming the medium to have an  $n^2$ -linear sound speed variation locally. We can then determine the constants from the boundary conditions of continuity of pressure and displacement at depth  $z' + \epsilon$ . Since the amplitudes of the WKB solutions were assumed to be real, the phase of the downgoing ray is determined by the difference between  $z^+$  and  $z^-$ . However, for simplicity we can choose these to be identical,  $z^- = z^+$ , and instead allow  $B^\pm$  to be complex entities.

We now determine  $B^+$  by solving a standard reflection problem,  $B^+ = \mathcal{R} B^-$ , with  $\mathcal{R}$  being the reflection coefficient. Since energy must be conserved, the ray must be totally reflected, requiring  $|B^+| = |B^-|$ . By representing the Airy function in terms of Bessel functions, the solution of the reflection problem shows that in the high-frequency limit, the ray must have a  $\pi/2$  phase shift [7], i.e.,

$$B^+ = B^- e^{-i\pi/2}. \quad (2.268)$$

An important feature of the WKB solution is its direct physical interpretation in terms of rays, and we can therefore use it to address the physical significance of the exact solution in (2.254) for the  $n^2$ -linear medium. Assume that a plane wave, represented by a *ray*, of horizontal wavenumber  $k_r$  is launched upward from a source at depth  $z_s > z' = a(k_r^2/\omega^2 - b)$ , in a medium with  $a > 0$ , i.e., the sound speed is decreasing with depth. At the source the argument to the Airy function  $\text{Ai}(\xi)$  is negative. At the depth  $z'$  the horizontal wavenumber is equal to the local medium wavenumber,  $k_r = k(z')$ , corresponding to a horizontally propagating plane wave, with the argument to the Airy function being  $\xi = 0$ . Above this *turning point*, the field will decay rapidly for  $z \rightarrow -b/a$ . This evanescent field is only predicted by the exact Airy function solution, but not by the WKB ray solution. After reaching the turning point the ray will refract downward, superimposed with the upgoing component yielding a standing wave solution in the vertical above the source, represented by the Airy function  $\text{Ai}(\xi)$ . Below the source the ray as well as the exact depth solution must propagate downward to infinity, a behavior represented by the linear combination of the Airy functions  $\text{Ai}(\xi) - i \text{Bi}(\xi)$ .

The difference between the WKB approximation and the exact solution is most dramatic at and beyond the turning point. However, when the turning points are close to the waveguide boundaries in terms of wavelengths, such that the reflection of the evanescent “tail” cannot be neglected, then the field elsewhere in the waveguide will be affected as well. These fundamental differences between the WKB ray approximation and exact solutions for the  $n^2$ -linear medium will be illustrated by numerical examples in Chap. 3.

The WKB approach is rarely used in *wavenumber integration* approaches. However, it has been used extensively in relation to *ray tracing* in range-independent environments as described in Chap. 3. In addition, the WKB approach provides a very simple means of determining approximations to the modal eigenvalues in the *normal mode* approach. As described earlier, the modal wavenumbers are those for which two ray multiples are in phase. We can therefore use the WKB approach to trace a ray upward from some depth  $z_s$ , through a turning point, incorporating the phase shift, or through a surface reflection. The downgoing ray is then traced similarly through the deep ocean turning point or the bottom reflection until it again reaches the depth  $z_s$ . If the up- and downgoing field components at this point are in phase, then the horizontal wavenumber is a modal wavenumber. The use of the WKB mode approximation is described in more detail in Chap. 5.

## Appendix 1: Principle of Reciprocity

In deriving *Green's theorem* in Sect. 2.3.3, we had to assume that  $G_\omega(\mathbf{r}, \mathbf{r}_0)$  is symmetric in  $\mathbf{r}$  and  $\mathbf{r}_0$ . In Sect. 2.3.2, we showed that the free-field Green's function  $g_\omega(\mathbf{r}, \mathbf{r}_0)$  is symmetric, but the same is not the case unconditionally for  $G_\omega$ , in spite of the fact that the two functions satisfy the same differential equation. For example, if we choose the homogeneous solution as a plane wave,  $H_\omega(\mathbf{r}) = \exp(i\mathbf{k} \cdot \mathbf{r})$ , then  $G_\omega$  satisfies (2.60), but is clearly not symmetric.

The symmetry of the Green's function is a result of the general *principle of reciprocity* of linear acoustics, and in this appendix we shall derive this very important principle.

Let  $G_\omega(\mathbf{r}, \mathbf{r}_1)$  and  $G_\omega(\mathbf{r}, \mathbf{r}_2)$  be two pressure Green's functions satisfying the differential equations

$$\rho(\mathbf{r}) \nabla \cdot [\rho^{-1}(\mathbf{r}) \nabla G_\omega(\mathbf{r}, \mathbf{r}_1)] + k^2 G_\omega(\mathbf{r}, \mathbf{r}_1) = -\delta(\mathbf{r} - \mathbf{r}_1), \quad (2.269)$$

$$\rho(\mathbf{r}) \nabla \cdot [\rho^{-1}(\mathbf{r}) \nabla G_\omega(\mathbf{r}, \mathbf{r}_2)] + k^2 G_\omega(\mathbf{r}, \mathbf{r}_2) = -\delta(\mathbf{r} - \mathbf{r}_2). \quad (2.270)$$

Now, multiplying the first equation by  $G_\omega(\mathbf{r}, \mathbf{r}_2)$  and the second by  $G_\omega(\mathbf{r}, \mathbf{r}_1)$ , and subtraction of the two, followed by integration over a volume  $V'$ , yield

$$\begin{aligned} \frac{G_\omega(\mathbf{r}_1, \mathbf{r}_2)}{\rho(\mathbf{r}_1)} - \frac{G_\omega(\mathbf{r}_2, \mathbf{r}_1)}{\rho(\mathbf{r}_2)} &= \int_{V'} \{G_\omega(\mathbf{r}', \mathbf{r}_2) \nabla \cdot [\rho^{-1}(\mathbf{r}') \nabla G_\omega(\mathbf{r}', \mathbf{r}_1)] \\ &\quad - G_\omega(\mathbf{r}', \mathbf{r}_1) \nabla \cdot [\rho^{-1}(\mathbf{r}') \nabla G_\omega(\mathbf{r}', \mathbf{r}_2)]\} dV'. \end{aligned} \quad (2.271)$$

Using integration by parts in the form of *Green's identity*,

$$\int_V g \nabla \cdot \mathbf{f} dV = - \int_V (\nabla g) \cdot \mathbf{f} dV + \oint_S g \mathbf{f} \cdot \mathbf{n} dS \quad (2.272)$$

with  $\mathbf{f} = \rho^{-1} \nabla G_\omega$ , we change the volume integral to a surface integral over the surface  $S'$  of the volume  $V'$ ,

$$\begin{aligned} & \frac{G_\omega(\mathbf{r}_1, \mathbf{r}_2)}{\rho(\mathbf{r}_1)} - \frac{G_\omega(\mathbf{r}_2, \mathbf{r}_1)}{\rho(\mathbf{r}_2)} \\ &= \int_{S'} \left[ G_\omega(\mathbf{r}', \mathbf{r}_2) \rho^{-1}(\mathbf{r}') \frac{\partial G_\omega(\mathbf{r}', \mathbf{r}_1)}{\partial \mathbf{n}} - G_\omega(\mathbf{r}', \mathbf{r}_1) \rho^{-1}(\mathbf{r}') \frac{\partial G_\omega(\mathbf{r}', \mathbf{r}_2)}{\partial \mathbf{n}} \right] dS'. \end{aligned} \quad (2.273)$$

Now it is clear that the Green's function satisfies the *reciprocity relation*

$$\rho(\mathbf{r}_2) G_\omega(\mathbf{r}_1, \mathbf{r}_2) = \rho(\mathbf{r}_1) G_\omega(\mathbf{r}_2, \mathbf{r}_1), \quad (2.274)$$

if there exists a boundary  $S'$  where  $G_\omega$  satisfies boundary conditions of the form

$$\frac{\partial G_\omega(\mathbf{r}', \mathbf{r})}{\partial \mathbf{n}} - \eta(\mathbf{r}') G_\omega(\mathbf{r}', \mathbf{r}) = 0, \quad (2.275)$$

where  $\eta(\mathbf{r}')$  is an arbitrary factor.

Boundary conditions of the form given in (2.275) are called *natural boundary conditions* and include as special cases both the *Dirichlet* boundary condition ( $\eta(\mathbf{r}') = \infty$ ) and the *Neumann* boundary condition ( $\eta(\mathbf{r}') = 0$ ). As shown in Sect. 2.3.3, the *radiation condition* in infinite media can also be expressed in this form. Other boundary conditions covered by (2.275) are *impedance conditions* with prescribed ratio between pressure and normal particle velocity.

Equation (2.275) is clearly a sufficient condition for reciprocity, but not a necessary one. However, all physically realistic environmental models will have natural boundary or radiation conditions. Thus, for example, the Pekeris waveguide has a Dirichlet boundary condition at the free surface, and radiation conditions at  $(r, z) \rightarrow \infty$ . On the other hand, the boundary conditions do not have to be *natural* on any surface  $S'$ . Thus in the Pekeris waveguide the boundary conditions at the seabed cannot be written in the form given in (2.275). The reason is that (2.275) represents only *local* boundary conditions, whereas the boundary conditions at the Pekeris waveguide seabed are *non-local*, involving the field propagating to a point on the boundary from everywhere else on the same boundary. However, the surface integral will still vanish along the seabed. This is easily verified by inserting the wavenumber integral representation for the Green's functions into the surface integral, interchanging the order of integration, and reformulating the boundary conditions for the *depth-dependent Green's function* at the seabed to an impedance condition using the radiation condition in the lower halfspace.

We will see in Chap. 7 that the natural boundary conditions play an important role in formulating the finite-element solution to the wave equation.

## Problems

**2.1.** Sound propagating in a moving medium is governed by a so-called *convected wave equation*. Consider the case where the background flow velocity is uniform in the  $x$ -direction with velocity  $V$ .

- Following the procedure in Sect. 2.1, derive the convected wave equation for sound in a one-dimensional environment with flow velocity  $V$ :

$$\left(1 - \frac{V^2}{c^2}\right) p_{xx} - \frac{2V}{c^2} p_{xt} - \frac{1}{c^2} p_{tt} = 0.$$

Note that setting  $V = 0$  gives the usual wave equation.

- Show that this equation can also be derived from the standard wave equation by changing to a moving coordinate system  $(\xi, \tau) = (x + Vt, t)$ .
- What is the form of this equation in three dimensions?

**2.2.** Assume an acoustic source is designed as a small, spherical balloon of radius  $a$ , within which the pressure is oscillating with frequency  $f$ , with maximum pressure amplitude  $P$ .

- Derive the expression for the acoustic pressure vs range.
- Determine the expression for  $P$  which directly yields transmission loss, i.e., unit pressure at  $r = 1$  m.

**2.3.** Derive *Green's theorem* for a fluid medium with variable density, where the wave equation is of the form given in (2.14).

**2.4.** Make a computer code for computing the magnitude and phase of the plane-wave reflection coefficient at an interface separating two fluid halfspaces.

- As a test of your code reproduce the results of Figs. 2.10 and 2.11.
- Discuss in physical terms the grazing angle dependence of the results.
- Add a second fluid layer in the bottom and then add frequency as an independent variable to your computer program. Contour your reflection results as a function of angle and frequency. Discuss the resulting structure of the contoured output.

**2.5.** For an ideal waveguide bounded above by a pressure-release surface and below by an infinitely rigid wall, derive a ray expansion for the acoustic field.

**2.6.** Write a code evaluating the ray expansion in (2.138) for the pressure field in an ideal waveguide with pressure-release boundaries.

- For a 100-m deep waveguide, compute the transmission loss for both source and receiver at depth 36 m, at every 100 m range out to 2 km. Compare your results to Fig. 2.23b.
- Perform a convergence analysis for a few selected ranges and discuss the range dependence.

**2.7.** Show that (5.299) represents the sum of the residues of the wavenumber kernel in (2.146).

**2.8.** Consider an isovelocity waveguide of thickness  $D$ , bounded above and below by infinitely rigid walls.

- Derive the characteristic equation for the horizontal wavenumber of the normal modes.
- Sketch the vertical pressure distribution of the first few normal modes.
- Derive the dispersion relation for the normal modes. Discuss the differences compared to the waveguide with pressure release boundaries.

**2.9.** Consider an environment similar to the Pekeris waveguide in Fig. 2.25, but with the bottom speed being changed to  $c_2 = 1300$  m/s.

- Make a sketch of the complex wavenumber plane for this problem (similar to Fig. 2.26), indicating the integration contour and the EJP branch cuts.
- Discuss the existence of normal modes in this case. If they exist, show their approximate positions.
- Make a sketch of the branch cuts corresponding to the vertical wavenumber being purely imaginary, with the corresponding closed integration contour.

**2.10.** Consider a Pekeris waveguide with the speed of sound  $c_1 = 1500$  m/s and density  $\rho_1 = 1000$  kg/m<sup>3</sup> in the water column, and with  $c_2 = 1800$  m/s and  $\rho_2 = 2000$  kg/m<sup>3</sup> in the bottom. The water depth is 100 m. A line source at depth  $z_s$  is generating a plane acoustic field in the waveguide.

- Defining the slowness of the  $m$ th normal mode as

$$p_m = \frac{k_{xm}}{\omega},$$

where  $k_{xm}$  is the horizontal wavenumber of the mode, state the upper and lower limit of  $p_m$  for modes propagating in the positive  $x$ -direction.

- For a source frequency exciting 3 modes, make a sketch of the mode functions for pressure and for the particle velocity potential. Discuss the differences.
- Derive the expression for the vertical wavelength of the modes.
- Using the results from questions (a) and (c), state the lower limit for the vertical wavelength of a mode at angular frequency  $\omega$ .
- Use the result from (d) to determine how many modes you have at frequency  $f = 30$  Hz.

**2.11.** In (2.189),  $a_m(k_{rm})$  represents a waveguide-specific modal excitation function.

- Derive the expression for  $a_m(k_{rm})$  for the Pekeris waveguide.
- Show that the modal excitation function has its maximum at the Airy phase frequency, i.e., the frequency where the mode has its minimum group velocity.

- c. Compute and plot vs frequency the magnitude of the excitation function for the first 3 modes in the Pekeris waveguide in Fig. 2.25. Discuss the results.

**2.12.** A storm has created a 1 m thick surface layer with a uniform distribution of small air bubbles. The fraction of the volume occupied by the bubbles is  $10^{-3}$ .

- What assumption(s) do you have to make to treat the bubble layer as a homogeneous acoustic medium?
- Under these assumptions, find the numerical values of the sound speed  $c$  and density  $\rho$  of the bubble layer. The sound speed of water and air are  $c_w = 1500 \text{ m/s}$  and  $c_a = 340 \text{ m/s}$ , respectively, and the corresponding densities are  $\rho_w = 1000 \text{ kg/m}^3$  and  $\rho_a = 1.2 \text{ kg/m}^3$ .
- Show that the characteristic equation for normal modes in the bubble layer is

$$\cot(k_z h) = -\frac{\alpha_w}{k_z} \frac{\rho}{\rho_w},$$

where  $h$  is the thickness of the bubble layer, and

$$\alpha_w = \sqrt{k_r^2 - \left(\frac{\omega}{c_w}\right)^2},$$

$$k_z = \sqrt{\left(\frac{\omega}{c}\right)^2 - k_r^2}.$$

- Discuss the physical significance of  $\alpha_w$  and  $k_z$ .
- What is the value of the cutoff frequency below which no normal modes can exist in the bubble layer?

**2.13.** In seismics, volume attenuation is often expressed in terms of the *quality factor*, defined as the ratio between the real and the imaginary part of the bulk modulus, i.e.,  $Q = K'/K''$  for  $K = K' - iK''$ . For small attenuations, ( $Q \gg 1$ ), derive the relation between  $Q$  and the loss tangent  $\delta$ , and the loss factor  $\alpha$  in dB per wavelength.

**2.14.** Consider the reflection of plane waves from a bottom with the sound speed profile

$$c(z) = \begin{cases} (az + b)^{-1}, & 0 < z < 100 \text{ m}, \\ 1600 \text{ m/s}, & z \geq 100 \text{ m}. \end{cases}$$

The sound speed is continuous at the seabed ( $z = 0$ ) and at  $z = 100 \text{ m}$ , and the speed of sound in the water column ( $z < 0$ ) is  $1500 \text{ m/s}$ .

- Determine the constants  $a$  and  $b$ .
- What is the critical grazing angle for waves incident from the water column?

- c. Use the WKB approximation to derive expressions for the magnitude and phase of the reflection coefficient. Derive the result for grazing angles smaller and larger than critical. *Hint:*

$$\int \sqrt{\alpha + \beta x^2} dx = \frac{1}{2} \left[ x \sqrt{\alpha + \beta x^2} + \frac{\alpha}{\sqrt{\beta}} \log \left( x \sqrt{\beta} + \sqrt{\alpha + \beta x^2} \right) \right].$$

- d. For a frequency of 100 Hz, compute the phase of the reflection coefficient at grazing angles of incidence  $30^\circ, 40^\circ, 50^\circ, 60^\circ, 70^\circ, 80^\circ$ , and make a sketch of the result.

- 2.15.** Using the procedure to derive generalized invariants, derive the corresponding invariant quantities in which range can be taken as the independent variable. In particular, show that

$$\gamma_{r:\omega,D,c} = 1, -2, 1.$$

Next, show that the ideal waveguide trajectory of constant-intensity interference maxima along a horizontal array (with elements at  $r$ ) for a changing sound speed  $c$  would be described by

$$\frac{\delta c}{\delta r} = \frac{c}{r}.$$

## References

1. P.G. Bergmann, The wave equation in a medium with a variable index of refraction. *J. Acoust. Soc. Am.* **17**, 329–333 (1946)
2. L.M. Brekhovskikh, O.A. Godin, *Acoustics of Layered Media II* (Springer, Berlin, 1992)
3. C.L. Pekeris, Theory of propagation of explosive sound in shallow water. *Geol. Soc. Am. Mem.* **27** (1948)
4. W.M. Ewing, W.S. Jardetzky, F. Press, *Elastic Waves in Layered Media* (McGraw-Hill, New York, 1957)
5. C.B. Officer, *Introduction to the Theory of Sound Transmission* (McGraw-Hill, New York, 1958)
6. P.M. Morse, K.U. Ingard, *Theoretical Acoustics* (McGraw-Hill, New York, 1968)
7. I. Tolstoy, C.S. Clay, *Ocean Acoustics: Theory and Experiment in Underwater Sound* (American Institute of Physics, New York, 1987)
8. L.M. Brekhovskikh, O.A. Godin, *Acoustics of Layered Media I* (Springer, Berlin, 1990)
9. G.V. Frisk, *Ocean and Seabed Acoustics: A Theory of Wave Propagation* (Prentice-Hall, Englewood Cliffs, NJ, 1994)
10. W. Munk, P. Worcester, C. Wunsch, *Ocean Acoustic Tomography* (Cambridge University Press, New York, 1995)
11. H. Medwin, C.S. Clay, *Fundamentals of Acoustical Oceanography* (Academic Press, San Diego, 1997)
12. P.M. Morse, H. Feshbach, *Methods of Mathematical Physics, Part I* (McGraw-Hill, New York, 1953)
13. J. Miklowitz, *The Theory of Elastic Waves and Waveguides* (North-Holland, New York, 1984)
14. J.W.S. Rayleigh, *The Theory of Sound, Vol. I* (Dover, New York, 1945)
15. S.D. Chuprova, Interference structure of a sound field in a layered ocean. in *Ocean Acoustics, Current State*, ed. by L.M. Brekhovskikh, I.B. Andreev (Nauka, Moscow, 1982), pp. 71–91

16. L.M. Brekhovskikh, Yu. Lysanov, *Fundamentals of Ocean Acoustics*, 3rd edn. (Springer, Berlin, 2003)
17. D.E. Weston, A.A. Horrigan, S.J.L. Thomas, R. Revie, Studies in sound transmission fluctuations in shallow water. *Philos. Trans. R. Soc. London, Ser. A* (1969)
18. G.A. Grachev, Theory of acoustic field invariants in layered waveguides. *Acoust. Phys.* **39**, 67–71 (1993)
19. W.A. Kuperman, G.L. D'Spain (eds.), *Ocean Acoustic Interference Phenomena and Signal Processing* (AIP, New York, 2002).
20. F.R. DiNapoli, R.L. Deavenport, Theoretical and numerical Green's function solution in a plane layered medium. *J. Acoust. Soc. Am.* **67**, 92–105 (1980)
21. M. Abramowitz, I.A. Stegun, *Handbook of Mathematical Functions* (Dover, New York, 1965)



# Chapter 3

## Ray Methods

### 3.1 Introduction

Ray-based models have been used for many years in underwater acoustics. In the early 1960s, virtually all modeling was done using either normal modes or ray tracing and primarily the latter. Today, however, ray tracing codes have fallen somewhat out of favor in the research community, the problem being the inherent (high frequency) approximation of the method which leads to somewhat coarse accuracy in the results. On the other hand, ray methods are still used extensively in the operational environment where speed is a critical factor and environmental uncertainty poses much more severe constraints on the attainable accuracy. Furthermore, much of the insight derived from studying ray theory is important in interpreting the results of other models.

From a historical point of view, it is interesting that the behavior of ray paths was understood long before ray theory was mathematically formalized. Ray theory originally emerged from optics where it was used to understand the propagation of light even before the more fundamental equations for light propagation (Maxwell's equations) were known. Indeed, propagation and reflection of rays was originally studied by Euclid [1], while Snell's law governing the refraction of the rays dates back to 1626. This development is analogous to the manner in which classical mechanics has come to be understood as an approximation to the more complete and complicated equations of quantum mechanics. One of the earliest papers on ray tracing in underwater acoustics is due to Lichte [2] who compared model results to measured data for a variety of shallow-water sites. This remarkable paper also anticipates the excellent long-range propagation attained in deep-water SOFAR channels. Today, ray theory is important in virtually all areas of wave propagation including optics, electromagnetics, and seismics [3].

For simplicity we shall present ray tracing first in a very physical, intuitive manner. In subsequent sections, we shall put the method on a formal mathematical basis. As we go through this, it is interesting to consider that ray methods are often thought of as primitive relics suited to the computers of decades gone by. In fact, ray theory is deceptively complicated both theoretically and in terms of computer

implementation. The reward for the hard work of implementing a good ray/beam code is a tool that beautifully captures the physics and in fact is practical for perhaps the majority of propagation problems.

As we shall discuss, the ray trajectories are often very sensitive to details of the environment or the numerical discretization of the problem. The sensitivity becomes particularly obvious as one traces rays to long ranges. Interestingly, the ray equations themselves may easily generate trajectories that in a formal sense are chaotic and this led to a great deal of research in recent years (see [4] and references therein). Nevertheless, ray methods are widely applicable.

### 3.2 Ray Bending

The school child who has played with a flashlight or a magnifying glass already has an idea of a ray of light that can be refracted. To make this formal, we should recognize that what we call a ray is defined as a normal to a wavefront. Ray tracing is therefore fundamentally about understanding how these rays bend or refract, thereby tracing out the propagation of wavefronts. We can imagine rays propagating in every direction in free space; however, the ones we trace are the ones that help us understand the propagation from a particular source. Thus plane waves and spherical waves in free space are understood in terms of different wavefronts and different rays. The relevant picture for a point source generating a field  $p(r) = e^{i\omega\tau}/r = e^{i\omega r/c}/r$  is indicated in Fig. 3.1. The rays or normals to the wavefronts are straight lines.

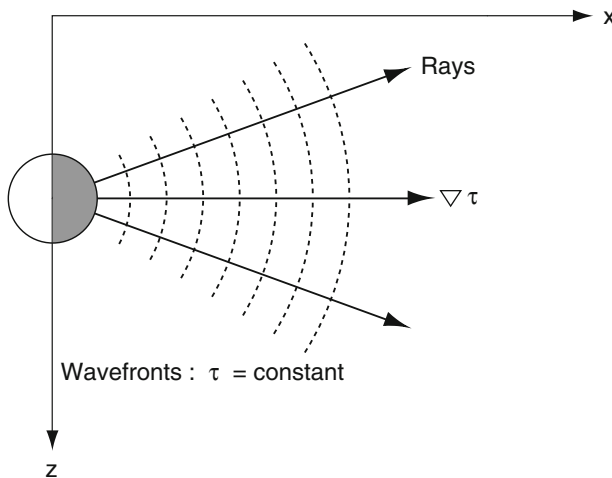
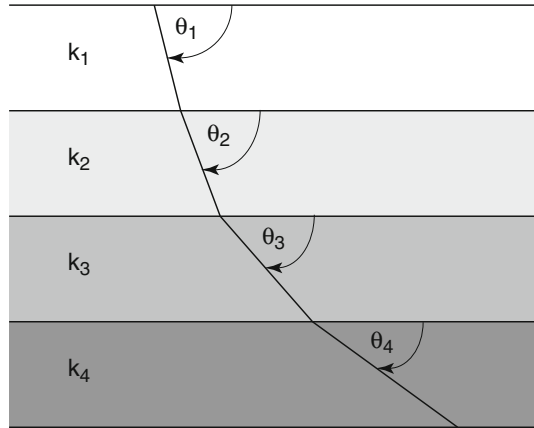


**Fig. 3.1** Rays and wavefronts

**Fig. 3.2** A ray refracting through a stack of layers



We consider next a fluid–fluid interface. In Sect. 1.6.1 we saw a traditional derivation showing how the incident wave gives rise to reflected and transmitted waves. In addition, we presented Snell’s law:

$$k_1 \cos \theta_1 = k_2 \cos \theta_2 \quad (3.1)$$

relating the angle of the incident wave  $\theta_1$  to the angle of the transmitted wave  $\theta_2$ . Now, in an intuitive way we can imagine a stack of layers (Fig. 3.2) and follow the transmitted wave through the stack. As the transmitted wave becomes incident on the next layer down, Snell’s law remains in effect, so that

$$k_2 \cos \theta_2 = k_3 \cos \theta_3 \quad (3.2)$$

and so *ad infinitum*. If we now envision the discrete stack of layers is approximating a fluid with a continuously varying wavenumber  $k(z)$ , then we can rewrite the above as,

$$k(z_1) \cos \theta(z_1) = k(z_2) \cos \theta(z_2). \quad (3.3)$$

The reflected waves are now ignored since our study of the fluid–fluid interface demonstrated that the reflected wave becomes progressively weaker as the sound speed discontinuity becomes weaker.

At this point, we have all the equations we need to trace rays in a stratified medium. We assume a ray starting point is provided, consisting of the ray origin  $z_0$  and its declination angle  $\theta_0$ . Then, the ray angle at a specified receiver depth  $z_r$  is simply

$$\theta(z_r) = \arccos \left[ \frac{k(z_0)}{k(z_r)} \cos \theta(z_0) \right]. \quad (3.4)$$

We can also see from Fig. 3.2 that in the  $i$ th layer,

$$\frac{\Delta r}{\Delta z} = \cot \theta_i. \quad (3.5)$$

Thus again passing to the limit of an infinite number of fine layers, we get a differential equation for the range of the ray as a function of depth,

$$\frac{dr}{dz} = \cot \theta(z). \quad (3.6)$$

This can then be integrated to yield,

$$r(z) = \int_{z_0}^{z_f} \cot \theta(z) dz. \quad (3.7)$$

At this point we have essentially a complete prescription for tracing a ray through a stratified medium. The integration of the ray trajectory is done through fine increments in depth. To fix ideas, imagine a sound-speed profile that is continually increasing with depth as implied by the ray trajectory in Fig. 3.2. The ray is continually refracted, apparently steering itself away from the higher-speed parts of the medium. In practice, it is just that to an observer facing in the direction of the ray propagation, the wavefronts to the left of the ray are in a slower medium than those to the right. Thus, the wavefront is continually turned like a wagon with one wheel in the mud. Eventually, the ray will turn to the point where it is horizontal. The ray integration must then be reversed with steps  $dz$  becoming negative.

Setting  $\theta(z_2) = 0$  (for a horizontal ray) in Snell's law give us:

$$k(z_1) \cos \theta(z_1) = k(z_2). \quad (3.8)$$

From this equation we can calculate a take-off angle  $\theta(z_1)$  causing a ray to turn at a given depth. This is useful, for instance, if we want to find the take-off angle that turns at the ocean bottom in a case where we want to limit a ray trace to waterborne paths.

### 3.3 Mathematical Derivation

Our starting point is the Helmholtz equation in Cartesian coordinates  $\mathbf{x} = (x, y, z)$ ,

$$\nabla^2 p + \frac{\omega^2}{c^2(\mathbf{x})} p = -\delta(\mathbf{x} - \mathbf{x}_0), \quad (3.9)$$

where  $c(\mathbf{x})$  is the sound speed and  $\omega$  is the angular frequency of the source located at  $\mathbf{x}_0$ . To obtain the ray equations, we seek a solution of the Helmholtz equation in the form

$$p(\mathbf{x}) = e^{i\omega \tau(\mathbf{x})} \sum_{j=0}^{\infty} \frac{A_j(\mathbf{x})}{(i\omega)^j}. \quad (3.10)$$

This is called the *ray series*. It is generally divergent, but in certain cases it can be shown to be an asymptotic approximation to the exact solution. Taking derivatives of the ray series, we obtain

$$p_x = e^{i\omega \tau} \left[ i\omega \tau_x \sum_{j=0}^{\infty} \frac{A_j}{(i\omega)^j} + \sum_{j=0}^{\infty} \frac{A_{j,x}}{(i\omega)^j} \right], \quad (3.11)$$

and

$$p_{xx} = e^{i\omega \tau} \left\{ [-\omega^2(\tau_x)^2 + i\omega \tau_{xx}] \sum_{j=0}^{\infty} \frac{A_j}{(i\omega)^j} + 2i\omega \tau_x \sum_{j=0}^{\infty} \frac{A_{j,x}}{(i\omega)^j} + \sum_{j=0}^{\infty} \frac{A_{j,xx}}{(i\omega)^j} \right\}. \quad (3.12)$$

Thus, we can write

$$\begin{aligned} \nabla^2 p = e^{i\omega \tau} & \left\{ [-\omega^2 |\nabla \tau|^2 + i\omega \nabla^2 \tau] \sum_{j=0}^{\infty} \frac{A_j}{(i\omega)^j} \right. \\ & \left. + 2i\omega \nabla \tau \cdot \sum_{j=0}^{\infty} \frac{\nabla A_j}{(i\omega)^j} + \sum_{j=0}^{\infty} \frac{\nabla^2 A_j}{(i\omega)^j} \right\}. \end{aligned} \quad (3.13)$$

Substituting this result into the Helmholtz equation and equating terms of like order in  $\omega$ , we obtain the following infinite sequence of equations for the functions  $\tau(\mathbf{x})$  and  $A_j(\mathbf{x})$ ,

$$\begin{aligned} O(\omega^2) & : |\nabla \tau|^2 = c^{-2}(\mathbf{x}), \\ O(\omega) & : 2\nabla \tau \cdot \nabla A_0 + (\nabla^2 \tau) A_0 = 0, \\ O(\omega^{1-j}) & : 2\nabla \tau \cdot \nabla A_j + (\nabla^2 \tau) A_j = -\nabla^2 A_{j-1}, \quad j = 1, 2, \dots \end{aligned} \quad (3.14)$$

The  $O(\omega^2)$  equation for  $\tau(\mathbf{x})$  is known as the *eikonal* equation. The remaining equations for  $A_j(\mathbf{x})$  are known as the *transport* equations.

At this stage, it would appear that we have made very little progress having converted a single linear partial differential equation (PDE) into a nonlinear PDE (the eikonal equation) plus an infinite series of linear PDEs (the transport equations). The standard simplification made is to ignore all but the first term in the ray series, which is evidently a high-frequency approximation. In the following sections, we show that the eikonal and the first transport equation can be solved quite easily.

### 3.3.1 Solving the Eikonal Equation

The eikonal equation

$$|\nabla \tau|^2 = \frac{1}{c^2(\mathbf{x})} \quad (3.15)$$

is a first-order nonlinear PDE that can be solved by a variety of techniques. For instance, eikonal solvers based on finite-differences have been widely considered in recent years [5–8]. However, the nonlinearity of the eikonal equation leads to multiple solutions, which causes some complications. In practice, the eikonal equation is usually solved by the *method of characteristics* [9]. In brief, one introduces a family of curves (rays) which are perpendicular to the level curves (wavefronts) of  $\tau(\mathbf{x})$  as shown in Fig. 3.1. This family of rays defines a new coordinate system, and it turns out that in *ray coordinates* the eikonal equation reduces to a far simpler, linear, ordinary differential equation.

Since  $\nabla \tau$  is a vector perpendicular to the wavefronts, we can define the ray *trajectory*  $\mathbf{x}(s)$  by the following differential equation,

$$\frac{d\mathbf{x}}{ds} = c \nabla \tau. \quad (3.16)$$

The factor of  $c$  is introduced so that the tangent vector  $d\mathbf{x}/ds$  has unit length. This is easily verified since

$$\left| \frac{d\mathbf{x}}{ds} \right|^2 = c^2 |\nabla \tau|^2. \quad (3.17)$$

Now, from the eikonal equation (3.15) the term on the right is found to be unity. Since  $|d\mathbf{x}/ds| = 1$ , the parameter  $s$  is simply the arclength along the ray. The rays can also be conveniently parameterized with respect to travel time or any other quantity which increases monotonically along the ray.

Our definition for the rays is based on their being perpendicular to the level curves of  $\tau(\mathbf{x})$ , a function which for the moment is still unknown. However, with some manipulations we can write the ray equations in a form involving only  $c(\mathbf{x})$ . We consider first just the  $x$ -component of (3.16). Differentiation with respect to  $s$  yields

$$\begin{aligned} \frac{d}{ds} \left( \frac{1}{c} \frac{dx}{ds} \right) &= \frac{d}{ds} \left( \frac{\partial \tau}{\partial x} \right) \\ &= \frac{\partial^2 \tau}{\partial x^2} \frac{\partial x}{\partial s} + \frac{\partial^2 \tau}{\partial x \partial y} \frac{\partial y}{\partial s}. \end{aligned} \quad (3.18)$$

Using (3.16) this can be written as

$$\begin{aligned} \frac{d}{ds} \left( \frac{1}{c} \frac{dx}{ds} \right) &= c \left( \frac{\partial^2 \tau}{\partial x^2} \frac{\partial \tau}{\partial x} + \frac{\partial^2 \tau}{\partial x \partial y} \frac{\partial \tau}{\partial y} \right) \\ &= \frac{c}{2} \frac{\partial}{\partial x} \left[ \left( \frac{\partial \tau}{\partial x} \right)^2 + \left( \frac{\partial \tau}{\partial y} \right)^2 \right]. \end{aligned} \quad (3.19)$$

Then, using the eikonal equation (3.15) to replace the terms in square brackets, we obtain

$$\frac{d}{ds} \left( \frac{1}{c} \frac{dx}{ds} \right) = \frac{c}{2} \frac{\partial}{\partial x} \left( \frac{1}{c^2} \right), \quad (3.20)$$

or

$$\frac{d}{ds} \left( \frac{1}{c} \frac{dx}{ds} \right) = -\frac{1}{c^2} \frac{\partial c}{\partial x}. \quad (3.21)$$

By applying this process to each of the coordinates, we obtain the following vector equation for the ray trajectories,

$$\frac{d}{ds} \left( \frac{1}{c} \frac{d\mathbf{x}}{ds} \right) = -\frac{1}{c^2} \nabla c. \quad (3.22)$$

In cylindrical coordinates  $(r, z)$ , these ray equations may be written in the first-order form

$$\frac{dr}{ds} = c \xi(s), \quad \frac{d\xi}{ds} = -\frac{1}{c^2} \frac{\partial c}{\partial r}, \quad (3.23)$$

$$\frac{dz}{ds} = c \zeta(s), \quad \frac{d\zeta}{ds} = -\frac{1}{c^2} \frac{\partial c}{\partial z}, \quad (3.24)$$

where  $[r(s), z(s)]$  is the trajectory of the ray in the range–depth plane. We have introduced the auxiliary variables  $\xi(s)$  and  $\zeta(s)$  in order to write the equations in first-order form. Recall that the tangent vector to a curve  $[r(s), z(s)]$  parameterized by arc length is given by  $[dr/ds, dz/ds]$ . Thus, from the above equations the tangent vector to the ray is

$$\mathbf{t}_{\text{ray}} = c [\xi(s), \zeta(s)]. \quad (3.25)$$

Later on we shall also be interested in normal vectors to the ray:

$$\mathbf{n}_{\text{ray}} = c [-\zeta(s), \xi(s)]. \quad (3.26)$$

One may immediately verify that  $\mathbf{t}_{\text{ray}} \cdot \mathbf{n}_{\text{ray}} = 0$ . The tangent and normal are, of course, arbitrary with respect to sign. However, the sign convention used here is important for some of the later formulas.

This set of ordinary differential equations is solved numerically as discussed in subsequent sections. However, to complete the specification of the rays we also need initial conditions. As indicated in Fig. 3.3, the initial conditions are that the ray starts at the source position  $(r_0, z_0)$  with a specified take-off angle  $\theta_0$ . Thus, we have

$$r = r_0, \quad \xi = \frac{\cos \theta_0}{c(0)}, \quad (3.27)$$

$$z = z_0, \quad \zeta = \frac{\sin \theta_0}{c(0)}. \quad (3.28)$$

**Fig. 3.3** Schematic of 2-D ray geometry

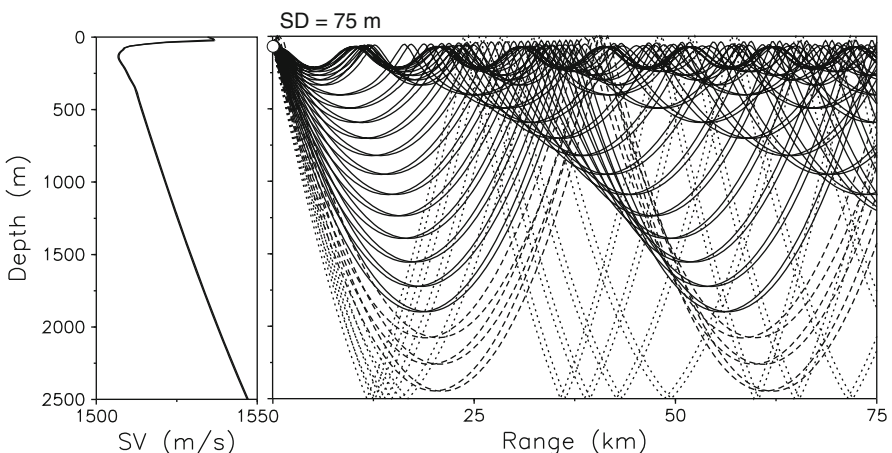
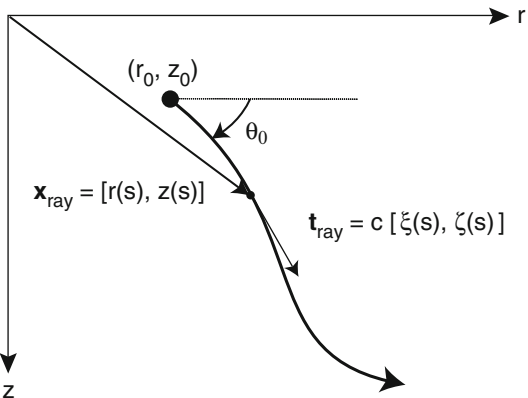


**Fig. 3.4** Sound-speed profile and ray trace in the Balearic Sea

The source coordinate is of course a given quantity whereas the take-off angle  $\theta_0$  for the moment is an unknown variable.

If the index of refraction is independent of frequency then the ray paths are also independent of frequency. However, the phase is frequency dependent. In practice, there is usually a frequency-dependent loss which adds an imaginary term to the index of refraction. This loss introduces an additional frequency dependence in the ray calculation.

As an example, we consider a sound-speed profile taken in the Balearic Sea (Western Mediterranean) with a source located at depth 75 m. The particular sound-speed profile and corresponding ray trace are shown in Fig. 3.4. For clarity the different classes of ray paths have been plotted using different line signatures. Thus, *refracted refracted* paths are given by solid lines, *refracted surface-reflected* paths by dashed lines, and *surface-reflected bottom-reflected* paths by dotted lines. To produce the plot in Fig. 3.4 the differential equations are integrated many times with initial conditions corresponding to different ray take-off angles.

Qualitatively, we observe that the rays veer away from regions with a higher sound speed so that the rays are bent away as they approach the surface and bottom. (In problems with more complicated sound-speed profiles the rays may change directions many times in a single cycle up and down through the water column.)

This type of plot is perhaps the most commonly used product of a ray tracing code although it represents only the “skeleton” of the acoustic field: it shows the direction in which energy propagates but not the pressure field or transmission loss. To obtain the pressure field we need to associate a phase and an amplitude with each ray. The phase is obtained by solving the eikonal equation in the coordinate system of the rays. Recall that

$$\nabla\tau \cdot \nabla\tau = \frac{1}{c^2}. \quad (3.29)$$

Therefore

$$\nabla\tau \cdot \frac{1}{c} \frac{d\mathbf{x}}{ds} = \frac{1}{c^2}, \quad (3.30)$$

or

$$\frac{d\tau}{ds} = \frac{1}{c}. \quad (3.31)$$

This is the eikonal equation written in terms of the ray coordinate  $s$ . Note that the original nonlinear PDE has been reduced to a linear ordinary differential equation which is readily solved to yield

$$\tau(s) = \tau(0) + \int_0^s \frac{1}{c(s')} ds'. \quad (3.32)$$

The integral term in this equation is the *travel time* along the ray, so from a physical point of view the phase of the wave is simply delayed in accordance with its travel time.

### 3.3.2 Solving the Transport Equation

The final step in computing the pressure is to associate an amplitude with each ray, that is, to solve the transport equation which we repeat here:

$$2 \nabla\tau \cdot \nabla A_0 + (\nabla^2\tau) A_0 = 0. \quad (3.33)$$

This can also be written in the form,

$$\nabla \cdot (A_0^2 \nabla\tau) = 0. \quad (3.34)$$

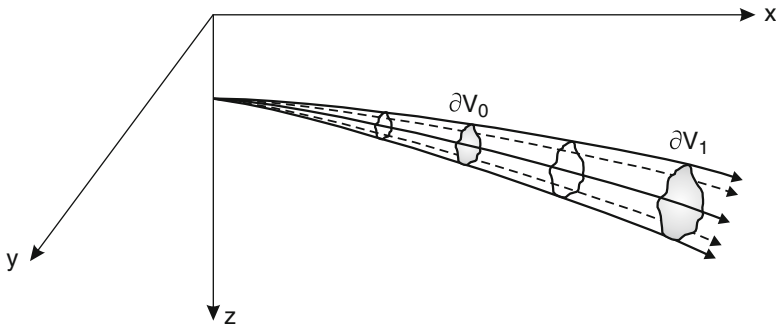


**Fig. 3.5** Construction of a ray tube

Consider an arbitrary field  $F$  and arbitrary volume  $V$ . Recall that Gauss's theorem (the divergence theorem) equates the integral of the divergence of  $F$ , throughout the volume to its flux through the boundary of that same volume:

$$\int_V \nabla \cdot F dV = \int_{\partial V} F \cdot \mathbf{n} dS, \quad (3.35)$$

where  $\mathbf{n}$  is an outward pointing normal. From this, we conclude

$$\int_{\partial V} A_0^2 \nabla \tau \cdot \mathbf{n} dS = 0. \quad (3.36)$$

We next define a *ray tube* as the volume enclosed by a family of rays as shown in Fig. 3.5. Since the rays are normal to the phase fronts,  $\nabla \tau \cdot \mathbf{n}$  vanishes on the sides of the ray tube. Meanwhile, on the ends of the ray tube the ray itself is the normal vector:  $\mathbf{n} = \pm d\mathbf{x}/ds$  and (3.31) shows us that the directional derivative  $\nabla \tau \cdot \mathbf{n} = 1/c$ . Therefore, we obtain the following energy conservation law:

$$\int_{\partial V_0} \frac{A_0^2}{c} dS = \int_{\partial V_1} \frac{A_0^2}{c} dS = \text{const}, \quad (3.37)$$

where  $\partial V_0$  and  $\partial V_1$  denote the endcaps of the ray tube, as indicated in Fig. 3.5. This is an important result that affirms our intuitive view of energy propagating within a ray tube. It further implies a rising or falling amplitude as the ray tube shrinks and expands. In particular, if we let the ray tube become infinitesimally small and use values at an arbitrary  $s = 0$  as a reference, we conclude that

$$A_0(s) = A_0(0) \sqrt{\frac{c(s)}{c(0)} \frac{J(0)}{J(s)}}, \quad (3.38)$$

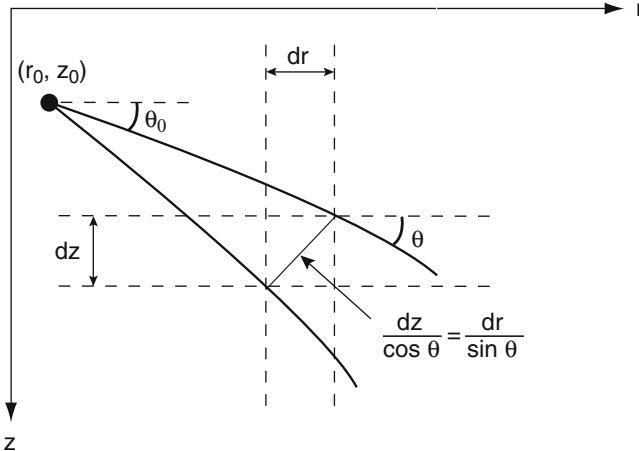


**Fig. 3.6** The ray-tube cross section

where  $J(s)$  is any quantity proportional to the cross-sectional area of the ray tube. We will see later that this cross-sectional area is also related to a certain Jacobian  $J$ . Let us now specialize to the common case of a point source in a cylindrically symmetric ocean. Then, we consider a “ray tube” formed by the boundary of two rays launched with adjacent take-off angles, separated by  $d\theta_0$ , as shown in Fig. 3.6. The cross-sectional area is just the hypotenuse  $J d\theta_0$  with:

$$J = r \left[ \left( \frac{\partial z}{\partial \theta_0} \right)^2 + \left( \frac{\partial r}{\partial \theta_0} \right)^2 \right]^{1/2}. \quad (3.39)$$

The extra factor of  $r$  accounts for the fact that we have assumed cylindrical symmetry so that Fig. 3.6 is really just showing a slice through a ray tube that is rotated around the  $z$ -axis. Again from the geometry, we can see that the following are equivalent forms:

$$J = \frac{r}{\cos \theta} \frac{\partial z}{\partial \theta_0} = \frac{r}{\sin \theta} \frac{\partial r}{\partial \theta_0}, \quad (3.40)$$

where  $\theta$  is the angle of the ray at the receiver. Sometimes one or the other of these various representations are convenient for numerical implementation.

In many early codes, the cross-sectional area was calculated by putting calipers on the ray trajectories, i.e. using finite-difference approximations. For instance, (3.40) yields the approximation:

$$J(s) = \frac{r_i(s)}{\sin \theta} \frac{r_{i+1}(s) - r_i(s)}{\delta \theta_0}, \quad (3.41)$$

where  $r_i(s) = r(s; \theta_0)$  and  $r_{i+1}(s) = r(s; \theta_0 + \delta \theta_0)$  are bracketing rays forming a ray tube.

### 3.3.3 Ray Amplitudes and Jacobians

The above derivation takes advantage of the divergence theorem to provide a simple and intuitive view of how the ray amplitude evolves. It is also useful to be able to view the rays as providing a change of coordinate system, whose Jacobian expresses the amplitude along the ray. To pursue that approach, recall that the rays are defined in (3.16) as being perpendicular to the wavefronts. This allows us to rewrite the transport equation (3.33) as

$$\frac{2}{c} \frac{d\mathbf{x}}{ds} \cdot \nabla A_0 + (\nabla^2 \tau) A_0 = 0. \quad (3.42)$$

The first term represents a directional derivative along the ray path so that

$$\frac{2}{c} \frac{dA_0}{ds} + (\nabla^2 \tau) A_0 = 0. \quad (3.43)$$

In principle, we could calculate  $\nabla^2 \tau$  and then integrate this equation along a ray path. On the other hand,

$$\nabla^2 \tau = \nabla \cdot \nabla \tau = \nabla \cdot \frac{d\mathbf{x}}{ds}, \quad (3.44)$$

so  $\nabla^2 \tau$  is given by the divergence of the rays. Loosely, (3.43) states that the amplitude along a ray changes in relation to the spreading of a ray tube. To make this statement precise, we introduce the *Jacobian*. For a three-dimensional problem we have

$$J = \left| \frac{\partial \mathbf{x}}{\partial(s, \theta_0, \varphi_0)} \right| = \begin{vmatrix} \frac{\partial x}{\partial s} & \frac{\partial x}{\partial \theta_0} & \frac{\partial x}{\partial \varphi_0} \\ \frac{\partial y}{\partial s} & \frac{\partial y}{\partial \theta_0} & \frac{\partial y}{\partial \varphi_0} \\ \frac{\partial z}{\partial s} & \frac{\partial z}{\partial \theta_0} & \frac{\partial z}{\partial \varphi_0} \end{vmatrix}, \quad (3.45)$$

where  $\theta_0$  and  $\varphi_0$  are, respectively, the declination and azimuthal take-off angles of the ray. For a cylindrically symmetric problem this reduces to

$$J = r \left( \frac{\partial r}{\partial s} \frac{\partial z}{\partial \theta_0} - \frac{\partial z}{\partial s} \frac{\partial r}{\partial \theta_0} \right), \quad (3.46)$$

or

$$J = r \left[ \left( \frac{\partial z}{\partial \theta_0} \right)^2 + \left( \frac{\partial r}{\partial \theta_0} \right)^2 \right]^{1/2}. \quad (3.47)$$

Other forms for the Jacobian were given in the previous section. In Appendix 2, we show that the Jacobian satisfies

$$\nabla^2 \tau = \frac{1}{J} \frac{d}{ds} \left( \frac{J}{c} \right), \quad (3.48)$$

so we can write (3.43) as

$$2 \frac{dA_0}{ds} + \left[ \frac{c}{J} \frac{d}{ds} \left( \frac{J}{c} \right) \right] A_0 = 0. \quad (3.49)$$

Integrating this equation we obtain our final result for the solution of the transport equation,

$$A_0(s) = A_0(0) \left| \frac{c(s) J(0)}{c(0) J(s)} \right|^{1/2}, \quad (3.50)$$

which, of course, agrees with the result derived previously.

### 3.3.4 Initial Conditions

In order to complete the solution of the eikonal and transport equations we must specify the initial conditions. This is done using the *method of canonical problems*: One constructs a simpler problem for which the exact solution is known and the initial conditions are chosen so that the ray result agrees with the exact solution. In ocean acoustics we are normally interested in a point source which suggests we take the problem of a point source in an infinite homogeneous medium as the canonical problem. We take the sound speed of the homogeneous medium to be that of the original inhomogeneous problem evaluated at the source, i.e.,  $c_0 = c|_{s=0}$ .

As discussed in Sect. 2.3.2, the solution to this problem is given by

$$p^0(s) = \frac{e^{i\omega s/c_0}}{4\pi s}, \quad (3.51)$$

where  $s$  is the distance from the source. Thus, the amplitude and phase associated with this solution are

$$\begin{aligned} A^0(s) &= \frac{1}{4\pi s}, \\ \tau^0(s) &= \frac{s}{c_0}. \end{aligned} \quad (3.52)$$

Now, taking  $s = 0$  we obtain  $\tau(0) = 0$  as the initial condition for the eikonal. The amplitude  $A^0(s)$  goes to infinity as  $s \rightarrow 0$  posing a slight complication. This difficulty is resolved by considering initial conditions for the product  $A_0(0) |J(0)|^{1/2}$  which turns out to be a bounded quantity.

To compute the Jacobian we first need the solution of the ray equations in a homogeneous medium. When the sound speed is constant the ray equations (3.22) are easily solved, yielding

$$\mathbf{x}(s) = \mathbf{x}_0 + s (\cos \theta_0 \cos \varphi_0, \cos \theta_0 \sin \varphi_0, \sin \theta_0). \quad (3.53)$$

Thus, the rays are simply straight lines fanning out from the source point as indicated in Fig. 3.1.

From the rays the Jacobian determinant in (3.45) is calculated to be

$$J(s) = -s^2 \cos \theta_0, \quad (3.54)$$

which is seen to be consistent with the cross-sectional area of the ray tube in Fig. 3.6. Thus,

$$\lim_{s \rightarrow 0} A(s) |J(s)|^{1/2} = \frac{1}{4\pi} |\cos \theta_0|^{1/2}. \quad (3.55)$$

Substituting this into (3.50), we obtain

$$A_0(s) = \frac{1}{4\pi} \left| \frac{c(s) \cos \theta_0}{c(0) J(s)} \right|^{1/2}. \quad (3.56)$$

Combining this result with that for the eikonal, (3.32), we obtain the pressure field as

$$p(s) = \frac{1}{4\pi} \left| \frac{c(s) \cos \theta_0}{c(0) J(s)} \right|^{1/2} e^{i\omega \int_0^s \frac{1}{c(s')} ds'}. \quad (3.57)$$

Thus, the pressure field is obtained by dividing the energy of the point source among each of the “ray tubes” (the tubes formed by pairs of adjacent rays). The change in intensity along a ray tube is then inversely proportional to the cross section of that tube. Finally, the phase associated with a ray is calculated from the travel time along a ray.

### 3.3.5 Intensity Calculations

#### 3.3.5.1 Dynamic Ray Tracing

We have seen that the amplitude along a ray depends on the change in area of the ray tube. It turns out that there is a simple differential equation which provides information about how the ray paths change for infinitesimal perturbations in either the ray take-off angle or the ray source point. These equations form the basis of *dynamic ray tracing* and can be used to calculate the amplitude along a ray. Here, we shall present only the final results. For a more detailed discussion the reader is referred to [10].

The dynamic ray equations are

$$\frac{dq}{ds} = c p(s), \quad \frac{dp}{ds} = -\frac{c_{nn}}{c^2(s)} q(s), \quad (3.58)$$

where  $c_{nn}$  is the curvature of the sound speed in a direction normal to the ray path. To get a formula for  $c_{nn}$  we begin by noting that the derivative of  $c$  in the normal direction is

$$c_n = \nabla c \cdot \mathbf{n}, \quad (3.59)$$

where  $\mathbf{n} = (n_{(r)}, n_{(z)})$  is the ray normal, which is viewed as a fixed quantity in the following derivatives. Thus,

$$c_n(r, z) = c_r(r, z)n_{(r)} + c_z(r, z)n_{(z)}. \quad (3.60)$$

Repeating the process we obtain:

$$\begin{aligned} c_{nn}(r, z) &= \nabla c_n(r, z) \cdot \mathbf{n}, \\ &= c_{rr}(r, z)n_{(r)}^2 + 2c_{rz}n_{(r)}n_{(z)} + c_{zz}n_{(z)}^2. \end{aligned} \quad (3.61)$$

The ray normal is given in (3.26) in terms of the auxiliary variables  $\xi$  and  $\zeta$ , yielding

$$c_{nn} = c^2 \left( \frac{\partial^2 c}{\partial r^2} \zeta^2 - 2 \frac{\partial^2 c}{\partial r \partial z} \zeta \xi + \frac{\partial^2 c}{\partial z^2} \xi^2 \right). \quad (3.62)$$

Thus, we have obtained a simple formula for the curvature of the sound speed in the normal direction, which uses only the second partial derivatives of the sound speed with respect to the Cartesian coordinates  $r$  and  $z$ .

The initial conditions determine the type of ray perturbation. If we take

$$q(0) = 0, \quad p(0) = \frac{1}{c(0)}, \quad (3.63)$$

then we are perturbing the rays with respect to angle and it can be shown that

$$rq(s) = J(s). \quad (3.64)$$

Thus,  $q$  is proportional to the Jacobian determinant. We can then write the ray amplitude as

$$A_0(s) = \frac{1}{4\pi} \left| \frac{c(s) \cos \theta_0}{rc(0)q(s)} \right|^{1/2}. \quad (3.65)$$

In summary, the intensity along a ray is found to be inversely proportional to a function  $q(s)$  that is easily calculated by integrating an extra pair of differential equations along with the ray equations.

### 3.3.5.2 Coherent Transmission Loss

The expressions we have derived so far yield the pressure associated with a single ray path. The pressure field at any point then involves identifying all the *eigenrays*, that is, the rays which pass through that point. For instance, the eigenrays for a receiver at 75 km in range and 500 m in depth in the Balearic Sea case are shown in Fig. 3.7. We can see clearly the different classes of refracted, surface, and bottom reflected rays that form the echo pattern at the receiver location.

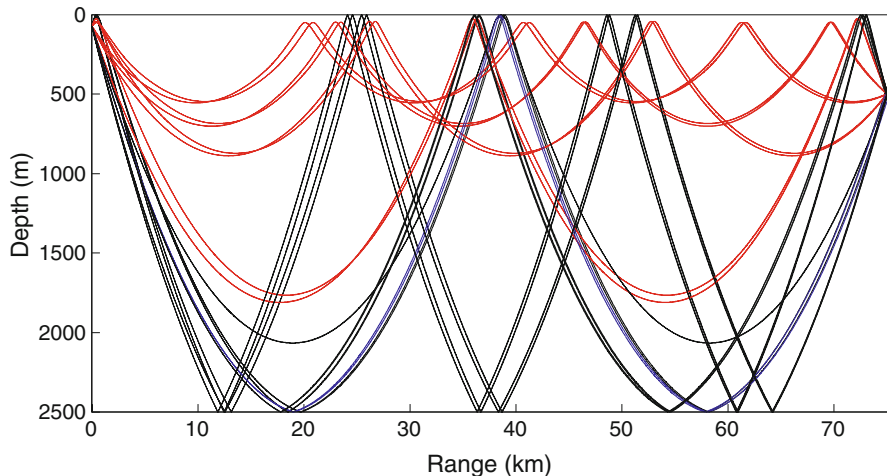


**Fig. 3.7** Eigenrays for a receiver at 75 km in range and 500 m in depth in the Balearic Sea

Each eigenray makes a contribution to the complex pressure field based on its intensity and phase at that point. The intensity is calculated by simply summing up the contributions of each of the eigenrays leading to

$$p^{(C)}(r, z) = \sum_{j=1}^{N(r,z)} p_j(r, z), \quad (3.66)$$

where  $N(r, z)$  denotes the number of eigenrays contributing to the field at a particular receiver position and  $p_j(r, z)$  is the pressure due to that eigenray. The number of contributing eigenrays can vary considerably. In the nearfield there may just be three important eigenrays: a direct ray, a bottom-bounce ray and a surface-bounce ray. The remaining eigenrays strike the bottom at steeper angles than the critical angle and are therefore strongly attenuated. At longer ranges there often will be contributions from paths which strike the surface and bottom several times or eigenrays following different refracted paths.

Once we have associated a phase and intensity with the ray paths we can complete the calculation of the pressure field. As discussed in Chap. 2, (2.77), transmission loss is then defined as

$$\text{TL}(s) = -20 \log \left| \frac{p(s)}{p^0(s=1)} \right|, \quad (3.67)$$

where  $p^0(s)$  given by (3.51) is the pressure for a point source in free space to be evaluated at a distance of 1 m from the source. Thus,

$$p^0(s=1) = \frac{1}{4\pi}. \quad (3.68)$$

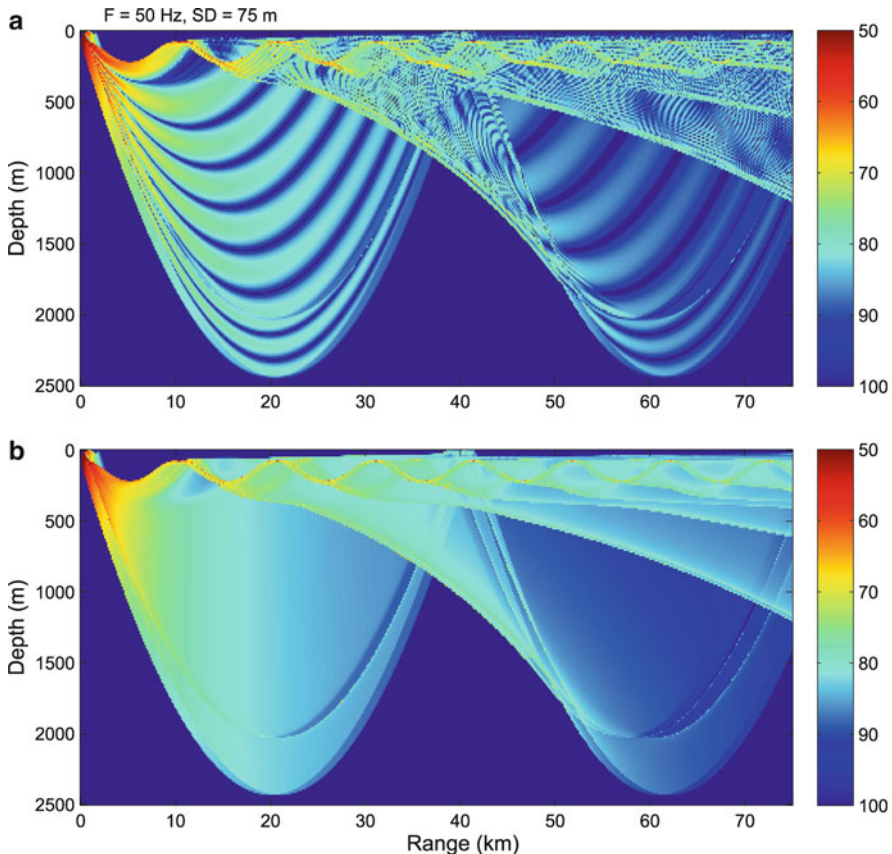


**Fig. 3.8** Transmission loss result for the Balearic Sea. (a) Coherent ray theory. (b) Incoherent ray theory

For the Balearic Sea problem this yields the transmission-loss plot shown in Fig. 3.8a. In the nearfield we can now see the role of phase in that the surface-reflected and direct ray paths interfere constructively and destructively to form the Lloyd-mirror pattern discussed in Sects. 1.4.2 and 2.4.2. Note that we have arbitrarily limited the ray fan to exclude the bottom-bounce rays, which would make a further contribution to the field depending on the reflectivity of the bottom. Results of this type of coherent calculation are most directly comparable to full wave theory solutions.

### 3.3.5.3 Incoherent Transmission Loss

Ray methods are most commonly used for high-frequency problems: they are derived under that assumption and other methods become less practical at higher

frequencies. However, as we go to high frequencies, the details of the interference pattern are less stable, in the sense that extremely detailed environmental knowledge is necessary for accurate predictions, and this knowledge is generally lacking. On the other hand, sonar performance evaluation may require only a smoothed transmission loss result.

Under these conditions an incoherent calculation may be acceptable in which the phase of the pressure associated with each eigenray is ignored. This leads to

$$p^{(I)}(r, z) = \left[ \sum_{j=1}^{N(r,z)} |p_j(r, z)|^2 \right]^{1/2}. \quad (3.69)$$

This form also has some computational advantages. Generally, the sampling in terms of the number of rays and the ray step size is less critical since the phase term which leads to a detailed interference pattern is missing. An incoherent transmission-loss calculation for the Balearic Sea is shown in Fig. 3.8b. Clearly the incoherent result is much smoother than the coherent result.

### 3.3.5.4 Semicohherent Transmission Loss

While the coherent transmission loss may represent a result which is so detailed that it could never be observed in reality, the incoherent calculation can smooth out features which are quite stable even at high frequencies. Perhaps the simplest example of such a feature is the Lloyd-mirror pattern which is seen in the coherent calculation in the nearfield. Evidently, what is needed in many practical applications is some intermediate solution which retains features that are insensitive to the detailed environmental knowledge but smoothes out other features which we cannot hope to predict.

There are a variety of techniques for accomplishing this. They all tend to be somewhat informal and partially empirically based. We shall mention just one example, namely the *semicoherent* loss calculation defined by

$$p^{(S)}(r, z) = \left[ \sum_{j=1}^{N(r,z)} S(\theta_0) |p_j(r, z)|^2 \right]^{1/2}. \quad (3.70)$$

Here,  $S(\theta_0)$  is a shading function which weights the amplitude of a ray as a function of its take-off angle. This type of formula is also appropriate for treating a source which is not omni-directional in its radiation pattern. However, our interest here is to reconstruct the Lloyd-mirror pattern that we expect in the nearfield. For a source in a homogeneous halfspace, the Lloyd-mirror pattern is given by

$$S(\theta_0) = 2 \sin^2 \left( \frac{\omega z_0 \sin \theta_0}{c_0} \right). \quad (3.71)$$

A similar correction can be used for the receiver to correct for a directionality pattern resulting from the interference of a surface-reflected and direct ray to the receiver.

### 3.3.5.5 Geometric Beams

The ray approach as described so far, solves the wave equation by introducing a new curvilinear coordinate system formed by the rays. The magic of this coordinate system is that one can easily construct travel times and amplitudes by simply solving a set of ordinary differential equation along each ray. The travel times and amplitudes, of course, yield immediately the pressure field along each ray. However, the user of a ray model typically needs the field on a rectangular grid whose nodes will generally lie in between the curvilinear grid formed by the fan of rays.

One simple way to interpolate from the ray grid onto the receiver grid is to construct a beam around each ray. Borrowing an idea from the finite-element literature, we consider triangular or hat-shaped beams as shown in Fig. 3.9 and introduced in [11]. The amplitude of these beams is tapered so that it varies linearly from  $A_0(s)$  on the central ray of the beam and decays linearly to zero on either side. The halfwidth  $W(s)$  of the beam is defined by the distance from the central ray where the beam amplitude is made to vanish. This width is chosen precisely so that the beam vanishes at the location of its neighboring ray. (Therefore the beam width depends on the density chosen for the ray fan.) Thus, the pressure for the beam is given by

$$P^{\text{beam}}(s, n) = A^{\text{beam}}(s) \phi(s, n) e^{i\omega\tau(s)}, \quad (3.72)$$

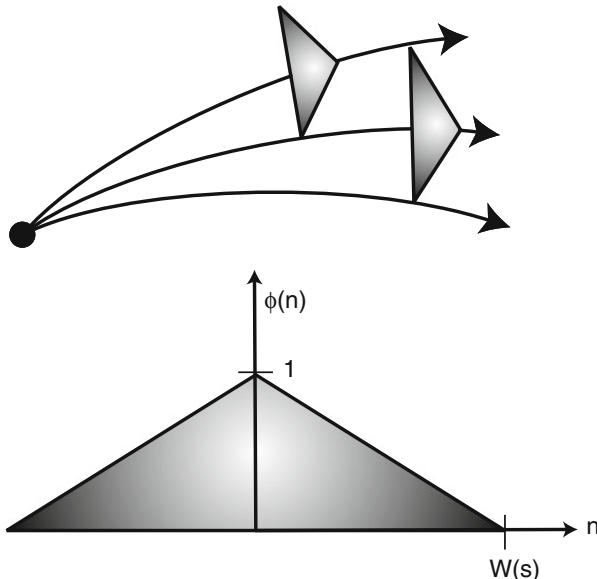


**Fig. 3.9** Construction of geometric beams around each ray

where  $\phi(s, n)$  is the hat-shaped function:

$$\phi(s, n) = \begin{cases} \frac{W(s)-n}{W(s)} & \text{for } n \leq W(s) \\ 0 & \text{else} \end{cases} \quad (3.73)$$

and  $n(s)$  is the normal distance from the receiver to the central ray of the beam.

We require that the amplitude of this beam on its central ray (where  $n = 0$ ) should match the geometric ray theory result, therefore  $A^{\text{beam}} = A_0(s)$  is derived directly from the dynamic ray equations given in (3.65).

The key remaining question is that of how to calculate the beam halfwidth  $W(s)$ . One tends to think of the amplitude as being a consequence of the spreading of the ray tube; however, one may also reverse the process and use the amplitude to calculate the width of the ray tube. The result is:

$$W(s) = |q(s) \delta\theta_0|, \quad (3.74)$$

where  $\delta\theta_0$  is the angular spacing between adjacent rays and  $q(s)$  is our spreading term from the dynamic ray equations.

Note that with this construction, we have accomplished a piecewise linear interpolation of the pressure field between rays; however, the field of each beam can be constructed independently. We refer to this as *Geometric Beam Tracing* since the behavior of the beams is determined by the geometry of the ray field. When properly implemented, this approach reproduces precisely a ray theoretic result and this is the method used to produce such results in this chapter. However, small errors in the implementation may cause large problems because the beams produced must have precisely the right width to fill the space between adjacent beams.

A slightly more forgiving formulation can be done by simply replacing the hat-functions with Gaussian shapes:

$$\phi(s, n) = e^{-\left(\frac{n}{W(s)}\right)^2}. \quad (3.75)$$

The resulting Gaussian beams have a slightly larger integrated energy across a beam, so the amplitude of each beam must be reduced accordingly:

$$A^{\text{beam}}(s) = \frac{1}{(2\pi)^{1/4}} \sqrt{\frac{\delta\theta_0}{r} \frac{c(s)}{c(0)} \frac{2 \cos \theta_0}{W(s)}}. \quad (3.76)$$

The use of the Gaussian shapes produces some smoothing of the pressure field; however, the beamwidth  $W(s)$  vanishes at caustics yielding singularities as discussed in the next section. Weinberg and Keenan [12] suggested limiting the ability of the beam to focus to a point, by imposing a minimum beam width of  $\pi\lambda$  where  $\lambda$  is the wavelength. That empirically-derived focal limit eliminates the singularities at caustics and generally improves the accuracy. These latter approaches may be viewed as derivatives of the Gaussian beam tracing approach originally proposed by Bucker

in the early 1970s. In Bucker's original work, the beamwidth was chosen fairly arbitrarily; however, in later work he proposed an approach based on the arc-length of the ray [13]. The beams serve simply to interpolate the field and are not intended to approximate the physics of a true Gaussian beam propagating in the ocean.

## 3.4 Ray Anomalies

### 3.4.1 Caustics and Shadow Zones

There are a few flaws in the transmission loss calculation in Fig. 3.8 which are typical of ray-theory results. The first is the occurrence of *shadow zones* where no rays pass and therefore the pressure field is identically zero. The second is the occurrence of *caustics* which are curves where the cross-section of a ray tube vanishes and therefore the predicted intensity is infinite. The exact solution of the wave equation generally is finite, so this is a ray artifact. In practice, these curves of infinite intensity would normally be missed unless a receiver is placed precisely on a caustic. Nevertheless, the problem can be significant, because the intensity is high not just at the caustic but in a zone surrounding the caustic. Furthermore, there is a phase change that occurs when a ray passes through a caustic. Neglecting this phase change causes an error at subsequent ranges which can be arbitrarily far from the caustic.

To illustrate these points, we consider a simpler sound-speed profile in which the square *index of refraction* varies linearly with depth, i.e.,  $n^2 = (c_0/c)^2 = a + bz$ . This kind of problem was studied in detail by Jones [14] and Pedersen and Gordon [15]. We consider the particular form

$$c(z) = \frac{c_0}{\sqrt{1 + 2.4z/c_0}} \quad (3.77)$$

with  $c_0 = 1550$  m/s.

The sound-speed profile and resulting ray trace are shown in Fig. 3.10 for a source depth of 75 m. The transmission loss at 2000 Hz for a receiver located at a depth of 75 m is shown in Fig. 3.11 using both an exact spectral integral representation (see Chap. 4) and ray theory.

In the range of 0 to about 0.88 km, the pressure field is composed of contributions from a direct ray and a surface-reflected ray. As we go out in range these two types of rays interfere constructively and destructively to produce an oscillatory transmission-loss pattern. Beyond about 0.88 km we can see clearly from the ray trace that we are entering a shadow zone where there are no rays. The ray that forms the border between the shadow zone and the two-ray region is called the *limiting ray*. In the shadow zone, the transmission loss predicted by ray theory drops off abruptly while the exact solution shows a gradual decay in energy.

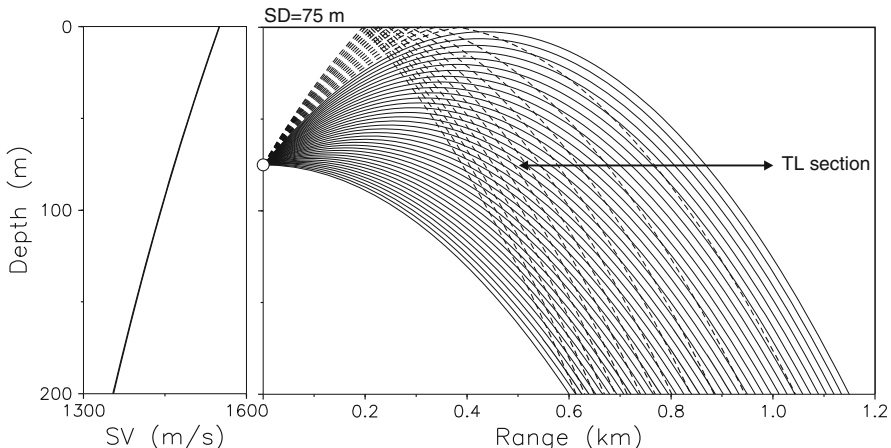


**Fig. 3.10** Sound-speed profile and ray trace for the  $n^2$ -linear profile with a shallow source

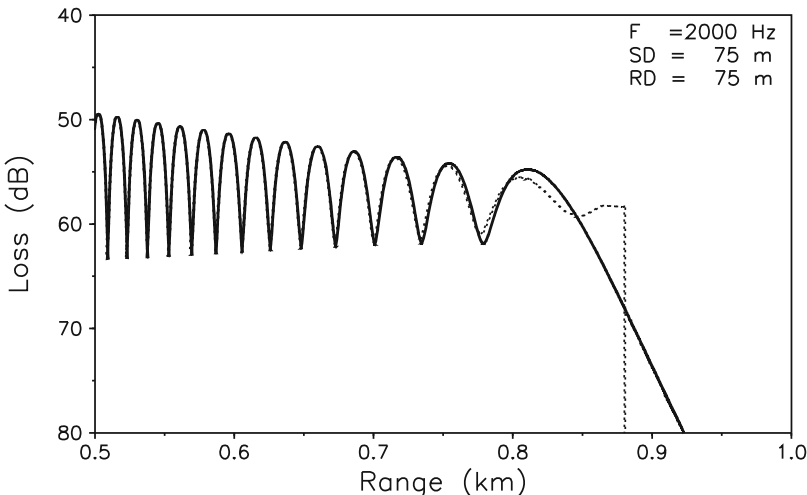


**Fig. 3.11** Transmission loss for the  $n^2$ -linear profile with a shallow source. *Solid curve:* Exact solution. *Dashed curve:* Ray theory

In fact, the shadow zone is an artifact of our method of constructing the rays. The ray plot was done using a certain fan of ray angles, and by limiting the fan, we introduce shadow zones in the ray plot. However, it is clear that even with a complete fan of angles covering  $\pm 90^\circ$ , no rays would enter the shadow zone beyond the limiting ray. But why should we restrict ourselves to real take-off angles? In fact, with complex ray angles one finds that *complex eigenrays* exist in what we had previously considered a shadow zone. These complex rays can be used to complete the ray theory result and provide a useful prediction into the shadow zone. However,

in practical ray tracing programs these complex rays are almost never used. The reason is that they introduce an increased complexity in identifying eigenrays.

For the purpose of illustrating caustic formation we increase the source depth to 1000 m, although our particular profile assumes unrealistic values at these depths. The corresponding profile and ray trace are shown in Fig. 3.12. Here, the range divides into three zones, which are echoed in the transmission-loss plot in Fig. 3.13. In the nearfield, out to about 3.04 km, we have a two-ray interference pattern as before. From about 3.04 to 3.08 km the surface-reflected ray is not present and the

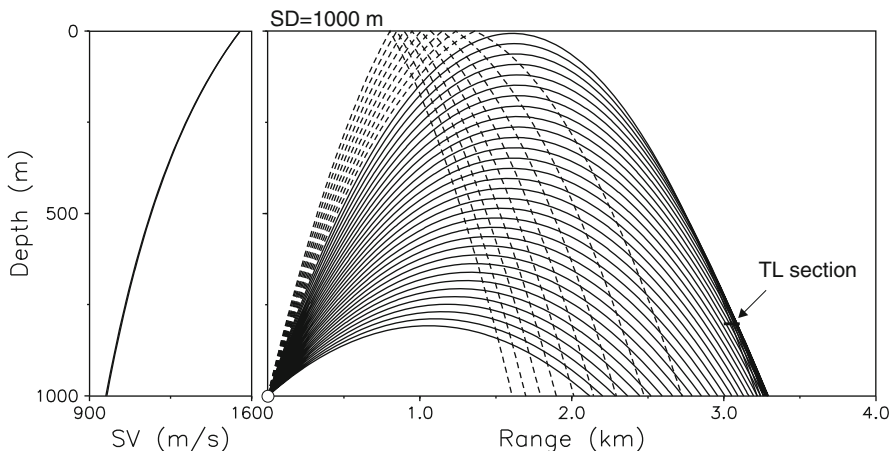


**Fig. 3.12** Sound-speed profile and ray trace for the  $n^2$ -linear profile with a deep source

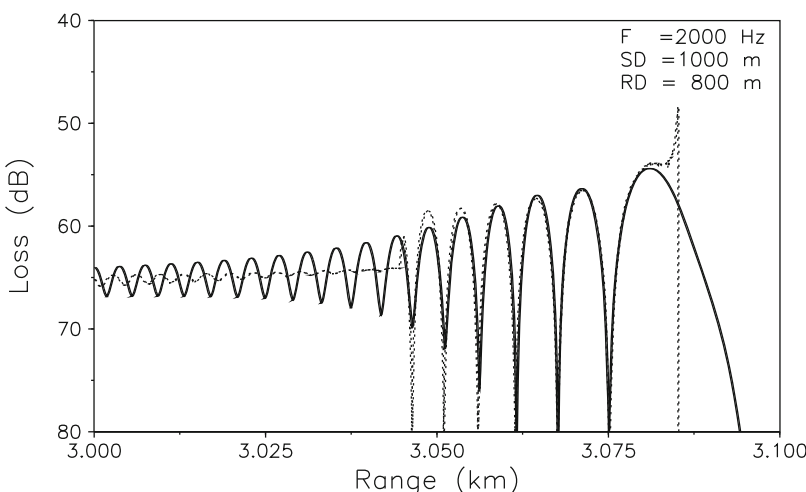


**Fig. 3.13** Transmission loss for the  $n^2$ -linear profile with a deep source. *Solid curve:* Exact solution. *Dashed curve:* Ray theory

interference pattern involves contributions from two rays with are both refracted. Beyond 3.08 km we again enter a shadow zone, but at the boundary of the shadow zone we see that the loss plot has a sharp peak. This peak occurs at the caustic and, properly sampled, actually assumes an infinitely large value. In the ray trace, the caustic is a line which divides the insonified zone from the shadow zone. The caustic starts at a depth  $z$  satisfying

$$c^2(z) = c^2(0) - c^2(z_0), \quad (3.78)$$

that is, at about 400 m. Above that depth the division between the shadow and insonified zones is formed by the limiting ray which just grazes the surface. The caustic curve itself corresponds to no single ray path but rather is the envelope of a family of ray paths.

From a computational point of view, a caustic occurs when the Jacobian, which appears in the amplitude term of (3.50), vanishes. As a ray passes through a caustic, the Jacobian changes sign. This brings us to an important point: How should the ray amplitude be continued as it goes through such a singular point? The analysis is somewhat complicated and we shall provide only the final solution here. (In Sect. 2.5.2 we proved an analogous result for the simple case of plane waves in a stratified medium.) The result is that we can continue to use (3.50) but we need to introduce a phase shift of  $\pi/2$  into the solution. (In the time domain, this corresponds to Hilbert transforming the waveform.) Thus, we write the solution of the amplitude equation as

$$A_0(s) = A_0(0)(-\mathrm{i})^{m(s)} \sqrt{\left| \frac{c(s) J(0)}{c(0) J(s)} \right|}, \quad (3.79)$$

and  $\sqrt{x}$  denotes the principal value, i.e., the branch of the square root that yields a positive number. The integer-valued function  $m(s)$  gives the number of time  $J(s)$  vanishes in  $[0, s]$ , i.e., the number of caustics crossed by the ray. This function is sometimes referred to as the KMAH index after Keller, Maslov, Arnol'd, and Hörmander. If this correction is not made, the resulting interference pattern is incorrect as illustrated in Fig. 3.14.

There are several approaches to producing improved approximations to the field in the vicinity of a caustic. These uniform asymptotic expansions were developed independently and at about the same time by Kravtsov [16, 17] and Ludwig [18] for simple caustics. However, caustics are classified into a taxonomy with a finite number of forms (e.g. cusps, swallow-tails), categorized using catastrophe theory. A complete theory requires both classifying the caustic and applying the appropriate uniform asymptotic expansion. More details may be found in [19].

### 3.4.2 Region of Validity of the Ray Solution

The previous section illustrated some of the ways in which ray theory can fail. Given the derivation of the ray equations as a high-frequency approximation it is natural to

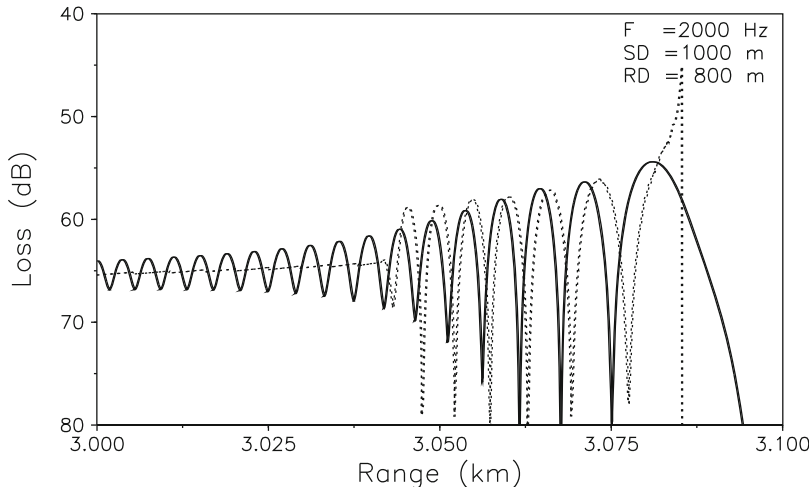


**Fig. 3.14** Transmission loss for the  $n^2$ -linear profile with a deep source. *Solid curve:* Exact solution. *Dashed curve:* Ray theory without correction for the phase shift at the caustic

ask how high is high? That is, at how low a frequency can we expect the ray theory to be valid. Clearly this is not a question we can answer without first setting some definition of what constitutes a sufficiently accurate solution. Unfortunately, even with a well-defined accuracy requirement it is difficult to predict a priori whether the ray solution will meet that requirement.

A complicating factor is that many ray codes produce a result which differs from the above prescription of ray theory due to implementation errors such as neglecting phase shifts at caustics, failing to identify all possible eigenrays, or introducing false caustics. These practical implementation problems are discussed in subsequent sections.

A second complication is that production codes are often altered to produce smoothed transmission loss curves. These smoothing schemes are done in a variety of ways with the objective of producing more physically reasonable results. In the final analysis, one can end up with substantially different results depending on the particular ray code used.

Nevertheless, there are guide lines that at least indicate which types of problems are likely to be more difficult. An often-quoted rule is that the acoustic wavelength should be substantially smaller than any physical scale in the problem. That is, the wavelength should be small compared to the water depth, bathymetric features and internal features such as surface ducts. Often, improved results can be obtained by smoothing out such features before doing the ray tracing [20]. Simply pruning the sound-speed profile by throwing away sample points can improve both the accuracy and the run time.

## 3.5 Gaussian Beams

### 3.5.1 Gaussian Beams in Free Space

Frequently, one is interested in generating focused beams. A simple and useful approach to this uses a *complex source point* as introduced by Deschamps [21]. This will also enable us to discuss some interesting basic physics of beam propagation.

We recall first that the field due to a point source in free space is given by

$$p(\mathbf{x}) = \frac{e^{ik|\mathbf{x}-\mathbf{x}_0|}}{|\mathbf{x}-\mathbf{x}_0|}, \quad (3.80)$$

where  $\mathbf{x} = (x, z)$  is the field coordinate and we consider only slices of the field where  $y = 0$ . This is an exact solution to the Helmholtz equation for any arbitrary source coordinate  $\mathbf{x}_0$ . Without loss of generality, we pick  $\mathbf{x}_0 = (ia, 0)$  so that the  $x$ -coordinate of the source has been offset into the complex plane. Then,

$$|\mathbf{x} - \mathbf{x}_0| = \sqrt{(x - ia)^2 + z^2}. \quad (3.81)$$

This offset into the complex plan produces a beam with central ray on the  $x$ -axis. To see this we consider paraxial solutions, that is, solutions in the neighborhood of the axis of the beam. To be precise, we assume  $z \ll x$ . Then, making an implicit choice about the branch of the square root, we can use the approximation  $\sqrt{a + \epsilon} \approx \sqrt{a} + \epsilon/(2\sqrt{a})$  to get

$$|\mathbf{x} - \mathbf{x}_0| \approx (x - ia) + \frac{z^2}{2(x - ia)}, \quad (3.82)$$

which yields the pressure field

$$p(\mathbf{x}) \approx \frac{e^{ik(x-ia)}}{x - ia} e^{i\frac{k}{2}\frac{z^2}{x-ia}}, \quad (3.83)$$

where we have also taken a paraxial, farfield approximation to the denominator. This, in turn, can be rewritten as

$$p(\mathbf{x}) \approx \frac{e^{ka} e^{ikx}}{x - ia} e^{i\frac{k}{2} K z^2} e^{-(\tilde{W})^2}, \quad (3.84)$$

where,

$$K(x) = \frac{x}{x^2 + a^2}, \quad (3.85)$$

$$W(x) = \sqrt{\frac{2}{k} \left( a + \frac{x^2}{a} \right)}. \quad (3.86)$$

It is easy to see that  $W(x)$  corresponds to a beamwidth, which evolves along the axis  $x$  of the beam. (There are many definitions of beamwidth. If we define the width of the beam by the  $e^2$ -folding distance, then  $W(x)$  should properly be called a half beamwidth.) In addition, we can see that the phase fronts are defined by

$$x + \frac{Kz^2}{2} = \text{const} = x_0, \quad (3.87)$$

which, neglecting the variation in  $K(x)$ , are parabolas. One may verify that  $K$  is the curvature of those parabolic phase fronts. In summary, if we shift the source point into the complex plane, we generate a beam in the real plane that is approximately Gaussian. The curvature of the phase fronts and width of the beam are then given by (3.85) and (3.86). By shifting both components of  $\mathbf{x}_0$  into the complex plane we can generate a Gaussian beam propagating in an arbitrary direction.

This analysis shows the effect of a complex source point. However, in practice we should generally use the exact form given in (3.80), which has the advantage of being an exact beam solution to the Helmholtz equation. In Fig. 3.15, we have calculated the magnitude of this field for a homogeneous medium with a sound speed of 1500 m/s and for a frequency of 100 Hz. The offset  $a$  into the complex plane was chosen to be 200, 1000, 7000 in sequence. Further, to focus on the hyperbolic shape of the beam, we have removed the cylindrical spreading term.

For  $a = 200$  in the upper panel, the beam is narrow at the waist and therefore diverges rapidly. In the middle panel, we have increased the offset to  $a = 1000$ . The beam is wider at the beginning but diverges more slowly, and ends up with a smaller width at the end. In the lower panel, we have increased  $a$  further to 7000. The divergence angle is narrower; however, the beam started out broader and ends up having a larger width at the end, than in the middle panel. In summary, if we wish to control the size of the beam, there is an optimal offset, corresponding to an initial beamwidth.

Equation (3.86) shows explicitly what is going on. The beamwidth  $W(x)$  is a hyperbola. We can solve for the complex offset  $a$  so as to minimize  $W(x)$  at any given range. Differentiating  $W(x; a)$  with respect to  $a$  and setting the result to 0, we find that the optimal  $a$  to minimize the beamwidth is  $a = x$ . In the example above, the maximum range was 1000 m so  $a = 1000$  minimizes the spot size at that range as indicated in the middle panel. The beamwidth at the origin corresponding to any particular  $a$  is  $W(0; a) = \sqrt{2a/k}$  or about 70 m in this case. This analysis assumes the beam waist is at the origin.

### 3.5.2 Gaussian Beam Tracing

As discussed in Sect. 3.3.5, there have been a number of informal attempts to smooth the ray-tracing results by taking into account the inherent variation of the

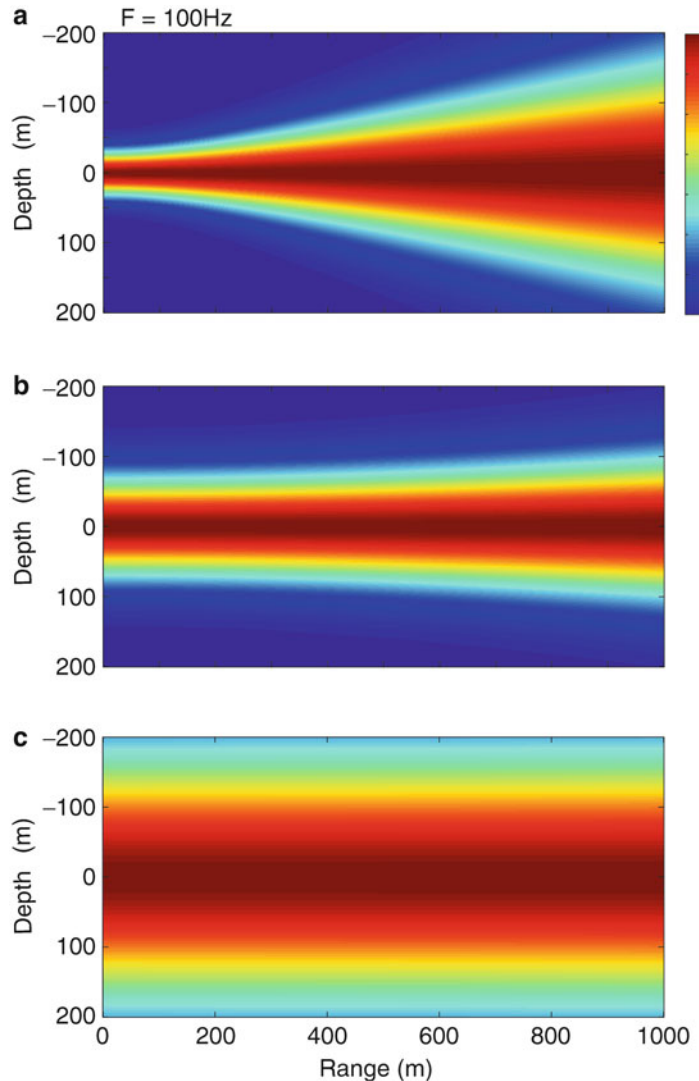


**Fig. 3.15** Propagation of a Gaussian beam in free space, generated by the complex source point method and for (a)  $a = 200$ , (b)  $a = 1000$ , and (c)  $a = 7000$ . The middle panel uses the optimal initial beamwidth that minimizes the spot size at the maximum range of 1000 m

medium, thus achieving an answer which more closely resembles reality. One popular approach is based on the idea that a ray should be considered a statistically varying curve with Gaussian statistics. This leads informally to associating a Gaussian intensity distribution with each ray. The ray then becomes the central ray of a Gaussian beam.

These “fuzzy” rays provide a smoother transition into a shadow zone and through a caustic—a result which is more consistent with that of full wave models. An unsatisfying aspect of this approach is that some recipe must be concocted for specifying the width of the Gaussian.

Porter and Bucker introduced a more formal Gaussian beam tracing technique based on work in the seismic community principally by Červený and co-workers (see [22, 23] and references therein). Here, the Gaussian beam is given an initial beamwidth and curvature at the source point, but is allowed to expand and contract or change curvature as it propagates away from the source. The evolution of the beam is governed by the quantities  $p$  and  $q$  which we have already seen in the context of dynamic ray tracing.

Formally, the method is derived by constructing a solution in the neighborhood of the central ray which in an asymptotic sense governs the behavior of a beam. The final equation for the beam is then given by

$$p^{\text{beam}}(s, n) = A \sqrt{\frac{c(s)}{rq(s)}} \exp \left\{ -i\omega \left[ \tau(s) + \frac{p(s)}{2q(s)} n^2 \right] \right\}, \quad (3.88)$$

where  $A$  is an arbitrary constant,  $n$  is the normal distance from the central ray, and  $\tau(s)$  is the phase delay along the ray.

In order for the above equation to have the form of a beam, with energy concentrated about the central ray,  $p$  and  $q$  are chosen to be complex. Then, the real and imaginary parts of  $p/q$  may be related to beamwidth  $W$  and curvature  $K$  via

$$W(s) = \sqrt{\frac{-2}{\omega \operatorname{Im}[p(s)/q(s)]}}, \quad (3.89)$$

$$K(s) = -c(s) \operatorname{Re}[p(s)/q(s)]. \quad (3.90)$$

Thus, the dynamic ray equations are simply solved with complex initial conditions representing an initial beamwidth and curvature. The optimal choice of these initial conditions is a matter of current research. However, the discussion in the previous section provides some useful intuition. Typically the initial beam curvature  $K(0)$  is set to zero. Then the initial beamwidth should be chosen so that the beams are not large compared to the water depth, but not so small that the beams diverge rapidly and become large compared to the water depth in the farfield. Typically, this will lead to an initial beamwidth of 10–50 wavelengths. In summary, the initial conditions for  $p$  and  $q$  are:

$$p(0) = 1, \quad q(0) = i\omega W^2(0)/2. \quad (3.91)$$

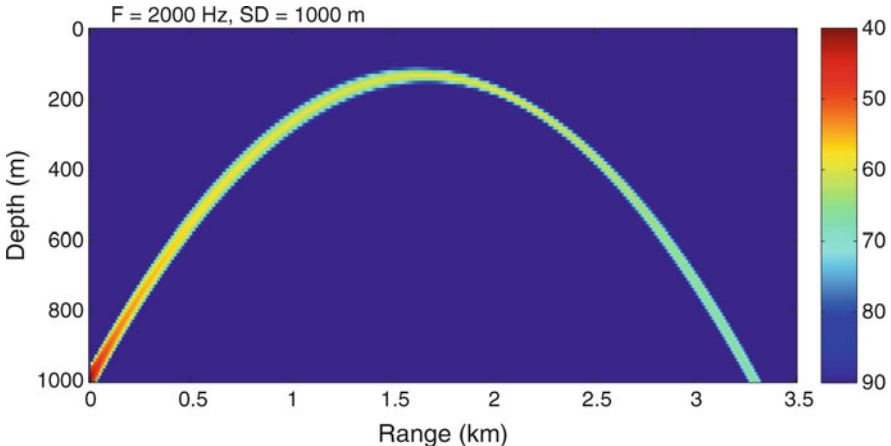


**Fig. 3.16** Propagation of a Gaussian beam for the  $n^2$ -linear profile

As an example of this type of calculation, we return to the  $n^2$ -linear problem (deep source) considered in Sect. 3.4. A plot of the intensity of a *single beam* is given in Fig. 3.16. The beam is associated with a central ray which refracts under the influence of the refractive profile. The beamwidth is also seen to vary along the ray. The phase fronts of the beam are hidden in an intensity plot like this, however, the curvature of the phase fronts also varies along the ray.

The final step is the summing up of all of the beams to obtain the complex pressure. The weightings of the beams are determined by considering a canonical problem of a point source in a homogeneous medium. The appropriate weighting of the beams for a point source is

$$A(\theta_0) = \delta\theta_0 \frac{1}{c_0} \sqrt{\frac{q(0) \omega \cos \theta_0}{2\pi}} e^{i\pi/4}, \quad (3.92)$$

where  $\delta\theta_0$  is the angular spacing between beams. The resulting transmission loss for the  $n^2$ -linear profile is shown in Fig. 3.17. Notice that the caustic spike which occurred with standard ray tracing is no longer present, the sharp fall-off into the shadow zone is more gradual, and the agreement with the exact solution is now very close. A more detailed description of Gaussian beam tracing is given in [23].

The above described technique is very appealing in that it is based on the physics of a true propagating beam. However, at lower frequencies the physics may imply that the beam is large compared to the channel, which causes a variety of problems. The geometric beams described in Sect. 3.3.5 have generally proven to be more satisfactory.

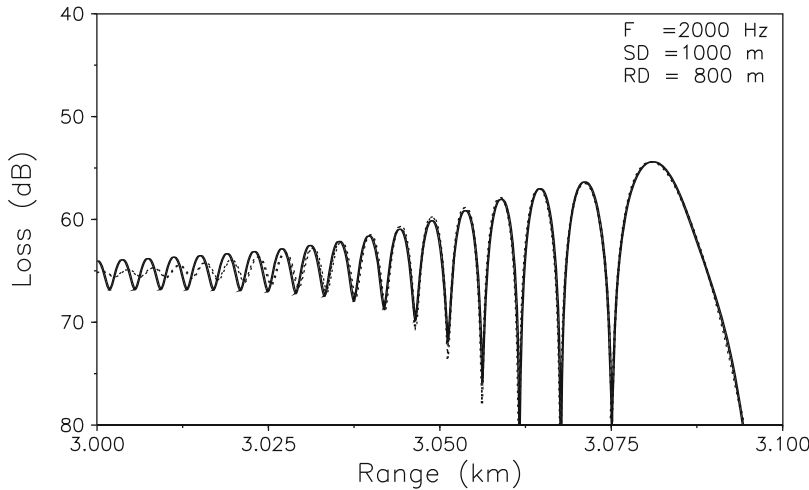


**Fig. 3.17** Transmission loss for the  $n^2$ -linear profile with a deep source. *Solid curve:* Exact solution. *Dashed curve:* Gaussian beam theory

## 3.6 Additional Mathematical Properties

### 3.6.1 Alternate Forms of the Ray Equations

We have derived the ray equations using arclength as the independent variable. The equations are also often written using range or depth as independent variables or with the arclength scaled in various ways. Below we present some of the more useful forms.

#### 3.6.1.1 $\sigma$ -Form

The  $\sigma$ -form is obtained by parameterizing the rays by a scaled arclength. As discussed earlier the ray equations can be conveniently parameterized by any quantity which varies monotonically along the ray. The particular form we consider here will turn out to be convenient for considering problems in which the square index of refraction varies linearly. To derive this form we introduce the parameter  $\sigma$  related to arclength via

$$\frac{ds}{d\sigma} = n, \quad (3.93)$$

where  $n = c_0/c$  is the index of refraction. The ray equations become

$$\frac{dr}{d\sigma} = \xi(s), \quad \frac{d\xi}{d\sigma} = nn_r, \quad (3.94)$$

$$\frac{dz}{d\sigma} = \zeta(s), \quad \frac{d\zeta}{d\sigma} = nn_z, \quad (3.95)$$

or, equivalently,

$$\frac{d^2\mathbf{x}}{d\sigma^2} = \frac{1}{2}\nabla(n^2). \quad (3.96)$$

The phase equation then becomes

$$\tau(\sigma) = \tau(\sigma_0) + \frac{1}{c_0} \int_{\sigma_0}^{\sigma} n^2(\sigma') d\sigma'. \quad (3.97)$$

### 3.6.1.2 $z(r)$ and $r(z)$ Forms

To obtain equations with  $r$  as the independent variable, we divide the equation for  $dr/ds$  into the other equations in (3.23) and (3.24). This yields

$$\frac{dz}{dr} = \frac{\zeta}{\xi}, \quad (3.98)$$

$$\frac{d\xi}{dr} = -\frac{c_r}{\xi c^3}, \quad (3.99)$$

$$\frac{d\zeta}{dr} = -\frac{c_z}{\xi c^3}. \quad (3.100)$$

With some manipulations, this third-order ODE can be reduced to a second order ODE. We differentiate the first equation with respect to  $r$  to obtain

$$\frac{d^2z}{dr^2} = \frac{\zeta_r \xi - \zeta \xi_r}{\xi^2}. \quad (3.101)$$

Then, using (3.99) and (3.100) to eliminate  $\zeta_r$  and  $\xi_r$  yields

$$\frac{d^2z}{dr^2} = \frac{-c_z + (\zeta/\xi)c_r}{\xi^2 c^3}. \quad (3.102)$$

From (3.98)  $\zeta/\xi = dz/dr$ . In addition,

$$\begin{aligned} \xi^2 &= \frac{1}{c^2} \left( \frac{dr}{ds} \right)^2 = \frac{1}{c^2} \frac{(dr)^2}{(dr)^2 + (dz)^2} \\ &= \frac{1}{c^2} \frac{1}{1 + (dz/dr)^2}. \end{aligned} \quad (3.103)$$

Substituting these results into (3.102) yields

$$\frac{d^2z}{dr^2} = \left[ 1 + \left( \frac{dz}{dr} \right)^2 \right] \left[ -\frac{c_z}{c} + \left( \frac{dz}{dr} \right) \frac{c_r}{c} \right]. \quad (3.104)$$

An analogous procedure (exchanging the roles of  $z$  and  $r$ ) yields the following differential equation for the ray range  $r$  as a function of depth  $z$ ,

$$\frac{d^2r}{dz^2} = \left[ 1 + \left( \frac{dr}{dz} \right)^2 \right] \left[ -\frac{c_r}{c} + \left( \frac{dr}{dz} \right) \frac{c_z}{c} \right]. \quad (3.105)$$

### 3.6.2 Treatment of Attenuation

As discussed in Chap. 1, volume attenuation can be included by simply adding an imaginary part to the sound speed. One way of motivating this process is to seek a particular decay rate for a plane wave propagating in an inhomogeneous medium. Here, we will essentially reverse those steps, taking the problem as defined in terms of a complex sound speed and seeing how the ray result is modified.

With a complex sound speed, rays with real take-off angles assume trajectories which are complex, that is, not confined to the real  $rz$ -plane. This makes the problem of finding eigenrays more complicated. In practice, it is seldom necessary to go through the complicated process of complex ray tracing to include attenuation. Instead one can simply neglect the imaginary part of the sound speed, trace the real rays and add a loss corresponding to the path length of the real rays. Let us see formally how this physically intuitive result derives from perturbation theory.

Recall that the eikonal equation reads,

$$c^2(\mathbf{x}) |\nabla \tau|^2 = 1. \quad (3.106)$$

We next write the perturbed sound speed as

$$c = c_0 + \epsilon c_1 + \dots \quad (3.107)$$

and seek a solution in the form

$$\tau = \tau_0 + \epsilon \tau_1 + \dots \quad (3.108)$$

The  $O(1)$  term is just the usual eikonal equation,

$$|\nabla \tau_0|^2 = \frac{1}{c_0^2(\mathbf{x})}, \quad (3.109)$$

which we solve using rays as described previously. The unperturbed problem has a purely real index of refraction and so the rays with real take-off angles stay in the real plane.

The  $O(\epsilon)$  term is

$$c_0^2(\nabla \tau_0) \cdot (\nabla \tau_1) + c_0 c_1 |\nabla \tau_0|^2 = 0. \quad (3.110)$$

From the definition of the ray paths given in (3.16) we can write this as

$$\left( \frac{d\mathbf{x}}{ds} \right) \cdot (\nabla \tau_1) = -\frac{c_1}{c_0^2}, \quad (3.111)$$

or

$$\frac{d\tau_1}{ds} = -\frac{c_1(s)}{c_0^2(s)}. \quad (3.112)$$

This is immediately solved to yield

$$\tau_1(s) = - \int_0^s \frac{c_1(s')}{c_0^2(s')} ds'. \quad (3.113)$$

Now, suppose the perturbation is due to a loss  $\alpha$  given in nepers/m. As we have seen in Chap. 1 this introduces an imaginary part to the sound speed given by

$$ic_i \simeq -i\alpha \frac{|c_r|}{\omega}. \quad (3.114)$$

Substituting this into (3.113) yields

$$\tau_1(s) = i \int_0^s \frac{\alpha(s')}{\omega} ds'. \quad (3.115)$$

Next, by introducing this additional phase factor into our representation of the pressure, (3.57), we obtain

$$p(s) = \frac{1}{4\pi} \left| \frac{c(s) \cos \theta_0}{c(0) J(s)} \right|^{1/2} e^{i\omega \int_0^s \frac{1}{c(s')} ds'} e^{-\int_0^s \alpha(s') ds'}. \quad (3.116)$$

If  $\alpha$  is a constant, then this gives a loss proportional to the path length times the loss per meter.

Losses can result from either volume attenuation or loss due to bottom or surface reflection. For rays that strike the boundaries, the volume attenuation is usually small compared to the reflection loss and can therefore be neglected. For purely refracted paths the volume attenuation can be important, but such paths typically propagate at very narrow angles so that the above loss integral is about the same for each path. The loss can then be included by simply adding to the transmission loss a term of the form  $\alpha r$  where  $\alpha$  is the attenuation in dB/km and  $r$  is the range. This approximation is used in many ray models.

### 3.6.3 Interfaces and Boundaries

When a ray strikes the ocean bottom it splits its energy into a reflected and a transmitted ray as illustrated in Fig. 3.18. The transmitted ray may then interact with a

**Fig. 3.18** Reflection and transmission at a fluid–fluid interface

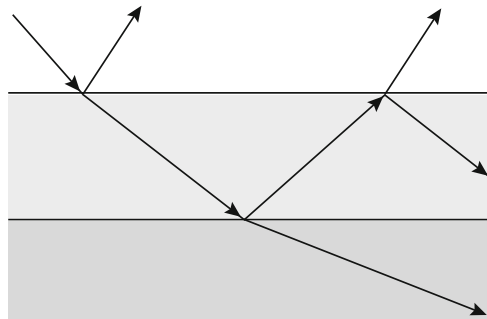
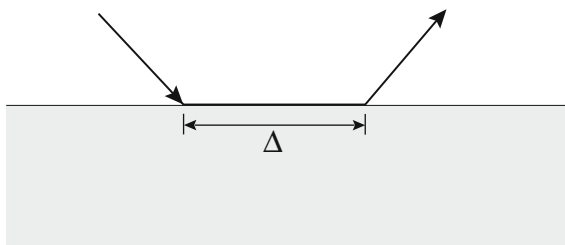


**Fig. 3.19** Ray displacement at fluid–fluid interfaces



still deeper interface in the sediment or be refracted back to the ocean bottom and generate yet another pair of rays. Thus, a single ray leads to a cascade of rays after hitting a sequence of interfaces.

While it is possible to keep track of all the newly generated rays [24], most ray codes treat the bottom simply as a reflector ignoring the transmitted ray and its subsequent splittings. Furthermore, the amplitude of the reflected ray is often calculated by reading in a user-supplied reflection coefficient tabulated at particular angles. The phase of the ray may also be changed in accordance with the phase of the (complex) reflection coefficient.

Treating bottom reflection in this way is somewhat informal, however, the resulting inaccuracies are consistent with the intended application of the model. For instance, transmission-loss modeling may often begin with a bottom characterized as mud, sand, or rock. This type of bottom description allows for a fair amount of variation in geoacoustic parameters (see Sect. 1.6) so it makes little sense to calculate the details of the phase of bottom-reflected energy.

If a detailed geoacoustic model of the bottom is available, then the amplitude and phase of the reflected wave can be calculated based on the plane-wave reflection and transmission coefficients discussed in Chap. 1. However, even this is an approximation since the incoming field is not, in general, a plane wave. Further corrections take into account the curvature of the wavefront and also the curvature of the interface as discussed by Bleistein [9]. Tindle and Bold [25] provide persuasive evidence that improved accuracy is obtained by displacing the reflected ray upon reflection as illustrated in Fig. 3.19. Similarly, Murphy and Davis [26] showed that such displacements should be included when the ray turns close to a boundary. The ray displacement concept was dealt with in some detail in Sect. 2.4.3.

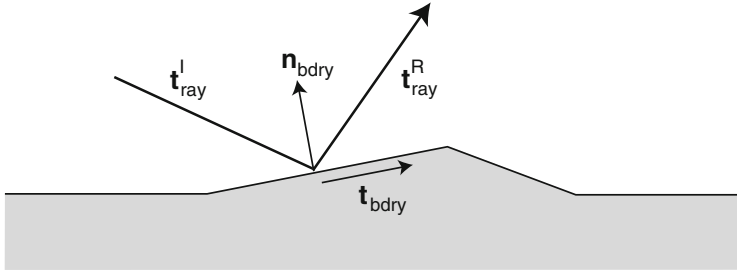


**Fig. 3.20** Ray reflecting from a piecewise linear boundary

As with the ocean sound-speed profile, the details of how the boundaries and interfaces are interpolated are important in terms of both the efficiency and the accuracy of the overall method. A very simple approach is to use piecewise linear interpolation, leading to a faceted model of the boundary. For instance, an idealized model of a seamount might be represented as shown in Fig. 3.20. The analysis in Sect. 1.6.1 showed us that a ray (associated with a plane wave) has an angle of reflection equal to its angle of incidence. To express this in a compact vector notation, we denote ray tangents for the incident and reflected rays by  $\mathbf{t}_{\text{ray}}^I$  and  $\mathbf{t}_{\text{ray}}^R$ , respectively. In addition, we denote unit tangents and normals to the boundary by  $\mathbf{t}_{\text{bdry}}$  and  $\mathbf{n}_{\text{bdry}}$ . These are easily pre-computed from the nodal coordinates defining the faceted boundary. The tangent and normal have an arbitrary sign. To eliminate this ambiguity, we chose an inward pointing normal and pick the sign of the tangent so that  $(\mathbf{t}_{\text{bdry}}, \mathbf{n}_{\text{bdry}}, \mathbf{y})$  is a right-handed coordinate system.

We can then represent the incident ray as a combination of components parallel and perpendicular to the boundary:

$$\mathbf{t}_{\text{ray}}^I = \alpha \mathbf{n}_{\text{bdry}} + \beta \mathbf{t}_{\text{bdry}}, \quad (3.117)$$

where,

$$\alpha = \mathbf{t}_{\text{ray}}^I \cdot \mathbf{n}_{\text{bdry}}, \quad (3.118)$$

$$\beta = \mathbf{t}_{\text{ray}}^I \cdot \mathbf{t}_{\text{bdry}}. \quad (3.119)$$

From the geometry in Fig. 3.20, it is easy to see that the reflected ray maintains the same component parallel to the boundary; however, the perpendicular component is negated. Thus,

$$\mathbf{t}_{\text{ray}}^R = -\alpha \mathbf{n}_{\text{bdry}} + \beta \mathbf{t}_{\text{bdry}}, \quad (3.120)$$

which may be written in terms of the tangent of the incident ray as:

$$\mathbf{t}_{\text{ray}}^R = \mathbf{t}_{\text{ray}}^I - 2\alpha \mathbf{n}_{\text{bdry}}. \quad (3.121)$$

To complete the specification of the reflection process, we must also know how to continue the dynamic ray equations. The result follows from a phase matching across the interface as described in [27, 28]:

$$p^R = p^I + q^I N, \quad q^R = q^I, \quad (3.122)$$

where

$$N = \pm \frac{2\kappa}{\alpha c^2} + M(4c_n - 2Mc_s)/c^2, \quad M = \beta/\alpha \quad (3.123)$$

and  $\kappa$  is the boundary curvature, which vanishes here for the case of a piecewise linear boundary. The plus sign is used for bottom reflection, and the minus sign for top reflection. Further, the normal and tangential derivatives of the sound speed are calculated in terms of the derivatives in Cartesian coordinates using a directional derivative,

$$c_n = \nabla c \cdot \mathbf{n}_{\text{ray}}, \quad c_s = \nabla c \cdot \mathbf{t}_{\text{ray}}, \quad (3.124)$$

where the unit tangent and normal to the ray are given by (3.25) and (3.26). Since  $q$  is associated with amplitude, we may interpret these equations as implying that there is no change of energy on reflection, but there is a change in wavefront curvature.

Typically, there is a boundary reflection loss provided in tabular form or derived from simple formulas, e.g. for an acoustic halfspace. The boundary reflection formula may represent true losses due to scatter or apparent losses due to partial coherence of the reflected field. We denote this complex reflection coefficient by  $\mathcal{R}(\theta_0)$ , where  $\theta_0$  is an angle of incidence. Given the generality of mechanisms, it is convenient to track such losses in extra variables  $A(s), \phi(s)$  providing the amplitude and phase of such cumulated losses as a function of arc length along the ray. At the ray origin we select  $A(0), \phi(0) = 1, 0$ , i.e., unit amplitude and zero phase. These variables do not change along a ray, until the ray interacts with a boundary, at which point they are corrected by the amplitude and phase change at the boundary,

$$A^R = |\mathcal{R}(\theta_0)| A^I, \quad \phi^R = \phi^I + \arg[\mathcal{R}(\theta_0)]. \quad (3.125)$$

Thus, considering all the parameters characterizing the ray, we may summarize the ray reflection process as follows:

$$\begin{aligned} \mathbf{x}^R &= \mathbf{x}^I, \\ \mathbf{t}^R &= \mathbf{t}^I - 2\alpha \mathbf{n}_{\text{bdry}}, \\ \tau^R &= \tau^I, \\ A^R &= |\mathcal{R}(\theta_0)| A^I, \\ \phi^R &= \phi^I + \arg[\mathcal{R}(\theta_0)]. \end{aligned} \quad (3.126)$$

For efficiency, one may elect at this stage to terminate the tracing of a particular ray based on the number of boundary interactions or an amplitude threshold.

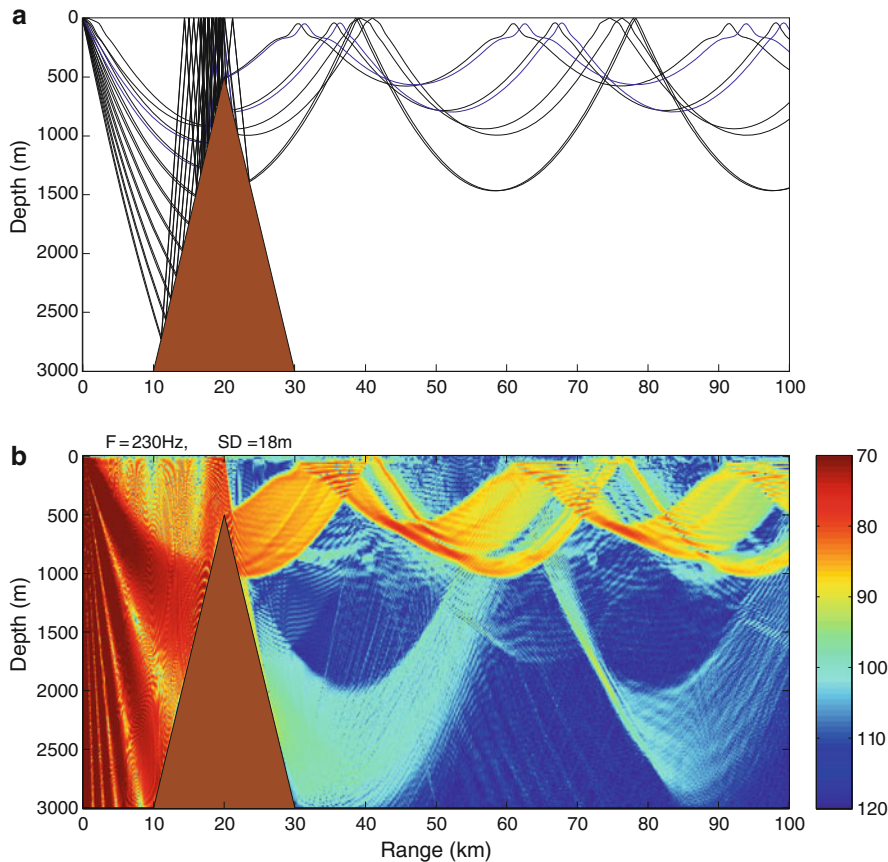


**Fig. 3.21** Propagation across the Dickins seamount. (a) Ray trace for source at 18-m depth and (b) transmission loss at 230 Hz

As an example, we consider propagation over a seamount with a source depth of 18 m. The ray trace in Fig. 3.21a clearly shows the rays becoming steeper as they reflect from the face of the seamount, then more horizontal as they reflect off the back. The associated transmission loss for a source frequency of 230 Hz is shown in Fig. 3.21b. This ray theoretic result compares well with the parabolic equation result in Sect. 6.9.3.

Another interesting test case for boundary interactions is the parabolic bottom profile described by McGirr et al. [29] in their evaluation of range-dependent ray theory models. (It is notable that this 1985 report concluded that none of the Navy's then standard ray models tested were capable of producing both satisfactory ray traces and intensities.) The specific parabolic bottom profile is

$$z = 0.002 b \sqrt{1 + r/c}, \quad (3.127)$$

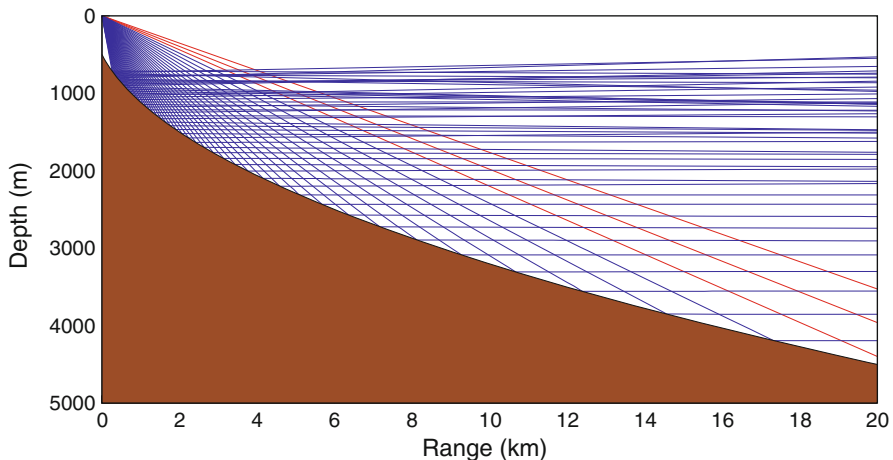


**Fig. 3.22** Ray reflecting from a piecewise linear boundary

with  $b = 250000$  and  $c = 250$ . Ranges  $r$  and depths  $z$  are given in meters. With these parameters a source at the origin is at the focal point, so the bottom-reflected rays should, ideally, emerge parallel to the surface, much as the reflector in a flashlight produces a uniform beam. As we go out to 20 km in range, the position of the rays is extremely sensitive to the tilt of the bottom facets, and therefore an interesting metric on how well the bathymetry interpolation works. With the bathymetry sampled every 25 m in depth, we derive the ray trace shown in Fig. 3.22. The flaws are obviously revealed in the irregular ray structure.

It should be noted that this result is not intrinsically wrong. The ray model has no way of knowing how the user intended to interpolate the bathymetry. In the Dickins seamount we really wanted the piecewise linear model. In this parabolic bottom case, we really intended a smoother quadratic fit between bathymetry points, rather than the faceted option. In any case, to accommodate both needs one must offer a smoother interpolation option.

Splines have often been proposed as an improvement. They produce smoother interpolates; however, in the quest to provide a smooth solution, splines often wiggle to extremes, causing their own artifacts. Splines under tension (T-Splines) have been used with greater success (Bucker [13], Foreman [30]). However, it becomes increasingly difficult to locate the intercept of the ray with the boundary as one becomes more sophisticated in the boundary interpolation. We present one particularly simple option. Clearly, to get the rays to reflect in a more uniform fashion, one requires a more accurate estimate of the bottom normal. Thus, we linearly interpolate the boundary normals to calculate the angle at which the ray reflects. This approach is illustrated in Fig. 3.23. Even though the normals vary in a smooth way along the boundary, we can still maintain the simplicity of using the piecewise linear boundary interpolation to determine the ray reflection point. However, the boundary curvature

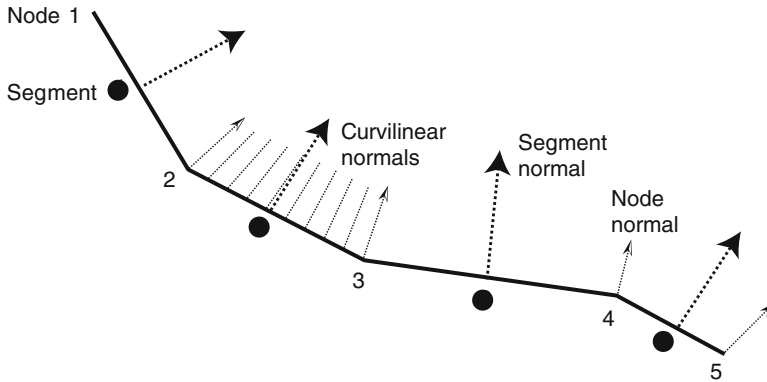


**Fig. 3.23** Curvilinear boundary interpolation: Segment normals derived directly from the facet model; Node normals interpolated from neighboring segment normals; Curvilinear normals interpolated from node normals

term in (3.123) must be included to correctly track the ray intensity. The boundary curvature is just the rate of change of the angle  $\phi$  of the normals:

$$\kappa = d\phi/ds, \quad (3.128)$$

which may also be pre-calculated for each segment.

As shown in the upper panel of Fig. 3.24, this improved boundary interpolation provides a set of perfectly (as far as the eye can see) parallel rays, as expected. A final check is performed by looking at the intensity (or transmission loss) as shown in the lower panel of Fig. 3.24. We see the desired smooth pattern in the Gaussian beam tracing result.

### 3.6.4 Weak Interfaces and Ocean Sound-Speed Discontinuities

Section 3.7.4 discusses various options for interpolating ocean sound-speed profiles. Within the ocean volume, these interpolating functions are normally continuous; however, they often have weak interfaces where the derivative has a discontinuity. For instance, this occurs when a piecewise-linear approximation is used. Changes in the beam curvature occur on crossing such interfaces. The formula for boundary reflection in (3.123) is essentially just a special case of such interface formulas. For ocean sound-speed profiles the interfaces are usually flat so that the curvature term disappears. One then applies a phase matching across the interface as described in [27, 28], yielding:

$$p^T = p^I + q^I N, \quad q^T = q^I, \quad (3.129)$$

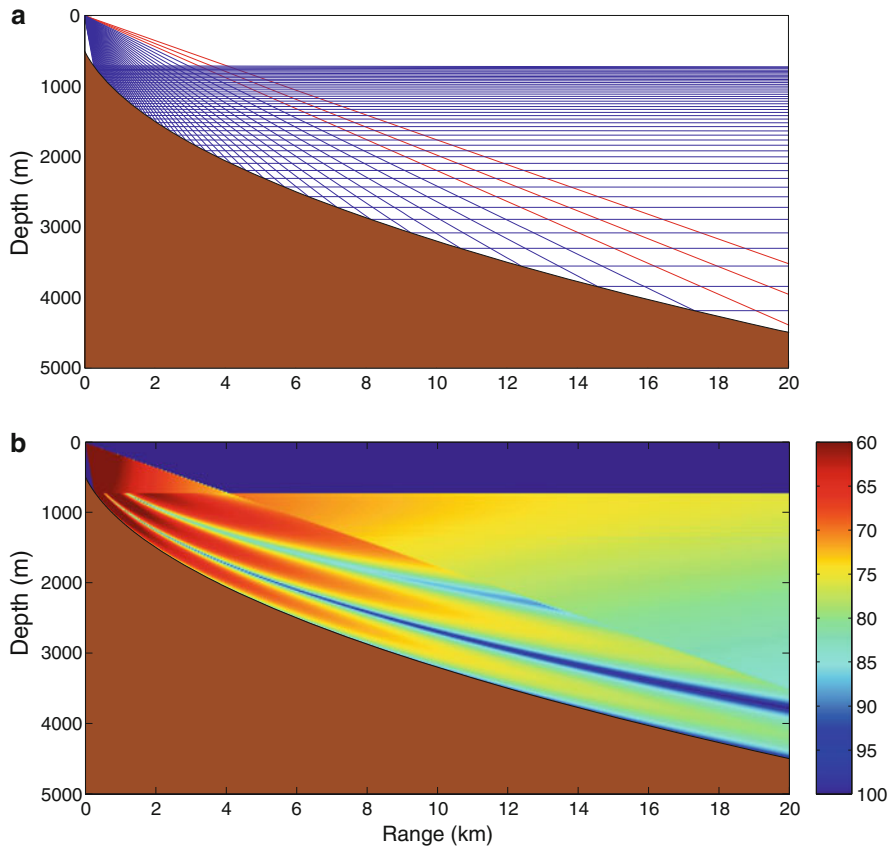


**Fig. 3.24** Curvilinear boundary interpolation for the parabolic bathymetry profile. (a) Ray trace and (b) transmission loss

where

$$N = -M(2[c_n] - M[c_s])/c^2, \quad M = \beta/\alpha \quad (3.130)$$

and  $[c_n]$ ,  $[c_s]$  are the jumps in normal and tangential derivatives of the sound speed across the interface, and  $\alpha$ ,  $\beta$  are given by (3.118) and (3.119). In addition,  $p^I$  and  $p^T$  denote values of  $p$  and  $q$  for the incident and transmitted waves, i.e., on either side of the weak interface.

### 3.6.5 Fermat's Principle

Fermat's principle states that the travel time for a ray path is stationary. This is often referred to in a less precise fashion as the principle of least travel time. Sometimes this is taken as a definition of the ray paths and their differential equations are derived from this principle. Let us see how this is carried out.

The travel time along a curve from a point  $x_0$  to another point  $x_1$  is given by

$$\tau = \int_{x_0}^{x_1} \frac{1}{c(s)} ds. \quad (3.131)$$

Since  $|dx(s)/ds|^2 = 1$  we can write this as

$$\tau = \int_{x_0}^{x_1} \frac{\sqrt{x_0^2 + y_0^2 + z_0^2}}{c(s)} ds. \quad (3.132)$$

This is now in the form of a variational problem,

$$S\{y\} = \int_{x_0}^{x_1} L(y, y', x) dx, \quad (3.133)$$

which is made stationary when  $L$  satisfies the Euler–Lagrange equations,

$$\frac{\partial L}{\partial y} - \frac{d}{dx} \left( \frac{\partial L}{\partial y'} \right) = 0. \quad (3.134)$$

This variational result is discussed in standard texts such as [31]. Thus, the travel time is stationary provided that

$$\frac{d}{ds} \left( \frac{1}{c} \frac{dx}{ds} \right) + \frac{1}{c^2} \frac{\partial c}{\partial x} = 0, \quad (3.135)$$

$$\frac{d}{ds} \left( \frac{1}{c} \frac{dy}{ds} \right) + \frac{1}{c^2} \frac{\partial c}{\partial y} = 0, \quad (3.136)$$

$$\frac{d}{ds} \left( \frac{1}{c} \frac{dz}{ds} \right) + \frac{1}{c^2} \frac{\partial c}{\partial z} = 0. \quad (3.137)$$

These are, of course, the usual differential equations for the rays.

### 3.6.6 Simplifications for Stratified Media

The above forms of the ray equations are all suitable for treating fully 2-D varying environments. An important special case is when the medium is horizontally stratified. We first consider the  $z(r)$  form, (3.104), which now reduces to

$$\frac{d^2 z}{dr^2} = - \left[ 1 + \left( \frac{dz}{dr} \right)^2 \right] \frac{c_z}{c}, \quad (3.138)$$

or

$$\frac{d}{dr} \left[ c \frac{dz}{dr} \right] - c_z = 0. \quad (3.139)$$

We next turn to the  $r(z)$  form. Equation (3.105) reduces to

$$\frac{d^2r}{dz^2} = \frac{dr}{dz} \frac{c_z}{c} \left[ 1 + \left( \frac{dr}{dz} \right)^2 \right], \quad (3.140)$$

which can be rearranged as

$$\frac{m'}{(1+m^2)m} = \frac{c_z}{c}, \quad (3.141)$$

where  $m(z) = dr/dz$ . This, in turn, can be written as

$$\frac{m'}{m} - \frac{mm'}{1+m^2} = \frac{c_z}{c}, \quad (3.142)$$

which is immediately integrated to give

$$\frac{m}{\sqrt{1+m^2}} = ac, \quad (3.143)$$

where  $a$  is an arbitrary constant of integration. Solving for  $m$  we obtain

$$m = \frac{ac}{\sqrt{1-a^2c^2}}. \quad (3.144)$$

Since  $m(z) = dr/dz$  we can integrate the above expression with respect to  $z$  to obtain:

$$r(z) = r(z_0) + \int_{z_0}^z \frac{ac}{\sqrt{1-a^2c^2}} dz'. \quad (3.145)$$

The phase equation has a similar representation as an integral with respect to  $z$ . We observe that

$$ds = \sqrt{(dr)^2 + (dz)^2} = dz \sqrt{1 + \left( \frac{dr}{dz} \right)^2}. \quad (3.146)$$

Then, using the expression for  $dr/dz$  given in (3.144) we obtain

$$ds = \frac{1}{\sqrt{1-a^2c^2}} dz. \quad (3.147)$$

Thus, the phase equation

$$\tau(s) = \tau(0) + \int_0^s \frac{1}{c(s')} ds' \quad (3.148)$$

becomes

$$\tau(z) = \tau(z_0) + \int_{z_0}^z \frac{1}{c(z') \sqrt{1 - a^2 c^2(z')}} dz'. \quad (3.149)$$

### 3.6.7 Snell's Law

Snell's law provides a simple formula for calculating the ray declination angle at any depth  $z$  based only on the declination angle at any other depth and a knowledge of the sound-speed profile. The result is

$$c(z_0) \cos \theta(z) = c(z) \cos \theta(z_0), \quad (3.150)$$

or equivalently,

$$n(z) \cos \theta(z) = n(z_0) \cos \theta(z_0). \quad (3.151)$$

In other words,  $n(z) \cos \theta(z)$  is a constant along the ray path.

A common use of Snell's law is to find the steepest angle  $\theta_0$  for which a ray emanating from the source would be turned just before striking the bottom as indicated in Fig. 3.25. Rays with steeper take-off angles will interact with the bottom and hence lose energy at every bounce. Thus, for a long-range calculation they might be discarded at the start. For this grazing ray, we want  $\cos \theta(D) = 1$  where  $D$  is the depth of the ocean bottom. Solving for the ray take-off angle we find,

$$\theta(z_0) = \arccos \left[ \frac{c(z_0)}{c(D)} \right]. \quad (3.152)$$

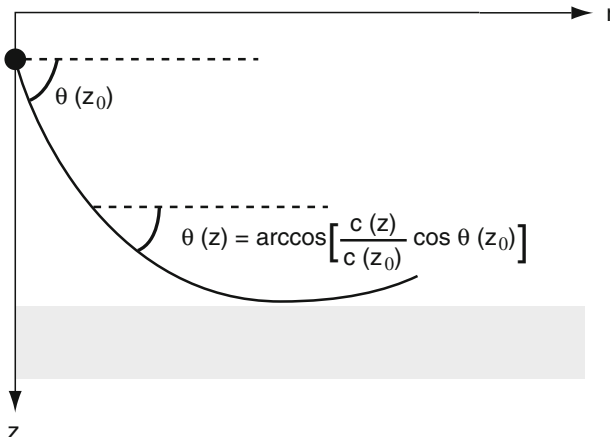


**Fig. 3.25** Snell's law and the calculation of the grazing ray

Of course, if the ray encounters a region where  $c(z)$  is greater than the sound speed at the bottom, the ray will be turned in that region and will not graze the bottom. On the other hand, if the sound speed at the bottom is lower than the sound speed at the source, then all rays (with real take-off angles) will strike the bottom.

Snell's law can be derived quite easily using the equations for ray paths in a range-independent medium. Recall from (3.143) that

$$\frac{m}{\sqrt{1+m^2}} = ac, \quad (3.153)$$

where  $m = dr/dz$ , i.e., the slope of the ray. Substituting  $m = \cot \theta_0$ , we obtain

$$\cos \theta_0 = a c(z), \quad (3.154)$$

where  $a$  is a constant. More generally, Snell's law holds in range-independent media even with discontinuities in the sound speed.

### 3.6.8 Reciprocity

As we saw in Sect. 2.4.5, the wave equation has the interesting property of reciprocity, meaning that if we exchange the positions of the source and a receiver in a given environment, the received field is unchanged. (The field in between the source and receiver is, in general, different.) Since ray theory provides only an approximate solution, it is not obvious whether reciprocity will be preserved.

It is clear that the eigenray connecting source and receiver is an eigenray regardless of which ends correspond to the source and the receiver. Similarly, the travel time integral is clearly independent of the direction of integration along the ray. Therefore, to validate reciprocity we need only verify that the ray amplitude is independent regardless of the direction of integration along the ray. As a notational convenience, let us consider the source and receiver to lie at arclengths  $s_1$  and  $s_2$ , respectively. Furthermore, we recall that the amplitude is derived from the dynamic ray equations, which can be written in second order form as

$$\mathcal{L}q = \left(\frac{q'}{c}\right)' + \frac{c_{nm}}{c^2(s)} q(s) = 0, \quad (3.155)$$

$$q(s_1) = 0, \quad (3.156)$$

$$q'(s_1) = \frac{1}{c(s_1)}. \quad (3.157)$$

Given any two linearly independent solutions of the differential equation  $q_1(s)$  and  $q_2(s)$ , we seek to satisfy the initial conditions as a linear combination  $q(s) = A q_1(s) + B q_2(s)$ . Solving for the unknown coefficients one finds

$$q(s) = \frac{q_1(s_1) q_2(s) - q_2(s_1) q_1(s)}{W(s_1)/c(s_1)}, \quad (3.158)$$

where  $W(s)$  is the Wronskian of the two independent solutions,

$$W(s) = q_1(s)q'_2(s) - q_2(s)q'_1(s). \quad (3.159)$$

One may verify by inspection that  $q(s)$  so constructed, satisfies the initial conditions. Now we wish to point out that  $W(s)/c(s)$  is a constant, i.e., that its derivative vanishes. This is verified by simply differentiating the above equation:

$$\begin{aligned} \left( \frac{W(s)}{c(s)} \right)' &= \left( \frac{q_1 q'_2 - q_2 q'_1}{c} \right)' \\ &= q_1 \left( \frac{q'_2}{c} \right)' - q_2 \left( \frac{q'_1}{c} \right)' \\ &= q_1 \mathcal{L} q_2 - q_2 \mathcal{L} q_1 \\ &= 0. \end{aligned} \quad (3.160)$$

Thus we see the pivotal result that we have a symmetry in exchanging source and receiver, that is,  $q(s_2; s_1) = q(s_1; s_2)$ . Said another way, the spreading function  $q$  at  $s_2$  due to a source at  $s_1$  is the same as the field at  $s_1$  due to a source at  $s_2$ . This symmetry of the spreading function is the desired property of reciprocity.

### 3.7 Numerical Solution

Among existing codes there are two principal techniques which are used for solving the ray equations. In the first class, the ray equations are integrated using standard numerical integrators such as the Runge–Kutta method. Off-the-shelf codes are not quite sufficient, however, since provision must be made for boundary interactions. Furthermore, the ocean sound-speed profile is often provided at discretely sampled points in depth (and range) and careful thought must be given to the problem of interpolating this data. For lack of a better term, we refer to the above solution techniques as *direct integration*.

In the second class, the domain of the problem is divided into subdomains, typically triangles. Within each triangle the sound speed is fitted by some simple form for which an analytic solution of the ray equations is possible. Following Červený [10], we refer to these techniques as *cell methods*. This technique was first developed for ocean-acoustic applications by Bucker as discussed in [32].

Regardless of the eigenray finding method, most codes will provide a ray thinning scheme which discontinues the ray tracing for rays whose associated intensity is below some threshold. For instance, rays which have interacted with the bottom a number of times might be discarded. This would be justified by assuming that the pressure field is dominated by purely refracted or surface-reflected paths. In the following sections, we treat each of these numerical approaches in some detail.

### 3.7.1 Direct Integration

#### 3.7.1.1 Tracing the Rays

Let us recall again the governing equations for the rays as given in (3.23) and (3.24). These are

$$\frac{dr}{ds} = c \xi(s), \quad \frac{d\xi}{ds} = -\frac{1}{c^2} \frac{\partial c}{\partial r}, \quad (3.161)$$

$$\frac{dz}{ds} = c \zeta(s), \quad \frac{d\zeta}{ds} = -\frac{1}{c^2} \frac{\partial c}{\partial z}, \quad (3.162)$$

together with the initial conditions,

$$r = r_0, \quad \xi = \frac{\cos \theta_0}{c(0)}, \quad (3.163)$$

$$z = z_0, \quad \zeta = \frac{\sin \theta_0}{c(0)}, \quad (3.164)$$

where  $\theta_0$  is a specified ray take-off angle. Evidently these equations take the standard form

$$\mathbf{y}' = \mathbf{f}(x, \mathbf{y}), \quad (3.165)$$

where  $\mathbf{y} = (r, z, \xi, \zeta)$  and  $x = s$ . The treatment of such initial-value problems is well-developed in standard texts on numerical methods so we shall make our remarks brief.

A simple numerical discretization is given by *Euler's method*. This is derived by using the Taylor series to write

$$\mathbf{y}_{i+1} = \mathbf{y}_i + \mathbf{y}'_i h + \mathbf{y}''_i \frac{h^2}{2!} + \dots, \quad (3.166)$$

where  $\mathbf{y}_i$  denotes  $\mathbf{y}(i h)$  and  $h$  is some fixed step length. This can also be written as

$$\mathbf{y}_{i+1} = \mathbf{y}_i + h \mathbf{f}(x, \mathbf{y}_i). \quad (3.167)$$

Euler's method is about the simplest numerical integrator that one can devise, but it is grossly inefficient. For a quick implementation of a ray-tracing code it may be suitable, however, one needs to be aware that while it will theoretically converge to the exact answer in the limit  $h \rightarrow 0$ , in finite-precision arithmetic it may never yield a sufficiently accurate answer.

Euler's method is characterized by a local truncation error of  $O(h)$ . There exists a whole family of  $O(h^2)$  methods which, for the same step size, generally yield a more accurate answer. These methods also require more computational work per

step, but, in practice, the trade-off is generally favorable to the higher-order schemes. One such scheme is the second-order *Runge–Kutta method*,

$$\mathbf{y}_{i+1/2} = \mathbf{y}_i + \frac{h}{2} \mathbf{f}(x_i, \mathbf{y}_i), \quad (3.168)$$

$$\mathbf{y}_{i+1} = \mathbf{y}_i + h \mathbf{f}(x_{i+1/2}, \mathbf{y}_{i+1/2}). \quad (3.169)$$

A further improvement in efficiency can be obtained by varying the step size  $h$ . Typically a larger step size is allowable below 500 m where the sound-speed profile is more smoothly varying.

One might expect that standard packaged codes could be easily used to solve the ray equations. There are two principal problems. First, the sound-speed profile is typically not available as a simple analytic function: In general, it is provided in the form of tabulated data. The interpolation of that function introduces its own errors that can be more important than the errors of the numerical integrator. This is shown in Sect. 3.7.4. Second, the ray integration must be interrupted and restarted whenever the ray reflects off a boundary. This process is especially complicated when the bottom boundary must also be interpolated from a discrete grid.

### 3.7.1.2 Boundary Reflections

With simple numerical integrators and uncomplicated boundaries, reflections are easy to implement. Consider Euler's scheme given in (3.167). In particular, we shall focus attention on the equation for the depth of the ray,

$$z_{i+1} = z_i + h c_i \xi_i. \quad (3.170)$$

Suppose that we wish to reflect a downgoing ray off a horizontal bottom at depth  $D$ . Obviously, we can test to see if the ray should have been reflected by checking whether  $z_{i+1} < D$ , that is, whether the ray has penetrated the bottom. If it has, then we simply repeat the Euler step with a step size chosen so that  $z_{i+1} = D$ , that is, so that the ray lands precisely on the bottom. Clearly, the reduced step size  $\tilde{h}$  that accomplishes this is

$$\tilde{h} = \frac{D - z_i}{c_i \xi_i}. \quad (3.171)$$

Lastly, we must restart the ray tracing from the lower boundary but with the take-off angle reflected. The appropriate conditions are, therefore,

$$\tilde{r} = r, \quad \tilde{\xi} = \xi, \quad (3.172)$$

$$\tilde{z} = z, \quad \tilde{\xi} = -\xi, \quad (3.173)$$

where we have used a tilde for the variables after reflection from the interface.

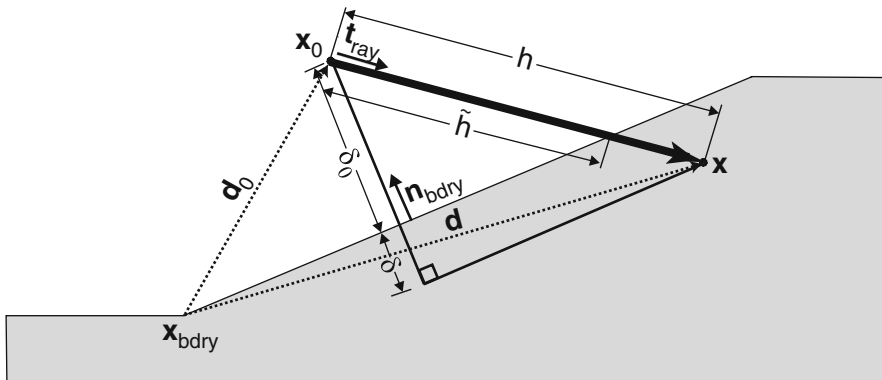


**Fig. 3.26** Geometry to calculate a reduced step that lands on a boundary or interface

In the more general case, the bottom is approximated in a piecewise-linear fashion as shown in Fig. 3.26. The process is essentially the same but involves slightly more complicated vector analysis. First, we consider a hypothetical step that crosses the boundary, as shown in the figure. We define vectors pointing from the beginning of the boundary segment to two adjacent points on the ray:

$$\mathbf{d}_0 = |\mathbf{x}_0 - \mathbf{x}_{\text{bdry}}|, \quad (3.174)$$

$$\mathbf{d} = |\mathbf{x} - \mathbf{x}_{\text{bdry}}|. \quad (3.175)$$

The first question is whether these points straddle the boundary indicating that the hypothetical step was too large. To test this we simply calculate the projections of these vectors onto the boundary normals,

$$\delta_0 = \mathbf{d}_0 \cdot \mathbf{n}_{\text{bdry}}, \quad (3.176)$$

$$\delta = \mathbf{d} \cdot \mathbf{n}_{\text{bdry}}. \quad (3.177)$$

If the offsets  $\delta_0$  and  $\delta$  have opposite signs, then the points straddle the boundary and the step size must be reduced. Further, we adopt the convention that the boundary normal points inward, so the crossing occurs when  $\delta_0$  is negative and  $\delta$  is positive. To correct the step  $h$ , we evidently need to reduce it in proportion to the amount we overstepped. The reduced step is, therefore,

$$\tilde{h} = \frac{-\delta_0}{-\delta_0 + \delta} h. \quad (3.178)$$

We can derive an alternative formula for  $\tilde{h}$  by noting that  $\delta_0$  is just the projection of the ray onto the normal to the boundary, so that

$$\delta_0 = \tilde{h} \cos \theta_0 = \tilde{h} \mathbf{t}_{\text{ray}} \cdot \mathbf{n}_{\text{bdry}}. \quad (3.179)$$

Solving for  $\tilde{h}$  we obtain

$$\tilde{h} = \frac{\delta_0}{\mathbf{t}_{\text{ray}} \cdot \mathbf{n}_{\text{bdry}}}. \quad (3.180)$$

This result reduces to that of (3.171) when the boundary is horizontal.

We have presented the mathematics here for reducing the step when a ray hits a sloped interface. More generally, the step needs to be reduced whenever the ray crosses any of a number of boundaries or interfaces. These may be defined by sound-speed points in depth or range, and bathymetry or altimetry points in range. These are just special cases of sloped interfaces so the above formula is applicable. All such crossings need to be considered to calculate the reduced step based on the nearest event.

### 3.7.1.3 Intensity Calculations

Sometimes the ray trace itself is all that is needed. However, if the pressure field is also needed then we recommend constructing a beam around each ray as described in Sect. 3.3.5. We further assume that the field is required on a rectangular grid of receiver coordinates. The principal problem then is to efficiently and reliably map each receiver location  $\mathbf{x}_{\text{rcvr}} = (r_{\text{rcvr}}, z_{\text{rcvr}})$  in a Cartesian coordinate system, to its corresponding ray-centered coordinates  $(s, n)$ . This part of the code can easily consume most of the computer time, if badly implemented. We have found the following approach works well. We march sequentially along the ray, working with one segment of the ray at a time. At step  $i$ , we have a ray segment with endpoints in range given by  $(r_{i-1}, r_i)$ . We now identify the range indices of all the receivers that are bracketed in range by those endpoints, as indicated in Fig. 3.27. We consider

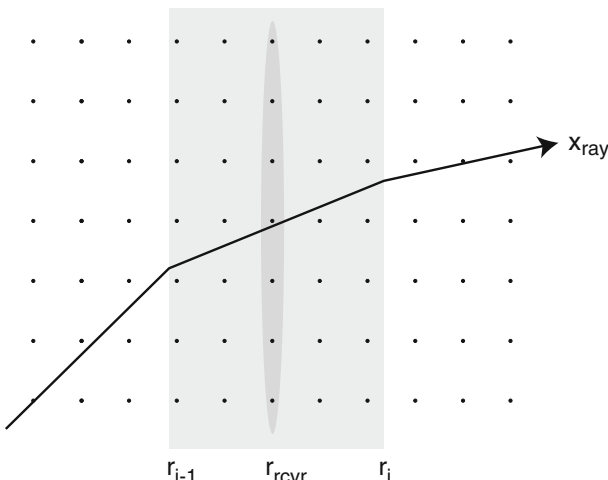


**Fig. 3.27** Active receivers in the zone of influence for a single segment of the ray

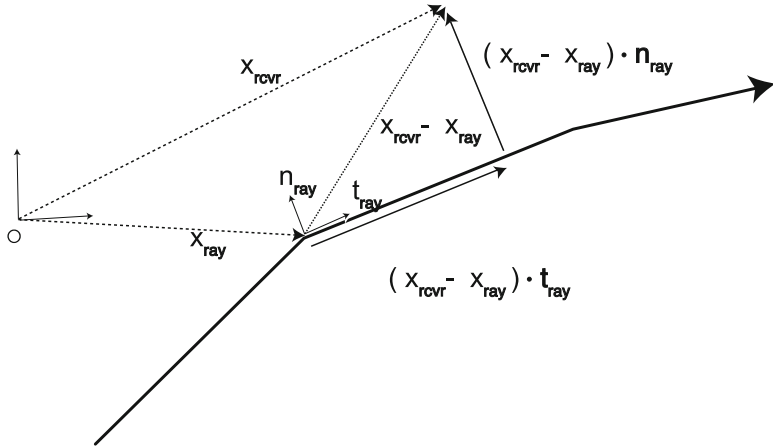


**Fig. 3.28** Receiver location expressed in ray-centered coordinates

cases where the ray may reverse in range and therefore are agnostic about whether  $r_i > r_{i-1}$ . Then an appropriate “containment” test for the receiver is whether:

$$r_{\text{rcvr}} \geq \min(r_i, r_{i-1}) \text{ and } r_{\text{rcvr}} < \max(r_i, r_{i-1}). \quad (3.181)$$

We next pass sequentially across columns of receivers, and for each column we work sequentially down from the surface receiver to the bottom receiver. The ray-centered coordinates  $(s, n)$  of each receiver follow from simple vector analysis as shown in Fig. 3.28:

$$s = (\mathbf{x}_{\text{rcvr}} - \mathbf{x}_{\text{ray}}) \cdot \mathbf{t}_{\text{ray}}, \quad (3.182)$$

$$n = |(\mathbf{x}_{\text{rcvr}} - \mathbf{x}_{\text{ray}}) \cdot \mathbf{n}_{\text{ray}}|, \quad (3.183)$$

where  $\mathbf{x}_{\text{ray}} = (r_{\text{ray}}, z_{\text{ray}})$  is one endpoint of the ray, with associated unit tangent  $\mathbf{t}_{\text{ray}}$  and unit normal  $\mathbf{n}_{\text{ray}}$ . Then, any required value for the beam in the vicinity of the ray segment can be computed by a linear fit between values at the endpoints. For instance,  $q(s)$ , which governs the beam amplitude, is computed as

$$q = q_{i-1} + \alpha(q_i - q_{i-1}), \quad (3.184)$$

where  $\alpha = s / \| r_i - r_{i-1} \|$  is the proportional distance along the ray segment. It varies from 0 to 1 for receivers on this segment of the ray, implying an interpolation of values between the endpoints. However, a receiver not lying exactly on the ray, but bracketed in range by a particular segment of the ray may involve a value of  $\alpha$  less than 0 or greater than 1, implying an extrapolation of values between the endpoints. Finally, we also remind that sign changes in  $q(s)$  must also be counted as we march along the ray to accumulate the KMAH index as discussed in Sect. 3.4.

The above described process is not necessarily using the segment of the ray that is closest to the receiver to construct the influence of the beam. However, it provides a particularly simple algorithm for mapping a receiver field in Cartesian coordinates to the beam field defined in ray-centered coordinates.

The direct integration approach is used in several models, e.g. those developed by Foreman [30], Bowlin et al. [33] and Cornyn [34].

### 3.7.2 Cell Methods: $n^2$ Linear

The philosophy of cell methods is to divide the domain into a patchwork of elements within which the medium has simple properties. An example of such a triangular discretization is provided in Fig. 3.29.

For two-dimensional problems the  $c$ -linear and  $n^2$ -linear approximations are popular choices. Let us consider the  $n^2$ -linear case first. The derivation is simplest if we start from the ray equations written as a function of  $\sigma$  as given in (3.96). Written out for each component, these equations read

$$\frac{d^2r}{d\sigma^2} = \frac{1}{2} \frac{\partial(n^2)}{\partial r}, \quad (3.185)$$

$$\frac{d^2z}{d\sigma^2} = \frac{1}{2} \frac{\partial(n^2)}{\partial z}. \quad (3.186)$$

In this form, it is clear that with a general linear form for the square index of refraction,

$$n^2(r, z) = n_0^2 + g_r(r - r_0) + g_z(z - z_0), \quad (3.187)$$

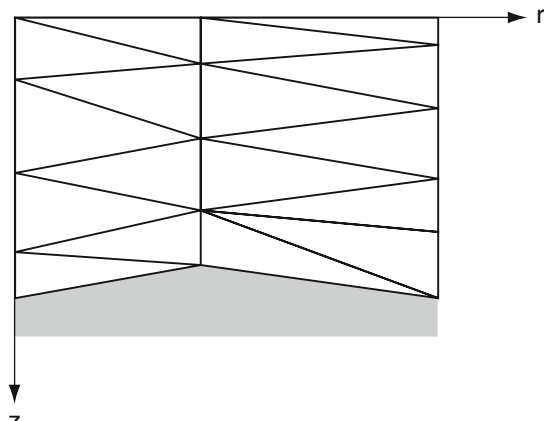


**Fig. 3.29** Triangulation for cell-type ray tracing

the ray equations can be integrated exactly yielding

$$r(\sigma) = \frac{gr}{4}\sigma^2 + a_1\sigma + a_2, \quad (3.188)$$

$$z(\sigma) = \frac{gz}{4}\sigma^2 + b_1\sigma + b_2. \quad (3.189)$$

We choose in the following to take  $\sigma = 0$  as the starting point of this ray and let  $r(0) = r_0$  and  $z(0) = z_0$ . We further assume the ray take-off angle is given by  $\theta_0$ , which implies  $dr/d\sigma = n_0 \cos \theta_0$  and  $dz/d\sigma = n_0 \sin \theta_0$  at the origin. Then we can solve for the unknown constants of integration  $a_1, a_2, b_1, b_2$  to obtain

$$r(\sigma) = \frac{gr}{4}\sigma^2 + (n_0 \cos \theta_0)\sigma + r_0, \quad (3.190)$$

$$z(\sigma) = \frac{gz}{4}\sigma^2 + (n_0 \sin \theta_0)\sigma + z_0, \quad (3.191)$$

where  $\theta_0$  is the take-off angle of the ray.

The phase is also easily calculated along these trajectories. Substituting the index of refraction given in (3.187) into the travel time formula given in (3.97), we obtain

$$\tau(\sigma) = \tau_0 + \frac{1}{c_0} \int_0^\sigma [n_0^2 + g_r(r - r_0) + g_z(z - z_0)] d\sigma'. \quad (3.192)$$

Substituting from (3.190) to (3.191) and integrating then yields

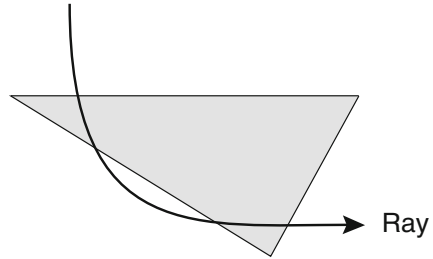
$$\begin{aligned} \tau(\sigma) &= \tau_0 + \frac{n_0^2}{c_0}\sigma \\ &\quad + \frac{gr}{c_0} \left[ \frac{gr}{12}\sigma^3 + \frac{n_0 \cos \theta_0}{2}\sigma^2 \right] \\ &\quad + \frac{gz}{c_0} \left[ \frac{gz}{12}\sigma^3 + \frac{n_0 \sin \theta_0}{2}\sigma^2 \right]. \end{aligned} \quad (3.193)$$

We have derived these equations assuming that the medium varies linearly as a function of  $r$  and  $z$ . In fact, it is sufficient to treat the case of a medium that only varies linearly in the  $z$ -direction since by rotating the coordinate system through an angle  $\phi = \arctan(g_r/g_z)$ , we obtain equations that only vary as a function of one variable. In other words, the transformation

$$\begin{bmatrix} r \\ z \end{bmatrix} = \begin{bmatrix} \cos \phi & \sin \phi \\ -\sin \phi & \cos \phi \end{bmatrix} \begin{bmatrix} \hat{r} \\ \hat{z} \end{bmatrix} \quad (3.194)$$

converts the sound speed  $c(r, z)$  to  $c(\hat{z})$  depending linearly on  $\hat{z}$ . Therefore, we can assume without loss of generality that  $g_r = 0$  and then solve (3.190)–(3.191) for  $z$  as a function of  $r$  yielding

$$z(r) = \frac{gz}{4} \left( \frac{r - r_0}{n_0 \cos \theta_0} \right)^2 + (\tan \theta_0)(r - r_0) + z_0. \quad (3.195)$$

**Fig. 3.30** Ray intercepts

Thus, the ray paths follow parabolic trajectories. This implies that, in the general case with linear variation in  $r$  and  $z$ , the rays trace out a segment of a rotated parabola.

The procedure then for tracing a ray involves solving for the intercept of the ray with each of the sides of the triangle. In some cases, the ray may intercept more than one side or the same side twice as illustrated in Fig. 3.30. When more than one intercept occurs, the intercept with the smallest  $\sigma$  is accepted. The ray is then continued into the next triangle, using the requirement of continuity of position and slope to solve for the constants  $a_1, a_2, b_1, b_2$  in the next triangle.

Analytic solutions may also be derived for the  $p, q$  equations, (3.58), which give the ray amplitude [23]. Finally, we should note that this technique is equally applicable—indeed simpler—when applied to a stratified medium. Then, instead of dividing the medium into triangles it is divided into a number of layers.

An example of a production model based on  $n^2$ -linear triangles is described by Roberts [35].

### 3.7.3 Cell Methods: $c$ Linear

The derivation proceeds most directly if we assume that the medium is range independent, i.e.,

$$c(z) = c_0 + g_z z. \quad (3.196)$$

We remind that for the general case with linear variations in both depth and range,

$$c(z) = c_0 + g_z z + g_r r, \quad (3.197)$$

we can simply rotate our coordinates so that the range dependence disappears.

Recall from (3.145) that in a range-independent medium the rays satisfy the equation,

$$r(z) = r(z_1) + \int_{z_1}^z \frac{ac}{\sqrt{1 - a^2 c^2}} dz'. \quad (3.198)$$

Since  $dc = g dz$  this can be written as

$$r(z) = r(z_1) + \int_{c(z_1)}^{c(z)} \frac{ac}{g\sqrt{1-a^2c^2}} dc, \quad (3.199)$$

which can be integrated analytically yielding

$$r = r(z_1) + \left. \frac{\sqrt{1-a^2c^2}}{ag} \right|_{c(z_1)}^{c(z)}. \quad (3.200)$$

This equation can be rearranged in the form

$$\left[ r - [r(z_1) - b] \right]^2 + \left[ z + \frac{c_0}{g} \right]^2 = R^2, \quad (3.201)$$

where

$$R = \frac{1}{ag}, \quad b = \frac{\sqrt{1-a^2(c_0+gz_1)^2}}{ag}. \quad (3.202)$$

Thus, the rays in a medium with linear variation of the sound speed follow circular trajectories as illustrated in Fig. 3.31. The circles are centered along the line where the sound speed vanishes and have an arbitrary radius depending on the choice of  $a$ .

An analytic expression for the phase is obtained from (3.149) with the usual change of integration variable,  $dc = gdz$ ,

$$\tau(z) = \tau(z_0) + \int_{c(z_0)}^{c(z)} \frac{1}{gc\sqrt{1-a^2c^2}} dc. \quad (3.203)$$

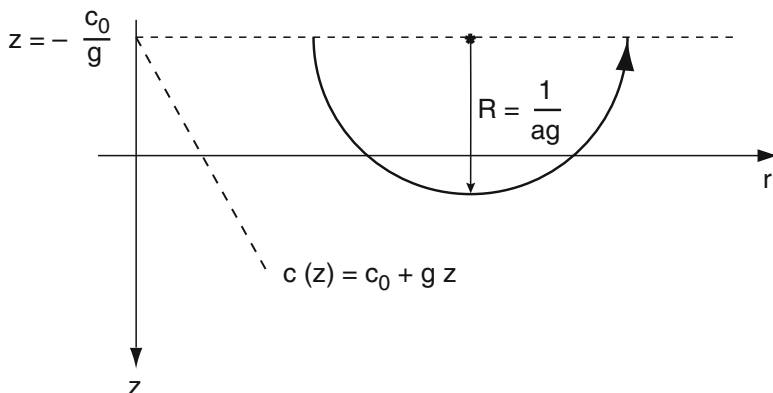


**Fig. 3.31** Ray path in a medium with linear sound-speed variation

This integral is found from tables to be

$$\tau(z) = \tau(z_0) + \left| \frac{1}{g} \log \left[ \frac{1 + \sqrt{1 - a^2 c^2}}{ac} \right]_{c(z_0)}^{c(z)} \right|. \quad (3.204)$$

This equation is valid for one of the endpoints being the singular turning point, where  $ac = 1$ , yielding a vanishing logarithm. However, it cannot be applied for a ray path through the turning point. In this case, the ray crosses each depth twice, and the travel time therefore becomes ambiguous. However, this case is easily handled by using (3.204) for each side of the turning point separately. Thus, a ray launched at depth  $z_0$  and received at depth  $z$ , after passing through the turning point, has the following phase:

$$\tau(z) = \tau(z_0) + \frac{1}{|g|} \left[ \log \left( \frac{1 + \sqrt{1 - a^2 c(z_0)^2}}{ac(z_0)} \right) + \log \left( \frac{1 + \sqrt{1 - a^2 c(z)^2}}{ac(z)} \right) \right]. \quad (3.205)$$

Analytic solutions for the  $p, q$  equations, (3.58), are also readily obtained. One of the earliest models based on  $c$ -linear triangles was developed by Bucker. The current version is documented in [32].

In addition to its use in cell methods, the analytic solution for the ray paths in the case of a horizontally stratified waveguide with a linear sound-speed profile is useful as a reference solution for the development of new ray codes. In this case the value of  $a$  is determined by the initial conditions for the ray at the source, e.g. a ray launched from depth  $z_0$  at grazing angle  $\theta_0$ . As described in Sect. 3.6.7, Snell's law requires the sound speed at the deepest point  $z_{\max}$  of the array, the *turning point*, to be

$$c(z_{\max}) = c(0) + g z_{\max} = \frac{c(z_0)}{\cos \theta_0}, \quad (3.206)$$

yielding

$$z_{\max} = \frac{c(z_0)}{g \cos \theta_0} - \frac{c(0)}{g}. \quad (3.207)$$

The last term is the depth of the center of the circular arcs, and the first term is, therefore, the radius, yielding

$$R = \frac{c(z_0)}{g \cos \theta_0} = \frac{c(z_{\max})}{g}. \quad (3.208)$$

Thus, the arbitrary parameter  $a$  is simply the constant in Snell's law,

$$a = g/R = \frac{\cos \theta_0}{c(z_0)}. \quad (3.209)$$

Now one can easily compute the ray paths in range and depth as a reference solution. Thus, the arc length is

$$s = R(\theta_0 - \theta) \quad (3.210)$$

yielding, together with simple projection of the circular arc,

$$\begin{aligned} r(s) &= R \sin \theta_0 - R \sin \theta \\ &= R [\sin \theta_0 + \sin(s/R - \theta_0)], \end{aligned} \quad (3.211)$$

$$\begin{aligned} z(s) &= R \cos \theta - c(0)/g \\ &= R \cos(s/R - \theta_0) - c(0)/g. \end{aligned} \quad (3.212)$$

### 3.7.4 False Caustics and Profile Interpolation

In the case of cell methods, the profile interpolation is implicit in the construction of the algorithm involving either  $c$ -linear or  $n^2$ -linear approximations to the sound-speed profile. When sound speed data is provided at a sequence of ranges at discretely tabulated depths it is a fairly simple manner to devise an algorithm which automatically generates a triangulation of those grid points. Obviously, the ray tracing will proceed more rapidly if fewer triangles are used so it is advantageous to subsample the profile in depth if there are a large number of depth points. In practice, it is seldom necessary to use more than 20 points in depth to define the sound-speed profile. In principle, extra points increase the accuracy but we need to bear in mind the limits in accuracy imposed by undersampling in range as well as the intrinsic inaccuracy of ray theory due to its high-frequency approximation. The fact that the medium is also time-varying poses an additional limit on the attainable accuracy.

The methods which rely on direct integration allow for a variety of schemes for profile interpolation. One approach is to use the same piecewise linear scheme used by the cell methods. More commonly, cubic splines are used which yield a smoother fit to the profile [36].

The effect on the ray trace of using piecewise linear approximations and cubic splines is shown in Fig. 3.32 for a source frequency of 500 Hz. Note that the cubic spline interpolation yields a much more regular ray trace corresponding more closely to the exact ray paths. The irregular ray pattern in Fig. 3.32a leads to corresponding anomalies in the calculated intensities, and indeed can cause false caustics as discussed by Pedersen [37]. In Fig. 3.33, we have calculated the transmission loss using both  $n^2$ -linear and spline interpolation, and using both geometric ray theory (left panels) and a full-wave solution based on normal modes (right panels).

Note that the  $n^2$ -linear approximation produces caustics in the geometric ray approximation, which are not seen in the spline fit. Ray theory is particularly sensitive to these caustics; however, they also affect the full-wave result as seen in the upper-right panel, which was generated using normal modes. Thus, the artifacts are a fundamental characteristic of piecewise-linear interpolation. (They can be mitigated

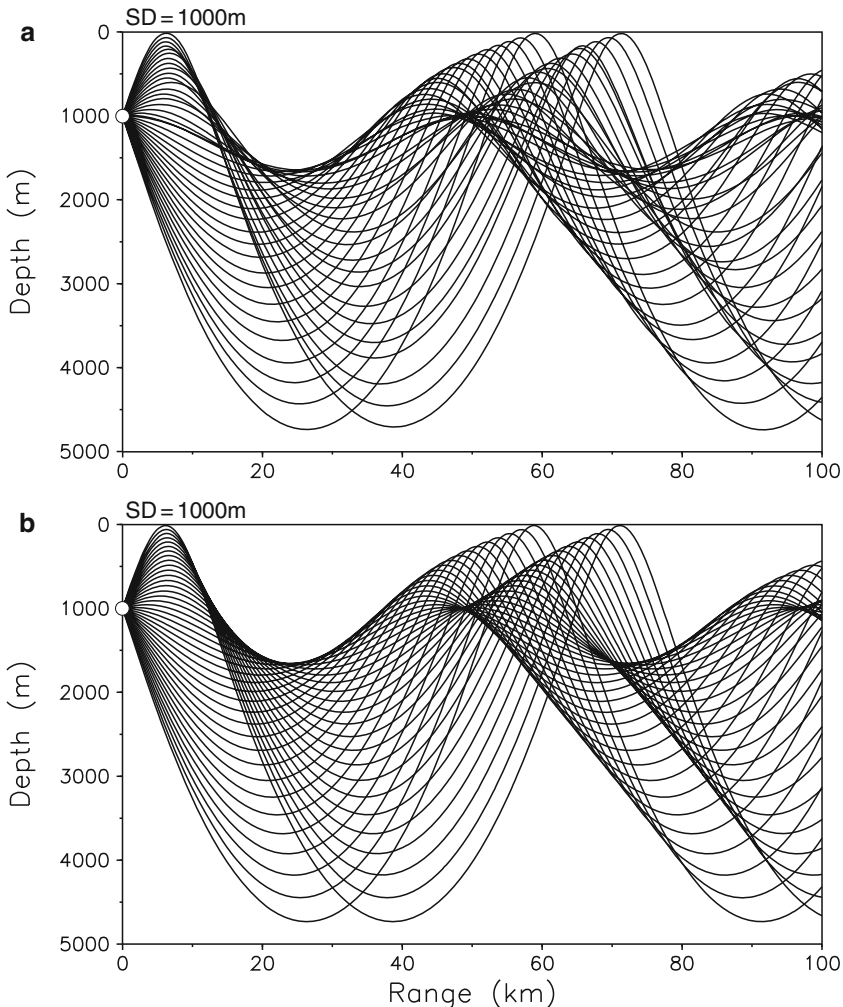


**Fig. 3.32** Rays for the Munk profile using (a) c-linear interpolation and (b) cubic-spline interpolation

by sampling the sound-speed profile more finely.) Gaussian beam tracing smoothes out the caustics yielding a result that is closer to the full wave solution. However, the best agreement is achieved using the spline-fit as seen in the lower panels.

A further feature of interest is the formation of an acoustic jet emanating horizontally from the source when piecewise-linear interpolation is used, and when the source is located at the discontinuity in the gradient of the sound speed.

The cell methods we have described use piecewise linear approximations and are therefore also prone to false caustics. However, it is fairly simple to construct cell-type methods which have continuous gradients across the cell interfaces while

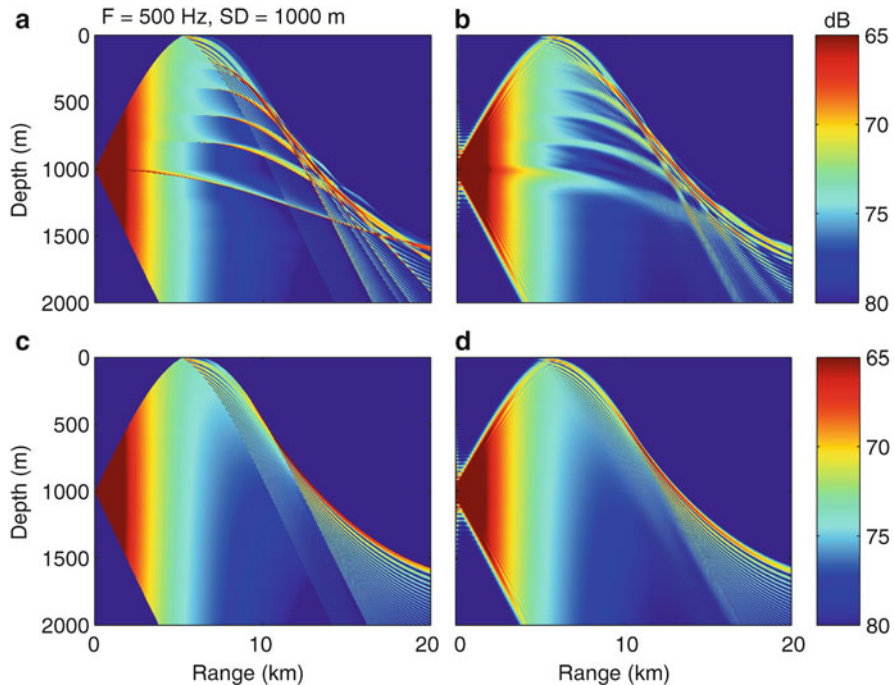


**Fig. 3.33** Transmission loss for the Munk profile using  $n^2$ -linear (top panels) and spline interpolation (bottom panels). The left panels were computed using geometric ray theory; the right panels are full-wave solutions computed using normal modes

retaining simple analytic solutions within a cell. On the other hand, in many practical cases these types of ray irregularities are tolerable. It should also be noted that while the cubic splines have the advantage of smoothness they often suffer from large amplitude wiggles between points in the sound-speed profile. This can be easily detected automatically but fixing the problem often requires human intervention to add or delete points in the profile.

### 3.7.5 Finding Eigenrays

We have seen how the phase and intensity along a ray can be found by simply solving a system of ordinary differential equations. In practice, however, our problem is usually not to find the solution along a ray but rather to find the solution at fixed points in the  $rz$ -plane, e.g., transmission loss for a fixed receiver depth. Thus, we are faced with the problem of finding *eigenrays*, that is, rays which connect the source and the specified receiver positions.

Mathematically this is a root-finding problem. The roots are the take-off angles  $\theta_0$  and the equation whose roots are sought can be defined as

$$f(\theta_0) = z(r_r; \theta_0) - z_r, \quad (3.213)$$

where  $(r_r, z_r)$  is the coordinate of the receiver and  $z(r; \theta_0)$  is the trajectory of the ray.

### 3.7.5.1 Interpolation

This approach is perhaps the most common. One begins by tracing a fan of rays from the origin. A search is then done to identify pairs of rays with adjacent take-off angles which bracket the receiver in depth as illustrated in Fig. 3.34. The phase delay and amplitude are then found by linear interpolation of the values obtained for the two bracketing rays. (Some models search for rays which bracket the receiver in range.)

There is one additional complication to be dealt with. As shown in Fig. 3.34, two rays with adjacent take-off angles may bracket a receiver in depth but have different ray histories. The first ray strikes the surface and loses energy in accordance with the surface reflection loss, while the second ray is turned before hitting the surface. As a result, a linear interpolation of phase and amplitude results in severe errors. To avoid this, one typically accumulates a ray history for each ray, counting the number of surface and bottom reflections as well as the number of times the ray has been turned. A test is then performed to disallow interpolation between rays with different ray histories.

As we have seen, the intensity associated with a ray requires the calculation of the Jacobian determinant,

$$J = r \left[ \left( \frac{\partial z}{\partial \theta_0} \right)^2 + \left( \frac{\partial r}{\partial \theta_0} \right)^2 \right]^{1/2}. \quad (3.214)$$

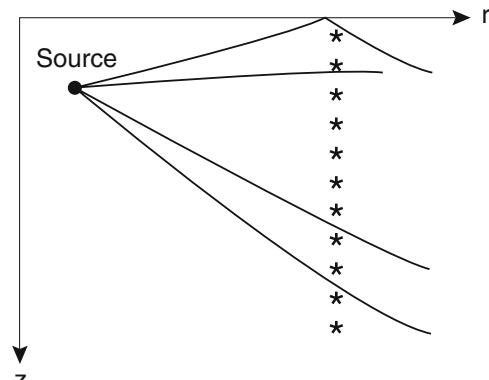


**Fig. 3.34** Ray interpolation

We have shown how this quantity can be derived by integrating the dynamic ray equations along with the usual ray equations. Alternatively, with two rays bracketing a receiver we can calculate the above derivatives directly.

### 3.7.5.2 Iteration

As mentioned above, the location of eigenrays is a root-finding problem for which standard techniques such as Newton's method or the secant method may be used. To initialize these root finders one again begins by tracing a fan of rays in order to find rays with adjacent take-off angles and identical ray histories which bracket the receiver point. This information is then passed to a root finder which iteratively adjusts the ray take-off angle to find a ray which passes to within a specified distance of the receiver. The interpolation method described above may be viewed as a member of this class of method in which the secant method is used with just a single iteration.

### 3.7.5.3 The Bending Method

This approach has received little attention in underwater acoustics but is quite popular in the seismic community. One begins by constructing a curve which connects the source and receiver and is described by a finite number of parameters. For instance, the curve could be composed of  $N-1$  line segments so that it is defined by  $N$  coordinates as illustrated in Fig. 3.35. The coordinates are then simultaneously perturbed to yield a path with reduced travel time. This process is continued until a path with a local minimum in travel time is obtained, i.e., a Fermat path, which therefore is a ray trajectory. Details along with references to earlier papers may be found in [38].

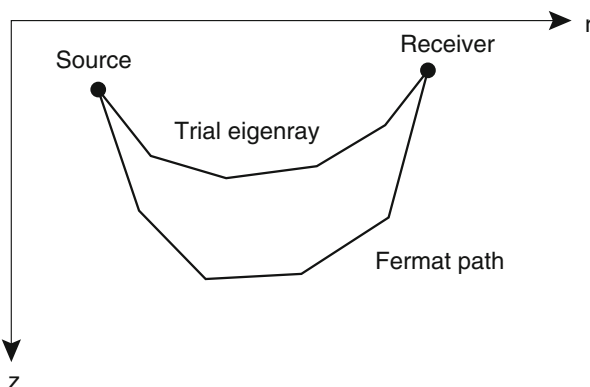


**Fig. 3.35** The bending method

### 3.7.5.4 The Continuation Method

The continuation method is closely related to the bending method in that one starts with an initial guess to the ray path which is subsequently altered. However, in the continuation method the ray is taken to satisfy a simpler problem and the sound-speed profile is gradually adjusted to the profile whose solution is desired. As the profile is changed the ray path is updated so that at any time it represents an eigenray for that problem. This technique is discussed by Keller and Perozzi [39].

## 3.8 Extensions and Related Techniques

The basic ray method can be extended and improved in a variety of ways and in some cases it may even be difficult to decide whether the resulting method should even still be referred to as ray theory. For instance, in the next section we will see how high-frequency asymptotics (ray theory) can be applied to a depth-separated form of the Helmholtz equation. The resulting algorithm can then be viewed as a hybrid ray–FFP or ray–mode method.

The parabolic equation method discussed in Chap. 6 is normally constructed as a paraxial solution valid for energy propagating near the horizontal. The parabolic equation can also be formulated paraxially about a ray path leading to a hybrid ray–PE model [40]. In a further approximation, this reduces back to the Gaussian beam tracing technique described in Sect. 3.5.2.

Ray theory can also be extended to treat elastic problems [41], although the literature on this subject is much more extensive in seismology than in ocean acoustics. Finally, ray models have also been developed to take account of the small-scale variability of the ocean. For instance, a model developed by Schneider [42] treats these effects in a Monte-Carlo form by randomly perturbing the take-off angle of the rays at certain points on their trajectories. The magnitude of the change in take-off angle is determined by a depth-dependent diffusion parameter characterizing the variability of the medium.

In the following sections, we shall discuss some other extensions of standard ray tracing.

### 3.8.1 The WKB Method

The WKB method, named after Wentzel, Kramers, and Brillouin, is a general technique for obtaining approximations to a certain class of linear differential equations [43]. Jeffreys, Liouville, and Green actually used the technique earlier so the method is variously referred to as WKBJ or LGJWKB, etc. The WKB method may also be viewed as the application of ray theory to one-dimensional problems.

A one-dimensional problem is obtained when the acoustic medium is range independent so that by applying a Hankel transform,

$$p(k_r, z) = \int_0^\infty p(r, z) J_0(k_r r) r dr \quad (3.215)$$

the Helmholtz equation reduces to

$$\left( \frac{\partial^2}{\partial z^2} + k_z^2 \right) p(k_r, z) = 0, \quad (3.216)$$

where we have introduced the vertical wavenumber

$$k_z^2(z) = \frac{\omega^2}{c^2(z)} - k_r^2. \quad (3.217)$$

Equation (3.216) is supplemented with appropriate boundary conditions at the ocean surface and bottom which for the moment shall be ignored.

Solved exactly, this equation forms the basis of the wavenumber-integration and normal-mode methods discussed in Chaps. 4 and 5. The pressure field is obtained by performing the inverse Hankel transform,

$$p(r, z) = \int_0^\infty p(k_r, z) J_0(k_r r) k_r dk_r, \quad (3.218)$$

which we can interpret as summing up the contributions of a continuum of waves each one with a different take-off angle parameterized by  $k_r$ .

The derivation of the WKB approximation now proceeds exactly as for the original ray representation except that all the vector equations become scalar equations involving the single variable  $z$ . Thus, we seek an asymptotic solution of the form

$$p(z) = e^{i\omega\tau(z)} \sum_{j=0}^{\infty} \frac{A_j(z)}{(i\omega)^j}. \quad (3.219)$$

In substituting this series into (3.216) and equating terms of like order in  $\omega$ , we obtain the following infinite sequence of equations for the functions  $\tau(z)$  and  $A_j(z)$ ,

$$\left| \frac{d\tau}{dz} \right|^2 = \frac{k_z^2(z)}{\omega^2}, \quad (3.220)$$

$$2 \frac{d\tau}{dz} \frac{dA_0}{dz} + \frac{d^2\tau}{dz^2} A_0 = 0, \quad (3.221)$$

$$2 \frac{d\tau}{dz} \frac{dA_j}{dz} + \frac{d^2\tau}{dz^2} A_j = -\frac{d^2A_{j-1}}{dz^2}, \quad j = 1, 2, \dots \quad (3.222)$$

In this one-dimensional form, the eikonal and transport equations can be solved immediately without need of the transformation into ray coordinates. We obtain

$$\tau(z) = \pm \frac{1}{\omega} \int k_z(z) dz. \quad (3.223)$$

The first transport equation then becomes

$$2 k_z(z) \frac{dA_0}{dz} + \frac{dk_z}{dz} A_0 = 0 \quad (3.224)$$

implying

$$A_0(z) = \frac{B}{\sqrt{k_z(z)}}, \quad (3.225)$$

where  $B$  is an arbitrary constant. Putting this all together we obtain our final result

$$p(k_r, z) \simeq \frac{B e^{\pm i \int_{z_0}^z k_z(z') dz'}}{\sqrt{k_z(z)}}, \quad (3.226)$$

which, of course, is identical to the result derived as (2.263) in Chap. 2. Substituting our definition for  $k_z(z)$  from (3.217) we obtain

$$p(k_r, z) \simeq \frac{B e^{\pm i \int_{z_0}^z [\omega^2/c^2(z') - k_r^2]^{1/2} dz'}}{[\omega^2/c^2(z') - k_r^2]^{1/4}}. \quad (3.227)$$

Like the general N-dimensional ray theory, this approximation breaks down in certain regions where  $A_0$  becomes infinite. In this case, it is clear that these infinities occur at points where  $\omega^2/c^2 - k_r^2$  vanishes. These are referred to as *turning points* since they correspond to depths where a ray with take-off angle corresponding to  $k_r$  is turned, i.e., it becomes horizontal.

Note that the one-dimensional WKB approximation breaks down in different regions from the two-dimensional ray theory which we have considered up till now. That is, the WKB approximation breaks down in the neighborhood of turning points while the 2-D ray theory breaks down in the vicinity of caustics of the 2-D ray system. The two approximations, while closely related, differ in some fundamental respects. Most notably, the 2-D ray result gives the field at a given point directly in terms of the contributions of a finite number of eigenray contributions. The WKB result given in (3.226) represents a single spectral component, and the field at any point is obtained by summing up an infinite number of contributions. In this respect, the WKB solution is more closely related to the Gaussian beam tracing discussed in Sect. 3.5.2. In fact, the WKB method can be obtained as a special case of Gaussian beam tracing. Like the standard ray tracing approach, the WKB method is readily adapted to broadband propagation problems as described by Brown [44].

The WKB seismogram can also be generalized to range-dependent problems as introduced by Maslov and further developed by Chapman and Drummond [45]. A similar approach has been developed by Tindle and Deane [46] for ocean acoustic applications.

### 3.8.2 Ray Theory via the WKB Approximation

The final step in computing the pressure field via the WKB approximation is to perform the inverse Hankel transform

$$p(r, z) = B \int_0^\infty \frac{e^{\pm i \int_{z_0}^z k_z(z') dz'}}{\sqrt{k_z(z)}} J_0(k_r r) k_r dk_r. \quad (3.228)$$

For ranges more than a few wavelengths from the source, it is usually sufficient to approximate the Bessel function by its large argument asymptotic formula. This gives

$$p(r, z) = B \int_0^\infty \frac{e^{\pm i \int_{z_0}^z k_z(z') dz'}}{\sqrt{k_z(z)}} e^{ik_r r} \sqrt{k_r} dk_r. \quad (3.229)$$

This integral is of the general form

$$p(z; \omega) = \int_\alpha^\beta A(\xi) e^{i\omega\tau(\xi)} d\xi, \quad (3.230)$$

which can be evaluated asymptotically in the limit  $\omega \rightarrow \infty$  by the method of *stationary phase* described in the discussion associated with (2.161). The result is

$$p(z; \omega) \simeq \sqrt{\frac{2\pi}{\omega |\tau''(\xi_0)|}} A(\xi_0) e^{i\omega\tau(\xi_0) \pm i\pi/4}, \quad (3.231)$$

where  $\xi_0$  is a point of stationary phase, i.e., a point where  $\tau'(\xi_0)$  vanishes. The sign  $\pm$  in the above is taken as the same as the sign of  $\tau''(\omega)$ . This formula basically states that in the limit of large  $\omega$  the integral is dominated by contributions in the vicinity of stationary points. There are various assumptions in its derivation, for instance that  $\tau''(\xi_0)$  does not also vanish and that there is only one stationary point in the domain of the integral. If there is more than one stationary point then each point contributes a term of this same form.

Applying this formula to the WKB integral we find that the phase is given by

$$\omega\tau(k_r) = \pm \int_{z_0}^z k_z(z') dz' + k_r r. \quad (3.232)$$

The condition  $\tau'(k_r) = 0$  then becomes

$$\pm \int_{z_0}^z \frac{dk_z}{dk_r} dz' + r = 0. \quad (3.233)$$

For a fixed range  $r$  this formula implicitly defines points  $k_r$  which provide a dominant contribution to the integral. (The  $k_r$ -points which dominate correspond to the take-off angles of the eigenrays.) We can also think of the equation as giving trajectories  $r(k_r)$  for which a fixed  $k_r$  is a stationary point. Substituting our definition of  $k_z(z, k_r)$  from (3.217) and rearranging we find that

$$r(z) = r(z_1) + \int_{z_1}^z \frac{ac}{\sqrt{1 - a^2 c^2}} dz', \quad (3.234)$$

where  $a = k_r/\omega$ . This we recognize as (3.145) giving the trajectories of rays in a stratified medium.

In summary, ray theory may be viewed as the combination of WKB theory and the method of stationary phase. The fact that the solution at a given point is obtained from summing up the contributions of eigenrays is equivalent to the fact that the spectral integral is asymptotically dominated by particular points in the  $k_r$ -spectrum. Just as the take-off angle for the eigenrays is different for different receiver ranges and depths, different parts of the spectral integral produce dominant contributions depending on the source and receiver depth. This insight is useful in understanding the wavenumber-integration technique discussed in Chap. 4.

### 3.8.3 The Ray Invariant and the Waveguide Invariant

In this section, we present the ray interpretation of the waveguide invariant [47]. We use slowness, the inverse of speed, to simply deal with frequency-independent ray paths. As per the definition given in (2.214), we must find the ray version of the phase and group slowness. All propagating rays in a waveguide cycle between a maximum and minimum depth determined by Snell's law of refraction or reflection. In addition, the trajectory of a ray satisfies

$$\frac{dr}{dz} = \frac{1}{\tan \theta}, \quad (3.235)$$

where  $\theta$  is the grazing angle of the ray with respect to the horizontal. Then, the horizontal range traversed of one ray cycle, often referred to as the skip distance  $\Lambda$ , is given by

$$\Lambda = 2 \int_{z_l}^{z_u} \frac{dz}{|\tan \theta|}, \quad (3.236)$$

where  $z_l, z_u$  are the lower and upper turning points determined by Snell's law. Now, by Snell's law we also have that the horizontal phase speed  $s_h$ , and therefore horizontal phase slowness of a particular ray is constant,

$$s_h = s(z) \cos \theta(z) = s(z_0) \cos \theta_0, \quad (3.237)$$

where  $s(z) \equiv 1/c(z)$ , and the subscript 0 refers to the launch angle and launch depth. Of course, the ray slowness is also clearly the medium slowness at the turning points (i.e., the depths at which  $s_v(z)$  vanish) and one can clearly identify a ray by its slowness. Similarly, vertical slowness is given by

$$s_v = s(z) |\sin \theta(z)| = \sqrt{s^2(z) - s_h^2}. \quad (3.238)$$

Combining (3.236)–(3.238), we obtain an expression for the skip distance as

$$\Lambda = 2 \int_{z_l}^{z_u} \frac{s_h}{s_v(z)} dz. \quad (3.239)$$

Similarly, using the expression for the ray travel time given by (3.32) together with (3.238), we obtain an expression for the cycle time  $T$ ,

$$T = 2 \int_{z_l}^{z_u} \frac{s(z)}{|\sin \theta(z)|} dz = 2 \int_{z_l}^{z_u} \frac{s^2(z)}{s_v(z)} dz. \quad (3.240)$$

The group slowness  $s_g$  of a ray is simply

$$s_g = \frac{T}{\Lambda}, \quad (3.241)$$

so that the waveguide invariant, from (2.214), is given by

$$\beta^{-1} = -\frac{ds_g}{ds_h} = -\frac{d(T/\Lambda)}{ds_h} = -\left(\frac{dT}{\Lambda ds_h} - \frac{T d\Lambda}{\Lambda^2 ds_h}\right). \quad (3.242)$$

Besides cycle distance and time, a third parameter, the ray invariant [48] will prove useful for determining the waveguide invariant. We start from relation  $\sin^2 \theta = 1 - \cos^2 \theta$  to construct the identity

$$\sin \theta = \frac{1}{\sin \theta} - \frac{\cos^2 \theta}{\sin \theta} \quad (3.243)$$

and together with Snell's law as per (3.237) we obtain

$$s_v = s(z) \sin \theta = \frac{s(z)}{\sin \theta} - s(z_0) \cos \theta_0 \frac{1}{\tan \theta}. \quad (3.244)$$

Note that the first term on the *rhs* is the integrand of (3.240) and similarly, the second term is the integrand of (3.236) so that we can introduce a ray invariant  $I_r$  as

$$\begin{aligned} I_r &= T - s_h \Lambda = \Lambda(s_g - s_h) = 2 \int_{z_l}^{z_u} s_v(z) dz \\ &= 2 \int_{z_l}^{z_u} \sqrt{s^2(z) - s_h^2} dz \equiv \oint s_v(z) dz, \end{aligned} \quad (3.245)$$

where the *rhs* integral representation for the whole cycle is for future reference to the Hamiltonian formulation of ray acoustics. Clearly, for a given ray, the ray invariant is constant since  $T, s_h, \Lambda$  are constants for any particular ray. Further from (3.239) and (3.240) we have,

$$\frac{dT}{ds_h} = s_h \frac{d\Lambda}{ds_h}, \quad (3.246)$$

so that, in combination with (3.245) we also obtain

$$\frac{dI_r}{ds_h} = -\Lambda. \quad (3.247)$$

Combining (3.242), (3.245) and (3.247), we obtain an alternative, very useful form of the waveguide invariant for a ray,

$$\beta^{-1} = -I_r \frac{d(\frac{1}{\Lambda})}{ds_h} = -I_r \sin \theta_0 \frac{d(\frac{1}{\Lambda})}{d\theta_0} = \frac{I_r \sin \theta_0}{\Lambda^2} \frac{d\Lambda}{d\theta_0} = -\frac{I_r}{\Lambda} \frac{d\Lambda}{d\theta_0} \frac{d\theta_0}{dI_r}. \quad (3.248)$$

### 3.8.3.1 Example 1: Ideal Waveguide

In this case, the slowness is constant,  $s(z) = s_0$  and the difference between the upper and lower boundaries is the waveguide thickness,  $z_u - z_l = D$ . The cycle distance and ray invariant are given by:

$$\Lambda = \frac{2D}{|\tan \theta_0|}, \quad \frac{d\Lambda}{d\theta_0} = -\frac{2D \operatorname{sign}(\theta_0)}{\sin^2 \theta_0}, \quad (3.249)$$

$$I_r = 2Ds_0 |\sin \theta_0|, \quad \frac{dI_r}{d\theta_0} = 2Ds_0 \cos \theta_0 \operatorname{sign}(\theta_0). \quad (3.250)$$

We then substitute into (3.248) to obtain

$$\beta^{-1} = \frac{1}{\cos^2 \theta_0}. \quad (3.251)$$

For a Pekeris waveguide associated with a shallow-water ocean environment, the grazing angles are typically small so that the waveguide invariant is approximately unity as already discussed in Sect. 2.4.6.

### 3.8.3.2 Example 2: $n^2$ -Linear Refracting Waveguide

Recall that the index of refraction is defined by  $n = c_0/c(z)$ , where  $c_0$  is a reference sound speed. An  $n^2$ -linear sound-speed profile is given by

$$s(z) = s_0 \sqrt{1 - az} \rightarrow s_v(z) = s_0 \sin \theta \sqrt{1 - az} = s_0 \sqrt{\sin^2 \theta_0 - az}, \quad (3.252)$$

where  $a$  is an arbitrary sound speed parameter and we have used Snell's law to derive the last equality. For simplicity, we take the “lower” ( $z$  is positive downward) boundary at  $z_l = 0$  from where we also launch the rays (by Snell's law, the results will be valid for any launch depth). For a launch angle of  $\theta_0$ , Snell's law provides the lower boundary where the vertical slowness is zero,  $z_u = (1/a) \sin^2 \theta_0$ . Then, from (3.239), we have

$$\Lambda = 2 \cos \theta_0 \int_{z_l}^{z_u} \frac{dz}{\sqrt{\sin^2 \theta_0 - az}} = \frac{2}{a} \cos \theta_0 |\sin \theta_0|, \quad (3.253)$$

so that

$$\frac{d\Lambda}{d\theta_0} = \frac{2}{a} \operatorname{sign}(\theta_0) (\cos^2 \theta_0 - \sin^2 \theta_0). \quad (3.254)$$

Next, we find the ray invariant from (3.245),

$$I_r = 2s_0 \int_{z_l}^{z_u} \sqrt{\sin^2 \theta_0 - az} dz = \frac{4s_0}{3a} |\sin^3 \theta_0|, \quad (3.255)$$

$$\frac{dI_r}{d\theta_0} = \frac{4s_0}{a} \sin^2 \theta_0 \cos \theta_0 \operatorname{sign}(\theta_0) \quad (3.256)$$

and by substituting these expressions into (3.248), we obtain

$$\beta^{-1} = -\frac{1}{3}(1 - \tan^2 \theta_0) \approx -\frac{1}{3}, \quad (3.257)$$

where the latter approximation is for small launch angles. The above result is also true for an  $n^2$ -linear profile symmetric about any depth without a reflecting surface since both the cycle time and the cycle distance would be doubled.

### 3.8.4 Hamiltonian Formulation of Ray Acoustics

One sometimes finds the Hamiltonian version of ray acoustics in the literature, particularly when studying perturbations about known solutions. First we recall that Fermat's principle is also referred to as the *Principle of Least Action* for which action is a quantity minimized by the actual trajectory, see (3.131). In a mechanical

**Table 3.1** Particle-ray analogy for Hamiltonian formulation. For Fermat’s principle,  $l$  is used as ray path length and  $s$  is slowness

Variable	Particle	Ray
Time $\leftrightarrow$ range	$t$	$r$
Space coordinate	$z$	$z$
Momentum, $p$	$mv$	$c_0 s_v$
Lagrangian, $L$	$KE - PE$	$c_o s = n$
Principle of Least Action, Fermat’s Principle	$\delta \int_{t_0}^{t_f} L dt = 0$	$\delta \int_{r_0}^{r_f} n dl = 0$
Hamiltonian, $H$	$KE + PE$	$-c_0 s_h = -\sqrt{n^2 - p^2}$
Action variable, $I$	$\frac{1}{2\pi} \oint p dz$	$\frac{1}{2\pi} \oint p dz = \frac{1}{2\pi} c_0 I_r$

The line integrals in the columns for the Principle of Least Action, Fermat Principle row is often called the “action,” as opposed to the “action variable” defined in the last row of the table. The particle Hamiltonian is the sum of kinetic and potential energy,  $KE + PE$ , and is a constant. The ray analogy to the Hamiltonian is the horizontal slowness which, by Snell’s law, is a constant for a ray path. The minus sign for the ray Hamiltonian is for consistency in Hamilton’s equations. As written, the ray momentum, Lagrangian, and Hamiltonian are dimensionless. Actually, note that the ray invariant is proportional to the action variable and that the “conjugate variable” to the action variable is an angle variable, see (3.261)

system the action is the path integral of the Lagrangian between two times. This leads to the ray analogy of the Lagrange equations of motion as per (3.134). A Legendre transformation of the Lagrangian yields the Hamiltonian which is a function of position and momentum coordinates. The ray analogy to momentum is a quantity proportional to the vertical slowness. To help the reader with the ray literature using the Hamiltonian formulation, we briefly summarize the relevant relations. Table 3.1 relates the ray variables in a range-independent waveguide to the quantities found in the Hamiltonian description [49, 50].

Hamilton’s equations, written in terms of  $r \equiv t, z$  and  $p$  are given by

$$\frac{dz}{dr} = \frac{\partial H}{\partial p}, \quad \frac{dp}{dr} = -\frac{\partial H}{\partial z}, \quad (3.258)$$

which, using Table 3.1 and the definitions in (3.28),  $s_h, s_v \equiv \xi, \zeta$ , gives,

$$\frac{dz}{dr} = -\frac{p}{H} = \frac{s_v}{s_h} = \frac{\zeta}{\xi}, \quad (3.259)$$

$$\frac{dp}{dr} = c_0 \frac{\partial s_h}{\partial z} = \frac{n (\partial n / \partial z)}{c_0 s_h},$$

$$\frac{d\xi}{dr} = -\frac{1}{\xi c^3} \frac{\partial c}{\partial z}, \quad (3.260)$$

which, in turn, are identical to the ray equations (3.98) and (3.100). Equation (3.99) is automatically satisfied by the Hamiltonian formulation for a range-independent environment since  $H$  is not a function of  $r$ , or, in terms of energy-conserving

particle motion,  $H$  is time independent. Note also the relation between the Hamiltonian and the action variable (as opposed to the action as per Fermat's principle) from Table 3.1 and (3.247),

$$\frac{dI}{dH} = \frac{2\pi}{\Lambda} \equiv \Omega(I) \quad (3.261)$$

the *rhs* being a spatial frequency. This leads to the usefulness of employing *action-angle coordinates* [50] without actually solving the ray equations. For the ray-particle analogy, the frequency of oscillations are constant when the Hamiltonian is not a function of time (or range for the ray case).

### 3.8.5 Three-Dimensional Ray Tracing

At the present, full three-dimensional ray tracing models are used much less frequently than 2-D versions. This is partly because the environmental information is more difficult to obtain and partly because the computational costs are much greater. The mathematical formulation is however fairly straightforward. In fact, our derivation for the 2-D case essentially covers the 3-D case at the same time. Written out explicitly the ray equations are

$$\frac{dx}{ds} = c \xi(s), \quad \frac{d\xi}{ds} = -\frac{1}{c^2} \frac{\partial c}{\partial x}, \quad (3.262)$$

$$\frac{dy}{ds} = c \eta(s), \quad \frac{d\eta}{ds} = -\frac{1}{c^2} \frac{\partial c}{\partial y}, \quad (3.263)$$

$$\frac{dz}{ds} = c \zeta(s), \quad \frac{d\zeta}{ds} = -\frac{1}{c^2} \frac{\partial c}{\partial z}. \quad (3.264)$$

These equations are solved with the initial conditions

$$\mathbf{x} = \mathbf{x}_0, \quad (3.265)$$

$$\frac{d\mathbf{x}}{ds} = (\cos \theta_0 \cos \varphi_0, \cos \theta_0 \sin \varphi_0, \sin \theta_0), \quad (3.266)$$

where  $\theta_0$  and  $\varphi_0$  are, respectively, the declination and azimuthal take-off angles of the ray as shown in Fig. 3.36.

The equations for the phase and amplitude along a ray retain the form

$$\tau(s) = \tau(0) + \int_0^s \frac{1}{c(s')} ds' \quad (3.267)$$

and

$$A_0(s) = A_0(0) \left| \frac{c(s) J(0)}{c(0) J(s)} \right|^{1/2}, \quad (3.268)$$

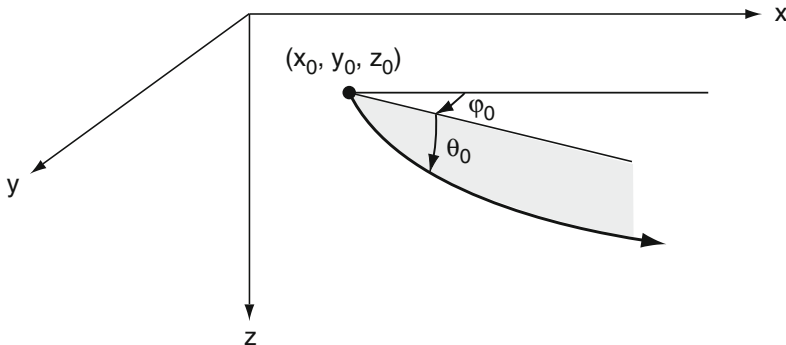


**Fig. 3.36** Schematic of 3-D ray geometry

with the Jacobian determinant given by

$$J = \left| \frac{\partial \mathbf{x}}{\partial(s, \theta_0, \varphi_0)} \right| = \begin{vmatrix} \frac{\partial x}{\partial s} & \frac{\partial x}{\partial \theta_0} & \frac{\partial x}{\partial \varphi_0} \\ \frac{\partial y}{\partial s} & \frac{\partial y}{\partial \theta_0} & \frac{\partial y}{\partial \varphi_0} \\ \frac{\partial z}{\partial s} & \frac{\partial z}{\partial \theta_0} & \frac{\partial z}{\partial \varphi_0} \end{vmatrix}. \quad (3.269)$$

This Jacobian can be calculated based on the area of three rays defining a ray tube or by integrating a modified form of the dynamic ray equations. As in the 2-D case, the various differential equations can be solved using standard integrators or by the cell method using  $n^2$ -linear or  $c$ -linear tetrahedrons (rather than triangles). The task of finding eigenrays becomes somewhat more complicated since the search now involves the two dimensions of declination angle and azimuthal angle.

The significance of 3-D effects is discussed more completely in Sect. 5.13 in the context of normal modes. In the case of long-range (global) propagation, 3-D effects can be very important. In such cases, the ray equations must also be altered to take into account the deviation of the Earth from a perfect sphere. Examples of 3-D ray and beam tracing may be found in [13, 51].

## Appendix 1: Recipe for Simple Ray Code

The easiest approach to writing a ray code is to use the direct integration method described in Sect. 3.7.1. As discussed in more detail there, the system of four coupled ordinary differential equations defining the rays, (3.23), are successively integrated using a simple Euler scheme. These ray equations are solved repeatedly using a sequence of different initial conditions corresponding to different ray take-off angles as given in (3.28). Improved efficiency is easily obtained using standard Runge–Kutta methods.

Depending on the sound-speed profile and the source position the ray trajectories may cycle within the ocean channel without striking the boundaries. However, eventually one will likely wish to account for surface and bottom reflections. To do this, we must find a means of interrupting the numerical solution of the ray equations when the ray just hits the boundary. The ray is then reflected as described in Sect. 3.6.3 and the numerical integrator is restarted from the boundary.

Terminating the integration of the ray equations precisely at the boundary is complicated if high-order sophisticated numerical integrators are used. Generally, an iterative scheme is used in which the step size is adjusted to provide precisely the right step. However, with simple integrators like Euler's method one can often solve directly for the appropriate step. This is discussed in Sect. 3.6.3.

Often this ray trace is the key product of interest from a ray model. The intensity along a ray is easily obtained by solving the dynamic ray equations as discussed in Sect. 3.3.5. The ray take-off angles are typically equally spaced yielding results on a complicated curvilinear grid. In contrast, the acoustic field is typically desired on a regular rectangular grid. This takes us beyond our stated goal of describing a *simple* ray model. One must either interpolate between the points on the ray grid or adjust the ray take-off angles so that they pass precisely through the receiver points. These options are discussed in Sect. 3.7.5.

## Appendix 2: A Useful Property of the Jacobian

In solving the transport equation, we used a relation for  $\tau$  in terms of the Jacobian given in (3.48). We shall prove this result for the two-dimensional case. The Jacobian is then defined as

$$J(s, \theta_0) = \frac{\partial x}{\partial s} \frac{\partial y}{\partial \theta_0} - \frac{\partial y}{\partial s} \frac{\partial x}{\partial \theta_0}. \quad (3.270)$$

Differentiating with respect to  $s$  we obtain

$$\frac{\partial J}{\partial s} = \frac{\partial^2 x}{\partial s^2} \frac{\partial y}{\partial \theta_0} + \frac{\partial^2 y}{\partial \theta_0 \partial s} \frac{\partial x}{\partial s} - \frac{\partial^2 y}{\partial s^2} \frac{\partial x}{\partial \theta_0} - \frac{\partial^2 x}{\partial \theta_0 \partial s} \frac{\partial y}{\partial s}. \quad (3.271)$$

Using the chain rule we can then write

$$\begin{aligned} \frac{\partial J}{\partial s} &= \left[ \frac{\partial}{\partial x} \left( \frac{\partial x}{\partial s} \right) \frac{\partial x}{\partial s} + \frac{\partial}{\partial y} \left( \frac{\partial x}{\partial s} \right) \frac{\partial y}{\partial s} \right] \frac{\partial y}{\partial \theta_0} \\ &\quad + \left[ \frac{\partial}{\partial x} \left( \frac{\partial y}{\partial s} \right) \frac{\partial x}{\partial \theta_0} + \frac{\partial}{\partial y} \left( \frac{\partial y}{\partial s} \right) \frac{\partial y}{\partial \theta_0} \right] \frac{\partial x}{\partial s} \\ &\quad - \left[ \frac{\partial}{\partial x} \left( \frac{\partial y}{\partial s} \right) \frac{\partial x}{\partial s} + \frac{\partial}{\partial y} \left( \frac{\partial y}{\partial s} \right) \frac{\partial y}{\partial s} \right] \frac{\partial x}{\partial \theta_0} \\ &\quad - \left[ \frac{\partial}{\partial x} \left( \frac{\partial x}{\partial s} \right) \frac{\partial x}{\partial \theta_0} + \frac{\partial}{\partial y} \left( \frac{\partial x}{\partial s} \right) \frac{\partial y}{\partial \theta_0} \right] \frac{\partial y}{\partial s}. \end{aligned} \quad (3.272)$$

Many of the terms in the above equation cancel yielding

$$\frac{\partial J}{\partial s} = \left[ \frac{\partial}{\partial x} \left( \frac{\partial x}{\partial s} \right) + \frac{\partial}{\partial y} \left( \frac{\partial y}{\partial s} \right) \right] \left( \frac{\partial x}{\partial s} \frac{\partial y}{\partial \theta_0} - \frac{\partial y}{\partial s} \frac{\partial x}{\partial \theta_0} \right). \quad (3.273)$$

The second term in parentheses is just the Jacobian determinant so we may rewrite the equation as

$$\frac{dJ}{ds} = \left( \nabla \cdot \frac{dx}{ds} \right) J. \quad (3.274)$$

Since there are no longer any derivatives with respect to  $\theta_0$  we have chosen to treat  $\theta_0$  as a parameter of  $J(s; \theta_0)$  and replace partial derivatives by ordinary derivatives. Now, by simply differentiating  $J/c$  we obtain

$$\frac{d}{ds} \left( \frac{J}{c} \right) = \frac{d}{ds} \left( \frac{1}{c} \right) J + \frac{1}{c} \frac{dJ}{ds}. \quad (3.275)$$

We next substitute the formula for  $dJ/ds$  given in (3.274) to obtain

$$\begin{aligned} \frac{d}{ds} \left( \frac{J}{c} \right) &= \left[ \frac{d}{ds} \left( \frac{1}{c} \right) + \frac{1}{c} \nabla \cdot \frac{dx}{ds} \right] J \\ &= \left[ \nabla \left( \frac{1}{c} \right) \cdot \frac{dx}{ds} + \frac{1}{c} \nabla \cdot \frac{dx}{ds} \right] J \\ &= \left[ \nabla \cdot \left( \frac{1}{c} \frac{dx}{ds} \right) \right] J. \end{aligned} \quad (3.276)$$

By definition  $dx/ds$  is related to the gradient of the phase  $\tau$  by (3.16) so that

$$\frac{d}{ds} \left( \frac{J}{c} \right) = (\nabla \cdot \nabla \tau) J. \quad (3.277)$$

Thus, we obtain the following simple relation between  $\tau$  and the Jacobian,

$$\nabla^2 \tau = \frac{1}{J} \frac{d}{ds} \left( \frac{J}{c} \right). \quad (3.278)$$

## Problems

**3.1.** Assume a deep ocean is represented by an infinite halfspace with a linear sound speed profile

$$c(z) = az + b, \quad a > 0.$$

A high-frequency source is radiating from a point  $(r, z) = (0, h)$ . Consider a ray emitted from the source at grazing angle  $\theta_0$ .

- a. Derive a parameter representation for the ray path before the first surface bounce,

$$r = r(\theta, \theta_0),$$

$$z = z(\theta, \theta_0),$$

where  $\theta$  is the local grazing angle for the ray.

- b. Show that the ray path describes a circular arc and that the center of the circle falls at a depth  $z = z_c$ , where  $z_c$  is independent of the launch angle  $\theta_0$ .
- c. Derive the expression for the range  $r_1(\theta_0)$ , where the ray launched at angle  $\theta_0$  bounces off the sea surface.
- d. Derive the parameter representation for the ray in the second ray cycle, i.e., after the first surface bounce.
- e. Derive the expression for  $dr/d\theta_0$  in the second ray cycle. Discuss the physical significance of the points where  $dr/d\theta_0 = 0$ .

### 3.2. An acoustic waveguide has the sound speed profile

$$c(z) = c_0 \cosh bz.$$

- a. Show that for a source at  $z = 0$ , all rays will refocus at ranges  $r = n\Delta r$ , where  $n$  is an integer and  $\Delta r$  is independent of the launch angle. State the expression for  $\Delta r$ .
- b. Discuss the physical significance of this phenomenon.
- c. Write a simple ray code to demonstrate the refocusing.
- d. Use your code to duplicate the result in Fig. 3.32.

### 3.3. Consider a source at depth $z_s = 2000$ m, range 0 and a receiver at depth $z_r = 4000$ m and range 2 km. Suppose that the sound speed depends only on depth, and that the values at the source and receiver depths are 1500 m/s and 1530 m/s, respectively.

- a. Use an  $n^2$ -linear approximation to estimate the travel time between source and receiver.
- b. If the receiver is moved farther out in range there comes a point where the eigen-ray is turned before reaching the receiver. At what range does this first happen?
- c. Is there a range where no real ray reaches the receiver? (Assume the water depth is infinite.)

### 3.4. Suppose we have a 500-Hz source launching a Gaussian beam in an isovelocity ocean with sound speed 1500 m/s.

- a. If the beamwidth and curvature at the source are 100 m and zero, respectively, what will the approximate beamwidth and curvature be 10 km away?
- b. Suppose we want the beam to be as narrow as possible at 10 km. What initial beamwidth and curvature will do this?
- c. Suppose the initial beam curvature has to be zero. What choice of the initial beamwidth will now give us the narrowest possible beam at 10 km?

**3.5.** A certain SSP has a sound speed of 1530 m/s at the surface, 1500 m/s at the source depth, 1550 m/s at the ocean bottom and 1800 m/s just below the bottom in the sediment. We will trace a fan of rays over angles  $[-\theta, +\theta]$ . How should we pick  $\theta$  to include:

- Only RR paths.
- Only RR and RSR paths.
- Only RR, RSR, and RSRBR paths striking the bottom with a grazing angle below the critical angle.

**3.6.** Show that the waveguide invariant for a waveguide defined by an upward-refracting, linear sound-speed profile,  $c(z) = c_0(1 + az)$ , and a perfectly reflecting upper boundary is given by

$$\beta^{-1} = \frac{|\sin \theta_0| - H}{|\sin^3 \theta_0|},$$

where

$$H = \ln \frac{1 + |\sin \theta_0|}{\cos \theta_0}.$$

Therefore, show that in the small launch angle limit, this waveguide invariant is the same as that of the  $n^2$ -linear profile.

## References

1. J.B. Keller, Rays, waves and asymptotics. *Bull. Am. Math. Soc.* **84**, 727–750 (1978)
2. H. Lichte, On the influence of horizontal temperature layers in seawater on the range of underwater sound signals. *Phys. Z.* **17**, 385–389 (1919). (translated by A.F. Wittenborn)
3. V. Červený, *Seismic Ray Theory* (Cambridge University Press, Cambridge, 2001)
4. F.D. Tappert, Theory of explosive beam spreading due to ray chaos. *J. Acoust. Soc. Am.* **114**, 2775–2781 (2003)
5. J. Vidale, Finite-difference calculation of traveltimes. *Bull. Seis. Soc. Am.* **78**, 2062–2076 (1988)
6. J.A. Sethian, Fast marching methods. *SIAM Rev.* **41**, 199–235 (1999)
7. S. Kim, R. Cook, 3D traveltimes computations using second-order ENO scheme. *Geophysics* **64**, 1867–1876 (1999)
8. W.-K. Jeong, R.T. Whitaker, A fast iterative method for eikonal equations. *SIAM J. Sci. Comput.* **30**, 2512–2534 (2008)
9. N. Bleistein, *Mathematical Methods for Wave Phenomena* (Academic, Orlando, FL, 1984)
10. V. Červený, Ray tracing algorithms in three-dimensional laterally varying layered structures. in *Seismic Tomography*, ed. by G. Nolet (Reidel, Boston, MA, 1987)
11. M.B. Porter, Y-C. Liu, Finite-Element Ray Tracing. in *Proceedings of the International Conference on Theoretical and Computational Acoustics*, ed. by D. Lee, M.H. Schultz (World Scientific, Singapore, 1994), pp. 947–956
12. H. Weinberg, R.E. Keenan, Gaussian ray bundles for modeling high-frequency propagation loss under shallow-water conditions. *J. Acoust. Soc. Am.* **100**, 1421–1431 (1996)
13. H.P. Bucker, A simple 3-D Gaussian beam sound propagation model for shallow water. *J. Acoust. Soc. Am.* **95**, 2437–2440 (1994)

14. D.S. Jones, High-frequency refraction and diffraction in general media. *Phil. Trans. R. Soc. Lond.* **255**, 341–387 (1963)
15. M.A. Pedersen, D.F. Gordon, Normal-mode and ray theory applied to underwater acoustic conditions of extreme downward refraction. *J. Acoust. Soc. Am.* **51**, 323–368 (1972)
16. Yu.A. Kravtsov, A modification of the geometrical optics method. *Radiofizika* **7**, 664–673 (1964)
17. Yu.A. Kravtsov, Asymptotic solutions of Maxwell's equations near a caustic. *Radiofizika* **7**, 1049–1056 (1964)
18. D. Ludwig, Uniform asymptotic expansion at a caustic. *Commun. Pure Appl. Math.* **19**, 215–250 (1966)
19. Yu.A. Kravtsov, Yu.I. Orlov, *Caustics, Catastrophes and Wave Fields*, 2nd edn. (Springer, New York, 1999)
20. T. Rekdal, B. Biondi, Ray methods in rough models. *Stanford Exploration Project Rep.* **80** (2001)
21. G.A. Deschamps, Gaussian beam as a bundle of complex rays. *Elect. Lett.* **7**, 1–2 (1971)
22. V. Červený, M.M. Popov, I. Pšenčík, Computation of wave fields in inhomogeneous media – Gaussian beam approach. *Geophys. J. R. Astron. Soc.* **70**, 109–128 (1982)
23. M.B. Porter, H.P. Bucker, Gaussian beam tracing for computing ocean acoustic fields. *J. Acoust. Soc. Am.* **82**, 1349–1359 (1987)
24. E.K. Westwood, P.J. Vidmar, Eigenray finding and time series simulation in a layered bottom. *J. Acoust. Soc. Am.* **81**, 912–924 (1987)
25. C.T. Tindle, G.E.J. Bold, Improved ray calculations in shallow water. *J. Acoust. Soc. Am.* **70**, 813–819 (1981)
26. E.L. Murphy, J.A. Davis, Modified ray theory for bounded media. *J. Acoust. Soc. Am.* **56**, 1747–1760 (1974)
27. V. Červený, I. Pšenčík, Gaussian beams in elastic 2-D laterally varying layered structures. *Geophys. J. R. Astron. Soc.* **78**, 65–91 (1984)
28. G. Muller, Efficient calculation of Gaussian-beam seismograms for two-dimensional inhomogeneous media. *Geophys. J. R. Astron. Soc.* **79**, 153–166 (1984)
29. R.W. McGirr, D.B. King, J.A. Davis, J. Campbell, An evaluation of range-dependent ray theory models. Rep. 115. Naval Ocean Research and Development Activity, Bay St. Louis, MS, 1985
30. T.L. Foreman, Ray modeling methods for range dependent ocean environments. Rep. TR-83-41. Applied Research Laboratories, Austin, TX, 1983
31. F.B. Hildebrand, *Advanced Calculus for Applications*, 2nd edn. (Prentice-Hall, Englewood Cliffs, NJ, 1976), pp. 360–361
32. W.H. Watson, R.W. McGirr, RAYWAVE II: A propagation loss model for the analysis of complex ocean environments. Rep. TN-1516. Naval Ocean Systems Center, San Diego, CA, 1975
33. J.B. Bowlin, J.L. Spiesberger, T.F. Duda, L.F. Freitag, Ocean acoustical ray-tracing software RAY. Rep. WHOI-93-10. Woods Hole Oceanographic Institution, Woods Hole, MA, 1992
34. J.J. Cornyn, GRASS: A digital-computer ray-tracing and transmission-loss-prediction system. Rep. 7621. Naval Research Laboratory, Washington, DC, 1973
35. B.G. Roberts, Horizontal-gradient acoustical ray-trace program TRIMAIN. Rep. 7827. Naval Research Laboratory, Washington, DC, 1974
36. C.B. Moler, L.P. Solomon, Use of splines and numerical integration in geometrical acoustics. *J. Acoust. Soc. Am.* **48**, 739–744 (1970)
37. M.A. Pedersen, Acoustic intensity anomalies introduced by constant velocity gradients. *J. Acoust. Soc. Am.* **33**, 465–474 (1961)
38. B.R. Julian, D. Gubbins, Three-dimensional seismic ray tracing. *J. Geophys.* **43**, 95–113 (1977)
39. H.B. Keller, P.J. Perozzi, Fast seismic ray tracing. *SIAM J. App. Math.* **43**, 981–992 (1983)
40. F.D. Tappert, D. Lee, H. Weinberg, The hybrid parabolic equation. in *Recent Progress in the Development and Application of the Parabolic Equation*, Rep. TD-7145. Naval Underwater Systems Center, New London, CT, 1984
41. K. Aki, P.G. Richards, *Quantitative Seismology: Theory and Methods* (Freeman, New York, 1980)

42. H.G. Schneider, Excess sound propagation loss in a stochastic environment. *J. Acoust. Soc. Am.* **62**, 871–877 (1977)
43. C.M. Bender, S.A. Orszag, *Advanced Mathematical Methods for Scientists and Engineers* (McGraw-Hill, New York, 1978)
44. M.G. Brown, Application of the WKBJ Green's function to acoustic propagation in horizontally stratified oceans. *J. Acoust. Soc. Am.* **71**, 1427–1432 (1982)
45. C.H. Chapman, *Fundamentals of Seismic Wave Propagation* (Cambridge University Press, Cambridge, 2004)
46. C.T. Tindle, G.B. Deane, Shallow water sound propagation with surface waves. *J. Acoust. Soc. Am.* **117**, 2783–2794 (2005)
47. P. Gerstoft, G.L. D'Spain, W.A. Kuperman, W.S. Hodgkiss, Calculating the waveguide invariant by ray-theoretic approaches. Rep. TM-468. Marine Physical Laboratory, San Diego, CA, 2001
48. L.M. Brekhovskikh, Yu. Lysanov, *Fundamentals of Ocean Acoustics*, 2nd edn. (Springer, Berlin, 1991)
49. L.D. Landau, E.M. Lifshitz, *Mechanics*, 3rd edn. (Pergamon, London, 1976)
50. A.L. Virovlyansky, Ray travel times at long ranges in acoustic waveguides. *J. Acoust. Soc. Am.* **113**, 2523–2532 (2003)
51. R.M. Jones, J.P. Riley, T.M. Georges, HARPO: A versatile three-dimensional Hamiltonian ray-tracing program for acoustic waves in an ocean with irregular bottom. U.S. Dept. of Commerce Rep. Environmental Research Laboratories, Boulder, CO, 1986

# Chapter 4

## Wavenumber Integration Techniques

### 4.1 Introduction

The wavenumber integration technique is basically a numerical implementation of the integral transform technique for horizontally stratified media described in Sect. 2.4.1. The field solution is in the form of a spectral (wavenumber) integral of solutions to the depth-separated wave equation. The normal mode approach described in the next chapter has the same mathematical basis but employs a different technique for evaluating the integral. Thus, the normal mode approach uses complex contour integration to reduce the integral representation to a sum of residues, whereas the wavenumber integration approach evaluates the integrals directly by numerical quadrature.

In underwater acoustics, wavenumber integration approaches are often called FFPs (Fast Field Programs) because of the use of Fast Fourier Transforms (FFTs) for evaluation of the spectral integrals in early implementations [1, 2]. However, many different quadrature schemes are used, and the term *wavenumber integration* is more accurate in terms of describing the approach. In seismology, the wavenumber integration methods are often referred to as *reflectivity* methods [3–6] or *discrete wavenumber* methods [7].

The principle of wavenumber integration for horizontally stratified media was introduced into underwater acoustics by Pekeris [8], who treated the problem of acoustic propagation in plane, layered waveguides using simple two and three-layer environmental models. Later, Jardetzky [9] and Ewing et al. [10] used the same technique to investigate seismic propagation in few-layer waveguides. The technique was to apply a series of integral transforms to the Helmholtz equation to reduce the original four-dimensional partial differential equation (three space dimensions and one time dimension) to a series of ordinary differential equations in the depth coordinate. These equations were then solved analytically within each layer in terms of unknown amplitudes which were determined by matching boundary conditions at the interfaces. The displacement and stress quantities were finally determined by evaluation of the inverse integral transforms.

For the few-layer cases originally presented, the linear system of equations in the unknown wavefield amplitudes expressing the boundary conditions, can easily be solved analytically. For more complicated environmental models, however, this procedure is inconvenient and must be replaced by a numerical approach.

Traditionally, the computation of the depth dependence of the field has been performed by means of propagator matrix methods as introduced by Thomson [11] and Haskell [12]. The propagator matrix approach has the computational advantage that it only requires a small amount of computer memory due to its recursive nature. However, it was realized quite early that special numerical treatment is required in order to ensure numerical stability, and several modified propagator matrix schemes have been proposed. In general, however, these have resulted in much more time-consuming codes. Further, the propagator technique is not well-suited to problems where the field has to be determined at more than a single receiver depth. A review of the propagator approaches is given by Kennett [6] who himself introduced the so-called invariant embedding formulation [4, 5], which has the interpretational advantage that arrivals resulting from reflections from a single interface can be isolated.

The propagator matrix approach has formed the basis of several application codes in both underwater acoustics [2] and seismology [3]. The so-called Fast Field Program developed by DiNapoli [1] applies an elegant recursive technique to determine the depth-dependent solution for many horizontal wavenumbers simultaneously, and is therefore extremely efficient. In contrast to the other techniques, however, the depth-dependent solution is approximate, and the technique is only applicable to a limited class of fluid problems.

More recently, Schmidt [13–15] developed a direct, global matrix approach which basically is a numerically stable implementation of the approaches of Pekeris [8] and Ewing, Jardetzky and Press [10]. Thus, the wavefield in each layer is simply represented by a superposition of the field produced by an arbitrary number of sources and an unknown field satisfying homogeneous wave equations. These unknown fields are then determined from the boundary conditions to be satisfied at all interfaces. The local boundary conditions at each interface are expressed as a linear system of equations in the Hankel transforms of the potentials in the adjacent layers. These *local* systems of equations are then assembled in a *global* system of equations expressing the boundary conditions at all interfaces. The numerical solution of the global system of equations then yields the field in all layers simultaneously.

Despite the common mathematical basis, there are a number of important differences between the various solution techniques, with each method having both advantages and disadvantages in terms of versatility and numerical stability. In the following, we describe all these approaches and point out the advantages and disadvantages. Moreover, Appendix 1 provides a recipe for implementing a simple wavenumber integration (FFP) code.

## 4.2 Mathematical Derivation

The wavenumber integration approach is applicable to *range independent* or *horizontally stratified* environments, as shown in Fig. 4.1. All interfaces are plane and parallel, and the layer properties are functions of depth only.

The wavenumber integration technique is based on the fact that for a horizontally stratified environment, it is possible to obtain exact integral representations for the field within each layer in terms of a set of unknown coefficients. These coefficients are found by matching the boundary conditions simultaneously at all interfaces, and the total field is determined by evaluation of the integral representations, as described in Sect. 2.4. However, the wavenumber integration approach is not restricted to stratifications of ideal, homogeneous fluid layers, but is straightforwardly extended to treat problems with depth-varying sound speed as well as elastic layers. In the following, we briefly summarize the basic principles of the integral transform approach described in Sect. 2.4, followed by a description of the integral representations for the various types of media that can be handled, as well as the appropriate boundary conditions the field must satisfy. The various numerical implementations of the wavenumber integration approach will be discussed subsequently.

### 4.2.1 Integral Transform Solution

For a source distribution along a vertical axis in a horizontally stratified environment, a cylindrical coordinate system  $(r, \varphi, z)$  is introduced, Fig. 4.1, with the  $z$ -axis passing through the sources, making the field independent of azimuthal angle  $\varphi$ . For the isotropic media considered here, the acoustic field with time dependence

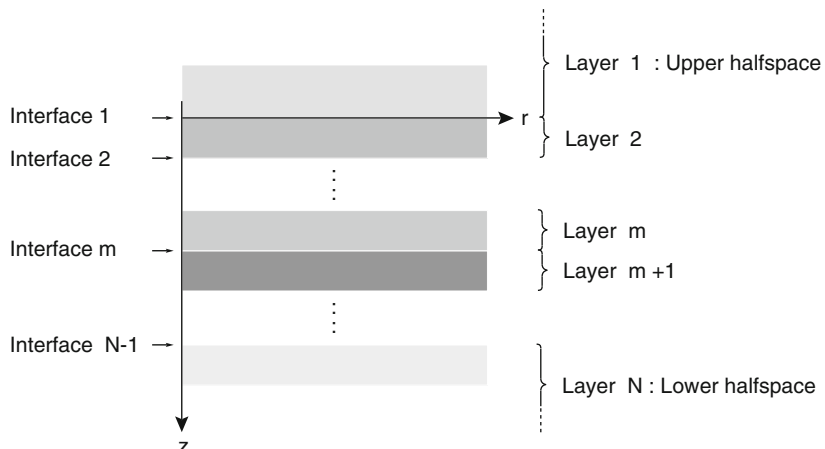


**Fig. 4.1** Horizontally stratified environment

$\exp(-i\omega t)$  in layer  $m$  containing the source can then be expressed in terms of scalar displacement potentials  $\psi_m(r, z)$ , which satisfy the Helmholtz equation,

$$[\nabla^2 + k_m^2(z)] \psi_m(r, z) = f_s(z, \omega) \frac{\delta(r)}{2\pi r}, \quad (4.1)$$

where  $k_m(z)$  is the medium wavenumber for layer  $m$ ,

$$k_m(z) = \frac{\omega}{c(z)}. \quad (4.2)$$

Similarly, for layers without sources the field must satisfy the homogeneous Helmholtz equation, i.e., (4.1) with  $f_s(z, \omega) = 0$ . Applying the forward Hankel transform, (2.95), to (4.1), we obtain the depth-separated wave equation,

$$\left[ \frac{d^2}{dz^2} - [k_r^2 - k_m^2(z)] \right] \psi_m(k_r, z) = \frac{f_s(z)}{2\pi} \quad (4.3)$$

i.e., an ordinary differential equation in depth. The solution is the sum of a particular solution  $\tilde{\psi}_m(k_r, z)$  to (4.3) and any linear combination of the two independent solutions  $\psi_m^+(k_r, z)$  and  $\psi_m^-(k_r, z)$  to the homogeneous equation.

The total solution for the depth-dependence of the field, the so-called *depth dependent Green's function*, is therefore

$$\psi_m(k_r, z) = \tilde{\psi}_m(k_r, z) + A_m^+(k_r) \psi_m^+(k_r, z) + A_m^-(k_r) \psi_m^-(k_r, z), \quad (4.4)$$

where  $A_m^+(k_r)$  and  $A_m^-(k_r)$  are arbitrary coefficients to be determined from the boundary conditions at the interfaces between the layers. The particular solution to (4.3) is most conveniently chosen to be the field produced by the sources in the absence of boundaries. When the unknown coefficients are found, the total field at the angular frequency  $\omega$  is found at any range  $r$  by evaluating the inverse Hankel transform, (2.94).

In most wavenumber integration implementations, the depth-dependence of  $k_m^2(z)$  is limited to cases where (4.3) can be solved analytically, limiting the numerical effort to the determination of the unknown coefficients  $A_m^+(k_r)$  and  $A_m^-(k_r)$  from the boundary conditions and to the evaluation of the inverse integral transforms. Alternatively, the depth-separated wave equations can be solved numerically, e.g., by finite differences. For computational reasons this is rarely done in wavenumber integration implementations. However, many normal mode implementations use this approach, thus eliminating the need for subdividing the environment into layers within which analytical solutions can be obtained. The finite difference approach is described in Chap. 5.

In the following, analytical field representations will be given for media for which the depth-separated equations can be solved in closed form, followed by a discussion of the boundary conditions to be satisfied at the interfaces between the various types of layers.

### 4.2.2 Homogeneous Fluid Layers

In a homogeneous, ideal fluid layer, the bulk modulus  $K$  and the density  $\rho$  are constant, corresponding to a constant sound speed,

$$c = \sqrt{\frac{K}{\rho}}. \quad (4.5)$$

The medium wavenumber  $k_m(z) = k_m = \omega/c$  is therefore constant as well. As described in Sect. 2.4, the homogeneous solutions to (4.3) are simply exponential functions,

$$\phi^+(k_r, z) = e^{ik_z z}, \quad (4.6)$$

$$\phi^-(k_r, z) = e^{-ik_z z}, \quad (4.7)$$

where  $\phi$  denotes a compressional or  $p$ -wave potential, and  $k_z$  is the vertical wavenumber,

$$k_z = \sqrt{k_m^2 - k_r^2}. \quad (4.8)$$

If no sources are present in the layer, the total field then follows directly from (2.94) as

$$\phi(r, z) = \int_0^\infty \left[ A^- e^{-ik_z z} + A^+ e^{ik_z z} \right] J_0(k_r r) k_r dk_r. \quad (4.9)$$

In physical terms, (4.9) is a decomposition of the total wavefield in upgoing,  $e^{-ik_z z}$ , and downgoing,  $e^{ik_z z}$ , conical waves with horizontal wavenumber  $k_r$ .

The boundary conditions for fluid layers – discussed in Sect. 4.2.5 – involve the vertical displacement  $w$  and the normal stress  $\sigma_{zz}$  ( $= -p$  in fluid media). The vertical displacement is

$$\begin{aligned} w(r, z) &= \frac{\partial \phi}{\partial z} \\ &= \int_0^\infty \left[ -ik_z A^- e^{-ik_z z} + ik_z A^+ e^{ik_z z} \right] J_0(k_r r) k_r dk_r, \end{aligned} \quad (4.10)$$

whereas the normal stress follows from the constitutive equation, or Hooke's law, (2.23),

$$\begin{aligned} \sigma_{zz}(r, z) &= K \nabla^2 \phi(r, z) \\ &= -\rho \omega^2 \phi(r, z) \\ &= -\rho \omega^2 \int_0^\infty \left[ A^- e^{-ik_z z} + A^+ e^{ik_z z} \right] J_0(k_r r) k_r dk_r. \end{aligned} \quad (4.11)$$

If a source is present in the layer, the particular solution to (4.3) has to be added. In the case of an omni-directional point source, the forcing term in (4.3) has the form

$$f_s(z, \omega) = S_\omega \delta(z - z_s), \quad (4.12)$$

where  $S_\omega$  is the source strength and  $z_s$  is the source depth. As shown in Sect. 2.4.2, the particular solution to (4.3) is then

$$\hat{\phi}(k_r, z) = \frac{S_\omega}{4\pi} \frac{e^{ik_z|z-z_s|}}{ik_z}, \quad (4.13)$$

whereas the corresponding source contribution to the total field follows from (2.94),

$$\hat{\phi}(r, z) = \frac{S_\omega}{4\pi} \int_0^\infty \frac{e^{ik_z|z-z_s|}}{ik_z} J_0(k_r r) k_r dk_r. \quad (4.14)$$

If more sources are present in the layer, their contributions are simply superimposed. The displacements and stresses are derived analogously to (4.10)–(4.11) and become

$$\hat{w}(r, z) = \frac{S_\omega}{4\pi} \int_0^\infty \text{sign}(z - z_s) e^{ik_z|z-z_s|} J_0(k_r r) k_r dk_r, \quad (4.15)$$

$$\hat{\sigma}_{zz}(r, z) = -\frac{S_\omega \rho \omega^2}{4\pi} \int_0^\infty \frac{e^{ik_z|z-z_s|}}{ik_z} J_0(k_r r) k_r dk_r. \quad (4.16)$$

### 4.2.3 $n^2$ -Linear Fluid Layers

Consider a fluid medium with constant density  $\rho$  and a depth variation of the medium wavenumber given by

$$k_m^2(z) = \omega^2(az + b) \quad (4.17)$$

corresponding to the index of refraction squared being linear. As described in Sect. 2.5.1, the homogeneous depth-separated wave equation for such a medium becomes

$$\left[ \frac{d^2}{dz^2} - [k_r^2 - \omega^2(az + b)] \right] \phi(k_r, z) = 0. \quad (4.18)$$

As shown in Sect. 2.5.1, independent solutions to this equation are

$$\phi^+(k_r, z) = \text{Ai}(\xi), \quad (4.19)$$

$$\phi^-(k_r, z) = \text{Ai}(\xi) - i \text{Bi}(\xi) \quad (4.20)$$

with

$$\zeta = (\omega^2 a)^{-2/3} [k_r^2 - \omega^2(az + b)]. \quad (4.21)$$

Note that we use a linear combination of the Airy functions as the second independent solution. In this way, the two independent solutions are those existing above and below a point source, as in (2.254). There are also computational reasons for this choice. The basic Airy functions  $\text{Ai}(\zeta)$  and  $\text{Bi}(\zeta)$  are theoretically independent, but for certain complex arguments they are numerically indistinguishable, leading to numerical stability problems when solving for the amplitudes. The solutions used here are always independent, even numerically.

The total field at angular frequency  $\omega$  is again obtained by evaluation of the inverse Hankel transform, (2.94),

$$\phi(r, z) = \int_0^\infty \{A^+ \text{Ai}(\zeta) + A^- [\text{Ai}(\zeta) - i\text{Bi}(\zeta)]\} J_0(k_r r) k_r dk_r \quad (4.22)$$

with the corresponding displacement and stress,

$$w(r, z) = -(\omega^2 a)^{1/3} \int_0^\infty \{A^+ \text{Ai}'(\zeta) + A^- [\text{Ai}'(\zeta) - i\text{Bi}'(\zeta)]\} J_0(k_r r) k_r dk_r, \quad (4.23)$$

$$\sigma_{zz}(r, z) = -\omega^2 \int_0^\infty \{A^+ \text{Ai}(\zeta) + A^- [\text{Ai}(\zeta) - i\text{Bi}(\zeta)]\} J_0(k_r r) k_r dk_r, \quad (4.24)$$

where a prime denotes the derivative with respect to the argument. The wavenumber kernel for a point source in a pseudo-linear layer is given in (2.254), yielding the source field

$$\begin{aligned} \hat{\phi}(r, z) = & -\frac{S_\omega}{4\pi} \int_0^\infty J_0(k_r r) k_r dk_r \\ & \times \begin{cases} \frac{2(\omega^2 a)^{-1/3} [\text{Ai}(\zeta_s) - i\text{Bi}(\zeta_s)] \text{Ai}(\zeta)}{\text{Ai}'(\zeta_s) [\text{Ai}(\zeta_s) - i\text{Bi}(\zeta_s)] - \text{Ai}(\zeta_s) [\text{Ai}'(\zeta_s) - i\text{Bi}'(\zeta_s)]}, & a(z - z_s) \leq 0 \\ \frac{2(\omega^2 a)^{-1/3} \text{Ai}(\zeta_s) [\text{Ai}(\zeta) - i\text{Bi}(\zeta)]}{\text{Ai}'(\zeta_s) [\text{Ai}(\zeta_s) - i\text{Bi}(\zeta_s)] - \text{Ai}(\zeta_s) [\text{Ai}'(\zeta_s) - i\text{Bi}'(\zeta_s)]}, & a(z - z_s) \geq 0. \end{cases} \end{aligned} \quad (4.25)$$

The corresponding stresses and displacements are derived as they are for the homogeneous case. As was the case for a source in a homogeneous layer, the kernel in the integral representation for  $\hat{\phi}(r, z)$  is continuous at the source depth, but the depth derivative is discontinuous.

#### 4.2.4 Homogeneous Elastic Layers

For a homogeneous, isotropic elastic solid with Lamé constants  $\lambda$  and  $\mu$ , and density  $\rho$ , it can be shown ([16], Chap. 2) that the equation of motion is satisfied if the displacements are expressed in terms of scalar potentials  $\{\phi, \psi\}$  as

$$u(r, z) = \frac{\partial}{\partial r} \phi(r, z) + \frac{\partial^2}{\partial r \partial z} \psi(r, z), \quad (4.26)$$

$$w(r, z) = \frac{\partial}{\partial z} \phi(r, z) - \frac{1}{r} \frac{\partial}{\partial r} r \frac{\partial}{\partial r} \psi(r, z), \quad (4.27)$$

where the potentials in the absence of sources satisfy the uncoupled, homogeneous Helmholtz equations,

$$[\nabla^2 + k_m^2] \phi(r, z) = 0, \quad (4.28)$$

$$[\nabla^2 + \kappa_m^2] \psi(r, z) = 0, \quad (4.29)$$

where  $k_m = \omega/c_p$  and  $\kappa_m = \omega/c_s$  are the wavenumbers corresponding to the compressional and shear velocities, respectively,

$$c_p = \sqrt{\frac{\lambda + 2\mu}{\rho}}, \quad (4.30)$$

$$c_s = \sqrt{\frac{\mu}{\rho}}. \quad (4.31)$$

Both equations are of the same form as (4.1) and can therefore be depth separated. As in the case of a homogeneous fluid, the constant wave speeds lead to simple exponential functions in depth, and the potentials therefore have the following integral representations for angular frequency  $\omega$ ,

$$\phi(r, z) = \int_0^\infty [A^- e^{-ik_z z} + A^+ e^{ik_z z}] J_0(k_r r) k_r dk_r, \quad (4.32)$$

$$\psi(r, z) = \int_0^\infty k_r^{-1} [B^- e^{-ik_z z} + B^+ e^{ik_z z}] J_0(k_r r) k_r dk_r \quad (4.33)$$

with the vertical wavenumbers

$$k_z = \sqrt{k_m^2 - k_r^2}, \quad (4.34)$$

$$\kappa_z = \sqrt{\kappa_m^2 - k_r^2}. \quad (4.35)$$

Since the expressions for the displacements in (4.26) and (4.27) involve one more spatial derivative of the shear potential than the compressional one, (4.33) has a factor  $k_r^{-1}$  stated explicitly, to make the dimension of the unknowns  $A^\pm$  and  $B^\pm$  identical. As will be discussed later, this is important to the numerical stability of the solution. Insertion of the integral representations for the potentials into (4.26)–(4.27) yields the following integral representations for the displacements,

$$u(r, z) = \int_0^\infty \left\{ -k_r A^- e^{-ik_z z} - k_r A^+ e^{ik_z z} + ik_z B^- e^{-ik_z z} - ik_z B^+ e^{ik_z z} \right\} J_1(k_r r) k_r dk_r, \quad (4.36)$$

$$w(r, z) = \int_0^\infty \left\{ -ik_z A^- e^{-ik_z z} + ik_z A^+ e^{ik_z z} + k_r B^- e^{-ik_z z} + k_r B^+ e^{ik_z z} \right\} J_0(k_r r) k_r dk_r \quad (4.37)$$

and the normal stress  $\sigma_{zz}$  and tangential stress  $\sigma_{rz}$  follow from Hooke's law,

$$\begin{aligned} \sigma_{zz}(r, z) &= (\lambda + 2\mu) \frac{\partial w}{\partial z} + \lambda \frac{\partial u}{\partial r} \\ &= \mu \int_0^\infty \left\{ (2k_r^2 - \kappa_m^2) [A^- e^{-ik_z z} + A^+ e^{ik_z z}] - 2ik_r \kappa_z [B^- e^{-ik_z z} - B^+ e^{ik_z z}] \right\} J_0(k_r r) k_r dk_r, \end{aligned} \quad (4.38)$$

$$\begin{aligned} \sigma_{rz}(r, z) &= \mu \left( \frac{\partial u}{\partial z} + \frac{\partial w}{\partial r} \right) \\ &= \mu \int_0^\infty \left\{ 2ik_r k_z [A^- e^{-ik_z z} - A^+ e^{ik_z z}] - (2k_r^2 - \kappa_m^2) [B^- e^{-ik_z z} + B^+ e^{ik_z z}] \right\} J_1(k_r r) k_r dk_r. \end{aligned} \quad (4.39)$$

In an elastic medium, integral representations for several types of sources can be derived, including point forces and force couples. A number of examples are given by Harkrider [17]. The compressional point source involves the compressional potential  $\phi$  only, with the integral representation

$$\hat{\phi}(r, z) = \frac{S_\omega}{4\pi} \int_0^\infty \frac{e^{ik_z |z-z_s|}}{ik_z} J_0(k_r r) k_r dk_r. \quad (4.40)$$

The corresponding displacement and stresses follow from (4.26) to (4.27) and Hooke's law,

$$\hat{u}(r, z) = -\frac{S_\omega}{4\pi} \int_0^\infty \frac{k_r e^{ik_z |z-z_s|}}{ik_z} J_1(k_r r) k_r dk_r, \quad (4.41)$$

$$\widehat{w}(r, z) = \frac{S_\omega}{4\pi} \int_0^\infty \text{sign}(z - z_s) e^{ik_z|z-z_s|} J_0(k_r r) k_r dk_r, \quad (4.42)$$

$$\widehat{\sigma}_{zz}(r, z) = \frac{S_\omega \mu}{4\pi} \int_0^\infty (2k_r^2 - \kappa_m^2) \frac{e^{ik_z|z-z_s|}}{ik_z} J_0(k_r r) k_r dk_r, \quad (4.43)$$

$$\widehat{\sigma}_{rz}(r, z) = -\frac{S_\omega \mu}{4\pi} \int_0^\infty 2k \text{sign}(z - z_s) e^{ik_z|z-z_s|} J_1(k_r r) k_r dk_r. \quad (4.44)$$

Another source often used in seismology is the vertical point force, which has the following integral representations for the potentials [10],

$$\widehat{\phi}(r, z) = -\frac{S_\omega}{4\pi} \int_0^\infty \text{sign}(z - z_s) e^{ik_z|z-z_s|} J_0(k_r r) k_r dk_r, \quad (4.45)$$

$$\widehat{\psi}(r, z) = \frac{S_\omega}{4\pi} \int_0^\infty \frac{e^{ik_z|z-z_s|}}{ik_z} J_0(k_r r) k_r dk_r. \quad (4.46)$$

Integral representations for the displacements and stresses are again obtained from (4.26) to (4.27) and Hooke's law, see [13].

#### 4.2.5 Boundary Conditions

The field at each interface now has two distinct integral representations, one from the layer above and one from the layer below. Depending on the type of interface, a certain set of boundary conditions must be satisfied.

- At a fluid–fluid interface, both the vertical displacement  $w$  and the normal stress  $\sigma_{zz}$  must be continuous. If one of the media is a vacuum, the normal stress  $\sigma_{zz}$  vanishes.
- At a fluid–solid interface, both  $w$  and  $\sigma_{zz}$  must be continuous while  $\sigma_{rz}$  vanishes. If the fluid layer is replaced by a vacuum, both  $\sigma_{zz}$  and  $\sigma_{rz}$  must vanish.
- At a “welded” interface between two solid media, all four parameters ( $w, u, \sigma_{zz}, \sigma_{rz}$ ) must be continuous.

Table 4.1 summarizes the boundary conditions for the different types of interfaces discussed above.

**Table 4.1** Boundary conditions (= continuous; 0 vanishing; – not involved)

Interface type	Field parameter			
	$w$	$u$	$\sigma_{zz}$	$\sigma_{rz}$
Fluid–vacuum	—	—	0	—
Fluid–fluid	=	—	=	—
Fluid–solid	=	—	=	0
Solid–vacuum	—	—	0	0
Solid–solid	=	=	=	=

Since the boundary conditions have to be satisfied at all ranges  $r$ , it is clear that they must be satisfied by the kernels in the integral representations as well. By imposing the appropriate interface conditions together with the radiation conditions for  $z \rightarrow \pm\infty$ , we obtain a linear system of equations in the unknown kernel coefficients  $A^+, A^-, B^+$  and  $B^-$ . In principle, this system has to be solved for all values of the horizontal wavenumber  $k_r$ , and the total field can then be determined by evaluating the inverse transforms. Except for a few trivial cases, however, both the solution of the linear system of equations and the evaluation of the inverse transforms must be done numerically, requiring truncation and discretization of the horizontal wavenumber axis.

The difference between the various numerical implementations concerns the method used for solving the linear system of equations in the unknown amplitudes and for the numerical evaluation of the inverse Hankel transform, (2.94). The various methods used for determining the depth-dependent solutions and carrying out the numerical integration will be discussed in Sects. 4.3 and 4.5, respectively.

#### 4.2.6 Attenuation

As described in Sect. 2.4.5, viscoelastic attenuation is included in wavenumber integration approaches by assuming the medium wavenumbers to be complex,

$$\tilde{k}_m = k_m(1 + i\delta_p), \quad \delta_p > 0. \quad (4.47)$$

with  $\delta_p$  being the *loss tangent* for acoustic waves in fluid layers and compressional waves in elastic media. Similarly for shear waves in elastic media, we have

$$\tilde{\kappa}_m = \kappa_m(1 + i\delta_s), \quad \delta_s > 0. \quad (4.48)$$

It has been experimentally observed [10, 18] that most elastic media have wave attenuations that increase linearly with frequency. Introducing the complex Lamé constants

$$\tilde{\lambda} = \lambda - i\lambda', \quad (4.49)$$

$$\tilde{\mu} = \mu - i\mu', \quad (4.50)$$

we find that the linear frequency dependence of attenuation requires that the ratios

$$\frac{\lambda' + 2\mu'}{\lambda + 2\mu} = \frac{1}{Q_p}, \quad (4.51)$$

$$\frac{\mu'}{\mu} = \frac{1}{Q_s} \quad (4.52)$$

be constant.  $Q_p$  and  $Q_s$  are called the *quality factors* for compression and shear, respectively. It is easily shown from the definition of the compressional and shear speeds that for small attenuations ( $Q$  large), the following relation exists between the loss tangent and the quality factor,

$$\delta = \frac{1}{2Q} \quad (4.53)$$

leading to the following relation between the attenuation  $\alpha$  in dB per wavelength and the quality factor,

$$\alpha = 40\pi \delta \log e \simeq \frac{27.29}{Q}. \quad (4.54)$$

Although the solution technique is valid for any value of the attenuations  $\alpha_p$  and  $\alpha_s$ , these have to be physically meaningful. Thus, it is required that a pure dilatation of an elastic medium does not produce energy. Therefore, the bulk modulus  $K = \lambda + \frac{2}{3}\mu$  must have a positive imaginary part, which is easily shown to require,

$$\frac{\alpha_s}{\alpha_p} = \frac{\delta_s}{\delta_p} < \frac{3}{4} \left( \frac{c_p}{c_s} \right)^2. \quad (4.55)$$

### 4.3 Numerical Solution of the Depth Equation

The numerical solution of the full wavefield problem divides naturally into three parts. Firstly, the depth-dependent Green's function is found at a discrete number of horizontal wavenumbers for the selected receiver depths. Secondly, the wavenumber integral, (2.94), is evaluated, yielding the transfer function at the selected depths and ranges. Finally, upon repetition of the first two steps at selected frequencies, the frequency integration, (2.27), can be performed to yield the total response in time.

It is clear that the three steps are not independent. In particular, the frequency and wavenumber sampling cannot be chosen arbitrarily, but is controlled by the numerical integration scheme used for evaluating the transforms. The frequency interval depends on the bandwidth of the source and the time window must be sufficiently large to contain the whole signal in order to avoid wrap-around, which again imposes requirements on the frequency sampling. Similarly, the wavenumber sampling must be capable of accurately integrating the often rapidly-varying and oscillating integrand in (2.94). Later in this chapter these numerical integration issues are discussed in detail.

Depending on the time–frequency and range–depth requirements, the evaluation of the depth-dependent Green's function may have to be performed a substantial number of times. The overall efficiency of the wavenumber integration approach is, therefore, closely related to the efficiency with which the depth equation is solved.

### 4.3.1 Direct Global Matrix Approach

The Direct Global Matrix (DGM) approach developed by Schmidt [13–15] is a numerically stable implementation of the original technique used by Pekeris [8] and Ewing et al. [10] for solving the depth-separated wave equation.

The DGM approach uses a *finite element* solution of the depth-separated wave equation, with each layer in the stratification being a finite element and with the unknown amplitudes of the homogeneous solutions within the layer being the degrees-of-freedom. Let  $A_m^-, A_m^+, B_m^-$ , and  $B_m^+$  be the amplitudes of the conical waves in layer number  $m$ . These amplitudes are conveniently collected in a *local* degree-of-freedom vector  $\mathbf{a}_m(k_r)$ , where  $k_r$  is the horizontal wavenumber,

$$\mathbf{a}_m(k_r) = \begin{Bmatrix} A_m^-(k_r) \\ B_m^-(k_r) \\ A_m^+(k_r) \\ B_m^+(k_r) \end{Bmatrix}, \quad m = 1, 2 \dots N. \quad (4.56)$$

If the kernels for the field parameters involved in the boundary conditions are expressed in vector form as

$$\mathbf{v}_m(k_r, z) = \begin{Bmatrix} w(k_r, z) \\ u(k_r, z) \\ \sigma_{zz}(k_r, z) \\ \sigma_{rz}(k_r, z) \end{Bmatrix}_m, \quad m = 1, 2 \dots N \quad (4.57)$$

the following matrix relation is obtained for the homogeneous part of the solution in layer  $m$ ,

$$\mathbf{v}_m(k_r, z) = \mathbf{c}_m(k_r, z) \mathbf{a}_m(k_r), \quad m = 1, 2 \dots N. \quad (4.58)$$

The local coefficient matrix  $\mathbf{c}_m(k_r, z)$  is a function of the horizontal wavenumber  $k_r$  and the depth  $z$ . For the homogeneous layers the depth appears in the exponential functions only, and in these cases the coefficient matrix can be factorized as

$$\mathbf{c}_m(k_r, z) = \mathbf{d}_m(k_r) \mathbf{e}_m(k_r, z), \quad (4.59)$$

where  $\mathbf{d}_m(k_r)$  is a depth-independent matrix containing only simple functions of  $k_r$ , and  $\mathbf{e}_m(k_r, z)$  is a diagonal matrix containing the exponentials.

The kernels for the source field  $\widehat{\mathbf{v}}_m(k, z)$  are now superimposed on the kernels for the homogeneous solution, and the continuity of the field parameters at interface number  $m$  separating the layers  $m$  and  $m + 1$  can then be expressed as

$$\mathbf{v}_m^m(k_r) + \widehat{\mathbf{v}}_m^m(k_r) = \mathbf{v}_{m+1}^m(k_r) + \widehat{\mathbf{v}}_{m+1}^m(k_r), \quad m = 1, 2 \dots N - 1, \quad (4.60)$$

where the depth  $z$  of the interface has been removed and replaced by a superscript indicating the interface number. If (4.60) is rewritten as

$$\mathbf{v}_m^m(k_r) - \mathbf{v}_{m+1}^m(k_r) = \widehat{\mathbf{v}}_{m+1}^m(k_r) - \widehat{\mathbf{v}}_m^m(k_r), \quad m = 1, 2 \dots N-1 \quad (4.61)$$

it expresses the cancellation of the discontinuity in the source field by the discontinuity in the homogeneous solution. The interface discontinuity vector  $\mathbf{v}^m(k_r)$  is, therefore, introduced as

$$\mathbf{v}^m(k_r) = \mathbf{v}_m^m(k_r) - \mathbf{v}_{m+1}^m(k_r), \quad m = 1, 2 \dots N-1 \quad (4.62)$$

and similarly for the source-field discontinuity vector  $\widehat{\mathbf{v}}^m(k_r)$ .

In order to assemble the local (4.61) into a global system, the *global* degree-of-freedom vector  $\mathbf{A}(k_r)$  in the up- and downgoing wavefield amplitudes is first introduced, defined by the unique local-to-global mapping

$$\mathbf{a}_m(k_r) = \mathbf{S}_m \mathbf{A}(k_r), \quad m = 1, 2 \dots N. \quad (4.63)$$

After insertion of (4.58) and (4.63), the discontinuity vector, (4.62), takes the form

$$\mathbf{v}^m(k_r) = [\mathbf{c}_m^m(k_r) \mathbf{S}_m - \mathbf{c}_{m+1}^m(k_r) \mathbf{S}_{m+1}] \mathbf{A}(k_r), \quad m = 1, 2 \dots N-1. \quad (4.64)$$

We now introduce a second unique mapping, collecting the local field discontinuity vectors  $\mathbf{v}^m(k_r)$  into one global discontinuity vector  $\mathbf{V}(k_r)$ ,

$$\mathbf{V}(k_r) = \sum_{m=1}^{N-1} \mathbf{T}^m \mathbf{v}^m(k_r), \quad (4.65)$$

which, after insertion of (4.64), becomes

$$\mathbf{V}(k_r) = \sum_{m=1}^{N-1} \mathbf{T}^m [\mathbf{c}_m^m(k_r) \mathbf{S}_m - \mathbf{c}_{m+1}^m(k_r) \mathbf{S}_{m+1}] \mathbf{A}(k_r). \quad (4.66)$$

Similarly, the global source-field discontinuity vector  $\widehat{\mathbf{V}}(k_r)$  is

$$\widehat{\mathbf{V}}(k_r) = \sum_{m=1}^{N-1} \mathbf{T}^m [\widehat{\mathbf{v}}_m^m(k_r) - \widehat{\mathbf{v}}_{m+1}^m(k_r)]. \quad (4.67)$$

The global cancellation of (4.66) by (4.67), therefore, requires the following linear system of equations to be satisfied,

$$\mathbf{C}(k_r) \mathbf{A}(k_r) = -\widehat{\mathbf{V}}(k_r), \quad (4.68)$$

where  $\mathbf{C}(k_r)$  is the global coefficient matrix,

$$\mathbf{C}(k_r) = \sum_{m=1}^{N-1} \mathbf{T}^m [\mathbf{c}_m^m(k_r) \mathbf{S}_m - \mathbf{c}_{m+1}^m(k_r) \mathbf{S}_{m+1}]. \quad (4.69)$$

The topology matrices  $\mathbf{S}_m$  and  $\mathbf{T}^m$  are extremely sparse, containing only zeroes and ones. Since the mappings of (4.63) and (4.65) are unique, the corresponding summations and matrix multiplications in (4.67) and (4.69) need never actually be performed, but can be replaced by a unique set of *pointers*, connecting the elements of the *local* systems with those of the *global* system, as illustrated in Fig. 4.2. As is the case in finite element programs, the topology matrices are therefore never set

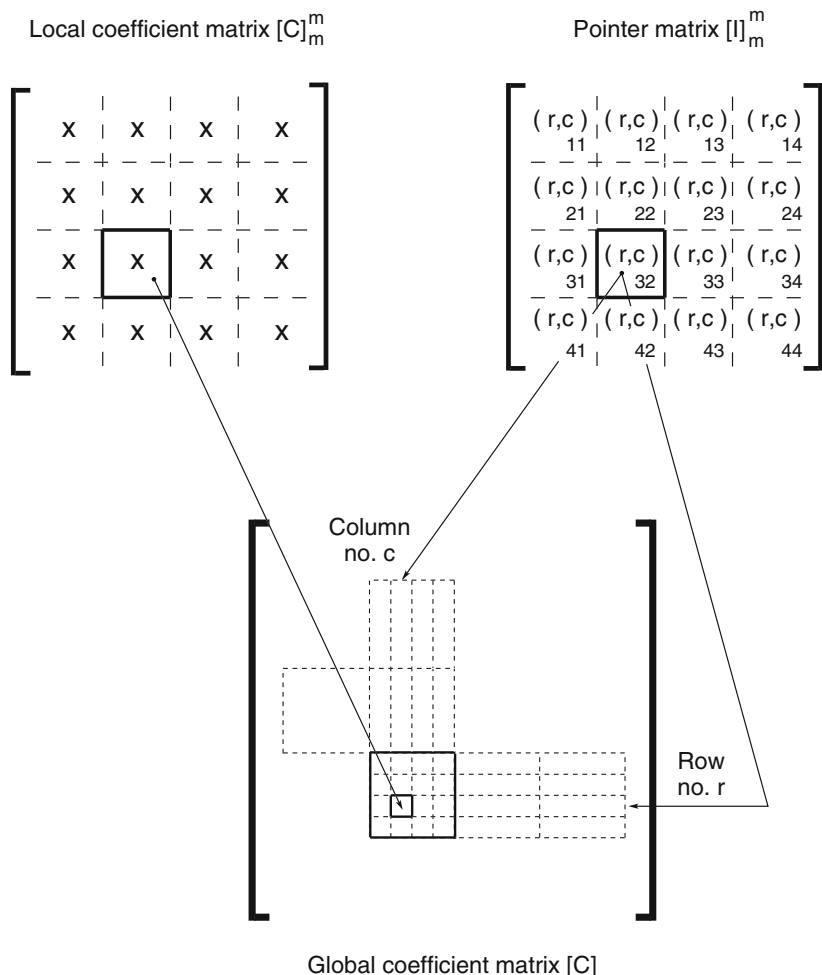


**Fig. 4.2** Mapping between local and global coefficient matrices by means of row and column pointers

up in the actual computer code. However, their formal use in (4.67) and (4.69) is very convenient in the general fluid–solid–vacuum case. The topology matrix  $\mathbf{S}_m$  is set up to include only the non-vanishing wavefield amplitudes, i.e., in the upper and lower halfspaces only those corresponding to upgoing ( $A^-, B^-$ ) and downgoing ( $A^+, B^+$ ) waves respectively, and in fluid media only  $A^-$  and  $A^+$ . Similarly,  $\mathbf{T}^m$  is set up to include only the actual number of boundary conditions at interface  $m$ , as described in Sect. 4.2.5. This ensures that the global coefficient matrix is a square matrix and reduces the total number of equations and unknowns compared to the purely elastic case.

The pointer indices defined by the mappings of (4.63) and (4.65) depend solely on the number of unknowns within each layer and the boundary conditions at each interface. They are, therefore, both frequency and wavenumber independent and can be determined a priori.

In this notation, the set-up of the global coefficient matrix requires only the calculation of the elements of the local coefficient matrices  $\mathbf{c}_m(k_r)$ , followed by the indexed move defined by the mappings, Fig. 4.2. The subsequent solution of (4.68) then yields the unknown wavefield amplitudes in all layers simultaneously.

#### 4.3.1.1 Numerical Stability

Although the global system of (4.68) is analytically well-conditioned, apart from poles corresponding to normal modes and seismic interface waves, its numerical solution is not necessarily stable. This important issue will be discussed here in some detail.

The difference in absolute dimension between the displacements and stresses can yield a difference of several orders of magnitude between the coefficients in the corresponding rows for both the local and global systems. As is well-known in such cases, simple Gaussian elimination, with or without partial pivoting, will not guarantee unconditional numerical stability. The coefficient matrices should therefore be scaled to make all elements physically dimensionless.

Although from a theoretical point of view the origin of the depth axis can be chosen arbitrarily, its choice is quite critical for numerical stability. First of all, a common origin for all layers is inconvenient due to the limited allowed arguments to the exponential functions. A local origin is therefore used for each layer, but this still does not ensure numerical stability for large layer thicknesses and large horizontal wavenumbers where the real parts of arguments to the exponential functions become large in *the evanescent regime*. For lossless cases the vertical wavenumber is purely imaginary in this regime,

$$k_z = i\gamma \quad (4.70)$$

with the two exponential solutions being

$$\phi_m^+(k_r, z) = e^{-\gamma z}, \quad (4.71)$$

$$\phi_m^-(k_r, z) = e^{+\gamma z} \quad (4.72)$$

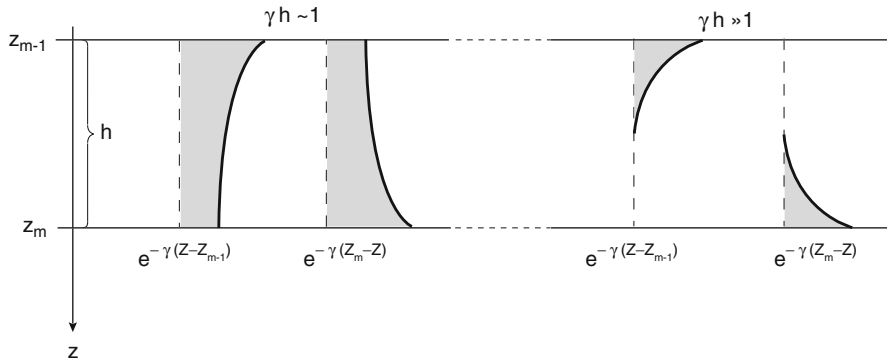


**Fig. 4.3** Physical significance of evanescent spectral components. In this regime the field is a superposition of two contributions, one decaying exponentially from the interface above, the other decaying exponentially from the interface below. For  $\gamma h \sim 1$ , the two components contribute throughout the layer. For  $\gamma h \gg 1$  the two components only contribute locally near the two interfaces

and similarly for the shear solutions in elastic layers. In these cases, argument overflow may of course occur, but this problem is easily eliminated by choosing the origin for the downward decaying field at the interface above the layer, and the origin of the upward decaying field at the lower boundary of the layer,

$$\phi_m^+(k_r, z) = e^{-\gamma(z-z_{m-1})}, \quad (4.73)$$

$$\phi_m^-(k_r, z) = e^{-\gamma(z_m-z)}. \quad (4.74)$$

This ensures that all layer exponentials have negative exponents in the evanescent regime.

The physical significance of the evanescent regime is illustrated in Fig. 4.3. If no sources are present in a layer the evanescent wavefield is a superposition of two exponentially decaying fields, one arising from a non-vanishing field at the interface above, the other from the interface below. Now assume that sources are only present above the actual layer. Then the field decaying away from the lower interface,  $\exp[-\gamma(z_m - z)]$ , can only be due to “reflection” from this interface of the field decaying away from the upper interface,  $\exp[-\gamma(z - z_{m-1})]$ . If, however, the layer is very thick or the horizontal wavenumber is large, i.e.,  $\gamma h \gg 1$ , the amplitude at the lower interface of the downward decaying field is insignificant, and the upward decaying field will be practically non-existent. In other words, the evanescent layer will behave exactly like an infinite halfspace in this part of the spectrum.

Therefore, in a computer with limited precision, the solution above the evanescent layer should be insensitive to the presence of the lower stratification once the relative difference between the coefficients at the two interfaces becomes smaller than the machine precision. However, if we force the global coefficient matrix to couple the solutions in the two domains, the coupling terms will not properly cancel due to the limited precision, which in turn causes numerical instability.

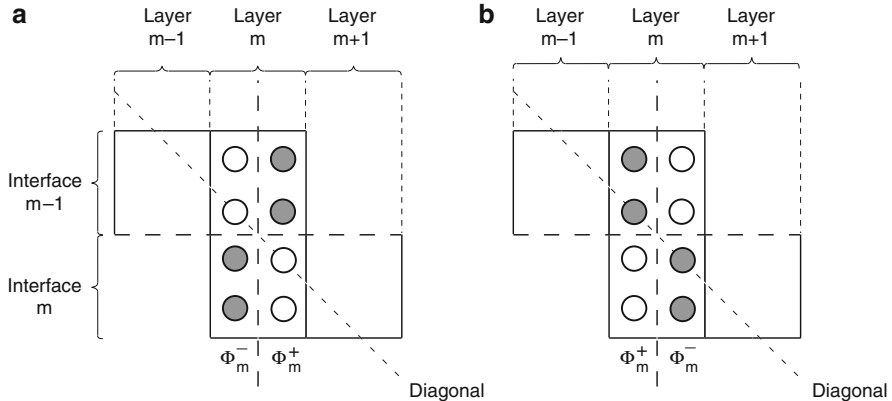


**Fig. 4.4** Mapping between local and global coefficient matrices: (a) Unstable mapping (b) Stable mapping

However, we can make the solution of the global system of equation *unconditionally stable*, simply by applying the knowledge about the physical uncoupling of the upper and lower stratifications in the evanescent regime. Thus, we can force the global system of equations to exhibit the same behavior at absolutely no additional computational cost by choosing a particular mapping between the local and global systems of equations. This is illustrated in Fig. 4.4, showing the two possible mappings for an intermediate fluid layer  $m$  in the extreme evanescent regime. With the present choice of local coordinate systems, (4.73) and (4.74), half of the coefficients in the coefficient matrices for layer  $m$  are small due to the large argument to the exponential functions, whereas the other half is of order one.

The mapping shown in Fig. 4.4a has the upward decaying components to the left and the downward decaying components to the right. When Gaussian elimination is applied to reduce the system to an upper triangular matrix, this mapping will couple the solutions above and below layer  $m$ , allowing truncation errors to propagate from the lower to the upper part and vice versa, thus, causing the solution to become numerically unstable. If, however, the two solutions are switched in the global system as shown in Fig. 4.4b, then the off-diagonal coefficients are numerically small: the global coefficient matrix is then divided into two numerically decoupled systems, one for the layering above layer  $m$  and one for the layering below, and both being well-conditioned. This mapping, therefore, totally eliminates the propagation of truncation errors across layer  $m$ , making this layer numerically equal to a halfspace in the evanescent regime, as seen both from above and below, in accordance with the physically correct behavior. The mapping shown in Fig. 4.4b is, therefore, unconditionally stable in the evanescent regime, and at absolutely no computational cost [13].

Concerning the pseudo-linear fluid layers described in Sect. 4.2.3, the two independent solutions  $A_i(\zeta)$  and  $A_i(\zeta) - iB_i(\zeta)$  exponentially decay and grow respectively for  $\zeta \rightarrow \infty$ . The stability in cases where these are involved is therefore

ensured in exactly the same way as described above, by normalizing the two solutions at the interface where they have the largest amplitude in this regime [13].

In summary, unconditionally stable solutions are obtained simply by choosing a proper local coordinate system and a proper local-to-global mapping in connection with Gaussian elimination with partial pivoting. The DGM solution technique is then unconditionally stable for any machine precision.

#### 4.3.1.2 Advantages and Disadvantages

When the global system of (4.68) has been solved, the kernels in the integral representations can be readily evaluated at any depth. The global matrix approach is, therefore, highly efficient in cases where the total wavefield is to be determined at many depths, e.g., for depth–range contouring of transmission loss and for simulation of vertical array responses. Another advantage is the fact that multiple sources can be treated simply by superimposing their contributions on the right side of (4.68). Therefore, the DGM approach is directly applicable to propagation problems involving beams generated by vertical arrays of sources, as will be demonstrated through a numerical example in Sect. 4.10.3. Since the basic solutions obtained by the DGM approach are the amplitudes of the up- and downgoing waves in each layer, the total solution is directly decomposed into these components. This feature is particularly important in the interpretation of propagation in an elastic bottom, where the total field is often a complicated interference of compressional and shear components.

The most important advantage of the DGM approach is, however, its unconditional stability, obtained at no additional computational cost, yielding a very efficient numerical solution of the depth-separated wave equation.

The memory requirement of the DGM approach is proportional to the number of layers, which causes practical limitations for the application of this solution technique on small computers without virtual memory. In cases where such computers are used to model environments with many layers, one of the alternative solution techniques described in the following should be used. Another disadvantage of the DGM approach is the relatively complicated coding necessary to establish the local-to-global mappings, and it is therefore more suited for general-purpose propagation models than for small, problem-dedicated user codes.

#### 4.3.2 Propagator Matrix Approach

Although the DGM approach is basically a direct numerical implementation of the original method of Pekeris [8] – a conceptually simple approach, representing the standard way of solving boundary-value problems in the spectral domain, this method was not pursued until the early 1980s. The reason was, first of all, that the DGM approach was believed to be inherently unstable (H.W. Kutschale, Private

communication 1983) for the reasons discussed earlier. Secondly, the computers available in the 1950s were very limited in terms of computational power and memory in particular. The early numerical solutions of the depth-separated wave equation performed by Thomson [11] and Haskell [12] therefore attempted to reduce both computational and memory requirements by developing the *propagator matrix* scheme for the solution. Since the original work of Thomson and Haskell, many modified versions of the propagator matrix approach have been developed, differing principally in the way they address the issue of numerical stability. Although the details vary among the implementations, the basic approach is the same.

Using the notation of the DGM solution, the vector of field parameters at interface  $m$ , bounding layer  $m$  below, is given by the matrix relation,

$$\mathbf{v}_m(k_r, z_m) = \mathbf{c}_m(k_r, z_m) \mathbf{a}_m(k_r), \quad (4.75)$$

where the vector  $\mathbf{v}_m(k_r, z_m)$  contains the displacements and stresses at interface  $m$ , and  $\mathbf{a}_m(k_r)$  is a vector containing the wavefield amplitudes in layer  $m$ , i.e.,  $A_m^-$ ,  $A_m^+$  for fluid layers and  $A_m^-$ ,  $A_m^+$ ,  $B_m^-$ ,  $B_m^+$  for elastic layers. Similarly, at the top interface,  $m - 1$ , of layer  $m$ ,

$$\mathbf{v}_m(k_r, z_{m-1}) = \mathbf{c}_m(k_r, z_{m-1}) \mathbf{a}_m(k_r). \quad (4.76)$$

We can now solve (4.75) for the wavefield amplitudes and insert the result in (4.76) to yield

$$\mathbf{v}_m(k_r, z_{m-1}) = \mathbf{P}_m(k_r) \mathbf{v}_m(k_r, z_m) \quad (4.77)$$

with  $\mathbf{P}_m$  being the *propagator matrix* for layer  $m$ ,

$$\mathbf{P}_m(k_r) = \mathbf{c}_m(k_r, z_{m-1}) [\mathbf{c}_m(k_r, z_m)]^{-1}. \quad (4.78)$$

Due to the small dimension of the local coefficient matrices, their inverses in (4.78) can be obtained in closed form, leading to closed-form expressions also for the coefficients of the propagator matrix. Using the continuity of the field parameters at the interfaces, (4.77) can now be used recursively to establish a matrix relation between the field parameters at some interface  $m$  and the parameters at a lower interface  $n$ ,

$$\mathbf{v}_m(k_r, z_m) = \mathbf{R}_n^m(k_r) \mathbf{v}_{n+1}(k_r, z_n) \quad (4.79)$$

with

$$\mathbf{R}_n^m(k_r) = \prod_{\ell=m+1}^n \mathbf{P}_\ell(k_r). \quad (4.80)$$

At the source depth  $z_s$  it is clear from the expressions for the kernels for the displacements and stresses given in Sect. 4.2, that some of these are continuous and some are discontinuous. Thus, for a source in a fluid medium, (4.15) and (4.16) imply that the normal stress or pressure kernel is continuous, and that the vertical displacement kernel is discontinuous, i.e.,

$$\begin{Bmatrix} \widehat{w}(k_r, z_s^-) \\ \widehat{\sigma}_{zz}(k_r, z_s^-) \end{Bmatrix} - \begin{Bmatrix} \widehat{w}(k_r, z_s^+) \\ \widehat{\sigma}_{zz}(k_r, z_s^+) \end{Bmatrix} = \begin{Bmatrix} -S_\omega/2\pi \\ 0 \end{Bmatrix} = \widehat{\mathbf{v}}(k_r, z_s). \quad (4.81)$$

We can now use (4.79) to “propagate” the solution from the lowermost interface to an artificial interface number  $s$  introduced at the source depth, add the discontinuity in the field parameters and continue to propagate the solution up to the uppermost interface, yielding

$$\mathbf{v}_1(k_r, z_1) = \mathbf{R}_s^1(k_r) [\mathbf{R}_{N-1}^s(k_r) \mathbf{v}_N(k_r, z_{N-1}) + \widehat{\mathbf{v}}(k_r, z_s)]. \quad (4.82)$$

For a purely fluid stratification, (4.82) provides two equations for the four unknown field parameters at the uppermost and lowermost interfaces in the stratification, or, for an elastic stratification, four equations in eight unknown field parameters. In either case, the boundary conditions at the uppermost and lowermost interfaces, or the radiation conditions in the limiting halfspaces, provide the necessary additional equations to determine the unknowns from (4.82). For example, at a free surface the pressure or normal stress must vanish,

$$\sigma_{zz}(k_r, z_1) = 0 \quad (4.83)$$

and in a lower fluid-bottom halfspace, the radiation condition requires the solution to be in terms of downgoing waves only, imposing the following impedance condition at the lowermost interface,

$$\sigma_{zz}(k_r, z_{N-1}) = -\frac{\rho_N \omega^2}{ik_{z,N}} w(k_r, z_{N-1}). \quad (4.84)$$

This condition follows directly from the form of the kernels of the integral representations given in (4.10) and (4.11).

The propagator matrix approach reduces the number of equations to be solved, from  $2(N - 1)$  in the DGM approach to just 2 in the purely fluid case, and from  $4(N - 1)$  to 4 in the elastic case. In addition, the coefficient matrices in (4.82) are determined by successive multiplication of small matrices. Consequently, the propagator matrix approach has insignificant memory requirements and is easily implemented on small computers.

In the propagator matrix approach the received field is determined by introducing a dummy interface at the receiver depth and then using the recurrence, (4.79), to determine the kernel at the receiver depth, once the field parameters are found at the lowermost interface from the solution of (4.82).

#### 4.3.2.1 Numerical Stability

In the preceding section, we described how the physical uncoupling of stratification above and below an evanescent layer introduces numerical instability unless the two regions are forced to uncouple numerically. Since the standard propagator

matrix approach couples the field at the lowermost and uppermost interfaces in the stratification, it is not surprising that this approach encounters numerical instability problems of the same nature.

Let layer  $m$  be an isovelocity fluid of thickness  $h_m$ . Inserting (4.59) into (4.78) then yields the following propagator matrix,

$$\mathbf{P}_m(k_r) = \mathbf{d}_m(k_r) \mathbf{e}_m(k_r, z_{m-1}) [\mathbf{e}_m(k_r, z_m)]^{-1} [\mathbf{d}_m(k_r)]^{-1}, \quad (4.85)$$

where the product of the two diagonal matrices including the exponentials are easily shown to be

$$\mathbf{e}_m(k_r, z_{m-1}) [\mathbf{e}_m(k_r, z_m)]^{-1} = \begin{bmatrix} e^{-ik_{z,m}h_m} & 0 \\ 0 & e^{ik_{z,m}h_m} \end{bmatrix}. \quad (4.86)$$

For wavenumbers where the field in layer  $m$  is evanescent, one of the exponentials in (4.86) becomes large and the other small. The terms involving the growing exponentials will theoretically cancel in (4.82), but due to the limited machine precision this will not be the case numerically. Truncation errors may therefore magnify significantly across this layer in the evanescent regime, in turn yielding unstable solutions to (4.82).

Several approaches have been applied to re-establish numerical stability in this regime, basically factorizing out the growing exponentials. Examples of such approaches are those of Gilbert and Backus [19], and Franssens [20]. However, the additional computational effort involved is significant. For example, Franssens' approach leads to  $6 \times 6$  propagators for elastic layers instead of the standard  $4 \times 4$ , thus more than doubling the computational effort.

#### 4.3.2.2 Advantages and Disadvantages

A major advantage of the propagator matrix approach over the DGM is the relative ease with which it is implemented. Only few lines of code are needed to complete the computation of the propagator matrices and the recursion in (4.82), and the solution of these few equations do not require particular numerical considerations.

Although the resulting system of equations is small, the computations are not more efficient than in the DGM approach. This is due to several factors. First of all, the simple propagator matrix formulation in (4.82) is not unconditionally stable as discussed above. In addition, in the common ocean-acoustic case of mixed fluid and elastic layers, the propagator matrices must be of the same dimension for all layers. Therefore, in these cases a  $4 \times 4$  propagator must be used also for fluid layers. These modified fluid propagator matrices are described by Kutschale [2], but basically they are derived as limits of the elastic propagators for the shear speed approaching zero. As a result, the recursion in (4.79) will involve a large number of zero multiplications for standard ocean-acoustic problems. In contrast, the DGM approach requires only  $2 \times 2$  coefficient matrices for fluid layers, independent of whether the stratification involves elastic layers or not.

Finally, while the DGM approach solves for the field everywhere in the stratification yielding the field for multiple receivers in depth at minimal computational cost, the propagator matrix approach requires the addition of a dummy interface at every receiver depth. Consequently, the computation time is proportional to the sum of the number of layers and the number of receivers, whereas that of the DGM approach is proportional to the number of layers only. For the same reason, multiple sources are not treated efficiently by the propagator matrix approach.

### 4.3.3 Invariant Embedding Approach

The problem of solving the wave equation in horizontally stratified media is common to ocean acoustics and seismology. However, the nature of the problems are quite different. Thus, in ocean acoustics, the field is often required over the entire water depth, and the bottom is important only in terms of its reflectivity. In seismology, on the other hand, source and receivers are usually confined to the surface of the solid earth or at shallow depths in the ocean, and the purpose of experiments and modeling is to image the properties of the layers within the crust. Therefore, surface effects at the seabed associated with reflection and interface waves as well as ocean waveguide effects such as modes, are usually considered disturbances and of no interest to the seismic problem. In contrast, these are the wave effects of importance to the underwater acoustician.

Due to this different focus, it is natural that the development of solution techniques has taken different routes in the two fields over the past decades. Thus, for the global solutions required in underwater acoustics, the DGM approach described earlier is the dominant solution technique today; the seismic field, with its emphasis on body-wave propagation within the crust, generally favors the *invariant embedding* approach of Kennett et al. [4, 5].

Although the many different implementations of the invariant embedding approach are for elastic stratifications only, the basic principle is most easily demonstrated for a fluid stratification. Here, the invariant embedding solution is basically a numerical implementation of the technique described in Sects. 1.5.3 and 1.5.4. Thus, the reflection coefficient  $\mathcal{R}_m$  for a plane wave incident from above on interface  $m - 1$ , bounding layer  $m$  above, is given in terms of the local reflection coefficients as

$$\mathcal{R}_m = \frac{\mathcal{R}_{m-1,m} + \mathcal{R}_{m,m+1} \exp(2ik_{z,m}h_m)}{1 + \mathcal{R}_{m-1,m} \mathcal{R}_{m,m+1} \exp(2ik_{z,m}h_m)}, \quad (4.87)$$

where  $h_m$  is the thickness of layer  $m$ .  $\mathcal{R}_{m-1,m}$  is the local reflection coefficient at interface  $m$ , assuming that layers  $m - 1$  and  $m$  are halfspaces. Similarly,  $\mathcal{R}_{m,m+1}$  is the reflection coefficient for the lower interface  $m + 1$ . However, there are no assumptions concerning layer  $m + 1$  being a halfspace, and we can therefore replace

the halfspace reflection coefficient  $\mathcal{R}_{m,m+1}$  by the total reflection coefficient  $\mathcal{R}_{m+1}$  to yield the recurrence relation for the total reflection coefficient,

$$\mathcal{R}_m = \frac{\mathcal{R}_{m-1,m} + \mathcal{R}_{m+1} \exp(2ik_{z,m}h_m)}{1 + \mathcal{R}_{m-1,m} \mathcal{R}_{m+1} \exp(2ik_{z,m}h_m)}. \quad (4.88)$$

The reflection coefficient  $\mathcal{R}_N$  at the lowermost interface  $N - 1$ , is given by (2.127), and we can now use the recurrence relation, (4.88), to determine the resulting reflection coefficient at any interface in the stratification. The fact that the recurrence in (4.88) is *invariant* to the layering below the actual layer is the reason for assigning the name *invariant embedding* to this solution technique.

As mentioned earlier, in reflection and refraction seismology the surface multiples are of minor interest, and the modeling has therefore traditionally eliminated such effects by using the so-called *reflectivity method* [3], which replaces the uppermost layer by a halfspace, and propagates the field without reflections from the source down to an interface, below which – *the reflectivity zone* – all multiples are included. The resulting reflection from the reflectivity zone is then propagated up to the receivers. The reflectivity zone is totally described by the reflection coefficient of the layered halfspace representing it, and here the invariant embedding approach is obviously a natural choice as the solution technique.

#### 4.3.3.1 Numerical Stability

It is clear from the form of the recurrence relation, (4.88), that the invariant embedding approach does not have stability problems similar to those of the traditional propagator matrix approach. Thus, for a thick layer in the evanescent regime, the exponentials in (4.88) will have negative real arguments, and when the relative magnitude of the exponentials is smaller than the machine precision, the recurrence relation will be numerically equivalent to the simple form

$$\mathcal{R}_m \simeq \mathcal{R}_{m-1,m}, \quad (4.89)$$

which is the reflection coefficient for layer  $m$  being a halfspace. The invariant embedding approach is, therefore, inherently consistent with the physical uncoupling of the upper and lower stratification in the evanescent regime for layer  $m$ , eliminating numerical stability problems in this regime.

#### 4.3.3.2 Advantages and Disadvantages

The advantages of the invariant embedding approach are the inherent numerical stability, the simplicity of the recurrence algorithms and the direct suitability for reflectivity modeling. In addition, invariant embedding has definite interpretational

advantages for crustal seismology in particular. This is due to the fact that the recurrence for layer  $m$  has the alternate form, (1.66),

$$\begin{aligned}\mathcal{R}_m &= \mathcal{R}_{m-1,m} + \mathcal{R}_{m+1} (1 - \mathcal{R}_{m-1,m}^2) \exp(2ik_{z,m}h_m) \\ &\quad \times \sum_{n=0}^{\infty} [\mathcal{R}_{m+1} \mathcal{R}_{m,m-1} \exp(2ik_{z,m}h_m)]^n.\end{aligned}\quad (4.90)$$

In this form, the summation represents the contributions from the various multiples within layer  $m$ , and the recurrence can therefore be tailored to include only a particular multiple. This feature is very important for the interpretation of seismic reflection and refraction data, where the origin of individual arrivals is usually far from obvious.

Invariant embedding is not well-suited to the solutions of the global problem of interest in ocean acoustics and borehole seismology, where sources and receivers are within the layering. Here, the total field is a superposition of reflections from the layering below as well as above the source, and for sources and receivers in different layers, the transmission recurrence must be included as well. Although it is possible to develop an invariant embedding scheme for such problems, the book-keeping becomes very complex, and only a few attempts have been made to use this method for the global problem. One of the few examples is the work of Stephen [21], who developed a modified invariant-embedding reflectivity method allowing for receivers within the layering of the reflectivity zone, but still requiring the source to be in an upper halfspace.

Although a hybridization of the DGM and invariant embedding is possible, no attempts so far have been made to develop such a model. This is because the computational effort involved in the two methods is similar, making it more convenient to use one or the other, depending on the nature of the propagation problem. On the other hand, such a hybrid method could have some advantages, in particular for problems in marine seismology.

## 4.4 Reflection Coefficients

The determination of plane-wave reflection coefficients of a stratified halfspace is of great interest in both underwater acoustics and seismology for several reasons: It is required as input to the widespread ray-tracing codes and it forms the basis of the synthetic reflectivity seismograms commonly used in crustal seismology [15]. Furthermore, plane-wave reflection coefficients are often used as input to geoacoustic inversion schemes.

The wavenumber integration technique is based on a decomposition of the total wavefield into conical waves for a cylindrical propagation geometry and into plane waves for a plane Cartesian propagation geometry. Here, we have given the field representations in cylindrical geometry, but the similar plane-geometry representations

are obtained simply by replacing the Hankel transform with the Fourier transform; the kernels are identical in the two cases as described in Chap. 2. The relation between the horizontal wavenumber and the grazing angle of propagation  $\theta$  for a homogeneous layer is

$$k_r = k_m \cos \theta, \quad (4.91)$$

where the medium wavenumber  $k_m$  may correspond to compressional or shear waves. As can be observed, only wavenumbers  $k_r \leq k_m$  correspond to real angles.

The plane-wave reflection coefficient  $\mathcal{R}(\theta)$  for a wave incident from above at angle  $\theta$  on a certain interface is straightforwardly found by one of the above techniques for solving the depth-separated wave equation.

The reflection coefficient is obviously most directly determined by *invariant embedding*, but the other methods are applicable as well. For example, in the DGM approach let the layer above the interface be replaced by an infinite half-space and the source field be a plane wave incident at angle  $\theta$  and amplitude  $A^-(k_r) = A^-(k_m \cos \theta)$  at the interface. The solution of the global system of equations for this new layered problem will directly yield the complex amplitude of the reflected plane wave  $A^+(k_r) = A^+(k_m \cos \theta)$ , and the reflection coefficient is simply,

$$\mathcal{R}(\theta) = \frac{A^+(k_m \cos \theta)}{A^-(k_m \cos \theta)}. \quad (4.92)$$

Both incident and reflected waves may, of course, in general be either compressional or shear waves. Since the solution of the depth-separated wave equation is exact to within machine accuracy, the same is the case for the reflection coefficients, i.e., there are no approximations except for the environmental model.

It should be pointed out that the reflection coefficients calculated in this way are for *true plane waves*. Plane-wave reflection coefficients are difficult to determine experimentally [22], which should be kept in mind when comparing synthetic and experimental reflection data.

## 4.5 Wavenumber Integration

Integral transform techniques such as wavenumber integration are important modeling approaches in all disciplines dealing with wave propagation in plane stratified media, such as crustal and exploration seismology, electromagnetics, and, of course, underwater acoustics.

To determine the acoustic or seismic field parameters at a particular receiver range  $r$  and depth  $z$ , we must numerically evaluate the inverse Hankel transform of the solution to the depth-separated wave equation at depth  $z$ ,

$$g(r, z) = \int_0^\infty g(k_r, z) J_m(k_r r) k_r dk_r, \quad (4.93)$$

where  $g(r, z)$  represents the field parameter of interest, e.g., acoustic pressure, or a particular displacement or stress component. The function  $g(k_r, z)$  is the associated wavenumber kernel. The order of the Bessel function is  $m = 0$ , except for the horizontal displacement and shear stress where  $m = 1$ , given in (4.36) and (4.39). The numerical evaluation of this integral is complicated by the following features, which must be considered when choosing an integration technique:

- The *infinite* integration interval.
- The *wavenumber discretization* giving rise to *aliasing* and *wrap-around* problems because of the oscillatory nature of the Bessel function, and the variation of the kernel  $g(k_r, z)$  which, for waveguide problems, has poles on or close to the real wavenumber axis.

While the issues associated with the solution of the depth-separated wave equation (e.g. numerical stability), and therefore the solution techniques, are universal, the evaluation of the wavenumber integral in general is performed differently, depending on the application and the underlying physics. Thus, e.g., exploration and crustal seismology typically deal with predominantly steep propagation angles because of the relatively short horizontal distance between the sources and a horizontal receiver array on the surface or in the water column. Also, for modeling a vertical borehole receiver array, the vertical and horizontal propagation scale are comparable, leading to propagation angles much steeper than those of significance to ocean acoustics. Consequently, the response is dominated by reflection and refraction at individual interfaces, with the reflectivity being the property of interest for the environmental characterization. Thus, modal propagation is in general insignificant and is often ignored in the modeling, e.g. by removing the surface of the ocean. In the absence of modal singularities only the relatively smooth *continuous spectrum* remains, which is much less susceptible to discretization problems. Further, with the field required at only a few receivers, the integration, and the associated sampling of the kernel, and therefore the solution of the depth-separated wave equation, may be performed individually. Thus, the accuracy can be managed by traditional *convergence analysis* by uniform sampling refinement, or by modern *adaptive integration* techniques, as described later.

In contrast, modeling in underwater acoustics has typically been aimed at predicting the transmission loss over very large horizontal distances, typically 2–3 orders of magnitude larger than the vertical scales of the ocean and the seabed. As a result, the shallow, subcritical propagation angles dominate, with a modal propagation pattern typically dominating beyond ranges of about 10 water depths. Therefore the underwater acoustics propagation is a true *waveguide* problem with dominance of the *discrete spectrum*, and the *continuous spectrum* is significant only at very low frequencies and short ranges. In addition, for passive sonar applications the transmission loss is needed for the entire range interval, and the number of receivers is therefore in general very large. For computational reasons the sampling of the wavenumber kernels, and therefore the solution of the depth equations, are performed on a common frequency–wavenumber grid for all receivers. As a consequence, the accuracy must be ensured more generically than in the seismic problem.

In modern underwater acoustics the role of transmission loss remains important, but new signal processing techniques such as Matched Field Processing (Sect. 10.6), require efficient models that provide field estimates on discrete horizontal or vertical arrays, including both magnitude and phase. Also, for active sonar systems, modern computer technology has made possible the full time-domain simulation of noise, target scattering, and reverberation for specific sonar scenarios. Therefore, the integration techniques applied to similar seismic problems have been adapted also to underwater-acoustic modeling frameworks.

In the following, we first describe the classical FFT-based integration schemes that allow for very efficient evaluation of the acoustic field at a large number of receiver ranges. The FFT technique is also well-suited to illustrate the *discretization problem* because of the direct analogy to periodic solutions of cylindrical problems. Then the more direct numerical integration schemes based on either fixed or adaptively-determined wavenumber sampling will be described.

#### 4.5.1 Fast Field Approximation

It has been shown that except for ranges shorter than a few wavelengths and very steep propagation angles, accurate evaluation of the inverse Hankel transform, (4.93), can be obtained by the so-called FFP (Fast Field Program) integration technique introduced by DiNapoli and Deavenport [1].

First the Bessel function is expressed in terms of Hankel functions,

$$J_m(k_r r) = \frac{1}{2} \left[ H_m^{(1)}(k_r r) + H_m^{(2)}(k_r r) \right]. \quad (4.94)$$

With the present choice of the time–frequency transform,  $H_m^{(1)}$  corresponds to outgoing waves and  $H_m^{(2)}$  to incoming waves. This latter term is important only for representing the standing wavefield at very short ranges and is therefore neglected. Next, we replace  $H_m^{(1)}(k_r r)$  by its asymptotic form [23],

$$\lim_{k_r r \rightarrow \infty} H_m^{(1)}(k_r r) = \sqrt{\frac{2}{\pi k_r r}} e^{i[k_r r - (m + \frac{1}{2})\frac{\pi}{2}]} \quad (4.95)$$

to arrive at the following expression for the inverse Hankel transform,

$$g(r, z) \simeq \sqrt{\frac{1}{2\pi r}} e^{-i(m + \frac{1}{2})\frac{\pi}{2}} \int_0^\infty g(k_r, z) \sqrt{k_r} e^{ik_r r} dk_r. \quad (4.96)$$

The approximation of (4.93) by (4.96) has not removed any of the complications concerning the integration interval or the oscillatory nature of the integrand. However, the exponential function is more suitable for numerical integration than the

Bessel function, particularly in terms of computation time. Since the numerical implementations used in underwater acoustics are almost without exception based on the fast-field approximation, we will focus on the evaluation of this integral in the following. It should be pointed out, however, that the truncation and sampling considerations discussed here apply as well to any direct numerical evaluation of (4.93).

### 4.5.2 Truncation of Integration Interval

To numerically evaluate the FFP integral, (4.96), we must either use a quadrature scheme for semi-infinite integration intervals or truncate the integration interval at a wavenumber beyond which the contribution to the integral is insignificant.

Although the first approach seems desirable in terms of accuracy, it is rarely used in the numerical implementations of the wavenumber integration approaches in underwater acoustics and seismology. The reason is, in part, that such a quadrature scheme would have to incorporate the oscillation of the exponential function in (4.96), which is different for the various ranges considered. It would therefore lead to different quadrature points for each range, with a significant additional computational effort as a result. Secondly, the variation of the kernel is strongly dependent on the environmental model and frequency, and moreover characterized by features such as poles and branch cuts which are not suited for quadrature schemes with infinite intervals.

Instead, the wavenumber axis is truncated, allowing for numerical quadrature without the complication of a semi-infinite integration interval. The reason this approach is applicable is that the kernel in general decays very rapidly beyond a certain wavenumber  $k_{\max}$ . For example, consider the depth-dependent solution for the Pekeris waveguide, (2.176), consisting of a source contribution and two homogeneous solutions. For large values of the horizontal wavenumber, the exponential functions all have real arguments, corresponding to evanescent waves with an exponential decay in depth. It is easily verified that in the source layer, the source term will have the slowest decay rate for large wavenumbers. Thus, for large source-receiver separations in depth, the integration kernel will be rapidly decaying with increasing  $k_r$ . For small separations the decay is slower, and in the extreme situation of source and receiver at the same depth, the kernel only decays as  $k_r^{-1}$  for  $k_r \rightarrow \infty$ , as illustrated in Fig. 2.6. Based on this information, it is usually straightforward to truncate the integration interval to obtain any degree of accuracy, except for the extreme case mentioned above where additional measures must be taken. Of course, it is desirable also for computational reasons to limit the integration interval as much as possible.

To appropriately truncate the integration interval, we can take advantage of the oscillatory nature of the exponential function in (4.96). Thus, for  $r \neq 0$  the alternating sign of exponential will ensure the convergence of the integral for  $k_r \rightarrow \infty$ , even for source and receiver at the same depth where the kernel alone is non-integrable. Therefore, the contribution to the integral beyond a certain wavenumber  $k_{\max}$  will

be negligible. However,  $k_{\max}$  will depend on range, and for multiple ranges it is not desirable to truncate at different wavenumbers. Instead it is desirable to have a wavenumber interval which is independent of range. An easy solution is to taper the kernel close to the maximum wavenumber selected such that the kernel is forced to gradually vanish over a wavenumber interval where the exponential function oscillates over several periods [13].

It should be stressed, that although the tapering of the kernel can be used to eliminate truncation errors, the actual choice of  $k_{\max}$  is not easily automated. On the contrary, a proper choice usually requires a fundamental understanding of wave-guide acoustics, in particular for elastic bottoms and ice covers, where significant components of the field have propagation wavenumbers far out in the evanescent regime.

### 4.5.3 Wavenumber Discretization: Aliasing

To numerically evaluate the wavenumber integral in (4.96), the integration kernel must be evaluated at a discrete number of wavenumbers. Even though dedicated quadrature schemes may be devised for certain canonical problems, the truncated wavenumber space in general is discretized equidistantly,

$$k_\ell = k_{\min} + \ell \Delta k_r, \quad \ell = 0, 1 \dots (M - 1), \quad (4.97)$$

where  $M$  is the total number of sample points, and  $\Delta k_r = (k_{\max} - k_{\min})/(M - 1)$ . Inserting (4.97) in (4.96) then yields the discrete wavenumber representation of the field integral

$$\hat{g}(r, z) = \frac{\Delta k_r}{\sqrt{2\pi r}} e^{i[k_{\min}r - (m + \frac{1}{2})\frac{\pi}{2}]} \sum_{\ell=0}^{M-1} \left[ g(k_\ell, z) \sqrt{k_\ell} \right] e^{i\ell \Delta k_r r}. \quad (4.98)$$

It is well-known from the discretization of time–frequency transforms that undersampling in one domain causes aliasing (wrap-around) in the other domain (see e.g., [24], Sect. 3.2), and being a Fourier transform, the wavenumber integral is exposed to the same problem.

Since, as discussed below, this aliasing problem is directly related to the periodicity of the exponential functions, its effect can in fact be quantified, and remedies can be designed to make its effect insignificant. The Fast Field approximation to the wavenumber integral, (4.96), can be written in the form

$$g(r, z) \simeq h(r) f(r, z). \quad (4.99)$$

Here,  $h(r)$  represents the range-dependent amplitude and phase factor,

$$h(r) = \sqrt{\frac{1}{2\pi r}} e^{-i(m + \frac{1}{2})\frac{\pi}{2}}, \quad (4.100)$$

and  $f(r, z)$  is the depth-dependent wavenumber integral,

$$f(r, z) = \int_0^\infty g(k_r, z) \sqrt{k_r} e^{ik_r r} dk_r. \quad (4.101)$$

In this form,  $f(r, z)$  represents the entire field variability except for the geometric spreading. Therefore, although the present analysis assumes cylindrical geometry, the results apply directly to the plane problem, with the only change being elimination of the cylindrical spreading factor  $r^{-1/2}$ .

In analogy, the discrete form in (4.98) is written as

$$\hat{g}(r, z) = e^{ik_{\min} r} h(r) \hat{f}(r, z) \quad (4.102)$$

with  $\hat{f}(r, z)$  representing the evaluation of the wavenumber integral by discrete summation,

$$\hat{f}(r, z) = \Delta k_r \sum_{\ell=0}^{M-1} g(k_\ell, z) \sqrt{k_\ell} e^{ir\ell\Delta k_r}. \quad (4.103)$$

In this form, it is clear that adding  $R = 2\pi/\Delta k_r$  to the range  $r$  simply adds an integer multiple of  $2\pi$  to the argument of the exponential function. Equation (4.103), therefore, yields a periodic solution,

$$\hat{f}(r + nR, z) \equiv \hat{f}(r, z), \quad n \in [-\infty \dots \infty]. \quad (4.104)$$

Therefore, whereas the continuous integral represents a solution over an infinite range interval, the discrete summation in (4.103) represents a solution over a limited range window  $r = [r_{\min}, r_{\min} + R]$ , with the solution at all other ranges being determined through the periodicity condition in (4.104).

In addition, since adding  $R = 2\pi/\Delta k_r$  to the range simply adds an integer multiple of  $2\pi$  to the argument of the exponential function, (4.103) also constrains the field and all its derivatives to be continuous at all the window boundaries,  $r = r_{\min} + nR$ , for integer  $n = -\infty \dots \infty$ . This property is the true culprit of the aliasing problem.

Consider the problem of computing the field produced by a physical source at the origin  $r = 0$  in a Pekeris waveguide. The integration kernel  $g(k_r, z)$  is shown schematically in the upper frame in Fig. 4.5, with the dashed portion near the origin indicating the square-root singularity introduced by the geometric  $\sqrt{k_r}$  factor. Because of the continuity condition at range window boundaries  $r = nR$ , all wave components produced by the physical source in the range window  $n = 0 : [0, R]$ , propagating in the positive direction at  $r = R$ , must be matched by identical wave components propagating in the positive direction in the neighboring window  $n = 1 : [R, 2R]$ . Because of the periodicity these wave components will therefore also exist in the current window  $n = 0$ , where they will appear to be originating from sources in the previous range window  $n = -1$ . Similarly, if the Hankel function in (4.94) representing the incoming components were retained, all wave components

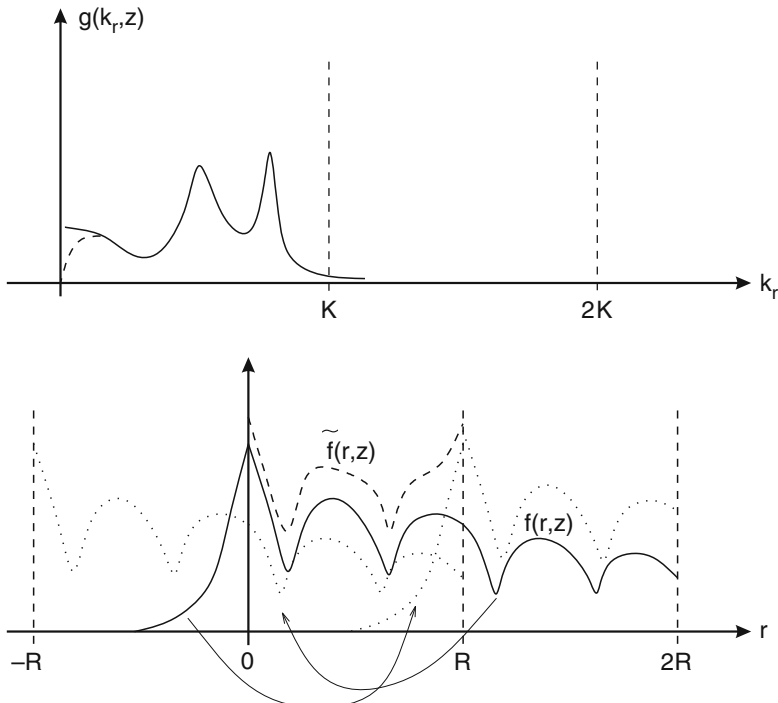


**Fig. 4.5** Aliasing associated with discrete wavenumber integration for a typical Pekeris waveguide problem. The wavenumber kernel showing the presence of two attenuated modes is sketched in the upper plot, with the square-root singularity introduced by the geometric  $\sqrt{k_r}$  indicated by the *dashed curve* near the origin. The discrete wavenumber integration yields the periodic result shown in the lower frame by a *dashed curve*, approximating the correct continuous result shown as a *solid curve*. The discrete result is a superposition of the “true” field produced by the mirror sources in all the range windows

propagating in the negative direction at  $r = 0^+$  will also appear as negatively propagating waves at  $r = R^-$ , appearing to originate at the periodic source at  $r = R^+$  in the neighbor window  $n = 1$ . This will be the situation in the *Fast Hankel Transform* described later in Sect. 4.5.6. Even though these incoming wave components are ignored here, the positive wavenumbers will contribute at small negative ranges, as indicated in the figure, yielding a non-vanishing field which will also wrap into the current window at  $r = R$ .

Similarly, if the true field extends beyond the neighboring windows, the field from the virtual sources in these windows will be wrapped into the current window as well. As a consequence the field represented by the Fourier summation in (4.103) will be the *superposition* of the field produced by an infinity of *periodic sources*, with the resulting field being

$$\hat{g}(r, z) = e^{ik_{\min}r} h(r) f^*(r, z) = h(r) \sum_{n=-\infty}^{\infty} f(r + nR, z), \quad (4.105)$$

where  $f(r, z)$  represents the true field as expressed by the continuous integral in (4.96).

This behavior of the discrete solution is consistent with the fact that for integer values of  $\ell$ , (4.103) provides an exact representation of the synthesis of circumferential waves of wavenumber  $\ell \Delta k_r$ ,  $\ell = 0, \dots, M - 1$  on the surface of a cylinder with radius  $\Delta k_r^{-1}$ , with all wave components on the cylinder, of course, having to be continuous at  $[0, 2\pi]$ , and the total field being periodic.

Thus, in summary, the discretization of the wavenumber integral forces a periodic solution, with the inherent property that the discrete Fourier transform  $f^*(r, z)$  in each range window of width  $R$  is a superposition of the “true” field  $f(r, z)$  produced by an infinite number of periodic source “images,” as illustrated in Fig. 4.5.

As a consequence, for the discrete wavenumber integral to be correct, the field produced by each source must vanish outside the range interval considered, otherwise it will be wrapped into the neighboring windows, and vice versa for the sources in the neighboring windows. This is the fundamental aliasing or wrap-around problem associated with discrete Fourier transforms, requiring the range window to be large enough for the periodic components to be insignificant, in turn requiring the wavenumber sampling to be small. On the other hand, if the signal dies out before reaching the neighboring window, the discrete form will approach the exact solution. In the cylinder analogy, this corresponds to a wave field which is attenuated enough to reduce the periodic multiples to insignificance.

Because of the two-sided nature of the discrete Fourier transform, aliasing occurs from both sides of the actual interval and therefore also from ranges smaller than  $r_{\min}$ . For  $r_{\min} > 0$  the strong signals in the interval  $[0, r_{\min}]$  are wrapped into the interval  $[R, r_{\min} + R]$ . Therefore *the maximum range is always  $R = 2\pi/\Delta k_r$ , independent of the choice of  $r_{\min}$* .

#### 4.5.4 FFP: Fast Field Program

The acoustic field is often required at a large number of ranges  $r_j$ , in particular in connection with the common underwater acoustics problem of determining transmission loss as function of range. In these cases, the Fourier series summation in (4.103) is very efficiently evaluated by means of an FFT. In this Fast-Field-Program (FFP) approach introduced by DiNapoli and Deavenport [1], the range axis  $r$  is discretized as

$$r_j = r_{\min} + j \Delta r, \quad j = 0, 1, \dots, (M - 1), \quad (4.106)$$

where the range step  $\Delta r$  is constrained by the wavenumber discretization through the relation

$$\Delta r \Delta k_r = \frac{2\pi}{M} \quad (4.107)$$

and  $M$  is an integral power of 2. The following discrete approximation of (4.96) is then obtained,

$$g^*(r_j, z) = \frac{\Delta k_r}{\sqrt{2\pi r_j}} e^{i[k_{\min} r_j - (m + \frac{1}{2})\frac{\pi}{2}]} \sum_{\ell=0}^{M-1} \left[ g(k_\ell, z) e^{ir_{\min} \ell \Delta k_r} \sqrt{k_\ell} \right] e^{i\frac{2\pi \ell j}{M}}, \quad (4.108)$$

where the summation can be performed by means of an FFT, yielding the field at all  $M$  ranges simultaneously. Note that

$$e^{i(-\ell \Delta k_r)(j \Delta r)} = e^{i(2\pi j - \ell \Delta k_r(j \Delta r))} = e^{i(M - \ell) \Delta k_r(j \Delta r)}. \quad (4.109)$$

Therefore, for  $k_{\min} = 0$  the upper half of the wavenumber components in (4.103) is indistinguishable from the negative wavenumbers in regard to the value of the exponential, such that, even though the original integral in (4.98) was one-sided, the summation is equivalent to a two-way propagation problem. With  $r_{\min} = 0$  this makes the discrete approximation of the wavenumber integral valid only up to a range  $r = R/2$ , consistent with the Nyquist sampling criterion [24]. Here, however, the one-sided nature of the original integral in (4.96) may yield a solution which is valid at ranges longer than the Nyquist range. Thus, with only positive wavenumbers considered, the wrap-around of the negative spectrum will correspond to the wavenumbers  $k_r > M \Delta k_r / 2$ . Therefore, as illustrated in Fig. 4.5, one can choose a wavenumber interval  $[0, 2K]$  such that the upper half is all beyond the significant evanescent components. This makes the negative spectrum wrap-around insignificant, and the range of validity will extend beyond  $R/2$ . However, as also illustrated in Fig. 4.5, the field will never vanish entirely at negative ranges because of the finite contribution from the small wavenumber components, and, more importantly, because of the numerical artifact associated with the discontinuity of the kernel at  $k_r = [0, 2K]$ . Even though the  $\sqrt{k_r}$  factor introduced by the FFP approximation forces the kernel to vanish, the derivatives remain discontinuous, and an artificial backward propagating field will result, which will be wrapped into the current range window near  $r = R$  as illustrated in the figure. Therefore, even though a simple zero-padding at large wavenumbers is a computationally efficient method for extending the range beyond the Nyquist limit  $R/2$ , it is not in general recommended. Instead, the range should be extended by simply reducing the wavenumber sampling  $\Delta k_r$ .

We will illustrate the effect of aliasing by using the FFP integration scheme, (4.108), to evaluate the transmission loss versus range at 46-m depth in the Pekeris waveguide shown in Fig. 2.25. The source depth is 36 m and the frequency is 20 Hz. The magnitude of the integration kernel along the real wavenumber axis is shown in Fig. 4.6a. Since an attenuation of  $0.5 \text{ dB}/\lambda$  is assumed in the bottom, no poles exist on the real axis, but the pole corresponding to the first propagating mode is evident as an extremely sharp peak. Figure 4.6b shows the exact transmission loss out to a range of 15 km as the solid curve. The dashed curve is the FFP result obtained by integrating the kernel in Fig. 4.6a using 1024 sample points equidistantly spaced between  $k_{\min} = 10^{-9} \text{ m}^{-1}$  and  $k_{\max} = 0.2 \text{ m}^{-1}$ . This implies  $\Delta k_r = 2 \times 10^{-4} \text{ m}^{-1}$ ,

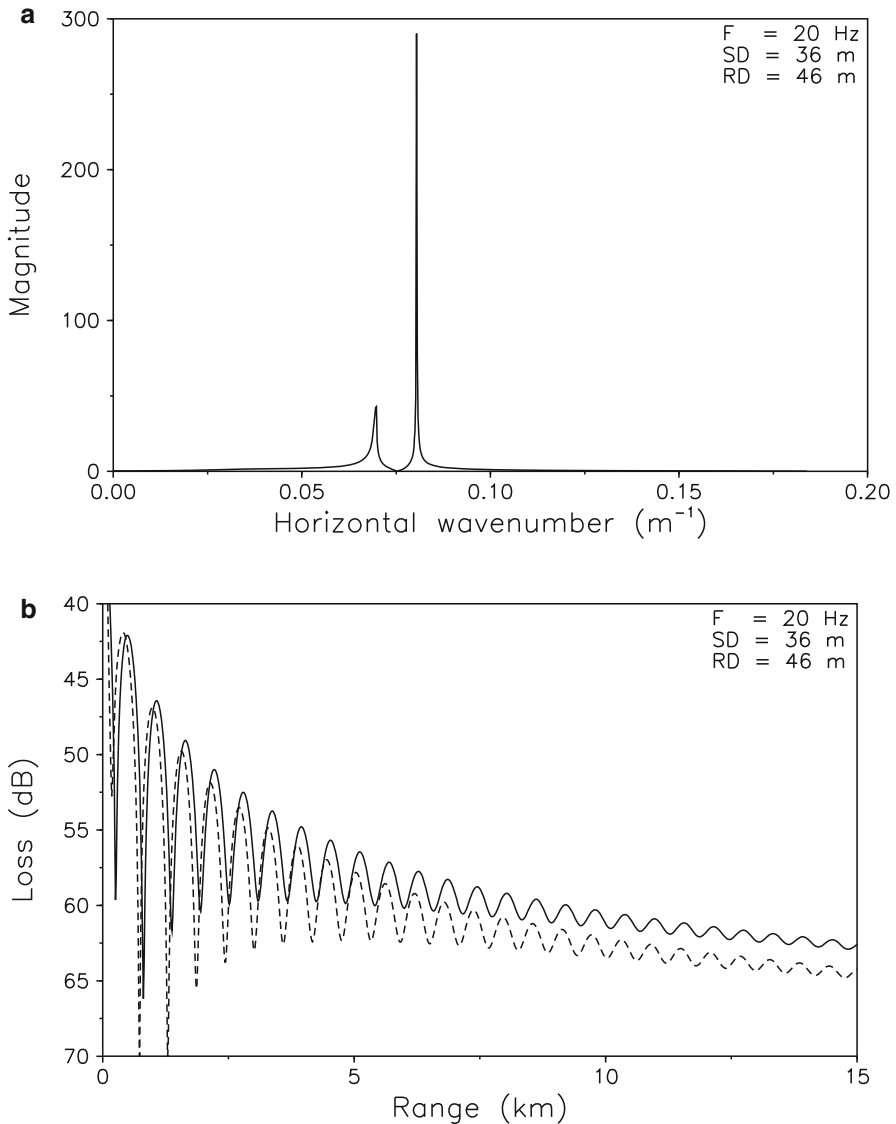


**Fig. 4.6** Acoustic field at 46-m depth in a Pekeris waveguide with a water speed of 1500 m/s and a bottom speed of 1800 m/s. (a) Magnitude of integration kernel along real wavenumber axis. (b) Transmission loss. *Solid curve*: Exact solution. *Dashed curve*: Real-axis FFP integration with  $k_{\max} = 0.2 m^{-1}$  and 1024 sample points

corresponding to a range window  $R = 2\pi/\Delta k_r \simeq 30 \text{ km}$ . The aliasing due to undersampling of the sharp peak in Fig. 4.6a clearly introduces errors of up to 2 dB in the predicted transmission loss, with the largest errors at longer ranges. However, even at short ranges the aliasing introduces errors in the modal interference pattern.

### 4.5.5 Complex Contour Integration

The aliasing from ranges larger than  $r_{\min} + R$  can be reduced by choosing  $R$  so large that the signal is known to die out within the range window. Here, it is important to note that the cylindrical spreading of the point-source waveguide field is accounted for by the  $r^{-1/2}$  factor in (4.100). Therefore, it has no implication for the wrap-around problem. As described above, the wrap-around is purely an effect of the replacement of the integral by the summation in (4.103), and to avoid the wrap-around it is necessary that the field decays more rapidly with range than the geometrical spreading decay  $r^{-1/2}$ . For a perfectly lossless waveguide, the modal field decays only due to geometrical spreading. In this case, the range window cannot be made large enough to eliminate the wrap-around, which is consistent with the fact that the normal modes appear as singularities on the real wavenumber axis, and these poles can never be properly sampled.

Therefore, direct numerical evaluation of the wavenumber integral in (4.96) along the real axis is possible only for waveguides with some form of attenuation. In the real ocean, both the water and the bottom have a finite volume attenuation, but in particular for environments with little bottom interaction, the attenuation loss is very small. In these cases a large range window, and therefore very fine wavenumber sampling, must be chosen to avoid wrap-around. This is clearly undesirable for computational reasons, particularly in cases where the field is needed only at relatively short ranges.

The aliasing problem can, however, be eliminated by moving the integration contour out into the complex plane. According to *Cauchy's theorem* the integral in the complex plane between two points is invariant to a change in the integration contour provided that the integrand is analytical between the contours. Thus, (4.96) can be replaced by

$$g(r, z) \simeq h(r) f(r, z) = h(r) \int_C g(k_r, z) \sqrt{k_r} e^{ik_r r} dk_r, \quad (4.110)$$

where  $C$  is the contour shown in Fig. 4.7. The contour consists of three linear sections  $C_1$ ,  $C_2$ , and  $C_3$ , where the vertical sections of length  $\epsilon$  are chosen at the points where the wavenumber axis would in any case be truncated. If these points are chosen where the kernels are small, i.e., where  $g(k_{\min}, z) \sqrt{k_{\min}} \simeq 0$ ,  $g(k_{\max}, z) \sqrt{k_{\max}} \simeq 0$ , and  $\epsilon \ll k_{\max} - k_{\min}$ , then the contributions from the vertical sections become insignificant compared to the integral along the horizontal section defined by  $\tilde{k} = k - i\epsilon$ . By inserting  $\tilde{k}$  in (4.110), we obtain

$$\begin{aligned} g(r, z) &\simeq h(r) f(r, z) \\ &= h(r) \int_{k_{\min}}^{k_{\max}} g(k_r - i\epsilon, z) \sqrt{k_r - i\epsilon} e^{i(k_r - i\epsilon)r} dk_r, \end{aligned} \quad (4.111)$$

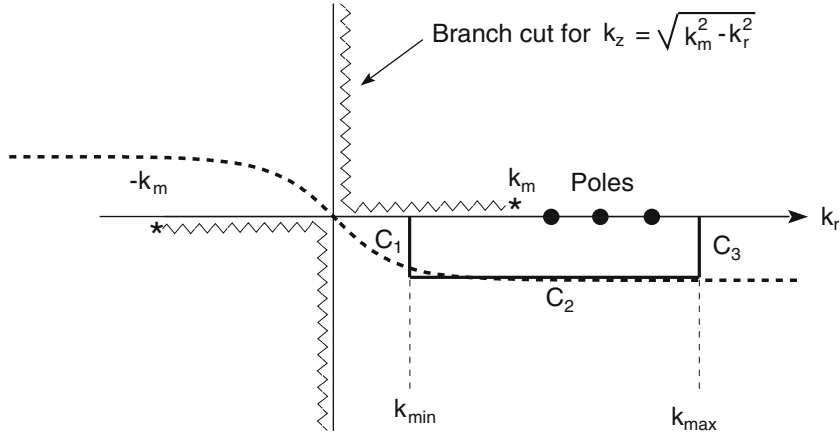


**Fig. 4.7** Complex integration contours for evaluation of wavenumber integral. The contour  $C_2$  is used for FFP integration, while the “exact” hyperbolic tangent contour indicated by the dashed line is used for trapezoidal rule integration

which after multiplication by  $e^{-\epsilon r}$  takes the form

$$\begin{aligned} g(r, z) e^{-\epsilon r} &\simeq h(r) f(r, z) e^{-\epsilon r} \\ &= h(r) \int_{k_{\min}}^{k_{\max}} g(k_r - i\epsilon, z) \sqrt{k_r - i\epsilon} e^{ik_r r} dk_r. \end{aligned} \quad (4.112)$$

As described above, a periodic approximation to the integral in (4.112) can be determined by means of an FFT, with the result

$$\begin{aligned} \widehat{g}(r_j, z) e^{-\epsilon r_j} &= e^{ik_{\min} r_j - \epsilon r_j} h(r_j) \widehat{f}(r_j, z) \\ &= h(r_j) \sum_{n=-\infty}^{\infty} f(r_j + nR, z) e^{-\epsilon(r_j + nR)} \\ &\simeq \Delta k_r e^{ik_{\min} r_j} h(r_j) \sum_{\ell=0}^{M-1} \left[ g(k_\ell - i\epsilon, z) e^{ir_{\min} \ell \Delta k_r} \sqrt{k_\ell - i\epsilon} \right] e^{i \frac{2\pi \ell j}{M}} \end{aligned} \quad (4.113)$$

or, after multiplication with  $e^{\epsilon r_j}$ , rearrangement of terms, and use of the (4.99),

$$\begin{aligned} g(r_j, z) &\simeq h(r_j) f(r_j, z) \\ &= \Delta k_r e^{(\epsilon + ik_{\min}) r_j} h(r_j) \sum_{\ell=0}^{M-1} \left[ g(k_\ell - i\epsilon, z) e^{ir_{\min} \ell \Delta k_r} \sqrt{k_\ell - i\epsilon} \right] e^{i \frac{2\pi \ell j}{M}} \\ &\quad - h(r_j) \sum_{n \neq 0} f(r_j + nR, z) e^{-\epsilon n R}. \end{aligned} \quad (4.114)$$

In this form, it is clear that all signals wrapped around from ranges larger than  $r_{\min} + R$  will be attenuated by at least  $\exp(-\epsilon R)$ . On the other hand, signals wrapped around from ranges smaller than  $r_{\min}$  will be amplified by at least  $\exp(\epsilon R)$ . As was the case for the real-axis integration, the maximum range is therefore still  $r_{\max} = R$ .

The explanation for this is as follows. The contour offset moves the integration path away from singularities such as branch points and poles associated with modes, resulting in a similar but smoother integration kernel. It is well-known that a smoother kernel yields a more rapidly decaying Fourier transform, corresponding to adding an artificial attenuation in range, and the corresponding field is therefore less likely to wrap into the neighboring range window. The multiplication of the transform result by the spatial exponential  $e^{\epsilon r}$  compensates for this artificial attenuation and restores the correct field decay with range.

The actual value of  $\epsilon$  is not extremely critical. However, if it is chosen too large the contributions from the two vertical parts of the contour may become significant. On the other hand, a too small value will require a very large number of sampling points. For most practical purposes an attenuation of the wrap-around by 60 dB is more than sufficient [13]. The corresponding value of the *contour offset* is

$$\epsilon = \frac{3}{R \log e} = \frac{3}{2\pi (M - 1) \log e} (k_{\max} - k_{\min}), \quad (4.115)$$

which even for a relatively small number of sample points  $M$  will ensure that  $\epsilon \ll k_{\max} - k_{\min}$ , and thus yield insignificant contributions from the vertical contours.

Figure 4.8 illustrates the effects of using the complex integration contour for evaluation of the field in the Pekeris waveguide treated above. Figure 4.8a shows the magnitude of the kernel of the summation in (4.114) for two contour offsets defined by (4.115). The solid curve is the kernel along a contour with an offset corresponding to  $M = 1024$  sampling points in the wavenumber interval shown, whereas the dashed curve is the kernel for  $M = 512$  sampling points over the same interval. When compared to Fig. 4.6a, it is clear that the contour offset has a smoothing effect on the integration kernel, and also results in lower amplitudes as is evident at the poles in particular. The effect of the lower amplitudes is compensated by the exponential outside the summation in (4.114).

Figure 4.8b shows the transmission loss computed from (4.114) for the two contours. On the dB-scale used here, the loss computed with  $M = 1024$  (solid curve) is identical in the whole range window to the exact loss shown as the solid curve in Fig. 4.4b. However, the loss computed with  $M = 512$  (dashed curve) is correct only out to a range of approximately 10 km, after which the result shows increasing errors. These errors appear in spite of the fact that the maximum range for this sampling is  $R = 2\pi/\Delta k_r \simeq 15$  km. This is due to the fact that even though we have removed the negative wavenumber spectrum represented by the Hankel function  $H_m^{(2)}(k_r r)$ , the value of the integral in (4.110) does not vanish for negative ranges  $r$ . According to the arguments above, the field for negative  $r$  will therefore wrap into the actual window, magnified by at least  $\exp(\epsilon R)$ . However, these

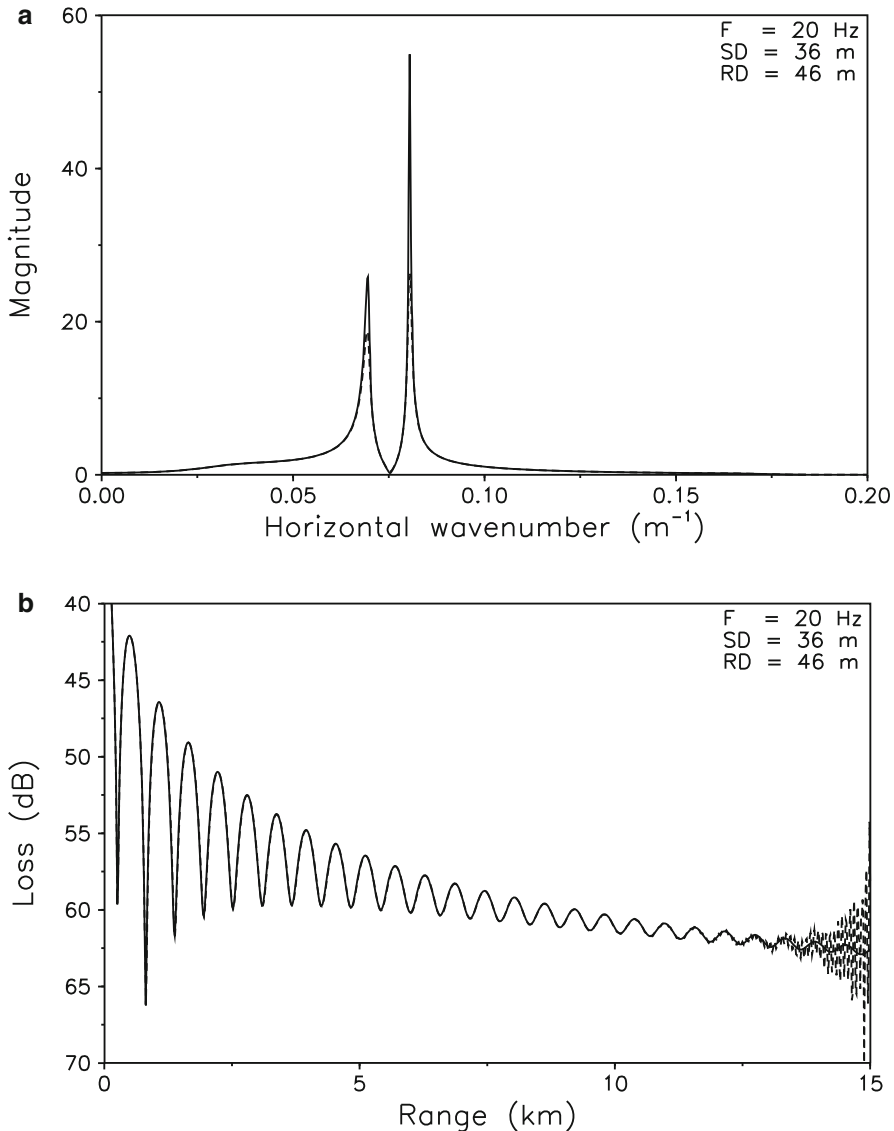


**Fig. 4.8** Acoustic field in a Pekeris waveguide computed with complex integration contours. (a) Magnitude of integration kernel along contours offset  $\epsilon$  given by (4.115) with  $k_{\max} = 0.2 \text{ m}^{-1}$ , and  $M = 1024$  (solid curve) and  $M = 512$  (dashed curve). (b) Transmission loss computed with  $M = 1024$  (solid curve) and  $M = 512$  (dashed curve)

components decay rapidly with negative range, and the wrap-around will therefore be confined to ranges close to the maximum range  $R$ . In general, experience shows that the solution obtained from (4.114) is correct to within a fraction of a decibel at least out to the Nyquist range  $r = R/2 = \pi/\Delta k_r$ .

Whereas the fast-field integration is very efficient for single-frequency transmission loss calculations, its use is inconvenient in the case of wideband pulse calculations. If the pulse response is required at more than a single range, the wavenumber sampling distance  $\Delta k_r$  would have to be frequency independent in order to satisfy (4.107). Furthermore, since the pulse response is usually required only for a relatively small number of ranges, one of the direct numerical quadrature schemes described in the following is generally more efficient.

#### 4.5.6 Fast Hankel Transforms

The Fast Field Program (FFP) approach described above has gained popularity because of its efficiency in producing field estimates at a large number of ranges. However, being based on the large-argument asymptotic of the Hankel functions it is associated with errors for small arguments  $k_r r$  of the Bessel function, i.e., for short ranges or small wavenumbers. Since the energy in the steep angles associated with small horizontal wavenumbers in general attenuates rapidly with range due to bottom interaction, the FFP provides good solution accuracy for many long-range propagation problems. The minimum range for which the error is acceptable is a complicated function of frequency and environment. Without full Hankel transform reference solutions there is no way of defining this limit of validity, and the use of the FFP has therefore been associated with a significant degree of uncertainty at short ranges, at low frequencies in particular. This problem needs to be dealt with when the short-range field is important, such as for seabed reverberation synthesis [25].

Compared to the simple exponential function, the generation of Bessel functions is relatively time consuming, and, in general, a direct, brute-force numerical integration technique for evaluating the Hankel transforms in (4.93) is not feasible. On the other hand algorithms are available for directly evaluating the Hankel transform, (4.93), using dedicated quadrature schemes. The one developed by Tsang et al. [26], however, requires the evaluation of an FFT for every receiver range, but, more importantly, it requires a numerical separation parameter which is not easily selected. The so-called Fast Hankel Transform [27] is very efficient for relatively smooth kernels, but not well-suited for the rapidly varying kernels of waveguide problems. More efficient *Fast Hankel Transforms* have been developed recently [28–30], but they are in general restrictive in terms of sampling requirements and therefore not easily adapted to ocean acoustic problems, where the sampling is controlled by the waveguide physics, and where the field is desired at a predetermined grid of horizontal ranges.

The advantage of the FFP technique described above is that it efficiently approximates the Hankel transform on a regular grid of wavenumbers and ranges. As shown below, it is possible to design a numerically efficient correction to the FFP which provides accurate accounting for the small-argument contributions.

The Hankel transform integrals are of the form

$$\begin{aligned} g(r) &= \int_0^\infty g(k_r) k_r J_m(k_r r) dk_r \\ &= \frac{1}{2} \int_0^\infty g(k_r) k_r [H_m^{(1)}(k_r r) + H_m^{(2)}(k_r r)] dk_r. \end{aligned} \quad (4.116)$$

For  $\exp(-i\omega t)$  time-dependence,  $H_m^{(1)}$  corresponds to outgoing waves and  $H_m^{(2)}$  to incoming waves, both of azimuthal Fourier order  $m$  dependence. Typically, acoustic forward propagation modeling ignores incoming waves, eliminating the second term. However, for short range, and for backscattering problems, e.g., it must be retained. Next, the Hankel functions  $H_m^{(1,2)}(k_r r)$  are replaced by their asymptotic form [23],

$$\lim_{k_r r \rightarrow \infty} H_m^{(1,2)}(k_r r) = \sqrt{\frac{2}{\pi k_r r}} e^{\pm i[k_r r - (m + \frac{1}{2})\frac{\pi}{2}]}, \quad (4.117)$$

to arrive at the following approximation to the Hankel transform,

$$\begin{aligned} g(r) \simeq \hat{g}(r) &= \sqrt{\frac{1}{2\pi r}} \int_0^\infty g(k_r) \sqrt{k_r} \left[ e^{i[k_r r - (m + \frac{1}{2})\frac{\pi}{2}]} \right. \\ &\quad \left. + e^{-i[k_r r - (m + \frac{1}{2})\frac{\pi}{2}]} \right] dk_r. \end{aligned} \quad (4.118)$$

This integral can be rewritten as a two-sided Fourier transform,

$$\hat{g}(r) = \int_{-\infty}^{\infty} f(k_r) e^{ik_r r} dk_r \quad (4.119)$$

with the kernel

$$f(k_r) = \begin{cases} g(-k_r) \sqrt{\frac{-k_r}{2\pi r}} e^{i[(m + \frac{1}{2})\frac{\pi}{2}]} & k_r < 0 \\ g(k_r) \sqrt{\frac{k_r}{2\pi r}} e^{-i[(m + \frac{1}{2})\frac{\pi}{2}]} & k_r \geq 0. \end{cases} \quad (4.120)$$

Similar to the FFP discussed above, (4.119) is efficiently evaluated using a standard FFT if the range  $r$  and wavenumber  $k_r$  are discretized equidistantly, with the sampling intervals being constrained by (4.107).

The error associated with using (4.119) is clearly associated with the approximation of the Bessel function in terms of the asymptotic expressions of the Hankel functions. Figure 4.9 shows the exact absolute value of the Bessel function  $J_0(k_r r)$  for  $k_r r \leq 100$  as a solid curve and the asymptotic values indicated by the dots. The absolute error is indicated by the dashed curve, and it is clear that the error of the approximation is less than  $10^{-4}$  for  $k_r r \geq 20\pi$ . Consequently, to achieve a more accurate evaluation of the Hankel Transforms of order 0 in (4.93) it is only necessary to correct the contributions corresponding to values of  $k_r r \leq KR = 20\pi$ .

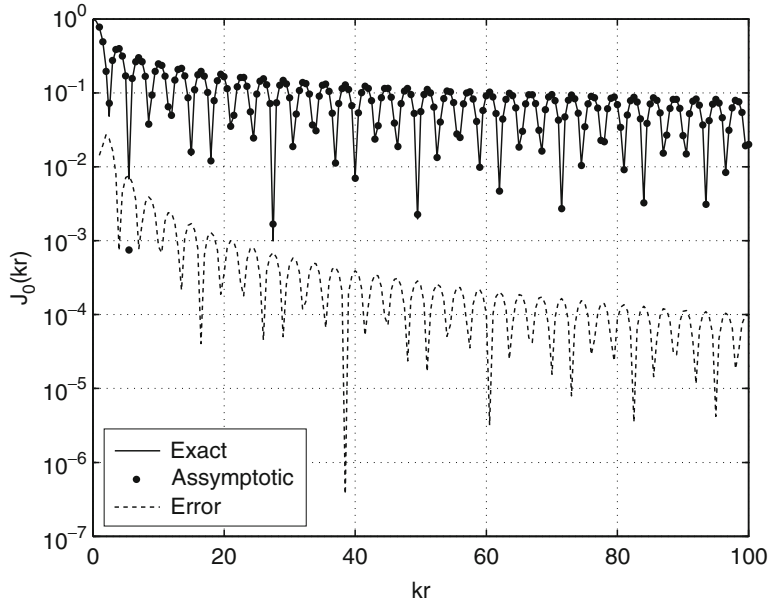


**Fig. 4.9** Error of farfield approximation of  $J_0(kr)$ . *Solid*: Exact; *Dots*: Large-argument approximation; *Dashed*: Error

This is performed in a numerically stable manner by a Hanning weighted average of the contributions of the exact Bessel function and the approximate FFP kernel,

$$g(r) = g^*(r) + \int_0^{KR} g(k_r r) w(k_r r) \times \left\{ k_r J_0(k_r r) - \sqrt{\frac{k_r}{2\pi r}} \left[ e^{i[k_r r - (m+\frac{1}{2})\frac{\pi}{2}]} + e^{-i[k_r r - (m+\frac{1}{2})\frac{\pi}{2}]} \right] \right\} dk_r, \quad (4.121)$$

where the tapered weight function  $w(k_r r)$  is

$$w(k_r r) = \begin{cases} 1, & k_r r \leq KR/2 \\ \{1 + \cos [\pi(k_r r - KR/2)/(KR/2)]\}/2, & KR/2 < k_r r < KR. \end{cases} \quad (4.122)$$

Equation (4.121) can be evaluated very efficiently. First, with the wavenumber and range sampling constrained by (4.107), all values of the exponentials are computed as part of the FFT evaluation of (4.118). Second, the Bessel functions will only be needed for a limited number of discrete values of the argument,

$$kr = n \Delta k_r \Delta r, \quad n = 0, \dots, \frac{KR}{\Delta k_r \Delta r}, \quad (4.123)$$

which can be pre-computed into a look-up table.

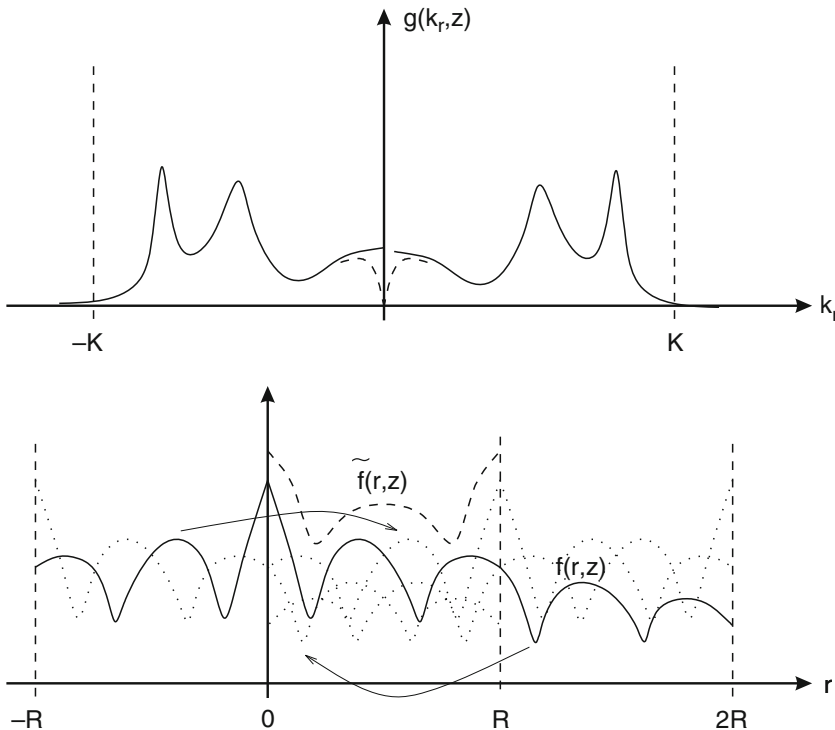


**Fig. 4.10** Aliasing associated with Fast Hankel Transform integration for typical Pekeris waveguide problem. The symmetric wavenumber kernel showing the presence of two attenuated modes is sketched in the upper plot, with the  $\sqrt{k_r}$ -effect introduced by the FFP approximation indicated by the dashed curve near the origin. The discrete wavenumber integration yields the periodic result shown in the lower frame by a dashed curve, approximating the correct continuous result shown as a solid curve. The discrete result is a superposition of the “true” field produced by the mirror sources in all the range windows

As in all other discrete wavenumber integration approaches, the present Fast Hankel Transform is susceptible to aliasing and wrap-around as described in Sect. 4.5.3. However, the fact that the negative wavenumber spectrum is included makes the aliasing issue slightly different, see Fig. 4.10. The full Hankel transform inherently contains both forward (positive) and backward (negative) propagating wavenumber components, with the real-argument Bessel function in (4.93) representing the superposition of the two. The  $\sqrt{k_r}$ -effect in the FFP is again shown near the origin as a dashed curve section, but this geometric artifact is obviously replaced by the true Bessel function by the algorithm. As illustrated in Fig. 4.10 the inherent symmetry (symmetric kernels for  $m$  even, antisymmetric for  $m$  odd) in the wavenumber integral yields a symmetric (or antisymmetric) solution in each range window. Therefore, the forward and backward wrap-around will be of the same order of magnitude, and the field approximation will be symmetric within each range window. Thus, the maximum range of validity is always the Nyquist

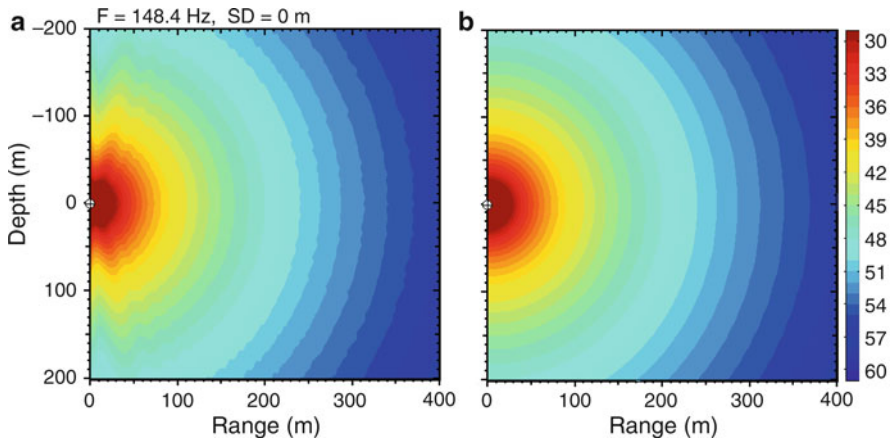


**Fig. 4.11** Acoustic point source field. (a) Shows the FFP approximation which clearly breaks down at steep angles and short ranges, while (b) obtained from the Fast Hankel Transform shows the correct spherical spreading behavior at all propagation angles

range  $r_{\max} = R/2 = \pi/\Delta k_r$  for the full Hankel Transform methods, assuming, of course, that  $R$  is chosen large enough to make the wrap-around insignificant in this part of the range window.

The performance of the Fast Hankel Transform is illustrated by Fig. 4.11, which shows the evaluation of the integral

$$p(r, z) = \int_0^\infty \frac{e^{ik_z|z|}}{ik_z} k_r J_0(k_r r) dk_r \quad (4.124)$$

representing the field due to a point source in free space.  $k_z = \sqrt{(\omega/c)^2 - k_r^2}$  is the vertical wavenumber at angular frequency  $\omega$ . Note that only the Fast Hankel Transform result based on (4.121) shows the correct spherical spreading behavior at all propagation angles, Fig. 4.11b.

#### 4.5.7 Trapezoidal Rule Integration

For propagation problems involving a relatively small number of receivers, such as a vertical line array for matched-field processing (see Chap. 10), or broadband time simulations, the FFT-based techniques are not computationally attractive. On the contrary, the sampling constraint in (4.107) has to be combined with the geometry of the array, often requiring a wavenumber sampling which is fixed for all frequencies, and that is not optimal.

As a consequence broadband and discrete array computations are generally performed by direct numerical quadrature schemes such as the trapezoidal rule integration. This scheme approximates the integrand by a function varying linearly between the sampling points, and hence is applicable only out to ranges where the

product of the kernel and the exponential function is well represented by a linear function. The kernel can be smoothed by moving the contour out into the complex plane as described earlier, but the exponential function varies rapidly for long ranges. To ensure that the exponential function alone is well represented by a linear function, the wavenumber sampling must satisfy the following inequality [31],

$$\Delta k_r R < \frac{\pi}{4}, \quad (4.125)$$

which, by comparison with (4.107), translates into a maximum range which is much shorter than the one obtained by the fast-field technique. However, for equidistant sampling, the trapezoidal rule yields a result which is identical to (4.108), except for insignificant differences at the ends of the integration interval. It should be pointed out, however, that the FFP technique has a degraded accuracy at longer ranges, which is insignificant on the logarithmic scale used for displaying transmission loss, but it may become important in connection with wideband pulse calculations. For accurate pulse calculations, the maximum ranges for the two techniques are identical and determined by (4.125).

In addition to allowing frequency-dependence of the wavenumber sampling, another advantage of the direct numerical integration schemes is that they are less restricted in terms of the wavenumber integration contour, even though they are obviously susceptible to the same aliasing problems. Thus, e.g., they do not need to use an integration contour parallel to the real axis, such as the contour  $C_2$  in Fig. 4.7, but these schemes can instead apply an “exact” contour such as the one shown by the dashed line in Fig. 4.7, thus totally eliminating the contributions from the two vertical contour sections. This is particularly important for short-range problems where the contribution from contour  $C_1$  becomes significant. Dawson and Fawcett [32] suggested the hyperbolic tangent contour for use with trapezoidal rule integration. The following contour is found to work well for most ocean acoustic and seismic problems,

$$\bar{k}_r = \begin{cases} k_r(1 - i\epsilon \tanh k_r / 6\Delta k_r), & k_r / 6\Delta k_r \leq 20 \\ k_r(1 - i\epsilon), & k_r / 6\Delta k_r > 20, \end{cases} \quad (4.126)$$

where the asymptotic offset  $\epsilon$  is given by (4.115).

Also, with its relatively small additional computational cost, it is strongly recommended to use the Fast Hankel Transform approach described in Sect. 4.5.6, but obviously implemented in a modified form, without using an FFT. Thus, (4.121) is easily re-arranged into a form directly suitable for trapezoidal rule integration, for the omni-directional field components,  $m = 0$ :

$$\begin{aligned} g(r) = \int_0^\infty g(k_r) \left\{ w(k_r r) k_r J_0(k_r r) + [1-w(k_r r)] \right. \\ \times \sqrt{\frac{k_r}{2\pi r}} \left. \left( e^{i[k_r r - (m+\frac{1}{2})\frac{\pi}{2}]} + e^{-i[k_r r - (m+\frac{1}{2})\frac{\pi}{2}]} \right) \right\} dk_r \end{aligned} \quad (4.127)$$

with the weight function

$$w(k_r r) = \begin{cases} 1, & k_r r \leq 10\pi \\ \{1 + \cos [\pi(kr - 10\pi)/(10\pi)]\}/2, & 10\pi < k_r r < 20\pi \\ 0, & k_r r > 20\pi. \end{cases} \quad (4.128)$$

As before, the Bessel functions can be pre-computed on a fixed grid up to the maximum argument  $k_r r = 20\pi$ , with the values at any intermediate argument being determined by interpolation. Here it has been found that for all practical applications, a sampling of  $\pi/20$  is more than adequate if combined with fourth-order Lagrange interpolation.

#### 4.5.8 Filon Integration

While the trapezoidal rule integration is accurate only for ranges which satisfy (4.125) for the product of the kernel and the exponential function in (4.110), it is possible to obtain accurate solutions at longer ranges by applying the generalized Filon integration scheme [33],

$$\int_a^b f(k_r) e^{Sg(k_r)} dk_r = \begin{cases} \frac{\Delta k_r}{S \Delta g} \left[ \Delta \{f e^{Sg}\} - \frac{\Delta f \Delta \{e^{Sg}\}}{S \Delta g} \right], & \Delta g \neq 0 \\ \frac{\Delta k_r}{2} [f(a) e^{Sg(a)} + f(b) e^{Sg(b)}], & \Delta g = 0, \end{cases} \quad (4.129)$$

where  $\Delta f = f(b) - f(a)$ , and similarly for the other functions. This quadrature scheme is exact for linear variations of the kernel  $f(k_r)$  and of the exponent  $g(k_r)$ . In the present case,  $S = ir$  and  $g(k_r) = k_r$ , i.e., the exponent is inherently a linear function of  $k_r$ . For the equidistant sampling given in (4.97), it is easily shown that the Filon integration scheme leads to the following quadrature scheme for evaluation of the wavenumber integral in (4.110),

$$g(r_j, z) \simeq \frac{w_j}{\sqrt{2\pi r_j}} e^{i[k_{\min} r_j - (m + \frac{1}{2}) \frac{\pi}{2}]} \sum_{\ell=0}^{M-1} \left[ g(k_\ell, z) e^{ir_{\min} \ell \Delta k_r} \sqrt{k_\ell} \right] e^{i \frac{2\pi \ell j}{M}}. \quad (4.130)$$

Here,  $w_j$  are the range-dependent quadrature weights given by

$$w_j = \Delta k_r \left[ \frac{\sin(\Delta k_r r_j / 2)}{\Delta k_r r_j / 2} \right]^2. \quad (4.131)$$

It is interesting to note that (4.130) is identical to (4.108) except for the simple change in integration weight from  $\Delta k_r$  to  $w_j$ , basically applying a sinc-function

squared to the field amplitude vs. range. The summation can again be performed by means of an FFT or by direct summation for the ranges of interest, and is therefore insignificantly more computationally intensive than the simple FFT or trapezoidal rule integrations. The Filon quadrature scheme is obviously applicable to the integration along the complex contour as well, again involving only the change of quadrature weights to those given in (4.131).

The Filon scheme is accurate as long as the kernels are well represented by linear interpolation between the sample points. On the other hand, the error due to the nonlinear behavior of the kernel will increase with range, and the Filon scheme therefore also has a practical range limitation. Since this range limitation depends on the smoothness of the kernel, it is not possible to give any specific value. Mallick and Frazer [31] found that whereas the wavenumber sampling required for the trapezoidal rule integration is inversely proportional to  $\omega r$ , the Filon scheme requires a sampling which is approximately inversely proportional to  $\sqrt{\omega r}$ . However, they considered seismic reflectivity problems characterized by relatively smooth wavenumber kernels. In ocean acoustics the kernel singularities are usually the controlling factor, and since the number of singularities increase with frequency, and since singularities are not necessarily better represented by a linear than a constant kernel, the improvement in computational efficiency is much less pronounced for underwater acoustic problems, and the Filon schemes are therefore rarely used.

#### 4.5.9 Adaptive Integration

The nonlinearity of the wavenumber kernel is obviously most severe near singularities introduced by the poles and branch cuts. In other regions, e.g., in the continuous and evanescent spectra and between the modes, the kernel may be adequately represented by linear interpolation even for a relatively coarse sampling. Therefore, the sampling requirements are not uniform, and in some cases computational advantages can be obtained by varying the sampling along the wavenumber axis.

While the FFP integration scheme requires an equidistant sampling, the trapezoidal and Filon schemes do not have this restriction. For some problems it is known a priori that the integration kernel is smooth in the continuous and evanescent parts of the spectrum, and a coarse wavenumber sampling can therefore be used in these regimes, combined with a finer sampling of the discrete spectrum. However, this is not a general behavior since poles may exist in the evanescent regime for waveguides with an elastic bottom and, as illustrated by the Pekeris example, poles may even exist close to the real axis in the continuous spectrum.

These integration problems may be overcome by an adaptive selection of the wavenumber sampling. Shown in Fig. 4.12 is an example of such an adaptive scheme, developed by Krenk et al. [34]. Here, the kernel is first sampled on a coarse wavenumber grid, which is then subsequently subdivided by bisection, until a stable value of the integral over the sub-interval is obtained. Adaptive integration

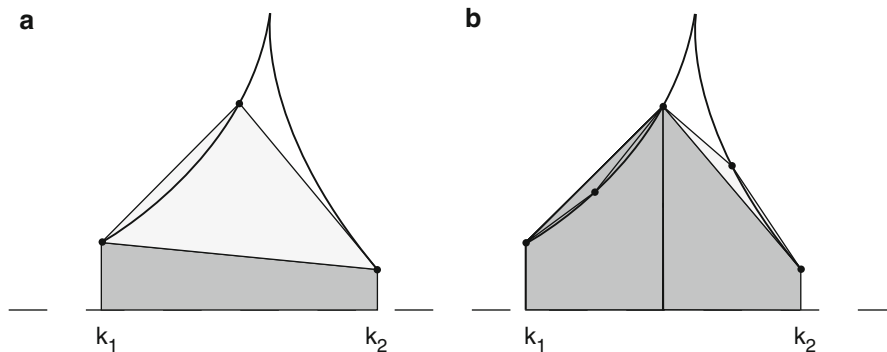


**Fig. 4.12** Adaptive evaluation of wavenumber integral

schemes involve more book-keeping in the implementation, but may improve the computational efficiency. However, for most underwater acoustic problems the computational advantages of adaptive schemes are found to be rather insignificant. Further, for computation of transmission loss, usually performed on a dense spatial grid, the fact that the adaptive sampling has to be performed individually for each receiver makes it rather intensive computationally. However, for time-domain computations for a small number of receivers, it may be computationally advantageous, but since this is not the most common application of modeling in ocean acoustics, the adaptive integration techniques have never achieved the popularity they hold in crustal and exploration seismology.

## 4.6 Frequency Integration

The last step involved in determining the full time-domain response is the evaluation of the inverse Fourier transform,

$$g(r, z, t) = \int_{-\infty}^{\infty} g(r, z, \omega) e^{-i\omega t} d\omega. \quad (4.132)$$

This integral must be evaluated for all field parameters, ranges, and depths of interest. Although simple in principle, the numerical implementation of (4.132) is non-trivial. The reason is that the numerical evaluation is susceptible to the same numerical artifacts as those discussed earlier for the evaluation of the wavenumber integral. Therefore, the same issues of windowing and sampling must be properly addressed. Since the evaluation of the frequency integral is common to all numerical approaches solving the Helmholtz equation, the associated numerical issues will

be deferred to Chap. 8. However, we present time-domain calculations also here (Sect. 4.10.4), due primarily to their importance in terms of interpreting the physical significance of features in the wavenumber integration kernels.

## 4.7 Range-Dependent Propagation

The wavenumber integration approach is applicable only to environments where the wave equation can be separated in range and depth. For a general layering of the ocean waveguide, this requires the environmental model to be horizontally stratified, with infinite extent in the horizontal plane, or spherically stratified for global propagation problems. If idealized boundary conditions and velocity profiles are acceptable, separation of variables can be applied to other geometries as well, e.g., to the ideal wedge. However, such models are mainly useful as benchmarks and are not sufficiently general to represent realistic ocean-acoustic scenarios.

An important feature of the wavenumber integration approaches is the direct representation of the solution in terms of physically meaningful wave components. In order to extend this feature to more general range-dependent problems, a significant effort has gone into the development of hybrid schemes involving wavenumber integration. A detailed description of these methods is beyond the scope of this book, and only a few references to the recent literature shall be given here.

Kuperman and Schmidt [35] combined the wavenumber integration with a self-consistent perturbational approach to model the rough interface scattering and the associated coherent propagation loss. The extention of this approach to allow modeling the reverberation in a stratified ocean environment with a rough seafloor is described later in Sect. 4.9.

Lu and Felsen [36] derived an adiabatic transformation of the wavenumber integrals for weakly range-dependent problems. Their approach is basically the integral equivalent of the adiabatic mode method described in Chap. 5.

Several attempts have been made to combine the wavenumber integration approach with the boundary integral method to model scattering by spatially confined inhomogeneities in an otherwise stratified environment. Shuster and Smith [37] used such an approach to model the scattering from objects in a stratified fluid bottom. Kawase [38] used a similar method to analyze the earthquake response of canyons in an elastic halfspace. In underwater acoustics, Dawson and Fawcett [32] used a hybrid wavenumber-integration/boundary-integral method to model propagation in an ocean waveguide with an irregular, but perfectly reflecting bottom. Essentially combining all these approaches, Gerstoft and Schmidt [39] used a hybrid wavenumber-integration/boundary-element approach to model scattering and reverberation from elastic inclusions in a stratified elastic bottom.

Finally, Seong [40] developed a fully range-dependent solution similar to the coupled mode approach described in Chap. 5. He basically divides the range-dependent environment into range-independent sectors and then couples the solutions by a hybrid boundary-element/finite-element method.

## 4.8 3-D Wavenumber Integration

The discussion of the wavenumber integration approach has so far been restricted to the case of a single point or line source, producing a two-dimensional acoustic field, axisymmetric or plane, respectively, in a stratified ocean waveguide. However, as shown by Schmidt and Glatting [41], it is straightforwardly generalized to computing the three-dimensional seismo-acoustic field produced by sources with horizontal directionality, such as horizontal or volumetric source arrays. Even though such fields can be represented as superpositions of offset point-source fields, the 3-D wavenumber integral representation becomes important for point sources with horizontal directionality, such as seismic moment sources. Also, as described in the following section, the use of wavenumber integration to handle scattering and reverberation problems inherently leads to wavenumber integral representations which are three-dimensional in nature.

Since the three-dimensional formulation is particularly useful for seismic problems, we will here describe it for stratifications involving elastic media. In the general 3-D case, the wavenumber integration formulation decomposes the wavefield in each layer  $\ell$  into one compressional and two shear potentials,

$$\chi_\ell = \{\phi_\ell, \psi_\ell, \Lambda_\ell\}, \quad (4.133)$$

where  $\chi_\ell$  is a generic potential representing the compressional potential  $\phi_\ell$  and the two scalar shear potentials  $\psi_\ell$  and  $\Lambda_\ell$ , representing SH and SV waves, respectively [41]. Obviously, in a fluid medium  $\chi_\ell$  represents the compressional potential only. For propagation and scattering in a horizontally stratified medium, it is convenient to introduce a coordinate system  $(\mathbf{x}, z)$ , where the vertical coordinate  $z$  is represented by a separate scalar, while the horizontal coordinates are represented in vector form  $\mathbf{x} = (x, y)$ .

Away from physical sources the seismo-acoustic field potentials of time dependence  $\exp(-i\omega t)$  must satisfy the homogeneous Helmholtz equations of the form,

$$[\nabla^2 + k_\ell^2] \chi_\ell(\mathbf{x}, z) = 0, \quad (4.134)$$

where  $k_\ell$  represents the appropriate medium wavenumbers  $k$  and  $\kappa$  for compressional and shear waves, respectively.

As in the 2-D case, the field must satisfy the boundary conditions at all interfaces  $z_\ell$  in the stratification, as well as the source conditions. Assuming the *physical sources* are limited to a single depth  $z_s$ , a dummy interface is added at this depth, and the interface conditions may then be written in the operator form,

$$B_\ell \chi_{\ell;\ell+1}(\mathbf{x}, z_\ell) = -f_s(\mathbf{x}) \delta_{\ell s}, \quad \ell = 1, 2 \dots N, \quad (4.135)$$

where  $\delta_{\ell s}$  is the Kronecker delta, having unit value at the source interface, and zero at all other interfaces.  $N$  is the total number of physical and dummy interfaces in the stratification. The differential matrix operator  $B_\ell$  represents the derivatives relating

the physical parameters involved in the boundary conditions to the potentials [35]. Thus, (4.135) represents the continuity of the pertinent displacements and stresses at all physical interfaces, and discontinuity conditions imposed by the physical source distribution  $f_s(\mathbf{x}, z_s)$ .

For problems with source distributions of finite horizontal extent, (4.134) and (4.135) are most conveniently solved in cylindrical coordinates. Here, the Helmholtz equation (4.134) have solutions in the form of an azimuthal Fourier–Neumann series, with the azimuthal Fourier coefficients being given by the Hankel transform integrals,

$$\begin{aligned} \chi_\ell(r, \varphi, z) = & \sum_{m=0}^{\infty} \left\{ \begin{array}{l} \cos m\varphi \\ \sin m\varphi \end{array} \right\} \int_0^\infty k_r J_m(k_r r) \\ & \times \left[ \widetilde{\chi}_{m;\ell}^+(k_r) e^{ik_z z} + \widetilde{\chi}_{m;\ell}^-(k_r) e^{-ik_z z} \right] dk_r. \end{aligned} \quad (4.136)$$

Here  $r, z$  are the depth and range coordinates, and  $k_r$  is the horizontal wavenumber. The depth dependence of the field is represented by the exponentials, with  $k_z$  being the vertical wavenumber, defined as

$$k_z = \begin{cases} \sqrt{k_\ell^2 - k_r^2}, & k_r \leq k_\ell \\ i\sqrt{k_r^2 - k_\ell^2}, & k_r > k_\ell, \end{cases} \quad (4.137)$$

where  $k_\ell = \omega/c_\ell$  is the medium wavenumber for layer  $\ell$ . In this form, the integral representation clearly separates the field into waves *propagating* vertically in the layer ( $k_r \leq k_\ell$ ), and waves which are exponentially growing or decaying, the *evanescent* waves ( $k_\ell \leq k_r$ ), separated by the critical wavenumber  $k_r = k_\ell$ . The amplitudes  $\chi_{m;\ell}^\pm(k_r)$  are found by matching the boundary conditions of continuous particle motion and stresses (pressure) at all interfaces in the stratification. Since these boundary conditions must be satisfied at all ranges  $r$ , they must be satisfied at each wavenumber component, in accordance with *Snell's law*. Assembled for all interfaces, these conditions are expressed in matrix form as

$$\widetilde{B}_\ell(k_r) \widetilde{\chi}_{m;\ell,\ell+1}^\pm(k_r) = -\widetilde{f}_{s;m}(k_r) \delta_{\ell s}, \quad \ell = 1, 2, \dots, N. \quad (4.138)$$

This equation is formally obtained as the Fourier–Hankel transform of the spatial boundary conditions, (4.135). At the depth of the source  $z_s$ , the *rhs* represents the discontinuity of the Hankel transforms of the particle motion and pressure due to the presence of the source. As shown by Schmidt and Glattetre [41], the global coefficient matrix  $\widetilde{B}_\ell$  in (4.138) can be made independent of the Fourier order  $m$ , which has obvious computational advantages when solving for many Fourier orders. This is achieved by expressing the boundary conditions, and therefore the source term  $\widetilde{f}_{s;m}$ , in terms of the following scalar equivalents

$$\widetilde{f}_{s;m}(k_r)^T \approx \Delta \left[ (\widetilde{u}^m + \widetilde{v}^m), (\widetilde{u}^m - \widetilde{v}^m), \widetilde{w}^m, \widetilde{\sigma}_{zz}^m, (\widetilde{\sigma}_{zr}^m + \widetilde{\sigma}_{z\varphi}^m), (\widetilde{\sigma}_{zr}^m - \widetilde{\sigma}_{z\varphi}^m) \right], \quad (4.139)$$

where  $\tilde{w}_m, \tilde{u}_m, \tilde{v}_m$  are the azimuthal expansion coefficients for the displacements [42]:

$$\begin{aligned}\tilde{w}(k_r, \varphi, z) &= \sum_{m=0}^{\infty} \tilde{w}^m(k_r, z) \begin{Bmatrix} \cos m\varphi \\ \sin m\varphi \end{Bmatrix} \\ \tilde{u}(k_r, \varphi, z) &= \sum_{m=0}^{\infty} \tilde{u}^m(k_r, z) \begin{Bmatrix} \cos m\varphi \\ \sin m\varphi \end{Bmatrix} \\ \tilde{v}(k_r, \varphi, z) &= \sum_{m=0}^{\infty} \tilde{v}^m(k_r, z) \begin{Bmatrix} \sin m\varphi \\ -\cos m\varphi \end{Bmatrix}\end{aligned}\quad (4.140)$$

and similarly for the stresses,

$$\begin{aligned}\tilde{\sigma}_{zz}(k_r, \varphi, z) &= \sum_{m=0}^{\infty} \tilde{\sigma}_{zz}^m(k_r, z) \begin{Bmatrix} \cos m\varphi \\ \sin m\varphi \end{Bmatrix} \\ \tilde{\sigma}_{rz}(k_r, \varphi, z) &= \sum_{m=0}^{\infty} \tilde{\sigma}_{rz}^m(k_r, z) \begin{Bmatrix} \cos m\varphi \\ \sin m\varphi \end{Bmatrix} \\ \tilde{\sigma}_{\varphi z}(k_r, \varphi, z) &= \sum_{m=0}^{\infty} \tilde{\sigma}_{\varphi z}^m(k_r, z) \begin{Bmatrix} \sin m\varphi \\ -\cos m\varphi \end{Bmatrix}.\end{aligned}\quad (4.141)$$

As in the 2-D case, the wavefield amplitude solutions to (4.138) are *exact*, but the numerical evaluation of the wavenumber integrals in (4.136) will exhibit the same truncation and discretization errors described earlier. However, the mitigation techniques described in Sect. 4.5 apply equally here.

## 4.9 Scattering and Reverberation in a Stratified Ocean

Even though the wavenumber integration approach is based on the assumption that the medium is horizontally stratified, it can be combined with e.g. Boundary Element methods to handle propagation in range-dependent media. However, for such problems other numerical techniques, such as Finite Element methods may often be advantageous. There are, however, a couple of classes of inherently range-dependent problems, where the wavenumber integration approach provides an attractive alternative. Those are the common underwater acoustics problems of scattering from an object in the ocean waveguide, and scattering and reverberation from small-scale perturbations to an otherwise horizontally stratified medium.

### 4.9.1 Target Scattering

Using a 3-D adaptation of the approach of Ingenito [43], the target is represented by a *virtual source* with a radiation pattern determined by convolving the incident field by a target scattering function. In this *single-scatter* approach, the stratification is ignored in the actual scattering process, with the target assumed to be in an infinite medium.

Following the derivation by Schmidt and Lee [44], the target is represented by a *virtual point source* at the target depth, with a radiation pattern determined by convolving the plane-wave components of the incident field by the plane-wave scattering function. Makris [45] rigorously derived the Fourier–Hankel representation of the 3-D waveguide field for a finite-size spherical target, and then formally investigated the validity of representing the target as a point scatterer. Using this *point-scatter* assumption, the Fourier–Hankel transform of the scattered field is performed numerically, in a form which is directly compatible with the Fourier-harmonics, 3-D extension of the wavenumber integral described in Sect. 4.8. Thus, following the derivation above, for an incident plane wave of wavenumber  $k$ , and horizontal azimuthal angle  $\varphi_0$ , the target scattering is represented by a 3-D shaded point source term,

$$\phi(R, q_r, \varphi) = \frac{\exp(i k R)}{R} T^\pm(q_r, \varphi, \varphi_0), \quad (4.142)$$

where  $T^\pm(q_r, \varphi, \varphi_0)$  are the angular-dependent target strengths or scattering amplitudes, with the  $\pm$  representing the up- and downward propagating components. The scattering amplitudes are here represented in terms of the horizontal wavenumbers  $k_r$  and  $q_r$  of the incident and scattered field, respectively, directly related to the grazing angles by the relation  $k_r = k \cos \theta$ . With the incident field being inherently decomposed into plane-wave components, the following integral representation is achieved from (4.9) for the scattering amplitudes for a target at depth  $z_T$ , and range and azimuth  $r_T$  and  $\varphi_T$  relative to the source,

$$\begin{aligned} T^+(q_r, \varphi, \varphi_0) = k^{-1} \int_0^\infty & \left[ S(\theta, \varphi, -\theta_0, \varphi_0) A^- e^{-ik_z z_T} \right. \\ & \left. + S(\theta, \varphi, \theta_0, \varphi_0) A^+ e^{ik_z z_T} \right] J_0(k_r r_T) k_r dk_r, \end{aligned} \quad (4.143)$$

$$\begin{aligned} T^-(q_r, \varphi, \varphi_0) = k^{-1} \int_0^\infty & \left[ S(-\theta, \varphi, -\theta_0, \varphi_0) A^- e^{-ik_z z_T} \right. \\ & \left. + S(-\theta, \varphi, \theta_0, \varphi_0) A^+ e^{ik_z z_T} \right] J_0(k_r r_T) k_r dk_r. \end{aligned} \quad (4.144)$$

with

$$\theta = \arccos[q_r / k(z)],$$

$$\theta_0 = \arccos[k_r / k(z)].$$

For a target in a stratified waveguide, (4.142) must be transformed into a wavenumber integral representation. As described in Sect. 2.4.2 for the point source, the transformation of the  $\exp(ikR)/R$  term is provided by the *Sommerfeld–Weyl* integral, (2.106), with the kernel  $i\exp(iq_z|z - z_t|)/q_z$  at depth  $z$ . Applying the *stationary phase* or *farfield* approximation, the corresponding wavenumber kernel for the scattered field is then achieved by simply shading the kernel of the Sommerfeld–Weyl integral by the scattering function,

$$\tilde{\phi}(z, q_r, \varphi) = i \frac{e^{-q_z|z-z_t|}}{q_z} T^\pm(q_r, \varphi, \varphi_0). \quad (4.145)$$

For simple bistatic configurations, where the field is required only at a few azimuthal angles  $\varphi$ , one can use the standard wavenumber integral representation in (2.140) with the source term in the kernel simply replaced by (4.145).

Except for monostatic and simple bistatic sonar configurations, the scattered field will in general be required at a large number of angles in azimuth. In such cases this simple “slice” method is computationally expensive. Alternatively, following Schmidt and Glatting [41], the wavenumber integration method is directly adapted to sources with azimuthal anisotropy by replacing the omni-directional wavenumber integral by its Fourier–Neumann equivalent,

$$\begin{aligned} \phi(r, \varphi, z) &= \sum_{m=0}^{\infty} \left\{ \begin{array}{l} \cos m\varphi \\ \sin m\varphi \end{array} \right\} \int_0^{\infty} q_r J_m(q_r r) \\ &\quad \times i^{m+1} \frac{e^{iq_z|z-z_t|}}{q_z} \tilde{T}_m^\pm(q_r, k_r, \varphi_0) dq_r, \end{aligned} \quad (4.146)$$

where  $i^m \tilde{T}_m^\pm(q_r, k_r, \varphi_0)$  are the Fourier–Hankel transforms of the target scattering functions in (4.143) and (4.144). It should be pointed out that these can be determined directly using higher-order spherical harmonics [46], thus avoiding a computationally intensive, two-dimensional numerical Fourier–Hankel transform. For each Fourier order  $m$ , we instead solve for the propagated field using standard wavenumber integration, simply replacing the *rhs* of the global boundary condition equation, (4.138), by the discontinuity in pressure and particle velocity above and below the nominal target depth  $z_T$ , associated with the source kernel at Fourier order  $m$ ,

$$\tilde{\phi}_m(q_r, z) = i^{m+1} \frac{e^{iq_z|z-z_t|}}{q_z} \tilde{T}_m^\pm(q_r, k_r, \varphi_0). \quad (4.147)$$

The Fourier–Neumann azimuthal expansion of the wavenumber integration approach now directly yields the target scattering at all bistatic angles in arbitrary, fluid–elastic stratifications [41]. The use of Fourier expansion in azimuth, as opposed to evaluating the wavenumber integral for each desired azimuthal angle, in general leads to significant computational savings, since the number of Fourier terms required is approximately equal to the  $ka$  value of the target, i.e., typically of order 1–10. For bi- and multistatic dynamic scenarios, the number of required azimuths in general far exceeds that.

In contrast to the modal formulation, described later in Sect. 5.12, the wavenumber representation inherently incorporates the scattering function for evanescent incident and scattered field components, which, e.g., is crucial to the modeling of scattering by buried targets interacting with seismic interface waves, etc. Also, the computed scattered field incorporates the steeper angle, continuous spectrum, which is important for ranges shorter than typically 5–10 water depths.

The wavenumber integration approach requires the target to be in an isovelocity layer to yield the decomposition into up- and downgoing plane waves. However, this is easily achieved simply by adding an infinitesimally thin layer at the target depth, consistent with the point scatter formulation. Even though the inclusion of the large-wavenumber, evanescent scattering components is an advantage of the wavenumber integration approach, it also causes problems. Thus, it can be shown [47] that the wavenumber kernel for sources of vertical extent diverges for large wavenumbers at depths covered by the source. This problem is inherent to the wavenumber scattering formulation. Thus, for depth-separations smaller than the target radius, the kernel in (4.146) will diverge. The integral converges theoretically due to cancellation by the oscillating Bessel function, but the numerical stability of the evaluation requires very special consideration in these cases, similar to those described in Sect. 4.5, but much more severe here because of the vertical extent of the target.

### 4.9.2 Rough Interface Reverberation

The 3-D wavenumber integration formulation in Sect. 4.8 can be combined with a perturbational approach to allow full wave-theory modeling of the three-dimensional field scattered by bottom roughness and propagated in the ocean waveguide. This approach handles consistently both the coherent component of the full waveguide field, including the evanescent bottom penetration, and the scattering and reverberation produced by anisotropic seabed roughness. Even though the modeling approach described here treats the scattered field deterministically, and therefore coherently, we will maintain the traditional scattering theory terminology, with the field in the absence of scatters being referred to as the *coherent* field, and the field perturbation being denoted the *scattered* field.

Following the computation of the coherent field by standard wavenumber integration, the scattering by rough interfaces can be consistently handled using the method of small perturbations developed by Kuperman and Schmidt [35]. For arbitrary fluid–elastic stratifications, this theory decomposes the wavefield into coherent and scattered components of the field potentials in layer number  $\ell$ , as illustrated in Fig. 4.13,

$$\chi_\ell = \langle \chi_\ell \rangle + s_\ell = \begin{cases} \phi_\ell = \langle \phi_\ell \rangle + p_\ell \\ \psi_\ell = \langle \psi_\ell \rangle + q_\ell \\ \Lambda_\ell = \langle \Lambda_\ell \rangle + r_\ell, \end{cases} \quad (4.148)$$

where  $\chi_\ell$  again is a generic potential representing the compressional potential and shear potentials in layer  $\ell$ .

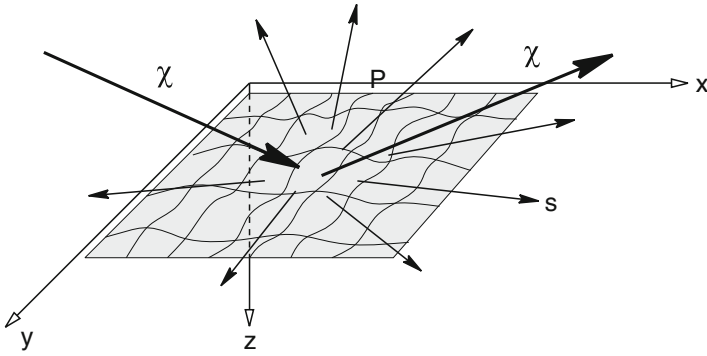


**Fig. 4.13** Rough interface patch in stratified waveguide, insonified by a seismo-acoustic field

The coherent field satisfies the Helmholtz equation (4.134) and a boundary conditions similar to (4.135), but with a modified boundary operator  $B_\ell$ . The self-consistent modification is important for evaluating coherent scattering losses [35, 48]. However, for evaluating the scattered field, the unperturbed conditions may be applied for the coherent field in what is equivalent to the *Born approximation*. Similarly, the scattered potentials satisfy homogeneous Helmholtz equations,

$$[\nabla^2 + k_\ell^2] s_\ell(\mathbf{x}, z) = 0 \quad (4.149)$$

and a set of boundary conditions, which according to the perturbation theory are of the form,

$$B_\ell s_{\ell;\ell+1}(\mathbf{x}, z_\ell) = -f_v(\mathbf{x}) \delta_{\ell,v}, \quad \ell = 1, 2 \dots N, \quad (4.150)$$

where  $z_v$  is the depth of the rough interface, and the distribution function  $f_v(\mathbf{x})$  is given by [35, 48, 49],

$$f_v(\mathbf{x}) = \left[ \overbrace{\gamma_v(\mathbf{x}) \frac{\partial B_v}{\partial z}}^{\text{elevation}} + \overbrace{\nabla \gamma_v(\mathbf{x}) \circ \mathbf{b}_v}^{\text{rotation}} \right] \langle \chi_{v;v+1}(\mathbf{x}, z_v) \rangle. \quad (4.151)$$

Here,  $\gamma_v(\mathbf{x})$  is the roughness elevation of interface  $v$  at depth  $z_v$ .  $B_v$  is the same boundary operator as above, while  $\mathbf{b}_v$  is a vector operator, representing the rotation of the boundary conditions due to the roughness slope. Note that the  $\circ$  operation represents the inner product of the local slope vector  $\nabla \gamma_v = (\gamma_x, \gamma_y)$  with the rotation operator  $\mathbf{b}_v$ .

Obviously, (4.150) is totally equivalent to (4.135), with the physical source distribution  $f_s(\mathbf{x})$  replaced by the distribution function  $f_v(\mathbf{x})$  at the depth of the rough

interface. Thus,  $f_v(\mathbf{x})$  represents a *virtual source distribution*, the amplitude and phase distributions of which are determined by the coherent field and the roughness through (4.151).

#### 4.9.2.1 Wavenumber Representation

For horizontal stratifications with rough interfaces of infinite extent, the perturbation theory proceeds by transforming the boundary equations (4.150) into the wavenumber domain, yielding for the wavenumber spectrum of the scattered field [48],

$$\begin{aligned} \tilde{s}_{\ell;\ell+1}^{\mp}(\mathbf{q}) = & -\tilde{B}_{\ell}^{-1}(\mathbf{q}) \frac{\delta_{\ell v}}{2\pi} \int d^2\mathbf{k} \tilde{\gamma}_v(\mathbf{q} - \mathbf{k}) \\ & \times \left[ \frac{\partial \tilde{B}_v(\mathbf{k})}{\partial z} + i(\mathbf{q} - \mathbf{k}) \cdot \tilde{\mathbf{b}}_v(\mathbf{k}) \right] \langle \tilde{\chi}_{v;v+1}^{\mp}(\mathbf{k}) \rangle, \quad \ell = 1, 2, \dots, N. \end{aligned} \quad (4.152)$$

Here, the matrix operators  $\tilde{B}_{\ell}$  and  $\tilde{\mathbf{b}}_{\ell}$  are the Fourier transforms of the corresponding differential operators in (4.151), and  $\langle \tilde{\chi}_{v;v+1}^{\mp} \rangle$  represents the expectation value of the wavefield components in the two layers, the *coherent* or *mean field*. For the mean and scattered fields to be consistent, the *mean field* must satisfy the modified boundary conditions [48],

$$\left[ \tilde{B}_{\ell}(\mathbf{k}) + \frac{\langle \gamma^2 \rangle}{2} \frac{\partial^2}{\partial z^2} \tilde{B}_{\ell}(\mathbf{k}) + I_1(\mathbf{k}) + I_2(\mathbf{k}) \right] \langle \tilde{\chi}_{\ell;\ell+1}^{\mp}(\mathbf{k}) \rangle = 0, \quad (4.153)$$

where  $I_1(\mathbf{k})$  and  $I_2(\mathbf{k})$  are the *scattering integrals*,

$$\begin{aligned} I_1(\mathbf{k}) = & -\frac{\langle \gamma^2 \rangle}{2\pi} \int d^2\mathbf{q} P_{\ell}(\mathbf{q} - \mathbf{k}) \frac{\partial \tilde{B}_{\ell}(\mathbf{q})}{\partial z} \\ & \times \tilde{B}_{\ell}^{-1}(\mathbf{q}) \left[ \frac{\partial \tilde{B}_{\ell}(\mathbf{k})}{\partial z} + i(\mathbf{q} - \mathbf{k}) \cdot \tilde{\mathbf{b}}_{\ell}(\mathbf{k}) \right], \end{aligned} \quad (4.154)$$

$$\begin{aligned} I_2(\mathbf{k}) = & \frac{\langle \gamma^2 \rangle}{2\pi} \int d^2\mathbf{q} P_{\ell}(\mathbf{q} - \mathbf{k}) i(\mathbf{q} - \mathbf{k}) \cdot \tilde{\mathbf{b}}(\mathbf{q}) \\ & \times \tilde{B}_{\ell}^{-1}(\mathbf{q}) \left[ \frac{\partial \tilde{B}_{\ell}(\mathbf{k})}{\partial z} + i(\mathbf{q} - \mathbf{k}) \cdot \tilde{\mathbf{b}}_{\ell}(\mathbf{k}) \right], \end{aligned} \quad (4.155)$$

where  $P_{\ell}(\mathbf{p})$  is the roughness power spectrum, and the matrix operators  $\tilde{B}_{\ell}$  and  $\tilde{\mathbf{b}}_{\ell}$  are the same as those appearing in (4.152). Their derivation is described in Appendix 2 for the common cases involving a fluid–fluid and a fluid–elastic interface. The use of the self-consistent boundary equations in (4.153) is important in cases where the coherent scattering loss is to be estimated. However, in cases where

the first-order scattering and reverberation is to be estimated, one may apply the *Born approximation* and simply use the unperturbed field solution for driving the scattered field in (4.152).

For random, spatially homogeneous interface roughness, the roughness statistics is given by the spatial correlation function  $N_v(\Delta\mathbf{r})$ , or its Fourier transform, the normalized roughness power spectrum  $P_v(\mathbf{p})$ , and the roughness variance  $\langle \gamma_v^2 \rangle$ ,

$$N_v(\Delta\mathbf{r}) = \langle \gamma_v(\mathbf{r}) \gamma_v(\mathbf{r} + \Delta\mathbf{r}) \rangle, \quad (4.156)$$

$$\langle \gamma_v^2 \rangle P_v(\mathbf{p}) = \frac{1}{2\pi} \int d^2 \Delta\mathbf{r} N_v(\Delta\mathbf{r}) e^{-i\mathbf{p} \cdot \Delta\mathbf{r}}. \quad (4.157)$$

Then the following expression is achieved for the spatial correlation function for the scattered field [48],

$$C_S(\mathbf{r}_1, z_1, \mathbf{r}_2, z_2) = \frac{\langle \gamma_v^2 \rangle}{(2\pi)^3} \int d^2 \mathbf{p} P_v(\mathbf{p}) \left[ \int d^2 \mathbf{q} A_m(z_1, \mathbf{q}, \mathbf{q} + \mathbf{p}) e^{i\mathbf{q} \cdot \mathbf{r}_1} \right]^\dagger \times \left[ \int d^2 \mathbf{q} A_n(z_2, \mathbf{q}, \mathbf{q} + \mathbf{p}) e^{i\mathbf{q} \cdot \mathbf{r}_2} \right]^\dagger, \quad (4.158)$$

where  $(\mathbf{r}_1, z_1)$  and  $(\mathbf{r}_2, z_2)$  are the coordinates of receivers in layers  $m$  and  $n$ , respectively, and  $A_m(z, \mathbf{q}, \mathbf{k})$  is the scattering kernel,

$$A_m(z, \mathbf{q}, \mathbf{k}) = e_m(z, \mathbf{q}) \tilde{T}_{v;m}^*(\mathbf{q}, \mathbf{k}) \langle \tilde{\chi}_{v;v+1}^\mp(\mathbf{k}) \rangle.$$

Here  $e_\ell(z, \mathbf{q})$  contains the exponentials representing the up- and downgoing scattered wavefield in layer  $\ell$ , and  $\tilde{T}_{v;\ell}$  is a generalized *transition matrix* for the field in layer  $\ell$  produced by scattering from rough interface number  $v$ ,

$$\tilde{T}_{v;\ell}(\mathbf{q}, \mathbf{k}) = -\tilde{B}_\ell^{-1}(\mathbf{q}) \frac{\delta_{\ell v}}{2\pi} \left[ \frac{\partial \tilde{B}_v(\mathbf{k})}{\partial z} + i(\mathbf{q} - \mathbf{k}) \cdot \tilde{\mathbf{b}}_v(\mathbf{k}) \right], \quad \ell = 1, 2 \dots N. \quad (4.159)$$

The scattering integrals of both (4.152) and (4.158) are of a form convolving a medium-dependent boundary operator term by the roughness spectrum at the difference wavenumber. This *Bragg scattering* condition is illustrated graphically in Fig. 4.14. An incident field with a wavenumber spectrum centered around the wave vector  $\mathbf{k}$  is convolved with an anisotropic roughness spectrum with skewness  $\varphi$ , creating a scattered field composed of wave vectors  $\mathbf{q}$  within the lightly shaded envelope in Fig. 4.14, representing the roughness spectrum. The modal structure of the waveguide, represented by the inverse boundary operator  $\tilde{B}_\ell^{-1}(\mathbf{q})$  in (4.159), is indicated by the circles in Fig. 4.14. Thus, the resulting scattered field will have a modal structure in all directions, but shaded by the roughness spectrum centered at the incident wavenumber.

Even though the wavenumber representation of the scattered field statistics is not used directly, the *Bragg scattering* condition is convenient for interpreting the

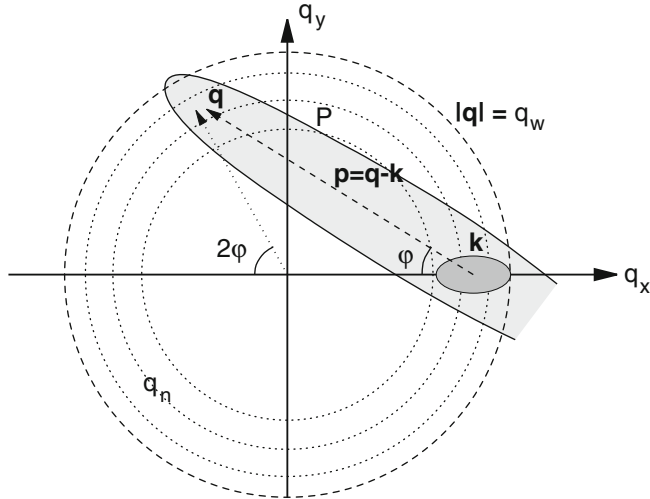


**Fig. 4.14** Graphical representation of the scattering wavenumber kernel. The scattered field is a convolution in the wavenumber plane of the incident field by the anisotropic roughness wavenumber spectrum

numerical results, and diagrams similar to Fig. 4.14 will be used in the following to explain the spatial and temporal *super sensitivity* of the reverberation environment associated with rippled seabeds.

#### 4.9.2.2 Finite Roughness Patch

For realistic two-dimensionally rough interfaces, the convolution integrals in the correlation function, (4.158), become four-dimensional. Even though a normal-mode expansion of (4.158) has recently been developed, yielding orders of magnitude in computational savings [50], the full numerical evaluation of the three-dimensional field statistics through (4.158) is computationally prohibitive. Consequently, numerical implementations have been limited to plane or axisymmetric problems with one-dimensional roughness [48, 50].

For a finite-size roughness patch, or sonar footprint, the scattered field can instead be represented by a spatial integral over the patch \$P\$,

$$s_\ell(\mathbf{x}; z) = \int_P G_\ell(\mathbf{x}, \mathbf{x}_v; z, z_v) d^2 \mathbf{x}_v, \quad (4.160)$$

where \$G\_\ell(\mathbf{x}, \mathbf{x}\_v; z, z\_v)\$ is a *Generalized Green's Function* satisfying the standard Helmholtz equation, and the boundary conditions,

$$B_\ell(\mathbf{x}) G_{\ell; \ell+1}(\mathbf{x}, \mathbf{x}_v; z, z_v) = -\delta(\mathbf{x} - \mathbf{x}_v) f_v(\mathbf{x}) \delta_{\ell v}, \quad \ell = 1, 2 \dots N \quad (4.161)$$

with the virtual source distribution  $f_v(\mathbf{x})$  given by (4.151). This equation is obviously of a form identical to the coherent equation (4.135) and can, therefore, be solved in cylindrical coordinates using the Fourier–Hankel transform, with solutions of the form of (4.136). Inserting these solutions into (4.160), and reversing the order of integration, yields for the scattered field,

$$s_\ell(r, \varphi, z) = \sum_{m=0}^{\infty} \left\{ \begin{array}{l} \cos m\varphi \\ \sin m\varphi \end{array} \right\} \int dq_r q_r J_m(q_r r) \times \left[ \int_P \tilde{G}_\ell^m(q_r, z, r_v, \varphi_v) r_v dr_v d\varphi_v \right]. \quad (4.162)$$

As was the case for the coherent field produced by the physical sources, the scattered field can then be computed using the three-dimensional wavenumber integration approach described in Sect. 4.8, with the physical source kernels being replaced by the virtual source equivalents, obtained as the Fourier–Hankel transforms of (4.151). The details of this transformation are described by Fan [51].

The Fourier series in (4.162) converges very fast for orders larger than the dimensionless size  $ka$  of the patch, due to the asymptotic behavior of the virtual source kernels,

$$\tilde{G}_\ell^m(q_r, z, r_v, \varphi_v) \sim J_m(q_r r_v) \rightarrow 0, \quad \text{for } m > q_r r_v \quad (4.163)$$

and the truncation of the azimuthal Fourier series is therefore easily determined *a priori*. Thus, the number of significant terms in the series depends only on the patch size with the typical number being equal to a few times the *patch size* in wavelengths. In contrast, the number of terms in the numerical evaluation of each of the two dimensions of the equivalent Fourier transform in Cartesian coordinates is determined by the *receiver range*. For finite-size patches, the virtual source range is typically much shorter than the receiver ranges, which is the key to the numerical efficiency of the cylindrical form.

### 4.9.3 Scattering from Volume Inhomogeneities

It has been shown by LePage and Schmidt [25, 52] that a perturbational approach can be used to model the monostatic reverberation caused by three-dimensionally distributed volume inhomogeneities in stratified media. The theory combines a wavenumber integration formulation for propagation to and from the scatterers with a two-dimensional spectral representation of the azimuthally-averaged scatterer realizations, totally consistent with the theory for rough interface reverberation described in the previous section. Together, the volume and interface scattering formulations can be combined with any spectral integral modeling framework to provide an efficient, high-fidelity, time-series realization generator for monostatic reverberation from realistic sediments in stratified ocean environments.

The first-order scattered pressure observed at the field point  $(x, y, z)$  due to small-perturbation volume inhomogeneity scattering from sound-speed perturbations  $\Delta c/c$  in the depth interval  $[z_1, z_2]$  is given by the convolution integral,

$$p_s(x, y, z) = 2k_b^2 \int_{-\infty}^{\infty} dx' \int_{-\infty}^{\infty} dy' \int_{z_1}^{z_2} dz' G(\vec{r}, \vec{r}') \times \frac{\Delta c}{c}(x', y', z') p(x', y', z'), \quad (4.164)$$

where, under the zeroth-order Born approximation,  $p$  is the pressure incident on the scatterers in the absence of multiple scattering effects,  $G(\vec{r}, \vec{r}')$  is the Green's function from the scatterer at  $\vec{r}' = (x', y', z')$  to the observer at  $\vec{r} = (x, y, z)$ , and the three-dimensional integral integrates over the space of contributing scatterers  $\frac{\Delta c}{c}$ . As described above, in a spectral integral modeling framework for a horizontally stratified medium, the Green's function has the wavenumber integral representation,

$$G(r, z, z') = \int_0^{\infty} g(q_r; z, z') J_0(r q_r) q_r dq_r \quad (4.165)$$

with  $r = \sqrt{(x - x')^2 + (y - y')^2}$  representing the horizontal separation of scatterer and observer.  $g(q_r; z, z')$  is the *depth-separated Green's function* which, e.g., in the case of a homogeneous background medium with acoustic wavenumber  $k_0$ , is given by the (2.105),

$$g(q_r; z, z') = \frac{i}{4\pi} \frac{e^{i|z-z'| \sqrt{k_0^2 - q_r^2}}}{\sqrt{k_0^2 - q_r^2}}. \quad (4.166)$$

As described in Sect. 4.8, the incident acoustic pressure for a general, horizontally anisotropic source are represented by a Fourier–Bessel integral,

$$p(x', y', z') = \sum_{n=0}^{\infty} \left\{ \begin{array}{l} \cos m\varphi' \\ \sin m\varphi' \end{array} \right\} \int_0^{\infty} \tilde{p}_m(k_r, z') J_m(k_r r') k_r dk_r, \quad (4.167)$$

where  $r' \equiv \sqrt{x'^2 + y'^2}$  and  $\varphi' \equiv \arccos(x'/r')$ .

#### 4.9.3.1 Monostatic Backscatter

In the case of observations of scattering in a laterally monostatic geometry  $x, y \equiv 0$ , (4.164) considerably simplifies when the source is horizontally omni-directional. Then the only non-zero Fourier harmonic in the source expansion is  $m = 0$ , and upon substitution of (4.165) and (4.167), (4.164) may be written as

$$p_s(z) = 2k_b^2 \int_{-\infty}^{\infty} dx' \int_{-\infty}^{\infty} dy' \int_{z_1}^{z_2} dz' \frac{\Delta c}{c}(x', y', z') \\ \times \int_0^{\infty} g(q_r; z, z') J_0(q_r r') q_r dq_r \int_0^{\infty} \tilde{p}_0(k_r, z') J_0(k_r r') k_r dk_r, \quad (4.168)$$

or, equivalently, converting to cylindrical coordinates and setting  $\delta c \equiv \Delta c/c$ ,

$$p_s(z) = 2k_b^2 \int_0^{\infty} r' dr' \int_{z_1}^{z_2} dz' \int_0^{2\pi} d\varphi \delta c(r', \varphi, z') \\ \times \int_0^{\infty} g(q_r; z, z') J_0(q_r r') q_r dq_r \int_0^{\infty} \tilde{p}_0(k_r, z') J_0(k_r r') k_r dk_r. \quad (4.169)$$

The angular integral in (4.169) indicates that the scattered field observed monostatically is averaged over non-dimensional sound speed perturbations  $\delta c$  in the cylindrical angle  $\varphi$ , yielding only a contribution from the zeroth-order harmonic of the perturbations,

$$\delta c_0(r, z') \equiv \int_0^{2\pi} \delta c(r, \varphi, z') d\varphi \\ = \int_0^{\infty} \tilde{\delta c}_0(p_r, z') J_0(p_r r) p_r dp_r. \quad (4.170)$$

By definition the spatial distribution of scatterers is related to its complex spectrum through the Fourier integral,

$$\delta c(x, y, z') = \int_{-\infty}^{\infty} \int_{-\infty}^{\infty} \tilde{\delta c}(k_x, k_y, z') e^{ik_x x} e^{ik_y y} dk_x dk_y, \quad (4.171)$$

which may be expressed in cylindrical coordinates as

$$\delta c(r, \varphi, z') = \int_{-\infty}^{\infty} \int_{-\infty}^{\infty} \tilde{\delta c}(k_x, k_y, z') e^{ik_x r \cos \varphi} e^{ik_y r \sin \varphi} dk_x dk_y \\ = \int_0^{\infty} p'_r dp'_r \int_0^{2\pi} d\varphi' \\ \times \tilde{\delta c}(p'_r \cos \varphi', p'_r \sin \varphi', z') e^{ip'_r r \cos \varphi' \cos \varphi} e^{ip'_r r \sin \varphi' \sin \varphi}. \quad (4.172)$$

The  $m$ th Fourier harmonic of the Fourier–Bessel transformation of  $\delta c(r, \varphi)$  is defined by the relation

$$\tilde{\delta c}_m(p_r, z') = \int_0^{\infty} J_m(p_r r) r dr \int_0^{2\pi} d\varphi \left\{ \begin{array}{l} \cos m\varphi \\ \sin m\varphi \end{array} \right\} \delta c(r, \varphi, z'). \quad (4.173)$$

For monostatic backscatter the form of (4.169) and (4.170) suggests that only the  $m \equiv 0$  order Fourier–Bessel transform of the perturbation  $\delta c$  is required. Insertion of (4.172) into (4.173) for  $m = 0$  yields,

$$\begin{aligned}\tilde{\delta c}_0(p_r, z') &= \int_0^{2\pi} d\varphi \int_0^{2\pi} d\varphi' \int_0^{\infty} r dr \int_0^{\infty} J_0(p_r r) p'_r dp'_r \\ &\times \tilde{\delta c}(p'_r \cos \varphi', p'_r \sin \varphi', z') e^{ip'_r r \cos \varphi' \cos \varphi} e^{ip'_r r \sin \varphi' \sin \varphi}. \quad (4.174)\end{aligned}$$

Equation (4.174) may be simplified through the variable transformation

$$\varphi' = \varphi + \varphi'',$$

which yields

$$\begin{aligned}\cos \varphi' &= \cos(\varphi + \varphi'') = \cos \varphi \cos \varphi'' - \sin \varphi \sin \varphi'' \\ \sin \varphi' &= \sin(\varphi + \varphi'') = \sin \varphi \cos \varphi'' + \cos \varphi \sin \varphi''.\end{aligned}$$

In this case, the complex exponentials in (4.174) may be considerably simplified as

$$e^{ip'_r r \cos \varphi' \cos \varphi} e^{ip'_r r \sin \varphi' \sin \varphi} \equiv e^{ip'_r r \cos \varphi''}, \quad (4.175)$$

so that (4.174) may be written as

$$\begin{aligned}\tilde{\delta c}_0(p_r, z') &= \int_0^{\infty} J_0(p_r r) r dr \int_0^{\infty} p'_r dp'_r \int_0^{2\pi} d\varphi \int_{-\varphi}^{2\pi-\varphi} d\varphi'' \\ &\times \tilde{\delta c}[p'_r \cos(\varphi + \varphi''), p'_r \sin(\varphi + \varphi''), z'] e^{ip'_r r \cos \varphi''} \\ &= \int_0^{\infty} J_0(p_r r) r dr \int_0^{\infty} p'_r dp'_r \int_0^{2\pi} \tilde{\delta c}(p'_r \cos \varphi''', p'_r \sin \varphi''', z') d\varphi''' \\ &\times \int_0^{2\pi} \cos[p'_r r \cos(\varphi''' - \varphi)] d\varphi. \quad (4.176)\end{aligned}$$

The integral over  $\varphi$  in (4.176) is evaluated as the Bessel function  $2\pi J_0(p'_r r)$ . If  $\tilde{\delta c}(k_x, k_y, z')$  is isotropic and composed of  $p'_r/2\pi$  independent normally-distributed random variables of variance  $P_{\delta c}(p'_r)$ , where  $P_{\delta c}$  is the power spectrum of the perturbations  $\delta c$ , then the integral over  $\varphi'''$  may be evaluated as [25],

$$\int_0^{2\pi} \tilde{\delta c}(p'_r \cos \varphi''', p'_r \sin \varphi''', z') d\varphi''' = N[0, 2\pi P_{\delta c}(p'_r, z')/p'_r], \quad (4.177)$$

where  $N[0, 2\pi P_{\delta c}(p'_r, z')/p'_r]$  is a normally-distributed random variable with variance  $\sigma^2 = 2\pi P_{\delta c}(p'_r, z')/p'_r$ . Thus (4.176) may be written as

$$\tilde{\delta c}_0(p_r, z') = 2\pi \int_0^{\infty} J_0(p_r r) r dr \int_0^{\infty} \sqrt{p'_r} N[0, 2\pi P_{\delta c}(p'_r, z')] J_0(p'_r r) dp'_r, \quad (4.178)$$

so that, by the Fourier–Bessel transform relation, we obtain,

$$\tilde{\delta}c_0(p_r, z') = 2\pi N[0, 2\pi P_{\delta c}(p_r, z')/p_r]. \quad (4.179)$$

Insertion of (4.179) into (4.170) then yields the azimuth-averaged perturbation realization,

$$\delta c_0(r', z') = 2\pi \int_0^\infty \sqrt{2\pi p_r} N[0, P_{\delta c}(p'_r, z')] J_0(p_r r') dp_r.$$

Equation (4.169) then takes the form,

$$\begin{aligned} p_s(z) &= 4\pi \sqrt{2\pi} k_b^2 \int_0^\infty r' dr' \int_{z_1}^{z_2} dz' \int_0^\infty \sqrt{p_r} N[0, P_{\delta c}(p_r, z')] J_0(p_r r') dp_r \\ &\times \int_0^\infty g(q_r; z, z') J_0(q_r r') q_r dq_r \\ &\times \int_0^\infty \tilde{p}_0(k_r, z') J_0(k_r r') k_r dk_r. \end{aligned} \quad (4.180)$$

Changing the orders of integration, (4.180) can be cast into a form which is directly suited for implementation in a wavenumber integration modeling framework for ocean waveguides,

$$\begin{aligned} p_s(z) &= 4\pi \sqrt{2\pi} k_b^2 \int_0^\infty q_r dq_r \int_{z_1}^{z_2} g(q_r; z, z') dz' \int_0^\infty J_0(q_r r') r' dr' \\ &\times \int_0^\infty \sqrt{p_r} N[0, P_{\delta c}(p_r, z')] J_0(p_r r') dp_r \\ &\times \int_0^\infty \tilde{p}_0(k_r, z') J_0(k_r r') k_r dk_r. \end{aligned} \quad (4.181)$$

In this form, the two inner integrals are uncoupled and may be evaluated directly a priori for a selected grid of scatterers in the spatial  $(r', z')$  domain. The integral over  $k_r$  represents the incident pressure field, while the integral over  $p_r$  represents the cylindrically-averaged scattering strength at  $(r', z')$ . The product of these integrals then represents the horizontal distribution of virtual sources at depth  $z'$  contributing to the scattered field. The Hankel transform integral over  $r'$  converts this sheet of virtual sources into an equivalent wavenumber spectrum, which, multiplied by the depth-dependent Green's function, represents the scattered field component at horizontal wavenumber  $q_r$ . The depth integral then superimposes the contributions from all scatterer depths to produce the total kernel of the Hankel wavenumber integral for the monostatic reverberant field on the coordinate axis  $r = 0$ , which is evaluated using any of the standard wavenumber integration techniques described in Sect. 4.5.

## 4.10 Numerical Examples

We apply here the wavenumber integration approach to a few seismo-acoustic propagation scenarios for which this solution technique is either unique or particularly convenient. These examples also illustrate how the inherent spectral decomposition of the field can be used to address the basic physics of this class of propagation problems.

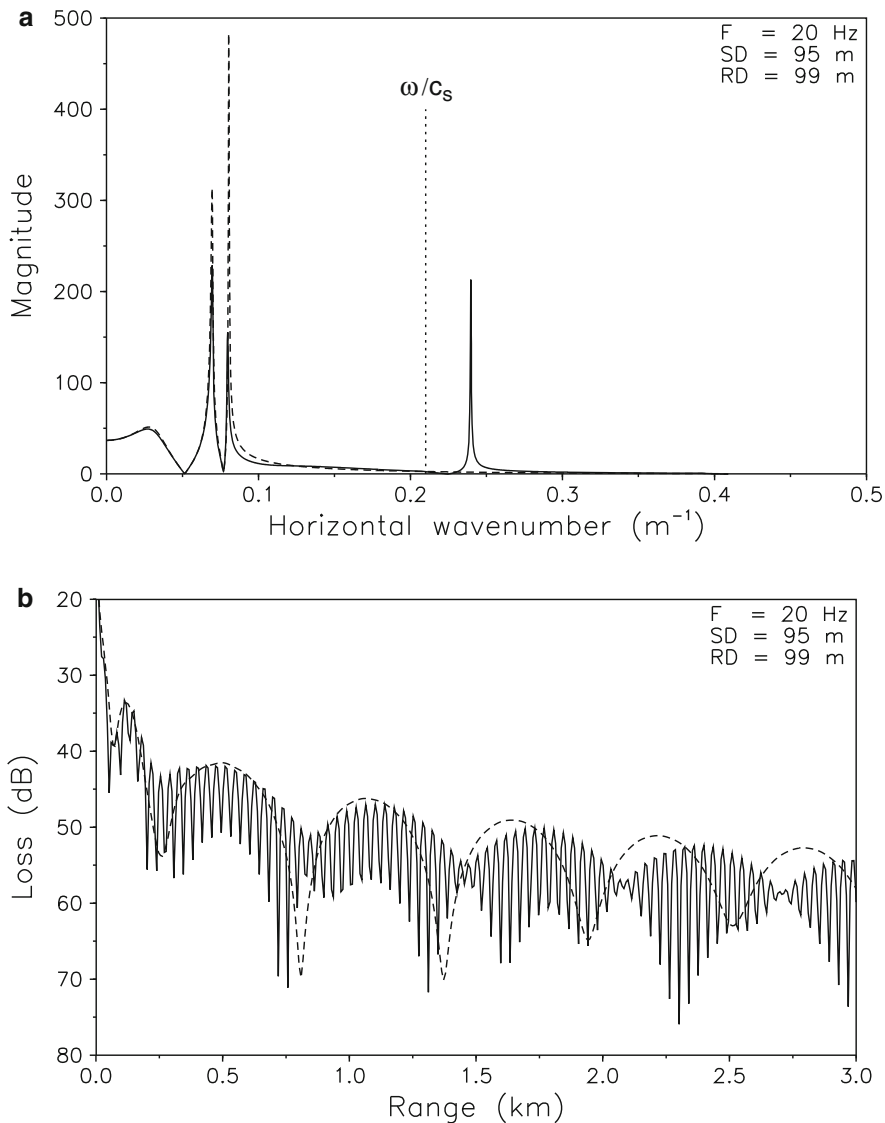
### 4.10.1 Waveguide with an Elastic Bottom

To illustrate the importance of correctly treating the shear properties of an elastic bottom, we modify the Pekeris waveguide shown in Fig. 2.25 to include shear in the bottom halfspace. First, it is assumed that the bottom material is sand with a compressional speed  $c_p = 1800 \text{ m/s}$  and density  $\rho_2 = 1800 \text{ kg/m}^3$  as before, but now with a shear speed  $c_s = 600 \text{ m/s}$ . To highlight the effect of shear we place both source and receiver close to the bottom, at 95- and 99-m depth, respectively.

Figure 4.15a shows the magnitude of the depth-dependent Green's function at 20 Hz as the solid curve, and for comparison, the corresponding Green's function for the Pekeris waveguide is indicated by the dashed curve. In the *continuous spectrum*, i.e., for wavenumbers up to  $k_r = 2\pi f/c_p = 0.07 \text{ m}^{-1}$ , the effect of shear is insignificant, except for a decrease in amplitude of the virtual mode. Similarly, the main difference in the *discrete spectrum* is a decrease in the amplitude of the single propagating normal mode. The reason for the decrease in amplitude of the two modes is the fact that for wavenumbers smaller than the shear wavenumber  $\kappa_2 = 2\pi f/c_s = 0.21 \text{ m}^{-1}$  indicated by the dotted line in Fig. 4.15a, the shear waves are propagating in the bottom, thus leaking energy away from the water column, in effect moving both poles away from the real wavenumber axis.

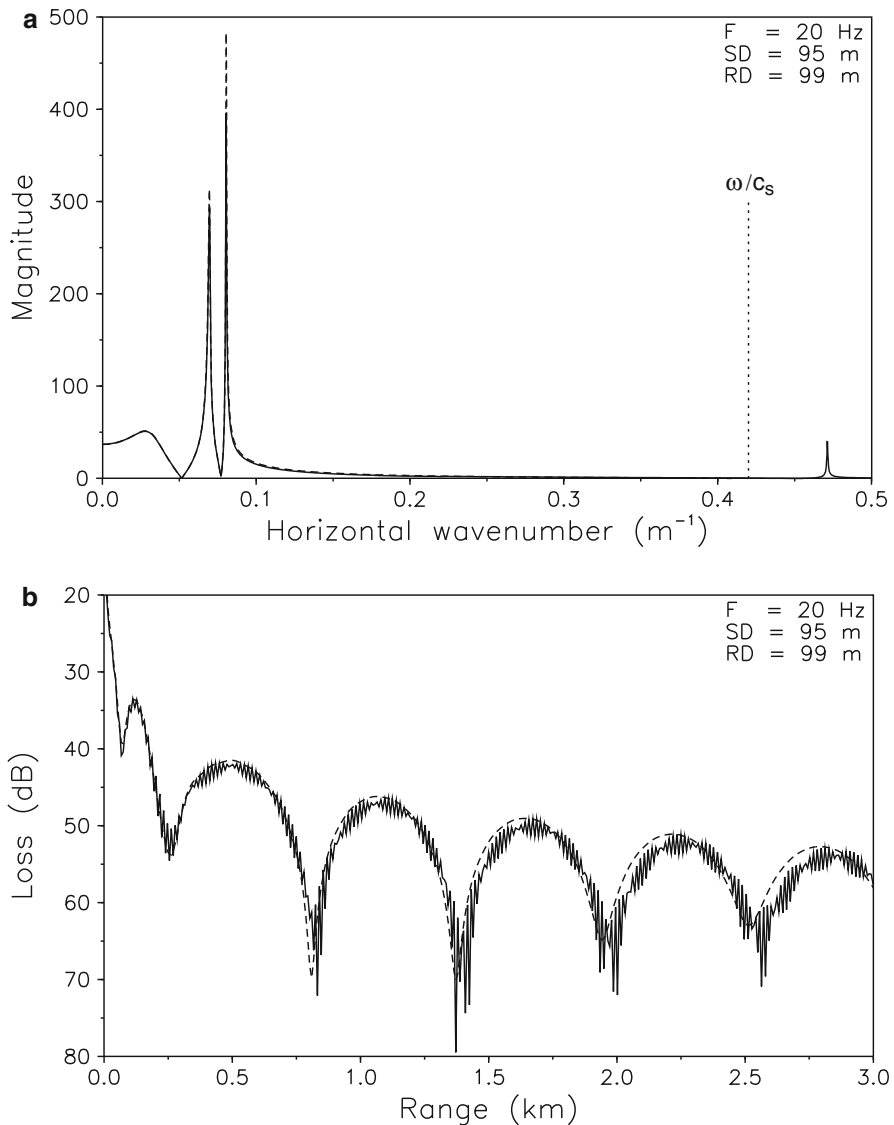
A more dramatic shear effect is the existence of an additional pole ( $k_r = 0.24 \text{ m}^{-1}$ ) in the part of the spectrum for which the field in the water is evanescent and for which both compression and shear waves are evanescent in the bottom. It can be shown that such a pole always exists for an elastic bottom, with a propagation wavenumber that is slightly larger than the shear wavenumber. This pole corresponds to an additional mode of propagation, *a seismic interface wave*; in underwater acoustics it is called a *Scholte wave*, and in seismology a *Stoneley wave*. Due to the fact that this mode is evanescent in both the water column and the bottom, its effect is most pronounced close to the water–bottom interface.

Figure 4.15b shows the corresponding transmission loss for the elastic case as the solid curve, and for comparison the fluid-bottom result as the dashed curve. The slowly changing interference structure is due to the interference of the normal and virtual modes similar to those of the Pekeris waveguide. The presence of shear not only affects the amplitude of the modes with higher transmission loss as a result, but the propagation wavenumbers change as well, modifying the modal interference length. This difference will be evident at all depths, but rapid fluctuations due to the Scholte wave interference will be most pronounced close to the bottom.



**Fig. 4.15** Acoustic field at 99 m depth in shallow-water waveguide with elastic bottom for 20-Hz point source at 95 m depth. **(a)** Magnitude of depth-dependent Green's function. **(b)** Transmission loss. Solid curve: Shear speed 600 m/s. Dashed curve: Fluid bottom

Most shallow sediments have much smaller shear speeds than the 600 m/s assumed above, and for such bottoms the effect of shear will diminish. This is illustrated in Fig. 4.16 showing results for a shear speed  $c_s = 300 \text{ m/s}$  in the bottom halfspace. Although the amplitudes of the two modes have decreased due to the shear, the effect is much less pronounced than in the high-shear-speed case above.



**Fig. 4.16** Acoustic field at 99-m depth in shallow-water waveguide with elastic bottom for 20-Hz point source at 95-m depth. **(a)** Magnitude of depth-dependent Green's function. **(b)** Transmission loss. *Solid curve:* Shear speed 300 m/s. *Dashed curve:* Fluid bottom

In addition, the Scholte wave at  $k_r = 0.47 \text{ m}^{-1}$  has diminished in amplitude. As a result, the effect of a low shear speed is relatively insignificant, even close to the bottom for this scenario, as illustrated in Fig. 4.16b. On the other hand, for lower frequencies where the normal modes are cut off, the Scholte wave still exists, and therefore dominates the transmission loss. Consequently, shear must be included at low frequencies to properly predict the transmission loss.

It should be emphasized that the results shown here are all steady-state solutions. The various modes may separate in the time domain at long ranges, yielding arrivals at field points where the transmission loss is vanishing. Examples of slow Scholte-wave arrivals separated from the faster waterborne modes are given in Chap. 8.

#### 4.10.2 The Bucker Waveguide

The fluid waveguide shown in Fig. 4.17 has been suggested by Bucker as a benchmark for ocean-acoustic propagation models [53]. The reason is partly that this environment is characterized by a strong density contrast at the bottom, which some earlier PE implementations had difficulties treating. Further, the sound speed contrast is very small, yielding a small number of normal modes with real propagation wavenumbers. On the other hand, the density contrast yields a significant number of virtual modes close to the real wavenumber axis. Therefore, normal mode models ignoring the continuous spectrum will not be able to provide accurate predictions of the transmission loss. On the other hand, the wavenumber integration has no restrictions on the density contrast nor on the spectral composition and is therefore capable of providing exact solutions for this environment.

The importance of the continuous spectrum is evident from Fig. 4.18a, showing the magnitude of the depth-dependent Green's function at depth 90 m for a 100-Hz point source at 30-m depth. The discrete spectrum, indicated by the dotted lines, covers only a minor part of the total spectrum.

The resultant transmission loss versus range is shown in Fig. 4.18b as a solid curve. The dashed curve indicates the solution obtained if the continuous spectrum

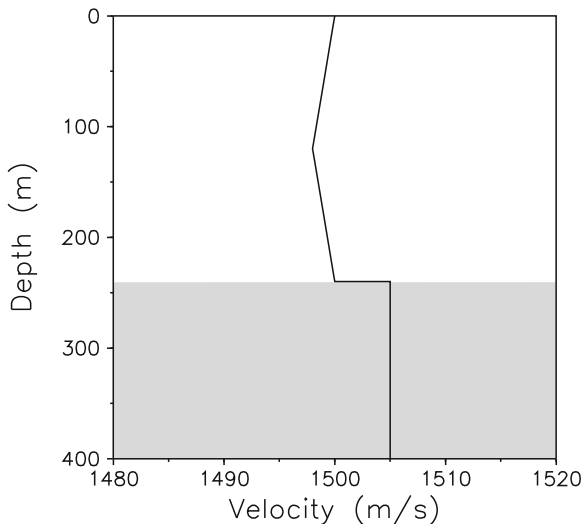


**Fig. 4.17** Sound-speed profile for Bucker waveguide of depth 240 m. The densities are  $1000 \text{ kg/m}^3$  for the water and  $2100 \text{ kg/m}^3$  for the fluid-bottom halfspace

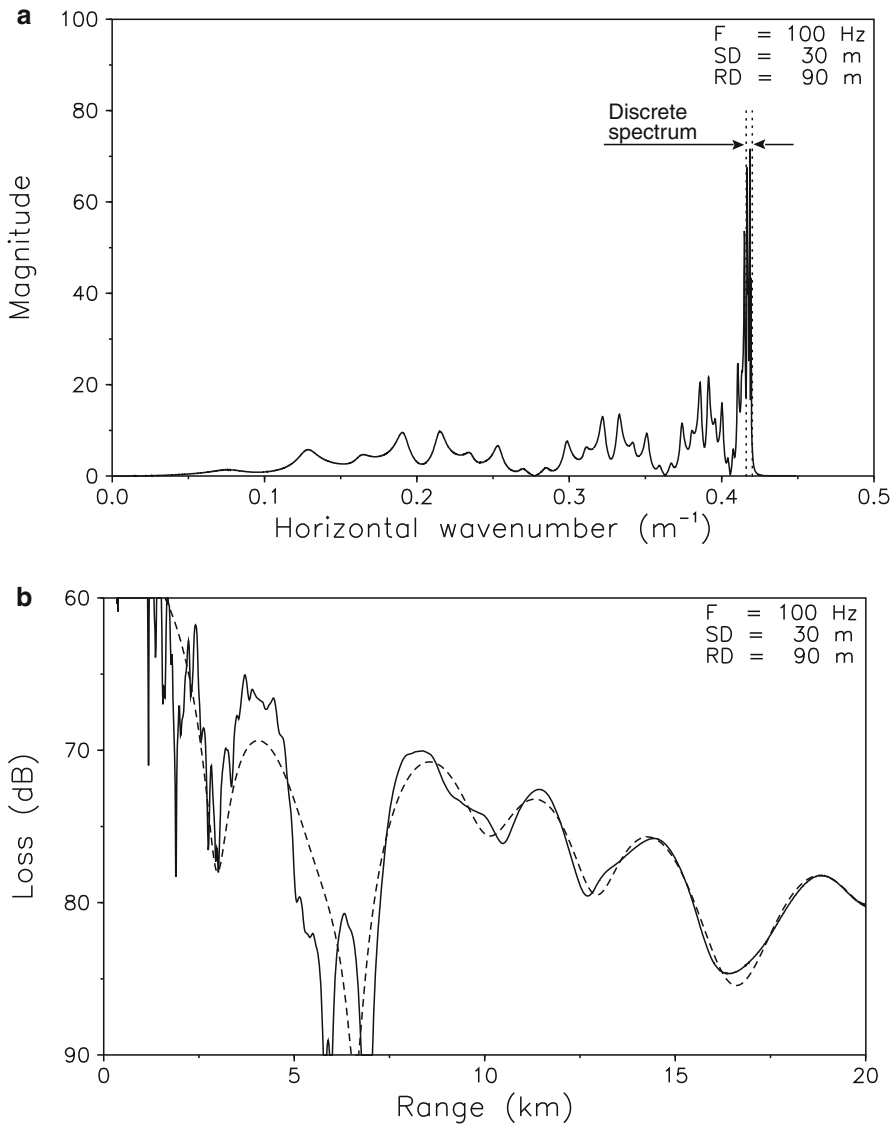


**Fig. 4.18** Propagation in the Bucker waveguide for a 100-Hz point source at 30 m depth: (a) Magnitude of depth-dependent Green's function at 90 m depth. (b) Transmission loss vs. range with the *solid curve* showing the full spectrum solution and the *dashed curve* the discrete spectrum solution (normal modes)

is ignored, i.e., the field predicted by normal-mode models including only modes on the real wavenumber axis. In most ocean-acoustic environments the significance of the continuous spectrum is limited to a few water depths in range, but here the influence of the continuous spectrum is clearly important even at very long ranges.

### 4.10.3 Beam Reflection and Transmission

Since the wavenumber integration approaches are not limited to propagation problems where the normal modes are dominant, they are well-suited to the analysis of short-range propagation problems where bottom interaction is important. Such problems are typically encountered in relation to experiments aimed at determining bottom properties. Such an experimental scenario is the use of high-frequency beams to determine the reflectivity characteristics of the seabed. We will here use wavenumber integration modeling to illustrate the physics involved in such an experimental scenario, with emphasis on the significance of the deeper layering.

In order to specifically address the bottom interaction problem, we ignore the free surface and replace the water column by an infinite upper halfspace with a constant sound speed of 1500 m/s. As shown in Fig. 4.19, the seabed is assumed to be at depth 100 m. A sediment layer of thickness 20 m has a pseudo-linear sound speed profile ranging from 1600 m/s at the seabed to 1700 m/s at the subbottom. Two subbottoms are considered: One is a homogeneous halfspace with sound speed 1800 m/s (solid line), whereas the second has a 1-m thick layer with speed 1800 m/s overlying a halfspace with 1700 m/s (dashed line). The densities of all layers in the bottom are assumed to be 1800 kg/m<sup>3</sup>.

A 1-kHz Gaussian beam is generated by a vertical array of 41 line sources with  $\lambda/2$  spacing (7.5 m), centered 50 m above the seabed. The Gaussian shape of the beam is obtained by applying a Gaussian shading of the the array, and the elements are phased to provide a nominal grazing angle of 25° of the beam. As discussed by Jensen and Schmidt [54] such a finite-width beam has a finite wavenumber spectrum, as is evident from Fig. 4.20, with Fig. 4.20a showing the wavenumber spectrum, and Fig. 4.20b showing the corresponding power spectrum versus grazing angle. The nominal horizontal wavenumber of the beam is  $k_r = 3.80 \text{ m}^{-1}$ ,

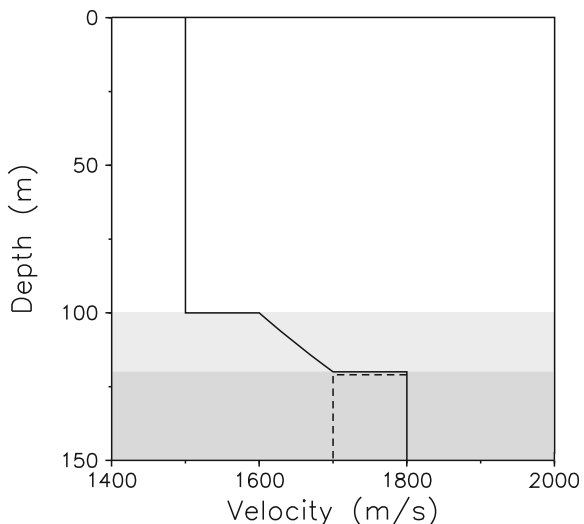


**Fig. 4.19** Sound-speed profile for beam reflection example. *Solid line:* Homogeneous subbottom halfspace with sound speed 1800 m/s. *Dashed line:* 1 m thick layer with speed 1800 m/s overlying a halfspace with 1700 m/s

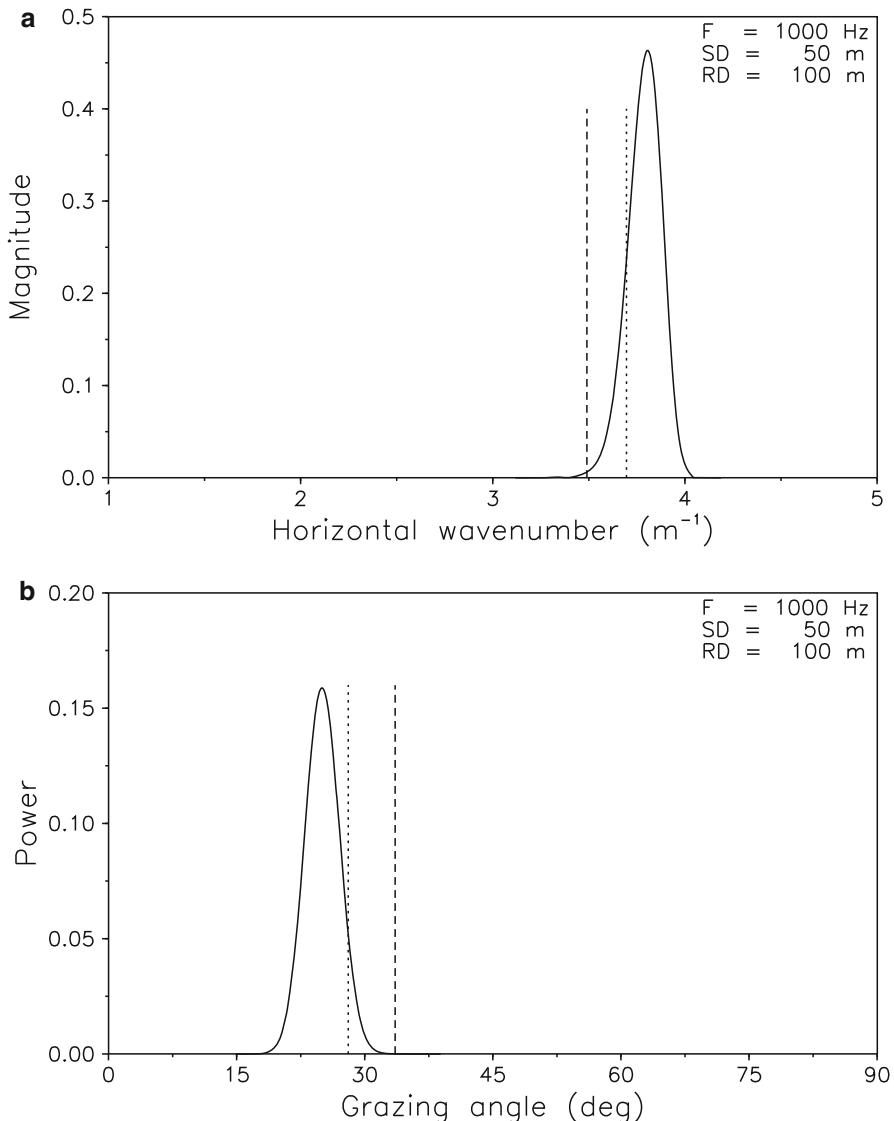


**Fig. 4.20** Plane wave spectra of the insonifying Gaussian beam at the seabed. **(a)** Horizontal wavenumber spectrum. **(b)** Power spectrum vs. grazing angle. The critical wavenumbers and angles for bottom speeds 1700 and 1800 m/s are indicated by the dotted and dashed lines, respectively

corresponding to a horizontal phase velocity of 1655 m/s, which is less than the sound speeds 1800 and 1700 m/s considered in the two subbottom examples. The corresponding bottom wavenumbers are indicated in Fig. 4.20a by the dashed and dotted lines respectively, and similarly for the corresponding critical grazing angles in Fig. 4.20b. The beam has significant plane-wave components propagating

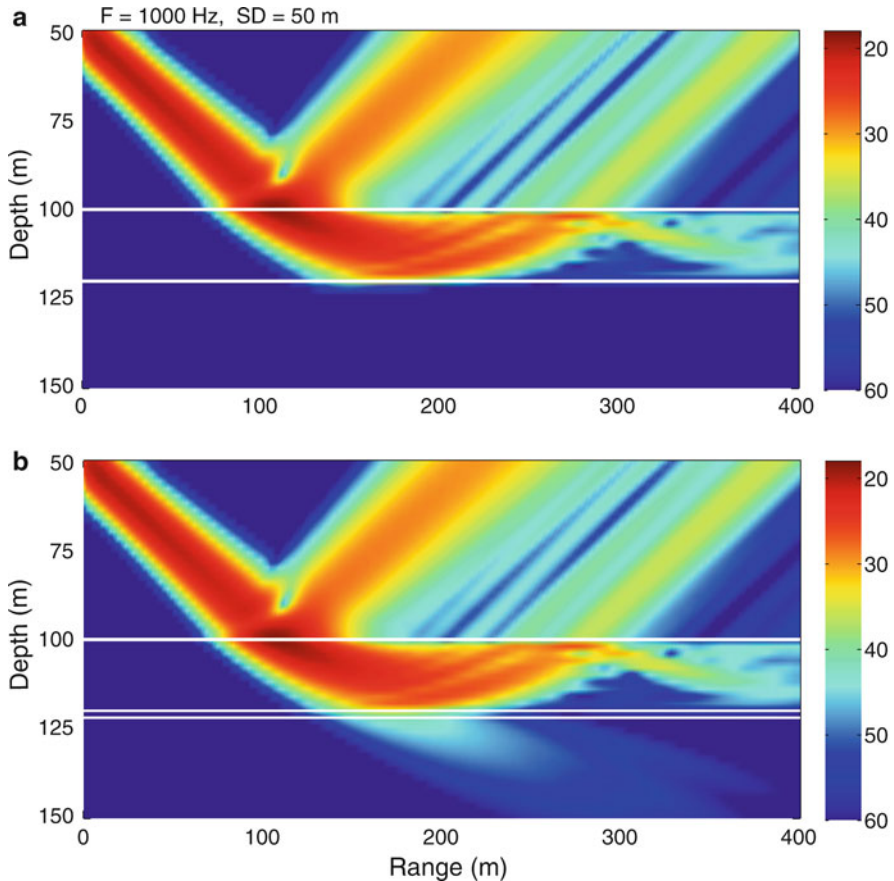


**Fig. 4.21** Contours of acoustic pressure produced by a Gaussian beam at nominal grazing angle  $25^\circ$  onto the seabed. (a) Halfspace subbottom with sound speed 1800 m/s. (b) 1-m thick fast layer over subbottom halfspace with speed 1700 m/s

vertically in the 1700 m/s bottom,  $k_r < 3.70 \text{ m}^{-1}$ , whereas the spectral components propagating vertically in the 1800 m/s bottom are insignificant. In other words, all significant plane-wave components of the beam are below critical grazing angle for the fast bottom, but some components are above critical for the 1700 m/s bottom.

Figure 4.21 shows the computed fields in the form of pressure contours versus depth and range. Figure 4.21a shows the result for the fast subbottom halfspace with sound speed 1800 m/s. Since all significant components of the beam have grazing angles below critical for this bottom, the field in the lower halfspace is evanescent, with all energy being reflected back into the sediment layer and subsequently into the water column. Therefore, the reflection coefficient for this bottom is of unit magnitude in the spectral regime covered by the beam. However, if this beam experiment is used to determine the reflection coefficient simply by measuring the field in the

specularly reflected beam, a 6 dB bottom loss will be observed. The rest of the beam energy is in part upwardly refracted in the sediment layer and in part reflected off the subbottom interface, and this energy will, therefore, re-enter the water column at longer ranges, generating a very complicated interference pattern as shown in Fig. 4.21a. It is interesting to note, that for this particular problem, a significant part of the energy will be trapped in the sediment layer, spreading the leakage back into the water column over a very long range interval. A correct determination of the plane-wave reflection coefficient would, therefore, in this case require a very long horizontal array in the water column. This example, therefore, clearly illustrate the limitations of traditional experimental techniques for determining reflection coefficients, as discussed in detail by Schmidt and Jensen [22].

The result for the 1700 m/s subbottom underlying a 1-m thick 1800 m/s layer is shown in Fig. 4.21b. The fast layer obviously provides a strong barrier, making the field in both the water column and in the sediment layer qualitatively similar to that of the homogeneous subbottom example. As described above, all significant components of the incoming beam will be evanescent in this layer, making it a strong reflector. However, the depth of the evanescent “tail” is finite, and in this case deeper than the thickness of the layer, yielding a non-vanishing field at the lower interface. Since parts of the beam spectrum are vertically propagating in the 1700 m/s halfspace, they will therefore convert from evanescent waves in the fast layer to propagating waves in the slower halfspace, generating a beam transmitted into the bottom, as is evident in Fig. 4.21b. This phenomenon of energy leaking through a layer through evanescent components is called wave *tunneling*, and is often observed in seismic refraction experiments such as the present example, due to the fact that these components may be reflected by deeper interfaces and detected at the seabed at longer ranges.

The tunneling phenomenon is not handled by classical ray theory, which would assume perfect reflection of all beam components by the fast layer, and therefore yield a field identical to that shown in Fig. 4.21a. This would obviously only be the case for higher frequencies where the evanescent “tails” are much shorter than the layer thickness. This example therefore clearly shows the limitations of classical ray theory as compared to full wave solutions, even at relatively high frequencies such as the present 1-kHz example. An additional example of wave tunneling not handled by ray theory is given in Sect. 8.5.6.

#### 4.10.4 Arctic Propagation

The ice-covered Arctic environment is oceanographically very stable due to the limited interaction with the atmosphere. Therefore, the sound speed variation is generally limited to the vertical. In addition, the low surface temperature makes the sound-speed profile strongly upward refracting at all depths, limiting the influence of the bottom, at least over the deep Abyssal plains. In terms of the water column, the Arctic environment therefore provides an almost ideal range-independent

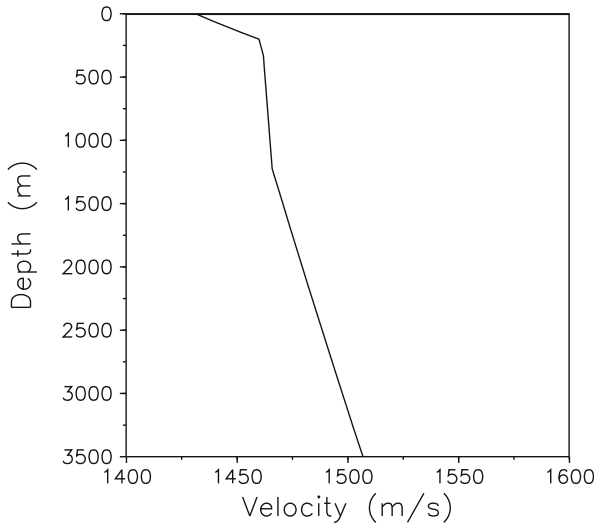


**Fig. 4.22** Sound-speed profile in ice-covered Arctic environment. The ice cover is 4 m thick and is treated as a homogeneous elastic medium with compressional speed 3500 m/s and shear speed 1800 m/s

waveguide, where sound can propagate over very long distances without bottom interaction. On the other hand, the ice cover is a complicating factor, and due to the upward-refracting sound-speed profile all significant propagation paths will interact with the ice cover. Ever since the pioneering work of Kutschale [2], the wavenumber integration approaches have provided a unique tool for modeling under-ice propagation in the Arctic ocean.

Figure 4.22 shows an example of a sound-speed profile in an Arctic environment covered by a 4-m thick, uniform ice plate with compressional speed 3500 m/s and shear speed 1800 m/s. Due to thermal radiation through the ice into the atmosphere, the water temperature decreases toward the surface, yielding a strongly upward-refracting thermocline in the upper few hundred meters. Beyond 1000 m depth, the sound speed is dominated by the pressure gradient, yielding a weaker upward-refracting profile. For shallow sources a significant amount of energy will be trapped in the surface channel, in contrast to the warmer latitudes, where fields produced by shallow sources will be dominated by the deeper-penetrating convergence-zone propagation as described in Chap. 1.

Transmission loss contours for the Arctic environment given in Fig. 4.22 are shown in Fig. 4.23 for a 20-Hz source at 100 m depth. It is evident that the field at depth down to 200 m is totally dominated by the surface-duct propagation, whereas the convergence-zone structure is dominating in the deeper parts of the ocean. A small increase in field strength can be observed in the convergence zones near the surface, but the detection of shallow sources in the Arctic is obviously not restricted to the convergence zones as is the case at lower latitudes. In Chap. 10, we use this Arctic environment to illustrate modern source localization processing.

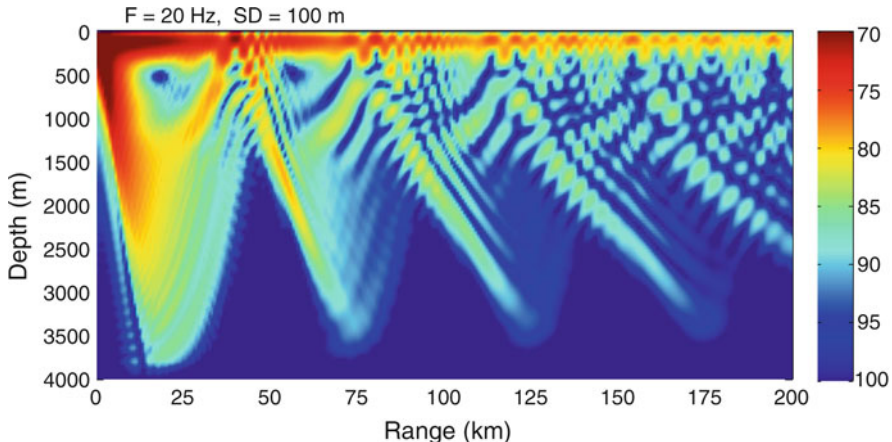


**Fig. 4.23** Contours of transmission loss vs. range and depth in Arctic environment

In Fig. 4.23, the ice cover was assumed to be a homogeneous, range-independent plate with realistic attenuations of  $0.4 \text{ dB}/\lambda$  for compressional waves and  $1.0 \text{ dB}/\lambda$  for shear waves. However, it has been demonstrated that the loss computed for such an environment is too low and not in agreement with experimental observations [55]. The obvious reason for this discrepancy is the fact that the ice cover is extremely inhomogeneous along the propagation path, being characterized by significant roughness as well as many discrete features such as ridges with keels extending deep into the surface channel. Although significant effort has gone into the theoretical description of this phenomenon, it is not yet properly understood. However, there is strong experimental evidence that a significant amount of energy is scattered into seismic waves in the ice cover [56], and this is therefore a plausible explanation for the observed excess loss in the Arctic.

Several seismic wave components have been measured in the ice, including horizontally polarized shear waves, the presence of which can only be explained by a three-dimensional scattering theory. However, the presence of other seismic modes such as the compressional and flexural plate waves are at least qualitatively explained by a two-dimensional theory. Although the scattering of energy into these waves due to inhomogeneities in the ice is beyond the capability of classical wave-number integration, we can illustrate how the excitation of these waves is predicted by a range-independent model. We use the same environmental model as above, but compute the particle velocities as they would be observed by geophones on the surface of the ice.

In order to specifically address the ice interaction problem, we ignore the wave-guide nature of the real ocean and replace the water column by a homogeneous lower halfspace with a constant sound speed of 1438 m/s, as shown in Fig. 4.24. For a 20-Hz source at 20-m depth, the kernels of the wavenumber integrals for the particle velocity on the surface of the ice are shown in Fig. 4.25, with the solid

**Fig. 4.24** Sound-speed profile in uppermost 50 m in ice-covered Arctic environment. The ice cover is 4 m thick and is treated as a homogeneous elastic medium with compressional speed 3500 m/s and shear speed 1800 m/s

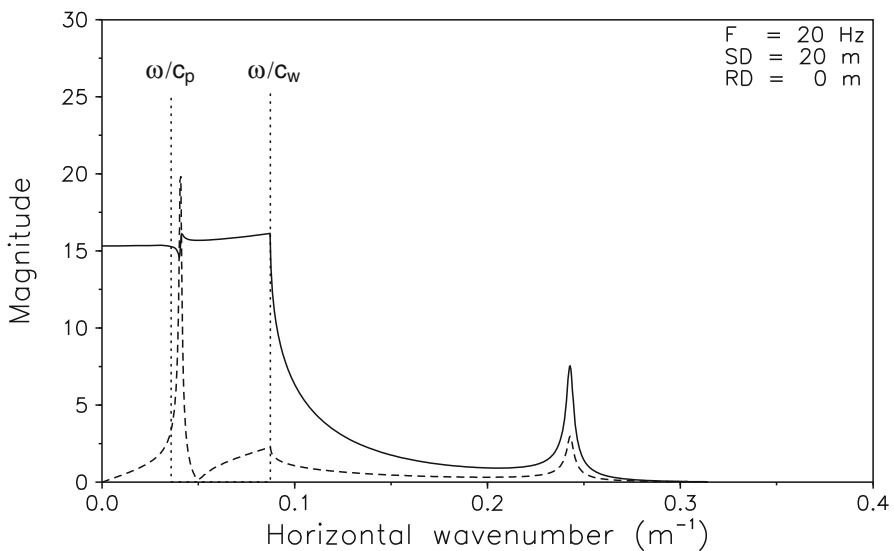
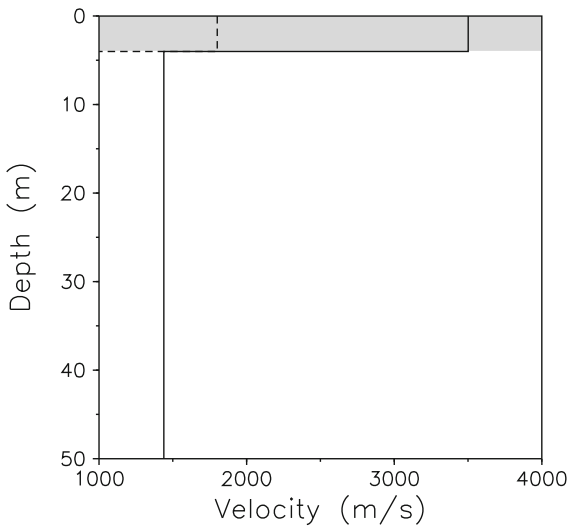


**Fig. 4.25** Magnitude of wavenumber integration kernels for particle velocities on the ice surface. *Solid curve*: Vertical component. *Dashed curve*: Radial component. *Dotted lines* indicate wavenumbers for compressional waves in ice and in water

curve representing the vertical component and the dashed curve the radial component. The dotted lines indicate the wavenumbers for compressional waves in the ice,  $k_r = 0.0359 \text{ m}^{-1}$ , and in the water,  $k_r = 0.0874 \text{ m}^{-1}$ .

The kernel for the radial particle velocity has a sharp peak at a wavenumber slightly larger than the compressional wavenumber in the ice, corresponding to the

fundamental compressional plate mode. Since this wavenumber is smaller than the water wavenumber, this mode will be propagating vertically in the water, leaking energy away from the ice plate. Therefore, the compressional mode is a *leaky mode* with complex propagation wavenumber. The compressional mode is also visible in the vertical particle velocity kernel as a small N-shaped wiggle. The branch point at the water wavenumber is evident in both components as a discrete change in slope. The third distinct feature of the kernels is the peak at wavenumber  $k_r \simeq 0.24 \text{ m}^{-1}$ . This is the fundamental *flexural wave* in the ice plate, with the largest amplitude in the vertical direction. This wave is obviously evanescent in the water column and is therefore not leaking. In the absence of attenuation, its propagation wavenumber would, therefore, be real. However, in this case the ice attenuation moves the singularity away from the real axis, yielding a finite amplitude in Fig. 4.25.

The physical significance of these three wavenumber components becomes particularly clear in the time domain solution. Thus, Fig. 4.26 shows the synthetic seismograms computed for a horizontal array of geophones on the ice surface, with 10 geophones spaced 100 m apart out to 1-km range. The source at 20-m depth is assumed to generate a Blackman–Harris pressure pulse (the second derivative of the Blackman window function, see [24], Sect. 7.4), with center frequency 20 Hz. Figure 4.26a shows the vertical geophone component and Fig. 4.26b the radial component. The first arrival is the compressional wave in the ice, which is most prominent in the radial component. The second arrival with *move-out* speed 1438 m/s is the waterborne arrival. It is most evident in the vertical component and has a pulse shape identical to the Ricker source wavelet. The third arrival, with the largest amplitude in the vertical component, is the flexural mode. This mode is highly dispersive, with the low frequencies propagating at extremely low group velocities.

The wavenumber integration approach is particularly well-suited and efficient for this type of short-range time-domain problem. Thus, the time domain solutions in Fig. 4.26 are computed in a few seconds on a standard workstation.

#### 4.10.5 Seabed Target Scattering and Reverberation

The detection of targets below a rough seabed is a challenging sonar problem of importance to minehunting and marine archeology. The detection of such buried objects are particularly difficult for insonification angles below critical, where the sonar penetration is limited to the evanescent lateral wave in the sediment [44]. A characteristic subcritical incidence scenario using narrow-beam sonars is shown in Fig. 4.27. The water sound speed is 1525 m/s, while the bottom is sand represented by a fluid halfspace with compressional velocity 1685 m/s and density  $1900 \text{ kg/m}^3$ . The corresponding critical grazing angle is  $25.2^\circ$ . The seabed is insonified by a narrow-beam sonar at a nominal grazing angle of  $18^\circ$ . The sonar footprint is approximately  $10 \times 5 \text{ m}$ .

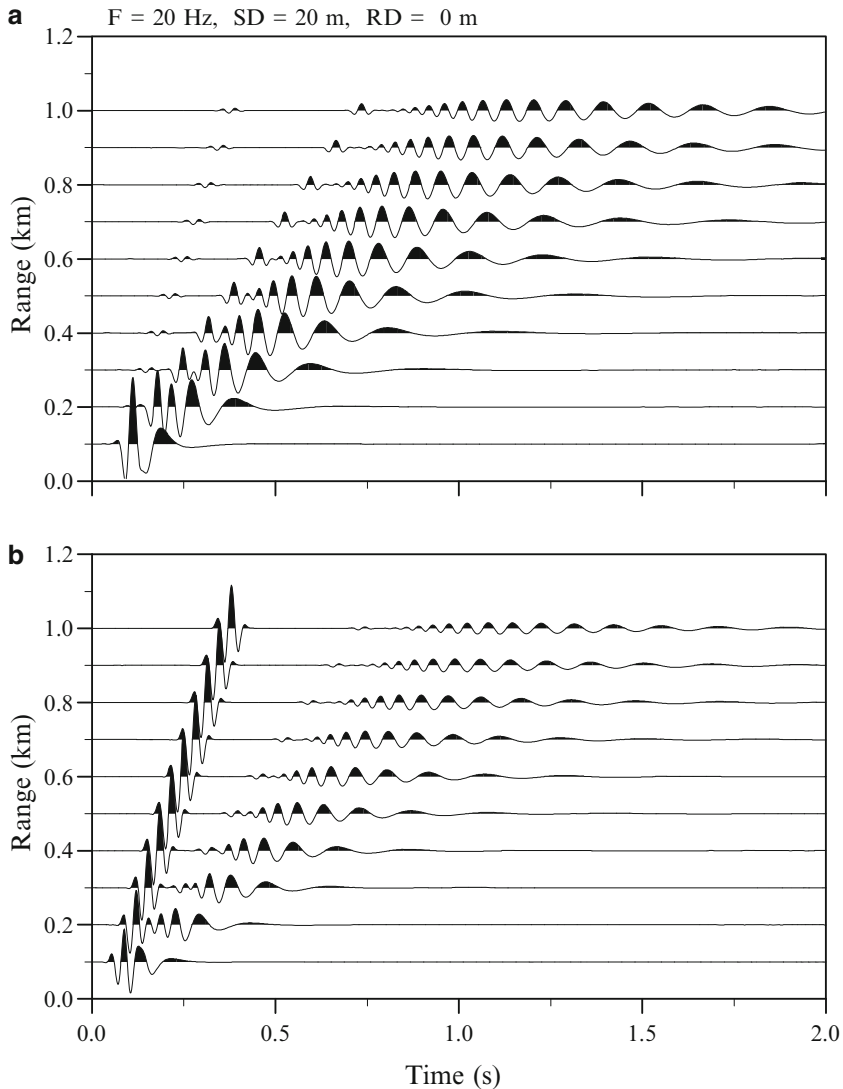


**Fig. 4.26** Range-stacked synthetic seismograms for receivers on top of the ice cover for a Ricker-wavelet source with center frequency 20 Hz at 20 m depth. **(a)** Vertical particle velocity. **(b)** Radial particle velocity. Amplitudes are multiplied by range to compensate for geometrical spreading and attenuation

The seabed is assumed to be covered by a ripple field with  $45^\circ$  aspect angle. Figure 4.28a shows the ripple field weighted by the amplitude of the sonar footprint, while Fig. 4.28b shows the corresponding wavenumber spectrum. The ripple field is generated by the ripple model developed by Pouliquen et al. [57], based on experimentally determined statistics. The short correlation length  $L$  of the ripples

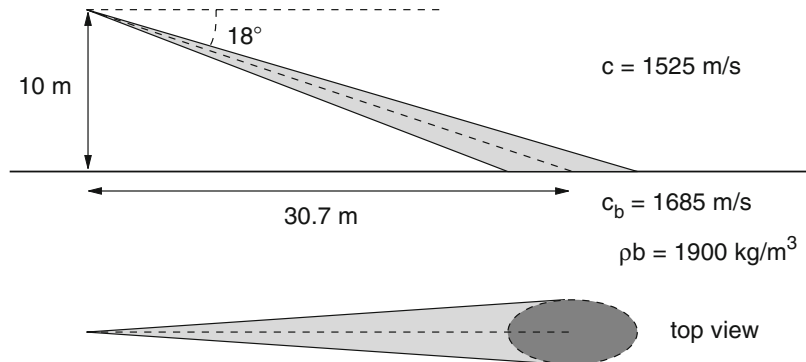


**Fig. 4.27** Geometry configuration for seabed target and reverberation modeling. A parametric sonar is used to insonify a seabed patch of approximately  $10 \times 5$  m, at a nominal grazing angle of  $18^\circ$

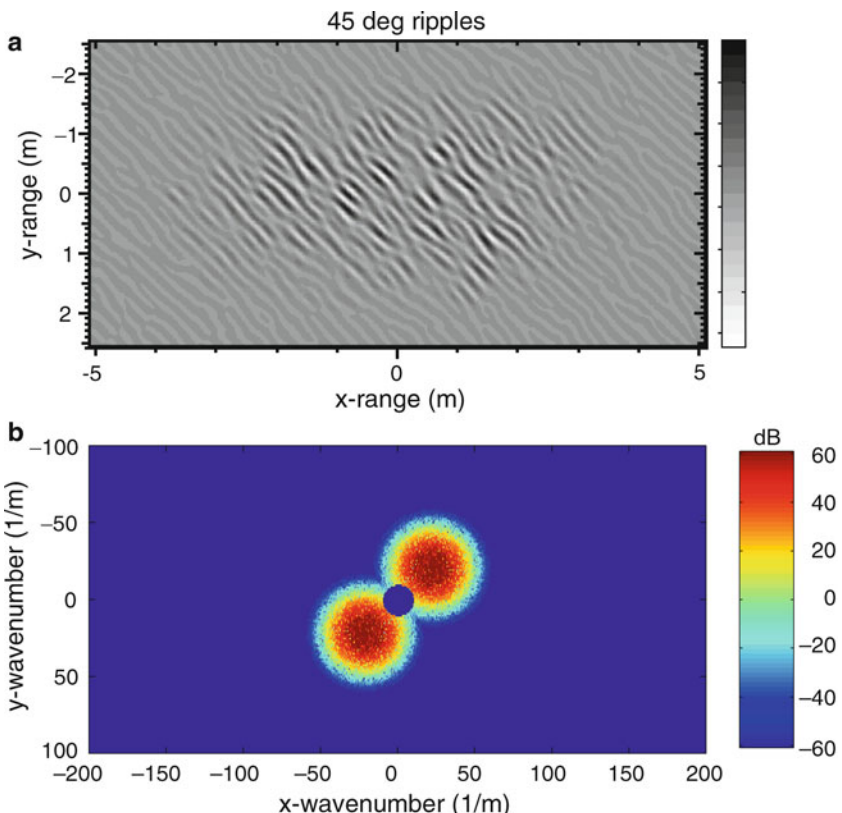


**Fig. 4.28** Rippled seabed insonified by a narrow-beam sonar at  $18^\circ$  grazing angle. The ripple aspect is  $45^\circ$  relative to the beam incident from the left. **(a)** Ripple elevation weighted with the sonar footprint. **(b)** Two-dimensional wavenumber spectrum of ripple patch [44]

is 20 cm, and the *rms* roughness height is 2.5 cm. Note the strongly polarized, almost monochromatic nature of the roughness spectrum, and the filtering of the low-wavenumber components, inherent to this seabed model [57].

The roughness patch is shaded by a Hanning window consistent with the spatial width of the incident beam, an approach justified by the fact that the perturbation theory is linear in both the roughness  $\gamma_v$  and the coherent field  $\chi_v$  in (4.151). All the results shown in the following are, therefore, generated using a plane wave of unit amplitude (0 dB) incident at the nominal 18° grazing angle.

#### 4.10.5.1 Reverberant Field

The spatial and temporal distribution of the scattered field was computed in the band 1–10 kHz, and covering ranges out to 50 m from the center of the footprint. Figure 4.29 shows the CW power level in dB in a horizontal plane at the source depth, 10 m above the seabed, at a frequency of (a) 2 kHz and (b) 6 kHz. The dimensionless correlation length of the ripples at the two frequencies are  $k_w L = 2\pi f L / c = 1.6$  and 4.9, respectively. The dynamic range of the contour levels is 60 dB, with red indicating high field values and blue low values.

As expected, the principal scattering is in the general direction corresponding to “specular” scattering, but with the 2 kHz result deviating significantly, both in terms of level and direction. The reason for this behavior is illustrated in Fig. 4.30 showing the wavenumber diagram similar to Fig. 4.14, but consistent with the specific ripple statistics. Thus, the grey-shading indicates schematically the power spectrum of Fig. 4.28b, centered at the incident wavenumber  $k_i$  corresponding to 18°. The circles

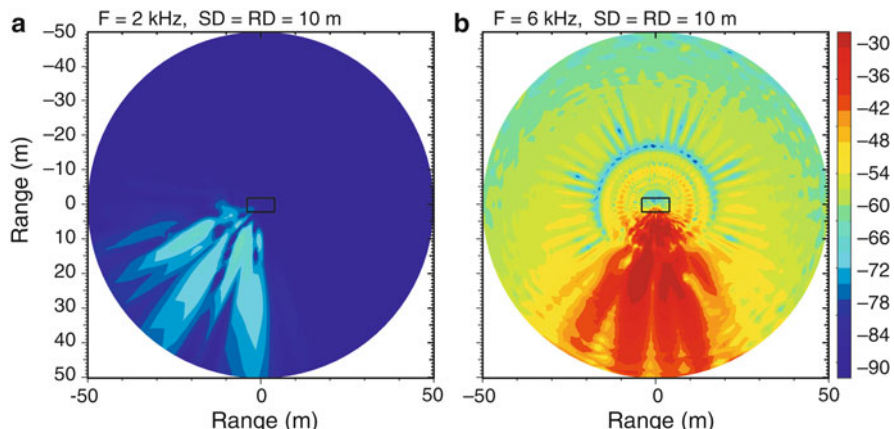


**Fig. 4.29** 3-D scattering from rippled sand bottom insonified by narrow-beam sonar incident from the left at a 45° aspect angle relative to the ripple axis. The incident field is a plane wave of 0 dB amplitude and 18° grazing angle. The plots show pressure level contours in decibels at (a) 2 kHz and (b) 6 kHz, in a horizontal plane 10 m above the seabed, centered at the sonar footprint [44]

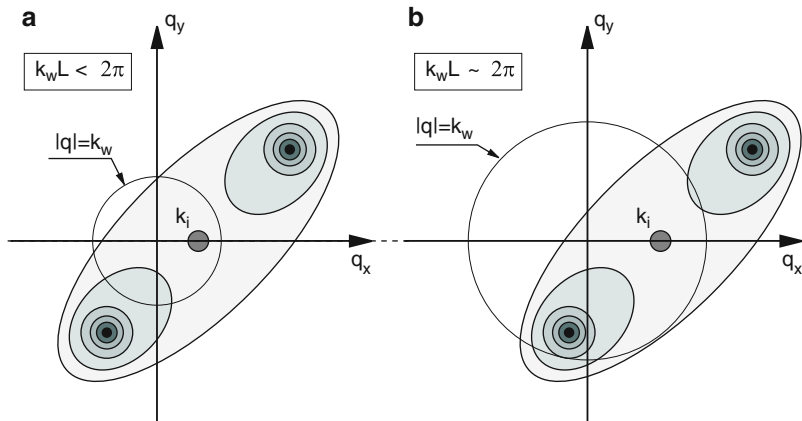


**Fig. 4.30** Bragg scattering conditions for ripples of aspect angle  $45^\circ$  relative to incident field. The shading indicates the level of the roughness power spectrum, centered at the incident wavenumber  $k_i$ . The short correlation length of the ripples is  $L$ , and the water wavenumber is  $k_w$ . (a) Low frequency ( $k_w L < 2\pi$ ). (b) Medium frequency ( $k_w L \approx 2\pi$ ) [44]

indicate the medium wavenumber at the two frequencies, separating the *propagating* ( $qr < k_w$ ) and *evanescent* components of the scattered field in the water column. At low frequencies ( $k_w L < 2\pi$ ) most of the roughness power is outside the circle and the associated scattering is, therefore, evanescent in the water column and not reaching the receiver at 10-m altitude. In contrast, at 6 kHz the peak of the roughness spectrum enters the propagating spectrum, with a significant specular scattering as a result.

#### 4.10.5.2 Target Scattering

The implications of the temporal and spatial characteristics of the ripple reverberation become particularly evident when compared to the scattering produced by a seabed target. To illustrate this, the theory in Sect. 4.9.1 has been applied to compute the 3-D scattered field produced by a solid sphere of radius 30 cm, buried flush at the center of the sonar footprint, and insonified by a plane wave of  $18^\circ$  grazing incidence. Analogous to the reverberation results above, Fig. 4.31 shows the scattered power in dB in a horizontal plane 10 m above the seabed, centered at the target and covering ranges out to 50 m. The spatial structure of the target scattering is obviously significantly different from the reverberation. Thus, the target scattering at 6 kHz, corresponding to  $ka \simeq 6.7$ , shown in Fig. 4.31b, is dominated by steep scattering angles, with a sharp drop in scattered power beyond a range of approximately 22 m, corresponding to the critical angle of  $25.2^\circ$ . At shorter ranges, the target scattering path corresponds to waves propagating in the bottom, while at longer ranges the coupling of the target scattering back into the water column is occurring through evanescent coupling, or “tunneling.” For  $r > 22$  m a radial interference pattern is

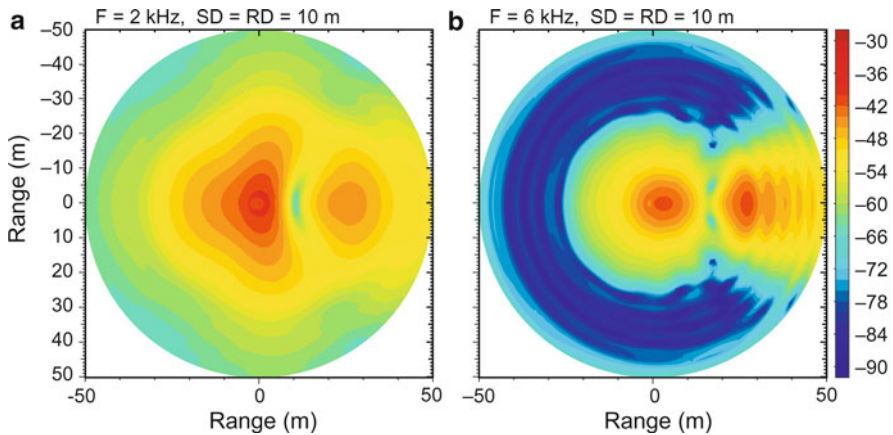


**Fig. 4.31** 3-D scattering from 30-cm radius sphere buried flush in sand bottom insonified from the left by a plane wave of 0 dB amplitude and  $18^\circ$  grazing angle. The plots show pressure level contours in dB at (a) 2 kHz ( $ka \approx 2.2$ ) and (b) 6 kHz ( $ka \approx 6.7$ ), in a horizontal plane 10 m above the seabed, centered at the sonar footprint [44]

evident, being associated with interference between the “tunneled” direct arrival and a second diffracted (creeping wave) arrival from the target [44]. Another characteristic feature at the higher frequency is the strong forward lobe, even in the evanescent regime.

The corresponding result at 2 kHz ( $ka \approx 2.2$ ) is shown in Fig. 4.31a. Here, the critical angle transition is much less distinct, and the scattering at the longer ranges is significantly higher than at higher frequencies. The reason for this is the slower decay of the evanescent “tail” at subcritical angles, yielding improved penetration, as well as more efficient energy tunneling back into propagating waves in the water column.

The most striking difference between the target scattering and the reverberation is the opposite frequency dependencies. Thus, from a monostatic as well as bistatic point of view, the target scattering beyond the “critical” cone is increasing with decreasing frequency, in contrast to the reverberation, which increases dramatically with increasing frequency.

#### 4.10.6 Reverberation from Seabed Volume Inhomogeneities

We shall here demonstrate the use of the wavenumber integration formulation of the reverberation from volume inhomogeneities, presented by LePage and Schmidt [25], to model the reverberation from a random distribution of volume inhomogeneities in a stratified seabed. The wavenumber integration result shall be compared the results using a ray-theoretic approach developed by Rogers and Holland [58].

#### 4.10.6.1 Fast Sediment Layer with Volume Inhomogeneities

One significant advantage of using the spectral integral approach to modeling sediment volume inhomogeneity scattering is that the Green's function is accurately modeled. Failings in the ray theory approximation to the Green's functions are especially evident near turning points in refractive sediments and near the critical angle for fast sediments. Another significant advantage is that the spectral integral approach correctly includes the scattering response of scatterers which have been excited by evanescent, or non-propagating waves. This type of scattering is typically found in fast sediments along the water-sediment interface at ranges where the incident angle of the source is smaller than the critical angle. For scatterers insonified by these types of waves, the differential plane-wave scattering cross section is undefined. Yet it is known that scatterers insonified by these types of waves can be important contributors to the total scattered field [59]. In fact, subcritical penetration and scattering is the basis for advanced mine-hunting sonar concepts for buried object detection [60,61]. If this mechanism is going to be included for modeling target response, it is important that a similar mechanism be included for modeling the reverberation from sediment volume inhomogeneities, especially for smooth bottoms. For these reasons we compare the scattering predictions of the spectral integral approach to a ray approach [62] for a fast sediment scattering scenario in order to evaluate the differences between the two approaches in the presence of a critical angle of reflection. The scenario is illustrated in Fig. 4.32. A point source is situated 25 m above a fast sediment layer, 100-m thick, with a background sound speed of 1600 m/s, density of 2000 kg/m<sup>3</sup> and attenuation of 0.01 dB/λ. In the sediment layer there is a distribution of volume inhomogeneities with *rms* sound speed fluctuation of 1 m/s, and *rms* density fluctuation of 8.75 kg/m<sup>3</sup>, with the corresponding correlation length scales of  $\ell_x = \ell_y = 10$  m and  $\ell_z = 2$  m.

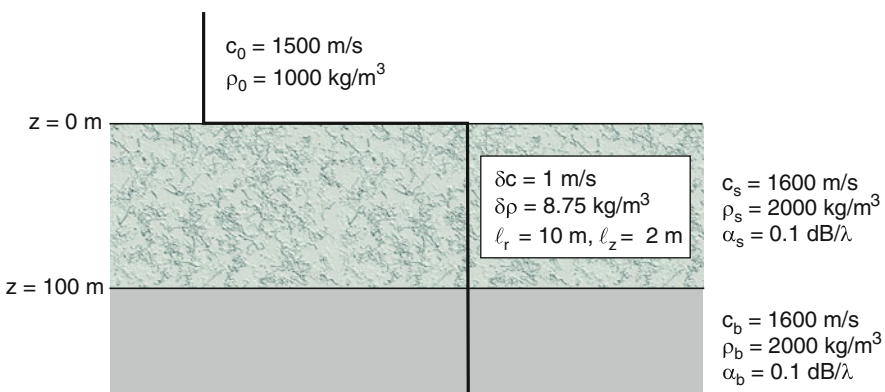


**Fig. 4.32** Volume scattering scenario: A 100-m thick sandy sediment layer with a background sound speed of 1600 m/s, density of 2000 kg/m<sup>3</sup> and attenuation of 0.01 dB/λ. The basement properties are identical to the background properties of the sediment

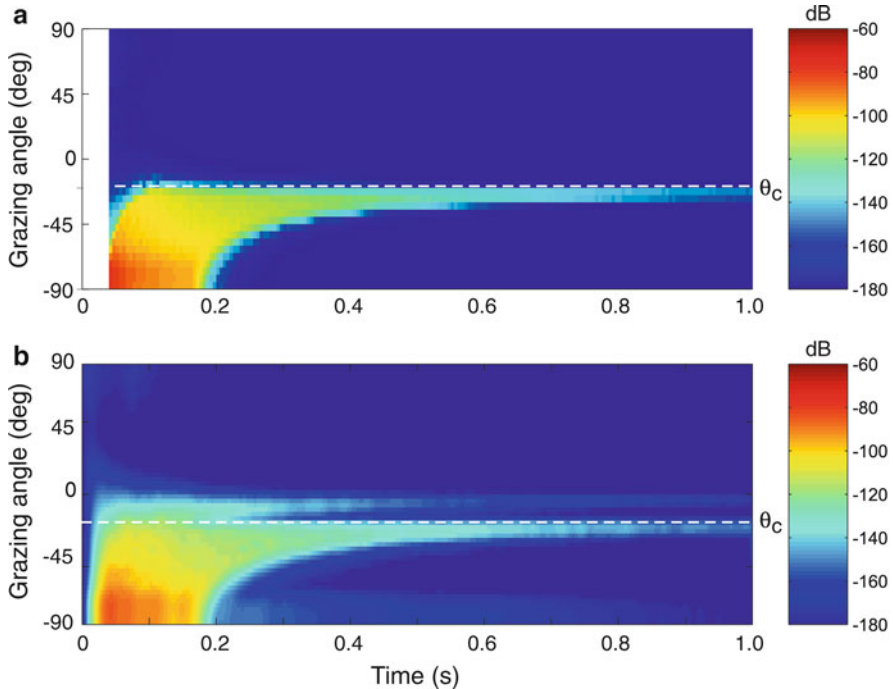


**Fig. 4.33** The time–beam evolution of scattered intensity for volume inhomogeneities in an isovelocity sediment layer, computed using (a) a ray-theoretic approach, and (b) wavenumber integration. The subcritical evanescent scattering branch following the time–angle trajectory of the water–sediment interface is missing in the ray result

In Fig. 4.33, the time–angle evolution of backscattered intensity is illustrated for this fast sandy bottom case. The ray tracing result is shown in the top plot and the spectral integral result is shown in the bottom plot. The results are in good agreement for angles greater than the critical angle of  $20^\circ$ , but the spectral integral result also shows a shallower angle branch at late time which conforms to the time–angle trajectory of the water–sediment interface. This upper trace corresponds to the inhomogeneous forcing of scatterers by the evanescent lateral wave at the interface. Since the lateral waves are not propagating vertically in the sediment, there is no differential scattering cross section for ray-tracing approaches to use to estimate this branch. Instead, the ray-tracing result estimates that the only propagation path of importance to scatterers near the water–sediment interface is the headwave path, which enters the sediment at the critical angle and propagates at near-horizontal angles to these scatterers and back. It is a fundamental limitation of the ray-tracing assumption that all of the scattering of the sediment volume inhomogeneities must be parameterized in terms of a differential scattering cross section.

Figure 4.34 shows the scattered intensity received monostatically for the lowloss case in red. It is clear that although the ray-tracing result neglects the

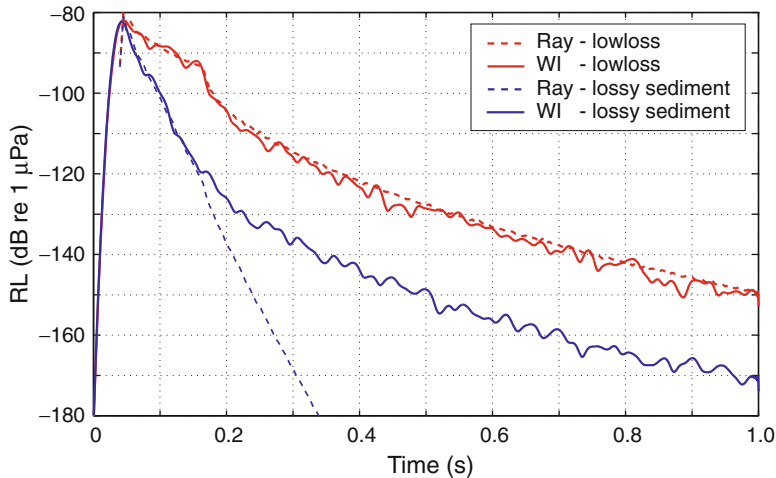


**Fig. 4.34** Single-phone average intensity estimates for the lowloss case (red) and for realistic bottom (blue) with a higher sediment attenuation of  $0.5 \text{ dB}/\lambda$ . The equivalent ray-tracing predictions are indicated by the dashed lines of the appropriate color. The disagreement for the lossy case is caused by the ray-tracing ignoring the dominating evanescent scattering effects

inhomogeneous scattering mechanism, the overall agreement between the two approaches is quite good. This is because in this case the attenuation in the sediment,  $0.01 \text{ dB}/\lambda$ , is sufficiently small that the headwave propagation path is the strongest contributor to the total scattered field for the times of interest in this simulation. If the sediment attenuation is increased to a more realistic  $0.5 \text{ dB}/\lambda$ , one obtains the intensity indicated by the blue curves in Fig. 4.34. In this case, the spectral integral result no longer agrees for times later than about 0.16 s. This is due to the fact that for realistic sediment attenuation the evanescent wave scattering, which is not modeled by the ray tracing approach, will be dominating at later times, as is evident from the beam-time response shown in Fig. 4.35. Comparing the results for the two cases suggests that the evanescent scattering mechanism is about 20 dB down from the headwave mechanism in the absence of loss.

#### 4.10.6.2 Upward Refracting Sediment Layer

Gradients in the background properties of sediments are commonly observed in coring data and in bottom sound speed inversions [62, 63]. Gradients are important to the physics of the scattering process because they control both how the subbottom is illuminated [64] and how the scattered field propagates back to the receivers. These gradients are often composed of microstructure with significant sound speed and density variance. However, some of the characteristics of scattering from these types of sediments may be accounted for by assuming that the background properties are smoothly varying over the depth of the sediment layer. As discussed in

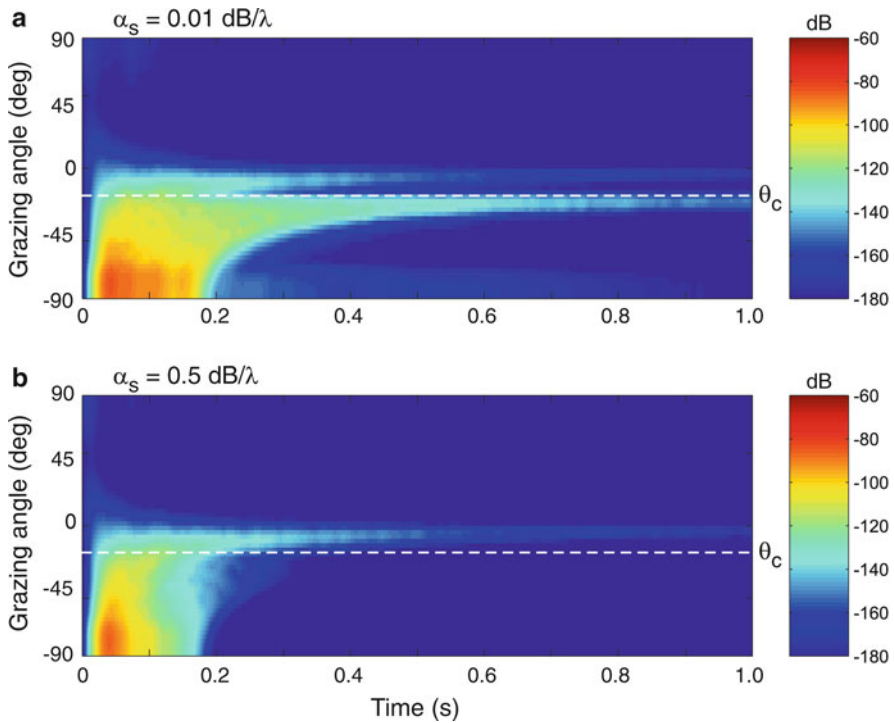


**Fig. 4.35** The time-beam evolution of scattered intensity for (a) a lowloss sediment and (b) a realistic, lossy sediment. In the lossier sediment case, the headwave scattering branch is attenuated after about 0.3 s. At times greater than this, the evanescent scattering path associated with the water–sediment interface is the only scattering mechanism of importance

Sect. 2.5.1, a  $c^2$ -linear sound-speed profile leads to analytical solutions of the depth-separated Helmholtz equation in terms of Airy functions. To illustrate the effect of the common upward-refracting sound-speed profiles found in the seabed, such a gradient is introduced into the background sound speed properties of the fast sandy sediment treated above. The sound speed at the bottom of the layer is increased to 1700 m/s, while all the other properties of the sediment layer remain fixed. To eliminate multipath artifact from the analysis, the basement sound speed is also set at 1700 m/s.

The effect of the sound-speed gradient on the incident field is illustrated in Fig. 4.36, where the range–depth pressure contours in decibels are shown for the point source 25 m above the sediment–water interface at 500 Hz for the isovelocity and gradient sediment cases. In both scenarios, the incident field passes unhindered into the sediment layer, except for a small reflection loss, up to the critical range of 67 m. However, in the isovelocity scenario above, the field then continues to propagate down into the lower halfspace, while here a significant portion of the transmitted energy is refracted back up into the sediment layer.

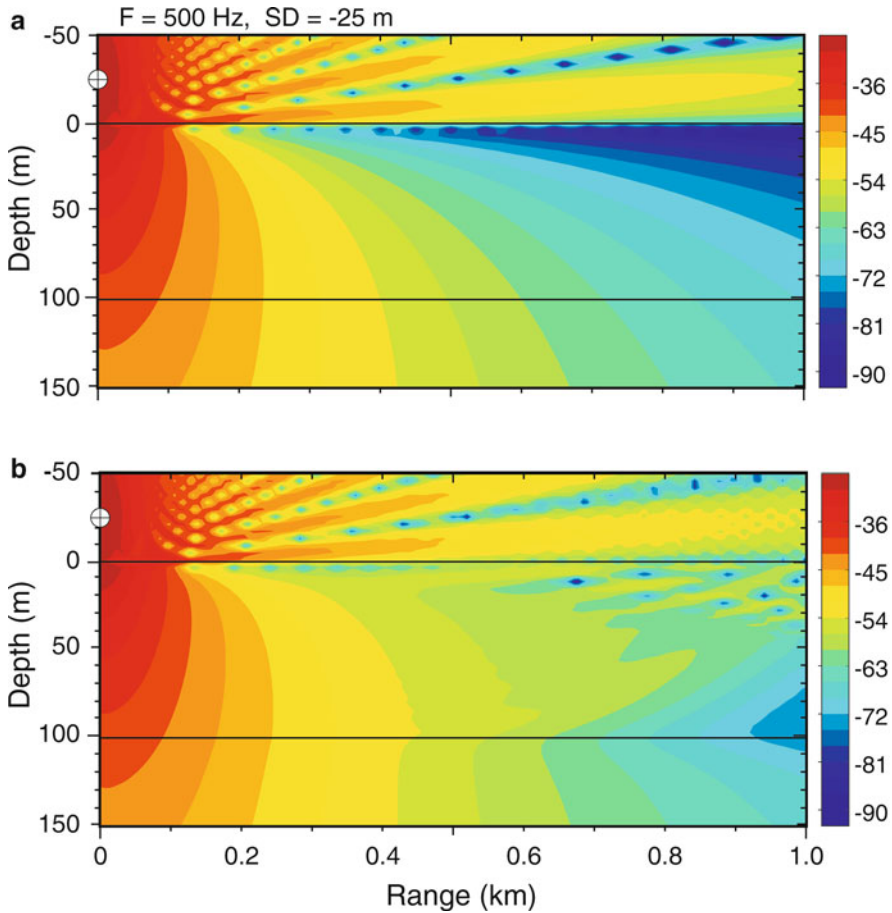


**Fig. 4.36** Range–depth pressure contours for (a) an isovelocity sediment, and (b) an upward-refracting sound-speed profile, at 500 Hz. The upward-refracting sediment sound speed causes a significant amount of the incident energy to be retained at longer ranges from the source

Figure 4.37 shows the time–angle distributions of backscattered intensity for the two scenarios. Clearly these distributions are quite different. While the high-angle, early-time backscatter and the forced inhomogeneous backscatter associated with the water–sediment interface are identical for the two scenarios, the deep refracted, or headwave, path contains significantly more energy at late time for the gradient sediment than it does for the isovelocity sediment. The angular width of the refracted scattering branch is also wider in the gradient case, because higher-angle energy is able to insonify the sediment layer at late times due to the refraction of this energy back into the sediment layer before it can escape into the basement.

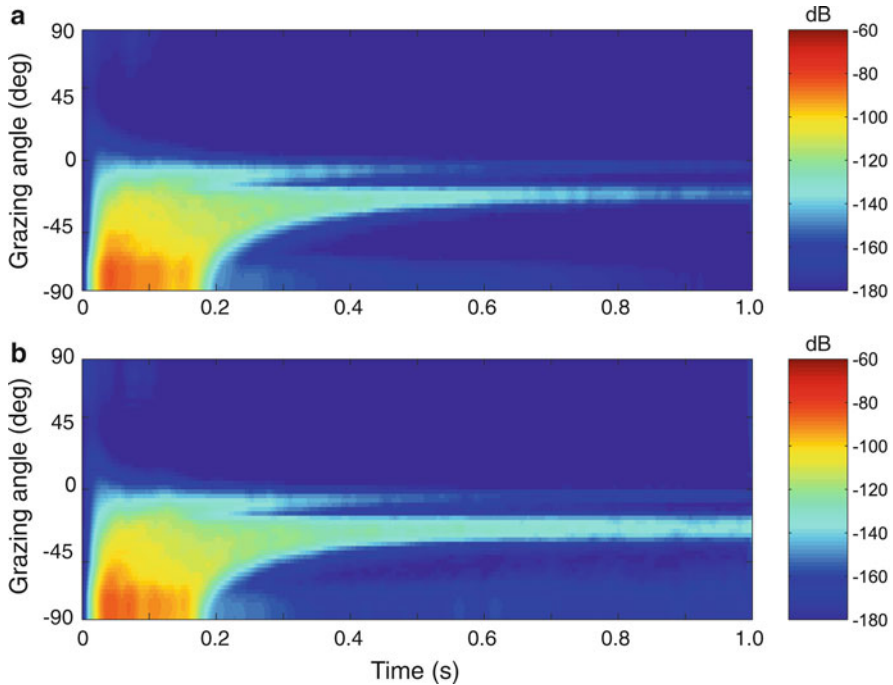


**Fig. 4.37** Time–angle evolution of scattered intensity for (a) the isospeed fast bottom, and (b) the upward refracting sediment. The results for the latter suggest that upward refracting sediments can have significantly more late-time reverberation over a broader range of grazing angles than otherwise similar sediment layers without gradients

## Appendix 1: Recipe for Simple WI/FFP Code

We here provide a recipe for writing a simple wavenumber integration (or FFP) code for modeling propagation in a stratified ocean. For simplicity, we assume all layers to be fluid and with constant speed and density. The stratification is limited above by the pressure-release surface, and below by a fluid halfspace.

There are basically two components to such a code; the first is the computation of the depth-dependent Green’s function, and the second is the numerical evaluation of the wavenumber integral yielding the field versus range and depth. The first part is generally the most computer intensive of the two.

### ***Depth-Dependent Green’s Function***

The first step is to develop a subroutine GREEN for computing the depth-dependent Green’s function  $g(k_r, z, z_s)$ , which forms the kernel of the wavenumber integral

in (4.93). The horizontal wavenumber should be assumed complex to allow for complex contour integration.

We have earlier described three different methods for computing the depth dependent Green's function: The *DGM* (Sect. 4.3.1), the *propagator matrix* (Sect. 4.3.2), and the *invariant embedding* (Sect. 4.3.3) approaches. Since the trapped waveguide field generally dominates the ocean acoustic field, the last method is inconvenient as discussed earlier. The global matrix approach is unconditionally stable, but the numerical implementation is rather involved. For simplicity we choose here to present the *propagator matrix* approach.

The development of a Green's function subroutine involves the following steps:

1. Introduce dummy interfaces at the source depth  $z_s$  and the receiver depth  $z$ . We assume the receiver is below the source. If the opposite is the case they can simply be switched due to reciprocity, properly accounting for a possible difference in density through (2.194).
2. Define the local vector  $\mathbf{v}$  in (4.75) and (4.76) as the wavenumber kernels of the vertical displacement and normal stress,

$$\mathbf{v} \equiv \begin{Bmatrix} w(k_r, z) \\ \sigma_{zz}(k_r, z) \end{Bmatrix}. \quad (4.182)$$

Similarly, define the degree-of-freedom vector  $\mathbf{a}_m$  for layer number  $m$  as composed of the complex amplitudes of the downgoing and upgoing solutions,

$$\mathbf{a}_m \equiv \begin{Bmatrix} A_m^-(k_r) \\ A_m^+(k_r) \end{Bmatrix}. \quad (4.183)$$

3. Use (4.10) and (4.11) to define the local *coefficient matrix*  $\mathbf{c}_m$  expressing the relation between  $\mathbf{v}$  and  $\mathbf{a}_m$ , i.e., with the above definitions,

$$\mathbf{c}_m(k_r, z) = \begin{bmatrix} -ik_z e^{-ik_z z} & ik_z e^{ik_z z} \\ -\rho_m \omega^2 e^{-ik_z z} & -\rho_m \omega^2 e^{ik_z z} \end{bmatrix}, \quad (4.184)$$

where  $k_z$  is the vertical wavenumber defined by (2.178). In layers with attenuation the medium wavenumber  $k_m$  is made complex as described in Sect. 2.4.5.

4. Invert  $\mathbf{c}_m$  either analytically or numerically, and use (4.78) to make a subroutine **PROPMAT** for the *propagator matrix* for layer  $m$ .
5. Use (4.84) to define the vector  $\mathbf{v}$  at the lowermost interface  $N - 1$  as

$$\mathbf{v}_{N-1} = \begin{Bmatrix} 1 \\ -\frac{\rho_N \omega^2}{ik_{z,N}} \end{Bmatrix} w(k_r, z_{N-1}). \quad (4.185)$$

6. Now, setting  $w(k_r, z_{N-1}) = 1$ , use (4.79) recursively up through the stratification, using the subroutine **PROPMAT** for each layer, until you reach the receiver interface  $r$ . Save the vector  $\mathbf{v}_r$ .

7. Continue the same recursion until you reach the source interface  $s$ , with the result  $\mathbf{v}_s$ .
8. Now continue the recursion in (4.79) all the way to the surface to yield the field vector corresponding to the first term in (4.82), except for the factor  $w(k_r, z_{N-1})$ . In parallel, use exactly the same recursion for the source discontinuity  $\hat{\mathbf{v}}$ , defined in (4.81), to yield the second term in (4.82). To make your code compute transmission loss use the definition of the source strength  $S_\omega$  given in (2.79).
9. With the surface stresses  $\sigma_{zz}(k_r, z_1)$  and  $\hat{\sigma}_{zz}(k_r, z_1)$  being determined from the two recursions, proceed to calculate  $w(k_r, z_{N-1})$  from the expression

$$w(k_r, z_{N-1}) = -\frac{\hat{\sigma}_{zz}(k_r, z_1)}{\sigma_{zz}(k_r, z_1)}, \quad (4.186)$$

which is derived from the pressure-release surface condition.

10. To determine the field vector at the receiver depth, simply multiply the resulting bottom interface displacement with the earlier saved normalized field vector  $\mathbf{v}_r$  to yield

$$\mathbf{v}(k_r, z) = w(k_r, z_{N-1}) \mathbf{v}_r. \quad (4.187)$$

Let the result returned from subroutine **GREEN** be the negative of the stress component to directly yield *transmission loss pressure* (if  $S_\omega$  was chosen according to (2.79)).

## **Wavenumber Integration**

The most efficient approach to the evaluation of the wavenumber integral is the FFP technique described in Sect. 4.5.4. To allow for field calculations in lossless waveguides, it is recommended to use the complex wavenumber form in (4.114), which is why we allowed the horizontal wavenumber to be complex in the subroutine **GREEN** described above.

As discussed in Sect. 4.5.4, the most critical component of computing the field versus range is the proper selection of the integration parameters. We here list the various considerations forming the foundation for an accurate representation of the field by the FFP summation in (4.114):

1. The first step is to select the integration interval  $[k_{\min}, k_{\max}]$ . Although for long ranges, the steep propagation angles are insignificant due to the loss incurred at each bottom bounce, it is recommended to initially include these components by choosing  $k_{\min} = 0$ . If  $k_{\min}$  is chosen larger, as will often be done by experienced modelers to reduce computation time, one must be careful to avoid numerical artifacts, as described in Sect. 4.5.2. Since the evanescent spectrum in fluid media

is only important for source and receiver at approximately the same depth, the highest significant spatial frequency in the horizontal corresponds to the lowest wave speed in the problem. It is, therefore, in general, conservative to choose  $k_{\max}$  as

$$k_{\max} \simeq 1.1 \frac{\omega}{c_{\min}}. \quad (4.188)$$

2. The next step is to choose the wavenumber sampling  $\Delta k_r$ . As discussed in Sect. 4.5.4, we can in most cases eliminate the aliasing by choosing a value according to

$$\Delta k_r \leq \frac{\pi}{r_{\max}}, \quad (4.189)$$

where  $r_{\max}$  is the range to the most distant receiver of interest. This corresponds to an FFT size for evaluating (4.114) of

$$M \geq \frac{(k_{\max} - k_{\min}) r_{\max}}{\pi}, \quad (4.190)$$

where  $M$  must be an integer power of two,  $M = 2^n$ .

3. The range sampling of the result produced by (4.114) is governed by (4.107), i.e.,

$$\Delta r = \frac{2\pi}{M \Delta k_r}. \quad (4.191)$$

The asymptotic form of the Hankel transform yields infinite pressure at range zero; therefore, choose the minimum range to be

$$r_{\min} = \Delta r. \quad (4.192)$$

4. The imaginary value of the horizontal wavenumber is now chosen according to (4.115), and the depth-dependent Green's function is computed using the subroutine **GREEN** for all  $M$  values of the horizontal wavenumber, and multiplied by the factors in the summation kernel in (4.114).
5. Now use a complex FFT to evaluate the sum, and the resulting vector is then multiplied by the factors outside the sum in (4.114). The result then represents the complex pressure at the discrete ranges,

$$r_j = r_{\min} + j\Delta r, \quad j = 0, \dots, (M-1) \quad (4.193)$$

of which only approximately the first half are valid.

6. Convert to transmission loss using (2.77).
7. To check that the wavenumber sampling is sufficient, double the value of  $M$ , and compare the results. Here, it is often useful to plot the depth-dependent Green's function as well, to visually ensure that no abrupt truncation occurs at  $k_{\max}$ .

## Appendix 2: Roughness Perturbation Operators

We shall here provide detailed, implementation-ready forms of the roughness perturbation operators in (4.152) for the special cases of a rough interface between two fluid media and a fluid–elastic layer interface.

### Fluid–Fluid Interface

Consider an interface  $\ell$  separating two fluid media, with displacement potentials  $\phi_\ell$  and  $\phi_{\ell+1}$ , respectively. In this case the boundary operator  $B_\ell \phi_{\ell;\ell+1}$  represents the discontinuity of vertical particle velocity and normal stress (negative of pressure),

$$B_\ell \phi_{\ell;\ell+1} = \Delta \begin{Bmatrix} w \\ \sigma_{zz} \end{Bmatrix} = \begin{Bmatrix} \frac{\partial \phi_{\ell+1}}{\partial z} - \frac{\partial \phi_\ell}{\partial z} \\ -\rho_{\ell+1} \omega^2 \phi_{\ell+1} - (-\rho_\ell \omega^2 \phi_\ell) \end{Bmatrix} \quad (4.194)$$

and the first term in (4.151) takes the form,

$$\gamma_\ell \frac{\partial B_\ell}{\partial z} \phi_{\ell;\ell+1} = \gamma_\ell \begin{Bmatrix} \frac{\partial^2 \phi_{\ell+1}}{\partial z^2} - \frac{\partial^2 \phi_\ell}{\partial z^2} \\ \rho_\ell \omega^2 \frac{\partial \phi_\ell}{\partial z} - \rho_{\ell+1} \omega^2 \frac{\partial \phi_{\ell+1}}{\partial z} \end{Bmatrix}. \quad (4.195)$$

The operator  $b_\ell$  represents the modification of the boundary conditions due to the rotation  $\gamma_\ell(\mathbf{x})$  of the interface. The scalar pressure is unaffected by the rotation, while a rotation of the boundary introduces the horizontal displacement  $\mathbf{u}$  in the boundary condition. As a result, the rotation term takes the form [48],

$$\begin{aligned} \nabla \gamma_v(\mathbf{x}) \circ \mathbf{b}_\ell \phi_{\ell;\ell+1} &= \begin{Bmatrix} \gamma_{,x} u_{x;\ell} - \gamma_{,y} u_{y;\ell} - \gamma_{,x} u_{x;\ell+1} + \gamma_{,y} u_{y;\ell+1} \\ 0 \end{Bmatrix} \\ &= \begin{Bmatrix} \gamma_{,x} \frac{\partial \phi_\ell}{\partial x} + \gamma_{,y} \frac{\partial \phi_\ell}{\partial y} - \gamma_{,x} \frac{\partial \phi_{\ell+1}}{\partial x} - \gamma_{,y} \frac{\partial \phi_{\ell+1}}{\partial y} \\ 0 \end{Bmatrix}. \end{aligned} \quad (4.196)$$

The perturbation matrices are straightforwardly evaluated in the case of a fluid–fluid interface, here for brevity assumed to be at depth  $z = 0$ . The depth-separated wavefield in the fluid layers are of the form,

$$\phi_\ell(\mathbf{k}, z) = A_\ell^+(\mathbf{k}) e^{ik_{z;\ell} z} + A_\ell^-(\mathbf{k}) e^{-ik_{z;\ell} z} \quad (4.197)$$

and similarly for layer  $\ell + 1$ . Due to the exponential depth dependence, the wavenumber matrix operators in (4.152) are easily derived from (4.194) to (4.196).

First, organizing the field components above and below the interface in the stable form,

$$\phi_{\ell;\ell+1}(\mathbf{k}) = \text{diag} \left[ e^{ik_{z;\ell} z}, e^{-ik_{z;\ell} z}, e^{ik_{z;\ell+1} z}, e^{-ik_{z;\ell+1} z} \right] \begin{Bmatrix} A_\ell^+(\mathbf{k}) \\ A_\ell^-(\mathbf{k}) \\ A_{\ell+1}^+(\mathbf{k}) \\ A_{\ell+1}^-(\mathbf{k}) \end{Bmatrix} \quad (4.198)$$

the wavenumber equivalent of the standard boundary operator in (4.194) is

$$\widetilde{\mathcal{B}}_\ell(\mathbf{k}) = \begin{bmatrix} -ik_{z;\ell} & ik_{z;\ell} & ik_{z;\ell+1} & -ik_{z;\ell+1} \\ \rho_\ell \omega^2 & \rho_\ell \omega^2 & -\rho_{\ell+1} \omega^2 & -\rho_{\ell+1} \omega^2 \end{bmatrix}. \quad (4.199)$$

Applying the depth derivatives to the exponentials in (4.198), the depth derivative in the first term in (4.152) follows directly as,

$$\frac{\partial \widetilde{\mathcal{B}}_\ell(\mathbf{k})}{\partial z} = \begin{bmatrix} k_{z;\ell}^2 & k_{z;\ell}^2 & -k_{z;\ell+1}^2 & -k_{z;\ell+1}^2 \\ ik_{z;\ell} \rho_\ell \omega^2 & -ik_{z;\ell} \rho_\ell \omega^2 & -ik_{z;\ell+1} \rho_{\ell+1} \omega^2 & ik_{z;\ell+1} \rho_{\ell+1} \omega^2 \end{bmatrix}. \quad (4.200)$$

In the wavenumber representation, the rotational operator is a horizontal vector,  $\widetilde{\mathbf{b}}_\ell = (\widetilde{b}_{x;\ell}, \widetilde{b}_{y;\ell})$ , with

$$\widetilde{b}_{x;\ell}(\mathbf{k}) \phi_{\ell;\ell+1}(\mathbf{k}) = \Delta \begin{Bmatrix} -u_x \\ 0 \end{Bmatrix} = \begin{bmatrix} ik_x & ik_x & -ik_x & -ik_x \\ 0 & 0 & 0 & 0 \end{bmatrix} \phi_{\ell;\ell+1}(\mathbf{k}) \quad (4.201)$$

and similarly for the  $y$ -component.

## Fluid–Elastic Interface

We next consider an interface  $\ell$  separating an upper fluid layer and a lower elastic layer. For the general problem of scattering from a two-dimensional rough interface involving an elastic medium, one must incorporate not only the out-of-plane scattering, but also the scattering into the horizontally-polarized shear waves. This adds another shear potential in the formulation, and the boundary operators in (4.152) become  $3 \times 8$  matrices. LePage [49, 65] used the perturbation theory to model three-dimensional scattering from an elastic ice cover in the Arctic and provided detailed expressions for the wavenumber boundary operators for this case. We shall here provide the much simpler expressions for the boundary operators in the plane strain case, ignoring both out-of-plane scattering and the scattering into the horizontally polarized shear waves. This approximation is usually justified in cases involving only monostatic sonar configurations. In the axisymmetric, plane strain

case ( $\partial/\partial\varphi \equiv 0$ ), the wavefields are described by the compressional potentials  $\phi_\ell$  and  $\phi_{\ell+1}$  in the fluid and elastic layer, respectively, and the vertically polarized shear waves in the elastic medium is represented by the SV potential  $\psi_{\ell+1}$ .

The boundary operator  $B_\ell \chi_{\ell;\ell+1}$  in this case represents the discontinuity of vertical particle displacement and normal stress, and the vanishing shear stress at the interface, which for axisymmetric propagation, using (4.39), is

$$B_\ell \chi_{\ell;\ell+1} = \Delta \begin{Bmatrix} w \\ \sigma_{zz} \\ \sigma_{rz} \end{Bmatrix} = \begin{Bmatrix} w_{\ell+1} - \frac{\partial \phi_\ell}{\partial z} \\ \rho_\ell \omega^2 \phi_\ell + (\lambda + 2\mu) \frac{\partial w_{\ell+1}}{\partial z} + \lambda \frac{\partial u_{\ell+1}}{\partial r} \\ 0 + \mu \left( \frac{\partial u_{\ell+1}}{\partial z} + \frac{\partial w_{\ell+1}}{\partial r} \right) \end{Bmatrix}, \quad (4.202)$$

where  $\lambda$  and  $\mu$  are the Lamé constants for the elastic layer, and  $w_{\ell+1}$  and  $u_{\ell+1}$  are the horizontal and vertical displacements at the interface, evaluated in the elastic layer, (4.26) and (4.27),

$$u_{\ell+1}(r, z) = \frac{\partial}{\partial r} \phi_{\ell+1}(r, z) + \frac{\partial^2}{\partial r \partial z} \psi_{\ell+1}(r, z), \quad (4.203)$$

$$w_{\ell+1}(r, z) = \frac{\partial}{\partial z} \phi_{\ell+1}(r, z) - \frac{1}{r} \frac{\partial}{\partial r} r \frac{\partial}{\partial r} \psi_{\ell+1}(r, z). \quad (4.204)$$

The first term in (4.151) is now simply the depth derivative of the standard boundary operator in (4.202).

The operator  $b_\ell$  represents the modification of the boundary conditions due to the rotation  $\gamma_\ell(\mathbf{x})$  of the interface. The rotation of the boundary introduces the horizontal displacement  $\mathbf{u}$  in the normal displacement boundary condition, and mixes the stress boundary conditions [48].

In the wavenumber domain, the kernels for the compressional and shear potentials in the elastic medium are, from (4.32) and (4.33),

$$\phi_{\ell+1}(k_r, z) = A_{\ell+1}^+(\mathbf{k}) e^{ik_{z;\ell+1}z} + A_{\ell+1}^-(\mathbf{k}) e^{-ik_{z;\ell+1}z}, \quad (4.205)$$

$$\psi_{\ell+1}(k_r, z) = k_r^{-1} [B_{\ell+1}^+(\mathbf{k}) e^{ik_{z;\ell+1}z} + B_{\ell+1}^-(\mathbf{k}) e^{-ik_{z;\ell+1}z}] \quad (4.206)$$

with  $\kappa_z = \sqrt{\kappa^2 - k_r^2}$  being the vertical wavenumber for the shear waves of wavenumber  $\kappa$  in layer  $\ell + 1$ .

Organizing the wavefield components in the stable order,

$$\chi_{\ell;\ell+1}(k_r) = \text{diag} \left[ e^{ik_{z;\ell}z}, e^{-ik_{z;\ell}z}, \right. \\ \left. e^{ik_{z;\ell+1}z}, e^{ik_{z;\ell+1}z}, e^{-ik_{z;\ell+1}z}, e^{-ik_{z;\ell+1}z} \right] \begin{Bmatrix} A_\ell^+(k_r) \\ A_\ell^-(k_r) \\ A_{\ell+1}^+(k_r) \\ B_{\ell+1}^+(k_r) \\ A_{\ell+1}^-(k_r) \\ B_{\ell+1}^-(k_r) \end{Bmatrix} \quad (4.207)$$

the corresponding wavenumber-domain operators in (4.152) are obtained from the kernels of the integral representations for the displacements and stresses in (4.36) to (4.39),

$$\begin{aligned} \widetilde{\mathcal{B}}_\ell(k_r)\chi_{\ell;\ell+1}(k_r) &= \Delta \begin{Bmatrix} w(k_r) \\ \sigma_{zz}(k_r) \\ \sigma_{rz}(k_r) \end{Bmatrix} = \begin{bmatrix} -ik_{z;\ell} & ik_{z;\ell} & ik_{z;\ell+1} \\ \rho_\ell \omega^2 & \rho_\ell \omega^2 & (2k_r^2 - \kappa^2)\mu \\ 0 & 0 & -2ik_r k_{z;\ell+1}\mu \end{bmatrix} \\ &\quad \begin{bmatrix} k_r & -ik_{z;\ell+1} & k_r \\ 2ik_r \kappa_z \mu & (2k_r^2 - \kappa^2)\mu & -2ik_r \kappa_z \mu \\ -(2k_r^2 - \kappa^2)\mu & 2ik_r k_{z;\ell+1}\mu & -(2k_r^2 - \kappa^2)\mu \end{bmatrix} \chi_{\ell;\ell+1}(k_r). \end{aligned} \quad (4.208)$$

Obviously, this *local* interface matrix cannot be inverted to solve for the scattered field amplitudes through the matrix  $\widetilde{\mathcal{B}}_\nu^{-1}(\mathbf{q})$ . To incorporate all multiple scattering in the waveguide, one must first assemble all the local interface matrices into an invertible *Global Matrix*. However, this would rarely make sense since the interface roughness is usually given in terms of its statistics, with a correlation length much shorter than the thickness of the layers. Instead, a much more efficient and physically justified approach is to solve for the scattered field locally to define the virtual source distribution in (4.151), and then use the full Global Matrix approach to incorporate the waveguide multiples in the reverberant field. This is done simply by ignoring the incoming scattered wave amplitudes  $A_\ell^+$ ,  $A_{\ell+1}^-$  and  $B_{\ell+1}^-$  to yield

$$\widetilde{\mathcal{B}}_\ell^{-1}(q_r) = \begin{bmatrix} iq_{z;\ell} & iq_{z;\ell+1} & qr \\ \rho_\ell \omega^2 & (2q_r^2 - \kappa^2)\mu & 2iq_r \kappa_z \mu \\ 0 & -2iq_r q_{z;\ell+1}\mu & -(2q_r^2 - \kappa^2)\mu \end{bmatrix}^{-1}. \quad (4.209)$$

The first term in (4.151) is straightforwardly determined by taking the depth derivatives of the exponentials in (4.207) and apply the resulting factors to the corresponding columns in the coefficient matrix in (4.202) to yield,

$$\begin{aligned} \frac{\partial \widetilde{\mathcal{B}}_\ell(k_r)}{\partial z} &= \begin{bmatrix} k_{z;\ell}^2 & k_{z;\ell}^2 & -k_{z;\ell+1}^2 \\ ik_{z;\ell} \rho_\ell \omega^2 & -ik_{z;\ell} \rho_\ell \omega^2 & ik_{z;\ell+1} (2k_r^2 - \kappa^2)\mu \\ 0 & 0 & 2k_r k_{z;\ell+1}^2 \mu \end{bmatrix} \\ &\quad \begin{bmatrix} ik_r \kappa_{z;\ell+1} & -k_{z;\ell+1}^2 & -ik_r \kappa_{z;\ell+1} \\ -2k_r \kappa_{z;\ell+1}^2 \mu & -ik_{z;\ell+1} (2k_r^2 - \kappa^2)\mu & -2k_r \kappa_{z;\ell+1}^2 \mu \\ -ik_{z;\ell+1} (2k_r^2 - \kappa^2)\mu & 2k_r k_{z;\ell+1}^2 \mu & ik_{z;\ell+1} (2k_r^2 - \kappa^2)\mu \end{bmatrix}. \end{aligned} \quad (4.210)$$

The rotational operator for the axisymmetric, plane strain case is,

$$\begin{aligned} \tilde{b}_{r;\ell}(k_r) \chi_{\ell;\ell+1}(k_r) &= \Delta \left\{ \begin{array}{c} -iu(k_r) \\ -2i\sigma_{rz}(k_r) \\ -i[\sigma_{zz}(k_r) - \sigma_{rr}(k_r)] \end{array} \right\} \\ &= \begin{bmatrix} -ik_r & -ik_r & ik_r \\ 0 & 0 & -4k_r k_{z;\ell+1} \mu \\ 0 & 0 & -2i(2k_r^2 - \kappa^2) \mu \\ -\kappa_{z;\ell+1} & ik_r & \kappa_{z;\ell+1} \\ 2i(2k_r^2 - \kappa^2) \mu & 4k_r k_{z;\ell+1} \mu & 2i(2k_r^2 - \kappa^2) \mu \\ 4k_r \kappa_{z;\ell+1} \mu & -2i(2k_r^2 - \kappa^2) \mu & -4k_r \kappa_{z;\ell+1} \mu \end{bmatrix} \chi_{\ell;\ell+1}(k_r). \end{aligned} \quad (4.211)$$

Note here that the kernels for displacement and stress components are multiplied by  $i$  to compensate for the different order of Bessel functions in the integral representations in (4.36)–(4.39), making the operators consistent with the plane-geometry ones derived by LePage [49].

## Problems

**4.1.** Consider the reflection of a plane wave from an isovelocity fluid layer of thickness  $H$  overlying an isovelocity fluid halfspace for which  $c_2 < c_1 < c_3$  and  $\rho_1 < \rho_2 < \rho_3$ .

- a. What is the critical grazing angle for waves incident from medium 1?
- b. If  $k_2 H \ll 1$ , show that to leading order the plane-wave reflection coefficient reduces to the plane-wave reflection coefficient without the layer present.

Now, suppose that  $\rho_1 = \rho_3 < \rho_2$  and  $c_1 = c_3 < c_2$ , and that the plane wave is incident at grazing angle  $\theta_1 < \arccos(c_1/c_2)$ .

- c. What is the angle of the transmitted wave in the lower halfspace, and what kind of wave is it (radiating or evanescent)?
- d. What is the form of the solution in the layer?
- e. Derive the expression for the reflection coefficient in the upper halfspace and the transmission coefficient in the lower halfspace.
- f. By your intuition, what happens when  $k_2 H \rightarrow \infty$ ? Verify your answer by examining the leading order behavior of the reflection and transmission coefficients.

**4.2.** Make a direct numerical implementation of the expression in (2.146) for the wavenumber representation of the field in an ideal waveguide. Allow the horizontal wavenumber to be complex.

- For sound speed 1500 m/s and depth 100 m, compute the wavenumber kernel at 20 Hz for source and receiver both at depth 36 m. Sample the kernel at 200 points equidistantly placed over the interval  $k_r \in [k_w/100, 2k_w]$ , where  $k_w$  is the water wavenumber. Let the imaginary value of the horizontal wavenumber be  $-k_w/100$  to avoid the modal singularities. *Note:* Your code will crash!
- Determine the wavenumber interval for which your code produces a result which is qualitatively consistent with Fig. 2.23a.
- Describe the nature of the numerical problem, and rewrite (2.146) into a form which remedies the problem. Implement it and compare your result to Fig. 2.23a (qualitatively).

**4.3.** In matched field processing for source localization the sensitivity to environmental mismatch is a critical issue due to the fact that the environment is never known perfectly in a deterministic sense. The sensitivity to a sound speed perturbation in a stratified or range-independent ocean depends on the change in the depth-dependent Green's function associated with that perturbation. Let the wave-number profile  $k(z) = \omega/c(z)$  for such an ocean be given by a set of parameters  $\mathbf{A} = [A_1, A_2, \dots, A_N]$ . Show that the partial derivatives of the depth-dependent Green's function with respect to the parameter  $A_i$  are given by the depth integral

$$\frac{\partial G_\omega(k_r, z, z_s)}{\partial A_i} = \int_0^\infty \frac{\partial(k^2(z))}{\partial A_i} G_\omega(k_r, z_s, z') G_\omega^*(k_r, z, z') dz'.$$

**4.4.** The homogeneous displacement equation of motion in a homogeneous and isotropic elastic medium has the vector form,

$$(\lambda + \mu) \nabla(\nabla \cdot \mathbf{u}) + \mu \nabla^2 \mathbf{u} = \rho \ddot{\mathbf{u}}.$$

- Show that this equation is satisfied by displacement fields of the form,

$$\mathbf{u} = \nabla\phi + \nabla \times \Psi,$$

where  $\phi$  is a scalar potential satisfying the equation

$$\nabla^2 \phi - \frac{1}{c_p^2} \ddot{\phi} = 0,$$

and  $\Psi$  is a vector potential satisfying the equation

$$\nabla^2 \Psi - \frac{1}{c_s^2} \ddot{\Psi} = 0,$$

and where  $\Psi$  satisfies the *gauge condition*  $\nabla \cdot \Psi = 0$ .

- Express  $c_p$  and  $c_s$  in terms of the Lamé constants  $\lambda$  and  $\mu$ , and the density  $\rho$ .
- What is the physical significance of the *gauge condition*?
- Explain the physical significance of  $\phi$  and  $\Psi$ .

**4.5.** Consider a homogeneous, isotropic, and elastic halfspace with compressional speed  $c_p$ , shear speed  $c_s$  and density  $\rho$ .

- For a plane compressional (P) wave incident on the free surface, derive the expressions for the reflected compression and shear potentials.
- Discuss the existence of *total conversion* (no reflected P-wave) and *no conversion* (no reflected shear wave).

**4.6.** Consider a homogeneous, isotropic, and elastic halfspace with compressional speed  $c_p$ , shear speed  $c_s$  and density  $\rho$ .

- For a plane shear (SV) wave incident on the free surface, derive the expressions for the reflected compression and shear potentials.
- Discuss the existence of *total conversion* (no reflected SV-wave) and *no conversion* (no reflected compressional wave).

**4.7.** Consider the problem of a water halfspace with sound speed  $c_1$  and density  $\rho_1$  overlying an elastic halfspace with compressional speed  $c_p$ , shear speed  $c_s$ , and density  $\rho_2$ .

- Show that the depth-dependent Green's function for a point source in the water, at height  $H$  above the interface, has a denominator of the form,

$$d(k_r) = (2k_r^2 - k_s^2)^2 + 4k_r^2 k_{z,2} \kappa_{z,2} + k_s^4 \frac{\rho_1 k_{z,2}}{\rho_2 k_{z,1}},$$

where  $k_s$  is the shear wavenumber in the solid halfspace,  $k_r$  is the horizontal wavenumber and  $k_{z,1}$  and  $k_{z,2}$  are the vertical wavenumbers for compressional waves in the two media, and  $\kappa_{z,2}$  is the vertical wavenumber for shear waves.

- Show that  $d(k)$  always has a real root  $k_{\text{SCH}}$ ,

$$k_{\text{SCH}} > \max[k_1, k_s],$$

where  $k_1$  is the wavenumber for acoustic waves in the water. The wave associated with this pole is called the *Scholte wave*.

- Describe the frequency dispersion characteristics of the Scholte wave.
- Make a sketch of the particle displacement associated with the Scholte wave on the surface of the elastic medium.
- Assume the source is placed just above the bottom  $H \simeq 0$ , and emits a broadband signal. The field is measured by means of a bottom mounted vertical array far away from the source, where the field is dominated by the Scholte wave. If the frequency spectrum measured at the receiver on the interface is  $F(\omega)$ , what is the frequency spectrum at height  $h$  above the interface?

**4.8.** The denominator of the depth-dependent Green's function for the fluid–elastic halfspace problem described in the previous problem also has a symmetric pair of complex roots which become important for the propagation characteristics in certain cases.

- Employ a numerical root finding scheme (e.g., a complex Newton–Raphson scheme) to determine the complex root with positive real value. (*Warning: take care how you choose the branch cuts for the square root.*)
- Assuming the sound speed in water to be 1500 m/s and the density 1000 kg/m<sup>3</sup>, compressional speed 5000 m/s and density 2500 kg/m<sup>3</sup> in the solid, map the position of the root as a function of shear speed in the range 1500–3500 m/s.
- Discuss the physical significance of the real and imaginary part of the root.

**4.9.** An infinite elastic plate of thickness  $2h$  is made of an elastic material with wave speeds  $c_p$  and  $c_s$  for compressional and shear waves, respectively, and density  $\rho_s$ . The plate is assumed to have free surfaces.

- Show that the characteristic equation for the modes in the plate has the form

$$\frac{\tan(\kappa_z h)}{\tan(k_z h)} = - \left[ \frac{4k_r^2 k_z \kappa_z}{(2k_r^2 - k_s^2)^2} \right]^{\pm 1},$$

where the “+” corresponds to symmetric modes and the “−” corresponds to antisymmetric modes.  $k_s$  is the shear wavenumber, and  $k_z$  and  $\kappa_z$  are the vertical wavenumbers for compression and shear, respectively.  $k_r$  is the horizontal wavenumber.

- Show that in the low-frequency limit,

$$\Omega = \frac{2h\omega}{\pi c_s} \rightarrow 0,$$

the characteristic equations reduce to,

$$\sinh \pi \gamma \pm \pi \gamma = 0,$$

where  $\gamma$  is a dimensionless horizontal wavenumber,

$$\gamma = \frac{2hk_r}{\pi}.$$

- Solve the frequency equation numerically and graphically represent the  $\omega - k_r$  relations for the first (fundamental) symmetric and antisymmetric modes for the elastic plate.
- Discuss the cutoff properties and the static limits of the phase and group velocities for the two fundamental modes.

**4.10.** Equation (2.182) represents a DGM formulation for the Pekeris waveguide.

- Is the direct numerical solution of (2.182) by Gaussian elimination numerically stable for all values of the horizontal wavenumber?
- Modify (2.182) to make the solution unconditionally stable.

**4.11.** Consider an ocean waveguide similar to the Pekeris waveguide, but with an  $n^2$ -linear sound speed profile  $c^2(z) = (az + b)^{-1}$  in the water column. Set up the corresponding global coefficient matrix in numerically stable forms for downward-refracting ( $a > 0$ ) and upward-refracting ( $a < 0$ ) profiles.

**4.12.** Assume you have to make a simple wavenumber integration code for propagation in Pekeris waveguides.

- Make a subroutine which computes the wavenumber kernel, or depth-dependent Green's function, along a contour below the positive real wavenumber axis. Make sure your code is numerically stable for large wavenumbers,  $k_r \gg (k_1, k_2)$ .
- Check your code by qualitatively reproducing the kernels shown in Fig. 4.8a.

You decide to use FFP integration with a contour offset equal to the wavenumber sampling interval  $\Delta k_r$ .

- What is the associated minimum attenuation of the wrap-around?
- Using this offset, perform a numerical convergence analysis for the integration by computing the transmission loss at 46 m depth and 10 km range for the Pekeris waveguide in Fig. 2.25, assuming an attenuation of  $0.5 \text{ dB}/\lambda$  in the bottom. *Note:* You don't have to use FFT integration for this, use simple trapezoidal rule integration.
- Repeat the convergence analysis without contour offset and discuss the difference in convergence rate.

**4.13.** Develop an adaptive Filon integration scheme for general wavenumber integrals based on the FFP approximation (large-argument Hankel function approximation).

- Implement and test your algorithm using the Green's function subroutine developed for the previous problem.
- Using the number of Green's function calculations as a performance measure, compare this approach to the simple direct trapezoidal rule integration in terms of computational efficiency for cases where the field is to be determined at a single range only.
- Discuss qualitatively the performance of the adaptive scheme relative to use of an FFT to compute transmission loss at a large number of ranges.

## References

- F.R. DiNapoli, R.L. Deavenport, Theoretical and numerical Green's function solution in a plane layered medium. *J. Acoust. Soc. Am.* **67**, 92–105 (1980)
- H.W. Kutschale, Rapid computation by wave theory of propagation loss in the Arctic ocean. Rep. CU-8-73. Lamont-Doherty Geological Observatory, Columbia University, New York, 1973
- K. Fuchs, G. Mueller, Computation of synthetic seismograms with the reflectivity method and comparison with observations. *Geophys. J. R. Astron. Soc.* **23**, 417–433 (1971)

4. B.L.N. Kennett, Reflections, rays and reverberations. *Bull. Seism. Soc. Am.* **65**, 1685–1696 (1974)
5. B.L.N. Kennett, N.J. Kerry, Seismic waves in a stratified half-space. *Geophys. J. R. Astron. Soc.* **57**, 557–583 (1979)
6. B.L.N. Kennett, *Seismic Wave Propagation in Stratified Media* (Cambridge University Press, Cambridge, 1983)
7. A.H. Olson, J.A. Orcutt, G.A. Fisher, The discrete wavenumber/ finite element method for synthetic seismograms. *Geophys. J. R. Astron. Soc.* **77**, 421–460 (1984)
8. C.L. Pekeris, Theory of propagation of explosive sound in shallow water. *Geol. Soc. Am. Mem.* **27** (1948)
9. W.S. Jardetzky, Period equation for an N-layered halfspace and some related questions. *Tech. Rep. Seism. No. 29*. Lamont-Doherty Geological Observatory, Columbia University, New York, 1953
10. W.M. Ewing, W.S. Jardetzky, F. Press, *Elastic Waves in Layered Media* (McGraw-Hill, New York, 1957)
11. W.T. Thomson, Transmission of elastic waves through a stratified solid. *J. Appl. Phys.* **21**, 89–93 (1950)
12. N.A. Haskell, The dispersion of surface waves in multilayered media. *Bull. Seism. Soc. Am.* **43**, 17–34 (1953)
13. H. Schmidt, SAFARI: Seismo-acoustic fast field algorithm for range independent environments. User's Guide. Rep. SR-113. SACLANT Undersea Research Centre, La Spezia, Italy, 1988
14. H. Schmidt, F.B. Jensen, A full wave solution for propagation in multilayered viscoelastic media with application to Gaussian beam reflection at fluid–solid interfaces. *J. Acoust. Soc. Am.* **77**, 813–825 (1985)
15. H. Schmidt, G. Tango, Efficient global matrix approach to the computation of synthetic seismograms. *Geophys. J. R. Astron. Soc.* **84**, 331–359 (1986)
16. J. Miklowitz, *The Theory of Elastic Waves and Waveguides* (North-Holland, New York, 1984)
17. D.G. Harkrider, Surface waves in multilayered elastic media. Part I: Rayleigh and Love waves from buried sources in a multilayered elastic halfspace. *Bull. Seism. Soc. Am.* **54**, 627–679 (1964)
18. H. Kolsky, *Stress Waves in Solids* (Dover, New York, 1963)
19. F. Gilbert, G.E. Backus, Propagator matrices in elastic waves and vibration problems. *Geophysics* **31**, 326–332 (1965)
20. G.R. Franssens, Calculation of the elasto-dynamic Green's function in layered media by means of a modified propagator matrix method. *Geophys. J. R. Astron. Soc.* **75**, 669–691 (1983)
21. R.A. Stephen, Synthetic seismograms for the case of a receiver within the reflectivity zone. *Geophys. J. R. Astron. Soc.* **51**, 169–181 (1977)
22. H. Schmidt, F.B. Jensen, Evaluation of experimental techniques for determining the plane wave reflection coefficient at the seafloor. in *Ocean Seismo-Acoustics*, ed. by T. Akal, J.M. Berkson (Plenum, New York, 1986), pp. 721–730
23. M. Abramowitz, I.A. Stegun, *Handbook of Mathematical Functions* (Dover, New York, 1965)
24. A.V. Oppenheim, R.W. Schafer, *Discrete-Time Signal Processing* (Prentice Hall, New Jersey, 1989)
25. K.D. LePage, H. Schmidt, Spectral integral representations of monostatic backscattering from three dimensional distributions of sediment volume inhomogeneities. *J. Acoust. Soc. Am.* **113**, 789–799 (2001)
26. L. Tsang, R. Brown, J.A. Kong, G. Simmons, Numerical evaluation of electromagnetic fields due to dipole antennas. *J. Geophys. Res.* **79**, 2077–2080 (1974)
27. W.L. Anderson, Computation of Green's tensor integrals for three-dimensional electromagnetic problems using fast Hankel transforms. *Geophysics* **49**, 1754–1759 (1984)
28. J.A. Ferrari, D. Perciante, A. Dubra, Fast Hankel transform of  $n$ th order. *J. Opt. Soc. Am.* **16**, 2581–2582 (1999)
29. Q.H. Liu, W.C. Chew, Applications of the conjugate gradient fast Fourier Hankel transfer method with an improved fast Hankel transform algorithm. *Radio Sci.* **29**, 1009–1022 (1994)

30. Q.H. Liu, Z.Q. Zhang, Nonuniform fast Hankel transform (NUFHT) algorithm. *Appl. Opt.* **38**, 6705–6708 (1999)
31. S. Mallick, L.N. Frazer, Practical aspects of reflectivity modeling. *Geophysics* **52**, 1355–1364 (1987)
32. T.W. Dawson, J.A. Fawcett, A boundary integral equation method for acoustic scattering in a waveguide with nonplanar surfaces. *J. Acoust. Soc. Am.* **87**, 1110–1125 (1990)
33. L.N. Frazer, J.F. Gettrust, On the generalization of Filon's method and the computation of oscillatory integrals of seismology. *Geophys. J. R. Astron. Soc.* **76**, 461–481 (1984)
34. S. Krenk, P. Gerstoft, O. Vilmann, Computational aspects of synthetic seismograms. Extended Abstracts, Annual Meeting of the Society of Exploration Geophysicists, Dallas, TX, 1086–1089 (1989)
35. W.A. Kuperman, H. Schmidt, Self-consistent perturbation approach to rough surface scattering in stratified elastic media. *J. Acoust. Soc. Am.* **86**, 1511–1522 (1989)
36. I.T. Lu, L.B. Felsen, Adiabatic transforms for spectral analysis of weakly range-dependent shallow ocean Green's functions. *J. Acoust. Soc. Am.* **81**, 897–911 (1987)
37. G.T. Schuster, L.C. Smith, Modeling scatterers embedded in a plane-layered media by a hybrid Haskell–Thomson and boundary integral equation method. *J. Acoust. Soc. Am.* **78**, 1387–1394 (1985)
38. H. Kawase, Time-domain response of a semi-circular canyon for incident SV, P, and Rayleigh waves calculated by the discrete wavenumber boundary element method. *Bull. Seis. Soc. Am.* **78**, 1415–1437 (1988)
39. P. Gerstoft, H. Schmidt, A boundary element approach to seismo-acoustic facet reverberation. *J. Acoust. Soc. Am.* **89**, 1629–1642 (1991)
40. W. Seong, Hybrid Galerkin boundary element – wavenumber integration method for acoustic propagation in laterally inhomogeneous media. Ph.D. thesis. Massachusetts Institute of Technology, Cambridge, MA, 1991
41. H. Schmidt, J. Glattetre, A fast field model for three-dimensional wave propagation in stratified environments based on the global matrix method. *J. Acoust. Soc. Am.* **78**, 2105–2114 (1985)
42. S. Krenk, H. Schmidt, Elastic wave scattering by a circular crack. *Phil. Trans. R. Soc. Lond. A* **308**, 167–198 (1982)
43. F. Ingenito, Scattering from an object in a stratified medium. *J. Acoust. Soc. Am.* **82**, 2051–2059 (1987)
44. H. Schmidt, J. Lee, Physics of 3D scattering by rough interfaces and buried targets in shallow water. *J. Acoust. Soc. Am.* **105**, 1605–1617 (1999)
45. N.C. Makris, A spectral approach to 3-D object scattering in layered media applied to scattering from submerged spheres. *J. Acoust. Soc. Am.* **104**, 2105–2113 (1998)
46. I. Lucifredi, Scattering from sub-critically insomfied buried elastic shells. Ph.D. thesis. Massachusetts Institute of Technology, Cambridge, MA, 2004
47. J.T. Goh, H. Schmidt, A hybrid coupled waveguide integration approach to range-dependent seismo-acoustic modeling. *J. Acoust. Soc. Am.* **100**, 1409–1420 (1996)
48. H. Schmidt, W.A. Kuperman, Spectral representations of rough interface reverberation in stratified ocean waveguides. *J. Acoust. Soc. Am.* **97**, 2199–2209 (1995)
49. K.D. LePage, Elastic scattering in oceanic waveguides. Ph.D. thesis. Massachusetts Institute of Technology, Cambridge, MA, 1992
50. B. Tracey, H. Schmidt, Seismo-acoustic field statistics in shallow water. *IEEE J. Oceanic Eng.* **OE-22**, 317–331 (1997)
51. H. Fan, Wave theory modeling of three-dimensional seismo-acoustic reverberation in ocean waveguides. Ph.D. thesis. Massachusetts Institute of Technology, Cambridge, MA, 1995
52. K.D. LePage, H. Schmidt, Spectral integral representations of volume scattering in sediments in layered waveguides. *J. Acoust. Soc. Am.* **108**, 1557–1567 (2000)
53. D. Lee, S.T. McDaniel, Ocean acoustic propagation by finite difference methods. *Comp. Math. Appl.* **14**, 305–423 (1987)
54. F.B. Jensen, H. Schmidt, Subcritical penetration of narrow Gaussian beams into sediments. *J. Acoust. Soc. Am.* **82**, 574–579 (1987)

55. F.R. DiNapoli, R.H. Mellen, Low frequency attenuation in the Arctic Ocean. in *Ocean Seismo-Acoustics*, ed. T. Akal, J.M. Berkson (Plenum, New York, 1986), pp. 387–395
56. B.E. Miller, H. Schmidt, Observation and inversion of seismo-acoustic waves in a complex Arctic ice environment. *J. Acoust. Soc. Am.* **89**, 1668–1685 (1991)
57. E. Pouliquen, A. Lyons, N.G. Pace, Penetration of acoustic waves into sandy seafloors at low grazing angles: The Helmholtz–Kirchhoff approach. Rep. SR-290. SACLANT Undersea Research Centre, La Spezia, Italy, 1998
58. A. Rogers, C.W. Holland, SCARAB version 1.01, Users Manual. Planning Systems Incorporated, 1997
59. P.C. Hines, Theoretical model of acoustic backscatter from a smooth seabed. *J. Acoust. Soc. Am.* **88**, 324–334, (1990)
60. A. Maguer, W.L.J. Fox, H. Schmidt, E. Pouliquen, E. Bovio, Mechanisms for subcritical penetration into a sandy bottom: Experimental and modeling results. *J. Acoust. Soc. Am.* **107**, 1215–1225 (2000)
61. A. Maguer, E. Bovio, W.L.J. Fox, H. Schmidt, “*In situ* estimation of sediment sound speed and critical angle. *J. Acoust. Soc. Am.* **108**, 987–996 (2000)
62. C.W. Holland, R. Hollett, L. Troiano, Measurement technique for bottom scattering in shallow water. *J. Acoust. Soc. Am.* **108**, 997–1011 (2000)
63. C.W. Holland, J. Osler, High resolution geoacoustic inversion in shallow water: A joint time and frequency domain technique. *J. Acoust. Soc. Am.* **107**, 1263–1279 (2000)
64. C.W. Holland, P. Neumann, Sub-bottom scattering: A modeling approach. *J. Acoust. Soc. Am.* **104**, 1363–1373 (1998)
65. K.D. LePage, H. Schmidt, Modeling of low frequency transmission loss in the Central Arctic. *J. Acoust. Soc. Am.* **96**, 1783–1795 (1994)



# Chapter 5

## Normal Modes

### 5.1 Introduction

Normal-mode methods have been used for many years in underwater acoustics. An early and widely cited reference is due to Pekeris [1], who developed the theory for a simple two-layer model of the ocean. At about the same time Ide et al. [2] had been using normal modes to interpret propagation in the Potomac River and Chesapeake Bay. Progress in the development of normal-mode methods is presented in an excellent summary given by Williams [3]. Numerical techniques now exist which can treat problems with an arbitrary number of fluid and viscoelastic layers.

The normal-mode method involves solving a depth-dependent equation which is precisely an unforced version of the equation solved in the wavenumber integration technique of Chap. 4. The numerical techniques are in fact very closely related. This unforced problem has a set of modes of vibration which are roughly akin to the modes of a vibrating string. The “frequencies” of vibration give the horizontal wavenumbers associated with the modal propagation. The complete acoustic field is then constructed by summing up contributions of each of the modes weighted in accordance to the source depth. An outline of a simple numerical code for computing normal modes is given in Appendix 1.

We begin with a simple derivation of the normal-mode equations based on separation of variables. This provides a quick means of introducing the gross features of the normal-mode approach as illustrated for the ideal, rigid-bottom waveguide in Sect. 5.4. In Sect. 5.5, we present a generalized derivation which starts with the spectral representation presented in Chap. 4. Apart from clarifying the relationship between normal mode and spectral integral solutions, this derivation is necessary for treating the more complex problems involving homogeneous-halfspace bottoms, interfacial roughness or even more complicated boundary conditions.

## 5.2 Mathematical Derivation

### 5.2.1 Point Source in Cylindrical Geometry

We begin with the Helmholtz equation in two dimensions with sound speed and density depending only on depth  $z$ ,

$$\frac{1}{r} \frac{\partial}{\partial r} \left( r \frac{\partial p}{\partial r} \right) + \rho(z) \frac{\partial}{\partial z} \left( \frac{1}{\rho(z)} \frac{\partial p}{\partial z} \right) + \frac{\omega^2}{c^2(z)} p = -\frac{\delta(r) \delta(z - z_s)}{2\pi r}. \quad (5.1)$$

Using the technique of *separation of variables*, we seek a solution of the unforced equation in the form  $p(r, z) = \Phi(r)\Psi(z)$ . After substituting into the above equation and dividing through by  $\Phi(r)\Psi(z)$  we find,

$$\frac{1}{\Phi} \left[ \frac{1}{r} \frac{d}{dr} \left( r \frac{d\Phi}{dr} \right) \right] + \frac{1}{\Psi} \left[ \rho(z) \frac{d}{dz} \left( \frac{1}{\rho(z)} \frac{d\Psi}{dz} \right) + \frac{\omega^2}{c^2(z)} \Psi \right] = 0. \quad (5.2)$$

The contents in the square brackets are functions of  $r$  and  $z$ , respectively. Thus, the only way the equation can be satisfied is if each component is equal to a constant. Denoting this separation constant by  $k_{rm}^2$ , we obtain the modal equation,

$$\rho(z) \frac{d}{dz} \left[ \frac{1}{\rho(z)} \frac{d\Psi_m(z)}{dz} \right] + \left[ \frac{\omega^2}{c^2(z)} - k_{rm}^2 \right] \Psi_m(z) = 0, \quad (5.3)$$

with

$$\Psi(0) = 0, \quad \left. \frac{d\Psi}{dz} \right|_{z=D} = 0. \quad (5.4)$$

Here,  $\Psi_m(z)$  denotes the particular function  $\Psi(z)$  obtained with the separation constant  $k_{rm}$ . The boundary conditions imposed imply a pressure-release surface located at  $z = 0$  and a perfectly rigid bottom located at  $z = D$ . In a later section, we discuss more complicated boundary conditions.

The modal equation is a classical *Sturm–Liouville* eigenvalue problem whose properties are well-known [5]. (We assume for the moment that  $\rho(z)$  and  $c(z)$  are real functions.) A brief summary of these properties are as follows: The modal equation has an infinite number of solutions which are like the modes of a vibrating string. The modes are characterized by a mode shape function  $\Psi_m(z)$  and a horizontal propagation constant  $k_{rm}$ . These horizontal propagation constants, which are analogous to a frequency of vibration, are all distinct. The function  $\Psi_m(z)$  is an *eigenfunction* and  $k_{rm}$  or  $k_{rm}^2$  is an *eigenvalue*. The  $m$ th mode has  $m$  zeroes in the interval  $[0, D]$  and the corresponding eigenvalues  $k_{rm}^2$  are all real and are ordered as  $k_{r1}^2 > k_{r2}^2 > \dots$ . One can also show that all the eigenvalues are less than  $\omega/c_{\min}$ ,

where  $c_{\min}$  is the lowest sound speed in the problem. In addition, the modes of such Sturm–Liouville problems are *orthogonal*, i.e.,

$$\int_0^D \frac{\Psi_m(z) \Psi_n(z)}{\rho(z)} dz = 0, \quad \text{for } m \neq n. \quad (5.5)$$

The solutions of the modal equation are arbitrary to a multiplicative constant as is easily seen from (5.3). In order to simplify certain results, we shall assume that the modes are scaled (normalized) so that

$$\int_0^D \frac{\Psi_m^2(z)}{\rho(z)} dz = 1. \quad (5.6)$$

Finally, the modes form a complete set, which means we can represent an arbitrary function as a sum of the normal modes. Thus, we write the pressure as

$$p(r, z) = \sum_{m=1}^{\infty} \Phi_m(r) \Psi_m(z). \quad (5.7)$$

Substituting this into (5.1), we obtain

$$\begin{aligned} & \sum_{m=1}^{\infty} \left\{ \frac{1}{r} \frac{d}{dr} \left( r \frac{d\Phi_m(r)}{dr} \right) \Psi_m(z) \right. \\ & \left. + \Phi_m(r) \left[ \rho(z) \frac{d}{dz} \left( \frac{1}{\rho(z)} \frac{d\Psi_m(z)}{dz} \right) + \frac{\omega^2}{c^2(z)} \Psi_m(z) \right] \right\} = -\frac{\delta(r) \delta(z - z_s)}{2\pi r}. \end{aligned} \quad (5.8)$$

The term in square brackets can be further simplified using the modal equation (5.3). This yields

$$\sum_{m=1}^{\infty} \left\{ \frac{1}{r} \frac{d}{dr} \left( r \frac{d\Phi_m(r)}{dr} \right) \Psi_m(z) + k_{rm}^2 \Phi_m(r) \Psi_m(z) \right\} = -\frac{\delta(r) \delta(z - z_s)}{2\pi r}. \quad (5.9)$$

Next, we apply the operator

$$\int_0^D (\cdot) \frac{\Psi_n(z)}{\rho(z)} dz \quad (5.10)$$

to (5.9). Because of the orthogonality property given in (5.5), only the  $n$ th term in the sum remains, yielding

$$\frac{1}{r} \frac{d}{dr} \left[ r \frac{d\Phi_n(r)}{dr} \right] + k_{rn}^2 \Phi_n(r) = -\frac{\delta(r) \Psi_n(z_s)}{2\pi r \rho(z_s)}. \quad (5.11)$$

This is a standard equation whose solution is given in terms of a Hankel function as

$$\Phi_n(r) = \frac{i}{4\rho(z_s)} \Psi_n(z_s) H_0^{(1,2)}(k_{rn}r). \quad (5.12)$$

As discussed in Chap. 2, the choice of  $H_0^{(1)}$  or  $H_0^{(2)}$  is determined by the radiation condition stating that energy should be radiating outward as  $r \rightarrow \infty$ . Since we have suppressed a time dependence of the form  $\exp(-i\omega t)$  we shall take the Hankel function of the first kind. Putting this all together, we find that

$$p(r, z) = \frac{i}{4\rho(z_s)} \sum_{m=1}^{\infty} \Psi_m(z_s) \Psi_m(z) H_0^{(1)}(k_{rm}r) \quad (5.13)$$

or, using the asymptotic approximation to the Hankel function,

$$p(r, z) \simeq \frac{i}{\rho(z_s) \sqrt{8\pi r}} e^{-i\pi/4} \sum_{m=1}^{\infty} \Psi_m(z_s) \Psi_m(z) \frac{e^{ik_{rm}r}}{\sqrt{k_{rm}}}. \quad (5.14)$$

As discussed in Chap. 2, we normally plot transmission loss rather than the complex pressure field. For the case where the density at the source and field points are the same, transmission loss is given by

$$TL(r, z) = -20 \log \left| \frac{p(r, z)}{p_0(r = 1)} \right|, \quad (5.15)$$

where

$$p_0(r) = \frac{e^{ik_0r}}{4\pi r} \quad (5.16)$$

is the pressure for the source in free space. Thus, one may write

$$TL(r, z) \simeq -20 \log \left| \frac{1}{\rho(z_s)} \sqrt{\frac{2\pi}{r}} \sum_{m=1}^{\infty} \Psi_m(z_s) \Psi_m(z) \frac{e^{ik_{rm}r}}{\sqrt{k_{rm}}} \right|. \quad (5.17)$$

In some cases, it is useful to calculate an incoherent transmission loss defined by

$$TL_{Inc}(r, z) \simeq -20 \log \frac{1}{\rho(z_s)} \sqrt{\frac{2\pi}{r}} \sqrt{\sum_{m=1}^{\infty} \left| \Psi_m(z_s) \Psi_m(z) \frac{e^{ik_{rm}r}}{\sqrt{k_{rm}}} \right|^2}. \quad (5.18)$$

When comparing theory to measured data which has been averaged over frequency, one can often simulate the resulting smoothed transmission loss by an incoherent modal summation. Incoherent transmission loss is also often appropriate for

shallow-water problems, where the modes are bottom-interacting. Since bottom properties are usually poorly known, the detailed interference pattern predicted by a coherent transmission-loss calculation is not always physically meaningful.

### 5.2.2 Line Source in Plane Geometry

Normally, a point source is appropriate for practical problems in underwater acoustics. However, for inter-model comparisons it is sometimes useful to work with a line source in plane geometry. The derivation requires minor changes with respect to the point-source case. Our starting point is the Helmholtz equation,

$$\frac{\partial^2 p}{\partial x^2} + \rho(z) \frac{\partial}{\partial z} \left( \frac{1}{\rho(z)} \frac{\partial p}{\partial z} \right) + \frac{\omega^2}{c^2(z)} p = -\delta(x) \delta(z - z_s). \quad (5.19)$$

We seek a solution in the form

$$p(x, z) = \sum_{m=1}^{\infty} \Phi_m(x) \Psi_m(z), \quad (5.20)$$

where  $\Psi_m(z)$  are the usual eigenfunctions of the depth-separated equation (5.3). Substituting (5.20) into (5.19) yields

$$\begin{aligned} \sum_{m=1}^{\infty} \left\{ \frac{d^2 \Phi_m(x)}{dx^2} \Psi_m(z) \right. \\ \left. + \Phi_m(x) \left[ \rho(z) \frac{d}{dz} \left( \frac{1}{\rho(z)} \frac{d \Psi_m(z)}{dz} \right) + \frac{\omega^2}{c^2(z)} \Psi_m(z) \right] \right\} = -\delta(x) \delta(z - z_s). \end{aligned} \quad (5.21)$$

Making use of the modal equation (5.3) we can simplify the term in square brackets and obtain

$$\sum_{m=1}^{\infty} \left[ \frac{d^2 \Phi_m(x)}{dx^2} \Psi_m(z) + k_{xm}^2 \Phi_m(x) \Psi_m(z) \right] = -\delta(x) \delta(z - z_s). \quad (5.22)$$

As before, we apply the operator,

$$\int_0^D (\cdot) \frac{\Psi_n(z)}{\rho(z)} dz, \quad (5.23)$$

to (5.22). Because of the orthogonality property only the  $n$ th term in the sum remains, yielding

$$\frac{d^2 \Phi_n(x)}{dx^2} + k_{xn}^2 \Phi_n(x) = \frac{-\delta(x) \Psi_n(z_s)}{\rho(z_s)}. \quad (5.24)$$

The solution of this equation gives us the range dependency associated with a particular mode. Where previously we had a Hankel equation to solve, we now have a somewhat simpler equation whose solution is given in terms of sines and cosines or, equivalently, in terms of complex exponentials as

$$\Phi_n(x) = \frac{i}{2\rho(z_s)} \Psi_n(z_s) \frac{e^{\pm ik_{xn}x}}{k_{xn}}. \quad (5.25)$$

As discussed in Chap. 2, the radiation condition fixes the sign in the exponential and we obtain our final solution,

$$p(x, z) = \frac{i}{2\rho(z_s)} \sum_{m=1}^{\infty} \Psi_m(z_s) \Psi_m(z) \frac{e^{ik_{xm}|x|}}{k_{xm}}. \quad (5.26)$$

Note that in comparison to the point-source result given in (5.14), the key difference is in the  $k_{xm}$  weighting in the denominator. Thus, normal mode codes – like any other solution method – can be modified to provide a line-source result with a trivial change.

Next, we follow the convention from the point-source geometry and define transmission loss with respect to the field 1 m from the source. The pressure field due to a line source in free space satisfies,

$$\frac{1}{r} \frac{\partial}{\partial r} \left( r \frac{\partial p_0}{\partial r} \right) + \frac{\omega^2}{c^2(z)} p_0 = -\frac{\delta(r)}{2\pi r}, \quad (5.27)$$

where  $r$  denotes a slant range from the source. The solution of this equation is given by

$$p_0(r) = \frac{i}{4} H_0^{(1)}(k_0 r), \quad (5.28)$$

where  $k_0 = \omega/c_0$  is the medium wavenumber at the source. Thus, the normalized pressure is given by

$$\frac{p(x, z)}{p_0(r)|_{r=1}} = \frac{2}{\rho(z_s) H_0^{(1)}(k_0)} \sum_{m=1}^{\infty} \Psi_m(z_s) \Psi_m(z) \frac{e^{ik_{xm}|x|}}{k_{xm}}. \quad (5.29)$$

This form is somewhat inconvenient since it requires the evaluation of a Hankel function. In virtually every other case where such functions have occurred, we have invoked the large-argument asymptotic representation to simplify the results. The difficulty here is that the argument  $k_0$  is generally not large. Since we are only seeking a normalization that is consistent with that of the point-source case, we may go ahead and use the asymptotic form (2.39), yielding

$$\frac{p(x, z)}{p_0(r=1)} \simeq \frac{\sqrt{2\pi k_0}}{\rho(z_s)} e^{-i(k_0 - \pi/4)} \sum_{m=1}^{\infty} \Psi_m(z_s) \Psi_m(z) \frac{e^{ik_{xm}|x|}}{k_{xm}}. \quad (5.30)$$

Transmission loss is then defined by

$$\text{TL}(x, z) = -20 \log \left| \frac{p(x, z)}{p_0(r = 1)} \right|. \quad (5.31)$$

We emphasize that there is no well-established convention for normalizing such line-source results and so care must be taken in comparing to published results. One should also be alert in performing broadband calculations with this normalization: the scale factor is frequency dependent and if it is not removed during the frequency synthesis, the pulse will be distorted.

### 5.3 Modal Expansion of the Green's Function

In the previous chapter, we obtained a representation of the pressure field in terms of the Green's function for the depth-separated problem,

$$\rho(z) \frac{d}{dz} \left[ \frac{1}{\rho(z)} \frac{dg(z)}{dz} \right] + \left[ \frac{\omega^2}{c^2(z)} - k_r^2 \right] g(z) = -\frac{\delta(z - z_s)}{2\pi}. \quad (5.32)$$

Sometimes it is useful to have a modal representation of this Green's function. This is easy to obtain. We first seek an expansion of the delta function as a sum of modes,

$$\delta(z - z_s) = \sum_m a_m \Psi_m(z). \quad (5.33)$$

Here, we assume that there is no continuous spectrum so that the modes form a complete set. To find the coefficients  $a_m$  we apply the operator

$$\int_0^D (\cdot) \frac{\Psi_n(z)}{\rho(z)} dz, \quad (5.34)$$

to this sum. Because of the orthogonality property given in (5.5) only the term in the series with  $m = n$  remains, i.e.,

$$a_n = \frac{\Psi_n(z_s)}{\rho(z_s)}. \quad (5.35)$$

To summarize, the delta function is represented by the following mode sum:

$$\delta(z - z_s) = \sum_m \frac{\Psi_m(z_s) \Psi_m(z)}{\rho(z_s)}. \quad (5.36)$$

The above relation is sometimes referred to as the *completeness relation* since it implies the mode set converges in the mean to an arbitrary piecewise continuous function.

We next seek a solution of the depth-separated problem as a sum of modes,

$$g(z) = \sum_m b_m \Psi_m(z). \quad (5.37)$$

Substituting this form into (5.32) yields

$$\begin{aligned} & \sum_{m=1}^{\infty} b_m \left[ \rho(z) \frac{d}{dz} \left( \frac{1}{\rho(z)} \frac{d\Psi_m(z)}{dz} \right) + \left( \frac{\omega^2}{c^2(z)} - k_r^2 \right) \Psi_m(z) \right] \\ &= -\frac{1}{2\pi} \sum_m \frac{\Psi_n(z_s)}{\rho(z_s)} \Psi_m(z). \end{aligned} \quad (5.38)$$

From the modal equation (5.3) we can rewrite this as

$$\sum_{m=1}^{\infty} b_m (k_{rm}^2 - k_r^2) \Psi_m(z) = -\frac{1}{2\pi} \sum_m \frac{\Psi_n(z_s)}{\rho(z_s)} \Psi_m(z). \quad (5.39)$$

Again, we apply the integral operator given in (5.34) and conclude from the orthogonality property that only the  $n$ th term in the sum remains. This gives

$$(k_{rn}^2 - k_r^2) b_n = -\frac{\Psi_n(z_s)}{2\pi\rho(z_s)}. \quad (5.40)$$

Solving this for  $b_n$  and substituting back into (5.37) gives our final result for the depth-separated Green's function,

$$g(z) = \frac{1}{2\pi\rho(z_s)} \sum_m \frac{\Psi_m(z_s) \Psi_m(z)}{k_r^2 - k_{rm}^2}. \quad (5.41)$$

In this form, one can clearly see that the Green's function has singularities at values of  $k_r$  corresponding to the modal wavenumbers  $k_{rm}$ .

## 5.4 The Isovelocity Problem

The principal numerical problem is to solve (5.3) and (5.4) for the normal modes  $\Psi_m(z)$ . The sound-speed profile  $c(z)$  assumes a fairly arbitrary form so simple analytical techniques are generally not useful. On the other hand, it is instructive to consider some simple profiles in order to understand the qualitative features of modal problems. The simplest such case is the *isovelocity* profile with constant density as shown in Fig. 5.1. The general solution is

$$\Psi_m(z) = A \sin(k_z z) + B \cos(k_z z), \quad (5.42)$$

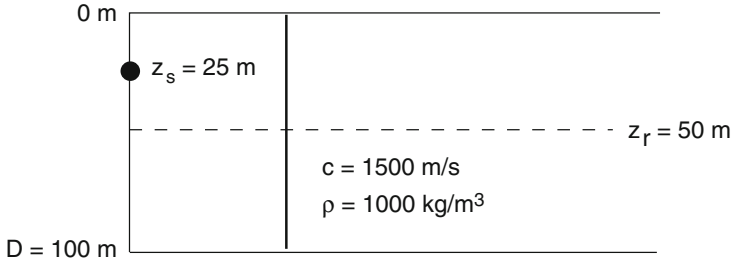


**Fig. 5.1** Schematic of the isovelocity problem

where the vertical wavenumber  $k_z$  is given by

$$k_z = \sqrt{\left(\frac{\omega}{c}\right)^2 - k_r^2}. \quad (5.43)$$

The surface boundary condition implies that  $B = 0$  while the bottom boundary condition leads to

$$Ak_z \cos(k_z D) = 0, \quad (5.44)$$

where  $D$  is the depth of the bottom. Thus, either  $A = 0$  (the trivial solution) or we must have

$$k_z D = \left(m - \frac{1}{2}\right)\pi, \quad m = 1, 2, \dots, \quad (5.45)$$

that is,  $k_r$  must assume particular values,

$$k_{rm} = \sqrt{\left(\frac{\omega}{c}\right)^2 - \left[\left(m - \frac{1}{2}\right)\frac{\pi}{D}\right]^2}, \quad m = 1, 2, \dots \quad (5.46)$$

The corresponding eigenfunctions are given by

$$\Psi_m(z) = \sqrt{\frac{2\rho}{D}} \sin(k_{rm} z), \quad (5.47)$$

where we have chosen the constant  $A$  so that the modes have unit norm as specified in (5.6).

Equation (5.46), which relates the frequency  $\omega$  to the horizontal wavenumber  $k_{rm}$ , is known as the *dispersion relation*. Plots of  $\omega$  versus  $k_{rm}$  are in turn called the dispersion curves. The quantities  $v_m(\omega) = \omega/k_{rm}$  and  $u_m(\omega) = d\omega/dk_{rm}$  are, respectively, the *phase velocity* and the *group velocity* of the  $m$ th mode. As discussed in Chap. 2, the group velocity is associated with the radial speed of propagation for a pulse in a waveguide.

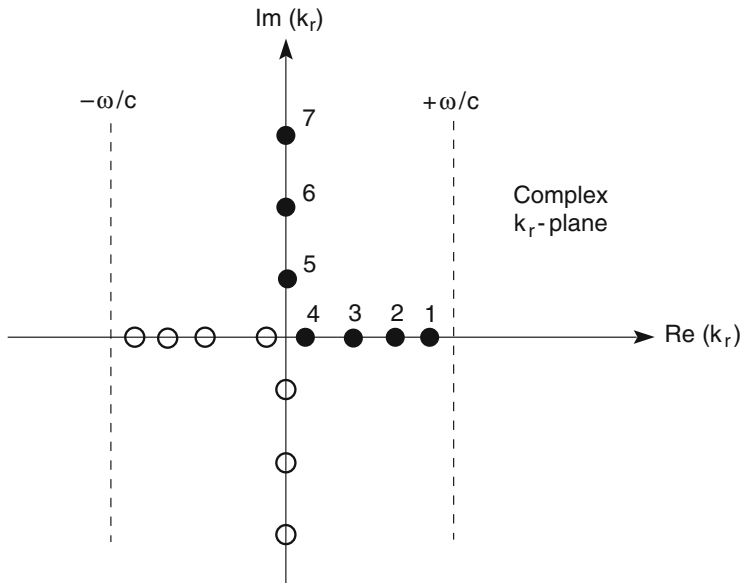


**Fig. 5.2** Location of eigenvalues for the isovelocity problem

The eigenvalues divide into two classes corresponding to *propagating* and *evanescent* modes depending on whether the argument of the square root in (5.46) is positive or negative. In either case, the square root admits two values  $k_{rm}$  and  $-k_{rm}$ . The positions of these eigenvalues are indicated schematically in Fig. 5.2. (Their precise positions depend on frequency, depth, and sound speed.)

For the propagating modes we select the branch which gives an outgoing wave. Since we have suppressed a time dependence of the form  $\exp(-i\omega t)$  we should take the positive value for  $k_{rm}$ . These eigenvalues are indicated by the filled circles lying on the positive real axis in Fig. 5.2.

For the evanescent modes we have to choose between roots of the form  $i\xi$  and  $-i\xi$  where  $\xi$  is a positive real number. These modes have the property of being either growing or decaying in range. In order to have a bounded solution, we take the branch for which  $k_{rm}$  lies in the upper halfplane, i.e.,  $k_{rm} = i\xi$  with  $\xi$  positive. These eigenvalues are indicated by the filled circles lying on the positive imaginary axis in Fig. 5.2.

The real eigenvalues have an upper bound of  $\omega/c$ . As we reduce the frequency, the eigenvalues on the real axis slide to the left and up the imaginary axis. At a sufficiently low frequency, the first mode will make the transition leaving no propagating modes in the problem. The frequency at which this occurs is called the *cutoff* frequency for the waveguide, found from (5.46) to be

$$f_0 = \frac{c}{4D}. \quad (5.48)$$

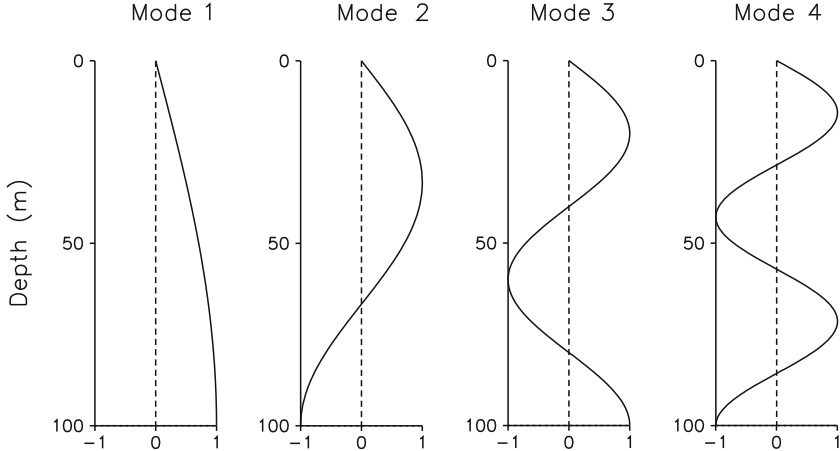


**Fig. 5.3** Selected modes of the isovelocity problem

As an example, consider the isovelocity problem with sound speed  $c = 1500 \text{ m/s}$ , depth  $D = 100 \text{ m}$ , and source frequency  $f = 100 \text{ Hz}$ . In this case, there are 13 propagating modes of which the first 4 are plotted in Fig. 5.3. Note that the  $m$ th mode has  $m$  zeroes.

Substituting the formula for the isovelocity modes given in (5.47) into (5.13) we obtain a representation of the pressure field

$$p(r, z) = \frac{i}{2D} \sum_{m=1}^{\infty} \sin(k_{zm} z_s) \sin(k_{zm} z) H_0^{(1)}(k_{rm} r). \quad (5.49)$$

Similarly, from (5.17) we obtain a representation for transmission loss as  $-10 \log I$  where  $I$  is an intensity defined by

$$I(r, z) = \left| \frac{1}{D} \sqrt{\frac{8\pi}{r}} \sum_{m=1}^{\infty} \sin(k_{zm} z_s) \sin(k_{zm} z) \frac{e^{ik_{rm} r}}{\sqrt{k_{rm}}} \right|^2. \quad (5.50)$$

In Fig. 5.4, we display the transmission loss for this problem keeping 1, 2, and 3 modes, respectively, in the modal sum. The source depth is  $z_s = 25 \text{ m}$  and the receiver depth is  $z = 50 \text{ m}$  in these calculations. Note that as we increase the number of modes the detail in the transmission-loss curves also increases. This can be understood by writing the intensity as

$$\begin{aligned} I(r, z) &= \frac{8\pi}{r D^2} \left| \sum_{m=1}^{\infty} A_m e^{ik_{rm} r} \right|^2 \\ &= \frac{8\pi}{r D^2} \left[ \sum_m A_m^2 + \sum_m \sum_{n>m} 2A_m A_n \cos(\Delta k_{mn} r) \right], \end{aligned} \quad (5.51)$$

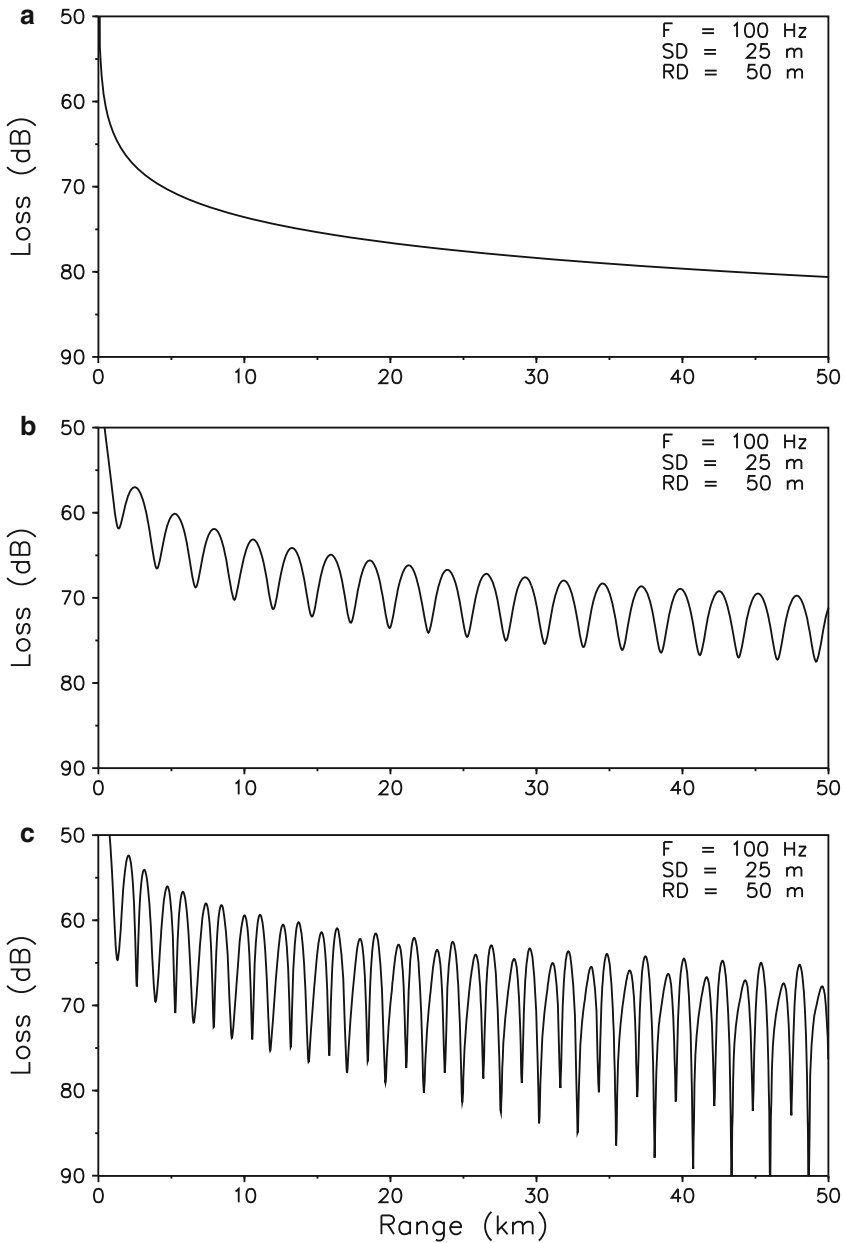


**Fig. 5.4** Transmission loss for the isovelocity problem using (a) 1 mode, (b) 2 modes, and (c) 3 modes

where

$$\Delta k_{mn} = k_{rm} - k_{rn} \quad (5.52)$$

and

$$A_m = \frac{\sin(k_{zm}z_s) \sin(k_{zm}z)}{\sqrt{k_{rm}}}. \quad (5.53)$$

With just one mode in the series, the complex pressure involves an oscillatory term of the form  $e^{ik_r r}$ , however, its envelope (the intensity) is smooth as indicated in Fig. 5.4a. With two modes in the series the intensity is seen to include a term  $\cos[(k_{r1} - k_{r2})r]$  giving the two-mode *interference* pattern in Fig. 5.4b. Note that the interference pattern occurs over a scale significantly larger than the wavelength. Finally, with 3 modes the interference structure shows a further increase in complexity as shown in Fig. 5.4c.

Many of the properties we see for the isovelocity profile will carry through to more general profiles. On the other hand, while it may still be useful to speak of propagating and evanescent modes, the distinction is blurred when attenuation is included because all the modes are then displaced into the first quadrant. As a result, the modes then have both a propagating and an evanescent component. Similarly, the cutoff frequency is poorly defined in such cases. These points will be made clearer as we consider more complex propagation situations.

## 5.5 A Generalized Derivation

The derivation of the modal equation followed in Sect. 5.2 is inapplicable in many ocean-acoustic problems. The key assumption was that after applying the separation of variables we obtained a Sturm–Liouville problem which was non-singular and therefore possessed a complete set of normal modes. As we shall see, even fairly simple scenarios can lead to singular problems for which the normal modes do not form a complete set. More generally, one obtains a mixed spectrum composed of a *discrete* and a *continuous* part. The discrete spectrum in such cases leads to a representation involving a sum of modes while the continuous spectrum involves an integral over a continuum of points in  $k$ -space in a manner similar to the spectral integral representation considered in Chap. 4.

A simple example of such a problem is the *Pekeris* waveguide shown in Fig. 5.5. It consists of an isovelocity water layer over an isovelocity halfspace bottom. Applying the separation of variables technique to this problem we obtain the modal equation (5.3) but with the bottom depth  $D$  going to infinity: the modal equation is singular. We can make the domain finite by constructing a boundary condition to be applied at the interface between the two layers. To construct the equivalent boundary condition, we observe that the general solution in the halfspace is given by

$$\Psi_b(z) = B e^{-\gamma_b z} + C e^{\gamma_b z}, \quad (5.54)$$

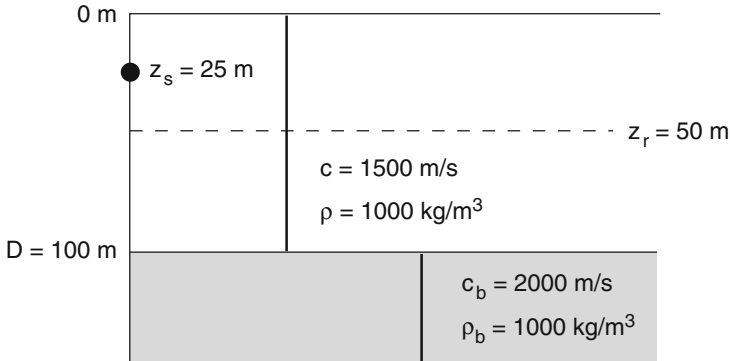


**Fig. 5.5** Schematic of the Pekeris waveguide

where

$$\gamma_b \equiv -ik_{z,b} = \sqrt{k_r^2 - \left(\frac{\omega}{c_b}\right)^2} \quad (5.55)$$

and \$c\_b\$ denotes the sound speed in the bottom. Let us assume for the moment that \$\gamma\_b\$ is positive. Then, in order to have a bounded solution at infinity, we require \$C\$ to vanish. At the interface, we require continuity of pressure and normal velocity as discussed in Chap. 2,

$$\Psi(D) = B e^{-\gamma_b D}, \quad (5.56)$$

$$\frac{d\Psi(D)/dz}{\rho} = -B \frac{\gamma_b e^{-\gamma_b D}}{\rho_b}, \quad (5.57)$$

where \$\rho\$ and \$\rho\_b\$ denote the density in the water and bottom, respectively. Dividing these two equations we find that \$\Psi(z)\$ must satisfy the boundary condition

$$\frac{\rho \Psi(D)}{d\Psi(D)/dz} = -\frac{\rho_b}{\gamma_b(k_r^2)}. \quad (5.58)$$

Our modal problem then reads,

$$\frac{d^2\Psi(z)}{dz^2} + \left[ \frac{\omega^2}{c^2(z)} - k_r^2 \right] \Psi(z) = 0, \quad (5.59)$$

$$\Psi(0) = 0, \quad (5.60)$$

$$f(k_r^2) \Psi(D) + \frac{g(k_r^2)}{\rho} \frac{d\Psi(D)}{dz} = 0, \quad (5.61)$$

where

$$f(k_r^2) = 1, \quad g(k_r^2) = \rho_b \sqrt{k_r^2 - \left(\frac{\omega}{c_b}\right)^2}. \quad (5.62)$$

Now we have a modal problem defined on a finite domain, but the boundary condition involves the eigenvalue  $k_r^2$ . Furthermore, the eigenvalue enters through a square root function which introduces a branch cut in the  $k_r$ -plane. Thus, we can convert a modal problem from an infinite domain to a finite domain but the problem remains singular and we are not assured of the completeness of the eigenfunctions.

We shall take another approach which, briefly stated, is to take the spectral integral representation of the solution (as given in Chap. 4), close the contour and calculate the integral as a sum of residues. The terms due to the residues will turn out to correspond to the modes of the problem. Thus, we start with the spectral integral representation,

$$\begin{aligned} p(r, z) &= \int_0^\infty G(z, z_s; k_r) J_0(k_r r) k_r dk_r \\ &= \frac{1}{2} \int_{-\infty}^\infty G(z, z_s; k_r) H_0^{(1)}(k_r r) k_r dk_r, \end{aligned} \quad (5.63)$$

where the Green's function  $G(z, z_s; k_r)$  satisfies

$$\rho(z) \left[ \frac{1}{\rho(z)} G'(z) \right]' + \left[ \frac{\omega^2}{c^2(z)} - k_r^2 \right] G(z) = -\frac{\delta(z - z_s)}{2\pi}, \quad (5.64)$$

$$f^T(k_r^2) G(0) + \frac{g^T(k_r^2)}{\rho(0)} \frac{dG(0)}{dz} = 0, \quad (5.65)$$

$$f^B(k_r^2) G(D) + \frac{g^B(k_r^2)}{\rho(D)} \frac{dG(D)}{dz} = 0, \quad (5.66)$$

where primes denote differentiation with respect to  $z$ . The top and bottom boundary conditions involve functions  $f^{T,B}$  and  $g^{T,B}$  representing an angle-dependent impedance. Incidentally, this form allows for fairly complicated bottom types. For instance, in Sect. 5.10.3 we show how to construct an impedance condition equivalent to an elastic bottom.

We shall write this problem symbolically as

$$\mathcal{L}(k_{rm})G = -\frac{\delta(z - z_s)}{2\pi}, \quad \mathcal{B}_1 G = \mathcal{B}_2 G = 0. \quad (5.67)$$

The solution of this boundary-value problem is given in standard texts (e.g., [5]) as

$$G(z, z_s; k_r) = -\frac{1}{2\pi} \frac{p_1(z_<; k_r) p_2(z_>; k_r)}{W(z_s; k_r)}, \quad (5.68)$$

where  $z_< = \min(z, z_s)$  and  $z_> = \max(z, z_s)$ . Furthermore,  $W(z; k)$  is the Wronskian

$$W(z; k_r) = p_1(z; k_r) p_2'(z; k_r) - p_1'(z; k_r) p_2(z; k_r), \quad (5.69)$$

where  $p_1, p_2$  are any non-trivial solutions satisfying the top and bottom boundary conditions respectively. That is,

$$\mathcal{L}(k_r)p_1 = 0, \quad \mathcal{B}_1 p_1 = 0, \quad (5.70)$$

$$\mathcal{L}(k_r)p_2 = 0, \quad \mathcal{B}_2 p_2 = 0. \quad (5.71)$$

Let us consider the Pekeris waveguide problem, which has a single branch cut from a lower-halfspace boundary condition. We next close the contour in the spectral integral representation by adding the semicircle  $C_\infty$  and the branch cut integral  $C_{\text{EJP}}$  as shown in Fig. 5.6. (This particular choice of the branch cut along the axes is called the EJP cut after Ewing et al. [7].) Then, assuming simple roots and using Cauchy's theorem we can write the integral as a sum of residues,

$$\int_{-\infty}^{\infty} + \int_{C_\infty} + \int_{C_{\text{EJP}}} = 2\pi i \sum_{m=1}^M \text{res}(k_{rm}), \quad (5.72)$$

where  $\text{res}(k_{rm})$  denotes the residue of the  $m$ th pole enclosed by the contour. These poles are indicated schematically by the filled circles in Fig. 5.6. (Their precise positions depend on both the frequency and the parameters of the waveguide.) Additional poles, which are not enclosed, will also occur as indicated by the open circles. Furthermore, depending on the particular problem and the choice of the branch cut, the number of such residues may be zero, finite, or infinite.

As the radius of the semicircle  $C_\infty$  goes to infinity, the contribution of that contour goes to zero because the Hankel function decays exponentially as the radius

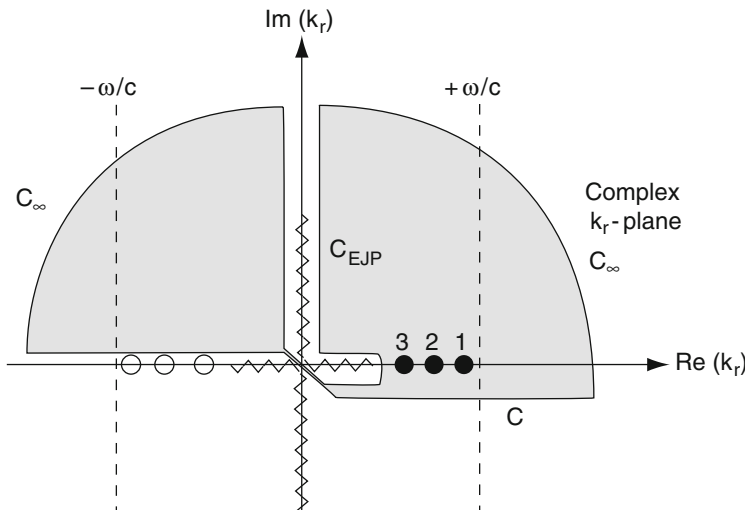


**Fig. 5.6** Location of eigenvalues for the Pekeris problem using the EJP branch cut

increases. Substituting the representation of the Green's function given in (5.68) into (5.63) we then obtain a representation of the field as a sum of residues plus a branch-line integral,

$$p(r, z) = \frac{i}{2} \sum_{m=1}^M \frac{p_1(z_-; k_{rm}) p_2(z_+; k_{rm})}{\partial W(z_s; k_r)/\partial k_r|_{k_r=k_{rm}}} H_0^{(1)}(k_{rm}r) k_{rm} - \int_{C_{\text{EJP}}}, \quad (5.73)$$

where  $k_{rm}$  is the  $m$ th zero of the Wronskian, ordered so that  $\text{Re}\{k_{r1}\} > \text{Re}\{k_{r2}\} > \dots$ . The equation defining these roots or eigenvalues [ $W(k_{rm}) = 0$ ] is known as the *characteristic equation* or *secular equation*. (In general, any equation whose roots are the eigenvalues will be called a characteristic equation.) Here, we have assumed that the zeroes of the Wronskian are simple. It is possible to construct environments where the Wronskian has multiple roots [8], but the probability of encountering such a problem is very small. Note that for proper Sturm–Liouville problems we cannot have multiple eigenvalues. The cases with multiple eigenvalues involve properties such as elasticity or complex sound speeds that destroy the self-adjointness of proper Sturm–Liouville problems.

Now if  $W(k_{rm}) = 0$  then  $p_{1,2}(z; k_{rm})$  are linearly dependent and we can simply scale them so that they are equal. We shall, therefore, define  $\Psi_m(z) = p_1(z; k_{rm}) = p_2(z; k_{rm})$  which satisfies

$$\mathcal{L}(k_{rm})\Psi_m = 0, \quad \mathcal{B}_1\Psi_m = \mathcal{B}_2\Psi_m = 0. \quad (5.74)$$

This is, of course, the standard modal equation. If  $k_{rm}$  and  $\Psi_m(z)$  form a non-trivial solution of this modal equation, then  $k_{rm}$  is a zero of the Wronskian and vice versa. In terms of  $\Psi_m$  we can write

$$p(r, z) = \frac{i}{2} \sum_{m=1}^M \frac{\Psi_m(z_s) \Psi_m(z)}{\partial W(z_s; k_r)/\partial k_r|_{k_r=k_{rm}}} H_0^{(1)}(k_{rm}r) k_{rm} - \int_{C_{\text{EJP}}}. \quad (5.75)$$

This representation of the pressure field is somewhat inconvenient since it requires the evaluation of  $\partial W/\partial k_r$ , which is defined in terms of functions  $p_{1,2}(z; k_r)$  that may not be readily available in a particular numerical scheme. In order to simplify this expression, we seek an alternate form for  $\partial W/\partial k_r$ . The derivation is complicated and not enlightening and, therefore, is relegated to Appendix 2. The final result is

$$\begin{aligned} \left. \frac{\partial W/\partial k_r}{\rho(z_s)} \right|_{k_{rm}} &= 2k_{rm} \int_0^D \frac{\Psi_m^2(z)}{\rho(z)} dz \\ &- \left. \frac{d(f/g)^T}{dk_r} \right|_{k_{rm}} \Psi_m^2(0) + \left. \frac{d(f/g)^B}{dk_r} \right|_{k_{rm}} \Psi_m^2(D). \end{aligned} \quad (5.76)$$

By properly scaling  $\Psi_m(z)$  we can make  $\partial W(z_s; k_r)/\partial k_r|_{k_r=k_{rm}} = 1$ . Thus, we obtain our final representation for the pressure field as

$$p(r, z) = \frac{i}{4\rho(z_s)} \sum_{m=1}^M \Psi_m(z_s) \Psi_m(z) H_0^{(1)}(k_{rm}r) - \int_{C_{\text{EIP}}}, \quad (5.77)$$

where the modes are normalized such that

$$\int_0^D \frac{\Psi_m^2(z)}{\rho(z)} dz - \frac{1}{2k_{rm}} \left. \frac{d(f/g)^T}{dk_r} \right|_{k_{rm}} \Psi_m^2(0) + \frac{1}{2k_{rm}} \left. \frac{d(f/g)^B}{dk_r} \right|_{k_{rm}} \Psi_m^2(D) = 1. \quad (5.78)$$

An alternate derivation of this result is given by Bucker [9] for the constant-density problem.

It appears that we have only made the problem more complicated by converting the original spectral-integral form to one involving a sum of modes plus another integral term. In practice, however, the branch-line integral can generally be neglected if we are sufficiently far from the source.

The particular nature of the boundary conditions is important in determining the representation. As we have seen, if the upper boundary is a pressure-release boundary and the lower boundary is perfectly rigid, then there are no branch-cut contributions, i.e., the solution is represented entirely as an infinite sum of modes. In problems with an elastic halfspace, there will be branch-cut terms associated with both  $s$ - and  $p$ -wave velocities in the halfspace.

The number of terms in the residue series depends on the particular branch cut taken. For instance, if we take the Pekeris branch cut shown in Fig. 5.7, it turns out that an additional (typically infinite) set of poles is exposed. These poles are represented by the filled circles numbered 4 to 6 in the figure. The poles in this second set lie off the real axis in the first quadrant and as a result decay exponentially in range. For this reason the corresponding modes are referred to as *leaky* modes. Thus, we can obtain an infinite variety of representations of the field depending on the choice of branch cut.

In principle, the Pekeris cut offers an advantage in exposing the leaky modes since, as we shall see in the next section, by including the leaky modes we can obtain a solution which is more accurate in the nearfield. In practice, it is somewhat difficult to reliably locate the leaky modes so the potential gain may come at the expense of robustness in the model. In addition, the leaky modes grow exponentially in depth and at some ranges and depths yield a diverging series. Alternatively, it is also possible to calculate the branch cut term numerically as discussed by Stickler [10].

In order to clarify some of these points, let us return to the Pekeris waveguide problem. The solution in the ocean layer which satisfies the pressure-release surface condition is given by

$$\Psi(z) = A \sin(k_z z), \quad (5.79)$$

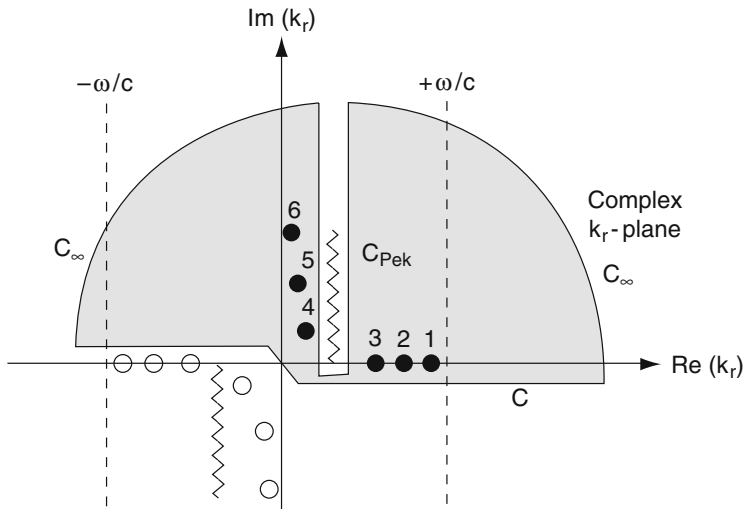


**Fig. 5.7** Location of eigenvalues for the Pekeris problem using the Pekeris branch cut

where

$$k_z = \sqrt{\left(\frac{\omega}{c}\right)^2 - k_r^2}. \quad (5.80)$$

In order to obtain a non-trivial solution that satisfies the bottom boundary conditions, (5.58), we must have

$$\tan(k_z D) = -\frac{i\rho_b k_z}{\rho k_{z,b}}, \quad (5.81)$$

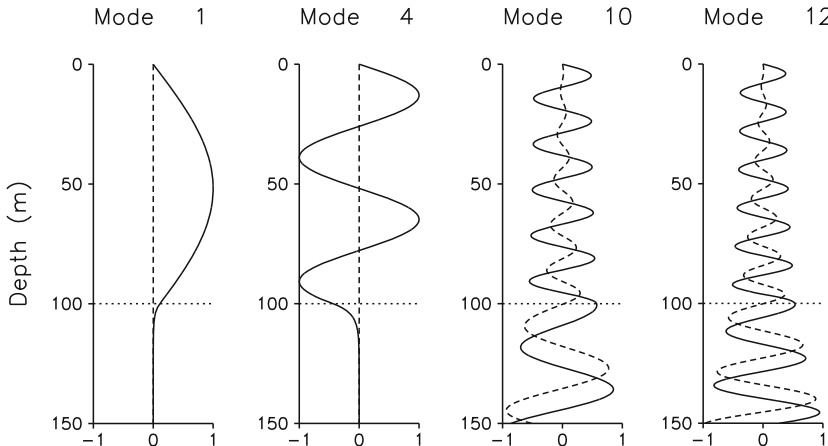
which is a transcendental equation for the eigenvalues  $k_{rm}(\omega)$ .

Figure 5.8 shows selected modes of the Pekeris waveguide. We see that modes 1 and 4 are qualitatively similar to those of the previous isovelocity problem (Fig. 5.3). Thus, the solution in the water column is again a sinusoid; however, the vertical wavenumber is different due to the change in phase associated with the bottom reflection coefficient. Also plotted in Fig. 5.8 are modes 10 and 12 which are leaky modes with a non-zero imaginary part as indicated by the dashed line.

Neglecting the cylindrical spreading term, the contribution of an individual mode to the pressure field is proportional to

$$p = \left( e^{ik_{zm} z} + e^{-ik_{zm} z} \right) e^{ik_{rm} r}. \quad (5.82)$$

Thus, a mode can be thought of as consisting of an up- and downgoing plane wave with an angle of propagation  $\theta_m$  defined by  $\tan \theta_m = k_{zm}/k_{rm}$ . The branch point occurs at  $k_r = \omega/c_b$  which in the angle domain corresponds precisely to the critical angle. Thus, the modes whose angles are less than the critical angle are trapped, i.e., they radiate no energy into the halfspace. The leaky modes, however, have angles above the critical angle and therefore lose energy to the lower halfspace.



**Fig. 5.8** Selected modes of the Pekeris waveguide. The water–bottom interface at 100 m is indicated by the horizontal *dotted line*

## 5.6 A Deep Water Problem: The Munk Profile

The Munk profile [11] is an idealized ocean sound-speed profile which allows us to illustrate many features that are typical of deep-water propagation. In its general form, the profile is given by

$$c(z) = 1500.0 \left[ 1.0 + \epsilon \left( \tilde{z} - 1 + e^{-\tilde{z}} \right) \right]. \quad (5.83)$$

The quantity  $\epsilon$  is taken to be

$$\epsilon = 0.00737,$$

while the scaled depth  $\tilde{z}$  is given by

$$\tilde{z} = \frac{2(z - 1300)}{1300}.$$

The resulting profile is plotted in Fig. 5.9. Taking a homogeneous, halfspace bottom with density  $1000 \text{ kg/m}^3$  and sound speed  $1600 \text{ m/s}$ , we obtain for a source frequency of  $50 \text{ Hz}$  the modes shown in Fig. 5.10. (An analytic solution for the modes is not available in this case so we use a numerical technique as described in Sect. 5.7.) Notice that the mode shapes are no longer perfect sinusoids; however, the  $m$ th mode still has  $m$  zero crossings. In addition, the modes are oscillatory near the sound-channel axis and exponentially decaying both near the surface and near the bottom. The size of the oscillatory region is larger for the higher-order modes.

**Fig. 5.9** The Munk sound-speed profile

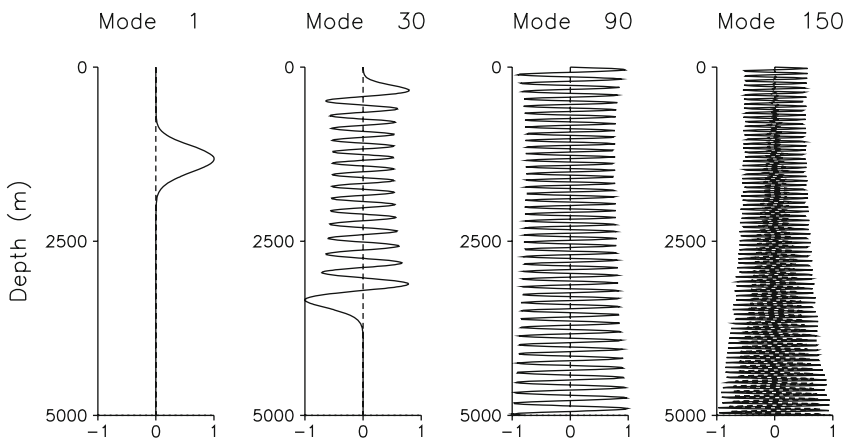
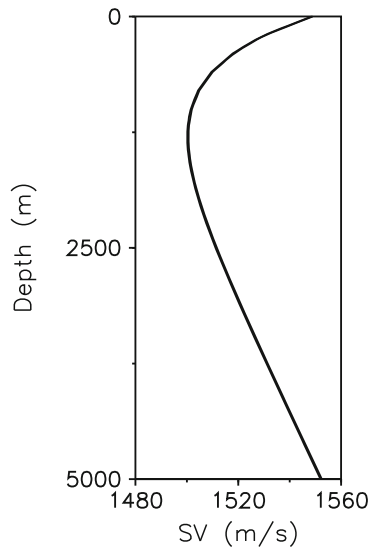


**Fig. 5.10** Selected modes for the Munk sound-speed profile

Some insight into the behavior of the modes can be obtained from the WKB approximation discussed in Sect. 2.5.2. The WKB approximation to the eigenfunctions is given by

$$\Psi(z) \simeq A \frac{e^{i \int_0^z k_z(z) dz}}{\sqrt{k_z(z)}} + B \frac{e^{-i \int_0^z k_z(z) dz}}{\sqrt{k_z(z)}}, \quad (5.84)$$

where

$$k_z^2(z) = \frac{\omega^2}{c^2(z)} - k_r^2. \quad (5.85)$$

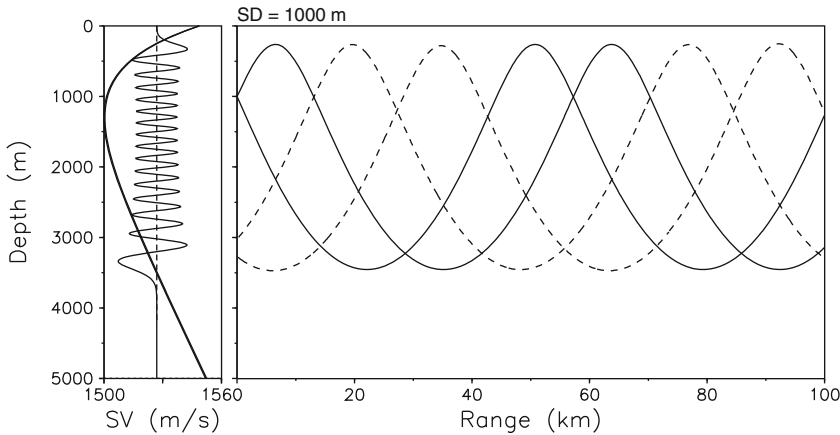


**Fig. 5.11** Ray equivalent of mode 30 for the Munk profile

Thus, locally the solution assumes the oscillating form of sines and cosines near the sound-channel axis (where  $k_z$  is real) and transitions to a solution involving exponentially growing and decaying functions near the surface and bottom (where  $k_z$  is imaginary). The depths where this transition occurs are the *turning points* and are precisely defined by depths where  $k_z^2(z) = 0$ . In addition, the amplitude term is seen to be governed by  $1/k_z(z)$  so that as we move away from the sound-channel axis (where  $k_z$  is large) toward the turning point (where  $k_z$  is small) the amplitude tends to increase.

These features are easily visualized if we superimpose the plot of an individual mode on top of the sound-speed profile. The axis of the mode is shifted to a position on the sound-speed axis corresponding to the phase speed of the mode. For instance, in Fig. 5.11 we have re-plotted mode 30 of the deep-water profile with its axis at 1525.9 m/s (corresponding to its phase speed). Where the axis of the mode crosses through the sound-speed profile,  $k_z^2(z)$  switches sign, and thus the mode behavior changes from oscillatory to evanescent. At the turning point the WKB approximation is actually singular. The correct solution, however, has a smooth behavior in the transition region as is clearly seen in Fig. 5.11.

The WKB representation of the solution also yields a geometric picture of an individual mode. Locally a mode assumes the form of a pair of up- and downgoing plane waves. The horizontal wavenumber is just the constant  $k_{rm}$  for the mode while the vertical wavenumber is a depth-dependent quantity  $k_{zm}(z)$ . We can identify a local angle of propagation as  $\theta_m = \arctan(k_{zm}/k_{rm})$ . Thus, we can plot the family of rays normal to the wavefronts of an individual mode. For instance, in Fig. 5.11 we show the family of rays associated with mode 30. These rays manifest a caustic at the

upper and lower turning points reflecting the singularity in the WKB approximation. At any receiver between the turning points there are exactly two ray arrivals, one coming from above and one from below.

One may define a mode *loop length* (cycle distance) as

$$L_m = \frac{-2\pi}{dk_{rm}/dm}, \quad (5.86)$$

which corresponds to the range over which the ray associated with a mode performs a complete loop up and down the channel. When analytic formulas are available for  $k_{rm}$  one may formally evaluate the required derivative with respect to the mode index  $m$ . Alternatively, one may approximate the derivative by a simple finite difference formula,

$$L_m \simeq \frac{2\pi}{k_{rm} - k_{r(m+1)}}. \quad (5.87)$$

In the case of mode 30 in Fig. 5.11, we find  $L_{30} = 57.4$  km. Additional aspects of the *ray-mode analogy* have been developed by Tindle and Guthrie, see for instance [12] and references therein.

In Fig. 5.12 we illustrate the effect of using different numbers of modes to calculate transmission loss. The source depth is chosen to be 100 m. Figure 5.12a includes only the *waterborne* modes, i.e., modes which have their lowest turning point above the ocean bottom. These modes (1–63) are exponentially decaying below the turning point and in this sense are not bottom interacting. In ray terms, these modes correspond to paths which are refracted within the water column.

The transmission loss shows a *convergence-zone* pattern involving a beam of energy that emerges from the source and refracts under the influence of the ocean sound-speed profile. Since we are using a restricted number of modes, we in effect are producing an angle-limited source. We observe that the transmission loss shows large *shadow zones* where the acoustic field is negligible. These quiet zones result not from the depth dependence of the eigenfunctions but from the phasing in range which causes the modes to add up destructively.

In Fig. 5.12b, we have added in the *bottom-bounce* modes (64–102). These modes have no turning points and correspond to ray paths which strike the bottom at a subcritical angle. By including these modes, we effectively widen the source beamwidth. A second beam is now visible emanating from the source and reflecting off the bottom.

In Fig. 5.12c, we have added a large number of *leaky* modes (103–400). As discussed earlier these modes are leaky in the sense that they are displaced from the real axis and therefore lose energy as a function of range. In ray terms, they correspond to paths which strike the bottom above the critical angle and therefore are very weakly reflected. In the transmission loss plot, we can see that the source angle has now been increased to  $\pm 90^\circ$  revealing the full Lloyd-mirror pattern of beams. For details on the nearfield Lloyd-mirror pattern, see Sects. 1.4.2 and 2.4.2.

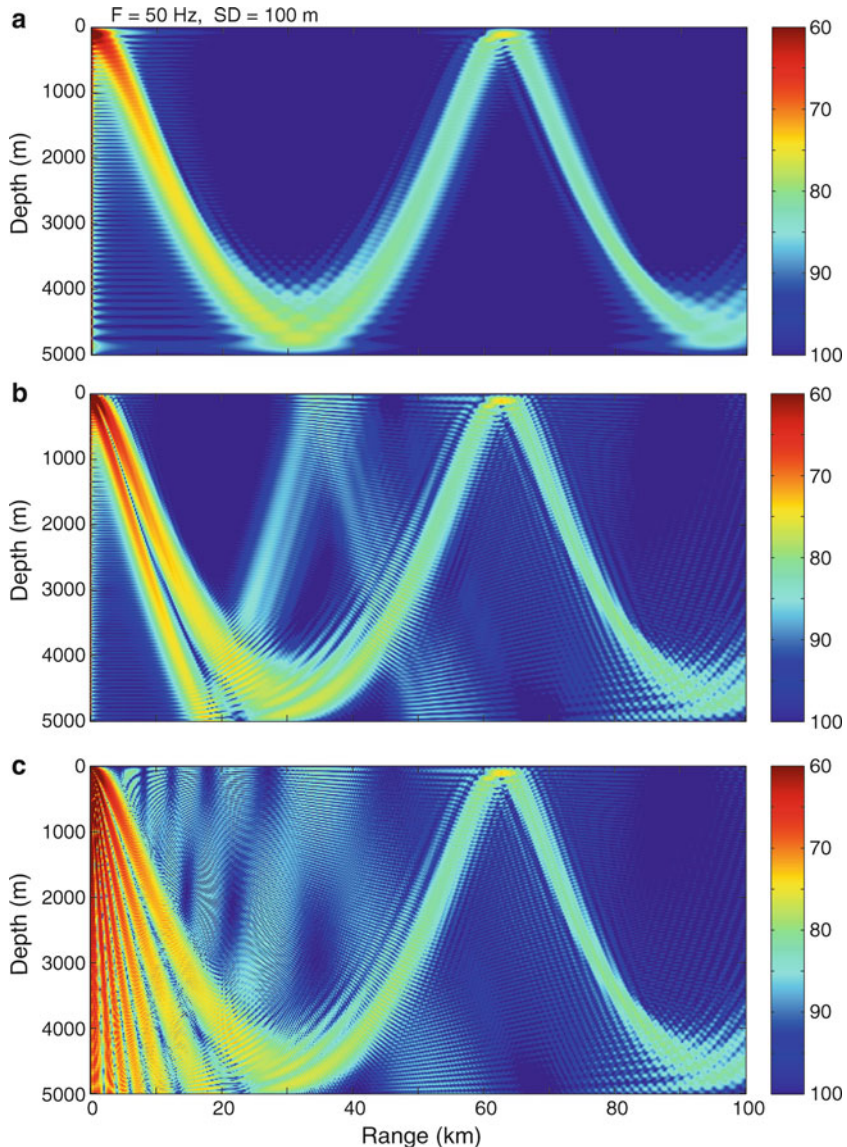


**Fig. 5.12** Transmission loss for the Munk profile including (a) waterborne modes only, (b) bottom bounce modes, and (c) leaky modes

## 5.7 Numerical Approaches

The numerical techniques which have been applied to the modal equation are very closely related to those used for the spectral integral approach of Chap. 4. The normal-mode equation is a classic Sturm–Liouville eigenvalue problem while the

spectral integral form is a forced version of that same equation. This relation is echoed in the discretized versions of normal-mode and spectral-integral models, regardless of the numerical technique which is applied. For instance, if we use a finite-difference method as described in the next section, the discretized modal problem will lead to an *algebraic eigenvalue problem* of the form

$$(\mathbf{A} - k_r^2 \mathbf{I}) \mathbf{x} = \mathbf{0}. \quad (5.88)$$

This same finite-difference technique applied to the spectral integral representation leads to a *linear system of equations* of the form

$$(\mathbf{A} - k_r^2 \mathbf{I}) \mathbf{x} = \mathbf{b} \quad (5.89)$$

with the matrix  $\mathbf{A}$  unchanged. The vector  $\mathbf{b}$  corresponds to the delta function forcing.

However, there are important differences between the two types of problems which affect the choice of numerical method. For instance, as we pass from a simple problem with say a free surface and rigid bottom with no loss mechanisms to more complicated problems with attenuating media and halfspace boundary conditions, the spectral integral solution requires little more than a change to complex arithmetic. The modal solution, however, involves solving a root-finding problem for the eigenvalues  $k_{rm}$ . Considering again a finite-difference method, the characteristic equation is simply a polynomial equation

$$\det \mathbf{C}(k_r^2) = 0. \quad (5.90)$$

When halfspace boundary conditions are introduced, the polynomial becomes a transcendental function; attenuation makes the coefficients of the polynomial complex. Many techniques which are suitable for the polynomial characteristic equations with real coefficients are either invalid or unreliable as the above complications are introduced. To avoid these problems, many models based on normal modes treat directly the non-attenuating problem. As will be described in Sect. 5.9, perturbation theory is then used to estimate the imaginary part of the eigenvalues.

Another difference between spectral and modal solutions is that the basic structure of a modal solution makes it appealing to first solve for the modes and then have a separate module for calculating the field. In this fashion, source depth, receiver depth, and receiver range can all be varied without having to recalculate the modes. This requires, however, that the modes be sampled on a scale of roughly half a wavelength in depth so that modal values can be accurately computed at any depth by interpolation. Therefore, numerical methods that can efficiently provide a fine depth sampling are favored.

In the next few sections, we give an overview of the various numerical solution techniques. As we shall see, all of the methods lead to a root-finding problem of the form  $\Delta(k_r) = 0$  with the roots defining the eigenvalues  $k_{rm}$ . The robust and efficient location of the roots of this equation is one of the key issues in a modal code and is treated in a separate section.

### 5.7.1 Finite-Difference Methods

As illustrated in Fig. 5.13 we divide the interval  $0 \leq z \leq D$  into  $N$  equal intervals to construct a mesh of equally spaced points  $z_j = jh$ ,  $j = 0, 1, \dots, N$ , where  $h$  is the mesh width given by  $h = D/N$ . Furthermore, we shall use the notation  $\Psi_j = \Psi(z_j)$ . The number  $N$  should be chosen large enough that the modes are adequately sampled; usually 10 points per wavelength are sufficient.

We shall assume for the moment that the density is constant, yielding the modal problem

$$\Psi''(z) + \left[ \frac{\omega^2}{c^2(z)} - k_r^2 \right] \Psi(z) = 0, \quad (5.91)$$

where the primes denote differentiation with respect to  $z$ . Following a standard procedure for deriving finite difference equations, we use the Taylor series expansion to obtain

$$\Psi_{j+1} = \Psi_j + \Psi'_j h + \Psi''_j \frac{h^2}{2!} + \Psi'''_j \frac{h^3}{3!} + \dots \quad (5.92)$$

Rearranging terms, we obtain a *forward difference* approximation for the first derivative,

$$\Psi'_j = \frac{\Psi_{j+1} - \Psi_j}{h} - \Psi''_j \frac{h}{2} + \dots \quad (5.93)$$

An  $O(h)$  approximation to the first derivative is therefore,

$$\Psi'_j \simeq \frac{\Psi_{j+1} - \Psi_j}{h}. \quad (5.94)$$

An improved approximation is obtained by using the governing equation (5.91) to evaluate the first term in the forward difference approximation. That is, we substitute

$$\Psi''(z) = - \left[ \frac{\omega^2}{c^2(z)} - k_r^2 \right] \Psi(z). \quad (5.95)$$

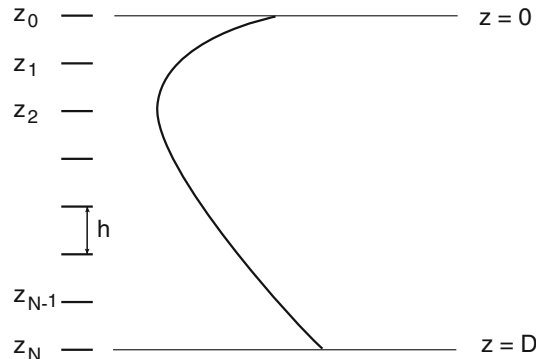


**Fig. 5.13** Finite difference mesh

This yields the  $O(h^2)$  approximation

$$\Psi'_j \simeq \frac{\Psi_{j+1} - \Psi_j}{h} + \left[ \frac{\omega^2}{c^2(z_j)} - k_r^2 \right] \Psi_j \frac{h}{2}. \quad (5.96)$$

Similarly, a *backward difference* approximation is obtained starting with the Taylor series

$$\Psi_{j-1} = \Psi_j - \Psi'_j h + \Psi''_j \frac{h^2}{2!} - \Psi'''_j \frac{h^3}{3!} + \dots \quad (5.97)$$

yielding the  $O(h)$  approximation

$$\Psi'_j \simeq \frac{\Psi_j - \Psi_{j-1}}{h} \quad (5.98)$$

and the  $O(h^2)$  approximation

$$\Psi'_j \simeq \frac{\Psi_j - \Psi_{j-1}}{h} - \left[ \frac{\omega^2}{c^2(z_j)} - k_r^2 \right] \Psi_j \frac{h}{2}. \quad (5.99)$$

Finally, adding (5.92) and (5.97) we obtain a *centered difference* approximation to the second derivative,

$$\Psi''_j = \frac{\Psi_{j-1} - 2\Psi_j + \Psi_{j+1}}{h^2} + O(h^2). \quad (5.100)$$

With these finite-difference approximations in hand, we can proceed to replace the derivatives in the continuous problem with discrete analogues. Let us recall the continuous problem,

$$\Psi''(z) + \left[ \frac{\omega^2}{c^2(z)} - k_r^2 \right] \Psi(z) = 0, \quad (5.101)$$

$$f^T(k_r^2) \Psi(0) + \frac{g^T(k_r^2)}{\rho} \frac{d\Psi(0)}{dz} = 0, \quad (5.102)$$

$$f^B(k_r^2) \Psi(D) + \frac{g^B(k_r^2)}{\rho} \frac{d\Psi(D)}{dz} = 0. \quad (5.103)$$

Using the centered, forward, and backward difference approximations for the ordinary differential equation and the top and bottom boundary conditions, we obtain

$$\begin{aligned} \Psi_{j-1} + \left\{ -2 + h^2 \left[ \frac{\omega^2}{c^2(z_j)} - k_r^2 \right] \right\} \Psi_j + \Psi_{j+1} &= 0, \quad j = 1, \dots, N-1, \\ \frac{f^T}{g^T} \Psi_0 + \frac{1}{\rho} \left\{ \frac{\Psi_1 - \Psi_0}{h} + \left[ \frac{\omega^2}{c^2(0)} - k_r^2 \right] \Psi_0 \frac{h}{2} \right\} &= 0, \\ \frac{f^B}{g^B} \Psi_N + \frac{1}{\rho} \left\{ \frac{\Psi_N - \Psi_{N-1}}{h} - \left[ \frac{\omega^2}{c^2(D)} - k_r^2 \right] \Psi_N \frac{h}{2} \right\} &= 0. \end{aligned} \quad (5.104)$$

We next write the first of these equations as

$$\frac{1}{h\rho} \Psi_{j-1} + \frac{-2 + h^2 [\omega^2/c^2(z_j) - k_r^2]}{h\rho} \Psi_j + \frac{1}{h\rho} \Psi_{j+1} = 0. \quad (5.105)$$

Then collecting the difference equations together we obtain an algebraic eigenvalue problem of the form

$$\mathbf{C}(k_r^2) \Psi = 0. \quad (5.106)$$

Here,  $\Psi$  is the vector with components  $\Psi_0, \Psi_1, \dots, \Psi_N$ . These components are approximations of the eigenfunctions of (5.3) evaluated at the mesh points. In addition,  $\mathbf{C}$  is a symmetric tri-diagonal matrix defined by

$$\mathbf{C} = \begin{bmatrix} d_0 & e_1 & & & & \\ e_1 & d_1 & e_2 & & & \\ & e_2 & d_2 & e_3 & & \\ & & \ddots & \ddots & \ddots & \\ & & & e_{N-2} & d_{N-2} & e_{N-1} \\ & & & & e_{N-1} & d_{N-1} & e_N \\ & & & & & e_N & d_N \end{bmatrix}, \quad (5.107)$$

where the coefficients  $d_j$  and  $e_j$  are defined by

$$d_0 = \frac{-2 + h^2 [\omega^2/c^2(z_0) - k_r^2]}{2h\rho} + \frac{f^T(k_r^2)}{g^T(k_r^2)}, \quad (5.108)$$

$$d_j = \frac{-2 + h^2 [\omega^2/c^2(z_j) - k_r^2]}{h\rho}, \quad j = 1, \dots, N-1, \quad (5.109)$$

$$d_N = \frac{-2 + h^2 [\omega^2/c^2(z_N) - k_r^2]}{2h\rho} - \frac{f^B(k_r^2)}{g^B(k_r^2)} \quad (5.110)$$

and

$$e_j = \frac{1}{h\rho}, \quad j = 1, \dots, N.$$

We have intentionally introduced a scaling factor of  $1/(h\rho)$  in every row here. For a constant-density problem with a single mesh width this would serve no purpose; however, later we shall consider multiple layers for which this scaling is the natural one.

Note that for a pressure-release surface the ratio  $f/g$  which appears in the boundary condition goes to infinity. In this case,  $\Psi_0$  vanishes and we can simply delete the first row and column from the matrix eigenvalue problem. Furthermore, if the functions  $f^{T,B}$ ,  $g^{T,B}$  are independent of  $k_r$  (as happens for the pressure-release surface and rigid bottom conditions), then the above problem is a standard algebraic eigenvalue problem and can be solved using standard routines. In general, only the

lower-order modes will be sufficiently accurate; the higher-order modes are undersampled by the finite-difference mesh. Thus, routines which are designed to extract a subset of the eigenvectors and eigenvalues are desired.

There are principally two types of techniques that are suitable. The first is a variant of the so-called *QR algorithm* designed for subsets of the modes. The second uses *Sturm's method* combined with inverse iteration.

For problems with large attenuation that cannot be treated by a perturbation method, the matrix is complex and Sturm's method must be replaced with some other determinant search method. However, in underwater acoustics a more common approach is to assume the attenuation is small and can therefore be accounted for through a perturbation method, as described later. In this case, one can use the Sturm sequence method for the real eigenvalue problem associated with the lossless problem.

The details of these algorithms may be found in standard texts, e.g., [13], but we shall here describe the efficient and stable method based on Sturm sequences, inverse iteration and Richardson extrapolation which is used extensively in several legacy normal mode codes, and which is easily implemented for those who wish to write their own mode code.

Sturm's method is essentially a determinant search technique applicable to both coefficient approximation and shooting techniques. Secondly, the inverse iteration technique is used to find the eigenvector after the eigenvalue has been found using Sturm's method. It is this aspect of the finite-difference method which eliminates the stability problem common to most shooting methods.

### 5.7.1.1 Sturm's Method

Sturm's method is basically an efficient, recursive approach for calculating the determinant of a tri-diagonal matrix with certain properties characteristic of the ocean waveguide mode problem. Thus, as described above, the modal problem in the case of a penetrable bottom is described by the algebraic eigenvalue problem in (5.106), which cannot be reformulated into a standard Sturm–Liouville eigenvalue problem. However, we can rewrite the eigenvalue problem into a *Pseudo Sturm–Liouville* form,

$$\begin{aligned} \det \mathbf{C}(\lambda) &= 0, \\ &\Leftrightarrow \\ \det [\mathbf{A}(\lambda) - \mathbf{I}\lambda] &= 0 \end{aligned} \tag{5.111}$$

with  $\lambda = k_r^2$ , and then use Sturm's method calculating the determinant. We can use this method in combination with any root-finding scheme, such as Newton–Ralphson's or Brent's methods. A major preliminary step, however, is to isolate the eigenvalues to intervals within which these methods will converge. Such methods, including bisection and deflation are described later. We shall describe here Sturm's method as it applies to the ocean acoustic mode problem.

It is clear that the finite difference equations from which a term linear in  $\lambda = k_r^2$  cannot be isolated are the ones at the top boundary, (5.108), and at the bottom boundary, (5.110). Thus, letting  $a_k(\lambda) = d_k(\lambda) + \lambda$ , the algebraic eigenvalue problem in (5.111) can be formulated as finding the zeros of the determinant of the tri-diagonal matrix

$$\mathbf{C}(\lambda) = \begin{bmatrix} \lambda - a_0(\lambda) & -e_1 & & & \\ -e_1 & \lambda - a_1 & -e_2 & & \\ & -e_2 & \lambda - a_2 & -e_3 & \\ & & \ddots & \ddots & \ddots \\ & & -e_{N-2} & \lambda - a_{N-2} & -e_{N-1} \\ & & & -e_{N-1} & \lambda - a_{N-1} & -e_N \\ & & & & -e_N & \lambda - a_N(\lambda) \end{bmatrix}. \quad (5.112)$$

Letting  $p_k$  denote the determinant of the upper-left  $k \times k$  submatrix, it is easily shown that  $p_k$  can be evaluated using the recursion

$$p_1(\lambda) = \lambda - a_0, \quad (5.113)$$

$$p_k(\lambda) = (\lambda - a_{k-1}) p_{k-1}(\lambda) - e_{k-1}^2 p_{k-2}(\lambda). \quad (5.114)$$

Thus, introducing the values  $p_{-1}$  and  $p_0$ , the following recursion formula, the so-called *Sturm Sequence*, can be used for evaluating the determinant for any value of  $\lambda = k_r^2$ ,

$$p_{-1} = 0,$$

$$p_0 = 1,$$

$$p_k(\lambda) = [\lambda - a_{k-1}(\lambda)] p_{k-1}(\lambda) - e_{k-1}^2 p_{k-2}(\lambda), \quad k = 1, 2, \dots, N+1. \quad (5.115)$$

The recurrence in (5.115) is highly efficient, and unconditionally stable for computing the determinant, and therefore forms a convenient cornerstone in any root-finding scheme. In addition, there is a property of the Sturm sequence which is extremely useful in isolating intervals around each mode for which one of the root-finding schemes may be applied.

Thus, the Sturm sequence can be shown to have the following property, that in terms of the physics is related to the oscillating nature of the normal modes:

- For a symmetric, tri-diagonal matrix the number of real eigenvalues larger than  $\lambda$  is equal to the number of zero-crossings of the Sturm sequence

$$p_0, p_1, \dots, p_{N+1}(\lambda).$$

Obviously, the tri-diagonal matrix in (5.112) is symmetric, and consequently this property of the Sturm sequence can be applied to isolate the propagating modes in ocean waveguides with a penetrable bottom, e.g. in combination with bisection as described later. Subsequently, the Sturm sequence can then be in a Newton–Ralphson or Brent root finding scheme.

It may be shown [14] that the Sturm sequence is identical to the sequence that would be obtained by a shooting method using the same underlying difference scheme. Thus we may interpret the elements in the sequence as representing values of a trial eigenfunction obtained by integrating from the top to the bottom of the waveguide with the final value representing the error in satisfying the bottom boundary condition.

This perspective is important in several ways. First, the traditional Sturm method is not applicable to nonlinear eigenvalue problems. The nonlinearity enters through the boundary conditions leading to  $a_0(\lambda)$  and  $a_n(\lambda)$ . If such boundary conditions are due to an acoustic or elastic halfspace without attenuation, then the sign changes in the sequence can still be used to determine the number of modes less than a trial wavenumber. Then the standard bisection algorithm based on Sturm sequences is shown to be valid.

In addition, as discussed later, there are well-known stability issues associated with the shooting method when shooting into regions where the modes are exponentially growing or decaying. These stability problems are easily handled by re-scaling the elements of the Sturm sequence. Interestingly, the instability does not affect the accuracy of the eigenvalues. In eigenvalue solvers this instability is usually handled by introducing a new sequence  $q_i = p_i / p_{i-1}$ . However,  $q_i(\lambda)$  then has poles that introduce complications when the bisection method is replaced by more sophisticated root finders.

### 5.7.1.2 Inverse Iteration

Once an estimate of the modal eigenvalues has been determined, e.g using the Sturm sequences in combination with a root finding scheme such as Newton–Ralphson or Brent, the next step in the numerical procedure is to evaluate the associated modal eigenfunction. A highly efficient method for this step is the concept of *Inverse Iteration*.

Let us assume that we have achieved an estimate  $\kappa$  of the  $m$ th eigenvalue of the matrix  $\mathbf{A}$ ,

$$\kappa = \lambda_m - \epsilon \quad (5.116)$$

with  $\epsilon$  being small. The eigenvector  $\Psi_m$  associated with the eigenvalue  $\lambda_m$  obviously satisfies the equation

$$[\mathbf{A}(\lambda_m) - \lambda_m \mathbf{I}] \Psi_m = \mathbf{0}. \quad (5.117)$$

Now we apply the iteration process

$$[\mathbf{A}(\lambda_m) - \kappa \mathbf{I}] \mathbf{w}_k = \mathbf{w}_{k-1}, \quad k = 1, 2, \dots, \infty. \quad (5.118)$$

Assuming  $\kappa$  is not exactly equal to the correct eigenvalue  $\lambda_m$ , this equation can be solved to yield the recursion

$$\mathbf{w}_k = [\mathbf{A}(\lambda_m) - \kappa \mathbf{I}]^{-1} \mathbf{w}_{k-1}. \quad (5.119)$$

Now it is well-known that the inverse matrix  $(\mathbf{A} - \kappa \mathbf{I})^{-1}$  has the same eigenvectors as the matrix  $\mathbf{A}$ , with the corresponding eigenvalues  $(\lambda_m - \kappa)^{-1}$ . Then, assuming the estimate  $\kappa$  is closer to  $\lambda_m$  than to any other eigenvalue, the recursion in (5.119) will converge towards the eigenvector  $\Psi_m$  associated with the eigenvalue  $\lambda_m$ ,

$$\mathbf{w}_k \rightarrow \Psi_m, \quad k \rightarrow \infty \quad (5.120)$$

provided the starting vector  $\mathbf{w}_0$  is not orthogonal to  $\Psi_m$ . A simple starting vector that will rarely fail is  $w_0 = [1, 1, \dots, 1]$ .

In addition, the inverse iteration provides an improved estimate of the eigenvalue, due to the limiting property

$$\frac{(w_r)_k}{(w_r)_{k-1}} \rightarrow \frac{1}{\lambda_m - \kappa}, \quad k \rightarrow \infty \quad (5.121)$$

or

$$\lambda_m \leftarrow \kappa + \frac{(w_r)_{k-1}}{(w_r)_k}, \quad k \rightarrow \infty. \quad (5.122)$$

This limiting property also suggests that, if the initial estimate  $\kappa$  is close to the real eigenvalue, a renormalization scheme may have to be applied to avoid having the inverse iteration blow up numerically. This is easily performed by normalizing the eigenvectors in each iteration step, e.g. requiring  $|w_k| = 1$ .

### 5.7.1.3 Richardson Extrapolation

In this section, we have introduced the most basic finite-difference schemes for solving the modal problem. While a stable scheme can be easily constructed using these techniques, an *efficient* scheme requires, as usual, a few enhancements. In practice, two alternatives have been found to be most useful.

The first approach is to use *Richardson extrapolation*. In brief, the method makes use of the fact that the numerically derived eigenvalues vary as a function of the mesh width  $h$  as

$$k_r^2(h) = k_0^2 + b_2 h^2 + b_4 h^4 + \dots, \quad (5.123)$$

where  $k_0^2$  denotes the exact eigenvalue of the continuous problem. It is, of course,  $k_0^2$  which is sought; however, it is computationally expensive to evaluate  $k_r^2(h)$  with small values of  $h$ . Instead, one solves the discretized problem for a series of meshes and fits a polynomial in  $h^2$  through the mesh points. The value of the polynomial evaluated at  $h = 0$  provides the Richardson extrapolation of the eigenvalue. This type of approach was introduced by Porter and Reiss [15] and is implemented in the models described in [16, 17].

The second approach is to use higher-order difference schemes. A scheme which may be recommended is *Numerov's method* [18] in which the differential equation

$$\Psi''(z) + \left[ \frac{\omega^2}{c^2(z)} - k_r^2 \right] \Psi(z) = 0 \quad (5.124)$$

is approximated by

$$\left( \frac{1}{h^2} + \frac{1}{12} k_{z,j-1}^2 \right) \Psi_{j-1} + \left( -\frac{2}{h^2} + \frac{10}{12} k_{z,j}^2 \right) \Psi_j + \left( \frac{1}{h^2} + \frac{1}{12} k_{z,j+1}^2 \right) \Psi_{j+1} = 0, \quad (5.125)$$

where

$$k_{z,j}^2 = \frac{\omega^2}{c^2(z_j)} - k_r^2. \quad (5.126)$$

Numerov's scheme yields  $O(h^4)$  accuracy versus  $O(h^2)$  accuracy for the standard scheme. From a practical point of view this makes a lot of difference in the CPU time required to achieve a certain level of accuracy. Thus, for the same mesh, Numerov's method requires approximately twice as much CPU time; however, for the *same* accuracy Numerov's method is typically much faster.

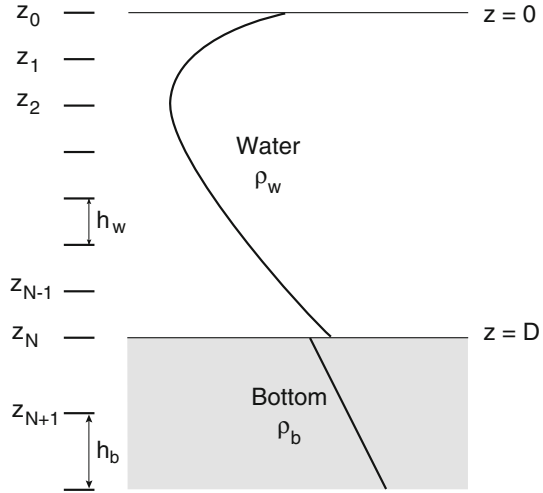
### 5.7.1.4 Treatment of Interfaces

Frequently ocean-acoustic problems involve discontinuities in the sound speed or density, for instance, in passing from water to bottom. Such problems can be treated by dividing the problem into layers such that within a layer these material properties vary smoothly. Within a layer the previous finite difference equations are applicable. At the interface one then derives a special condition to tie together the individual layer solutions.

As an example, we consider a single interface between two layers representing the water and the bottom. Within each layer we construct independent finite-difference meshes with grid spacing  $h_w$  and  $h_b$  as illustrated in Fig. 5.14. In the water, the finite-difference approximation to (5.91) is

$$\Psi_{j-1} + \left\{ -2 + h_w^2 \left[ \frac{\omega^2}{c^2(z_j)} - k_r^2 \right] \right\} \Psi_j + \Psi_{j+1} = 0, \quad j = 1, \dots, N-1 \quad (5.127)$$

**Fig. 5.14** Finite difference mesh for an interface



and in the bottom the finite-difference approximation is

$$\Psi_{j-1} + \left\{ -2 + h_b^2 \left[ \frac{\omega^2}{c^2(z_j)} - k_r^2 \right] \right\} \Psi_j + \Psi_{j+1} = 0, \quad j = N+1, \dots \quad (5.128)$$

At the interface, the pressure must be continuous, a condition which is imposed implicitly by allowing for a unique value  $\Psi_N$  at the interface. We must also impose continuity of normal velocity, i.e.,

$$\frac{d\Psi(D)/dz}{\rho_w} = \frac{d\Psi(D)/dz}{\rho_b}, \quad (5.129)$$

where  $\rho_w$  and  $\rho_b$  denote the densities in the water and sediment, respectively. This interface condition can then be approximated by

$$\begin{aligned} & \left\{ \frac{\Psi_N - \Psi_{N-1}}{h_w} - \left[ \frac{\omega^2}{c^2(D^-)} - k_r^2 \right] \Psi_N \frac{h_w}{2} \right\} / \rho_w \\ &= \left\{ \frac{\Psi_{N+1} - \Psi_N}{h_b} + \left[ \frac{\omega^2}{c^2(D^+)} - k_r^2 \right] \Psi_N \frac{h_b}{2} \right\} / \rho_b, \end{aligned} \quad (5.130)$$

where we have used the backward difference formula for the water and the forward difference for the bottom. Furthermore,  $c(D^\pm)$  denotes the limiting value of the sound speed at the interface as approached from  $z < D$  ( $D^-$ ) and  $z > D$  ( $D^+$ ). Rearranging we obtain

$$\begin{aligned} & \frac{\Psi_{N-1}}{h_w \rho_w} + \frac{-\Psi_N + [\omega^2/c^2(D^-) - k_r^2] \Psi_N h_w^2/2}{h_w \rho_w} \\ & + \frac{-\Psi_N + [\omega^2/c^2(D^+) - k_r^2] \Psi_N h_b^2/2}{h_b \rho_b} + \frac{\Psi_{N+1}}{h_b \rho_b} = 0. \quad (5.131) \end{aligned}$$

Note that if  $h_w = h_b$ ,  $\rho_w = \rho_b$  and  $c(z)$  is continuous we obtain the same finite-difference formula given in (5.127) for a point not on the interface.

This process can obviously be repeated for every interface in the problem and we obtain, just as for the single-layer case, a symmetric matrix eigenvalue problem. Incidentally, the resulting problem is precisely equivalent to what one would obtain by using finite elements with hat-shaped basis functions and “mass-lumping.” This is discussed further in Sect. 7.4.3.

It should be noted that the change in density at the interface breaks the symmetry of the tri-diagonal matrix. Thus, to write the algebraic eigenvalue problem into the *Pseudo Sturm–Liouville* form in (5.111), all finite difference equations must be normalized to have the same coefficient of  $k_r^2$ . This creates a difference between the two off-diagonal elements above and below the interface, modifying the last term  $e_{N-1}^2$  in the Sturm sequence. However, the product of the two terms is still positive, retaining the properties of the Sturm sequence.

### 5.7.1.5 Mode Normalization

Recall that the evaluation of the pressure requires the *normalized* modes. The normalization constant is, as described in Appendix 2,

$$N_m = \int_0^D \frac{\Psi_m^2(z)}{\rho(z)} dz - \frac{1}{2k_{rm}} \left. \frac{d(f/g)^T}{dk_r} \right|_{k_{rm}} \Psi_m^2(0) + \frac{1}{2k_{rm}} \left. \frac{d(f/g)^B}{dk_r} \right|_{k_{rm}} \Psi_m^2(D). \quad (5.132)$$

The integral term can be evaluated by the trapezoidal rule. That is,

$$I_m = \int_0^D \frac{\Psi_m^2(z)}{\rho(z)} dz \simeq \frac{D}{N} \left( \frac{1}{2} \phi_0 + \phi_1 + \phi_2 + \cdots + \phi_{N-1} + \frac{1}{2} \phi_N \right), \quad (5.133)$$

where

$$\phi_j = \frac{\Psi_j^2}{\rho(z_j)}. \quad (5.134)$$

In problems with density discontinuities, the trapezoidal rule is applied separately within each smooth region. Finally, the derivatives  $d(f/g)^{T,B}/dk_r$  can be evaluated either analytically or by a simple centered-difference formula depending on their complexity.

In cases where the bottom is represented by a fluid halfspace, such as the Pekeris waveguide problem, the mode normalization is more easily performed by extending the depth integral to infinity to include the evanescent “tail” of the modal function in the bottom halfspace, i.e.,

$$N_m = I_m + \int_D^\infty \frac{\Psi_m^2(z)}{\rho(z)} dz, \quad (5.135)$$

where the bottom portion of the integral is easily evaluated analytically. The mode shape in the bottom is exponential,

$$\Psi_m(z) = \Psi_m(D) e^{-\gamma_m(z-D)} \quad (5.136)$$

with  $\gamma_m = \sqrt{k_{rm}^2 - (\omega/c_b)^2}$ , yielding

$$N_m = I_m + \frac{\Psi_m^2(D)}{2\gamma_m \rho_b} \quad (5.137)$$

with  $I_m$  given in (5.133).

### 5.7.2 Layer Methods

The layer methods divide the problem into a number of depth segments and approximate the sound-speed profile by simple functional forms within each segment. This method is sometimes called *coefficient approximation* or, in seismology, the Thomson–Haskell method. This type of approach was discussed in detail in Chaps. 2 and 4 so we shall pass over it fairly quickly here. This technique, however, is widely used in normal-mode models, e.g., those developed by Stickler [10], Tolstoy and May [19], Pedersen and Gordon [20], Bartherger [21], Levinson et al. [22], Westwood et al. [23], Clark and Smith [24], and others. More details may also be found in the text of Boyles [25]. As discussed earlier, the only significant change in applying these techniques to normal-mode problems is that the resulting system of equations is unforced and assumes the form of an eigenvalue problem.

Probably the simplest form involves isovelocity layers. The single-layer and two-layer cases—treated in Sects. 5.4 and 5.5, respectively—provide a simple introduction to the technique. Within each layer we write the solution in the form

$$\Psi_\ell(z) = A_\ell \cos [k_z(z - z_\ell)] + B_\ell \sin [k_z(z - z_\ell)], \quad (5.138)$$

where  $z_\ell$  denotes the depth at the top of the  $\ell$ th layer. This gives us  $2N$  unknowns:  $\{A_\ell, B_\ell, \ell = 1, \dots, N\}$  where  $N$  is the number of layers. We obtain  $2N$  equations by requiring continuity of pressure and normal velocity at every interface ( $2N - 2$

equations), and that  $\Psi(z)$  vanishes at the surface and  $d\Psi/dz$  vanishes at the bottom. Thus, we obtain an eigenvalue problem of the form

$$\mathcal{L}(k_r^2)(A/B) = 0, \quad (5.139)$$

where  $(A/B)$  is the vector of coefficients  $A_\ell, B_\ell$ . In order for this eigenvalue problem to have a solution, the determinant of the matrix must vanish which presents a root-finding problem. The determinant can be evaluated for a particular value of  $k_r$  using standard linear algebra packages.

For acoustic problems, methods based on piecewise *linear* approximation to the index of refraction squared have usually been preferred. As discussed in Sect. 2.5.1, the solution in an  $n^2$ -linear layer involves Airy functions. These functions are somewhat more expensive to evaluate, however fewer layers are needed to approximate the sound-speed profile. The net result is that for a given accuracy less computation time is generally required for the Airy-function approach.

### 5.7.3 Shooting Methods

In the shooting methods, we recast the original boundary-value problem as an initial-value problem (IVP). Starting for instance from the surface, we take the pressure-release boundary condition and additionally impose an arbitrary derivative condition. This gives us the IVP,

$$\Psi_m(0) = 0,$$

$$\frac{d\Psi_m}{dz}(0) = 1,$$

$$\frac{d^2\Psi_m}{dz^2} + \left[ \frac{\omega^2}{c^2(z)} - k_{rm}^2 \right] \Psi_m = 0, \quad (5.140)$$

where we have added the condition  $d\Psi_m/dz = 1$  at  $z = 0$ . This may be thought of as a mode normalization condition.

The process then is to solve this IVP, integrating from the surface to the bottom, to calculate  $\Psi_m(D; k_r^2)$ . The IVP can be solved using any of a number of standard solvers. For instance, using the finite-difference equations derived in Sect. 5.7.1, we obtain the recursion

$$\Psi_0 = 0,$$

$$\Psi_1 = h,$$

$$\Psi_{j+1} = -\Psi_{j-1} + \left\{ 2 - h^2 \left[ \frac{\omega^2}{c^2(z_j)} - k_r^2 \right] \right\} \Psi_j, \quad j = 1, \dots, N. \quad (5.141)$$

Using a centered difference for the derivative, the rigid-bottom boundary condition can then be stated as

$$\Delta(k_r^2) = \frac{\Psi_{N+1} - \Psi_{N-1}}{2h} = 0. \quad (5.142)$$

For an arbitrary  $k_r^2$  this boundary condition will generally not be satisfied. Therefore, a sequence of shots with different values of  $k_r$  is performed and  $k_r$  is “adjusted” to satisfy the bottom boundary condition. The process of finding  $k_r$ -values that satisfy the bottom boundary condition is, once again, a root-finding problem.

The above finite-difference approach has been used by Newman and Ingiento [26]; however, any of the standard procedures for solving IVPs may be applied including the Runge–Kutta method. An example of the latter is described by Beisner [27]. The shooting technique may also be applied to the Prüfer phase-amplitude variables as described in Sect. 5.8. This latter approach has been used by Baggeroer [28].

One of the problems with one-sided shooting is numerical instability. To understand this problem, consider the Munk profile treated in Sect. 5.6. Let us further assume that we seek one of the refracted-refracted modes  $\Psi_m(z)$  whose eigenvalue  $k_{rm}$  lies in the interval

$$\left. \frac{\omega}{c(z)} \right|_{z=0} < k_{rm} < \frac{\omega}{c_{\min}}, \quad (5.143)$$

where  $c_{\min}$  denotes the sound speed at the sound-channel axis.

The true solution, as indicated schematically by the solid line in Fig. 5.15, should pass from an exponentially growing region A to an oscillatory region B and finally to an exponentially decaying region C. The transitions in solution behavior occur at the turning points. Instead, for some particular value  $k_{\text{trial}} \simeq k_{rm}$ , the solution of the IVP will show the correct behavior down to the lower turning point. In region C,

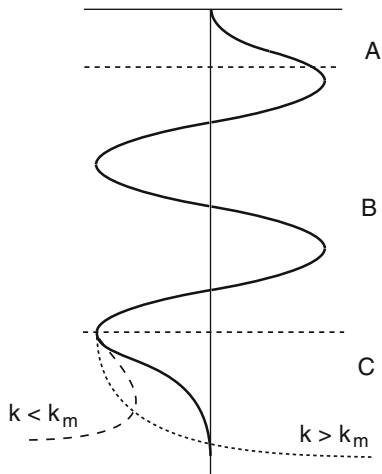


**Fig. 5.15** Trial eigenfunctions obtained with one-sided shooting

the general solution is composed of an exponentially growing and an exponentially decaying solution. The exponentially growing solution must be suppressed in order to satisfy the boundary condition, but if that component is excited at all, it tends to manifest itself due to its exponential growth with depth.

With one-sided shooting it is impossible to suppress the growing component. However, the eigenvalue  $\omega$  is accurately computed since a slight change in  $k_{\text{trial}}$  causes the resulting  $\Psi(z)$  to flip to the opposite side as indicated by the dotted line in Fig. 5.15. (The growing component may easily lead to floating-point overflow; however, this problem is easily solved by rescaling during the shooting process.)

In some cases, it is possible to circumvent this problem by simply shooting in the right direction. For instance, in Arctic problems the sound speed generally increases in depth so by shooting from the bottom toward the surface one is always integrating in the direction in which the true solution is either exponentially increasing or oscillatory. Alternatively, in a problem like the Munk profile which contains two turning points for some of the modes, it is possible to shoot from both the bottom and the top and match the two solutions at the sound-channel axis. This scheme is called *parallel shooting* and is described by Dozier and Tappert [18]. Problems with several turning points may occur when there is more than one duct, e.g., when there is a mixed layer near the surface. In such cases, one may use *multiple shooting* in which the problem is divided into numerous layers and shooting is applied in each layer. This is discussed in more detail by Keller [29].

### 5.7.4 Root Finders

One of the most difficult aspects of normal-mode computations is finding the roots of the characteristic equation. The fundamental difficulty is that many familiar root-finding algorithms, such as the secant method or Newton's method, will only converge to a particular root if a sufficiently close initial guess is provided. Unfortunately, even though the eigenvalues of a purely acoustic problem are guaranteed to be distinct, they can be very nearly degenerate. As a result, many existing mode codes provide accurate but *incomplete* mode sets. The problem is further complicated if we include attenuation directly, rather than using a perturbation approach. In that case, one gets a complex eigen-problem and a complex characteristic equation. In addition, if half-space boundary conditions are used then branch cuts are present in the characteristic function. Finally, if elasticity is present then double roots may also occur. In the following sections, we discuss various approaches for handling these issues.

#### 5.7.4.1 Bisection

For a purely acoustic problem, a bisection approach in combination with the use of *Sturm Sequences* is generally the most attractive [15]. For this fairly broad class

of problems the method will calculate a particular subset in a predictable amount of time *without fail*. It is typically as efficient or more efficient than any of the other schemes described below. However, for more complicated problems, for instance problems involving elasticity or complex wave speeds, this technique is not applicable.

In brief, using the finite-difference formulation, the bisection algorithm relies on the property that the number of zero crossings of the Sturm sequence  $p_k(\kappa)$  in (5.115) is equal to the number of eigenvalues larger than  $\kappa = k_r^2$ . Thus, by simply counting zero-crossings in a calculated Sturm sequence we can isolate intervals with only a single mode, which can then be found using, e.g., Newton's or Brent's methods. In fact, a stronger result is available: the number of zeroes in the Sturm sequence increases monotonically as the trial wavenumber  $k_r$  decreases.

In more detail this process proceeds as follows. Recall that the wavenumber corresponding to the lowest-order mode is bounded above by  $\omega/c_{\min}$ , where  $c_{\min}$  is the lowest sound speed in the problem. This provides an upper bound for the mode search. There are an infinite number of modes so that a lower bound must be selected in some fashion. This bound is user-specified, but if it exceeds the halfspace velocity in the problem, the bound is reduced to eliminate leaky modes from the analysis.

Next, we take the midpoint  $\kappa_{1/2}$  of the interval and compute the number of modes to the right of the midpoint, simply counting the number of zero crossings of the Sturm sequence  $p_k(\kappa_{1/2})$ . Based on the number of zero-crossings in the trial eigenfunction one may decide whether the wavenumber corresponding to the first eigenvalue lies to the left or to the right of the midpoint. The midpoint then becomes either a new lower bound or a new upper bound for the modal wavenumber. This process of interval halving is repeated until the interval contains precisely one modal eigenvalue. With the isolating interval computed for the first mode, one then performs the same process for the second mode and so on. For subsequent modes an upper bound is available from the lower bound of the previous mode. In addition, information generated during the bisection for the first mode provides useful bounds for higher modes. As a result the generation of all  $M$  of the isolating intervals typically requires little more than  $M$  bisection steps.

Once isolating intervals have been constructed one can either continue the bisection until the desired eigenvalue accuracy is obtained or switch to a more sophisticated root finder. With isolating intervals available there are a number of root finders available which will guarantee convergence, e.g. Brent's method [30].

We have described the bisection technique in the context of the numerically stable finite difference method, but it is applicable to both the shooting method and coefficient approximation schemes. In fact, the analogy is a perfect computational identity [14] if the same finite-difference scheme is used for the shooting method.

As mentioned above, the traditional Sturm-sequence method is only directly applicable to purely acoustic problems without attenuation and without halfspace boundaries that generate branch cuts in the characteristic equation. However, the

technique may be generalized to allow for trapped-mode calculations in problems with homogeneous acoustic [14] or elastic halfspaces. Further, the work of Woodhouse [31] suggests a generalization for a similar class of elastic problems with depth-dependent wave speeds.

### 5.7.4.2 Deflation

The philosophy of the deflation method is to start above the first eigenvalue and use the secant method to find the first eigenvalue. Once that eigenvalue is located it is deflated, that is, divided out of the characteristic equation, and the process is repeated for each eigenvalue in turn. Interestingly, one may formally prove that the secant method will *always* converge to the first eigenvalue if started at a point above that same eigenvalue [13]. Naturally, there are some footnotes to this sweeping statement. The key one is that the characteristic function should be a polynomial. Some care is required in defining the characteristic function to avoid violating this requirement. Secondly, the eigenvalues should all be real. In practice, the deflation procedure works fairly well for most realistic ocean-acoustic problems—even when there are complex eigenvalues. When problems do occur, they usually happen when a root is sought near a branch cut of the characteristic function.

The deflation of previous eigenvalues is a trivial process. Instead of computing the characteristic function  $\Delta(k_r^2)$ , one computes

$$\tilde{\Delta}(k_r^2) = \frac{\Delta(k_r^2)}{\prod_j k_r^2 - k_{r,j}^2}, \quad (5.144)$$

where  $k_{r,j}$  are the previously computed eigenvalues which are to be removed or deflated.

We have described deflation here as an approach for systematically locating the eigenvalues by calculating them sequentially from one end of the spectrum. However, the deflation approach is broadly useful for any root-finding scheme where we simply wish to avoid finding the same root twice.

### 5.7.4.3 Brute-Force Search

Given user-specified upper and lower bounds one selects a certain  $\Delta k_r$  and simply steps along the  $k_r$ -axis evaluating the determinant at each point. The eigenvalues lie within the intervals where a sign-change is encountered. Faster root finders can then be used to refine the estimate.

The  $\Delta k_r$  required can be unpredictably small since it is difficult to know a priori how closely spaced the nearest eigenvalues may be. The more conservatively one picks this step, the more robust the method is, but then the efficiency suffers.

#### 5.7.4.4 Analytic Estimates

A number of people have applied their skills to devising formulas for estimating eigenvalues. Generally, one constructs a simpler profile which resembles the given profile as closely as possible but for which one knows the eigenvalues. Another alternative is to use the WKB estimate of the eigenvalue. This approach is discussed by Bartberger [21].

Once the lower-order modes are found, extrapolation is often used to estimate the positions of higher modes from lower-order ones.

#### 5.7.4.5 Continuation Methods

Another approach to finding eigenvalues is to track them as they evolve from some other problem. For instance, in range-dependent modal calculations, each new environment may be viewed as an evolution in range. Thus, we imagine the eigenvalues also having a trajectory in range, which one may track. One way to do this is simply to use the eigenvalues from a previous range to initialize the search for eigenvalues at a new range.

In a similar spirit, one may solve for eigenvalues of a complex problem involving material attenuation by gradually increasing the attenuation and tracking the eigenvalues as the attenuation increases to the desired value. In this case, the problem may be started with no attenuation, taking advantage of the robustness of the bisection method.

There is now a large literature on such *continuation* or *homotopy* methods in a variety of fields.

#### 5.7.4.6 Approaches Unique to the Complex Plane

Complex roots occur in the presence of (a) material absorption, (b) halfspaces (leading to leaky modes), and, possibly, (c) elasticity. Some of the approaches described above generalize immediately. For instance, one may use Newton or secant methods in the complex plane. However, the bisection method, which *guarantees* convergence, does not apply. In general, none of the approaches provide the same reliability in the complex plane.

Lehmer [32] developed a well-known approach that may be viewed as a generalization of bisection to the complex plane. He contemplates a mechanism for identifying whether a root exists within a disc, and then develops a process of translating and dilating/contracting discs to map out roots in the complex plane.

Whether or not there is a root in a given domain may be determined by the *principle of the argument*, which states that the number of zeros of an analytic function in a given domain is found by counting phase changes around its boundary. Delves and Lyness [33] developed an extension of the Lehmer approach that used not just the presence of a zero, but the actual count of enclosed zeros. Some care is needed to choose the step for the contour integration.

Once a zero is enclosed one may attempt to speed up the process by following contours where the real or imaginary part of the function is zero. The zeros lie at the intersection of such contours. The text by Hamming [34] provides a good discussion of these methods.

These or similar approaches have been used in a variety of applications leading to eigenvalue problems. In radio [35], one finds the Shellman–Morfitt root-finding algorithm. Dubbelday [36] studies fluid-loaded plates. Cristini [37] modified an acousto-elastic mode code to use the Davies [38] approach, which is also based on the Delves–Lyness method.

The above discussion views the root-finding as an essentially two-dimensional problem in the complex plane. Tindle and Chapman [39] showed how such roots could be traced along a contour in the complex plane defined by a phase function. The attraction of this approach is that the main search is confined to a 1-D search along a single contour. However, roots may exist on additional contours that may be difficult to locate. This approach has been successfully implemented in a general-purpose code for acousto-elastic modes [23].

### 5.7.5 *Choice of Numerical Algorithm*

As we have mentioned, examples of each of the above numerical techniques exist in practical models, which is an indicator that the choice of algorithm is not clear-cut. One can often demonstrate the superiority of a given scheme by simply choosing the test cases carefully. For instance, methods based on layer matrices are generally more efficient than finite-difference-based methods for problems with few layers, e.g., the Pekeris waveguide, especially at a high source frequency. Thus the number of modes increases linearly with frequency as does the computational cost for layer-matrix methods. On the other hand, the finite-difference models must also increase the number of mesh points leading to a *quadratic* increase in execution time.

In practice, the sound-speed profile may be tabulated at tens (or even hundreds) of points in which case one would have to increase the number of layers in layer methods as well. However, if hundreds of layers are needed, one starts to question also the effect of range dependence. For high-frequency problems one may then settle for fewer layers and hope to predict only the broad features such as convergence-zone and surface-duct propagation.

An appealing aspect of the finite-difference approach is that it automatically provides sampling on a fine grid. For a layer method every depth point requires the evaluation of somewhat complicated Airy functions. Thus, a requirement for fine sampling – e.g., to produce a snapshot of the pressure field throughout the water column–tends to favor finite-difference methods.

Another important consideration is model *robustness*. In normal-mode codes, two principal problem areas appear: (1) stability and (2) mode location (skipping over modes or including the same mode several times). Stability problems can be overcome in finite-difference methods by using inverse iteration, in layer methods

as described in Chap. 4, and in shooting methods by using multiple shooting. The mode location problem can be solved using the bisection method which is most efficiently applied to finite-difference approaches.

In short, the relative computational costs are a function of the frequency and other aspects of the problem and, consequently, it is not possible to make universal statements about which method is most efficient.

## 5.8 Prüfer Transformations and Mode Counting

We consider here a general Sturm–Liouville problem given by

$$\begin{aligned} \left[ \frac{p'}{a(z; k)} \right]' + b(z; k) p &= 0, \\ p(0) &= 0, \\ p(D) &= 0, \end{aligned} \tag{5.145}$$

where  $a, b$  are arbitrary real functions. For the standard modal problem,

$$\begin{aligned} a(z; k) &= 1, \\ b(z; k) &= \omega^2/c^2(z) - k^2. \end{aligned} \tag{5.146}$$

In the presence of a shear flow with velocity  $V(z)$  one finds

$$\begin{aligned} a(z; k) &= [\omega - k V(z)]^2, \\ b(z; k) &= \frac{1}{c^2(z)} - \frac{k^2}{[\omega - k V(z)]^2} \end{aligned} \tag{5.147}$$

(see problem 5.11). For simplicity we assume pressure-release boundaries for now – later on we will consider more complicated boundary conditions.

A variety of important properties of the modal equation can be understood by working with an amplitude–phase representation of the solution. In particular, we define the Prüfer variables  $A(z), \phi(z)$  implicitly by:

$$\begin{aligned} p(z) &= A(z) \sin \phi(z), \\ \frac{p'(z)}{a(z; k)} &= A(z) \cos \phi(z). \end{aligned} \tag{5.148}$$

Differentiating both these equations with respect to  $z$  yields:

$$\begin{aligned} p'(z) &= A' \sin \phi + A(\cos \phi)\phi', \\ \left[ \frac{p'(z)}{a(z; k)} \right]' &= A' \cos \phi - A(\sin \phi)\phi'. \end{aligned} \tag{5.149}$$

The first of these equations gives an expression for  $p'$  which must also be equal to  $a(z; k)A(z) \cos \phi(z)$ . The second equation is just the first term of the Sturm–Liouville problem. Summarizing:

$$\begin{bmatrix} \sin \phi & A \cos \phi \\ \cos \phi & -A \sin \phi \end{bmatrix} \begin{bmatrix} A' \\ \phi' \end{bmatrix} = \begin{bmatrix} aA \cos \phi \\ -bA \sin \phi \end{bmatrix}. \quad (5.150)$$

The matrix on the left-hand side is easily inverted yielding the final equations:

$$\begin{bmatrix} A' \\ \phi' \end{bmatrix} = \begin{bmatrix} (a-b)A \sin \phi \cos \phi \\ a \cos^2 \phi + b \sin^2 \phi \end{bmatrix}. \quad (5.151)$$

These are the Prüfer differential equations, which, together with surface and bottom boundary conditions, provide an alternative formulation of the modal problem. The first equation may be further simplified using the double-angle formula  $2 \sin \phi \cos \phi = \sin 2\phi$ . The equation for  $A(z)$  may be integrated to yield:

$$A(z) = A(0) e^{\int_0^z [a(\tilde{z}) - b(\tilde{z})] \frac{\sin 2\phi(\tilde{z})}{2} d\tilde{z}} \quad (5.152)$$

from which we can see that the amplitude  $A(z)$  never vanishes. Thus zeros of the modes  $p(z) = A(z) \sin \phi(z)$  occur where the phase  $\phi(z)$  is an integer multiple of  $\pi$ . We may also view the phase as a function of the wavenumber  $k$ , writing it as  $\phi(z; k)$ . Interestingly, if the coefficients  $a(z; k), b(z; k)$  in the modal equation are monotonic in  $k$ , then so is  $\phi$ . The significance of this statement is that we can now place a trial wavenumber  $k_{\text{trial}}$  in the spectrum by simply counting the number of phase rolls in  $\phi(z; k_{\text{trial}})$ . The  $m$ th mode has a terminal phase  $\phi(D) = m\pi$  so if  $m = \lfloor \phi(D; k_{\text{trial}}) \rfloor$  then  $k_{\text{trial}}$  lies in the interval  $[k_m, k_{m+1}]$ , where  $k_m$  denotes the  $m$ th mode.

The traditional proof of the monotonicity of the phase  $\phi(z; k)$  is fairly straightforward. One considers two problems:

$$\begin{aligned} \left[ \frac{p'}{a} \right]' + b p &= 0, \quad p(0) = 0, \quad p'(0) = 0, \\ \left[ \frac{\tilde{p}'}{\tilde{a}} \right]' + \tilde{b} \tilde{p} &= 0, \quad \tilde{p}(0) = 0, \quad \tilde{p}'(0) = 0, \end{aligned} \quad (5.153)$$

where it is assumed  $\tilde{a} > a$ , and  $\tilde{b} > b$  for all  $z$ . Each of these problems has associated Prüfer variables  $A, \phi, \tilde{A}$ , and  $\tilde{\phi}$ . Now suppose that the phase functions  $\phi(z)$  and  $\tilde{\phi}(z)$  have a crossing at some depth  $z_0$ . At such a point,

$$\begin{aligned} \phi'(z_0) &= a(z_0) \cos^2 \phi_0 + b(z_0) \sin^2 \phi_0, \\ \tilde{\phi}'(z_0) &= \tilde{a}(z_0) \cos^2 \phi_0 + \tilde{b}(z_0) \sin^2 \phi_0 \end{aligned} \quad (5.154)$$

from which it is clear that  $\tilde{\phi}'(z_0) > \phi'(z_0)$ , i.e., the slope of the  $\tilde{\phi}$  curve is greater than the slope of the  $\phi$  curve at that point. Thus, if the curves cross, then the  $\tilde{\phi}$

curve must approach from below the  $\phi$  curve. This implies there can be at most one crossing and since the initial conditions give the same starting point for both curves, that point must be the only crossing. Then we have  $\tilde{\phi}(z) > \phi(z)$  from that point on.

In this derivation, we considered two independent problems with coefficients  $a, b$  and  $\tilde{a}, \tilde{b}$ . If we view those cases simply as samples of the monotonic functions  $a(z; k), b(z; k)$ , then we conclude that the phase  $\phi(z; k)$  at any point  $z$  must vary monotonically with the wavenumber. In the standard acoustic problem,  $b(z; k) = \omega^2/c^2(z) - k^2$  increases as  $k$  decreases, so the number of phase wraps also increases as  $k$  decreases.

The practical implication of this theory is that we calculate the number of modes less than any trial wavenumber by simply counting the number of zeros in the trial eigenfunction derived by shooting from one boundary to the other. For instance, if we want to know the number of propagating modes, we set  $k_{\text{trial}} = \min[\omega/c(z)]$  and count the resulting zeros. The results above are cast in terms of the wraps in the Prüfer phase function; however, this is equivalent to a zero-crossing in the trial eigenfunction.

### 5.8.1 Top Halfspaces

The above discussion is general in the sense of considering more complicated modal problems, such as those with shear flows. However, we had assumed simple pressure-release boundary conditions at both ends. We will now show that for the trapped modes, the same process is valid for acousto-elastic halfspaces. To introduce the method, we consider an artificial scenario in which a homogeneous acoustic halfspace with a sound speed of 2000 m/s overlies an ocean layer with a sound speed of 1500 m/s. The interface between the top halfspace and the ocean occurs at  $z = 0$ . The ocean is assumed to be terminated with a pressure-release boundary at some greater depth.

To begin the shooting process, we start with the analytic solution in the top (upper halfspace):

$$\Psi_t(z) = e^{\gamma_t z}, \quad (5.155)$$

where

$$\gamma_t \equiv -ik_{z,t} = \sqrt{k_r^2 - \left(\frac{\omega}{c_t}\right)^2} \quad (5.156)$$

and  $c_t$  denotes the sound speed in the top. We observe that the Prüfer phase in the top is given by the constant

$$\phi = \arctan(p/p') = 1/\gamma_t. \quad (5.157)$$

Similarly, the Prüfer amplitude is given by

$$A(z) = p(z)/\sin \phi. \quad (5.158)$$

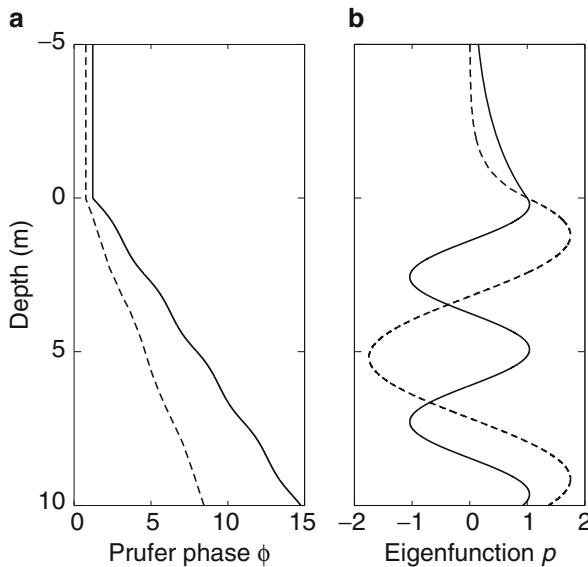


**Fig. 5.16** Shooting from a halfspace, through an isovelocity ocean for two different trial eigenvalues. (a) Prüfer phase (b) trial eigenfunction

Together these equations give the initial conditions for the Prüfer differential equations, which may be integrated using standard numerical techniques. We show the phase,  $\phi(z)$  and the resulting trial eigenfunction in Fig. 5.16 for two different trial eigenvalues.

There are a number of features of interest in this plot. First, we observe that, within the phase interval for trapped modes, i.e.,  $\omega/k_r$  in  $[c_0, c_1]$ , the initial Prüfer phase  $\phi(0)$  is a monotonically decreasing function of  $k_r$ . Thus, as we decrease  $k_r$ , going towards higher-order modes, we transition from the dashed curve to the solid curve. The latter curve is entirely to the right of the former, indicating that the number of phase wraps continues to be a monotonic function of the trial eigenvalue and therefore can still be used to identify where it lies in the spectrum. The important feature in this analysis is that the phase of the top reflection coefficient is also monotonic in the trial eigenvalue in a sense that is consistent with the monotonic properties of the phase in the ocean. With this property we can continue to use the number of zeros crossings as an indicator of the position of a trial wavenumber in the spectrum.

Note that in this example the Prüfer phase is not a strictly linear function in the ocean. Since the eigenfunction is a perfect sine wave, one might think that it should be characterized by a linear phase. However, the Prüfer variables require the same phase and amplitude to capture the function and its derivative in a particular form. To achieve this, both functions may assume complicated shapes, which in turn can require fine step sizes in the numerical integrators. Various modified

transformations can reduce the complexity of these functions and improve the efficiency of the numerical procedures. The text by Pryce [40] is a good starting point for the interested reader.

### 5.8.2 Bottom Halfspaces

The above discussion treats a halfspace as an initial condition for the shooting process. Shooting can be done from the top down, or in the reverse direction so that bottom halfspaces may often be treated in the same fashion. However, if shooting is used not just to get the eigenvalue, but also to directly solve for the eigenfunction, then the shooting direction may be dictated by stability conditions. For instance, in typical Arctic profiles, which are upward refracting, shooting for the eigenfunctions should be done from the bottom up. Conversely, in shallow water problems in lower latitudes, the profile is often downward refracting and so the shooting would often be done in the downward direction. Finally, in deep-water problems there is often a sound speed minimum in the interior. Then the stable shooting process proceeds from both ends towards an interior point,  $z_{\text{mid}}$  (parallel shooting). We consider this more general case here.

In this case, we shoot from the top to  $z_{\text{mid}}$  yielding  $A_t(z), \phi_t(z)$  and from the bottom to yield  $A_b(z), \phi_b(z)$ . At the point where these two shooting solutions meet we must have continuity of the function and its first derivative (we assume there is no density discontinuity at the join). However, we may scale the solutions to obtain the match. Thus, we seek:

$$\begin{aligned} a A_t(z_{\text{mid}}) \sin[\phi_t(z_{\text{mid}})] &= b A_b(z_{\text{mid}}) \sin[\phi_b(z_{\text{mid}})], \\ a A_t(z_{\text{mid}}) \cos[\phi_t(z_{\text{mid}})] &= b A_b(z_{\text{mid}}) \cos[\phi_b(z_{\text{mid}})] \end{aligned} \quad (5.159)$$

or, in matrix form,

$$\begin{bmatrix} A_t(z_{\text{mid}}) \sin[\phi_t(z_{\text{mid}})] & -A_b(z_{\text{mid}}) \sin[\phi_b(z_{\text{mid}})] \\ A_t(z_{\text{mid}}) \cos[\phi_t(z_{\text{mid}})] & -A_b(z_{\text{mid}}) \cos[\phi_b(z_{\text{mid}})] \end{bmatrix} \begin{bmatrix} a \\ b \end{bmatrix} = \begin{bmatrix} 0 \\ 0 \end{bmatrix}. \quad (5.160)$$

In order for there to be a non-trivial solution, the determinant must vanish implying

$$A_t(z_{\text{mid}}) A_b(z_{\text{mid}}) \left\{ \sin[\phi_t(z_{\text{mid}})] \cos[\phi_b(z_{\text{mid}})] - \cos[\phi_t(z_{\text{mid}})] \sin[\phi_b(z_{\text{mid}})] \right\} = 0. \quad (5.161)$$

Since the amplitudes  $A_t, A_b$  never vanish, this in turn implies

$$\sin[\phi_t(z_{\text{mid}}) - \phi_b(z_{\text{mid}})] = 0. \quad (5.162)$$

Thus, we see that the difference of the phases in the down- and upgoing directions must have the form  $(n + 1/2)\pi$  where  $n$  is an integer. Also, we have shown that both phase functions are monotonic (with the correct sense) in the trial eigenvalue. Therefore, as before, we can identify the position of a trial eigenvalue within the spectrum by counting the number of phase wraps in this total phase.

This result has been derived using the Prüfer variables; however, again, it is applicable to any shooting technique that provides an estimate of  $p$  since that may be converted to an equivalent phase by zero-counting.

There is no generalization of these mode-counting procedures to arbitrary elastic media. However, in the case of an elastic halfspace and for trapped modes, one can show that the boundary condition has the required monotonicity of phase. Then one may count modes as described above.

## 5.9 Modal Perturbation Theory

### 5.9.1 Modal Propagation Loss

Loss may be caused by material absorption or by scattering at boundaries or interfaces. In the former case the loss is manifest as a complex sound speed while in the latter case the interfacial condition is modified. Both of these mechanisms can be handled by straightforward modifications of the numerical algorithm; however, the eigenvalues become complex, requiring the use of complex arithmetic. More importantly, the root-finder must be modified to perform not just a line search on the real axis but a 2-D search in the complex  $k_r$ -plane. While robust and efficient root finders can be constructed for the real problem, the complex root finders are failure-prone.

An attractive alternative to complex eigenvalue searches is to compute the real eigenvalues and then obtain an approximation to the imaginary parts using perturbation theory. To illustrate the technique we consider the modal problem with simple pressure-release and rigid-bottom boundary conditions. That is,

$$\rho(z) \left[ \frac{1}{\rho(z)} \Psi_m'(z) \right]' + [k^2(z) - k_{rm}^2] \Psi_m(z) = 0 \quad (5.163)$$

with

$$\Psi_m(0) = 0, \quad \frac{d\Psi_m(D)}{dz} = 0, \quad \int_0^D \frac{\Psi_m^2(z)}{\rho(z)} dz = 1, \quad (5.164)$$

where  $k^2(z) = \omega^2/c^2(z)$ . We then introduce a perturbation in the square of the medium wavenumber

$$k^2(z) = k_0^2(z) + \epsilon k_1^2(z) + \dots, \quad (5.165)$$

where  $k_0^2(z)$  corresponds to the unperturbed sound-speed profile which for lossy problems is simply the square of the real part of the medium wavenumber  $k(z) = \omega/c(z)$ . The next step is to seek a solution of the form

$$\Psi(z) = \Psi_0(z) + \epsilon \Psi_1(z) + \dots \quad (5.166)$$

and the associated perturbed eigenvalue is

$$k_{rm}^2 = k_{r0}^2(z) + \epsilon k_{r1}^2 + \dots \quad (5.167)$$

Substituting into (5.163) and (5.164) and collecting terms of like order, we obtain

$$O(1) : \rho(z) \left[ \frac{1}{\rho(z)} \Psi'_0(z) \right]' + [k_0^2(z) - k_{r0}^2] \Psi_0(z) = 0, \quad (5.168)$$

$$\Psi_0(0) = 0, \quad \frac{d\Psi_0(D)}{dz} = 0, \quad \int_0^D \frac{\Psi_0^2(z)}{\rho(z)} dz = 1. \quad (5.169)$$

This is the lossless eigenvalue problem and can be solved on the real axis. The next-higher-order equation is

$$O(\epsilon) : \rho(z) \left[ \frac{1}{\rho(z)} \Psi'_1(z) \right]' + [k_0^2(z) - k_{r0}^2] \Psi_1(z) = -[k_1^2(z) - k_{r1}^2] \Psi_0(z), \quad (5.170)$$

$$\Psi_1(0) = 0, \quad \frac{d\Psi_1(D)}{dz} = 0, \quad \int_0^D \frac{\Psi_1^2(z)}{\rho(z)} dz = 1. \quad (5.171)$$

From the Fredholm Alternative Theorem, the inhomogeneous term on the right-hand side must be orthogonal to all solutions of the homogeneous adjoint problem in order for a solution to exist [5]. (In terms of an undamped vibrating string, this means that a steady-state solution does not exist when the string is forced at a resonance frequency.) The solutions of the adjoint problem are simply the modes  $\Psi_0(z)$ . Therefore, we must have

$$\int_0^D [k_1^2(z) - k_{r1}^2] \frac{\Psi_0^2(z)}{\rho(z)} dz = 0, \quad (5.172)$$

which implies

$$k_{r1}^2 = \int_0^D \frac{k_1^2(z) \Psi_0^2(z)}{\rho(z)} dz, \quad (5.173)$$

where we have used the fact that the modes  $\Psi_0(z)$  are normalized as specified in (5.169). This is the first correction due to an arbitrary perturbation  $k_1^2(z)$ .

To apply the perturbation approach to estimate the modal attenuation due to material absorption we introduce an imaginary component to the medium wavenumber  $k(z) = \omega/c(z) + i\alpha$ .

The perturbation method above is performed in the square of the wavenumber, which in this case for small attenuation is

$$k^2(z) \approx \left[ \frac{\omega}{c(z)} \right]^2 + 2i\alpha(z) \frac{\omega}{c(z)}. \quad (5.174)$$

The first term involving only the real wavenumber component  $\omega/c(z)$  is used to generate the zeroth-order unperturbed problem which is easily solved to provide eigenvalues  $k_{rm}$  and eigenfunctions  $\Psi_m(z)$ .

We next denote the perturbation term by  $\epsilon k_1^2 = 2i\alpha(z)\omega/c(z)$  and the corresponding perturbation to the eigenvalue by  $\epsilon k_{r1}^2 = 2i\alpha_m k_{rm}$ . Inserting these into (5.173) then yields

$$2i\alpha_m k_{rm} = \int_0^D \frac{2i\alpha(z) \omega/c(z) \Psi_m^2(z)}{\rho(z)} dz \quad (5.175)$$

or

$$\alpha_m = k_{rm}^{-1} \int_0^D \frac{\alpha(z) \omega \Psi_m^2(z)}{c(z) \rho(z)} dz. \quad (5.176)$$

In practice, this first-order perturbational approximation is usually adequate. It gives poor numerical accuracy when the imaginary part is very large, i.e., when the mode decays very rapidly in range. In such cases, the accuracy is normally not critical since the pressure field is then usually dominated by other modes which are less severely attenuated.

At intermediate and lower frequency the attenuation in the water column can usually be ignored. Thus, the only attenuation of significant is due to the material absorption in the bottom. The perturbation approach was here derived for the ideal waveguide with homogeneous boundary conditions. However, the result in (5.176) is still valid, provided the integration interval is extended into the bottom to include the evanescent “tail” of the modal function, i.e.,

$$\begin{aligned} \alpha_m &= k_{rm}^{-1} \int_0^\infty \frac{\alpha(z) \omega \Psi_m^2(z)}{c(z) \rho(z)} dz \\ &= k_{rm}^{-1} \int_0^D \frac{\alpha(z) \omega \Psi_m^2(z)}{c(z) \rho(z)} dz + \delta\alpha_m, \end{aligned} \quad (5.177)$$

where the contribution from the bottom portion is easily evaluated analytically. The mode shape in the bottom is exponential

$$\Psi_m(z) = \Psi_m(D) e^{-\gamma_m(z-D)} \quad (5.178)$$

with

$$\gamma_m = \sqrt{k_{rm}^2 - (\omega/c_b)^2} \quad (5.179)$$

yielding

$$\begin{aligned}\delta\alpha_m &= k_{rm}^{-1} \int_D^\infty \frac{\alpha_b \omega \Psi_m^2(z)}{c_b \rho_b} dz \\ &= \frac{\Psi_m^2(D) \alpha_b \omega}{2k_{rm} \gamma_m c_b \rho_b}.\end{aligned}\quad (5.180)$$

It is interesting to note that the depth integral in (5.180) directly provides mathematical justification for the “optimum frequency” characteristic of shallow water propagation, discussed in Sect. 1.4.3. As is obvious from (5.178), the pressure field associated with a trapped mode is exponentially decreasing with depth. However, as is evident from (5.179), it is also exponentially decreasing with frequency, thus leading to a decrease in the integration kernel at higher frequencies. On the other hand the imaginary part of the medium wavenumber for marine sediments has a power law dependency with frequency,  $\alpha \sim f^\beta$ , with  $\beta$  being somewhere between 1 and 2, depending on the sediment type and frequency range. At low frequencies the increase in the depth of the exponential tail leads to an increase in the bottom integral contribution, which will more than compensate for the power law decrease in the material dissipation, thus resulting in the low frequency increase in transmission loss observed in Fig. 1.17.

In turn, this trade-off between the exponential increase in the modal amplitude and the power-law decrease in intrinsic attenuation with decreasing frequency has a somewhat counter-intuitive effect. Thus, at high frequencies, the bottom attenuation is rather insignificant compared to other attenuation effects, due to the strong evanescence of the field in the bottom. On the other hand, the change in intrinsic attenuation has a strong effect at the low frequencies where bottom attenuation dominates. As a result the frequency with minimum loss will trend higher in frequency for increasing intrinsic bottom attenuation. This somewhat surprising phenomenon is illustrated in Fig. 5.17, where the transmission loss in a shallow-water environment is plotted vs. range and frequency, for two different values of the intrinsic attenuation in a sandy bottom. The water depth is 100 m, and a summer sound-speed profile similar to the one shown in Fig. 1.17 is assumed. The source and receiver depths are 10 and 50 m, respectively. The bottom sound speed is 1700 m/s. Figure 5.17a shows contours of the incoherent transmission loss, computed using (5.18) for an intrinsic bottom attenuation of 0.1 dB/λ, indicating an optimal frequency of approximately 160 Hz for this source–receiver configuration. Figure 5.17b shows the equivalent result when the bottom attenuation is increased to 0.5 dB/λ, increasing the optimum frequency to approximately 500 Hz.

A perturbational approach is also useful for treating loss due to surface or bottom roughness. Kuperman and Ingemito [41] derive the result,

$$\gamma^{(\text{scat})} = \frac{\sigma^2 k_{zm}}{2\rho k_{rm}} \left[ \frac{d\Psi_m(z)}{dz} \right]_{z=0}^2 \quad (5.181)$$

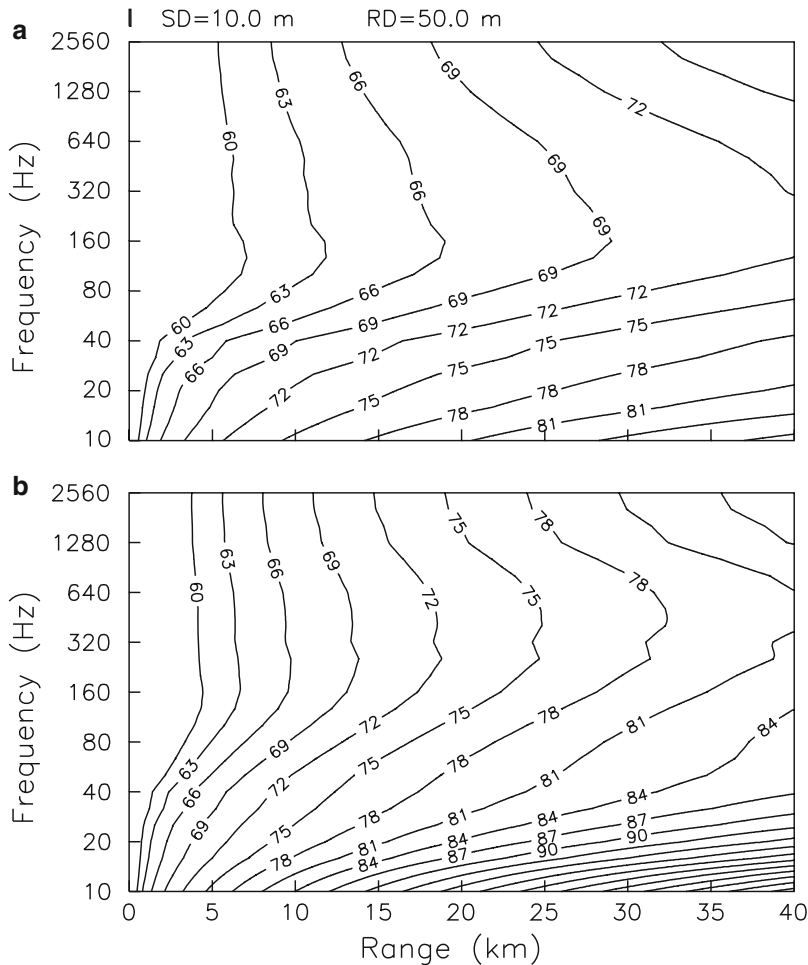


**Fig. 5.17** Frequency–range contours of incoherent transmission loss in 100-m deep shallow water environment with summer sound-speed profile and a sand bottom, illustrating the bottom attenuation effects on the optimum frequency. (a) Bottom attenuation  $0.1 \text{ dB}/\lambda$ : Optimum frequency 160 Hz. (b) Bottom attenuation  $0.5 \text{ dB}/\lambda$ : Optimum frequency 500 Hz

for the perturbation in the eigenvalues due to surface scattering loss. Here,  $\sigma$  denotes the *rms* roughness of the sea surface, and  $k_{zm}$  is again the vertical wavenumber,

$$k_{zm} = \sqrt{\frac{\omega^2}{c^2(0)} - k_{rm}^2}. \quad (5.182)$$

### 5.9.2 Modal Group Velocity

As discussed in Chap. 2, each mode has its own group velocity that in turn varies with the source frequency. The group velocity is defined as

$$u_n(\omega) = \frac{d\omega}{dk_{rn}}. \quad (5.183)$$

Numerically, this velocity may be computed using a simple finite-difference formula. For instance, we may use the formula

$$u_n \simeq \frac{(\omega + \Delta\omega) - \omega}{k_{rn}(\omega + \Delta\omega) - k_{rn}(\omega)}. \quad (5.184)$$

Thus, we evaluate the modal wavenumbers at two closely spaced frequencies  $\omega$  and  $\omega + \Delta\omega$  and compute the derivative based on the ratio of the change in wavenumber to the change in frequency.

The only difficulty with this approach is that of choosing the frequency spacing. If  $\Delta\omega$  is too large, then the difference formula is inaccurate; if it is too small then round-off error can corrupt the answer.

An alternative is to compute the group velocity from perturbation theory. The formulas from the preceding section can be applied directly. The perturbed problem has

$$k^2(z) = \frac{(\omega + \Delta\omega)^2}{c^2(z)} \simeq \frac{\omega^2}{c^2(z)} + \frac{2\Delta\omega\omega}{c^2(z)}. \quad (5.185)$$

This can be written as  $k^2 = k_0^2 + \epsilon k_1^2$  where  $k_0^2 = \omega^2/c^2$ ,  $k_1^2 = 2\omega/c^2$ , and  $\epsilon = \Delta\omega$ . Substituting in (5.173) we obtain

$$k_{r1}^2 = \int_0^D \frac{2\omega}{c^2(z)} \frac{\Psi_0^2(z)}{\rho(z)} dz. \quad (5.186)$$

With this result we can calculate the wavenumber for the perturbed problem as  $k_r^2(\omega + \Delta\omega) \simeq k_{r0}^2(\omega) + \Delta\omega k_{r1}^2$ . Let us rearrange this equation as follows:

$$\frac{k_r^2(\omega + \Delta\omega) - k_{r0}^2(\omega)}{\Delta\omega} \simeq k_{r1}^2. \quad (5.187)$$

We now pass to the limit of vanishing  $\Delta\omega$  and find

$$\frac{d(k_r^2)}{d\omega} = 2k_r \frac{dk_r}{d\omega} = k_{r1}^2. \quad (5.188)$$

Putting this all together we find

$$\frac{dk_r}{d\omega} = \frac{\omega}{k_r} \int_0^D \frac{\Psi_0^2(z)}{\rho(z) c^2(z)} dz. \quad (5.189)$$

The reciprocal of this formula gives the group velocity. Such formulas have been used for many years in various branches of wave propagation. Unfortunately, they become quite tedious as the problem complexity increases, e.g., to elastic or poro-elastic media with complicated boundary conditions.

## 5.10 Elastic Media

The ocean bottom is commonly modeled as an acoustic medium; however, it can be more accurately modeled by including elasticity, leading to compressional and shear waves. In many ocean sediments, the shear-wave speeds are less than a few hundred m/s, in which case the coupling to shear is weak and the elastic effects are typically negligible. However, where the shear speed is higher, elastic wave effects can be critically important. For instance, much of the Pacific Ocean has a thin sediment (<200 m) with very low shear speeds, overlying a basalt with shear speeds that can exceed the speed of sound in the ocean. For lower frequencies, the sound readily penetrates the thin sediment and couples to compression and shear waves in the basalt. These waves refract in the basalt and can re-radiate into the ocean volume, leading to a continuous coupling of the two media.

Further refinements are possible. For instance, poro-elastic models that treat the physics of fluid flow through granular media have been widely studied. Elastic models may also consider anisotropy in which the shear and compressional wave speeds depend also on the direction of propagation through the medium. In this section, we will consider isotropic, elastic media. These types of problems have been studied extensively in seismology. We refer the reader to that literature for additional information. The text by Aki and Richards [4] is an excellent starting point.

### 5.10.1 Governing Equations

The field in the elastic medium is represented by  $x$ ,  $y$ , and  $z$ -components of the particle displacement and denoted by  $\mathbf{u} = (u, v, w)$ . The displacements respond to external forces  $\mathbf{f}$  and internal stresses  $\tau$  according to the equations of motion:

$$\rho \ddot{u}_i = f_i + \tau_{ji,j}, \quad (5.190)$$

where the over-dot indicates a time-derivative. This is essentially a statement of Newton's second law equating mass-times-acceleration to the forces. The stress  $\tau$  is related to the strain  $e_{ij}$  according to:

$$\tau_{ij} = \lambda \delta_{ij} e_{kk} + 2\mu e_{ij}, \quad (5.191)$$

where  $\lambda$  and  $\mu$  are the Lamé constants. These parameters are related to the shear and compressional wave speeds via

$$c_s = \sqrt{\frac{\mu}{\rho}}, \quad c_p = \sqrt{\frac{\lambda + 2\mu}{\rho}}. \quad (5.192)$$

In addition, the strains are related to the displacements via:

$$e_{ij} = \frac{1}{2} \left( \frac{\partial u_i}{\partial x_j} + \frac{\partial u_j}{\partial x_i} \right). \quad (5.193)$$

We now seek a solution of the form  $\mathbf{u} = \hat{\mathbf{u}} e^{ik_x x - \omega t}$  assuming a dependence in the  $x$ -direction that is appropriate for line sources in range-independent environments. The process for point sources assumes a Hankel function in range and yields identical depth-separated equations. Then, substituting into the above equations yields:

$$-\omega^2 \rho \hat{\mathbf{u}} = \begin{bmatrix} -k^2(\lambda + 2\mu)\hat{u} + ik\lambda\hat{w}_{,z} + [\mu(\hat{u}_{,z} + ik\hat{w})]_{,z} \\ -\mu k^2 \hat{v} + [\mu\hat{v}_{,z}]_{,z} \\ ik\mu\hat{u}_{,z} - k^2\mu\hat{w} + [ik\lambda\hat{u} + (\lambda + 2\mu)\hat{w}_{,z}]_{,z} \end{bmatrix}. \quad (5.194)$$

Note that the equations for  $u$  and  $w$  are decoupled from the equation for  $v$ . It turns out that there is also no coupling induced by boundary or interface conditions and so these equations may be solved separately. The resulting solutions for  $u$  and  $w$  are termed Rayleigh waves, and the solution for  $v$  is termed a Love wave. We will not consider Love waves further here. They cannot be excited by pressure waves in the ocean volume (at least under the assumption of range-independent media). Furthermore, the resulting differential equation assumes the same form as that used for the acoustic wave equation so the numerical techniques are identical.

These equations could be discretized directly in this form. However, they contain the wavenumber  $k$ , which will become the eigenvalue, in both linear and squared forms. In addition, the equations are complex. As discussed in [6], a simpler eigenproblem can be obtained by introducing a scaled stress-displacement vector  $\mathbf{r}$  defined by

$$(r_1, r_2, r_3, r_4) = \left( \frac{u}{ik}, w, \frac{\tau_{zx}}{ik}, \tau_{zz} \right). \quad (5.195)$$

The governing equation for the Rayleigh waves then becomes

$$-\omega^2 \rho \mathbf{r} = \begin{bmatrix} -k^2(\lambda + 2\mu)r_1 + \lambda r_{2,z} + [\mu(r_{1,z} + r_2)]_{,z} \\ -k^2\mu(r_{1,z} + r_2) + [-k^2\lambda r_1 + (\lambda + 2\mu)r_{2,z}]_{,z} \end{bmatrix}. \quad (5.196)$$

In practice, the equations will normally become complex once attenuation is added. However, the above form makes clear that the wavenumbers come in pairs corresponding to the two roots of  $k^2$ .

From the definition of the stresses in (5.191):

$$\begin{aligned} r_3 &= \frac{\tau_{zx}}{ik} = \mu(r_{1,z} + r_2), \\ r_4 &= \tau_{zz} = (\lambda + 2\mu)r_{2,z} - k^2\lambda r_1 \end{aligned} \quad (5.197)$$

yielding,

$$\mathbf{r}' = \mathbf{E}\mathbf{r}, \quad (5.198)$$

where,

$$\mathbf{E}(z, k) = \begin{bmatrix} 0 & -1 & 1/(\rho c_s^2) & 0 \\ k^2\eta(z) & 0 & 0 & 1/(\rho c_p^2) \\ k^2\xi(z) - \rho\omega^2 & 0 & 0 & -\eta(z) \\ 0 & -\rho\omega^2 & k^2 & 0 \end{bmatrix} \quad (5.199)$$

with the quantities  $\eta(z)$  and  $\xi(z)$  defined by

$$\eta(z) = \frac{c_p^2 - 2c_s^2}{c_p^2}, \quad \xi(z) = \frac{\rho [c_p^4 - (c_p^2 - 2c_s^2)^2]}{c_p^2} \quad (5.200)$$

and where  $c_p, c_s$  denote the P and S-wave velocities, respectively. In this form, certain properties of elastic waves are immediately obvious. For instance, since the eigenvalue occurs only as a squared quantity, the eigenvalues will come in pairs. That is, if  $(k_j, \mathbf{r}_j)$  is an eigensolution then  $(-k_j, \mathbf{r}_j)$  is also an eigensolution.

The above equations for  $\mathbf{r}$  are combined with interfacial and boundary conditions to completely specify the acousto-elastic modal problem. Various combinations were discussed in Sect. 4.2.5. At an elastic–elastic interface, one requires continuity of  $\mathbf{r}$  (i.e., continuity of displacements and stresses). At an acousto-elastic interface the condition of continuity of horizontal displacement is relaxed. Noting that (a) pressure is the negative of the normal stress  $\tau_{zz}$ , (b)  $\tau_{zx}$  vanishes in an acoustic medium, and (c) the gradient of the pressure gives the time derivative of the velocity field, one obtains

$$\begin{aligned} \omega^2 r_2(z) &= \Psi'(z), \\ r_3(z) &= 0, \\ r_4(z) &= -\Psi(z). \end{aligned} \quad (5.201)$$

The appropriate normalization condition [4] for such elastic modes is that

$$\int \left[ -k^2\xi(z)r_1^2(z) + \eta(z)r_1(z)r_4(z) - r_2(z)r_3(z) \right] dz = 1, \quad (5.202)$$

where the integral is taken over the domain of the problem.

### 5.10.2 Numerical Discretization

As in the acoustic case, there are many techniques for discretizing the elastic equations. One popular approach is to use analytic solutions for piecewise-constant layers. The techniques are similar to those covered in Chap. 4 for the spectral integral formulation. Note that in purely acoustic problems, piecewise-linear approximations to the sound speed have been found to be particularly effective. Those approaches lead to Airy-function solutions. In elastic layers, there is continuous coupling between P and S-wave solutions in such layers and an exact Airy-function solution is not available. Various approximate solutions for such layers may be derived.

Instead, we consider the finite-difference approach here. As illustrated in Fig. 5.13 we divide the interval  $0 \leq z \leq D$  into  $N$  equal intervals to construct a mesh of equally spaced points  $z_j = jh$ ,  $j = 0, 1, \dots, N$ , where  $h$  is the mesh width given by  $h = D/N$ . Furthermore, we shall use the notation  $\Psi_j = \Psi(z_j)$ . The number  $N$  should be chosen large enough that the modes are adequately sampled; usually 10 points per wavelength are sufficient. It should be noted that there are two wavelengths corresponding to the P and S-wave speeds, respectively. For a fixed frequency the shear-wave speed produces the shorter wavelength and produces the stricter requirement on the sampling. The shear waves can have very short wavelengths for low-velocity materials.

The governing equations for elastic media are easily discretized by standard finite-difference techniques. We construct a uniform grid  $z_j = z_0 + jh$ ,  $j = 0, 1, \dots, N$ , where  $h$  is the mesh width. Then writing  $\mathbf{r}_j = \mathbf{r}(z_j)$ , (5.199) can be approximated by the trapezoidal rule:

$$\mathbf{r}_{j+1} - \mathbf{r}_j = \frac{h}{2} [\mathbf{E}(z_j)\mathbf{r}_j + \mathbf{E}(z_{j+1})\mathbf{r}_{j+1}]. \quad (5.203)$$

Another suitable alternative is the box method,

$$\mathbf{r}_{j+1} - \mathbf{r}_j = \frac{h}{2} \mathbf{E}(z_{j+1/2}) [\mathbf{r}_j + \mathbf{r}_{j+1}]. \quad (5.204)$$

These difference formulas may be assembled into a matrix leading to an algebraic eigenvalue problem for  $k^2$ . The section of the matrix corresponding to the elastic layers will then have a block form. For instance, with the trapezoidal rule above, the blocks assume the form:

$$\left[ \begin{array}{cccc|cccc} \frac{2}{h} & -1 & \frac{1}{\rho c_s^2(z_j)} & 0 & -\frac{2}{h} & -1 & \frac{1}{\rho c_s^2(z_{j+1})} & 0 \\ k^2\eta_j & \frac{2}{h} & 0 & \frac{1}{\rho c_p^2(z_j)} & k^2\eta_{j+1} & -\frac{2}{h} & 0 & \frac{1}{\rho c_p^2(z_{j+1})} \\ k^2\zeta_j - \rho\omega^2 & 0 & \frac{2}{h} & -\eta_j & k^2\zeta_{j+1} - \rho\omega^2 & 0 & -\frac{2}{h} & -\eta_{j+1} \\ 0 & -\rho\omega^2 & k^2 & \frac{2}{h} & 0 & -\rho\omega^2 & k^2 & -\frac{2}{h} \end{array} \right]. \quad (5.205)$$

This leads to a band-matrix with nine diagonals. If the boundary conditions do not introduce more complicated functions of the eigenvalues  $k^2$ , it may be solved using

standard packages. One may also directly discretize the equations in second-order form as given in (5.194). This has the computational advantage of reducing the size of the matrix, since the stress terms are eliminated from the equations.

### 5.10.3 Shooting Methods and Compound Matrices

Shooting methods may also be used for solving the combined acoustic and elastic equations as discussed by Porter and Reiss [6]. To illustrate the concept, we consider first a single fluid layer over an elastic layer, with a pressure-release surface boundary and a perfectly-rigid bottom terminating the elastic layer. We shoot in parallel from the surface down, and from the bottom up seeking to satisfy the interface conditions at the fluid–elastic interface. The process for the fluid layer is exactly as described in Sect. 5.7.3 for the purely acoustic case. In the elastic layer, we apply the two initial conditions for a perfectly rigid bottom; however, the IVP for a fourth-order equation requires a total of four initial conditions. The strategy is to pick two additional initial conditions so as to generate two linearly-independent solutions, denoted by  $\mathbf{r}$  and  $\mathbf{s}$ . Then, we can solve for scalar multiples of all the solutions so as to satisfy the interface condition. For an elastic medium with a rigid bottom, both displacements must vanish,

$$r_1(D) = r_2(D) = 0. \quad (5.206)$$

Thus, two linearly-independent solutions can be obtained using the initial conditions,

$$\mathbf{r} = (0, 0, 1, 0), \quad \mathbf{s} = (0, 0, 0, 1). \quad (5.207)$$

We then pick a trial value for the wavenumber  $k$  and solve for the pressure  $\Psi(z)$  and the stress-displacement vectors  $r(z)$  and  $s(z)$ . An example is shown in Fig. 5.18.

We then seek a linear combination of  $a\mathbf{r} + b\mathbf{s}$  and a scaling  $c\Psi$  to satisfy the interface condition which requires continuity of the normal and tangential stresses, and continuity of the normal displacement as given in (5.201). In terms of the linearly independent solutions we have

$$\begin{aligned} \omega^2 [ar_2(z) + bs_2(z)] &= c\Psi'(z), \\ ar_3(z) + bs_3(z) &= 0, \\ ar_4(z) + bs_4(z) &= -c\Psi(z). \end{aligned} \quad (5.208)$$

In matrix form this can be written as

$$\begin{bmatrix} \omega^2 r_2 & \omega^2 s_2 & -\Psi' \\ r_3 & s_3 & 0 \\ r_4 & s_4 & \Psi \end{bmatrix} \begin{bmatrix} a \\ b \\ c \end{bmatrix} = \begin{bmatrix} 0 \\ 0 \\ 0 \end{bmatrix}. \quad (5.209)$$

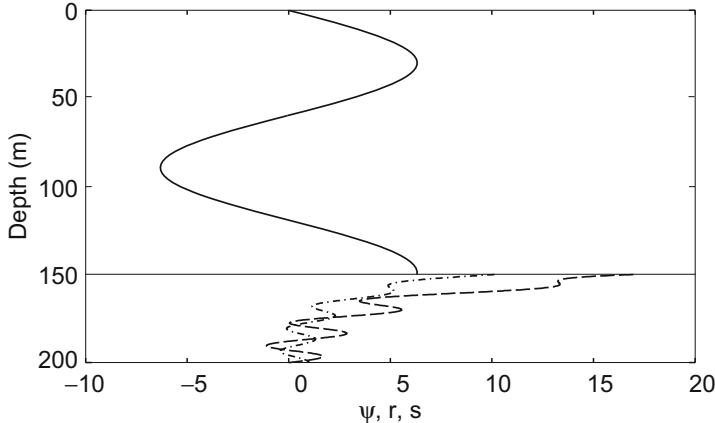


**Fig. 5.18** Parallel shooting for acousto-elastic modes. The trial acoustic solution is obtained by integrating down from the surface for the pressure  $\Psi(z)$ . The trial elastic solution is obtained by integrating up from the bottom for the stress-displacement vectors  $r(z)$  and  $s(z)$

In order for there to be a non-trivial solution, the determinant must vanish, implying,

$$f^B(k^2)\Psi_j(D) + g^B(k^2) \frac{d\Psi_j(D)}{dz} = 0 \quad (5.210)$$

with

$$f^B(k^2) = \omega^2 y_4, \quad g^B(k^2) = y_2 \quad (5.211)$$

and

$$y_2 = r_3 s_4 - r_4 s_3, \quad y_4 = r_2 s_3 - r_3 s_2. \quad (5.212)$$

Note that  $y_2$  and  $y_4$  are determinants of a  $2 \times 2$  matrix of the two solutions  $\mathbf{r}$  and  $\mathbf{s}$ . The condition that the determinant vanishes given in (5.210) is then the secular equation for the eigenvalue  $k$ . In the usual shooting approach for such eigenvalue problems, we must adjust  $k$  using a root-finder until the determinant vanishes.

This provides a complete numerical algorithm for finding the eigenvalues. To summarize, we shoot from the bottom up with two different initial conditions, yielding linearly independent solutions  $\mathbf{r}$  and  $\mathbf{s}$ . Then we shoot from the top down to calculate  $\Psi$  which must satisfy the condition given by (5.210). This latter equation may be viewed as an impedance condition on the acoustic pressure. Then we can see that the coefficients of the impedance are derived by upward shooting through the elastic medium. That impedance condition can also be included directly in a finite-difference formulation as described in the introductory sections of this chapter.

There are, however, some practical problems with the above described procedure. The solutions  $\mathbf{r}$  and  $\mathbf{s}$  are mathematically independent, but their numerical approximations commonly are not. For instance, for wavenumbers generating exponentially growing and decaying solutions for either the shear or pressure wave components,

the growing solution is inevitably excited, dominating the behavior of both  $\mathbf{r}$  and  $\mathbf{s}$ . Then, the numerical solutions become proportional to each other, even though they are mathematically independent.

To mitigate this problem, one seeks differential equations yielding the determinants  $y_2$  and  $y_4$  directly. To get a complete set of equations one must consider all the determinants of  $2 \times 2$  sub-matrices of the two solutions  $\mathbf{r}$  and  $\mathbf{s}$ . Thus, we introduce dependent variables defined by,

$$\begin{bmatrix} y_1 \\ y_2 \\ y_3 \\ y_4 \\ y_5 \\ y_6 \end{bmatrix} = \begin{bmatrix} r_1 s_2 - r_2 s_1 \\ r_3 s_4 - r_4 s_3 \\ r_1 s_3 - r_3 s_1 \\ r_2 s_3 - r_3 s_2 \\ r_1 s_4 - r_4 s_1 \\ r_2 s_4 - r_4 s_2 \end{bmatrix}, \quad (5.213)$$

where  $\mathbf{r}$  and  $\mathbf{s}$  denote two linearly-independent solutions in the elastic medium. Note that  $\mathbf{y}$  involves all permutations of  $r_i, s_j$  with an ordering chosen to obtain a simple form for the  $\mathbf{y}$ -equations. By differentiating the above equations and substituting into (5.199) we find that  $\mathbf{y}$  satisfies a system of differential equations:

$$\mathbf{y}' = \mathbf{W}\mathbf{y}, \quad (5.214)$$

where

$$\mathbf{W} = \begin{bmatrix} 0 & 0 & 0 & 1/(\rho c_s^2) & -1/(\rho c_p^2) \\ 0 & 0 & 0 & -\omega^2 \rho & -[k^2 \zeta(z) - \omega^2 \rho] \\ 0 & 0 & 0 & 1 & \eta(z) \\ k^2 \zeta(z) - \omega^2 \rho & 1/(\rho c_p^2) & -k^2 \eta(z) & 0 & 0 \\ \omega^2 \rho & -1/(\rho c_s^2) & -2k^2 & 0 & 0 \end{bmatrix}. \quad (5.215)$$

The differential equation for  $y_6$  reduces to  $y_6 = -k^2 y_5$  and has been eliminated from the system. After integrating these differential equations we obtain directly  $y_2$  and  $y_4$  defining the impedance condition at the fluid–elastic interface. This is called the *compound matrix method* or the *delta matrix formulation*. In the following section, we summarize the form of the various boundary and interface conditions in terms of the formulations for  $\mathbf{r}$  and  $\mathbf{y}$ .

## 5.10.4 Boundary and Interface Conditions

### 5.10.4.1 Perfectly Free Boundary (Dirichlet BC)

The free surface condition is an approximation for the surface boundary condition. (A more sophisticated boundary condition is obtained by using a homogeneous

acoustic halfspace to model the atmosphere above the ocean. The impedance contrast is, however, so large that there is no practical need for modeling the atmosphere.) For an acoustic medium this yields

$$\Psi(0) = 0, \quad (5.216)$$

while for an elastic medium both stresses must vanish:

$$r_3(0) = r_4(0) = 0. \quad (5.217)$$

Thus, two linearly independent solutions can be obtained using

$$\mathbf{r} = (1, 0, 0, 0), \quad \mathbf{s} = (0, 1, 0, 0). \quad (5.218)$$

From the definitions of  $\mathbf{y}$  in (5.213) we obtain the following boundary conditions

$$\mathbf{y} = (0, 1, 0, 0, 0). \quad (5.219)$$

#### 5.10.4.2 Perfectly Rigid Boundary (Neumann BC)

The perfectly rigid assumption enjoys some popularity for a bottom boundary. For a purely acoustic problem, this becomes,

$$\Psi'(D) = 0. \quad (5.220)$$

For an elastic medium, this implies that both displacements must vanish,

$$r_1(D) = r_2(D) = 0. \quad (5.221)$$

Thus, two linearly independent solutions can be obtained using,

$$\mathbf{r} = (0, 0, 1, 0), \quad \mathbf{s} = (0, 0, 0, 1). \quad (5.222)$$

From the definitions of  $\mathbf{y}$  in (5.213) we obtain the following boundary conditions,

$$\mathbf{y} = (1, 0, 0, 0, 0). \quad (5.223)$$

#### 5.10.4.3 Acoustic Halfspace Conditions (Robin BC)

We consider first an acoustic bottom halfspace characterized by a single wave speed  $c_{pb}$  and a density  $\rho_b$ . The general solution in the halfspace is given by,

$$\Psi_{HS}(z) = Ae^{-\gamma_b z} + Be^{\gamma_b z}, \quad (5.224)$$

where

$$\gamma_b = \sqrt{k^2 - \frac{\omega^2}{c_{pb}^2}}, \quad (5.225)$$

and the Pekeris branch of the square root is used to expose the leaky modes. In order to have a bounded solution at infinity, we require  $B$  to vanish. At the interface, we require continuity of pressure and normal displacement which implies

$$\Psi(D) = A e^{-\gamma_b D}, \quad (5.226)$$

$$\Psi'(D) = -A \gamma_b e^{-\gamma_b D}. \quad (5.227)$$

Thus, we obtain the bottom impedance condition

$$\Psi(D) + \frac{\rho_b}{\gamma_b} \Psi'(D) = 0. \quad (5.228)$$

A similar procedure yields the result for a top homogeneous halfspace

$$\Psi(D) - \frac{\rho_t}{\gamma_t} \Psi'(D) = 0, \quad (5.229)$$

which differs by a sign change. Note that by letting  $\rho \rightarrow 0$  we obtain the free-surface boundary condition and  $\rho \rightarrow \infty$  gives the perfectly rigid boundary condition.

#### 5.10.4.4 Elastic Halfspace Conditions

The solution for a homogeneous elastic medium is given in terms of P and S-wave potentials,  $\phi$  and  $\psi$  respectively. For a bounded solution these potentials take the form:

$$\phi(z) = A e^{-\gamma_p z}, \quad \psi(z) = B e^{-\gamma_s z}, \quad (5.230)$$

where

$$\gamma_p = \sqrt{k^2 - \frac{\omega^2}{c_{pb}^2}}, \quad \gamma_s = \sqrt{k^2 - \frac{\omega^2}{c_{sb}^2}}. \quad (5.231)$$

In terms of these potentials, the elastic displacements are given by

$$u = \phi_x - \psi_z, \quad w = \phi_z + \psi_x. \quad (5.232)$$

So in terms of  $u$  and  $w$  we can write the most general form of the halfspace solution as:

$$\begin{bmatrix} u \\ w \end{bmatrix} = \begin{bmatrix} ik & -\gamma_s ik \\ -\gamma_p & -k^2 \end{bmatrix} \begin{bmatrix} A \\ B \end{bmatrix}. \quad (5.233)$$

Recall,

$$(r_1, r_2) = \left( \frac{u}{ik}, w \right) \quad (5.234)$$

and from (5.199) we obtain

$$r_3 = \mu(r'_1 + r_2), \quad (5.235)$$

$$r_4 = (\lambda + 2\mu)r'_2 - k^2\lambda r_1, \quad (5.236)$$

so that the most general solution in the lower halfspace is

$$\begin{bmatrix} r_1 \\ r_2 \\ r_3 \\ r_4 \end{bmatrix} = \begin{bmatrix} 1 & \gamma_s \\ -\gamma_p & -k^2 \\ -2\mu\gamma_p & -\mu(\gamma_s^2 + k^2) \\ \mu(\gamma_s^2 + k^2) & 2\mu\gamma_s k^2 \end{bmatrix} \begin{bmatrix} A \\ B \end{bmatrix}. \quad (5.237)$$

Taking the columns of the above matrix as two linearly-independent solutions and substituting into the the definitions of  $\mathbf{y}$  in (5.213) we obtain the following boundary conditions,

$$\begin{bmatrix} y_1 \\ y_2 \\ y_3 \\ y_4 \\ y_5 \end{bmatrix} = \begin{bmatrix} (\gamma_s\gamma_p - k^2)/\mu \\ [(\gamma_s^2 + k^2)^2 - 4\gamma_s\gamma_p k^2]\mu \\ 2\gamma_s\gamma_p - \gamma_s^2 - k^2 \\ \gamma_p(k^2 - \gamma_s^2) \\ \gamma_s(\gamma_s^2 - k^2) \end{bmatrix}. \quad (5.238)$$

Note that the classical dispersion relation for Rayleigh waves is obtained by taking the free-surface condition  $y_2 = 0$ . In addition, one may show that within the interval generating trapped modes,  $y_2$  and  $y_4$  are monotonic functions of the wavenumber, allowing the Prüfer results from Sect. 5.8 to be used to identify the modes.

### 5.10.5 Numerical Example

As an example of the role of shear we consider a simple shallow-water case with a downward-refracting sound-speed profile as depicted in Fig. 5.19. The source frequency is 50 Hz. The sediment overlays a faster basement that is eventually terminated at a depth of 600 m by a perfectly rigid boundary. First, we consider the case where shear in the sediment is neglected. The  $\tau_{zz}$  component of selected modes is shown in Fig. 5.20a. Recall, that pressure is just the negative of  $\tau_{zz}$ .

For the most part these modes resemble those of a purely acoustic problem. However, mode 2 is a Scholte wave with energy mostly confined at the sediment–basement interface as discussed previously in Sect. 4.10.1. The phase speed of these Scholte waves is generally about 0.85 times the minimum shear-wave speed. Mode 3 shows characteristics of both a Scholte wave and a body wave in the ocean medium.

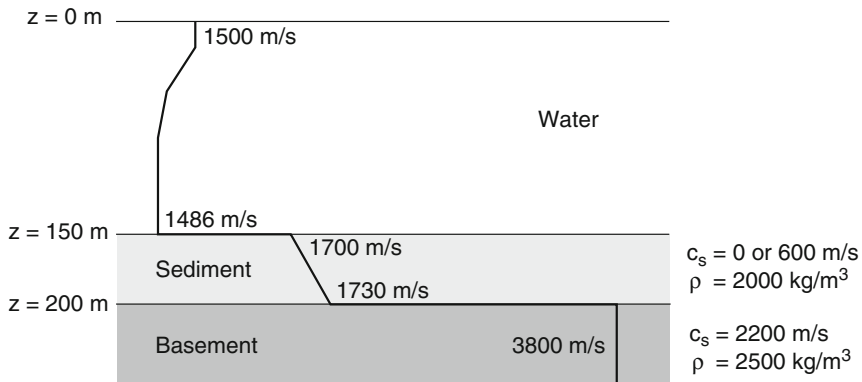


Fig. 5.19 Shallow-water test environment with layered elastic bottom

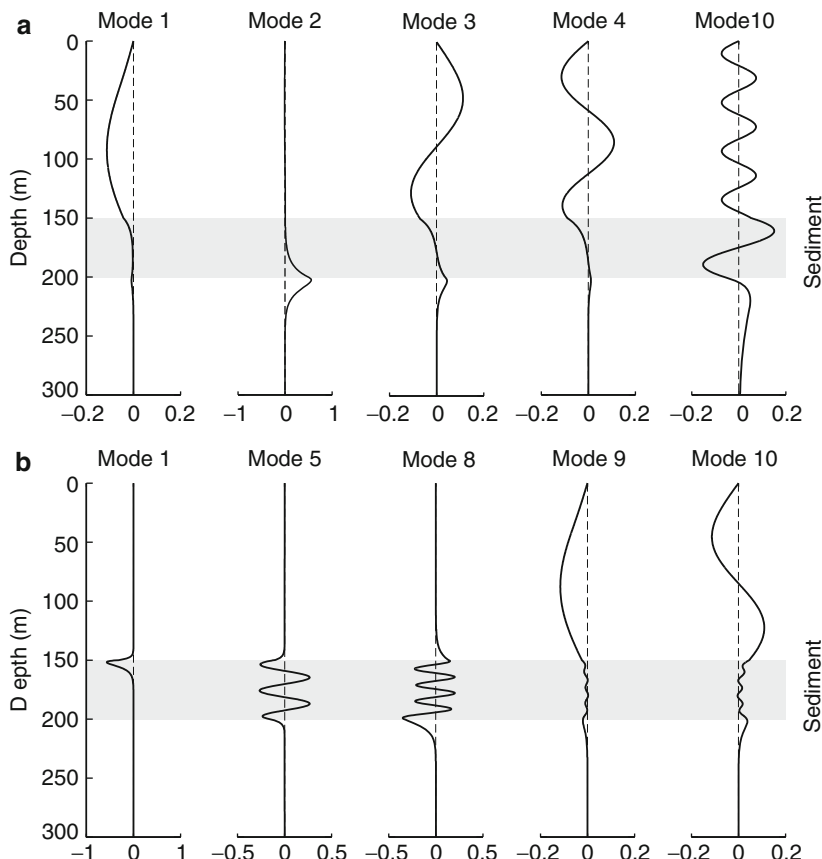
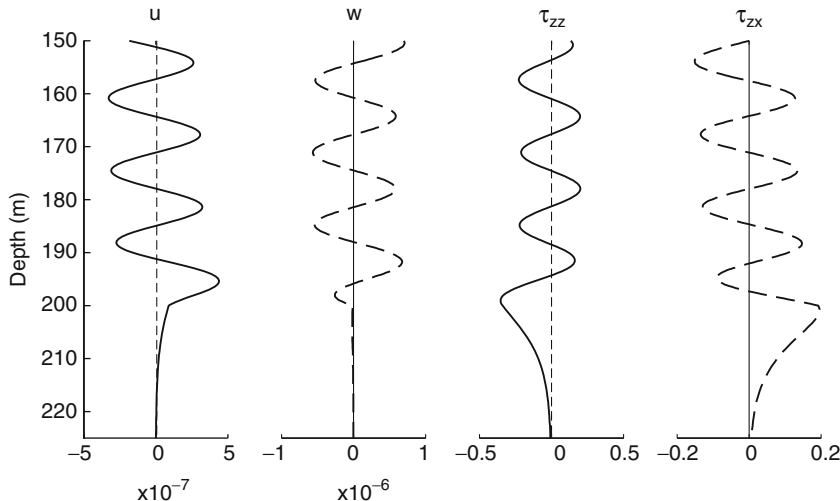


Fig. 5.20 Selected modes at 50 Hz for layered elastic bottom. (a) Sediment without shear, (b) Sediment with a shear speed of 600 m/s. The  $\tau_{zz}$  component is displayed



**Fig. 5.21** All components of the stress–displacement vector for mode 8 with the layered elastic bottom

In Fig. 5.20b, we have included the shear waves in the sediment layer. Mode 1 has the character of a Scholte wave with energy confined to a layer around the water–sediment interface. Modes 5 and 8 are part of a whole family of new modes that are trapped in the sediment layer. Modes 9 and 10 in this case with shear, compare to modes 1 and 3 respectively from the case without shear.

Such modes can be displayed in various ways. The full stress-displacement vector within the elastic layers is shown in Fig. 5.21. The real and imaginary parts of these complex vectors are plotted with a solid and dashed line, respectively. Note that the  $u$  and  $\tau_{zz}$  components are purely real, while the  $w$  and  $\tau_{zx}$  components are purely imaginary as anticipated by (5.195) that defines the  $\mathbf{r}$ -vector in terms of scaled values of these components. However, one may also find modes that have mixed real and imaginary parts, and complex wavenumbers. Furthermore, if we introduce attenuation into the problem then all the modes will have both real and imaginary parts.

For vector sensors, the stress–displacement vector is usually the key interest. Such components could also be calculated within the water column since the stress displacements can be derived from the pressure vector. The stress–displacement vector can also be converted to equivalent P and S-wave potentials.

## 5.11 Normal Modes for Range-Dependent Environments

We tend to think of normal-mode models as primarily suitable for range independent problems, however, it is in principle easy to extend them to provide range-dependent solutions. One way of doing this is to divide the range axis into a number of

segments and approximate the field as range independent within each segment. The solution within a range-independent segment is constructed using the standard normal-mode solution and interface conditions (continuity of pressure and radial velocity) are then used to “glue” the solutions together.

This coupled-mode approach is straightforward but leads to a computationally intensive procedure. For this reason it is, at least at the present, primarily used for providing a reference solution for checking simpler approximate models such as the PE techniques discussed in Chap. 6. After developing the coupled-mode solution we will go on to explore two successive simplifications in which we ignore (1) the backscattered component of the field and (2) coupling between different-order modes at the segment interfaces – the “adiabatic” approximation. These approximations are frequently a reasonable compromise between accuracy and run time.

### 5.11.1 Coupled Modes

Following the derivation by Evans [42], we begin by dividing the axisymmetric problem into  $N$  segments in range as illustrated in Fig. 5.22. Neglecting contributions from higher-order modes (or the continuous spectrum), the general solution in the  $j$ th segment can be written as

$$p^j(r, z) = \sum_{m=1}^M \left[ a_m^j \widehat{H}1_m^j(r) + b_m^j \widehat{H}2_m^j(r) \right] \Psi_m^j(z), \quad (5.239)$$

where  $\widehat{H}1, 2$  are the following ratios of Hankel functions,

$$\widehat{H}1_m^j(r) = \frac{H_0^{(1)}(k_{rm}^j r)}{H_0^{(1)}(k_{rm}^j r_{j-1})}, \quad (5.240)$$

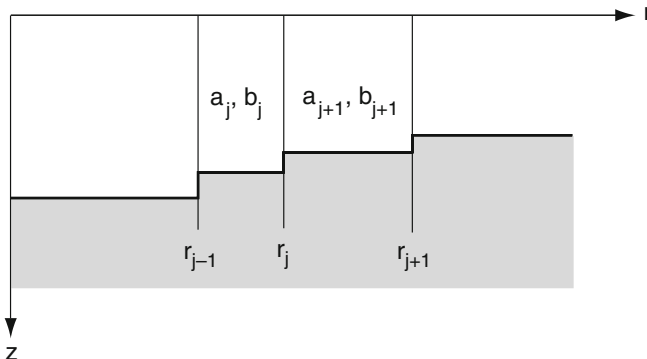


**Fig. 5.22** Range segmentation for coupled-mode formulation

$$\hat{H}2_m^j(r) = \frac{H_0^{(2)}(k_{rm}^j r)}{H_0^{(2)}(k_{rm}^j r_j)} \quad (5.241)$$

and we define  $r_{j-1} = r_1$  in the special case where  $j = 1$ . This scaling of the Hankel functions is done to avoid overflow problems for the leaky modes, which involve growing and decaying exponentials. In practice, it is convenient to replace the Hankel functions by their large-argument asymptotic representation yielding

$$\hat{H}1_m^j(r) \simeq H1_m^j(r) = \sqrt{\frac{r_{j-1}}{r}} e^{ik_{rm}^j(r-r_{j-1})}, \quad (5.242)$$

$$\hat{H}2_m^j(r) \simeq H2_m^j(r) = \sqrt{\frac{r_j}{r}} e^{ik_{rm}^j(r_j-r)}. \quad (5.243)$$

Note that the use of the ranges of the inner and outer boundaries of the segment for normalizing  $H_0^{(1)}$  and  $H_0^{(2)}$ , respectively, is consistent with the numerically stable *Direct Global Matrix* normalization described in Sect. 4.3.1, ensuring that the normalized Hankel functions only involve decaying exponentials inside each segment. We shall use this asymptotic representation in the remainder of the analysis.

Next, we impose continuity of pressure at the  $j$ th interface,

$$\sum_{m=1}^M [a_m^{j+1} + b_m^{j+1} H2_m^{j+1}(r_{j+1})] \Psi_m^{j+1}(z) = \sum_{m=1}^M [a_m^j H1_m^j(r_j) + b_m^j] \Psi_m^j(z). \quad (5.244)$$

This matching condition involves a continuum of depth points in that we require continuity of pressure for all  $z$ -values. In practice, however, we are going to work with a limited mode set and therefore we need a finite set of conditions which relate the  $M$  mode coefficients  $a_m, b_m$ . This can be done in several ways. For instance, we could require continuity of pressure at  $M$  discrete depth points. We shall impose a moment condition that the error considered as a function of depth should have vanishing components of each of the first  $M$  modes. Thus, we apply the operator

$$\int (\cdot) \frac{\Psi_\ell^{j+1}(z)}{\rho_{j+1}(z)} dz \quad (5.245)$$

to our matching equation where  $\ell = 1, \dots, M$ . Because of the orthogonality property

$$\int \frac{\Psi_m^{j+1}(z) \Psi_\ell^{j+1}(z)}{\rho_{j+1}(z)} dz = \delta_{\ell m}, \quad (5.246)$$

where  $\delta_{\ell m}$  is the Kronecker delta, only one term remains from the sum on the left of (5.244). We therefore have

$$a_\ell^{j+1} + b_\ell^{j+1} H2_m^{j+1}(r_{j+1}) = \sum_{m=1}^M [a_m^j H1_m^j(r_j) + b_m^j] \tilde{c}_{\ell m}, \quad \ell = 1, \dots, M, \quad (5.247)$$

where

$$\tilde{c}_{\ell m} = \int \frac{\Psi_{\ell}^{j+1}(z) \Psi_m^j(z)}{\rho_{j+1}(z)} dz. \quad (5.248)$$

In matrix notation, we can write this equation as

$$\mathbf{a}^{j+1} + \mathbf{H}_2^{j+1} \mathbf{b}^{j+1} = \widetilde{\mathbf{C}}^j \left( \mathbf{H}_1^j \mathbf{a}^j + \mathbf{b}^j \right), \quad (5.249)$$

where  $\mathbf{H}_1^j$  and  $\mathbf{H}_2^{j+1}$  denote the diagonal matrices with entries  $H1_m^j(r_j)$  and  $H2_m^{j+1}(r_j)$  respectively. In addition,  $\widetilde{\mathbf{C}}$  is the matrix with entries  $\tilde{c}_{\ell m}$  and  $\mathbf{a}, \mathbf{b}$  are column vectors with entries  $a_{\ell}, b_{\ell}$ , respectively.

We next impose continuity of radial particle velocity. The particle velocity is proportional to

$$\frac{1}{\rho_j} \frac{\partial p^j(r, z)}{\partial r} \simeq \frac{1}{\rho_j} \sum_{m=1}^M k_{rm}^j [a_m^j H1_m^j(r) - b_m^j H2_m^j(r)] \Psi_m^j(z). \quad (5.250)$$

This time we apply the operator

$$\int (\cdot) \Psi_{\ell}^{j+1}(z) dz \quad (5.251)$$

to obtain

$$a_{\ell}^{j+1} - b_{\ell}^{j+1} H2_m^{j+1}(r_j) = \sum_{m=1}^M [a_m^j H1_m^j(r_j) - b_m^j] \hat{c}_{\ell m}, \quad \ell = 1, \dots, M, \quad (5.252)$$

where

$$\hat{c}_{\ell m} = \frac{k_{rm}^j}{k_{rl}^{j+1}} \int \frac{\Psi_{\ell}^{j+1}(z) \Psi_m^j(z)}{\rho_j(z)} dz. \quad (5.253)$$

Note that  $\hat{c}$  differs from  $\tilde{c}$  in the density term of the integral and by a ratio of horizontal wavenumbers.

In matrix notation, this matching condition can be written as

$$\mathbf{a}^{j+1} - \mathbf{H}_2^{j+1} \mathbf{b}^{j+1} = \widehat{\mathbf{C}}^j \left( \mathbf{H}_1^j \mathbf{a}^j - \mathbf{b}^j \right). \quad (5.254)$$

Combining this equation with the pressure-matching (5.249) we can obtain an explicit expression for  $\mathbf{a}^{j+1}$  and  $\mathbf{b}^{j+1}$ ,

$$\begin{bmatrix} \mathbf{a}^{j+1} \\ \mathbf{b}^{j+1} \end{bmatrix} = \begin{bmatrix} \mathbf{R}_1^j & \mathbf{R}_2^j \\ \mathbf{R}_3^j & \mathbf{R}_4^j \end{bmatrix} \begin{bmatrix} \mathbf{a}^j \\ \mathbf{b}^j \end{bmatrix}, \quad (5.255)$$

where

$$\begin{aligned}\mathbf{R}_1^j &= \frac{1}{2} (\tilde{\mathbf{C}}^j + \hat{\mathbf{C}}^j) \mathbf{H}_1^j, \\ \mathbf{R}_2^j &= \frac{1}{2} (\tilde{\mathbf{C}}^j - \hat{\mathbf{C}}^j), \\ \mathbf{R}_3^j &= \frac{1}{2} (\tilde{\mathbf{C}}^j - \hat{\mathbf{C}}^j) (\mathbf{H}_2^{j+1})^{-1} \mathbf{H}_1^j, \\ \mathbf{R}_4^j &= \frac{1}{2} (\tilde{\mathbf{C}}^j + \hat{\mathbf{C}}^j) (\mathbf{H}_2^{j+1})^{-1}.\end{aligned}\quad (5.256)$$

Finally, we need to include the boundary condition at  $r = 0$  and a radiation condition as  $r \rightarrow \infty$ . The latter is imposed by requiring that  $b_m^N = 0$ , for  $m = 1, \dots, M$ . The appropriate condition at  $r = 0$  can be shown to be

$$a_m^1 = \frac{i}{4\rho(z_s)} \Psi_m(z_s) H_0^{(1)}(k_{rm}^1 r_1) + b_m^1 \frac{H_0^{(1)}(k_{rm}^1 r_1)}{H_0^{(2)}(k_{rm}^1 r_1)}, \quad m = 1, \dots, M. \quad (5.257)$$

Collecting all of these equations together we obtain a block matrix problem of the following form,

$$\left[ \begin{array}{ccccccccc} \mathbf{I} & -\mathbf{D} & 0 & & & & & & \\ \mathbf{R}_1^1 & \mathbf{R}_2^1 & \mathbf{I} & 0 & & & & & \\ \mathbf{R}_3^1 & \mathbf{R}_4^1 & 0 & \mathbf{I} & & & & & \\ \ddots & \ddots & \ddots & \ddots & & & & & \\ & & & & \mathbf{R}_1^{N-2} & \mathbf{R}_2^{N-2} & \mathbf{I} & 0 & \\ & & & & \mathbf{R}_3^{N-2} & \mathbf{R}_4^{N-2} & 0 & \mathbf{I} & \\ & & & & & & \mathbf{R}_1^{N-1} & \mathbf{R}_2^{N-1} & \mathbf{I} \\ & & & & & & \mathbf{R}_3^{N-1} & \mathbf{R}_4^{N-1} & 0 \end{array} \right] \begin{bmatrix} \mathbf{a}^1 \\ \mathbf{b}^1 \\ \mathbf{a}^2 \\ \mathbf{b}^2 \\ \vdots \\ \mathbf{a}^{N-1} \\ \mathbf{b}^{N-1} \\ \mathbf{a}^N \end{bmatrix} = \begin{bmatrix} \mathbf{s} \\ \mathbf{0} \\ \mathbf{0} \\ \mathbf{0} \\ \vdots \\ \mathbf{0} \\ \mathbf{0} \\ \mathbf{0} \end{bmatrix}, \quad (5.258)$$

where  $\mathbf{D}$  is the diagonal matrix with entries

$$d_{ii} = \frac{H_0^{(1)}(k_{ri}^1 r_1)}{H_0^{(2)}(k_{ri}^1 r_1)} \quad (5.259)$$

and  $\mathbf{s}$  is the column vector with entries

$$s_m = \frac{i}{4\rho(z_s)} \Psi_m(z_s) H_0^{(1)}(k_{rm}^1 r_1). \quad (5.260)$$

Computationally, this approach requires the solution of a whole family of normal-mode problems, one for each range segment, followed by the solution of a large banded, block-linear system. To obtain numerical convergence in cases of continuously varying properties (sloping bottoms, ocean fronts) the range segments

are frequently required to be less than a wavelength, leading to extremely long computation times. Depending on the use of range functions, numerical instabilities can occur. These are analogous to the problems that occur in solving the global equations obtained with wavenumber integration for layered media (see Sect. 4.3). The methods of eliminating the instabilities are also similar to those used for wavenumber integration, see for instance [43]. The *Direct Global Matrix* normalization of the Hankel functions in (5.240) and (5.241) is among the range functions that are unconditionally stable numerically.

Finally, we should also mention that it is possible to formulate the coupled-mode problem in a differential form. In fact, we shall follow this approach in a subsequent section since it leads more naturally to the adiabatic mode approximation. The above development in terms of piecewise range-independent segments may then be viewed as simply one way of solving the coupled differential equations in range.

### 5.11.2 One-Way Coupled Modes

The full two-way coupled-mode formulation allows for interactions between each segment in range and as a result leads to a global problem rather than a marching type of solution provided by, for instance, the parabolic equation. Computation time can be reduced by neglecting these multiple interactions, usually with only a minor degradation in accuracy.

An efficient marching implementation of coupled modes can be done in several ways with different degrees of accuracy. This is discussed in detail by Porter et al. [44]. A good compromise between accuracy and complexity is provided by the *single-scatter* formulation which treats each interface in range as an independent process thus neglecting the higher-order multiple-scattering terms. To derive this form we begin with the matching condition for the  $j$ th interface given in (5.255),

$$\begin{bmatrix} \mathbf{a}^{j+1} \\ \mathbf{b}^{j+1} \end{bmatrix} = \begin{bmatrix} \mathbf{R}_1 & \mathbf{R}_2 \\ \mathbf{R}_3 & \mathbf{R}_4 \end{bmatrix} \begin{bmatrix} \mathbf{a}^j \\ \mathbf{b}^j \end{bmatrix}. \quad (5.261)$$

For the single-scatter approximation, the incoming wave in the left segment is assumed to be given, and we require that the solution is purely outgoing in the right segment, i.e.,  $\mathbf{b}^{j+1} = \mathbf{0}$ . Solving for the backscattered amplitudes  $\mathbf{b}^j$  yields

$$\mathbf{b}^j = -\mathbf{R}_4^{-1} \mathbf{R}_3 \mathbf{a}^j. \quad (5.262)$$

Therefore, the forward-scattered amplitudes  $\mathbf{a}^{j+1}$  are given by

$$\mathbf{a}^{j+1} = (\mathbf{R}_1 - \mathbf{R}_2 \mathbf{R}_4^{-1} \mathbf{R}_3) \mathbf{a}^j, \quad (5.263)$$

which is an explicit equation for the forward-scattered field.

For problems where backscattering is important, the marching, single-scatter solution can be performed sequentially in a scattering-series approach, first in the

outgoing direction, then in the backscattering direction, and so on, until the solution has converged. For all practical purposes only one backward propagation marching is required. Section 5.13.3 provides an example of this approach using the two-way marching scheme for solving the three-dimensional mode coupling around a circular seamount [45]. Thus, while backscattering in most cases can be ignored for 2-D problems, the coupled mode formulation of the out-of-plane forward scattering around a circular seamount inherently involves both incoming and outgoing components of the modal field.

In practice, an *approximate single-scatter* solution works nearly as well. This solution is obtained by neglecting lower-order terms in the single-scatter recursion,

$$\mathbf{a}^{j+1} = \mathbf{R}_1 \mathbf{a}^j. \quad (5.264)$$

It can be shown that the matrix  $\mathbf{R}_1$  is an arithmetic mean of coupling matrices based on pressure matching and velocity matching.

### 5.11.3 The Adiabatic Approximation

Even though the one-way coupled-mode approach discussed in the previous section provides a significant speed-up in execution time, it may still be too time consuming for many practical applications. For this reason a further approximation is often invoked in which one neglects the cross-coupling terms which allow energy from one mode to transfer into other modes. Instead, one assumes that in going from one range to the next the modes will couple *adiabatically*, i.e., without any transfer of energy to higher or lower modes. This approximation was introduced into underwater acoustics by Pierce [46] based on analogous results for the Schrödinger equation. Our derivation follows Pierce's, however we note that a somewhat more formal derivation is given by Weinberg and Burridge [47].

To derive this approximation, we return to the Helmholtz equation in cylindrical coordinates,

$$\frac{\rho}{r} \frac{\partial}{\partial r} \left( \frac{r}{\rho} \frac{\partial p}{\partial r} \right) + \rho \frac{\partial}{\partial z} \left( \frac{1}{\rho} \frac{\partial p}{\partial z} \right) + \frac{\omega^2}{c^2(r, z)} p = -\frac{\delta(r) \delta(z - z_s)}{2\pi r}. \quad (5.265)$$

Since the modes form a complete set, we can represent the solution at any range as a sum of local modes. We, therefore, seek a solution of the range-dependent problem in the form

$$p(r, z) = \sum_m \Phi_m(r) \Psi_m(r, z), \quad (5.266)$$

where  $\Psi_m(r, z)$  are the local modes defined by

$$\rho(r, z) \frac{\partial}{\partial z} \left[ \frac{1}{\rho(r, z)} \frac{\partial \Psi_m(r, z)}{\partial z} \right] + \left[ \frac{\omega^2}{c^2(r, z)} - k_{rm}^2(r) \right] \Psi_m(r, z) = 0. \quad (5.267)$$

Thus, at any range  $r$ ,  $\Psi_m(r, z)$  is found by solving the depth-separated modal equation with the environmental properties at that range. Substituting in the Helmholtz equation yields

$$\sum_m \frac{\rho}{r} \frac{\partial}{\partial r} \left( \frac{r}{\rho} \frac{\partial(\Phi_m \Psi_m)}{\partial r} \right) + \sum_m k_{rm}^2(r) \Phi_m \Psi_m = -\frac{\delta(r) \delta(z - z_s)}{2\pi r}, \quad (5.268)$$

where we have used (5.267) to eliminate the  $z$ -derivatives. Rearranging terms leads to

$$\begin{aligned} & \sum_m \left[ \frac{\rho}{r} \frac{\partial}{\partial r} \left( \frac{r}{\rho} \frac{\partial \Phi_m}{\partial r} \right) \Psi_m + 2 \frac{\partial \Phi_m}{\partial r} \frac{\partial \Psi_m}{\partial r} + \frac{\rho}{r} \frac{\partial}{\partial r} \left( \frac{r}{\rho} \frac{\partial \Psi_m}{\partial r} \right) \Phi_m \right] \\ & + \sum_m k_{rm}^2(r) \Phi_m \Psi_m = -\frac{\delta(r) \delta(z - z_s)}{2\pi r}. \end{aligned} \quad (5.269)$$

For simplicity we now assume that  $\rho$  is independent of  $r$ . Then we can apply the operator

$$\int (\cdot) \frac{\Psi_n(r, z)}{\rho} dz \quad (5.270)$$

and because of the orthogonality property many of the terms in the sum will disappear. The result is

$$\frac{1}{r} \frac{d}{dr} \left( r \frac{d\Phi_n}{dr} \right) + \sum_m 2B_{mn} \frac{d\Phi_m}{dr} + \sum_m A_{mn} \Phi_m + k_{rn}^2(r) \Phi_n = -\frac{\delta(r) \Psi_n(0, z_s)}{2\pi r}, \quad (5.271)$$

where

$$A_{mn} = \int \frac{1}{r} \frac{\partial}{\partial r} \left( r \frac{\partial \Psi_m}{\partial r} \right) \frac{\Psi_n}{\rho} dz, \quad (5.272)$$

$$B_{mn} = \int \frac{\partial \Psi_m}{\partial r} \frac{\Psi_n}{\rho} dz. \quad (5.273)$$

Note that  $B_{mn} = -B_{nm}$ , since differentiating

$$\int \frac{\Psi_m(z) \Psi_n(z)}{\rho(z)} dz = \delta_{mn} \quad (5.274)$$

gives

$$\int \frac{\partial \Psi_m(z)}{\partial r} \frac{\Psi_n(z)}{\rho(z)} dz + \int \frac{\Psi_m(z)}{\rho(z)} \frac{\partial \Psi_n(z)}{\partial r} dz = 0. \quad (5.275)$$

Equation (5.271) is a statement of coupled modes written for the case of continuous variation of sound speed. It can be solved directly by, for instance, finite differences. The adiabatic approximation can now be stated simply as the assumption

that the coupling matrices  $A_{mn}$  and  $B_{mn}$  are negligible. (Some authors retain the diagonal terms  $A_{nn}$  which alters the results slightly.) We then obtain a set of *decoupled* equations,

$$\frac{1}{r} \frac{d}{dr} \left( r \frac{d\Phi_n}{dr} \right) + k_{rn}^2(r) \Phi_n = -\frac{\delta(r) \Psi_n(0, z_s)}{2\pi r}, \quad (5.276)$$

which in the WKB approximation has the solution

$$\Phi_n(r) \simeq A \frac{e^{i \int_0^r k_{rn}(r') dr'}}{\sqrt{k_{rn}(r) r}}. \quad (5.277)$$

The value of  $A$  is found by requiring that the WKB solution matches our standard solution, (5.13), when the problem is range independent. Thus,

$$A = \frac{i}{\rho(z_s) \sqrt{8\pi}} e^{-i\pi/4} \Psi_n(0, z_s). \quad (5.278)$$

By substituting this results back into (5.266), we obtain the final result,

$$p(r, z) \simeq \frac{i}{\rho(z_s) \sqrt{8\pi r}} e^{-i\pi/4} \sum_{m=1}^{\infty} \Psi_m(0, z_s) \Psi_m(r, z) \frac{e^{i \int_0^r k_{rm}(r') dr'}}{\sqrt{k_{rm}(r)}}. \quad (5.279)$$

In practice, the eigenfunctions and eigenvalues are normally calculated at a discrete set of ranges: values at intermediate ranges are then calculated by linear interpolation. Note that the adiabatic form is sensitive to the polarity of the modes; that is, if one flips the sign of  $\Psi_m(r, z)$  at some particular range, the computed pressure is changed. Therefore, care must be taken that the modes are polarized in a consistent fashion in range.

An unfortunate aspect of this particular adiabatic approximation is that it fails to satisfy reciprocity. This is a consequence of the assumption that the environment is azimuthally symmetric about the source. Thus, when we exchange source and receiver we are also implicitly changing the environment to make it azimuthally symmetric about the new source position. These effects are discussed in [48, 49]. A reciprocal formulation can be derived by assuming the environmental is invariant with respect to translations perpendicular to the radial connecting the source to the receiver. The result is

$$p(r, z) \simeq \frac{i}{\rho(z_s) \sqrt{8\pi}} e^{-i\pi/4} \sum_{m=1}^{\infty} \Psi_m(0, z_s) \Psi_m(r, z) \frac{e^{i \int_0^r k_{rm}(r') dr'}}{\sqrt{k_{rm}(0) k_{rm}(r) \int_0^r \frac{1}{k_{rm}(r')} dr'}}. \quad (5.280)$$

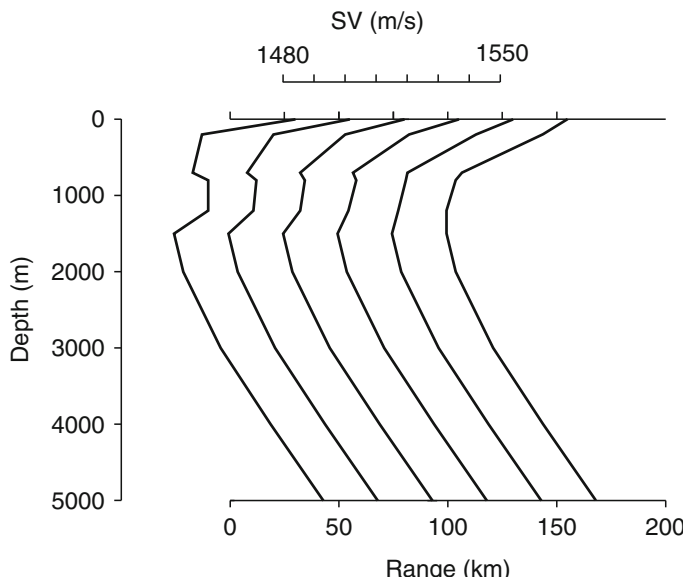
To decide which of these forms to use, one must decide whether a translationally or rotationally symmetric model better characterizes the true ocean around the source point. However, in practice there is usually not much difference between the two cases.

### 5.11.4 Example: A Warm-Core Eddy

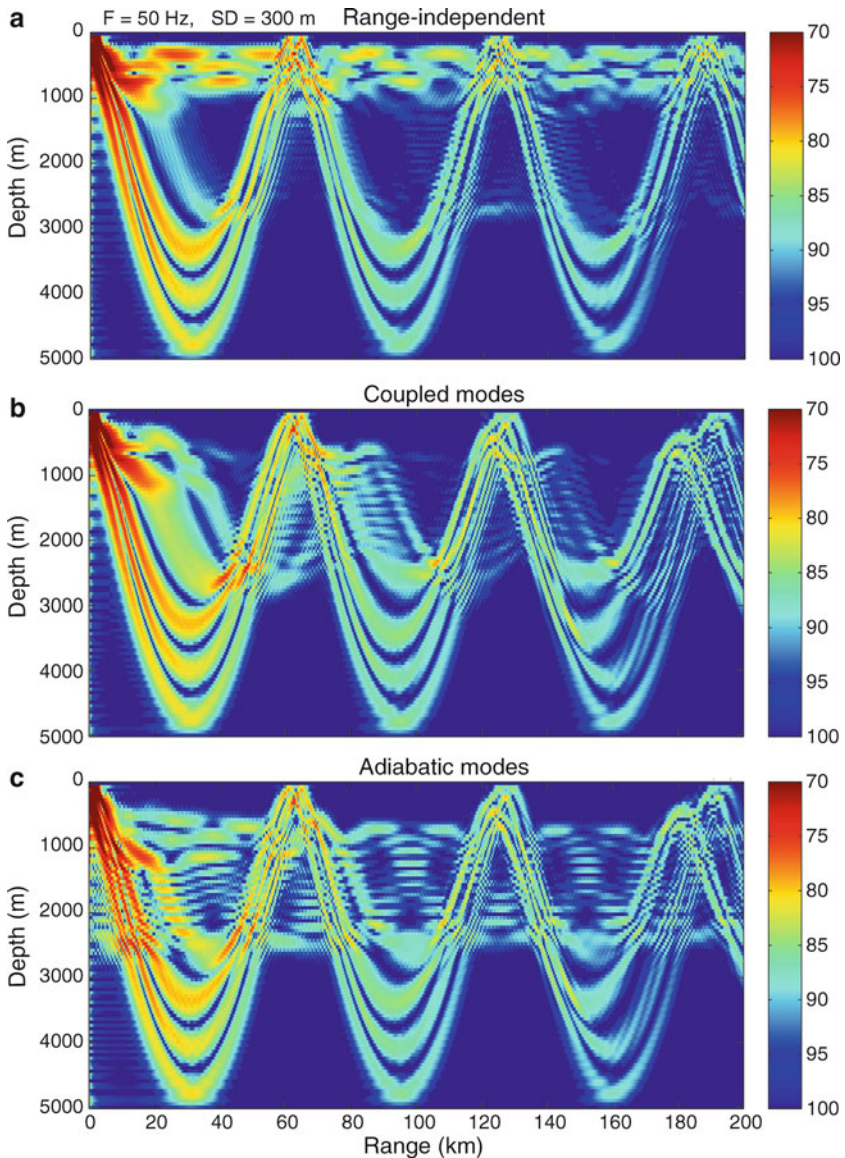
Range dependence can be due to both bathymetric variations (seamounts, continental slopes) and variations in material properties (oceanographic features such as fronts and eddies or changes in bottom type). We consider here a flat-bottom problem involving an eddy in deep water. The actual sound-speed profiles are shown in Fig. 5.23. The warm-core eddy which is centered at roughly 1000 m depth and at zero range (axisymmetric problem), shows up as a zone of increased sound speed.

Figure 5.24 shows plots of the transmission loss obtained with (a) range independent normal modes using the first sound-speed profile throughout, (b) coupled-mode theory using all profiles, and (c) adiabatic mode theory using all profiles. The source frequency is 50 Hz and the source depth is 300 m. The range-independent calculation in Fig. 5.24a shows deep-cycling convergence-zone paths. A band of energy is also seen to propagate in the duct which is roughly centered at the source depth in the first profile.

The one-way coupled mode calculation in Fig. 5.24b shows that as the duct disappears in range the energy passes into the main SOFAR duct. The result is a great increase in transmission loss for a receiver located at, for instance, 100 m depth. Thus, in this particular case a range-independent calculation would almost certainly be considered inadequate. The faster adiabatic calculation shown in Fig. 5.24c provides an intermediate result in terms of accuracy: it correctly shows the transition of energy from the near-surface duct into the main SOFAR duct but fails to reproduce the details of the pattern. Whether this result would be considered adequate depends on the application.



**Fig. 5.23** Sound-speed profiles through the eddy



**Fig. 5.24** Transmission loss for the eddy problem using (a) range-independent, (b) coupled, and (c) adiabatic mode theory

The adiabatic approximation provides accurate predictions when the range dependence is sufficiently weak. What constitutes “weak” range-dependence is a question which has been addressed in numerous papers but is difficult to answer in any general sense. In some cases, the adiabatic approximation provides very

poor results. An interesting example of such a problem is obtained by introducing a seamount into our eddy problem. If the seamount is placed in the shadow zone between 100 and 150 km then the convergence zone paths will pass over it unaffected. If the seamount is placed in the insonified area centered at 90 km, then the convergence zone paths will reflect off the seamount and be displaced in range. However, past the seamount the adiabatic formula depends only on the integral of the wavenumbers and is therefore *insensitive* to the location of the seamount. Despite these problems, the adiabatic approximation is frequently a very useful approach, especially in shallow-water problems where a lack of knowledge about bottom properties imposes a more severe limit on the attainable accuracy.

## 5.12 Scattering from Objects in a Waveguide

The scattering from an object or a target in a waveguide field can be thought of as a mode coupling problem in which the coupling coefficients are related to both the object and its position in the waveguide. In this section, we present Ingenito's [50] solution to this scattering problem which is based on this mode-coupling premise. Thus, the central idea behind the approach is to ultimately formulate the scattering of an incident waveguide field given by (5.13) off an object by representing the object by its plane-wave scattering function. The object is taken to be in an imaginary isovelocity vertical cylinder so that the modal wave field within the cylinder can be represented by a set of plane waves. The incident amplitudes of the plane waves are determined by continuity of pressure and normal particle velocity at the water-column imaginary-cylinder interface. The scattered field is computed using a plane-wave scattering function and then the continuity conditions are invoked again to determine the scattered modal field. We start by constructing the expression for the plane-wave scattering function. Next, we use Green's theorem to place an object in the waveguide as described above. From there we compute the object-generated modal coupling. To be consistent with [50] we use velocity potential  $\phi$ , as defined by (2.17).

### 5.12.1 Scattering Geometry

The problem of a sphere in a waveguide will be considered though the results will ultimately be extended to an object of arbitrary shape and composition whose scattering properties can be described by a farfield plane-wave scattering function. As shown in Fig. 5.25, the surface and bottom of the waveguide is at  $z = -D$  and  $z = H - D$ , respectively; the center of the spherical object is taken at the origin. The source is at  $(x_0, y_0, z_0)$ ; the field point is at  $(x, y, z)$  while a point on the surface of the sphere is  $(x', y', z')$ . We will also use spherical coordinates  $(R, \theta, \varphi)$  with

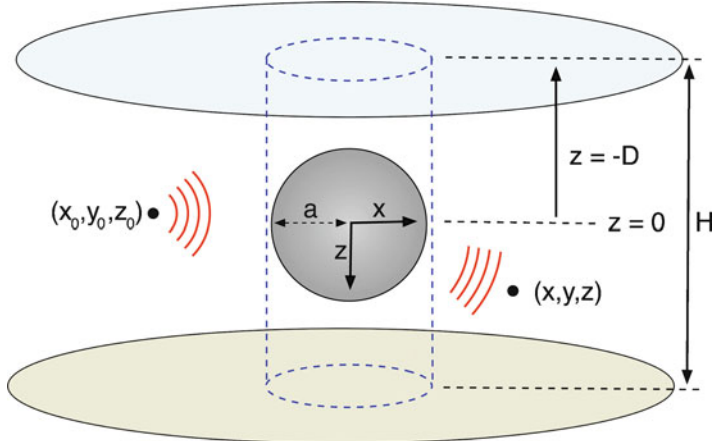


**Fig. 5.25** Geometry of scattering from sphere in a waveguide of depth  $H$ . The origin is taken at the center of the sphere and  $z$  is positive in the downward direction so that the ocean surface is at  $z = -D$  and the ocean bottom at  $z = H - D$ . Relative to the Cartesian coordinate system, we also use spherical coordinates  $(R, \theta, \varphi)$  and cylindrical coordinates  $(r, \varphi, z)$ . The dashed-line “imaginary” cylinder is a constant sound speed region used for the purpose of matching the modal field with plane waves in the immediate vicinity of the scatterer

$R = \sqrt{x^2 + y^2 + z^2}$  and with  $\theta$  defined as the grazing angle meaning the complement of the standard polar angle measured with respect to the  $z$ -axis and cylindrical coordinates  $(r, \varphi, z)$  with  $r = \sqrt{x^2 + y^2}$ , both systems consistent with the above Cartesian system.

### 5.12.2 The Plane-Wave Scattering Function

The coordinate system is shown in Fig. 5.25. The plane-wave scattering function  $S(\theta, \varphi; \theta_0, \varphi_0)$  for an incident field  $\phi_i = e^{ik\mathbf{R}}$  is defined for the farfield in free space through the relation of the total field  $\phi$ ,

$$\phi(\mathbf{R}) = \phi_i(\mathbf{R}) + \phi_s(\mathbf{R}) \quad (5.281)$$

and

$$\phi_s(\mathbf{R}) = \frac{e^{ikR}}{kR} S(\theta, \varphi; \theta_0, \varphi_0), \quad (5.282)$$

where the field point is  $(r, \theta_m, \varphi)$  and the argument of the function  $S$  is

$$\cos \beta = \sin \theta \sin \theta_0 + \cos \theta \cos \theta_0 \cdot \cos(\varphi - \varphi_0), \quad (5.283)$$

which is the cosine of the angles between the directions  $(\theta_m, \varphi)$  and  $(\theta_{m'}, \varphi_0)$ , the incident and scattered directions, respectively. Note that [51] uses a quantity called *scattered amplitude*,  $\phi_s \equiv S/k$ .

Applying Green's theorem as given by (2.63) over an infinite spherical region in which there are no sources but an incoming plane wave, it turns out that the surface integral over the sphere at infinity gives the incident wave so that we are just left with a surface integral over the object [51],

$$\phi(\mathbf{R}) = \phi_i(\mathbf{R}) + \int_{A'_{\text{object}}} \left\{ G(\mathbf{R}, \mathbf{R}') \frac{\partial \phi(\mathbf{R}')}{\partial \mathbf{n}'} - \phi(\mathbf{R}') \frac{\partial G(\mathbf{R}, \mathbf{R}')}{\partial \mathbf{n}'} \right\} dA', \quad (5.284)$$

where

$$\phi_i(\mathbf{R}') = e^{-ikR'\eta(\theta_0, \varphi_0)}, \quad (5.285)$$

$$G(\mathbf{R}, \mathbf{R}') = \frac{1}{4\pi} \left( \frac{e^{ik|\mathbf{R}-\mathbf{R}'|}}{|\mathbf{R}-\mathbf{R}'|} \right) \xrightarrow{R \gg R'} \frac{1}{4\pi} \left( \frac{e^{ik[R-R'\eta(\theta, \varphi)]}}{R} \right) \quad (5.286)$$

and

$$\eta(\theta, \varphi) = \sin \theta \sin \theta' + \cos \theta \cos \theta' \cos(\varphi - \varphi'). \quad (5.287)$$

We consider the three types of boundary conditions between the fluid and the object that we have most often dealt with in this book. Since  $\phi$  represents the velocity potential, these boundary conditions are

$$\phi = 0, \quad \text{pressure release or "soft" object}, \quad (5.288)$$

$$\frac{\partial \phi}{\partial \mathbf{n}} = 0, \quad \text{rigid object}, \quad (5.289)$$

and the two-fluid boundary conditions (fluid object with different sound speed and density than background fluid) between the background medium (denoted as 1) and object (denoted as 2),

$$\begin{aligned} \rho_1 \phi_1 &= \rho_2 \phi_2, && \text{continuity of pressure,} \\ \frac{\partial \phi_1}{\partial n} &= \frac{\partial \phi_2}{\partial n}, && \text{continuity of normal particle velocity.} \end{aligned} \quad (5.290)$$

If we use the rigid or pressure-release boundary conditions, the first or the second term of the surface integral vanishes, respectively. If we use the two-fluid boundary conditions, we can use (5.281) and (5.290) to rewrite (5.284) in the form

$$\phi_s(\mathbf{R}) = \int_{A'_{\text{object}}} \left\{ G(\mathbf{R}, \mathbf{R}') \frac{\partial [\phi_i(\mathbf{R}) + \phi_s(\mathbf{R})]}{\partial \mathbf{n}'} - [\phi_i(\mathbf{R}) + \phi_s(\mathbf{R})] \frac{\partial G(\mathbf{R}, \mathbf{R}')}{\partial \mathbf{n}'} \right\} dA'. \quad (5.291)$$

We now substitute the farfield versions (5.285) and (5.286) into (5.291) and obtain

$$\begin{aligned} \phi_s(\mathbf{R}) = \frac{1}{4\pi} \frac{e^{ikR}}{R} \int_{A'_{\text{object}}} & \left\{ e^{-ikR'\eta(\theta,\varphi)} \frac{\partial}{\partial n'} \left[ e^{-ikR'\eta(\theta_0,\varphi_0)} + \phi_s(\mathbf{R}') \right] \right. \\ & \left. - \left[ e^{-ikR'\eta(\theta_0,\varphi_0)} + \phi_s(\mathbf{R}') \right] \frac{\partial}{\partial n'} e^{-ikR'\eta(\theta,\varphi)} \right\} dA', \end{aligned} \quad (5.292)$$

where  $\phi_s(\mathbf{R}')$  is determined by the boundary conditions as per (5.288), (5.289) or (5.290). Comparing (5.282) with (5.292) we can write down the general expression for the scattering function,

$$\begin{aligned} S(\theta, \varphi; \theta_0, \varphi_0) = \frac{k}{4\pi} \int_{A'_{\text{object}}} & \left\{ e^{-ikR'\eta(\theta,\varphi)} \frac{\partial}{\partial n'} \left[ e^{-ikR'\eta(\theta_0,\varphi_0)} + \phi_s(\mathbf{R}') \right] \right. \\ & \left. - \left[ e^{-ikR'\eta(\theta_0,\varphi_0)} + \phi_s(\mathbf{R}') \right] \frac{\partial}{\partial n'} e^{-ikR'\eta(\theta,\varphi)} \right\} dA'. \end{aligned} \quad (5.293)$$

Using the above boundary conditions, the scattering functions for the soft and rigid objects, are given by the first and second terms of the integral, respectively,

$$S_s(\theta, \varphi; \theta_0, \varphi_0) = \frac{k}{4\pi} \int_{A'_{\text{object}}} e^{-ikR'\eta(\theta,\varphi)} \frac{\partial}{\partial n'} \left[ e^{-ikR'\eta(\theta_0,\varphi_0)} + \phi_s(\mathbf{R}') \right] dA', \quad (5.294)$$

$$S_r(\theta, \varphi; \theta_0, \varphi_0) = -\frac{k}{4\pi} \int_{A'_{\text{object}}} \left[ e^{-ikR'\eta(\theta_0,\varphi_0)} + \phi_s(\mathbf{R}') \right] \frac{\partial}{\partial n'} e^{-ikR'\eta(\theta,\varphi)} dA', \quad (5.295)$$

where  $\phi_s(\mathbf{R}')$  is determined by the above boundary conditions.

The evaluation of any of these scattering integrals is quite involved, even for simple spheres or cylinders [51, 52]. For example, for the case of an infinite cylinder of radius  $a$  whose axis goes through the origin and is perpendicular to the incoming plane wave, the latter is expanded into cylindrical waves and the scattered field is represented as a series of outgoing cylindrical waves. Then the appropriate boundary conditions are applied to determine the amplitudes of the outgoing cylindrical waves in the series expansion for the scattered field. The procedure is the same for the sphere except the expansions are in terms of spherical waves. For the more general case of complex-shaped and/or internally-structured targets, the modeling requires numerical methods such as the Finite Difference or Finite Element methods, as described in Chap. 7. However, these methods are rarely practical for treating both propagation and scattering problems due to the vastly different scales,

and the methodology described here for the coupling of the target scattering to the waveguide propagation physics therefore applies equally to complex targets treated numerically. Such hybrid methods are described in detail in Sect. 7.4.5.

### 5.12.3 Scattering from Spherical Objects in a Waveguide

We want to describe the waveguide scattered field in terms of the plane-wave scattering function that was derived in the last section. We start with Ingenito's example of a rigid sphere in the water column of a waveguide using Green's theorem to provide guidance on how to develop the theory using a plane-wave scattering function. The boundary condition at the surface of the rigid sphere is

$$\left. \frac{\partial \phi(\mathbf{R})}{\partial \mathbf{n}} \right|_{R=a} = 0. \quad (5.296)$$

Applying Green's theorem as given by (2.63) to a large volume containing both the source,  $f = \delta(\mathbf{r}' - \mathbf{r}_0)$ , and the sphere, we obtain, as per (2.60),

$$\begin{aligned} \phi(\mathbf{R}) &= \int_{V'} \delta(\mathbf{R}' - \mathbf{R}_0) G(\mathbf{R}, \mathbf{R}') dV' \\ &\quad + \int_{A'_{\text{object}}} \left[ G(\mathbf{R}, \mathbf{R}') \frac{\partial \phi(\mathbf{R}')}{\partial \mathbf{n}'} - \psi(\mathbf{R}') \frac{\partial G(\mathbf{R}, \mathbf{R}')}{\partial \mathbf{n}'} \right] dA', \end{aligned} \quad (5.297)$$

where we note that since we are in a waveguide, we have the added complication of cylindrical coordinates being the most convenient system but the sphere's boundary condition is most easily described in spherical coordinates. As shown in Fig. 5.25, the origin of our coordinate system is at the center of the sphere and the ocean surface is at  $z = -D$ . Then, if we take the bounding surfaces to be the surface of the sphere, the ocean surface, and a surface at infinite depth where the waveguide field vanishes, the surface integral part of (5.297) reduces to surface integrals over the ocean-air and sphere surfaces. Since the volume integral is the waveguide Green's function for a source at  $\mathbf{r}_0$  [as given by (5.13)], it can be denoted as simply the incident field  $\psi_i(\mathbf{R})$ . Further, the surface integral vanishes at the ocean surface where both the Green's function and the total field vanish. The surface integral then needs only to be evaluated at the surface of the sphere for which the derivative of the field vanishes as per (5.296). Writing the total field as

$$\phi(\mathbf{r}) = \phi_i(\mathbf{R}) + \phi_s(\mathbf{R}), \quad (5.298)$$

we then have that the incident and the scattered fields are given by

$$\phi_i(\mathbf{R}) = \frac{i}{4\rho_0} \sum_m \Psi_m(z) \Psi_m(z_0) H_0^{(1)}(k_{rm} |\mathbf{r} - \mathbf{r}_0|), \quad (5.299)$$

$$\phi_s(\mathbf{R}) = \int_{S'_\text{sphere}} \phi(\mathbf{R}') \frac{\partial G(\mathbf{R}, \mathbf{R}')}{\partial \mathbf{n}'} dA' \quad (5.300)$$

and the Green's function by

$$G(\mathbf{R}, \mathbf{R}') = \frac{i}{4\rho_0} \sum_m \Psi_m(z) \Psi_m(z_0) H_0^{(1)}(k_{rm} |\mathbf{r} - \mathbf{r}'|). \quad (5.301)$$

Our goal now is to expand the incident wave into a set of plane waves and the scattered field into a set of spherical waves. Then, we will be able to express the waveguide scattered field as a sum of terms related to the scattering functions derived in Sect. 5.12.2. Let us assume that just the spherical object is circumscribed by a vertical cylinder such that the source and field points are outside this cylinder. Further, we assume that the sound speed is constant within this cylinder so that in this region the modes are sine functions, (5.82), and can be written as

$$\Psi(z) = N_m \left[ e^{ik_{zm}(z+D)} + e^{-ik_{zm}(z+D)} \right], \quad (5.302)$$

where

$$k_{zm} = \sqrt{\frac{\omega^2}{c^2} - k_{rm}^2}, \quad (5.303)$$

and  $N_m$  is the normalization constant. For a waveguide with a depth-dependent sound speed profile, the modes are nearly plane waves in the vicinity of the object so that using the appropriate mode functions and wavenumbers is still a good approximation.

Assuming the object is far from the source, we can use the asymptotic form of the Hankel function, (2.39), in (5.299). Then, together with (5.302), we get that the incident field in the region near the sphere is a sum of up- and down-traveling plane waves for each mode. We then can use the same formulation in this region as developed in Sect. 5.12.2 for plane-wave scattering provided that we express the Green's function, and the incoming and scattered fields, in terms of spherical waves. This method becomes tractable only if the scattered field is restricted to outgoing spherical waves which translates to a single-scatter approximation. After the boundary condition at the surface of the sphere is invoked and the surface integral is carried out, the field is once again expressed in a cylindrical coordinate system in terms of modes and Hankel functions found in the solution to the waveguide. Further, the symmetry of the scattering function for a spherical object is also used:

$$\begin{aligned} S(-\theta_m, \varphi; \theta_{m'}, \varphi_0) &= S(\theta_m, \varphi; -\theta_{m'}, \varphi_0), \\ S(-\theta_m, \varphi; -\theta_{m'}, \varphi_0) &= S(\theta_m, \varphi; \theta_{m'}, \varphi_0). \end{aligned} \quad (5.304)$$

The result is that the scattered field is given by

$$\begin{aligned}\phi_s(\mathbf{r}) = & \frac{i}{2\rho^2 k} \sum_{m,m'} \frac{\Psi_m(z)\Psi_{m'}(z_0)}{\sqrt{k_{rm} k_{rm'} r r_0}} e^{i(k_{rm}r + k_{rm'}r_0)} N_m N_{m'} \\ & \times \left[ (e^{ik_{zm}D} e^{ik_{zm'}D} + e^{-ik_{zm}D} e^{-ik_{zm'}D}) S(\theta_m, \varphi; \theta_{m'}, \varphi_0) \right] \\ & \times \left[ (e^{ik_{zm}D} e^{-ik_{zm'}D} + e^{-ik_{zm}D} e^{ik_{zm'}D}) S(\theta_m, \varphi; -\theta_{m'}, \varphi_0) \right], \quad (5.305)\end{aligned}$$

where the argument of the scattering function is given by (5.283) and is the cosine of the angle between the incident and scattered waves. From (5.302), the modes are composed of up- and downgoing plane waves with grazing angles  $\theta_m = \pm \arcsin(k_{zm}/k)$ . Further, using (5.302), we can write (5.305) as

$$\begin{aligned}\phi_s(\mathbf{r}) = & \frac{i}{4\rho^2 k} \sum_{m,m'} \frac{\Psi_m(z)\Psi_{m'}(z_0)}{\sqrt{k_{rm} k_{rm'} r r_0}} e^{i(k_{rm}r + k_{rm'}r_0)} \\ & \times \left\{ \left[ \Psi_m(0)\Psi_{m'}(0) - \frac{\Psi'_m(0)\Psi'_{m'}(0)}{k_{zm}k_{zm'}} \right] S(\theta_m, \varphi; \theta_{m'}, \varphi_0) \right. \\ & \left. + \left[ \Psi_m(0)\Psi_{m'}(0) + \frac{\Psi'_m(0)\Psi'_{m'}(0)}{k_{zm}k_{zm'}} \right] S(\theta_m, \varphi; -\theta_{m'}, \varphi_0) \right\}, \quad (5.306)\end{aligned}$$

where we note that the center of the spherical object is at the origin of the coordinate system. Interpreting (5.306), we see that the double sum represents a scattered field that is a redistribution of the modal terms. Each of the four terms in the curly brackets represent the up- or downgoing modal components scattering into up- and downgoing waves with amplitudes determined by the scattering function whose argument depends on the angle between each pair of incident/scattered plane waves. One further simplification expresses the scattered field in a rather transparent modal representation. In a realistic waveguide, the propagating modes represent near-horizontal propagation, i.e.,  $k_{rm} \approx k \rightarrow \theta = 0$ . With this approximation, (5.306) reduces to

$$\phi_s(\mathbf{r}) = \frac{i}{2k} S(0, \varphi; 0, \varphi_0) \sum_m \frac{\psi_m(z)\psi_m(0)}{\sqrt{k_{rm}r}} e^{ik_{rm}r} \sum_{m'} \frac{\psi_{m'}(z_0)\psi_{m'}(0)}{\sqrt{k_{rm'}r_0}} e^{ik_{rm'}r_0}, \quad (5.307)$$

where we have also used the completeness relationship, (5.36). Equation (5.307) now has the simple interpretation that the scattered field emanates from a point source at the center of the sphere with an amplitude that is the product of the incident modal field at that point and the farfield scattering function evaluated at the azimuthal angle between the source and the field point. While we use as an example scattering from a rigid sphere, the formulation is valid for other spherical

objects [52]. For reference purposes, below is the farfield scattering function for a soft and rigid sphere of radius  $a$ ,

$$S_s(\theta_m, \varphi_m; \theta_{m'}, \varphi_{m'}), = i \sum_n \frac{j_n(ka)}{h_n^{(1)}(ka)} (-1)^n (2n+1) P_n(\cos \beta_{mm'}), \quad (5.308)$$

$$S_r(\theta_m, \varphi_m; \theta_{m'}, \varphi_{m'}), = i \sum_n \frac{j'_n(ka)}{h'^{(1)}_n(ka)} (-1)^n (2n+1) P_n(\cos \beta_{mm'}), \quad (5.309)$$

where the arguments of the Legendre polynomials  $P_n$  are determined via (5.283) and the spherical Bessel and Hankel functions are,

$$j_n(x) = \sqrt{\frac{\pi}{2\pi}} J_{n+1/2}(x), \quad (5.310)$$

$$h_n^{(1)}(x) = \sqrt{\frac{\pi}{2\pi}} H_{n+1/2}^{(1)}(x). \quad (5.311)$$

We have here derived the expressions for the modal scattering by targets in an ocean waveguide. However, the analogous expressions for the wavenumber integration representation of the scattering are straightforwardly achieved due the fact that this approach, as described in Chap. 4, is inherently based on a decomposition of the waveguide field into plane or cylindrical wave components, and therefore directly compatible with the plane-wave scattering formulation described here.

The validity of the single-scatter approach for targets near interfaces is obviously an issue, but as shown by Fawcett [53] the approach appears sufficiently accurate for objects buried in sedimentary bottoms. However, the single-scatter approximation may be inadequate when modeling the temporal details of the scattered signals. Here, the late secondary multiples may be of lower amplitude than the primary response, but separated enough in time to provide important classification information. Another related issue, in particular for objects close to the seabed interface, is the treatment of the target as a *point scatterer* which is a key feature of this approach. The validity of this approximation was rigorously addressed by Makris [54] who concluded that the point scatterer approximation for the sphere is valid for ranges in excess of a sphere diameter from the centroid, consistent with the wavenumber integral discussion above.

Figure 5.26 shows the scattering function in (a) the vertical and (b) the horizontal plane, for a 10-m diameter, rigid sphere at mid water depth in a Pekeris waveguide of 100-m depth. The frequency is 1.5 kHz, and the source is placed at 30-m depth and at a range of 500 m. Note that the scattering functions are scaled by -60 dB. Figure 5.27 shows the corresponding scattered acoustic pressure in the waveguide in three different vertical slices through the target at bistatic angles 0°, 45° and 90°.

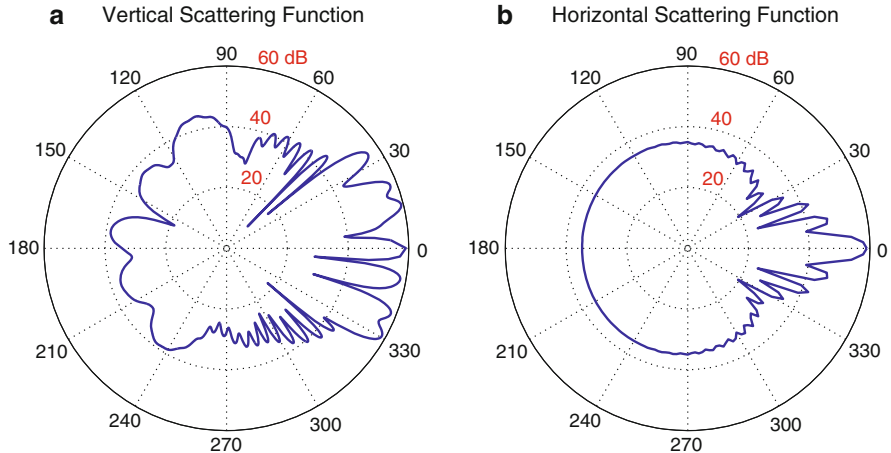


**Fig. 5.26** Scattering function for 10-m diameter, rigid sphere at mid-depth in 100 m deep Pekeris waveguide, insonified by a 1.5-kHz point source at depth 30 m and distance 500 m. The scattering functions are scaled by  $-60 \text{ dB}$ . (a) In-plane vertical scattering function; (b) Horizontal scattering function at target depth

#### 5.12.4 Scattering from Non-Spherical Objects

The scattering from non-spherical objects satisfying any of the above boundary conditions can be derived in the same manner as in Sect. 5.12.3 with the exception that the symmetry properties of the farfield scattering function as expressed by (5.304) cannot be invoked [50]. The scattered field can then be approximated by

$$\phi_s(R) \approx \frac{4\pi}{k} \sum_{m m'} \left\{ A_{m'}(\mathbf{R}_0) [A_m(\mathbf{R}) S(-\theta_m, \varphi; -\theta_{m'}, \varphi_0) - B_m(\mathbf{R}) S(\theta_m, \varphi; -\theta_{m'}, \varphi_0)] - B_{m'}(\mathbf{R}_0) [A_m(\mathbf{R}) S(-\theta_m, \varphi; \theta_{m'}, \varphi_0) - B_m(\mathbf{R}) S(\theta_m, \varphi; \theta_{m'}, \varphi_0)] \right\}, \quad (5.312)$$

where

$$A_m(\mathbf{R}) = \frac{i\Psi_m(z) N_m e^{i(k_{rm}r + k_{zm}D - \pi/4)}}{\rho \sqrt{8\pi k_{rm}r}},$$

$$B_m(\mathbf{R}) = \frac{i\Psi_m(z) N_m e^{i(k_{rm}r - k_{zm}D - \pi/4)}}{\rho \sqrt{8\pi k_{rm}r}}. \quad (5.313)$$

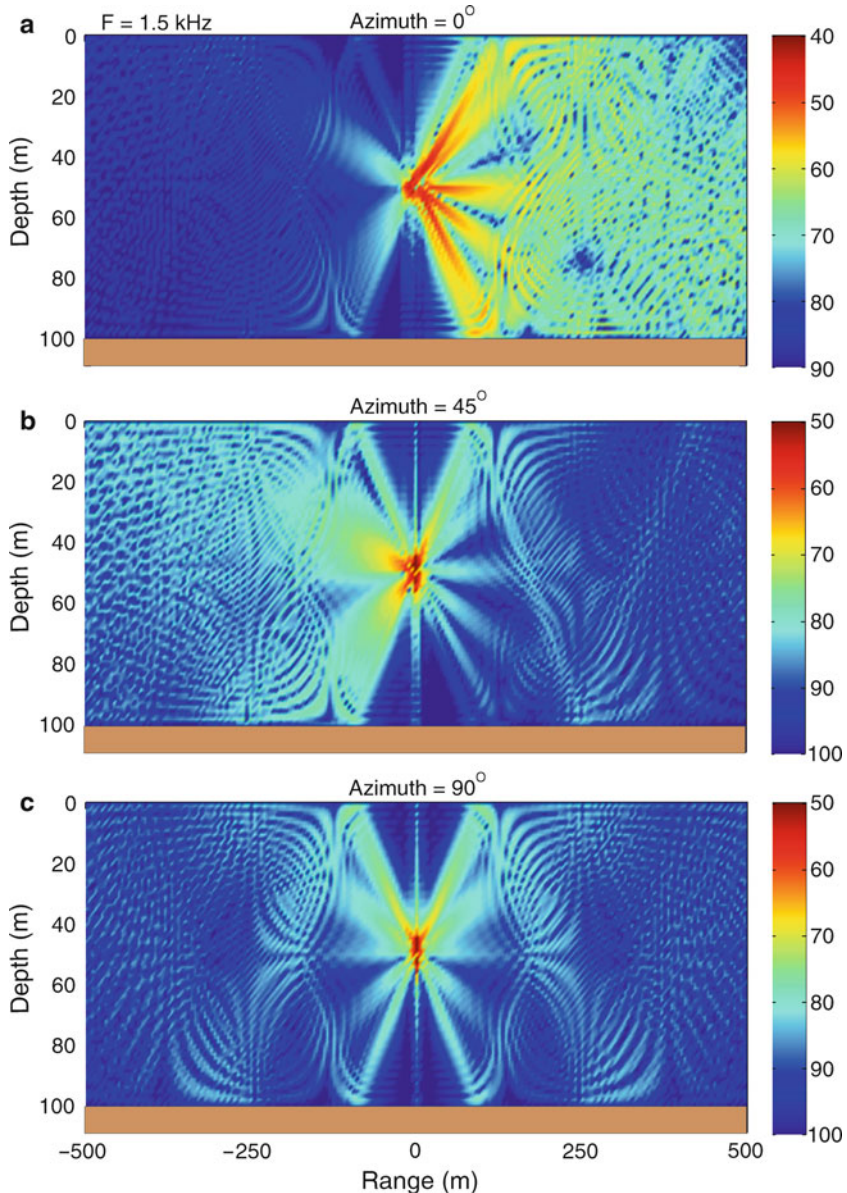


**Fig. 5.27** Scattering from a 10-m diameter, rigid sphere at mid water depth in a Pekeris waveguide. The frequency is 1.5 kHz, and the source is at 30 m depth, 500 m from the target. The three plots show contours of the range-depth dependence of the scattered acoustic field at various azimuthal angles. (a)  $0^\circ$ , with left being the backscatter direction towards the source and the right being forward scatter, (b) Azimuth =  $45^\circ$ , and (c) Azimuth =  $90^\circ$

## 5.13 Normal Modes for 3-D Varying Environments

As with all of the range-dependent 2-D models, a direct extension to 3-D problems is possible by simply running the 2-D models repeatedly along a number of different bearings. Along each bearing one then uses the sound-speed profile and bathymetry for that track. Combining these results along numerous bearings allows one to build-up a 3-D image of the acoustic field, which, however, is just an  $N \times 2$ -D calculation where horizontal refraction has been ignored. The issue of azimuthally-coupled solutions is dealt with in the following sections.

As in the 2-D problem it is convenient to calculate the mode sets on a coarse grid and calculate intermediate values by interpolation. As an example, we consider a scenario in the North Atlantic which encompasses a segment of the Gulf Stream as shown in Fig. 5.28a. The environment is sampled at a number of different points in the  $xy$ -plane and modes are calculated at each of these points. The nodes are then used to construct a triangulation of the environment as shown in Fig. 5.28b. The position of the Gulf stream, two eddies that have spun off from it, and other features of the environment are echoed in the triangulation. (Regular grids are also suitable: they are easier to set up but may require more nodal points to produce an acceptable sampling of the environment.)

Once the modes are calculated and stored, 3-D acoustic fields can be rapidly computed by applying the adiabatic formula in (5.279) along a fan of radials emanating from the source. Where the adiabatic formula requires modes in a triangle, they are computed by bilinear interpolation. An example of this type of calculation is given in Fig. 5.29 where we have plotted transmission loss in the  $xy$ -plane at a constant receiver depth of 400 m. The source depth is also at 400 m and the frequency is 50 Hz. Note how the Gulf Stream casts an acoustic shadow behind it. (In fact, the energy is really just redirected to other depths.) The eddies, in turn, also produce visible perturbations in the transmission-loss field.

### 5.13.1 Horizontal Refraction Equations

The range-dependent 2-D models assume azimuthally-symmetric environments; however we violate this assumption in applying the model with different profiles for each bearing. In practice, this approximation is generally adequate and indeed is normally implicit in a 2-D run of a range-dependent model. That is, we normally use environmental information on a bearing-line between source and receiver, not intending the slice to define an azimuthally-symmetric environment.

In some cases, effects of horizontal refraction must be included. In principle, this is easily done. The derivation follows the pattern developed in the previous section for adiabatic modes in two dimensions. We start with the Helmholtz equation in three dimensions,

$$\rho \nabla \cdot \left( \frac{1}{\rho} \nabla p \right) + \frac{\omega^2}{c^2(x, y, z)} p = -\delta(x) \delta(y) \delta(z - z_s), \quad (5.314)$$

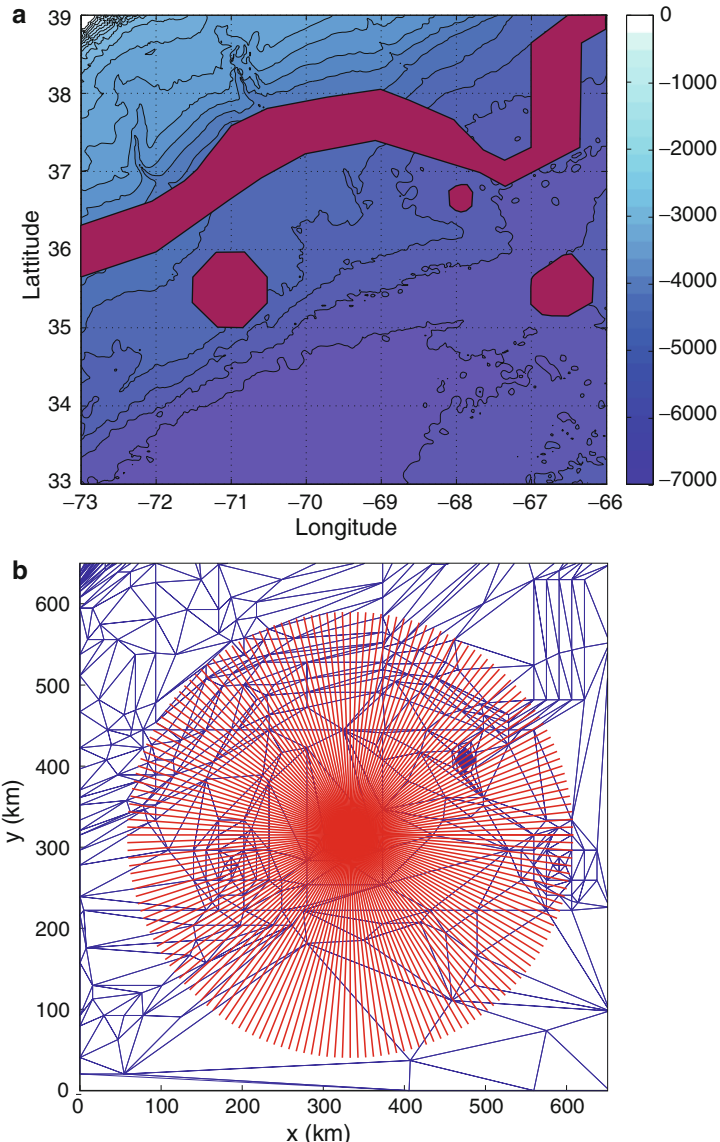


**Fig. 5.28** Gulf Stream environment for 3-D transmission loss calculation. (a) Bathymetry and position of the Gulf Stream and two eddies. (b) Triangulation for the Gulf Stream problem

or, written out in full,

$$\begin{aligned} \rho \frac{\partial}{\partial x} \left( \frac{1}{\rho} \frac{\partial p}{\partial x} \right) + \rho \frac{\partial}{\partial y} \left( \frac{1}{\rho} \frac{\partial p}{\partial y} \right) + \rho \frac{\partial}{\partial z} \left( \frac{1}{\rho} \frac{\partial p}{\partial z} \right) \\ + \frac{\omega^2}{c^2(x, y, z)} p = -\delta(x) \delta(y) \delta(z - z_s). \end{aligned} \quad (5.315)$$

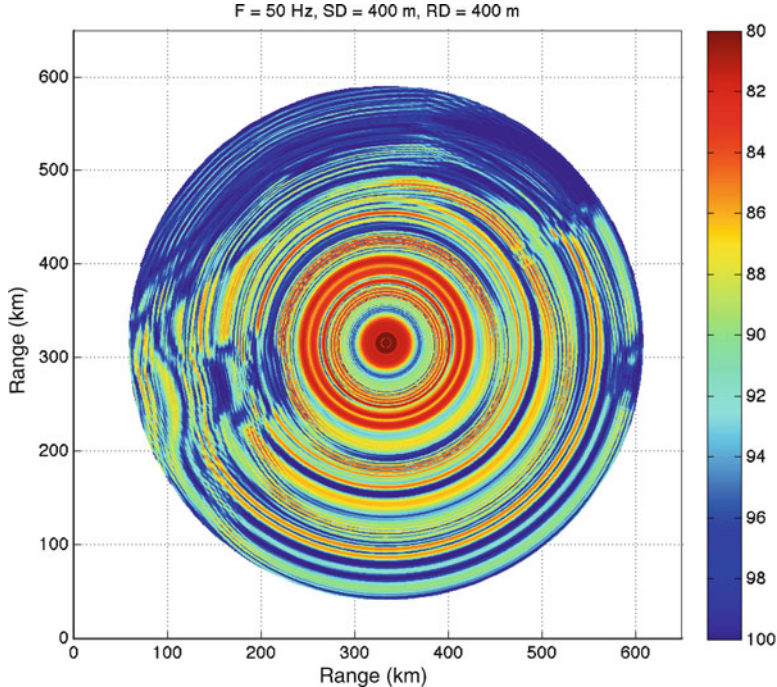


**Fig. 5.29** Transmission loss for the Gulf Stream problem

We next seek a solution of the form

$$p(x, y, z) = \sum_m \Phi_m(x, y) \Psi_m(x, y, z), \quad (5.316)$$

where  $\Psi_m(x, y, z)$  are the local modes. Substituting into the Helmholtz equation and applying the operator

$$\int (\cdot) \frac{\Psi_n(x, y, z)}{\rho} dz, \quad (5.317)$$

yields

$$\begin{aligned} & \frac{\partial^2 \Phi_n}{\partial x^2} + \frac{\partial^2 \Phi_n}{\partial y^2} + k_{rn}^2(x, y) \Phi_n + \sum_m A_{mn} \Phi_m \\ & + \sum_m 2B_{mn} \frac{\partial \Phi_m}{\partial x} + \sum_m 2C_{mn} \frac{\partial \Phi_m}{\partial y} = -\delta(x) \delta(y) \delta(z - z_s), \end{aligned} \quad (5.318)$$

where

$$\begin{aligned} A_{mn} &= \int \left( \frac{\partial^2}{\partial x^2} + \frac{\partial^2}{\partial y^2} \right) \Psi_m \frac{\Psi_n}{\rho} dz, \\ B_{mn} = -B_{nm} &= \int \frac{\partial \Psi_m}{\partial x} \frac{\Psi_n}{\rho} dz, \\ C_{mn} = -C_{nm} &= \int \frac{\partial \Psi_m}{\partial y} \frac{\Psi_n}{\rho} dz. \end{aligned} \quad (5.319)$$

Here, we have assumed that the density  $\rho(z)$  depends only on depth  $z$ . The adiabatic approximation can then be obtained by neglecting the contributions of the coupling matrices  $A$ ,  $B$ , and  $C$ . This yields the horizontal refraction equation

$$\frac{\partial^2 \Phi_n}{\partial x^2} + \frac{\partial^2 \Phi_n}{\partial y^2} + k_{rn}^2(x, y) \Phi_n = -\Psi_n(z_s) \delta(x) \delta(y). \quad (5.320)$$

Using the local normal modes, we have eliminated the  $z$ -dimension from the problem and obtained a new Helmholtz equation, but now in the lateral coordinates  $x$  and  $y$ . The effective index of refraction is given by the horizontal wavenumber  $k_{rn}(x, y)$  so that every mode generates a corresponding Helmholtz equation. Such 2-D Helmholtz equations have been treated earlier in this chapter using normal modes, and in other chapters by ray, spectral integral, and PE methods. These same techniques may be applied also to the horizontal refraction equation. An early solution of the horizontal refraction equations by ray theory was presented by Weinberg and Burridge [47].

There is continuing debate about when it is necessary to include the effects of horizontal refraction. Oceanographic features are certainly capable of inducing refraction as discussed by Baer [55]; however, it appears that the largest effects are due to variations in the bottom topography. Doolittle et al. [56] present experimental evidence of such effects for a path over the East Australian Continental Slope.

In Sect. 5.13.3, it is shown that horizontal refraction can become extremely important in regard to propagation around deep ocean seamounts.

### 5.13.2 Global Propagation

The effects of horizontal refraction are accentuated when very-long-range transmission is considered (implying very high signal levels at the source). An interesting data set involving paths halfway around the world from Perth to Bermuda was considered by Heaney et al. [57]. On this global scale ( $r \simeq 20000$  km) prediction accuracy is closely tied to the available environmental information on bathymetry and sound-speed profiles along the various propagation paths. Moreover, 3-D effects due to Earth curvature and horizontal refraction must be taken into account in order to provide accurate estimates of both travel time and signal dispersion.

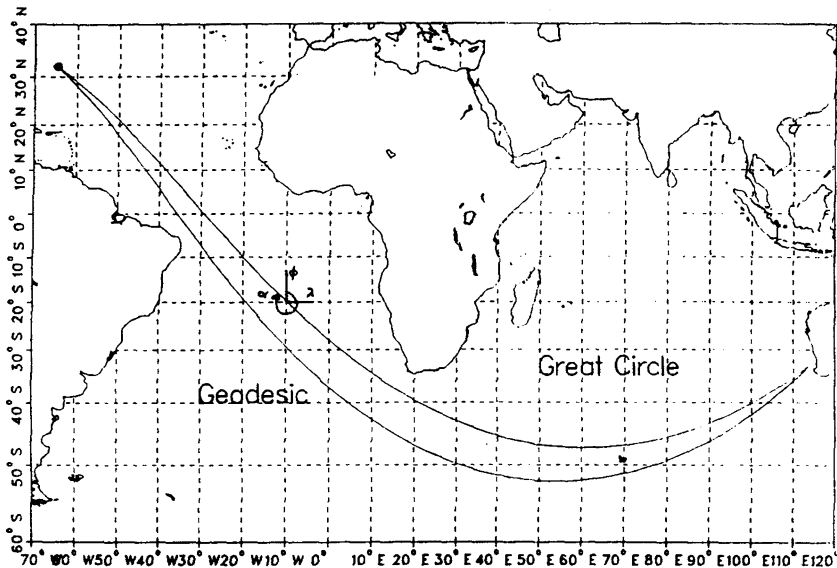


**Fig. 5.30** Shortest paths between Perth and Bermuda for a spherical Earth (great circle) and for an ellipsoidal Earth (geodesic) distorted by rotation (from Heaney et al. [57])

The propagation geometry is shown in Fig. 5.30. The difference between a great-circle path (spherical Earth) and a geodesic path (ellipsoidal Earth) is seen to be very significant. The geodesic path is displaced up to 800 km to the south, thus traversing cold, slow waters near Antarctica. The result is an increased travel time of approximately 30 s compared to the great-circle path. Since the experimental results show a two-pulse arrival structure with the first arrival at  $13364 \pm 5$  s and the second appearing 30–40 s later, we require a modeling accuracy of at least 5–10 s on travel time in order to explain the experimental data. Consequently, the geodesic path associated with the flattened Earth geometry must be invoked.

The modeling of the Perth–Bermuda propagation experiment was done by adiabatic mode theory in the vertical and by ray theory in the horizontal. For a source frequency of 15 Hz (estimated peak energy of received pulse), the modal structure was calculated on the horizontal grid shown as dots in Fig. 5.31. Both sound-speed profiles and bathymetry were available from data bases on the same 230 grid points. Next, a horizontal ray tracing was performed for each mode and for a series of horizontal launch angles to find unobstructed propagation paths from Perth to Bermuda. This ray modeling includes horizontal refraction due both to transverse sound-speed gradients and to bottom interaction near land masses.

Examples of successful mode 1 paths are shown in Fig. 5.31. There are five paths connecting Perth with Bermuda, four paths to the north (group A) and one path almost 1000 km further south (group B). Intermediate rays are blocked by islands. The higher-order modes show exactly the same behavior, with six unobstructed paths for mode 2 (three in A and three in B), and one each for modes 3 and 4.

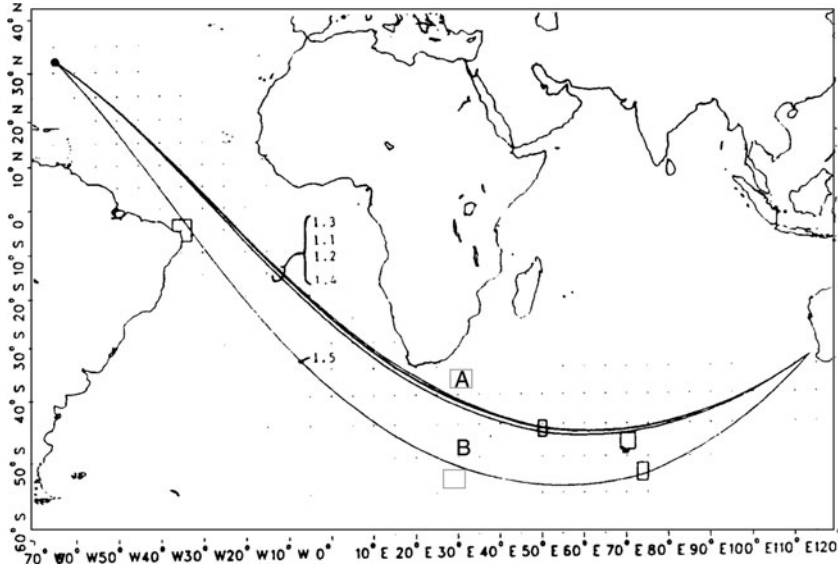


**Fig. 5.31** Five successful mode 1 rays between Perth and Bermuda. Sound-speed profiles are specified on the longitude–latitude grid points shown (from Heaney et al. [57])

The signal *travel time* along a ray is easily found by integrating up the modal group delay given by (5.189),

$$t_m = \int_0^S \frac{\omega}{k_{rm}} \int_0^D \frac{1}{\rho(z)} \left[ \frac{\Psi_m(z)}{c(z)} \right]^2 dz ds. \quad (5.321)$$

Here,  $s$  is the arclength along a ray,  $\omega$  the angular frequency,  $k_{rm}$  the modal eigenvalue,  $\rho$  the water density,  $\Psi_m$  the modal eigenfunction, and  $c$  the sound speed over depth  $z$ .

Figure 5.32 displays the recorded time series at Bermuda from three consecutive explosions near Perth. The horizontal time scale is 25 s per tick mark, while the vertical decibel scale is 10 dB per two tick marks. Note the characteristic double-pulse arrival structure for all three shots. In the upper left inset is shown computed mode arrivals with amplitudes relative to 0-dB bottom loss. First, we see a set of mode 2 arrivals followed by several mode 1 arrivals, all pertaining to the faster group A rays. Approximately 30–40 s later comes the slower (and weaker) group B rays composed again of both mode 2 and mode 1 arrivals. Considering the environmental uncertainties in the data bases used in the calculations, the overall model–data agreement for this global propagation experiment is more than satisfactory.

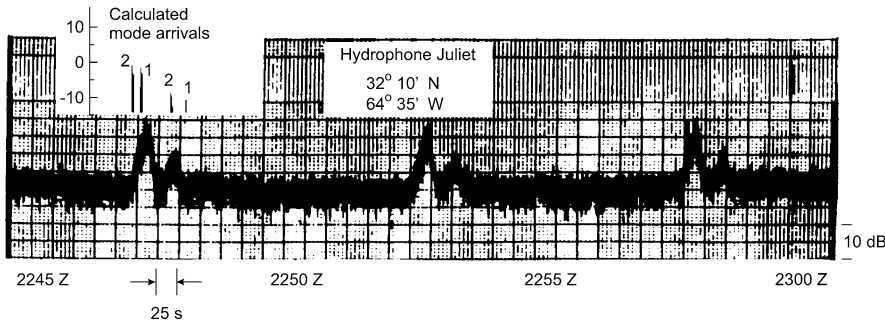


**Fig. 5.32** Data record of 21 March 1960 for three successive 300-lb explosive charges. The *upper left insert* gives arrival times and strengths relative to 0-dB bottom loss for successful mode 1 and mode 2 arrivals (adapted from Heaney et al. [57])

### 5.13.3 3-D Mode Coupling Around Seamounts

The propagation over and around a seamount is inherently a three-dimensional problem, except for the trivial case of the source located at the top of a cylindrically symmetric seamount. With the interest in exploring global propagation for climate monitoring, etc., a significant effort has been invested in the development of adequate numerical models capable of addressing the effect of mid-ocean seamounts on long-range propagation.

A wave-theoretic model of acoustic propagation in the ocean around a conical seamount was first developed by Buckingham [58]. In this model, the surface of the seamount was assumed to be a perfect reflector, with the apex of the seamount reaching the surface of the ocean. This model provided early insight into the phenomenon of azimuthal mode coupling, but the use is rather limited due to the highly idealized geometry and boundary conditions.

A 3-D, coupled-mode solution, based on a cylindrically symmetric inclusion with an asymmetric incident field, was developed by Evans [59] and applied by Fawcett [53] to a single-region, penetrable inclusion. More recently Evans [60] used this coupled-mode model to investigate the interaction of underwater ambient noise with a cylindrically symmetric seamount. Another 3-D coupled-mode solution for a source-generic field around a conical seamount was developed by Taroudakis [61]. However, this formulation becomes numerically unstable for even moderate frequencies and small seamounts.

To allow the modeling of 3-D propagation and scattering around realistic seamounts at relevant frequencies, a spectral coupled-mode model was proposed by Luo and Schmidt [45] for the field generated by an offset acoustic source in an ocean with axisymmetric bathymetry. Based on the same theoretical foundation as the formulation presented by Taroudakis [61], this approach combines a spectral decomposition in azimuth with a coupled-mode theory for two-way,

range-dependent propagation. Numerical stability and high efficiency is achieved by making a number of significant modifications to the theoretical and numerical formulation, leading to orders-of-magnitude improvement in numerical efficiency for realistic problems. Further, by using a standard normal-mode model for determining the fundamental modal solutions and coupling matrices, and by applying a simple superposition principle [45, 62], the computational requirements are made independent of the distance between the seamount and the source and receivers, and dependent only on the geometry of the seamount and the frequency of the source. As a result, realistic propagation and scattering scenarios can then be modeled, including effects of seamount roughness and realistic sedimentary structure.

The 3-D, coupled-mode model has been used to analyze the mode coupling occurring at the edge of a conical seamount, demonstrating that the out-of-plane scattering leads to significantly stronger shadowing behind the seamount than predicted by traditional two-dimensional models.

### 5.13.3.1 Mathematical Formulation

An acoustic source is offset horizontally relative to a conical seamount, as illustrated in Fig. 5.33. This is a 3-D problem in which the acoustic field depends not only on range and depth, but also on azimuth.

In the coupled-mode approach, a number of range-independent ring-shaped sectors are used to approximate such a conical seamount. The notation  $r^j$  is used to denote the range at the vertical interface between sector  $j$  and sector  $j + 1$ , for  $j = 1, 2, \dots, J - 1$ , with  $J$  denoting the total number of sectors, as illustrated in Fig. 5.33.

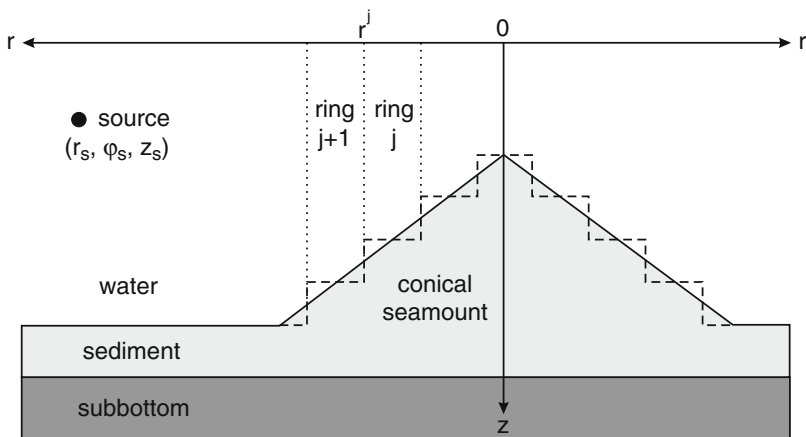


**Fig. 5.33** An ocean waveguide with a conical seamount, which is approximated by a number of range-independent, ring-shaped sectors of different properties

A cylindrical-polar coordinate system is introduced, centered at the axis of the seamount. The location of the point source is denoted by  $\mathbf{r}_s = (r_s, \varphi_s, z_s)$ , and the location of a field point is denoted by  $\mathbf{r} = (r, \varphi, z)$ . The 3-D Helmholtz equation for the field produced by the source, in the outer source ring-shaped sector, is [45, 61],

$$\begin{aligned} \frac{1}{r} \frac{\partial}{\partial r} \left( r \frac{\partial p}{\partial r} \right) + \frac{1}{r^2} \frac{\partial^2 p}{\partial \varphi^2} + \rho(z) \frac{\partial}{\partial z} \left( \frac{1}{\rho(z)} \frac{\partial p}{\partial z} \right) + \frac{\omega^2}{c^2(z)} p \\ = -\frac{\delta(r - r_s)}{r} \delta(z - z_s) \delta(\varphi - \varphi_s), \end{aligned} \quad (5.322)$$

where  $p = p(r, \varphi, z)$  is the acoustic pressure (factoring out the harmonic time dependence  $e^{-i\omega t}$ ,  $\omega$  being the angular frequency), and  $\rho(z)$  and  $c(z)$  are density and sound-speed profiles in the outer source ring-shaped sector, respectively.

In ring-shaped sector  $j$  ( $j = 1, 2, \dots, J - 1$ ), which is a range-independent environment, the density and sound-speed profiles are denoted by  $\rho^j(z)$  and  $c^j(z)$ . The 3-D Helmholtz equation is

$$\frac{1}{r} \frac{\partial}{\partial r} \left( r \frac{\partial p^j}{\partial r} \right) + \frac{1}{r^2} \frac{\partial^2 p^j}{\partial \varphi^2} + \rho^j(z) \frac{\partial}{\partial z} \left( \frac{1}{\rho^j(z)} \frac{\partial p^j}{\partial z} \right) + \frac{\omega^2}{c^{j2}(z)} p^j = 0, \quad (5.323)$$

where  $p^j = p^j(r, \varphi, z)$  is the acoustic pressure in ring-shaped sector  $j$ .

### 5.13.3.2 Spectral Coupled-Mode Solution

The seamount environment is divided into three regions, one being the innermost, cylindrical sector containing the summit of the seamount (region I), one containing all the ring-shaped sectors between the central cylinder and the base of the seamount (region II), and the third being a semi-infinite, ring-shaped sector outside the base of the seamount (region III).

The acoustic field in the external region of the seamount, i.e., region III, is represented as a superposition of the unperturbed field produced by the source in the absence of the seamount, and a scattered field produced by the seamount. This basically reformulates the seamount propagation problem into a scattering problem. Scattering problems are traditionally handled using this fundamental superposition principle of decomposing the total field into its incident and scattered components. Although rather trivial, this reformulation has significant impact on the numerical efficiency. Thus, the number of azimuthal orders required for the Fourier–Neumann expansion of the source field is roughly proportional to the source range [63], while the number of Fourier orders for treating the seamount region depends on the radius of the seamount [45]. This was one of the major reasons for the severe frequency limitations of earlier approaches.

Using  $J$  to denote the total number of sectors,  $r_1$  to denote the range of the base of a seamount, and  $r^j$  to denote the range of the vertical interface between sector  $j$  and sector  $j + 1$ , the two-way normal-mode representation of the pressure field in the three regions is:

*Inner cylinder*,  $r \leq r^1$ ,

$$p^1(r, \varphi, z) = \sum_{m=0}^{\infty} \sum_{n=1}^{\infty} b_{mn}^1 \hat{J}_m(k_{rn}^1 r) \Psi_n^1(z) \Phi_m(\varphi). \quad (5.324)$$

*Intermediate sectors*,  $r^1 < r \leq r_1$ . In sector  $j$ , i.e.,  $r^{j-1} < r \leq r^j$ ,

$$\begin{aligned} p^j(r, \varphi, z) = & \sum_{m=0}^{\infty} \sum_{n=1}^{\infty} \left[ a_{mn}^j \hat{H}_m^{(1)}(k_{rn}^j r) + b_{mn}^j \hat{J}_m(k_{rn}^j r) \right] \\ & \times \Psi_n^j(z) \Phi_m(\varphi). \end{aligned} \quad (5.325)$$

*Outer region* containing the source,  $r > r_1$ ,

$$p(r, \varphi, z) = p_i(r', z) + \sum_{m=0}^{\infty} \sum_{n=1}^{\infty} a_{mn}^J \hat{H}_m^{(1)}(k_{rn}^J r) \Psi_n^J(z) \Phi_m(\varphi), \quad (5.326)$$

where  $r'$  is the range of a field point with respect to the source, and  $p_i(r', z)$  is the two-dimensional (2-D) solution in the absence of the seamount

$$r'(r, \varphi) = \sqrt{r^2 + r_s^2 - 2rr_s \cos(\varphi_s - \varphi)}, \quad (5.327)$$

$$p_i(r', z) = \frac{i}{4} \frac{1}{\rho(z_s)} \sum_{n=1}^{\infty} \Psi_n^J(z_s) \Psi_n^J(z) H_0^{(1)}(k_{rn}^J r'). \quad (5.328)$$

The coefficients  $a_{mn}^j$  and  $b_{mn}^j$  represent the amplitudes of the diverging and converging normal modes of azimuthal order  $m$ . They are determined from a system of equations representing the source, boundary, and radiation conditions at each vertical interface. The fact that these equations are uncoupled azimuthally is a principal key to the efficiency of the spectral approach. Basically, the solution is performed independently at each azimuthal order, with the total scattered field following by Fourier synthesis.  $\Psi_n^j(z)$  are local, depth-dependent mode functions, independent of azimuthal order, satisfying the standard modal orthogonality relation

$$\int_0^{\infty} \frac{1}{\rho^j(z)} \Psi_n^j(z) \Psi_v^j(z) dz = \delta_{nv}, \quad n, v = 1, 2, \dots \quad (5.329)$$

Similarly,  $\Phi_m(\varphi)$  are azimuthal eigenfunctions

$$\Phi_m(\varphi) = e_m \cos[m(\varphi - \varphi_s)], \quad m = 0, 1, \dots \quad (5.330)$$

satisfying the orthogonality relation

$$\int_{-\pi}^{\pi} \Phi_m(\varphi) \Phi_\mu(\varphi) d\varphi = \delta_{m\mu}, \quad m, \mu = 0, 1, \dots \quad (5.331)$$

with  $e_m = \sqrt{1/2\pi}$  for  $m = 0$ , and  $e_m = \sqrt{1/\pi}$  otherwise. The functions  $\widehat{J}_m(k_{rn}^j r)$  and  $\widehat{H}_m^{(1)}(k_{rn}^j r)$  in (5.324)–(5.326) are normalized Bessel and Hankel functions defined as

$$\widehat{J}_m(k_{rn}^j r) = J_m(k_{rn}^j r) H_m^{(1)}(k_{rn}^j r^j), \quad (5.332)$$

$$\widehat{H}_m^{(1)}(k_{rn}^j r) = \frac{H_m^{(1)}(k_{rn}^j r)}{H_m^{(1)}(k_{rn}^j r^{j-1})} \quad (5.333)$$

with  $k_{rn}^j$  denoting the horizontal wavenumber of mode  $n$  in sector  $j$ .

Applying the source condition, the coefficients  $b_{mn}^J$  in the external sector are found as

$$b_{mn}^J = \frac{i}{2} \frac{\Psi_n(z_s)}{\rho(z_s)} \Phi_m(\varphi_s). \quad (5.334)$$

With  $b_{mn}^J$  known, the remaining coefficients, i.e.,  $b_{mn}^j$ ,  $j = 1, \dots, J-1$ , and  $a_{mn}^j$ ,  $j = 1, \dots, J$  can be determined by solving the system of equations representing the boundary conditions at each vertical sector interface. The coefficients do not couple among azimuthal orders, but are found independently for each azimuthal order by solving the coupling equations globally, or using a numerically efficient marching, single-scatter scheme [45]. Once the coefficients are found, the field can be computed everywhere using the modal summations in (5.324)–(5.326).

A realistic mid-ocean seamount problem that can be handled by this spectral coupled mode approach is shown in Fig. 5.34. Two conical seamounts of radius 20 km, and height 1000 and 3800 m, respectively, are insonified by a 10-Hz source at 100-km distance. The water depth is 5000 m, and a Munk sound speed profile is assumed with an axis depth of 1300 m.

Figure 5.35 shows contour plots of the transmission loss in dB in a horizontal plane at 300-m depth. Figure 5.35a is the 3-D spectral coupled-mode solution for the 1000-m tall seamount, while Fig. 5.35b shows the result for the 3800-m tall seamount. Not surprisingly, the taller seamount interacts much more strongly with the cylindrical convergence zone propagation pattern than the lower one, with a significant shadow zone being present behind the seamount.

Figures 5.35c, d show the corresponding results obtained using an  $N \times 2$ -D approach, i.e., utilizing a standard 2-D coupled-mode model along vertical slices over and around the seamount. It is clear that the 2-D model is perfectly capable of capturing the physics of the three-dimensional problem for the low seamount. However, for the taller seamount the difference is dramatic, with a much “deeper” shadow zone behind the seamount when the 3-D modal scattering effects are included. Surprisingly this phenomenon exists even for propagation straight over the summit of

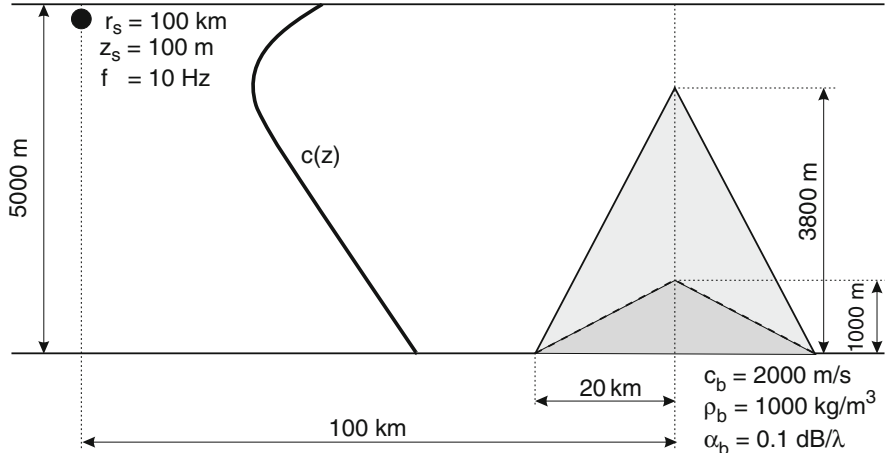


**Fig. 5.34** Seamount propagation and scattering scenario. Conical seamounts of radius 20 km, and height 1000 and 3800 m, respectively, are insonified by a 10-Hz source at 100-km distance. The water depth is 5000 m, and a Munk sound-speed profile is assumed with an axis depth of 1300 m below the sea surface

the seamount, implying the counter-intuitive result that the shadow zone behind a circular seamount is “deeper” than one generated behind an ocean ridge of the same cross-section. This, in turn, suggests that even for the relatively benign slopes associated with the tall seamount, the out-of-plane scattering is significant, refracting the modal energy away from the principal propagation direction over the summit.

A major advantage of the spectral coupled-mode approach is the inherent decomposition of the scattered field into components of physical significance, the azimuthal and vertical normal modes, which allows us to provide a physical interpretation without having to apply any post-processing of the numerical results. Thus, the spectral formulation allows the modeler to directly assess the modal composition of the scattered field versus azimuth around the seamount.

### 5.13.3.3 Azimuthally Scattered Mode Amplitudes

From (5.326), the scattered field in the region outside the base of the seamount is

$$\begin{aligned}
 p_s(r, \varphi, z) &= \sum_{m=0}^{\infty} \sum_{n=1}^{\infty} a_{mn}^J \hat{H}_m^{(1)}(k_{rn}^J r) \Psi_n^J(z) \Phi_m(\varphi) \\
 &= \sum_{n=1}^{\infty} \left[ \sum_{m=0}^{\infty} a_{mn}^J \hat{H}_m^{(1)}(k_{rn}^J r) \Phi_m(\varphi) \right] \Psi_n^J(z). \quad (5.335)
 \end{aligned}$$

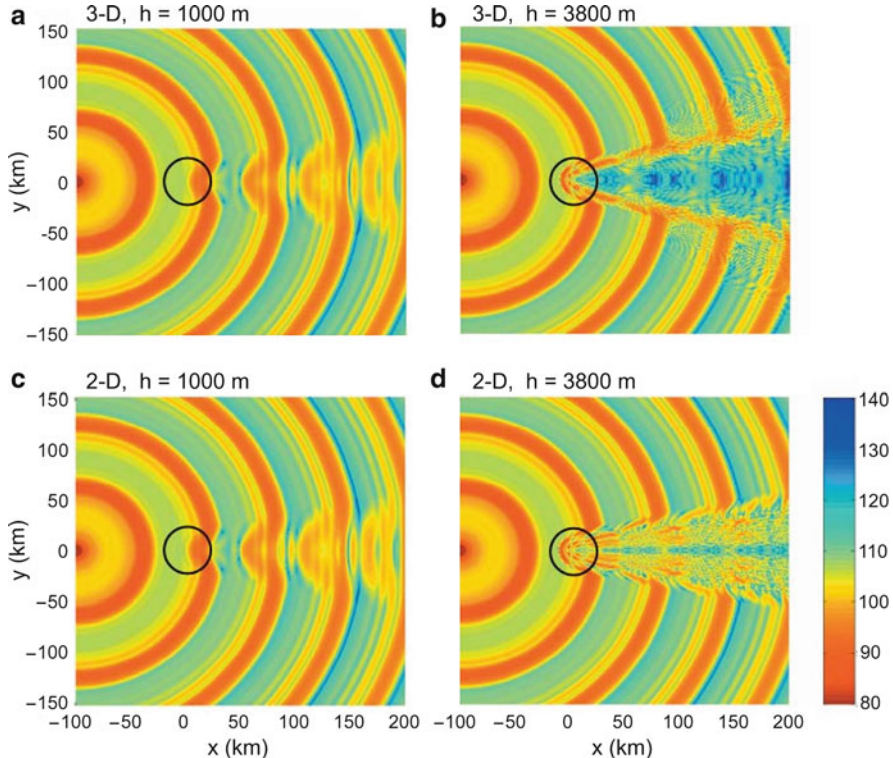


**Fig. 5.35** Transmission loss in dB in a horizontal plane at 300-m depth above a conical seamount of radius 20 km, insonified by a 10-Hz source at 100-km distance from the summit. (a) 1000-m tall seamount, computed using the 3-D spectral coupled mode approach. (b) 3800-m tall seamount, 3-D spectral coupled mode result. (c) 1000-m tall seamount,  $N \times 2$ -D coupled mode result. (d) 3800-m tall seamount,  $N \times 2$ -D coupled mode result [45]

At the boundary of the seamount  $r = r_l$ , we notice that  $\hat{H}_m^{(1)}(k_{rn}^J r_l) = 1$  and, therefore, (5.335) becomes

$$p_s(r_l, \varphi, z) = \sum_{n=1}^{\infty} \left[ \sum_{m=0}^{\infty} a_{mn}^J \Phi_m(\varphi) \right] \Psi_n^J(z). \quad (5.336)$$

The scattered mode amplitude function is defined as

$$A_n(\varphi) = \sum_{m=0}^{\infty} a_{mn}^J \Phi_m(\varphi) \quad (5.337)$$

and  $A_n(\varphi)$  is used to investigate how the energy of an incident mode is coupled into the excited modes at different azimuthal angles, as illustrated in Fig. 5.36.

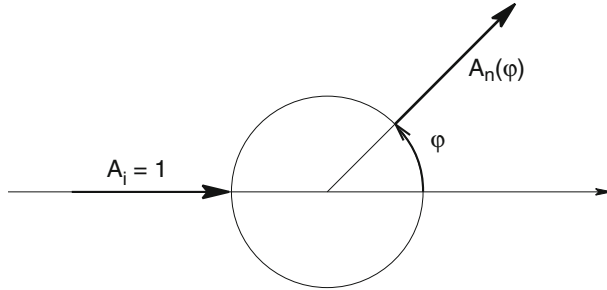


**Fig. 5.36** Top view of seamount problem. A single mode number  $i$  of unit amplitude  $A_i = 1$  is incident from the left, and the amplitudes  $A_n(\varphi)$  of the modes along a radial slice of azimuthal angle  $\varphi$  is a measure of the significance of 3-D mode coupling by the seamount

In the farfield of the seamount, the asymptotic form of the normalized Hankel function in (5.335) is used

$$\hat{H}_m^{(1)}(k_{rn}^J r) \sim \sqrt{\frac{r_1}{r}} e^{ik_{rn}^J(r-r_1)} \quad (5.338)$$

and, therefore, the scattered field by the seamount can be expressed as

$$p_s(r, \varphi, z) \approx \sqrt{\frac{r_1}{r}} \sum_{n=1}^{\infty} \left[ \sum_{m=0}^{\infty} a_{mn}^J \Phi_m(\varphi) \right] \Psi_n^J(z) e^{ik_{rn}^J(r-r_1)} \quad (5.339)$$

or

$$p_s(r, \varphi, z) \approx \sqrt{\frac{r_1}{r}} \sum_{n=1}^{\infty} A_n(\varphi) \Psi_n^J(z) e^{ik_{rn}^J(r-r_1)}, \quad (5.340)$$

which shows that in the farfield, the scattered field by the seamount is equivalent to an azimuthally shaded source with the azimuthal source strength  $A_n(\varphi)$ .

At the base of the seamount  $r = r_1$ , we have  $\hat{H}_m^J(r_1) = 1$ , and (5.335) gives

$$\begin{aligned} p_s(r_1, \varphi, z) &= \sum_{m=0}^{\infty} \sum_{n=1}^{\infty} a_{mn}^J \Psi_n^J(z) \Phi_m(\varphi) \\ &= \sum_{n=1}^{\infty} A_n(\varphi) \Psi_n^J(z), \end{aligned} \quad (5.341)$$

where the amplitude of mode number  $n$  scattered into the azimuthal direction  $\varphi$  is given by (5.337).

A contour plot of the magnitude of  $A_n(\varphi)$  versus azimuthal scattering angle and mode number is a useful tool for determining the amount of mode coupling by the seamount. Thus, Fig. 5.37 shows the result for the two seamount problems defined

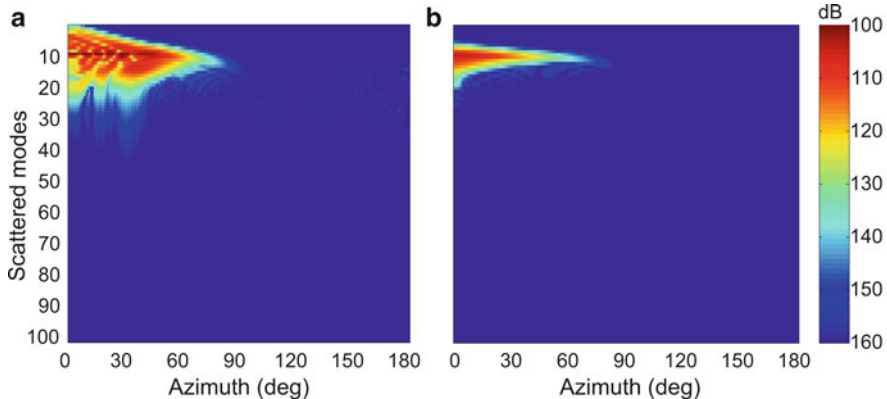


**Fig. 5.37** Contours in dB of scattered mode amplitudes vs. azimuthal angle and mode number for a conical seamount of radius 20 km in a 5000-m deep ocean with a Munk sound-speed profile. The incident field consists of mode 10 only, at 10 Hz. The seamount is represented by 512 ring sectors. The two plots correspond to a seamount of height (a) 3800 m, and (b) 1000 m

in Fig. 5.34. The seamounts are here insonified by mode 10 only. For the Munk profile, mode 10 is evanescent in depth below 4000 m, and therefore only interacts slightly with the 1000-m high seamount, Fig. 5.37b. As a result the vertical and horizontal mode coupling is here significantly less than for the 3800-m high seamount, consistent with the total field results in Fig. 5.35a, b.

It is well-established in two-dimensional, coupled-mode modeling that the discretization step size must be small enough to eliminate artificial backscattering. As shown by Jensen [64], diffraction lobes form when the spacing  $\Delta x$  is larger than  $\lambda/2$ , where  $\lambda$  denotes the wavelength, in particular in the backscatter direction. As a result of that study  $\Delta x \leq \lambda/4$  is considered an appropriate discretization criterion for facet slopes of up to  $60^\circ$ .

Even in cases where backscattering is not of interest, the discretization problem can be severe for the seamount problem. This is due to the fact that the two-way coupling is happening in all azimuthal directions, and reflection artifacts can therefore become an issue even in the forward direction. The number of ring sectors is critical to the numerical efficiency, and for realistic seamounts and relevant frequencies the  $\lambda/4$  criterion will in general prohibit modeling at relevant sonar frequencies. However, by randomizing the discretization, the diffraction lobes can be reduced significantly to yield better approximate solutions with significantly fewer sectors than required by the criterion  $\Delta r < \lambda/2$  (or the even stricter criterion  $\Delta r < \lambda/4$ ).

Again we will use the seamount problem in Fig. 5.34 to illustrate this important numerical modeling issue. The wavelength at 10 Hz is roughly 150 m, so to avoid the diffraction beams, the horizontal step size should be less than 75 m if the uniform horizontal spacing technique is used. If we use 512 sectors,  $\Delta r < \lambda/2$  is satisfied and no artificial diffraction beams are formed, as illustrated in the contour plots of scattered mode amplitudes versus azimuthal angle in Fig. 5.37. The forward scatter

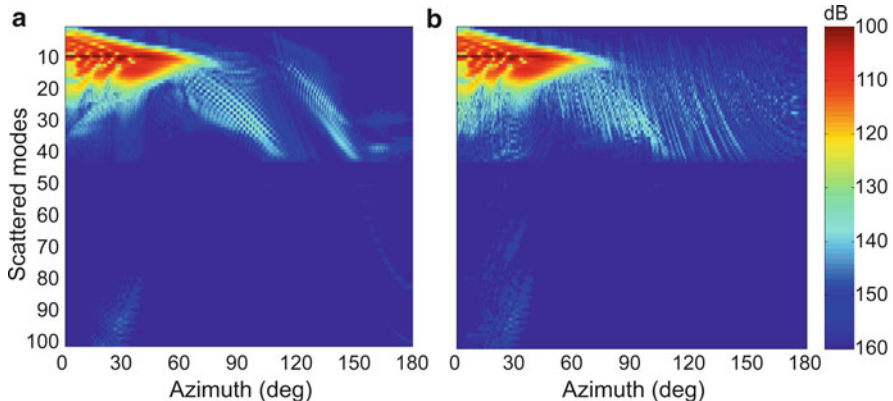


**Fig. 5.38** Contours in dB of scattered mode amplitudes vs. azimuthal angle and mode number for a conical seamount of height 3800 m and radius 20 km in a 5000-m deep ocean with a Munk sound speed profile. The incident field consists of mode 10 only, at 10 Hz. The seamount is here represented by 128 ring sectors. (a) Equidistant sector discretization, (b) Random sector discretization

direction corresponds to azimuthal angle zero, i.e., to the left in the contour plot, and as expected the forward scattering is dominating, with significant normal mode and azimuthal coupling. No diffraction lobes appear for neither the 3800-m tall nor the 1000-m tall seamount.

Figure 5.38a shows the scattered mode amplitude plot using 128 sectors, corresponding to  $\Delta r \approx (4/3)\lambda$ , and by comparison to Fig. 5.37a, it is obvious that two backscattering diffraction lobes have been generated over a wide modal regime. Figure 5.38b shows the corresponding result when the sector discretization is randomized. The reduction in the diffraction lobes is achieved at the cost of an increase in the diffuse backscatter, but one could argue that this is actually a more realistic representation of the seamount than the smooth, idealized representation.

## 5.14 Waveguide Invariant and Dispersion for Realistic Environments

We have already discussed the basic theory for waveguide invariants in Sect. 2.4.6 where the properties of the invariant were introduced in the context of the ideal and Pekeris waveguides. In those cases, the modes correspond to ray paths that reflect but do not refract. In Sect. 3.8.3, we computed invariants using ray methods and included a simple refracting profile and showed that the sign of the invariant  $\beta$  was negative for the refracting case vs. positive for the reflecting cases. Since, the invariant relates group velocity to phase velocity, clearly it represents the most salient aspects of broadband propagation. Straightforward simulation of a

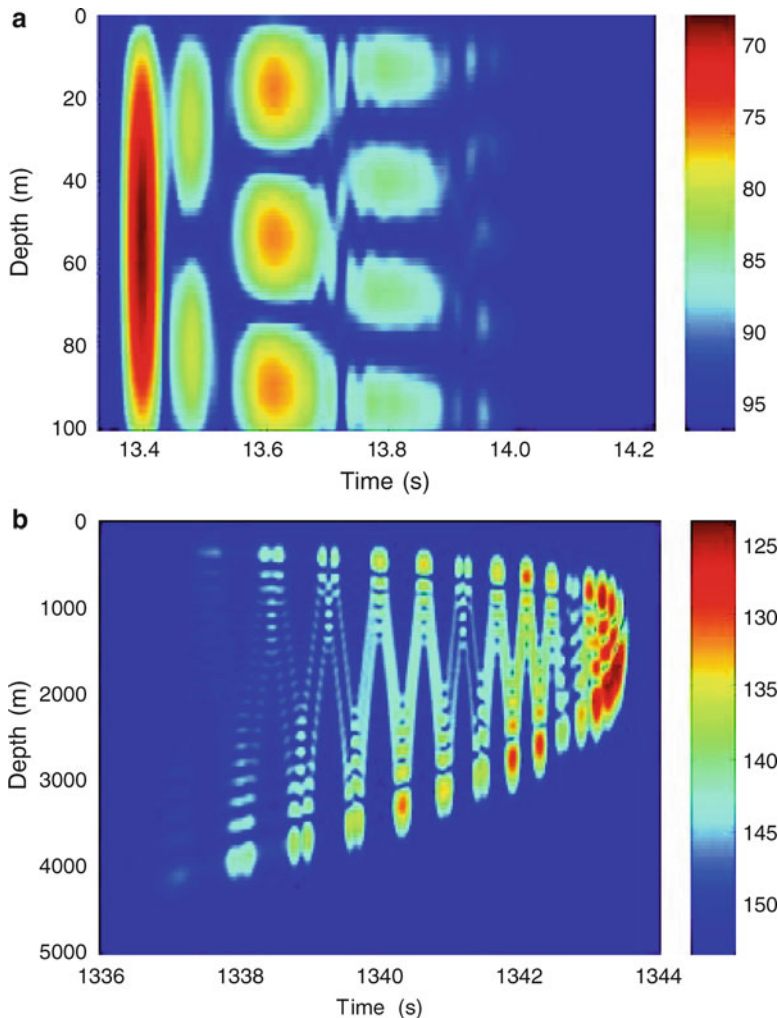


**Fig. 5.39** Pulse propagation. (a) Pulse structure at 20-km range in a shallow-water, 100 m Pekeris waveguide with sound speed of 1500 m/s, and bottom sound-speed and density of 1600 m/s and 1800 kg/m<sup>3</sup>. The bandwidth is 50 Hz, the central frequency is 100 Hz and the source depth is 40 m. The first mode has the fastest group speed and makes up the first arrival at a range of 20 km. (b) Pulse structure at 2000-km range in a deep-water, Munk-profile environment. Source depth is 900 m, source frequency is 22.5 Hz with a 15-Hz bandwidth. All the arrivals shown do not interact with the surface or bottom. For these arrivals, the deep refracted paths, which are made up of higher modes, arrive earlier than the lowest modes propagating near the channel axis

pulse propagating in a Pekeris waveguide and in deep water, as shown in Fig. 5.39, immediately shows the basic features of the propagation for these two environments. In shallow water, lower modes, meaning lower phase velocities, tend to arrive first whereas in deep water they arrive last.

In this section, we review the application of the invariant to describing refraction and reflection-dominated propagation paths in shallow and deep water and its application to range-dependent environments. Along the way, we discuss some important aspects of dispersion in range-dependent environments.

Recalling that all speeds we discuss are the horizontal components of the velocities in a waveguide, the central issue is how the invariant is related to phase and group speeds,  $v$  and  $u$ , respectively, or slowness  $S$  (inverse of speed); below we repeat (2.214),

$$\frac{1}{\beta} \equiv -\frac{dS_g}{dS_p} = -\left(\frac{v}{u}\right)^2 \frac{du}{dv}. \quad (5.342)$$

Clearly, if  $\beta$  changes sign, the group speed vs. phase speed relation is reversed. Now, phase speeds do not change their fundamental nature between different environments. Intuitively, the phase speed of a particular path launched at a source and received at a receiver is simply related to the local angle of a particular path with respect to the horizontal. In particular, it is basically  $c(z)/\cos \theta$ , where  $c(z)$  is the local sound speed and  $\theta$  is the local angle of the ray path with respect to the horizontal. By Snell's law, it is also the value of the sound-speed profile at the turning depth, or for a mode, the depth at which it transitions between oscillatory and exponential decaying. However, the group-speed dependence on phase speed changes depending on the nature of the environment – with refraction and reflection-dominated environments denoting major categories.

In reflection-dominated environments, the group speed is fastest when the path is shortest and typically the shortest path is the one with the smallest grazing angle (or equivalently, lowest mode and lowest phase speed). On the other hand, for a refraction-dominated environment, such as deeply-refracted convergence-zone paths, rays turn around at the higher sound speeds as specified by Snell's law. The net effect is that the steeper launch angles penetrate to higher sound speed regions and the total travel time is smaller for these paths than for other, shallower launch angle paths more localized to regions of lower sound speed such as the sound speed in the vicinity of the deep sound channel axis. The modal picture, as represented by the group speed discussion associated with Sect. 5.9.2 and explicitly written down in (5.346), is consistent with the ray picture; in deep water, the higher modes have higher group speeds as can be seen because the mode shapes are weighted with respect to sound speed ("bulge" in regions of low sound speed) and, further, the group speed is proportional to  $c(z)$  as can be seen in the integral of (5.346).

### 5.14.1 The Waveguide Invariant Is Variable!

Consider the generic shallow-water summer profile shown in Fig. 5.40. The group vs. phase-speed curves for 1000Hz propagation show that there are two types of paths: ray paths that refract at the thermocline before they can reflect at the ocean surface and ray paths that reflect at the ocean surface. All paths are bottom reflecting. As explained in the invariant section of Chap. 3, the reflection-dominated path

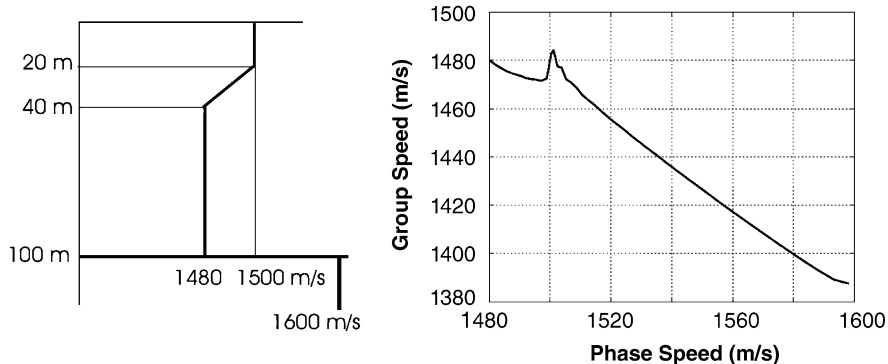


**Fig. 5.40** Sound-speed profile and group speed vs. phase speed curve for 1000 Hz propagation. Negative slope regions correspond to positive  $\beta$  and the positive slopes to negative  $\beta$ . We see at 1000 Hz there is a refraction-dominated region in the thermocline

has a positive  $\beta$  whereas the refraction-dominated path has a negative  $\beta$ . Hence,  $\beta$  is variable for an environment that supports different types of propagation paths (see also deep-water example in next section). Further, we already know from the discussion associated with Figs. 5.10 and 5.11 that the turning points of the refracted paths correspond to the evanescent (in the  $z$ -direction) regions of the modes. The thermocline region where the slope changes is particularly interesting in the context of real ocean environments. This region, which contains the turning points of many paths, is typically where there tends to be high internal wave activity. In this region, we see that there are pairs of modes (phase speeds) with the same group speed. Since, by Snell's law, horizontal rays are most affected by the sound-speed profile, we can expect that it is modes in this region that will cause significant fluctuations.

### 5.14.2 Range-Dependent Group Speed and Adiabatic Mode Theory

We think of phase speed as a local concept and we can relate it to either a launch angle or receive angle; in the case of either a moving source or receiver in a range-dependent environment, the phase speed at the particular transducer moving through range changes. In any event, modal phase speed is simply the local quantity  $v_n = \omega / k_{rn}$ . However, modal group speed is a range-integrated quantity. In a range dependent environment, we can derive an effective average modal group speed  $u_n$  from the range-averaged slowness. That is, we note that the pulse observables at range  $r$  are arrival times which are given by  $r/u_n$ . Hence, for a range-dependent environment we are concerned with  $1/u_n \equiv \bar{S}_{gn}$ , where the overbar denotes range averaging and  $S_{gn}$  is referred to as the (local) modal group slowness. Since the

adiabatic mode approximation has a range-averaged modal wavenumber associated with each term, it follows from the definition of group speed as per (2.158), that

$$\bar{S}_{gn}(r, \omega) = \frac{\partial}{\partial \omega} \left( \frac{1}{r} \int_0^r k_{rn}(r', \omega) dr' \right) \quad (5.343)$$

and the range-dependent effective group speed is

$$\langle u_n(r, \omega) \rangle = \frac{1}{\bar{S}_{gn}(r, \omega)}. \quad (5.344)$$

Hence, the range-dependent effective group speed is obtained from the average,

$$\frac{1}{\langle u_n(r, \omega) \rangle} = \frac{1}{r} \sum_{\Delta r'_n} \frac{\Delta r'_n}{u_n(r', \omega)}, \quad (5.345)$$

where the sum is taken over the  $n$  range-independent subintervals  $\Delta r'_n$  of the propagation path. Finally, we note that we can interchange the partial with the integral sign in (5.343) and can use the modal formula for the (local or range independent) modal group speed of Sect. 5.9.2, yielding

$$\frac{\partial k_{rn}}{\partial \omega} = \frac{1}{u_n(\omega)} = \frac{\omega}{k_{rn}(\omega)} \int_0^\infty \frac{\Psi_n^2(\omega; z)}{\rho(z) c^2(z)} dz, \quad (5.346)$$

where  $\Psi_n(\omega; z)$  are the normal mode eigenfunctions of the pressure field in the ocean waveguide and  $\rho(z)$  and  $c(z)$  are the density and sound-speed profiles as a function of depth.

Figure 5.41 shows a plot of the effective group speed (as per (5.345) and (5.346)) vs. phase speed for a North Pacific environment. Notice that the slope changes sign. In the context of the discussion following (5.342), we note that the slope on the left part of the curve is dominated by refraction and the right by bottom reflection; hence bottom-bounce paths in deep water have a shallow-water-like behavior. Since the slope of this curve is related to the invariant as per (5.342), it is clear that the waveguide invariant is variable!

As explained in Chaps. 2 and 3, the invariant  $\beta$  expresses the change in group slowness (speed) as a function of phase slowness (speed) for a mode interval over a frequency interval. Inherent to the discussion and utility of the invariant is that we always consider it to be a propagation property centered about an average mode number and frequency. This assumption comes from the derivation of the invariant and in particular, the linearization expressed by (2.212). Hence, change the frequency and/or the mode group for the same invariant, and one ends up with a different  $\beta$ . *The waveguide invariant is only invariant within a mode group and frequency interval consistent with (2.212).*

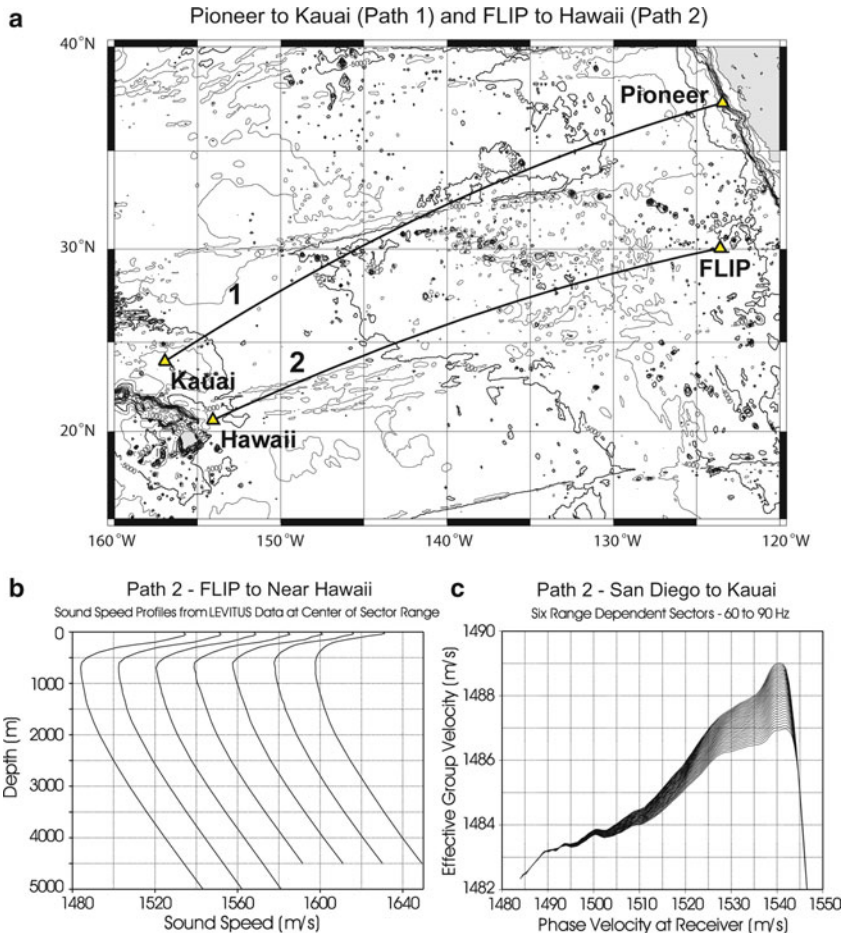


**Fig. 5.41** Sound propagation in the North Pacific. (a) The map shows two paths used in the Acoustic Thermometry of the Ocean Experiment [65]. (b) Climatology-derived sound speeds for Path 2. (c) Group velocity as a function of phase velocity as parameterized by frequency (60–90 Hz) [66]

### 5.14.3 Waveguide Invariant for Range-Dependent Environments

As long as modes maintain their identity, the waveguide invariant is a meaningful parameter. Hence, we present the form of the waveguide invariant in the adiabatic approximation [67]. To keep the derivation general, we will also include propagation along different azimuthal angles [68], the so-called  $N \times 2$ -D description of propagation, as discussed in Sect. 5.13. In analogy to (2.206), the condition for a line of constant intensity is

$$dI(r, \varphi, \omega) = \frac{\partial I}{\partial \omega} \delta\omega + \frac{\partial I}{\partial r} \delta r + \frac{\partial I}{\partial \varphi} \delta\varphi = 0, \quad (5.347)$$

where  $\varphi$  is the azimuthal angle of propagation. The expression for intensity, (2.207), is modified by the pertinent adiabatic quantities,

$$\begin{aligned}\Delta k_{mn}(\omega) &\longrightarrow \frac{1}{r} \int_0^r \Delta k_{mn}(r, \varphi, \omega) dr \equiv \Delta \bar{k}_{mn}, \\ B_n &\longrightarrow B_n^{s,r} \approx \Psi_n^s(z_s) \Psi_n^r(z_r) / \sqrt{\int_0^r k_n dr}.\end{aligned}\quad (5.348)$$

The partial derivatives of (5.347) for a pair of modes which correspond to the range-independent quantities of (2.210) and (2.211) are now given by

$$\begin{aligned}\frac{\partial I(r, \varphi, \omega)}{\partial \omega} &\propto -r \frac{\partial \Delta \bar{k}_{mn}}{\partial \omega} \sin(\Delta \bar{k}_{mn} r), \\ \frac{\partial I(r, \varphi, \omega)}{\partial r} &\propto -\Delta k_{mn}(\text{re}) \sin(\Delta \bar{k}_{mn} r), \\ \frac{\partial I(r, \varphi, \omega)}{\partial \varphi} &\propto -r \frac{\partial \Delta \bar{k}_{mn}}{\partial \varphi} \sin(\Delta \bar{k}_{mn} r),\end{aligned}$$

where  $\Delta \bar{k}_{mn}(\text{re})$  represents the wavenumber difference at that range where environmental changes affect the phase velocity, i.e., where the  $\delta r$  of (5.347) is created. Typically in a range-independent case, the  $\delta r$  is created by the horizontal physical aperture of the receiver. However, for a case where the moving source is creating the  $\delta r$ , the resulting changes need to be evaluated at the source and not at the receiver. Plugging these partial derivatives into (5.347) and rearranging gives the following:

$$\frac{\partial \Delta \bar{k}_{mn}/\partial \omega}{\Delta k_{mn}(\text{re})/\omega} \frac{r}{\omega} \delta \omega + \delta r + \frac{r}{\Delta k_{mn}(\text{re})} \frac{\partial \Delta \bar{k}_{mn}}{\partial \varphi} \delta \varphi = 0,\quad (5.349)$$

which clearly reduces to the form and (2.219) for an azimuthally independent environment. Consistent with (2.214) and (2.219), the definition of a range-dependent  $\beta(r)$  from a source at zero range to a receiver at range  $r$  is therefore [69],

$$\frac{1}{\beta(r)} = -\frac{\partial \bar{S}_g}{\partial S_p} = \frac{\partial \Delta \bar{k}_{mn}/\partial \omega}{\Delta k_{mn}(\text{re})/\omega}.\quad (5.350)$$

Note that  $\beta(r)$  is dependent on the *range-averaged group slowness*  $\bar{S}_g$ , defined by the numerator of the first fraction in (5.349), and the *local phase slowness*  $S_p$  at the transducer associated with the changing range in the environment defined by the denominator.

The azimuthal term in (5.349) can be re-arranged by noting that  $\Delta \bar{k}_{mn} = \int (\partial \Delta \bar{k}_{mn} / \partial \omega) d\omega$ . Reversing the order of integration over range and frequency, this last terms becomes

$$\frac{r}{\Delta k_{mn}(\text{re})} \frac{\partial}{\partial \varphi} \left\{ \int \left[ \frac{\Delta k_{mn}(\text{re})}{\omega} \left( \frac{1}{r} \int \frac{\partial \Delta \bar{k}_{mn}}{\partial \omega} dr \right) \left( \frac{\Delta k_{mn}(\text{rcr})}{\omega} \right)^{-1} \right] d\omega \right\} \delta \varphi,$$

which can be rewritten using the definition of  $\beta(r)$  given in (5.350) as

$$-\frac{r}{\Delta k_{mn}(\text{re})} \left[ \int \frac{\Delta k_{mn}(\text{re})}{\omega} d\omega \right] \frac{\partial}{\partial \varphi} \left[ \frac{1}{\beta(r, \varphi)} \right] \delta\varphi.$$

We now differentiate over  $\varphi$ , and again use (5.350) to help with the integral of  $\omega$  so that (5.349) finally becomes,

$$\frac{\delta\omega}{\omega} = \beta(r, \varphi) \frac{\delta r}{r} - \frac{\beta(\text{re})}{\beta(r, \varphi)} \frac{\partial}{\partial \varphi} [\beta(r, \varphi)] \delta\varphi. \quad (5.351)$$

This equation is the generalization of the waveguide invariant formulation for a range and azimuthally-varying environment using the adiabatic approximation and has been experimentally verified [68].

## Appendix 1: Recipe for Simple Mode Code

The easiest approach to writing a normal-mode code is to use the finite-difference technique described in Sect. 5.7.1. As discussed in more detail there, one replaces the continuous (differential) eigenvalue problem given in (5.3) with a discrete (matrix) eigenvalue problem given in (5.106). For ideal waveguides with homogeneous boundary conditions, the discrete eigenvalue problem is readily solved by calling standard routines for symmetric tri-diagonal matrices. The resulting eigenvectors and eigenvalues are approximations to the lowest-order eigenfunctions and eigenvalues of the original continuous problem.

Note that the matrix eigenvalue problem has exactly  $N$  eigenvalues and eigenvectors where  $N$  is both the dimension of the matrix and the number of mesh points used. In contrast, the continuous problem has an infinite number of eigensolutions. As  $N$  is increased we approximate the lowest-order modes more accurately. Simultaneously, we obtain approximations to still higher order modes, however, the highest-order mode of the matrix problem is always a poor approximation to the corresponding mode of the continuous problem.

For more realistic problems, e.g., those involving a penetrable bottom like the Pekeris waveguide problem, the use of standard eigenvalue routines is inapplicable because the algebraic eigenvalue problem in (5.106) is not a proper Sturm–Liouville problem. It can be changed to a proper Sturm–Liouville problem by adding a false bottom, deep enough for the propagating modes with their evanescent tails to be unaffected. This, on the other hand, will introduce false reflections at steeper angles, manifesting themselves as higher-order modes with oscillations in the bottom. To eliminate the significance of these reflections in the calculated field, one must make sure that the false bottom is sufficiently deep for the bottom attenuation to eliminate their significance in the water column. One way of thinking about the transformation of the complex eigenvalue problem into a real one and

subsequently adding the attenuation through an imaginary horizontal wavenumber is a transformation of the plane-wave attenuation represented by the imaginary part of the medium wavenumber to an attenuation operating only in range. Thus, one just has to ensure that the false bottom is deep enough to eliminate the significance of the false modes at the first range point of interest, easily estimated using the equivalent modal angles. Ideally, one should perform a convergence analysis increasing the bottom depth to verify the result.

Another straightforward way to solve the mode problem in such cases is to maintain the formulation with the inhomogeneous boundary condition at the bottom, and directly use the finite difference formulation with *Bisection* in combination with *Sturm Sequences* and *Inverse Iteration* for determining the eigenvalues and eigenvectors. The procedure is as follows:

1. Determine the interval of wavenumbers of interest for the problem at hand. For most long-range propagation problems only discrete modes are important, with propagation wavenumbers between  $k_{\min} = k_b = \omega/c_b$  and  $k_{\max} = \omega/c_{\min}$ .
2. Choose a depth discretization which reasonably samples the highest mode expected, i.e. 5–10 sample points per wavelength.
3. Determine the total number of modes as equal to the number of zero-crossings of the Sturm sequence calculated using the recursion (5.115).
4. Use bisection as described in Sect. 5.7.4.1 to isolate intervals with only one modal eigenvalue  $\lambda_m = k_{rm}^2$  in each.
5. Use a root-finding scheme such as Newton’s method in combination with the Sturm sequence to achieve an estimate  $k_{rm}$  of each of the modal wavenumbers.
6. For each of the modes, use the inverse iteration procedure in Sect. 5.7.1.2 with  $\kappa = k_{rm}^2$  to determine the associated eigenfunctions and an improved estimate of the modal wavenumbers.
7. Refine the discretization mesh by a factor 1.5–2 and repeat the procedures from step 3.
8. Use Richardson extrapolation to achieve an estimate of the eigenvalues of the continuous problem and determine the error. If unacceptable, repeat the mesh refinement and repeat the procedure from step 3.
9. Once the modal eigenvalues are determined with satisfactory accuracy, the next step is to normalize the modes according to (5.6). Numerically, this is done using the trapezoidal rule as discussed in Sect. 5.7.1, with the bottom halfspace contribution given in (5.135).
10. Next, the modal attenuation is accounted for by computing the imaginary part of the propagation wavenumber in (5.177).
11. Lastly, the modes are summed to compute the transmission loss using the formula in (5.17). Since the eigenfunctions are only tabulated on the discrete points of the finite-difference mesh, the transmission loss is most readily calculated for sources and receivers lying at those same depths. If the source or receiver lies between points of the finite-difference mesh, the eigenfunctions may be approximated by simple linear interpolation.

## Appendix 2: Evaluation of the Normalization Term

We consider the problem

$$\rho(z) \frac{d}{dz} \left[ \frac{1}{\rho(z)} \frac{dG(z)}{dz} \right] + \left( \frac{\omega^2}{c^2(z)} - k_r^2 \right) G(z) = -\frac{\delta(z - z_s)}{2\pi}, \quad (5.352)$$

$$f^T(k_r^2) G(0) + \frac{g^T(k_r^2)}{\rho(0)} \frac{dG(0)}{dz} = 0, \quad (5.353)$$

$$f^B(k_r^2) G(D) + \frac{g^B(k_r^2)}{\rho(D)} \frac{dG(D)}{dz} = 0, \quad (5.354)$$

where primes denote differentiation with respect to  $z$ . We shall write this problem symbolically as

$$\mathcal{L}(k_{rm})G = -\frac{\delta(z - z_s)}{2\pi}, \quad \mathcal{B}_1 G = \mathcal{B}_2 G = 0. \quad (5.355)$$

The Wronskian is defined by

$$W(z; k_r) = p_1(z; k_r) \frac{dp_2(z; k_r)}{dz} - \frac{dp_1(z; k_r)}{dz} p_2(z; k_r), \quad (5.356)$$

where  $p_1, p_2$  are any non-trivial solutions that satisfy the top and bottom boundary conditions respectively. That is,

$$\mathcal{L}(k_r)p_1 = 0, \quad \mathcal{B}_1 p_1 = 0, \quad (5.357)$$

$$\mathcal{L}(k_r)p_2 = 0, \quad \mathcal{B}_2 p_2 = 0. \quad (5.358)$$

Our objective is to obtain an expression for  $\partial W/\partial k$ . Let  $\Psi_m$  be a solution of the unforced boundary value problem

$$\mathcal{L}(k_{rm})\Psi_m = 0, \quad \mathcal{B}_1\Psi_m = \mathcal{B}_2\Psi_m = 0. \quad (5.359)$$

Then

$$p_2 \mathcal{L}(k_{rm})\Psi_m - \Psi_m \mathcal{L}(k_r)p_2 = 0 \quad (5.360)$$

or, equivalently,

$$\left[ p_2 \left( \frac{\Psi'_m}{\rho} \right)' - \Psi_m \left( \frac{p'_2}{\rho} \right)' \right] + (k_r^2 - k_{rm}^2) \frac{\Psi_m p_2}{\rho} = 0. \quad (5.361)$$

This can also be written

$$\left( p_2 \frac{\Psi'_m}{\rho} - \Psi_m \frac{p'_2}{\rho} \right)' + (k_r^2 - k_{rm}^2) \frac{\Psi_m p_2}{\rho} = 0. \quad (5.362)$$

Taking the integral then gives

$$\left[ \frac{p_2 \Psi'_m - \Psi_m p'_2}{\rho} \right]_0^D + (k_r^2 - k_{rm}^2) \int_0^D \frac{\Psi_m p_2}{\rho} dz = 0. \quad (5.363)$$

We shall need two intermediate results giving the value of the term in square brackets at  $z = 0$  and  $z = D$ . To obtain the value at  $z = 0$  we note that  $W(z)/\rho(z)$  is constant since,

$$\left( \frac{W}{\rho} \right)' = \left( \frac{p_1 p'_2 - p'_1 p_2}{\rho} \right)' = \frac{p_1 \mathcal{L} p_2 - p_2 \mathcal{L} p_1}{\rho} = 0. \quad (5.364)$$

Thus, we can write

$$\frac{W(z_s)}{\rho(z_s)} = \frac{W(0)}{\rho(0)} = \frac{p_1(0) dp_2(0)/dz - dp_1(0)/dz p_2(0)}{\rho(0)} \quad (5.365)$$

and solving for  $dp_2(0)/dz$  one obtains

$$dp_2(0)/dz = \frac{dp_1(0)/dz p_2(0) + W(z_s) \rho(0)/\rho(z_s)}{p_1(0)}. \quad (5.366)$$

This enables us to write

$$\left. \frac{p_2 \Psi'_m - \Psi_m p'_2}{\rho} \right|_0 = \frac{p_2(0) d\Psi_m(0)/dz - dp_1(0)/dz p_2(0) \Psi_m(0)/p_1(0)}{\rho(0)} - \frac{W(z_s)}{\rho(z_s)}. \quad (5.367)$$

We can eliminate the derivatives from this equation using the upper boundary conditions,

$$\frac{d\Psi_m(0)}{dz} = -\frac{\rho(0) f^T(k_{rm})}{g^T(k_{rm})} \Psi_m(0), \quad (5.368)$$

$$\frac{dp_1(0)}{dz} = -\frac{\rho(0) f^T(k_r)}{g^T(k_r)} p_1(0). \quad (5.369)$$

Thus, (5.367) becomes,

$$\left. \frac{p_2 \Psi'_m - \Psi_m p'_2}{\rho} \right|_0 = -\left[ \frac{f^T(k_r)}{g^T(k_r)} - \frac{f^T(k_{rm})}{g^T(k_{rm})} \right] p_2(0) \Psi_m(0) - \frac{W(z_s)}{\rho(z_s)}. \quad (5.370)$$

This gives us the value of the term in square brackets in (5.363) evaluated at  $z = 0$ . The value at  $z = D$  can be written down directly as

$$\frac{p_2 \Psi'_m - \Psi_m p'_2}{\rho} \Big|_D = - \left[ \frac{f^B(k_r)}{g^B(k_r)} - \frac{f^B(k_{rm})}{g^B(k_{rm})} \right] p_2(D) \Psi_m(D), \quad (5.371)$$

where we have used the bottom boundary conditions,

$$\frac{d\Psi_m(D)}{dz} = - \frac{\rho(D) f^B(k_{rm})}{g^B(k_{rm})} \Psi_m(D), \quad (5.372)$$

$$\frac{dp_1(D)}{dz} = - \frac{\rho(D) f^B(k_r)}{g^B(k_r)} p_1(D). \quad (5.373)$$

Using the results of (5.370) and (5.371) in (5.363) we obtain,

$$-\left[ \frac{f^B(k_r)}{g^B(k_r)} - \frac{f^B(k_{rm})}{g^B(k_{rm})} \right] p_2(D) \Psi_m(D) + \left[ \frac{f^T(k_r)}{g^T(k_r)} - \frac{f^T(k_{rm})}{g^T(k_{rm})} \right] p_2(0) \Psi_m(0) \\ + \frac{W(z_s; k_r) - W(z_s; k_{rm})}{\rho(z_s)} + (k_r^2 - k_{rm}^2) \int_0^D p_2 \frac{\Psi_m}{\rho} dz = 0, \quad (5.374)$$

where we have added the term  $W(z_s; k_{rm})$ . This is permissible since  $W(z; k_{rm}) = 0$ , i.e., the Wronskian vanishes when  $k_r$  is an eigenvalue.

The functions  $p_{1,2}(z; k_r)$  and  $\Psi_m(z)$  may all be scaled freely and still satisfy their respective governing equations. Therefore, without loss of generality, we take  $p_2(D; k_r) = \Psi_m(D)$ . Now, dividing both sides of the equation by  $k_r - k_{rm}$  and taking the limit as  $k_r \rightarrow k_{rm}$ , we obtain the final result,

$$\frac{\partial W / \partial k_r}{\rho(z_s)} \Big|_{k_{rm}} = 2k_{rm} \int_0^D \frac{\Psi_m^2(z)}{\rho(z)} dz - \frac{d(f/g)^T}{dk_r} \Big|_{k_{rm}} \Psi_m^2(0) \\ + \frac{d(f/g)^B}{dk_r} \Big|_{k_{rm}} \Psi_m^2(D). \quad (5.375)$$

## Problems

**5.1.** Write a simple code to calculate the modes in a channel with a pressure-release surface and a rigid bottom. Compare your model results to those shown for the Munk profile in Fig. 5.10.

**5.2.** Consider a 300 m deep Pekeris waveguide with ocean sound speed of 1500 m/s and sediment sound speed of 1800 m/s.

- For a source frequency of 500 Hz, how many trapped modes are present? What are the horizontal wavenumbers for the first two modes?
- What is the cutoff frequency?
- What will the modes look like? (Sketch.)

**5.3.** For a certain frequency there is a mode for the Munk profile in Fig. 5.9 with phase speed 1535 m/s. Does it have an upper and lower turning point? If so, at what depth(s)?

**5.4.** Suppose we wish to write a normal mode code using Numerov's method.

- Write down a difference scheme to handle the ocean–sediment interface.
- What is the form of the final matrix of difference equations? (Assume a pressure-release surface and perfectly rigid bottom.)
- Discuss how you might solve the resulting algebraic eigenvalue problem.

**5.5.** How will the modes change across the eddy whose SSP is shown in Fig. 5.23 (Sketch).

**5.6.** Consider the following eigenproblem:

$$\begin{aligned} u'' + \lambda^2 u &= 0, \\ u(0) + u'(0) &= 0, \\ u(1) + u'(1) &= 0. \end{aligned}$$

The exact eigenvalues are  $\lambda_k = k\pi$ . If we solve this problem using finite differences with the standard formula, we will get approximations to these eigenvalues  $\beta_k(N) = 2N \sin \frac{k\pi}{2N}$  where  $N$  is the number of points in the mesh and  $k = 1, \dots, N - 1$ .

- How can we use our formula for  $\beta_k(N)$  to obtain a similar result for the approximate eigenvalues of an isovelocity acoustic problem?
- Calculate  $\beta_1(10)$ ,  $\beta_1(20)$ ,  $\beta_1(40)$ .
- Use Richardson extrapolation to estimate  $\beta_1(N)$  from these numbers in the limit  $N \rightarrow \infty$ .
- Roughly, how large would  $N$  have to be to obtain this value by simple mesh refinement?
- How much slower would the mesh refinement be? (Solving the finite difference equations for  $\beta(N)$  requires roughly  $20N$  operations.)

**5.7.** Ray–mode analogy: Consider a isovelocity waveguide bounded above and below by pressure-release surfaces.

- Draw a diagram (see Fig. 2.20) with a “ray” reflecting with phase change, first from the bottom, and then from the surface. Construct a wavefront perpendicular to this ray such that it intersects both the ray when it is incident on the bottom and after it is reflected from the surface. What is the condition for angle and frequency that this wavefront be the result of perfect constructive interference?

- b. What are the normal modes and eigenvalues of a waveguide with the above boundary conditions? (Note that Sect. 5.4 discusses the rigid bottom case).
- c. Compare the two results.
- d. Now assume that the bottom is a fluid and consider a ray more grazing than critical. It will be perfectly reflected but will undergo a phase change at the bottom given by the results in problem 1.5. What is the condition for perfect constructive interference. Compare this result with (5.81).
- e. Which is a better approximation of a shallow water environment: a waveguide with a rigid or pressure-release bottom?

**5.8.** An alternative to using standard perturbation theory to compute the mode attenuation coefficients is to use a reflection coefficient argument. For an isovelocity waveguide, assume the magnitude of the bottom reflection coefficient to be close to unity, i.e., approximately  $|R| = 1 - \epsilon$ .

- a. Derive an expression for the cycle distance associated with a mode. Using this cycle distance, express the change in the acoustic field as a function of the acoustic field itself, the cycle distance and the loss per bounce. This simple differential equation gives the modal attenuation coefficient.
- b. What happens for the non-isovelocity case? Compute a skip distance by taking advantage of the fact that the horizontal wavenumber of a mode is constant whereas the vertical wavenumber varies with depth.

**5.9.** Another technique to compute bottom attenuation, which works for non-isovelocity cases is to assume a thin isovelocity layer just above the bottom. In this layer, normal modes are represented by up- and downgoing waves with a reflection coefficient which includes the bottom attenuation term as in the problem above. The field and its derivative must be continuous in the water column. Take the limit of zero layer thickness to obtain the ratio of the normal mode to its derivative in terms of the reflection coefficient. Assume the modes and wavenumbers are complex and write down the eigenvalue equation and its complex conjugate. Multiply these equations by their complex conjugate mode function, respectively. Taking the difference of these two equations and integrating by parts will yield a relation connecting the imaginary part of the wavenumber with the normal mode and its derivative. Use this method to derive an expression for the modal attenuation coefficient.

**5.10.** The technique of the last problem can be used to approximate the effects of a low-shear-speed bottom. In this case, a shear wave is an additional mechanism to transmit sound out of the water column; hence, it acts as a loss mechanism.

- a. Use a small parameter expansion of the fluid–elastic reflection coefficient to derive the effective modal attenuation coefficient due to the existence of a low shear speed  $c_s$  in the bottom sediment.
- b. At what shear speed do you expect this approximation to break down?

**5.11.** Ocean currents affect sound propagation. For simplicity consider sound from a line source propagating in a laminar flow velocity  $V(z)$  parallel to the ocean bottom

and in the positive  $x$ -direction. Linearizing about the background state as in Sect. 2.1 one can derive the following convected wave equation:

$$\begin{aligned}\rho(u_t + Vu_x + wV_z) &= -p_x, \\ \rho(w_t + Vw_x) &= -p_z, \\ p_t + Vp_x + c^2\rho(u_x + w_z) &= 0,\end{aligned}$$

where  $u$  and  $w$  are the acoustic particle velocities in the  $x$  and  $z$ -directions, respectively.

- a. Show that the normal modes of this equation satisfy

$$\left[ \frac{1}{(\omega - kV)^2} \psi_z \right]_z + \left[ \frac{1}{c^2} - \frac{k^2}{(\omega - kV)^2} \right] \psi = 0.$$

Note that  $V(z) = 0$  gives the usual modal equation.

- b. Ocean currents will satisfy a no-slip condition implying that the flow velocity vanishes at the bottom. Nevertheless, consider an ocean with uniform flow, uniform sound speed and with a perfectly rigid bottom. What is the dispersion relation? Plot representative curves for different modes and flow speeds. Include the asymptotes.

### 5.12. It is informative to study the invariant over a band of frequencies.

- a. Compute and plot the invariant  $\beta$  as a function of phase speed for the generic environment depicted in Fig. 5.40. Pay particular attention to any singularities.
- b. Now consider a 100 Hz bandwidth and make plots of both group velocity and  $\beta$  as a function of phase speed parameterized by frequency. Discuss any features of the arrival structure of a 100 Hz pulse you would expect as learned from this plot.

## References

1. C.L. Pekeris, Theory of propagation of explosive sound in shallow water. *Geol. Soc. Am. Mem.* **27** (1948)
2. J.M. Ide, R.F. Post, W.J. Fry, The propagation of underwater sound at low frequencies as a function of the acoustic properties of the bottom. *J. Acoust. Soc. Am.* **19**, 283 (1947)
3. A.O. Williams, Normal-mode methods in propagation of underwater sound. in *Underwater Acoustics*, ed. by R.W.B. Stephens (Wiley-Interscience, New York, 1970), pp. 23–56
4. K. Aki, P.G. Richards, *Quantitative Seismology: Theory and Methods* (Freeman, New York, 1980)
5. I. Stakgold, *Green's Functions and Boundary Value Problems* (Wiley, New York, 1979)
6. M.B. Porter, E.L. Reiss, A numerical method for bottom interacting ocean acoustic normal modes. *J. Acoust. Soc. Am.* **77**, 1760–1767 (1985)
7. W.M. Ewing, W.S. Jardetzky, F. Press, *Elastic Waves in Layered Media* (McGraw-Hill, New York, 1957)
8. R.B. Evans, The existence of generalized eigenfunctions and multiple eigenvalues in underwater acoustics. *J. Acoust. Soc. Am.* **92**, 2024–2029 (1992)

9. H.P. Bucker, Sound propagation in a channel with lossy boundaries. *J. Acoust. Soc. Am.* **48**, 1187–1194 (1970)
10. D.C. Stickler, Normal-mode program with both the discrete and branch line contributions. *J. Acoust. Soc. Am.* **57**, 856–861 (1975)
11. W.H. Munk, Sound channel in an exponentially stratified ocean with applications to SOFAR. *J. Acoust. Soc. Am.* **55**, 220–226 (1974)
12. C.T. Tindle, The equivalence of bottom loss and mode attenuation per cycle in underwater acoustic. *J. Acoust. Soc. Amer.* **66**, 250–255 (1979)
13. J.H. Wilkinson, *The Algebraic Eigenvalue Problem* (Oxford University Press, Oxford, 1965)
14. M.B. Porter, E.L. Reiss, A note on the relationship between finite-difference and shooting methods for ODE eigenvalue problems. *SIAM J. Numer. Anal.* **23**, 1034–1039 (1986)
15. M.B. Porter, E.L. Reiss, A numerical method for ocean acoustic normal modes. *J. Acoust. Soc. Am.* **76**, 244–252 (1984)
16. F.B. Jensen, C.M. Ferla, SNAP: The SACLANTCEN normal-mode acoustic propagation model. Rep. SM-121. SACLANT Undersea Research Centre, La Spezia, Italy, 1979
17. M.B. Porter, The KRAKEN normal mode program. Rep. SM-245. SACLANT Undersea Research Centre, La Spezia, Italy, 1991
18. L.B. Dozier, F.D. Tappert, Statistics of normal mode amplitudes in a random ocean. *J. Acoust. Soc. Am.* **64**, 533–547 (1978)
19. I. Tolstoy, J. May, A numerical solution for the problem on long-range sound propagation in continuously stratified media, with applications to the deep ocean. *J. Acoust. Soc. Am.* **32**, 655–660 (1960)
20. D.F. Gordon, Underwater sound propagation loss program. Rep. TR-393. Naval Ocean Systems Center, San Diego, CA, 1979
21. C.L. Bartberger, The computation of complex normal mode eigenvalues in underwater acoustic propagation. in *Computational Acoustics: Algorithms and Applications*, ed. by D. Lee, R.L. Sternberg, M.H. Schultz (North-Holland, Amsterdam, The Netherlands, 1988)
22. S.J. Levinson, E.K. Westwood, R.A. Koch, S.K. Mitchell, C.V. Sheppard, An efficient and robust method for underwater acoustic normal-mode computations. *J. Acoust. Soc. Am.* **97**, 1576–1585 (1995)
23. E.K. Westwood, C.T. Tindle, N.R. Chapman, A normal mode model for acousto-elastic ocean environments. *J. Acoust. Soc. Am.* **100**, 3631–3645 (1996)
24. C.A. Clark, K.B. Smith, An efficient normal mode solution to wave propagation prediction. *IEEE J. Oceanic Eng.* **33**, 462–476 (2008)
25. C.A. Boyles, *Acoustic Waveguides* (Wiley, New York, 1984)
26. A.V. Newman, F. Ingenito, A normal mode computer program for calculating sound propagation in shallow water with an arbitrary velocity profile. Memo. Rep. 2381. Naval Research Laboratory, Washington, DC, 1972
27. H.M. Beisner, Numerical calculation of normal modes for underwater sound propagation. *IBM J. Res. Develop.* **18**, 53–58 (1974)
28. A.B. Baggeroer, Prüfer transformations for the normal modes in ocean acoustics. in *Proceedings of the Shallow Water Acoustics Conference 2009* ed. J. Simmen, E.S. Livingston, J.-X. Zhou, F.-H. Li (American Institute of Physics, New York, 2010)
29. H.B. Keller, *Numerical Solution of Two Point Boundary Value Problems* (SIAM, Philadelphia, 1976)
30. R.P. Brent, An algorithm with guaranteed convergence for finding a zero of a function. *Comput. J.* **14**, 422–425 (1971)
31. J.H. Woodhouse, The calculation of eigenfrequencies and eigenfunctions of the earth and the sun. in *Seismological Algorithms*, ed. by D.J. Doombos (Academic, London, 1988), pp. 321–370
32. D.H. Lehmer, A machine method for solving polynomial equations. *J. Assoc. Comput. Mach.* **8**, 151–162 (1961)
33. L.M. Delves, J.N. Lyness, A numerical method for locating the zeros of an analytic function. *Math. Comput.* **21**, 543–560 (1967)

34. R.W. Hamming, *Introduction to Applied Numerical Analysis* (McGraw-Hill, New York, 1971)
35. H.V. Hitney, J.H. Richter, R.A. Pappert, K.D. Anderson, G.B. Baumgartner Jr., Tropospheric radio propagation assessment. Proc. IEEE **73**, 265–283 (1985)
36. P.S. Dubbelday, Application of a new complex root-finding technique to the dispersion relations for elastic waves in a fluid-loaded plate. SIAM J. Appl. Math. **43**, 1127–1139 (1983)
37. P. Cristini, Implementation of a new root finder for KRAKEN, in *Proceedings of the Fourth European Conference Underwater Acoustics*, ed. by A. Alippi, G.B. Cannelli (Italian National Research Council, Rome, 1998), pp. 775–780
38. B. Davies, Locating the zeros of an analytic function. J. Comput. Phys. **66**, 36–49 (1986)
39. C.T. Tindle, N.R. Chapman, A phase function for finding normal mode eigenvalues over a layered elastic bottom. J. Acoust. Soc. Am. **96**, 1777–1782 (1994)
40. J.D. Pryce, *Numerical Solution of Sturm–Liouville Problems* (Clarendon, Oxford, 1993)
41. W.A. Kuperman, F. Ingenito, Attenuation of the coherent component of sound propagating in shallow water with rough boundaries. J. Acoust. Soc. Am. **61**, 1178–1187 (1977)
42. R.B. Evans, A coupled mode solution for acoustic propagation in a waveguide with stepwise depth variations of a penetrable bottom. J. Acoust. Soc. Am. **74**, 188–195 (1983)
43. R.B. Evans, The decoupling of stepwise coupled modes. J. Acoust. Soc. Am. **80**, 1414–1419 (1986)
44. M.B. Porter, F.B. Jensen, C.M. Ferla, The problem of energy conservation in one-way models. J. Acoust. Soc. Am. **89**, 1058–1067 (1991)
45. W. Luo, H. Schmidt, Three-dimensional propagation and scattering around a conical seamount. J. Acoust. Soc. Am. **125**, 52–65 (2009)
46. A.D. Pierce, Extension of the method of normal modes to sound propagation in an almost-stratified medium. J. Acoust. Soc. Am. **37**, 19–27 (1965)
47. H. Weinberg, R. Burridge, Horizontal ray theory for ocean acoustics. J. Acoust. Soc. Am. **55**, 63–79 (1974)
48. L.M. Brekhovskikh, O.A. Godin, *Acoustics of Layered Media II* (Springer, Berlin, 1992)
49. M.B. Porter, Adiabatic modes for a point source in a plane-geometry ocean. J. Acoust. Soc. Am. **96**, 1918–1921 (1994)
50. F. Ingenito, Scattering from an object in a stratified medium. J. Acoust. Soc. Am. **82**, 2051–2059 (1987)
51. P.M. Morse, K.U. Ingard, *Theoretical Acoustics* (Princeton University Press, Princeton, 1968)
52. J.J. Bowman, T.B.A. Senior, P.L.E. Uslenghi (eds.), *Electromagnetic and Acoustic Scattering by Simple Shapes* (North-Holland, Amsterdam, 1969)
53. J.A. Fawcett, Coupled-mode modeling of acoustic scattering from three-dimensional, axisymmetric objects. J. Acoust. Soc. Am. **102**, 3387–3393 (1997)
54. N.C. Makris, A spectral approach to 3-D object scattering in layered media applied to scattering from submerged spheres. J. Acoust. Soc. Am. **104**, 2105–2113 (1998)
55. R.N. Baer, Propagation through a three-dimensional eddy including effects on an array. J. Acoust. Soc. Am. **69**, 70–75 (1981)
56. R. Doolittle, A. Tolstoy, M.J. Buckingham, Experimental confirmation of horizontal refraction of CW acoustic radiation from a point source in a wedge-shaped ocean environment. J. Acoust. Soc. Am. **83**, 2117–2125 (1988)
57. K.D. Heaney, W.A. Kuperman, B.E. McDonald, Perth–Bermuda sound propagation (1960): Adiabatic mode interpretation. J. Acoust. Soc. Am. **90**, 2586–2594 (1991)
58. M.J. Buckingham, Theory of acoustic propagation around a conical seamount. J. Acoust. Soc. Am. **80**, 256–277 (1986)
59. R.B. Evans, Three dimensional acoustic scattering from a cylindrical inclusion in a waveguide. in *Computational Acoustics: Scattering, Gaussian Beams and Aeroacoustics*, vol. 2, ed. by D. Lee, A. Cakmak, R. Vichnevetsky (North-Holland, Amsterdam, 1990), pp. 123–132
60. R.B. Evans, Stepwise coupled mode scattering of ambient noise by a cylindrically symmetric seamount. J. Acoust. Soc. Am. **119**, 161–167 (2006)
61. M.I. Taroudakis, A coupled-mode formulation for the solution in the presence of a conical sea-mount. J. Comput. Acoust. **4**, 101–121 (1996)

62. G.A. Athanassoulis, K.A. Belibassakis, All-frequency normal-mode solution of the three-dimensional acoustic scattering from a vertical cylinder in a plane-horizontal waveguide. *J. Acoust. Soc. Am.* **101**, 3371–3384 (1997)
63. H. Schmidt, J. Glattetre, A fast field model for three-dimensional wave propagation in stratified environments based on the global matrix method. *J. Acoust. Soc. Am.* **78**, 2105–2114 (1985)
64. F.B. Jensen, On the use of stair steps to approximate bathymetry changes in ocean acoustic models. *J. Acoust. Soc. Am.* **104**, 1310–1315 (1998)
65. ATOC Consortium, Ocean climate change: Comparison of acoustic tomography, satellite altimetry and modeling. *Science* **281**, 1327–1332 (1998)
66. W.A. Kuperman, G.L. D'Spain, K.D. Heaney, Long range source localization from single hydrophone spectrograms. *J. Acoust. Soc. Am.* **109**, 1935–1943 (2001)
67. S.V. Burenkov, Distinctive features of the interference structure of a sound field in a two-dimensionally inhomogeneous waveguide. *Sov. Phys. Acoust.* **35**, 465–467 (1989)
68. W.A. Kuperman, G.L. D'Spain, H.C. Song, A.M. Thode, The generalized waveguide invariant concept with application to vertical arrays in shallow water. in *Ocean Acoustics Interference Phenomena and Signal Processing*, ed. by W.A. Kuperman, G.L. D'Spain (American Institute of Physics, Melville, New York, 2002)
69. S.D. Chuprov, Interference structure of a sound field in a layered ocean. in *Ocean Acoustics, Current State*, ed. by L.M. Brekhovskikh, I.B. Andreevoi (Nauka, Moscow, 1982), pp. 71–91



# Chapter 6

## Parabolic Equations

### 6.1 Introduction

The pioneering work on parabolic wave equations goes back to the mid-1940s when Leontovich and Fock [1] applied a PE method to the problem of radio wave propagation in the atmosphere. Since then, parabolic equations have been used in several branches of physics, including the fields of optics, plasma physics, seismics, and underwater acoustics. It is the application of PE methods to wave-propagation problems in the ocean that is the subject of this chapter.

The parabolic-equation method was introduced into underwater acoustics in the early 1970s by Hardin and Tappert [2], who devised an efficient numerical solution scheme based on fast Fourier transforms. Since then, interest in PE techniques has grown steadily within the acoustic modeling community, to the point that the PE method has now become the most popular wave-theory technique for solving *range-dependent* propagation problems in ocean acoustics. This development is clearly reflected in the considerable number of publications which have appeared, relating both to new theoretical developments and to the actual use of PE codes to study complex propagation situations in the ocean.

A 1990 literature survey revealed that more than 120 articles and technical reports addressing new PE developments in underwater acoustics had been published over a period of 15 years. While the number of publications was low in the 1970s, the average during the 1980s and 1990s was around 10 publications per year. Our purpose here is not to provide an exhaustive list of references to the PE literature, but rather to point to some important papers, which may provide additional information on particular topics.

Three key references have formed the basis for much of the material presented in this chapter: First of all the lecture notes entitled “The parabolic approximation method” published by Tappert in 1977 [3], which presents the fundamental theory behind parabolic wave equations. Next, the proceedings from the PE Workshop held in 1981 [4], which presents the state-of-the-art in PE modeling as of 1981. Finally, a more recent monograph by Lee and McDaniel [5] entitled “Ocean acoustic propagation by finite difference methods,” which describes a variety of numerical solution schemes for PE-type wave equations.

In this chapter, we concentrate on PE solutions for a harmonic source in a 2-D fluid environment, with Appendix 1 providing a recipe for implementing a simple PE code. PE implementations for 2-D *elastic* media are briefly discussed, but readers are referred to the literature for details. Three-dimensional PE implementations for fluid media are discussed in Sect. 6.8, and illustrative numerical examples of both 2-D and 3-D propagation effects are shown at the end of the chapter. The issue of computing scattering at rough boundaries in the PE seems not yet to have found a satisfactory solution for general applications and scattering is therefore not dealt with here. However, a numerical implementation of rough-surface scattering by Rosenberg [6] has been used with some success in the community. Broadband PE solutions (2-D and 3-D) are addressed in Chap. 8, which deals with pulse modeling in general, either by Fourier synthesis of single-frequency solutions or by direct solution of the wave equation in the time domain.

## 6.2 Derivation of Parabolic Equations

The starting point is the 3-D Helmholtz equation for a constant-density medium in cylindrical coordinates  $(r, \varphi, z)$  as derived from (2.29) and (2.35),

$$\frac{1}{r} \frac{\partial}{\partial r} \left( r \frac{\partial p}{\partial r} \right) + \frac{1}{r^2} \frac{\partial^2 p}{\partial \varphi^2} + \frac{\partial^2 p}{\partial z^2} + \frac{\omega^2}{c^2(r, \varphi, z)} p = 0. \quad (6.1)$$

Assuming azimuthal symmetry and hence no dependence on the  $\varphi$ -coordinate, this reduces to the standard 2-D Helmholtz equation,

$$\frac{\partial^2 p}{\partial r^2} + \frac{1}{r} \frac{\partial p}{\partial r} + \frac{\partial^2 p}{\partial z^2} + k_0^2 n^2 p = 0, \quad (6.2)$$

where  $p(r, z)$  is the acoustic pressure,  $k_0 = \omega/c_0$  is a reference wavenumber, and  $n(r, z) = c_0/c(r, z)$  is the index of refraction.

### 6.2.1 Standard PE Derivation

There are several ways to arrive at the standard form of the 2-D parabolic wave equation. However, here we shall closely follow Tappert [3] by assuming the solution of (6.2) to take the form

$$p(r, z) = \psi(r, z) H_0^{(1)}(k_0 r), \quad (6.3)$$

which is an outgoing cylindrical wave solution in a form similar to that obtained in Chap. 5 for the propagation of a single adiabatic normal-mode. The envelope function  $\psi(r, z)$  is assumed to be slowly varying in range.

The Hankel function, which satisfies the Bessel differential equation

$$\frac{\partial^2 H_0^{(1)}(k_0 r)}{\partial r^2} + \frac{1}{r} \frac{\partial H_0^{(1)}(k_0 r)}{\partial r} + k_0^2 H_0^{(1)}(k_0 r) = 0 \quad (6.4)$$

is generally replaced by its asymptotic form for  $k_0 r \gg 1$ ,

$$H_0^{(1)}(k_0 r) \simeq \sqrt{\frac{2}{\pi k_0 r}} e^{i(k_0 r - \frac{\pi}{4})}. \quad (6.5)$$

Substituting our trial solution, (6.3), into the 2-D Helmholtz equation (6.2), and making use of the Hankel-function property given by (6.4), we obtain

$$\frac{\partial^2 \psi}{\partial r^2} + \left( \frac{2}{H_0^{(1)}(k_0 r)} \frac{\partial H_0^{(1)}(k_0 r)}{\partial r} + \frac{1}{r} \right) \frac{\partial \psi}{\partial r} + \frac{\partial^2 \psi}{\partial z^2} + k_0^2 (n^2 - 1) \psi = 0. \quad (6.6)$$

Next, we make the farfield assumption,  $k_0 r \gg 1$ , and use (6.5) to obtain the simplified elliptic wave equation

$$\frac{\partial^2 \psi}{\partial r^2} + 2ik_0 \frac{\partial \psi}{\partial r} + \frac{\partial^2 \psi}{\partial z^2} + k_0^2 (n^2 - 1) \psi = 0. \quad (6.7)$$

Finally, we introduce the crucial *paraxial approximation* in order to arrive at the standard parabolic wave equation. This small-angle approximation is expressed by

$$\frac{\partial^2 \psi}{\partial r^2} \ll 2ik_0 \frac{\partial \psi}{\partial r}. \quad (6.8)$$

The exact meaning of this approximation shall become clear in the next section where we develop a generalized operator formalism for deriving an entire family of parabolic equations. For now, we can provide a qualitative justification for this approximation noting that the main radial dependence of the field is contained in the Hankel function through the term  $\exp(ik_0 r)$ , while the envelope  $\psi$  will vary slowly with range over a wavelength  $\lambda$ . This can be expressed mathematically as  $\partial\psi/\partial r \ll \psi/\lambda \sim ik_0 \psi$ , and consequently the paraxial approximation is justified.

By making use of the paraxial approximation in (6.7) we obtain the following wave equation,

$$2ik_0 \frac{\partial \psi}{\partial r} + \frac{\partial^2 \psi}{\partial z^2} + k_0^2 (n^2 - 1) \psi = 0, \quad (6.9)$$

which is the *standard parabolic equation* introduced into underwater acoustics by Hardin and Tappert [2].

### 6.2.2 Generalized PE Derivation

As mentioned earlier there exist an infinity of parabolic approximations to the elliptic wave equation. In the previous section we derived the standard narrow-angle equation, which is considered accurate only for propagation angles within 10–15° off the horizontal. However, more wide-angled equations can be formulated and numerically solved.

Here we derive a series of parabolic wave equations based on an operator formalism [4], which has become increasingly popular over recent years. We start by defining the two operators

$$P = \frac{\partial}{\partial r}, \quad Q = \sqrt{n^2 + \frac{1}{k_0^2} \frac{\partial^2}{\partial z^2}} \quad (6.10)$$

and write the elliptic wave equation (6.7) in the following form,

$$[P^2 + 2ik_0 P + k_0^2 (Q^2 - 1)] \psi = 0. \quad (6.11)$$

The next step is to factor this equation into two components, an outgoing and an incoming wave component, according to

$$(P + ik_0 - ik_0 Q)(P + ik_0 + ik_0 Q) \psi - ik_0 [P, Q] \psi = 0, \quad (6.12)$$

where

$$[P, Q] \psi = PQ \psi - QP \psi \quad (6.13)$$

is the commutator of the operators  $P$  and  $Q$ . For range-independent media where  $n \equiv n(z)$ , the two operators commute and the last term in (6.12) is equal to zero. Here we assume that the range dependence given by  $n(r, z)$  is weak enough that we can ignore the commutator term. Selecting only the outgoing wave component we then obtain

$$P \psi = ik_0 (Q - 1) \psi,$$

or

$$\frac{\partial \psi}{\partial r} = ik_0 \left( \sqrt{n^2 + \frac{1}{k_0^2} \frac{\partial^2}{\partial z^2}} - 1 \right) \psi. \quad (6.14)$$

This equation is a genuine *one-way* wave equation, which for range-independent environments is exact within the limits of the farfield approximation. The equation is evolutionary in range and provides the basis for obtaining various forms of parabolic approximations, i.e., partial differential equations in first order with respect to  $r$ . These forms will follow as a result of approximations to the pseudo-differential operator  $Q$ , whose properties preclude the solution of (6.14) itself.

Before proceeding to introduce approximations to  $Q$ , it is useful to recapitulate the approximations on which (6.14) is based for general range-dependent

environments. These are: (a) that we are in the farfield, (b) that the commutator term  $[P, Q]\psi$  is negligible, and (c) that backscattering is negligible. The last two assumptions generally limit the validity of (6.14) to “weak” range dependence.

### 6.2.3 Expansion of the Square-Root Operator

For convenience we introduce the abbreviations,

$$\varepsilon = n^2 - 1, \quad \mu = \frac{1}{k_0^2} \frac{\partial^2}{\partial z^2}, \quad q = \varepsilon + \mu \quad (6.15)$$

and write the square-root operator  $Q$  given by (6.10) as

$$Q = \sqrt{1 + q}. \quad (6.16)$$

A solvable parabolic wave equation is now obtained by making a *Taylor series* expansion of  $Q$ ,

$$\sqrt{1 + q} = 1 + \frac{q}{2} - \frac{q^2}{8} + \frac{q^3}{16} + \dots \quad (6.17)$$

with the requirement of  $|q| < 1$  for convergence of the expansion.

Let us briefly analyze the implications of requiring the operator  $q = \varepsilon + \mu$  to be small. We consider a trial plane-wave solution of the form

$$\psi = e^{i(k_r r \pm k_z z)}, \quad (6.18)$$

where the horizontal and vertical wavenumbers are related to the medium wavenumber  $k$  through the *dispersion relation*,

$$k^2 = k_r^2 + k_z^2 \quad (6.19)$$

with the angle of propagation  $\theta$  with respect to horizontal defined by

$$\sin \theta = \pm \frac{k_z}{k}. \quad (6.20)$$

By using (6.18) the differential operator  $\mu$  is easily evaluated to be

$$\mu = \frac{1}{k_0^2} \frac{\partial^2}{\partial z^2} = -\frac{k_z^2}{k_0^2}, \quad (6.21)$$

or

$$\mu = -n^2 \sin^2 \theta. \quad (6.22)$$

We now make use of Snell's law

$$\frac{\cos \theta_0}{\cos \theta} = n \quad (6.23)$$

to relate propagation angles to the index of refraction in the ocean, and obtain

$$q = \varepsilon + \mu = (n^2 - 1) - n^2 \sin^2 \theta, \quad (6.24)$$

or

$$q = -\sin^2 \theta_0. \quad (6.25)$$

This expression shows that when selecting  $c_0$  equal to the sound speed at the source, the operator  $q$  is only a function of the source radiation angle. Hence,  $q$  is indeed small for propagation near the horizontal, and an expansion of  $(1 + q)^{1/2}$  around  $q = 0$  is equivalent to introducing a paraxial approximation.

If we retain only the first two terms in the expansion given by (6.17), we get the following approximate form of the square-root operator,

$$Q \simeq 1 + \frac{q}{2} = 1 + \frac{n^2 - 1}{2} + \frac{1}{2k_0^2} \frac{\partial^2}{\partial z^2}. \quad (6.26)$$

Substituting this expression for  $Q$  into the generalized one-way wave equation (6.14), we obtain

$$\frac{\partial \psi}{\partial r} = \frac{ik_0}{2} \left( n^2 - 1 + \frac{1}{k_0^2} \frac{\partial^2}{\partial z^2} \right) \psi, \quad (6.27)$$

which is the *standard* parabolic equation derived earlier as (6.9).

The above derivation based on a series expansion of the square-root operator  $Q$  opens up the road for formulating better PE approximations with a wide-angle capability. In principle, one could just retain some of the higher order terms in the Taylor series, but the presence of  $q$ -terms raised to second or higher power complicates the numerical implementation. However, there are other rational-function approximations to the square-root operator which have proven very successful. A general form of these approximations are given by

$$\sqrt{1 + q} \simeq \frac{a_0 + a_1 q}{b_0 + b_1 q}, \quad (6.28)$$

where the coefficients can be chosen so as to minimize the error over a given angle interval. We shall here present three different sets of coefficients associated with some common PE implementations.

We first choose  $a_0 = 1$ ,  $a_1 = 0.5$ ,  $b_0 = 1$ , and  $b_1 = 0$  to obtain

$$\sqrt{1 + q} \simeq 1 + 0.5 q, \quad \text{Tappert} \quad (6.29)$$

which again is the two-term Taylor expansion of (6.17) leading to the standard parabolic equation.

Next we select  $a_0 = 1$ ,  $a_1 = 0.75$ ,  $b_0 = 1$ , and  $b_1 = 0.25$ , which yields

$$\sqrt{1+q} \simeq \frac{1 + 0.75q}{1 + 0.25q}, \quad \text{Claerbout} \quad (6.30)$$

which is the wide-angle PE due to Claerbout [7]. We shall show later that the Tappert and the Claerbout equations both have increasing phase error with increasing angle.

The last approximation has the form

$$\sqrt{1+q} \simeq \frac{0.99987 + 0.79624q}{1 + 0.30102q}, \quad \text{Greene} \quad (6.31)$$

which is the high-angle PE derived by Greene [8] based on the criterion of minimum phase errors over an angle interval of  $0\text{--}40^\circ$ . Note that this approximation has coefficients very similar to those used by Claerbout. Application of Greene's optimization criteria for other angle intervals will, of course, alter the values of the coefficients  $a_0$ ,  $a_1$ ,  $b_0$ , and  $b_1$ .

By making use of (6.14) and (6.28) we find that a rational linear approximation in the general form given above leads to a parabolic wave equation of the form

$$A_1 \frac{\partial \psi}{\partial r} + A_2 \frac{\partial^3 \psi}{\partial z^2 \partial r} = A_3 \psi + A_4 \frac{\partial^2 \psi}{\partial z^2}, \quad (6.32)$$

where

$$\begin{aligned} A_1 &= b_0 + b_1(n^2 - 1), \\ A_2 &= b_1/k_0^2, \\ A_3 &= ik_0 [(a_0 - b_0) + (a_1 - b_1)(n^2 - 1)], \\ A_4 &= i(a_1 - b_1)/k_0. \end{aligned}$$

This is a convenient compact form of the parabolic wave equation, whose numerical implementation shall be dealt with later. However, it can be anticipated that while the general form of (6.32) can be solved by finite-difference or finite-element techniques, only the Tappert equation, which has  $A_2 = 0$ , can be solved by the split-step Fourier technique [2].

We have so far presented parabolic equation approximations which have limited accuracy for propagation angles beyond  $\pm 40^\circ$  relative to the main propagation direction, which need not be the horizontal. However, in recent years considerable effort has gone into deriving still more wide-angled PE approximations [9–12], using different rational-function representations for the operator  $(1+q)^{1/2}$ .

An overview of several different families of approximants was given by Halpern and Trefethen [13]. They found that a Padé series expansion, which has become popular recently, is not the optimal choice in terms of minimizing phase errors

over a wide range of propagation angles. However, the Padé series does provide highest accuracy in the main propagation direction, which is important for under-water acoustics applications. Moreover, numerical implementations are facilitated by the use of Padé series.

We shall here present a generalized very-wide-angle PE based on a Padé series expansion proposed by Bamberger et al. [11] and first implemented by Collins [12],

$$\sqrt{1+q} = 1 + \sum_{j=1}^m \frac{a_{j,m} q}{1 + b_{j,m} q} + O(q^{2m+1}), \quad (6.33)$$

where  $m$  is the number of terms in the expansion and

$$a_{j,m} = \frac{2}{2m+1} \sin^2\left(\frac{j\pi}{2m+1}\right), \quad (6.34)$$

$$b_{j,m} = \cos^2\left(\frac{j\pi}{2m+1}\right). \quad (6.35)$$

It is instructive to write out this expansion when including one term only from the sum,

$$\sqrt{1+q} \simeq 1 + \frac{0.50 q}{1 + 0.25 q}, \quad (6.36)$$

which is easily seen to be equivalent to the expansion given in (6.30). Thus, the Padé series includes as a special case the standard 40° PE derived by Claerbout [7]. When including two terms from the Padé series sum we have the following approximation,

$$\sqrt{1+q} \simeq 1 + \frac{0.13820 q}{1 + 0.65451 q} + \frac{0.36180 q}{1 + 0.09549 q}, \quad (6.37)$$

which is a wider-angle PE accurate to nearly 55° from the main propagation direction. By including even more terms it is possible to cover almost the full  $\pm 90^\circ$  spectrum of forward propagating waves. Collins [12] has shown that most ocean-acoustic problems can be adequately handled by less than five terms.

By substituting (6.33) into (6.14) we obtain the generalized *very-wide-angle* parabolic equation based on the Padé series expansion of the square-root operator,

$$\frac{\partial \psi}{\partial r} = ik_0 \left[ \sum_{j=1}^m \frac{a_{j,m} \left( n^2 - 1 + \frac{1}{k_0^2} \frac{\partial^2}{\partial z^2} \right)}{1 + b_{j,m} \left( n^2 - 1 + \frac{1}{k_0^2} \frac{\partial^2}{\partial z^2} \right)} \right] \psi, \quad (6.38)$$

which can be solved by finite-difference or finite-element techniques. Equation (6.38) is a PE approximation which virtually eliminates inherent phase errors associated with high-angle propagation. Of course, the higher accuracy is not achieved without additional computational cost.

For completeness we shall consider one final operator splitting which has been used extensively in PE codes based on the split-step Fourier solution technique. Recall that the operator  $Q$  is given by

$$Q = \sqrt{1 + \varepsilon + \mu}, \quad (6.39)$$

where  $\varepsilon$  and  $\mu$  are defined in (6.15). The expansions considered so far were all based on the assumption that  $q = \varepsilon + \mu$  is small compared to unity. Several  $Q$  approximations for either  $\varepsilon$  small (small variations in the index of refraction) or  $\mu$  small (small propagation angles) were proposed by Tappert [3]. However, we shall here concentrate on the particular splitting proposed by Feit and Fleck [14] and introduced into underwater acoustics by Thomson and Chapman [15].

We write  $Q$  in the form

$$Q \simeq \sqrt{1 + \mu} + \sqrt{1 + \varepsilon} - 1, \quad (6.40)$$

which is seen to be an exact splitting for a uniform medium ( $\varepsilon = 0$ ). We expect this form also to have a good wide-angled behavior for realistic ocean acoustic environments with moderate changes in the refraction index. By substituting the above expression for  $Q$  into the generalized one-way wave equation, (6.14), we obtain the following PE approximation,

$$\frac{\partial \psi}{\partial r} = ik_0 \left( n - 2 + \sqrt{1 + \frac{1}{k_0^2} \frac{\partial^2}{\partial z^2}} \right) \psi. \quad (6.41)$$

As was the case for the Tappert equation, (6.27), the above form of the parabolic wave equation can be solved by the efficient split-step Fourier algorithm.

An alternative PE form proposed by Berman et al. [16] also allows a split-step solution. This equation, referred to as the **LOGPE**, takes the form

$$\frac{\partial \psi}{\partial r} = ik_0 \left\{ \ln n + \frac{1}{2} \ln \left[ \cos^2 \left( -\frac{i}{k_0} \frac{\partial}{\partial z} \right) \right] \right\} \psi, \quad (6.42)$$

which to leading order is identical to (6.41). The LOGPE has the particular property that its rays are identical to the rays of the Helmholtz equation in a range independent environment.

Numerical examples [15, 16] indicate that (6.41) and (6.42) have smaller phase errors than the standard PE and hence can be considered more wide-angled ( $\sim \pm 20^\circ$ ). It should be emphasized, however, that all true wide-angle PE approximations ( $> 20^\circ$ ) are of the forms given by (6.32) or (6.38), and require solution by finite-difference or finite-element techniques.

Despite the fact that parabolic wave equations are approximate, it can be shown that they satisfy the fundamental principle of reciprocity of linear acoustics [17].

### 6.2.4 Phase Errors and Angular Limitations

In the derivation of the various parabolic approximations, we repeatedly referred to the goodness of the approximations in terms of the angular spectrum of forward propagating plane waves treated accurately by each of the PEs. It is clear that depending on the acceptable phase error, a particular PE can be considered, for instance, a 20° equation for one application and a 30° equation for another application with less stringent accuracy requirements.

In order to make a meaningful statement on the angular limitations of the various PEs, we here address the issue of inherent phase errors in a unified approach. We follow McDaniel [18] by considering propagation of a single normal mode in the parabolic approximations and comparing the results with those obtained in Chap. 5 for the full elliptic wave equation. The analysis is based on the assumption of a stratified medium with the index of refraction,  $n(z) = k(z)/k_0$ , being a function of depth only.

For illustrative purposes we carry through the analysis for Claerbout's wide-angle PE, which is obtained by substituting expression (6.30) into the generalized one-way wave equation (6.14). We get

$$\frac{\partial \psi}{\partial r} = ik_0 \left( \frac{1 + 0.75q}{1 + 0.25q} - 1 \right) \psi, \quad (6.43)$$

where the operator  $q$  is defined in (6.15). An explicit differential form is obtained without difficulty as

$$\left( k^2(z) + 3k_0^2 + \frac{\partial^2}{\partial z^2} \right) \frac{\partial \psi}{\partial r} = 2ik_0 \left( k^2(z) - k_0^2 + \frac{\partial^2}{\partial z^2} \right) \psi. \quad (6.44)$$

This equation may be solved by the method of *separation of variables*. We write

$$\psi = \Phi(r) \Psi(z), \quad (6.45)$$

where  $\Phi(r)$  is a function only of range and  $\Psi(z)$  is a function only of depth. By substituting (6.45) into (6.44), and collecting terms appropriately, we arrive at the following equation,

$$\left[ \frac{d^2 \Psi}{dz^2} + k^2(z) \Psi \right] \left( \frac{d\Phi}{dr} - 2ik_0 \Phi \right) + \left[ 3k_0^2 \frac{d\Phi}{dr} + 2ik_0^3 \Phi \right] \Psi = 0, \quad (6.46)$$

which may be separated into two differential equations by equating the terms in the first brackets to  $k_{rm}^2 \Psi$  and the terms in the second brackets to  $-k_{rm}^2 (d\Phi/dr - 2ik_0 \Phi)$ , with  $k_{rm}^2$  being the separation constant. We now obtain the depth and range-separated equations in the form

$$\frac{d^2 \Psi}{dz^2} + [k^2(z) - k_{rm}^2] \Psi = 0 \quad (6.47)$$

and

$$\frac{d\Phi}{dr} - ik_0 \frac{2k_{rm}^2 - 2k_0^2}{3k_0^2 + k_{rm}^2} \Phi = 0. \quad (6.48)$$

We immediately notice that (6.47) is identical to the depth-separated part of the Helmholtz equation, (5.3), which has solutions in terms of a set of normal modes with amplitude functions  $\Psi_m(z)$  and horizontal wavenumbers  $k_{rm}$ . Hence, it is clear that a normal mode is propagated in this particular parabolic approximation with the correct amplitude and mode shape. This is an important result, which can be shown to be valid for all PEs based on the rational linear approximation, (6.32).

Next, we examine the radial part of the wave equation which has the solution

$$\Phi(r) = \Phi(r_0) \exp \left[ ik_0 \left( \frac{2k_{rm}^2 - 2k_0^2}{3k_0^2 + k_{rm}^2} \right) (r - r_0) \right]. \quad (6.49)$$

In order to return to pressure, we recall from (6.3) that we initially factored out a range dependence of the form  $H_0^{(1)}(k_0 r)$ , which in the farfield results in a phase factor  $\exp(ik_0 r)$ . By substituting (6.49) into (6.3) we obtain

$$p(r, z) = p(r_0, z) \sqrt{\frac{r_0}{r}} \exp \left[ ik_0 \left( \frac{k_0^2 + 3k_{rm}^2}{3k_0^2 + k_{rm}^2} \right) (r - r_0) \right]. \quad (6.50)$$

We know from the solution of the Helmholtz equation that the correct modal phase is  $\exp[ik_{rm}(r - r_0)]$ , which shows that there is a phase error in the Claerbout equation. We notice that the error is dependent on the choice of  $k_0$ . One can select  $k_0$  such that the phase error is zero for the  $m$ th mode, i.e.,  $k_0 = k_{rm}$ , but all other modes will propagate with a slightly wrong phase velocity.

It is convenient to relate phase velocity errors in (6.50) to errors in propagation angles, which can be done by introducing the identity  $k_{rm} = k_0 \cos \theta_m$ . We furthermore simplify results by choosing  $k_0 = 1$  to obtain the modal phase in the Claerbout equation as

$$\varphi = \frac{1 + 3 \cos^2 \theta_m}{3 + \cos^2 \theta_m}, \quad (6.51)$$

while the phase in the Helmholtz equation is given by  $\cos \theta_m$ . Dropping the subscript  $m$  and expressing phase angles in terms of  $\sin^2 \theta$ , we arrive at the following phases,

$$\varphi = \sqrt{1 - \sin^2 \theta} \quad \text{Helmholtz} \quad (6.52)$$

and

$$\varphi = \frac{1 - 0.75 \sin^2 \theta}{1 - 0.25 \sin^2 \theta}. \quad \text{Claerbout} \quad (6.53)$$

If we now compare these two expressions with the square-root operator expansion given in (6.30), using also (6.25) to relate the operator  $q$  to the propagation angle, we realize that (6.52) and (6.53) are just a restatement of the fact that we have

approximated the actual propagation angle in the Helmholtz equation  $(1 - \sin^2 \theta)^{1/2}$  with a rational function in  $\sin^2 \theta$ . This fact immediately allows us to write down the phases associated with each of the parabolic approximations considered earlier. Including also the exact form of the square-root operator  $Q$  we have

$$Q = \sqrt{1 - \sin^2 \theta}, \quad \text{Helmholtz} \quad (6.54)$$

$$Q_1 = 1 - \frac{\sin^2 \theta}{2}, \quad \text{Tappert} \quad (6.55)$$

$$Q_2 = \frac{1 - 0.75 \sin^2 \theta}{1 - 0.25 \sin^2 \theta}, \quad \text{Claerbout, Padé (1)} \quad (6.56)$$

$$Q_3 = \frac{0.99987 - 0.79624 \sin^2 \theta}{1 - 0.30102 \sin^2 \theta}, \quad \text{Greene} \quad (6.57)$$

$$Q_4 = 1 - \frac{0.13820 \sin^2 \theta}{1 - 0.65451 \sin^2 \theta} - \frac{0.36180 \sin^2 \theta}{1 - 0.09549 \sin^2 \theta}. \quad \text{Padé (2)} \quad (6.58)$$

We can now define the phase errors for the various PE approximations as  $|Q - Q_i|$ , a quantity which is displayed graphically as a function of angle in Fig. 6.1. For completeness we here show results also for a very-wide-angle 5-term Padé equation.

In the upper graph, the acceptable error has been arbitrarily set to 0.002, as indicated by the horizontal dashed line. This is seen to result in the following approximate angle limitations:  $20^\circ$  (Tappert),  $35^\circ$  (Claerbout, Padé (1)),  $45^\circ$  (Greene),  $55^\circ$  (Padé (2)), and  $75^\circ$  (Padé (5)). With the vertical scale expanded ten times and an acceptable error of only 0.0002, we see from the lower graph that the maximum angles for the various PE approximations are now  $10^\circ$ ,  $25^\circ$ ,  $40^\circ$ ,  $45^\circ$ , and  $70^\circ$ , respectively. We also notice that while the phase error increases with angle for the Tappert, Claerbout, and Padé equations, Greene's  $40^\circ$  expansion has errors of equal magnitude over the entire range from 0 to  $40^\circ$ . More results on phase errors in narrow and wide-angle PEs are given by Hill [19].

The best PE approximation is clearly the Padé (5) equation, which has small phase errors for angles within  $\pm 60^\circ$  of the main propagation direction. As mentioned earlier, this high-angle capability can be extended to nearly  $\pm 90^\circ$  by including more Padé terms in the expansion given by (6.38).

An often-used example illustrating the effects of phase errors on computed transmission loss is shown in Fig. 6.2. This test problem was first presented at the PE Workshop in 1981 [4]. We consider a Pekeris waveguide of depth 100 m with both source and receiver placed near the bottom at 99.5 m. The water speed is 1500 m/s and the bottom speed 1590 m/s, resulting in a critical angle of  $19.4^\circ$ . The density ratio between bottom and water is 1.2 and the bottom attenuation is  $0.5 \text{ dB}/\lambda$ . At a frequency of 250 Hz there are 11 propagating modes with propagation angles between  $1.7^\circ$  and  $18.5^\circ$ . Considering the phase error results given in Fig. 6.1b,

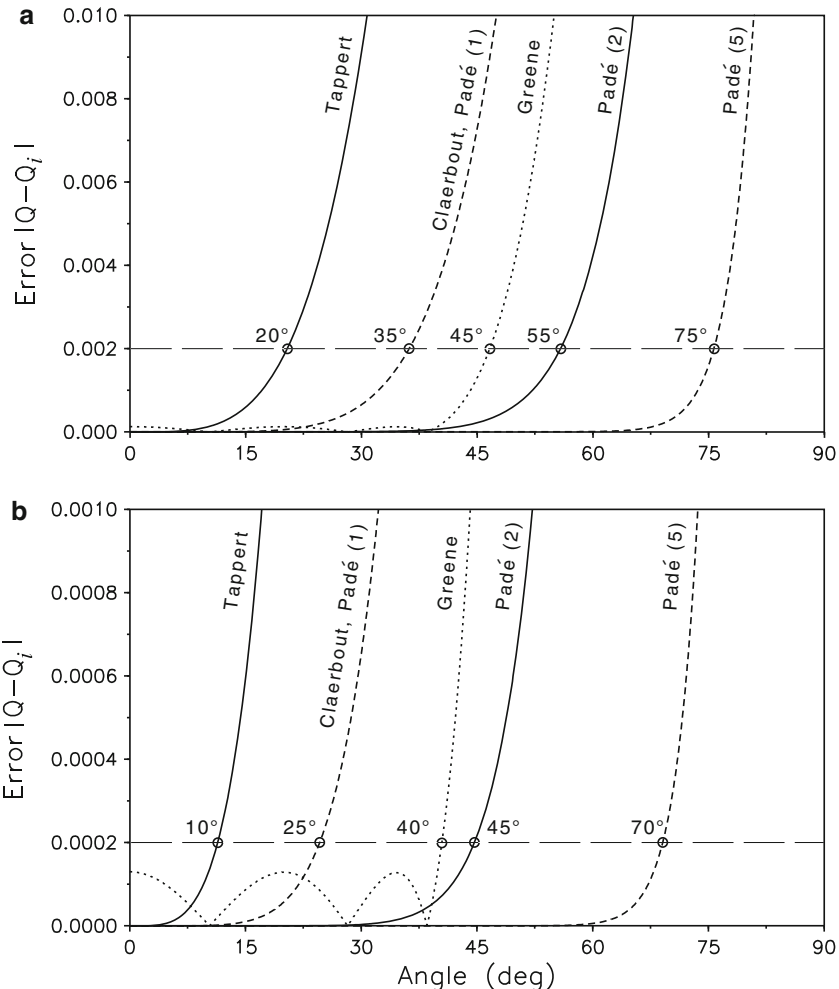


**Fig. 6.1** Phase error vs. propagation angle for different parabolic equation approximations. **(a)** Nominal beamwidths for an acceptable phase error of 0.002. **(b)** Nominal beamwidths for an acceptable phase error of 0.0002

it is not surprising that the result from the standard PE (Tappert Eq.) matches poorly the FFP reference solution in Fig. 6.2. On the other hand, the wide-angle Claerbout equation is seen to provide accurate results for this test problem. For completeness we mention that the two PE results were obtained using a modal starter (Sect. 6.4.1).

In summary, we have shown that while the various parabolic approximations to the Helmholtz equation propagate normal modes with the correct amplitude distribution over depth in stratified media, the approximations all have inherent phase errors, which limit their applicability to a certain range of angles around the main propagation direction. However, recent developments based on Padé series

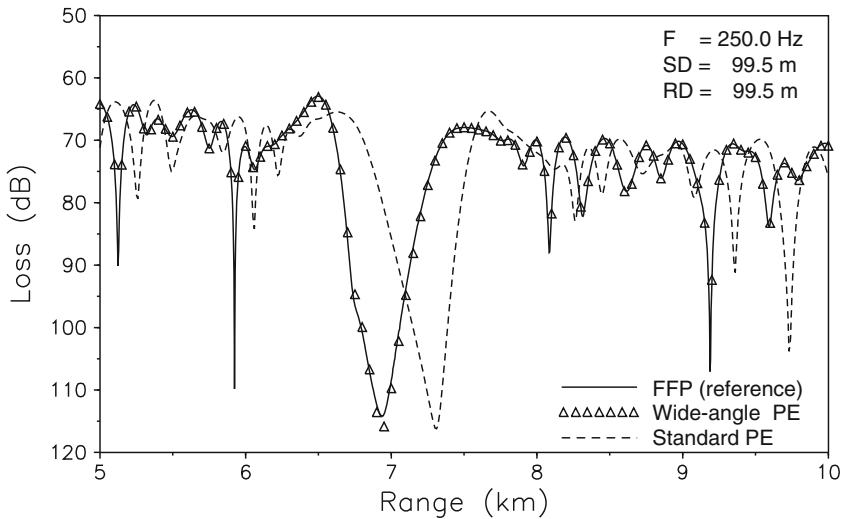


**Fig. 6.2** Comparison of transmission loss results for narrow and wide-angle PEs with FFP reference solution

expansions have practically eliminated the small-angle restrictions generally associated with parabolic wave equations. Of course, this high-angle capability is not achieved without additional computational effort.

### 6.3 The Elastic PE

Over the years, various attempts have been made to formulate and solve parabolic equations for elastic media. The first successful code implementations date back to around 1990 and were done independently by Collins [20, 21] and by Wetton and Brooke [22]. In this section, we briefly outline the derivation of the elastic PE and its numerical solution, following closely the approach by Collins [21].

One of the standard farfield formulations of elasticity is given by the system [23],

$$\mu \frac{\partial^2 u}{\partial r^2} + \mu \frac{\partial^2 u}{\partial z^2} + \rho \omega^2 u + (\lambda + \mu) \frac{\partial \Delta}{\partial r} + \frac{\partial \mu}{\partial z} \frac{\partial u}{\partial z} + \frac{\partial \mu}{\partial z} \frac{\partial w}{\partial r} = 0, \quad (6.59)$$

$$\mu \frac{\partial^2 w}{\partial r^2} + \mu \frac{\partial^2 w}{\partial z^2} + \rho \omega^2 w + (\lambda + \mu) \frac{\partial \Delta}{\partial z} + \frac{\partial \lambda}{\partial z} \Delta + 2 \frac{\partial \mu}{\partial z} \frac{\partial w}{\partial z} = 0, \quad (6.60)$$

where

$$\Delta = \frac{\partial u}{\partial r} + \frac{\partial w}{\partial z}. \quad (6.61)$$

Here,  $u$  and  $w$  are the displacements,  $\Delta$  the dilatation,  $\rho$  the density, and  $\lambda$  and  $\mu$  the Lamé constants. Due to the presence of terms involving  $\partial/\partial r$ , it is difficult to factor (6.59) into incoming and outgoing operators. Greene [24] proposed a non-standard formulation that is easy to factor. Differentiating (6.59) with respect to  $r$  and (6.60) with respect to  $z$  and summing, we obtain

$$\begin{aligned} & (\lambda + 2\mu) \frac{\partial^2 \Delta}{\partial r^2} + (\lambda + 2\mu) \frac{\partial^2 \Delta}{\partial z^2} + \rho \omega^2 \Delta + 2 \frac{\partial \mu}{\partial z} \frac{\partial^2 w}{\partial r^2} + \omega^2 \frac{\partial \rho}{\partial z} w \\ & + \left( \frac{\partial \lambda}{\partial z} + 2 \frac{\partial \mu}{\partial z} \right) \frac{\partial \Delta}{\partial z} + \frac{\partial}{\partial z} \left( \frac{\partial \lambda}{\partial z} \Delta \right) + 2 \frac{\partial}{\partial z} \left( \frac{\partial \mu}{\partial z} \frac{\partial w}{\partial z} \right) = 0. \end{aligned} \quad (6.62)$$

Equations (6.60) and (6.62) provide a formulation of the form

$$\mathbf{L} \frac{\partial^2}{\partial r^2} \begin{pmatrix} \Delta \\ w \end{pmatrix} + \mathbf{M} \begin{pmatrix} \Delta \\ w \end{pmatrix} = \begin{pmatrix} 0 \\ 0 \end{pmatrix}, \quad (6.63)$$

where the matrices  $\mathbf{L}$  and  $\mathbf{M}$  contain depth operators. Since  $\mathbf{L}$  and  $\mathbf{M}$  commute with  $\partial/\partial r$ , (6.63) has the outgoing factor,

$$\frac{\partial}{\partial r} \begin{pmatrix} \Delta \\ w \end{pmatrix} = ik_0 \sqrt{\mathbf{I} + \mathbf{X}} \begin{pmatrix} \Delta \\ w \end{pmatrix}, \quad (6.64)$$

$$\mathbf{X} = k_0^{-2} (\mathbf{L}^{-1} \mathbf{M} - k_0^2 \mathbf{I}), \quad (6.65)$$

where  $k_0$  is the reference wavenumber and  $\mathbf{I}$  the identity matrix.

An elastic PE is derived from (6.64) by introducing a Padé series expansion of the square-root operator,

$$f(q) \equiv \sqrt{1+q} \simeq g(q) \equiv 1 + \sum_{j=1}^m \frac{a_{2j-1,m} q}{1 + a_{2j,m} q}, \quad (6.66)$$

where the coefficients are designed to guarantee both accuracy and stability. For elastic waveguides, some eigenvalues corresponding to evanescent modes have negative real parts [25]. Due to this fundamental difference between acoustic and elastic waveguides, the Padé coefficients given by Bamberger et al. [11] provide accuracy but not stability for the elastic PE. To guarantee that evanescent modes do not grow as the elastic PE solution is marched in range,  $g$  must map part of the lower left quadrant of the complex plane into the upper half of the complex plane, as shown by Wetton and Brooke [22]. The Padé coefficients are obtained by placing  $2m$  constraints on  $g$  and applying Newton's method [21]. The accuracy constraints require that derivatives of  $f$  and  $g$  agree at  $q = 0$ . The stability constraints require that  $g$  map all of the squared eigenvalues into the upper half of the complex plane. The coefficients tabulated by Collins [21] were derived by enforcing only one stability constraint, but they provide stability for most problems and are nearly as accurate as the coefficients of Bamberger et al. [11].

Applying the Padé approximation, we obtain the *elastic PE*

$$\frac{\partial}{\partial r} \begin{pmatrix} \Delta \\ w \end{pmatrix} = ik_0 \left\{ 1 + \sum_{j=1}^m \frac{a_{2j-1,m} (\mathbf{L}^{-1}\mathbf{M} - k_0^2 \mathbf{I})}{k_0^2 \mathbf{I} + a_{2j,m} (\mathbf{L}^{-1}\mathbf{M} - k_0^2 \mathbf{I})} \right\} \begin{pmatrix} \Delta \\ w \end{pmatrix}. \quad (6.67)$$

The numerical solution of (6.67) is based on a splitting method [20], which requires numerical solutions of

$$\frac{\partial}{\partial r} \begin{pmatrix} \Delta \\ w \end{pmatrix} = ik_0 \begin{pmatrix} \Delta \\ w \end{pmatrix} \quad (6.68)$$

and

$$[k_0^2 \mathbf{L} + a_{2j,m} (\mathbf{M} - k_0^2 \mathbf{L})] \frac{\partial}{\partial r} \begin{pmatrix} \Delta \\ w \end{pmatrix} = ik_0 a_{2j-1,m} (\mathbf{M} - k_0^2 \mathbf{L}) \begin{pmatrix} \Delta \\ w \end{pmatrix}. \quad (6.69)$$

The numerical solution of (6.68) is trivial. The solution of (6.69) as implemented by Collins [20] is based on a finite-difference depth discretization that is valid for piecewise-continuous depth variations and Crank–Nicolson integration in range.

For more details on the elastic PE, readers are referred to key references by Collins and co-workers [26–28]. A benchmark solution for propagation in an elastic wedge was published in the proceedings of the PE Workshop II held in 1991 [29]. Additional PE results illustrating the importance of shear for propagation over sloping elastic bottoms are given in Sect. 6.9.4.

## 6.4 Starting Fields

As stated earlier, the principal advantage of the parabolic wave equation over the elliptic Helmholtz equation is that the PE is a one-way wave equation which can be solved by a range-marching solution technique. This, however, requires specification of both initial and boundary conditions for the ocean environment considered. Although this section deals primarily with the starting field problem, we shall briefly outline how to treat the sea surface and the seafloor.

The free surface is traditionally treated as a pressure-release boundary requiring  $\psi(r, 0) = 0$ , which is easily implemented in any numerical solution scheme. The lower boundary condition is more complicated. We essentially wish to terminate the solution domain in depth ( $0 \leq z \leq z_{\max}$ ) by a radiation condition to simulate a bottom continuation by a homogeneous halfspace. In practice, this is accomplished by terminating the physical solution domain by an artificial absorption layer of several wavelengths thickness, so as to ensure that no significant energy is reflected from the lower boundary at  $z = z_{\max}$ . Within the physical solution domain the seabed generally exhibits a layered structure with strong impedance ( $\rho c$ ) contrasts at the interfaces. Consequently, we need to address the question of how to handle discontinuities and varying density in the PE. Moreover, for a realistic treatment of bottom

effects on wave propagation in the ocean, it is necessary to include absorption in the bottom material. All these issues related to the modeling of a layered seabed in the PE are addressed in Sects. 6.5 and 6.6.

We now return to the problem of establishing initial data for the PE, i.e., a specification of the complex pressure over depth  $\psi(r_0, z)$  at the starting range  $r_0$  of the computation. In principle, one could specify the actually measured field over depth (amplitude and phase) resulting from a source with some complicated radiation pattern. In practice, one is primarily interested in modeling a point source, or, to be more precise, a beam-limited source with an aperture that is compatible with the angular limitations of the PE to be solved. Both numerical and analytical techniques can be used to generate an appropriate PE starting field.

### 6.4.1 Numerical Starters

In principle, any numerical model based on ray tracing, normal-mode theory, or wavenumber integration techniques can be used to generate the acoustic field over depth at the initial range  $r_0$ . However, the modeling community has favored the normal-mode starter, which provides the initial field for a point source in a horizontally stratified medium. If we assume the environment to be locally range-independent near the source, the modal starter is appropriate, and if, in addition, only long-range propagation is considered, we can limit the modal sum to include just the discrete modal spectrum.

#### 6.4.1.1 Modal Starter

Before proceeding to derive an expression for a normalized modal starter, we introduce a simplified form of (6.3), which relates pressure  $p(r, z)$  to the PE envelope function  $\psi(r, z)$ , as

$$p(r, z) = \frac{\psi(r, z)}{\sqrt{r}} e^{i(k_0 r - \frac{\pi}{4})}. \quad (6.70)$$

When solving the parabolic wave equation in  $\psi(r, z)$  with a starting field normalized to the strength of a point source at 1-m distance from the source, transmission loss can be calculated as

$$TL = -20 \log \frac{|\psi|}{\sqrt{r}}, \quad (6.71)$$

where  $|\psi|$  denotes the modulus of the complex pressure.

The normalized modal field is obtained from (5.14) and (5.16) as

$$p(r, z) = \frac{1}{\rho(z_s)} \sqrt{\frac{2\pi}{r}} \sum_{m=1}^M \frac{\Psi_m(z_s) \Psi_m(z)}{\sqrt{k_{rm}}} e^{i(k_{rm} r - \frac{\pi}{4})}, \quad (6.72)$$

where  $\rho$  is the density,  $\Psi_m(z)$  the eigenfunctions,  $k_{rm}$  the eigenvalues, and  $z_s$  the source depth. By substituting this expression into (6.70) it is easily seen that the normalized starting field for  $\psi$  at  $r = 0$  takes the form

$$\psi(0, z) = \frac{\sqrt{2\pi}}{\rho(z_s)} \sum_{m=1}^M \frac{\Psi_m(z_s) \Psi_m(z)}{\sqrt{k_{rm}}}, \quad (6.73)$$

which is the *modal source*. By considering only the discrete modal spectrum we have implicitly limited the angular spectrum at the source to a halfwidth of  $\theta_1 = \arccos(c_0/c_{\max})$ , where  $c_0$  is the sound speed at the source and  $c_{\max}$  is the maximum speed in the bottom. A narrower source spectrum can be used by just summing over a subset of discrete modes.

The modal source is particularly useful when benchmarking PE solutions against normal-mode results in stratified environments. In this way, we ensure that the initial conditions are identical. It is also important to point out that the modal source has no source-depth restrictions, i.e., the source is allowed to be on the bottom as well as in the bottom. Only when the source is placed over a down-sloping bottom is the discrete modal starter inappropriate. This is because part of the continuous modal spectrum then can be coupled into the propagating spectrum, as shown by Tindle et al. [30]. Hence, it is important under these circumstances to use a source field with a wide angular spectrum, which can be obtained either numerically from the PE self starter described below or analytically from one of the wide-angle source function described in Sect. 6.4.2.

#### 6.4.1.2 PE Self Starter

The self starter developed by Collins [31, 32] is as accurate as the normal-mode starter but requires much less computational effort. This starter, which has been implemented for both the acoustic and the elastic PE, is obtained by solving a boundary-value problem involving the PE depth operator (hence the name) with a forcing delta function. The self starter is as efficient as the analytic starters. In contrast to the analytic starters, however, the self starter satisfies all interface and boundary conditions, depends on the depth-dependent properties of the medium, is valid for wide propagation angles for a source in a region of rapid depth dependence (such as near an interface), and properly excites interface waves.

Let us consider the case of a line source in a fluid layer of an otherwise layered elastic medium. The derivation of the self starter for a purely fluid case is similar. We assume that the environment is range independent in a small range interval (less than a wavelength) containing the source. In plane geometry with a forcing function, the equations of motion are of the form

$$\mathbf{L} \frac{\partial^2}{\partial x^2} \begin{pmatrix} \Delta \\ w \end{pmatrix} + \mathbf{M} \begin{pmatrix} \Delta \\ w \end{pmatrix} = \begin{pmatrix} \delta(x) \delta(z - z_0) \\ 0 \end{pmatrix}, \quad (6.74)$$

where the depth operators  $\mathbf{L}$  and  $\mathbf{M}$  are defined in the Sect. 6.3. The elastic PE is obtained by factoring (6.74) for  $x > 0$  to obtain

$$\frac{\partial}{\partial x} \begin{pmatrix} \Delta \\ w \end{pmatrix} = i(\mathbf{L}^{-1}\mathbf{M})^{1/2} \begin{pmatrix} \Delta \\ w \end{pmatrix}. \quad (6.75)$$

By integrating (6.74) over an arbitrarily small range interval about the origin, we obtain

$$\lim_{x \rightarrow 0^+} \mathbf{L} \frac{\partial}{\partial x} \begin{pmatrix} \Delta \\ w \end{pmatrix} = \begin{pmatrix} \frac{1}{2} \delta(z - z_0) \\ 0 \end{pmatrix}. \quad (6.76)$$

Substituting (6.75) into (6.76), we obtain

$$\mathbf{L} (\mathbf{L}^{-1}\mathbf{M})^{1/2} \begin{pmatrix} \Delta \\ w \end{pmatrix} = \begin{pmatrix} -\frac{1}{2}i \delta(z - z_0) \\ 0 \end{pmatrix}. \quad (6.77)$$

In principle, one could solve (6.77) directly by replacing the operator square root with a Padé approximation. Since the solution of (6.74) is singular at  $z = z_0$ , however, this approach is numerically difficult.

There is a numerically robust solution of (6.77) that involves three steps. We first write (6.77) as

$$\mathbf{M} (\mathbf{L}^{-1}\mathbf{M})^{-1/2} \begin{pmatrix} \Delta \\ w \end{pmatrix} = \begin{pmatrix} -\frac{1}{2}i \delta(z - z_0) \\ 0 \end{pmatrix}. \quad (6.78)$$

The first step involves solving

$$\mathbf{M} \begin{pmatrix} \Delta_0 \\ w_0 \end{pmatrix} = \begin{pmatrix} -\frac{1}{2}i \delta(z - z_0) \\ 0 \end{pmatrix}, \quad (6.79)$$

where

$$\begin{pmatrix} \Delta_0 \\ w_0 \end{pmatrix} \equiv (\mathbf{L}^{-1}\mathbf{M})^{-1/2} \begin{pmatrix} \Delta \\ w \end{pmatrix}. \quad (6.80)$$

Since the solution of (6.79) is related to the wavenumber spectrum, which is bounded, it may be obtained numerically using a finite-difference approach [21]. In the normal-mode representation, the solution of (6.79) differs from the solution of (6.77) only by the power of the eigenvalue that appears as a factor in each term. The second step involves using the solution of (6.79) to initialize the elastic PE and marching out a short distance in range to  $x = x_0$  to eliminate the evanescent modes, which compose the singularity at  $z = z_0$ . The third step involves operating on the field to correct the power of the eigenvalue factors as follows,

$$\begin{pmatrix} \Delta \\ w \end{pmatrix} = (\mathbf{L}^{-1}\mathbf{M})^{1/2} \begin{pmatrix} \Delta_0 \\ w_0 \end{pmatrix} \simeq ik_0 \prod_{j=1}^m \frac{k_0^2 \mathbf{L} + \alpha_{j,m} (\mathbf{M} - k_0^2 \mathbf{L})}{k_0^2 \mathbf{L} + \beta_{j,m} (\mathbf{M} - k_0^2 \mathbf{L})} \begin{pmatrix} \Delta_0 \\ w_0 \end{pmatrix}, \quad (6.81)$$

where the field quantities in (6.81) depend on both  $x$  and  $z$ . As in Sect. 6.3 on the elastic PE, the operator square root is replaced with a Padé approximation, written here as a product rather than a sum for convenience.

The self starter for the elastic PE is easily generalized to the case of a point source. Since the normal-mode expansions for the line source and point source solutions differ in the farfield only by the power of the eigenvalue factors (see Sect. 5.2), the third step for the point-source case involves operating on the field with  $(\mathbf{L}^{-1}\mathbf{M})^{3/4}$  rather than  $(\mathbf{L}^{-1}\mathbf{M})^{1/2}$ . Padé coefficients for the self starter are tabulated in [31].

## 6.4.2 Analytical Starters

### 6.4.2.1 Gaussian Source

The analytical source functions are all designed to closely match the farfield result for a point-source solution of the Helmholtz equation in a homogeneous medium. Following this logic and taking into account also the requirement to limit the source aperture to be consistent with the angular limitations associated with a particular parabolic wave equation, Tappert [3] originally proposed a Gaussian starter for use with the standard PE. This source function has the form

$$\psi(0, z) = A e^{-\frac{(z-z_s)^2}{W^2}}, \quad (6.82)$$

where  $A$  is the effective source level,  $W$  is the beamwidth, and  $z_s$  is the source depth. In order to determine  $A$  and  $W$ , we follow Brock [33] and solve the standard PE for a homogeneous medium with the above starting field. We see from (6.27) that the PE with  $n^2(r, z) = 1$  takes the form

$$\frac{\partial \psi}{\partial r} = \frac{i}{2k_0} \frac{\partial^2 \psi}{\partial z^2}, \quad (6.83)$$

which is similar to the well-studied, one-dimensional heat diffusion equation.

The solution of the initial-value problem given by (6.82) and (6.83) is most easily carried out in the transform domain defined by the complex Fourier transform pair,

$$\psi(r, z) = \int_{-\infty}^{\infty} \psi(r, k_z) e^{ik_z z} dk_z, \quad (6.84)$$

$$\psi(r, k_z) = \frac{1}{2\pi} \int_{-\infty}^{\infty} \psi(r, z) e^{-ik_z z} dz, \quad (6.85)$$

where  $k_z$  is the vertical wavenumber.

We first transform (6.83) to obtain

$$\int_{-\infty}^{\infty} \left( \frac{\partial}{\partial r} - \frac{i}{2k_0} \frac{\partial^2}{\partial z^2} \right) \psi(r, z) e^{-ik_z z} dz = 0. \quad (6.86)$$

The only term in this integral that requires attention is the second term in the parentheses. For a well-behaved function with  $\psi(r, z)$  and  $\partial\psi/\partial z$  both approaching zero as  $z \rightarrow \pm\infty$ , it is easily verified through integration by parts that we have

$$\int_{-\infty}^{\infty} \frac{\partial^2 \psi(r, z)}{\partial z^2} e^{-ik_z z} dz = -k_z^2 \psi(r, k_z), \quad (6.87)$$

where  $\psi(r, k_z)$  is given by (6.85). This is an important result which shall be used repeatedly in this section.

Equation (6.86) now becomes

$$\left( \frac{\partial}{\partial r} + \frac{ik_z^2}{2k_0} \right) \psi(r, k_z) = 0, \quad (6.88)$$

which is a linear, first-order differential equation with the solution

$$\psi(r, k_z) = \psi(0, k_z) e^{-\frac{ik_z^2 r}{2k_0}}. \quad (6.89)$$

Next we transform the initial condition given by (6.82) to obtain

$$\begin{aligned} \psi(0, k_z) &= \frac{1}{2\pi} \int_{-\infty}^{\infty} A e^{-\frac{(z-z_s)^2}{W^2}} e^{-ik_z z} dz \\ &= \frac{A}{2\pi} e^{-ik_z z_s} \int_{-\infty}^{\infty} e^{-\frac{t^2}{W^2}} e^{-ik_z t} dt, \end{aligned} \quad (6.90)$$

where we have introduced the substitution  $t = z - z_s$ .

From integral tables we find that the solution of (6.90) in its most general form is given by

$$\int_{-\infty}^{\infty} e^{-at^2} e^{\pm ibt} dt = \sqrt{\frac{\pi}{a}} e^{-\frac{b^2}{4a}} \quad (6.91)$$

leading to the following expression for the transformed initial field

$$\psi(0, k_z) = \frac{AW}{2\sqrt{\pi}} e^{-ik_z z_s} e^{-\frac{k_z^2 W^2}{4}}. \quad (6.92)$$

By substituting this result into (6.89) and transforming back to the  $z$ -domain we obtain

$$\psi(r, z) = \frac{AW}{2\sqrt{\pi}} \int_{-\infty}^{\infty} e^{-\left(\frac{W^2}{4} + \frac{ir}{2k_0}\right)k_z^2} e^{i(z-z_s)k_z} dk_z. \quad (6.93)$$

This integral is again of the general form given by (6.91), and, consequently, we can proceed to write the desired field solution as

$$\psi(r, z) = \frac{A}{\sqrt{1 + \frac{i2r}{k_0 W^2}}} \exp \left[ -\frac{(z - z_s)^2}{W^2 \left( 1 + \frac{i2r}{k_0 W^2} \right)} \right]. \quad (6.94)$$

This solution is seen to be a Gaussian distribution with decreasing peak level and increasing beamwidth as a function of range.

In order to match pressure amplitudes in the farfield, we next evaluate  $|p|^2 = r^{-1} \psi \psi^*$ , where  $*$  denotes the complex conjugate. Introducing the abbreviation  $\varepsilon = k_0^2 W^4 / 4r^2$  we obtain

$$|p|^2 = \frac{k_0 A^2 W^2}{2r^2 \sqrt{1 + \varepsilon}} \exp \left[ -\frac{k_0^2 W^2 (z - z_s)^2}{2r^2 (1 + \varepsilon)} \right], \quad (6.95)$$

where  $\varepsilon \ll 1$  in the farfield. Neglecting the  $\varepsilon$ -term and retaining two terms of the series expansion of the exponential function, we arrive at the following approximate expression for the PE pressure variation in the farfield,

$$|p|^2 \simeq \frac{k_0 A^2 W^2}{2r^2} \left[ 1 - \frac{k_0^2 W^2}{2r^2} (z - z_s)^2 \right]. \quad (6.96)$$

We now turn to the normalized point-source field in a homogeneous medium given by

$$|p|^2 = \frac{1}{R^2}; \quad R^2 = r^2 + (z - z_s)^2. \quad (6.97)$$

We can rewrite this as

$$|p|^2 = \frac{1}{r^2 \left[ 1 + \frac{(z - z_s)^2}{r^2} \right]} \quad (6.98)$$

and for  $r \gg z - z_s$ , expand the second factor in the denominator to obtain

$$|p|^2 \simeq \frac{1}{r^2} \left[ 1 - \frac{(z - z_s)^2}{r^2} \right]. \quad (6.99)$$

By comparing (6.96) and (6.99) it is easily verified that a field matching is achieved by using the following values for  $A$  and  $W$ ,

$$A = \sqrt{k_0}, \quad W = \frac{\sqrt{2}}{k_0}. \quad (6.100)$$

The starting field given in (6.82) can now be written

$$\psi(0, z) = \sqrt{k_0} e^{-\frac{k_0^2}{2}(z - z_s)^2}, \quad (6.101)$$

which is the standard *Gaussian source*.

The advantage of an analytical source is that the starting field is generated with minimum computational effort. The Gaussian source has therefore been used extensively in the community, and it is an appropriate starter for use with the standard parabolic equation. However, when solving wide-angle propagation problems, a more wide-angle starter is required.

#### 6.4.2.2 Greene's Source

One example of a source with good wide-angle properties is a weighted Gaussian of the form

$$\psi(0, z) = \sqrt{k_0} [1.4467 - 0.4201 k_0^2 (z - z_s)^2] e^{-\frac{k_0^2(z-z_s)^2}{3.0512}}, \quad (6.102)$$

which is *Greene's source* [8]. As shown in the next section, this source is ideal for use with wide-angle PEs.

#### 6.4.2.3 Thomson's Source

Some effort has gone into constructing analytic starters with better spectral properties than both the Gaussian and Greene's source, i.e., with a sharper cutoff outside a specified source aperture. One such source proposed by Thomson [34] models the spectrum of a point source in a homogeneous halfspace, i.e., the surface boundary condition is built into the source spectrum. The *Thomson halfspace source* is defined in vertical wavenumber space for  $0 \leq |k_z| \leq k_0 \sin \theta_1$  by

$$\psi(0, k_z) = \sqrt{\frac{8\pi}{k_0}} \sin(k_z z_s) \left(1 - \frac{k_z^2}{k_0^2}\right)^{-1/4}, \quad (6.103)$$

where  $\theta_1$  is the half-beamwidth of the source. Outside this aperture  $\psi(0, k_z)$  is set to zero. The field in  $z$ -space is determined by taking an inverse Fourier transform, i.e.,  $\psi(0, z) = \mathcal{F}^{-1}\{\psi(0, k_z)\}$ .

As demonstrated numerically in the next section, the Thomson source provides the correct farfield solution for a point source in a homogeneous halfspace when propagated with an exact one-way wave equation. This, in turn, means that the Thomson source is ideal for use with the very-wide-angle PEs. Moreover, a beam-limited aperture is easily introduced by truncating the integration interval in  $k_z$ -space where the function  $\sin(k_z z_s)$  vanishes, i.e., for  $k_z = m(\pi/z_s)$ , where  $m$  indicates the number of surface-interference (Lloyd-mirror) beams to be included in the source field. Note that no amplitude tapering is required when choosing a source aperture that coincides with a null in the Lloyd-mirror beam pattern.

#### 6.4.2.4 Generalized Gaussian Source

For completeness we finally derive a Gaussian source with both variable beamwidth and beam tilt. In the expression for the farfield pressure distribution given by (6.95), we neglect the small  $\varepsilon$ -term and introduce the propagation angle with respect to horizontal as  $\tan \theta = (z - z_s)/r$  to obtain

$$|p|^2 = \frac{k_0 A^2 W^2}{2r^2} e^{-\frac{k_0^2 W^2}{2} \tan^2 \theta}. \quad (6.104)$$

As is customary for Gaussian beams, we define the beamwidth as the 1/e-decay point perpendicular to the axis. Denoting the angle associated with this particular beamwidth by  $\theta_1$ , we find  $W$  from the requirement that the exponent to the exponential in (6.104) be equal to  $-1$ , i.e.,

$$W^2 = \frac{2}{k_0^2 \tan^2 \theta_1}. \quad (6.105)$$

The source amplitude  $A$  is again determined so that the on-axis pressure in the farfield agrees with the point source result of (6.99),

$$A = \sqrt{k_0} \tan \theta_1. \quad (6.106)$$

We can now write the *generalized Gaussian source* as

$$\psi(0, z) = \sqrt{k_0} \tan \theta_1 e^{-\frac{k_0^2}{2}(z-z_s)^2 \tan^2 \theta_1} e^{ik_0(z-z_s) \sin \theta_2}, \quad (6.107)$$

where  $\theta_1$  is the halfwidth of the source aperture as defined above and  $\theta_2$  is the beam tilt with respect to the horizontal, measured positive downward. The beam tilt, which can be applied to any of the sources presented in this section, has been introduced by simply adding a linear phase delay across the vertical source “array”. Note that the standard Gaussian source, (6.101), is retrieved from the variable-beamwidth formula with  $\theta_1 = 45^\circ$ .

The generalized Gaussian source, (6.107), is particularly useful in modeling highly directional sources tilted toward the sea surface or the seafloor. On the other hand, the Gaussian source should not be used to model sources with a halfwidth larger than  $45^\circ$ , since better results here are obtained with the wide-angle sources proposed by Greene, (6.102), and Thomson, (6.103). A detailed comparison of farfield radiation patterns for different sources propagated with different PEs is given in Sect. 6.4.3.

Since all the analytic starters presented in this section were set up for a homogeneous medium, special precautions must be taken when the source is near a boundary. The sea surface (already included in Thomson’s source) is handled by simply subtracting the contribution from the image source,

$$\psi(0, z) = \psi(0, z - z_s) - \psi(0, z + z_s), \quad (6.108)$$

which ensures that the surface boundary condition  $\psi = 0$  is fulfilled. The bottom boundary, on the other hand, is not easily incorporated in the source field, and analytic starters are generally considered inappropriate when the source is within a wavelength of the seafloor.

The effect of placing the source on or near the seafloor can be illustrated through a numerical example. We again turn to test problem 3B from the PE workshop [4], which is a Pekeris problem with an isovelocity (1500 m/s) water column of 100-m depth overlying a homogeneous bottom with a wave speed of 1590 m/s and an attenuation of  $0.5 \text{ dB}/\lambda$ . In order to maximize the effect of the water–bottom interface on the source field, we place the source right on the bottom ( $SD = 100 \text{ m}$ ) and also increase the density contrast from 1.2 to 2.0.

The computed propagation loss for a frequency of 250 Hz and a receiver depth of 100 m is shown in Fig. 6.3. The solid line is the reference solution obtained with the Claerbout equation using a modal source that incorporates the bottom-boundary condition. The dashed line, on the other hand, is an approximate result obtained using Greene's source derived for a homogeneous medium. We notice that the prediction error in this case is around 2.5 dB. Numerical tests indicate that the error primarily is dependent on the density contrast across the water–bottom interface and on the distance of the source from the interface. Thus, the prediction error was negligible in the original test problem with a density contrast of only 1.2 and the source positioned 0.5 m above the interface.

It is easily seen from (6.102) that the source field decays to zero within a vertical distance of approximately  $\lambda/3$  from the nominal source position. This, in turn,

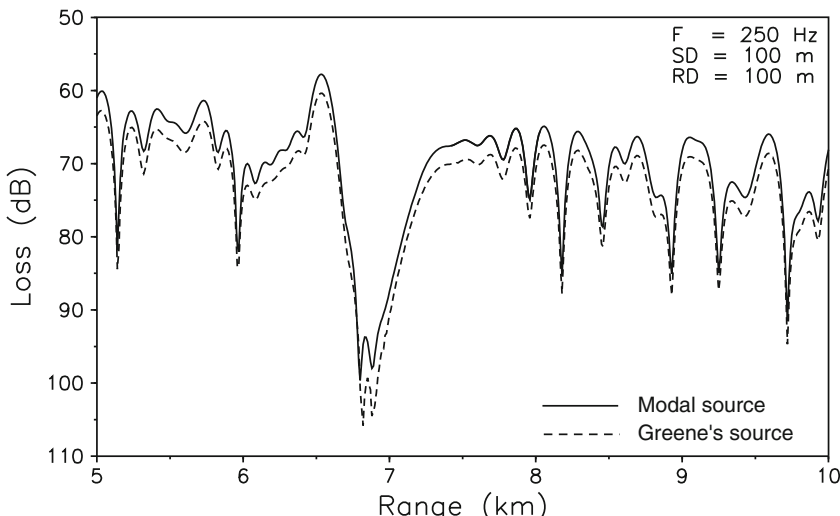


**Fig. 6.3** Comparison of transmission loss results for sources placed on the seafloor. The modal source includes the bottom boundary condition, while Greene's source assumes a homogeneous medium at the source range

means that the source needs to be within  $\lambda/3$  of the interface for the error to be significant. Moreover, the fact that the prediction error in Fig. 6.3 is mainly a level error, with the multipath interference structure being only weakly affected, seems to suggest that a first-order error correction could be achieved by a simple renormalization of the source level. This idea, however, still needs formal justification.

### 6.4.3 Spectral Properties of Sources

Various analytical sources were derived to provide a farfield radiation pattern which, within a beam-limited aperture, matches a point-source solution of the Helmholtz equation in a homogeneous medium. However, since each form of the parabolic wave equation (Tappert Equation, Claerbout Equation, etc.) leads to a different farfield radiation pattern for the same starting field, it is not possible to define a source beamwidth without specifying also the wave equation used for propagating the field. In fact, the generalized Gaussian source with variable beamwidth, (6.107), was derived using the Tappert equation as a propagator, and, consequently, the effective beamwidth will change if this same source field is propagated with, for example, the wide-angle Claerbout equation.

Since the various analytical sources presented in the previous section are not equally suited for use with both narrow and wide-angle PEs, it is of interest to investigate the effective (farfield) beam pattern of these sources when propagated with different parabolic equations in, for instance, a homogeneous halfspace. In this way, we can provide specific guidance on which source field to use with a particular PE.

We shall numerically generate a series of farfield radiation patterns for three different analytical sources (Gaussian, Greene, Thomson) propagated by three different wave equations: the narrow-angle Tappert equation, (6.27), the Thomson–Chapman equation, (6.41), and the wide-angle Claerbout equation, (6.43). The test problem is a homogeneous halfspace with a sound speed of 1500 m/s, a density of 1000 kg/m<sup>3</sup>, and no volume attenuation. The reference solution is obtained by numerically evaluating the field from a point source located at  $(0, z_s)$  and given by

$$p(r, z) = \frac{e^{ikR_1}}{R_1} - \frac{e^{ikR_2}}{R_2}, \quad (6.109)$$

where

$$R_1 = \sqrt{r^2 + (z - z_s)^2}, \quad R_2 = \sqrt{r^2 + (z + z_s)^2},$$

are the distances from a field point to the source and its image, respectively. This image solution is known to produce a beam pattern resulting from constructive and destructive interference between the two possible propagation paths connecting the source with a given field point: the direct path and the surface-reflected (image

source) path. This Lloyd-mirror beam pattern, analyzed in detail in Sect. 1.4.2, consists of a finite number of beams  $m$  with directions far from the source given by

$$\sin \theta_m = (2m - 1) \frac{\lambda}{4z_s}, \quad (6.110)$$

where  $\lambda = 2\pi/k$  is the acoustic wavelength,  $z_s$  is the source depth, and  $\theta_m$  is the beam angle relative to horizontal.

The reference solution given by (6.109) is displayed in Fig. 6.4a as a contour map of transmission loss,  $TL = -10 \log(pp^*)$ . The frequency is 100 Hz and the source depth 75 m. For this particular source depth there are ten Lloyd-mirror beams with tilt angles varying between  $2.87^\circ$  for the most horizontal beam to  $71.8^\circ$  for the steepest beam. For comparison an approximate solution obtained from the Tappert PE with a  $45^\circ$  Gaussian source is shown in Fig. 6.4b. Note that only the first three or four beams propagating within  $15$ – $20^\circ$  with respect to the horizontal are in the right positions, which is entirely consistent with the phase-error analysis of Sect. 6.2.4. The observed decay in beam intensity toward steeper angles is a direct consequence of the limited aperture of the Gaussian source.

To quantify differences between the various PE solutions and the reference solution given in Fig. 6.4a, we compare propagation losses along a circular path with a radius of 500 m centered on the origin. The resulting display of propagation loss versus declination angle is shown in Fig. 6.5 for three different sources (Gaussian source in row 1, Greene's source in row 2, and Thomson's source in row 3) propagated with three different parabolic equations as indicated at the top of each column. Note that the Thomson–Chapman PE (T&C), (6.41), has no phase errors nor angular limitations for a homogeneous medium and hence can be considered a reference solution in this case. We consequently take the T&C results in the last column to represent the very-wide-angle PEs, i.e., “exact” one-way wave-equation solutions. Hence, the hierarchy in Fig. 6.5 is the following: We have increasingly accurate PE solutions moving from left to right, and we have increasing source aperture moving from top to bottom. The solid line is the reference solution showing both position and intensity of the ten Lloyd-mirror beams. Indicated on each figure is also the 3-dB half-beamwidth associated with the various PE results (dashed lines).

It is evident from the sequence of plots in column 1 of Fig. 6.5 that the Gaussian source is well matched to the Tappert equation yielding a gradual amplitude decay toward steeper angles ( $\theta_{3\text{dB}} \simeq 52^\circ$ ). The two wide-angle sources, on the other hand, cause amplitude overshoots of 3–4 dB and these sources should not be used with this narrow-angle PE.

Looking next at the plots in column 2 for Claerbout's wide-angle PE, we notice that the best results here are obtained with Greene's source. The Gaussian source is too narrow-angled and Thomson's source again causes a 3-dB amplitude overshoot in directions between  $40$  and  $60^\circ$ . Note that the smaller phase errors in the Claerbout equation result in an accurate positioning of the first five beams compared to only two beams in the Tappert equation.

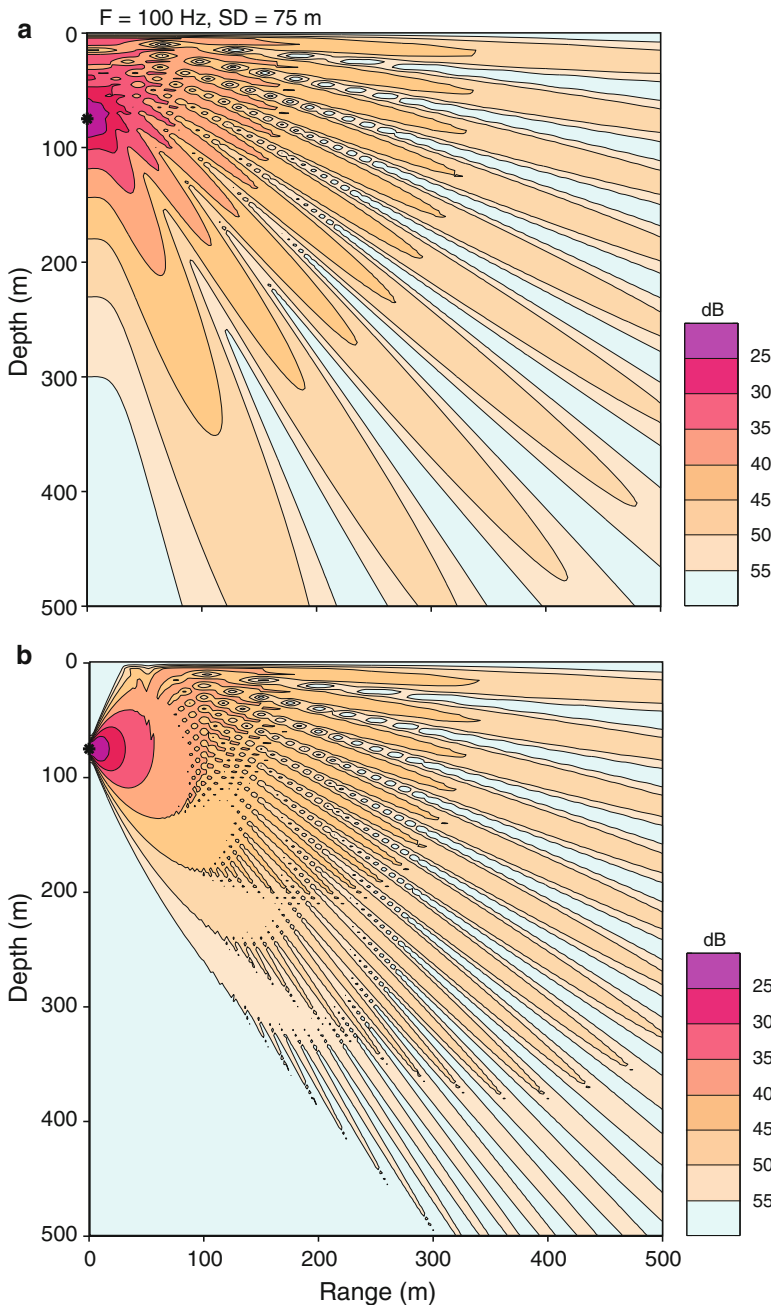


**Fig. 6.4** Angular radiation patterns for source near a free surface in a homogeneous halfspace. (a) Lloyd-mirror reference solution for a point source. (b) PE solution for a 45° Gaussian source propagated with the narrow-angle Tappert equation

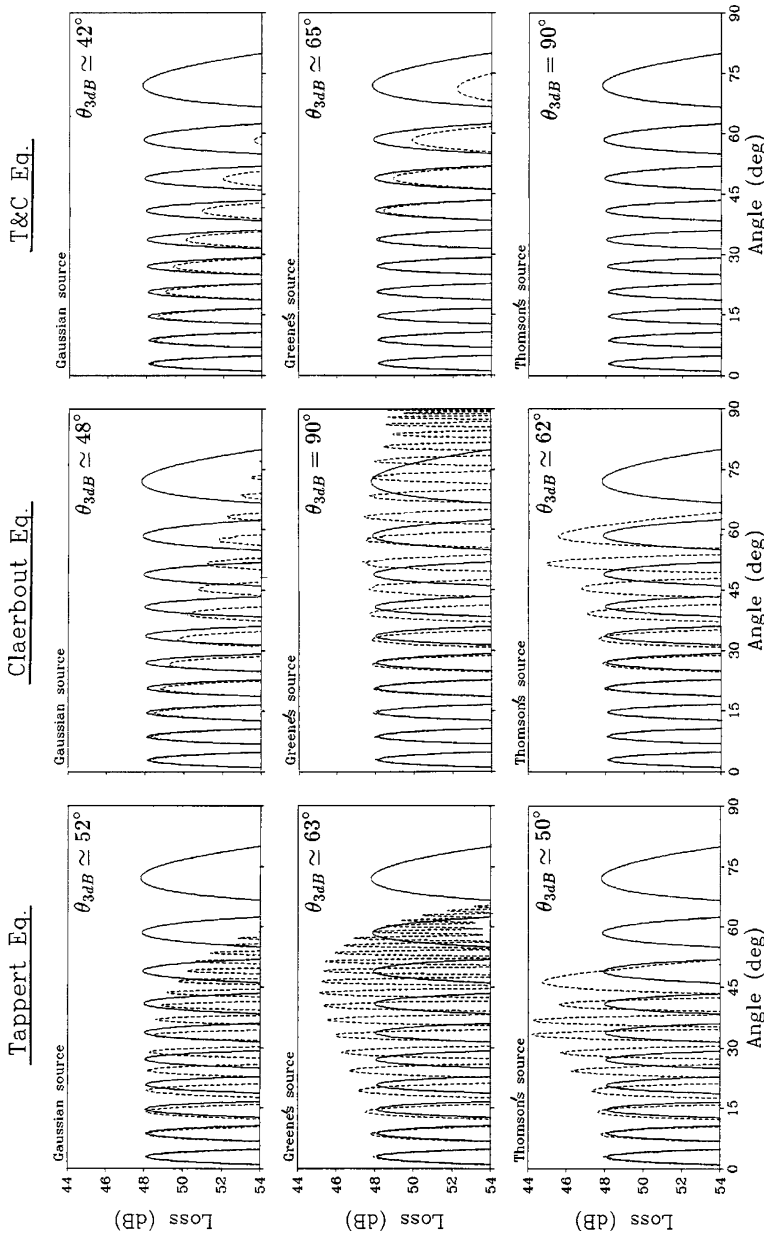


**Fig. 6.5** Farfield radiation patterns (dashed lines) for three different sources ( $45^\circ$  Gaussian source, Greene's wide-angle source, and Thomson's halfspace source) propagated with three different parabolic equations: The narrow-angle Tappert PE, the wide-angle Claerbout PE, and the Thomson-Chapman PE. The full line is the Lloyd-mirror reference solution at a distance of 500 m from the origin. The 3-dB half-beamwidth is indicated on each graph

The last column represents very-wide-angle PE results with zero phase errors and, hence, all beams are correctly positioned. Moreover, there is a smooth amplitude decay with increasing angle for both the Gaussian source ( $\theta_{3\text{dB}} \approx 42^\circ$ ) and Greene's source ( $\theta_{3\text{dB}} \approx 65^\circ$ ). However, Thomson's source here provides a full-spectrum result indistinguishable from the Lloyd-mirror reference solution.

While the Gaussian sources is seen to result in similar farfield radiation patterns for the various wave equations (though with varying beamwidth) wide-angle sources must be carefully selected and matched to a particular PE in order to ensure optimal farfield radiation characteristics. It is seen from Fig. 6.5 that the optimal choice of an analytic source function goes along the upper-left to lower-right diagonal, with a Gaussian source for the narrow-angle Tappert equation, Greene's source for the wide-angle Claerbout equation, and Thomson's halfspace source for any of the very-wide-angle PEs. Of course, the numerical self starter discussed in Sect. 6.4.1 is automatically matched to any PE propagator and hence constitutes the optimal starter in general terms.

## 6.5 Solutions by FFTs

The principal advantage of the various parabolic wave equations derived in Sect. 6.2 is that they constitute an initial-value problem in range and hence can be solved by a range-marching numerical technique, given a source-field distribution over depth at the initial range. Over the years, several different solution techniques have been implemented in computer codes [5], but only the split-step Fourier technique and various finite-difference/ finite-element techniques have gained widespread use in the underwater acoustics community.

Before going into details on the numerical solution schemes, let us briefly point out some advantages and disadvantages of these two main solution techniques. The split-step algorithm has been used extensively to solve the standard PE ever since it was devised by Hardin and Tappert [2] in the early 1970s. This technique is computationally efficient for long-range, narrow-angle propagation problems with negligible bottom interaction. For short-range, deep-water problems and shallow-water problems in general, propagation is basically more wide-angled and bottom-interacting paths become important. This requires use of one of the wide-angle PEs, which can be solved only by finite differences or finite elements. Moreover, the strong speed and density contrasts encountered at the water–bottom interface adversely affect the computational efficiency of the split-step technique, which in cases of strong bottom interaction requires an excessively fine computational grid ( $\Delta r, \Delta z$ ). Hence, the advantage of higher computational efficiency of the split-step technique is entirely lost in situations with strong bottom interaction.

Finite-difference/ finite-element techniques are applicable to any of the PE forms derived in Sect. 6.2. The main disadvantage of these techniques is that they are less efficient than the split-step technique for long-range, narrow-angle problems with little or no bottom interaction. Since many practical ocean-acoustic problems of

naval interest are of this type, it is likely that the split-step technique will remain the preferred technique for sonar-performance predictions for some time to come. The FD/FE methods, on the other hand, are more generally applicable and provide higher accuracy in wide-angle, bottom-interacting situations. Consequently, these techniques are likely to dominate PE modeling in the scientific community in the future.

The most recent development in terms of efficient PE solution schemes is a “split-step” Padé solution devised by Collins [35]. He uses higher-order Padé approximations not of the square-root operator itself but rather of a composition of the exponential and square-root operators. The result is a considerable efficiency gain through the use of larger range steps. Thus the scheme is claimed to be more than an order-of-magnitude faster than standard FD/FE solution schemes. This, in turn, could lead to a unified PE solution approach where the accurate high-angle PEs can be solved with the efficiency of the classical split-step Fourier technique.

### 6.5.1 The Split-Step Fourier Algorithm

As was the case when deriving the standard parabolic equation in Sect. 6.2.1, we shall also here start with a rather heuristic approach to solving this PE by Fourier transform techniques. Subsequently, we present a more complete derivation based on a generalized operator formalism.

In the heuristic approach, we start by transforming the entire parabolic equation, (6.9), under the assumption that the refraction index  $n$  is constant. With the forward transform given by (6.84) and making use also of the transform property derived in (6.87), we easily see that the transformed wave equation in  $\psi(r, k_z)$  takes the form

$$2ik_0 \frac{\partial\psi}{\partial r} - k_z^2 \psi + k_0^2 (n^2 - 1) \psi = 0 \quad (6.111)$$

or by rearranging the terms

$$\frac{\partial\psi}{\partial r} + \frac{k_0^2 (n^2 - 1) - k_z^2}{2ik_0} \psi = 0. \quad (6.112)$$

This is a linear, first-order differential equation with the solution

$$\psi(r, k_z) = \psi(r_0, k_z) e^{-\frac{k_0^2(n^2-1)-k_z^2}{2ik_0}(r-r_0)}. \quad (6.113)$$

We now transform back to the  $z$ -domain and get the field solution

$$\psi(r, z) = e^{\frac{ik_0}{2}(n^2-1)(r-r_0)} \int_{-\infty}^{\infty} \psi(r_0, k_z) e^{-\frac{i(r-r_0)}{2k_0}k_z^2} e^{ik_z z} dk_z. \quad (6.114)$$

We next denote the range increment  $r - r_0$  by  $\Delta r$  and introduce the symbol  $\mathcal{F}$  for the Fourier transform from the  $z$ -domain to the  $k_z$ -domain and  $\mathcal{F}^{-1}$  as the inverse transform. The field solution can then be written in the compact form

$$\psi(r, z) = e^{\frac{i k_0}{2} [n^2(r_0, z) - 1] \Delta r} \mathcal{F}^{-1} \left\{ e^{-\frac{i \Delta r}{2 k_0} k_z^2} \mathcal{F} \{ \psi(r_0, z) \} \right\}, \quad (6.115)$$

which is the split-step marching algorithm proposed by Hardin and Tappert [2] for solving the standard parabolic equation. The solution was derived for the trivial case of a uniform medium, but, as we shall see, the error incurred for  $n = n(r, z)$  is of order  $(\Delta r)^2$  and hence can be made arbitrarily small by choosing a small computational range step. The algorithm was shown by Tappert to be unconditionally stable.

We next develop a solution scheme based on a generalized operator formalism, which has proven convenient for a detailed error analysis of the various approximations involved.

Let us write the parabolic wave equation (6.9) in the form

$$\frac{\partial \psi}{\partial r} = \left[ \frac{i k_0}{2} (n^2 - 1) + \frac{i}{2 k_0} \frac{\partial^2}{\partial z^2} \right] \psi \quad (6.116)$$

and introduce the two operators

$$A = \frac{i k_0}{2} [n^2(r, z) - 1]; \quad B = \frac{i}{2 k_0} \frac{\partial^2}{\partial z^2} \quad (6.117)$$

to arrive at the following compact form of the PE, a first-order differential equation in  $r$ ,

$$\frac{\partial \psi}{\partial r} = (A + B) \psi = U(r, z) \psi. \quad (6.118)$$

Here,  $U = A + B$  is the composite operator, which depends on both  $r$  and  $z$ .  $A = A(r, z)$  is seen to be a multiplication operator and  $B = B(z)$  a differential operator.

We now write the solution to (6.118) formally as

$$\begin{aligned} \psi(r, z) &= e^{\int_{r_0}^{r_0 + \Delta r} U(r, z) dr} \psi(r_0, z) \\ &\simeq e^{\widetilde{U} \Delta r} \psi(r_0, z), \end{aligned} \quad (6.119)$$

where we have approximated the behavior of  $U(r, z)$  over the range interval  $\Delta r$  by the quantity  $\widetilde{U}$ . In the next section, we demonstrate that the error involved is of order  $(\Delta r)^2$  or  $(\Delta r)^3$  depending on the choice of  $\widetilde{U}$ .

The next step toward a numerical solution is to split the exponential operator  $\exp[(A + B)\Delta r]$  in one of the following ways, arriving at forms which have all appeared in the literature,

$$(I) : \quad e^{(A+B)\Delta r} \simeq e^{A\Delta r} e^{B\Delta r}, \quad (6.120)$$

$$(II) : \quad e^{(A+B)\Delta r} \simeq e^{B\Delta r} e^{A\Delta r}, \quad (6.121)$$

$$(III) : \quad e^{(A+B)\Delta r} \simeq e^{\frac{A}{2}\Delta r} e^{B\Delta r} e^{\frac{A}{2}\Delta r}, \quad (6.122)$$

$$(IV) : \quad e^{(A+B)\Delta r} \simeq e^{\frac{B}{2}\Delta r} e^{A\Delta r} e^{\frac{B}{2}\Delta r}. \quad (6.123)$$

These forms are approximate except when the operators  $A$  and  $B$  commute. We later show that the errors are of order  $(\Delta r)^2$  or  $(\Delta r)^3$  depending on the form of the splitting.

The mathematical meaning of the exponential operators shall become clear shortly. Terms of form  $\exp(A \Delta r)$  are multiplication operators, which are easily handled in a numerical context. The  $\exp(B \Delta r)$  terms are to be evaluated by Fourier transforms. Let us take as an example the  $B$ -term from (6.120) and denote it by  $V$ ,

$$V(r_0, z) = e^{B\Delta r} \psi(r_0, z); \quad B = \frac{i}{2k_0} \frac{\partial^2}{\partial z^2}. \quad (6.124)$$

We next expand the exponential function to obtain

$$\begin{aligned} V(r_0, z) &= \left[ 1 + \Delta r B + \frac{(\Delta r)^2}{2} BB + \dots \right] \psi(r_0, z) \\ &= \left[ 1 + \frac{i\Delta r}{2k_0} \frac{\partial^2}{\partial z^2} + \frac{1}{2} \left( \frac{i\Delta r}{2k_0} \right)^2 \frac{\partial^4}{\partial z^4} + \dots \right] \psi(r_0, z), \end{aligned} \quad (6.125)$$

which shows explicitly the meaning of the exponential operator in  $B$ . Carrying out a Fourier transformation of the entire equation, and making use of the result obtained earlier in (6.87), yields

$$V(r_0, k_z) = \left[ 1 - \frac{i\Delta r}{2k_0} k_z^2 + \frac{1}{2} \left( \frac{i\Delta r}{2k_0} \right)^2 k_z^4 - \dots \right] \psi(r_0, k_z) \quad (6.126)$$

or, simply

$$V(r_0, k_z) = e^{-\frac{i\Delta r}{2k_0} k_z^2} \psi(r_0, k_z). \quad (6.127)$$

An inverse transform of this equation immediately leads to a solution for  $V$  in terms of two Fourier transforms,

$$V(r_0, z) = \mathcal{F}^{-1} \left\{ e^{-\frac{i\Delta r}{2k_0} k_z^2} \mathcal{F} \{ \psi(r_0, z) \} \right\}. \quad (6.128)$$

Having established how to numerically evaluate the exponential operators in  $B$  in transform space, it is straightforward to write down the split-step marching solutions related to each of the four splittings given in (6.120)–(6.123),

$$\psi_1(r, z) = e^{\frac{ik_0}{2}[n^2(r_0, z)-1]\Delta r} \mathcal{F}^{-1} \left\{ e^{-\frac{i\Delta r}{2k_0} k_z^2} \mathcal{F} \{ \psi(r_0, z) \} \right\}, \quad (6.129)$$

$$\psi_{\text{II}}(r, z) = \mathcal{F}^{-1} \left\{ e^{-\frac{i\Delta r}{2k_0} k_z^2} \mathcal{F} \left\{ e^{\frac{ik_0}{2} [n^2(r_0, z) - 1]\Delta r} \psi(r_0, z) \right\} \right\}, \quad (6.130)$$

$$\psi_{\text{III}}(r, z) = e^{\frac{ik_0}{4} [n^2(r_0, z) - 1]\Delta r} \mathcal{F}^{-1} \left\{ e^{-\frac{i\Delta r}{2k_0} k_z^2} \mathcal{F} \left\{ e^{\frac{ik_0}{4} [n^2(r_0, z) - 1]\Delta r} \psi(r_0, z) \right\} \right\}, \quad (6.131)$$

$$\psi_{\text{IV}}(r, z) = \mathcal{F}^{-1} \left\{ e^{-\frac{i\Delta r}{4k_0} k_z^2} \mathcal{F} \left\{ e^{\frac{ik_0}{2} [n^2(r_0, z) - 1]\Delta r} \mathcal{F}^{-1} \left[ e^{-\frac{i\Delta r}{4k_0} k_z^2} \mathcal{F}[\psi(r_0, z)] \right] \right\} \right\}. \quad (6.132)$$

Details on the numerical implementation of any of these forms in terms of a discrete FFT shall be dealt with in Sect. 6.5.3. However, a few general comments on the four different solution algorithms are in order at this point.

First of all we notice that the refraction index  $n(r_0, z)$  in all cases has been evaluated at range  $r_0$ . There is a subtlety associated with this choice, since, as shown in the next section, some of the error terms can be made an order smaller in  $\Delta r$  by choosing  $n^2 = n^2(r_0 + \frac{\Delta r}{2}, z)$ . However, all of the above forms are accurate to order  $(\Delta r)^2$ .

The first two forms are very similar in structure and we shall be dealing only with (6.129) in what follows. The last two forms involve a double splitting of either the  $A$  or the  $B$  operator. Both forms have similar accuracy, but (6.131) is clearly preferable, since it involves only two transforms per range step compared with four transforms for (6.132).

As a final comment, it is interesting to note that the split-step algorithm given by (6.129) advances the solution in two distinct stages. The first stage is to advance the solution as if the medium were homogeneous thus accounting for the effects of *diffraction* only. In the second step, we explicitly include effects of *refraction* through  $n^2(r_0, z)$ . This observation explains the true sense of the term *split-step* Fourier algorithm as coined by Tappert [33].

### 6.5.2 Error Analysis

The material presented here follow closely the rather complete error analysis given by Davis et al. [4]. We start with the parabolic wave equation in the form given by (6.118)

$$\psi' = U\psi = (A + B)\psi, \quad (6.133)$$

where we now use primes to indicate differentiation with respect to range. Next, assume that  $\psi_j = \psi(r_j, z)$  is known at range  $r_j$ . In order to obtain the field at range  $r_{j+1} = r_j + \Delta r$ , we use a Taylor series expansion of  $\psi(r, z)$ ,

$$\psi_{j+1} = \psi_j + \psi'_j \Delta r + \psi''_j \frac{(\Delta r)^2}{2} + \psi'''_j \frac{(\Delta r)^3}{6} + \dots, \quad (6.134)$$

which together with (6.133) leads to the following power series solution to the standard parabolic equation,

$$\begin{aligned} \psi_{j+1} = & \left[ 1 + U \Delta r + (U' + U^2) \frac{(\Delta r)^2}{2} \right. \\ & \left. + (U'' + 2UU' + U'U + U^3) \frac{(\Delta r)^3}{6} \right]_j \psi_j. \end{aligned} \quad (6.135)$$

This solution, which is accurate to third order in  $\Delta r$ , is used as a reference solution in what follows.

The first approximation introduced in deriving the split-step algorithm was associated with the exponentiation of the solution as given by (6.119). It is clear that only if  $U$  is independent of range is this expression exact. If we evaluate  $U$  at range  $r_j$  the inherent error is found by first expanding the exponential function to third order in  $\Delta r$  to obtain

$$\psi_{j+1} = \left[ 1 + U \Delta r + U^2 \frac{(\Delta r)^2}{2} + U^3 \frac{(\Delta r)^3}{6} \right] \psi_j. \quad (6.136)$$

The error is found as the difference between the expressions given in (6.135) and (6.136),

$$E_1 = \frac{(\Delta r)^2}{2} U'_j \psi_j + O((\Delta r)^3) \psi_j, \quad (6.137)$$

where  $U'$  is evaluated to be

$$U'_j = A'_j = \frac{ik_0}{2} \frac{\partial n^2}{\partial r}. \quad (6.138)$$

Hence, the first error is of order  $(\Delta r)^2$  and is proportional to the horizontal gradient of the index of refraction.

Alternatively one could assume a linear variation of  $U$  over the range interval  $\Delta r$  and evaluate  $U$  at the mid-point as

$$\tilde{U} = U_j + U'_j \frac{\Delta r}{2}, \quad (6.139)$$

which leads to an error that is third order in  $\Delta r$ ,

$$\widetilde{E}_1 = \frac{(\Delta r)^3}{12} (2U'' + UU' - U'U)_j \psi_j. \quad (6.140)$$

Let us now turn to the second type of error caused by the operator splittings given in (6.120)–(6.123). We first consider a simple splitting of the form

$$e^{(A+B)\Delta r} = e^{A\Delta r} e^{B\Delta r}. \quad (6.141)$$

The error is again found by expanding the exponentials to third order in  $\Delta r$  and comparing terms on both sides of the equality sign,

$$\begin{aligned} E_2 &= -\frac{(\Delta r)^2}{2}(AB - BA)\psi_j, \\ &= -\frac{(\Delta r)^2}{2}[A, B]\psi_j, \end{aligned} \quad (6.142)$$

where the commutator  $[A, B]\psi$  is evaluated to be

$$[A, B]\psi = \frac{1}{4} \left( \frac{\partial^2 n^2}{\partial z^2} \psi + 2 \frac{\partial n^2}{\partial z} \frac{\partial \psi}{\partial z} \right). \quad (6.143)$$

Hence, the simple splitting causes errors that are second order in  $\Delta r$  and dependent on the  $z$ -gradient of the sound speed (through  $n$ ). This is definitely a more serious error than the one given in (6.137), simply because depth gradients in sound speed generally are orders of magnitude greater than range gradients.

It is important to try to reduce the errors caused by the non-commutativity of operators  $A$  and  $B$ , which can be achieved by the more elaborate splitting given in (6.122) and (6.123). As an example, we consider the form

$$e^{(A+B)\Delta r} = e^{\frac{A}{2}\Delta r} e^{B\Delta r} e^{\frac{A}{2}\Delta r}, \quad (6.144)$$

which leads to an error term that is third order in  $\Delta r$ ,

$$\begin{aligned} E_3 &= \frac{(\Delta r)^3}{6} BAB - \frac{(\Delta r)^3}{12} (AB^2 + B^2 A + ABA) + \frac{(\Delta r)^3}{24} (A^2 B + BA^2) \\ &= \frac{(\Delta r)^3}{24} (2B[A, B] - [A, B]2B + A[A, B] - [A, B]A). \end{aligned} \quad (6.145)$$

This is a significant improvement over the previous splitting error and the optimal form of the solution algorithm is clearly the one given in (6.131). Note that all error terms vanish in a homogeneous medium, where the split-step algorithm permits arbitrarily large range steps. For a non-uniform medium, the range step must be small in order to keep the errors small. In particular, error type  $E_3$ , which is proportional to the depth gradient of the sound speed, will require small range steps, when trying to handle a speed discontinuity at the water–bottom interface. This is precisely the situation, where the split-step algorithm loses its computational speed advantage over finite-difference and finite-element techniques.

### 6.5.3 Numerical Implementation

A schematic of the solution domain is shown in Fig. 6.6. The solution is obtained on a regular spatial grid ( $\Delta r, \Delta z$ ), onto which the environmental parameters ( $c, \rho, \alpha$ ) are mapped. The marching solution algorithm requires specification of initial conditions  $\psi(r_0, z)$  as well as boundary conditions at the sea surface ( $z = 0$ ) and at the bottom boundary ( $z = z_{\max}$ ). Since the issue of starting fields was treated in Sect. 6.4, we shall here concentrate on formulating appropriate upper and lower boundary conditions.

The free surface is traditionally treated as a pressure-release boundary requiring  $\psi(r, 0) = 0$ , which is easily implemented in the numerical solution scheme. The lower boundary condition is more complicated. We essentially wish to terminate the solution domain in depth ( $z = z_{\max}$ ) by a radiation condition to simulate a bottom continuation by a homogeneous halfspace. The usual approach is to terminate the physical solution domain ( $z = H$ ) by an *artificial absorption layer* of several wavelengths thickness (Fig. 6.6), so as to ensure that no significant energy is reflected from the lower boundary at  $z = z_{\max}$ . Following Brock [33], the absorption layer is modeled with a complex index of refraction of the form

$$n^2 = n_b^2 + i\alpha \exp\left[-\left(\frac{z - z_{\max}}{D}\right)^2\right], \quad (6.146)$$

which results in an exponentially increasing wave attenuation with depth in the absorption layer. In this expression  $n_b = c_0/c_b$ , while the constants  $\alpha$  and  $D$  are generally picked as  $\alpha = 0.01$  and  $D = (z_{\max} - H)/3$ . The thickness of the artificial absorption layer is taken to be  $H/3$ , which seems to work well in typical

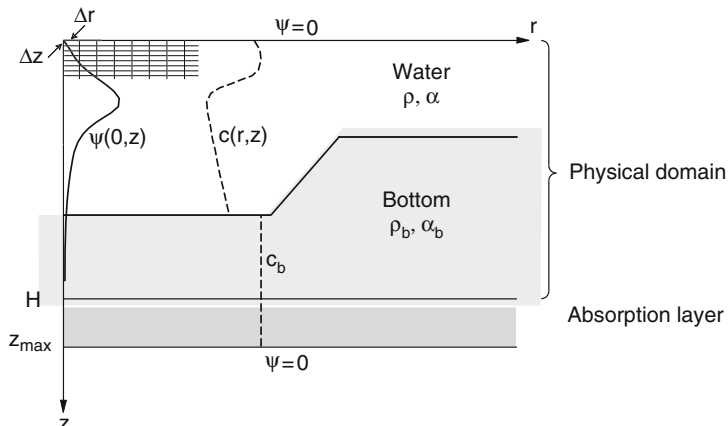


**Fig. 6.6** Schematic of solution domain for parabolic wave equations

deep-water situations. However, to ensure meaningful results in shallow water, it is prudent to include a real physical bottom of several wavelengths thickness and with real sediment attenuation.

Having now set up a finite solution domain in depth, we can straightforwardly implement the split-step algorithm. Thus, the Fourier transform over depth is performed by a discrete FST (fast sine transform), applied separately to real and imaginary parts of the field. The use of a sine transform ensures that the upper boundary condition  $\psi = 0$  is automatically satisfied.

It is clear that the requirement of a uniform grid over depth causes problems with rapid variations (discontinuities) in sound speed, density, and attenuation – quantities which are all included in the index of refraction (Sects. 6.5.4 and 6.5.5). The remedy is simple but costly: model discontinuities by a continuous change in parameters over a small depth interval and increase the transform size to ensure proper sampling in depth. Not only are large transforms needed to handle discontinuities, but small range steps are necessary as well in order to keep numerical errors small. The overall result is that the split-step technique becomes computationally inefficient when having to deal with strong discontinuities in environmental parameters.

Finally, we address an issue of considerable practical importance to users of PE codes: What grid size ( $\Delta r, \Delta z$ ) should be used to obtain an accurate numerical solution to a particular propagation problem? It is clear from the error analysis in Sect. 6.5.2 that all error terms can be made arbitrarily small by selecting a sufficiently small range step  $\Delta r$ . How small it should be depends on the acceptable error in transmission loss (1 dB, 3 dB, ...) at the maximum propagation range considered. Moreover, since range-dependent environments generally exhibit a non-uniform variation with range, error contributions are not constant per meter or kilometer for a fixed range step  $\Delta r$ . For instance, if propagation is partially over a flat bottom (no range dependence) and partially over a steep seamount (strong range dependence), a much smaller range step  $\Delta r$  is clearly required across the seamount to keep the numerical error constant per kilometer. Hence, an optimal choice of  $\Delta r$  as a function of range requires an adaptive process which permits local changes in range step size based on pre-established accuracy criteria.

The choice of  $\Delta z$  depends on the spectral width of the source ( $\Delta z = 2\pi/k_{z,\max}$ ) as well as on the required depth sampling of environmental “discontinuities.” However, when using one of the analytical sources described in Sect. 6.4.2, a minimum sampling criterion in depth is easily established based on the need for an adequate sampling of the source field over depth. Thus, the vertical extent of the standard Gaussian source, (6.101), defined as the distance between the two 1/e-decay points, is seen to be  $z_\ell = 2\sqrt{2}/k_0 \sim \lambda/2$ . Hence, the depth sampling must be less than half a wavelength, and an adequate upper bound is given by

$$\Delta z \leq \frac{\lambda}{4}. \quad (6.147)$$

This criterion can be shown to apply equally well to Greene’s wide-angle source, (6.102), while a less stringent sampling criterion ( $\Delta z \leq \lambda/2$ ) is required for Thomson’s halfspace source, (6.103).

The only safe way to ensure numerically accurate PE results is through a convergence test, where  $\Delta r$  and  $\Delta z$  are systematically reduced until a stable answer is obtained to within the prescribed accuracy. For this purpose, a good initial guess for  $\Delta z$  is obtained from (6.147) while a somewhat larger range step is generally adequate, i.e.,  $\Delta r = 2 - 5 \Delta z$  for bottom-interacting propagation and  $\Delta r = 20 - 50 \Delta z$  for long-range deep-water propagation.

The test of solution convergence is a tedious process, which most model users would rather avoid. Moreover, fixed  $\Delta r$  and  $\Delta z$  are not optimal in terms of computational efficiency. Therefore, adaptive schemes for automatic determination of both  $\Delta r$  and  $\Delta z$  as a function of range have been devised. One such scheme implemented by Brock [33] has proven to work quite well for deep-water environments with negligible bottom interaction. However, in cases of strong bottom interaction (seamounts in deep water, shallow water in general) there is presently no automatic scheme available which guarantees accurate numerical results with minimum computational effort. In these situations, a careful test of solution convergence with decreasing  $\Delta r$  and  $\Delta z$  is the only way to obtain accurate numerical results.

### 6.5.4 Variable Density

For a realistic treatment of bottom effects on propagation, it is important to include density changes at the water–bottom interface, as well as within the bottom itself. This can be achieved by solving the reduced wave equation for a variable-density medium in the form [3, 36],

$$\rho \nabla \cdot \left( \frac{1}{\rho} \nabla p \right) + k_0^2 n^2 p = 0, \quad (6.148)$$

where  $\nabla$  is the gradient operator. If we now define the new variable

$$\tilde{p} = \frac{p}{\sqrt{\rho}} \quad (6.149)$$

it is not difficult to show that (6.148) transforms into the standard Helmholtz form in  $\tilde{p}$ ,

$$\nabla^2 \tilde{p} + k_0^2 \tilde{n}^2 \tilde{p} = 0, \quad (6.150)$$

where  $\tilde{n}$  is the *effective* index of refraction given by

$$\tilde{n}^2 = n^2 + \frac{1}{2k_0^2} \left[ \frac{1}{\rho} \nabla^2 \rho - \frac{3}{2\rho^2} (\nabla \rho)^2 \right]. \quad (6.151)$$

Hence, density effects can be accounted for by solving the standard Helmholtz equation in the variable  $p/\sqrt{\rho}$  with a density-dependent index of refraction given by (6.151).

It is easily seen that the above argument holds for the various parabolic wave equations as well. Consequently, we solve the PE for a density-reduced pressure  $\tilde{\psi} = \psi/\sqrt{\rho}$ , remembering to also express the initial conditions in the variable  $\tilde{\psi}$ . When the field solution  $\tilde{\psi}(r, z)$  has been obtained numerically, we multiply through by  $\sqrt{\rho(r, z)}$  to obtain  $\psi(r, z)$  and then compute transmission loss in the usual manner from (6.71).

Since we are primarily interested in horizontal interfaces, we need only evaluate the  $z$ -derivatives in (6.151), that is

$$\tilde{n}^2 = n^2 + \frac{1}{2k_0^2} \left[ \frac{1}{\rho} \frac{\partial^2 \rho}{\partial z^2} - \frac{3}{2\rho^2} \left( \frac{\partial \rho}{\partial z} \right)^2 \right]. \quad (6.152)$$

It is clear that a density discontinuity with infinite derivatives causes problems in the numerical algorithm. We, therefore, follow Tappert [3] and introduce a smoothing function of the form

$$\rho(z) = \frac{1}{2}(\rho_2 + \rho_1) + \frac{1}{2}(\rho_2 - \rho_1) \tanh\left(\frac{z - D_0}{L}\right), \quad (6.153)$$

where  $D_0$  is the depth of the interface and  $L$  the distance over which the density changes from  $\rho_1$  to  $\rho_2$ . In order that the reflection from this density jump be correctly modeled,  $L$  must be small compared to the vertically projected wavelength. An appropriate value of  $L$  is given by

$$k_0 L = 2. \quad (6.154)$$

A generalization of the above result to handle arbitrary density variations in depth is straightforward. In practice, a simplified bottom description based on a number of constant-density layers is generally used. Each density discontinuity is then approximated by a smooth density profile of the form given by (6.153).

### 6.5.5 Attenuation

Volume attenuation is included in the standard fashion by adding a small imaginary part  $i\alpha$  to the medium wavenumber,

$$k = \frac{\omega}{c} + i\alpha, \quad \alpha > 0. \quad (6.155)$$

The attenuation coefficient  $\alpha$  here has the units nepers/m. However, as shown in Sect. 1.5.1, it is common in underwater acoustics to work with the quantity  $\alpha^{(\lambda)}$  in dB/ $\lambda$ , defined as

$$\alpha^{(\lambda)} = -20 \log \left( \frac{e^{-\alpha(r+\lambda)}}{e^{-\alpha r}} \right) = \alpha \lambda 20 \log e, \quad (6.156)$$

where  $\lambda$  is the acoustic wavelength.

In the PE context we need to introduce a complex index of refraction as

$$n^2 = \left( \frac{k}{k_0} \right)^2 \simeq \left( \frac{c_0}{c} \right)^2 \left[ 1 + i \frac{2\alpha c}{\omega} \right]. \quad (6.157)$$

By introducing  $\alpha^{(\lambda)}$  from (6.156) and evaluating the constants, we obtain the final form of  $n^2$ ,

$$n^2 \simeq \left( \frac{c_0}{c} \right)^2 \left[ 1 + i \frac{\alpha^{(\lambda)}}{27.29} \right]. \quad (6.158)$$

Hence, volume attenuation can be accounted for by simply adding an imaginary part to the index of refraction squared. The attenuation coefficient  $\alpha$  can be easily made a function of both depth and range, which, in fact, is the proper way to handle attenuation in range-dependent environments.

## 6.6 Solutions by FDs and FEs

Finite-difference (FD) and finite-element (FE) methods are general-purpose numerical schemes which are used for solving partial differential equations in many branches of physics; the theory and development of these techniques is described in most textbooks on numerical analysis. Both schemes are based on the concept of discretization of the physical problem and its solution in order to facilitate a numerical evaluation. Since the two formulations lead to a similar set of equations for a given problem, we shall here concentrate on the more popular finite-difference scheme for solving the parabolic wave equation [5], referring readers to a paper by Huang [37] for details on the finite-element implementation. As to the relative merits of the two schemes, Huang [37] claims that a variable vertical mesh spacing is more readily included in the finite-element technique making this scheme better suited for treating sloping interfaces. However, finite-difference schemes with equidistant grid spacing in both depth and range are favored in the modeling community due to its simplicity.

A variety of finite-difference schemes (explicit or implicit) can be applied to the parabolic wave equation. We here derive an implicit scheme (IFD) of the Crank–Nicolson type, which has been thoroughly analyzed and described by Lee and McDaniel [5]. We closely follow their approach in first deriving field equations that include horizontal interfaces with impedance contrasts, and then formulating the IFD solution scheme.

While the split-step technique outlined in Sect. 6.5 was applicable only to a few narrow-angle PE forms, the finite-difference technique is universally applicable to

both narrow and wide-angle forms of the parabolic wave equation. To emphasize this point, we carry through the derivation of the IFD formulation for the generalized rational-function form of the parabolic wave equation given by (6.32). As a special case this form comprise the Tappert equation as well as two wide-angle forms due to Claerbout and Greene. For FD/FE implementations of very-wide-angle PE forms – including the computationally efficient “split-step” Padé solution–readers are referred to a series of papers by Collins [12, 20, 21, 35] and references therein.

### 6.6.1 Field Equations on Horizontal Interfaces

As pointed out earlier, the correct treatment of wave reflection and transmission at horizontal interfaces with density and speed contrasts is of paramount importance to a realistic modeling of propagation in the ocean waveguide. These interfaces represent not only the water–bottom interface but also layer interfaces within the bottom itself created through varying sedimentation processes. At each interface, the standard acoustic boundary conditions requiring continuity of pressure and the normal component of the particle velocity must hold.

The derivation presented here deals with a horizontal interface  $z_B$  separating two media with different sound speeds and densities (Fig. 6.7). As the governing wave equation we take the farfield Helmholtz form given by (6.7)

$$\frac{\partial^2 \psi}{\partial r^2} + 2ik_0 \frac{\partial \psi}{\partial r} + k_0^2 (n^2 - 1) \psi + \frac{\partial^2 \psi}{\partial z^2} = 0 \quad (6.159)$$

with boundary conditions mathematically expressed as

$$\psi_1(r, z_B) = \psi_2(r, z_B) \quad (6.160)$$

and

$$\frac{1}{\rho_1} \frac{\partial \psi_1}{\partial z} \Big|_{z_B} = \frac{1}{\rho_2} \frac{\partial \psi_2}{\partial z} \Big|_{z_B}. \quad (6.161)$$



**Fig. 6.7** Notation for finite-difference grid along horizontal interface

Following Botseas et al. [38], we next introduce a finite-difference grid  $(\Delta r, \Delta z)$  as shown in Fig. 6.7. The discretized field variable is denoted  $\psi_\ell^m$ , where  $\ell$  and  $m$  are integer indices indicating the depth level and the range level, respectively. Assuming that the field is known at range level  $m$ , we proceed to determine the field at level  $m + 1$  such that the boundary conditions imposed by (6.160) and (6.161) are satisfied.

### Medium 1:

Denoting the field variable  $\psi_\ell^m$  on the interface in medium 1 by  $\psi_1$ , this quantity must satisfy (6.159), i.e.,

$$\frac{\partial^2 \psi_1}{\partial r^2} + 2ik_0 \frac{\partial \psi_1}{\partial r} + k_0^2 (n_1^2 - 1) \psi_1 + \frac{\partial^2 \psi_1}{\partial z^2} = 0. \quad (6.162)$$

We next introduce a Taylor series expansion of  $\psi_{\ell-1}^m$  upon  $\psi_\ell^m$

$$\psi_{\ell-1}^m = \psi_\ell^m - \Delta z \frac{\partial \psi_\ell^m}{\partial z} + \frac{(\Delta z)^2}{2} \frac{\partial^2 \psi_\ell^m}{\partial z^2} + \dots \quad (6.163)$$

and solve for the second derivative of  $\psi$  to obtain

$$\frac{\partial^2 \psi_1}{\partial z^2} = -\frac{2}{(\Delta z)^2} (\psi_1 - \psi_{\ell-1}^m) + \frac{2}{\Delta z} \frac{\partial \psi_1}{\partial z}. \quad (6.164)$$

Finally, substituting (6.164) into (6.162) yields

$$\frac{\partial \psi_1}{\partial z} = -\frac{\Delta z}{2} \left[ \frac{\partial^2 \psi_1}{\partial r^2} + 2ik_0 \frac{\partial \psi_1}{\partial r} + k_0^2 (n_1^2 - 1) \psi_1 - \frac{2}{(\Delta z)^2} (\psi_1 - \psi_{\ell-1}^m) \right]. \quad (6.165)$$

### Medium 2:

It is not difficult to show that an equivalent equation for the field on the interface in medium 2 takes the form

$$\frac{\partial \psi_2}{\partial z} = \frac{\Delta z}{2} \left[ \frac{\partial^2 \psi_2}{\partial r^2} + 2ik_0 \frac{\partial \psi_2}{\partial r} + k_0^2 (n_2^2 - 1) \psi_2 + \frac{2}{(\Delta z)^2} (\psi_{\ell+1}^m - \psi_2) \right]. \quad (6.166)$$

In order to satisfy the boundary conditions given by (6.160) and (6.161), we require first of all that  $\psi_1 = \psi_2 = \psi$  in (6.165) and (6.166). Next, we multiply through by  $1/\rho_1$  in (6.165) and  $1/\rho_2$  in (6.166) and equate the two right-hand-sides to obtain a field equation that satisfies also the second boundary condition,

$$\begin{aligned} & \frac{\partial^2 \psi}{\partial r^2} + 2ik_0 \frac{\partial \psi}{\partial r} + k_0^2 \frac{\rho_2}{\rho_1 + \rho_2} \left( n_1^2 + \frac{\rho_1}{\rho_2} n_2^2 \right) \psi - k_0^2 \psi \\ & + \frac{2}{(\Delta z)^2} \frac{\rho_2}{\rho_1 + \rho_2} \left( \psi_{\ell-1}^m - \frac{\rho_1 + \rho_2}{\rho_2} \psi_\ell^m + \frac{\rho_1}{\rho_2} \psi_{\ell+1}^m \right) = 0. \end{aligned} \quad (6.167)$$

This equation is the desired farfield Helmholtz equation valid along a horizontal interface separating media with different sound speeds and densities. In a homogeneous medium with  $n_1 = n_2 = n$  and  $\rho_1 = \rho_2 = \rho$ , it is easily seen that (6.167) reduces to

$$\frac{\partial^2 \psi}{\partial r^2} + 2ik_0 \frac{\partial \psi}{\partial r} + k_0^2 (n^2 - 1) \psi + \frac{\psi_{\ell+1}^m - 2\psi_\ell^m + \psi_{\ell-1}^m}{(\Delta z)^2} = 0, \quad (6.168)$$

which again is the Helmholtz form given in (6.159), only with the second depth derivative replaced by a central finite-difference form.

For economy in writing we next introduce the abbreviations

$$\Gamma_{zz} \psi = \frac{2}{(\Delta z)^2} \frac{\rho_2}{\rho_1 + \rho_2} \left( \psi_{\ell-1}^m - \frac{\rho_1 + \rho_2}{\rho_2} \psi_\ell^m + \frac{\rho_1}{\rho_2} \psi_{\ell+1}^m \right), \quad (6.169)$$

$$\eta = \frac{\rho_2}{\rho_1 + \rho_2} \left( n_1^2 + \frac{\rho_1}{\rho_2} n_2^2 \right) - 1, \quad (6.170)$$

$$G = k_0^2 \eta + \Gamma_{zz}, \quad (6.171)$$

which allows us to cast the governing wave equation, (6.167), in the familiar form

$$\frac{\partial^2 \psi}{\partial r^2} + 2ik_0 \frac{\partial \psi}{\partial r} + G \psi = 0, \quad (6.172)$$

which, with

$$G = k_0^2 (Q^2 - 1) \quad (6.173)$$

is identical to the two-way Helmholtz form given in (6.11). Hence, following the procedure outlined in Sect. 6.2.2, we can directly write down the corresponding one-way wave equation

$$\begin{aligned} \frac{\partial \psi}{\partial r} &= ik_0 (Q - 1) \psi \\ &= ik_0 \left( \sqrt{1 + q} - 1 \right) \psi, \end{aligned} \quad (6.174)$$

where  $q = G/k_0^2$ . This equation is the generalized parabolic wave equation valid on horizontal interfaces.

## 6.6.2 IFD Formulation

To solve (6.174) we follow Lee and McDaniel [5] and introduce the *Crank–Nicolson* finite-difference scheme given by

$$\frac{\psi^{m+1} - \psi^m}{\Delta r} = ik_0 \left( \sqrt{1 + q} - 1 \right) \frac{\psi^{m+1} + \psi^m}{2}, \quad (6.175)$$

which, in turn, leads to the following implicit equation

$$\left[ 1 - \frac{ik_0 \Delta r}{2} (\sqrt{1+q} - 1) \right] \psi^{m+1} = \left[ 1 + \frac{ik_0 \Delta r}{2} (\sqrt{1+q} - 1) \right] \psi^m. \quad (6.176)$$

To proceed further we need to introduce a rational-function approximation of the operator  $\sqrt{1+q}$ . We here choose the form given by (6.28)

$$\sqrt{1+q} \simeq \frac{a_0 + a_1 q}{b_0 + b_1 q}, \quad (6.177)$$

which was shown to comprise three well-known PE forms due to Tappert, Claerbout, and Greene. Substituting this expression for the square-root operator into (6.176) and making use of the definition of  $q$ , we obtain

$$\begin{aligned} & \left[ 1 - \frac{ik_0 \Delta r}{2} \left( \frac{a_0 + a_1 \left( \eta + \frac{\Gamma_{zz}}{k_0^2} \right)}{b_0 + b_1 \left( \eta + \frac{\Gamma_{zz}}{k_0^2} \right)} - 1 \right) \right] \psi^{m+1} \\ &= \left[ 1 + \frac{ik_0 \Delta r}{2} \left( \frac{a_0 + a_1 \left( \eta + \frac{\Gamma_{zz}}{k_0^2} \right)}{b_0 + b_1 \left( \eta + \frac{\Gamma_{zz}}{k_0^2} \right)} - 1 \right) \right] \psi^m. \end{aligned} \quad (6.178)$$

By assuming the operator  $b_0 + b_1 \left( \eta + \frac{\Gamma_{zz}}{k_0^2} \right)$  to be constant across a range step, the above expression simplifies to

$$\begin{aligned} & \left[ b_0 + b_1 \eta - \frac{ik_0 \Delta r}{2} [(a_0 - b_0) + (a_1 - b_1)\eta] \right] \psi^{m+1} \\ &+ \frac{1}{k_0^2} \left[ b_1 - \frac{ik_0 \Delta r}{2} (a_1 - b_1) \right] \Gamma_{zz} \psi^{m+1} \\ &= \left[ b_0 + b_1 \eta + \frac{ik_0 \Delta r}{2} [(a_0 - b_0) + (a_1 - b_1)\eta] \right] \psi^m \\ &+ \frac{1}{k_0^2} \left[ b_1 + \frac{ik_0 \Delta r}{2} (a_1 - b_1) \right] \Gamma_{zz} \psi^m. \end{aligned} \quad (6.179)$$

Next, define

$$w_1 = b_0 + \frac{ik_0 \Delta r}{2} (a_0 - b_0), \quad (6.180)$$

$$w_1^* = b_0 - \frac{ik_0 \Delta r}{2} (a_0 - b_0), \quad (6.181)$$

$$w_2 = b_1 + \frac{ik_0 \Delta r}{2} (a_1 - b_1), \quad (6.182)$$

$$w_2^* = b_1 - \frac{ik_0 \Delta r}{2} (a_1 - b_1). \quad (6.183)$$

and substitute these abbreviations into (6.179) together with the expression for  $\Gamma_{zz}$  given by (6.169) to obtain

$$\begin{aligned} & \left( \frac{w_1^*}{w_2^*} + \eta \right) \psi_\ell^{m+1} + \frac{1}{k_0^2} \left[ \frac{2}{(\Delta z)^2} \frac{\rho_2}{\rho_1 + \rho_2} \right] \\ & \times \left( \psi_{\ell-1}^{m+1} - \frac{\rho_1 + \rho_2}{\rho_2} \psi_\ell^{m+1} + \frac{\rho_1}{\rho_2} \psi_{\ell+1}^{m+1} \right) \\ & = \left( \frac{w_1 + w_2 \eta}{w_2^*} \right) \psi_\ell^m + \frac{1}{k_0^2} \left( \frac{w_2}{w_2^*} \right) \left[ \frac{2}{(\Delta z)^2} \frac{\rho_2}{\rho_1 + \rho_2} \right] \\ & \times \left( \psi_{\ell-1}^m - \frac{\rho_1 + \rho_2}{\rho_2} \psi_\ell^m + \frac{\rho_1}{\rho_2} \psi_{\ell+1}^m \right). \end{aligned} \quad (6.184)$$

Finally, by multiplying both sides of this equation by  $k_0^2 (\Delta z)^2 (\rho_1 + \rho_2) / (2\rho_2)$ , reintroducing  $\eta$  from (6.170) and regrouping terms, we can express the solution in vector form as

$$[1, u, v] \begin{bmatrix} \psi_{\ell-1}^{m+1} \\ \psi_\ell^{m+1} \\ \psi_{\ell+1}^{m+1} \end{bmatrix} = \frac{w_2}{w_2^*} [1, \hat{u}, v] \begin{bmatrix} \psi_{\ell-1}^m \\ \psi_\ell^m \\ \psi_{\ell+1}^m \end{bmatrix}, \quad (6.185)$$

where

$$\begin{aligned} u &= \frac{\rho_1 + \rho_2}{\rho_2} \left[ \frac{k_0^2 (\Delta z)^2}{2} \left( \frac{w_1^*}{w_2^*} \right) - 1 \right] \\ &+ \frac{k_0^2 (\Delta z)^2}{2} \left[ (n_1^2 - 1) + \frac{\rho_1}{\rho_2} (n_2^2 - 1) \right], \end{aligned} \quad (6.186)$$

$$v = \frac{\rho_1}{\rho_2}, \quad (6.187)$$

$$\begin{aligned} \hat{u} &= \frac{\rho_1 + \rho_2}{\rho_2} \left[ \frac{k_0^2 (\Delta z)^2}{2} \left( \frac{w_1}{w_2} \right) - 1 \right] \\ &+ \frac{k_0^2 (\Delta z)^2}{2} \left[ (n_1^2 - 1) + \frac{\rho_1}{\rho_2} (n_2^2 - 1) \right]. \end{aligned} \quad (6.188)$$

To complete the IFD formulation we finally collect the local solutions given by (6.185) into a global matrix solution over  $N$  mesh points in depth,

$$\begin{aligned}
& \left[ \begin{array}{ccc} u_1 & v_1 & \\ 1 & u_2 & v_2 \\ 1 & u_3 & v_3 \\ \ddots & \ddots & \ddots \\ 1 & u_{N-2} & v_{N-2} \\ 1 & u_{N-1} & v_{N-1} \\ 1 & u_N & \end{array} \right] \left[ \begin{array}{c} \psi_1 \\ \psi_2 \\ \psi_3 \\ \vdots \\ \psi_{N-2} \\ \psi_{N-1} \\ \psi_N \end{array} \right]^{m+1} \\
& = \left( \frac{w_2}{w_2^*} \right) \left[ \begin{array}{ccc} \hat{u}_1 & v_1 & \\ 1 & \hat{u}_2 & v_2 \\ 1 & \hat{u}_3 & v_3 \\ \ddots & \ddots & \ddots \\ 1 & \hat{u}_{N-2} & v_{N-2} \\ 1 & \hat{u}_{N-1} & v_{N-1} \\ 1 & \hat{u}_N & \end{array} \right] \left[ \begin{array}{c} \psi_1 \\ \psi_2 \\ \psi_3 \\ \vdots \\ \psi_{N-2} \\ \psi_{N-1} \\ \psi_N \end{array} \right]^m. \quad (6.189)
\end{aligned}$$

Note that this solution involves two tri-diagonal matrices, which can be easily symmetrized by multiplying through row-wise by the appropriate density ratios, i.e.,  $v_1$  in row 2,  $v_1 v_2$  in row 3, etc.

The IFD computer code developed by Lee et al. [5, 38] in the early 1980s solves (6.189). The numerical scheme has been shown to be unconditionally stable and provide accurate solutions for a variety of ocean acoustic problems. The fact that the code permits solution of both narrow and wide-angle PEs has definitely contributed to its widespread use in the modeling community.

### 6.6.3 Error Analysis

The local truncation error associated with the Crank–Nicolson finite difference scheme is here evaluated following a procedure similar to the one developed in Sect. 6.5.2 for the split-step Fourier algorithm.

Recall that the standard parabolic wave equation can be written in the compact form

$$\frac{\partial \psi}{\partial r} = (A + B) \psi = U(r, z) \psi, \quad (6.190)$$

where the two operators  $A$  and  $B$  are given by

$$A = \frac{ik_0}{2} [n^2(r, z) - 1], \quad B = \frac{i}{2k_0} \frac{\partial^2}{\partial z^2}. \quad (6.191)$$

In Sect. 6.5.2, we derived the following power-series solution to (6.190), accurate to third order in the range step  $\Delta r$ ,

$$\begin{aligned}\psi_{j+1} = & \left[ 1 + U\Delta r + (U' + U^2) \frac{(\Delta r)^2}{2} \right. \\ & \left. + (U'' + 2UU' + U'U + U^3) \frac{(\Delta r)^3}{6} \right]_j \psi_j.\end{aligned}\quad (6.192)$$

This solution, in which primes indicate differentiation with respect to range, is used as a reference solution in what follows.

The Crank–Nicolson range-marching algorithm for the standard parabolic equation, (6.190), takes the form

$$\frac{\psi_{j+1} - \psi_j}{\Delta r} = \frac{U_{j+1} \psi_{j+1} + U_j \psi_j}{2} \quad (6.193)$$

or

$$\psi_{j+1} = \frac{1 + U_j \frac{\Delta r}{2}}{1 - U_{j+1} \frac{\Delta r}{2}} \psi_j. \quad (6.194)$$

Two steps are required to arrive at the desired power-series solution for  $\psi_{j+1}$ . We first introduce a series expansion of the denominator to third order in  $\Delta r$  to obtain

$$\psi_{j+1} = \left[ \left( 1 + U_j \frac{\Delta r}{2} \right) \left( 1 + U_{j+1} \frac{\Delta r}{2} + U_{j+1}^2 \frac{(\Delta r)^2}{4} + U_{j+1}^3 \frac{(\Delta r)^3}{8} \right) \right] \psi_j. \quad (6.195)$$

Next, we eliminate  $U_{j+1}$  from this expression by using a Taylor series expansion of  $U_{j+1}$  upon  $U_j$ ,

$$U_{j+1} = U_j + U'_j \Delta r + U''_j \frac{(\Delta r)^2}{2} + \dots \quad (6.196)$$

The final result to third order in  $\Delta r$  is easily shown to be

$$\begin{aligned}\psi_{j+1} = & \left[ 1 + U\Delta r + (U' + U^2) \frac{(\Delta r)^2}{2} \right. \\ & \left. + (U'' + 2UU' + U'U + U^3) \frac{(\Delta r)^3}{4} \right]_j \psi_j.\end{aligned}\quad (6.197)$$

By comparing this expression with the reference solution given in (6.192), we find the truncation error associated with the Crank–Nicolson scheme to be

$$E_{\text{CN}} = -\frac{(\Delta r)^3}{12} (U'' + 2UU' + U'U + U^3)_j \psi_j. \quad (6.198)$$

Note that this error is third order in  $\Delta r$  as was the case for the split-step algorithm in its most efficient form, (6.140).

For completeness, we mention that the above result was also obtained by McDaniel and Lee [39], who performed a more elaborate error analysis that included the presence of horizontal interfaces with speed and density discontinuities. They found that the leading error term associated with the range-marching algorithm is of order  $(\Delta r)^3$ , while the error associated with the depth differencing is of order  $(\Delta r \Delta z)$  across interfaces and of order  $\Delta r (\Delta z)^2$  elsewhere.

#### 6.6.4 Numerical Implementation

The implementation of the IFD solution closely follows the scheme outlined in Sect. 6.5.3 for the split-step Fourier algorithm. Thus, as shown in Fig. 6.6, the solution is obtained on a regular spatial grid  $(\Delta r, \Delta z)$ , onto which the environmental parameters  $(c, \rho, \alpha)$  are mapped. Even though a uniform grid in depth is not required in the IFD technique, this solution is generally preferred for simplicity.

The range-marching algorithm requires specification of initial conditions  $\psi(r_0, z)$  as well as boundary conditions at the sea surface ( $z = 0$ ) and at the bottom boundary ( $z = z_{\max}$ ). Appropriate starting fields were discussed in Sect. 6.4, and boundary conditions are treated exactly as described in Sect. 6.5.3 for the split-step algorithm, i.e., the sea surface is treated as a pressure-release boundary with  $\psi(r, 0) = 0$ , while the lower boundary simulates a radiation condition. This is achieved by terminating the physical solution domain ( $z = H$ ) by an artificial absorption layer of several wavelengths thickness (Fig. 6.6), so as to ensure that no significant energy is reflected from the lower boundary at  $z = z_{\max}$ . The absorption layer is modeled with a complex index of refraction of the form given by (6.146).

Having established a finite solution domain in depth, we can straightforwardly implement the IFD algorithm using a standard tri-diagonal matrix solver. Since the formulation already incorporates horizontal interfaces with speed and density discontinuities, we only need to address the issue of volume attenuation, which is included in the usual fashion by adding an imaginary part to the index of refraction squared, see (6.158).

All comments made in Sect. 6.5.3 concerning an appropriate choice of the computational grid  $(\Delta r, \Delta z)$  for the split-step algorithm, apply equally well to the IFD technique. Thus, the only safe way to ensure numerically accurate PE results is through a convergence test, where  $\Delta r$  and  $\Delta z$  are systematically reduced until a stable answer is obtained to within the prescribed accuracy. For this purpose, a good initial guess for  $\Delta z$  is obtained from (6.147) while a somewhat larger range step,  $\Delta r = 2 - 5 \Delta z$ , is generally adequate.

## 6.7 The Problem of Energy Conservation in PEs

Since the early 1970s, when the first parabolic equation solution based on Fourier transforms appeared in the underwater acoustics community, the PE technique has been applied extensively to model propagation in range-dependent ocean environments with strong bathymetric changes. In fact, the rationale behind the continual search for more wide-angle PE forms during the 1980s was to obtain an accurate treatment of bottom-interacting propagation, which often involves steep propagation angles (critical reflection angles of 20–30° are typical for sandy seafloors). With phase errors practically eliminated from the wide-angle PE codes, these were subsequently used with confidence to model propagation in sloping bottom situations, both on continental shelves and over seamounts. There is, however, a fundamental problem of energy conservation in the standard PE implementation of sloping interfaces, leading to *energy loss* for upslope propagation and *energy gain* for downslope propagation. The problem is accentuated by increasing bottom slope and impedance contrast, and prediction errors of several decibels may occur.

The first evidence of inaccurate PE results for upslope propagation in a wedge-shaped ocean appeared among the range-dependent benchmark solutions solicited by the Acoustical Society of America in 1987 [40]. Figure 6.8 presents results for a 2.86° wedge with a penetrable lossy bottom. As shown in Fig. 6.8a, the initial water depth is 200 m decreasing linearly to 0 at a range of 4 km. The source depth is 100 m and the source frequency 25 Hz.

The reference solution given by the solid line in Figs. 6.8b and 6.8c was obtained from a full-spectrum, two-way, coupled-mode solution. For comparison two different PE solutions to the exact same problem are shown as the dashed curves. Figure 6.8b shows the result obtained with a split-step implementation of the Thomson–Chapman PE, (6.41), while Fig. 6.8c displays a finite-difference implementation of the Claerbout PE, (6.43). Note that two types of errors are apparent in these PE solutions. Thus, the Thomson–Chapman PE clearly is too narrow-angled for this propagation problem ( $\theta_c \simeq 28^\circ$ ), causing phase errors and slight shifts in the multipath interference structure. The mean level, on the other hand, is quite accurately predicted.

Turning to the result obtained with the wide-angle Claerbout equation, Fig. 6.8c, we see that phase errors are negligible while the predicted level is approximately 2 dB too low at longer ranges. This level difference was initially thought to be due to the neglect of backscattering in the one-way PE solution, but it was subsequently realized that the backscattered field in this case is negligible. In fact, the strength of the backscattered field component extracted from the two-way coupled-mode result, is 40–50 dB lower than the outgoing field component.

Since the solution is fundamentally outgoing, then why are one-way PE results in error? This can be understood by looking at the consequences of the use of a stair-step approximation to a sloping interface. Figure 6.9 shows a few vertical segments separating media of different properties. The important interfaces with strong impedance contrasts are the horizontal interfaces  $I_h$  and the vertical interfaces  $I_v$

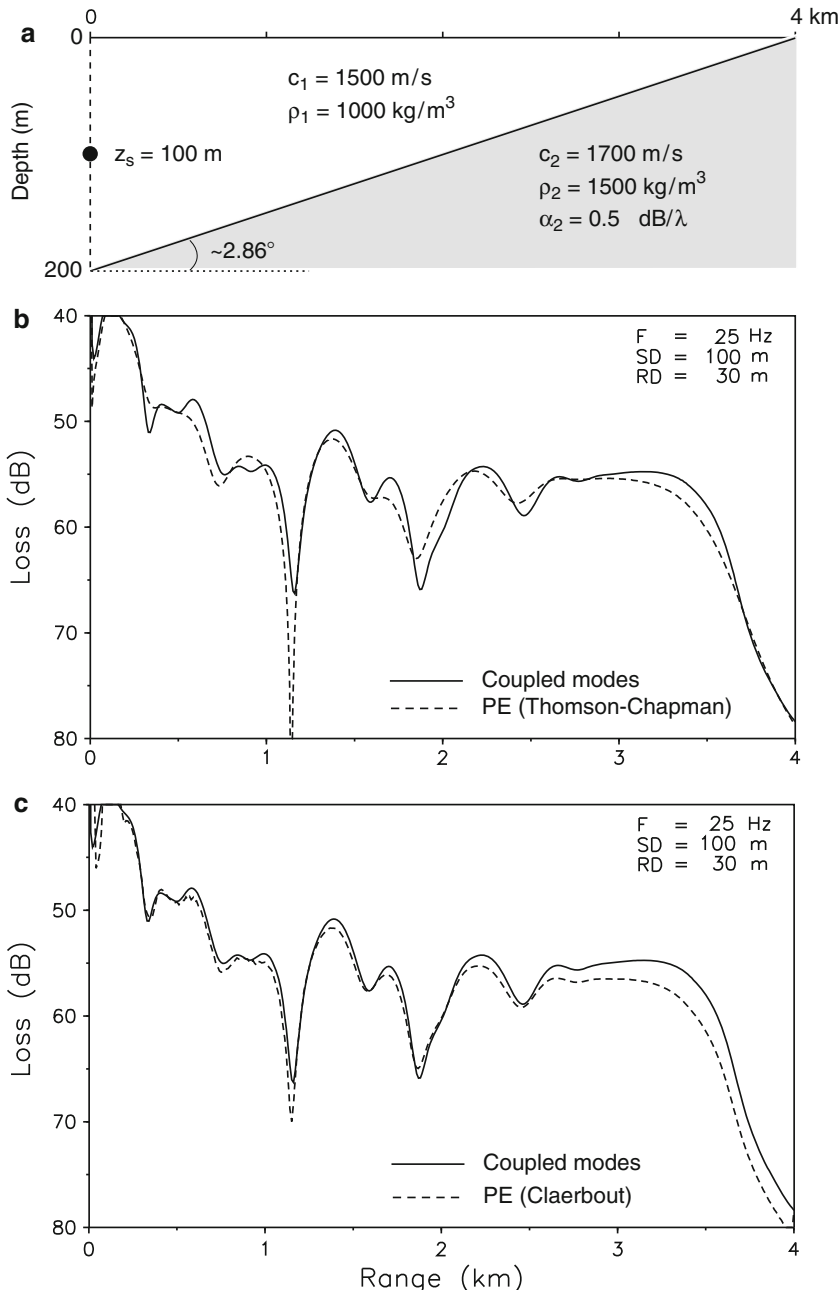


**Fig. 6.8** Comparison of PE results with coupled-mode reference solution for upslope propagation in a wedge. (a) Test environment. (b) Split-step result for the Thomson-Chapman equation. (c) Finite-difference result for the Claerbout equation (from Jensen and Ferla [40])

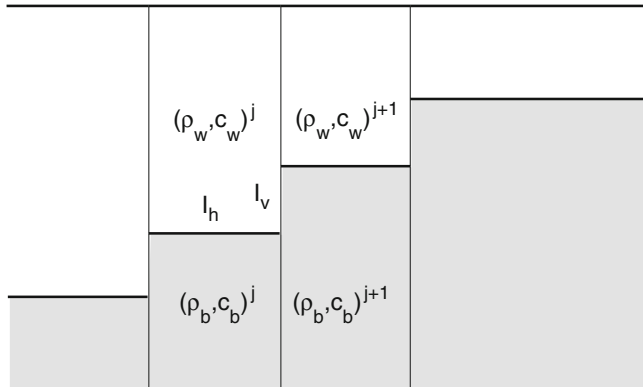


**Fig. 6.9** Stair-step representation of sloping interface

along the stair-steps. While boundary conditions at horizontal interfaces (continuity of pressure and vertical particle velocity) are accurately implemented, particularly in the IFD implementation, the vertical boundary conditions along  $I_v$  are treated very loosely. In fact, an a priori assumption of the solution being outgoing only, permits just one vertical boundary condition to be satisfied. When solving for pressure in a finite-difference implementation, the boundary condition being satisfied is continuity of pressure across vertical interfaces. Since split-step Fourier implementations generally solve for a density-reduced pressure,  $p/\sqrt{\rho}$ , these codes provide continuity of reduced pressure across vertical interfaces. It is clear, however, that the full boundary condition cannot be satisfied within the framework of a one-way solution.

The question of whether improved (energy conserving) interface conditions for one-way wave equations can be defined was addressed by Porter et al. [41]. Thus, it was shown that a solution which matches pressure alone show serious deficiencies for moderate density variations. Matching particle velocity is also a poor choice, however, matching density-reduced pressure corrects entirely for the density effect. A further improvement may be obtained using a  $p/\sqrt{\rho c}$  matching, which is energy conserving in a forward sense for *horizontally* propagating sound.

That the  $p/\sqrt{\rho c}$  matching is an appropriate solution to the energy conservation problem also in finite-difference PEs was demonstrated by Collins and Westwood [42], who provided numerical evidence that this type of interface condition leads to accurate one-way results for steep bottom slopes as well as for strong impedance contrasts. As an alternative, one could avoid the stair-step representation all together and implement directly a sloping-bottom boundary condition as proposed by Lee and McDaniel [43] and more recently by Huang [37]. However, numerical evidence of the accuracy of this type of interface representation is currently not available.

## 6.8 Three-Dimensional PEs

Three-dimensional PE implementations for fluid media were pioneered in the early 1980s by Baer [44], Perkins and Baer [45], and Siegmann et al. [46]. Since then, several implementations have been reported, and readers are referred to review papers by Tolstoy [47] and Sturm [48] for detailed references to the 3-D modeling literature.

In this section, we outline the theoretical basis for three-dimensional PE implementations, following closely the approach for 2-D PEs in Sect. 6.2.2. First, assume that the solution of the 3-D Helmholtz equation (6.1) takes the form of an outgoing cylindrical wave solution

$$p(r, \varphi, z) = \psi(r, \varphi, z) H_0^{(1)}(k_0 r), \quad (6.199)$$

where  $k_0 = \omega/c_0$  is an arbitrarily-defined reference wavenumber. Substituting this trial solution into the 3-D Helmholtz equation (6.1), and making use of (6.4) and (6.5), we obtain an elliptic wave equation in  $\psi$ ,

$$\frac{\partial^2 \psi}{\partial r^2} + 2ik_0 \frac{\partial \psi}{\partial r} + \frac{1}{r^2} \frac{\partial^2 \psi}{\partial \varphi^2} + \frac{\partial^2 \psi}{\partial z^2} + k_0^2 (n^2 - 1) \psi = 0, \quad (6.200)$$

which is the 3-D equivalent of (6.7).

Following the approach of Sect. 6.2.2, we can proceed to factorize (6.200) into incoming and outgoing wave components, and it is easily shown that we obtain a 3-D parabolic wave equation for the outgoing component in the form

$$\frac{\partial \psi}{\partial r} = ik_0 \left( \sqrt{n^2 + \frac{1}{k_0^2} \frac{\partial^2}{\partial z^2} + \frac{1}{(k_0 r)^2} \frac{\partial^2}{\partial \varphi^2}} - 1 \right) \psi. \quad (6.201)$$

As for the 2-D problem discussed earlier, the square-root operator must be replaced by an approximate functional form for numerical evaluation.

### 6.8.1 Expansion of the Square-Root Operator

For brevity we write the pseudo-differential operator in (6.201) as

$$Q = \sqrt{1 + q_z + q_\varphi}, \quad (6.202)$$

where

$$q_z = (n^2 - 1) + \frac{1}{k_0^2} \frac{\partial^2}{\partial z^2}, \quad q_\varphi = \frac{1}{(k_0 r)^2} \frac{\partial^2}{\partial \varphi^2}. \quad (6.203)$$

The 3-D environment is entered via the refraction index  $n(r, \varphi, z) = c_0/c(r, \varphi, z)$ , where  $c_0$  is a reference sound speed. Note that the depth operator  $q_z$  has the same form as for the 2-D case treated in Sect. 6.2.3. The azimuthal operator  $q_\varphi$  accounts for horizontal refraction.

Solvable three-dimensional parabolic equations can be obtained by using either Taylor or Padé series expansions of the square-root operator  $\mathcal{Q}$ . Here, it is commonly assumed that the 3-D effects are sufficiently gradual that cross terms in the operator expansions ( $q_z q_\varphi, q_z^2 q_\varphi, q_z q_\varphi^2, \dots$ ) may be ignored. This means, for instance, that the Taylor series expansion of  $\mathcal{Q}$ :

$$\sqrt{1 + q_z + q_\varphi} = 1 + \frac{q_z + q_\varphi}{2} - \frac{(q_z + q_\varphi)^2}{8} + \frac{(q_z + q_\varphi)^3}{16} + \dots \quad (6.204)$$

is approximated by

$$\sqrt{1 + q_z + q_\varphi} \simeq 1 + \frac{1}{2}q_z + \frac{1}{2}q_\varphi - \frac{1}{8}q_z^2 - \frac{1}{8}q_\varphi^2 + \frac{1}{16}q_z^3 + \frac{1}{16}q_\varphi^3 + \dots \quad (6.205)$$

Similarly, using Padé series expansions without cross terms gives

$$\sqrt{1 + q_z + q_\varphi} \simeq 1 + \sum_{j=1}^m \frac{a_{j,m} q_z}{1 + b_{j,m} q_z} + \sum_{j=1}^m \frac{a_{j,m} q_\varphi}{1 + b_{j,m} q_\varphi}, \quad (6.206)$$

where  $m$  is the number of terms in the expansion and

$$a_{j,m} = \frac{2}{2m+1} \sin^2 \left( \frac{j\pi}{2m+1} \right), \quad (6.207)$$

$$b_{j,m} = \cos^2 \left( \frac{j\pi}{2m+1} \right). \quad (6.208)$$

Even though some practical code implementations involving operator cross terms have been attempted, the majority of 3-D PE codes reported in the literature [48] are based on the above expansions, which separately provide functional approximations of  $q_z$  and  $q_\varphi$ . The above forms also allow solution by the method of alternating directions, which has become the solution method of choice over the past decade.

Let us briefly comment on a few 3-D code implementations in terms of their angular capabilities which now refer both to propagation in the vertical plane (similar to 2-D codes) and in the horizontal plane. The simplest form of a 3-D parabolic equation was derived by Tappert [2] in the early 1970s using just the linear terms in the Taylor expansion of (6.205). Substituting back into the generalized parabolic equation (6.201), we obtain

$$\frac{\partial \psi}{\partial r} = ik_0 \left( \frac{1}{2}q_z + \frac{1}{2}q_\varphi \right) \psi, \quad (6.209)$$

which is a narrow-angle solution in both depth and azimuth. It was quickly realized that a wide-angle capability was required in the vertical, where sound-speed gradients and, hence, refraction is greater than in the horizontal plane. Therefore, Lee et al. [49] implemented a code based on a second-order Taylor expansion in  $q_z$ , but retaining a first-order term in  $q_\varphi$ ,

$$\frac{\partial \psi}{\partial r} = ik_0 \left( \frac{1}{2} q_z - \frac{1}{8} q_z^2 + \frac{1}{2} q_\varphi \right) \psi, \quad (6.210)$$

which is wide-angle in the vertical but narrow-angle in the horizontal. One final improvement using Taylor series was proposed by Chen et al. [50] who went to second order in both  $q_z$  and  $q_\varphi$ , i.e.,

$$\frac{\partial \psi}{\partial r} = ik_0 \left( \frac{1}{2} q_z - \frac{1}{8} q_z^2 + \frac{1}{2} q_\varphi - \frac{1}{8} q_\varphi^2 \right) \psi. \quad (6.211)$$

As for the 2-D solutions, very-high-angle propagation can be obtained using the Padé series expansion given in (6.206). Collins and Chin-Bing [51] were first to implement this in a working code for 3-D, even though it was done only for the depth operator and only using one Padé term,

$$\frac{\partial \psi}{\partial r} = ik_0 \left( \frac{0.5 q_z}{1 + 0.25 q_z} + 0.5 q_\varphi \right) \psi. \quad (6.212)$$

This is the wide-angle Claerbout form [7] for propagation in the vertical, *cf.* (6.36), whereas the solution is narrow-angle in the horizontal.

The ultimate very-wide-angle PE implementation based on Padé approximants for both  $q_z$  and  $q_\varphi$  was reported by Sturm in 2005 [48]. Substituting (6.206) into the generalized parabolic wave equation (6.201) yields

$$\frac{\partial \psi}{\partial r} = ik_0 \left( \sum_{j=1}^m \frac{a_{j,m} q_z}{1 + b_{j,m} q_z} + \sum_{j=1}^m \frac{a_{j,m} q_\varphi}{1 + b_{j,m} q_\varphi} \right) \psi, \quad (6.213)$$

which can be made arbitrarily wide angled in both depth and azimuth by including enough terms in the Padé sums. Of course, this increased angular coverage is achieved at an increased computational cost, which ultimately make these fully 3-D solutions impractical, except at very low frequencies. Numerical results for 3-D propagation in a wedge-shaped waveguide using (6.213) are presented in Sects. 6.9.5 and 8.5.3.

## 6.9 Numerical Examples

We here illustrate the wide variety of acoustic problems, which can be solved with current PE implementations. These problems involve fundamental aspects of 2-D beam physics (reflection, refraction, and diffraction), mode conversion and mode cutoff in a wedge-shaped duct, propagation across a seamount, propagation over a sloping elastic bottom and finally 3-D propagation in a wedge showing horizontal refraction effects. In some of these examples, we consider an over-simplified propagation situation consisting of a homogeneous water column overlying a homogeneous (halfspace) bottom. This is done purely for illustrative purposes. In fact, the strength of the numerical models is that they allow for an arbitrary variation in depth and range of the acoustic parameters of the environment, i.e., wave speed, wave attenuation, and density, essentially without additional computational cost.

Since propagation problems in the ocean are generally not tractable by analytical techniques, we totally rely on numerical solutions of the type presented here for a detailed analysis of the complicated acoustics associated with the ocean environment. 2-D transmission-loss contours over depth and range (Figs. 6.10–6.12) have proven to be both a compact and convenient field representation, which, like a ray diagram, readily provides information on the spatial intensity distribution in a vertical slice through the ocean. Most of the 2-D results are for a line source in plane geometry. The cylindrical-geometry results can be obtained by simply adding a spreading loss of  $10 \log r$ , where  $r$  is the range in meters.

### 6.9.1 Beam Propagation

We first illustrate various aspects of beam propagation through an inhomogeneous medium. Three examples are considered: (1) beam splitting at grazing incidence upon the seafloor, Fig. 6.10a, (2) beam propagation and critical-angle effects in a wedge-shaped ocean, Fig. 6.10b, and (3) beam focusing by a thick acoustic lens, Fig. 6.10c. The numerical results are all generated with a finite-difference implementation of the Claerbout PE, (6.43). The source frequency is 100 Hz and the well-collimated beam is obtained with a Gaussian source of halfwidth  $2^\circ$ , (6.107).

#### 6.9.1.1 Beam Splitting

In Fig. 6.10a, we consider a simplified ocean with a constant-gradient profile ( $0.016 \text{ m/s/m}$ ) overlying a homogeneous bottom. The sound speed at the source is 1500 m/s increasing to 1506.4 m/s at the bottom. Hence, a downward tilt of the source beam of  $\theta_0 = \arccos(1500/1506.4) \simeq 5.28^\circ$  results in the equivalent ray having grazing incidence on the bottom. The bottom has a sound speed of 1655 m/s ( $\theta_c \simeq 24.5^\circ$ ), a density of  $1500 \text{ kg/m}^3$ , and no attenuation.

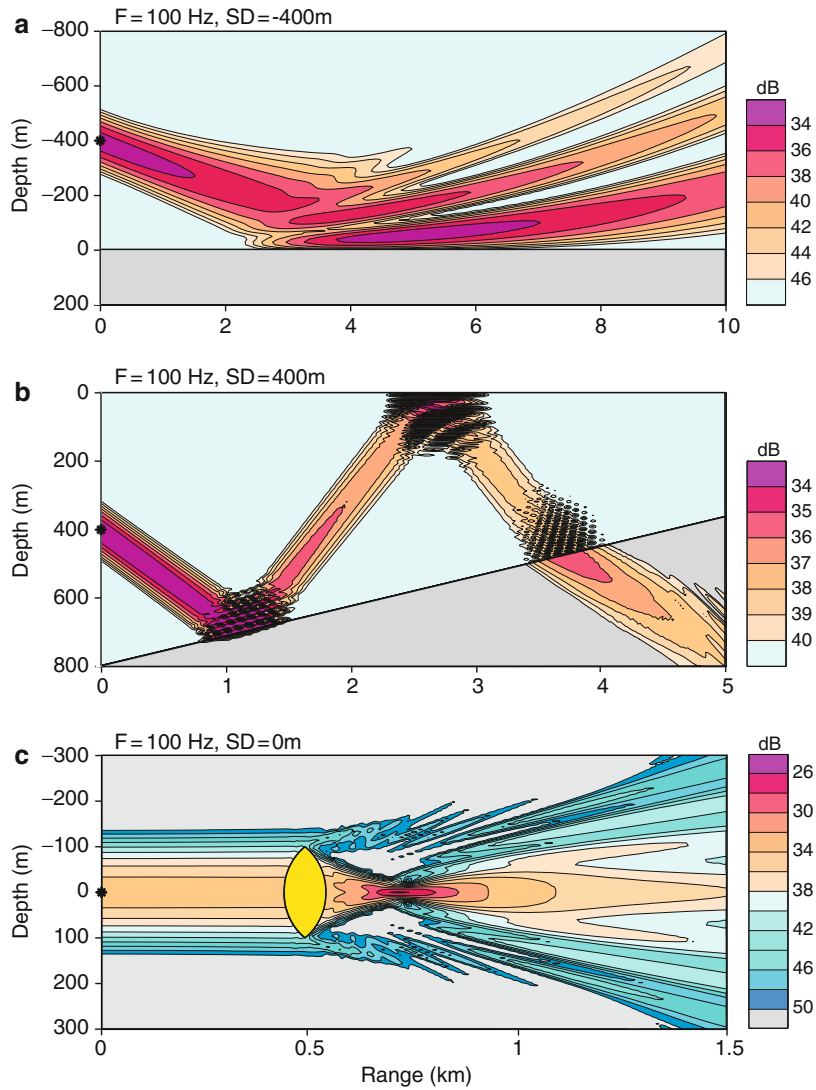


**Fig. 6.10** Numerical results illustrating fundamental aspects of beam propagation in inhomogeneous media. (a) Beam splitting at grazing incidence upon the seafloor. (b) Upslope propagation in a wedge with both subcritical and supercritical interaction with the seafloor. (c) Focusing by a thick acoustic lens

We see from the numerical solution in Fig. 6.10a that the incident Gaussian beam, after interaction with the perfectly reflecting boundary, is split into a series of interference lobes, with the lobe intensity decreasing away from the boundary (only three lobes are shown in the figure). This phenomenon is caused by the fact that narrow beams have wide angular spectra [52]. Thus, energy is propagating not only in the

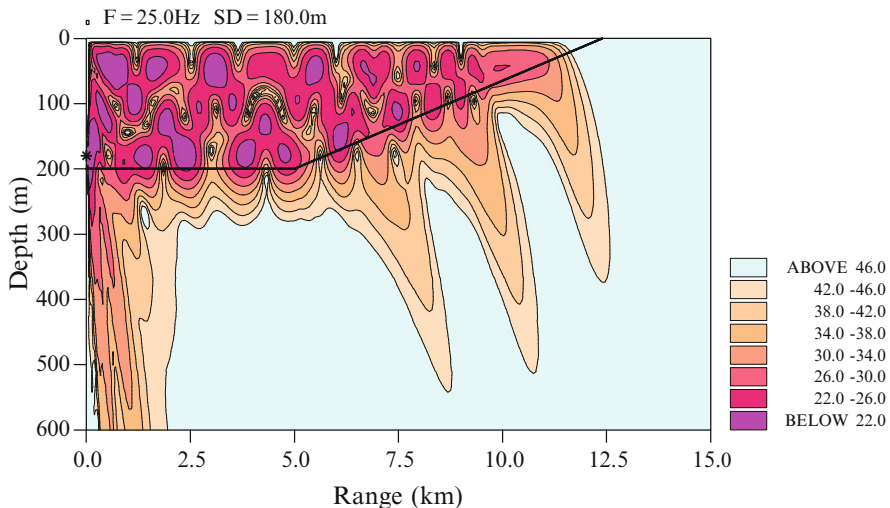


**Fig. 6.11** Mode cutoff during upslope propagation in a wedge-shaped ocean with a penetrable bottom

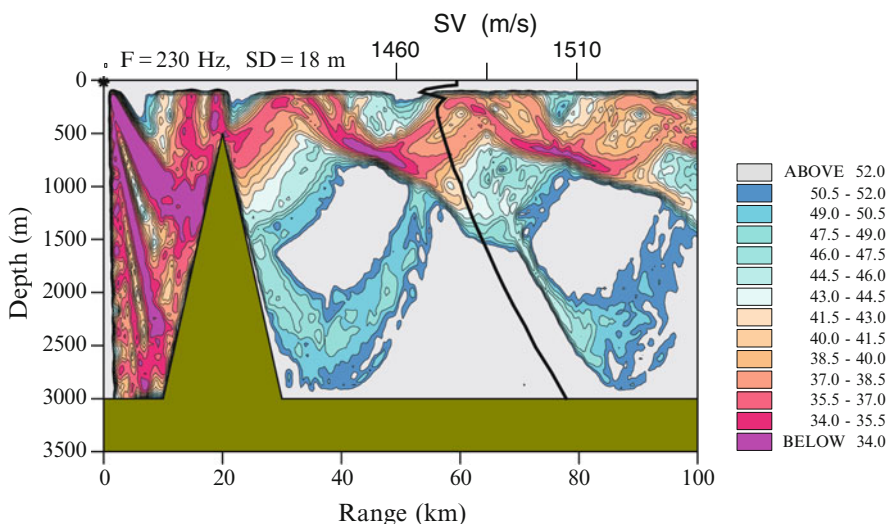


**Fig. 6.12** Sound propagation across a seamount

direction indicated by the beam axis, but also at steeper and shallower angles. The steep-angle energy is reflected at the boundary with a phase shift, while shallow-angle energy is entirely refracted within the water column. The beam splitting results from the interference between the different spectral components.

### 6.9.1.2 Beam Reflection and Transmission

We next consider beam propagation in a wedge-shaped ocean as shown in Fig. 6.10b. The water column here has a constant sound speed of 1500 m/s, while the bottom properties are the same as in the previous example. The bottom slope is 5° and the source beam has a downward tilt of 15°. In this geometry, the first interaction with the seafloor occurs at a grazing angle of 20°, which is subcritical ( $\theta_c \simeq 25.0^\circ$ ), and the beam is seen to be perfectly reflected. The second interaction, on the other hand, occurs at a grazing angle of 30° (easily verified by geometrical considerations), which is supercritical, and most of the energy is transmitted into the bottom. According to Snell's law the angle of the transmitted beam with respect to horizontal is around 12.2°.

This example of beam tracing in a tapered waveguide with a penetrable boundary clearly illustrates some of the fundamental reflection characteristics of ocean bottoms. Moreover, the example permits a detailed study of particular aspects of beam physics near critical incidence, such as non-specular reflection, subcritical penetration, and lateral displacement along the interface of both the reflected and transmitted beam axes. For more details on beam reflection and transmission problems at fluid–fluid interfaces, readers are referred to a numerical study by Jensen and Schmidt [52].

### 6.9.1.3 Beam Focusing

The last example, Fig. 6.10c, has been chosen to illustrate the full potential of numerical PE solutions to complex acoustic problems. We consider a 2° Gaussian beam propagating in a medium with a sound speed of 1500 m/s incident on a thick *acoustic lens* with a sound speed of 1200 m/s. There is no density contrast in the problem and wave attenuation is neglected. The lens consisting of two circular arcs has a height of 200 m ( $\simeq 13.3\lambda$ ) and a thickness of 100 m ( $\simeq 6.7\lambda$ ), where  $\lambda = 15$  m is the acoustic wavelength in the surrounding medium.

The computed field solution shown in Fig. 6.10c exhibits a complicated interference structure – including edge diffraction effects—outside the elongated focal region, where the intensity is approximately 8 dB higher than in the incident beam. This acoustic problem, with characteristic dimensions being of the order of a few wavelengths, is not tractable by analytical techniques. On the other hand, a numerical solution can be obtained for any frequency and any lens geometry in a matter of minutes.

## 6.9.2 Propagation in a 2-D Wedge

The study of wave phenomena such as mode conversion and mode cutoff during up-slope propagation in a wedge-shaped ocean represents one of the earliest successful

applications of PE techniques to practical ocean-acoustic problems. Numerical results similar to the one shown in Fig. 6.11 were first published by Jensen and Kuperman in 1980 [53]. We here consider a homogeneous ocean with a sound speed of 1500 m/s overlying a homogeneous bottom with a speed of 1700 m/s ( $\theta_c \simeq 28^\circ$ ), an attenuation of  $0.5 \text{ dB}/\lambda$ , and a density of  $1500 \text{ kg/m}^3$ . The bottom is flat out to a range of 5 km, then sloping toward the sea surface at an angle of  $1.55^\circ$ . The source frequency is 25 Hz and the source depth is 180 m. The field solution is, in this case, generated with a split-step implementation of the Thomson–Chapman PE, (6.41), using Greene’s wide-angle source, (6.102), to initialize the solution.

The principal feature of interest in Fig. 6.11 is the radiation of sound into the bottom, both at short ranges and on the slope. This phenomenon is closely related to the critical-angle effect demonstrated for beam propagation in Fig. 6.10b. Thus, the nearfield region out to about 2 km corresponds to sound radiated from the source at steep angles ( $>28^\circ$ ) propagating directly into the bottom at supercritical incidence. Energy radiated at shallower angles is trapped in the water column as three propagating modes. However, during upslope propagation there is a steepening of ray (mode) angles, which eventually leads to supercritical incidence also for the guided modes. The result is that modes are cut off, with the modal energy being radiated into the bottom as three well-defined beams. This phenomenon has by now been thoroughly investigated both experimentally and theoretically, with numerical PE simulations playing a decisive role [54].

### 6.9.3 Propagation Over a Seamount

The final 2-D, fluid-bottom example shown in Fig. 6.12 deals with long-range propagation in deep water at a frequency of 230 Hz. The source depth is 18 m, and a prominent seamount blocks propagation via deep refracted paths within the initial 20 km. The seamount has a slope of around  $14^\circ$ , with its peak reaching a depth of just 500 m below the sea surface. A measured North-Pacific sound-speed profile (heavy line on figure) is taken to represent water-column properties all along the track. The bottom is taken to be homogeneous with a sound speed of 1800 m/s, an attenuation of  $0.5 \text{ dB}/\lambda$ , and a density of  $1500 \text{ kg/m}^3$ . The field solution is, in this case, generated with a split-step implementation of the standard PE, (6.27), using a Gaussian source, (6.101), for initialization.

The 2-D field solution shown in Fig. 6.12 has been heavily smoothed in order to remove small-scale interference structure and emphasize the principal acoustic paths through the ocean. We see that propagation beyond the mount occurs along two distinctly different paths: one is channel propagation at a depth of around 500 m; the other is convergence-zone propagation starting on top of the seamount and having a cycle length of approximately 40 km. This particular example illustrates very well the kind of environmental complexity that can be treated with current parabolic-equation implementations. Further examples of PE modeling of 2-D, range-dependent propagation situations are given in Figs. 1.18 and 1.19.

### 6.9.4 Propagation Over a Sloping Elastic Bottom

To illustrate the importance of shear in the bottom, a couple of recently generated benchmark solutions for the elastic parabolic equations are presented [55]. We consider upslope propagation in a homogeneous water column overlying a homogeneous elastic bottom, see Fig. 6.13. The water sound speed and density are taken to be 1500 m/s and 1000 kg/m<sup>3</sup>, respectively. The bottom properties are given in the table of Fig. 6.13, which lists two bottom types ranging from moraine ( $c_s = 800$  m/s) to chalk ( $c_s = 1200$  m/s), hence covering a range of elastic sea floors with significant shear effects.

Numerical solutions for the above test problems were generated by a state-of-the-art, one-way, elastic parabolic equation code [28]. To clearly demonstrate the importance of shear for the investigated bottom types, both fluid and elastic solutions are displayed in Fig. 6.14. Moreover, the accuracy of the elastic PE solutions is verified by comparison to full-spectrum, two-way reference solutions generated by a finite-element propagation code, as described in Chap. 7. It is evident from the transmission-loss plots that shear is very important, as it causes level differences of 10–15 dB at longer ranges for bottom 1 (upper panel) and as much as 40–50 dB for bottom 2 (lower panel). The fact that the elastic PE result falls right on top of the FE reference solution in both cases indicates that backscattering is negligible for these test problems. Even though the two numerical codes give identical results, the computational efficiency differs by about a factor 100 in favor of the parabolic equation solution.

### 6.9.5 Propagation in a 3-D Wedge

The wedge-shaped waveguide considered for illustrating 3-D propagation effects is shown in Fig. 6.15. The bottom depth is 380 m in the deep part, followed by a linear slope of 2.86° and ending with a shallow depth of only 20 m. The slope area has a

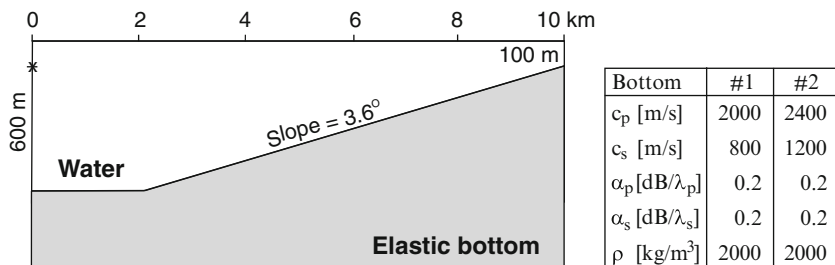


**Fig. 6.13** Test environment consisting of a constant water depth of 600 m out to 2 km, followed by a bottom slope of 3.6° until the water depth reaches 100 m. Two elastic bottoms are considered with the properties given in the table

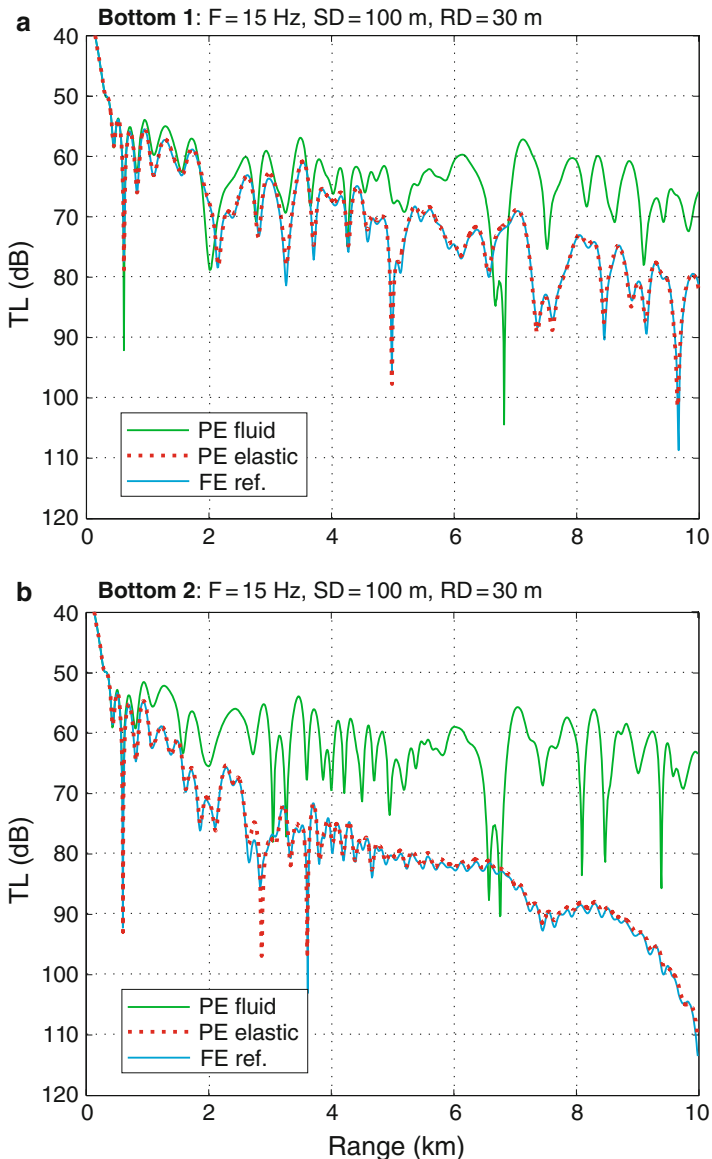


**Fig. 6.14** Propagation over a sloping elastic bottom. Transmission loss comparison for (a) bottom 1 and (b) bottom 2, both for a frequency of 15 Hz. Source and receiver depths are 100 and 30 m, respectively

horizontal extent in the  $x$ -direction of 7.2 km, and a 25-Hz point source is placed at the mid-point where the bottom depth is 200 m. The source is at 40-m depth. We consider a homogeneous ocean with a sound speed of 1500 m/s overlying a

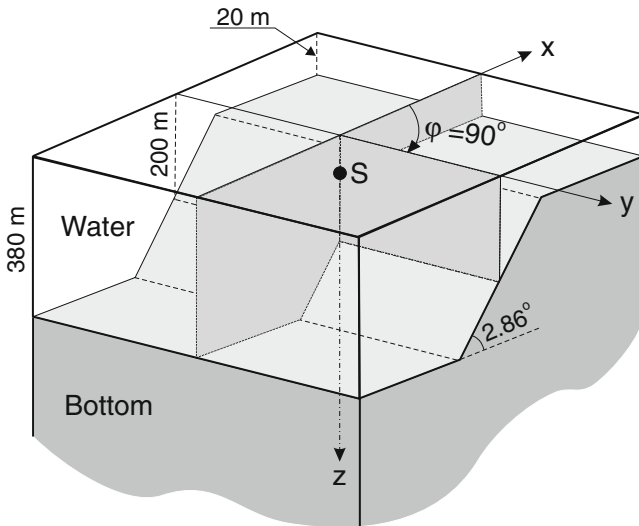


**Fig. 6.15** Geometry of truncated wedge-shaped waveguide

homogeneous fluid bottom with a speed of 1700 m/s, an attenuation of  $0.5 \text{ dB}/\lambda$ , and a density of  $1500 \text{ kg/m}^3$ , which results in a critical grazing angle of approximately  $28^\circ$ .

Propagation directly upslope in this environment (the  $x$ -direction) is a classical 2-D situation with no environmental variability perpendicular to the plane of propagation, i.e. the  $xz$ -plane. This case was treated in detail in Sect. 6.9.2 illustrating mode conversion and mode cutoff effects. Since parameters here are identical except for the bottom slope, we know that for a 25-Hz source in 200 m of water there are three propagating modes, which will reach their respective cutoff depths during upslope propagation and radiate energy into the bottom. For propagation in any other direction ( $0 < \varphi < 180^\circ$ ) 3-D effects will be present, and we wish to illustrate this explicitly by comparing approximate  $N \times 2$ -D PE solutions with fully 3-D solutions as reported by Sturm [48].

Before presenting the numerical results, we wish to recall that pseudo 3-D results can be generated by simply running 2-D codes along a number of different bearings and using the environmental information along each track as input to the models. Combining results along  $N$  different bearings allows one to build-up a 3-D image of the acoustic field, which, however, is just an  $N \times 2$ -D calculation where horizontal refraction has been ignored. The reason for using  $N \times 2$ -D approaches in practical applications is that fully 3-D computations are at least two orders of magnitude slower [48]. Also, the effect of horizontal refraction is small for weak azimuthal variability and moderate propagation ranges. One example of horizontal refraction effects on very-long-range propagation was discussed in Sect. 5.13.2.

Comparison of transmission-loss computations for the truncated-wedge environment (Fig. 6.15) is shown in Fig. 6.16. Each panel is a horizontal slice through the acoustic field at 30-m depth, the upper panel showing the approximate  $N \times 2$ -D

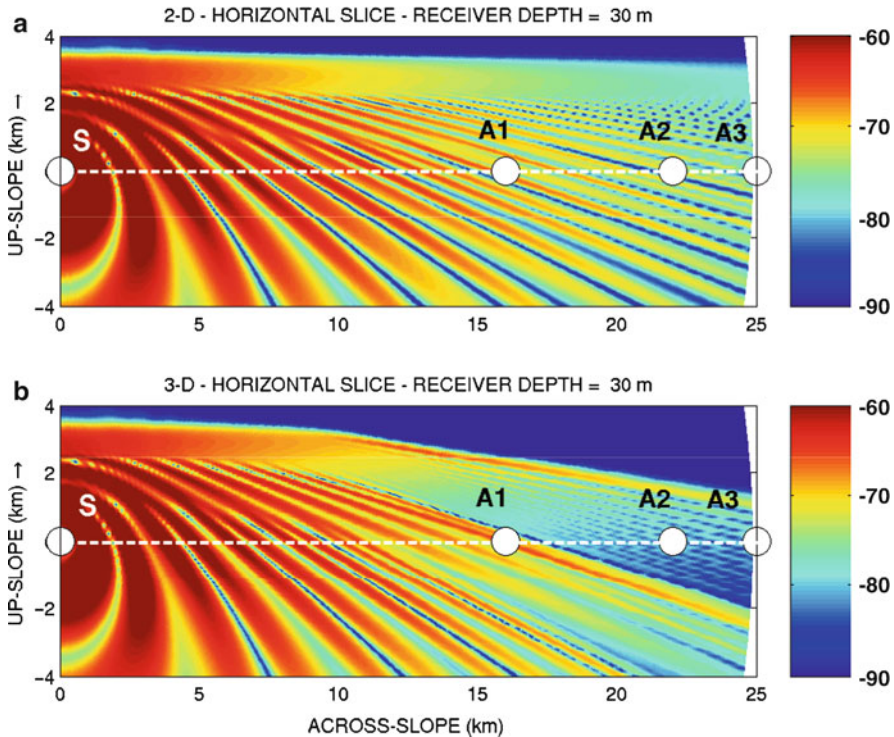


**Fig. 6.16** Transmission loss (in dB re 1 m) at 25 Hz in a horizontal plane  $z = 30$  m showing (a) the  $N \times 2$ -D result and (b) the 3-D result with horizontal refraction (from Sturm [48])

result and the lower panel the 3-D result. At a first glance, the two results are similar. However, beyond a cross-slope range of 10 km there are some differences in the interference structure, and there is clearly a more pronounced shadow zone (dark blue area) in the upper right corner of the lower panel, showing refraction of energy away from the wedge apex in the fully 3-D result.

A clearer picture of the 3-D effect is obtained by comparing losses in the cross-slope direction ( $\varphi = 90^\circ$ ) for a receiver at 30 m, see Fig. 6.17. Out to a range of around 17 km there are only small differences in the interference pattern between the two results, but then the 3-D solution drops by about 10 dB and stays lower out to 25 km. The reason for this behavior will be explained by studying single mode propagation over a sloping bottom.

Figure 6.18 illustrates the horizontal refraction of a single ray launched obliquely upslope in a wedge. At each bottom reflection the ray is deflected slightly away from the apex, with the result that an energy path which starts upslope is turned around and ends up propagating downslope. Steeper rays have more bottom reflections and will be turned around faster than shallow-angle rays. Invoking the ray-mode analogy, a mode with horizontal phase velocity  $v_m = \omega/k_m$ , where  $k_m$  is the modal eigenvalue, can be associated with an equivalent ray angle  $\theta_m = \arccos(c_0/v_m)$ ,

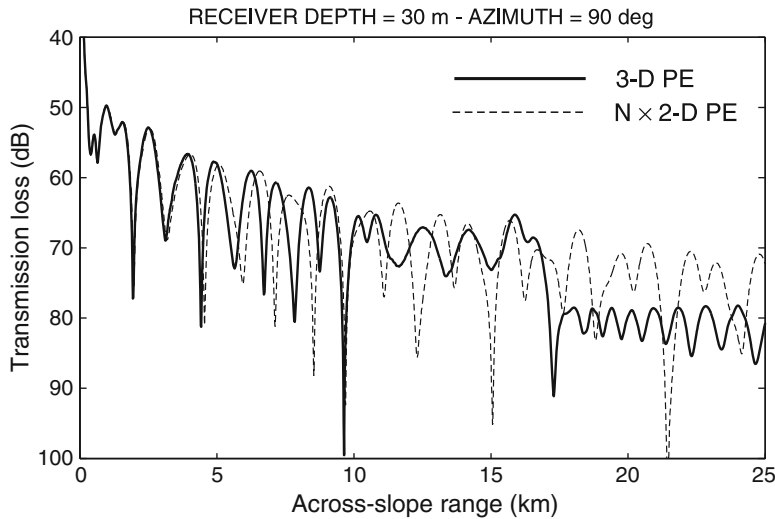


**Fig. 6.17** Comparison of  $N \times 2$ -D and 3-D transmission-loss results in the cross-slope direction indicated by the white dashed lines in Fig. 6.16. Frequency is 25 Hz, source depth 40 m and receiver depth 30 m (from Sturm [48])

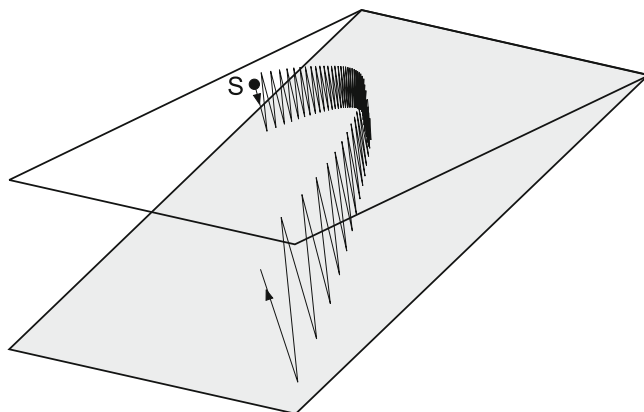


**Fig. 6.18** Illustration of horizontal deflection (refraction) of a single ray in a wedge-shaped ocean. The ray is launched obliquely upslope and is deflected away from the apex as a result of multiple boundary reflections

where  $c_0$  is the water sound speed, here 1500 m/s. It is easily seen that lower-order modes correspond to shallow ray angles, whereas higher modes correspond to steep ray angles. Consequently, higher modes exhibit stronger horizontal deflection than lower-order modes.

As shown by Sturm [48] the horizontal trace of individual mode paths can be computed with the result given in Fig. 6.19. In the upper panel, equivalent mode-1 rays have been launched from the source every  $2^\circ$  for  $0 < \varphi < 180^\circ$ . Rays reaching

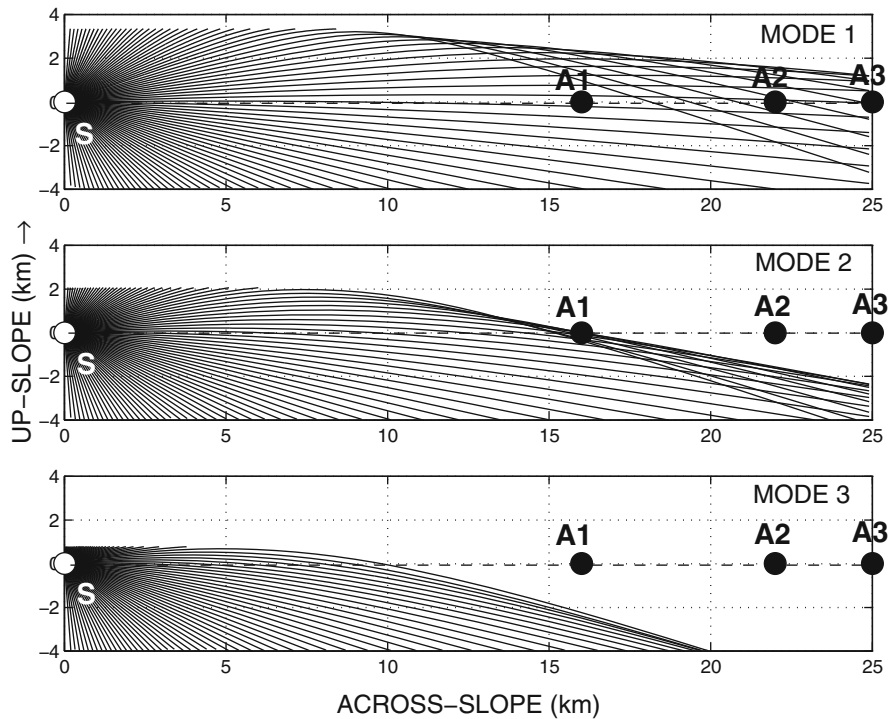


**Fig. 6.19** Ray diagrams showing horizontally-refracted mode paths for a 25-Hz source in 200 m of water (from Sturm [48])

the cutoff depth for the equivalent mode are interrupted, indicating that energy is being transmitted into the bottom. This occurs for all rays near the upslope direction. For rays launched toward the cross-slope direction ( $\varphi = 90^\circ$ ) there is a clear deflection away from the apex, causing an intra-modal interference at longer ranges, i.e., there are regions (positions A2 and A3) where two mode-1 paths exist, one associated with a smaller horizontal launch angle and one with a launch angle near  $90^\circ$ . A two-ray caustic delimits the shadow zone in the upper right corner of the panel.

Similar results are shown for modes 2 and 3 in the lower panels in Fig. 6.19. Note that positions A2 and A3 are both in the shadow zone for mode 2, and that mode 3 does not reach any of the three receiver positions.

Full 3-D PE computations for individual modes (Fig. 6.20) confirm the ray analysis results of horizontal refraction over a sloping bottom. Equally instructive are the contour plots of the pressure levels in the vertical plane passing through array positions A1, A2 and A3, see Fig. 6.21. In the upper panel, the computation is started off with just mode 1 as a source. Note the intra-modal interference at longer ranges (18–25 km). For mode 2 we clearly see the caustic at position A1 and the acoustic shadow beyond. Mode 3 only reaches a range of around 10 km. The lower panel shows the point-source result, where all three propagating modes are included. It is

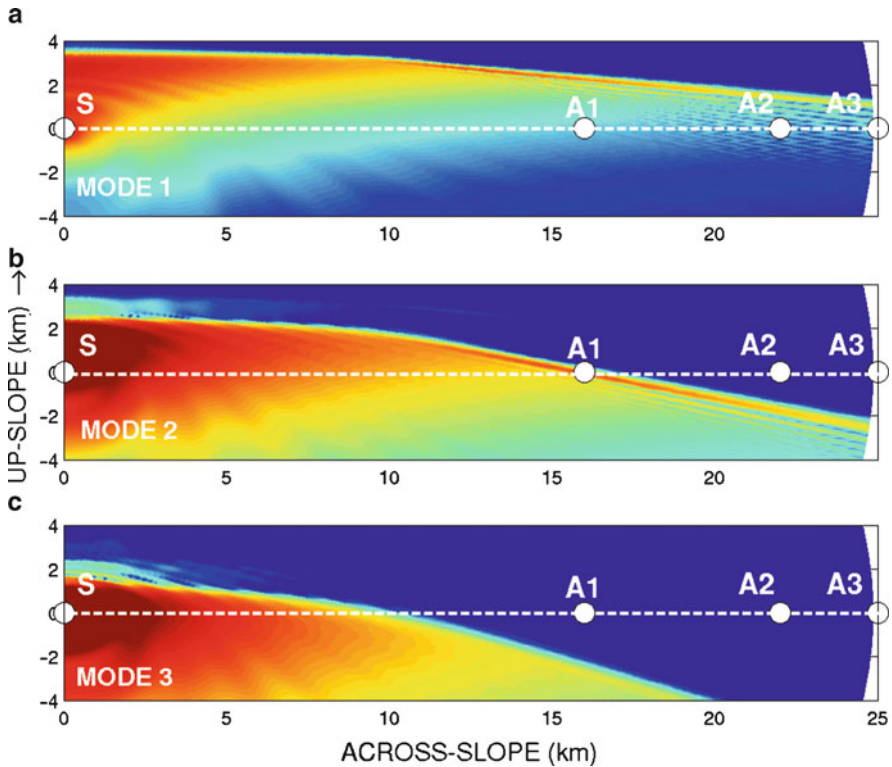


**Fig. 6.20** 3-D transmission-loss results (in dB re 1 m) at 25 Hz in a horizontal plane  $z = 30$  m using single-mode excitations: (a) mode 1, (b) mode 2, (c) mode 3 (from Sturm [48])

now clear that the abrupt decrease in pressure level at around 17 km in the cross-range direction (Fig. 6.17) is associated with the turn-around of mode 2, leaving only the contribution of mode 1 at longer ranges.

For a more detailed analysis of 3-D propagation effects, including a waveguide with a Gaussian-shaped canyon, readers are referred to the paper by Sturm [48], which also provides details on the numerical solution technique, spatial discretization, accuracy, convergence, etc. Broadband solutions for the same wedge-shaped waveguide are presented in Sect. 8.5.3.

## Appendix 1: Recipe for Simple PE Code

The easiest approach to writing a PE code is to use the split-step Fourier algorithm for solving the standard parabolic wave equation, as described in Sect. 6.5.1. An appropriate starting field is the Gaussian source, (6.101), which will be placed a  $r = 0$  in a lossy fluid environment of general range-dependent nature.

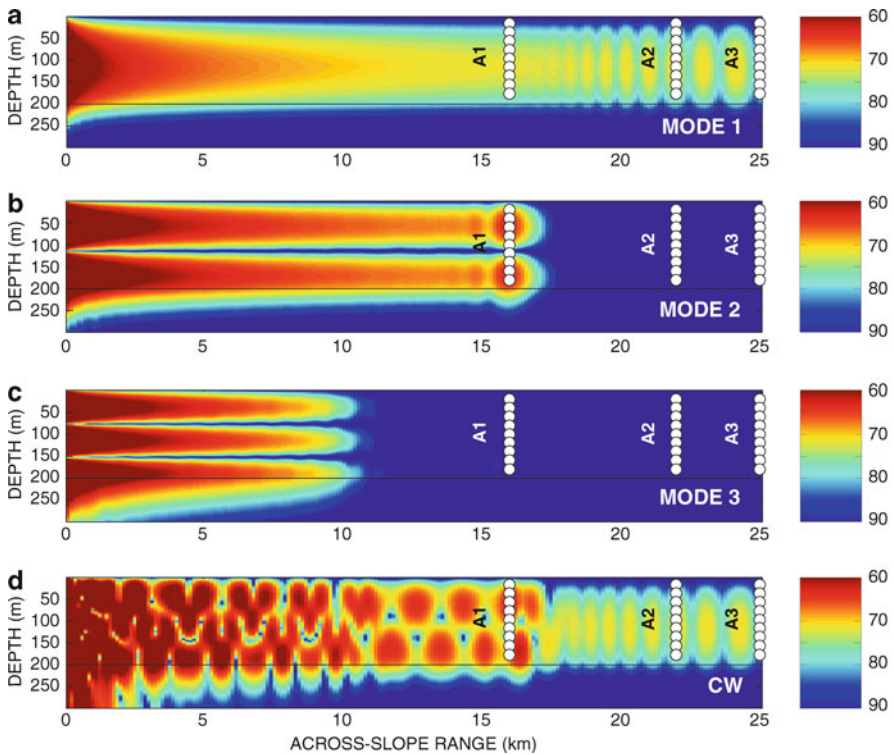


**Fig. 6.21** 3-D pressure contours (in dB re 1 m) at 25 Hz in a vertical plane  $x = 0$  m (cross-range direction) using single-mode excitations: (a) mode 1, (b) mode 2, (c) mode 3. The lower figure (d) shows the 3-D PE solution including all three modes (from Sturm [48])

As discussed in Sect. 6.5.3 and illustrated in Fig. 6.6, we first need to set up a finite solution domain in depth ( $0 \leq z \leq z_{\max}$ ), which covers the physical domain (water + bottom) as well as the “sponge” layer required to avoid spurious reflections off the lower computational boundary. An appropriate choice of  $z_{\max}$  is

$$z_{\max} = \frac{4H}{3}, \quad (6.214)$$

where  $H$  is the maximum depth of the physical domain along the propagation track.

The environmental information (sound speed, density, and attenuation) enters via the squared index of refraction  $n^2(r, z)$ , which should be used in the form given in (6.152) to include effects of density changes over depth, primarily at the water-bottom interface. A smoothing of the density change between layers is required, e.g., by using (6.153). The wave attenuation is included by adding an imaginary part to the squared index of refraction according to (6.158). Also, the exponentially increasing attenuation in the sponge layer must be included, (6.146). The final result of all this is an  $n^2$  depth array of complex numbers providing all the environmental

information. Range-dependent effects are included by updating the refraction-index array appropriately. Thus, a new sound-speed profile will change the real part of  $n^2(z)$  within the water column, while a change in water depth will change the index in the array associated with the change in properties at the water–bottom interface.

Having defined the initial field over depth from (6.101), we can proceed to apply the marching FFT algorithm given in (6.129). Note that this algorithm basically requires a Fourier transformation of the initial field over depth, followed by a multiplication by a phase factor, then an inverse Fourier transform, and finally a multiplication by another phase factor containing the environmental information (through  $n^2(z)$ ). As mentioned in Sect. 6.5.3, this marching scheme is generally implemented using a discrete FST (fast sine transform). We can, however, also use a standard, complex FFT, at the expense of doubling the calculation time.

In order to use the standard FFT, we double the computational domain to cover the depth interval  $-z_{\max} \leq z \leq +z_{\max}$ . At the same time we define the initial field to be antisymmetric in the surface by subtracting the contribution from the image source, i.e.,

$$\psi(0, z) = \psi(0, z - z_s) - \psi(0, z + z_s), \quad (6.215)$$

which ensures that the surface boundary condition  $\psi = 0$  is satisfied. Note that the field over depth must be made antisymmetric in the surface before advancing the solution another range step. This can be done by simply folding the real and imaginary parts of  $\psi(r_0, z)$  around the sea surface with a sign change.

The numerical solution now proceeds stepwise according to (6.129) until the desired maximum range has been reached. Transmission loss versus depth or range can then be calculated from (6.71).

The practical issue of which FFT size and which range step size to use was addressed in Sect. 6.5.3. It was concluded that the depth sampling must satisfy the relation

$$\Delta z \leq \frac{\lambda}{4}, \quad (6.216)$$

where  $\lambda$  is the acoustic wavelength. The FFT size is therefore determined by

$$M > \frac{8 z_{\max}}{\lambda}, \quad (6.217)$$

where  $M$  must be an integer power of two,  $M = 2^n$ .

A proper range step size is not as easily determined. However,  $\Delta r$  can generally be taken somewhat larger than  $\Delta z$ , i.e.,

$$\Delta r = (2 - 5) \Delta z, \quad (\text{shallow water}) \quad (6.218)$$

$$\Delta r = (20 - 50) \Delta z, \quad (\text{deep water}) \quad (6.219)$$

A final word of caution: The only way to ensure numerically accurate PE results is through a convergence test, where  $\Delta r$  and  $\Delta z$  are systematically reduced until a stable solution is obtained within the prescribed accuracy.

## Problems

**6.1.** The standard parabolic wave equation can be derived by introducing a narrow-angle approximation to a modal representation of the field in a waveguide. Let the modal solution be given by

$$p(r, z) = \sum_m a_m \Psi_m(z) \frac{e^{ik_m r}}{\sqrt{k_m r}},$$

where the eigenfunctions  $\Psi_m(z)$  satisfy the depth-separated wave equation

$$\frac{d^2 \Psi_m(z)}{dz^2} + [k_0^2 n^2(z) - k_m^2] \Psi_m(z) = 0.$$

Here,  $k_0$  is the reference wavenumber and  $n(z) = k/k_0$  the index of refraction. By assuming the modal eigenvalues to cluster around  $k_0$  (a narrow-angle approximation) and to be given in the form  $k_m = k_0(1 - \epsilon_m)^{1/2}$ , where  $\epsilon_m$  is small compared to unity, show that to leading order in  $\epsilon_m$  the field solution can be written in the form  $p(r, z) = \psi(r, z) \exp(ik_0 r)/(k_0 r)^{1/2}$ , where the envelope function  $\psi(r, z)$  satisfies the standard parabolic equation (6.9).

**6.2.** The effect of earth curvature on long-range propagation in the ocean can be easily accounted for in acoustic models via a modification of the local sound-speed profile.

- a. With  $r$  being the horizontal range from a source and  $R$  the earth radius, show that the sea surface on a sphere is displaced by  $\Delta z \simeq r^2/2R$ .
- b. By introducing the transformation

$$\psi(r, z) = \psi'(r, z') \exp\left[ik_0 r \left(\frac{z'}{R} - \frac{r^2}{6R^2}\right)\right], \quad z' = z - \Delta z,$$

and substituting into (6.9), derive a parabolic wave equation in  $\psi'(r, z')$ .

- c. Discuss the form of this equation and show that the earth curvature effect can be accounted for by a small linear increase in sound speed with depth.
- d. Estimate the percentage change in convergence-zone ranges due to earth curvature.

**6.3.** Rayleigh's principle for one-way wave propagation asserts that the average kinetic energy in the wave must be equal to the average potential energy, i.e.,

$$\int \frac{1}{4} (|u|^2 + |v|^2) dz = \int \frac{1}{4} \rho c^{-2} |p|^2 dz.$$

Here,  $u$  is the horizontal particle velocity,  $v$  the vertical particle velocity, and  $p$  the pressure. This energy conservation formula can be used to determine a “natural” reference wavenumber  $k_0$  for propagation in any of the parabolic approximations to the Helmholtz equation.

- a. Derive an approximate expression for  $k_0$  in terms of integrals of field quantities satisfying the standard parabolic equation (6.27).
- b. For a single mode propagating in an ideal, pressure-release waveguide show that the “natural” wavenumber found in (a) equals the modal eigenvalue.
- c. Discuss the implications of multi-mode propagation for the choice of a reference wavenumber, particularly in lossy environments with mode stripping.
- d. Consider next the alternative PE form given by (6.41). Derive the approximate expression for  $k_0$  and show that for single-mode propagation in an ideal, pressure-release waveguide the “natural” wavenumber now equals the water wavenumber.

**6.4.** Consider upslope propagation in an isovelocity wedge as illustrated in Fig. 6.11.

- a. Under the assumption of no bottom attenuation, derive an expression for the number of modes present in such a Pekeris waveguide. *Hint:* Use the information given in Sect. 2.4.5.
- b. Calculate the nominal cutoff ranges (depths) for the three propagating modes in Fig. 6.11 and compare with the PE-generated field solution.

## References

1. M.A. Leontovich, V.A. Fock, Zh. Eksp. Teor. Fiz. **16**, 557–573 (1946) [Engl. transl.: J. Phys. USSR **10**, 13–24 (1946)]
2. R.H. Hardin, F.D. Tappert, Applications of the split-step Fourier method to the numerical solution of nonlinear and variable coefficient wave equations. SIAM Rev. **15**, 423 (1973)
3. F.D. Tappert, The parabolic approximation method. in *Wave Propagation in Underwater Acoustics*, ed. by J.B. Keller, J.S. Papadakis (Springer, New York, 1977), pp. 224–287
4. J.A. Davis, D. White, R.C. Cavanagh, NORDA parabolic equation workshop. Rep. TN-143. Naval Ocean Research and Development Activity, Stennis Space Center, MS, 1982
5. D. Lee, S.T. McDaniel, *Ocean Acoustic Propagation by Finite Difference Methods* (Pergamon, New York, 1988)
6. A.P. Rosenberg, A new rough surface parabolic equation program for computing low-frequency acoustic forward scattering from the ocean surface. J. Acoust. Soc. Am. **105**, 144–153 (1999)
7. J.F. Claerbout, *Fundamentals of Geophysical Data Processing* (Blackwell, Oxford, 1985), pp. 194–207
8. R.R. Greene, The rational approximation to the acoustic wave equation with bottom interaction. J. Acoust. Soc. Am. **76**, 1764–1773 (1984)
9. D.F. St. Mary, Analysis of an implicit finite difference scheme for very wide angle underwater acoustic propagation. in *Proceedings of the 11th IMACS World Congress on System Simulation and Scientific Computing* (Oslo, Norway, 1985), pp. 153–156
10. G.H. Knightly, D. Lee, D.F. St. Mary, A higher-order parabolic wave equation. J. Acoust. Soc. Am. **82**, 580–587 (1987)

11. A. Bamberger, B. Engquist, L. Halpern, P. Joly, Higher order parabolic wave equation approximations in heterogeneous media. *SIAM J. Appl. Math.* **48**, 129–154 (1988)
12. M.D. Collins, Applications and time-domain solution of higher-order parabolic equations in underwater acoustics. *J. Acoust. Soc. Am.* **86**, 1097–1102 (1989)
13. L. Halpern, L.N. Trefethen, Wide-angle one-way wave equations. *J. Acoust. Soc. Am.* **84**, 1397–1404 (1988)
14. M.D. Feit, J.A. Fleck Jr., Light propagation in graded-index fibers. *Appl. Opt.* **17**, 3990–3998 (1978)
15. D.J. Thomson, N.R. Chapman, A wide-angle split-step algorithm for the parabolic equation. *J. Acoust. Soc. Am.* **74**, 1848–1854 (1983)
16. D.H. Berman, E.B. Wright, R.N. Baer, An optimal PE-type wave equation. *J. Acoust. Soc. Am.* **86**, 228–233 (1989)
17. L. Nghiem-Phu, F.D. Tappert, Modeling of reciprocity in the time domain using the parabolic equation method. *J. Acoust. Soc. Am.* **78**, 164–171 (1985)
18. S.T. McDaniel, Propagation of normal mode in the parabolic approximation. *J. Acoust. Soc. Am.* **57**, 307–311 (1975)
19. R.J. Hill, Wider-angle parabolic wave equation. *J. Acoust. Soc. Am.* **79**, 1406–1409 (1986)
20. M.D. Collins, A higher-order parabolic equation for wave propagation in an ocean overlying an elastic bottom. *J. Acoust. Soc. Am.* **86**, 1459–1464 (1989)
21. M.D. Collins, Higher-order parabolic approximations for accurate and stable elastic parabolic equations with application to interface wave propagation. *J. Acoust. Soc. Am.* **89**, 1050–1057 (1991)
22. B.T.R. Wetton, G.H. Brooke, One-way wave equations for seismoacoustic propagation in elastic waveguides. *J. Acoust. Soc. Am.* **87**, 624–632 (1990)
23. H. Kolsky, *Stress Waves in Solids* (Dover, New York, 1963), p. 11
24. R.R. Greene, A high-angle one-way wave equation for seismic wave propagation along rough and sloping interfaces. *J. Acoust. Soc. Am.* **77**, 1991–1998 (1985)
25. J. Miklowitz, *The Theory of Elastic Waveguides* (North-Holland, Amsterdam, The Netherlands, 1984), p. 198
26. M.D. Collins, W.L. Siegmann, A complete energy conserving correction for the elastic parabolic equation. *J. Acoust. Soc. Am.* **104**, 687–692 (1999)
27. W. Jerzak, W.L. Siegmann, M.D. Collins, Modeling Rayleigh and Stoneley waves and other interface and boundary effects with the parabolic equation. *J. Acoust. Soc. Am.* **117**, 3497–3503 (2005)
28. D.A. Outing, W.L. Siegmann, M.D. Collins, E.K. Westwood, Generalization of the rotated parabolic equation to variable slopes. *J. Acoust. Soc. Am.* **120**, 3534–3538 (2006)
29. S.A. Chin-Bing, D.B. King, J.A. Davis, R.B. Evans, *PE Workshop II: Proceedings of the Second Parabolic Equation Workshop* (Naval Research Laboratory, Washington, DC, 1993)
30. C.T. Tindle, H. Hobaek, T.G. Muir, Normal mode filtering for downslope propagation in a shallow water wedge. *J. Acoust. Soc. Am.* **81**, 287–294 (1987)
31. M.D. Collins, A self starter for the parabolic equation method. *J. Acoust. Soc. Am.* **92**, 2069–2074 (1992)
32. M.D. Collins, A stabilized self starter. *J. Acoust. Soc. Am.* **106**, 1724–1726 (1999)
33. H.K. Brock, The AESD parabolic equation model. Rep. TN-12. Naval Ocean Research and Development Activity, Stennis Space Center, MS, 1978
34. D.J. Thomson, Wide-angle parabolic equation solutions to two range-dependent benchmark problems. *J. Acoust. Soc. Am.* **87**, 1514–1520 (1990)
35. M.D. Collins, A split-step Padé solution for the parabolic equation method. *J. Acoust. Soc. Am.* **93**, 1736–1742 (1993)
36. P.G. Bergman, The wave equation in a medium with a variable index of refraction. *J. Acoust. Soc. Am.* **17**, 329–333 (1946)
37. D. Huang, Finite element solution to the parabolic wave equation. *J. Acoust. Soc. Am.* **84**, 1405–1413 (1988)
38. G. Botseas, D. Lee, K.E. Gilbert, IFD: Wide angle capability. Rep. TR-6905. Naval Underwater Systems Center, New London, CT, 1983

39. S.T. McDaniel, D. Lee, A finite-difference treatment of interface conditions for the parabolic wave equation: The horizontal interface. *J. Acoust. Soc. Am.* **71**, 855–858 (1982)
40. F.B. Jensen, C.M. Ferla, Numerical solutions of range-dependent benchmark problems in ocean acoustics. *J. Acoust. Soc. Am.* **87**, 1499–1510 (1990)
41. M.B. Porter, F.B. Jensen, C.M. Ferla, The problem of energy conservation in one-way models. *J. Acoust. Soc. Am.* **89**, 1058–1067 (1991)
42. M.D. Collins, E.K. Westwood, A higher-order energy-conserving parabolic equation for range-dependent ocean depth, sound speed, and density. *J. Acoust. Soc. Am.* **89**, 1068–1075 (1991)
43. D. Lee, S.T. McDaniel, A finite-difference treatment of interface conditions for the parabolic wave equation: The irregular interface. *J. Acoust. Soc. Am.* **73**, 1441–1447 (1983)
44. R.N. Baer, Propagation through a three-dimensional eddy including effects on an array. *J. Acoust. Soc. Am.* **69**, 70–75 (1981)
45. J.S. Perkins, R.N. Baer, An approximation to the three-dimensional parabolic-equation method for acoustic propagation. *J. Acoust. Soc. Am.* **72**, 515–522 (1982)
46. W.L. Siegmann, G.A. Kriegsmann, D. Lee, A wide-angle three-dimensional parabolic wave equation. *J. Acoust. Soc. Am.* **78**, 659–664 (1985)
47. A. Tolstoy, 3-D propagation issues and models. *J. Comput. Acoust.* **4**, 243–271 (1996)
48. F. Sturm, Numerical study of broadband sound pulse propagation in three-dimensional oceanic waveguides. *J. Acoust. Soc. Am.* **117**, 1058–1079 (2005)
49. D. Lee, G. Botseas, W.L. Siegmann, Examination of three-dimensional effects using a propagation model with azimuth-coupling capability (FOR3D). *J. Acoust. Soc. Am.* **91**, 3192–3202 (1992)
50. C.F. Chen, Y.-T. Lin, D. Lee, A three-dimensional azimuthal wide-angle model. *J. Comput. Acoust.* **7**, 269–288 (1999)
51. M.D. Collins, S.A. Chin-Bing, A three-dimensional parabolic equation model that includes the effects of rough boundaries. *J. Acoust. Soc. Am.* **87**, 1104–1109 (1990)
52. F.B. Jensen, H. Schmidt, Subcritical penetration of narrow Gaussian beams into sediments. *J. Acoust. Soc. Am.* **82**, 574–579 (1987)
53. F.B. Jensen, W.A. Kuperman, Sound propagation in a wedge-shaped ocean with a penetrable bottom. *J. Acoust. Soc. Am.* **67**, 1564–1566 (1980)
54. F.B. Jensen, C.T. Tindle, Numerical modeling results for mode propagation in a wedge. *J. Acoust. Soc. Am.* **82**, 211–216 (1987)
55. F.B. Jensen, P.L. Nielsen, M. Zampolli, M.D. Collins, W.L. Siegmann, Benchmark scenarios for range-dependent seismo-acoustic models. in *Theoretical and Computational Acoustics 2007*, ed. by M.I. Taroudakis, P. Papadakis (University of Crete, Heraklion, Greece, 2008), see addendum



# Chapter 7

## Finite Differences and Finite Elements

### 7.1 Introduction

In the preceding chapters, we have described the numerical solution techniques most commonly applied in ocean-acoustic propagation modeling. One or more of these approaches are numerically efficient for the majority of forward problems occurring in underwater acoustics, including propagation over very long ranges, with or without lateral variations in the environment. However, the numerical efficiency of these approaches is obtained by sacrificing generality through the various assumptions and approximations applied.

In spite of the success in explaining many of the observed phenomena by using these propagation models, there are still a number of unresolved scientific issues which cannot be accurately addressed by applying the traditional numerical approaches. Of particular importance in that regard is the low and medium-frequency scattering and reverberation from the ocean boundaries. These effects are inherently excluded from the approaches assuming horizontal stratification such as wavenumber integration and normal mode methods. Similarly, the classical parabolic equation approaches treat one-way propagation only and are therefore not capable of treating backscattering problems directly.

In view of the increased importance of scattering and reverberation in relation to the development of low-frequency active sonar systems, there has been a significant effort in recent years to generalize the various approaches to allow for modeling of some scattering and reverberation effects. Kuperman and Schmidt [1] combined a boundary perturbation approach with a wavenumber integration model to incorporate the effect of scattering from randomly rough interfaces in a stratified ocean with an elastic bottom. A similar perturbation approach has been applied to introduce sea-surface scattering loss in normal mode models. However, the perturbation approaches assume the roughness to be small in terms of both amplitude and slope, and this method is therefore of limited use for modeling of strong backscattering features. Here, the coupled mode approach [2] with its inherent incorporation of the backscattered field can be applied to model reverberation in two-dimensional representations of monostatic scenarios. However, the formulation of mode coupling for elastic bottoms is non-trivial, and elastic effects are of particular importance in the

low-frequency regime. Using a single-scatter approximation, Collins and Evans [3] have applied the PE approach to model ocean reverberation. By comparing to coupled mode simulations, the single-scatter approximation has been shown to work well for fluid discontinuities, but the generalization to elastic problems is again non-trivial.

Therefore, in spite of these recent advances, there is still a need for models capable of solving the two-way wave equation in inhomogeneous, fluid–elastic environments with complex geometry. A number of numerical approaches are available for this purpose, based on some form of *direct discretization* of the governing equations. In this chapter we will review three such discrete methods which have been applied to ocean acoustic propagation and scattering problems. The *Finite Difference Method* (FDM) is based on direct discretization of the governing differential equation by approximating the differential operators by finite differences over a discrete computational mesh. The *Finite Element Method* (FEM) instead discretizes the environment into discrete blocks or *elements*, connected in *nodes*, the field at which represents the degrees-of-freedom for the discretization. The discrete FEM equations are obtained through the use of an integral property of the field, representing either a variational principle or a weighted residual integral. The *Boundary Element Method* (BEM) is basically a finite-element method, but based on discretization of the surface integral representation of the field given by Green’s theorem, rather than a direct discretization of the wave equation.

All the discrete methods described here are computationally intensive due to the fact that the discrete solution must be able to represent the actual spatial and temporal variation of the acoustic field either in a volume for FDM and FEM or on a boundary for BEM. Therefore, these methods are rarely used for general ocean-acoustic propagation problems except for providing benchmark solutions. Their use in ocean acoustics is limited either to the solution of special short range scattering problems, or as a component in hybrid approaches where these methods are used to model the actual scattering process, but where the propagation of the reverberant field is treated by one of the much more efficient approaches described in earlier chapters. A detailed description of the discrete methods is therefore only necessary for the numerical specialists directly involved in the development of such codes. However, since these approaches are the only options for modeling certain classes of acoustic problems, we review here the fundamental principles to give the numerical modeler a basis for choosing the method most convenient for treating any particular problem. For details, the reader is referred to the abundant literature available on each of the discrete methods described below.

## 7.2 Differential Equations

The wave equation and the Helmholtz equation governing seismo-acoustic propagation are special cases of a general class of partial differential equations, which in two dimensions are of the form

$$a \frac{\partial^2 \psi}{\partial x^2} + b \frac{\partial^2 \psi}{\partial x \partial y} + c \frac{\partial^2 \psi}{\partial y^2} + d \frac{\partial \psi}{\partial x} + e \frac{\partial \psi}{\partial y} + f \psi + g = 0. \quad (7.1)$$

The independent variables ( $x, y$ ) may represent two space coordinates as in the case of the Helmholtz equation, or space and time as in the wave equation in one space dimension. Equation (7.1) is categorized according to the relation between the coefficients of the second derivatives. Thus, (7.1) is *elliptic* for  $b^2 - 4ac < 0$ , *parabolic* for  $b^2 - 4ac = 0$ , and *hyperbolic* for  $b^2 - 4ac > 0$ . The mathematical reason for this categorization is associated with the local interdependencies of the partial derivatives [4–6], but without going into detail it is easy to demonstrate physically why the numerical solution is dependent on where a particular differential equation falls in these categories.

Consider the wave equation in one space dimension,

$$\frac{\partial^2 \psi}{\partial x^2} - \frac{1}{c^2} \frac{\partial^2 \psi}{\partial t^2} = 0, \quad (7.2)$$

which is a *hyperbolic* differential equation. The knowledge of the physics implies that the solution at some time  $t$  is only dependent on the past history, i.e., the solution at times  $t' < t$ , but totally independent of the future  $t' > t$ . Therefore, a numerical solution for time  $t$  does not require knowledge of the future solution, and consequently this equation can be solved using a *time-marching* scheme. This fundamental feature of hyperbolic equations is of obvious importance to numerical efficiency, in particular because it limits the requirements to the approximation of the radiation conditions on the boundaries of the computational mesh. Thus, no special treatment of the boundaries is necessary if the mesh is made so large that the wavefield does not reach the artificial boundaries within the time period of interest. Similarly, *parabolic* equations can be solved using a marching scheme as described in Chap. 6.

The frequency-domain Helmholtz equation,

$$\frac{\partial^2 \psi}{\partial x^2} + k^2 \psi = 0 \quad (7.3)$$

is an example of an *elliptic* partial differential equation. Solutions to this equation are steady-state solutions, with the field at one point in space being dependent on the field everywhere else, including the real and artificial boundaries. This suggests that equations of this category must be solved using a global scheme. Clearly this requires that the boundary conditions are properly defined and included in the formulation. This feature of the elliptic equations is particularly critical in relation to problems involving radiation conditions due to the fact that the computational domain must be finite.

## 7.3 Finite-Difference Methods

### 7.3.1 Introduction

The finite-difference method (FDM) is a general numerical approach to the solution of ordinary and partial differential equations. Of particular importance here are the second-order differential equations describing the propagation of acoustic and seismic waves.

The finite-difference approximation to the wave equation is used extensively in the seismic exploration community. The reason is that the environments of interest are characterized by very complex environmental geometry and anisotropic material properties. None of the methods described earlier are capable of modeling the seismic propagation in and around *salt diapirs* or *fault zones*, areas which contain potential oil and gas traps.

In ocean acoustics, the *waveguide* physics dominates the propagation, and therefore the traditional methods are sufficiently accurate for most applications. However, the finite-difference approach has been used for analyzing acoustic interaction with elastic bottoms with geometrical irregularities such as rough interfaces or laterally varying elastic properties. A review of such applications is given by Stephen [7]. Another application of the FDM in ocean acoustics is the analysis of scattering from the underside of the Arctic ice cover. Fricke [8], for instance, has developed a finite-difference formulation for studying scattering from large-scale ice features such as keels and leads.

In addition to providing a solution capability for the full wave equation, the FDM has been used extensively for numerical solution of the reduced or approximate equations of the traditional approaches described in the earlier chapters. Thus, as described in Sect. 5.7.1, the FDM is commonly used for solving the modal equation numerically. It is also one of the most common approaches for solving the PE as described in Sect. 6.6.2.

### 7.3.2 Difference Approximations

The basic principle of the finite-difference method is the discretization of the governing differential equations by locally approximating the *differential operators* by *difference operators*. As illustrated in Fig. 7.1, we assume that the wave-propagation problem in the volume  $V$  is described by the differential equation

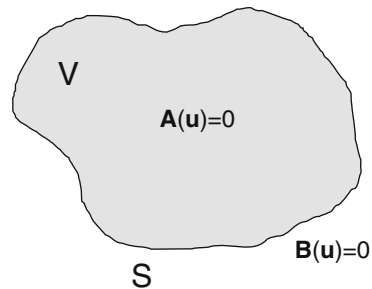
$$\mathbf{A}(\mathbf{u}) = 0 \quad (7.4)$$

with the associated boundary conditions on the surface  $S$  given by

$$\mathbf{B}(\mathbf{u}) = 0. \quad (7.5)$$

The solution  $\mathbf{u}$  may be a function of one or more spatial coordinates and time.

**Fig. 7.1** Volume  $V$  bounded by the surface  $S$ , with the field satisfying the differential equation  $\mathbf{A}(\mathbf{u}) = 0$  and the boundary condition  $\mathbf{B}(\mathbf{u}) = 0$



For a one-dimensional problem, we can express the solution  $u$  in the vicinity of the point with coordinate  $x$  by a Taylor series expansion, i.e.,

$$u(x + h) = u(x) + h u'(x) + \frac{1}{2}h^2 u''(x) + \frac{1}{6}h^3 u'''(x) + \dots \quad (7.6)$$

and

$$u(x - h) = u(x) - h u'(x) + \frac{1}{2}h^2 u''(x) - \frac{1}{6}h^3 u'''(x) + \dots \quad (7.7)$$

Addition of (7.6) and (7.7) now yields the following approximation to the second derivative,

$$u''(x) = \frac{d^2u}{dx^2} = \frac{u(x - h) - 2u(x) + u(x + h)}{h^2} + O(h^2). \quad (7.8)$$

Similarly, the subtraction of (7.7) from (7.6) yields

$$u'(x) = \frac{du}{dx} = \frac{u(x + h) - u(x - h)}{2h} + O(h^2). \quad (7.9)$$

Equation (7.9) represents the tangent at point  $x$  by the chord connecting the solutions at  $x - h$  and  $x + h$ , i.e., points  $A$  and  $B$  in Fig. 7.2. Equation (7.9) is called the *central difference* approximation to the derivative. Alternatively, (7.6) directly yields the *forward difference* approximation,

$$u'(x) = \frac{du}{dx} = \frac{u(x + h) - u(x)}{h} + O(h) \quad (7.10)$$

with errors of order  $h$  compared to  $h^2$  for the central difference approximation. The reason for the larger error is clear from Fig. 7.2: the forward difference approximates the tangent by the chord  $CB$ . Similarly, the *backward difference* representing the slope of the chord  $AC$  is obtained from (7.7) as

$$u'(x) = \frac{du}{dx} = \frac{u(x) - u(x - h)}{h} + O(h). \quad (7.11)$$

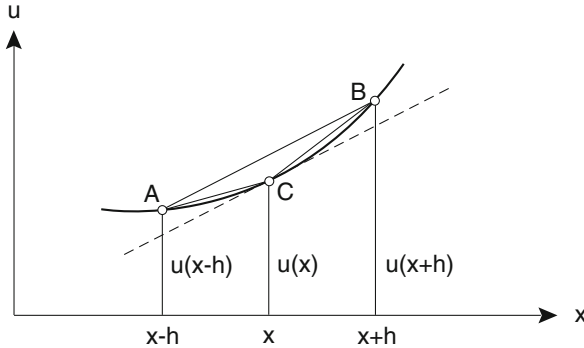


**Fig. 7.2** Approximation of derivatives by central, forward, and backward finite differences

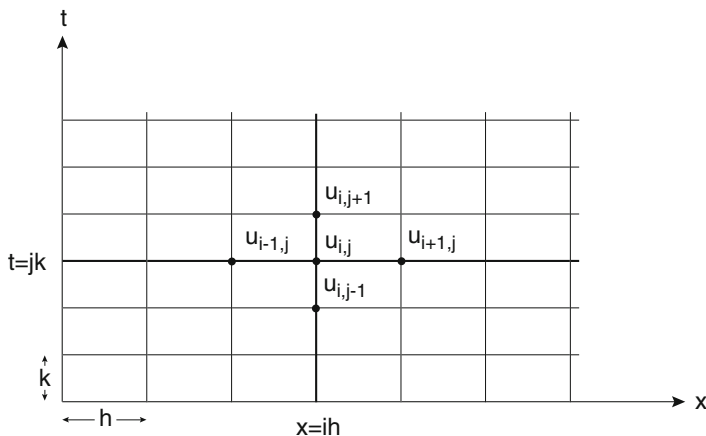


**Fig. 7.3** Finite-difference discretization of a two-dimensional domain

The finite-difference approximation is easily generalized to approximating the partial derivatives for problems in more than one dimension. Thus, for the time-domain wave equation in one space dimension,

$$\frac{\partial^2 u}{\partial x^2} - \frac{1}{c^2} \frac{\partial^2 u}{\partial t^2} = 0, \quad (7.12)$$

we can discretize the solution on a rectangular grid as shown in Fig. 7.3. The coordinates of the grid points are given by

$$x = i h, \quad (7.13)$$

$$t = j k. \quad (7.14)$$

From (7.8) we then have for  $u_{i,j} = u(ih, jk)$ ,

$$\frac{\partial^2 u}{\partial x^2} \Big|_{i,j} \simeq \frac{u_{i-1,j} - 2u_{i,j} + u_{i+1,j}}{h^2} \quad (7.15)$$

with errors of order  $h^2$ . Similarly, the time derivative is approximated by

$$\frac{\partial^2 u}{\partial t^2} \Big|_{i,j} \simeq \frac{u_{i,j-1} - 2u_{i,j} + u_{i,j+1}}{k^2} \quad (7.16)$$

with errors of order  $k^2$ . The insertion of (7.15) and (7.16) into (7.12) for all grid points then yields a linear system of equations to be satisfied by the approximate solution  $u_{i,j}$ . In addition, the solution on the boundary of the domain has to satisfy the conditions of (7.5). For problems in one space dimension, such as wave propagation in a thin rod, the boundary conditions are easily discretized by means of finite-difference approximations to the differential operators involved. This provides the additional linear equations necessary to determine the solution for  $u_{i,j}$ .

In spite of its conceptual simplicity, there are a number of numerical issues that must be addressed. We have here described the simplest finite-difference approximations, but there are a number of variants, using, for instance, higher-order Taylor series approximations. The alternatives need to be considered on the basis of efficiency, stability, and convergence. In addition, for wave propagation problems in more than one space dimension, the incorporation of boundary and radiation conditions generally requires special attention. In the following section, we will review these numerical issues in relation to the time-domain wave equation.

### 7.3.3 Convergence and Stability

The accuracy of the finite-difference approximation is associated with two different, but related problems. As described above, the discretization of the differential operators introduces errors of a certain order in the mesh sizes  $h, k, \dots$ . The exact solution  $\bar{u}$  to the discretized equations will therefore be an approximation to the exact solution  $u$  to the original differential equation. The associated error is called the *discretization error*,

$$e_D(h, k, \dots) = u - \bar{u}. \quad (7.17)$$

A finite-difference formulation for which the discretization error decreases to zero with decreasing mesh size is said to be *convergent*. Even though the finite-difference approximations in (7.8) and (7.9) are converging, the same is not necessarily the case for the discretization of the differential equation. For example, at internal or external boundaries the solution or its derivatives will be discontinuous, with the differential equation being invalid on the boundary itself. The discretization must

therefore incorporate the discontinuities explicitly, or the boundary must be properly smoothed for the discretization to converge. For multi-dimensional problems, convergence may require some relation to be satisfied between the various mesh lengths.

Another error is introduced by the numerical solution of the discretized equations due to the limited number of digits in the number representation. The nature of the equations may be such that round-off errors will propagate and magnify throughout the computational domain. Such a formulation is called numerically *unstable*. Similarly, a scheme for which round-off errors are local or propagating with decreasing amplitude are said to be numerically *stable*. In either case, the difference between the exact solution to the discretized equations  $\bar{u}$  and the numerical solution  $\hat{u}$  is called the *stability error* or *rounding error*,

$$e_S(h, k, \dots) = \bar{u} - \hat{u}. \quad (7.18)$$

As was the case for the discretization error, the stability error generally depends on the mesh lengths of the discretization, and the issues of convergence and stability are usually related.

Clearly, the total error of the finite-difference solution is the sum of the discretization and stability errors,

$$e = u - \hat{u} = e_D + e_S. \quad (7.19)$$

For problems of relatively simple nature, the convergence and stability of a certain finite-difference formulation can usually be demonstrated by one of the classical methods described in the literature [5, 6]. However, for complex problems, these important properties may be difficult to demonstrate mathematically, and, consequently, one often has to resort to numerical experiments. Below we demonstrate the stability analysis for finite-difference approximations to the acoustic wave equation.

### 7.3.4 The Wave Equation

The fundamental principles of finite-difference modeling will here be demonstrated for a relatively simple acoustic propagation problem. Although the derivations are obviously more involved, the basic principles described here are easily generalized to more complex environmental models involving elastic bottoms and ice covers.

Assume we want to determine the acoustic field produced by a transient line source of time dependence  $S(t)$  at  $(x_s, z_s)$  in the two-dimensional ocean shown in Fig. 7.4. The sea surface is represented by a pressure-release boundary, and the sound speed is allowed to vary arbitrarily throughout the volume. For simplicity we assume the density to be constant. The wave equation for this problem is

$$\frac{\partial^2 p}{\partial x^2} + \frac{\partial^2 p}{\partial z^2} - \frac{1}{c^2} \frac{\partial^2 p}{\partial t^2} = -S(t) \delta(x - x_s) \delta(z - z_s). \quad (7.20)$$

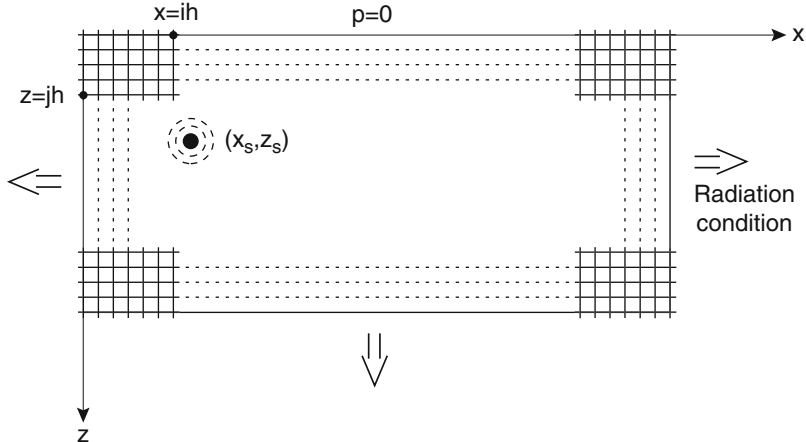


**Fig. 7.4** Line source in 2-D ocean model with space varying sound speed. A finite-difference approximation is sought on a rectangular mesh

The finite-difference approximation to (7.20) requires special consideration in relation to three different issues. The first concerns the derivation of a convergent and stable finite-difference scheme. The second issue is the representation of the singular source term, and finally the boundary and radiation conditions must be properly incorporated.

#### 7.3.4.1 Finite-Difference Scheme

Except for the source position, the propagation of the acoustic field is governed by the homogeneous form of (7.20). This equation is discretized by introducing a rectangular mesh with  $(x_i, z_j) = (ih, jh)$ ,  $i = 0, \dots, M$ ,  $j = 0, \dots, N$ , as shown in Fig. 7.4. The spatial operators are then replaced by finite differences of the form given in (7.15). Here, for simplicity, we have chosen a mesh with the same spacing in the  $x$ - and  $z$ -directions. We have also used a regular mesh with constant spacing throughout the domain. More sophisticated models may use irregular grid spacings. Similarly, the time is discretized as  $t^n = nk$ , with the time derivative being replaced by its finite-difference approximation, (7.16). Note that we use a superscript to identify the time discretization and subscripts to identify the spatial mesh. Insertion of  $t^n = nk$  into the homogeneous form of (7.20) then yields the recurrence relation for the field  $p_{i,j}^n = p(x_i, z_j; t^n)$ , valid everywhere except at the source point,

$$p_{i,j}^{n+1} = r^2 (p_{i-1,j}^n + p_{i+1,j}^n + p_{i,j-1}^n + p_{i,j+1}^n) + 2 (1 - 2r^2 p_{i,j}^n) - p_{i,j}^{n-1} \quad (7.21)$$

with

$$r = \frac{ck}{h}. \quad (7.22)$$

Clearly, the mesh sizes  $(h, k)$  must be small enough for the finite differences to accurately represent the curvature of the field in space and time, i.e., the spatial discretization size  $h$  must be much smaller than the acoustic wavelength throughout the frequency spectrum of the source function  $S(t)$ . Similarly, the time increment  $k$  must be small compared to the shortest time period of the spectral components. However, to obtain convergence and stability it is also necessary to constrain the ratio  $r$  between the spatial and temporal mesh sizes.

For smooth variations of the sound speed, the time marching scheme in (7.21) can be shown to be *convergent* for  $r \leq 1$  [4]. We show here that this condition is also sufficient to ensure *numerical stability*. As described above, the issue of stability concerns the propagation of truncation errors in the solution. In order to demonstrate this, we shall use the so-called *Neumann stability analysis* based on a Fourier representation of the error distribution. Other types of stability analyses are described in the specialized literature [4, 5].

An arbitrary error distribution at time  $t = t_0$  can be represented by the Fourier series

$$e_{p,q}^0 = \sum_{m=0}^M \sum_{n=0}^N A_{mn} e^{i\alpha_m p h} e^{i\beta_n q h}, \quad (7.23)$$

where  $\alpha_m = m\pi/Mh$  and  $\beta_n = n\pi/Nh$ . Since the problem is linear, each term in the expansion will propagate in time according to the recurrence in (7.21). Since the error amplitudes  $A_{mn}$  are arbitrary, each term must propagate in time with decreasing amplitude for the solution to be stable. To demonstrate stability, it is therefore sufficient to examine individually the propagation of each term in the expansion. We now assume the error at time  $t = t_0 + \ell k$  to be

$$e_{p,q}^\ell = e^{ih(\alpha p + \beta q)} e^{i\gamma \ell k} = e^{ih(\alpha p + \beta q)} \xi^\ell \quad (7.24)$$

with  $\xi = \exp(i\gamma k)$ . The requirement for the error to decay in time, and therefore for the scheme to be stable, clearly is

$$|\xi| \leq 1. \quad (7.25)$$

The actual value of  $\xi$  is determined by inserting (7.24) into the recurrence relation, (7.21), yielding a quadratic equation,

$$\xi^2 - 2A\xi + 1 = 0 \quad (7.26)$$

with  $A = 1 - 2r^2 \sin^2[(\alpha_m + \beta_n)h/2]$ . The solutions are

$$\xi = A \pm \sqrt{A^2 - 1}. \quad (7.27)$$

Stability is assured if both roots satisfy the condition  $|\xi| \leq 1$ , which leads to

$$-1 \leq A \leq 1 \quad (7.28)$$

or

$$r = \frac{ck}{h} \leq 1. \quad (7.29)$$

In physical terms, this equation states that for the finite-difference solution to be numerically stable, the time step must be smaller than the time it takes an acoustic wave to transverse one grid cell in the computational mesh. In contrast to this, the finite-difference approximation to the parabolic equation described in Chap. 6 is unconditionally stable, i.e., the ratio between the mesh sizes affect the accuracy, but does not have any implications in terms of numerical stability.

Equation (7.21) is an example of an *explicit* finite-difference scheme which is *conditionally stable*. Such schemes extrapolate the solution to time  $t^{n+1}$  from the value of the field and its spatial derivatives at time  $t^n$ . This scheme, therefore, ignores changes in the spatial derivatives between  $t^n$  and  $t^{n+1}$ .

Alternatively, *implicit* schemes based on the finite-difference representation of the spatial derivatives at  $t^{n+1}$  can be applied. Some implicit schemes are *unconditionally stable*. However, this stability is obtained at the cost of performing a matrix inversion for every step in the recursion. A general formulation for the time recurrence, incorporating both of these schemes as well as combinations of the two, has been developed by Newmark [9]. This method has found widespread use in the finite-element community and is discussed in Sect. 7.4.8. The derivation of convergent and stable finite-difference schemes for the elastic wave equation is obviously more involved, and the reader is here referred to the literature for details [7].

### 7.3.4.2 Source Representation

The incorporation of the source requires special consideration due to its singular nature. This problem is equivalent to the incorporation of the acoustic point or line sources in the parabolic equation described in Chap. 6. The reason is that the source term in (7.20) has a vanishing spatial extent and infinite amplitude. Despite these difficulties it is possible to directly include the source term in a finite-difference or finite-element formulation.

One method is based on the knowledge of the analytical solution for the same source placed in an infinite medium. This method was first applied to represent seismic sources in elastic media [10, 11] but it is equally applicable to the acoustic problem [12]. The solution to (7.20) for an infinite, homogeneous medium is determined by first applying the Fourier transform to obtain the Helmholtz equation which can then be solved in a cylindrical coordinate system as described in Chap. 2. The resulting time-domain solution is

$$\bar{p}(R, t) = \frac{i}{2} \int_{-\infty}^{\infty} S(\omega) H_0^{(1)}\left(\frac{\omega R}{c}\right) e^{-i\omega t} d\omega \quad (7.30)$$

with  $R = \sqrt{(x - x_s)^2 + (z - z_s)^2}$ . This solution must now be superimposed with the field reflected from boundaries and inhomogeneities. Thus, in a small region a

few mesh sizes wide and surrounding the source, the solution is expressed as a sum of the analytical solution and a perturbation,

$$p(x, z; t) = \bar{p}(R, t) + \hat{p}(x, z; t). \quad (7.31)$$

Assume that the solution outside the source region is known; then the perturbation inside the source region  $\hat{p}(x, z; t)$  can be found, using finite differences, from the continuity conditions on the boundary between the two domains. Subsequently, the exterior finite-difference solution can be updated. This procedure must now be continued in an iterative scheme for every time step until the solution has converged. However, unless the source is very close to a boundary or an inhomogeneity, the field inside the source region will be totally dominated by the analytical solution throughout the duration of the source pulse. In such cases, the iteration is unnecessary. Instead, the field and its derivatives are simply set equal to the analytic results throughout the duration of the source pulse. Once the source pulse has left the source region, the mesh points are returned to being normal ones without source contributions. This method is computationally much simpler, but obviously requires that the spatial extent of the source wavelet is small compared to the distance between the source point and any significant scattering feature.

#### 7.3.4.3 Boundary and Radiation Conditions

Homogeneous boundary conditions on plane boundaries parallel to the computational mesh are easily incorporated in the finite-difference formulation. Thus, the pressure-release boundary condition at the surface in Fig. 7.4 is satisfied by eliminating the boundary nodes  $(i, 0)$  from the recurrence, and instead setting  $p_{i,0} = 0$  in the recurrence for the neighboring interior nodes.

Similarly, a rigid boundary condition  $\partial p / \partial \mathbf{n} = 0$  is incorporated by assuming a solution which is symmetric with respect to the boundary and modifying the recurrence accordingly for the boundary nodes.

These homogeneous boundary conditions are special cases of the general *natural* boundary conditions of the form

$$\frac{\partial p}{\partial \mathbf{n}} = \eta \rho p, \quad (7.32)$$

where  $\rho$  is the density and  $\eta$  is a coefficient. Since the field outside the boundary is undetermined, the central difference cannot be used directly for the spatial derivative. A one-sided approximation such as (7.11) will increase the discretization error and, therefore, reduce the performance of the approximation. Alternatively, a higher-order *Lagrange extrapolation* [6] can be used to estimate the field outside the boundary, e.g., for the right boundary in Fig. 7.4,

$$p_{M+1,j} = 3(p_{M,j} - p_{M-1,j}) + p_{M-2,j} + O(h^3), \quad (7.33)$$

which inserted in (7.9) yields

$$\frac{\partial p}{\partial \mathbf{n}} = \frac{1}{2h} (3 p_{M,j} - 4 p_{M-1,j} + p_{M-2,j}) + O(h^2). \quad (7.34)$$

Inserting this into (7.32) then yields the approximation for the pressure on the boundary,

$$p_{M,j} \simeq \frac{4 p_{M-1,j} - p_{M-2,j}}{3 - 2\eta\rho h}. \quad (7.35)$$

The boundary condition in (7.32) is now approximated by inserting (7.35) into the recurrence for the node  $(M - 1, j)$ .

The incorporation of boundary conditions for elastic media is performed in a similar manner, but the derivations are clearly more involved. For curved or plane boundaries which are not parallel to the computational mesh, the incorporation of the boundary conditions becomes very complicated, in particular for those boundary conditions including spatial derivatives. For details, reference is again made to the specialized literature [4, 5].

One of the potential applications of FDM is for modeling acoustic scattering from objects and inhomogeneities within an acoustic medium. Here, it is important for convergence that the finite-difference formulation properly represents the internal boundary conditions. This is particularly crucial for problems with strong contrast, such as those encountered in relation to scattering and reverberation from bottom or ice features. In principle, it is possible to derive a finite-difference formulation with a computational mesh which follows the geometry of the internal boundary. However, this complicates the derivation of the difference operators significantly, in particular in elastic media, with the formulation becoming problem-specific. This method is therefore in general limited to the analysis of special problems with fixed geometry. More general finite-difference models use a uniform grid, with the assumption of smoothly varying properties across internal boundaries – an approach which significantly simplifies the numerical implementation. This representation of the internal boundaries, however, makes the issue of convergence important. Thus, the simple finite-difference schemes may cause numerical artifacts such as singularities at boundary corners. The elimination of these artifacts requires incorporation of special numerical features such as added dissipation, etc. A variety of such schemes have been developed, and their applicability to seismo-acoustic scattering problems have been discussed and evaluated by Fricke [12].

For computational reasons the finite-difference mesh must be of limited size, and it can therefore cover only a subdomain of the “infinite” environmental model usually used for representing the ocean. In addition to *physical boundaries* such as the sea surface or a rigid subbottom, it is necessary to introduce a *computational boundary*. This boundary, however, will give rise to artificial reflections unless some special precautions are taken. For transient problems, the reflections can be made insignificant within the time period of interest by making the computational domain sufficiently large. However, the computational effort increases sharply with an increased number of mesh points, and this solution is therefore, in general, very costly.

A more efficient approach is to prescribe a *radiation condition* on the computational boundary, ensuring that the field is only allowed to radiate out of the computational domain. The prescription of such conditions is complicated by the fact that on the computational boundary the relation between the field and its derivatives is non-local, i.e., it depends on the value of the field everywhere else on the boundary. This is clear from Green's theorem stated in (2.63). This non-local behavior is particularly critical for steady-state problems such as single-frequency solutions governed by the elliptic Helmholtz equation. For transient problems the non-local nature of the boundary conditions is less critical, and the radiation conditions are therefore usually approximated by some kind of local condition, such as an *impedance condition* on the computational boundary.

As described in Chap. 2 for a plane wave propagating in the  $x$ -direction, the ratio between the pressure and the particle velocity is equal to the acoustic impedance. Thus, for a pressure wave  $p^+(x, t) = f(x - ct)$  propagating in the positive  $x$ -direction, the associated particle velocity is  $v^+(x, t) = f(x - ct)/\rho c$ , i.e.,  $p^+(x, t) = \rho c v^+(x, t)$ . Similarly, for a pressure wave  $p^-(x, t) = f(x + ct)$  propagating in the negative  $x$ -direction we have  $p^-(x, t) = -\rho c v^-(x, t)$ . We can use this knowledge to force the solution on the computational boundary to be an outgoing wave only, with a propagation vector perpendicular to the boundary, by applying the condition

$$\mathbf{v} \cdot \mathbf{n} = \frac{p}{\rho c}, \quad (7.36)$$

where  $\mathbf{n}$  represents the outward-pointing normal on the boundary. Using Euler's equation, (2.11), this relation can be reformulated to a boundary condition for pressure,

$$\frac{1}{c} \frac{\partial p}{\partial t} + \frac{\partial p}{\partial \mathbf{n}} = 0. \quad (7.37)$$

Insertion of (7.9) for the time derivative, and (7.34) for the spatial derivative into (7.37) then yields a recurrence relation for the pressure. This relation is then used instead of (7.21) for mesh points on the computational boundary.

The impedance condition for the acoustic problem does not have a direct equivalent for elastic waves. However, Gottlieb et al. [13] have developed an equivalent scheme which reduces the artificial reflections from the computational boundary in both fluid and elastic media. Using eigenvalue decomposition, the boundary field is decomposed into outgoing and incoming waves, in turn allowing for explicit elimination of the incoming components at the boundary. In this approach, the radiated components will propagate through the boundary with a speed which minimizes the reflected components. In contrast, the impedance condition sets the speed equal to the speed of sound at the boundary. Therefore, the eigenvalue decomposition approach has an improved reduction of the reflections at oblique angles of incidence onto the boundary. On the other hand, this approach is much more complicated to implement than the impedance approach.

It should be stressed that the above reflection-reduction approaches are exact only for a plane wave of *normal* incidence onto a plane boundary. Their finite-difference implementation therefore only reduces the reflected field for moderate

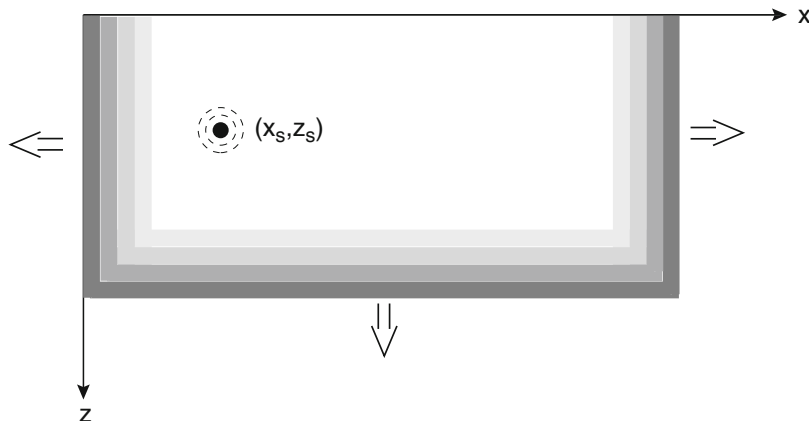


**Fig. 7.5** The computational region is divided into a region where the solution is sought and a sponge region with increasing attenuation toward the computational boundary

angles of incidence. The finite-difference mesh must be rectangular for the simple difference operators to be valid, with the computational boundary being rectangular as well. Therefore, the field in general involves waves with oblique angles of incidence on the computational boundary. To further reduce the artificial reflections, the impedance boundary condition must be combined with an attenuating “sponge” layer as shown in Fig. 7.5. The sponge layer must be designed such that the internal reflections are insignificant, which requires that the attenuation increases smoothly toward the computational boundary [12, 14].

## 7.4 Finite-Element Methods

### 7.4.1 Introduction

Whereas the FDM has gained widespread use in many areas of science, including acoustics and seismology, in some areas, engineering in particular, it has been overshadowed by another discrete method, the FEM. The reason is the close similarity between FEM and the traditional methods used in structural, mechanical, and hydrodynamic engineering, such as the variational principle and the principle of virtual work. The basis of the FEM is the division of the physical domain into subdomains, or *elements*, within which exact or approximate solutions can be obtained in terms of a finite number of degrees-of-freedom. The connectivity between the elements then leads to a linear system of equations in the degrees-of-freedom, closely analogous to the system of equations describing the mechanical behavior of discrete systems.

A fundamental difference between the FDM and FEM is the method of discretization: FDM discretizes the *governing equations* whereas FEM discretizes

the *physical domain*, treating the problem similarly to the treatment of a discrete mechanical system. However, the derivation of the discretized equations for both methods has the governing differential equations and the boundary conditions as the starting point, and in some cases the two approaches lead to identical discrete equations. The more important difference is the way the discrete approximation is obtained. In FDM, the differential operators of the governing equations are approximated using *local* accuracy criteria, and the boundary conditions are handled by special difference operators tailored to the particular boundary geometry. The derivation of the discretized FEM equations is based on *global* integral forms which combine the field equations and the prescribed boundary conditions. Therefore, FEM implementations become virtually independent of the boundary geometry and conditions. In addition, the FEM has no requirements in terms of regularity of the domain discretization, directly allowing for a discretization which is consistent with internal boundaries and discontinuities. These features makes FEM much more versatile than FDM for treatment of boundary-value problems with complex geometry.

Since the discretization requirements are similar for FDM and FEM, the use of FEM approaches are also, for computational reasons, restricted to acoustic propagation problems in relatively small physical domains, typically a few tens of wavelengths across. However, FEM is extremely versatile in terms of geometries and material properties that can be treated, and the fact that boundary conditions are directly incorporated in the FEM formulation makes this method an attractive alternative to the FDM for many deterministic scattering problems. In addition, the point and line sources of importance in ocean acoustics and seismology are directly incorporated in the FEM formulation, without applying any special numerical devices as in the FDM. In spite of this, most of the discrete solutions of the full wave equation in underwater acoustics have been based on the FDM.

Several FEM implementations of the reduced equation have appeared in the literature. Thus, Huang [15] used finite elements to solve the PE as mentioned in Chap. 6, and Olson et al. [16] used finite elements to solve the depth-separated wave equation in horizontally stratified media, allowing for arbitrary vertical variation of elastic properties. The direct global matrix approach to solving the depth-separated wave equation in stratified media, described in Sect. 4.3.1, is also, in principle, a FEM. However, it yields exact solutions to the depth-separated wave equation due to the fact that the trial functions are direct solutions to the equations within the layers (elements). A hybrid model (PE/FEM) for ocean-acoustic reverberation was developed by Murphy and Chin-Bing [17]. Here, the field is propagated to and from a scattering feature using a standard PE code, while the scattering problem is treated by a FEM solution of the Helmholtz equation over a relatively small region enclosing the scatterer. Other hybrid approaches such as the method of Seong [18] also bear close resemblance to FEM.

The wave equation is a particular case of a general class of differential equations for which accurate and efficient finite-element schemes have been developed. Others are the *heat equation*, the *Laplace equation* in fluid dynamics, and the equations of *structural mechanics and dynamics*. In fact, there is a substantial literature describing the various aspects of the finite-element solution to these equations, including

accuracy, convergence, and stability. Due to this and the fact that the applicability of the discrete numerical methods in ocean acoustics is relatively limited, we describe here only the basic principles, and refer to the extensive literature on the subject for details. The classic book by Zienkiewicz [19] gives a very comprehensive description of the finite-element method in all areas of engineering, as well as a large number of references to related literature. A more compact description of the method is given by Fletcher [20], who places the FEM in the context of more general Galerkin computational methods. An introductory text to finite-element analysis published by Burnett [21] provides several computational examples.

### 7.4.2 Mathematical Derivation

The finite-element method is a general numerical solution technique for field and boundary-value problems appearing in many areas of physics and engineering. We first present a general derivation, and then describe in some detail the finite-element solution of the wave equation.

Consider a volume  $V$  bounded by the surface  $S$  as shown in Fig. 7.1. The vector or scalar field  $\mathbf{u}(\mathbf{x})$  satisfies a set of differential equations

$$\mathbf{A}(\mathbf{u}) = 0 \quad (7.38)$$

inside the volume  $V$ , and the linear boundary conditions

$$\mathbf{B}(\mathbf{u}) = 0, \quad (7.39)$$

on  $S$ . The finite-difference approach described earlier directly discretizes (7.38) and (7.39) by locally approximating the differential operators by *difference operators*. In the finite-element method, we instead seek solutions in terms of a set of *trial* or *shape functions*, i.e., solutions of the form

$$\mathbf{u}(\mathbf{x}) \simeq \widehat{\mathbf{u}}(\mathbf{x}) = \sum_{m=1}^M \mathbf{N}_m(\mathbf{x}) a_m = \mathbf{N} \mathbf{a}, \quad (7.40)$$

where  $\mathbf{N}_m(\mathbf{x})$  is a function of the independent variables and  $a_m$  are expansion coefficients representing the degrees-of-freedom for the discrete approximation. To determine the  $M$  expansion coefficients we will need  $M$  equations. In the finite-element method, these equations are derived from scalar integral properties of the field, i.e., expressions of the form

$$\int_V G_n(\widehat{\mathbf{u}}) dV + \int_S H_n(\widehat{\mathbf{u}}) dS = 0, \quad n = 1, \dots, M. \quad (7.41)$$

There are basically two methods for deriving integrals of the form shown in (7.41). One is the method of *weighted residuals*, the other is the use of a *variational principle*.

### 7.4.2.1 Weighted Residuals

The left sides of (7.38) and (7.39) must vanish everywhere in the volume  $V$  and on the surface  $S$ , respectively. Therefore, the integral of these functions multiplied by any arbitrary function must vanish as well. We can directly write down a set of integrals of the form in (7.41), to yield a set of equations from which the expansion coefficients can be determined,

$$\int_V \mathbf{g}_n^T \mathbf{A}(\hat{\mathbf{u}}) dV + \int_S \mathbf{h}_n^T \mathbf{B}(\hat{\mathbf{u}}) dS = 0, \quad n = 1, \dots, M, \quad (7.42)$$

where  $\mathbf{g}_n$  and  $\mathbf{h}_n$  are vectors of dimension equal to that of  $A$ , with the elements being arbitrary functions of the independent variables. Because the differential operators  $\mathbf{A}$  and  $\mathbf{B}$  must vanish everywhere in the exact solution, (7.42) clearly represents a *weighted integral of residuals* of the approximation, (7.40). Moreover, since (7.42) expresses an integral of residuals rather than the local residuals directly, it is often referred to as a *weak form* of the governing equations [19].

Although the weighting functions are arbitrary, a proper choice of  $\mathbf{g}_n$  and  $\mathbf{h}_n$  is important for the accuracy of the solution. A number of weighting functions have been applied. Using *point collocation*, the sum of the residuals at  $M$  discrete points  $\mathbf{x}_n$  in the domain is forced to vanish by choosing the weighting functions,

$$\mathbf{g}_n(\mathbf{x}) = \delta(\mathbf{x} - \mathbf{x}_n), \quad n = 1, \dots, M \quad (7.43)$$

and similarly for the boundary weights  $h_n(\mathbf{x})$ . Although not necessarily true in general, improved accuracy and stability may be obtained by letting the weights be equal to the trial functions, i.e.,

$$\mathbf{g}_n(\mathbf{x}) = \mathbf{N}_n(\mathbf{x}), \quad (7.44)$$

which is the *Galerkin* approach [22]. Insertion of the Galerkin weights into (7.42) yields the following equations for the expansion coefficients to be satisfied,

$$\int_V \mathbf{N}^T \mathbf{A}(\mathbf{Na}) dV + \int_S \mathbf{N}^T \mathbf{B}(\mathbf{Na}) dS = 0. \quad (7.45)$$

An advantage of the Galerkin method is that for linear differential equations it always leads to symmetric coefficient matrices, a feature which highly simplifies the solution of the discretized equations. However, the coefficient matrices arising from the collocation approach can be symmetric as well, e.g., by using a regular FEM mesh. Other methods, such as *domain collocation* [19] have been applied, but the Galerkin method is used almost exclusively in modern FEM analysis.

### 7.4.2.2 Variational Principle

Another way of arriving at an integral form of the governing equations is to use a *variational principle*. Here, the governing equations are derived from the stationarity of a scalar functional,

$$\Pi = \int_V F \left( \mathbf{u}, \frac{\partial \mathbf{u}}{\partial x}, \dots \right) dV + \int_S G \left( \mathbf{u}, \frac{\partial \mathbf{u}}{\partial x}, \dots \right) dS. \quad (7.46)$$

The stationarity of  $\Pi$  requires that the variation of the functional vanishes for small variations of the dependent variables  $\delta \mathbf{u}$ , i.e.,

$$\delta \Pi = \int_V \delta \mathbf{u}^T \mathbf{A}(\mathbf{u}) dV + \int_S \delta \mathbf{u}^T \mathbf{B}(\mathbf{u}) dS = 0, \quad (7.47)$$

where  $\mathbf{A}(\mathbf{u})$  and  $\mathbf{B}(\mathbf{u})$  represent the variations of the kernels  $F(\mathbf{u})$  and  $G(\mathbf{u})$  in (7.46). For (7.47) to be satisfied for any variation  $\delta \mathbf{u}$ , the kernels  $\mathbf{A}$  and  $\mathbf{B}$  must vanish everywhere,

$$\mathbf{A}(\mathbf{u}) = 0, \quad (7.48)$$

$$\mathbf{B}(\mathbf{u}) = 0, \quad (7.49)$$

which are the *Euler equations* corresponding to the particular variational principle. Those variational principles for which the Euler equations are identical to the differential equations (7.38) and (7.39) are called *natural variational principles* and include Hamilton's principle of stationary energy often used in fluid and solid mechanics.

Again we seek approximate solutions of the form,

$$\mathbf{u} \simeq \widehat{\mathbf{u}} = \mathbf{N} \mathbf{a}. \quad (7.50)$$

The variation of this approximate solution is

$$\delta \widehat{\mathbf{u}} = \mathbf{N} \delta \mathbf{a}, \quad (7.51)$$

which inserted together with (7.50) into (7.47) yields

$$\delta \mathbf{a}^T \left[ \int_V \mathbf{N}^T \mathbf{A}(\mathbf{Na}) dV + \int_S \mathbf{N}^T \mathbf{B}(\mathbf{Na}) dS \right] = 0. \quad (7.52)$$

Equation (7.52) must be satisfied for all small variations  $\delta \mathbf{a}$ , requiring the term in the brackets to vanish. Therefore, comparing (7.45) and (7.52) it is clear that the approximation obtained from a *natural variational principle* is identical to that obtained by the Galerkin weighted-residual approach described above. However, (7.52) applies to any valid variational principle.

### 7.4.2.3 The FEM Equations

The discrete finite-element equations are obtained by insertion of (7.40) into (7.42), which leads to a system of equations in the expansion coefficients. If the differential equations (7.38) and (7.39) are linear, they can be written as

$$\mathbf{A}(\mathbf{u}) = \mathbf{L}\mathbf{u} + \mathbf{p} = 0 \quad \text{in } V, \quad (7.53)$$

$$\mathbf{B}(\mathbf{u}) = \mathbf{M}\mathbf{u} + \mathbf{q} = 0 \quad \text{on } S. \quad (7.54)$$

By inserting these equations together with (7.40) into the Galerkin form of the residual integral, (7.45), and interchanging the integration and summation, we obtain a linear system of equations in the expansion coefficients,

$$\mathbf{K}\mathbf{a} + \mathbf{f} = 0 \quad (7.55)$$

with the elements of the coefficient matrix  $\mathbf{K}$  and the vector  $\mathbf{f}$  being

$$K_{nm} = \int_V \mathbf{N}_n^T \mathbf{L} \mathbf{N}_m dV + \int_S \mathbf{N}_n^T \mathbf{M} \mathbf{N}_m dS, \quad (7.56)$$

$$f_n = \int_V \mathbf{N}_n^T \mathbf{p} dV + \int_S \mathbf{N}_n^T \mathbf{q} dS. \quad (7.57)$$

### 7.4.2.4 Trial Functions

The proper choice of trial functions is closely related to the physics of the problem at hand. Thus, for wave propagation problems, the trial functions must be capable of accurately approximating the shape of the wavelets in both space and time.

For certain problems with relatively simple boundary geometries and simple, homogeneous boundary conditions, trial functions spanning the whole volume  $V$  can be chosen. Such trial functions are called *global* shape functions, and methods based on this approach are often referred to as *pseudo-spectral methods*. However, the use of global trial functions is restricted to cases where the coefficients of the governing equations vary smoothly over the entire volume as well as on the boundary. Many problems for which discrete methods are the methods of choice, are characterized by internal discontinuities as well as smooth variations. Similarly, the boundary conditions will often be mixed. Therefore, a more general approach is to use *local* trial functions, with each trial function being non-vanishing in a subdomain where the coefficients, and therefore also the solutions, are smooth functions of the independent variables. This is the approach taken in the *finite-element method*. The volume is divided into a finite number of subdomains or *elements*, connected in discrete points or *nodes*. The fields at the nodes are the degrees-of-freedom of the discrete approximation, and the *trial functions* are chosen to be local *interpolation* functions for the field between the nodes.

### 7.4.2.5 Partial Discretization

So far we have assumed that the shape functions are functions of all independent parameters. For equations with many independent variables, such as equations in three space and one time dimensions, the requirements in terms of space and time windows, and in sampling, can lead to a huge dimension of the FEM equations (7.55). However, for field problems governed by hyperbolic and parabolic partial differential equations, the integration in one dimension may be performed by recursion. An example is the time-domain wave equation which is a hyperbolic PDE for which the time-domain solution can be obtained by recursion involving a few discrete time steps. For such equations the computational requirements can be reduced significantly by letting the expansion coefficients in (7.40) be functions of time, and letting the trial functions be functions of space only,

$$\hat{\mathbf{u}} = \mathbf{N}(\mathbf{x}) \mathbf{a}(t). \quad (7.58)$$

It is easy to show that if the governing equations involve first and second derivatives in time, the discretized FEM equations will take the form of an ordinary differential equation in time,

$$\mathbf{M} \ddot{\mathbf{a}} + \mathbf{C} \dot{\mathbf{a}} + \mathbf{K} \mathbf{a} + \mathbf{f} = 0. \quad (7.59)$$

Below we discuss the use of partial discretization and the associated time recurrence in relation to the FEM solution of the acoustic wave equation.

### 7.4.3 The Acoustic Wave Equation

An acoustic medium with space-varying sound speed  $c(\mathbf{x})$  and density  $\rho(\mathbf{x})$  occupies the volume  $V$ , bounded by the boundary  $S$  as shown in Fig. 7.6. In addition, the medium is assumed to be a viscous fluid with damping coefficient  $\alpha(\mathbf{x})$ . The medium

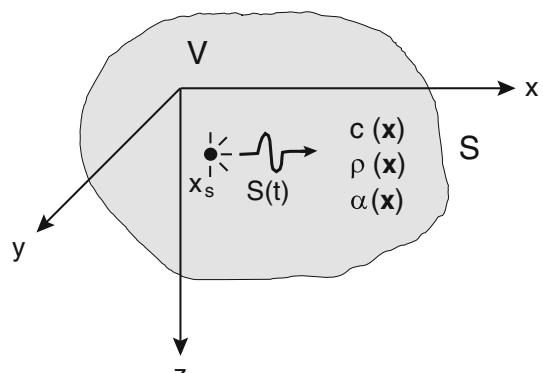


**Fig. 7.6** Acoustic medium occupying the volume  $V$  bounded by the surface  $S$

properties can be either smoothly varying or have discontinuities. The wave equation for the acoustic pressure  $p(\mathbf{x}, t)$  in such a medium is

$$\rho \frac{\partial}{\partial x} \left( \frac{1}{\rho} \frac{\partial p}{\partial x} \right) + \rho \frac{\partial}{\partial y} \left( \frac{1}{\rho} \frac{\partial p}{\partial y} \right) + \rho \frac{\partial}{\partial z} \left( \frac{1}{\rho} \frac{\partial p}{\partial z} \right) - \alpha \frac{\partial p}{\partial t} - \frac{1}{c^2} \frac{\partial^2 p}{\partial t^2} + S(t) \delta(\mathbf{x} - \mathbf{x}_s) = 0 \quad (7.60)$$

or in vector notation,

$$\nabla^T (\mathbf{R} \nabla p) + f = 0 \quad (7.61)$$

with  $\mathbf{R}$  being the diagonal matrix  $R_{ij} = \delta_{ij} \rho^{-1}$ . Since we use *partial discretization*, the source term of time dependence  $S(t)$ , as well as the inertial and damping force terms are collected in the scalar forcing function  $f$ ,

$$f = \frac{1}{\rho} \left[ S(t) \delta(\mathbf{x} - \mathbf{x}_s) - \frac{1}{c^2} \frac{\partial^2 p}{\partial t^2} - \alpha \frac{\partial p}{\partial t} \right]. \quad (7.62)$$

As described in Chap. 2, realistic boundary conditions on the physical boundaries of an acoustic medium are of the *natural* form,

$$\eta(p - p_s) - (\mathbf{R} \nabla p)^T \mathbf{n} = 0, \quad (7.63)$$

where  $\mathbf{n}$  is the boundary normal,  $\eta$  is a boundary-specific coefficient, and  $p_s$  represents induced surface pressure. It is clear from (2.11) that the second term in (7.63) represents the normal acceleration of the boundary. Therefore, the coefficient  $\eta$  represents the inverse of an *added mass* on the boundary. In the case of  $\eta = 0$ , (7.63) states that the normal acceleration, and therefore the displacement, vanishes. The other extreme case of  $\eta = \infty$  represents prescribed values of the pressure on the surface, e.g., for a free pressure-release surface we have  $p_s = 0$ . As shown below, natural boundary conditions of the form given in (7.63) can be directly incorporated in the finite-element equations. The term *natural* is used variably in the FEM literature. Thus, Zienkiewicz [19] uses the term for (7.63) with  $p_s \equiv 0$ , whereas others use it for the form with  $\eta \equiv 0$ . However, the important property of a *natural* boundary condition is the normal derivative term, which, as shown below, is necessary to cast the FEM equations into a numerically tractable form. The form of the first term can in fact be chosen rather arbitrarily, and, as shown later, this term can in fact be modified to directly incorporate impedance boundary conditions in the FEM equations.

We can now insert the operators given in (7.61) and (7.63) into the weighted residual integral, (7.42), to obtain

$$\int_V g \left[ \nabla^T \mathbf{R} \nabla p + f \right] dV - \int_S g \left[ (\mathbf{R} \nabla p)^T \mathbf{n} - \eta (p - p_s) \right] dS. \quad (7.64)$$

Using integration by parts in the form of Green's identity,

$$\int_V g \nabla^T \mathbf{f} dV = - \int_V (\nabla g)^T \mathbf{f} dV + \oint_S g \mathbf{f}^T \mathbf{n} dS \quad (7.65)$$

with  $\mathbf{f} = \mathbf{R} \nabla p$ , (7.64) can be rewritten as

$$\int_V [(\nabla g)^T \mathbf{R} (\nabla p) - g f] dV - \int_S g \eta (p - p_s) dS = 0. \quad (7.66)$$

Inserting the approximation  $\hat{p}(\mathbf{x}, t) = \mathbf{N}(\mathbf{x}) \mathbf{p}(t)$  together with the Galerkin weights  $g = N_n$  into (7.66) yields the FEM discretization for the acoustic wave equation,

$$\mathbf{C} \ddot{\mathbf{p}} + \mathbf{D} \dot{\mathbf{p}} + \mathbf{E} \mathbf{p} + \mathbf{f} = 0 \quad (7.67)$$

with

$$C_{ij} = \int_V N_i \rho^{-1} c^{-2} N_j dV, \quad (7.68)$$

$$D_{ij} = \int_V N_i \rho^{-1} \alpha N_j dV, \quad (7.69)$$

$$E_{ij} = \int_V (\nabla N_i)^T \rho^{-1} (\nabla N_j) dV - \int_S N_i \eta N_j dS, \quad (7.70)$$

$$\begin{aligned} f_i &= -S(t) \int_V N_i \rho^{-1} \delta(\mathbf{x} - \mathbf{x}_s) dV + \int_S N_i \eta p_s dS \\ &= -S(t) N_i(\mathbf{x}_s) \rho^{-1}(\mathbf{x}_s) + \int_S N_i \eta p_s dS. \end{aligned} \quad (7.71)$$

The discrete FEM equation (7.67) provides a general formulation applicable to problems in any number of space dimensions. The formulation is *complete* in the sense that the discrete equations include both the boundary conditions and the singular source representation. This contrasts to the finite-difference approach which requires special numerical devices to be incorporated for boundaries as well as for sources. This completeness is an important advantage of the finite-element method, in particular for complex geometry of the boundaries. Depending on the complexity of the problem, we can choose a set of *global* or *local* trial functions for the discretization. Although such methods only differ in terms of the choice of trial functions, the methods based on global trial functions are usually referred to as *spectral methods* or *Galerkin approaches*, whereas those based on local trial functions are called *finite-element methods*. We will here demonstrate the use of both approaches to obtain steady-state solutions for the 1-D wave equation.

### 7.4.3.1 Galerkin Approaches

For problems with simple boundary geometry and smooth variations of the medium properties, a spectral method based on *global* trial functions is often appropriate. Consider the one-dimensional form of the wave equation, (7.60), for a medium with sound speed  $c(z)$ . For a monochromatic source of time dependence  $S(t) = \exp(-i\omega t)$ , the pressure must be of the same time dependence, and, ignoring the viscous attenuation, the wave equation takes the form

$$\rho \frac{\partial}{\partial z} \left( \frac{1}{\rho} \frac{\partial p}{\partial z} \right) + k^2(z) p(z) = -\delta(z - z_s) \quad (7.72)$$

with  $k(z) = \omega/c(z)$ . Note that replacing  $k(z)$  with the vertical wavenumber  $k_z^2 = (\omega/c)^2 - k_r^2$ , (7.72) becomes identical to the inhomogeneous form of the depth-separated wave equation (5.3) for a horizontally stratified medium with density variation; therefore, the solution described here directly provides a finite element solution for the depth-dependent Green's function in a waveguide, and could be used as an alternative to the methods described in Chaps. 4 and 5. The boundary conditions are assumed to be,

$$p(0) = 0, \quad (7.73)$$

$$\left. \frac{dp}{dz} \right|_{z=D} = 0, \quad (7.74)$$

corresponding to  $\eta(0) = \infty$ ,  $p_S(0) = 0$ , and  $\eta(D) = 0$  in (7.63). This problem is a proper Sturm–Liouville problem for which the solution can be represented by an eigenfunction expansion. In the case of a *homogeneous medium*, i.e.,  $c(z) = c$  and  $\rho(z) = \rho$ , the solution is

$$p(z) = \sum_{n=1}^{\infty} p_n \sin(k_{zn} z), \quad (7.75)$$

where

$$k_{zn} = \frac{(n - 0.5)\pi}{D}, \quad (7.76)$$

$$p_n = \frac{2}{D (k_{zn}^2 - k^2)} \sin(k_{zn} z_s). \quad (7.77)$$

In the case of spatially-varying medium properties, the eigenfunctions cannot in general be determined analytically. We, therefore, seek an approximation of the form

$$p(z) = \sum_{n=1}^N p_n N_n(z). \quad (7.78)$$

If we choose a set of trial functions  $N_j(z)$  satisfying the boundary conditions in (7.73) and (7.74), we obtain the finite element discretization of (7.72),

$$\mathbf{E}\mathbf{p} + \mathbf{f} = 0 \quad (7.79)$$

with

$$E_{ij} = \int_0^D \rho^{-1} \left[ \frac{dN_i}{dz} \frac{dN_j}{dz} - k^2 N_i N_j \right] dz, \quad (7.80)$$

$$f_i = -N_i(z_s) \rho^{-1}(z_s). \quad (7.81)$$

The surface integrals in (7.70) and (7.71) vanish because of the choice of trial functions with  $N_i(0) = 0$  and the boundary conditions  $\eta(0) = \infty$ ,  $p_s(0) = 0$  and  $\eta(D) = 0$ .

Since the trigonometric functions in (7.75) satisfy the boundary conditions, they form a convenient choice of trial functions for a finite-element discretization of (7.72) in the general case with spatially varying properties. Inserting  $N_i(z) = \sin(\gamma_{zi} z)$  into (7.80) and (7.81) we obtain

$$E_{ij} = \int_0^D \rho^{-1} [\gamma_{zi} \gamma_{zj} \cos(\gamma_{zi} z) \cos(\gamma_{zj} z) - k^2(z) \sin(\gamma_{zi} z) \sin(\gamma_{zj} z)] dz, \quad (7.82)$$

$$f_i = -\sin(\gamma_{zi} z_s) \rho^{-1}(z_s). \quad (7.83)$$

For a homogeneous medium, the density can be eliminated, and  $\mathbf{E}$  becomes a diagonal matrix,  $E_{ij} = \delta_{ij} D(\gamma_{zi} \gamma_{zj} - k^2)/2$ , and (7.79) can then be directly solved to recover the solution given in (7.77). Therefore, if the *test functions* are chosen to be the *eigenfunctions* for a particular problem, then the *Galerkin finite element solution is identical to an eigenfunction expansion solution*. In the general inhomogeneous case,  $\mathbf{E}$  becomes a full matrix, requiring numerical solution of (7.79).

As described above, the homogeneous form of (7.72) with  $k^2$  replaced by  $k_z^2 = (\omega/c)^2 - k_r^2$  is identical to the mode equation (5.3). The determinant equation,

$$|\mathbf{E}| = 0 \quad (7.84)$$

directly provides an equation for the modal wavenumbers  $k_{rn}$  for the acoustic waveguide with a pressure-release surface and rigid bottom, but with arbitrary depth dependence of the medium properties. Some normal-mode solutions, e.g., the one used in the coupled-mode code of Evans [2], use such a Galerkin solution to the modal equations. The number of terms needed in the Galerkin expansion (7.78) clearly depends on the variation of the medium properties as well as the number of significant eigenfunctions or modes. Thus, the number of terms generally must be larger than the number of significant modes for the waveguide problem. An exception is for the homogeneous waveguide where the trial functions are themselves the eigenfunctions, and, consequently, the required number of Galerkin terms is exactly equal to the number of significant modes. However, the stronger the variation is in

the medium properties, the larger is the difference between the required number of trigonometric trial functions compared to the number of eigenfunctions. The magnitude of the off-diagonal terms in (7.84) is a measure of this difference. Therefore, the number of terms  $N$  must be chosen so large that the effective bandwidth of the coefficient matrix  $\mathbf{E}$  is smaller than its dimension.

#### 7.4.3.2 Finite Elements

In problems with discontinuous medium properties, the derivatives of the pressure become discontinuous as well. In such cases, a Galerkin approximation in terms of *global* trial functions will require a large number of expansion terms. Therefore, *local* trial functions are more appropriate as they allow for more accurate representations of discontinuous derivatives. Although the only difference is the choice of trial functions, this approach is usually called the *finite-element method*, whereas the technique based on global trial functions is referred to as the *Galerkin method*. For the one-dimensional wave equation (7.72), a finite-element discretization is illustrated in Fig. 7.7. The length  $D$  is divided into  $N - 1$  sectors or *elements*, connected in  $N$  points or *nodes*. The medium properties are assumed to vary smoothly within each element, but they are allowed to be discontinuous at the nodes.

Let the pressure  $p_n = p(z_n)$  at the nodes  $z_n$ ,  $n = 1, \dots, N$ , be the degrees-of-freedom for a discrete approximation,

$$p(z) = \sum_{n=1}^N p_n N_n(z). \quad (7.85)$$

As illustrated in Fig. 7.7, the trial functions  $N_n$  are chosen to be composed of linear interpolation functions for the pressure in the two elements connected by node  $n$ ,

$$N_n(z) = \begin{cases} 0 & z \leq z_{n-1}, z \geq z_{n+1} \\ \frac{z-z_{n-1}}{z_n-z_{n-1}} & z_{n-1} \leq z \leq z_n \\ \frac{z-z_{n+1}}{z_n-z_{n+1}} & z_n \leq z \leq z_{n+1} \end{cases}. \quad (7.86)$$

By inserting (7.86) into (7.80) and (7.81) and evaluating the local integrations over the elements, we obtain the discrete FEM equations of the form given in (7.79).

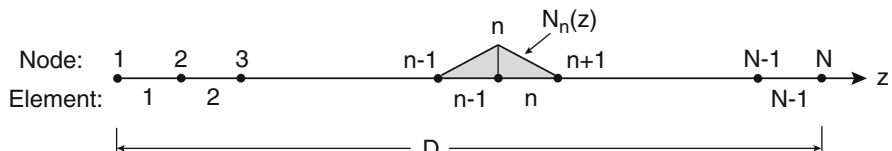


**Fig. 7.7** Finite-element discretization and associated trial functions for the one-dimensional wave equation in a region of length  $D$

For simplicity, we assume the density to be constant, and the wavenumber to be a constant  $k_n$  within each element. Further, we choose a regular mesh, i.e.,  $z_{n+1} - z_n = z_n - z_{n-1} = h$ ; then the  $n$ th *finite element* equation for a node outside the source region becomes

$$\begin{aligned} & -\frac{1}{h} \left[ \left( 1 + \frac{(hk_{n-1})^2}{6} \right) p_{n-1} - \left( 2 - \frac{(hk_{n-1})^2}{3} - \frac{(hk_n)^2}{3} \right) p_n \right. \\ & \quad \left. + \left( 1 + \frac{(hk_n)^2}{6} \right) p_{n+1} \right] = 0. \end{aligned} \quad (7.87)$$

By inserting the finite difference form of the second derivative, (7.15), into the wave equation (7.72) with  $\rho = \text{const}$ , it is easily verified that the corresponding *finite difference* discretization is

$$\frac{1}{h^2} [p_{n-1} - [2 - (hk_n)^2] p_n + p_{n+1}] = 0. \quad (7.88)$$

The two discretizations are clearly different, although they are consistent for  $hk \rightarrow 0$ . If instead of the Galerkin weights we had used point collocation weights, the two methods would lead to identical discrete equations for a regular mesh [19].

The pressure-release boundary condition  $p_S(0) = 0$  can be implemented in two ways. Since the solution is known to vanish, we can simply eliminate the boundary node from the expansion. However, for reasons of generality, it is usually desirable to maintain the boundary nodes in the expansion, and instead include the boundary contributions in (7.70) and (7.71), allowing for an arbitrary boundary pressure  $p_S$ . Thus, the pressure-release boundary condition is satisfied by enforcing  $\eta$  to a very large number, e.g.,  $\eta = 10^{20}$ . As described earlier, the Neumann boundary condition at  $z = D$  is inherent in the finite-element formulation. However, the discrete equation for the boundary node  $N$  becomes different from that governing the internal nodes due to the fact that it only involves integration over element  $N - 1$ . Thus, the resulting global finite-element equations (7.79) are, in matrix form,

$$\begin{bmatrix} a_1 & b_1 & & & & & \\ b_1 & a_2 & b_2 & & & & \\ & \ddots & & & & & \\ & & & & & & \\ & & & b_{n-1} & a_n & b_n & & & \\ & & & & \ddots & & & & \\ & & & & & & & & \\ & & & & & & & & \\ & & & & b_{N-2} & a_{N-1} & b_{N-1} & & \\ & & & & b_{N-1} & a_N & & & \end{bmatrix} \begin{bmatrix} p_1 \\ p_2 \\ \vdots \\ p_n \\ \vdots \\ p_{N-1} \\ p_N \end{bmatrix} = \begin{bmatrix} 0 \\ 0 \\ \vdots \\ \vdots \\ 1 \\ \vdots \\ 0 \\ 0 \end{bmatrix}, \quad (7.89)$$

where the source is assumed to be at node  $n$ . The coefficients are

$$a_i = \begin{cases} 10^{20}, & i = 1 \\ -h^{-1} \left[ 1 - \frac{(hk_{N-1})^2}{3} \right], & i = N \\ -h^{-1} \left[ 2 - \frac{(hk_{i-1})^2}{3} - \frac{(hk_i)^2}{3} \right], & \text{otherwise.} \end{cases} \quad (7.90)$$

$$b_i = -h^{-1} \left[ 1 + \frac{(hk_i)^2}{6} \right]. \quad (7.91)$$

The choice of the simple linear interpolation functions clearly does not correctly approximate the second derivative of the pressure. The accuracy of the FEM solution is therefore highly dependent on the number and size of the elements. In general, the second derivative of the field must be well represented by the nodal values themselves, a requirement which not surprisingly is identical to that of the FDM. For acoustic problems, the element size must therefore be short compared to the local acoustic wavelength, i.e.,  $kh$  must be small. Typically, the required number of elements per wavelength is at least ten, which translates into

$$hk_n \leq 0.6. \quad (7.92)$$

By introducing internal nodes within the elements, higher-order interpolation functions can be used, and fewer elements are therefore required. The computational savings, however, are generally limited because of the added number of nodes and, therefore, more degrees-of-freedom per element.

#### 7.4.3.3 Finite Elements in Two and Three Dimensions

The FEM equations (7.67) are valid for any number of space dimensions, allowing for both global and local trial functions. However, the global Galerkin approach is usually not convenient for problems in two or three dimensions, for which the environment is often characterized by a complex geometry of the external boundary as well as of internal interfaces. The discretization of such problems is therefore in general performed using the local finite-element discretization.

Many different types and shapes of elements have been used, and for a complete description reference is made to the literature, e.g., Zienkiewicz [19]. Here, we just describe the simplest two-dimensional triangular element shown in Fig. 7.8.

The element has three nodes, one in each corner at the points  $\mathbf{x}_1$ ,  $\mathbf{x}_2$ , and  $\mathbf{x}_3$ . Each node may be connected to one or more other elements or be on the boundary. The only element properties needed for setting up the discrete FEM equations (7.67) are the interpolation functions. The pressure inside the triangular element is assumed to be of the form

$$p^e(x, y) = \sum_{n=1}^3 N_n(x, y) p_n^e, \quad (7.93)$$

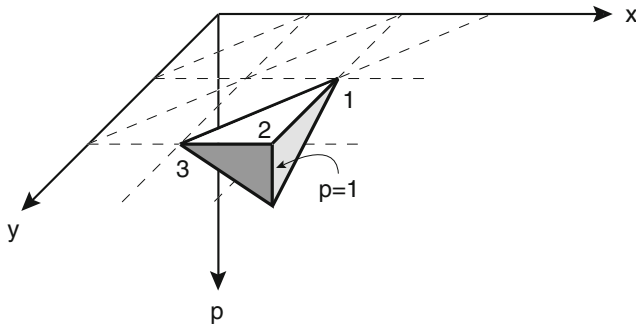


**Fig. 7.8** Two-dimensional finite element of *triangular shape* with nodes in each corner. The three interpolation functions are of unit amplitude in one node and vanishes in the other two

where  $p_n$  is the pressure at the nodes, and  $N_n(x, y)$  are linear interpolation functions

$$N_j^e = a_{1j} + a_{2j} x + a_{3j} y, \quad j = 1, \dots, 3 \quad (7.94)$$

with the coefficients  $a_{ij}$  chosen such that the interpolation function  $N_i^e$  is unity in node  $i$ , and zero in the two other nodes. The coefficients  $a_{ij}$  are therefore found from the matrix equation

$$\begin{bmatrix} a_{11} & a_{12} & a_{13} \\ a_{21} & a_{22} & a_{23} \\ a_{31} & a_{32} & a_{33} \end{bmatrix} = \begin{bmatrix} 1 & x_1 & y_1 \\ 1 & x_2 & y_2 \\ 1 & x_3 & y_3 \end{bmatrix}^{-1}. \quad (7.95)$$

In setting up the discretized equation (7.67), it is important to note that the integrals for a particular component of the coefficient matrices, e.g.,  $E_{ij}$  in (7.70), will have contributions from all elements where the two interpolation functions  $N_i$  and  $N_j$  have finite amplitudes. We, therefore, get contributions only for those elements which are common to nodes  $i$  and  $j$ . The coefficient matrices therefore in general become extremely sparse. It is very important for the numerical efficiency that only non-vanishing components of the matrices be computed. Due to the complex geometry often used for the finite-element mesh, the numerical implementation could become a book-keeping nightmare. However, the implementation can be performed very efficiently by means of *topology matrices*, describing the connectivity of the elements and nodes. Thus, we can define the mapping between the *global* node-pressure-vector  $\mathbf{p}$  and the *local* node-pressure-vector  $\mathbf{p}^m$  within element  $m$  by the matrix relation

$$\mathbf{p}^m = \mathbf{L}^m \mathbf{p}. \quad (7.96)$$

Identical expressions are obtained for the time derivatives of the pressure. Since each element only has a few degrees-of-freedom (3 for the triangular element), the

topology matrix is extremely sparse, with unity coefficients at positions for which the element node pressure occupies the corresponding position in the global node pressure vector.

By making use of (7.96), we can replace the global integrals of (7.68)–(7.71) by sums of element integrals to obtain

$$\mathbf{C} = \sum_{m=1}^M (\mathbf{L}^m)^T \mathbf{C}^m \mathbf{L}^m, \quad (7.97)$$

$$\mathbf{D} = \sum_{m=1}^M (\mathbf{L}^m)^T \mathbf{D}^m \mathbf{L}^m, \quad (7.98)$$

$$\mathbf{E} = \sum_{m=1}^M (\mathbf{L}^m)^T \mathbf{E}^m \mathbf{L}^m, \quad (7.99)$$

$$\mathbf{f} = \sum_{m=1}^M (\mathbf{L}^m)^T \mathbf{f}^m, \quad (7.100)$$

with  $\mathbf{C}^m$ ,  $\mathbf{D}^m$ ,  $\mathbf{E}^m$  and  $\mathbf{f}^m$  being the element matrices

$$C_{ij}^m = \int_{V_m} \rho^{-1} c^{-2} N_i^m N_j^m dV, \quad (7.101)$$

$$D_{ij}^m = \int_{V_m} \rho^{-1} \alpha N_i^m N_j^m dV, \quad (7.102)$$

$$E_{ij}^m = \int_{V_m} \rho^{-1} (\nabla N_i^m)^T (\nabla N_j^m) dV - \int_{S_m} N_i^m \eta N_j^m dS, \quad (7.103)$$

$$f_i^m = -S(t) N_i^m(\mathbf{x}_s) \rho^{-1}(\mathbf{x}_s) + \int_{S_m} N_i^m \eta p_s dS. \quad (7.104)$$

The global coefficient matrices are now determined by first evaluating the elements matrices given in (7.101)–(7.104), followed by the matrix multiplications in (7.97)–(7.100). For numerical efficiency, it is important to take advantage of the fact that, in particular for regular element grids, the local matrices are identical for many elements, requiring only computation of the element matrices for each type of element used. Furthermore, it is usually assumed that the medium properties are constant within each element, making the local matrices dependent on element geometry only, except for a proportionality factor.

It is even more important, however, to take advantage of the sparseness of the topology matrices in (7.96). Thus, a direct matrix multiplication in (7.97)–(7.100) will involve a very large number of zero multiplications and additions. The most efficient way of evaluating these matrix products is therefore to determine a priori a

set of *pointers* indicating where each element of the local matrices has to be added in the global coefficient matrices. These pointers are directly determined by the topology matrices representing the connection between the local and global degree-of-freedom vectors. Here, it is also of important to organize the mapping in (7.96) such that the resultant bandwidth of the global matrices becomes as small as possible. This will minimize storage requirements since only the non-vanishing band of the coefficient matrices needs to be stored. Since the matrices in (7.97)–(7.100) are symmetric, only half of the band needs to be stored. The fact that the coefficient matrices are banded and symmetric is clearly of significance for the matrix inversions involved in the solution of the finite-element equations. Furthermore, the matrices are diagonally dominant, which eliminates the need for pivoting for stability purposes.

#### 7.4.3.4 Boundary and Radiation Conditions

We have derived the finite-element equations under the assumption that the boundary conditions are of the *natural* form given by (7.63). While this equation accurately represents the *physical boundaries* of the environment, we need to be concerned also with the *computational boundary* limiting the finite-element mesh. As was the case for the finite-difference solution, we can formulate a radiation boundary condition which ensures only outgoing waves for normal incidence onto the computational boundary. The derivation is analogous to the one leading to the FDM boundary condition (7.37). The FEM result is

$$\frac{1}{\rho c} \frac{\partial p}{\partial t} + (\mathbf{R} \nabla p)^T \mathbf{n} = 0. \quad (7.105)$$

This condition is of the same form as the natural boundary conditions of (7.63), and can be incorporated into the finite-element equation (7.67) simply by modifying (7.69) to

$$D_{ij} = \int_V N_i \rho^{-1} \alpha N_j dV + \int_{S'} N_i (\rho c)^{-1} N_j dS', \quad (7.106)$$

where  $S'$  denotes the computational boundary. The element matrix in (7.102) is modified in a similar manner.

It should be stressed that this impedance condition is only exact for a plane wave of normal incidence onto a plane boundary. However, it significantly reduces the reflected field for moderate angles of incidence, and as was the case for the FDM approach, this impedance boundary condition may be combined with an attenuating sponge layer to further reduce the artificial reflections. In addition, the finite-element mesh and the computational boundary can be of arbitrary shape and can therefore often be designed to match the shape of the dominant wavefronts.

### 7.4.4 The Elastic Wave Equation

The *displacement equation of motion* for a homogeneous, isotropic elastic medium is of the form

$$(\lambda + \mu) \nabla (\nabla \cdot \mathbf{u}) + \mu \nabla^2 \mathbf{u} - \rho \ddot{\mathbf{u}} + \mathbf{f} = 0, \quad (7.107)$$

where  $\mathbf{u}(\mathbf{x})$  is the displacement vector at a point  $\mathbf{x}$ ,  $\lambda$ , and  $\mu$  are the Lamé constants, and  $\mathbf{f}(\mathbf{x})$  represents the volume forces. As described in Chap. 4, we can solve this equation in terms of displacement potentials. However, the displacement potentials are in general discontinuous at internal interfaces, requiring these to be treated as boundaries with associated continuity conditions for the displacements and stresses. The reason for using discrete methods such as FEM is to avoid exactly that. However, the displacement field is continuous for all internal interfaces which are assumed “welded.” It is, therefore, more convenient to base a FEM analysis on direct discretization of (7.107), which represents a set of coupled linear differential equations of the form given in (7.53), with boundary conditions of the form given in (7.54). Using partial discretization we can assume approximate solutions of the form

$$\mathbf{u} \simeq \sum_{m=1}^M \mathbf{N}_m(\mathbf{x}) \mathbf{v}_m(t) = \mathbf{N} \mathbf{v}, \quad (7.108)$$

where  $\mathbf{v}$  is a vector of node displacements. We then use the general method described in Sect. 7.4.2 to arrive at a discrete set of FEM equations of the form

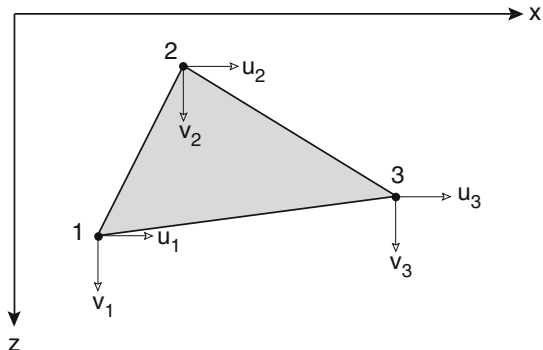
$$\mathbf{M} \ddot{\mathbf{v}} + \mathbf{D} \dot{\mathbf{v}} + \mathbf{K} \mathbf{v} + \mathbf{g} = 0. \quad (7.109)$$

Since the first term clearly represents inertial forces,  $\mathbf{M}$  is denoted the *mass matrix* for the FEM discretization. Similarly,  $\mathbf{D}$  is the *damping matrix*, while the matrix  $\mathbf{K}$  representing the elastic properties of the medium is the *stiffness matrix* for the discrete system.

As was the case for the acoustic wave equation treated in the previous section, either *global* or *local* trial functions can be applied. However, discrete methods will usually be chosen only for problems with complex boundary geometry, and therefore the *local* finite-element discretization is usually applied for wave propagation problems. The simplest 2-D element is again the triangle with nodes in the corners, as shown in Fig. 7.9. For the elastic problem this element has six degrees-of-freedom, representing the two displacement components  $u$  and  $v$  for each of the three nodes. Assuming linear interpolation, the displacement components within the element are given in terms of the node displacement vector  $\mathbf{v}^e$  by

$$\mathbf{u} = \begin{Bmatrix} u \\ v \end{Bmatrix} = [\mathbf{I} \mathbf{N}_1, \mathbf{I} \mathbf{N}_2, \mathbf{I} \mathbf{N}_3] \mathbf{v}^e = \mathbf{N} \mathbf{v}^e, \quad (7.110)$$

**Fig. 7.9** Two-dimensional finite element of *triangular shape* with nodes in each corner. The element has six degrees-of-freedom, representing the node displacements



where  $\mathbf{I}$  is a  $2 \times 2$  identity matrix and  $N_i$  are the same linear interpolation functions used for the triangular acoustic element,

$$N_j^e = a_{1j} + a_{2j} x + a_{3j} y, \quad j = 1, 2, 3 \quad (7.111)$$

with the coefficients  $a_{ij}$  given by (7.95). The element mass and damping matrices and the forcing vector then become

$$\mathbf{M}^e = \int_{V_e} \rho (\mathbf{N}^e)^T \mathbf{N}^e dV, \quad (7.112)$$

$$\mathbf{D}^e = \int_{V_e} \mu (\mathbf{N}^e)^T \mathbf{N}_j^e dV, \quad (7.113)$$

$$\mathbf{g}^e = S(t) [\mathbf{N}^e(\mathbf{x}_s)]^T \mathbf{f}(\mathbf{x}_S). \quad (7.114)$$

The element stiffness matrix represents the stored elastic energy for a certain node displacement field and is, therefore, equal to the inner product of the strain and stress vectors corresponding to that displacement field [19]. Insertion of (7.110) into the definition of the strain tensor  $\epsilon_{ij} = 1/2(u_{i,j} + u_{j,i})$  for plane strain, yields the vector relation between the node displacements and the strain components contributing to the elastic energy,

$$\begin{Bmatrix} \epsilon_{xx} \\ \epsilon_{yy} \\ 2\epsilon_{xy} \end{Bmatrix} = \mathbf{B}^e \mathbf{v}^e, \quad (7.115)$$

where  $\mathbf{B}$  is the *strain interpolation* matrix

$$\mathbf{B}^e = [\mathbf{B}_1, \mathbf{B}_2, \mathbf{B}_3] \quad (7.116)$$

with the  $3 \times 2$  submatrices given by

$$\mathbf{B}_i = \begin{bmatrix} \frac{\partial N_i}{\partial x} & 0 \\ 0 & \frac{\partial N_i}{\partial y} \\ \frac{\partial N_i}{\partial y} & \frac{\partial N_i}{\partial x} \end{bmatrix} = \begin{bmatrix} a_{2i} & 0 \\ 0 & a_{3i} \\ a_{3i} & a_{2i} \end{bmatrix}. \quad (7.117)$$

The strain interpolation function is clearly a constant, and this triangular element is therefore often referred to as a *constant strain* element. In plain strain, the stress-strain relation, or Hooke's law, is in matrix form

$$\begin{Bmatrix} \sigma_{xx} \\ \sigma_{yy} \\ \sigma_{xy} \end{Bmatrix} = \begin{bmatrix} \lambda + 2\mu & \lambda & 0 \\ \lambda & \lambda + 2\mu & 0 \\ 0 & 0 & \mu \end{bmatrix} \begin{Bmatrix} \epsilon_{xx} \\ \epsilon_{yy} \\ 2\epsilon_{xy} \end{Bmatrix} = \mathbf{D}^e \begin{Bmatrix} \epsilon_{xx} \\ \epsilon_{yy} \\ 2\epsilon_{xy} \end{Bmatrix} \quad (7.118)$$

or in terms of the node displacements by inserting (7.115),

$$\begin{Bmatrix} \sigma_{xx} \\ \sigma_{yy} \\ \sigma_{xy} \end{Bmatrix} = \mathbf{D}^e \mathbf{B}^e \mathbf{v}^e. \quad (7.119)$$

The element stiffness matrix then becomes

$$\mathbf{K}^e = \int_{V_e} (\mathbf{B}^e)^T \mathbf{D}^e \mathbf{B}^e dV. \quad (7.120)$$

The corresponding global coefficient matrices in (7.109) are again assembled using expressions in terms of topology matrices similar to those given in (7.97)–(7.100).

Although the derivation of the finite-element approximation was here based on the equation of motion for a homogeneous, isotropic elastic medium, this assumption only affects the equations on the element level. Therefore, if the FEM formulation is performed in continuous variables, such as the displacements in elastic media, and pressure in the acoustic case, problems involving spatial inhomogeneity can be treated simply by letting the finite-element mesh follow internal boundaries. The fact that the finite-element mesh can be deformed without changing the basic element formulation except for the numerical values, is a very important advantage of the FEM approach over discrete methods based on finite differences. In the next section, we described how the finite-element method is capable of coupling regions where the field is described by different governing equations.

### 7.4.5 Coupled Fluid–Elastic Domains

One of the most important applications of the finite-element method in relation to ocean acoustics is the modeling of acoustic waves interacting with elastic media in cases where the interface is of irregular geometry.

One approach to such problems is to represent the water as an elastic medium with a very low shear speed and associated large shear attenuation, virtually describing the water as a viscous fluid. We can then apply the FEM discretization in (7.109) for the combined problem. However, due to the large displacement gradients occurring in the water close to the interface, such an approach will usually require a very fine element grid in the fluid close to the elastic interface, and furthermore, this approach also represents the fluid problem by double the number of degrees-of-freedom needed physically. It is, therefore, more efficient to use a coupled approach, using the discretization in (7.67) for the fluid region and (7.109) for the elastic region and then couple the two using the proper boundary conditions.

At the boundary, the normal displacement must be continuous. As is clear from (2.11), the last term in the *natural* form of the fluid boundary condition, (7.63), represents the normal acceleration of the boundary. We can, therefore, write the boundary condition of continuous normal displacement to be satisfied on the fluid–elastic boundary in the equivalent acceleration form

$$-\ddot{u}_n - (\mathbf{R} \nabla p)^T \mathbf{n} = 0, \quad (7.121)$$

where  $u_n$  is the normal displacement of the elastic boundary. The normal displacement can be expressed in terms of interpolation functions on the boundary and the degrees-of-freedom for the elastic discretization,

$$u_n = \widehat{\mathbf{N}} \mathbf{v}. \quad (7.122)$$

Incorporating the boundary condition of (7.121) into the weighted residual integrals for the fluid then replaces (7.67) by

$$\mathbf{C} \ddot{\mathbf{p}} + \mathbf{E} \mathbf{p} + \mathbf{f} + \mathbf{F} \ddot{\mathbf{v}} = 0, \quad (7.123)$$

where the coefficient matrix for the coupling term is

$$F_{ik} = \int_{S_I} N_i \widehat{N}_k dS. \quad (7.124)$$

$S_I$  is the interface separating the elastic and fluid regions. Since the fluid attenuation is usually insignificant compared to the elastic attenuation, we have eliminated the damping term from (7.123).

The continuity of stress on the interface is satisfied by prescribing the normal stress in the elastic medium to be equal to the negative of the fluid pressure, which in a similar way leads to the modified form of (7.109),

$$\mathbf{M}\ddot{\mathbf{v}} + \mathbf{D}\dot{\mathbf{v}} + \mathbf{K}\mathbf{v} + \mathbf{g} + \mathbf{F}^T \mathbf{p} = 0. \quad (7.125)$$

Equations (7.123) and (7.125) now form a set of coupled equations that can be solved simultaneously for fluid pressure and elastic displacement.

### 7.4.6 Steady-State Solutions

As for all ocean acoustic modeling, the use of Fourier synthesis of steady-state solutions is computationally efficient by eliminating the time dimension from the governing equations. This is particularly the case for propagation problems in bounded domains where the field satisfies *natural* boundary conditions of the form given in (7.63). However, when applying FEM to problems with radiation conditions, which is often the case in ocean acoustics, the radiation condition can only be *approximated* by a boundary condition. The boundary of the computational grid will therefore introduce errors throughout the whole domain in steady-state solutions.

There are several ways of eliminating, or at least reducing these errors, all of which are associated with approximating the boundary integral representation of Green's theorem for the external, infinite medium:

- The finite-element method may be coupled with the finite-element discretization of Green's theorem, i.e., the BEM, which is described in the next section.
- Another method, similar to the “sponge” layer approach described earlier for the FD approach, is to make the medium highly attenuating in a region along the boundary, thus partially eliminating the artificial boundary reflections.
- A computationally efficient technique is the unconjugated infinite element (UIE) method [23–25]. The main disadvantages associated with the UIE are the need for nonstandard basis functions and the integration of highly oscillatory integrands over infinite intervals, which can cause difficulties when implementing the technique in generic FE tools.
- A viable and readily available alternative is the perfectly matched layer (PML) technique, introduced originally by Bérenger [26, 27]. The PML can be implemented either by introducing anisotropic material damping parameters or by a complex coordinate scaling [28–31]. This method has the advantage that it can be formally adapted to arbitrary external environments, including realistic representations of a stratified ocean environment. A version of this method has been very effectively adapted to ocean-acoustic scattering problems by Zampolli et al. [32]. It is summarized in the following section.

### 7.4.7 Perfectly Matched Layers

One method for converting a fluid layer into a Bérenger [26, 27] perfectly matched layer (PML) consists of applying a transformation to the coordinates [28, 31]. The

transformation is a scaling to complex coordinates such that the new medium becomes selectively dissipative in the direction perpendicular to the interface between the PML and the physical domain.

Here, we focus on the application of PML's specifically in the context of structural acoustics problems. For this purpose, the PML scaling and the PML reflection properties are analyzed in a planar 2-D geometry, with the underlying assumption that the conclusions on the applicability of the method can be extended to other curvilinear geometries in the same way as one can extend the coordinate scaling functions [28–30]. Considering a planar Cartesian coordinate system with the interface between PML and fluid being the  $z$ -axis (inset in Fig. 7.10), the coordinate scaling for a complex time dependence  $\exp(-i\omega t)$  is defined as:

$$\tilde{x}(x) = \frac{\lambda}{D}x + \frac{i}{\omega} \int_0^{\frac{\lambda}{D}x} \sigma(\xi) d\xi, \quad (7.126)$$

$$\frac{d\tilde{x}}{dx} = \frac{\lambda}{D} \cdot \frac{i\omega - \sigma(x)}{i\omega} \quad (7.127)$$

for  $x > 0$ .  $D$  is the thickness of the PML, and  $\lambda = c_f/f$  is the acoustic wavelength. The scaling satisfies the continuity property  $\sigma(0) = 0$ . It is also required

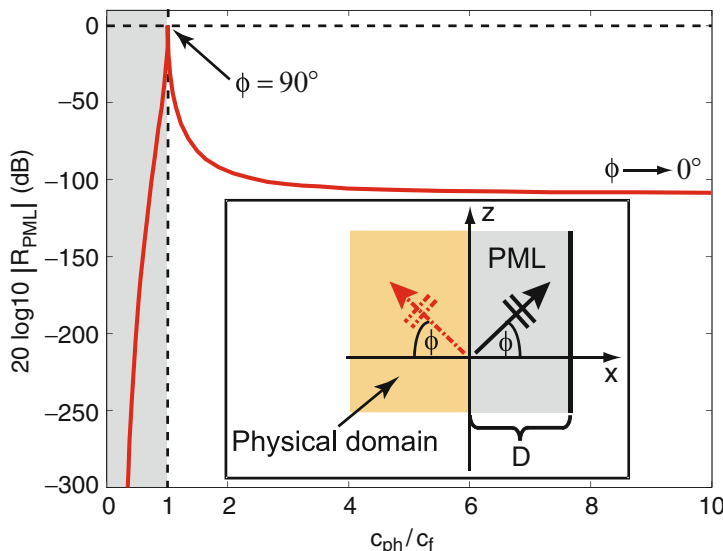


**Fig. 7.10** PML reflection coefficient for fluid-borne structural waves. At the coincidence frequency  $c_{ph}/c_f = 1$ , the waves transition from the evanescent regime (shaded area) to the propagating regime. The inset shows the PML in the domain  $x > 0$ , the plane wave launched into the PML at an angle  $\phi$  (black arrow) and the PML-reflected plane wave (red arrow) reflected back into the physical domain. In general, the physical domain can be an elastic structure or a fluid

that  $\tilde{x}(D) = (1 + i)\lambda$  and  $\text{Im}(\tilde{x}) > 0$ . The latter property implies that the PML is capable of absorbing evanescent plane waves as well as propagating ones, with the well-known limitations for angles near grazing incidence [33–35]. The coordinate stretching introduced in FDTD implementations of the PML [34, 36–38] can be chosen in a particularly convenient manner in frequency-domain models, such as the one presented here. By introducing the  $\lambda/D$  stretching in (7.126) and (7.127), the scaled coordinate is normalized with respect to  $\lambda$ . In the finite element model, this has the advantage that one can define one single PML geometry for a given multi-frequency problem, with one fixed discretization of  $\tilde{x}$  applicable throughout the frequency band of interest.

If the medium in the domain  $x \leq 0$  is a radiating or scattering elastic structure, the fluid waves in  $x > 0$  generated by the fluid–structure interaction can be represented by the homogeneous plane-wave spectrum [39, 40]

$$p(x, z) = e^{-k\beta x} e^{ik\sqrt{\beta^2 + 1}z} \quad (7.128)$$

with  $\beta = \sqrt{(c_f/c_{ph})^2 - 1}$ , and where  $c_{ph}$  is the phase speed at which the horizontal displacement component propagates along  $z$  (inset in Fig. 7.10). The evanescent spectrum of the homogeneous plane wave is in the range  $0 < c_{ph}/c_f < 1$ .

Placing the planar PML in direct contact with the physical domain  $x < 0$ , as shown in Fig. 7.10, considering homogeneous plane waves in the form of (7.128) incident onto the  $x = 0$  interface from the  $x < 0$  domain, and requiring the pressure and the normal displacement respectively to be continuous at the interface  $x = 0$  yields the reflection coefficient

$$|\mathcal{R}_{\text{PML}}| = e^{-4\pi\beta}. \quad (7.129)$$

The logarithmic plot of  $|\mathcal{R}_{\text{PML}}|$  in Fig. 7.10 exhibits a strong decay of the reflected plane waves away from the coincidence frequency. The steep decay of the evanescent waves makes it necessary to discretize the PML through the thickness with a sufficient number of degrees-of-freedom. When setting up a numerical model for a given frequency band of interest, one can a priori estimate the minimum phase speed  $c_{ph}$  of the structural waves using analytical methods, and discretize the PML accordingly.

Close to the coincidence frequency for elastic shells, the PML can exhibit significant reflections in both the evanescent and the propagating regime. This can in principle lead to inaccurate numerical solutions. Nevertheless, for a large number of cases of interest, the elastic structures have a curvature, so that the coupling angle of the structural waves is never above the threshold value beyond which numerical reflections become significant. This makes the PML widely applicable to problems of scattering and radiation from localized elastic structures surrounded by fluids.

### 7.4.8 Time Recurrence

In Sect. 7.4.3, we described the use of FEM to determine steady-state solutions to the wave equation. For time-invariant medium properties we can apply Fourier synthesis of such steady-state solutions to obtain the solution for arbitrary time dependence of the source function, as described in Chap. 8.

Although usually not seen as such, Fourier synthesis is an example of a Galerkin approach with *global*, orthogonal trial functions over the time interval  $T = 1/\Delta f$ . Since for transient problems the time period of physical interest is often very short, with artificial boundaries having no significant effect on the solution until the initial transient signal reaches them, we can often use direct time-domain integration by simply making the finite-element domain so large that interaction with the artificial boundaries happens outside the time interval of interest.

Since the linear wave equation has no “memory”, i.e., the time development of the solution depends only on the instantaneous value of the field and its time derivative, we can treat the finite-element equations (7.67) or (7.109) as an initial value problem which can be integrated by time-domain recurrence. In FEM terminology, this approach corresponds to using *local* trial functions in time. A variety of recurrence relations have been developed based on either finite differences or finite elements. A general class of recurrence algorithms is known as *Newmark’s method* [9], which for (7.67) takes the form

$$\begin{aligned} & [\mathbf{C} + \gamma \Delta t \mathbf{D} + \beta \Delta t^2 \mathbf{E}] \mathbf{p}_{n+1} \\ &= [2\mathbf{C} - (1 - 2\gamma) \Delta t \mathbf{D} - (1/2 - 2\beta + \gamma) \Delta t^2 \mathbf{E}] \mathbf{p}_n \\ &\quad - [\mathbf{C} - (1 - \gamma) \Delta t \mathbf{D} + (1/2 + \beta - \gamma) \Delta t^2 \mathbf{E}] \mathbf{p}_{n-1} \\ &\quad - \Delta t^2 [\beta \mathbf{f}_{n+1} + (1/2 - 2\beta + \gamma) \mathbf{f}_n + (1/2 + \beta - \gamma) \mathbf{f}_{n-1}], \end{aligned} \quad (7.130)$$

where  $\mathbf{p}_n = \mathbf{p}(t_0 + n \Delta t)$  is the solution vector at discrete points in time. This algorithm can be derived using a weighted-residual finite-element formulation with quadratic trial functions and the various values of  $\beta$  and  $\gamma$  corresponding to different weighting functions [19].

As discussed in [9, 19] the values of the parameters  $\beta$  and  $\gamma$  cannot be chosen arbitrarily. Thus,  $\gamma < 0.5$  can be shown to yield growing amplitudes if applied to free vibration problems, and is therefore unstable. Similarly,  $\gamma > 0.5$  yields decaying amplitudes, corresponding to stable but artificially damped solutions. The value  $\gamma = 0.5$  introduces no artificial damping, but does not guarantee stability. Thus, it can be shown that this value will only provide unconditionally stable solutions provided  $\beta \geq 0.25$ . On the other hand, schemes with smaller values of  $\beta$  are not necessarily unstable, but the stability depends on the length of the time step.

If  $f_m$  is the largest frequency component in the forcing function, then a scheme with  $\beta = 0$  and  $\gamma = 0.5$  is stable for time steps satisfying the condition

$$\Delta t \leq \frac{1}{\pi f_m}. \quad (7.131)$$

The reason for using this conditionally stable scheme rather than an unconditionally stable one, is its numerical efficiency. Thus, the mass and damping matrices are in general strongly diagonally dominant and may be replaced by *lumped* diagonal matrices without significant loss of accuracy. In the case of  $\beta = 0$ , the coefficient matrix on the left side of (7.130) becomes diagonal, eliminating the need for a matrix inversion in the recurrence algorithm, and therefore yielding a very efficient *explicit* scheme.

An advantage of the unconditionally stable *implicit* schemes is that they allow for much longer time steps than the conditionally stable ones. However, frequencies of the order  $1/\Delta t$  and larger are clearly not accurately represented. Therefore, the frequency content of the source pulse should be limited, or an artificial attenuation of the high frequencies should be introduced. By choosing  $\gamma > 0.5$ , a frequency-dependent attenuation is introduced, with very small attenuation for frequencies  $f < 1/10 \Delta t$  and strong attenuation for  $f > 1/\Delta t$ . Therefore, it is often desirable to choose  $\gamma > 0.5$  to obtain an unconditionally stable scheme which artificially damps the inaccurate high-frequency components of the solution [19].

In general, all the proposed versions of Newmark's method as well as other types of time integration schemes have merit in terms of stability, accuracy or efficiency, and the choice is therefore strongly dependent on the problem at hand as well as personal preferences.

## 7.5 Boundary-Element Methods

### 7.5.1 Introduction

The finite-difference and finite-element methods are extremely versatile in terms of the environmental complexity that can be treated. Thus, these methods are applicable to problems which cannot be solved with the traditional methods described in earlier chapters. Such problems include scattering from objects in fluid or elastic media, and scattering at a rough elastic seabed or at an irregular elastic ice cover.

The main limitation of the discrete methods (FDM, FEM) is that the computation time can be excessive. These methods must discretize the environment with a mesh size small compared to the acoustic or elastic wavelengths. This is even the case in regions where the environment is homogeneous and the field therefore is described by a simple wave equation. Further, as these methods do not directly allow for prescribed radiation conditions on the boundary, the computational domain must be made sufficiently large to eliminate artificial reflections within the time period of interest. For the same reason these discrete methods are not particularly well-suited for narrow-band or CW problems. As described earlier, the artificial reflection can be reduced by adding artificial attenuation close to the boundary of the computational domain. However, attenuation discontinuities produce reflections as well, and therefore the artificial attenuation must increase gradually toward the boundary. This method therefore still requires a computational grid which, in some cases, may be relatively large compared to the environmental feature of interest.

Many scattering and reverberation problems occurring in ocean acoustics are characterized by the limited extent of the scattering feature. This is the case, for example, in relation to the analysis of ice keel scattering or reverberation from bottom features such as faults, diapirs, or small sea mounts. In such cases, the major part of the propagation and reverberation takes place in an environment which is easily treated by one of the traditional methods. For example, a range-independent acoustic model is well-suited to describe Arctic propagation, except for the scattering introduced by discrete keel structures.

For such problems we can instead use a discretization of Green's theorem expressing the field in a volume in terms of an integral of the field and its derivative on the boundary. Thus, a real or artificial boundary separating an *interior* region from an *exterior* region is defined in such a way that the boundary integral can be used. The interior region includes the scatterer which is treated by either a boundary integral method or another discrete method, depending on the complexity. The advantage of such an approach is that only the boundary of the exterior domain needs to be discretized since the boundary integral formulation inherently satisfies the wave equation throughout the volume as well as the radiation conditions at infinity. As we shall see, this approach can, therefore, also be applied to provide radiation conditions on the boundary of the finite computational domain of the other discrete numerical methods.

The boundary integral method has been used extensively for solving scattering problems associated with objects in infinite media, but it is equally applicable to scattering from objects of finite extent in the ocean waveguide. Thus, Schuster and Smith [41] combined a wavenumber-integration approach for a stratified fluid medium with a boundary-integral formulation to model scattering from inclusions in the seabed. A similar approach was used by Kawase [42] to determine the earthquake response of semi-circular canyons in an elastic halfspace. Dawson and Fawcett [43] used a boundary-integral formulation to model scattering from a rough sea surface or bottom with ideal boundary conditions. Gerstoft and Schmidt [44] generalized this hybrid approach to model seismo-acoustic scattering and reverberation from penetrable inclusions in a stratified elastic bottom and from elastic ice covers.

### 7.5.2 The Boundary-Integral Equation

Consider the problem of acoustic propagation in a volume  $V$  of infinite extent, but including a *scatterer* bounded by the surface  $S$  along which the boundary conditions are known. This problem, illustrated in Fig. 7.11, is a special case of the general problem of propagation in bounded media described in Sect. 2.3.3. Here, it was shown that the displacement field of time dependence  $\exp(-i\omega t)$  is given by *Green's theorem*,

$$\psi(\mathbf{r}) = \int_S \left[ G_\omega(\mathbf{r}, \mathbf{r}') \frac{\partial \psi(\mathbf{r}')}{\partial \mathbf{n}'} - \psi(\mathbf{r}') \frac{\partial G_\omega(\mathbf{r}, \mathbf{r}')}{\partial \mathbf{n}'} \right] dS' - \int_V f(\mathbf{r}') G_\omega(\mathbf{r}, \mathbf{r}') dV', \quad (7.132)$$

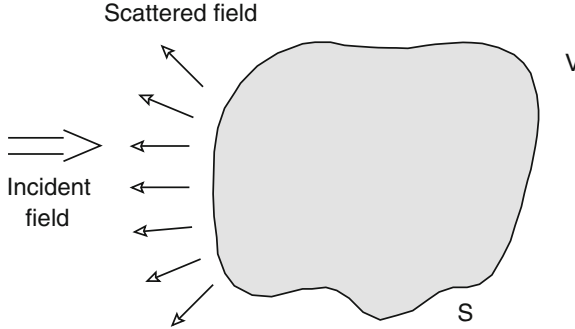


**Fig. 7.11** Volume  $V$  of infinite extent, bounded by an internal boundary  $S$

where  $\mathbf{n}'$  is the outward pointing normal on the surface  $S$ , and with the prime denoting the integration variables. Thus,  $\mathbf{r}'$  is a point on the boundary in the surface integral, whereas it represents all points in the volume in the second integral. Equation (7.132) states that the field throughout the volume  $V$  is totally determined by the volume sources within the volume, and the field and its derivative on the boundary  $S$ . The *Green's functions*  $G_\omega(\mathbf{r}, \mathbf{r}')$  are arbitrary as long as they satisfy the wave equation and boundary and radiation conditions, *except* those existing on  $S$ .

As described in Sect. 2.3.4, for some simple boundary geometries and conditions, the Green's functions can be chosen such that they also satisfy the boundary conditions on  $S$ , in turn eliminating the surface integral. In that case, (7.132) simply represents the superposition of the field produced by all volume sources. However, for general boundary conditions, the field and its derivative must be determined before (7.132) can be applied. In addition, a valid Green's function must obviously be known.

By letting the field points  $\mathbf{r}$  in (7.132) approach the boundary  $S$ , the *boundary integral equation* is obtained for the field and its derivative as

$$\begin{aligned} \psi(\mathbf{r}'') - \int_S \left[ G_\omega(\mathbf{r}'', \mathbf{r}') \frac{\partial \psi(\mathbf{r}')}{\partial \mathbf{n}'} - \psi(\mathbf{r}') \frac{\partial G_\omega(\mathbf{r}'', \mathbf{r}')}{\partial \mathbf{n}'} \right] dS' \\ + \int_V f(\mathbf{r}') G_\omega(\mathbf{r}'', \mathbf{r}') dV' = 0, \end{aligned} \quad (7.133)$$

where  $\mathbf{r}''$  is now also a point on the boundary  $S$ . This equation is a *Fredholm integral equation* of the second kind [20]. The numerical solution of (7.133) must properly account for the singular nature of the kernels of the surface integral. Thus, the singularity of the Green's function  $G_\omega(\mathbf{r}'', \mathbf{r}')$  is integrable, but the normal derivative is not. However, as we will see below, the finite element solution inherently eliminates this numerical singularity.

An additional equation is provided by the boundary conditions. If these are *natural*, then the boundary condition can be expressed as

$$\frac{\partial \psi(\mathbf{r}')}{\partial \mathbf{n}'} - \eta(\mathbf{r}') [\psi(\mathbf{r}') - \psi_S(\mathbf{r}')] = 0. \quad (7.134)$$

We can now use (7.134) to eliminate one of the unknown field properties in the boundary integral equation (7.133). Since  $\psi$  represents a displacement potential, the case of  $\eta = 0$  represents the perfectly rigid boundary, with the boundary integral equation becoming

$$\psi(\mathbf{r}'') + \int_S \psi(\mathbf{r}') \frac{\partial G_\omega(\mathbf{r}'', \mathbf{r}')}{\partial \mathbf{n}'} dS' + \int_V f(\mathbf{r}') G_\omega(\mathbf{r}'', \mathbf{r}') dV' = 0. \quad (7.135)$$

Similarly,  $\eta = \infty$ ,  $\psi_S = 0$ , represents the pressure-release boundary where the potential must vanish, and in this case the integral equation takes the form,

$$-\int_S G_\omega(\mathbf{r}'', \mathbf{r}') \frac{\partial \psi(\mathbf{r}')}{\partial \mathbf{n}'} dS' + \int_V f(\mathbf{r}') G_\omega(\mathbf{r}'', \mathbf{r}') dV' = 0. \quad (7.136)$$

A critical point in using Green's theorem is the availability of valid Green's functions. However, many problems occurring in ocean acoustics have known Green's functions, but complex boundary geometry. An example is the scattering by objects in infinite media where the Green's function for an infinite medium, (2.52), can be applied. Here the boundary integral forms the mathematical basis for the T-matrix approach commonly used for object scattering problems. Another example is that of waveguides with objects or localized boundary irregularities. For such problems the Green's functions can be determined efficiently either analytically for ideal waveguides or numerically using one of the approaches described earlier for the more general waveguide environments. However, except for a few trivial cases with simple boundary geometry, the boundary integral equation must be solved numerically. In the following, we describe a finite-element approximation to (7.133), a method usually called the BEM.

### 7.5.3 Boundary-Element Equations

In Sect. 7.3, we described the finite-element approximation to linear differential equations, but this method is also applicable to linear integral equations such as (7.133). We will, therefore, seek approximations to the field and its derivative on the boundary in the forms

$$\psi(\mathbf{r}'') = \sum_{n=1}^N N_n(\mathbf{r}'') a_n = \mathbf{N} \mathbf{a} \quad (7.137)$$

and

$$\frac{\partial \psi(\mathbf{r}'')}{\partial \mathbf{n}'} = \sum_{n=1}^N N_n(\mathbf{r}'') b_n = \mathbf{N} \mathbf{b}. \quad (7.138)$$

Inserting these approximations into (7.133), and multiplying by a set of weight functions  $g_m(\mathbf{r}'')$ ,  $m = 1, \dots, N$ , followed by integration over the surface coordinate  $\mathbf{r}''$ , we obtain the matrix equation for the expansion coefficients,

$$\mathbf{G}\mathbf{a} - \mathbf{H}\mathbf{b} + \mathbf{h} = 0 \quad (7.139)$$

with the coefficients given by

$$G_{ij} = \int_S \int_S g_i(\mathbf{r}'') \frac{\partial G_\omega(\mathbf{r}'', \mathbf{r}')}{\partial \mathbf{n}'} N_j(\mathbf{r}') dS' dS'' + \int_S g_i(\mathbf{r}'') N_j(\mathbf{r}'') dS, \quad (7.140)$$

$$H_{ij} = \int_S \int_S g_i(\mathbf{r}'') G_\omega(\mathbf{r}'', \mathbf{r}') N_j(\mathbf{r}') dS' dS'', \quad (7.141)$$

$$h_i = \int_S \int_V g_i(\mathbf{r}') f(\mathbf{r}') G_\omega(\mathbf{r}'', \mathbf{r}') dV' dS''. \quad (7.142)$$

Note here that the singularity of the surface integral of the derivative of the Green's function in (7.133) is eliminated by the second surface integral introduced by the weighted residual formulation. Thus, for smooth weight functions  $g_i(\mathbf{r}'')$ , the double integral in (7.140) is finite. On the other hand, if collocation weights are used, the elimination of one of the integrals should be associated with explicit treatment of the contribution from the singularity of the Green's function derivative through a limiting process [44]. The details are beyond the scope of this book, but the result is simply a factor 1/2 applied to the second term in (7.140).

An additional set of discrete equations is obtained from the boundary conditions. Inserting the expansions in (7.137) and (7.138) into (7.134), the residual integral yields the matrix equations

$$\widehat{\mathbf{G}}\mathbf{a} + \widehat{\mathbf{H}}\mathbf{b} + \widehat{\mathbf{h}} = 0 \quad (7.143)$$

with the coefficient matrices given by

$$\widehat{G}_{ij} = - \int_S g_i(\mathbf{r}'') \eta(\mathbf{r}'') N_j(\mathbf{r}'') dS'', \quad (7.144)$$

$$\widehat{H}_{ij} = \int_S g_i(\mathbf{r}'') N_j(\mathbf{r}'') dS'', \quad (7.145)$$

$$\widehat{h}_i = \int_S g_i(\mathbf{r}'') \eta(\mathbf{r}'') \psi_S(\mathbf{r}'') dS''. \quad (7.146)$$

Solution of (7.143) for  $\mathbf{b}$  yields

$$\mathbf{b} = -\hat{\mathbf{H}}^{-1} [\hat{\mathbf{G}} \mathbf{a} + \hat{\mathbf{h}}], \quad (7.147)$$

which inserted into (7.139) gives

$$[\mathbf{G} + \mathbf{H}\hat{\mathbf{H}}^{-1}\hat{\mathbf{G}}] \mathbf{a} + [\mathbf{h} + \mathbf{H}\hat{\mathbf{H}}^{-1}\hat{\mathbf{h}}] = 0. \quad (7.148)$$

We can now solve (7.148) for  $\mathbf{a}$ , with  $\mathbf{b}$  following from (7.147). Then, the approximation to the field can be found anywhere in the volume by inserting the resulting boundary expansions into (7.132) to yield

$$\psi(\mathbf{r}) = \int_S \left[ G_\omega(\mathbf{r}, \mathbf{r}') \mathbf{N} \mathbf{b} - \frac{\partial G_\omega(\mathbf{r}, \mathbf{r}')}{\partial \mathbf{n}'} \mathbf{N} \mathbf{a} \right] dS' - \int_V f(\mathbf{r}') G_\omega(\mathbf{r}, \mathbf{r}') dV'. \quad (7.149)$$

For problems with simple homogeneous boundary conditions, such as scattering from rigid inclusions or empty cavities, the solution can obviously be simplified by directly eliminating one of the terms in the kernel of the integral equation (7.133). However, these special cases are directly represented by the full matrix equations. Thus, for the rigid inclusion with  $\eta(\mathbf{r}'') \equiv 0$ , we have  $\hat{\mathbf{G}} = \mathbf{0}$  and  $\hat{\mathbf{h}} = \mathbf{0}$ , and half of the terms in (7.148) vanish. The general formulation given here is applicable to problems with mixed or non-homogeneous, natural boundary conditions of the form given in (7.134). However, as demonstrated Sect. 7.5.4, it also applies to the much more general coupled problems governed by boundary conditions which are not natural.

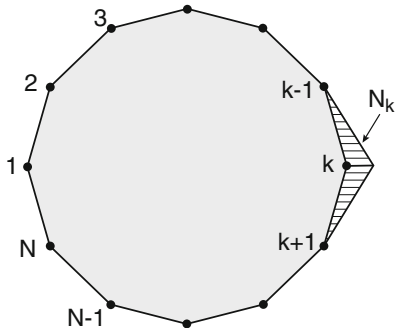
### 7.5.3.1 Trial and Weight Functions

As was the case for the finite-element method, the discretization of the boundary integral equation can be based on *global* as well as *local* trial functions. The global trial functions are convenient for relatively simple boundary geometries and continuously varying boundary conditions. The global trial functions are therefore used for scattering from cylinders, spheres etc., and this is the approach taken in the so-called T-matrix approach to object scattering.

As for FEM, local trial functions or *boundary elements* are of much more general applicability. A simple boundary-element discretization for a two-dimensional scattering problem is shown in Fig. 7.12. The boundary is divided into a number of *elements*, connected in an equal number of *nodes*. The trial functions are chosen to be linear interpolation functions in elements  $k$  and  $k + 1$ , with the degrees-of-freedom being the displacement potential and its normal derivative in the connecting node  $k$ , i.e., the expansion coefficients  $a_k$  and  $b_k$  in (7.137) and (7.138).

The weight functions  $g_n$  can again be chosen as either *collocation* weights,  $g_n = \delta(\mathbf{x} - \mathbf{x}_n)$  with  $\mathbf{x}_n$  being the node coordinates, or as *Galerkin* weights,

**Fig. 7.12** Boundary-element discretization with nodal values of the field as the degrees-of-freedom and trial functions in terms of linear interpolation functions



$g_n = N_n(\mathbf{x})$ . As was the case for FEM, the Galerkin weights yield symmetric matrices, which may improve accuracy. On the other hand the use of collocation eliminates the outer surface integrals in (7.140)–(7.142), and is therefore often more efficient numerically.

The size of the boundary elements depends on both the acoustic wavelength and the boundary geometry. Thus, since the field curvature is ignored for the linear elements, the number of elements should be of the order of ten per wavelength. In addition, the linear elements must accurately represent the curvature of the boundary. Higher-order elements as well as curved elements could be used, but for simplicity, the linear elements are the most common.

We have here derived the boundary-element formulation for an acoustic medium. A similar integral equation and associated boundary-element solutions can be derived for elastic scattering problems, and such an approach has for instance been applied to scattering and contact problems using *global*, orthogonal trial functions [45, 46].

### 7.5.4 Coupled Domains

In many scattering problems occurring in ocean acoustics, the boundary of the scatterer cannot be described by *natural* boundary conditions of the form given in (7.134) where the coefficients  $\eta(\mathbf{r}'')$  are functions of position only. In cases where the interior of the scatterer can itself contain a field (penetrable scatterer), the boundary conditions for the exterior field become dependent not only on the position on the boundary, but also on the field inside the scatterer. In such cases, we have to solve the total scattering problem as a *coupled problem*.

#### 7.5.4.1 Interior Boundary-Element Solution

For some scattering problems, e.g., those involving spatial inhomogeneities of the acoustic medium such as inclusions in a fluid bottom, the field in the interior of the scatterer is conveniently found using the boundary integral equation. In analogy to

the above, the boundary expansion coefficients  $\bar{\mathbf{a}}$  and  $\bar{\mathbf{b}}$  for the field and its normal derivative on the surface of the interior domain must satisfy a matrix equation of the form

$$\bar{\mathbf{G}}\bar{\mathbf{a}} - \bar{\mathbf{H}}\bar{\mathbf{b}} + \bar{\mathbf{h}} = 0. \quad (7.150)$$

On the surface  $S$  separating the two domains, the normal displacement must be continuous. The normal surface displacement for the exterior domain is given by

$$u_n = \frac{\partial \psi}{\partial \mathbf{n}}, \quad (7.151)$$

where the normal  $\mathbf{n}$  points away from the volume and therefore into the scatterer. Similarly, the normal surface displacement for the interior domain is

$$\bar{u}_n = \frac{\partial \bar{\psi}}{\partial \bar{\mathbf{n}}}, \quad (7.152)$$

where the surface normal  $\bar{\mathbf{n}}$  is pointing outward. Therefore, since  $\bar{\mathbf{n}} = -\mathbf{n}$ , the displacement boundary condition is

$$\frac{\partial \bar{\psi}}{\partial \bar{\mathbf{n}}} = -\frac{\partial \psi}{\partial \mathbf{n}} \quad \text{on } S. \quad (7.153)$$

In addition, the pressure  $p = -\rho \omega^2 \psi$  must be continuous, i.e.,

$$\bar{\rho} \bar{\psi} = \rho \psi \quad \text{on } S. \quad (7.154)$$

If the trial functions are chosen to be identical for the exterior and interior problems, then these boundary conditions require the expansion coefficients for the two solutions to satisfy the conditions

$$\bar{\mathbf{a}} = \frac{\rho}{\bar{\rho}} \mathbf{a}, \quad (7.155)$$

$$\bar{\mathbf{b}} = -\mathbf{b}. \quad (7.156)$$

The matrix equations for the interior can therefore be rewritten as

$$\frac{\rho}{\bar{\rho}} \bar{\mathbf{G}}\bar{\mathbf{a}} + \bar{\mathbf{H}}\bar{\mathbf{b}} + \bar{\mathbf{h}} = 0. \quad (7.157)$$

This equation is clearly of a form identical to that of the matrix equation corresponding to the *natural* boundary conditions, (7.143), and the expansion coefficients are again determined from (7.148) and (7.147), with

$$\widehat{\mathbf{G}} = \frac{\rho}{\bar{\rho}} \bar{\mathbf{G}}, \quad (7.158)$$

$$\widehat{\mathbf{H}} = \bar{\mathbf{H}}, \quad (7.159)$$

$$\widehat{\mathbf{h}} = \bar{\mathbf{h}}. \quad (7.160)$$

### 7.5.4.2 Interior Finite-Element Solution

For problems where the nature of the interior domain is such that the Green's functions are not easily obtainable, it must be treated by another numerical method. Here, the close similarity between the boundary-element and the finite-element methods makes it straightforward to combine a BEM formulation for the exterior with an FEM formulation for the interior, or vice versa. An example of such a hybrid discretization is shown in Fig. 7.13.

Assume the interior domain is a fluid medium, for which an approximate solution is determined from the FEM equations (7.67), which for steady-state solutions of time dependence  $\exp(-i\omega t)$  take the form

$$\mathbf{K}\mathbf{p} + \mathbf{f} = 0 \quad (7.161)$$

with  $\mathbf{K}$  being the complex coefficient matrix,

$$\mathbf{K} = [-\omega^2 \mathbf{C} - i\omega \mathbf{D} + \mathbf{E}]. \quad (7.162)$$

The coefficient matrices are obtained from the element matrices through the mappings defined by (7.97)–(7.100), with the element matrices determined by (7.101)–(7.104).

To be consistent with the finite-element representation for the interior domain, the boundary-element equations (7.139) are formulated in terms of nodal pressures  $\mathbf{p}$ , simply by multiplication by the ratio  $\rho\omega^2$  between the pressure and the displacement potential, i.e.,

$$\mathbf{G}\mathbf{p} - \rho\omega^2 [\mathbf{H}\mathbf{b} - \mathbf{h}] = 0. \quad (7.163)$$

It is clear from (7.64) to (7.66), together with (2.11), that the surface contributions to the finite-element matrices in (7.161) represent the acceleration flux into the elements, concentrated in the element nodes. We, therefore, introduce the equivalent

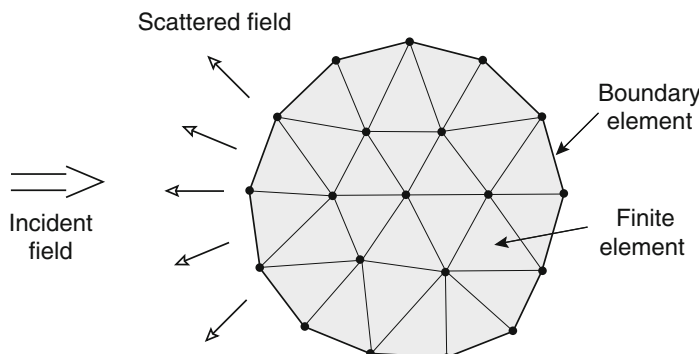


**Fig. 7.13** Coupled problem where the exterior domain is treated by BEM and the interior treated by FEM

node acceleration vector  $\mathbf{q}$  for the external domain, representing the acceleration flux into the exterior domain. Since  $\mathbf{b}$  in (7.139) represents the displacement flux out of the domain, we have  $\mathbf{q} = -(-\omega^2 \mathbf{b}) = \omega^2 \mathbf{b}$ , which inserted in (7.163) yields

$$\mathbf{q} = \omega^2 \mathbf{b} = \rho^{-1} \mathbf{H}^{-1} [\mathbf{G} \mathbf{p} + \rho \omega^2 \mathbf{h}]. \quad (7.164)$$

If we select the BEM discretization for the exterior domain such that the nodes coincide with the boundary nodes of the interior FEM discretization, we can then simply consider the exterior domain a special *infinite* element with the element matrix and forcing terms obtained from (7.164) as

$$\mathbf{K}^{M+1} = \rho^{-1} \mathbf{H}^{-1} \mathbf{G}, \quad (7.165)$$

$$\mathbf{f}^{M+1} = \omega^2 \mathbf{H}^{-1} \mathbf{h}. \quad (7.166)$$

The contribution from the infinite element is then included in the global finite-element equations by properly defining the topology mapping and incorporating it in the summations of (7.99) and (7.100).

The coupling of finite-element and boundary-element methods is particularly important for numerical solution of the Helmholtz equation for infinite domains with radiation conditions. As described earlier, an alternative approach is to use a pure finite element formulation over a finite-size domain by introducing artificial attenuation at the boundary or the related PML approach. However, by using the hybrid BEM–FEM formulation we basically introduce radiation boundary conditions into the boundary of the finite-element domain, thereby minimizing the required size of the discretized domain, and in principle also eliminating artificial boundary reflections.

Another important application is the modeling of scattering from complex elastic structures such as submersibles, where the interior domain is so complex that only FEM is applicable for a proper description. The coupling of the infinite fluid element with an internal elastic FEM formulation is performed using the procedure described in Sect. 7.4.5. Due to the vastly different length scales of the local scattering problem and the ocean waveguide propagation, for such problems a hybrid approach is an attractive alternative. These approaches use one of the classical methods described in the previous chapters for the propagation to and from the object, and then use a finite-element solution for the scattering problem.

While the boundary-element formulation for the external domain is formally consistent with the internal finite-element formulation, it is computationally intensive due to the large number of degrees-of-freedom for the combined problem. A computationally efficient alternative, which allows total decoupling of the internal and external solutions, is the Virtual Source Concept (VSC) described in the next section. Here, the target is represented by a “stiffness” or “impedance” matrix, allowing the scattering problem to be entirely solved through an efficient superposition principle approximation to the external surface integral.

### 7.5.5 Virtual Source Concept

The VSC is an approximate method for solving the integral equation for target scattering. It is based on the classical wavefield superposition approach and is applicable to targets of arbitrary shape and composition. As such, it is a generalization of the so-called internal source density method used by Stepanishen [47] and Sarkissian [48] to model 3-D scattering from objects of revolution with Dirichlet or Neumann boundary conditions in an infinite, homogeneous fluid. The virtual source approach provides an efficient approximation to the solution of the external integral equation problem for scattering from objects with complex boundary geometry and internal structure. The major advantage is its inherent independence of the external environment, with just a point-source Green's function being required. All the legacy acoustic propagation models can provide this information, and hence this method can be directly applied to scattering from objects in ocean waveguides. For example, Kessel [49] used an internal multipole expansion method in combination with a modal Green's function to model the scattering from objects in horizontally stratified waveguides using ideal, homogeneous boundary conditions. However, the method is easily generalized to the more complex boundary conditions associated with scattering from realistic objects in the ocean. In cases where the target scattering function can be represented by a single multipole expansion, such as is the case for spheres, where exact scattering functions can be expressed analytically in terms of spherical harmonics, Kessel's method becomes identical to the classical approach of Ingenito [50].

The virtual source approach, described in the following, involves three steps [51]. First, the incident field at the fully or partially buried target position in a stratified fluid–elastic waveguide is computed using standard wavenumber integration, as described in Chap. 4. The scattered field is then represented by removing the target and replacing it by a distribution of virtual sources inside the volume occupied by the target. After superimposing the incident field with the virtual source field, the virtual source strengths are determined by satisfying the boundary conditions on the surface of the target. The boundary conditions for any elastic target may be expressed in terms of the dynamic stiffness matrix, expressing the unique relationship between the surface pressure and the normal displacement. As opposed to other coupling approaches, such as the “scattering chamber” approach, the replacement of the target by its unique stiffness matrix does not require the treatment of the outer medium in the target model. Therefore, once the dynamic stiffness matrix for the target is determined, it can be used for arbitrary orientation and burial of the target. This characteristic of the approach facilitates the investigation of the sensitivity of the scattered field to parameters such as seabed properties, burial depth, and insonification geometry.

The extension of Stepanishen's [47] and Kessel's [49] methods to handle general elastic objects with full 3-D geometry is relatively straightforward, requiring only a frequency-dependent stiffness matrix, associated with the target's internal structure and composition. In addition, it can be generalized to problems where the target penetrates interfaces in a horizontally stratified environment. It, therefore, provides

a versatile numerical method for the analysis of scattering from partially and fully buried targets. Furthermore, it takes into account multiple scattering effects within the target, as well as between the target and the environmental stratification as further investigated in [52].

The modeling of the target stiffness matrix is flexible and can be done using any target-appropriate approach: a so-called “reverse” virtual source approach can be applied for homogeneous fluid objects, exact spherical harmonics representation can be used for spherical shells, or a more general numerical method such as Finite Elements can be used for other objects. A major benefit of such a hybrid VSC/FE approach is the fact that the object stiffness matrix is totally independent of the surrounding medium, and steady-state solutions can, therefore, be obtained without the complicating external radiation conditions.

The wavefield superposition principle is illustrated in Fig. 7.14. An arbitrarily-shaped object in a stratified ocean is partially buried in the seabed. The stratification can include fluid as well as elastic layers, but it is here for simplicity assumed that the layers containing the target are isovelocity fluid media. The actual target is removed and replaced by a continuously stratified medium with a discrete distribution of  $N$  simple point sources of unknown, complex strengths, which are represented by a dotted line vector  $\mathbf{s}$ . This source distribution is assumed to generate a field which is identical to the scattering produced by the target. Thus, if the surface of the target is discretized in  $N$  nodes, the total pressure  $\mathbf{p}$  and normal displacement  $\mathbf{u}$  are decomposed into the known incident field contribution  $\mathbf{p}_i$ ,  $\mathbf{u}_i$  and the scattered field  $\mathbf{p}_s$ ,  $\mathbf{u}_s$ ,

$$\mathbf{p} = \mathbf{p}_i + \mathbf{p}_s, \quad \mathbf{u} = \mathbf{u}_i + \mathbf{u}_s. \quad (7.167)$$

The scattered field is generated by the virtual source distribution  $\mathbf{s}$ ,

$$\mathbf{p}_s = \mathbf{Ps}, \quad \mathbf{u}_s = \mathbf{Us} \quad (7.168)$$

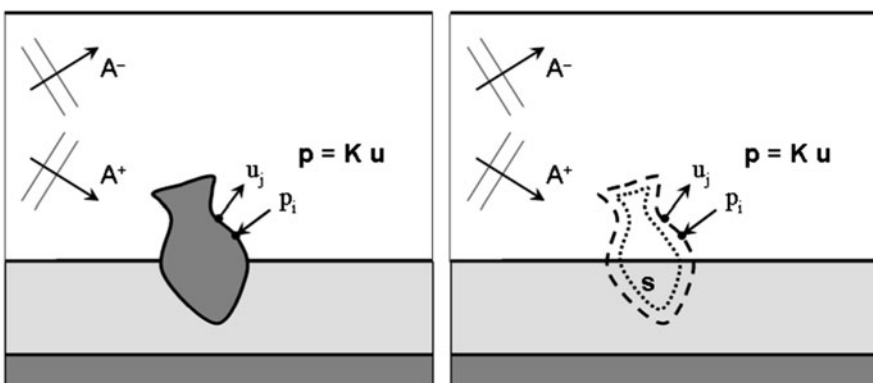


**Fig. 7.14** Virtual source approach to scattering from a partially buried target in a stratified ocean waveguide. The target is replaced by an internal, virtual source distribution generating a field in the background environment which, superimposed with the incident field, satisfies the boundary condition  $\mathbf{p} = \mathbf{Ku}$ , representing the target’s dynamic stiffness properties

with  $\mathbf{P}$  and  $\mathbf{U}$  representing  $N \times N$  matrices containing the pressure and normal displacement Green's functions, respectively, between  $N$  virtual sources and  $N$  surface nodes.

The superimposed field on the virtual target surface must satisfy the boundary conditions associated with the real target. Thus, the field inside the true target must satisfy Green's theorem, providing a unique relation between the pressure and normal displacement on the surface. In a discrete representation with  $N$  surface nodes, this relation can be expressed in terms of a dynamic, frequency-dependent stiffness matrix  $\mathbf{K}$ ,

$$\mathbf{p} = \mathbf{Ku}. \quad (7.169)$$

Combining (7.167)–(7.169) leads to the following matrix representation for the virtual source strengths:

$$\mathbf{s} = [\mathbf{P} - \mathbf{KU}]^{-1} [\mathbf{Ku}_i - \mathbf{p}_i]. \quad (7.170)$$

Once the virtual source strengths are found from (7.170), the scattered field is obtained anywhere in the external medium by superposition, using the continuous-medium Green's function, in this case the stratified ocean waveguide.

The virtual source method may also be used for solving problems involving scatter at rough boundaries as discussed by Fawcett [53] and Abawi and Porter [54].

### 7.5.5.1 Green's Functions

The Green's function for a stratified ocean is required for both the incident field, the external boundary influence matrices, and the final computation of the scattered field. Any of the classical waveguide modeling approaches may be applied to compute the incident and scattered fields. However, for an accurate evaluation of the boundary influence matrices, we require a technique which is valid in the immediate vicinity of the source and for all propagation angles. Here, we apply the exact Fourier–Bessel wavenumber integration formulation for stratified waveguides [55]. Thus, the field produced by a horizontal distribution of sources can be expressed in an azimuthal Fourier series of the displacement potential  $\phi(\mathbf{r}) = \phi(r, \varphi, z)$ ,

$$\phi(r, \varphi, z) = \phi_S + \phi_H = \sum_{m=0}^{\infty} \left[ \phi_S^m(r, z) + \phi_H^m(r, z) \right] \begin{Bmatrix} \cos(m\varphi) \\ \sin(m\varphi) \end{Bmatrix}, \quad (7.171)$$

where  $\phi_S^m(r, z)$  and  $\phi_H^m(r, z)$  are Fourier coefficients for the direct source contribution and the field produced by the boundary interactions, respectively. Both components are represented in terms of horizontal wavenumber integrals,

$$\phi_S^m(r, \varphi, z) = \frac{\epsilon_m}{4\pi} \int_0^\infty \left[ \sum_{j=1}^N s_j \begin{Bmatrix} \cos(m\varphi_j) \\ \sin(m\varphi_j) \end{Bmatrix} J_m(k_r r_j) \frac{e^{ik_r |z-z_j|}}{ik_z} \right] k_r J_m(k_r r) dk_r, \quad (7.172)$$

$$\phi_H^m(r, \varphi, z) = \int_0^\infty \left[ A_m^+(k_r) e^{ik_z z} + A_m^-(k_r) e^{-ik_z z} \right] k_r J_m(k_r r) dk_r, \quad (7.173)$$

where  $k_r, k_z$  are the horizontal and vertical numbers,  $s_j$  is the complex source strength of source  $j$  at  $(r_j, \varphi_j, z_j)$ , and  $A_m^+(k_r)$  and  $A_m^-(k_r)$  are the complex azimuthal Fourier coefficients of the up- and downgoing wavefield amplitudes produced by the multiple boundary interactions. They are found by matching the boundary conditions at all horizontal interfaces.  $\epsilon_m$  is a factor which is 1 for  $m = 0$  and 2 otherwise.

Considering only the multiple scattering between the target and the seabed, all that is needed for generating the Green's function matrices in (7.170) is the two-halfspace Green's function, which for the virtual source and receiver both being in the water column above the seabed becomes

$$G_\omega(\mathbf{r}_i, \mathbf{r}_j) = s_j \frac{e^{ik_1 |\mathbf{r}_i - \mathbf{r}_j|}}{4\pi |\mathbf{r}_i - \mathbf{r}_j|} + s_j \sum_{m=0}^{\infty} \left\{ \begin{array}{l} \cos(m\varphi_i) \cos(m\varphi_j) \\ \sin(m\varphi_i) \sin(m\varphi_j) \end{array} \right\} \times \frac{\epsilon_m}{4\pi} \int_0^\infty \left[ J_m(k_r r_j) \mathcal{R}_{11}(k_r) \frac{e^{ik_{z;1}(z_I - z_j - z_i)}}{ik_{z;1}} \right] k_r J_m(k_r r_i) dk_r, \quad (7.174)$$

where  $\mathcal{R}_{11}$  is the plane-wave reflection coefficient for the seabed. Similarly, for the virtual receiver in the seabed, the Fourier–Bessel integral representation for the Green's function is

$$G_\omega(\mathbf{r}_i, \mathbf{r}_j) = s_j \sum_{m=0}^{\infty} \left\{ \begin{array}{l} \cos(m\varphi_i) \cos(m\varphi_j) \\ \sin(m\varphi_i) \sin(m\varphi_j) \end{array} \right\} \times \frac{\epsilon_m}{4\pi} \int_0^\infty \left[ J_m(k_r r_j) \mathcal{T}_{12}(k_r) \frac{e^{i[k_{z;1}(z_I - z_j) + k_{z;2}(z_i - z_I)]}}{ik_{z;1}} \right] k_r J_m(k_r r_i) dk_r \quad (7.175)$$

with  $\mathcal{T}_{12}(k_r)$  being the transmission coefficient at horizontal wavenumber  $k_r$ .

### 7.5.5.2 Numerical Implementation Issues

Although the virtual source approach in principle is exact, the numerical stability of the solution is dependent on the virtual source distribution being such that it produces linearly independent Green's function distributions over the surface nodes. In that regard, it has been found empirically that a consistent convergence is achieved by distributing the surface nodes with a separation which is proportional to the local radii of curvature, and by placing a virtual source along the inward normal at each node, at a depth of approximately 0.6 times the node separation. This seems to provide the optimal compromise between diagonal dominance of the matrix to be inverted in (7.170) and efficient use of the dynamic range.

The numerical convergence of the virtual-source scattering model has been validated by comparisons to exact spherical-harmonic solutions for spherical shells [56], and by comparison to full finite-element solutions for general shapes [51].

The computationally most intensive component of the VSC approach is the evaluation of the  $N \times N$  pressure and displacement Green's function matrices  $\mathbf{P}$  and  $\mathbf{U}$  in (7.170) through the Fourier–Bessel representations in (7.174)–(7.175). Here, it is important to take advantage of any target symmetries and variables of limited dimension. Thus, e.g., for targets with vertical axisymmetry, the virtual sources and surface nodes are naturally placed in “rings” at constant depth, thus strongly reducing the number of required values of Bessel functions. Other computational gains can be achieved by careful use of numerical devices such as pre-computed tabulations of the exponential and Bessel functions, pre-computing the wavenumber functions, etc. Further gains are achieved by embedding the virtual source geometry within the integration kernels. In other words, instead of evaluating the spectral integrals for each source–receiver combination, the integral is performed simultaneously for all identical source–receiver combinations, leading to a reduction in computation from  $O(N^2)$  to  $O(N)$ , with  $N$  being the number of the virtual sources and surface nodes.

Another key to the convergence and efficiency is the adherence to all the standard sampling guidelines for wavenumber integration described in Chap. 4, including the use of complex integration contours.

Once the virtual source strengths have been determined, the total scattered field is computed as a superposition of the fields produced by all the virtual sources representing the target. Here, one can use the full 3-D spectral representation described in Sect. 7.5.5. However, if multiple reflections from the sea surface or deeper seabed interfaces can be ignored, a more efficient approximation based on the stationary evaluation of the spectral integrals can be applied, as described by Zampolli et al. [57].

## 7.6 Numerical Examples

We illustrate here the use of the discrete numerical methods for scattering problems which cannot be handled by any of the traditional methods described in the earlier chapters.

### 7.6.1 Scattering by Arctic Ice Features

As shown in Chap. 4, bottom elasticity plays an important role in relation to low-frequency propagation in shallow water. In the Arctic, the elasticity of the ice cover is equally important as illustrated in the examples given in Sect. 4.10.4. Although the plane-parallel model of the ice cover allows for analysis of the basic physics of

the ice interaction in relation to forward propagation problems, this model is highly unrealistic for scattering and reverberation problems. Thus, the Arctic ice cover is characterized by strong scattering features such as ridges, keels, floes, leads, etc. Since none of the traditional models treat two-way propagation in range-dependent elastic media, such ice-scattering problems can only be addressed using one of the discrete methods described above.

We illustrate here the use of a finite-difference model and a boundary-element model to predict the scattering by an ice floe and an ice keel. We use the idealized models shown in Fig. 7.15 and address the effect of properly including ice elasticity in the analysis.

The acoustic field is generated by a line source at 15-m depth in an infinitely deep ocean with constant sound speed of 1430 m/s. In Fig. 7.15a, a semi-cylindrical ice floe of 6-m radius is centered at a horizontal range of 85.5 m. In the second example, shown in Fig. 7.15b, the same ice volume is attached to an infinite ice plate of 3-m thickness to represent a semi-cylindrical ice keel.

A finite-difference model has been used to model the broadband scattering produced by the ice floe in Fig. 7.15a. The source pulse is assumed to be a Ricker wavelet, i.e., a pulse shape corresponding to the second derivative of a Gaussian pulse. The wavelet has a center frequency of 50 Hz and significant energy between

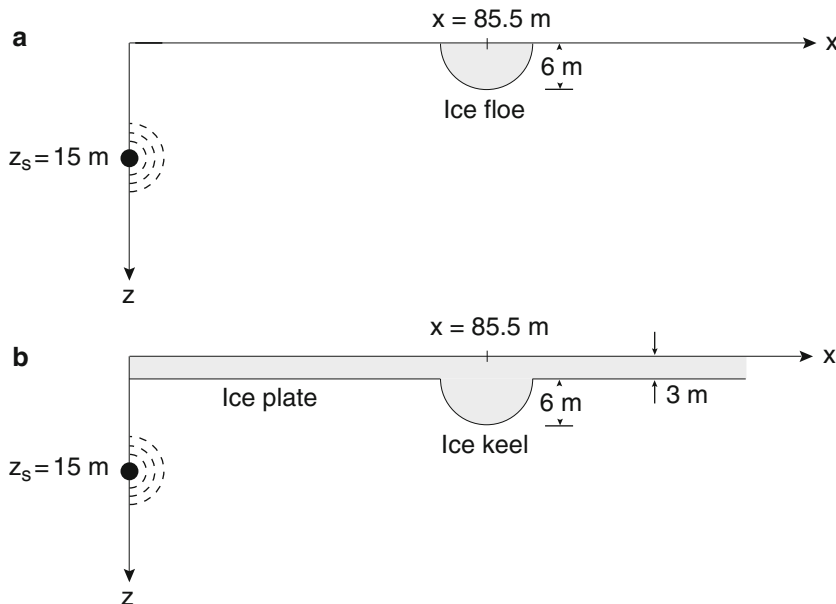


**Fig. 7.15** Environmental models used for numerical ice scattering experiments. The acoustic field is generated by a wideband line source at depth 15 m. (a) A half-cylindrical ice floe floating at range 85.5 m on an infinite halfspace of water. (b) A water halfspace is covered by a 3-m thick ice sheet with compressional speed 3500 m/s and shear speed 1600 m/s. A half-cylindrical ice keel with radius 6 m is centered at range 85.5 m

0 and 125 Hz. Two different ice models were considered: The first represents an old ice floe as an elastic medium with compressional speed 3500 m/s and shear speed 1600 m/s; the second is a young ice floe consisting of smaller chunks of ice suspended in water and represented by a fluid medium with compressional speed 3500 m/s.

### 7.6.1.1 Finite-Difference Solution

Figure 7.16a and b show contours of the scattered field for the elastic and fluid floes, respectively. The snapshots represent the field 55 ms after the source reaches its maximum amplitude. The scattered field has been isolated by subtracting the finite-difference solution for the homogeneous water halfspace from the full solution for the case with the floe. The significance of the ice elasticity is clear in both a qualitative and a quantitative sense. Thus, the elastic floe scatters in a quadrupole radiation pattern, whereas the fluid floe scatters in a way similar to a vertical dipole. Also, Fig. 7.16 shows that the scattered field produced by the elastic floe is of higher amplitude than that of the fluid floe.

The finite-difference computations used a grid spacing of 0.5 m, with the total computational domain ranging from  $x = -100$  m to  $x = 300$  m, in the horizontal and down to a depth of 100 m below the free surface. The sponge layer necessary to eliminate artificial reflections from the computational boundary, occupied the whole region outside the one shown in Fig. 7.16.

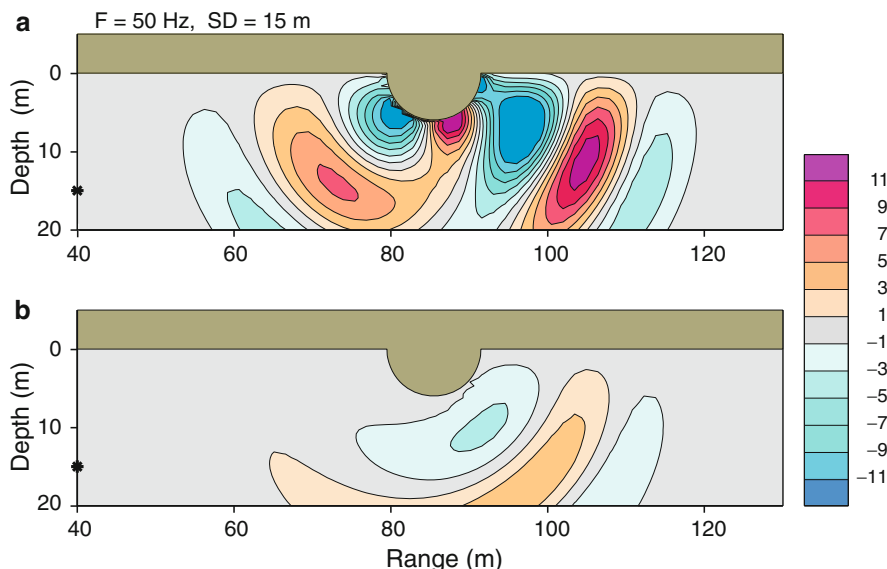


**Fig. 7.16** Snapshots of the scattered field computed by a finite-difference model [12]. (a) Elastic ice floe with compressional speed 3500 m/s and shear speed 1600 m/s. (b) Fluid ice floe with compressional speed 3500 m/s and no shear

### 7.6.1.2 Boundary-Element Solution

Whereas the finite-difference solution is most convenient for full time-domain solutions, a boundary-element solution is much more efficient for determining the single-frequency or narrow-band response for this type of problem. This is because the environment outside the area occupied by the scatterer is such that the Green's functions are readily determined either exactly or numerically. Thus, for the ice floe problem the Green's functions for both the exterior and interior domains are the simple ones for either a fluid or an elastic halfspace. Therefore, only the semi-circular boundary of the ice floe needs to be discretized. For a frequency of 50 Hz, a convergent solution is obtained using only 24 boundary elements, which is in sharp contrast to the 160000 grid points used for the finite-difference computation. On the other hand, the computations needed for each node in the boundary discretization are more involved, with the resulting difference in computation time being much less dramatic.

The boundary-element solutions for the ice floe problems are shown in Fig. 7.17 in the form of transmission loss contours of the scattered field at 50 Hz. The

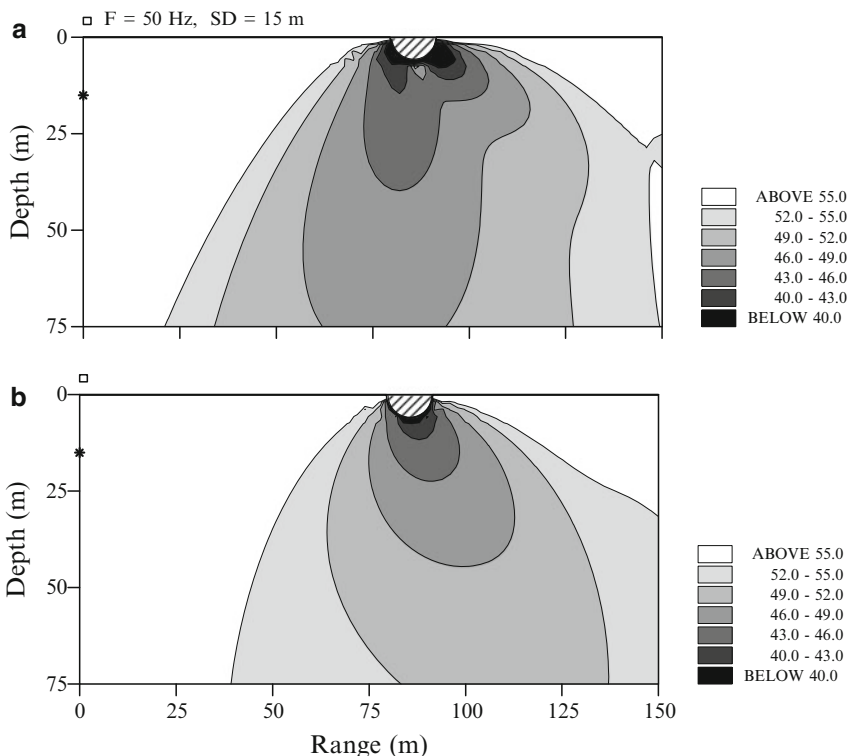


**Fig. 7.17** Contours of transmission loss at 50 Hz for the field scattered by a half-cylindrical ice floe, computed by a boundary-element model [44]. (a) Elastic ice floe with compressional speed 3500 m/s and shear speed 1600 m/s. (b) Fluid ice floe with compressional speed 3500 m/s and no shear

elimination of the incoming field is straightforward in the boundary-element approach, since it is simply a matter of ignoring the volume integral in (7.132) representing the exterior source term. Even though the FDM solutions in Fig. 7.16 illustrate time-domain results, the results shown in Fig. 7.17 agree qualitatively. The dipole nature of the fluid floe is evident, and similarly the quadrupole radiation pattern of the elastic floe is observable, although somewhat masked by a relatively strong dipole component at this frequency. Also, the stronger scattering produced by the elastic keel is evident.

For these simulations, we have used a boundary-element model which uses wavenumber integration to evaluate the Green's functions for both the exterior and interior domains [44]. This model, therefore, treats arbitrary stratification in both regions. It is straightforward in this model to include the homogeneous ice plate to represent the problem of scattering by ice keels. The environmental model for such a scenario is shown in Fig. 7.15b. We consider the scattering from a half-cylindrical keel attached to an otherwise uniform ice sheet of 3-m thickness. Figure 7.18 shows the transmission loss contours of the field scattered by elastic and fluid ice keels, each with the same properties as the ice floes treated above. Compared to the results

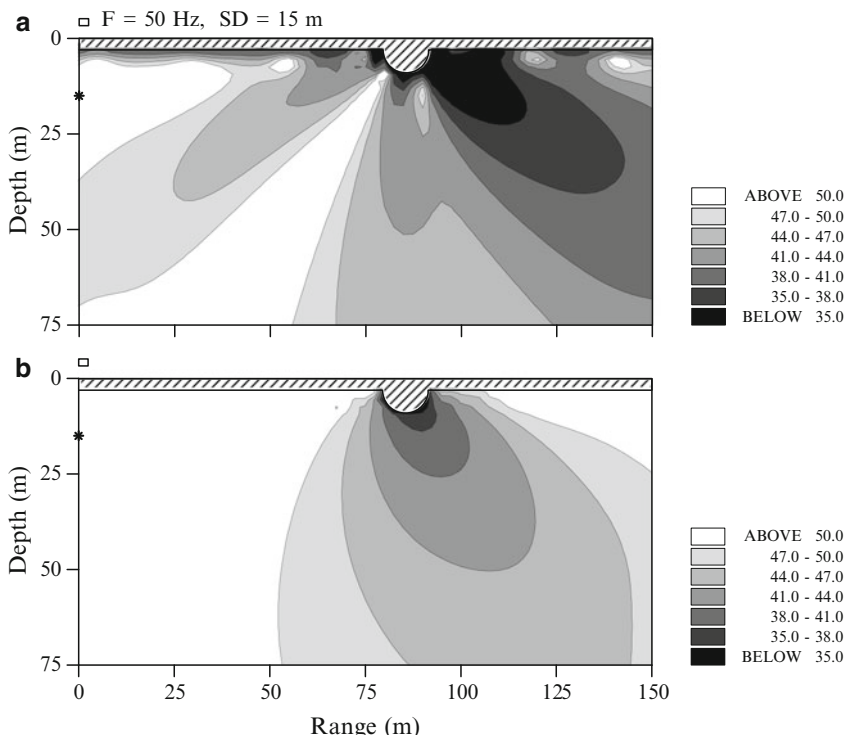


**Fig. 7.18** Contours of transmission loss at 50 Hz for the field scattered by a half-cylindrical ice keel below a 3-m thick ice cover, computed using a boundary-element model [44]. (a) Elastic ice keel with properties identical to those of the ice cover, i.e., compressional speed 3500 m/s and shear speed 1600 m/s. (b) Fluid ice keel with compressional speed 3500 m/s and no shear

in Fig. 7.17 for the floe problem, the radiation pattern for the elastic keel in Fig. 7.18a has changed dramatically, whereas the change for the fluid keel in Fig. 7.18b is mainly quantitative, showing the same dipole pattern, but at a higher level with the ice plate present.

Another significant difference is the strong evanescent field close to the ice plate and the associated interference pattern in Fig. 7.18a. This is due to the excitation of a *flexural wave* in the ice plate, which interferes with the waterborne acoustic field and the compressional wave in the ice. This is evident from Fig. 7.19a, which

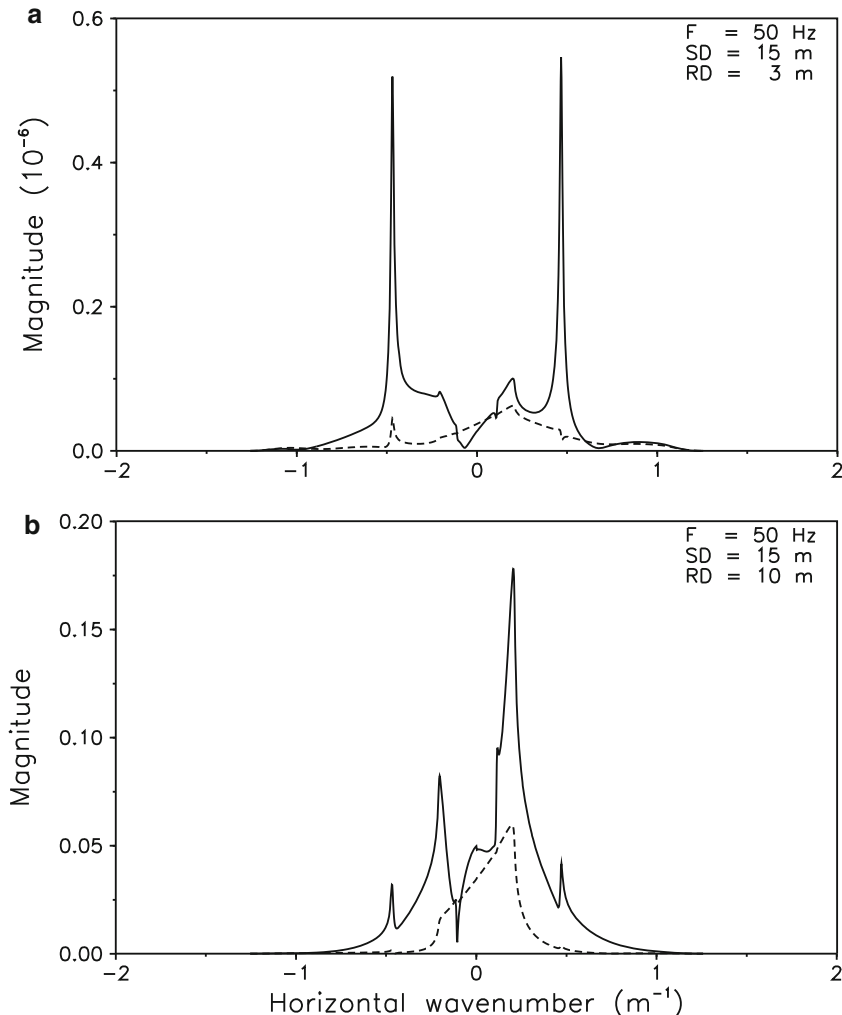


**Fig. 7.19** Wavenumber spectra of field scattered by ice keel at 50 Hz, computed using a boundary-element model [44]. *Solid* and *dashed curves* correspond to the elastic and fluid keels, respectively. (a) Wavenumber spectrum of vertical particle velocity at bottom of ice cover. (b) Wavenumber spectrum of acoustic pressure at 10-m depth

shows the wavenumber spectrum for the vertical particle velocity at the bottom of the ice cover. Negative wavenumbers correspond to back scattering and positive wavenumbers to forward scattering. The solid curve is the result for the elastic keel. Clearly, the field near the ice plate is dominated by the subsonic flexural mode with wavenumber  $k_x \simeq \pm 0.5 \text{ m}^{-1}$ , in both the forward and backward directions. The corresponding result for the fluid ice keel is shown in Fig. 7.19a as a dashed curve, and here the flexural wave is also excited, but at a much lower amplitude. This is not surprising in view of the vanishing shear rigidity of this keel. The evanescent nature of the flexural component is apparent in Fig. 7.19b, which shows the wavenumber spectrum of the acoustic field at 10-m depth. Even though the flexural components are still detectable at this depth, their amplitudes have decreased dramatically. The field is here dominated by the low-wavenumber components,  $|k_x| \leq 0.21 \text{ m}^{-1}$ , corresponding to a field propagating vertically in the water column. As expected, the peaks and valleys in this spectral regime are consistent with the angular dependence of the radiation pattern in Fig. 7.18a.

Through these numerical examples we have demonstrated the generality of the discrete methods, which provide solutions of propagation and scattering problems in environments with complex geometry and material properties. Additional examples involving bottom inhomogeneities and irregular interfaces can be found in the literature, see e.g., [7]. The discrete methods, however, are computationally intensive, and they should only be applied to problems not tractable by one of the more efficient numerical techniques described in Chaps. 3–6.

## 7.6.2 Scattering from Objects Near Interfaces

As mentioned earlier, the problems associated with scattering from complex objects in the ocean waveguide are most efficiently handled using one of the hybrid approaches, combining a discrete numerical method for the actual scattering problem with one of the standard approaches for waveguide propagation for the incident and scattered fields. Examples of scattering from both rigid and soft spheres in a waveguide using mode and wavenumber integration approaches were presented in Sect. 5.12. Here, we use finite-element and virtual-source techniques to solve scattering problems involving layered elastic spheres placed near the seabed.

### 7.6.2.1 Filled Spherical Shell on the Seabed

As shown by Zampolli et al. [32] the finite-element technique with PML's (FE-PML) is particularly attractive for computing the field scattered or radiated by an object located within a layered medium. As an example, the farfield scattering from a layered elastic sphere lying on the interface between two different fluids is considered in Fig. 7.20. The material properties are given in Table 7.1. The critical angle of reflection is around  $20^\circ$ . The outer radius of the sphere is  $a = 0.5 \text{ m}$ , and the

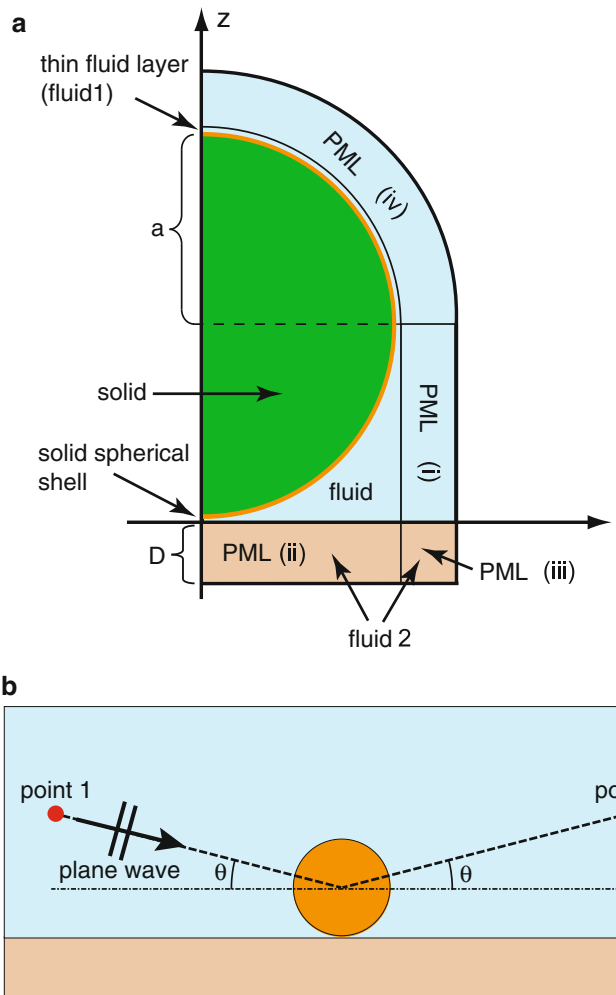


**Fig. 7.20** Finite element computational domain for scattering from an elastic layered sphere lying on the interface between two different fluid halfspaces (a), and definition of the problem geometry (b)

**Table 7.1** Material properties for object scattering examples.  
A  $p$ -wave attenuation of  $0.5 \text{ dB}/\lambda$  is assumed for the sediment

	$c_p(\text{m/s})$	$c_s(\text{m/s})$	$\rho(\text{kg/m}^3)$
Water	1500	0	1000
Sediment	1600	0	1800
Fiberglass casing	3500	1400	3000
Solid filling	2500	1200	2000

shell is 1 cm thick. Two different insonification angles are considered: subcritical insonification at  $\theta = 15^\circ$  and supercritical insonification at  $\theta = 25^\circ$ . The farfield is sought at the two points shown in the figure and located 50 m from the center of the sphere.

The FE computational domain is shown in Fig. 7.20a, where the PML for the upper fluid is in direct contact with the PML for the lower fluid at the interface  $z = 0$ . The sphere is lifted by a distance of 0.25 cm along  $z$  from the bottom interface to circumvent meshing difficulties arising from the presence of degenerate corners at  $(r, z) = (0, 0)$  and at  $(r, z) = (a, a)$ . This makes it necessary also to introduce the 0.25 cm thick layer of fluid between the upper hemisphere and the PML depicted in the figure. The domain is discretized using an unstructured mesh of triangular cubic Lagrange elements. The  $A_0^-$  phase speed estimated analytically for the spherical shell [58, 59] varies between a minimum of 167 m/s at approximately 550 Hz and a maximum of 600 m/s at 10 kHz. The shell and its surroundings are meshed with elements having a maximum edge length of 0.5 cm, whereas the element size away from the shell increases up to 1.5 cm. The result is a computation time of about 10 h on a standard workstation to compute the sweep from 100 Hz to 10 kHz in 5 Hz intervals.

The incident field applied on the interface between the elastic sphere and the fluid domain is

$$p^{\text{inc}}(r, \varphi, z) = p_\theta^{\text{inc}}(r, \varphi, z) + \mathcal{R}(k_2 \cos \theta) p_{-\theta}^{\text{inc}}(r, \varphi, z), \quad (7.176)$$

where  $p_\theta^{\text{inc}}$  is defined in (7.199) and (7.200), the reflection coefficient  $\mathcal{R}$  is given in (7.211) and the incident grazing angle  $\theta$  is defined in Fig. 7.20. The farfield target strength

$$\text{TS}(\mathbf{r}) = 20 \log (\mathbf{r} |p^{\text{scat}, \infty}(\mathbf{r})| / |p^{\text{inc}}|) \quad (7.177)$$

at the  $i$ th receiver is computed by approximating the 3-D Helmholtz–Kirchhoff integral for the scattered field, (7.207), via the discrete sum

$$p^{\text{scat}}(\mathbf{r}_i) = \left[ \frac{\partial G_{ij}^{(12)}}{\partial n_j} p_j^{\text{scat}} - \rho_f^{(1)} \omega^2 G_{ij}^{(12)} (u_n^{\text{scat}})_j \right] dA_j, \quad (7.178)$$

where the scattered pressure  $p_j^{\text{scat}} = p^{\text{scat}}(\mathbf{r}_j)$  and the normal displacement of the scattered field  $(u_n^{\text{scat}})_j = u_n^{\text{scat}}(\mathbf{r}_j)$  are obtained using the Fourier sum (7.201). The 2188 sampling points  $\mathbf{r}_j$  used here are approximately equi-distributed on the surface of the sphere, and  $dA_j$  is the area associated to each point. The Green's function for the two-layered medium  $G_{ij}^{(12)} = G^{(12)}(\mathbf{r}_i, \mathbf{r}_j)$  is used in the approximate form given in (7.212).

The solution computed with the FE-PML method is compared to a solution obtained with the VSC described in Sect. 7.5.5 [52, 55]. The VSC is here used with a single virtual multipole source representing the analytical, free-field scattering function for the spherical shell in terms of spherical harmonics, but using the full wavenumber integral for the two-layered-medium Green's function  $G^{(12)}$  [60].

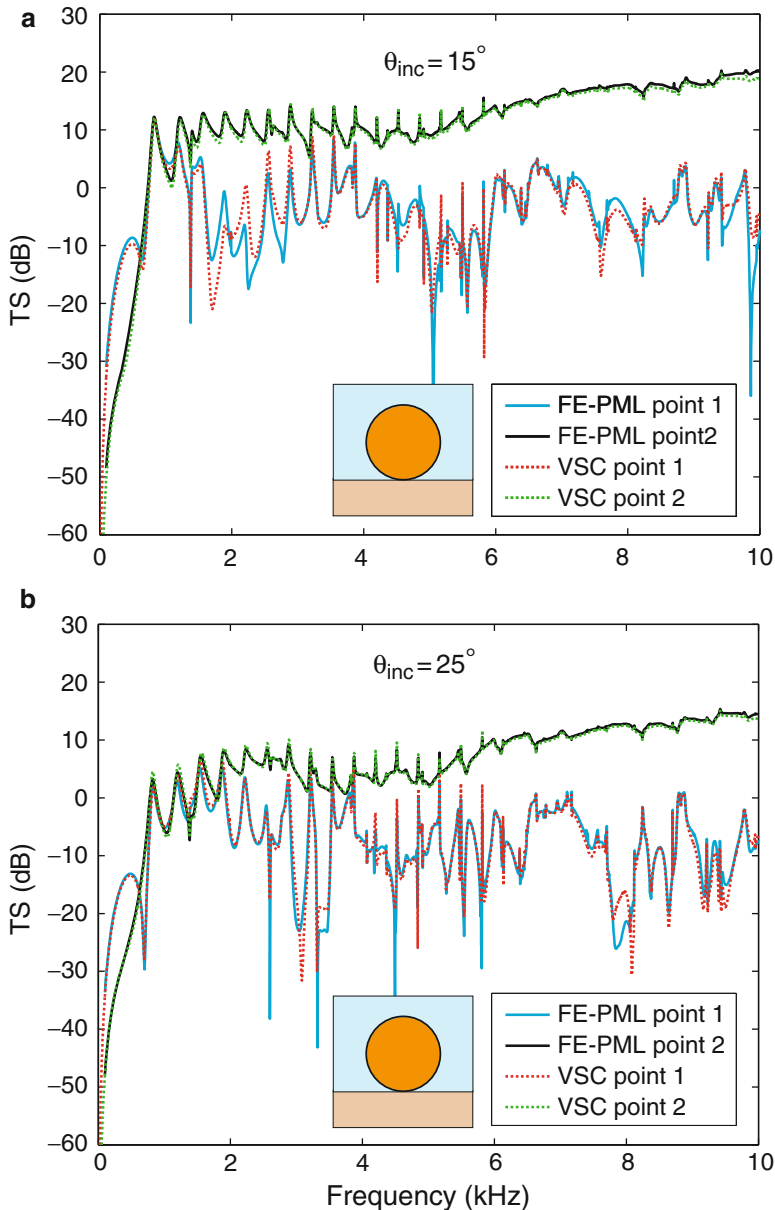


**Fig. 7.21** Farfield target strength for proud spherical shell on the seabed: (a) Subcritical incidence  $\theta = 15^\circ$ , (b) Supercritical incidence  $\theta = 25^\circ$

This version of the VSC neglects multiple scattering between the scatterer and the fluid–fluid interface beyond the first bounce. Figure 7.21 shows that the solutions agree well for both incidence angles, with some differences between the FE-PML and the VSC solutions being more evident in the subcritical case for backscattering

(Fig. 7.21a). These differences may be attributed to the approximation of the Green's function in the FE solution, (7.212), which degrades as the receiver angle moves closer to grazing, and to the fact that higher-order scattering between the fluid–fluid interface and the scatterer is neglected in the VSC solution. Nevertheless, the results demonstrate the applicability of both the FE-PML and the VSC approaches to scattering in complex geometries.

### 7.6.2.2 Buried, Filled Spherical Shell

We next consider scattering from a filled, spherical shell buried 20 cm below the water–sediment interface, Fig. 7.22a. The dimensions of the sphere are as in the previous example and the material properties are those given in Table 7.1. The solution computed with the FE-PML method is again compared to a solution obtained with the VSC described in Sect. 7.5.5. As for the case of the proud sphere, the VSC is used with a single virtual multipole source representing the analytical, free-field scattering function for the spherical shell in terms of spherical harmonics, but using the full wavenumber integral for the two-layered-medium Green's

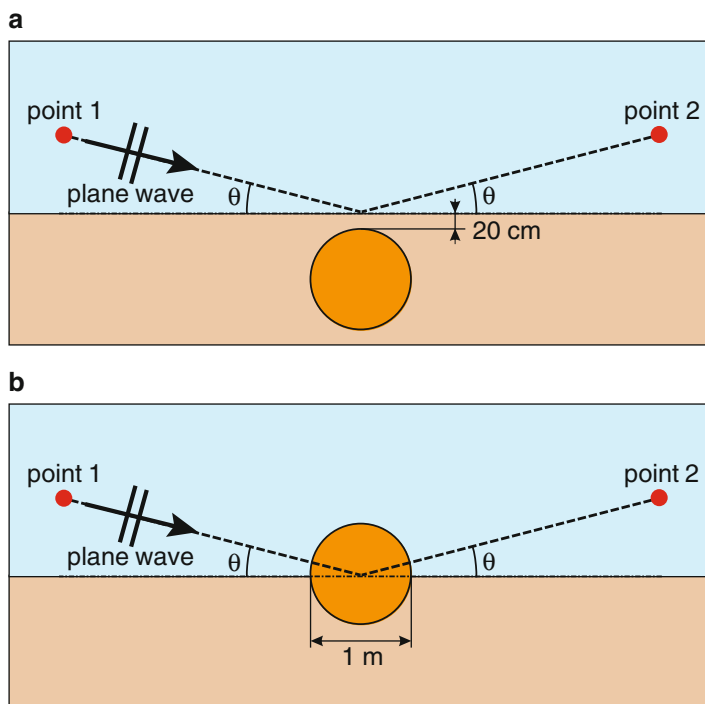


**Fig. 7.22** Scattering from a buried and a half-buried, *filled spherical shell*. (a) Problem geometry for the buried case and (b) the half-buried case

function  $G^{(12)}$  [60]. Hence, the VSC again neglects multiple scattering between the scatterer and the fluid–fluid interface beyond the first bounce. Figure 7.23 shows that the solutions agree well for both incidence angles, except above 4 kHz for backscattering with subcritical insonification, Fig. 7.23a. Here, levels are very low ( $-60$  to  $-90$  dB) and numerical accuracy may be a problem in both models. This test problem is a clear demonstration of the difficulty associated with long-range object detection in the seabed, which often involves insonification at low grazing angles.

### 7.6.2.3 Half-Buried, Filled Spherical Shell

As shown in the previous examples, the scattering from proud and buried targets can be accurately estimated using the highly efficient single-scatter approximation in combination with the free-field analytical scattering function. Not surprisingly, the same is not the case for objects penetrating the interfaces. On the other hand, both the FE-PML and VSC approaches can be used effectively in such cases, as demonstrated by Zampolli et al. [61]. Consider again scattering from a solid-filled, spherical shell half-buried in the sediment, Fig. 7.22b. The dimensions of the sphere are as in the previous examples and the material properties are those given in Table 7.1.

In this more complicated test problem, the multiple scattering interactions between the spherical target and the seafloor cannot be neglected. For this reason, it is necessary to compute the VSC solution using a nodal stiffness matrix describing the target surface impedance, in conjunction with the discrete representation of the Helmholtz–Kirchhoff integral for the layered medium. This requires the inversion of a dense matrix at each frequency, the size of which is equal to twice the number of surface points (pressure and pressure-gradient sources) required to characterize the target impedance. The computational burden of this approach has made it necessary to limit the maximum frequency of the computations for the VSC solutions to 5.5 kHz.

In Fig. 7.24, the FE-PML and VSC solutions are compared. The agreement in both backscattering and forward scattering is good at the low frequencies, with some differences, caused by the progressive degradation of the VSC stiffness-matrix-solution convergence, appearing as the frequency increases. For the lower part of the frequency band, the solutions can be regarded as being of benchmark quality. The FE-PML solutions were obtained by discretizations analogous to those successfully used for the completely buried sphere in the previous example. This, in turn, provides some degree of confidence in the accuracy of the FE-PML results throughout the entire frequency band.

Additional scattering results for axisymmetric targets (cylinders, spheres) placed in the free field or near the ocean bottom (proud, half-buried, or fully buried) may be found in [32, 57, 61].

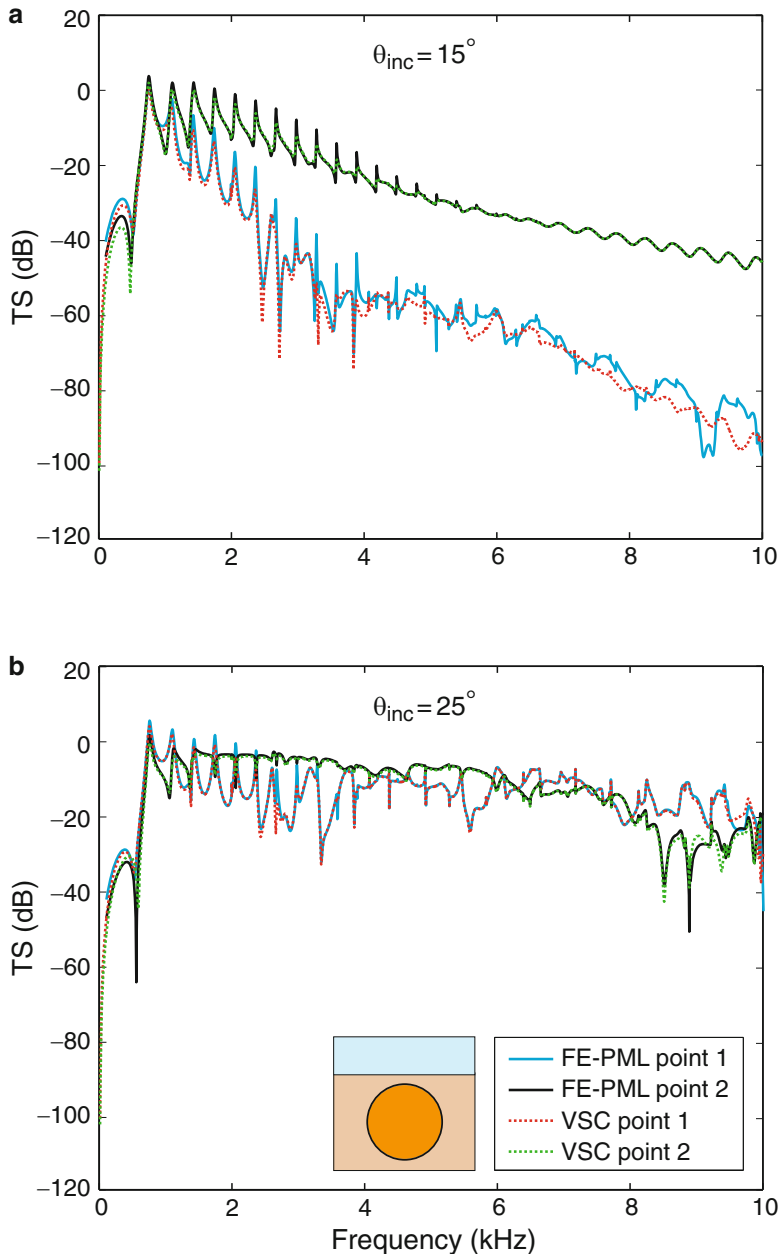


**Fig. 7.23** Farfield target strength for buried, filled spherical shell: **(a)** Subcritical incidence  $\theta = 15^\circ$ , **(b)** Supercritical incidence  $\theta = 25^\circ$

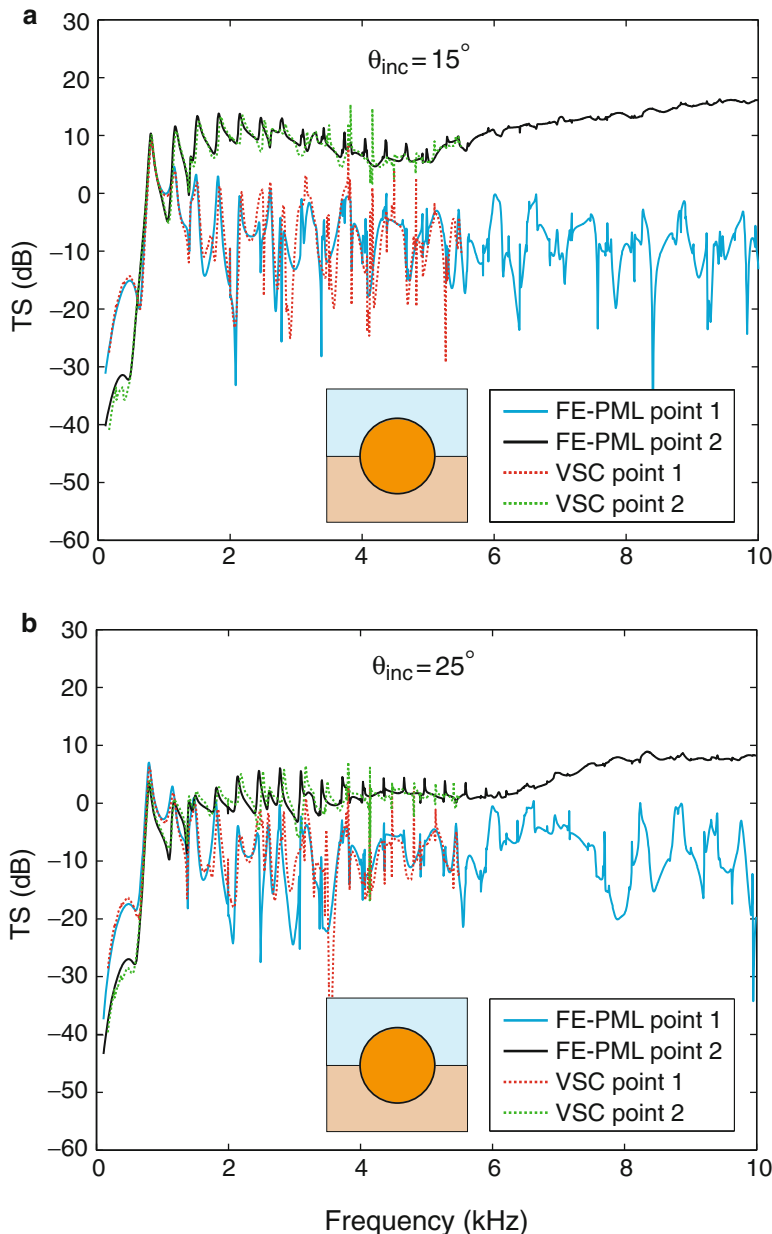


**Fig. 7.24** Farfield target strength for half-buried, *filled spherical shell*: (a) Subcritical incidence  $\theta = 15^\circ$ , (b) Supercritical incidence  $\theta = 25^\circ$

## Appendix 1: Variational Formulation for Fluid–Elastic Interaction

In ocean acoustics, the principal use of the FEM is for modeling scattering from complex, elastic objects embedded in the acoustic medium. Several general-purpose finite-element solvers are available for handling the discretization and solution of the resulting equations. All that is required for using such standard tools is the definition of the governing differential equations or the corresponding variational formulation. A convenient derivation for this general problem has been given by Zampolli et al. [32], and shall be summarized here. The derivation of the variational formulation for axisymmetric geometries is particularly useful for the large class of scattering problems involving elastic objects of revolution.

### The Elastic Medium

The propagation of stress-waves in an elastic medium  $\Omega_s$  are described by the elastic equation of motion [62]

$$(C_{ijkl} u_{k,l})_{,j} + \omega^2 \rho_s u_i = 0, \quad (7.179)$$

where  $\rho_s$  is the density of the solid. The indices are in the range  $i, j, k, l = 1, 2, 3$ . The summation convention is assumed for repeated indices. The notation “ $,_j$ ” indicates differentiation with respect to the  $j$ th coordinate, i.e. “ $\partial/\partial x_j$ ”. The vector  $\mathbf{u}$  describes the displacement of the solid particles,

$$\mathbf{u}(x_1, x_2, x_3) = u_i \mathbf{e}_i, \quad (7.180)$$

where  $\mathbf{e}_i$  denotes the unit vector of the  $i$ th coordinate, such as for example  $\mathbf{e}_x, \mathbf{e}_y, \mathbf{e}_z$  in Cartesian coordinates, or  $\mathbf{e}_r, \mathbf{e}_\varphi$  and  $\mathbf{e}_z$  in cylindrical coordinates. The deformation of the medium is described by the symmetric small-strain tensor,

$$\varepsilon_{ij} = \frac{1}{2} \left( \frac{\partial u_i}{\partial x_j} + \frac{\partial u_j}{\partial x_i} \right). \quad (7.181)$$

The stress tensor  $\sigma_{ij}$  is related linearly to the strain tensor  $\varepsilon_{ij}$  via the stress–strain equation,

$$\sigma_{ij} = C_{ijkl} \varepsilon_{kl}, \quad (7.182)$$

where, for an *elastically isotropic* material, the tensor of elastic constants  $C_{ijkl}$  obeys the relation [62],

$$C_{ijkl} = \lambda \delta_{ij} \delta_{kl} + \mu (\delta_{ik} \delta_{jl} + \delta_{il} \delta_{jk}) \quad (7.183)$$

with  $\lambda, \mu$  representing the Lamé elastic constants, and  $\delta_{ij}$  being the symmetric Kronecker delta tensor. This yields the Hooke’s law,

$$\sigma_{ij} = \lambda \varepsilon_{kk} \delta_{ij} + 2\mu \varepsilon_{ij}. \quad (7.184)$$

The longitudinal and transverse sound speeds  $c_p$  and  $c_s$  are related to the Lamé constants via

$$c_p = \sqrt{\frac{\lambda + 2\mu}{\rho_s}}, \quad c_s = \sqrt{\frac{\mu}{\rho_s}}. \quad (7.185)$$

The principle of virtual work for the elastic medium yields the variational equation [31, 62],

$$\int_{\Omega_s} (-\omega^2 \rho_s u_i \delta u_i + \sigma_{ij} \delta \varepsilon_{ij}) d\Omega - \int_{\partial \Omega_s} t_i \delta u_i dS = 0, \quad (7.186)$$

where  $i, j = 1, 2, 3$ ,  $\delta u_i$  and  $\delta \varepsilon_{ij}$  represent admissible variations of the unknown displacement vector and of the unknown strain tensor, respectively. The surface traction vector is given by Cauchy’s stress formula,

$$t_i = \sigma_{ij} n_j \quad (7.187)$$

with  $n_j$  being the components of the outward-pointing unit vector normal to  $\partial \Omega_s$ . Boundary conditions for the elastic domain can be applied as Neumann boundary conditions via the surface traction  $t_i$ , as Dirichlet boundary conditions by constraining  $u_i$  to conform to some known displacements, or as combinations of Neumann and Dirichlet conditions for the different components of the unknowns.

## The Fluid Medium

In the fluid  $\Omega_f$  the unknown pressure  $p(\mathbf{x})$  is modeled by the Helmholtz equation in the form admitting a position-dependent fluid density  $\rho_f(\mathbf{x})$  and sound speed  $c_f(\mathbf{x})$  [39, 63]:

$$\nabla \cdot \left( \frac{1}{\rho_f(\mathbf{x})} \nabla p(\mathbf{x}) \right) + \frac{k^2}{\rho_f(\mathbf{x})} p(\mathbf{x}) = 0, \quad \mathbf{x} \in \Omega_f, \quad (7.188)$$

where  $k = \omega/c_f(\mathbf{x})$  is the wavenumber.

For the unbounded fluid domain, the Sommerfeld radiation condition (2.67) must hold at infinity,

$$\lim_{R \rightarrow \infty} \left[ R \left( \frac{\partial p(R)}{\partial R} - ik p(R) \right) \right] = 0 \quad (7.189)$$

with  $R$  being the spherical radial coordinate, originating at a nominal center of the computational domain. Other boundary conditions for the pressure may be of Dirichlet, Neumann, or mixed Dirichlet/Neumann types.

Following the derivations presented in the literature [31, 64] one obtains the variational equation for the pressure in the fluid domain,

$$\int_{\Omega_f} \left( -\frac{1}{\omega^2 \rho_f} \nabla p \cdot \delta(\nabla p) + \frac{1}{\rho_f c_f^2} p \delta p \right) d\Omega + \int_{\partial\Omega_f} \frac{1}{\omega^2 \rho_f} \nabla p \cdot \mathbf{n} \delta p dS = 0. \quad (7.190)$$

The quantity

$$\frac{1}{\omega^2 \rho_f} \nabla p \cdot \mathbf{n} = u_n \quad (7.191)$$

represents the normal component of the particle displacement, applied at the surface of the boundary  $\partial\Omega_f$ . Using (7.191), Neumann boundary conditions and mixed boundary conditions can be applied via the boundary integral term in (7.190). In accordance with the symmetric potential formulation introduced by Everstine [65, 66], the scaling  $1/\omega^2$  is applied in (7.190) with the purpose of obtaining a symmetric coupled fluid–solid FE equation system [63]. This makes it possible to use a symmetric sparse solver in the numerical scheme, which is generally a more efficient option compared to non-symmetric solvers.

If the quantity of interest in the fluid domain is the acoustic field scattered by an obstacle, and the incident acoustic pressure  $p^{inc}$  and its normal derivative  $\nabla p^{inc}$  are known a priori, then one has:

$$p = p^{\text{scat}} + p^{\text{inc}}, \quad \nabla p = \nabla p^{\text{scat}} + \nabla p^{\text{inc}}, \quad (7.192)$$

where  $p^{\text{scat}}$  is the unknown scattered field component, and  $p$  represents the total acoustic pressure. Consequently, substitution of (7.192) into (7.190) yields

$$\begin{aligned} & \int_{\Omega_f} \left( -\frac{1}{\omega^2 \rho_f} \nabla p^{\text{scat}} \delta(\nabla p^{\text{scat}}) + \frac{1}{\rho_f c_f^2} p^{\text{scat}} \delta p^{\text{scat}} \right) d\Omega \\ & + \int_{\partial\Omega_f} \frac{1}{\omega^2 \rho_f} (\nabla p - \nabla p^{\text{inc}}) \cdot \mathbf{n} \delta p^{\text{scat}} dS = 0. \end{aligned} \quad (7.193)$$

The incident field may be given via some direct analytical expression, or by some other numerical method (such as for example a waveguide propagation model), or it may have been determined experimentally.

## Interface Boundary Conditions

Any two adjacent elastic domain components, say  $\Omega^{(1)}$  and  $\Omega^{(2)}$  in Fig. 7.25, are assumed to be perfectly bonded, which implies that the continuity of displacement  $u_i$  and stress  $t_i$  must be satisfied across the interface  $I$ . The finite-element method, which partitions the computational domain into a finite number of non-overlapping, finite-sized elements would for example yield two elements like  $\Omega^{(1)}$  and  $\Omega^{(2)}$ . In particular, the continuity of  $t_i$  across the interface between two adjacent solid volumes, implies that the boundary integral contributions over the interface  $I$  from  $\Omega^{(1)}$  and  $\Omega^{(2)}$  in (7.186) vanish:

$$\int_I \underbrace{\left( t_i^{(1)} + t_i^{(2)} \right)}_{\sigma_{ij}^{(1)} n_j^{(1)} - \sigma_{ij}^{(2)} n_j^{(1)}} \delta u_i \, dS = 0, \quad (7.194)$$

where the normal  $n_j^{(1)}$  is chosen to point from  $\Omega^{(1)}$  into  $\Omega^{(2)}$ . The continuity of the primary variables  $u_i$  in the solid is guaranteed by the inter-element continuity condition.

Similarly, the pressure and the normal displacement, (7.191), both must be continuous across the interface separating two adjacent portions of the fluid domain. The latter condition, in particular, implies that, if  $\Omega^{(1)}$  and  $\Omega^{(2)}$  belong to the fluid domain, the boundary integral contribution from the two subdomains in (7.190) becomes,

$$\int_I \left( \frac{1}{\omega^2 \rho_f^{(1)}} \nabla p \cdot \mathbf{n}^{(1)} - \frac{1}{\omega^2 \rho_f^{(2)}} \nabla p \cdot \mathbf{n}^{(1)} \right) \delta p \, dS = 0. \quad (7.195)$$

This is true also if the two volumes are occupied by two heterogeneous fluids. The continuity of the primary variable  $p$  is ensured also in this case by the inter-element continuity condition.

If one of the two subdomains, say  $\Omega^{(1)}$ , is a solid and the other one, say  $\Omega^{(2)}$ , is a fluid, then the normal displacement across the interface and the normal stress,

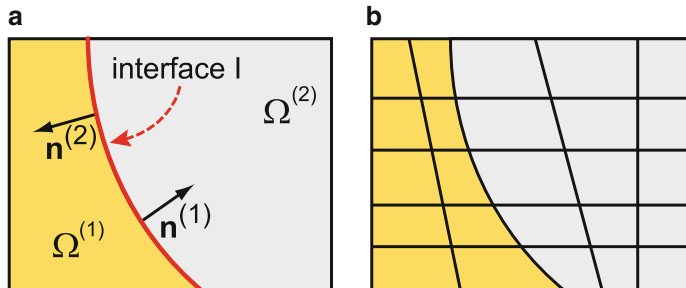


**Fig. 7.25** (a) Two generic components of the computational domain,  $\Omega^{(1)}$  and  $\Omega^{(2)}$ , separated by a common interface  $I$ . (b) Schematic representation of the subdivision of the two domain components into finite elements

which is related to the acoustic pressure by  $\sigma_{ij} = -p \delta_{ij}$ , must both be continuous across  $I$ . Equations (7.186), (7.190) and (7.193) imply in this case that

$$\int_I t_i \delta u_i \, dS = - \int_I \left\{ \frac{p}{p^{\text{scat}} + p^{\text{inc}}} \right\} n_i \delta u_i \, dS, \quad (7.196)$$

$$\int_I \frac{1}{\omega^2 \rho_f} \left\{ \nabla p - \nabla p^{\text{inc}} \right\} \cdot \mathbf{n} \delta p \, dS = - \int_I \left\{ \mathbf{u} - \frac{1}{\omega^2 \rho_f} \nabla p^{\text{inc}} \right\} \cdot \mathbf{n} \delta p \, dS. \quad (7.197)$$

The upper or lower expression in the brackets is chosen depending on whether the unknown is  $p$  or  $p^{\text{scat}}$ . In what follows, the attention is restricted to the scattered field equations in the fluid, knowing that the total-field case can always be recovered by the substitutions  $p^{\text{inc}} \mapsto 0$  and  $p^{\text{scat}} \mapsto p$ .

### Axially Symmetric Geometries

In the case where the geometry of the problem is axisymmetric (Fig. 7.26), but the loading is not necessarily axially symmetric, the variational equations for the 3-D problem presented previously are rewritten in cylindrical coordinates  $\mathbf{r} = r\mathbf{e}_r + \varphi\mathbf{e}_\varphi + z\mathbf{e}_z$ , with  $0 \leq \varphi < 2\pi$ . A generic incident acoustic field  $p^{\text{inc}}$  can be decomposed in a Fourier series

$$p^{\text{inc}}(r, \varphi, z) = p_m^{\text{inc}}(r, z) e^{im\varphi}, \quad -\infty < m < +\infty. \quad (7.198)$$

Of particular interest to the examples presented in Sect. 7.6.2 is the expansion of a plane wave having the wavenumber vector parallel to the  $rz$ -plane and forming an angle  $\theta$  with the  $r$ -axis [67]:

$$p^{\text{inc}}(r, \varphi, z) = \epsilon_m p_m^{\text{inc}}(r, z) \cos(m\varphi), \quad 0 \leq m < +\infty, \quad (7.199)$$

$$p_m^{\text{inc}}(r, z) = (-i)^m e^{(-ikz \sin \theta)} J_m(kr \cos \theta) \quad (7.200)$$

with  $\epsilon_0 = 1$  and  $\epsilon_m = 2$ ,  $m = 1, \dots, +\infty$ , and with  $J_m$  representing the Bessel function of order  $m$ .

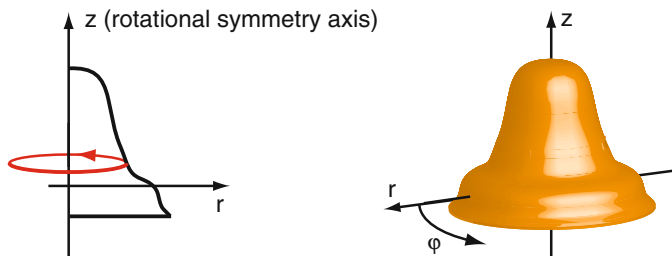


**Fig. 7.26** A 3-D axisymmetric geometry is obtained by rotating a generating line around the axis of symmetry

Consistent with the chosen decomposition of the applied load, the solid displacement  $(u_1, u_2, u_3) = (u, v, w)$  and the pressure  $p$  are decomposed in the same way

$$\begin{pmatrix} u(r, \varphi, z) \\ w(r, \varphi, z) \\ p(r, \varphi, z) \end{pmatrix} = \begin{pmatrix} u_m(r, z) \\ w_m(r, z) \\ p_m(r, z) \end{pmatrix} \left\{ \begin{array}{l} e^{im\varphi} \\ \cos(m\varphi) \end{array} \right\},$$

$$v(r, \varphi, z) = v_m(r, z) \left\{ \begin{array}{l} e^{im\varphi} \\ \sin(m\varphi) \end{array} \right\}. \quad (7.201)$$

The complex exponential or the trigonometric functions in the brackets are chosen depending on whether the forcing is decomposed according to (7.198) or (7.199). Applying the substitutions to the variational (7.186) and (7.193) written in cylindrical coordinates, with  $d\Omega = r dr d\varphi dz$ ,  $\Omega_{s/f}^0 = \{(r, \varphi, z) \in \Omega_{s/f} : \varphi = 0\}$ , carrying out the integration over  $\varphi$  explicitly, and making use of the orthogonality property of the Fourier basis, yields:<sup>1</sup>

$$\int_{\Omega_s^0} \left[ -\omega^2 \rho_s \left( (u_m \delta u_m + w_m \delta w_m) \left\{ \frac{2\pi}{I_{cc}} \right\} + v_m \delta v_m \left\{ \frac{2\pi}{I_{ss}} \right\} \right) \right. \\ + (\sigma_r^m \delta(\varepsilon_r^m) + \sigma_\varphi^m \delta(\varepsilon_\varphi^m) + \sigma_z^m \delta(\varepsilon_z^m)) \left\{ \frac{2\pi}{I_{cc}} \right\} \\ + (2\sigma_{r\varphi}^m \delta(\varepsilon_{r\varphi}^m) + 2\sigma_{\varphi z}^m \delta(\varepsilon_{\varphi z}^m)) \left\{ \frac{2\pi}{I_{ss}} \right\} \\ \left. + 2\sigma_{rz}^m \delta(\varepsilon_{rz}^m) \left\{ \frac{2\pi}{I_{cc}} \right\} \right] r dr dz + I_{\partial\Omega_s^0} = 0, \quad (7.202)$$

$$\int_{\Omega_f^0} \left[ -\frac{1}{\omega^2 \rho_f} \left( \frac{\partial p_m^{\text{scat}}}{\partial r} \delta \left( \frac{\partial p_m^{\text{scat}}}{\partial r} \right) \left\{ \frac{2\pi}{I_{cc}} \right\} + \frac{m^2}{r^2} p_m^{\text{scat}} \delta(p_m^{\text{scat}}) \left\{ \frac{2\pi}{I_{ss}} \right\} \right. \right. \\ + \frac{\partial p_m^{\text{scat}}}{\partial z} \delta \left( \frac{\partial p_m^{\text{scat}}}{\partial z} \right) \left\{ \frac{2\pi}{I_{cc}} \right\} \\ \left. \left. + \frac{1}{\rho_f c_f^2} p_m^{\text{scat}} \delta(p_m^{\text{scat}}) \left\{ \frac{2\pi}{I_{cc}} \right\} \right] r dr dz + I_{\partial\Omega_f^0} = 0. \quad (7.203) \right.$$

The factors for the case of a loading decomposed in a cosine series are:

$$I_{ss} = \begin{cases} \pi, & m \neq 0 \\ 0, & m = 0 \end{cases}, \quad I_{cc} = \begin{cases} \pi, & m \neq 0 \\ 2\pi, & m = 0. \end{cases} \quad (7.204)$$

---

<sup>1</sup> It should be noted that the summation convention for repeated indices does not apply to (7.202), (7.203), (7.205), and (7.206).

The boundary terms  $I_{\partial\Omega_s^0}$  and  $I_{\partial\Omega_f^0}$  can be split into contributions from the free faces  $\Gamma_{s\setminus\text{fsi}}$  and  $\Gamma_{f\setminus\text{fsi}}$ , and the contributions from the fluid–solid interfaces  $\Gamma_{\text{fsi}}$ . This yields the contour integral terms:

$$\begin{aligned} I_{\partial\Omega_s^0} &= \int_{\Gamma_{\text{fsi}}} (p_m^{\text{scat}} + p_m^{\text{inc}}) (n_r \delta u_m + n_z \delta w_m) \left\{ \frac{2\pi}{I_{\text{cc}}} \right\} r \, d\ell \\ &\quad + \int_{\Gamma_{s\setminus\text{fsi}}} \left[ (t_r^m \delta u_m + t_z^m \delta w_m) \left\{ \frac{2\pi}{I_{\text{cc}}} \right\} + t_\varphi^m \delta v_m \left\{ \frac{2\pi}{I_{\text{ss}}} \right\} \right] r \, d\ell, \end{aligned} \quad (7.205)$$

$$\begin{aligned} I_{\partial\Omega_f^0} &= \int_{\Gamma_{\text{fsi}}} \left[ u_m n_r + w_m n_z - \frac{1}{\omega^2 \rho_f} \left( \frac{\partial p_m^{\text{inc}}}{\partial r} n_r + \frac{\partial p_m^{\text{inc}}}{\partial z} n_z \right) \right] \left\{ \frac{2\pi}{I_{\text{cc}}} \right\} \delta p_m^{\text{scat}} r \, d\ell \\ &\quad + \int_{\Gamma_{f\setminus\text{fsi}}} \frac{1}{\omega^2 \rho_f} \left[ \frac{\partial}{\partial r} (p_m - p_m^{\text{inc}}) n_r + \frac{\partial}{\partial z} (p_m - p_m^{\text{inc}}) n_z \right] \left\{ \frac{2\pi}{I_{\text{cc}}} \right\} \delta p_m^{\text{scat}} r \, d\ell. \end{aligned} \quad (7.206)$$

In (7.205),  $t_r^m$ ,  $t_\varphi^m$ , and  $t_z^m$  represent the modal components of the applied traction vector  $t_i$  in cylindrical coordinates.

## Appendix 2: Farfield Computations

In Cartesian coordinates, the pressure field at a point  $\mathbf{r}$  exterior to a surface  $S_0$  enclosing a finite volume  $V_0$  can be computed from the pressure  $p$  and the normal displacement  $u_n$  sampled on  $S_0$  using the Helmholtz–Kirchhoff integral theorem [64]:

$$p(\mathbf{r}) = \int_{S_0} \left[ \frac{\partial G(\mathbf{r}, \mathbf{r}_0)}{\partial n(\mathbf{r}_0)} p(\mathbf{r}_0) - \rho_f \omega^2 G(\mathbf{r}, \mathbf{r}_0) u_n(\mathbf{r}_0) \right] dS. \quad (7.207)$$

If the quantity of interest is the scattered field, one simply needs to replace  $p$  by  $p^{\text{scat}}$  and  $u_n$  by the scattered-field normal displacement  $u_n^{\text{scat}}$ . If  $S_0$  is the interface between the elastic scatterer, on which  $u_n$  can be sampled from the solution in the elastic domain, and the fluid, one has  $u_n^{\text{scat}} = u_n - u_n^{\text{inc}}$  where  $u_n^{\text{inc}}$  is computed from the incident field gradient via (7.191). The Green’s function  $G(\mathbf{r}, \mathbf{r}_0)$  is the solution of

$$(\nabla^2 + k^2) G(\mathbf{r}, \mathbf{r}_0) = \delta(\mathbf{r} - \mathbf{r}_0), \quad \mathbf{r}, \mathbf{r}_0 \in V, \quad \mathbf{r} \neq \mathbf{r}_0, \quad (7.208)$$

where the volume  $V \supset V_0$  can be the free space, a multilayered medium, an under-water waveguide or any other suitable background configuration. To compute the scattering examples of Sect. 7.6.2 the cases of interest are where  $V$  is a free space, and where  $V$  is a two-layered fluid medium, with  $\mathbf{r}, \mathbf{r}_0$  both contained in the upper medium (see for example Fig. 7.20). The free-space Green’s function is, (2.52),

$$G(\mathbf{r}, \mathbf{r}_0) = \frac{e^{ik|\mathbf{r}-\mathbf{r}_0|}}{4\pi|\mathbf{r}-\mathbf{r}_0|}. \quad (7.209)$$

Using the cylindrical coordinates  $\mathbf{r} = (r, \varphi, z)$  and  $\mathbf{r}_0 = (r_0, \varphi_0, z_0)$ , the solution of (7.208) for the two-layered medium is represented by the plane-wave spectral integral in cylindrical coordinates [68],

$$\begin{aligned} G^{(12)}(\mathbf{r}, \mathbf{r}_0) &= \frac{\epsilon_m}{4\pi} \cos[m(\varphi - \varphi_0)] \int_0^\infty J_m(k_r r) J_m(k_r r_0) \\ &\quad \times \left[ e^{ik_r|z-z_0|} + \mathcal{R}(k_r) e^{ik_r(z+z_0)} \right] \frac{k_r}{k_{z1}} dk_r, \end{aligned} \quad (7.210)$$

where  $z > 0$  (the boundary coincides with the plane  $z = 0$ ),  $k_{z1} = \sqrt{k_1^2 - k_r^2}$  and  $k_1 = \omega/c_f^{(1)}$ . The density and the sound speed in the upper and lower fluids are represented respectively by  $\rho_f^{(1)}$  and  $\rho_f^{(2)}$  and by  $c_f^{(1)}$  and  $c_f^{(2)}$ . The reflection coefficient of each individual plane-wave component in the spectral integral is,

$$\mathcal{R}(k_r) = \frac{\rho_f^{(2)} k_{z1} - \rho_f^{(1)} k_{z2}}{\rho_f^{(2)} k_{z1} + \rho_f^{(1)} k_{z2}} \quad (7.211)$$

with  $k_{z2} = \sqrt{k_2^2 - k_r^2}$  and  $k_2 = \omega/c_f^{(2)}$ . A convenient approximation of (7.210), valid if  $\mathbf{r}$  is not closer than  $\lambda/2$  to the two-fluid interface, is the free-space point source–image point source superposition [68],

$$G^{(12)}(\mathbf{r}, \mathbf{r}_0) \approx G(\mathbf{r}, \mathbf{r}_0) + \mathcal{R}(k_2 \cos \theta) G(\mathbf{r}, \mathbf{r}'_0) \quad (7.212)$$

with  $k = k_1$ . The image point source is located at  $\mathbf{r}'_0 = (r_0, \varphi_0, -z_0)$  and  $\mathcal{R}(k_2 \cos \theta)$  is the plane-wave reflection coefficient at the interface  $z = 0$  for a ray connecting  $\mathbf{r}'_0$  and  $\mathbf{r}$ , which has an angle of incidence  $\theta = \arcsin[(z + z_0)/|\mathbf{r} - \mathbf{r}'_0|]$ . The approximation (7.212) is convenient since it allows to speed up the farfield calculations in the presence of a fluid–fluid interface by avoiding the integration of the full wavenumber spectrum in (7.210).

## Problems

**7.1.** For a two-dimensional finite difference grid of spacing  $h$  in  $x$  and  $y$ , derive an  $O(h^2)$  finite difference approximation to the derivative

$$\frac{\partial^2 u}{\partial x \partial y}.$$

**7.2.** Consider the one-dimensional wave equation

$$\frac{\partial^2 p(x, t)}{\partial x^2} - \frac{1}{c^2} \frac{\partial^2 p(x, t)}{\partial t^2} = 0,$$

subject to the boundary conditions

$$\begin{aligned} p(0, t) &= P(t), \\ \left. \frac{\partial p(x, t)}{\partial x} \right|_{x=D} - \alpha p(D, t) &= 0. \end{aligned}$$

You may assume the sound speed and density is constant for  $x \in [0, D]$ .

- a. Show that the boundary condition at  $x = D$  represents the reflection from a plane interface separating two fluid media.
- b. Assume that  $[0, D]$  represents an acoustic medium with  $c = 1500 \text{ m/s}$  and  $\rho = 1000 \text{ kg/m}^3$ , and that  $D$  represents an interface to an acoustic halfspace with  $c_2 = 1600 \text{ m/s}$  and  $\rho_2 = 1800 \text{ kg/m}^3$ . Find the corresponding value of  $\alpha$ .
- c. Assume that the boundary pressure  $P(t)$  is of the form

$$P(t) = \begin{cases} 0, & t \leq 0 \\ 1 - \cos^2(4\pi tc/D), & t < D/(4c) \\ 0, & t \geq D/(4c). \end{cases}$$

Derive the analytical solution for  $p(x, t)$  for  $t \in [0, 2D/c]$ .

**7.3.** Make a finite difference code for solving the previous problem for  $D = 1500 \text{ m}$ . Choose a simple explicit scheme similar to that described in Sect. 7.3.4.

- a. Perform a numerical convergence analysis and compare your results to the analytical result.
- b. Show that the convergence rate is consistent with the order of the finite difference approximations used.

**7.4.** Assume you want to solve the one-dimensional Helmholtz equation (7.72), with homogeneous boundary conditions  $p(0) = p(D) = 0$ , using FEM with global trial functions.

- a. Determine the set of trial functions which yield a diagonal coefficient matrix for a homogeneous medium.
- b. Determine the FEM solution for a point source at  $x = x_s$  in the case of a homogeneous medium.
- c. Discuss the relation between this solution and the normal mode solution for an ideal waveguide, Sect. 2.4.4.

**7.5.** Consider a fluid waveguide similar to the Pekeris waveguide, but with a continuously varying sound speed  $c(z)$  in the water column.

- a. Using the simple linear elements shown in Fig. 7.7, formulate the FEM equations for the depth-separated wave equation. You may assume the sound speed to be linear (but not constant) within each element.
- b. Discuss the factors affecting the choice of element size for this problem.

- c. Implement the formulation and perform a numerical convergence analysis for the isovelocity Pekeris waveguide. Compare your results to the analytical solution (e.g., by solving (2.182)).

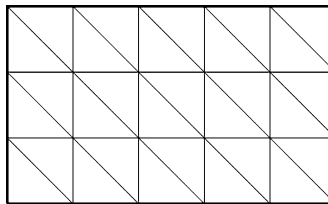
**7.6.** Assume a finite element mesh is composed of triangular elements which are all identical, but rotated versions of the one shown in Fig. 7.9. When setting up the global finite element equations, all node displacements must be aligned with the coordinate axes as shown in Fig. 7.9.

- a. Assume the stiffness matrix  $\mathbf{k}$  for one of the elements has been determined. Show that the stiffness matrix for another, rotated element can be determined by an expression of the form,

$$\mathbf{k}^* = \mathbf{A}^T \mathbf{k} \mathbf{A},$$

- b. Derive the expressions for the coefficients of  $\mathbf{A}$  for an element rotated by an angle  $\theta$ .

**7.7.** Assume you have to write a finite element code solving the Helmholtz equation in a rectangular domain using the following mesh of simple, triangular elements with nodes in the corners:



- a. Describe the strategy you would use for setting up the local element matrices.  
 b. Select a local element numbering for your elements, and determine the global node numbering which yields the minimum bandwidth of the global coefficient matrices.  
 c. Write out the topology matrix  $\mathbf{L}$  corresponding to the numbering you selected.

## References

1. W.A. Kuperman, H. Schmidt, Self-consistent perturbation approach to rough surface scattering in stratified elastic media. *J. Acoust. Soc. Am.* **86**, 1511–1522 (1989)
2. R.B. Evans, A coupled mode solution for acoustic propagation in a waveguide with stepwise depth variations of a penetrable bottom. *J. Acoust. Soc. Am.* **74**, 188–195 (1983)
3. M.D. Collins, R.B. Evans, A two way parabolic equation for acoustic backscattering in the ocean. *J. Acoust. Soc. Am.* **91**, 1357–1368 (1992)
4. G.E. Forsythe, W.R. Wasow, *Finite Difference Methods for Partial Differential Equations* (John Wiley, New York, 1960)
5. G.D. Smith, *Numerical Solution of Partial Differential Equations* (Oxford University Press, London, 1969)

6. G. Dahlquist, Å. Björk, *Numerical Methods* (Prentice Hall, Englewood Cliffs, NJ, 1974)
7. R.A. Stephen, A review of finite difference methods for seismo-acoustics problems at the seafloor. *Rev. Geophys.* **26**, 445–458 (1988)
8. J.R. Fricke, Acoustic scattering from elemental ice features: Numerical modeling results. *J. Acoust. Soc. Am.* **93**, 1784–1796 (1993)
9. N.M. Newmark, A method for computation of structural dynamics. *Proc. Am. Soc. Civ. Eng.* **85**, EM3, 67–94 (1959)
10. Z. Alterman, F.C. Karal Jr., Propagation of elastic waves in layered media by finite difference methods. *Bull. Seism. Soc. Am.* **58**, 367–398 (1968)
11. K.R. Kelly, R.W. Ward, S. Treitel, R.M. Alford, Synthetic seismograms: A finite-difference approach. *Geophysics* **41**, 2–27 (1976)
12. J.R. Fricke, Acoustic scattering from elastic ice: A finite difference solution. Ph.D. thesis. Massachusetts Institute of Technology, Cambridge, MA, 1991
13. D. Gottlieb, M. Gunzberger, E. Turkel, On numerical boundary treatment of hyperbolic systems for finite difference and finite element methods. *SIAM J. Num. Anal.* **19**, 671–682 (1982)
14. R. Kosloff, D. Kosloff, Absorbing boundaries for wave propagation problems. *J. Comput. Phys.* **63**, 363–376 (1986)
15. D. Huang, Finite element solution to the parabolic wave equation. *J. Acoust. Soc. Am.* **84**, 1405–1413 (1988)
16. A.H. Olson, J.A. Orcutt, G.A. Fisher, The discrete wavenumber/finite element method for synthetic seismograms. *Geophys. J. R. Astron. Soc.* **77**, 421–460 (1984)
17. J.E. Murphy, S.A. Chin-Bing, A seismo-acoustic finite element model for underwater acoustic propagation. in *Shear Waves in Marine Sediments*, ed. by J.M. Hovem, M.D. Richardson, R.D. Stoll (Kluwer Academic Publishers, The Netherlands, 1991), pp. 463–470
18. W. Seong, Hybrid Galerkin boundary element – wavenumber integration method for acoustic propagation in laterally inhomogeneous media. Ph.D. thesis. Massachusetts Institute of Technology, Cambridge, MA, 1991
19. O.C. Zienkiewicz, *The Finite Element Method* (McGraw-Hill, London, 1977)
20. C.A.J. Fletcher, *Computational Galerkin Methods* (Springer, New York, 1984)
21. D.S. Burnett, *Finite Element Analysis: From Concepts to Applications* (Addison-Wesley, Reading, MA, 1987)
22. B.G. Galerkin, Series solution of some problems of elastic equilibrium of rods and plates. (in Russian), *Vestn. Inzh. Tech.* **19**, 897–908 (1915)
23. D.S. Burnett, A three-dimensional acoustic infinite element based on a prolate spheroidal multipole expansion. *J. Acoust. Soc. Am.* **96**, 2798–2816 (1994)
24. J.J. Shirron, Solution of exterior Helmholtz problems using finite and infinite elements. Ph.D. thesis. University of Maryland, College Park, MD, 1995
25. J.J. Shirron, I. Babuska, A comparison of approximate boundary conditions and infinite element methods for exterior Helmholtz problems. *Comput. Methods Appl. Mech. Eng.* **164**, 121–139 (1998)
26. J.P. Bérenger, A perfectly matched layer for the absorption of electromagnetic waves. *J. Comput. Phys.* **114**, 185–200 (1994)
27. J.P. Bérenger, Perfectly matched layer for the FDTD solution of wave–structure interaction problems. *IEEE Trans. Antennas Propag.* **44**, 110–117 (1996)
28. F. Collino, P. Monk, The perfectly matched layer in curvilinear coordinates. *SIAM J. Sci. Comput.* **19**, 2061–2090 (1998)
29. E. Turkel, A. Yefet, Absorbing PML boundary layers for wave-like equations. *Appl. Numer. Math.* **27**, 533–557 (1998)
30. Q.H. Liu, Perfectly matched layers for elastic waves in cylindrical and spherical coordinates. *J. Acoust. Soc. Am.* **105**, 2075–2084 (1999)
31. F. Ihlenburg, *Finite Element Analysis of Acoustic Scattering* (Springer, New York, 1998)
32. M. Zampolli, A. Tesei, F.B. Jensen, N. Malm, J.B. Blottman, A computationally efficient finite element model with perfectly matched layers applied to scattering from axisymmetric objects. *J. Acoust. Soc. Am.* **122**, 1472–1485 (2007)

33. J.P. Bérenger, Evanescent waves in PML's: Origin of the numerical reflection in wave–structure interaction problems. *IEEE Trans. Antennas Propag.* **47**, 1497–1503 (1999)
34. J.P. Bérenger, Application of the CFS PML to the absorption of evanescent waves in wave-guides. *IEEE Microw. Wirel. Compon. Lett.* **12**, 218–220 (2002)
35. J.J. Shirron, T.E. Giddings, A finite element model for acoustic scattering from objects near a fluid–fluid interface. *Comput. Methods Appl. Mech. Eng.* **196**, 279–288 (2006)
36. Q.H. Liu, J. Tao, The perfectly matched layer for acoustic waves in absorptive media. *J. Acoust. Soc. Am.* **102**, 2072–2082 (1997)
37. Y.Q. Zeng, Q.H. Liu, A staggered-grid finite-difference method with perfectly matched layers for poroelastic wave equations. *J. Acoust. Soc. Am.* **109**, 2571–2580 (2001)
38. O.B. Matar, V. Preobrazhensky, P. Pernod, Two-dimensional axisymmetric numerical simulation of supercritical phase conjugation of ultrasound in active solid media. *J. Acoust. Soc. Am.* **118**, 2880–2890 (2005)
39. A.D. Pierce, *Acoustics: An Introduction to Its Physical Principles and Applications* (Acoustical Society of America, Melville, NY, 1991)
40. M.C. Junger, D. Feit, *Sound, Structures, and Their Interaction* (MIT, Cambridge, MA, 1972)
41. G.T. Schuster, L.C. Smith, Modeling scatterers embedded in a plane-layered media by a hybrid Haskell–Thomson and boundary integral equation method. *J. Acoust. Soc. Am.* **78**, 1387–1394 (1985)
42. H. Kawase, Time-domain response of a semi-circular canyon for incident SV, P, and Rayleigh waves calculated by the discrete wavenumber boundary element method. *Bull. Seism. Soc. Am.* **78**, 1415–1437 (1988)
43. T.W. Dawson, J.A. Fawcett, A boundary integral equation method for acoustic scattering in a waveguide with nonplanar surfaces. *J. Acoust. Soc. Am.* **87**, 1110–1125 (1990)
44. P. Gerstoft, H. Schmidt, A boundary element approach to seismo-acoustic facet reverberation. *J. Acoust. Soc. Am.* **89**, 1629–1642 (1991)
45. H. Schmidt, S. Krenk, Asymmetric vibrations of a circular elastic plate on an elastic half space. *Int. J. Solids Struct.* **18**, 91–105 (1982)
46. S. Krenk, H. Schmidt, Elastic wave scattering by a circular crack. *Phil. Trans. R. Soc. Lond. A* **308**, 167–198 (1982)
47. P. Stepanishen, A generalized internal source density method for the forward and backward projection of harmonic pressure fields from complex bodies. *J. Acoust. Soc. Am.* **101**, 3270–3277 (1997)
48. A. Sarkissian, Multiple scattering effects when scattering from a target in a bounded medium. *J. Acoust. Soc. Am.* **96**, 3137–3144 (1994)
49. R.T. Kessel, Scattering of elastic waves in layered media: A boundary integral – normal mode method. Ph.D. thesis University of Victoria, Victoria, Canada, 1996
50. F. Ingenito, Scattering from an object in a stratified medium. *J. Acoust. Soc. Am.* **82**, 2051–2059 (1987)
51. H. Schmidt, I. Veljkovic, M. Zampolli, Bistatic scattering from buried targets in shallow water – experiment and modeling. in *Proceedings of 7th ECWA Conference*, ed. by D.G. Simons (Delft University, The Netherlands, 2004), pp. 475–482
52. I. Lucifredi, H. Schmidt, Subcritical scattering from buried elastic shells. *J. Acoust. Soc. Am.* **120**, 3566–3583 (2006)
53. J.A. Fawcett, A scattering-chamber approach for solving finite rough surface scattering problems. *J. Acoust. Soc. Am.* **118**, 1348–1357 (2005)
54. A.T. Abawi, M.B. Porter, Propagation in an elastic wedge using the virtual source technique. *J. Acoust. Soc. Am.* **121**, 1374–1382 (2007)
55. H. Schmidt, J. Glattetre, A fast field model for three-dimensional wave propagation in stratified environments based on the global matrix method. *J. Acoust. Soc. Am.* **78**, 2105–2114 (1985)
56. H. Schmidt, Virtual source approach to scattering from partially buried elastic targets. in *High Frequency Acoustics Conference*, ed. by M.B. Porter, M. Siderius, W.A. Kuperman (AIP, Melville, NY, 2004), pp. 456–463

57. M. Zampolli, A. Tesei, G. Canepa, O.A. Godin, Computing the far-field scattered or radiated by objects inside layered fluid media using approximate Green's functions. *J. Acoust. Soc. Am.* **123**, 4051–4058 (2008)
58. S.G. Kargl, P.L. Marston, Observations and modeling of the backscattering of short tone bursts from a spherical shell: Lamb wave echoes, glory, and axial reverberations. *J. Acoust. Soc. Am.* **85**, 1014–1028 (1989)
59. J.D. Kaplunov, L.Y. Kossovich, E.V. Nolde, *Dynamics of Thin Walled Elastic Bodies* (Academic, San Diego, CA, 1998)
60. H. Schmidt, J. Lee, Physics of 3D scattering by rough interfaces and buried targets in shallow water. *J. Acoust. Soc. Am.* **105**, 1605–1617 (1999)
61. M. Zampolli, A. Tesei, F.B. Jensen, Benchmark problems for acoustic scattering from elastic objects in the free field and near the sea floor. *J. Acoust. Soc. Am.* **125**, 89–98 (2009)
62. J.D. Achenbach, *Wave Propagation in Elastic Solids* (North-Holland, Amsterdam, The Netherlands, 1993)
63. D.S. Burnett, M. Zampolli, FESTA: A 3-D finite element program for acoustic scattering from undersea targets. Rep. SR-394 NATO Undersea Research Center, La Spezia, Italy, 2004
64. A.D. Pierce, Variational formulation in acoustic radiation and scattering, in *Physical Acoustics*, vol. XXII, ed. by A.D. Pierce, R.N. Thurston (Academic, San Diego, CA, 1993)
65. G.C. Everstine, A symmetric potential formulation for fluid–structure interaction. *J. Sound Vib.* **79**, 157–160 (1981)
66. G.C. Everstine, Finite element formulations of structural acoustics problems. *Comput. Struct.* **65**, 307–321 (1997)
67. N.D. Veksler, *Resonance Acoustic Spectroscopy* (Springer, Berlin, 1993)
68. P.M. Morse, K.U. Ingard, *Theoretical Acoustics* (McGraw-Hill, New York, 1968)

# Chapter 8

## Broadband Modeling

### 8.1 Introduction

While time-series analysis and modeling has always been the approach used by geophysicists for studying low-frequency seismic wave propagation in the Earth's crust, underwater acousticians have traditionally favored spectral analysis techniques, which only provide information about the band-averaged energy distribution in space. There are several reasons for choosing this approach in ocean acoustics. Most importantly, the ocean is characterized by high temporal variability, which causes strong (and unpredictable) signal fluctuations for long-range propagation at traditional sonar frequencies. At best, only the mean signal energy seems to have a predictable behavior at these frequencies. However, for some years now, the trend in sonar development has been toward lower frequencies, which should lead to both higher signal stability and better predictability. Consequently, the powerful time-series analysis techniques of geophysics may well become a valuable tool also for studying the complex propagation situations encountered in the ocean.

Work on direct simulation of broadband signal dispersion in ocean waveguides has been under way for some time [1–6]. Within the framework of *linear* acoustics there are fundamentally two approaches to this modeling problem, see Fig. 8.1. The first is to solve the pulse propagation problem via the *frequency domain* by Fourier synthesis of CW (continuous wave) results. This approach is attractive since it requires little programming effort. In fact, any of the time-harmonic acoustic models described earlier in this book can be linked up with a pulse post-processor which numerically performs the Fourier synthesis based on a number of CW calculations within the frequency band of interest. Alternatively, one can solve the problem directly in the *time domain*, which, however, requires the development of an entirely new set of propagation codes.

Since a pulse calculation is typically 2–3 orders of magnitude slower than a single-frequency calculation, computational efficiency becomes of utmost importance in choosing between frequency-domain and time-domain models. Our experience is that most problems of practical importance in underwater acoustics (long-range propagation of pulses of “finite” bandwidth) clearly favor the Fourier synthesis technique. However, there also exist problems for which solutions are more conveniently generated with a time-domain model.

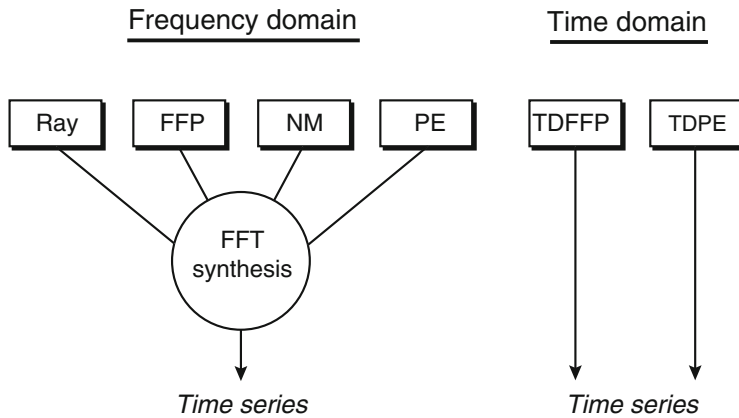


**Fig. 8.1** Schematic of two approaches to broadband modeling

Numerical results for pulse propagation modeling using both Fourier synthesis and time-domain techniques are presented in Sect. 8.5.

## 8.2 Fourier Synthesis of Frequency-Domain Solutions

As described in Chap. 2, the solution of the time-dependent wave equation can be obtained via a Fourier transform of the frequency-domain solution as

$$\begin{aligned}
 p(r, z, t) &= \frac{1}{2\pi} \int_{-\infty}^{\infty} p(r, z, \omega) e^{-i\omega t} d\omega \\
 &= \frac{1}{2\pi} \int_{-\infty}^{\infty} S(\omega) g(r, z, \omega) e^{-i\omega t} d\omega,
 \end{aligned} \tag{8.1}$$

where  $S(\omega)$  is the source spectrum and  $g(r, z, \omega)$  is the spatial transfer function. The main computational effort is associated with generating the transfer function at a number of discrete frequencies within the frequency band of interest. The evaluation of the integral in (8.1) is then done by an FFT at each spatial position  $(r, z)$  for which the pulse response is desired.

The strength of this method clearly lies in its simplicity and versatility. Once a post-processor has been developed for evaluating the integral in (8.1) and providing displays (stacks and snapshots), any existing CW code can be easily interfaced to produce a pulse result. This means that one can always use the most convenient and computationally efficient CW code for a given problem, independent of whether it is based on rays, spectral integrals, normal modes, or parabolic equations (PEs).

Although the Fourier synthesis approach is conceptually simple, there are several numerical issues that must be addressed in relation to the evaluation of the frequency integral. Thus, the necessary truncation and discretization of the integral is

susceptible to all the artifacts of discrete time series analysis, such as windowing and aliasing effects [7]. On the other hand, as described in the following, it is possible to use the physical knowledge of waveguide propagation, together with special numerical devices, to eliminate such artifacts, or at least reduce them to insignificance.

For completeness we write down the time-domain version of (8.1),

$$\begin{aligned} p(r, z, t) &= \frac{1}{2\pi} \int S(t') e^{i\omega t'} g(r, z, t'') e^{i\omega t''} e^{-i\omega t} d\omega dt' dt'' \\ &= \int_{\text{causal}} S(t') g(r, z, t - t') dt', \end{aligned} \quad (8.2)$$

where the last integral is a convolution of the source time function with the retarded time-domain Green's function, meaning that the time at the field point is later than the corresponding source emission time.

### 8.2.1 Evaluation by FFT

In general, the time-domain solution is sought at a large number of time values, typically at equidistant time sampling. It is well-established that the most efficient numerical integration approach for such problems is the Fast Fourier Transform (FFT). The literature is abundant on the properties and implementation of the FFT, (e.g., [7]), and we shall here only review the issues of particular concern to time-domain synthesis in ocean acoustics.

#### 8.2.1.1 Frequency Windowing

The first step in evaluating the frequency integral by means of an FFT is to truncate the integration interval. This is easily done since the frequency content of the signal is predetermined by the source spectrum, i.e., the frequency dependence of  $S(\omega)$ . Thus, assuming that the source does not emit any significant energy above a certain radial frequency  $\omega_{\max}$ , we replace (8.1) by

$$p(r, z, t) = \frac{1}{2\pi} \int_{-\omega_{\max}}^{\omega_{\max}} S(\omega) g(r, z, \omega) e^{-i\omega t} d\omega. \quad (8.3)$$

If  $g(r, z, \omega)$  represents transmission loss pressure, i.e., the solution to (2.83), then  $S(\omega)$  is the frequency spectrum of the source pressure at 1-m distance from the source. It is easily verified by changing the sign convention in the Fourier transform pair in (2.27) and (2.28) that the solutions to the Helmholtz equation are conjugate symmetric, i.e.,  $g(r, z, -\omega) = \overline{g(r, z, \omega)}$ . To yield a real time series,  $S(\omega)$  must also be conjugate symmetric. Thus, an alternative form is

$$p(r, z, t) = \operatorname{Re} \left\{ \frac{1}{\pi} \int_0^{\omega_{\max}} S(\omega) g(r, z, \omega) e^{-i\omega t} d\omega \right\}. \quad (8.4)$$

### 8.2.1.2 Fast Fourier Transforms

Let us assume that the response at a point  $(r, z)$  is sought in a time window of length  $T$ , starting at some time  $t_{\min}$ . The time and frequency axes are then discretized as

$$t_j = t_{\min} + j \Delta t, \quad j = 0, 1 \dots (N - 1), \quad (8.5)$$

$$\omega_\ell = \ell \Delta\omega, \quad \ell = -(N/2 - 1) \dots - 1, 0, 1 \dots (N/2 - 1) \quad (8.6)$$

with the samplings satisfying the relation

$$\Delta t \Delta\omega = \frac{2\pi}{N}. \quad (8.7)$$

With  $T = N\Delta t$ , this relation directly determines the necessary radial frequency sampling as  $\Delta\omega = 2\pi/T$ , or in terms of frequency sampling,

$$\Delta f = \frac{\Delta\omega}{2\pi} = \frac{1}{T}. \quad (8.8)$$

We now replace the integral by a discrete sum. However, according to standard sampling theory, the discretization in frequency introduces periodicity of  $T$  in time ([7], Sect. 3.2), with the result being a time-shifted sum of all the periodic responses,

$$\sum_n p(r, z, t_j + nT) = \frac{\Delta\omega}{2\pi} \sum_{\ell=-(N/2-1)}^{N/2-1} [p(r, z, \omega_\ell) e^{-it_{\min}\omega_\ell}] e^{-i\frac{2\pi\ell j}{N}} \quad (8.9)$$

or, by using the conjugate-symmetric property of the transfer functions,

$$\sum_n p(r, z, t_j + nT) = \frac{\Delta\omega}{2\pi} \operatorname{Re} \left\{ \sum_{\ell=0}^{N/2-1} \epsilon_\ell [p(r, z, \omega_\ell) e^{-it_{\min}\omega_\ell}] e^{-i\frac{2\pi\ell j}{N}} \right\} \quad (8.10)$$

with

$$\epsilon_\ell = \begin{cases} 1 & \text{for } \ell = 0, \\ 2 & \text{for } \ell > 0. \end{cases}$$

The actual response in the selected time window  $[t_{\min}, t_{\min} + T]$  then becomes

$$\begin{aligned} p(r, z, t_j) &= \frac{\Delta\omega}{2\pi} \operatorname{Re} \left\{ \sum_{\ell=0}^{N/2-1} \epsilon_\ell [p(r, z, \omega_\ell) e^{-it_{\min}\omega_\ell}] e^{-i\frac{2\pi\ell j}{N}} \right\} \\ &\quad - \sum_{n \neq 0} p(r, z, t_j + nT), \end{aligned} \quad (8.11)$$

where the last sum represents the *wrap-around* or *aliasing* from the periodic time windows.

If we choose  $N$  to be an integer power of 2, then very efficient algorithms, the so-called *Real Fast Fourier Transforms* (RFFT), are available for evaluating the first sum in (8.11), simultaneously for all  $N$  values of  $t_j$ . Alternatively, we could use a *Complex Fast Fourier Transform* to evaluate (8.9), at twice the computational cost, however, since this transform does not take advantage of the fact that the kernel is conjugate symmetric.

Note that we have not directly related the frequency sampling to the maximum frequency content of the source signal. The reason is that the most critical issue in replacing the continuous Fourier integral with the discrete summation is the aliasing represented by the last summation in (8.11). Thus, since the computational effort associated with the FFT is quite insignificant, it is convenient to properly select the time windowing  $T$  and sampling  $\Delta t$  needed to represent the response at all the receivers. This, in turn, constrains the frequency sampling through (8.8). It is clear, however, that to include the entire spectrum we must have

$$\frac{N\Delta\omega}{2} > \omega_{\max} \quad (8.12)$$

or, in terms of frequency,

$$\frac{N\Delta f}{2} > f_{\max}. \quad (8.13)$$

Using (8.8) it is evident that this inequality is identical to the *Nyquist criterion* for the sampling frequency  $f_s$ ,

$$f_s = \frac{1}{\Delta t} > 2f_{\max}. \quad (8.14)$$

### 8.2.1.3 Time Windowing and Sampling

The selection of the time window is critical due to the aliasing term in (8.11). For computational reasons, it is desirable to choose  $T$  as short as possible since the length of the time window determines the frequency sampling through (8.8). On the other hand, it must be selected large enough that it contains the entire transient response at each receiver so as to eliminate the aliasing. Unfortunately, the onset and duration of the transient response is not only controlled by the source signal, but also by the dispersive nature of the waveguide.

A proper start of the time window  $t_{\min}$  is easily determined from travel time considerations. Thus, for waveguide problems, a conservative estimate for a receiver at range  $r$  is to choose  $t_{\min}$  smaller than or equal to the travel time of a signal propagating at the highest wave speed in the problem, i.e.,

$$t_{\min} \leq \frac{r}{c_{\max}}. \quad (8.15)$$

If we choose  $t_{\min}$  to vary with range through (8.15), we effectively produce a “running” time window. The result is that arrivals propagating at a horizontal speed  $c_{\max}$ , such as the *head waves* described later on in the examples, will appear at the same *reduced time*  $t' = t - r/c_{\max}$  in a range-stacked plot of the time series. Therefore, such reduced-time stackings with varying *reduction velocity* is used routinely in seismology for associating particular arrivals with layers in the Earth stratification [8].

The selection of the time window  $T$  must be done in accordance with the waveguide physics, which clearly makes it quite a subtle issue. A sound approach for long-range waveguide problems dominated by modal propagation is to determine the minimum modal group velocity  $u_{\min}$  in the frequency interval covered by the source spectrum, and select  $T$  such that the signal at the longest range  $r_{\max}$  is included, i.e.,

$$T = t_{\max} - t_{\min} \geq r_{\max} \left[ \frac{1}{u_{\min}} - \frac{1}{c_{\max}} \right]. \quad (8.16)$$

On the other hand, for short-range problems where the continuous spectrum dominates the field, the steep bottom and surface-bounce signals and their multiples will constitute the “tail” of the signal. In such cases, the time window is best determined by trial and error, i.e., by increasing  $T$  until a stable result is obtained. Alternatively, one may use the complex frequency integration technique described below.

Once the time window  $T$  has been selected, we must choose an FFT size  $N$  which properly samples the signal. Here, the Nyquist criterion given in (8.14) must be satisfied. However, this criterion requires only two samples per period at the highest frequency  $f_{\max}$ , which is insufficient to yield a reasonably looking graphical signal display. A more appropriate value of  $\Delta t$  is

$$\Delta t = \frac{T}{N} < \frac{1}{8f_{\max}}, \quad (8.17)$$

which corresponds to more than eight samples per period.

### 8.2.2 Complex Frequency Integration

As mentioned earlier, the determination of a minimum time window via the medium and group velocities in (8.16) does not ensure inclusion of the steep-angle multiples. If these or other late arrivals are of interest, the time window must be extended. Here it should be remembered that the aliasing happens from both sides, and, hence, the initial part of the response must be included as well. For some propagation problems, in particular those involving high-frequency signals, this may lead to substantial computational requirements. Therefore, if such late arrivals are of no interest, it would be desirable to be able to compute only the early part of the signal. This can

be accomplished by using a complex integration approach analogous to the one used for eliminating aliasing for the wavenumber integrals in Chap. 4.

The *complex frequency integration* approach [9] evaluates (8.11) along a contour displaced into the positive imaginary frequency plane,  $\tilde{\omega} = \omega + i\delta$ . Inserting  $\tilde{\omega}$  into (8.11) yields

$$p(r, z, t_j) \simeq \frac{\Delta\omega}{2\pi} e^{\delta t_j} \operatorname{Re} \left\{ \sum_{\ell=0}^{N-1} \epsilon_\ell [p(r, z, \omega_\ell + i\delta) e^{-it_{\min}\omega_\ell}] e^{-i\frac{2\pi\ell j}{N}} \right\} - \sum_{n \neq 0} p(r, z, t_j + nT) e^{-\delta n T}. \quad (8.18)$$

The first summation can still be done by an RFFT, but due to the exponential in the second sum, the aliasing from the later time windows ( $n > 0$ ) is reduced by at least  $e^{-\delta T}$ . On the other hand, this approach magnifies the aliasing from earlier time windows ( $n < 0$ ), and it is therefore crucial to select  $t_{\min}$  such that the earliest possible arrival is included in the window, e.g., using (8.15). Mallick and Frazer [9] have found that  $\delta$  should not be chosen too large in order to avoid artificial arrivals due to the contour displacement. They suggest  $\delta = (\log 50)/T$  to be optimal, yielding a reduction of the wrap-around by a factor 50.

A complication of this approach is clearly that the transfer functions must be evaluated at complex frequencies, and existing frequency-domain propagation models must therefore be modified accordingly to allow for the use of (8.18). On the other hand, since most codes are already using complex arithmetic, the change to complex frequency is a trivial modification. It is clear from the form of (8.18) that the imaginary component of the frequency merely corresponds to an added damping in time, which is then compensated for by the exponential outside the summation.

## 8.3 Time-Domain Solutions

### 8.3.1 Ray Methods

The formulation of ray theory in the time domain has a particularly simple form. Perhaps the easiest way of obtaining the desired result is to start with the single-frequency representation given in Chap. 3 for the contribution of a single eigenray,

$$p(s) = A(s) e^{i\omega \tau(s)}, \quad (8.19)$$

where  $A(s)$  is the amplitude determined by the change in the cross-sectional area of a ray tube and  $\tau(s)$  is the phase delay along a ray path,

$$\tau(s) = \int_0^s \frac{1}{c(s')} ds'. \quad (8.20)$$

We further assume that the loss, and therefore the amplitude term  $A(s)$ , is independent of frequency. For a source with a narrow spectrum centered about some frequency  $f_0$ , we would calculate  $A(s)$  based on the loss obtained at  $f_0$ . Alternatively, if the loss has a simple frequency dependence, then the following derivation will proceed with minor modifications.

As discussed above, a time-domain solution can be obtained by Fourier synthesis as

$$p(s, t) = \frac{1}{2\pi} \int_{-\infty}^{\infty} S(\omega) p(s, \omega) e^{-i\omega t} d\omega, \quad (8.21)$$

where  $S(\omega)$  represents the spectrum of the source. Substituting our ray representation for  $p(s, \omega)$ , we obtain

$$p(s, t) = A(s) \frac{1}{2\pi} \int_{-\infty}^{\infty} S(\omega) e^{-i\omega[t - \tau(s)]} d\omega. \quad (8.22)$$

That is,

$$p[s, t + \tau(s)] = A(s) \frac{1}{2\pi} \int_{-\infty}^{\infty} S(\omega) e^{-i\omega t} d\omega. \quad (8.23)$$

Now, we can recognize the integral as simply the inverse Fourier transform so that

$$p[s, t + \tau(s)] = A(s) S(t) \quad (8.24)$$

or, equivalently,

$$p(s, t) = A(s) S[t - \tau(s)]. \quad (8.25)$$

Thus, the received signal is simply a scaled and delayed replica of the source signal. The scaling factor, i.e., the change in amplitude of the source signal, is determined by the change in the cross-sectional area of a ray tube. In focal regions, the ray result fails in the usual fashion by predicting an infinite intensity.

A key assumption in the above description is that the amplitude  $A(s)$  is purely real. As discussed in Chap. 3, boundary reflections typically cause phase changes. In addition, the wave encounters a  $90^\circ$  phase change as it passes through a caustic. Finally, Gaussian beam tracing creates more general phase changes. In short,  $A(s) = A_r(s) + iA_i(s)$  is generally a complex number. When  $A(s)$  is complex, we require  $A(s, \omega) = A^*(s, -\omega)$ , where  $\omega$  is the angular frequency. This ensures the resulting waveform is purely real. In the simplest case, one assumes  $A(s, \omega) = A_r(s) + i \operatorname{sgn}(\omega) A_i(s)$ , with the frequency dependence entirely embedded in the  $\operatorname{sgn}(\omega)$  function. The generalization of (8.22) to this complex amplitude is:

$$p(s, t) = \frac{1}{2\pi} \int_{-\infty}^{\infty} [A_r(s) + i \operatorname{sgn}(\omega) A_i(s)] S(\omega) e^{-i\omega[t - \tau(s)]} d\omega \quad (8.26)$$

or,

$$p(s, t) = A_r(s) \frac{1}{2\pi} \int_{-\infty}^{\infty} S(\omega) e^{-i\omega[t-\tau(s)]} d\omega + A_i(s) \frac{1}{2\pi} \int_{-\infty}^{\infty} i \operatorname{sgn}(\omega) S(\omega) e^{-i\omega[t-\tau(s)]} d\omega. \quad (8.27)$$

Recall that the Hilbert transform  $\hat{S}(t)$  is a  $90^\circ$  phase change of an arbitrary waveform  $S(t)$ , and is therefore defined by:

$$\hat{S}(t) = \frac{1}{2\pi} \int_{-\infty}^{\infty} -i \operatorname{sgn}(\omega) S(\omega) d\omega. \quad (8.28)$$

Since  $1/(\pi t)$  is the inverse transform of  $-i \operatorname{sgn}(\omega)$ , we may also write the Hilbert transform as the time-domain convolution of the source waveform with  $1/(\pi t)$ , i.e.,

$$\hat{S}(t) = \frac{1}{\pi} \int_{-\infty}^{\infty} \frac{S(t)}{t - \tau} d\tau; \quad (8.29)$$

however, the frequency-domain representation is usually more convenient. In either case,

$$p(s, t) = A_r(s) S[t - \tau(s)] - A_i(s) \hat{S}[t - \tau(s)], \quad (8.30)$$

which implies that the received waveform is a weighted sum of the original waveform and its Hilbert transform, with the weighting determined by the strengths of the real and imaginary parts of the amplitudes. Note that the Hilbert transform produces an acausal signal, reflecting an artifact of ray theory.

Equation (8.30) is the key result showing the form of a single echo or path, including phase changes due to propagation delay, boundary reflections, and caustic phase shifts. In the late 1960s, there was some debate in the literature about the role of such phase changes, culminating in some experiments at sea to verify the effects. The tutorial paper by Tolstoy [10] provides further detail.

We have interpreted ray theory in the time domain through Fourier transforms of the frequency-domain results. One may instead derive a geometric acoustics formulation directly in the time domain. The terms involving inverse powers of  $\omega$  in the ray series are then associated with the propagation of discontinuous waves, as discussed further in [11].

### 8.3.2 Spectral Integral Techniques

The wavenumber integration technique described in Chap. 4 was derived from the wave equation through two transforms: first, a Fourier transform with respect to frequency eliminated the time derivatives and reduced the problem to

the Helmholtz equation; second, a Hankel transform with respect to the range coordinate eliminated range derivatives and further reduced the problem to an ordinary differential equation involving only depth.

In order to derive a time-domain FFP we simply omit the step of Fourier transforming with respect to frequency. Let us go through the steps. We start with the acoustic wave equation in cylindrical coordinates,

$$\rho \nabla \cdot \left( \frac{1}{\rho} \nabla p \right) - \frac{1}{c^2(z)} \frac{\partial^2 p}{\partial t^2} = -\frac{S(t)}{r} \delta(z - z_s, r), \quad (8.31)$$

where  $p(r, z, t)$  is the acoustic pressure as a function of range  $r$ , depth  $z$ , and time  $t$ . In addition,  $S(t)$  is the isotropic point source,  $\rho(z)$  is the density, and  $c(z)$  is the sound speed. To completely specify the problem we require some boundary and initial conditions. We assume that the surface is a pressure-release boundary and that at some sufficiently great depth  $D$ , the boundary can be treated as perfectly rigid, i.e.,

$$p(r, 0, t) = 0, \quad p_z(r, D, t) = 0. \quad (8.32)$$

The subscript here denotes a partial derivative. We furthermore require

$$p(r, z, t) \text{ outgoing as } r \rightarrow \infty. \quad (8.33)$$

Finally, we assume that initially the medium is quiescent, i.e.,

$$p(r, z, 0) = p_t(r, z, 0) = 0. \quad (8.34)$$

The time-domain FFP is obtained by applying a Hankel transform in range to (8.31). Hence, we write

$$p(k_r, z, t) = \int_0^\infty p(r, z, t) J_0(k_r r) r dr, \quad (8.35)$$

which leads to

$$\left[ \rho \frac{\partial}{\partial z} \left( \frac{1}{\rho} \frac{\partial}{\partial z} \right) - k_r^2 - \frac{1}{c^2(z)} \frac{\partial^2}{\partial t^2} \right] p(k_r, z, t) = -S(t) \delta(z - z_s) \quad (8.36)$$

together with the boundary and initial conditions,

$$p(k_r, 0, t) = 0, \quad (8.37)$$

$$p_z(k_r, D, t) = 0, \quad (8.38)$$

$$p(k_r, z, 0) = p_t(k_r, z, 0) = 0. \quad (8.39)$$

Equations (8.36)–(8.39) are the governing equations for the time-marched FFP. If we were to go one step further and factor out an  $\exp(-i\omega t)$  time dependence, we would obtain the usual equations for the time-harmonic FFP described in Chap. 4.

We observe that for any fixed  $k_r$ , (8.36) assumes the form of a vibrating string embedded in an elastic membrane [12]. (It is also a special case of the Klein–Gordon equation in quantum mechanics.) The parameter  $k_r$  then governs the restoring force of the surrounding elastic medium, so that for  $k_r = 0$  we obtain the familiar equation for a vibrating string in free space. Numerically, the problem can be treated by a simple centered-difference scheme as discussed in standard texts for the wave equation.

Equations (8.36)–(8.39) are solved for a sequence of  $k_r$ -values and then the pressure is evaluated using the inverse Fourier–Bessel transform,

$$p(r, z, t) = \int_0^\infty p(k_r, z, t) J_0(k_r r) k_r dk_r. \quad (8.40)$$

As with the time-harmonic FFP, this integral may be evaluated using an FFT, and the same rules apply to the windowing and sampling in the horizontal wavenumber as those described in Chap. 4. The value of  $k_{\max}$  is chosen to sample the highest spatial frequency in the problem. In most purely acoustic problems the evanescent spectrum is insignificant, with the exception of problems with source and receiver at approximately the same depth. Thus, if the source is band-limited with upper frequency  $f_{\max}$  then the shortest wavelength is  $c_{\min}/f_{\max}$  where  $c_{\min}$  is the minimum sound speed present in the problem. So one sets  $k_{\max} = 2\pi f_{\max}/c_{\min}$  to ensure that the pulse is adequately sampled in space. Finer sampling of the pressure field can be obtained by increasing  $k_{\max}$ ; however, for  $|k_r| > k_{\max}$  the kernel essentially vanishes and can simply be zeroed out. Conversely,  $k_{\min}$  is governed by the longest wavelength and, for problems with a low-frequency cutoff, can be set at  $k_{\min} = 2\pi f_{\min}/c_{\max}$ . For a more rigorous description of the wavenumber sampling issues, the reader is referred to Chap. 4.

Unlike the time-harmonic FFP, this integral can normally be performed directly on the real axis. This is because the resulting pressure field is typically limited in space so that the kernel is band-limited. Thus, the kernel is evaluated for  $k_{r,j} = k_{\min} + j\Delta k_r$  where  $\Delta k_r = 2\pi/r_{\max}$  and  $r_{\max}$  is the maximum range to which the pulse will propagate before the calculation is terminated. More detail on the numerical implementation is given in [6].

### 8.3.3 Parabolic Equations

The PE is a one-way or “progressive” wave equation. Time domain solutions may be obtained by straightforward Fourier synthesis as described in Sect. 8.2. An alternative is to directly solve the time-domain wave equation in a form that is amenable to numerical treatment. This has been done by Collins [4, 5] for a linear, high-angle PE based on a Padé series approximation. However, we here present a solution

technique originally derived by McDonald and Kuperman [3] for studying shock propagation – a nonlinear wave phenomenon. By eliminating the nonlinear terms, a progressive time-domain wave equation is obtained which we show reduces to the standard frequency-domain PE derived in Chap. 6.

The starting point for the derivation is (2.9) which we rewrite below retaining only the lowest-order nonlinear term,

$$\frac{\partial^2 \chi}{\partial t^2} = \nabla^2 c^2 (\chi + \beta \chi^2), \quad (8.41)$$

where  $\chi = \rho'/\rho_0$  is the ratio of the acoustic perturbation density to the ambient density, and  $\beta = 1 + (\rho/c)[\partial c(\rho_0)/\partial \rho]$  is the nonlinear parameter of the medium.

Equation (8.41) as derived refers to the rest frame of the medium. Since our goal is to describe pulse propagation, then, in order to follow the evolution of the pulse as it traverses large distances, it is convenient to transfer to a reference frame moving with some average speed  $c_0$ . It will turn out that this average speed corresponds to the average wavenumber which appears in the PE. The total sound speed is then given by

$$c(r, z) = c_0 + c_1(r, z), \quad (8.42)$$

where the spatial dependence of the sound speed is in the small quantity  $c_1(r, z)$ . We use the time derivative in the moving frame,

$$D_t = \frac{\partial}{\partial t} + c_0 \frac{\partial}{\partial r} \quad (8.43)$$

to effect the transformation, where  $r$  is the range variable in the primary direction of propagation, i.e., the direction  $x$  in the discussion associated with (2.7). Note, for example, that a sinusoid in a homogeneous infinite space gives  $D_t \chi = 0$ . We now substitute (8.43) into (8.41) to obtain

$$\left[ \underbrace{D_t - c_0 \frac{\partial}{\partial r}}_a \right]^2 \chi = \left[ \frac{\partial^2}{\partial r^2} + \underbrace{\frac{1}{r} \frac{\partial}{\partial r}}_b + \underbrace{\frac{\partial^2}{\partial z^2}}_c \right] \left[ c_0 + \underbrace{c_1(r, z)}_d \right]^2 \left[ \chi + \underbrace{\beta \chi^2}_e \right], \quad (8.44)$$

where the underbraced quantities within each bracket are assumed to be small. Proceeding from left to right in (8.44), the smallness assumptions have the following physical interpretations: (a) the evolution of the pulse is gradual compared to its transit time past a given point; (b) the gradient scale size in range is much smaller than the total range; (c) the variation in the transverse direction is more gradual than that in range; (d) spatial variations in the sound speed are small; and (e) the nonlinear term is small. We now expand (8.44) keeping only the lowest order in small terms and then integrate with respect to  $r$ ,

$$D_t \chi = -\frac{c_0}{2r} \chi - \frac{\partial}{\partial r} \left( c_1 \chi + \frac{c_0}{2} \beta \chi^2 \right) - \frac{c_0}{2} \int \frac{\partial^2 \chi}{\partial z^2} dr. \quad \text{NPE} \quad (8.45)$$

An attractive feature of the above equation is that each term describes a distinct physical process. The first term on the right side is geometric spreading; the second term is refraction; the third term contains nonlinear effects; and the last is diffraction. Not only have the physical processes been separated, but we have also reduced the problem from second order in time to first order in time.

We refer to the above equation as the nonlinear *progressive* wave equation (NPE); a more formal perturbation-scaling derivation is given in [3]. The linear time domain version (TDPE) is obtained by turning off the nonlinear term,

$$D_t \chi = -\frac{c_0}{2r} \chi - \frac{\partial}{\partial r}(c_1 \chi) - \frac{c_0}{2} \int \frac{\partial^2 \chi}{\partial z^2} dr. \quad \text{TDPE} \quad (8.46)$$

Comparing the above two equations, we note an important feature of nonlinear propagation which is exhibited in the NPE: a finite amplitude disturbance affects the medium (the linear or “acoustic” approximation neglects this effect). That is, substitution of  $c_1 + 0.5 c_0 \beta \chi \equiv c_{\text{NL}}$  for  $c_1$  in TDPE, (8.46) indicates that the nonlinearity can be thought of as an effective perturbation in the local sound speed caused by the propagating wave, a kind of “self-refraction.” When the disturbance is positive/negative, the local propagation speed is increased/decreased. This leads to the well-known nonlinear steepening of initially smooth pulses into shock fronts [13].

The derivation of the progressive wave equations involved the same *paraxial approximation* as used to derive the PE. Hence, we expect that the frequency-domain version of the TDPE should be the PE. Indeed, if we introduce the envelope function  $\psi(r, z)$  which varies slowly with range into the TDPE and let

$$\chi(r, z) = \frac{e^{i(kr - \omega t)}}{\sqrt{r}} \psi(r, z); \quad \omega \equiv k c_0 \quad (8.47)$$

and take the limit of large  $kr$ , we obtain

$$\frac{\partial \psi}{\partial r} = -ik \frac{c_1}{c_0} \psi + \frac{i}{2k} \frac{\partial^2 \psi}{\partial z^2}. \quad (8.48)$$

Equation (8.48) is identical to the standard PE given by (6.9); in the latter let  $n = c_0/(c_0 + c_1)$  and take  $c_1$  small.

## 8.4 Doppler Shift in a Waveguide

Up to this point, we have discussed only solutions to the wave equation for stationary problems, i.e., for the environment and source–receiver configuration fixed throughout the duration of the propagation. However, for real sonar environments,

this is not always a valid assumption. Thus, we shall demonstrate in the following that the problem of a moving source or receiver is of broadband nature, even for a monochromatic CW source.

It is well-known that a moving source and/or receiver in free space results in a frequency Doppler shift which is described by the simple relation obtained from a Galilean transformation [13]. In a waveguide or stratified environment, source–receiver motion results in a more complicated Doppler structure because of multipath phenomena. Here we consider the simplest case: horizontal motion in a range-independent waveguide environment; each horizontal wavenumber component of the acoustic field will undergo a different Doppler shift. Previous waveguide derivations [14, 15] used normal-mode representations for deriving the Doppler-shifted field. Here, we present a simple derivation based on the spectral representation in a form which requires only a very simple modification of an existing wavenumber integration code to incorporate the source–receiver dynamics. The spectral formulation is then translated into a numerically tractable modal formulation.

We start with the wave equation governing the field produced by a moving source in a horizontally stratified ocean, as shown in Fig. 8.2. As we shall see later, once the expression for the field is found for the moving source, it is straightforwardly modified to incorporate receiver motion. The wave equation (2.26) in Cartesian coordinates, with the right-hand-side representing a harmonic point source of time dependence  $\exp(-i\Omega t)$  and moving with a constant horizontal velocity vector  $\mathbf{v}_S$ , is

$$\nabla^2 \psi(\mathbf{r}, z, t) - \frac{1}{c^2} \frac{\partial^2 \psi(\mathbf{r}, z, t)}{\partial t^2} = -\delta(\mathbf{r} - \mathbf{v}_S t) \delta(z - z_S) e^{-i\Omega t}. \quad (8.49)$$

We now apply the Fourier transform in (2.28) to arrive at the inhomogeneous Helmholtz equation,

$$[\nabla^2 + k_\omega^2] \psi(\mathbf{r}, z, \omega) = -\delta(z - z_S) \int \delta(\mathbf{r} - \mathbf{v}_S t) e^{i(\omega - \Omega)t} dt, \quad (8.50)$$

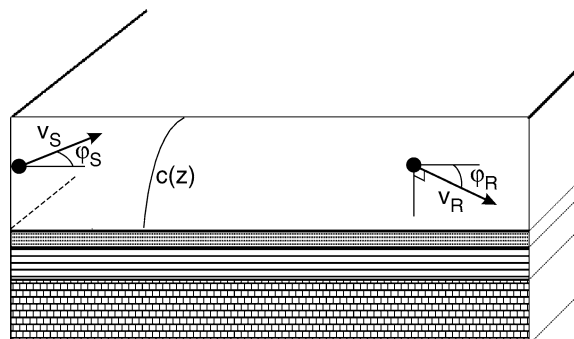


**Fig. 8.2** Horizontally stratified ocean with horizontally moving source and receiver. The source is moving at speed  $v_S$  and bearing  $\varphi_S$ , while the receiver is moving at speed  $v_R$  and bearing  $\varphi_R$ . Vertical motion is ignored

where  $k_\omega$  is the medium wavenumber at frequency  $\omega$ ,  $k_\omega = \omega/c$ . In the following we will first derive the wavenumber integral representation for the solutions to (8.50), followed by the normal mode equivalent.

### 8.4.1 Wavenumber Integral Representation

Because of the source motion, we do not assume the problem to be axisymmetric; rather than the Hankel transforms used in Sect. 2.4, we use a two-dimensional Fourier transform to reduce the spatial dimension of the Helmholtz equation. Thus, we use the transform pair,

$$\psi(\mathbf{r}, z; \omega) = \int \psi(\mathbf{k}_r, z; \omega) e^{i\mathbf{k}_r \cdot \mathbf{r}} d^2 \mathbf{k}_r, \quad (8.51)$$

$$\psi(\mathbf{k}_r, z; \omega) = \frac{1}{(2\pi)^2} \int \psi(\mathbf{r}, z; \omega) e^{-i\mathbf{k}_r \cdot \mathbf{r}} d^2 \mathbf{r} \quad (8.52)$$

to transform (8.50) into the depth-separated wave equation,

$$\begin{aligned} \frac{d^2 \psi(\mathbf{k}_r, z; \omega)}{dz} + [k_\omega^2 - k_r^2] \psi(\mathbf{k}_r, z; \omega) &= -\frac{\delta(z - z_S)}{(2\pi)^2} \int e^{i(\omega - \Omega - \mathbf{k}_r \cdot \mathbf{v}_S)t} dt \\ &= -\frac{\delta(z - z_S)}{2\pi} \delta(\omega - \Omega - \mathbf{k}_r \cdot \mathbf{v}_S), \end{aligned} \quad (8.53)$$

with  $k_r = |\mathbf{k}_r|$ , and where we have used the identities,

$$\int \delta(\mathbf{r} - \mathbf{v}_S t) e^{-i\mathbf{k}_r \cdot \mathbf{r}} d^2 \mathbf{r} = e^{-\mathbf{k}_r \cdot \mathbf{v}_S t} \quad (8.54)$$

and

$$\frac{1}{2\pi} \int e^{i(\omega - \Omega - \mathbf{k}_r \cdot \mathbf{v}_S)t} dt = \delta(\omega - \Omega - \mathbf{k}_r \cdot \mathbf{v}_S). \quad (8.55)$$

Equation (8.53) is a standard depth-separated wave equation of the form given in (4.3), with the solution

$$\psi(\mathbf{k}_r, z; \omega) = \delta(\omega - \Omega - \mathbf{k}_r \cdot \mathbf{v}_S) g(k_r, z; \omega) \quad (8.56)$$

with  $g(k_r, z; \omega)$  being the depth-dependent Green's function for the waveguide at frequency  $\omega$ , satisfying (2.92), and being determined for arbitrary stratifications by any of the methods described in Chap. 4.

The time-domain solution then follows by evaluation of the inverse Fourier transforms in (8.51) and (2.27),

$$\psi(\mathbf{r}, z, t) = \frac{1}{2\pi} \int e^{-i\omega t} d\omega \int \psi(\mathbf{k}_r, z, \omega) e^{i\mathbf{k}_r \cdot \mathbf{r}} d^2 \mathbf{k}_r, \quad (8.57)$$

which by insertion of (8.56) reduces to

$$\psi(\mathbf{r}, z, t) = \frac{1}{2\pi} \int g(k_r, z; \Omega + \mathbf{k}_r \cdot \mathbf{v}_S) e^{-i[(\Omega + \mathbf{k}_r \cdot \mathbf{v}_S)t - \mathbf{k}_r \cdot \mathbf{r}]} d^2 \mathbf{k}_r. \quad (8.58)$$

Thus, in evaluating the integral, we simply have to compute the depth-dependent Green's function for each wave vector  $\mathbf{k}_r$  at the frequency

$$\omega = \Omega + \mathbf{k}_r \cdot \mathbf{v}_S. \quad (8.59)$$

Equation (8.59) represents the *Doppler frequency shift* for each wavenumber component of the field resulting from a moving harmonic source. Now, it is clear that since the expression in (8.58) represents the field at all range vectors  $\mathbf{r}$ , we can straightforwardly modify it to include the receiver motion. Thus, the range vector for a receiver at position  $\mathbf{r}_0$  at time  $t = 0$ , and moving with a velocity vector  $\mathbf{v}_R$ , is given by  $\mathbf{r} = \mathbf{r}_0 + \mathbf{v}_R t$ . Insertion of this into (8.58) yields

$$\psi(\mathbf{r}_0 + \mathbf{v}_R t, z, t) = \frac{1}{2\pi} \int g(k_r, z; \Omega + \mathbf{k}_r \cdot \mathbf{v}_S) e^{-i[(\Omega + \mathbf{k}_r \cdot (\mathbf{v}_S - \mathbf{v}_R))t - \mathbf{k}_r \cdot \mathbf{r}_0]} d^2 \mathbf{k}_r. \quad (8.60)$$

Here, it is interesting to note the asymmetry between source and receiver motion. Thus, whereas both source and receiver motion yield a frequency shift through the exponential, only the source motion affects the integration kernel, i.e., the depth-dependent Green's function. Therefore, reciprocity does not hold for moving sources and receivers! Also note that, as expected, no Doppler shift is observed if source and receiver are moving at identical velocities, but the kernel is still affected, in a non-reciprocal way.

Therefore, the field observed at a receiver moving with the same speed and direction as the source is different from the field observed in the stationary case, a fact which is rarely appreciated when interpreting experimental data. On the other hand, as we shall demonstrate, this effect is rather small, making the static approximation valid for most realistic source–receiver motions. A joint source–receiver motion is clearly equivalent to stationary sources and receivers in a moving medium.

Even though (8.60) represents the field by a wavenumber integral, this expression is not well-suited for direct numerical implementation. The reason is that the source–receiver dynamics couples the time and wavenumber through the argument to the exponential function, requiring the integral to be evaluated for each individual time value. However, it turns out that this time–wavenumber coupling is closely tied to the formulation in the *source's* frame of reference, i.e. in terms of a harmonic source excitation of frequency  $\Omega$ , resulting in each received

wavenumber component to be of different frequency. Thus, as shown by Schmidt and Kuperman [16] a much simpler, and numerically tractable, formulation is achieved by assuming the source to have a finite bandwidth (which is obviously realistic) and transforming the field expression in (8.60) into the *receiver's* frame of reference. For a source with finite bandwidth  $S(\Omega)$ , the field at the receiver is simply determined by a Fourier integral of the above expression,

$$\begin{aligned}\psi(\mathbf{r}_0 + \mathbf{v}_R t, z, t) &= \frac{1}{4\pi^2} \int S(\Omega) d\Omega \\ &\times \int G(k_r, z; \Omega + \mathbf{k}_r \cdot \mathbf{v}_S) e^{-i[(\Omega + \mathbf{k}_r \cdot (\mathbf{v}_S - \mathbf{v}_R))t - \mathbf{k}_r \cdot \mathbf{r}_0]} d^2 \mathbf{k}_r.\end{aligned}\quad (8.61)$$

In the receiver's frame of reference the frequency spectrum of the field at the receiver now follows by applying the Fourier transform in (2.28) to (8.61),

$$\begin{aligned}\psi(\mathbf{r}_0 + \mathbf{v}_R t, z, \omega) &= \int e^{i\omega t} \psi(\mathbf{r}_0 + \mathbf{v}_R t, z, t) dt \\ &= \frac{1}{4\pi^2} \int S(\Omega) d\Omega \int e^{i\mathbf{k}_r \cdot \mathbf{r}_0} G(k_r, z; \Omega + \mathbf{k}_r \cdot \mathbf{v}_S) d^2 \mathbf{k}_r \\ &\quad \times \int e^{-i[\Omega - \omega + \mathbf{k}_r \cdot (\mathbf{v}_S - \mathbf{v}_R)]t} dt \\ &= \frac{1}{2\pi} \int e^{i\mathbf{k}_r \cdot \mathbf{r}_0} d^2 \mathbf{k}_r \\ &\quad \times \int S(\Omega) G(k_r, z; \Omega + \mathbf{k}_r \cdot \mathbf{v}_S) \delta[\Omega - \omega + \mathbf{k}_r \cdot (\mathbf{v}_S - \mathbf{v}_R)] d\Omega \\ &= \frac{1}{2\pi} \int e^{i\mathbf{k}_r \cdot \mathbf{r}_0} S(\Omega_k) G(k_r, z; \omega + \mathbf{k}_r \cdot \mathbf{v}_R) d^2 \mathbf{k}_r,\end{aligned}\quad (8.62)$$

where  $\Omega_k$  is the Doppler-shifted source frequency,

$$\Omega_k = \omega - \mathbf{k}_r \cdot (\mathbf{v}_S - \mathbf{v}_R).\quad (8.63)$$

Equation (8.62) represents stationary frequency components of the field in the receiver's frame of reference, with the time-domain response following by evaluation of the inverse Fourier transform in (2.27). Thus, simply by transforming into the receiver's frame of reference, i.e., changing from a representation in terms of “source frequency”  $\Omega$  in (8.61) to a representation in terms of “receiver frequency”  $\omega$ , the coupling between time and wavenumber has been eliminated. As a result, the wavenumber and frequency integrations are performed independently, as in the static case. In fact, the differences introduced by the dynamics are rather trivial. The first concerns the source spectrum  $S(\Omega_k)$  which is wavenumber-independent in the static case and therefore in that case may be applied outside the wavenumber integral, as part of the Fourier synthesis; the other difference is the change in frequency-argument to the depth-dependent Green's function. We will later discuss the physical significance of these differences.

In spite of its extraordinary simplicity, (8.62) is *exact* within the limitations of the linear theory of acoustics. Thus, the only assumption made is that source and receiver are moving at constant speeds.

Unfortunately, the evaluation of the two-dimensional wavenumber integral in (8.62) is computationally intensive. However, in underwater acoustics the range separation of the source and receiver is usually large compared to the track of each during the time duration of the signal. The angles  $\varphi_S$  and  $\varphi_R$  between the velocity vectors of the source and receiver, respectively, and the radial vector connecting them, can therefore be considered constant, and we can replace the 2-D Fourier integral in (8.62) by a Hankel transform representation in the horizontal wavenumber [17], i.e.,

$$\begin{aligned}\psi(\mathbf{r}_0 + \mathbf{v}_R t, z, \omega) &\simeq \int_0^\infty S(\Omega_k) G(k_r, z; \omega + k_r v_R \cos \varphi_R) J_0(k_r r_0) k_r dk_r \\ &= \frac{1}{2} \int_{-\infty}^\infty S(\Omega_k) G(k_r, z; \omega + k_r v_R \cos \varphi_R) H_0^{(1)}(k_r r_0) k_r dk_r\end{aligned}\quad (8.64)$$

with

$$\Omega_k = \omega - k_r(v_S \cos \varphi_S - v_R \cos \varphi_R). \quad (8.65)$$

Using this approximation it is straightforward to modify an existing wavenumber integration code to compute the Doppler-shifted acoustic field. The only change needed is to compute the depth-dependent Green's function at the shifted frequency  $\omega + k_r v_R \cos \varphi_R$  for every wavenumber  $k_r$  considered, and multiply it by the source spectrum at the shifted frequency  $\Omega_k$ . The resulting dynamic transfer functions are then transformed into the time-domain response by standard Fourier synthesis.

#### 8.4.2 Normal Mode Representation

Based on the spectral representations given above it is now straightforward to proceed to the normal-mode representation of the Doppler-shifted discrete part of the acoustic field. Ignoring the branch line contribution, the depth-dependent Green's function can be written in terms of normal modes through (5.41),

$$G(k_r, z; \omega) \simeq \frac{1}{2\pi\rho(z_S)} \sum \frac{\Psi_n(z) \Psi_n(z_S)}{k_r^2 - k_n^2}, \quad (8.66)$$

where  $k_n$  are the eigenvalues of the homogeneous form of (8.53), and  $\Psi_n$  are the associated eigenvectors. We can now replace the kernel in (8.64) by the modal expansion in (8.66), but with the wavenumber  $k_n$  replaced by the eigenvalues  $k_n^*$  at the Doppler-shifted frequency  $\omega + k_n v_R \cos \varphi_R$ , i.e. for  $v_R/c \ll 1$ ,

$$k_n^* \simeq k_n \left( 1 + v_R \cos \varphi_R \frac{dk_n}{d\omega} \right) = k_n \left( 1 + \frac{v_R}{u_n} \cos \varphi_R \right), \quad (8.67)$$

where  $u_n$  is the *group velocity* of the  $n$ th mode at angular frequency  $\omega$ . The wave-number integral in (8.64) can then, in analogy to the static case, be replaced by the modal sum,

$$\begin{aligned}\psi(\mathbf{r}_0 + \mathbf{v}_R t, z, \omega) &\simeq \frac{i}{4\rho(z_S)} \sum_n S(\Omega_n) \\ &\quad \times \Psi_n(z) \Psi_n(z_S) H_0^{(1)} \left[ k_n r_0 \left( 1 + \frac{v_R}{u_n} \cos \varphi_R \right) \right],\end{aligned}\quad (8.68)$$

where

$$\begin{aligned}\Omega_n &= \omega - k_n (v_S \cos \varphi_S - v_R \cos \varphi_R) \\ &= \omega \left( 1 - \frac{v_S}{v_n} \cos \varphi_S + \frac{v_R}{v_n} \cos \varphi_R \right)\end{aligned}\quad (8.69)$$

with  $v_n = \omega/k_n$  being the modal *phase velocity*. Here, it is assumed that the change in modal eigenfunctions is negligible. Further, this expression ignores any modal cutoff effects introduced by the Doppler shift, and as such (8.68) represents another level of approximation compared to the spectral representation in (8.64). The physical interpretation of the dynamic effects is very simple in the modal approximation. It is clear from (8.69) that the Doppler shift in observed frequency is associated with the horizontal *phase velocity* of the individual modes. Since each mode is a result of the constructive interference of up- and downgoing plane waves with distinct grazing angles  $\theta_n = \arccos(k_n/k_w)$ , different modes clearly have different phase velocities and therefore different Doppler shifts.

The source–receiver dynamics also yields a perturbation in the interference associated with the change in the modal propagation wavenumbers in (8.67). It is clear from (8.68) that this change in modal eigenvalue can alternatively be interpreted as a change in range. With this observation we can easily interpret this effect physically as being associated with the different distances the modes are traveling from being launched at the source to being received at the receiver, due to their different *group velocities*. Here, it is interesting to note that this effect only involves the receiver motion. However, this asymmetry, which is the reason for the earlier discussed lack of reciprocity, actually makes sense physically. Assume the source function is a delta function in time, i.e.,  $S(\Omega) \equiv 1$ . All modes in the waveguide will then be excited at the same instance in time, and their arrival time and therefore relative phase will be unaffected by the continued source motion. Therefore, if the receiver is at rest, the arrival time, and therefore relative phase, of the modes is independent of the source dynamics. On the other hand, if the receiver is moving, it will pick up the individual modal arrivals at different points in space due to their different group velocities. As a result, the relative phase between the modes is affected, reflected through the change in observed modal wavenumber given in (8.67). This *wavenumber Doppler shift* was ignored in the Doppler formulation of Fawcett and Maranda [18], but as is clear from (8.68) and (8.69), this effect can be equally important to the *frequency Doppler shift*, depending on the ratio between the relative source–receiver speed and the receiver speed itself.

It is easily verified that for a stationary receiver and a moving, monochromatic source,  $S(\Omega) = \delta(\Omega - \Omega_0)$ , the Fourier transform of (8.69) becomes identical to the expressions derived by Guthrie et al. [14] and Hawker [15] for this special case. Their results could also be derived by directly replacing the wavenumber integral in (8.58) by its modal expansion.

Next, we derive a simple modification of the adiabatic mode expansion, incorporating the source–receiver dynamics. This is easily done heuristically, based on the physical interpretation of the two effects of the dynamics stated above. For the static case, the adiabatic expansion of the field produced by a source of strength  $S(\omega)$  directly follows from (5.279) as,

$$\psi(r, z, \omega) \simeq \frac{iS(\omega)e^{-i\pi/4}}{\rho(z_S)\sqrt{8\pi}} \sum_n \Psi_n(z) \Psi_n(z_S) \frac{e^{i\int_0^r k_n(r') dr'}}{\sqrt{\int_0^r k_n(r') dr'}}. \quad (8.70)$$

Now it is clear from the above that the frequency Doppler shift depends on the phase velocities at the source and receiver, whereas the phase shift is associated with the different ranges the modes are traveling before reaching the moving receiver. Based on this observation, the adiabatic result directly follows as,

$$\psi(\mathbf{r}_0 + \mathbf{v}_R t, z, \omega) \simeq \frac{ie^{-i\pi/4}}{\rho(z_S)\sqrt{8\pi}} \sum_n S(\Omega_n^*) \Psi_n(z) \Psi_n(z_S) \frac{e^{i\int_0^{r_n^*} k_n(r') dr'}}{\sqrt{\int_0^{r_n^*} k_n(r') dr'}}, \quad (8.71)$$

where

$$\Omega_n^* = \omega \left( 1 - \frac{v_S}{v_n(0)} \cos \varphi_S + \frac{v_R}{v_n(r_0)} \cos \varphi_R \right) \quad (8.72)$$

and  $r_n^*$  is the perturbed ranges for the phase integrals,

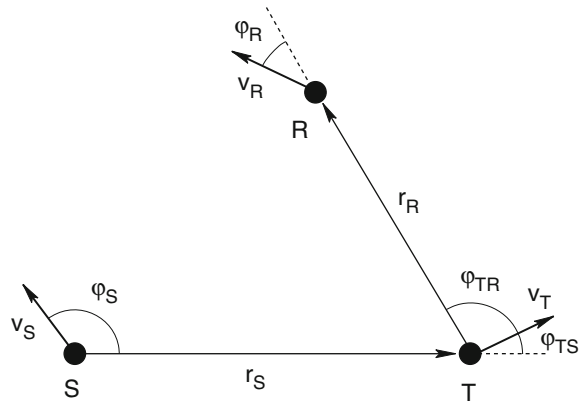
$$r_n^* = r_0 \left( 1 + \frac{v_R}{u_n(r_0)} \cos \varphi_R \right). \quad (8.73)$$

The modification of existing normal mode codes to account for the source–receiver dynamics is equally simple to the one described above for wavenumber integration codes.

### 8.4.3 *Doppler Shift for Active Sonar*

While Doppler shift plays some role in passive sonar systems by shifting frequency lines in the target spectrum, the effect is far more important for active sonar, where the transmitted signal is known exactly. A computationally efficient approach to modeling the active Doppler problem is easily derived using the modal formulation in the receiver’s frame of reference, described above.

**Fig. 8.3** Geometry of bistatic, active sonar configuration where the source S, the target T, and the receiver R all move with different speeds and in different directions



Consider the bistatic scenario shown in Fig. 8.3, where an acoustic source  $S$  with heading  $\varphi_S$  relative to target direction and speed  $v_S$  is transmitting an acoustic pulse with frequency spectrum  $S(\Omega)$ . A target  $T$  is moving at speed  $v_T$  and heading  $\varphi_{TS}$  relative to the direction from the source at range  $r_S$ , and heading  $\varphi_{TR}$  relative to the direction to the receiver at range  $r_R$ , corresponding to a bistatic scattering angle  $\varphi = \varphi_{TS} + \varphi_{TR}$ . The receiver  $R$  is moving at speed  $v_R$  on relative heading  $\varphi_R$ .

Taking the starting point in the receiver's frame of reference and considering the target scattering into mode number  $n$  as the source, the corresponding modal representation of the field at the receiver is given by (8.68),

$$\psi(\mathbf{r}_R + \mathbf{v}_R t, z, \omega) \simeq \frac{i}{4\rho(z_T)} \sum_n S_n(\Omega_n) \Psi_n(z) \Psi_n(z_T) H_0^{(1)}(k_n^* r_R), \quad (8.74)$$

where  $S_n(\Omega_n)$  is the modal excitation of mode number  $n$  by the target at frequency

$$\Omega_n = \omega - k_n(v_T \cos \varphi_{TR} - v_R \cos \varphi_R) \quad (8.75)$$

and the Doppler-shifted modal wavenumber for mode  $n$  is, from (8.67),

$$k_n^* = \left( 1 + \frac{v_R}{u_n} \cos \varphi_R \right). \quad (8.76)$$

Let the bistatic modal scattering matrix for the target at frequency  $\omega$  and bistatic angle  $\varphi$  be denoted  $M_{mn}(\omega, \varphi)$ . Then, the excitation of mode  $n$  by the target scattering for the mode- $m$  component of the incident field is,

$$S_n(\Omega_n) \simeq \frac{i}{4\rho(z_S)} \sum_m S(\Omega_{mn}) M_{mn}(\Omega_n, \varphi) \Psi_m(z_T) \Psi_m(z_S) H_0^{(1)}(k_{mn}^* r_S). \quad (8.77)$$

Here,  $S(\Omega_{mn})$  is the spectral density at the Doppler-shifted frequency for the mode  $n - m$  combination,

$$\begin{aligned}\Omega_{mn} &= \Omega_n - k_m (v_S \cos \varphi_S - v_T \cos \varphi_{TS}) \\ &= \omega - k_n (v_T \cos \varphi_{TR} - v_R \cos \varphi_R) - k_m (v_S \cos \varphi_S - v_T \cos \varphi_{TS}),\end{aligned}\quad (8.78)$$

and  $k_{mn}^*$  is the wavenumber for mode  $m$  at the bistatically Doppler-shifted frequency,

$$\begin{aligned}\omega_{mn}^* &= \Omega_n + k_m v_T \cos \varphi_{TS} \\ &= \omega - k_n (v_T \cos \varphi_{TR} - v_R \cos \varphi_R) + k_m v_T \cos \varphi_{TS},\end{aligned}\quad (8.79)$$

which, analogous to (8.67), is derived as,

$$\begin{aligned}k_{mn}^* &= k_m + (\omega_{mn}^* - \omega) \frac{dk_m}{d\omega} \\ &= k_m \left( 1 + v_T \cos \varphi_{TS} \frac{dk_m}{d\omega} \right) - k_n (v_T \cos \varphi_{TR} - v_R \cos \varphi_R) \frac{dk_m}{d\omega} \\ &= k_m \left( 1 + \frac{v_T}{u_m} \cos \varphi_{TS} \right) - k_n \frac{v_T \cos \varphi_{TR} - v_R \cos \varphi_R}{u_m}.\end{aligned}\quad (8.80)$$

As is clear from (8.77), the Doppler compensation for the *bistatic* configuration can be accounted for simply by replacing the static product of the source spectrum and the modal target scattering function,  $S(\omega) M_{mn}(\omega, \varphi)$ , by the Doppler-shifted product  $S(\Omega_{mn}) M_{mn}(\Omega_n, \varphi)$ , and using the Doppler-shifted wavenumbers in (8.76) and using (8.80) in the arguments to the Hankel functions for the scattered and incident modes. Thus, any off-the-shelf modal code is easily modified to handle general dynamic, bistatic configurations.

For *monostatic* configurations, the following geometric identities are determined from Fig. 8.3,

$$\begin{aligned}v_R &= v_S, \\ r_R &= r_S, \\ \varphi_R &= \pi - \varphi_S, \\ \varphi_{TR} &= \pi - \varphi_{TS},\end{aligned}$$

which, inserted into (8.74) and (8.77) yields,

$$\psi(\mathbf{r}_S + \mathbf{v}_S t, z, \omega) \simeq \frac{i}{4\rho(z_T)} \sum_n S_n(\Omega_n) \Psi_n(z_S) \Psi_n(z_T) H_0^{(1)}(k_n^* r_S) \quad (8.81)$$

and

$$S_n(\Omega_n) \simeq \frac{i}{4\rho(z_S)} \sum_m S(\Omega_{mn}) M_{mn}(\Omega_n, \pi) \Psi_m(z_T) \Psi_m(z_S) H_0^{(1)}(k_{mn}^* r_S) \quad (8.82)$$

with the monostatically Doppler-shifted frequency for the scattered mode number  $n$  being,

$$\Omega_n = \omega + k_n (v_T \cos \varphi_{TS} - v_S \cos \varphi_S). \quad (8.83)$$

The corresponding Doppler-shifted modal wavenumber is,

$$k_n^* = \left( 1 - \frac{v_S}{u_n} \cos \varphi_S \right) \quad (8.84)$$

and the Doppler-shifted frequencies and wavenumbers for the incident field are,

$$\Omega_{mn} = \omega + (k_m + k_n) (v_T \cos \varphi_{TS} - v_S \cos \varphi_S), \quad (8.85)$$

$$k_{mn}^* = k_m + (k_m + k_n) \frac{v_T}{u_m} \cos \varphi_{TS} - k_n \frac{v_S}{u_m} \cos \varphi_S. \quad (8.86)$$

## 8.5 Numerical Examples

This section presents a few examples of the kind of detailed insight into ocean-acoustic propagation which can be achieved only through time-series analysis. The geophysics literature is replete with references showing that even extremely complicated arrival structures in heterogeneous fluid–elastic environments can be completely untangled by exploiting the different propagation characteristics of the various wave types. Thus, it is often possible to explicitly identify compressional ( $p$ ) and shear bulk waves ( $sh$ ,  $sv$ ), various converted components of these waves, head waves, guided  $p$  and  $s$  modes, interface waves, etc. For illustrative examples we refer the reader to two recent publications dealing with the modeling aspect of seismic wave propagation: Schmidt and Tango [8] describe a pulse modeling technique for horizontally stratified media based on the wavenumber integration technique (Chap. 4) combined with Fourier synthesis; Dougherty and Stephen [19] present time-domain finite-difference solutions for range-dependent elastic media.

We shall concentrate on some fundamental aspects of acoustic propagation in both shallow and deep water. The problems are solved both in the time domain and via Fourier synthesis, and results are presented either as stacked time series versus range or depth, or as snapshots at fixed times.

### 8.5.1 The Head-Wave Problem

As shown in Fig. 8.4 we first consider a simple acoustic problem involving two lossless fluid halfspaces of equal density but with different sound speeds, 1500 and 2500 m/s. A point source located 50 m above the interface emits a wavelet given by

$$S(t) = \begin{cases} \sin(\omega_c t) - \frac{1}{2} \sin(2\omega_c t) & \text{for } 0 < t < 1/f_c \\ 0 & \text{else} \end{cases}. \quad (8.87)$$

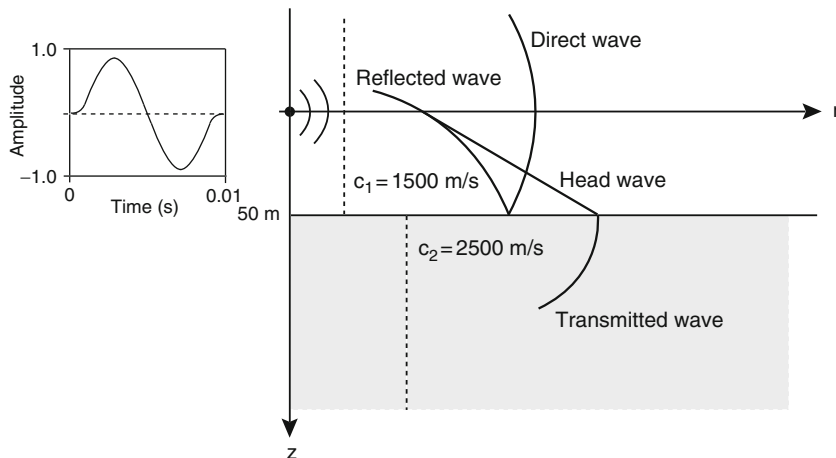


**Fig. 8.4** Schematic of the head-wave problem

This waveform is shown as an inset in Fig. 8.4 for a center frequency of 100 Hz. Also shown in the figure are the four distinct *wavefronts* expected to emerge after the pulse interacts with the sound-speed discontinuity 50 m below the source.

The computed time evolution of the field is plotted in Fig. 8.5 as a sequence of snapshots from 20 to 120 ms. Note that the pressure has been normalized so that the maximum is unity, and it has also been multiplied by a factor of  $\sqrt{r}$  to compensate for cylindrical spreading. In the initial frame, Fig. 8.5a, we see a spherical wave since the pulse has not yet contacted the interface. In Fig. 8.5b the pulse has interacted with the lower halfspace, and both a reflected (R) and a transmitted wave (T) are clearly visible. Since the sound speed is higher in the lower halfspace, the pulse is longer in the bottom than in the top. The transmission coefficient is less than unity so that the transmitted wave shows a decreased amplitude relative to the direct wave. Moreover, the reflected wave shows a critical-angle effect which causes a reduced amplitude at steep angles (beyond 53°).

In Fig. 8.5c, we see that the wave in the lower halfspace has pulled ahead of the direct wave due to the greater wave speed in the bottom. Note that we have changed the scale in order to highlight the weak *head-wave* arrival. The wave front of the head wave (H) is clearly visible forming a line segment starting from the transmitted wave in the lower halfspace touching tangentially the reflected wave front. (This is indicated schematically in Fig. 8.4.) While the reflected and transmitted waves both show the positive leader and negative trailer of the original wavelet, the head wave is an integrated version of the source wavelet and therefore has roughly the form of a pseudo-Gaussian pulse. (We refer the reader to the text of Aki and Richards [20] for a readable mathematical analysis of the head wave.)

It is clear from Fig. 8.5c that the head wave is the first arrival only near the interface in the upper medium. Further away from the interface, the direct wave is the first arrival, followed by the head wave and the reflected wave. Finally, there is a

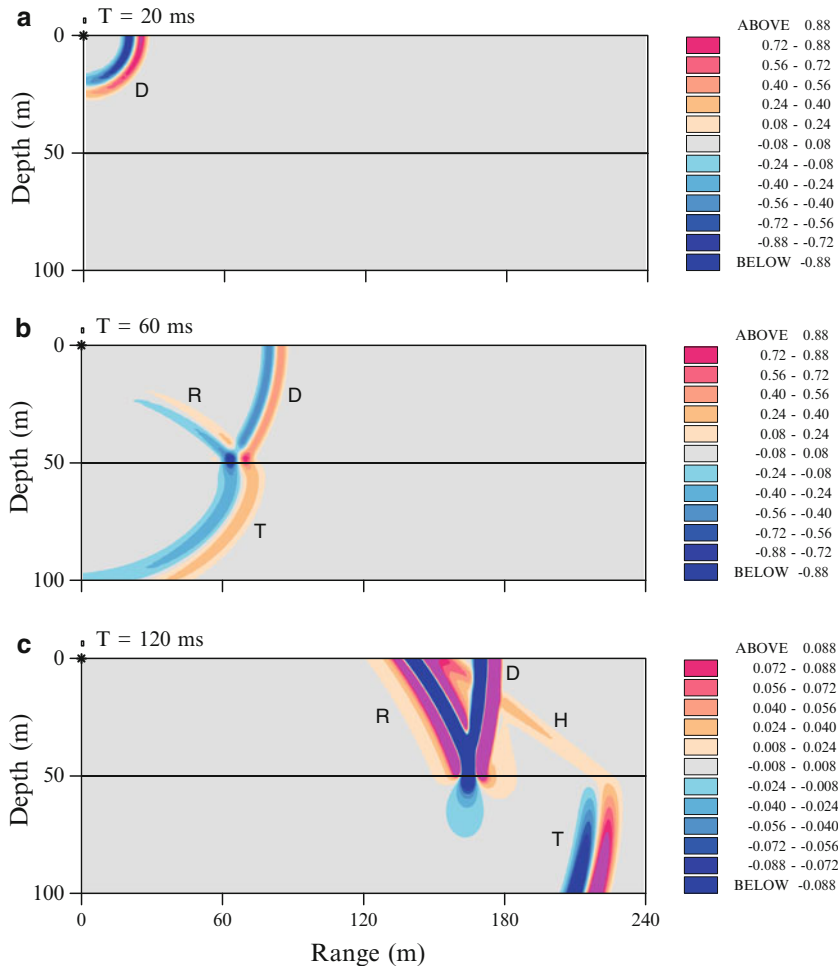


**Fig. 8.5** Snapshots of the pulse at 20, 60, and 120 ms showing the spatial positions of the direct wave (D), the reflected wave (R), the transmitted wave (T), and the head wave (H)

region where the head wave is not noticeable at all since it arrives coincident with the reflected wave. Again, it should be emphasized that the head wave is weakly excited, with an amplitude that is just a few percent of the amplitude of the direct wave. Note, however, that the amplitude of the head wave increases as we move away from the interface toward the point of contact with the reflected wave.

The head-wave problem was solved directly in the time domain using a time-marched FFP technique developed by Porter [6].

### 8.5.2 Mode Dispersion in a Waveguide

We next consider a shallow-water waveguide of the Pekeris type, i.e., a homogeneous water column overlying a homogeneous fluid bottom. The environmental parameters are given in Fig. 8.6. Note that we have introduced a bottom density of  $1500 \text{ kg/m}^3$  and an attenuation of  $0.2 \text{ dB}/\lambda$ .

Before presenting pulse results, we briefly discuss the important issue of signal dispersion in a waveguide. As shown in Chap. 5, a waveguide of this type supports modal propagation, where each mode is characterized by both a distinct shape function  $\Psi_m(z)$  and a distinct horizontal wavenumber  $k_m$ . The wavenumber relates to the *phase velocity* through  $v_m = \omega/k_m$ , where  $\omega = 2\pi f$  is the angular frequency. The modal phase velocity is the speed at which a constant phase front propagates horizontally through the waveguide. Each mode has a different phase velocity, and the phase velocity for a given mode varies with frequency. This latter effect is called *dispersion*. Since the dispersion considered here is solely due to the geometry of the waveguide, it is called *geometrical dispersion*. There also exists a small *intrinsic dispersion* in all real media with attenuation. The phase speed then is (weakly) frequency-dependent even in homogeneous environments without boundaries.

The more important quantity for describing pulse propagation in a waveguide is the *group velocity*

$$u_m = \frac{d\omega}{dk_m}, \quad (8.88)$$

which is the horizontal velocity at which energy travels in the waveguide. We can best illustrate the group velocity concept through an example, for which we use the Pekeris waveguide in Fig. 8.6. The computed dispersion curves for the first 4 modes

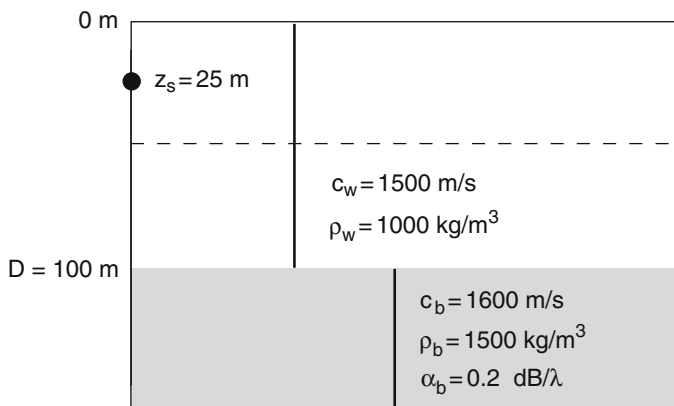


**Fig. 8.6** Schematic of the Pekeris waveguide

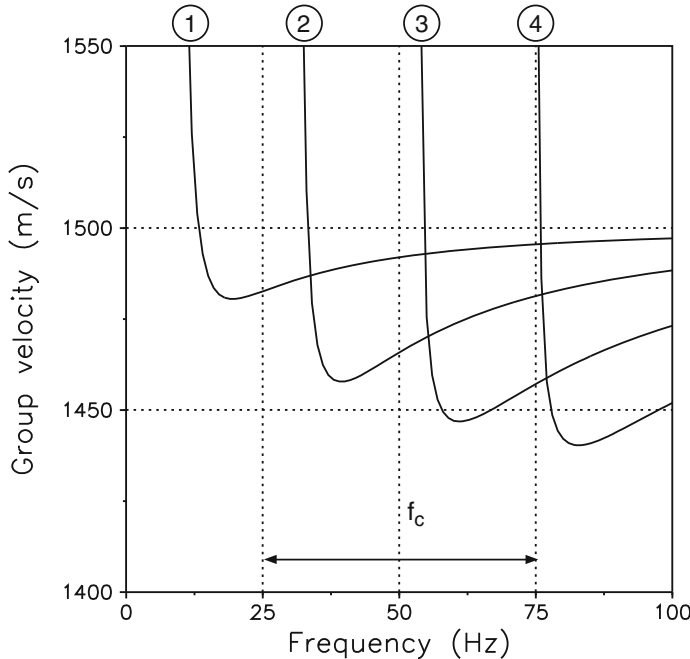


**Fig. 8.7** Dispersion characteristics of the Pekeris waveguide

are shown in Fig. 8.7. Note that each mode has a well-defined low-frequency cutoff determined by

$$f_{0m} = \frac{(m - 0.5) c_w}{2D \sqrt{1 - (c_w/c_b)^2}}. \quad (8.89)$$

Thus, the first mode only exists above 10.8 Hz, while mode 2 appears at 32.3 Hz, mode 3 at 53.9 Hz, and mode 4 at 75.4 Hz. Since we are interested in the propagation of a pulse centered at 50 Hz and with a 50-Hz bandwidth, we immediately see from Fig. 8.7 that only the first three modes will be excited. Moreover, since the peak (50 Hz) is below cutoff for mode 3, this mode will only be weakly excited.

The group velocity curves permit an estimate of the total time dispersion of the pulse at a given range. The fastest arrival is seen to be associated with modes near cutoff, where we have  $u_m = c_b = 1600$  m/s. However, modes near cutoff are weakly excited and therefore of minor importance. The part of the group velocity curve that is most important extends to the right of the local minimum (the *Airy phase*), where  $u_m$  asymptotically approaches the water speed.

Returning to the question of maximum signal dispersion in the frequency range 25–75 Hz at a distance of 30 km from the source, we see that the slowest arrival is the Airy phase of mode 3 ( $\sim 1446.5$  m/s), while the fastest arrival is the high-frequency part of mode 1 ( $\sim 1495.5$  m/s). These limiting group speeds imply arrival times of 20.06 s for the leading edge and 20.74 s for the trailing edge, i.e., a total time dispersion of around 0.7 s.

We now verify the dispersion analysis by presenting actual pulse simulations obtained by Fourier synthesis of single-frequency normal-mode solutions. We choose a source pulse given by

$$S(t) = \begin{cases} \frac{1}{2} \sin \omega_c t (1 - \cos \frac{1}{4}\omega_c t) & \text{for } 0 < t < 4/f_c \\ 0 & \text{else} \end{cases} \quad (8.90)$$

which is a Hanning-weighted four-period sine wave, see Fig. 8.8a. The pulse length is 0.08 s. The received pulse at a range of 30 km is shown in Fig. 8.8b for a source

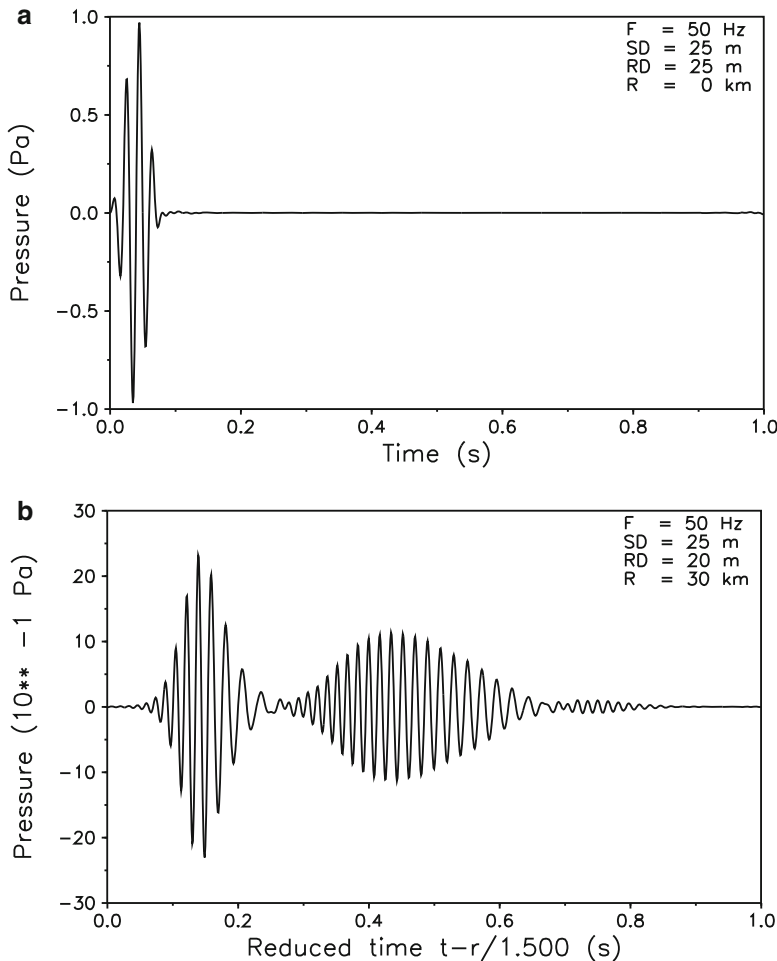


**Fig. 8.8** Comparison of (a) the source pulse with (b) the received signal at a distance of 30 km from the source. Note that the initial pulse of length 0.08 s becomes strongly dispersed with a final length of around 0.7 s

depth of 25 m and a receiver depth of 20 m. Note that the total signal dispersion is around 0.7 s as predicted from the group velocity curves. The time axis in Fig. 8.8b is reduced time, with the reference time  $t = 0$  corresponding to an absolute travel time of 20.0 s. We see that the received signal consists of two distinct wave packets, one centered at  $t = 0.15$  s, which is the first mode, and the other centered at  $t = 0.45$  s, which is the second mode. There also is a weak third-mode arrival centered at  $t = 0.75$  s. Note that the travel-time estimates from the dispersion curves are consistent with the computed time series. A closer examination of the arrival structure within each mode reveals that the leading edge consists of high-frequency contributions, whereas the trailing edge has a more low-frequency content (the Airy phase).

A more complete picture of the modal dispersion is given in Fig. 8.9, where we illustrate the pulse evolution with range at a receiver depth of 20 m (left panel) as well as the depth dependence of the field at a range of 30 km (right panel). The traces marked with arrows are common to the two plots. The apparent increase in amplitude of mode 1 with range is because all traces have been multiplied by a factor  $r$  to compensate for spherical spreading (a normalization adopted from geophysics).

The depth stack is indeed very instructive for analyzing the arrival structure. Note that the peak amplitude of the first wave packet is low near the surface, increasing toward mid-depth, and then slowly decaying toward the bottom. This corresponds

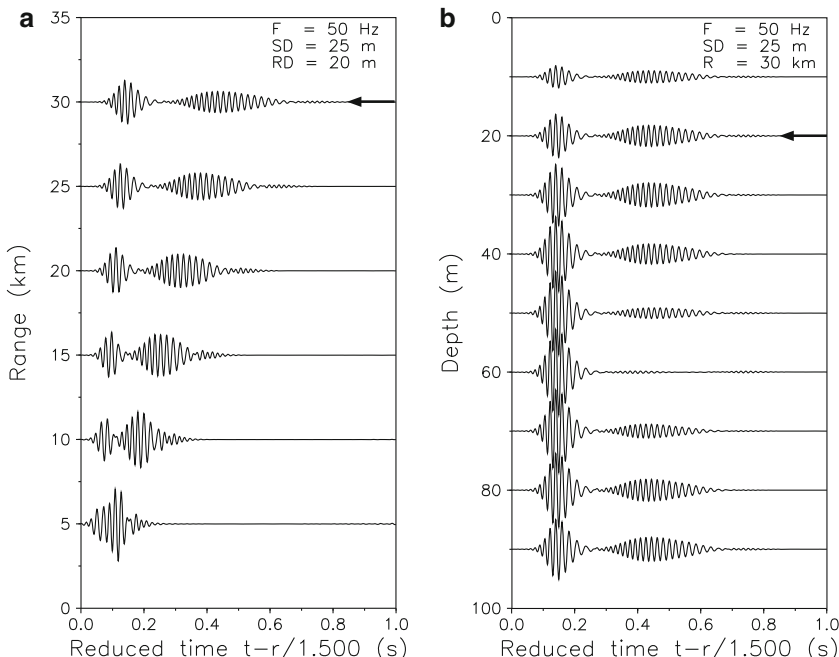


**Fig. 8.9** Stacked time series vs. range and depth for the Pekeris waveguide. Note the splitting up of the signal with range in two distinct wave packets corresponding to the first two modes of the waveguide

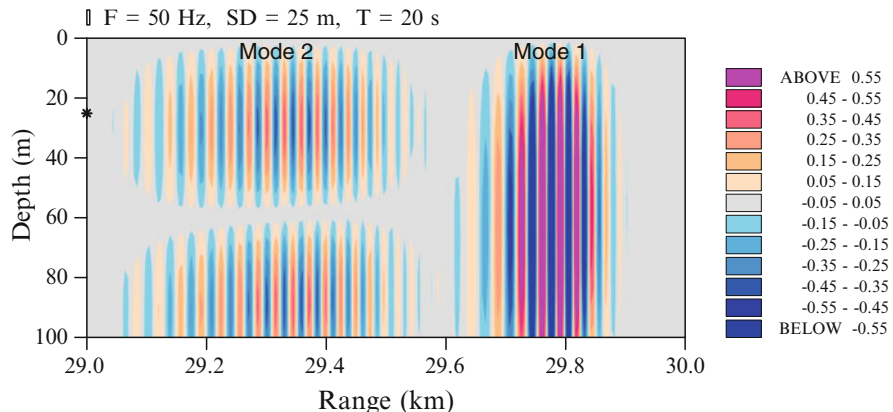


**Fig. 8.10** Snapshot of pulse in the Pekeris waveguide at  $t = 20$  s. The pulse has an extent of nearly 1 km in range with a clearly visible modal structure

exactly to the depth function of the first mode (see Chap. 5). Also, the signals are in phase all through the water column. For the second arrival, the peak amplitude clearly has a null around 60-m depth, but there are maxima at 30 and 90 m. This corresponds to the depth function of the second mode. Moreover, it is easily verified that the upper lobe is  $180^\circ$  out of phase with the lower lobe, as should be the case for mode 2. Hence, this picture illustrates all the basic properties of modal propagation in an idealized waveguide. To complement the stacked time-series plots, we finally present a snapshot (Fig. 8.10) of the pressure distribution in space at  $t = 20$  s. Again, the modal structure is clearly visible.

That the above picture of modal dispersion in a waveguide is not far from reality in real ocean environments was demonstrated by Ferris [21], who measured similar modal arrivals on a vertical array in shallow water. The experimental results, however, showed the second mode to arrive earlier than the first mode due to a particular sound-speed structure in the water column.

### 8.5.3 3-D Wedge Propagation

The wedge-shaped waveguide considered for illustrating 3-D propagation effects in the time domain is shown in Fig. 8.11. The bottom depth is 380 m in the deep part, followed by a linear slope of  $2.86^\circ$  and ending with a shallow depth of only 20 m. The slope area has a horizontal extent in the  $x$ -direction of 7.2 km, and a point source (25 Hz center frequency) is placed at the mid-point where the bottom depth is 200 m. The source depth is 40 m. We consider a homogeneous ocean with a sound speed of 1500 m/s overlying a homogeneous bottom with a speed of 1700 m/s, an attenuation of  $0.5 \text{ dB}/\lambda$ , and a density of  $1500 \text{ kg/m}^3$ .

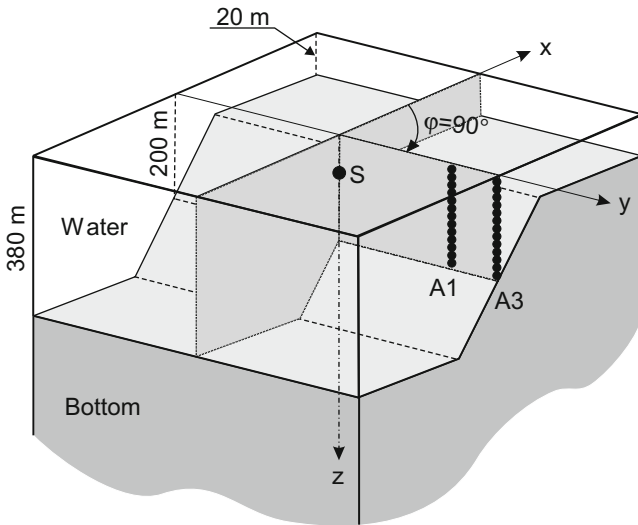


**Fig. 8.11** Geometry of truncated wedge-shaped waveguide

As discussed in Sect. 6.9.5, there are three propagating modes at the source at 25 Hz. Keeping in mind the dispersion characteristics illustrated for the Pekeris waveguide in the previous section (also three propagating modes), it is easy to interpret the modal arrival structure for a broadband pulse in the 3-D wedge shown in Fig. 8.11. The source pulse is again a Hanning-weighted four-period sine wave, (8.90), with a center frequency of 25 Hz, which results in a pulse length of 0.16 s. We shall study the arrival structure on two vertical arrays, A1 and A3, placed in the cross-slope direction ( $yz$ -plane) in 200 m of water. This is where 3-D effects are known to be strongest.

The ray diagrams of horizontally refracted mode paths, shown in Fig. 8.12 and discussed in detail in Sect. 6.9.5, are very helpful in interpreting the numerical results. In each panel equivalent modal rays have been launched from the source every  $2^\circ$  for  $0 < \varphi < 180^\circ$ . Rays reaching the cutoff depth for the equivalent mode are interrupted, indicating that energy is being transmitted into the bottom. This occurs for all rays near the upslope direction. For rays launched toward the cross-slope direction ( $\varphi = 90^\circ$ ) there is a clear deflection away from the apex, causing an intra-modal interference at longer ranges, i.e., there are regions (arrays A2 and A3) where two mode-1 paths exist, one associated with a smaller horizontal launch angle and one with a launch angle near  $90^\circ$ . A two-ray caustic delimits the shadow zone in the upper right corner of each panel, and array A1, for instance, is right at the caustic for mode 2.

Numerical results for the wedge environment were generated by Sturm [22] using a wide-angled 3-D PE model. Figure 8.13 shows the pulse arrival structure over depth at array position A1 situated 16 km from the source in the cross-slope direction (Fig. 8.11). The left panel shows the 2-D solution, where horizontal refraction is ignored. The correct 3-D result is to the right. Note that the total signal dispersion

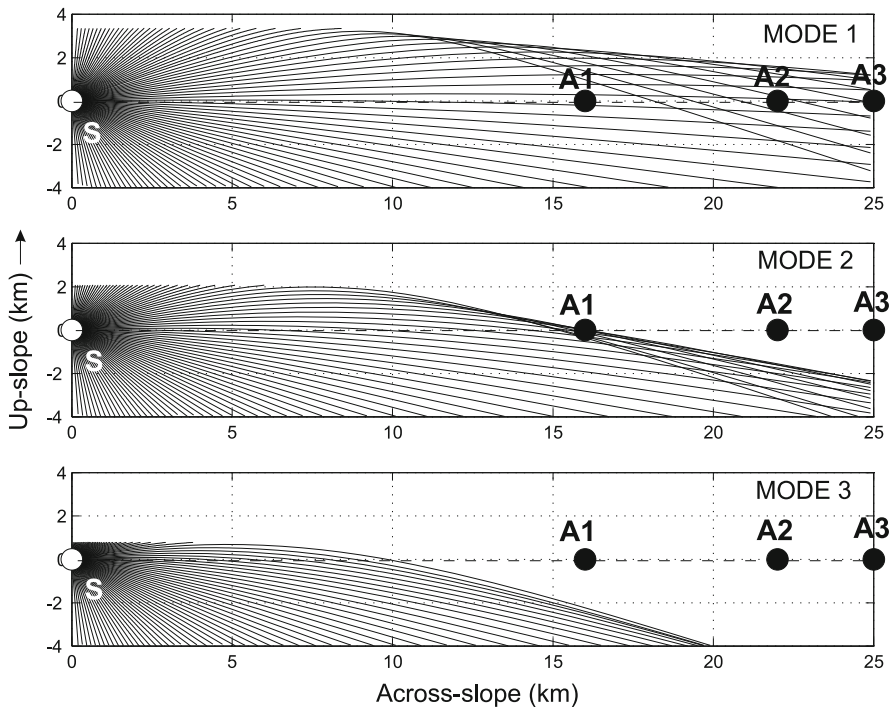


**Fig. 8.12** Ray diagrams showing horizontally refracted mode paths for a 25-Hz source in 200 m of water (from Sturm [22])

is similar in the two cases, around 1 s. The 2-D case to the left is a simple Pekeris result for a 200-m deep waveguide. The three mode arrivals are well separated: First, mode 1 with highest amplitude at mid-depth, then mode 2 with vanishing amplitude around mid-depth (110 m), and finally a weaker mode 3. The 3-D result in the right panel is quite different showing only two arriving modes, and mode 2 is strongly dispersed. Returning to the ray diagrams in Fig. 8.12, we see that array A1 is right at the caustic for mode 2 (middle panel) and in the shadow region for mode 3 (lower panel). Hence, there are two mode 2 arrivals with slightly different path lengths at position A1, which explains the strong dispersion observed for mode 2. Also, there clearly should not be any mode 3 contribution.

Finally, we compare 2-D and 3-D results at array A3, which is at a distance of 25 km from the source in the cross-slope direction, Fig. 8.14. Note that the differences between the approximate 2-D solution to the left and the full 3-D result to the right are quite pronounced. The 2-D solution shows three modal arrivals, with mode 3 being very weak due to reflection loss at the bottom. The 3-D result to the right shows two mode 1 arrivals, the first corresponding to a ray launch angle near 90° in the cross-slope direction, *cf.* the ray diagrams in Fig. 8.12, whereas the second arrival corresponds to a smaller launch angle, resulting in a longer path and more bottom loss.

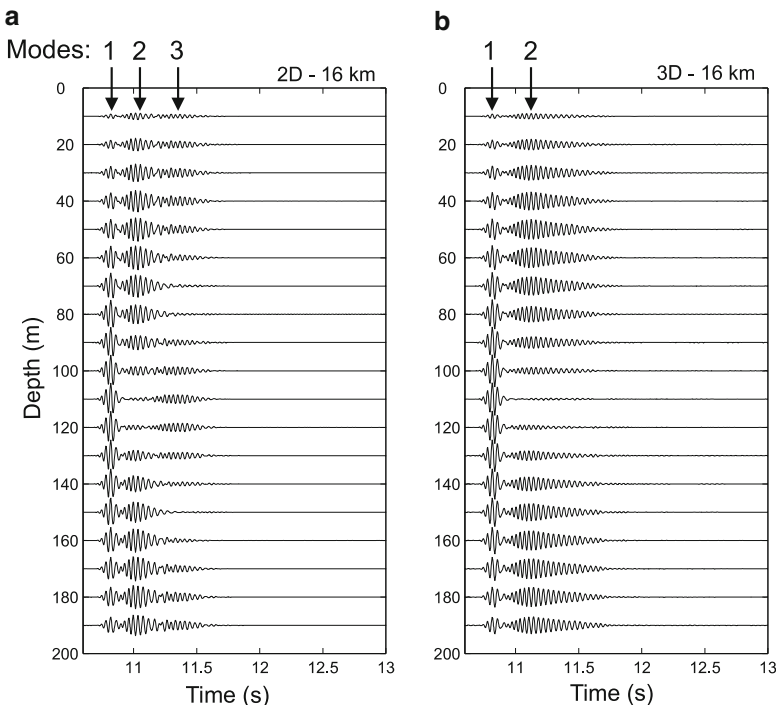


**Fig. 8.13** Stacked time series vs. depth for array A1 located 16 km away from the source in the cross-range direction: (a) 2-D result, (b) 3-D result with horizontal refraction (from Sturm [22])

For a more detailed analysis of 3-D propagation effects, including a waveguide with a Gaussian-shaped canyon, readers are referred to the paper by Sturm [22].

#### 8.5.4 Seismic Interface Waves

It is well-established that shear rigidity of the ocean bottom affects the propagation of waterborne sound through the coupling of acoustic energy into shear waves. This coupling mechanism is of particular importance in low-frequency shallow-water acoustics, where the excitation of shear waves in the bottom often becomes the dominant loss mechanism for waterborne sound. Under these circumstances, a realistic physical model of the ocean bottom is that of a viscoelastic solid described by compressional and shear-wave velocities, the attenuation factors associated with these waves, and the material density.

While the compressional-wave speed and the density of sediments can be determined by direct methods, the shear-wave properties are difficult to measure for two reasons: First, because of the usually high attenuation of these waves and, second, because it is difficult to generate a wave consisting predominantly

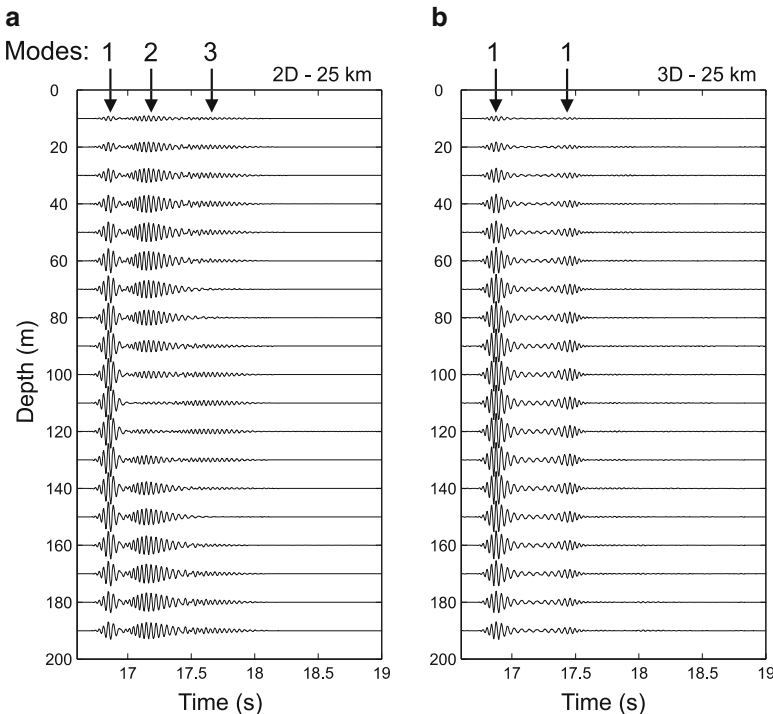


**Fig. 8.14** Stacked time series vs. depth for array A3 located 25 km away from the source in the cross-range direction: (a) 2-D result, (b) 3-D result with horizontal refraction (from Sturm [22])

of transverse particle motion. However, the shear speed and attenuation can be indirectly determined through the measured propagation characteristics of the ocean-bottom interface wave, whose existence is intrinsically related to the shear properties of the sediments.

A seismic interface wave is a guided wave propagating along the interface between two media with different shear speeds [23]. The wave is generally given different names according to the media properties involved. Hence, when propagating on a free surface of a solid it is called a *Rayleigh* wave, while it is a *Scholte* wave when propagating along a fluid–solid interface, and a *Stoneley* wave when associated with a solid–solid boundary. Note that at least one of the media must be a solid for the interface wave to exist. In the case of a water–sediment interface, the pertinent wave type is a Scholte wave with the following characteristics:

- The wave propagates along the seafloor with exponentially decaying amplitude away from the guiding interface (wave is evanescent in both media).
- Particle motion is elliptical in the depth–range plane.
- There is no low-frequency cutoff.
- Propagation speed and attenuation are closely related to the shear properties of the sediment.

To demonstrate how shear speed and shear attenuation profiles can be determined from Scholte-wave experiments in connection with a numerical model, we turn to the experimental records in Fig. 8.15. Here, stacked time signals are shown for both the vertical and the horizontal (radial) particle velocities as recorded by a geophone on the ocean bottom [24]. The source was an explosive charge detonated near the seafloor in 20 m of water. The charge size was increased with range as indicated by the black dots in Fig. 8.15. We clearly see the dispersed low-frequency Scholte-wave arrivals with group velocities between 78 and 235 m/s.

Before performing a detailed modeling of this propagation situation, it is convenient to carry out a dispersion analysis of the experimental data. By applying a multiple-filter technique developed by Dziewonski et al. [25] to the recorded time series at range 1.7 km, we obtain the dispersion diagrams shown in Fig. 8.16. The contours indicate energy levels in decibels (max. level = 99 dB). It is evident that the horizontal component of the particle velocity gives more information about the propagation situation than does the vertical component. Thus, Fig. 8.16b shows that energy is arriving in three discrete modes, of which the slowest arrival is the Scholte mode ( $M_0$ ) with its energy centered around 2 Hz. The first shear mode ( $M_1$ ) is well excited, with maximum energy around 2.8 Hz, while the second shear mode ( $M_2$ ) is only weakly excited.

The pulse modeling is done by Fourier synthesis of CW solutions from a wave-number integration code [8]. The aim is to construct an environment that leads to computed dispersion characteristics in agreement with the experimental results of Fig. 8.16. This is done in a trial-and-error fashion, where environmental parameters are changed in a systematic way until acceptable agreement is obtained between theory and experiment. Since we are interested in determining the shear properties for an unconsolidated sediment, we can a priori fix the compressional-wave properties and densities, which are known to have negligible effect on the propagation characteristics of bottom interface waves. The compressional-wave properties and densities used as input to the seismic model are given in Fig. 8.17. Also shown here are the final choices of shear-speed and shear-attenuation profiles for the bottom.

To confirm the validity of this modeling exercise, we have created synthetic seismograms for both the vertical and horizontal (radial) particle velocities (Fig. 8.18). As can be observed, the computed time series are in close agreement with the experimental results in Fig. 8.15, both with respect to signal shape and total dispersion with range. Note that signal amplitudes cannot be compared since experimental and theoretical results are normalized differently.

The computed low-frequency dispersion curves for the model environment are shown in Fig. 8.19. In the upper panel, we have superimposed the theoretical dispersion curves (dashed lines) on the experimental data from Fig. 8.16b, and there is clearly excellent agreement between theory and experiment for the modal arrival structure, which in turn means that we have chosen an appropriate shear-speed profile. Figure 8.19b shows the relative energy distribution in the first three modes as determined from the numerical model. Again, there is good agreement with the experimental results in Fig. 8.19a, indicating that the choice of shear-attenuation profile is also appropriate.

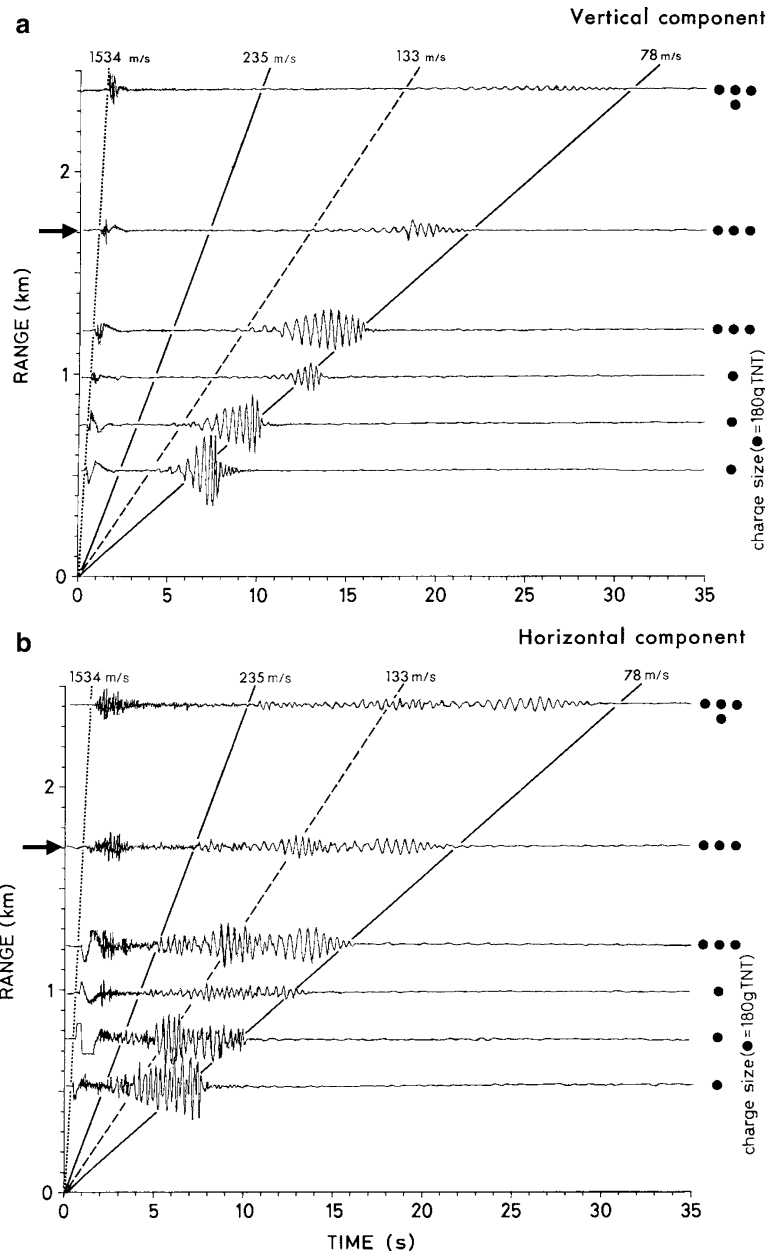


**Fig. 8.15** Stacked time signals for the vertical and horizontal particle velocities as recorded by a geophone on the seafloor. The explosive charge size is shown on the right. (From Schmalfeldt and Rauch [24])

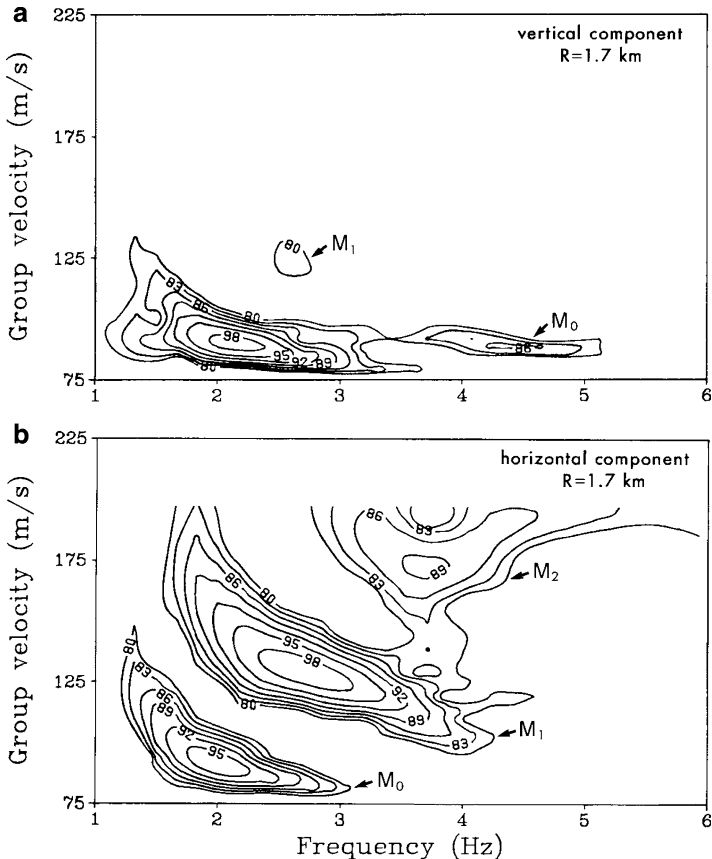


**Fig. 8.16** Dispersion curves obtained by applying a multiple filter technique to the experimental records at range 1.7 km. Energy is seen to be propagating in three discrete modes:  $M_0$ ,  $M_1$ , and  $M_2$

It should be emphasized that the inferred shear speeds (100–320 m/s) and shear-speed gradients ( $\sim 4$  m/s/m) agree well with values given by Hamilton [26] for sand–silt bottoms. Concerning the shear-attenuation profile, reported data are so sparse that no comparison with the literature can be made.

### 8.5.5 Deep-Water Propagation

To illustrate the detail with which we can analyze and explain multipath propagation situations by means of pulse modeling techniques, we consider propagation in a generic deep-water environment. A ray representation of the refracted sound paths from a 1000-m deep source is shown in Fig. 8.20 together with the sound-speed profile. We compute the pulse arrival structure at the spatial positions indicated by

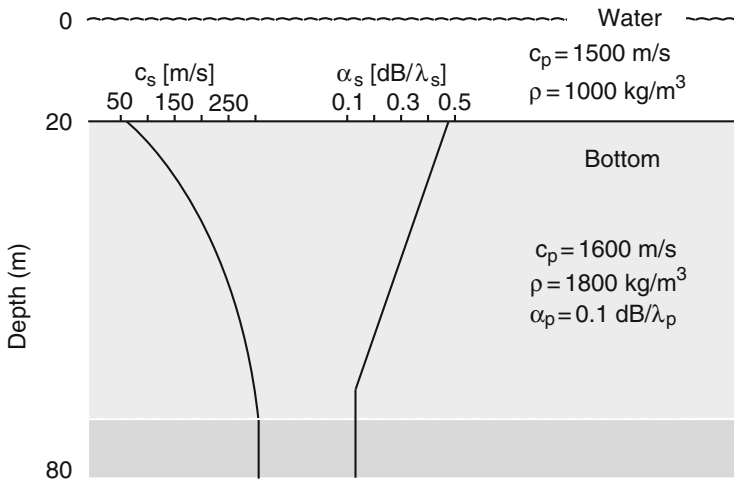


**Fig. 8.17** Model environment for generating synthetic seismograms

the two dotted lines, i.e., on a vertical “array” at 60-km range covering the upper 1000 m of the water column and on a horizontal “array” placed at 1000-m depth and covering ranges from 40 to 75 km.

The ray picture shows that up to four different ray arrivals can be expected at any receiver position. Thus there is one family of rays that leaves the source in the downward direction and which passes one lower turning point before arriving at the receivers. We designate this *ray family* a “–” arrival. Similarly, a ray that passes through one lower and one upper turning point is a “–+” arrival. For rays leaving the source in the upward direction, we can identify two different families. The rays which pass through one upper and one lower turning point are “+–” arrivals, while rays with one additional upper turning point are designated “+ – +” arrivals. As seen from Fig. 8.20, there are receivers beyond 60 km on the horizontal array with just one arrival, as well as receivers at closer ranges with three or four arrivals.

The computed pulse arrivals are displayed in Fig. 8.21 as range and depth-stacked time series in the standard format of geophysics. On the time axis, reduced time is displayed relative to a mean propagation velocity of 1520 m/s, and the pulse amplitudes are shown without spherical spreading. The traces marked by arrows (range = 60 km, receiver depth = 1000 m) are common to the two displays.

We first analyze the range-stacked result in Fig. 8.21a. Note that the four different ray arrivals described previously have been identified. We see that the – arrival (deep refracted path) comes in first followed by two coincident arrivals, the –+ and the +– paths. The last arrival is the + – + path. Of particular interest is the signal structure near the *cusped caustic* at range 50 km. Here, we record a high-amplitude pulse made up of three coincident ray arrivals. Since the pulse results are wave-theory based, the solution includes both real and diffracted arrivals. In fact, the – arrival is a *diffracted arrival* beyond 55 km on the horizontal array, and at all depths

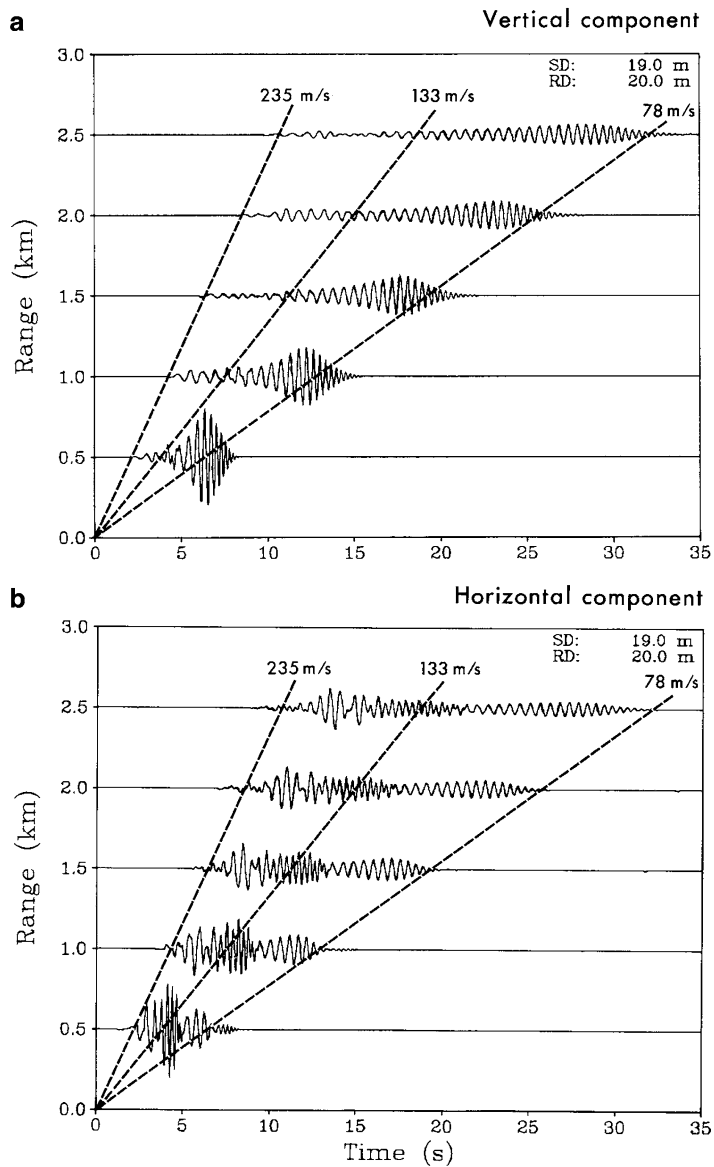


**Fig. 8.18** Synthetic seismograms for the vertical and horizontal particle velocities at the seafloor

on the vertical array. This diffracted arrival is easily observed on the depth stack in Fig. 8.21b, where the four different pulse arrivals have again been identified.

The modeling of this deep-water propagation situation was done by Fourier synthesis of normal-mode results. We selected a broadband pulse (center

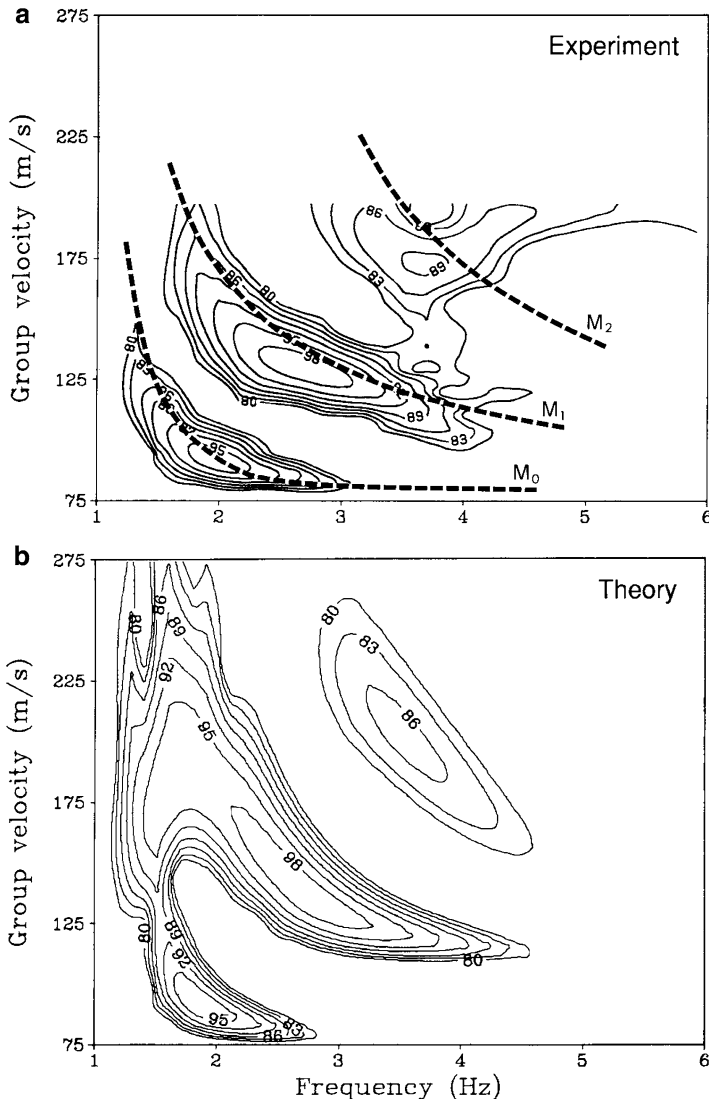


**Fig. 8.19** Comparison of experimental and theoretical dispersion curves for the horizontal particle velocity of the seafloor at range 1.7 km

frequency = 50 Hz, bandwidth = 125 Hz) requiring calculation of 125 frequency samples. The number of propagating modes increases linearly with frequency being 63 at 50 Hz. The calculation time on a workstation for a single-frequency solution is less than 1 min at the center frequency, but it increases with frequency squared. The full pulse calculation based on 125 CW solutions is therefore a considerable computational task.

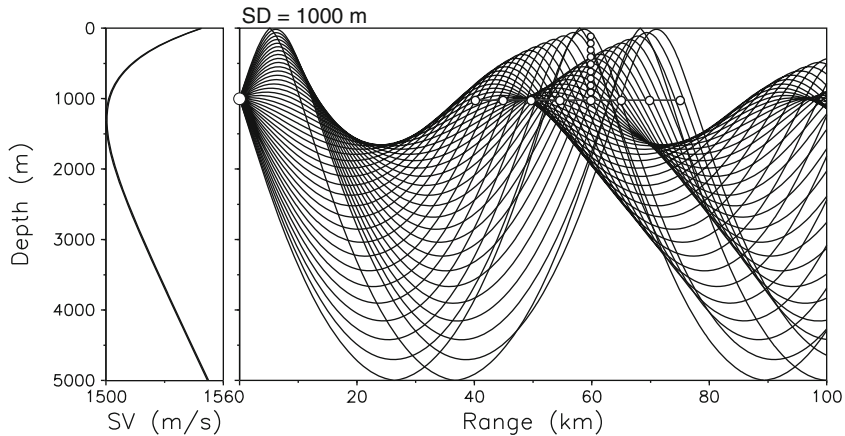


**Fig. 8.20** Ray representation of sound propagation in a generic deep-water environment

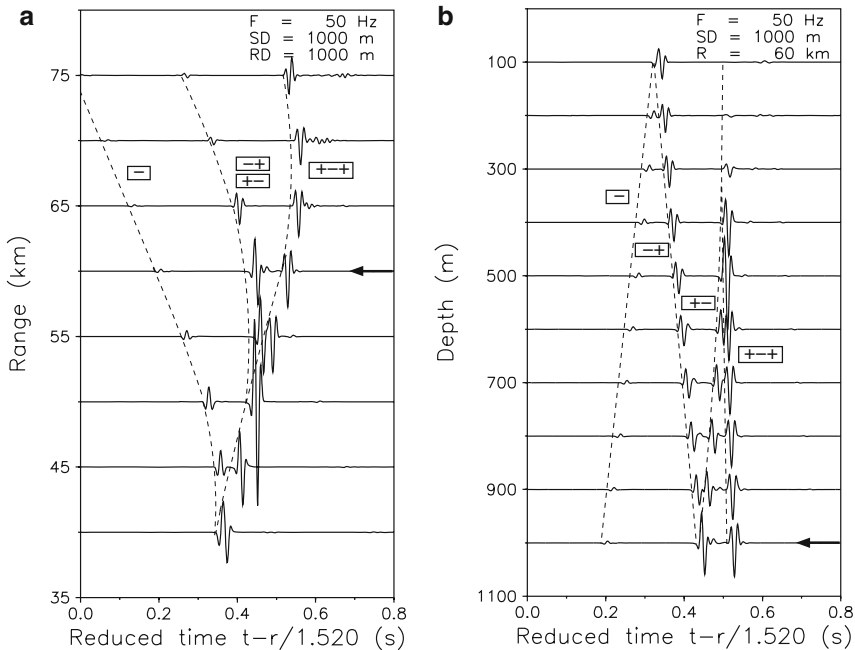


**Fig. 8.21** Computed pulse arrivals on (a) a horizontal array and (b) a vertical array. The + and - symbols indicate upper and lower turning points for particular energy paths (ray families)

In conclusion, it is clear that pulse modeling in deep water is practical only for frequencies below a few hundred hertz. However, this example demonstrates that pulse modeling permits a detailed analysis of ocean-acoustic propagation not achievable from CW results.

### 8.5.6 Surface-Duct Propagation with Leakage

In this final example, we study long-range propagation in a surface duct, in particular the existence of ducted “precursors” due to leakage. As shown in Fig. 8.22, the sound-speed profile is a slightly modified version of the profile used in the previous example, here with a 250-m deep surface duct. The ray diagram for a source at 50-m depth shows energy paths trapped in the duct as well as deep refracted paths being refocused near the surface at a range of 60 km (the convergence zone (CZ)).

In a wave-theory context, the surface duct allows for only one guided mode at a frequency of 100 Hz. This mode is a leaky (virtual) mode, which continuously sheds energy into the lower medium, as indicated by the dashed arrows. Also shown in Fig. 8.22 are examples of two leaky energy paths through the deep ocean (turning depth  $\sim 3500$  m), which return to the surface duct approximately 60 km down-range, in between the first and the second CZ. Hence, assuming the leakage (tunneling) to be significant, propagation for both source and receiver in the surface duct will consist of purely ducted energy out to the first CZ, and by interference between the ducted mode and the leaky energy beyond the first CZ. In fact, the problem gets increasingly complicated as we move out in range, with an additional leaky arrival appearing after each passing of a CZ.

We shall investigate this problem in the time domain by computing the pulse arrivals at various receiver locations. As an example, we note that the field point located at range 80 km and 1000-m depth will be reached by three different arrivals: (1) A leaky arrival directly from the surface duct, (2) a leaky arrival which has passed one lower turning point, (3) a leaky arrival which has gone through a lower turning point and a surface reflection. The modeling is again performed by Fourier synthesis of single-frequency normal mode solutions.

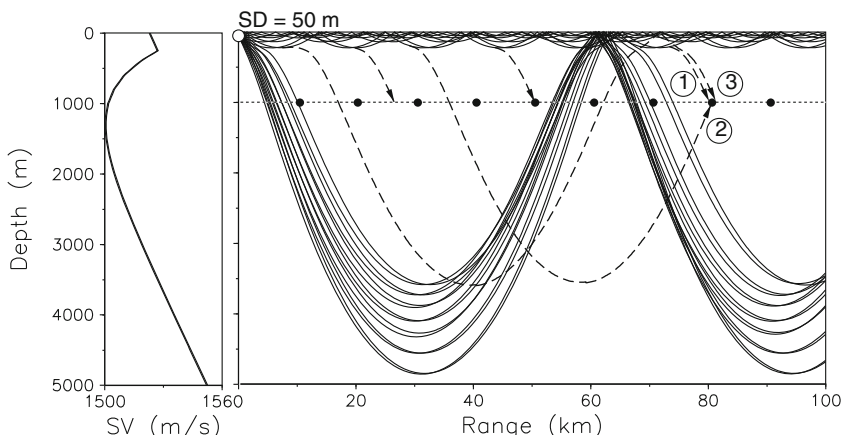


**Fig. 8.22** Sound-speed profile and associated ray diagram for the leaky surface duct problem. The leaky paths are indicated by *dashed lines*

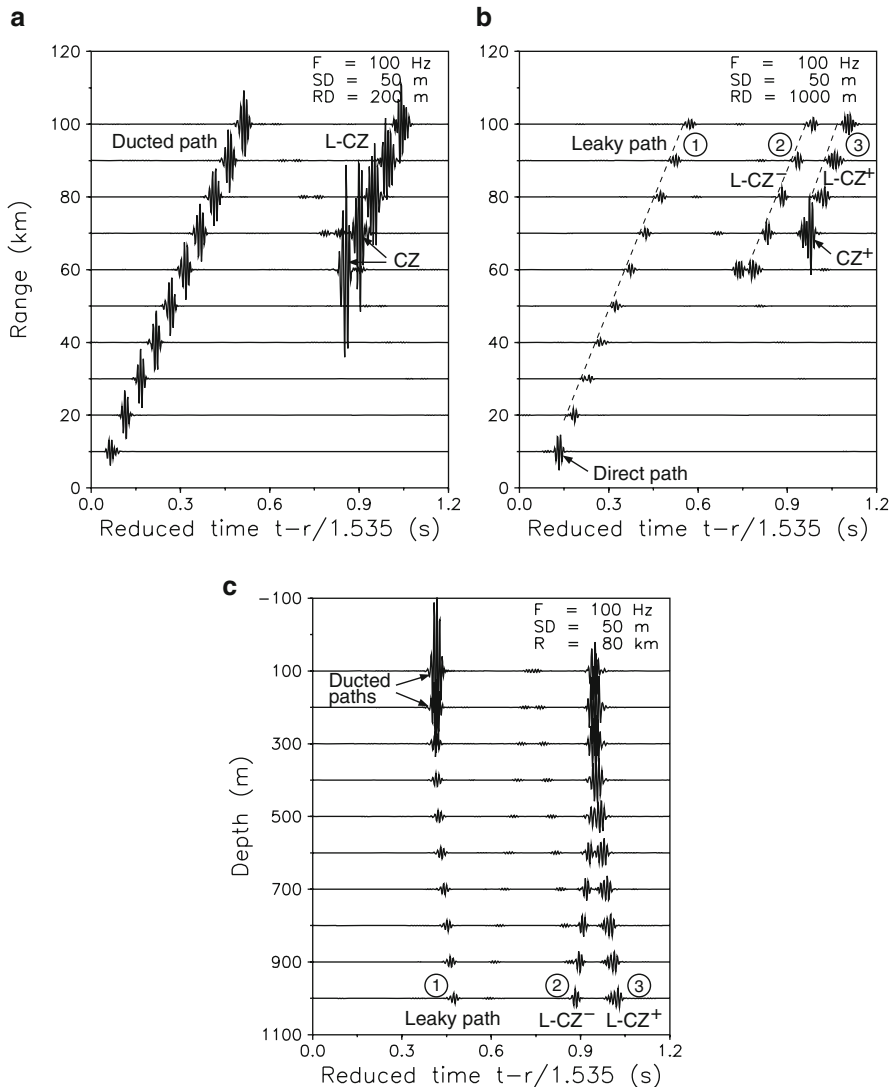


**Fig. 8.23** Stacked time series vs. range at two different depths (a) 200 m, (b) 1000 m, and vs. depth (c) at a range of 80 km. The arrivals denoted “L-CZ” indicate leaky surface-duct energy which has followed a deep refracted (or CZ) path to the receiver. The superscripts + and – indicate whether the ray path gets to the receiver from above or from below

Stacked time series versus range and depth are shown in Fig. 8.23, with a uniform scaling allowing for direct comparison of signal amplitudes between the three plots. The two range stacks are for a receiver within the duct,  $RD = 200$  m, and for a receiver below the duct,  $RD = 1000$  m. Note that the increase in amplitude with range of the ducted arrival in Fig. 8.23a is an artifact caused by the renormalization of all amplitudes with range  $r$ .

We first analyze the arrival structure within the surface duct as shown in Fig. 8.23a. The first arrival is due to the ducted mode, and this is the only arrival out to the first CZ ( $\sim 60$  km). Then we see a strong convergence-zone arrival (at 60 and 70 km), which persists at longer ranges even though the ray diagram in Fig. 8.22 shows that these field points are well beyond the first CZ. These “ghost” arrivals marked L-CZ in Fig. 8.23 are associated with leaky energy having followed deep refracted paths back to the surface duct. Note that the leaky arrivals carry as much, or even more, energy than the ducted arrivals. This, of course, will be true only for particular environmental conditions. However, energy leakage is definitely important in this case where only one mode is trapped in the surface duct.

Looking next at the pulse arrival structure on a receiver at depth 1000 m, Fig. 8.23b, we see that all arrivals have been identified. The notations L-CZ<sup>-</sup> and L-CZ<sup>+</sup> refer to leaky CZ paths arriving at the receiver from below and from above, respectively. The three main arrivals are numbered in accordance with the ray-path numbering in Fig. 8.22. Again we note that there is only one arrival out to the first CZ, the direct leaky path 1. At 70 km there is a strong CZ arrival preceded by two weaker arrivals often referred to as the *leaky precursors*. At longer ranges there are three leaky arrivals, and we notice that the last arrival is the strongest. This is because the duct is continuously leaking energy into the lower medium, causing a rapid decay of the ducted pulse amplitude with range. As a consequence, the leaky path 3 which originates at the shortest range will be the strongest arrival at long ranges.

We finally display in Fig. 8.23c the arrival structure over depth at a range of 80 km. Again the various ducted and leaky arrivals are identified; in addition, we see two low-amplitude diffracted arrivals. It is evident that only a wave-theory-based pulse solution allows an unambiguous and complete dissection of a propagation situation as complex as the surface-duct problem considered here.

### 8.5.7 Acoustic Emission from Ice Fractures

As an example of strong Doppler effect in the ocean, we consider the problem of recording acoustic emission from propagating fractures in an Arctic ice cover. This problem is of importance in relation to the use of acoustic remote sensing of ice mechanical processes, but it is also a particularly interesting physical problem due to the interplay of high fracture speeds and low phase- and group velocities of some of the dominant propagation modes in the ice cover.

To illustrate the dynamic fracture effects we use a simple environmental model. Thus, the ice cover is assumed to be a homogeneous and isotropic, elastic plate of constant thickness 4 m. The compressional and shear speeds are 3500 m/s and 1800 m/s, respectively, and the density is 900 kg/m<sup>3</sup>. The attenuations are assumed to be 0.5 and 1.0 dB/λ for compression and shear, respectively. Since we are here concerned about relatively short ranges and travel times, refraction in the water will be insignificant, and the water column is represented by an infinite halfspace with constant sound speed 1438 m/s.

It is well established that the ice will support two fundamental modes which are never cut off: the supersonic, and therefore leaky, *compressional mode*, and the subsonic *flexural mode* [27]. At high frequencies the ice plate may support a large number of modes, with the cutoff frequency for the first higher-order mode being approximately equal to the *thickness–shear frequency* for the plate [27, 28],

$$f_0 = \frac{c_s}{2H}, \quad (8.91)$$

where  $c_s$  is the shear speed and  $H$  is the ice thickness. For the present case, this translates into a cutoff frequency of  $f_0 = 225$  Hz, below which only the two fundamental modes exist.

We consider the scenario illustrated in Fig. 8.24. A tensile (e.g., thermal) crack, assumed to be at depth 1 m below the ice surface, is initiated at time  $t = 0$  s and propagates with a constant speed of 800 m/s for a total period of 20 ms, yielding a final crack length of 16 m. The acoustic emission is recorded by 3 vertical geophones, denoted G1, G2, and G3, placed at a range of 200 m from the crack initiation point, at bearings 120°, 90°, and 60°, respectively, relative to the fracture propagation direction.

The crack tip is represented by an omni-directional seismic moment source, with a bell-shaped time dependence, as shown in Fig. 8.25a. The associated frequency spectrum is shown in Fig. 8.25b, indicating the dominant components to be at frequencies less than 150 Hz. This source representation is not necessarily realistic, but it contains all the fundamental physics necessary for illustrating the dynamic effects of the fracture propagation and the coupling to the ice modes.

Since the range to the receivers is large compared to the length of the crack, we will again use (8.64) to simulate the response. Figure 8.26a shows the resulting time

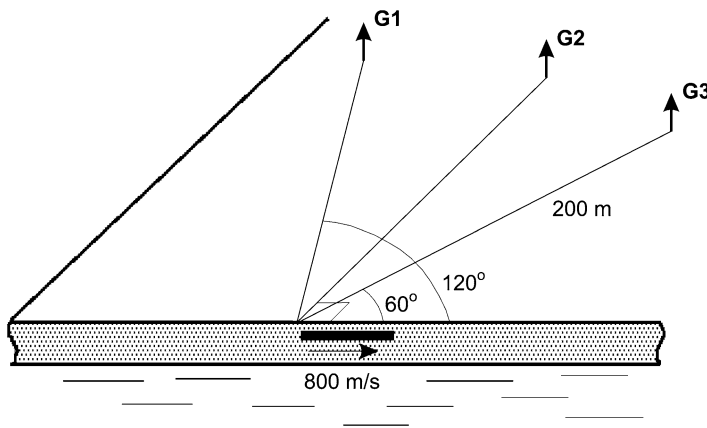


**Fig. 8.24** Scenario for simulation of acoustic emission from horizontally-propagating tensile crack in the Arctic ice cover. The emission is recorded by three vertical geophones at a range of 200 m from the crack initiation point

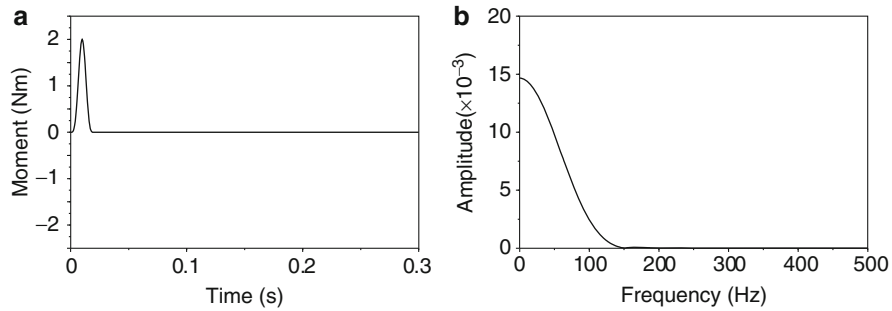


**Fig. 8.25** Seismic moment representation of tensile crack. (a) Time series, (b) Frequency spectrum

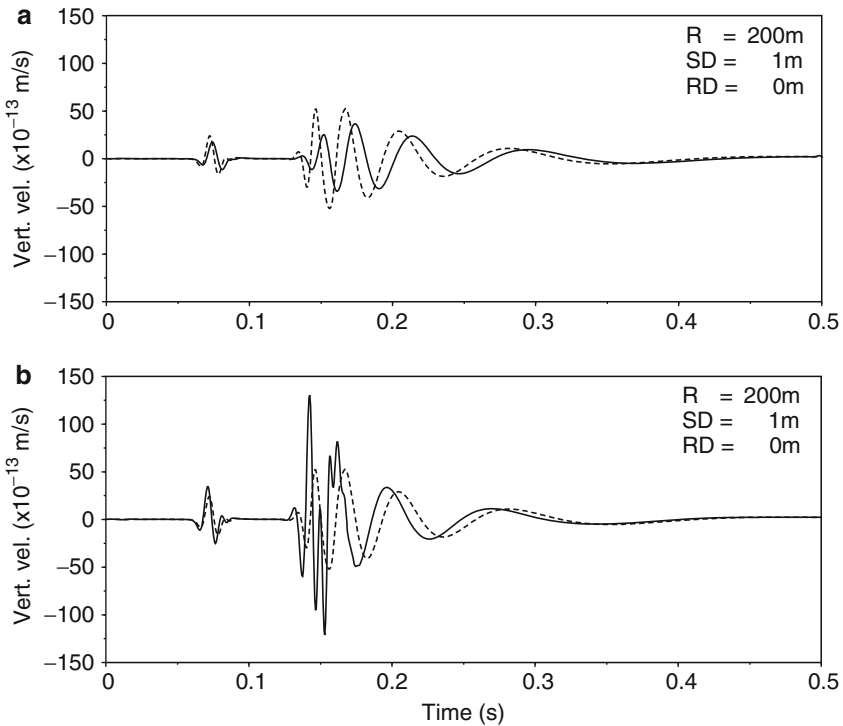


**Fig. 8.26** Comparison of signals received on different geophone pairs. (a) Results for geophones G1 (solid curve) and G2 (dashed curve), (b) Results for geophones G3 (solid curve) and G2 (dashed curve)

series for geophones G1 (solid curve) and G2 (dashed curve). It is clear from the geometry in Fig. 8.25 that the crack tip is moving away from the receiver at a projected speed of 400 m/s, in our notation corresponding to  $v_s \cos \varphi_s = -400$  m/s, whereas within our approximations the source is at rest relative to geophone G2.

A comparison of the two responses in Fig. 8.26a shows the expected frequency Doppler shifts, both for the fundamental *compressional mode* arriving at  $t = 0.06$  s, but much more clearly for the highly dispersive and slow fundamental *flexural mode* between  $t = 0.12$  and  $t = 0.5$  s. Another effect is a decrease in the observed amplitudes, primarily due to the longer mean range for geophone G1.

Similarly, Fig. 8.26b shows a comparison of the response of geophones G3 (solid curve) and G2 (dashed curve). For geophone G3, the crack tip is approaching with a projected speed of 400 m/s, i.e.,  $v_s \cos \varphi_s = 400$  m/s, and here the differences is obviously much more dramatic than for G1. We clearly observe the expected effects of upward Doppler shift and higher amplitudes for both fundamental modes. However, in addition we see a distinct high-frequency arrival interfering with the initial phase of the fundamental flexural wave. This is due to the excitation of a higher-order mode in the ice. As mentioned earlier, the cutoff frequency for the first higher-order mode is 225 Hz. As a result, this mode was not observed on geophone G1 and G2 due to the fact that the source contains energy only up to 150 Hz, and the signal on G1 has a negative Doppler shift. However, the relatively low phase velocity of the higher-order mode, in combination with the high source speed, will produce a positive Doppler shift in the forward direction, large enough to allow for its excitation, and therefore detection by geophone G3. This effect would clearly not be included in a modal expansion, which ignores cutoff effects and changes in mode shape.

## Problems

**8.1.** Defining the *bandwidth* of a source wavelet as the total width of the main lobe of its frequency spectrum, show that the bandwidth of the wavelet

$$S(t) = \begin{cases} \frac{1}{2} \sin(2\pi f_c t) \left[ 1 - \cos\left(\frac{\pi}{2N} f_c t\right) \right] & \text{for } 0 < t < 4N/f_c \\ 0 & \text{else} \end{cases}$$

is equal to  $f_c/N$ .

**8.2.** Using Fourier synthesis you have to compute a field produced by the source wavelet

$$S(t) = \begin{cases} \sin(2\pi f_c t) - \frac{1}{2} \sin(4\pi f_c t) & \text{for } 0 < t < 1/f_c \\ 0 & \text{else} \end{cases}$$

- Determine the frequency spectrum  $S(f)$  of this wavelet.
- At which frequency  $f_{\max}$  would you truncate the computation of the Green's functions? Justify your answer.
- The maximum time duration of the impulse response is  $T_I = 15/f_c$ . What is the frequency sampling required to avoid wrap-around in the computed response?

**8.3.** Assume you have a code for computing the transfer function  $p(r, z, \omega)$  for the reflection problem in Fig. 8.4, which you want to use together with Fourier synthesis to model the transient response on a horizontal receiver array 100 m above the interface. The array has 11 elements at a spacing of 50 m, with the first element at  $r = 0$ .

- Which array elements will record the *head wave*?
- If you use a *fixed* time window starting at time  $t = 0$ , determine the minimum length  $T_f$  of the time window necessary to avoid wrap-around of the response of any of the receivers.
- Similarly, determine the minimum length  $T_r$  of the time window if you allow the starting time  $t_{\min}$  to be receiver-dependent (*running* time window).
- In general, the computation time for the Fourier synthesis is insignificant compared to that associated with the computation of the transfer functions. Determine in relative terms the computational advantage of using the *running* time window for this problem.
- Would there be any computational advantage in using a receiver-dependent length of the window as well?

**8.4.** Write a computer program for solving the reflection problem described in problem 8.1 above. You may use library routines where feasible.

- Discuss your selection of time and frequency sampling.
- Make a plot of the stacked time series using a *running* time window with  $t_{\min} = r/2500$ .
- Identify the various arrivals on the plot, and discuss any possible differences in pulse shape.

**8.5.** A source and a receiver are moving horizontally in a horizontally stratified ocean with velocity vectors  $\mathbf{v}_s$  and  $\mathbf{v}_r$ , respectively.

- Show that in the frequency domain, the field observed by the receiver is given by the expression

$$\psi(\mathbf{r}_0 + \mathbf{v}_r t, z, \omega) = \frac{1}{2\pi} \int S(\Omega_k) G(k_r, z; \omega + \mathbf{k}_r \cdot \mathbf{v}_r) e^{i\mathbf{k}_r \cdot \mathbf{r}_0} d^2 \mathbf{k}_r,$$

where  $\Omega_k$  is the Doppler shifted source frequency

$$\Omega_k = \omega - \mathbf{k}_r \cdot (\mathbf{v}_s - \mathbf{v}_r).$$

- Discuss the computational advantages of using this representation together with Fourier synthesis to determine the time-domain solution, rather than using (8.60) directly.
- Derive the modal representation for the frequency-domain solution.

**8.6.** It is desired to send out an  $n$ -cycle CW pulse of center frequency  $f_c$  in shallow water such that the modes are temporally separated at range  $r$ . Using group velocity

arguments, determine the relationship between  $f_c$ ,  $n$  (taken together, bandwidth) and  $r$  for the onset of this mode separation. Confirm this with a numerical computation.

## References

1. J.E. Murphy, Finite-difference treatment of a time-domain parabolic equation: Theory. *J. Acoust. Soc. Am.* **77**, 1958–1960 (1985)
2. L. Nghiem-Phu, F.D. Tappert, Modeling of reciprocity in the time domain using the parabolic equation method. *J. Acoust. Soc. Am.* **78**, 164–171 (1985)
3. B.E. McDonald, W.A. Kuperman, Time domain formulation for pulse propagation including nonlinear behavior at a caustic. *J. Acoust. Soc. Am.* **81**, 1406–1417 (1987)
4. M.D. Collins, The time-domain solution of the wide-angle parabolic equation including the effects of sediment dispersion. *J. Acoust. Soc. Am.* **84**, 2114–2125 (1988)
5. M.D. Collins, Applications and time-domain solution of higher-order parabolic equations in underwater acoustics. *J. Acoust. Soc. Am.* **86**, 1097–1102 (1989)
6. M.B. Porter, The time-marched fast-field program (FFP) for modeling acoustic pulse propagation. *J. Acoust. Soc. Am.* **87**, 2013–2083 (1990)
7. A.V. Oppenheim, R.W. Schafer, *Discrete-Time Signal Processing* (Prentice Hall, New Jersey, 1989)
8. H. Schmidt, G. Tango, Efficient global matrix approach to the computation of synthetic seismograms. *Geophys. J. R. Astron. Soc.* **84**, 331–359 (1986)
9. S. Mallick, L.N. Frazer, Practical aspects of reflectivity modeling. *Geophysics* **52**, 1355–1364 (1987)
10. I. Tolstoy, Phase changes and pulse deformation in acoustics. *J. Acoust. Soc. Am.* **44**, 675–683 (1968)
11. G.B. Whitham, *Linear and Nonlinear Waves* (Wiley, New York, 1973), pp. 235–247
12. P.M. Morse, H. Feshbach, *Methods of Theoretical Physics* (McGraw-Hill, New York, 1953), pp. 138–141
13. A.D. Pierce, *Acoustics: An Introduction to Its Physical Principles and Applications* (American Institute of Physics, New York, 1989)
14. A.N. Guthrie, R.M. Fitzgerald, D.A. Nutile, J.D. Shaffer, Long-range low-frequency CW propagation in the deep ocean: Antigua–Newfoundland. *J. Acoust. Soc. Am.* **56**, 58–69 (1974)
15. K.E. Hawker, A normal mode theory of acoustic Doppler effects in the oceanic waveguide. *J. Acoust. Soc. Am.* **65**, 675–681 (1979)
16. H. Schmidt, W.A. Kuperman, Spectral and modal representations of the Doppler-shifted field in ocean waveguides. *J. Acoust. Soc. Am.* **96**, 386–395 (1994)
17. P.M. Morse, K.U. Ingard, *Theoretical Acoustics* (Princeton University Press, Princeton, 1968), pp. 364–365
18. J.A. Fawcett, B.H. Maranda, A hybrid target motion analysis/matched-field processing localization method. *J. Acoust. Soc. Am.* **94**, 1363–1371 (1993)
19. M.E. Dougherty, R.A. Stephen, Seismic energy partitioning and scattering in laterally heterogeneous ocean crust. *Pure Appl. Geophys.* **128**, 195–229 (1988)
20. K. Aki, P.G. Richards, *Quantitative Seismology* (Freeman, New York, 1980), pp. 211–214
21. R.H. Ferris, Comparison of measured and calculated normal-mode amplitude functions for acoustic waves in shallow water. *J. Acoust. Soc. Am.* **52**, 981–988 (1972)
22. F. Sturm, Numerical study of broadband sound pulse propagation in three-dimensional oceanic waveguides. *J. Acoust. Soc. Am.* **117**, 1058–1079 (2005)
23. W.M. Ewing, W.S. Jardetzky, F. Press, *Elastic Waves in Layered Media* (McGraw-Hill, New York, 1957)

24. B. Schmalfeldt, D. Rauch, Explosion-generated seismic interface waves in shallow water: Experimental results. Rep. SR-71. SACLANT Undersea Research Centre, La Spezia, Italy, 1983
25. A. Dziewonski, S. Block, M. Landisman, A technique for the analysis of transient seismic signals. Bull. Seis. Soc. Am. **59**, 427–444 (1969)
26. E.L. Hamilton, Geoacoustic modeling of the seafloor. J. Acoust. Soc. Am. **68**, 1313–1340 (1980)
27. B.E. Miller, H. Schmidt, Observation and inversion of seismo-acoustic waves in a complex Arctic ice environment. J. Acoust. Soc. Am. **89**, 1668–1685 (1991)
28. R.D. Mindlin, *An Introduction to Mathematical Theory of Vibration of Elastic Plates* (U.S. Army Signal Corps. Engineering Laboratories, Fort Monmouth, NY, 1955)

# Chapter 9

## Ambient Noise

### 9.1 Introduction

In this chapter, we address the modeling of ambient noise as an application of the concepts and methods discussed in the previous chapters. Ambient noise in the ocean impacts underwater acoustics in two ways:

- It is the resident acoustic field in the ocean and hence also a diagnostic of the ocean environment.
- It is the interference with respect to detecting or measuring signals.

We have already discussed some of the basic features of ambient noise in the ocean in Chap. 1. Below a few hundred hertz, a dominant component of ambient noise in the ocean originates from shipping and other man-made sources. We will not discuss this aspect because the resulting acoustic field is just a straightforward, though involved, summation of acoustic fields from geographically distributed discrete sources. In this chapter we shall be concerned with the distribution of surface-generated ambient noise. The relevant propagation phenomena have been qualitatively and quantitatively covered in previous chapters. In particular, wave theory methods such as wavenumber integration, normal mode, and parabolic equation techniques can be utilized for explaining the spatial distribution of surface-generated noise. The spatial distribution of noise is quantitatively defined as the spatial correlation between pairs of field points. The correlations between  $N$  field points is represented by a square matrix of dimension  $N \times N$ ; the diagonal entries are proportional to the intensity at each of the field points (or receivers) while the off-diagonal terms are proportional to the correlation between field points.

As an introduction, though, we start with two common models of noise. The first is white noise for which noise is uncorrelated between any two sensors. That means that the off-diagonal terms of the noise correlation matrix are zero. The second common noise model is isotropic (plane wave) noise meaning that the noise is made up of plane waves that are statistically equally distributed over all directions. We can calculate the isotropic noise correlation between the two points by computing the correlation for one plane wave between two points and then averaging over all polar angles. Without loss of generality we can choose the two points to be along

the  $z$ -axis separated by an arbitrary distance  $d$ . Then the noise at the two points separated by a distance  $d$  can be represented simply as

$$n_z = A e^{ik \cdot z} \text{ and } n_{z+d} = A e^{ik \cdot (z+d)} \rightarrow n_z n_{z+d}^* = e^{-ikd \cos \theta}. \quad (9.1)$$

The expectation of the normalized correlation function is computed by averaging over all polar and azimuthal angles,  $\theta$  and  $\varphi$ , respectively,

$$\langle n_z n_{z+d}^* \rangle = C \int_0^{2\pi} d\varphi \int_0^\pi \sin \theta e^{-ikd \cos \theta} d\theta = \frac{\sin kd}{kd}, \quad (9.2)$$

where  $C$  is a normalization factor such that the correlation function is unity at  $d = 0$ , meaning that the correlation matrix has unity entries on the diagonal. Note that for  $k = \lambda/2$ , the off-diagonal terms are zero and the noise appears to be white. Arrays typically have  $\lambda/2$  spacing and this has often led to the confusion that white noise and isotropic noise are the same. That is not the case; white noise is non-propagating local noise uncorrelated from sensor to sensor whereas isotropic noise is propagating noise with a sensor-to-sensor correlation as per (9.2). A more general approach for a non-isotropic distribution of plane waves with arbitrary sensor-to-sensor orientation is given in [1].

In this chapter, we will model noise using waveguide propagation theory. We begin by examining the problem of a homogeneous statistical distribution of sources near the surface in a stratified ocean. Spectral and normal-mode methods are most applicable for this range-independent case, providing analytically identifiable contributions associated with the continuous spectrum for overhead noise and the discrete spectrum for long-distance contributions, and evanescent spectral components for shallow-water seismo-acoustic noise. Next, we consider a range-dependent ocean in which the environment has three-dimensional (3-D) features and the distribution of surface sources is also position-dependent (e.g., higher surface source levels in storm regions). This 3-D problem is efficiently approached using adiabatic mode theory. We finally show how the PE approach can also be used to address this problem.

## 9.2 Surface Noise in a Stratified Ocean

In a halfspace bounded above by a surface with a homogeneous distribution of noise sources, the spatial distribution of the noise takes a simple form. In this idealized environment, the spatial correlation of the noise in the farfield of the surface is a function of only the separation of the field points. For a range-independent waveguide, this remains true only for the horizontal separation; in the vertical the cross-spectral density depends on the absolute depths of the field points. The derivations in this section, and in particular those of Sect. 9.2.3, are equally applicable to elastic media.

### 9.2.1 Mathematical Derivation

The distribution of sound from surface noise sources can be calculated by coupling these noise sources into the water column using any of the propagation models discussed in earlier chapters. We follow the derivation of Kuperman and Ingénito [2] and Schmidt and Kuperman [3]. Figure 9.1 shows the geometry for such a model, where the random source term on the plane  $z = z'$  in the frequency domain is denoted  $S_\omega(\mathbf{r}')$ , where  $\mathbf{r}' = (x', y')$ . The acoustic field from such a source distribution is the solution of the equation

$$(\nabla^2 + k^2) \phi_\omega(\mathbf{r}, z) = -S_\omega(\mathbf{r}') \delta(z - z'), \quad (9.3)$$

where  $k \equiv \omega/c(z)$ . To simplify notation, we suppress the frequency dependence of the spectral strength of the noise sources  $S_\omega$  and the acoustic field  $\phi_\omega$ . However, note that the total broadband noise field would be obtained by Fourier synthesis of  $\phi_\omega$ . Equation (9.3) has the solution

$$\phi(\mathbf{r}, z) = \int S(\mathbf{r}') g(\mathbf{r}, \mathbf{r}'; z, z') d^2\mathbf{r}', \quad (9.4)$$

where  $g(\mathbf{r}, \mathbf{r}'; z, z')$  is the Green's function, satisfying the Helmholtz equation

$$(\nabla^2 + k^2) g(\mathbf{r}, \mathbf{r}'; z, z') = -\delta^2(\mathbf{r} - \mathbf{r}') \delta(z - z') \quad (9.5)$$

and the appropriate boundary conditions.

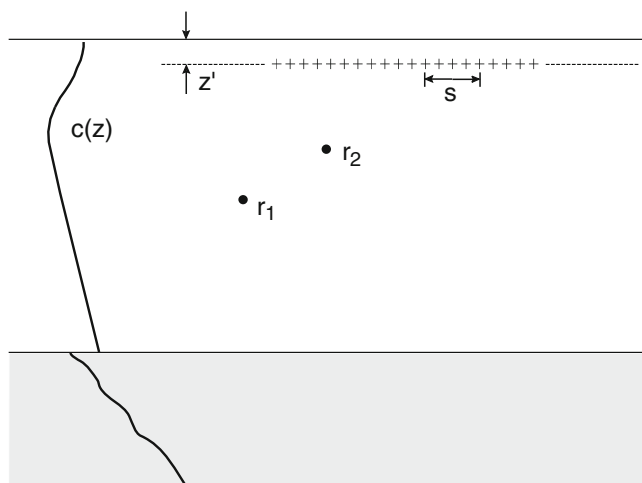


**Fig. 9.1** The geometry for the surface-distributed noise problem

The spatial distribution of the noise field is characterized by the ensemble average of the product of the acoustic field at a point  $(\mathbf{r}_1, z_1)$  and the complex conjugate of the field at a point  $(\mathbf{r}_2, z_2)$ . This quantity is called the *cross-spectral density*  $C_\omega(\mathbf{r}_1, \mathbf{r}_2, z_1, z_2)$ , and reduces to the local sound intensity when the two field points are at the same position. Otherwise, this quantity is representative of the directional/spatial properties of the noise field which would be measured by a distributed acoustic receiving array (Chap. 10). The cross-spectral density is

$$\begin{aligned} C_\omega(\mathbf{r}_1, \mathbf{r}_2, z_1, z_2) &= \langle \phi(\mathbf{r}_1, z_1) \phi^*(\mathbf{r}_2, z_2) \rangle \\ &= \int \int \langle S(\mathbf{r}') S^*(\mathbf{r}'') \rangle \\ &\quad \times g(\mathbf{r}_1, \mathbf{r}', z_1, z') g^*(\mathbf{r}_2, \mathbf{r}'', z_2, z') d^2\mathbf{r}' d^2\mathbf{r}'', \end{aligned} \quad (9.6)$$

where  $S$  is the surface noise source function. The correlation function of the surface noise sources  $q^2 N(\mathbf{s}) \equiv \langle S(\mathbf{r}') S^*(\mathbf{r}'') \rangle$  is taken to be homogeneous and, therefore, spatially dependent only on the separation,  $\mathbf{s} \equiv \mathbf{r}' - \mathbf{r}''$ , between sources;  $q$  is the surface source strength. A discussion of source strengths versus windspeed, e.g., is given by Kewley et al. [4] while an analysis of source strengths associated with more extreme winds can be found in Wilson and Makris [5]. An alternative approach is given by Knobles et al. [6]. Consistent shipping and wind noise sources levels are given by Evans and Carey [7].

We also express the noise field points through the difference of displacement vectors,  $\mathbf{R} \equiv \mathbf{r}_1 - \mathbf{r}_2$ , and denote the cross-spectral density given by (9.6) for angular frequency  $\omega$  as  $C_\omega(\mathbf{R}, z_1, z_2)$ . The Cartesian coordinate equivalents of the integral representation for the Green's function, (4.93), are of the form

$$g(\mathbf{r}_1, \mathbf{r}', z_1, z') = \frac{1}{2\pi} \int g(k, z_1, z') \exp[i\mathbf{k} \cdot (\mathbf{r}_1 - \mathbf{r}')] d^2\mathbf{k}, \quad (9.7)$$

$$g^*(\mathbf{r}_2, \mathbf{r}'', z_1, z') = \frac{1}{2\pi} \int g^*(k', z_2, z') \exp[-i\mathbf{k}' \cdot (\mathbf{r}_2 - \mathbf{r}'')] d^2\mathbf{k}'. \quad (9.8)$$

We now insert these expressions into (9.6), and substitute  $\mathbf{R}$  for  $\mathbf{r}_1 - \mathbf{r}_2$  and  $\mathbf{s}$  for  $\mathbf{r}' - \mathbf{r}''$ . Then the integration can be performed over  $\mathbf{r}''$  and  $\mathbf{k}'$  with the result

$$\begin{aligned} C_\omega(\mathbf{R}, z_1, z_2) &= q^2 \int \int N(\mathbf{s}) g(k, z_1, z') g^*(k, z_2, z') \\ &\quad \times \exp[i\mathbf{k} \cdot (\mathbf{R} - \mathbf{s})] d^2\mathbf{s} d^2\mathbf{k}. \end{aligned} \quad (9.9)$$

Performing the integration over the azimuth angle associated with  $\mathbf{k}$  gives,

$$\begin{aligned} C_\omega(\mathbf{R}, z_1, z_2) &= 2\pi q^2 \int N(\mathbf{s}) d^2\mathbf{s} \int_0^\infty g(k_r, z_1, z') g^*(k_r, z_2, z') \\ &\quad \times J_0(k_r |\mathbf{R} - \mathbf{s}|) k_r dk_r, \end{aligned} \quad (9.10)$$

where  $J_0$  is the Bessel function of zeroth order. Equations (9.9) and (9.10) involve an integral over the horizontal wavenumber  $k_r$ , and a spatial integral over the separation  $\mathbf{s} = \mathbf{r}' - \mathbf{r}''$ . The latter can be eliminated by introducing the wavenumber spectrum  $P(\mathbf{k})$  of the surface source correlation, in terms of which  $N(\mathbf{s})$  is given by the Fourier integral,

$$N(\mathbf{s}) = \frac{1}{2\pi} \int P(\mathbf{k}) \exp(i\mathbf{k} \cdot \mathbf{s}) d^2\mathbf{k}. \quad (9.11)$$

By inserting (9.11) into (9.9), the integration over  $\mathbf{s}$  can be performed, yielding

$$C_\omega(\mathbf{R}, z_1, z_2) = 2\pi q^2 \int P(\mathbf{k}) g(k, z_1, z') g^*(k, z_2, z') \exp(i\mathbf{k} \cdot \mathbf{R}) d^2\mathbf{k}. \quad (9.12)$$

If the surface noise source correlation  $N(\mathbf{s})$  is spatially isotropic, i.e.,  $N(\mathbf{s}) = N(|\mathbf{s}|)$ , then we can perform the integration over the azimuthal angle associated with  $\mathbf{k}$  to obtain,

$$C_\omega(R, z_1, z_2) = 4\pi^2 q^2 \int [P(k_r) g(k_r, z_1, z') g^*(k_r, z_2, z')] J_0(k_r R) k_r dk_r. \quad (9.13)$$

This form is particularly useful since it is equivalent to the wavenumber integral in (4.93), but with the depth-dependent Green's function  $g(k_r, z, z')$  in (4.93) replaced by the product in the bracket in (9.13). Wavenumber integration codes as described in Chap. 4 are, therefore, easily modified to compute the noise correlation function (NCF) in a stratified model of the ocean environment [3]. Finally, we mention for clarity in nomenclature and later use that the *correlation function*  $C_\tau$  of the noise field is given by

$$C_\tau(R, z_1, z_2) = \int_{-\infty}^{\infty} C_\omega(R, z_1, z_2) \exp(-i\omega\tau) d\omega. \quad (9.14)$$

### 9.2.2 Spatial Distribution of Noise Sources

In simple general terms, much of the noise sources can be categorized as and are associated with [8]:

1. *Monopole*: mass addition, heat addition, volume change – e.g., bubbles, rain droplet impact, etc.
2. *Dipole*: force, translation, acceleration (sloshing) – e.g., vibration of unbaffled rigid bodies.
3. *Quadrupole*: moment, shear, distortion, rotation, turbulence.

These noise sources can then be taken to be on the source plane in Fig. 9.1, and in the presence of the pressure-release surface these sources will then couple into the

water column as higher-order-pole radiators. If the noise sources are uncorrelated, their correlation function will be of the form of a delta function [9]. In general, it has been shown by Liggett and Jacobson [10] that the *correlation function* of surface sources which produce a farfield radiation pattern (of multipole order  $p$ )  $\cos^p \theta$  with respect to the vertical is given by

$$N(\mathbf{s}) = \begin{cases} 2\delta(s)/[k^2(z')s] & \text{uncorrelated noise sources} \\ 2^p p! J_p[k(z')s]/[k(z')s]^p & \cos^p \theta \text{ radiation pattern.} \end{cases} \quad (9.15)$$

### 9.2.3 Wavenumber Integral Representation

Since the Green's function  $g$  satisfies the pressure-release boundary condition, monopole sources near the surface couple into the water column as dipoles. For the case when the noise sources are *uncorrelated*, the first expression in (9.15) will represent a dipole sheet at the surface, corresponding to a sheet of uncorrelated monopole sources below the surface; substituting this expression into (9.10) yields the cross-spectral density,

$$C_\omega(R, z_1, z_2) = \frac{8\pi^2 q^2}{k^2(z')} \int_0^\infty g(k_r, z_1, z') g^*(k_r, z_2, z') J_0(k_r R) k_r dk_r, \quad (9.16)$$

which reduces to a quantity proportional to the noise intensity when evaluated at  $R = 0$  and  $z_1 = z_2$ ,

$$C_\omega(0, z, z) = \frac{8\pi^2 q^2}{k^2(z')} \int_0^\infty |g(k_r, z, z')|^2 k_r dk_r. \quad (9.17)$$

For *correlated* sources corresponding to a  $\cos^p \theta$  radiation pattern with respect to the vertical, we use the second expression in (9.15). In this case, the noise source spectrum is given by the Fourier transform of (9.15), which can be performed in closed form using the identity [11],

$$\int_0^\infty J_p(ax) J_0(bx) x^{1-p} dx = \begin{cases} 0 & a < b \\ [2^{-1} (a^2 - b^2)]^{p-1} a^{-p} [\Gamma(p)]^{-1} & a \geq b \end{cases}$$

with the result

$$P(k_r) = \frac{2p!}{k^{2p} \Gamma(p)} \begin{cases} 0 & k_r > k \\ (k^2 - k_r^2)^{p-1} & k_r \leq k, \end{cases} \quad (9.18)$$

where  $k = \omega/c(z')$  is the wavenumber at the sea surface and  $\Gamma(p)$  the standard Gamma function. Substituting (9.18) into (9.13), we obtain

$$C_\omega(R, z_1, z_2) = \frac{8\pi^2 p! q^2}{k^{2p} \Gamma(p)} \int_0^k (k^2 - k_r^2)^{p-1} \times g(k_r, z_1, z') g^*(k_r, z_2, z') J_0(k_r R) k_r dk_r, \quad (9.19)$$

which reduces to

$$C_\omega(R, z_1, z_2) = \frac{8\pi^2 p q^2}{k^{2p}} \int_0^k (k^2 - k_r^2)^{p-1} \times g(k_r, z_1, z') g^*(k_r, z_2, z') J_0(k_r R) k_r dk_r. \quad (9.20)$$

The source depth  $z'$  is here assumed to be small but arbitrary. However, for fixed source strength  $q$ , the depth-dependent Green's function at depth  $z > z'$  is then proportional to  $z'$  as is clear from the expressions given in (2.113) for the source in a halfspace and in (2.146) for a source in an ideal waveguide. As a result, the cross-spectral density function in (9.20) becomes proportional to  $(z')^2$ . To eliminate this dependence on the arbitrary source depth, the monopole *source strength*  $q$  is conveniently normalized to yield a certain pressure level  $Q$  in an infinitely deep ocean by assigning it the value [3],

$$q^2(z') = Q^2 / 16\pi(z')^2.$$

To summarize, the expressions derived in this section for the cross-spectral density of the noise field are amenable to direct numerical evaluation by the methods of Chap. 4. We shall later on investigate the structure of these integral expressions in some detail.

### 9.2.4 Normal Mode Representation

We can also evaluate the above expressions using the normal-mode representation of the Green's function. One advantage of going this route is that the physical understanding associated with the modal picture directly translates to the noise problem. Secondly, the application of adiabatic mode theory can be used to extend the noise formulation to range-dependent environments. We consider the most common case, the dipole surface distribution corresponding to  $p = 1$ .

Recall from Chaps. 2 and 5, that in the case of a penetrable bottom, the modal expansion of the field is only accurate in cases where the branch-line contribution representing the continuous spectrum is insignificant. In general, this requires the horizontal separation of source and receiver to be of the order of several water depths. However, in the present case, characterized by a uniform sheet of surface sources, the contribution of the continuous spectrum will always be significant due to the presence of sources with small horizontal offsets. Therefore, the branch-line integral must be evaluated or approximated. Here, as described in Chap. 5 for a lossy bottom, the branch-line contribution can be approximated by a sum of

complex modes by introducing a deep *false bottom*, virtually transforming the leaky waveguide problem into a proper Sturm–Liouville problem for which the depth-dependent Green's function is represented exactly by the eigenfunction (or modal) expansion, (5.41),

$$g(k_r, z, z') = \frac{1}{2\pi\rho} \sum_m \frac{\Psi_m(z') \Psi_m(z)}{k_r^2 - k_{rm}^2}, \quad (9.21)$$

where  $\Psi_m(z)$  is the normalized amplitude function and  $k_{rm}$  the propagation wave-number of the  $m$ th mode for the transformed problem. It is interesting to note that we must include attenuation in the system to obtain a finite cross-spectral density function. This is because sound trapped by the layered medium (represented by the discrete modes) suffers cylindrical spreading while the amount of energy radiated by the noise sources increases as the square of the range from the field points. Hence, the contributions to the energy from distant sources increase with range and the total intensity diverges. Any amount of attenuation will cause the intensity to decay exponentially with range and ensure convergence. We assume that  $k_{rm}$  is a complex number whose imaginary part is the modal attenuation coefficient,  $k_{rm} = \kappa_m + i\alpha_m$ , with  $\kappa_m, \alpha_m > 0$ . Furthermore, we use the relation  $J_0 = [H_0^{(1)} + H_0^{(2)}]/2$  together with the knowledge that  $g$  and  $g^*$  are even in  $k_r$  and  $-H_0^{(1)}(-x) = H_0^{(2)}(x)$  to rewrite (9.16) in a form more convenient for the modal representation,

$$C_\omega(R, z_1, z_2) = \frac{4\pi^2 q^2}{k^2} \int_{-\infty}^{\infty} g(k_r, z_1, z') g^*(k_r, z_2, z') H_0^{(1)}(k_r R) k_r dk_r. \quad (9.22)$$

We use (9.21) for  $g$  and  $g^*$  so that we end up with integrals of the form

$$I_{mn} \equiv \frac{q^2}{\rho^2 k^2} \int_{-\infty}^{\infty} \frac{k_r H_0^{(1)}(k_r R)}{[k_r^2 - k_{rm}^2][k_r^2 - (k_{rn}^*)^2]} dk_r, \quad (9.23)$$

which have simple poles at  $\pm k_{rm}, \pm k_{rn}^*$  of which the poles  $+k_{rm}$  and  $-k_{rn}^*$  are in the upper halfplane. Using standard methods of complex integration, we close the contour in the upper halfplane with a semicircle of large radius and evaluate the residues,

$$I_{mn} = \frac{i\pi q^2}{\rho^2 k^2} \left[ \frac{H_0^{(1)}(k_{rm} R)}{k_{rm}^2 - (k_{rn}^*)^2} + \frac{H_0^{(2)}(k_{rn}^* R)}{k_{rm}^2 - (k_{rn}^*)^2} \right],$$

where we have also used the Hankel function relation  $-H_0^{(1)}(-x) = H_0^{(2)}(x)$ . We can now write the normal-mode representation of the cross-spectral density as

$$\begin{aligned} C_\omega(R, z_1, z_2) &= \frac{i\pi q^2}{\rho^2 k^2} \sum_{m,n} \Psi_m(z') \Psi_m(z_1) \Psi_n(z') \Psi_n(z_2) f_{mn} \\ &\times \left[ H_0^{(1)}(k_{rm} R) + H_0^{(2)}(k_{rn}^* R) \right], \end{aligned} \quad (9.24)$$

where

$$f_{mn} = \frac{1}{k_{rm}^2 - (k_{rn}^*)^2}. \quad (9.25)$$

The quantity  $f_{mn}$  is a measure of the coherence between the normal modes which make up the noise field. Assuming that  $\kappa_m \gg \alpha_m, \kappa_n \gg \alpha_n$ , we get

$$f_{mn} = \begin{cases} \frac{1}{\kappa_m^2 - \kappa_n^2} & \text{for } m \neq n \\ \frac{1}{4i\alpha_m \kappa_m} & \text{for } m = n. \end{cases} \quad (9.26)$$

We see that the  $m = n$  terms become infinite in (9.24) in the absence of attenuation. This is due to the contributions of distant sources as discussed below (9.21). The  $m \neq n$  terms remain finite and because they are products of different modes with rapidly oscillating phases, distant sources give negligible contribution to the sum. Furthermore, from (9.26), if the attenuation coefficients  $\alpha_m$  are much smaller than the smallest separation between the eigenvalues (which is common in underwater acoustics), then the noise field can be approximated by an incoherent sum of modes. We further simplify (9.24) by approximating  $k_{rm}$  by its real part  $\kappa_m$  with the result,

$$C_\omega(R, z_1, z_2) = \frac{\pi q^2}{2\rho^2 k^2} \sum_m \frac{[\Psi_m(z')]^2 \Psi_m(z_1) \Psi_m(z_2) J_0(\kappa_m R)}{\alpha_m \kappa_m}. \quad (9.27)$$

It is clear that the structure of the noise is highly dependent on the attenuation  $\alpha_m$ . In fact, as discussed earlier, the attenuation must be finite for the solution to converge.

### 9.2.5 Noise in a Homogeneous Halfspace

Early work by Cron and Sherman [12] on the distribution of noise in the ocean was based on a heuristic model of the deep ocean as a homogeneous halfspace with a plane of sources having  $\cos^p \theta$  directionality distributed uniformly on the surface. In this section, we recover their result as a limiting case of the formal theory presented above.

The appropriate Green's function for a source in the vicinity of a pressure-release surface is given by the Sommerfeld–Weyl integral, (2.106). By inserting this expression into (9.20), we obtain, after some algebra, the following result [2],

$$\begin{aligned} C_\omega(R, z_1, z_2) &= \frac{2pq^2}{k^{2p}} \int_0^k (k^2 - k_r^2)^{p-1} \exp[iZ(k^2 - k_r^2)^{1/2}] \\ &\times \frac{\sin^2[z'(k^2 - k_r^2)^{1/2}]}{k^2 - k_r^2} J_0(k_r R) k_r dk_r, \end{aligned} \quad (9.28)$$

where we have taken  $Z \equiv z_1 - z_2$ . In order to recover the Cron and Sherman result, we let  $z' \rightarrow 0$  and take the normalized function  $\bar{C}_\omega(R, z_1, z_2)$  defined as

$$\bar{C}_\omega(R, z_1, z_2) \equiv \lim_{z' \rightarrow 0} \frac{\operatorname{Re}[C_\omega(R, z_1, z_2)]}{\{\operatorname{Re}[C_\omega(0, z_1, z_1)] \operatorname{Re}[C_\omega(0, z_2, z_2)]\}^{1/2}}. \quad (9.29)$$

For the normalized source strength we must then evaluate integrals of the form

$$I_p(R, Z) = \int_0^k (k^2 - k_r^2)^{p-1} \cos[Z(k^2 - k_r^2)^{1/2}] J_0(k_r R) k_r dk_r. \quad (9.30)$$

First, consider the case when  $z_1 = z_2$ ; then we have

$$I_p(R, 0) = \int_0^k (k^2 - k_r^2)^{p-1} J_0(k_r R) k_r dk_r, \quad (9.31)$$

which is a standard integral and is given by [11]

$$I_p(R, 0) = 2^{p-1} k^p R^{-p} (p-1)! J_p(kR). \quad (9.32)$$

Therefore,

$$\bar{C}_\omega(R, z_1, z_1) = 2^p p! \frac{J_p(kR)}{(kR)^p}, \quad (9.33)$$

which is exactly the correlation function of the surface sources, (9.15). Next, let  $R = 0$ , so that we deal with integrals of the form

$$I_p(0, Z) = \int_0^k (k^2 - k_r^2)^{p-1} \cos[Z(k^2 - k_r^2)^{1/2}] k_r dk_r, \quad (9.34)$$

which, after changing variables to  $\zeta \equiv (k^2 - k_r^2)^{1/2}$ , becomes

$$I_p(0, Z) = \int_0^k \zeta^{2p-1} \cos(Z\zeta) d\zeta. \quad (9.35)$$

For  $p = 1$ , this integral is simply

$$I_1(0, Z) = kZ^{-1} \sin(kZ) + Z^{-2} [\cos(kZ) - 1], \quad (9.36)$$

so that

$$\bar{C}_\omega(0, Z) = 2(kZ)^{-1} \sin(kZ) + (kZ)^{-2} [\cos(kZ) - 1]. \quad (9.37)$$

For  $p > 1$ , we note that

$$I_p(0, Z) = (-1)^{p-1} \frac{\partial^{2p-2}}{\partial Z^{2p-2}} I_1(0, Z), \quad (9.38)$$

so for  $p \geq 1$

$$\bar{C}_\omega(0, Z) = (-1)^{p-1} 2^p k^{-2p} \frac{\partial^{2p-2}}{\partial Z^{2p-2}} I_1(0, Z). \quad (9.39)$$

The results given by (9.33), (9.37), and (9.39) are the Cron and Sherman results [12]. However, the present derivation is more general. In fact, if instead of using the  $p = 1$  correlation function of (9.15) we chose the *uncorrelated* noise source case, a second term would be present which, however, would be negligible except near the surface. This second term is the contribution of the nearfield of the dipoles, corresponding to the evanescent spectrum  $k_r > k$  in (9.16). Such evanescent components have in fact been observed experimentally [13], and, as we shall see later, this evanescent spectrum becomes an important component of the low-frequency noise field in shallow water.

### 9.2.6 Noise in Stratified Media

Here, we present results for the noise fields in fluid media and an example comparing the physics of noise fields of fluid and elastic media. This latter comparison is of interest for very-low seismo-acoustic frequencies where significant interaction with the ocean basement occurs.

#### 9.2.6.1 Fluid Waveguide

In presenting stratified waveguide results of noise fields originating from homogeneously distributed surface sources, the following should be noted:

1. In a range-independent environment, the vertical directionality of the surface-generated noise field is controlled by the fundamental propagation properties of the waveguide, as illustrated in Fig. 9.2.
2. The horizontal structure of the noise field is spatially homogeneous meaning that the cross-spectral density is a function of the horizontal separation of field points and not the absolute horizontal location.
3. The vertical structure of the noise field is not spatially homogeneous so that the cross-spectral density is a function of the absolute position of the field points. This is not the case for the homogeneous halfspace which the simpler models [12] address.

We consider a 100-m deep waveguide bounded below by a fluid halfspace with a sound speed of 1800 m/s, an attenuation of 0.5 dB/ $\lambda$ , and a density of 1800 kg/m<sup>3</sup>. As shown in Fig. 9.3a, we consider two different sound-speed profiles. The one indicated by the solid curve is weakly downward refracting, whereas the one indicated by the dashed curve is characterized by a strong surface duct.

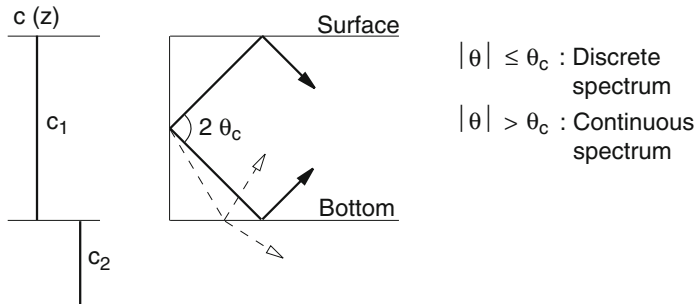


**Fig. 9.2** Spectral partitioning in ocean waveguide due to critical angle effect. Energy propagating within a cone of  $2\theta_c$  (the discrete spectrum) suffers little bottom loss; steeper paths associated with the continuous spectrum are very lossy with considerable energy being transmitted into the bottom

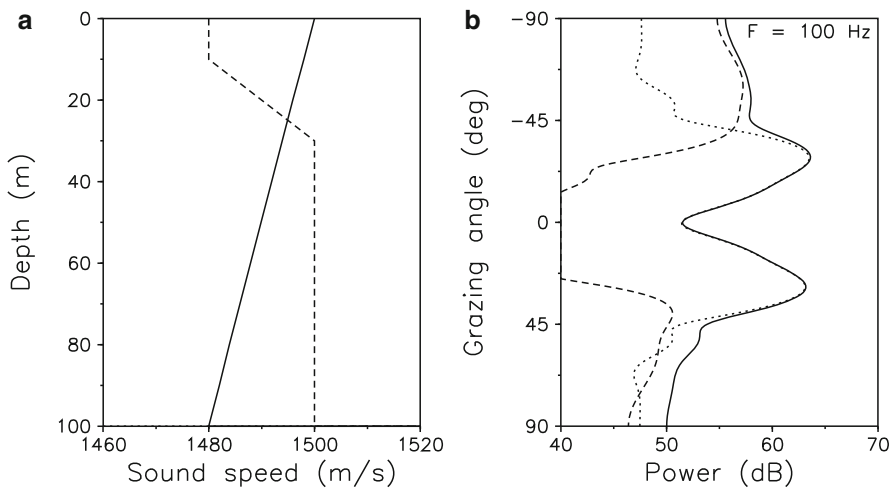


**Fig. 9.3** Noise in a range-independent waveguide. (a) Generic sound-speed profiles. (b) Vertical directionality. The individual contributions from the continuous and discrete spectra are indicated by the dashed and dotted curves, respectively

Item 1 above is clearly demonstrated by computing the *vertical directivity* of the noise. As described in Chap. 2, the depth-dependent Green's function in a stratified medium is inherently decomposed in up- and downgoing wave components. However, in the wavenumber representation for the noise field, (9.16), the two components are coupled through the cross-terms. Therefore, in contrast to what is the case for the signal produced by a single source or an array of coherent sources, the vertical directivity cannot be determined through a simple transformation of horizontal wavenumber to grazing angle. We will therefore demonstrate the vertical directivity by simulating the response of a vertical receiver array used as a steered antenna. This process is called beamforming and, as addressed in Sect. 10.2.1, uses the cross-spectral density function as an input.

For the environment with a downward refracting sound-speed profile, indicated by the solid curve in Fig. 9.3a, the output of the beamformer is shown in Fig. 9.3b where we have performed the computation using the spectral representation of the noise field. Negative angles are the upward direction from which we see the direct surface arrivals. The main features of the waveguide are clear. There is no horizontally propagating wave because such a wave cannot simultaneously satisfy the surface and bottom boundary conditions; hence, we see a *noise notch* in the horizontal. The actual depth of the noise notch varies with environmental conditions as discussed by Rouseff and Tang [14]. The actual directionality is a tradeoff between *discrete* modal energy contained within the angular cone shown in Fig. 9.2 and the *continuous*, more vertical portion of the field. It is easy to see that a relatively lossless bottom will permit discrete contributions from long ranges and the directionality will tend to be more horizontal than an extremely lossy bottom environment where the continuous spectrum will tend to dominate.

We can immediately understand Item 2 above since it is simply a result of horizontal translational invariance in a range-independent waveguide. However, it is interesting to note that the horizontal cross-spectral density is different for this case than for the homogeneous halfspace case. This is because of the above-mentioned tradeoff between the discrete and continuous spectra. For a frequency of 100 Hz, Fig. 9.4 shows the normalized contributions of the two spectral components of the total spatial correlation as a function of the horizontal separation. In the limit of the bottom speed and density approaching the corresponding parameter values for the water column, the contribution from the discrete spectrum disappears, and the continuous portion becomes equal to the correlation function for a homogeneous halfspace.

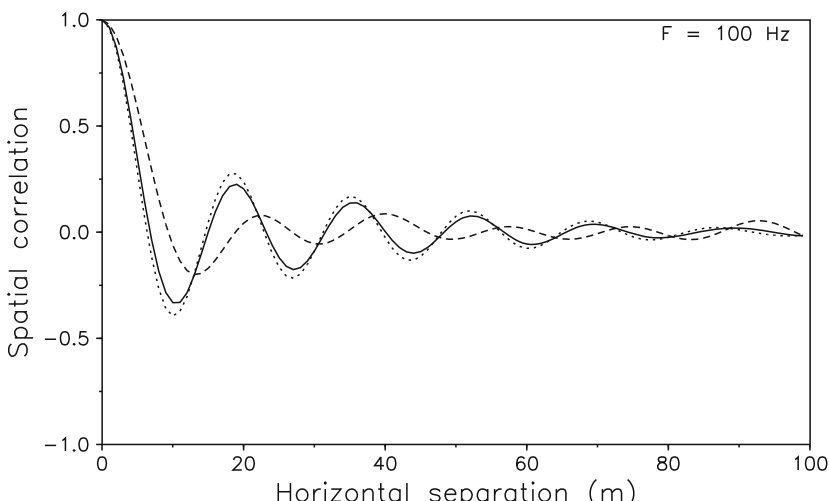


**Fig. 9.4** Normalized horizontal spatial correlation of the noise at depth 50 m in the environment shown in Fig. 9.3a. The *solid curve* shows the correlation of the total field, whereas the *dashed* and *dotted curves* show the normalized contributions from the continuous and discrete spectra, respectively

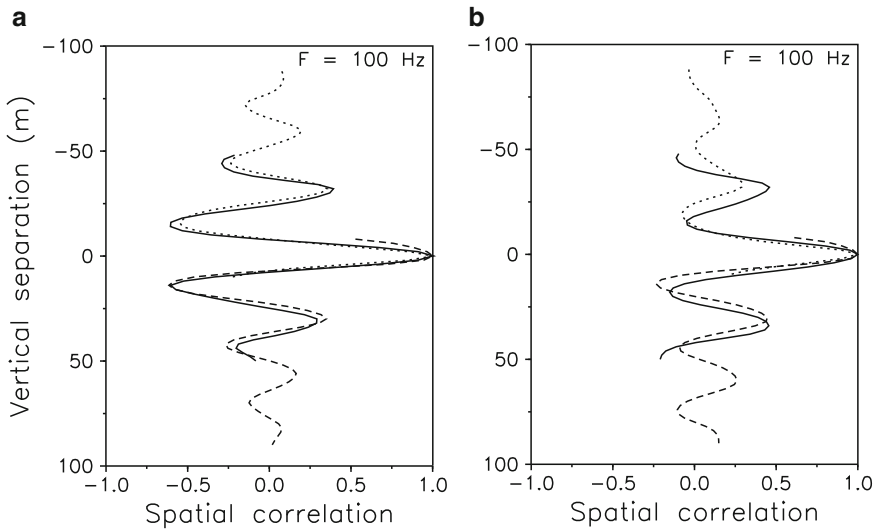


**Fig. 9.5** Normalized vertical spatial correlation at depth 50 m (solid curve), 10 m (dashed curve), and 90 m (dotted curve), demonstrating the spatial inhomogeneity of the waveguide noise field. **(a)** Downward-refracting profile; **(b)** Surface-duct profile

As mentioned in Item 3, the vertical *spatial correlation* is not stationary, even for isovelocity waveguides. This is illustrated in Fig. 9.5 which shows normalized vertical correlations for the two sound-speed profiles given in Fig. 9.3. The solid curves are for the reference receiver at mid-depth, 50 m, whereas the dashed and dotted curves correspond to receivers at 10 and 90 m depths, respectively. It is clear, for example, that the correlation is increased in the part of the water column where energy tends to be trapped. Furthermore, even in the isovelocity case, the waveguide correlation is different from that existing in a homogeneous halfspace, with the lack of spatial stationarity particularly evident near the ocean bottom as compared to elsewhere in the water column.

### 9.2.6.2 Elastic Waveguide

As discussed in Chap. 4, for low-frequency propagation one must consider the ocean bottom as a layered viscoelastic medium, which means that the waveguide supports not only body waves but also seismic interface waves. In a viscoelastic structure, cutoff never occurs even though discrete modes may not be present in the water column. The vertical amplitude distribution of an interface wave decays exponentially away from the bottom, which implies that the interface waves can only be excited in a stratified waveguide by sources close in terms of wavelength to the interface. Hence, at low frequencies, these interface waves provide a mechanism for sound to propagate and be sensed in the water column. The partitioning between body waves and interface waves can explain the spectral distribution of noise observed

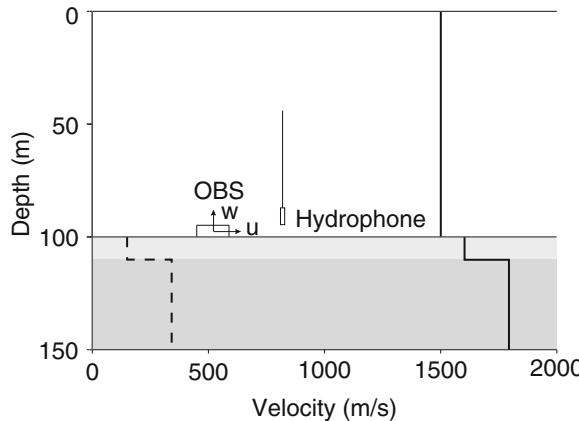


**Fig. 9.6** Environmental model of 10-m silt layer of density  $1800 \text{ kg/m}^3$  overlying a sand halfspace of density  $2000 \text{ kg/m}^3$  corresponding to a Mediterranean Sea experiment. Dashed line is for shear speed, solid line for compressional speed. The shear-wave attenuation for the layers are 0.5 and  $1.0 \text{ dB}/\lambda$  and the compressional attenuation for the layers are 0.1 and  $0.2 \text{ dB}/\lambda$ , respectively

experimentally in shallow water and reported for deep-water environments where the activity at the air-sea interface is the source of microseismic and low-frequency noise.

We consider the environment depicted in Fig. 9.6, representing the site of an experiment performed in the Mediterranean Sea [15]. To illustrate the physics associated with the elastic waveguide, it is enough to deal with the expectation of the intensity  $I$  for uncorrelated noise sources. This we obtain from (9.17) as

$$I = \frac{8\pi^2 q^2}{k^2(z')} \int_0^\infty |g_{p,w,u}(k_r, z, z')|^2 k_r \, dk_r, \quad (9.40)$$

where  $g_{p,w,u}(k_r, z, z')$  are the seismo-acoustic Green's functions for the pressure  $g_p$ , vertical particle velocity  $g_w$ , and horizontal particle velocity  $g_u$  as described in Chap. 4. A decibel level corresponding to the source level  $q$  yields the same decibel level as  $Q$  in a homogeneous halfspace in the examples that follow. For instance, a 50 dB noise source level would result in a uniform 50 dB noise level in a homogeneous halfspace. This is accomplished to first order in  $z'$  if  $q^2$  is assigned the value

$$q^2(z') = \frac{Q^2}{16\pi z'^2} \quad (9.41)$$

with the caveat that  $z'$  is chosen small enough compared to the vertical wavelengths involved that it will result in (9.40) being independent of  $z'$ .

As discussed in Chap. 4, plots of the kernels of (9.40) as a function of horizontal wavenumber for frequencies corresponding to regimes that range from discrete modal propagation through waterborne cutoff down to lower frequencies are valuable for physical interpretation. Figure 9.7 depicts the wavenumber kernels for 10, 5,

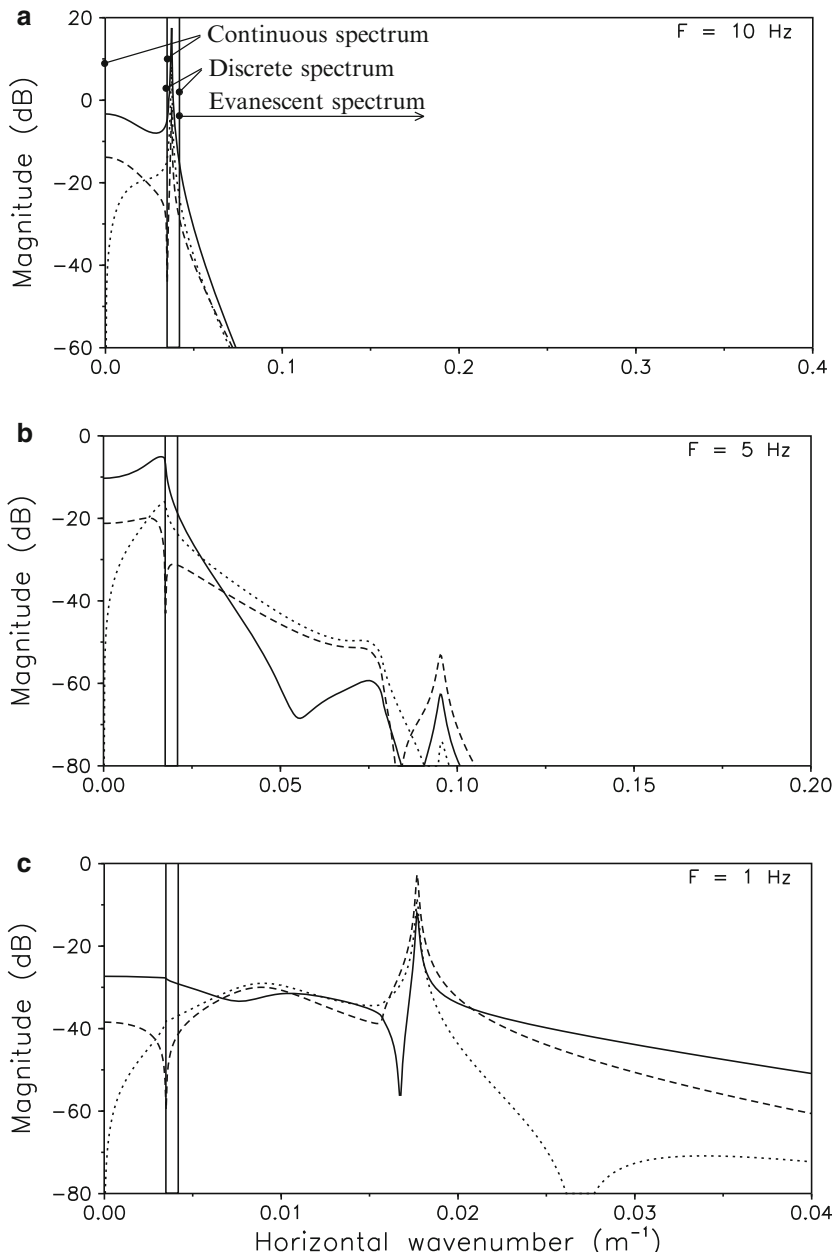


**Fig. 9.7** Wavenumber kernels  $|g_{p,w,u}(k_r, z, z')|^2$  at the seabed for frequencies of (a) 10 Hz, (b) 5 Hz and (c) 1 Hz. The solid curve is for  $g_p$ , the dashed curve for  $g_u$  and the dotted curve for  $g_w$ . The continuous, discrete, and evanescent parts of the wavenumber spectrum are indicated

and 1 Hz for the continuous, discrete (modal), and evanescent spectral intervals. The region to the left is the continuous portion of the spectrum that corresponds to steep propagation angles (grazing angles larger than the basement critical angle). The evanescent bottom interface waves appear to the right of the discrete spectrum since their phase speeds are lower than the speed of sound in the water column. At 10 Hz, we see that the Green's function for all three wavefield parameters has a peak in the discrete region corresponding to a single propagating normal mode, but no evanescent waves are significant.

At 5 Hz we see a larger contribution in the continuous regime, but no discrete modes are present; this frequency is below the 8-Hz cutoff of the fundamental waterborne mode. We also see some peaks to the right of the discrete region that corresponds to various interface waves. Though the height of each peak represents the excitation of the type of motion associated with that peak, the contribution to the noise is a direct integration of the kernel (i.e., it does not have the oscillatory exponential for the kernel associated with propagation from a point source, as in (4.96)). This makes the width of the peak important as well. Thus, a wide peak, indicating high attenuation, can still contribute significantly to the total noise intensity. This contrasts with propagation from a point source where a wide peak renders that spectral contribution insignificant at long ranges. This difference is due to the distribution of the noise sources over the entire surface. Thus, the theory predicts that highly attenuated interface waves can still be important propagation mechanisms for surface-generated noise; the important issue is that this excitation is relatively low at 5 Hz for this environment.

Finally, at 1 Hz we see dominant sharp peaks only in the interface-wave regime. This indicates that in this frequency regime the *interface wave* is the only significant carrier of the ambient noise. Since high, wide peaks correspond both to a significant noise contribution and highly attenuated propagation paths, we can conclude that only sources at short horizontal ranges relative to the field points contribute significantly to the ambient noise.

Figure 9.8 summarizes the picture that emerges from studying the Green's functions in Fig. 9.7. At higher frequencies, the noise field is composed mainly of continuous and discrete spectral components, with the higher frequencies tending

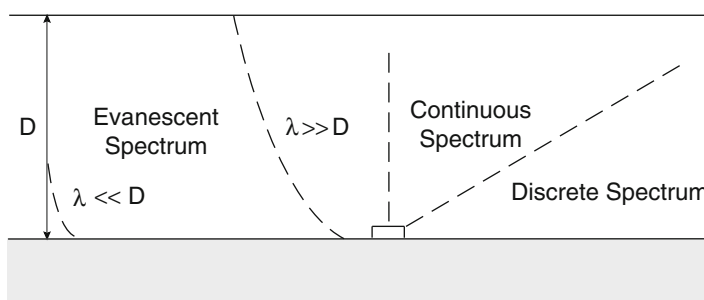


**Fig. 9.8** Schematic representation of the three spectral regimes

more toward the continuous spectrum because of attenuation. As the frequency is decreased, the ocean surface comes acoustically closer to the seabed and coupling to the evanescent portion of the spectrum therefore takes place.

The noise levels obtained by performing the integration in (9.40) are shown in Fig. 9.9 as a function of frequency. From Fig. 9.9a, we see a rise in the noise level from just above cutoff ( $\sim 10$  Hz) that corresponds to the maximum excitation of the first discrete mode. At lower frequencies, the noise decreases because there are no discrete contributions from distant noise sources. Finally, at very low frequencies, there is an increase in the noise corresponding to the surface noise sources that are now in the nearfield of the bottom and therefore excite interface waves. The increase is greater for the velocity components than for pressure due to the presence of the pressure-release surface. This low-frequency excitation does not occur for a purely fluid bottom as shown in Fig. 9.9b. Figure 9.9c which shows experimental results by Akal et al. [15] for this environment, confirms the above analysis. By subtracting the theoretical results for a white source spectrum, Fig. 9.9a, from the experimental data in Fig. 9.9c, we obtain a more realistic estimate of the actual source levels. These source levels adjusted for propagation effects are found to be significantly lower at the low frequencies than the levels obtained from the raw spectra [3]. This is because the acoustic waveguide by trapping energy magnifies the noise field over that which would be expected in a halfspace ocean.

### 9.3 Extracting Time-Domain Green's Functions from Noise Correlation Functions

Noise is typically considered a nuisance to overcome. Much of signal processing is devoted to extracting a signal that is embedded in noise. However, since the structure of ocean noise is determined by the environment, as shown earlier in this chapter, noise must contain information about the environment. Indeed, for example, the discussion accompanying Fig. 9.2 is about the dependence of noise on the critical angle and hence, the bottom sound speed. More quantitatively, it has been shown by Deane et al. [16, 17] that ocean bottom properties can be estimated from the vertical coherence of ocean noise. More recently, a rather elegant approach by Harrison and Simons [18, 19] demonstrated how to extract the bottom reflection coefficient by simply taking advantage of the fact that at any given angle with respect to the horizontal, noise coming from the bottom undergoes one more bottom reflection than noise coming from overhead. Even more ambitious is acoustic daylight, as proposed by Buckingham et al. [20–23], where surface-generated noise is used as the equivalent of diffuse light for the purpose of underwater imaging. This incoherent process is the acoustical analog to (incoherent) optics though a coherent acoustic version has also been theoretically explored [24]. In this section, however, we will confine the material to the basic question of how to recover propagation physics from an ocean ambient noise field.

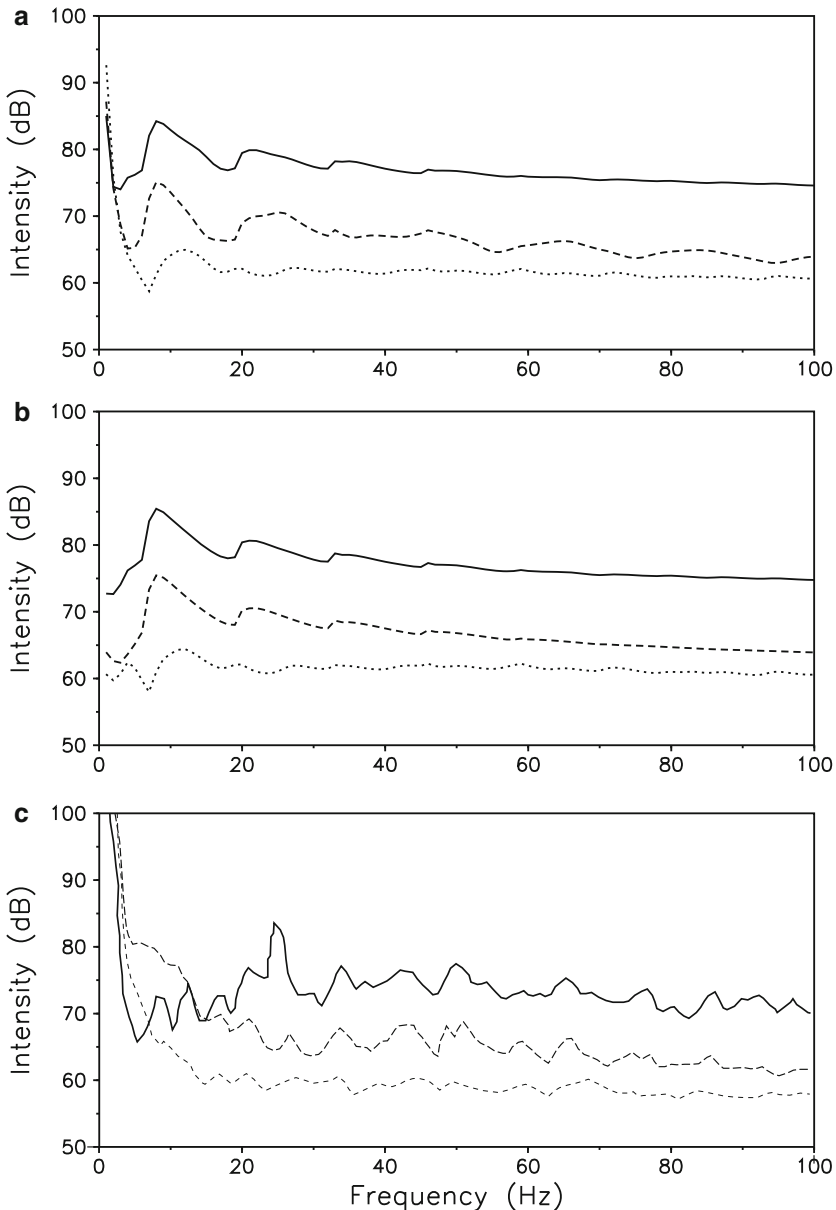


**Fig. 9.9** Noise level spectra for a  $q^2$  that in an infinitely deep ocean would yield a pressure amplitude  $Q$  corresponding to 70 dB. The *solid curve* is pressure, the *dashed curve* horizontal particle velocity, and the *dotted curve* vertical particle velocity. (a) Shear supporting bottom; (b) Fluid bottom; (c) Data from Mediterranean experiment [15]

### 9.3.1 The Time-Domain Green's Function

It has been shown [25–27] that if noise sources are homogeneously distributed over all space, then the time derivative of the time-domain NCF is related to the time-domain Green's function (TDGF) between the two points of the correlation. While this is a general result, for surface-generated noise the sources are not distributed over all space. However, we can show that the arrival times of the TDGF can be extracted from surface noise, but the arrival amplitudes will reflect the fact that the sources are dipoles which emphasize vertical propagation and hence higher modal arrivals.

We return to the simplified version of the frequency-domain waveguide noise correlation as expressed by (9.27), reinsert the Hankel functions' representation of the Bessel function and then take the Fourier transform with respect to frequency to obtain the time-domain NCF given by (9.14) between points 1 and 2 located at depths  $z_1, z_2$ , respectively (see Fig. 9.1) and separated by the horizontal distance  $R$ . The TDGF arrival times will therefore be related to the time-derivative of the correlation function,

$$\begin{aligned} \frac{\partial C_t(R, z_1, z_2)}{\partial t} &\propto \int_{-\infty}^{\infty} (-i\omega)e^{-i\omega t} \sum_m [\Psi_m(z')]^2 \frac{\Psi_m(z_1) \Psi_m(z_2)}{\alpha_m \kappa_m} \\ &\quad \times \left[ H_0^{(1)}(\kappa_m R) - H_0^{(1)}(-\kappa_m R) \right] d\omega. \end{aligned} \quad (9.42)$$

The first frequency factor disappears in the integrand because (see, e.g., (5.177)) of the approximate relationship  $\alpha_m \kappa_m \approx \omega \alpha_b$ . In any event, we note that the temporal arrival structure can be obtained from a stationary phase evaluation of the Fourier integral and therefore amplitude factors in the integrand are not consequential for the actual arrival times as opposed to phase factors. Comparing this result of (9.42) to the Fourier synthesis of (5.13), we see that the time-domain correlation function of the noise (which we now denote as NCF), or more precisely, its derivative, is directly related to a *shaded* impulse response or the TDGF between points 1 and 2. As mentioned above, the shading factor in the first brackets of the integrand comes from the fact that the original sources of the acoustic fields are dipoles as explained earlier in this chapter. If, e.g., the noise sources were isotropically distributed over the water volume, then the correlation function would also include an integration over  $z'$  resulting in the form of (9.42) without the bracketed  $z'$  factor and therefore a much better representation of the true Green's function.

Nevertheless, the important result is that a correlation between surface-generated noise received at two points results in a time of arrival structure as if there was a source at one of the points and a receiver at the other. The two Hankel-function terms indicate that the result is centered about  $t = 0$ , i.e., one is the time-reversed of the other, meaning either receiver point could be the analog of the source location.

### 9.3.2 Emergence of Coherent Wavefronts from Noise

Figure 9.10 schematically explains how these coherent wavefronts emerge from the random noise field. Only those propagation paths emanating from a random noise source that go through both receivers contribute to the NCF. The paths between the two points are the allowable propagation paths, so after a long time all propagation paths are accumulated in the NCF in the form of time delays. If one then correlates the time series at a point receiver with those at a set of vertical receivers, then the set time delays (peaks) in the NCF will naturally correspond to the wavefront arrivals at the vertical array as if there was a source at that first point receiver.

A time-domain image representation of the waveguide noise process not only quantitatively confirms this intuitive picture, but also reveals that it is the time derivative of the NCF that gives the TDGF [27]. In the image theory, the impulse responses of (2.139) are used as the TDGF's of the time-domain version of (9.6) and the subsequent integrations over surface area can be performed because of the delta functions in (2.139). After an elaborate combination of algebraic and geometric calculations, a closed-form solution results of which the time derivative is taken. The resulting series are the set of wavefronts between the correlation points, and the image solution can also be generalized to finite bandwidth intervals. An example of a finite bandwidth result of such a calculation is shown in Fig. 9.11 for the TDGF, and the time derivative of the NCFs for two different noise source layer depths. The effect of the dipole in the NCF calculation is to shade the more horizontal arrivals (more vertical wavefronts). The shallower noise sources behave more like true dipoles that have the greater vertical directivity as seen by comparing Figs. 9.11b, c.

Finally, an important issue is the length of time used to compute the NCF such that the wavefronts emerge from the background noise. For a homogeneous distribution of noise sources, the rate of emergence of the wavefronts from the correlation process has been shown to be proportional to  $\sqrt{tw}$ , the square root of the time-bandwidth product [26, 28, 29]. In reality, ocean noise sources are not uniformly distributed. In the lower frequency regime, shipping noise is a dominant factor and

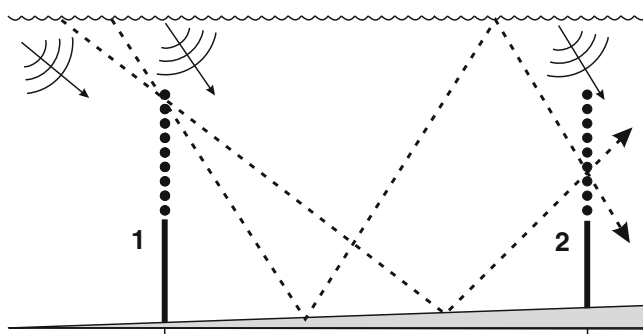


**Fig. 9.10** The noise correlation between receivers 1 and 2 is built up from noise events whose propagation paths go through both receivers

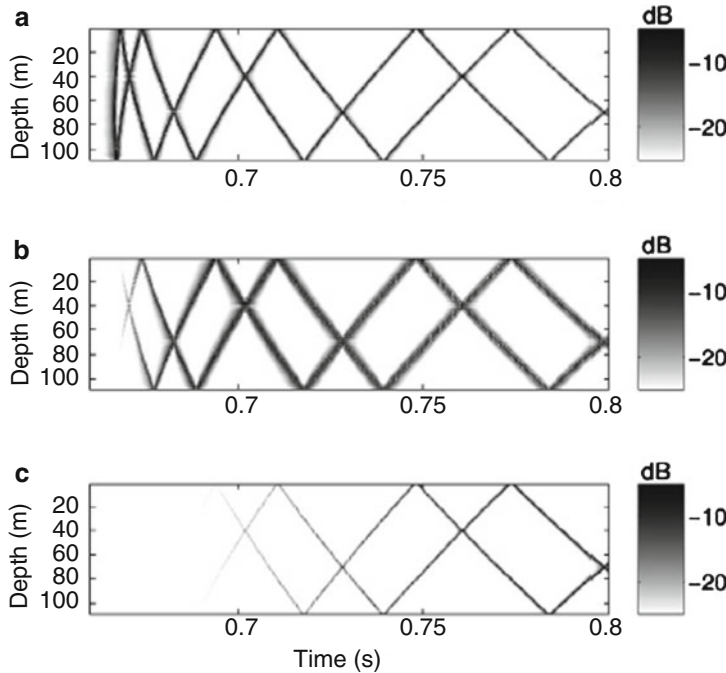


**Fig. 9.11** Ideal waveguide example constructed from image theory. We consider a source (receiver) at 70 m depth in a 110-m pressure-release waveguide at a range of 1 km from a vertical receive array. The impulsive field is filtered to a bandwidth between 1 and 3 kHz. **(a)** The TDGF from the source to the receiver array and **(b, c)** Positive time-delay waveforms of the correlation function between a receiver at 70-m depth and a vertical array and a distribution of noise sources at 1 m **(b)**, 0.1 m **(c)**. The shallower noise sources in **(c)** behave more like dipoles emphasizing the later, more vertical arrival structure as compared to **(b)** and to the true TDGF in **(a)**. Note that the arrival times for all three cases are the same

noise from specific ships will introduce error to the process. This can be minimized by eliminating specific events through some sort of clipping. The higher the frequency, the less the effects of shipping so that the criterion of homogeneous distribution of noise sources, at least in azimuth, is more likely to be satisfied. However, the angular distribution of noise in the vertical due to dipole sources on the surface of the waveguide is not isotropic.

### 9.3.3 Data Examples of Extracting Wavefronts from Noise

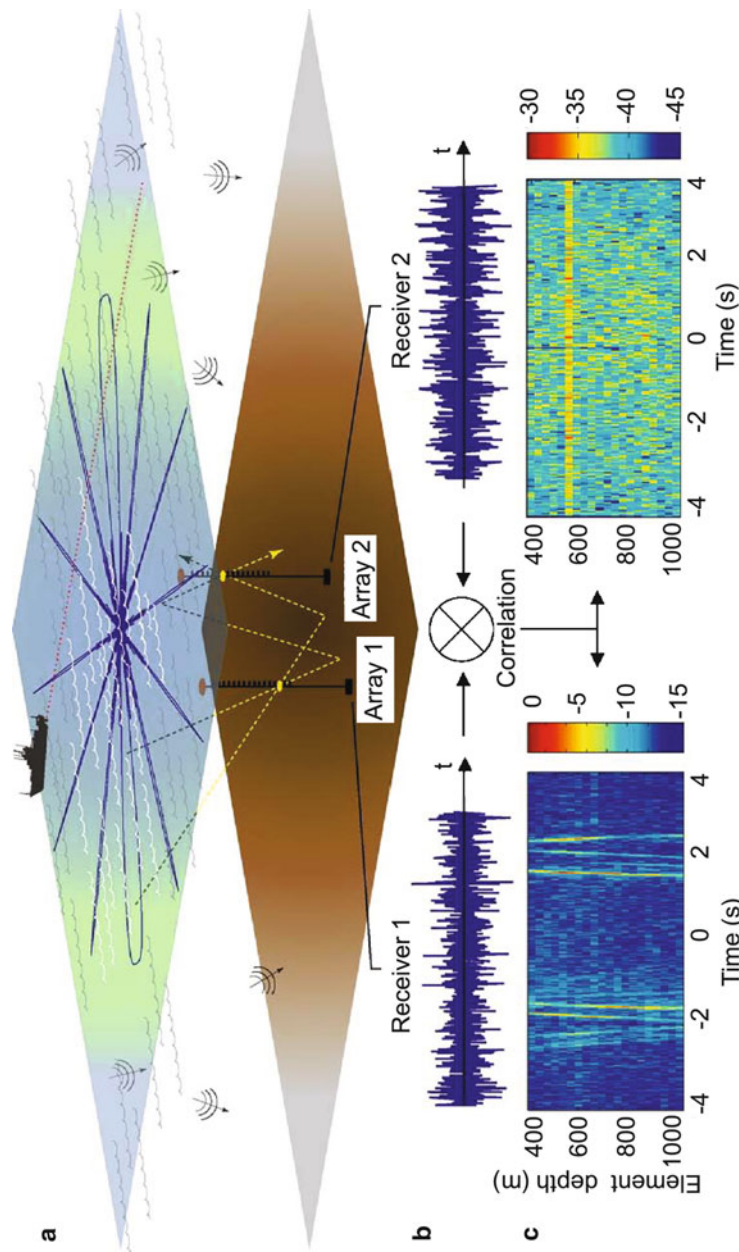
The process of constructing an NCF between receiver elements and arrays requires that all the receivers be synchronized. An example of such data comes from the long-range, North-Pacific Acoustic Laboratory (NPAL) [26] experiments which provides data of opportunity for computing the NCF over a considerable range. The data

used here was from four vertical arrays that were colinear in range in intervals up to 5 km. The NPAL experiments used a source at about 3000 km but the noise data used here was taken when the source was turned off. The processing bandwidth was 70–130 Hz so shipping noise was the dominant component. It was shown [26] that the TDGF's would also emerge from this scenario with appropriate processing and sufficient integration time.

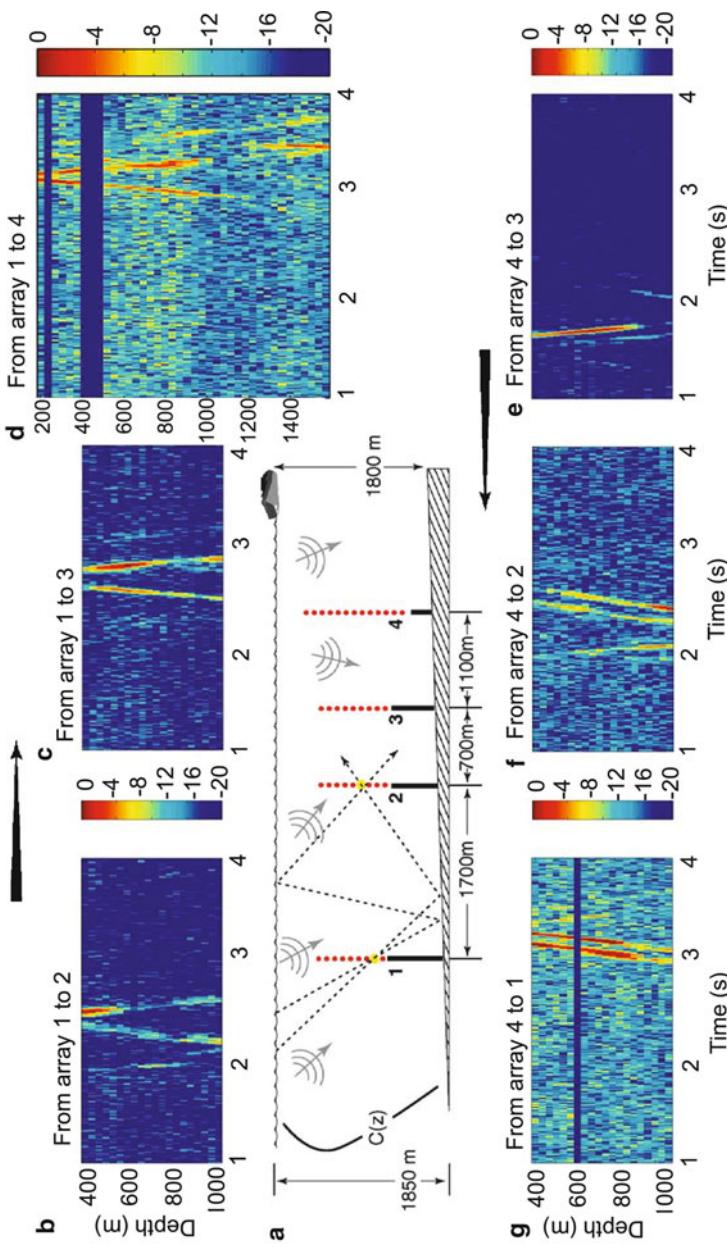
A receiver configuration and some results are shown in Fig. 9.12. The correlation beam pattern is shown superimposed on the surface. One can think of the lobes as the delay-time resolution. That is, in the endfire direction the lobes are broadest meaning that a ship transecting such a lobe will register at the same delay time for that whole transect while a ship transmitting a thinner, more broadside lobe has a shorter length of time for a specific delay time to register before smearing to another delay time. Therefore, over a long time, it is the endfire direction that will dominate and the above discussions on how the wavefronts emerge are valid for this case also. Further, note that whether or not we have discrete shipping or distributed surface sources, the largest time delay between receivers (for a particular path) always occurs for sources along the horizontal line between the receivers excluding those between the receivers (endfire). Intuitively, think of the opposite situation, broadside, a source perpendicular to that horizontal line between receivers. If the perpendicular intersect was midway, the time delay would be zero. The endfire direction provides the maximum allowable time delay; therefore the time derivative of the NCF would have a peak at that maximum allowable time delay corresponding to the travel time between the two points. Figure 9.12c is the two-sided correlation function showing the wavefronts as discussed above whereas Fig. 9.12d shows the same correlation process for time series that were not simultaneously recorded. The latter result is further evidence that the TDGF is build up from individual noise sources whose propagation path goes through both receivers.

Figure 9.13 is a range-depth schematic of the layout of receiving arrays together with examples of the NCF processing. Because of the multiple arrays were along a line, we actually see traveling wavefronts. A careful examination of the results shows that the effect of the slightly sloping bottom is contained in the results. That is, up-slope propagation results in steepening of the propagation angle with each bounce and the associated wavefront change that must be perpendicular to the propagation direction. Therefore, the forward and back-propagating wavefronts should accordingly have different tilts as the data analysis shows.

The correlated noise between array elements lying on the ocean bottom can also be used to extract the TDGF between the array elements. Data taken from such an array [30] lying on the bottom in 21-m deep, coastal-water location was used for just such an analysis, see Fig. 9.14. The noise was from croaker fish and therefore volume distributed. As pointed out earlier in the chapter, since the noise sources are distributed over the volume, we must also integrate over depth  $z'$  in (9.24). Invoking orthonormality of the modes, we obtain the same expression as that of (9.42) but without the factor of  $[\Psi_m(z')]^2$ . Hence, as expected for the homogeneous distribution of noise sources throughout the volume, the time derivative of the correlation function yields a more accurate representation of the TDGF rather than an amplitude shaded version of the temporal arrival structure.



**Fig. 9.12** Noise correlation processing of deep-water shipping noise in the 70–130 Hz band [26]. (a) Schematic of two vertical arrays in 1850-m deep water, 2200 m apart. The beam pattern projected on the surface is from the correlation process and indicates the widest lobe in the endfire directions. (b) The processing shown involves correlating time series between an element of array 1 at 500-m depth and each of the elements of array 2. (c) The left-hand result shows the resulting wavefronts as if the receive element on array 1 was a source. The right-hand result is a correlation result from which the two time series were not taken at the same time



**Fig. 9.13** The positive time-correlation traveling-wavefront result obtained by processing data from four arrays in the environment of Fig. 9.12. (a) Arrays geometry: note that array 4 has twice the elements of the others. (b)–(d) Traveling wavefronts obtained by correlating time series from elements of arrays 2–4 with the 500-m element of array 1. (e)–(g) Traveling wavefronts obtained by correlating time series from elements of arrays 1–3 with the 500-m element of array 4 revealing the wavefront traveling in the opposite direction of (b)–(d). Further, the sloping bottom is actually manifest in the different wavefront angles of (b)–(d) and (e)–(g)

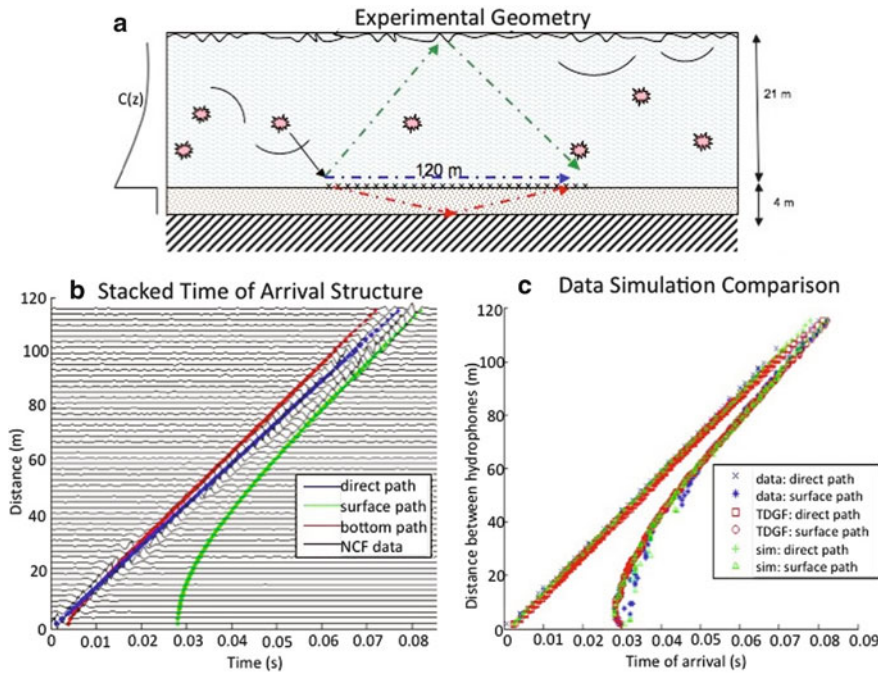


**Fig. 9.14** Time-of-arrival structure obtained from the correlation of croaker fish noise on a 64-element horizontal array. The analysis bandwidth was 250–750 Hz. (a) Schematic of experimental layout. (b) The temporal derivative of the correlation functions between elements. The processing yields the direct and surface-reflected paths. (c) A favorable comparison between data, simulation of data by using many random sources and the actual (using measured environmental input) time-domain Green’s function

As mentioned above, the data analysis requires synchronized arrays. However, it has also been shown [29] that with some basic environmental information, the noise correlation process can actually be used to synchronize arrays by “focusing” the correlation data into wavefronts in which the synchronization and/or array geometry parameters are used together with an optimization algorithm. Furthermore, an important application of this correlation processing has been to correlate beams from a vertical array of sensors (see Chap. 10) for the purpose of constructing a passive fathometer using only ambient noise, rather than the conventional active fathometer that uses its own source [31].

## 9.4 Surface Noise in a Three-Dimensional Ocean

Modeling range-dependent environments requires extensive changes since separation of variables, which underlies the derivations in Sect. 9.2 cannot be formally employed. Hence, the analytic integration over surface area or wavenumber space, as suggested by (9.9) and (9.10), is not possible.

The two wave models that are most practical for solving the range-dependent noise problem are adiabatic mode theory and the parabolic equation method. In this section, we generalize the earlier mode results to range-dependent environments by applying adiabatic mode theory.

### 9.4.1 Noise Modeling by Adiabatic Modes

Following the derivation of Perkins et al. [32], we begin our treatment with (9.4) and assume that the sound-speed profile, bathymetry, bottom properties and surface source strength can vary with range. To calculate the integral in (9.4) we divide the area of the plane into two regions: a large circular area  $A$  centered on the origin, and the remaining area outside  $A$ . Usually  $A$  is large enough so that the contribution to the field from the area outside  $A$  is highly attenuated and can be neglected. The area  $A$  is in turn divided up into a circular region of radius  $R$  centered on the origin plus  $N$  subregions of general shape, each having an area denoted by  $A_v$ . This is illustrated in Fig. 9.15a. We have that

$$A = A_0 + \sum_{v=1}^N A_v, \quad (9.43)$$

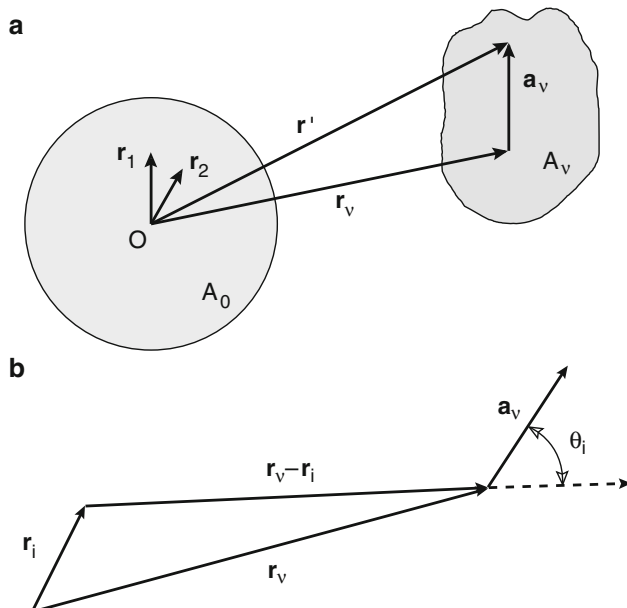


**Fig. 9.15** Geometry for the adiabatic mode solution of the surface-distributed noise problem

where  $A_0 = \pi R^2$ . The subregions are chosen so that the environment and source strength do not vary with range within a subregion. Hence, we have

$$\phi(\mathbf{r}, z) = \sum_{\nu=0}^N \int_{A_\nu} S(\mathbf{r}') g(\mathbf{r}, \mathbf{r}'; z, z') d^2 \mathbf{r}'. \quad (9.44)$$

We form the cross-spectral density between two points,  $C(\mathbf{r}_1, z_1; \mathbf{r}_2, z_2)$ , by multiplying the field at one point  $(\mathbf{r}_1, z_1)$  by the complex conjugate of the field at a second point  $(\mathbf{r}_2, z_2)$  and taking the ensemble average. We get

$$\begin{aligned} C(\mathbf{r}_1, z_1; \mathbf{r}_2, z_2) &\equiv \langle \phi(\mathbf{r}_1, z_1) \phi^*(\mathbf{r}_2, z_2) \rangle \\ &= \sum_{\nu, \mu} \int_{A_\nu} \int_{A_\mu} \left\langle \langle S(\mathbf{r}') S(\mathbf{r}'') \rangle \right. \\ &\quad \times g(\mathbf{r}_1, \mathbf{r}'; z_1, z') g^*(\mathbf{r}_2, \mathbf{r}''; z_2, z') \left. \right\rangle d^2 \mathbf{r}' d^2 \mathbf{r}'', \end{aligned} \quad (9.45)$$

where the asterisk indicates the complex conjugate and the brackets indicate the ensemble average. As in [2], we assume that the spatial coherence of the noise sources,  $\langle S(\mathbf{r}') S(\mathbf{r}'') \rangle$ , depends only on the difference between source points which we denote by  $\mathbf{s} \equiv \mathbf{r}' - \mathbf{r}''$ . Furthermore, we assume that the sources are uncorrelated, see (9.15), so that we get

$$\begin{aligned} C_\omega(\mathbf{r}_1, z_1; \mathbf{r}_2, z_2) &= \frac{2q^2}{k^2} \sum_{\nu, \mu} \int_{A_\nu} \int_{A_\mu} \left\{ \frac{\delta(\mathbf{R})}{\mathbf{R}} \right. \\ &\quad \times g(\mathbf{r}_1, \mathbf{r}'; z_1, z') g^*(\mathbf{r}_2, \mathbf{r}' - \mathbf{R}; z_2, z') \left. \right\} d^2 \mathbf{r}' d^2 \mathbf{R}, \end{aligned} \quad (9.46)$$

which reduces to

$$C(\mathbf{r}_1, z_1; \mathbf{r}_2, z_2) = \frac{4\pi q^2}{k^2} \sum_{\nu=0}^N \int_{A_\nu} g(\mathbf{r}_1, \mathbf{r}'; z_1, z') g^*(\mathbf{r}_2, \mathbf{r}'; z_2, z') d^2 \mathbf{r}', \quad (9.47)$$

where we have suppressed the  $\omega$  dependence. We will use adiabatic mode theory to express the range-dependent Green's functions, which from (5.280) is

$$\begin{aligned} g(\mathbf{r}_1, \mathbf{r}'; z_1, z') &= \frac{i}{\rho \sqrt{8\pi}} e^{-i\pi/4} \\ &\quad \times \sum_m \Psi_m(z_1; \mathbf{r}_1) \Psi_m(z'; \mathbf{r}') \frac{e^{i \int_{L_1} k_{rm}(\xi, \eta) ds}}{\sqrt{\int_{L_1} k_{rm}(\xi, \eta) ds}}, \end{aligned} \quad (9.48)$$

where the sum is over the local modes  $\Psi_m(z_1; \mathbf{r}_1)$ ; that is, the modes calculated using the sound-speed profile, water depth and bottom structure at the position  $\mathbf{r}_1$ .

The sum also involves integrals of the modal wavenumbers  $k_{rm}(\xi, \eta)$  over the straight-line path  $L_1$  connecting the points  $(x_1, y_1)$  and  $(x', y')$ . Also, in (9.48)  $ds$  is the element of arclength and equals  $[(d\xi)^2 + (d\eta)^2]^{1/2}$  such that

$$\xi = s(x' - x_1)/(|\mathbf{r}' - \mathbf{r}_1|) + x_1, \quad (9.49)$$

$$\eta = s(y' - y_1)/(|\mathbf{r}' - \mathbf{r}_1|) + y_1. \quad (9.50)$$

Substituting (9.48) and a similar expression for the second Green's function in the  $\nu \neq 0$  terms of (9.47) yields

$$\begin{aligned} C(\mathbf{r}_1, z_1; \mathbf{r}_2, z_2) &= C_0 + \frac{q^2}{2\rho^2 k^2} \sum_{v=1}^N \sum_{m,n} \Psi_m(z_1; \mathbf{r}_1) \Psi_m(z'; \mathbf{r}') \Psi_n(z_2; \mathbf{r}_2) \Psi_n(z'; \mathbf{r}') \\ &\times \int_{A_v} \frac{e^{i \int_{L_1} k_{rm}(\xi, \eta) ds - i \int_{L_2} k_{rn}^*(\xi, \eta) ds}}{\sqrt{\int_{L_1} k_{rm}(\xi, \eta) ds \int_{L_2} k_{rn}^*(\xi, \eta) ds}} d^2 \mathbf{r}', \end{aligned} \quad (9.51)$$

where  $L_2$  is the straight-line path connecting the points  $(x_2, y_2)$  and  $(x', y')$  and  $C_0(\mathbf{r}_1, z_1; \mathbf{r}_2, z_2)$  is the contribution of the area  $A_0$  to the cross-spectral density.

Next, we let  $\mathbf{r}' = \mathbf{r}_v + \mathbf{a}_v$  where  $\mathbf{r}_v$  is the radial vector from the origin to a selected point in  $A_v$  as indicated in Fig. 9.15b. Let the points  $(x_1, y_1)$  and  $(x_2, y_2)$  lie within the inner circle, i.e.,  $|\mathbf{r}_{1,2}| < R$ . We also require that  $|\mathbf{r}_v - \mathbf{r}_{1,2}| \gg |\mathbf{a}_v|$  with the result that

$$|\mathbf{r}' - \mathbf{r}_1| = |(\mathbf{r}_v - \mathbf{r}_1) + \mathbf{a}_v| \simeq |\mathbf{r}_v - \mathbf{r}_1| + \frac{(\mathbf{r}_v - \mathbf{r}_1) \cdot \mathbf{a}_v}{|\mathbf{r}_v - \mathbf{r}_1|}, \quad (9.52)$$

or

$$|\mathbf{r}' - \mathbf{r}_1| \simeq |\mathbf{r}_v - \mathbf{r}_1| + |\mathbf{a}_v| \cos \theta_1, \quad (9.53)$$

where  $\theta_1$  is the angle between the vectors  $\mathbf{r}_v - \mathbf{r}_1$  and  $\mathbf{a}_v$ , as shown in Fig. 9.15b. The line integral can therefore be written as

$$\begin{aligned} \int_0^{|\mathbf{r}' - \mathbf{r}_1|} k_{rm}[\xi(s), \eta(s)] ds &\simeq \int_0^{|\mathbf{r}_v - \mathbf{r}_1|} k_{rm}[\xi(s), \eta(s)] ds \\ &+ \int_{|\mathbf{r}_v - \mathbf{r}_1|}^{|\mathbf{r}_v - \mathbf{r}_1| + |\mathbf{a}_v| \cos \theta_1} k_{rm}[\xi(s), \eta(s)] ds. \end{aligned} \quad (9.54)$$

Since the limits of the second integral lie within the area  $A_v$  and we have assumed  $k_{rm}[\xi(s), \eta(s)]$  to be constant within  $A_v$ , we have

$$\int_0^{|\mathbf{r}' - \mathbf{r}_1|} k_{rm}[\xi(s), \eta(s)] ds \simeq \int_0^{|\mathbf{r}_v - \mathbf{r}_1|} k_{rm}[\xi(s), \eta(s)] ds + k_{rm}[\mathbf{r}_v] |\mathbf{a}_v| \cos \theta_1. \quad (9.55)$$

The remaining integral is not a function of  $\mathbf{a}_v$ . The  $L_1$  and  $L_2$  line integrals can now be written as

$$\int_{L_1} k_{rm}(\xi, \eta) ds \simeq \int_0^{|r_v - r_1|} k_{rm}(\xi, \eta) ds + k_{rm}(r_v) |\mathbf{a}_v| \cos \theta_1 \quad (9.56)$$

with  $\theta_1$  defined as in Fig. 9.15b and

$$\int_{L_2} k_{rn}^*(\xi, \eta) ds \simeq \int_0^{|r_v - r_2|} k_{rn}^*(\xi, \eta) ds + k_{rn}^*(r_v) |\mathbf{a}_v| \cos \theta_2 \quad (9.57)$$

with  $\theta_2$  defined in a similar way to  $\theta_1$ . Substituting (9.56) and (9.57) into (9.51), we get

$$\begin{aligned} C(r_1, z_1; r_2, z_2) = & C_0 + \frac{q^2}{2\rho^2 k^2} \sum_{v=1}^N \sum_{m,n} \Psi_m(z_1; r_1) \Psi_m(z'; r_v) \Psi_n(z_2; r_2) \Psi_n(z'; r_v) \\ & \times \frac{e^{i[(\bar{k}_{rm})_{v_1} - (\bar{k}_{rn}^*)_{v_2}]}}{\sqrt{(\bar{k}_{rm})_{v_1} (\bar{k}_{rn}^*)_{v_2}}} \int_{A_v} e^{i[k_{rm}(r_v) \cos \theta_1 - k_{rn}^*(r_v) \cos \theta_2] \mathbf{a}_v} d^2 \mathbf{a}_v, \end{aligned} \quad (9.58)$$

where

$$(\bar{k}_{rm})_{v_1} \equiv \int_0^{|r_v - r_1|} k_{rm}(\xi, \eta) ds \quad (9.59)$$

with  $\xi$  and  $\eta$  given by (9.49) and (9.50). We have neglected the second terms of (9.56) and (9.57) in approximating the term  $[\int_{L_1} k_{rm}(\xi, \eta) ds \int_{L_2} k_{rn}^*(\xi, \eta) ds]^{1/2}$  which appears in the denominator of (9.51).

As shown in Appendix 1, after much manipulation of integrals and Bessel functions, the final result becomes

$$\begin{aligned} C_0(r_1, z_1; r_2, z_2) \simeq & \frac{i\pi q^2}{\rho^2 k^2} \sum_{m,n} \frac{\Psi_m(z_1; 0) \Psi_m(z'; 0) \Psi_n(z_2; 0) \Psi_n(z'; 0)}{k_{rm}^2 - (k_{rn}^*)^2} \\ & \times \left\{ H_0^{(1)}(k_{rm}|r_2 - r_1|) + H_0^{(2)}(k_{rn}^*|r_2 - r_1|) \right. \\ & \left. - \left[ \sqrt{\frac{k_{rm}}{k_{rn}^*}} + \sqrt{\frac{k_{rn}^*}{k_{rm}}} \right] J_0(\gamma) e^{i(k_{rm} - k_{rn}^*)R} \right\}, \end{aligned} \quad (9.60)$$

where

$$\gamma = \sqrt{(k_{rm}r_1)^2 + (k_{rn}^*r_2)^2 - 2k_{rm}k_{rn}^*r_1r_2 \cos(\theta_2 - \theta_1)} \quad (9.61)$$

with  $\theta_1$  and  $\theta_2$  being the polar angles associated with  $\mathbf{r}_1$  and  $\mathbf{r}_2$ .

### 9.4.2 Simulated Noise Fields in 3-D Environments

In this section, we present two examples. The first is the intensity distribution of noise in a complex artificial environment which illustrates how noise, in a photographic negative sense, produces an “image” of the environment. The second is an example of the spatial distribution of noise expected in a complex region of the ocean: the example already discussed in Sect. 5.13.1 for the Gulf-Stream/continental-margin environment.

#### 9.4.2.1 “Image” of Noise Levels

Figure 9.16 shows an artificially constructed environment which simulates a seamount in the vicinity of a continental slope. This environment is insonified by a sheet of uncorrelated noise sources (for this numerical example, the sheet is a 1400-km square centered above the region shown) of equal strength except for the storm cases. Storms are simulated by 50-km radius circular regions whose source levels are 25 dB above the ambient sheet. For a more precise discussion of storm source

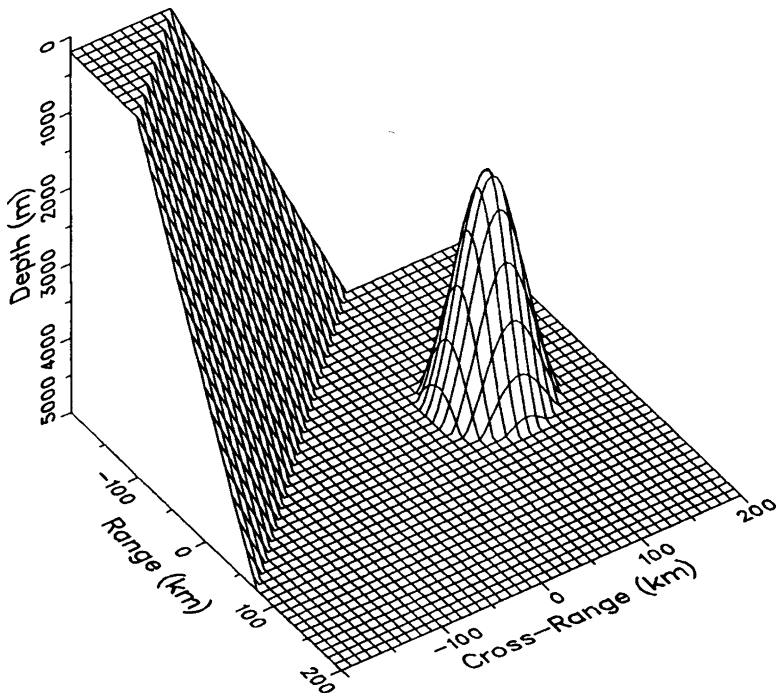


**Fig. 9.16** Idealized environment with continental slope and seamount for noise intensity calculation

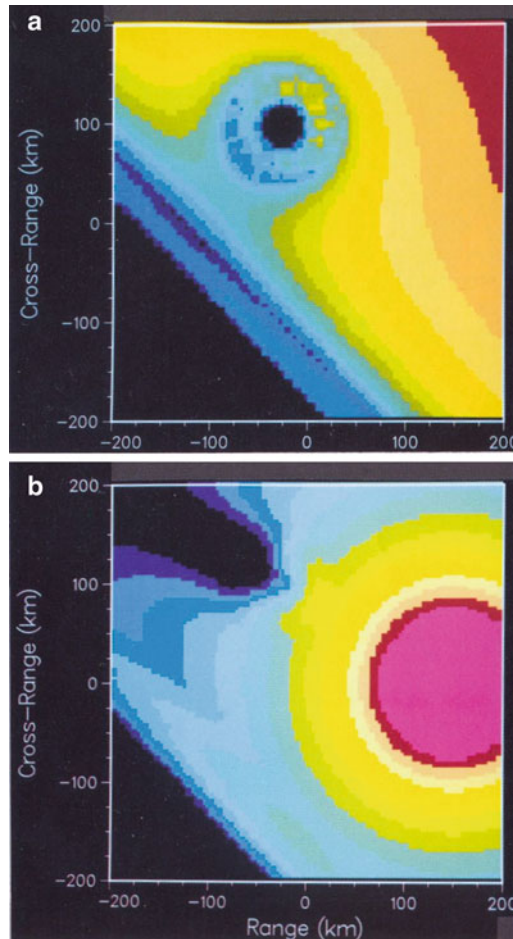


**Fig. 9.17** Contours of noise intensity at 10 Hz and a depth of 800 m appearing as a seascape image. (a) Noise intensity for a homogeneous distribution of uncorrelated sources; (b) The same with a storm southeast of the seamount

levels, see Wilson and Makris [5]. The noise levels in a storm-free region is shown in Fig. 9.17a. The intensity distribution appears as an image of the bathymetry, the image mostly resulting from various degrees of upslope cutoff. A storm in the region appears to be lighting up the seascape as a lantern. Figure 9.17b shows the region for a storm located to the right, with the seamount creating a shadow and the continental shelf affecting the intensity fall-off with respect to range. Note also that the presence of the storm, i.e., a strong, localized source distribution, results in an image of greater dynamic range than the homogeneous source distribution.

### 9.4.2.2 Noise Directionality

Figure 9.18a is the environment which we have already discussed vis-à-vis propagation in the vicinity of the Gulf Stream. The X marks the spot where we place a hypothetical vertical array for examining, using plane-wave beamforming, the vertical directionality of noise in the vicinity of a continental rise. We calculate the directionality for two cases: a circular storm of radius 50 km in either deep water,  $67.5^\circ W$ , or on the continental slope,  $72^\circ W$ . The source level is related to wind

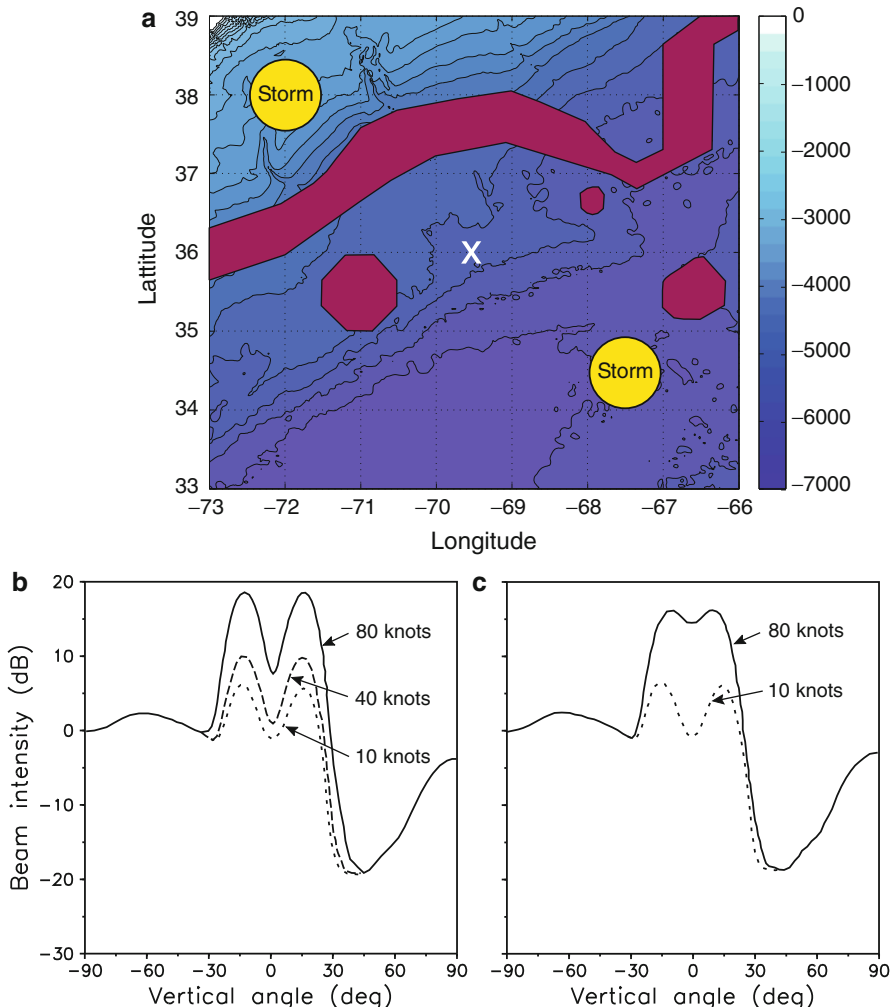


**Fig. 9.18** Noise directionality in a Gulf-Stream/continental-slope area. (a) Bathymetry and position of the Gulf Stream; (b) Vertical directionality from storm in deep water; (c) The same for storm on the continental slope

speed using Wilson [33] as subsequently interpreted by Kewley et al. [4]. We see in Figs. 9.18b and 9.18c that the vertical directionality shows a notch for the deep water storm case whereas the noise is more horizontal for the shallow storm. This effect of the disappearance of the horizontal *noise notch* caused by sources in shelf regions has been noted by Wagstaff [34], Wales and Diachok [35], and Dashen and Munk [36]. This effect may also be understood from a ray point of view since a ray specularly reflected from a downslope interface is more horizontal than its incident ray. The effect of the complex oceanography is not clearly represented in these plots. In Chap. 10, we will discuss certain signal processing techniques which show noise results that appear to image the oceanography of the environment.

### 9.4.3 Noise Modeling by PE

The PE model can be used, under certain conditions, to compute the vertical distribution of noise in a range-dependent environment. This technique is not only of interest from the point of view of calculating noise distributions, but it also is an interesting application of the parabolic equation.

In this section, we follow the derivation of Carey et al. [7, 37] using the notational conventions of Chap. 6. As in Sect. 9.4.1 we divide the ocean surface into an inner circular area  $A_0$  and an outer area. We will be concerned with evaluating the cross-spectral density in the inner region *far* from the outer region. For simplicity, we start by assuming that the ocean is range-dependent but azimuthally symmetric about the origin as depicted in Fig. 9.19 and we consider sources only in the outer region. Figure 9.19 shows an annulus in the outer region in which surface sources radiating with uniformly-distributed  $[0, 2\pi]$  random phase  $\chi$  are distributed with a density of

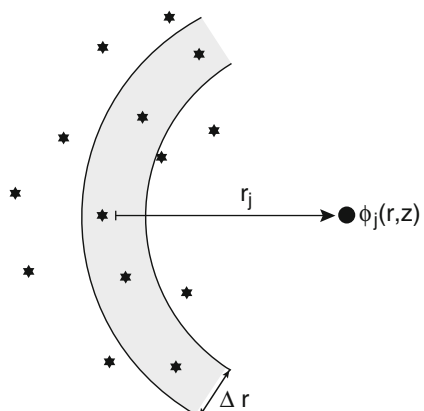


**Fig. 9.19** Geometry for the PE noise calculation

$\eta$  sources per unit area. Each of the  $N_j$  sources in the  $j$ th annulus of thickness  $\Delta r$  contribute to the field point  $(r, z)$  as

$$\phi_j(r, z) = \sum_{n=1}^{N_j} \exp(i\chi_n) p(r_j, z), \quad (9.62)$$

which represents an incoherent sum of sources. By taking advantage of the azimuthal symmetry, (9.62) becomes

$$\phi_j(r, z) = \sqrt{N_j} \exp(i\chi_n) p(r_j, z). \quad (9.63)$$

Since the number of sources is  $2\pi r_j \Delta r \eta$ , we can rewrite (9.63) as

$$\phi_j(r, z) = \beta \sqrt{r_j} p(r_j, z); \quad \beta = \sqrt{2\pi \Delta r \eta}. \quad (9.64)$$

We now sum up the contributions from all  $M$  annuli, again associating a random phase  $\chi$  with each one to get the total field from the outer region,

$$\phi(r, z) = \sum_{j=1}^M \exp(i\chi_j) \phi_j(r, z), \quad (9.65)$$

which together with (9.63) becomes

$$\phi(r, z) = \beta \sum_{j=1}^M \sqrt{r_j} \exp(i\chi_j) p(r_j, z). \quad (9.66)$$

Since we will ultimately be evaluating the fields using the PE model, we use (6.70)

$$p(r, z) = \frac{\psi(r, z)}{\sqrt{r}} \exp\left[i\left(k_0 r - \frac{\pi}{4}\right)\right],$$

to rewrite (9.66) in terms of the PE envelope function  $\psi$ ; the result is

$$\phi(r, z) = \beta \sum_{j=1}^M \exp[i(k_0 r_j + \chi_j)] \psi(r_j, z), \quad (9.67)$$

where we have omitted the  $\pi/4$  phase factor coming from the asymptotic form of the Hankel function. Next, we march the acoustic field according to the PE algorithm. From (6.119) we have

$$\psi(r + \Delta r, z) = e^{\tilde{U} \Delta r} \psi(r, z).$$

Following the procedures in Chap. 6 for deriving PE algorithms we consider small steps  $\Delta r$  over locally range-independent environments. We then evaluate (9.67) for two contiguous rings of  $\Delta r$  thickness and propagate from the first ring using its source excitation through the second picking up its additional excitation, i.e., we propagate two range steps  $\Delta r$ .

Let  $\psi(0, z) \equiv g_s(z)$  be the surface noise excitation, i.e., the starting field for the PE envelope function injecting noise into each annulus. Referring to Fig. 9.19, the first  $\Delta r$ -step consists of adding the second ring's noise to the noise which propagated from the first ring,

$$\psi(r + \Delta r, z) = e^{\tilde{U} \Delta r} g_s(z) + \exp(i\chi) g_s(z), \quad (9.68)$$

where again we use  $\chi$  to produce a random phase between the previously marched field and the newly injected noise. Now we take the second range step

$$\psi(r + 2\Delta r, z) = e^{\tilde{U} \Delta r} [e^{\tilde{U} \Delta r} g_s(z) + \exp(i\chi) g_s(z)] + \exp(i\chi) g_s(z), \quad (9.69)$$

so that the noise marching algorithm is

$$\psi(r + \Delta r, z) = e^{\tilde{U} \Delta r} [\psi(r, z) + \exp(i\chi) g_s(z)]. \quad (9.70)$$

This algorithm can be implemented with any version of the PE as described in Chap. 6.

#### 9.4.4 Downslope and Deep-Ocean-Basin Noise Field

The PE algorithm marches out vertical slices of the noise field and hence it is straightforward to apply this method to compute the vertical directionality. We present an example taken from Carey et al. [37] modeling the individual contributions of noise from the continental shelf and the deep ocean to a station positioned in the deep ocean. We have already shown in Sect. 9.4.2 that the adiabatic mode model predicts that noise originating from a storm over a continental shelf and received in deep water fills in the horizontal notch associated with noise originating only from deep-water regions.

The idealized ocean and geoacoustic environment with 3–6° slope is shown in Fig. 9.20; a 90-element vertical array centered about the SCA with half-wavelength spacing for 50 Hz was placed in the center of the basin. Figure 9.21 shows the response of the vertical array with the *noise notch* filled in by slope conversion [34,35]. Hence, the PE model of noise contains the appropriate physics. Reference [37] also contains discussions on variable oceanography. To date only computations for cylindrically symmetric oceans have been made; more realistic computations will require a reformulation of the algorithm in terms of sectors. Nevertheless, the method shows promise in that the PE algorithm is still the most accurate and practical method for computing acoustic fields over large and extremely variable ocean paths.

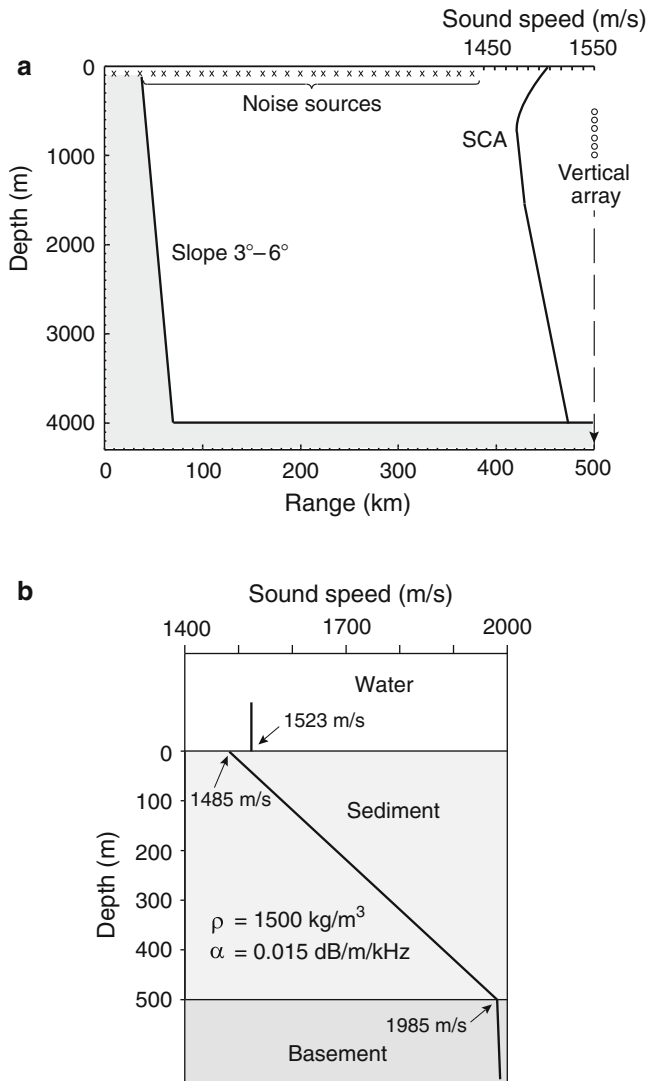


**Fig. 9.20** Downslope environment for PE noise calculation. (a) Distribution of noise sources and position of vertical array near the sound-channel axis (SCA). (b) Geoacoustic parameters

## Appendix 1: Evaluation of the Cross-Spectral Density

Here, we calculate the contribution to the cross-spectral density from noise sources distributed over a circular area with radius  $R$  and centered at the origin. From (9.47), the contribution of the area  $A_0$  to the cross spectral density is

$$C_0(\mathbf{r}_1, z_1; \mathbf{r}_2, z_2) = \frac{4\pi q^2}{k^2} \int_{A_0} g(\mathbf{r}_1, \mathbf{r}'; z_1, z') g^*(\mathbf{r}_2, \mathbf{r}'; z_2, z') d^2\mathbf{r}'. \quad (9.71)$$

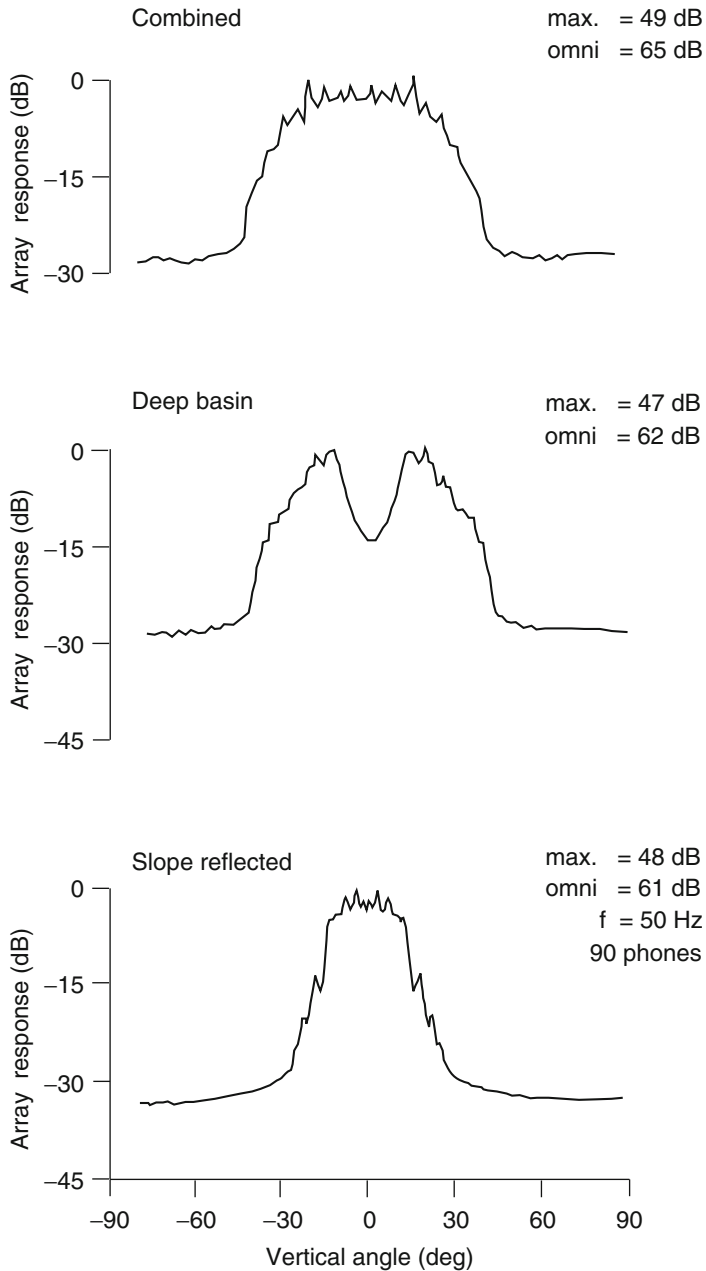


**Fig. 9.21** Computed vertical directionality of ambient noise (*top curve*). The *middle curve* shows the contribution from noise sources over the deep portion of the ocean, while the *lower curve* shows the contribution from sources on the continental slope (from Carey et al. [37])

We assume that the receivers are outside the source area,

$$|\mathbf{r}_{1,2}| > R. \quad (9.72)$$

For this case we use the range-independent Green's function given by (5.13),

$$g(\mathbf{r}_1, \mathbf{r}'; z_1, z') = \frac{i}{4\rho} \sum_m \Psi_m(z') \Psi_m(z_1) H_0^{(1)}(k_{rm} |\mathbf{r}_1 - \mathbf{r}'|). \quad (9.73)$$

Substituting (9.73) and a similar form for the second Green's function in (9.71), we get

$$\begin{aligned} C_0(\mathbf{r}_1, z_1; \mathbf{r}_2, z_2) &= \frac{\pi q^2}{4\rho^2 k^2} \sum_{m,n} \Psi_m(z_1; \mathbf{r}_1) \Psi_m(z'; \mathbf{r}') \Psi_n(z_2; \mathbf{r}_2) \Psi_n(z'; \mathbf{r}') \\ &\times \int_{A_0} H_0^{(1)}(k_{rm} |\mathbf{r}_1 - \mathbf{r}'|) H_0^{(2)}(k_{rn}^* |\mathbf{r}_2 - \mathbf{r}'|) d^2\mathbf{r}'. \end{aligned} \quad (9.74)$$

To evaluate the integral in (9.74) we assume that  $|\mathbf{r}_2| > |\mathbf{r}_1|$  and write

$$\begin{aligned} \int_0^{2\pi} \int_0^R [ ] r' dr' d\theta' &= \int_0^{2\pi} \int_0^{r_1} [ ] r' dr' d\theta' \\ &+ \int_0^{2\pi} \int_{r_1}^{r_2} [ ] r' dr' d\theta' + \int_0^{2\pi} \int_{r_2}^R [ ] r' dr' d\theta'. \end{aligned} \quad (9.75)$$

For the first integral we have  $r' < r_1 < r_2$ , so we can expand the Hankel functions as follows,

$$H_0^{(1)}(k_{rm} |\mathbf{r}_1 - \mathbf{r}'|) = \sum_{p=0}^{\infty} \epsilon_p J_p(k_{rm} r') H_p^{(1)}(k_{rm} r_1) \cos[p(\theta_1 - \theta')] \quad (9.76)$$

and

$$H_0^{(2)}(k_{rn}^* |\mathbf{r}_2 - \mathbf{r}'|) = \sum_{q=0}^{\infty} \epsilon_q J_q(k_{rn}^* r') H_q^{(2)}(k_{rn}^* r_2) \cos[q(\theta_2 - \theta')] \quad (9.77)$$

with  $\epsilon_0 = 1$  and  $\epsilon_p = 2$  for  $p = 1, 2, 3, \dots$ . Substituting (9.76) and (9.77) into the first term of (9.75) and carrying out the integration over  $\theta'$  yields,

$$\begin{aligned} \int_0^{2\pi} \int_0^{r_1} [ ] r' dr' d\theta' &= 2\pi \sum_{p=0}^{\infty} \epsilon_p H_p^{(1)}(k_{rm} r_1) H_p^{(2)}(k_{rn}^* r_2) \cos[p(\theta_2 - \theta_1)] \\ &\times \int_0^{r_1} J_p(k_{rm} r') J_p(k_{rn}^* r') r' dr'. \end{aligned} \quad (9.78)$$

The integral over  $r'$  is

$$\begin{aligned} & \int_0^{r_1} J_p(k_{rm}r') J_p(k_{rn}^*r') r' dr' \\ &= \frac{k_{rn}^* r_1 J_p(k_{rm}r_1) J_{p-1}(k_{rn}^*r_1) - k_{rm}r_1 J_{p-1}(k_{rm}r_1) J_p(k_{rn}^*r_1)}{k_{rm}^2 - (k_{rn}^*)^2}. \quad (9.79) \end{aligned}$$

Similarly, we have

$$\begin{aligned} \int_0^{2\pi} \int_{r_1}^{r_2} [ ] r' dr' d\theta' &= 2\pi \sum_{p=0}^{\infty} \epsilon_p J_p(k_{rm}r_1) H_p^{(2)}(k_{rn}^*r_2) \cos[p(\theta_2 - \theta_1)] \\ &\times \int_{r_1}^{r_2} H_p^{(1)}(k_{rm}r') J_p(k_{rn}^*r') r' dr' \quad (9.80) \end{aligned}$$

with

$$\begin{aligned} & \int_{r_1}^{r_2} H_p^{(1)}(k_{rm}r') J_p(k_{rn}^*r') r' dr' \\ &= \left[ \frac{k_{rn}^* r' H_p^{(1)}(k_{rm}r') J_{p-1}(k_{rn}^*r') - k_{rm}r' H_{p-1}^{(1)}(k_{rm}r') J_p(k_{rn}^*r')}{k_{rm}^2 - (k_{rn}^*)^2} \right]_{r_1}^{r_2}, \quad (9.81) \end{aligned}$$

and

$$\begin{aligned} \int_0^{2\pi} \int_{r_2}^R [ ] r' dr' d\theta' &= 2\pi \sum_{p=0}^{\infty} \epsilon_p J_p(k_{rm}r_1) J_p(k_{rn}^*r_2) \cos[p(\theta_2 - \theta_1)] \\ &\times \int_{r_2}^R H_p^{(1)}(k_{rm}r') H_p^{(2)}(k_{rn}^*r') r' dr', \quad (9.82) \end{aligned}$$

with

$$\begin{aligned} & \int_{r_2}^R H_p^{(1)}(k_{rm}r') H_p^{(2)}(k_{rn}^*r') r' dr' \\ &= \left[ \frac{k_{rn}^* r' H_p^{(1)}(k_{rm}r') H_{p-1}^{(2)}(k_{rn}^*r') - k_{rm}r' H_{p-1}^{(1)}(k_{rm}r') H_p^{(2)}(k_{rn}^*r')}{k_{rm}^2 - (k_{rn}^*)^2} \right]_{r_2}^R. \quad (9.83) \end{aligned}$$

Combining (9.79)–(9.83) we get

$$\begin{aligned}
& \int_0^{2\pi} \int_0^R H_0^{(1)}(k_{rm}|{\mathbf r}_1 - {\mathbf r}'|) H_0^{(2)}(k_{rn}^*|{\mathbf r}_2 - {\mathbf r}'|) r' d{\mathbf r}' d\theta' \\
&= 4i \sum_{p=0}^{\infty} \left[ \frac{J_p(k_{rm}r_1) H_p^{(1)}(k_{rm}r_2) + J_p(k_{rn}^*r_1) H_p^{(2)}(k_{rn}^*r_2)}{k_{rn}^2 - (k_{rm}^*)^2} \right] \cos p(\theta_2 - \theta_1) \\
&+ 2\pi \sum_{p=0}^{\infty} J_p(k_{rm}r_1) J_p(k_{rn}^*r_2) \\
&\times \left[ \frac{k_{rn}^* R H_p^{(1)}(k_{rm}R) H_{p-1}^{(2)}(k_{rn}^*R) - k_{rm}R H_{p-1}^{(1)}(k_{rm}R) H_p^{(2)}(k_{rn}^*R)}{k_{rm}^2 - (k_{rn}^*)^2} \right] \\
&\times \cos p(\theta_2 - \theta_1). \tag{9.84}
\end{aligned}$$

The first term of (9.84) reduces to

$$\frac{2i}{\pi} \left[ \frac{H_0^{(1)}(k_{rm}|{\mathbf r}_2 - {\mathbf r}_1|) + H_0^{(2)}(k_{rn}^*|{\mathbf r}_2 - {\mathbf r}_1|)}{k_{rn}^2 - (k_{rm}^*)^2} \right]. \tag{9.85}$$

We can simplify the second term of (9.84) assuming  $k_{rm}R, k_{rn}^*R \gg 1$ , by using the asymptotic form of the Hankel function,

$$H_p^{(1)}(z) \simeq \sqrt{\frac{2}{\pi z}} e^{i(z-p\pi/2-\pi/4)}.$$

Then, the second term of (9.84) becomes

$$-\left[ \frac{\sqrt{\frac{k_{rn}^*}{k_{rm}}} + \sqrt{\frac{k_{rm}}{k_{rn}^*}}}{k_{rm}^2 - (k_{rn}^*)^2} \right] J_0(\gamma) e^{i(k_{rm}-k_{rn}^*)R}, \tag{9.86}$$

where

$$\gamma = \sqrt{(k_{rm}r_1)^2 + (k_{rn}^*r_2)^2 - 2k_{rm}k_{rn}^*r_1r_2 \cos(\theta_2 - \theta_1)}.$$

Finally, substituting (9.84) into (9.74) and using (9.85) and (9.86) we get

$$C_0(\mathbf{r}_1, z_1; \mathbf{r}_2, z_2) = \frac{i\pi q^2}{\rho^2 k^2} \sum_{m,n} \frac{\Psi_m(z_1; 0) \Psi_m(z'; 0) \Psi_n(z_2; 0) \Psi_n(z'; 0)}{k_{rm}^2 - (k_{rn}^*)^2} \\ \times \left\{ H_0^{(1)}(k_{rm}|\mathbf{r}_2 - \mathbf{r}_1|) + H_0^{(2)}(k_{rn}^*|\mathbf{r}_2 - \mathbf{r}_1|) \right. \\ \left. - \left[ \sqrt{\frac{k_{rm}}{k_{rn}^*}} + \sqrt{\frac{k_{rn}^*}{k_{rm}}} \right] J_0(\gamma) e^{i(k_{rm} - k_{rn}^*)R} \right\}. \quad (9.87)$$

When  $R \rightarrow \infty$  this expression agrees with (9.24) for the range-independent waveguide.

## Problems

**9.1.** Let the ocean be a semi-infinite, isovelocity halfspace bounded above by a uniform distribution of monopole sources radiating with an intensity per unit area at a unit distance. What is the depth dependence of the intensity of the noise field? Now assume that the spreading law is cylindrical rather than spherical. What additional physical parameter must be included to give physically sensible results?

**9.2.** Define directionality of the noise field to be the noise intensity per unit solid angle. Derive an expression for the noise directionality in the ocean described in the above problem. How does the result change if the sources are dipoles rather than monopoles? (Take the intensity radiation pattern for a dipole to be proportional to  $\cos^2 \phi$ , where  $\phi$  is the angle measured from the normal to the surface).

**9.3.** The cross-spectral density and the directionality are related by a Fourier transform. What are the Fourier conjugate variables? Compare the monopole and dipole results derived in the last problem with the Cron and Sherman results discussed in Sect. 9.2.5.

**9.4.** Consider a sonar receiver array with baffled sensors which individually have a beam pattern  $W(\theta, \varphi) = W_1(\theta) W_2(\varphi)$ , where  $\theta$  is the vertical angle and  $\varphi$  is the azimuthal angle. The sonar is used in a stratified ocean with a uniform distribution of surface noise sources.

- a. Derive an expression for  $C_\omega(\mathbf{r}_1, \mathbf{r}_2, z_1, z_2)$ , the cross-spectral density function for the ambient noise as seen by the array.
- b. Show that your result is consistent with the result of Kuperman and Ingénito for  $W(\theta, \varphi) \equiv 1$ .

**9.5.** Develop an algorithm for generating a realization of noise time series for a receiver array in a stratified ocean with ambient noise generated by a homogeneous distribution of surface noise sources.

## References

1. H. Cox, Spatial correlation in arbitrary noise fields with application to ambient sea noise. *J. Acoust. Soc. Am.* **54**, 1289–1301 (1973)
2. W.A. Kuperman, F. Ingenito, Spatial correlation of surface generated noise in a stratified ocean. *J. Acoust. Soc. Am.* **67**, 1988–1996 (1980)
3. H. Schmidt, W.A. Kuperman, Estimation of surface noise source levels from low-frequency seismo-acoustic ambient noise measurements. *J. Acoust. Soc. Am.* **84**, 2153–2162 (1988)
4. D.J. Kewley, D.G. Browning, W.M. Carey, Low-frequency wind-generated ambient noise source levels. *J. Acoust. Soc. Am.* **88**, 1894–1902 (1990)
5. J.D. Wilson, N.C. Makris, Ocean acoustic hurricane classification. *J. Acoust. Soc. Am.* **119**, 168–181 (2006)
6. D.P. Knobles, S.M. Joshi, R.D. Gaul, H.C. Graber, N.J. Williams, Analysis of wind-driven ambient noise in a shallow water environment with a sandy seabed. *J. Acoust. Soc. Am.* **124**, EL157–162 (2008)
7. R.B. Evans, W.M. Carey, Basin scale computation of vertical and horizontal directivity of underwater ambient noise, due to shipping and wind. in *Proceeding of the 9th International Conference on Theoretical and Computational Acoustics*, ed. by S. Marburg (Dresden, Germany, 2010)
8. D. Ross, *Mechanics of Underwater Noise* (Pergamon, New York, 1976)
9. M.J. Beran, G.B. Parent, *Theory of Partial Coherence* (Prentice Hall, Englewood Cliffs, NJ, 1964)
10. W.S. Liggett, M.J. Jacobson, Covariance of surface generated noise in a deep ocean. *J. Acoust. Soc. Am.* **38**, 303–312 (1965)
11. F. Oberhettinger, *Tables of Bessel Transformations* (Springer, New York, 1972)
12. B.F. Cron, C.H. Sherman, Spatial correlation functions for various noise models. *J. Acoust. Soc. Am.* **34**, 1732–1736 (1962)
13. J.A. Orcutt, C.S. Cox, A.C. Kibblewhite, W.A. Kuperman, H. Schmidt, Observations and causes of ocean and seafloor noise at ultra-low and very-low frequencies. in *Natural Physical Sources of Underwater Sound: Sea Surface Sound* (2), ed. by B.R. Kerman (Kluwer, Dordrecht, 1993), pp. 203–232
14. D. Rouseff, D.J. Tang, Internal wave effects on the ambient noise notch in the East China Sea: Model/data comparison. *J. Acoust. Soc. Am.* **120**, 1284–1294 (2006)
15. T. Akal, A. Barbagelata, G. Guidi, M. Snoek, Time dependence of ambient seafloor noise on a continental shelf. in *Ocean Seismo-Acoustics*, ed. by T. Akal, J.M. Berkson (Plenum, New York, 1986), pp. 767–778
16. G.B. Deane, M.J. Buckingham, C.T. Tindle, Vertical coherence of ambient noise in shallow water overlying a fluid seabed. *J. Acoust. Soc. Am.* **102**, 3413–3424 (1997)
17. N.M. Carbone, G.B. Deane, M.J. Buckingham, Estimating the compressional and shear wave speeds of a shallow-water seabed from the vertical coherence of ambient noise in the water column. *J. Acoust. Soc. Am.* **103**, 801–813 (1997)
18. C.H. Harrison, D.G. Simons, Geoacoustic inversion of ambient noise: A simple method. *J. Acoust. Soc. Am.* **112**, 1377–1389 (2002)
19. C.H. Harrison, Sub-bottom profiling using ocean ambient noise. *J. Acoust. Soc. Am.* **115**, 1505–1515 (2004)
20. M.J. Buckingham, B.V. Berkhouw, S.A.L. Glegg, Imaging the ocean with ambient noise. *Nature* **356**, 327–329 (1992)

21. J.R. Potter, Acoustic imaging using ambient noise: Some theory and simulation results. *J. Acoust. Soc. Am.* **95**, 21–33 (1994)
22. C.L. Epifanio, J.R. Potter, G.B. Deane, M.L. Readhead, M.J. Buckingham, Imaging in the ocean with ambient noise: the ORB experiments. *J. Acoust. Soc. Am.* **106**, 3211–3225 (1999)
23. M.J. Buckingham, Acoustic daylight imaging in the ocean. in *Handbook of Computer Vision and Applications – Volume 1: Sensors and Imaging*, ed. by B. Jahne, H. Haussecker, P. Geissler (Academic, San Diego, 1999), pp. 415–442
24. N.C. Makris, F. Ingenito, W.A. Kuperman, Detection of a submerged object insonified by surface noise in an ocean waveguide. *J. Acoust. Soc. Am.* **96**, 1703–1724 (1994)
25. R.L. Weaver, O.I. Lobkis, Ultrasonics without a source: Thermal fluctuation correlations at MHz frequencies. *Phys. Rev. Lett.* **87**, 134301 (2001)
26. P. Roux, W.A. Kuperman, the NPAL Group, Extracting coherent wavefronts from acoustic ambient noise in the ocean. *J. Acoust. Soc. Am.* **116**, 1995–2003 (2004)
27. K.G. Sabra, P. Roux, W.A. Kuperman, Arrival-time structure of the time-averaged ambient noise cross-correlation function in an oceanic waveguide. *J. Acoust. Soc. Am.* **117**, 164–174 (2005)
28. K.G. Sabra, P. Roux, W.A. Kuperman, Emergence rate of the time-domain Green's function from the ambient noise cross-correlation function. *J. Acoust. Soc. Am.* **118**, 3524–3531 (2005)
29. K.G. Sabra, P. Roux, A.M. Thode, G.L. D'Spain, W.S. Hodgkiss, W.A. Kuperman, Using ocean ambient noise for array self-localization and self-synchronization. *IEEE J. Oceanic Eng.* **30**, 338–347 (2005)
30. S. Fried, W.A. Kuperman, K.G. Sabra, P. Roux, Extracting the local Green's function on a horizontal array from ambient ocean noise. *J. Acoust. Soc. Am.* **124**, EL:183–188 (2008)
31. M. Siderius, C.H. Harrison, M.B. Porter, A passive fathometer technique for imaging seabed layering using ambient noise. *J. Acoust. Soc. Am.* **120**, 1315–1323 (2006)
32. J.S. Perkins, W.A. Kuperman, F. Ingenito, L.T. Fialkowski, J. Glattetre, Modeling ambient noise in three-dimensional ocean environments. *J. Acoust. Soc. Am.* **92**, 739–752 (1993)
33. J.H. Wilson, Wind-generated noise modeling. *J. Acoust. Soc. Am.* **73**, 211–216 (1983)
34. R.A. Wagstaff, Low-frequency ambient noise in the deep sound channel—The missing component. *J. Acoust. Soc. Am.* **69**, 1009–1014 (1981)
35. S.C. Wales, O.I. Diachok, Ambient noise vertical directionality in the northwest Atlantic. *J. Acoust. Soc. Am.* **70**, 577–582 (1981)
36. R. Dashen, W. Munk, Three models of global ocean noise. *J. Acoust. Soc. Am.* **76**, 540–554 (1984)
37. W.M. Carey, R.B. Evans, J.A. Davis, G. Botseas, Deep-ocean vertical noise directionality. *IEEE J. Oceanic Eng.* **15**, 324–334 (1990)

# Chapter 10

## Signals in Noise

### 10.1 Introduction

Ocean acoustics often involves measuring or detecting a signal propagating in the ocean in the presence of noise. If the signal is weak, an array of sensors is used to coherently sum up or accumulate signal energy at a greater rate than noise. A simple example would be an array of hydrophones used to form a directional receiver in isotropic noise. For this case, there is a gain of signal over noise as compared to a single omni-directional hydrophone because, when “aimed” in the direction of the signal, the receiver picks up all the signal but only a fraction of the isotropic noise.

Associated with the evolution of sonar technology has been the development of a heuristic methodology for treating the energetics of signals and interference received at an acoustic array. This methodology is effectively summarized by the *sonar equation*. In this chapter, we will first review some material leading to the concept of *array gain* (AG) and then introduce the sonar equation for passive and active systems. An understanding of sonar equation energetics will be helpful in applying modeling results to complex problems. Next, we apply the modeling methods developed in the previous chapters to the subject of *array processing*. In its most elementary form, array processing in free space is called *plane-wave beamforming*. When the propagation medium is accounted for in the array processing, we refer to the procedure as *matched-field processing* (MFP). That is, we search for signals by matching the array data to solutions of the Helmholtz equation for a particular ocean waveguide environment.

In practice, acoustic measurements are performed in the time domain. Frequency-domain data are obtained by Fourier transforms requiring sophisticated procedures and sufficient data to make accurate spectral estimates. The simulations presented in this chapter are in the frequency domain.

## 10.2 The Energetics of Signals in Noise

### 10.2.1 Array Gain

An array of hydrophones is an acoustic antenna which can be used to enhance the received signal-to-noise ratio (SNR). This enhancement is often referred to as AG and is accomplished in three related ways. First, the level of the signal at the receiver can be increased by summing the outputs of the hydrophones coherently. Recall that the coherent sum refers to adding (complex) amplitudes; the total energy is then the square of the sum of amplitudes. This coherent sum can be related to a look or steering direction and a beamwidth. Second, the incoherent part of the noise – the white noise – adds incoherently so that the energies, not the amplitudes, add. Finally, the coherent part of the noise in general has directional properties so that an appropriately phased coherent sum of hydrophone outputs can be constructed to optimize AG. This limits the directional noise input by looking away from the noise and further limits the noise input in the direction of the noise by the restricted beamwidth associated with the look direction. We can illustrate these ideas quantitatively as follows: Consider the simple case of an array of  $m$  elements with signal  $s_i(t)$  and noise  $n_i(t)$  at the  $i$ th element of the array. The average SNR at the output of the array will be

$$\frac{S^2}{N^2} = \frac{\overline{\left[ \sum_{i=1}^m s_i(t) \right]^2}}{\overline{\left[ \sum_{i=1}^m n_i(t) \right]^2}}, \quad (10.1)$$

where the bar over a quantity denotes time average.

Summing the outputs of the hydrophones using various phase and amplitude shadings is called beamforming. The simplest example of AG is the situation in which the signal is a plane wave traveling in one direction and the noise field is isotropic, i.e., it is a uniform distribution of plane waves over all angles. A single omni-directional hydrophone receives all the signal and noise. An array of hydrophones can be used to coherently sum the signal by phasing the array to look in the direction of the plane wave. Hence the signal output of the array is the coherent sum of the signal at the hydrophones. On the other hand, only the noise in the look direction is output from the array beamformer, with the total energy of the noise related to the beamwidth. Hence an extremely narrow beam picks up all the signal but only a small portion of the noise, and there is an enhancement of the SNR relative to an omni-directional receiver. Below, we briefly derive these results. Equation (10.1) can be rewritten as

$$\frac{S^2}{N^2} \equiv \frac{\sum_{i,j=1}^m s_{ij}}{\sum_{i,j=1}^m n_{ij}}, \quad (10.2)$$

where the  $i, j$  subscripts imply a double summation, and the array signal and noise cross-correlation coefficients between the  $i$ th and  $j$ th hydrophones are given by  $s_{ij} \equiv s_i(t) s_j^*(t)$  and  $n_{ij} \equiv n_i(t) n_j^*(t)$ , respectively.

In the simple and common cases where both the signal and the noise have approximately the same amplitude at each hydrophone,  $s$  and  $n$ , respectively, we define  $s_{ij} \equiv s^2 \hat{s}_{ij}$  and  $n_{ij} \equiv n^2 \hat{n}_{ij}$ . For this case, (10.2) simplifies to

$$\frac{S^2}{N^2} = \frac{s^2}{n^2} \frac{\sum_{i,j=1}^m \hat{s}_{ij}}{\sum_{i,j=1}^m \hat{n}_{ij}}. \quad (10.3)$$

The second fraction on the right side of the expression above is a measure of the array performance in that it represents the increase in the SNR over a single omnidirectional hydrophone. AG is then defined in decibels as

$$AG = 10 \log \frac{S^2/N^2}{s^2/n^2} = 10 \log \frac{\sum_{i,j=1}^m \hat{s}_{ij}}{\sum_{i,j=1}^m \hat{n}_{ij}}, \quad (10.4)$$

so that AG is a function of the signal and noise structure projected onto the geometry of the array. The *directivity index* (DI) is a special case of AG and equals AG when the signal is a single plane wave and the noise is isotropic. For this case,  $\hat{n}_{ij}$  is stationary in space (i.e., depends only on the distance between hydrophones) and is given by

$$\hat{n}_{ij} = \frac{\sin(kd)}{kd}, \quad i \neq j, \quad (10.5)$$

where  $d$  is the hydrophone separation and  $k = 2\pi/\lambda$  is the acoustic wavenumber. Note that for isotropic noise and hydrophone spacing  $d = \lambda/2$ , the noise appears uncorrelated, i.e., cross terms vanish. For the purpose of illustration, we consider a two-element array. For this case (10.4) yields

$$DI = 10 \log \frac{2}{1 + \sin(kd)/(kd)} \quad (10.6)$$

and if the hydrophone separation is  $\lambda/2$ , we obtain a DI of  $10 \log 2$ . An important generalization is that a linear array of  $n$  hydrophones with  $\lambda/2$  spacing in isotropic noise has a DI of

$$\text{DI} = 10 \log n. \quad (10.7)$$

The quantity DI plays a central role in the sonar equation as discussed below.

### 10.2.2 Sonar Equation

In either case, passive or active (see Fig. 10.1), the performance of a sonar system can be estimated using the sonar equation. Because it is customary to use decibels in underwater acoustics, the form of sonar equations is such that individual phenomena contributing to the performance of a sonar appear as additive terms and can

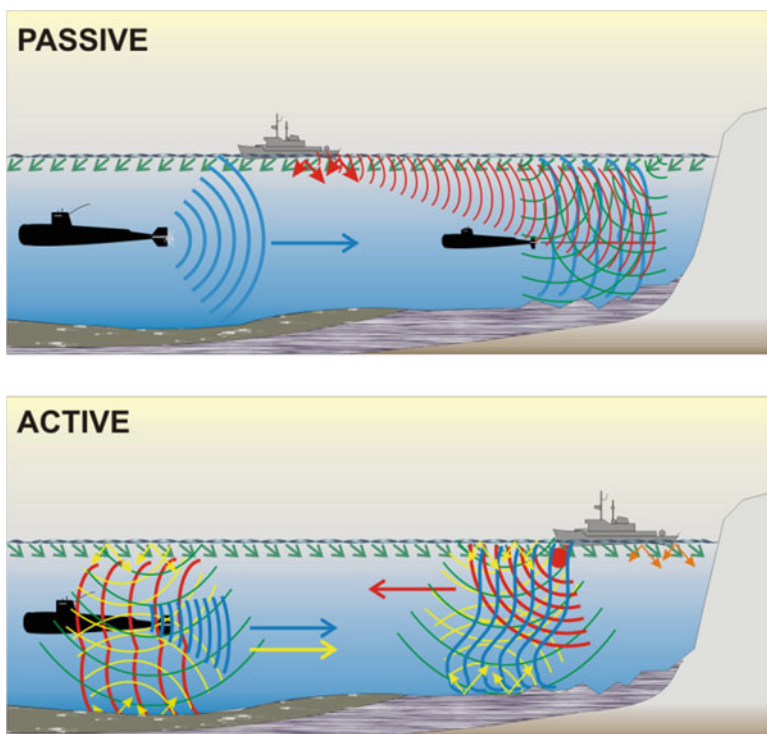


**Fig. 10.1** Passive and active sonar for submarine detection. *Passive*: The submarine on the right tries to detect sounds (blue) from the other submarine using a towed array (antenna). These sounds are distorted by the shallow water environment and are embedded in ocean surface noise (green) and surface shipping noise (red). *Active*: The ship on the right send out a pulse (red) and an echo (blue), distorted by the shallow water environment, is returned to the ship sonar which tries to distinguish it from backscattered reverberation (yellow) and ocean noise (green) (Taken from Physics Today, Oct 04)

normally be treated separately. Therefore, all terms in the sonar equations presented below are expressed in decibels. References for this material can be found in [1–4]. A more accurate representation of sonar system performance requires simulation of the relevant acoustic phenomena and subsequent insertion of these fields into a computer model of the system.

### 10.2.2.1 Detection Threshold and ROC Curves

The detection threshold DT [1] is a decibel number that essentially incorporates the sonar (which includes operator) ability to decide that a detection is made or not made, i.e., the SNR necessary for detection, which in dB we write as  $DT = SNR_{DT} \equiv 10 \log(S/N_0)$ , where  $S$  is the received signal and  $N_0$  the noise in a 1-Hz band. Detection is classically treated by probability theory such that there exists a probability of detection PD and a probability of false alarm PFA. PD is the probability a signal is detected if it is present and  $1 - PD$  is the probability it will not be detected if it is present. PFA is the probability that a signal is detected when it is not present and  $1 - PFA$  is the probability that the signal will not be detected when it is not present.

In practical terms, the signal and noise are fluctuating and a detection is made (over a time interval) when the fluctuating sum of the signal and noise exceeds a threshold. For example, the case that the noise alone rises above the threshold contributes to the PFA. Therefore, the criteria determining the measurement of a detection threshold involves associating it with a specific PD and PFA. Typically, numbers might be a PD of 0.5 and PFA of  $10^{-4}$ . But the probabilities will themselves be a function of the relation between the signal and noise statistics, as represented by their mean and variance. The detection index  $\mathcal{D}$  succinctly characterizes this relation in that it indicates how easy it is to see a signal in noise,

$$\mathcal{D} = \frac{(M_{SN} - M_N)^2}{\sigma_N^2}, \quad (10.8)$$

where  $M_{SN}$  is the mean of the signal-plus-noise,  $M_N$  is the noise mean and  $\sigma_N^2$  is the variance of the noise. Figure 10.2 schematically shows the implications of the detection index where the relative proximity of the two probability-density distributions indicate the statistics of the detectability. For example, if the mean of the signal-plus-noise probability density distribution was further to the right, the detection index and PD would be larger and the corresponding PFA would be smaller.

Receiver-operating-characteristic (ROC) curves are plots of PD vs. PFA parameterized by  $\mathcal{D}$ . Figure 10.3 is an example taken from [1]. We give a typical example of how to use this methodology and refer the reader to the sonar literature for a more complete treatment [1]. A square-law detector is commonly used for a passive system dealing with unknown signals. In that case, it has been shown that the detection index for a small SNR, narrowband signal in Gaussian noise is given by

$$\mathcal{D} = wt \left( \frac{S}{N} \right)^2, \quad (10.9)$$

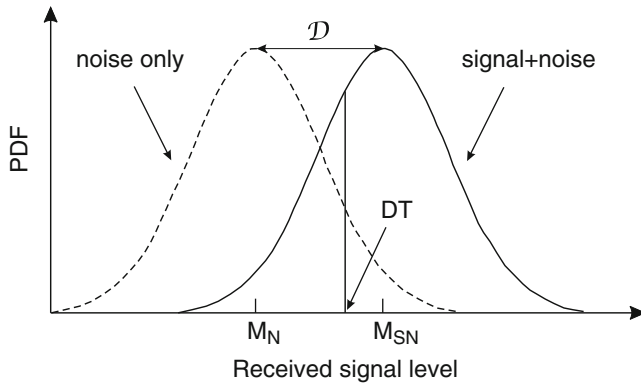


**Fig. 10.2** Probability-density distributions of noise and signal-plus-noise. The area under the Signal-plus-Noise curve to the right of the threshold DT is the probability of detection PD. The area under the Noise curve to the right of the threshold is the probability of false alarm PFA. The detection index  $\mathcal{D}$  is larger when the mean of the Signal-plus-Noise is further to the right of the mean of the Noise alone (from Urick [1])

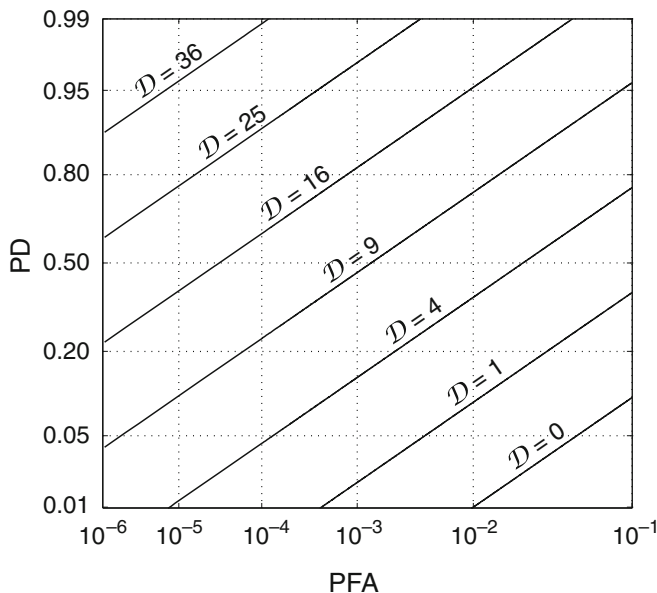


**Fig. 10.3** ROC curves: For a given signal-plus-noise, different threshold settings correspond to different PD and PFA as shown in Fig. 10.2. The ROC curves summarize the relation between PD and PFA for different thresholds as parameterized through the detection index  $\mathcal{D}$

where  $w$ ,  $t$ ,  $S$ ,  $N$  are the bandwidth (taken to be larger than the width of the spectral line of the signal), integration time, signal power, and noise power in the bandwidth, respectively. If one Hertz is the noise bandwidth reference, the detection index referenced to noise is  $\mathcal{D} = wt[S/(wN_0)]^2$ , where  $N_0$  is the noise in a 1-Hz band. This gives a relation of the SNR to the detection index for an energy detector of an unknown signal in Gaussian noise in decibels:

$$\text{SNR} = 5 \log \left( \frac{\mathcal{D}w}{t} \right) \equiv \text{DT}, \quad (10.10)$$

for detection criteria of a specified PD and PFA. In reality, there are correction factors for the detection threshold related to the length of observations used to make a decision, human factors, and others that we omit from this discussion. Since the criteria are specified through the ROC curves, we can now estimate the DT for specific cases. We simply go to the ROC curves for a selected PD vs. PFA and read off the detection index from which we can compute the detection threshold. For example, from Fig. 10.3 for a PD of 50% and a PFA of 0.01%, the detection index is  $\mathcal{D} \simeq 16$ . Using unit bandwidth and integration time, the detection threshold is  $\text{DT} = 5 \log 16 = 6 \text{ dB}$ .

The above methodology is an example of the meaning of the DT term below, though the relationship between DT and  $\mathcal{D}$  is different depending on the type of receiver and sonar. An important lesson from the discussion in this section is that a meaningful sonar performance prediction involves stochastic modeling of signal and noise. From a simulation point of view, this translates into modeling time series as the input to specific sonar signal processing algorithms, which is discussed in some detail in Sect. 10.9.

### 10.2.2.2 Passive Sonar Equation

A radiating object of source level SL (all units are expressed in decibels relative to an accepted standard – in this case one meter or one yard) will be received at a hydrophone of a sonar system at a lower signal level S because of the transmission loss TL it suffers; hence,

$$S = SL - TL, \quad (10.11)$$

where TL is given by (2.77) and is almost without exception a positive quantity. Any of the propagation models discussed in this book, or simpler geometric spreading laws with an estimate of attenuation, can be used to estimate TL.

The noise at a single hydrophone N is subtracted from (10.11) to obtain the SNR at a single hydrophone,

$$\text{SNR} = SL - TL - N. \quad (10.12)$$

A sonar system normally consists of an array of hydrophones which are beamformed to obtain signal-to-noise enhancement. The directivity index (DI) – see discussion below (10.4) – is added to (10.12) to obtain the SNR at the output of the beamformer,

$$\text{SNR}_{\text{BF}} = SL - TL - N + DI. \quad (10.13)$$

There exists a threshold SNR above which a sonar system will, with 50% probability (by convention), accomplish its detection purpose. Ideally, detection should occur when the signal is not masked by noise, i.e.,  $\text{SNR} > 0$ , but, normally, because of the nature of the sonar, the signal, the interference, the sonar operator's training and alertness, and an assortment of other factors, a certain additional signal level at the output of the beamformer is required for detection. This additional signal level above zero  $\text{SNR}_{\text{BF}}$  is referred to as the *recognition differential* RD or the *detection threshold* DT and was briefly introduced in the above subsection. Hence, if we include a term related to this detection threshold, we can write a sonar equation for the *signal excess* SE, the difference between the actual received signal at the output of the beamformer and the minimum signal for detection (i.e., extra signal above that needed for detection),

$$\text{SE} = \text{SL} - \text{TL} - \text{N} + \text{DI} - \text{DT}, \quad (10.14)$$

where, even though all the quantities are in decibels, only SL and N must be defined with respect to the same reference pressure and frequency bandwidth (e.g., 1 Hz or a fraction of an octave such as the standard one-third octave filter convention). We later show that an  $\text{SE} > 0$  can be used to increase our effective *probability of detection* PD which is defined as the probability that an existing signal will be detected.

Another quantity useful to the sonar engineer is the *figure of merit* FOM which is the transmission loss that gives zero signal excess for a  $\text{PD} = 50\%$ , i.e., the maximum allowable transmission loss for a detection. Hence, from (10.14),

$$\text{FOM} = \text{SL} - \text{N} + \text{DI} - \text{DT} \quad (10.15)$$

and we see that the FOM is a transmission-loss number which encompasses target source level and sonar system parameters. Therefore, a specification of an FOM can be translated into a detection range if the propagation conditions (loss vs. range) are known.

We note that the above sonar equations are for simplistic situations and must be modified accordingly to be applicable to more realistic situations. For example, the signal and noise levels have both vertical and azimuthal dependence so that they are functions of the beam steering angle  $\theta_s$ . The signal is also likely to have a dispersed arrival structure because of multipath propagation. Furthermore, the response of the sonar array is a function of  $\theta_s$ . All these complications can be included either in a more sophisticated sonar equation or by a more precise model simulation involving propagation, noise and sonar signal processing packages. The latter requires considerably more detailed knowledge of the ocean-acoustic environment and the sonar system under study.

Continuing with the simple sonar equation, we note that DT includes all the signal and noise processes associated with the sonar, including the operator, except for the AG. Hence, we are in the realm of probabilistic phenomena. The detection

threshold DT (in decibels) is the ratio of the signal power S in the receiver bandwidth to the noise power  $N_0$  in a 1-Hz band at which detection will occur according to some decision criterion.

To understand the effect of detection threshold setting, we consider two possible cases. If the detection criterion is set too stringently and the DT is, therefore, high, the probability of detection is low. However, the probability of false alarm (the probability that noise alone crosses the detection threshold DT) is also low. In this case, only targets with high source level will be detected. Alternatively, for a low DT, low-level targets are detected but there is a high probability of false alarms.

In reality, sonar-system performance has a more complicated behavior than the simplistic discussion above. For example, signal fluctuations may result in increased detection threshold crossings (for a fixed probability of false alarm). Hence, fluctuations in this case do not degrade sonar performance but result in a net increase in the probability of detection. More complete consideration of such phenomena lies within the specialized topic of ROC curves as briefly discussed above.

### 10.2.2.3 Active Sonar Equation

There are two fundamental configurations of active sonars. A *monostatic* sonar transmits a pulse which interacts with a target, resulting in an echo which returns to the receiver array co-located with the transmitter. A *bistatic* sonar has the receiver in a different location than the transmitter. While our main concern will be with monostatic sonars, we will point out some of the pertinent differences between the two configurations.

With respect to sonar equations, the principal differences between the passive and active cases are that (a) the source level is modified by a *target strength* TS, as defined in (1.82); (b) reverberation is the dominant interference; (c) the transmission loss results from two paths: transmitter to target and target to receiver.

In the monostatic case, the transmission loss is  $2 TL$ , where TL is the one-way transmission loss. In the bistatic case, the transmission loss is  $TL_1 + TL_2$  where the transmission loss is the sum (in decibels) over paths from the transmitter to the target and from the target to the receiver. The reverberation level is an additional interference term in the active problem that results primarily from scattering of the transmitted field from the boundaries and volume of the ocean. Boundary scattering is due to waves, ice or bottom features while volume scattering is caused by fish, plankton, etc. Hence, the reverberation level at the receiver is a function not only of the acoustic environment but also of the location of both the receiver and the transmitter. The total interference term in the sonar equation is a sum of reverberation and noise terms  $RL + N$ . The concept of detection threshold remains the same as for the passive case (though its specific determination is different [1]) so that we can rewrite (10.14) for the active case as

$$SE = SL - TL_1 + TS - TL_2 - (RL + N) + DI - DT. \quad (10.16)$$

In the monostatic case, the two transmission loss terms can be replaced by  $2 \text{ TL}$ . The first two terms are for the outgoing path; the next two terms are for the returning echo; the quantities in the parentheses are the interference and the last two terms are the system-operator parameters.

In most practical cases, reverberation is the dominant interference factor for active sonar performance. Hence, we drop the noise term, noting that it may have to be retained in highly specialized cases. The DI used in the passive sonar equation approximated the interference (i.e., the noise field) as isotropic; this is no longer a valid approximation for reverberation. It is, therefore, often convenient to define a quantity as equivalent plane-wave reverberation level  $\text{RL}_{\text{PW}}$  which replaces the terms  $\text{N} - \text{DI}$  in the passive sonar equation,

$$\text{SE} = \text{SL} - \text{TL}_1 + \text{TS} - \text{TL}_2 - \text{RL}_{\text{PW}} - \text{DT}. \quad (10.17)$$

The corresponding FOM for an active system is defined similarly to the passive system case, (10.15), but is for the maximum allowable two-way transmission loss with  $\text{TS} = 0 \text{ dB}$ . We can estimate the influence of surface and bottom reverberation on sonar performance by combining (1.83) and (1.85) with a propagation model from the earlier chapters. An additional level of sophistication with regard to some of the above topics is given by Baggeroer [5] which also includes an extensive bibliography.

## 10.3 Plane-Wave Beamforming

Beamforming goes beyond simple energetics; it is a spatial filtering process. In this section we present some of the fundamental aspects of plane-wave beamforming.

### 10.3.1 Linear Beamforming

We can shade the array by amplitude and phase factors at each hydrophone. The simplest example is phase shading of a horizontal array to search in bearing for a plane-wave signal, a procedure referred to as “steering the array.” We take  $\theta_s$  as the beam steering angle or the look direction.

As illustrated in Fig. 10.4, we consider a plane wave

$$s(\theta) = \exp(i\mathbf{k} \cdot \mathbf{r}), \quad (10.18)$$

where  $\theta$  is the bearing angle associated with the signal and we have suppressed the time dependence  $\exp(-i\omega t)$ . If the hydrophone input at position  $\mathbf{r}_i$  is multiplied by the complex conjugate of the plane-wave phase factor  $w_i = \exp(i\mathbf{k} \cdot \mathbf{r}_i)$ , the field is summed in phase. The AG does not change since both signal and noise are altered by

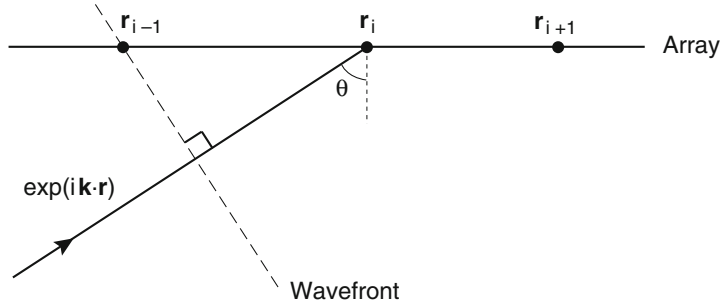


**Fig. 10.4** Geometry for plane-wave beamforming

this same factor. The output of this linear (*Bartlett*) beamforming process  $B_{\text{Bart}}(\theta_s)$  is a quadratic form obtained by summing the shaded signal-plus-noise from each hydrophone,

$$B_{\text{Bart}}(\theta_s) = \left| \sum_{i=1}^m w_i^*(\theta_s) [s_i(\theta) + n_i] \right|^2 = \sum_{i,j=1}^m w_i^*(\theta_s) (s_{ij} + n_{ij}) w_j(\theta_s), \quad (10.19)$$

where  $s_{ij} + n_{ij}$  are elements of a *Cross-Spectral Density Matrix* (CSDM) which, when obtained from data, would involve Fourier transforms and ensemble averages as mentioned in the introduction and in the discussion below (10.2). For simulation purposes we can construct these quantities directly, and subsequently obtain the CSDM if we assume that the signal and noise are mutually independent and uncorrelated. If the field at the receiving array is a plane wave at a particular angle of incidence, the beamformer has its greatest peak in that same direction; however, there also exists sidelobes because of the finite spatial sampling of the acoustic field with a finite-aperture array.

We can write the above expression in matrix notation where boldface lower-case letters denote vectors and boldface upper-case letters denote matrices. Define a steering column vector  $\mathbf{w}$  whose  $i$ th element is  $w_i$  and a CSDM,  $\mathbf{K}$ , of the signal and noise with elements  $K_{ij} = s_{ij} + n_{ij}$ . The signal and noise are here assumed to be independent. For later use we mention that the CSDM is Hermitian since it is constructed as the outer product of data vectors, say,  $\mathbf{d}$ :

$$\mathbf{K}^\dagger = (\mathbf{d}\mathbf{d}^\dagger)^\dagger = \mathbf{d}\mathbf{d}^\dagger = \mathbf{K}, \quad (10.20)$$

where  $\dagger$  denotes the complex transpose operation. Equation (10.19) can be rewritten as

$$B_{\text{Bart}}(\theta_s) = \mathbf{w}^\dagger(\theta_s) \mathbf{K}(\theta_{\text{true}}) \mathbf{w}(\theta_s) \equiv \mathbf{w}^\dagger \mathbf{K} \mathbf{w}. \quad (10.21)$$

The data across the array as represented in the matrix  $\mathbf{K}$  contains the information that the source is in the direction  $\theta_{\text{true}}$ . Sometimes  $\mathbf{w}(\theta_s)$  is referred to as a replica and the above beamforming process is viewed as matching the received data across

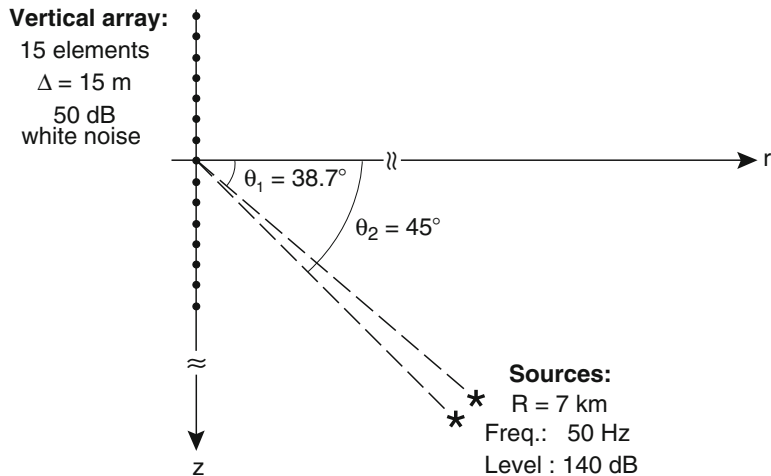


**Fig. 10.5** Geometry of plane-wave beamforming example

the array with a replica. In the previous example, the replica is a plane wave in the look direction. Because the array is finite, there will be sidelobes, i.e., energy will be received from directions other than the look direction for each steered or beamformed angle. Figure 10.5 shows a 15-element vertical array receiving signals from two CW sources, one at a true bearing of  $45^\circ$  and another adjacent to it as indicated by its coordinates and angularly separated by  $6.3^\circ$ . Figure 10.6a is the output of the Bartlett beamformer for a single source at  $45^\circ$  bearing together with the outputs of the MV and MCM beamformers which are described later. Though a point source is used, the geometry is such that the wavefront curvature does not appreciably disturb the performance of the plane-wave Bartlett beamformer, though the curvature does effect the performance of the other beamformers discussed below. For the case of sound received from both sources, Fig. 10.6b indicates that the Bartlett beamformer cannot, in this case, resolve the two sources.

### 10.3.2 Adaptive Beamforming

There are other methods of suppressing sidelobes, usually referred to as adaptive methods, since the signal processing procedure constructs weight vectors depending on the received data itself. We briefly describe one of these procedures: the *Minimum Variance distortionless processor* (MV or MVDR), sometimes also called the *Maximum Likelihood Method* directional-spectrum-estimation procedure, e.g., see Johnson [6]. In this section, we also briefly discuss the application of eigenvector methods [6] to beamforming. Eigenvector beamforming, under certain circumstances, provides some advantages with respect to issues concerning computation

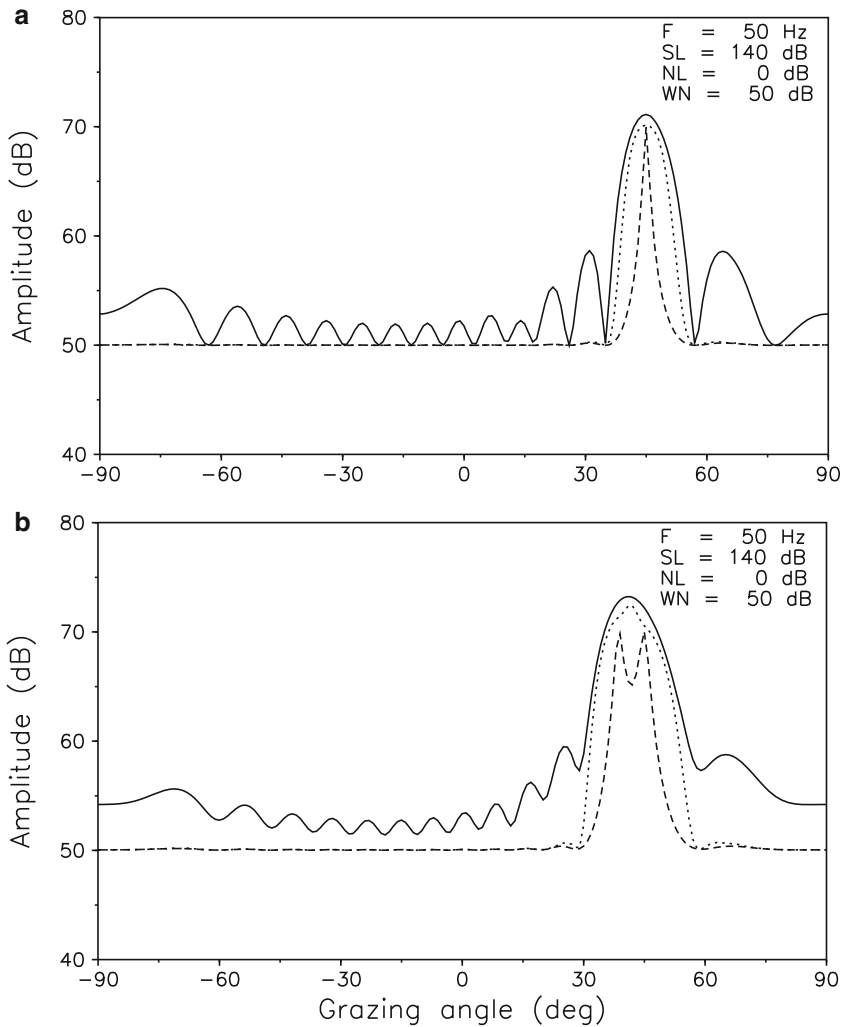


**Fig. 10.6** Beamformer outputs. (a) Single source at a bearing of  $45^\circ$ ; (b) Two sources with  $6.3^\circ$  angular separation. *Solid line*: Bartlett. *Dashed line*: MV. *Dotted line*: MCM

and resolution. There are many other types of adaptive beamforming algorithms which are discussed in Widrow and Stearns [7]. These adaptive methods are characteristically nonlinear functions of the received fields. As a matter of fact, these beamformers often have a SNR threshold above which their desirable properties appear. For this reason, the term nonlinear beamforming is often used interchangeably with adaptive beamforming.

### 10.3.2.1 Estimating the Cross-Spectral Density Matrix

Adaptive beamformers typically involve procedures related or equivalent to inverting the covariance or CSDM of the data across the array. Therefore, it can be quite misleading to simulate the performance of adaptive array processing using the deterministic procedures of the previous section that do not deal with the rank requirement of an invertible matrix. That is because we must treat our data as originating from a random process and therefore must “estimate” the covariance from a sampling process of the data. For the sample covariance estimation we assume we have an array with  $N$  sensors located at  $\mathbf{r}_i$ ,  $i = 1, \dots, N$ , and a narrowband model as illustrated in Fig. 10.7. While we assume in much of our discussion that these covariances are known, generally, these covariances must be estimated from the data. For this estimation the signal is windowed ( $W$ ) and segmented into “snapshots,”

$$R(\omega) = \int_{T_l}^{T_l + T_w} d_i(t) W(t - T_l) e^{i\omega t} dt. \quad (10.22)$$

We assume that window lengths and resolution bandwidths have been chosen so that bias errors are not an issue.

In most beamforming algorithms, the data vectors are averaged to form the sample covariance matrix,

$$\hat{\mathbf{K}}(\omega) = \frac{1}{L} \sum_{l=1}^L \mathbf{d}(\omega) \mathbf{d}^\dagger(\omega), \quad (10.23)$$

where  $L$  is the number of snapshots and  $\mathbf{d}(\omega)$  is the windowed frequency-domain data vector with elements  $R_i$ . We assume that there are  $L_{\text{eff}}$  “degrees-of-freedom”

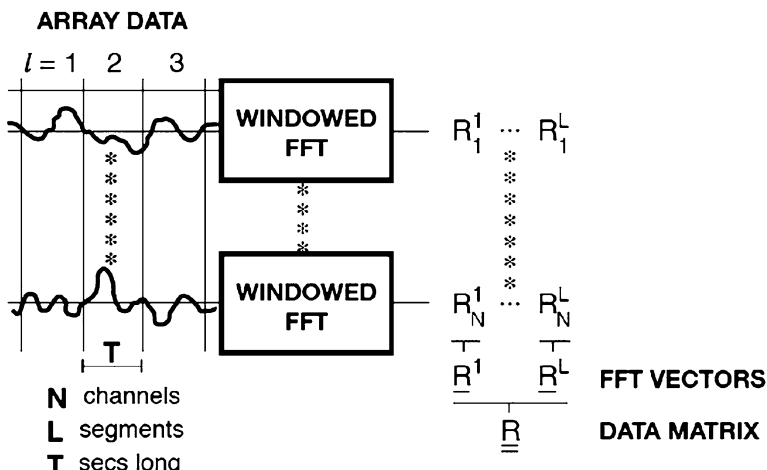


**Fig. 10.7** Schematic of processing flow to obtain narrowband snapshots for estimating the cross-spectral density matrix

in the sample covariance matrix. (One can also average across frequency if relative phase constraints across the array are observed.) We assume that the data vectors have zero mean and that the expected value of the sample covariance is the ensemble covariance  $\mathbf{K}(\omega)$ . In what follows, we assume that the CSDM has come from this process and that the sampling is sufficient to allow the required matrix operations so that we drop the hat notation for the sample CSDM.

### 10.3.2.2 Minimum Variance Distortionless Processor

We seek a weight vector  $\mathbf{w}_{\text{MV}}$  applied to the matrix  $\mathbf{K}$  such that its effect will be to minimize the output of the beamformer, (10.21), except in the look direction where we want the signal to pass through undistorted. In essence, the MV or MVDR processor optimizes the match to a signal in the look direction and therefore tries to reject signals *and correlated noise* from other directions. The weight vector is therefore chosen to minimize the functional

$$F = \mathbf{w}_{\text{MV}}^\dagger \mathbf{K} \mathbf{w}_{\text{MV}} + \gamma (\mathbf{w}_{\text{MV}}^\dagger \mathbf{w} - 1). \quad (10.24)$$

The first term is the mean-square output of the array and the second term incorporates the constraint of unity gain by means of the Lagrangian multiplier  $\gamma$ . Note that for this complex variable problem, there are two independent variables which we can take as  $\mathbf{w}_{\text{MV}}$  and  $\mathbf{w}_{\text{MV}}^*$ . Following the method of Lagrange multipliers, we need to take the gradients with respect to these variables but note that they are conjugates of each other. Taking one of these gradients (using the property that  $\mathbf{K}$  is Hermitian) and setting it equal to zero, we obtain,

$$2\mathbf{K} \mathbf{w}_{\text{MV}} + \gamma \mathbf{w} = 0, \quad (10.25)$$

so that

$$\mathbf{w}_{\text{MV}} = -\frac{\gamma}{2} \mathbf{K}^{-1} \mathbf{w} \longrightarrow \mathbf{w}_{\text{MV}}^\dagger = -\frac{\gamma}{2} (\mathbf{K}^{-1} \mathbf{w})^\dagger \quad (10.26)$$

and the constraint condition of unity in the look direction gives

$$\frac{\partial F}{\partial \gamma} = \mathbf{w}_{\text{MV}}^\dagger \mathbf{w} - 1 = 0. \quad (10.27)$$

Performing the complex transpose operation on the right-hand side of the second of (10.26) yields

$$\mathbf{w}_{\text{MV}}^\dagger = -\frac{\gamma}{2} \mathbf{w}^\dagger \mathbf{K}^{-1}, \quad (10.28)$$

where we have used the property that the inverse of a Hermitian matrix is Hermitian, which, taken together with the constraint of (10.27), gives an expression for the Lagrange multiplier,

$$\gamma = -2 \left( \mathbf{w}^\dagger \mathbf{K}^{-1} \mathbf{w} \right)^{-1}. \quad (10.29)$$

Combining (10.26) and (10.29) we obtain the MV weight vector,

$$\mathbf{w}_{\text{MV}} = \frac{\mathbf{K}^{-1} \mathbf{w}}{\mathbf{w}^\dagger \mathbf{K}^{-1} \mathbf{w}}. \quad (10.30)$$

Note that this new weight vector depends on the received data as represented by the CSDM; hence, the method is *adaptive*. Substituting back into the quadratic form of (10.21) (which has been constructed such that the second term on the right side vanishes) gives the output of our MV processor,

$$B_{\text{MV}}(\theta_s) = \left[ \mathbf{w}^\dagger(\theta_s) \mathbf{K}^{-1}(\theta_{\text{true}}) \mathbf{w}(\theta_s) \right]^{-1}. \quad (10.31)$$

The MV beamformer should have (if the signal was a plane wave) the same peak value at  $\theta_{\text{true}}$  as the Bartlett beamformer, (10.21), but with sidelobes suppressed and narrower main beam indicating that it is a high-resolution beamformer. The MV peak is not the same as the Bartlett because of a form of “mismatch.” Plane-wave beamforming matches plane waves to the signal which in this case, however, is emanating from a point source. The example given in Fig. 10.6 illustrates the increased resolution of the MV over the Bartlett, and only the MV is seen to resolve the two sources in Fig. 10.6b, see also [6, 8].

### 10.3.2.3 Eigenvector Beamformers

In principle, the estimate of the CSDM across a receiving array is made by taking an ensemble average over an appropriate time interval such that signals from sources are statistically independent of each other (uncorrelated) and of the background noise. We interpret this to mean that the source position vectors are linearly independent and furthermore, the noise subspace is orthogonal to the signal subspace.

We start by representing the CSDM in terms of its  $M$  eigenvectors  $\mathbf{v}_i$  and eigenvalues  $\lambda_i$ ,

$$\mathbf{K} = \sum_{i=1}^M \lambda_i \mathbf{v}_i \mathbf{v}_i^\dagger, \quad (10.32)$$

which satisfy the standard eigenvalue equation,

$$\mathbf{K}\mathbf{v}_i = \lambda_i \mathbf{v}_i, \quad i = 1, \dots, M. \quad (10.33)$$

Next, we write  $\mathbf{K}$  in terms of its signal and noise components  $\mathbf{K}_s + \mathbf{K}_n$ , respectively. If there are  $p$  independent signal sources of strength  $\sigma_i$  with signal vectors  $\mathbf{s}_i$ , then  $\mathbf{K}_s$  can be expressed in terms of these signal vectors such that the total CSDM can be written as

$$\mathbf{K} = \sum_{i=1}^p \sigma_i \mathbf{s}_i \mathbf{s}_i^\dagger + \mathbf{K}_n. \quad (10.34)$$

The simplest case is when the noise is spatially white (or a plane-wave beamforming case for an array with half-wavelength spacing in isotropic noise) for which the CSDM of the noise is proportional to the identity matrix; then (10.34) becomes

$$\mathbf{K} = \sum_{i=1}^p \sigma_i \mathbf{s}_i \mathbf{s}_i^\dagger + K_n \mathbf{I}. \quad (10.35)$$

Comparing (10.35) with (10.32) we see that there are  $p$  eigenvectors which correspond to the signal vectors so that the remaining  $M - p$  eigenvectors are orthogonal to the signal vector space. Note that the signal eigenvectors have eigenvalues  $\sigma_i + K_n$  which include the noise.

It is straightforward to simply use the eigenvalue decomposition of the CSDM to implement the Bartlett and MV processors. However, there are some interesting additional variants of interest. For the Bartlett processor, we can truncate the CSDM eigenvector representation and reduce the background noise by including only the signal vector space,

$$\mathbf{K}' = \sum_{i=1}^p \lambda_i \mathbf{v}_i \mathbf{v}_i^\dagger. \quad (10.36)$$

Equation (10.21) is a statement of scanning the space of the CSDM with the replica vectors and using  $\mathbf{K}'$  will result in sharp peaks at the source locations. Alternatively, we note that the inverse matrix required for the MV has the same eigenvectors,

$$\mathbf{K}^{-1} = \sum_{i=1}^M \lambda_i^{-1} \mathbf{v}_i \mathbf{v}_i^\dagger. \quad (10.37)$$

In this case, let us truncate the matrix representation of the CSDM so as to not include the signal subspace,

$$[\mathbf{K}'']^{-1} = \sum_{i=M-p}^M \lambda_i^{-1} \mathbf{v}_i \mathbf{v}_i^\dagger. \quad (10.38)$$

The replica scanning process produces a null for the source locations so that the MV prescription of the inverse of the process is infinite at source locations and finite otherwise. This provides an extremely high-resolution estimate of the source location. The MUSIC method [9] uses eigenvector decomposition where the eigenvalues of the (noise) subspace orthogonal to the signal subspace is set to unity by a “prewhitening” transformation of the CSDM.

Finally, note that when the noise is correlated so that the second term of (10.34) is not diagonal, then there is no one-to-one correspondence between eigenvectors and source location vectors. Nevertheless, one can expect that under certain conditions, such as highly directional noise conditions or with a priori knowledge about the noise field as modeled in Chap. 9, eigenvector methods may prove beneficial.

### 10.3.3 Multiple-Constraints Beamforming

Array processing represents an extremely large and active area of research, most of which is beyond the scope of this book. Although there are many other beamformers, in this section we present an example of one which provides an opportunity to combine environmental-acoustic issues with signal processing. The MV method is high resolution not only in the conventional search parameter, in this case bearing, but also in other parameters that may enter into the beamforming or search problem. This suggests that opening up the search window in one or more of these parameters would make the beamformer more tolerant of uncertainty in the other parameters. The more general beamforming algorithm discussed in the next section involves other parameters not likely to be known exactly, such as those describing the ocean environment. It may then be desirable to open up the MV method's search window and attempt to average out the effect of uncertainties.

Schmidt et al. [10] have combined the Bartlett and MV methods by opening up a central window having an increased number of constraints (multiple constraints) in (10.24). The idea is to suppress sidelobes by minimizing a functional constrained not by unity in the look direction but by a set of beams, each with its own Bartlett window, defining a lower-resolution look direction,

$$F_{\text{MCM}} = \mathbf{w}_{\text{MCM}}^\dagger \mathbf{K} \mathbf{w}_{\text{MCM}} + \sum_{m=1}^M \gamma_m \left( \mathbf{w}_{\text{MCM}}^\dagger \mathbf{w}_m - c_m \right), \quad (10.39)$$

where we have  $M$  constraints defining the local Bartlett window about each look direction  $\mathbf{w}_l$ . The elements of the constraint column vector  $\mathbf{c}$  is taken to be  $c_m = \mathbf{w}_l^\dagger \mathbf{w}_m$ . Performing the minimization (see [10] for details) yields

$$B_{\text{MCM}}(\theta_s) = \mathbf{c}^\dagger \left[ \mathbf{W}^\dagger(\theta_s) \mathbf{K}^{-1}(\theta_{\text{true}}) \mathbf{W}(\theta_s) \right]^{-1} \mathbf{c}, \quad (10.40)$$

where  $\mathbf{W}$  is a replica matrix composed of  $M$  replica vectors,

$$\mathbf{W} = [\mathbf{w}_1 | \mathbf{w}_2 | \cdots | \mathbf{w}_M]. \quad (10.41)$$

Figure 10.6 provides an example of the *Multiple Constraints Matching* (MCM) beamformer performance compared to the other beamformers. Figure 10.6a shows that the MCM beamformer behaves like the MV beamformer for sidelobe suppression but has a mainlobe width comparable to that of the Bartlett. On the other hand, Fig. 10.6b shows the decreased resolution, with the mainlobe unable to resolve the two sources. In Sect. 10.6, the advantages of a beamformer which is tolerant to environmental uncertainties will become apparent.

### 10.3.4 White-Noise Constraint Processor

The white-noise constraint (WN) processor essentially desensitizes the MVDR processor to mismatch by selectively loading the diagonal of the CSDM used for the adaptive weights.

#### 10.3.4.1 Derivation of the White-Noise Constraint Processor

The WN processor [11] is based on the idea that the maximum AG defined as the SNR at the output of the array in white noise is  $10 \log N$  as per Sect. 10.2, where  $N$  is the number of array elements. We can write the white-noise gain as

$$G = \frac{\mathbf{w}^\dagger \mathbf{K}_s \mathbf{w}}{\mathbf{w}^\dagger \mathbf{K}_n \mathbf{w}}, \quad (10.42)$$

so that the white-noise gain (the white-noise CSDM is proportional to the identity matrix) is simply

$$G_w = \frac{|\mathbf{w}^\dagger \mathbf{s}|^2}{\mathbf{w}^\dagger \mathbf{w}} \leq N, \quad (10.43)$$

where the equal sign refers to perfect match between the replica and the signal. Note that mismatch not only arises from modeling, but also from the lack of accurate knowledge of receiver element location. If we take the mismatch from either effect to introduce zero-mean uncorrelated random errors, the signal CSDM becomes  $\mathbf{K}_s + \chi \mathbf{I}$ , where  $\chi$  is the error strength parameter. The fractional sensitivity of the gain to these errors is therefore

$$S = \frac{dG/d\chi}{G} = \frac{1}{G_w} \quad (10.44)$$

meaning that we can reduce our sensitivity to errors by constraining the white-noise gain to be less than  $N$ . We accomplish this by adding a white-noise constraint to the functional of (10.24). But first note that the bore hole constraint of the term multiplied by  $\gamma$  tells us that the minimization problem is also equivalent to minimizing the same functional divided by  $\mathbf{w}^\dagger \mathbf{w}$ . Then, the equivalent expressions to minimizing the functional of (10.24) with respect to  $\mathbf{w}_{MV}$  are,

$$\min \left[ \frac{\mathbf{w}_{MV}^\dagger \mathbf{K} \mathbf{w}_{MV}}{|\mathbf{w}_{MV}^\dagger \mathbf{w}|^2} \right], \quad \mathbf{w}_{MV}^\dagger \mathbf{w} = 1. \quad (10.45)$$

Now we add the additional constraint which is, as per above, the inverse of a white-noise gain of (10.43) thereby reducing sensitivity to error:

$$\min \left[ \frac{\mathbf{w}_{WN}^\dagger \mathbf{K} \mathbf{w}_{WN}}{|\mathbf{w}_{WN}^\dagger \mathbf{w}|^2} + \gamma \frac{\mathbf{w}_{WN}^\dagger \mathbf{w}_{WN}}{|\mathbf{w}_{WN}^\dagger \mathbf{w}|^2} \right], \quad \mathbf{w}_{WN}^\dagger \mathbf{w} = 1, \quad (10.46)$$

which we can rewrite as

$$\min \left[ \frac{\mathbf{w}_{WN}^\dagger (\mathbf{K} + \gamma \mathbf{I}) \mathbf{w}_{WN}}{|\mathbf{w}_{WN}^\dagger \mathbf{w}|^2} \right], \quad \mathbf{w}_{WN}^\dagger \mathbf{w} = 1, \quad (10.47)$$

where  $\gamma$  is a Lagrange multiplier yet to be determined. By analogy to the minimization of the functional in (10.24) that yields (10.30), we can immediately write the solution to the WN problem:

$$\mathbf{w}_{WN} = \frac{(\mathbf{K} + \gamma \mathbf{I})^{-1} \mathbf{w}}{\mathbf{w}^\dagger (\mathbf{K} + \gamma \mathbf{I})^{-1} \mathbf{w}}. \quad (10.48)$$

In order to determine  $\gamma$ , we must specify the decrease in the white-noise gain. For later reference, we note that the second expression in (10.45) and (10.47) defines the MV-constraint subspace. We can specify the reduction in the white-noise gain by setting the white-noise gain to  $G_w = \delta^2 \leq N$ ; i.e., from (10.43) and the bore hole condition setting the numerator of (10.43) to unity, we have the condition

$$\mathbf{w}_{WN}^\dagger \mathbf{w}_{WN} = \delta^{-2}. \quad (10.49)$$

We determine the diagonal loading  $\gamma$  by selecting a  $\delta$ ; in dB, we can think of the constraint being so many dB below the white-noise gain. For a given  $\delta$ ,  $\gamma$  is different for each replica  $\mathbf{w}$  and one finds each  $\gamma$  by computing  $\mathbf{w}_{WN}$  from (10.48) and varying values of  $\gamma$  until (10.49) is satisfied. This is most efficiently accomplished by noting that the eigenvectors of  $\mathbf{K}$  and  $(\mathbf{K} + \gamma \mathbf{I})$  are the same so that  $(\mathbf{K} + \gamma \mathbf{I})^{-1}$  is easy to compute from (10.37) for any  $\gamma$ :

$$(\mathbf{K} + \gamma \mathbf{I})^{-1} = \sum_{i=1}^N \frac{\mathbf{v}_i \mathbf{v}_i^\dagger}{\lambda_i + \gamma}, \quad (10.50)$$

where  $\lambda_i$  and  $\mathbf{v}_i$  are the eigenvector and eigenvalue of the non-diagonally loaded CSDM.

When we use the full white-noise gain (“0-dB down”), the processor behaves as a the MVDR processor. For a larger constraint, the processor starts to behave a bit like the Bartlett. A typical constraint might be 3-dB down, with trial and error being an excellent starting guide. The robustness that is obtained is at the expense of decreasing the MVDR resolution.

## 10.4 Time-Domain Processing

Time delay is the time-domain analogy to phase shading in the frequency domain. For isovelocit environments, time-delay beamforming is straightforward. In general, time-delay beamforming takes advantage of the coherent properties of

the original pulse. For non-isovelocity cases, appropriate time delays as a function of depth have a powerful application in signal processing methods that depend on time-of-arrival structure, such as ocean tomography.

### 10.4.1 Isovelocity Time-Delay Beamforming

The formulas for isovelocity time-delay beamforming can be derived formally by taking the Fourier transform of the beamforming process. Using the property that the Fourier transform of a product of functions in one space is a convolution in the conjugate space, we can immediately write down, from the linear (rather than quadratic) form of (10.19) and the definitions above it, that

$$B(t) = \sum_i \int w_i(\tau) r_i(t - \tau) d\tau, \quad (10.51)$$

where  $r_i(t)$  is the signal-plus-noise time-domain data at the  $i$ th array element. The time-domain replica  $w_i(\tau)$  is the Fourier transform of the phase factor  $w_i$  in (10.19),

$$w_i(\tau) = \delta\left(\tau - \frac{d_i}{c} \sin \theta\right), \quad (10.52)$$

where  $d_i$  is the element spacing and  $c$  the sound speed. We can now write the beamformer output as

$$B(t) = \sum_i r_i\left(t - \frac{d_i}{c} \sin \theta\right). \quad (10.53)$$

This process is referred to as delay-and-sum beamforming; the delay is simply the time interval associated with the phase shift in the frequency-domain array processing.

### 10.4.2 Non-Isovelocity Time-Delay Beamforming: The Turning Point Filter

As discussed in Chap. 3, Snell's law relates a ray angle with the local sound speed. Specifically, if  $c(z_{TP})$  is the sound speed at depth  $z_{TP}$  where a ray has a turning point (is horizontal), then Snell's law takes the form  $\cos \theta(z)/c(z) = \cos \theta(z')/c(z') = 1/c(z_{TP})$ , where  $\theta$  is the angle of the ray with respect to the horizontal at any other depth  $z$ . By simply using Snell's law we can construct a “turning-point filter” [12] such that the beamformer of a vertical array scans through turning points rather than angles of plane waves.

For any element at depth  $z$  of a vertical array, the vertical wavenumber  $k_z$  of a ray with horizontal wavenumber  $k_r$  is

$$k_z = \sqrt{k^2(z) - k_r^2} = \omega \sqrt{\frac{1}{c^2(z)} - \frac{\cos^2 \theta_0}{c^2(d_0)}}, \quad (10.54)$$

where we have invoked Snell's law stating that the horizontal wavenumber of a ray is constant and we have chosen the array element depth at  $d_0$  as a reference. The phase difference between elements at depth  $d$  and  $d_0$  is just the integral of the vertical wavenumber between these two depths, and the associated time delay is this phase delay divided by  $\omega$ ,

$$\tau = \int_{d_0}^d \sqrt{\frac{1}{c^2(z)} - \frac{\cos^2(\theta)}{c^2(d_0)}} dz, \quad (10.55)$$

where we now define  $\theta$  as the scanning angle at the “phase center” of the array (at depth  $d_0$ ). The beamforming is then done by a time delay of the data at each depth as per (10.51) for a given angle and sum. Note that for a constant sound speed, (10.55) reduces to the time delay of the delay-and-sum beamformer as expressed in (10.53).

### 10.4.3 Example: Passive Fathometer

A conventional fathometer is active. In its simplest form, a monostatic sonar transmits a pulse, and an echo from a bottom reflection is received. The time difference between transmission and reception multiplied by the sound speed is twice the distance between the bottom and the sonar. A simple improvement on this process would be the use of an  $M$ -element vertical receiving array with equally spaced elements. Pick a reference receiver, say the top receiver. It receives the bottom echo at a time  $\tau_b$  after it was transmitted.

Now, for the passive fathometer [13], only ambient-noise correlations are utilized; there is no source attached to the device. Recall from Sect. 9.3 that the time-domain noise-correlation function (NCF) between receiver 1 and receiver 2 produces a time series as if one of the receivers was the source. The time series should then include a direct arrival from the source (receiver 1) and the bottom echo arrival to receiver 2. This is the same information as in the active case. The big difference, as mentioned in Sect. 9.3, is that it takes time to build up the NCF. One then uses the same process as in the active case. However, because of the statistical nature of the buildup of the NCF's from random noise, we can further take advantage of diversity to build up the endfire-beam time series. That is because in this case, we can use each receiver as a “source.” Now we can choose the next receiver as the reference, the only difference in the outputs is that the beam time series is now  $\Delta\tau$  shifted from the first beam. We continue the process to use each of the receivers as the reference noting the time shifts of their respective endfire-beam time series. Therefore, we can do another delay-and-sum process on all the beams. These two

delay-and-sum processes are analogous to having a directional receive array (as in the active fathometer example above) and also a directional source array. The results of a passive fathometer experiment [13] is shown in Fig. 10.8, which includes a comparison with an active fathometer operating over the same location. More advanced signal processing than that used to produce the results in Fig. 10.8 have since been developed [14–17].

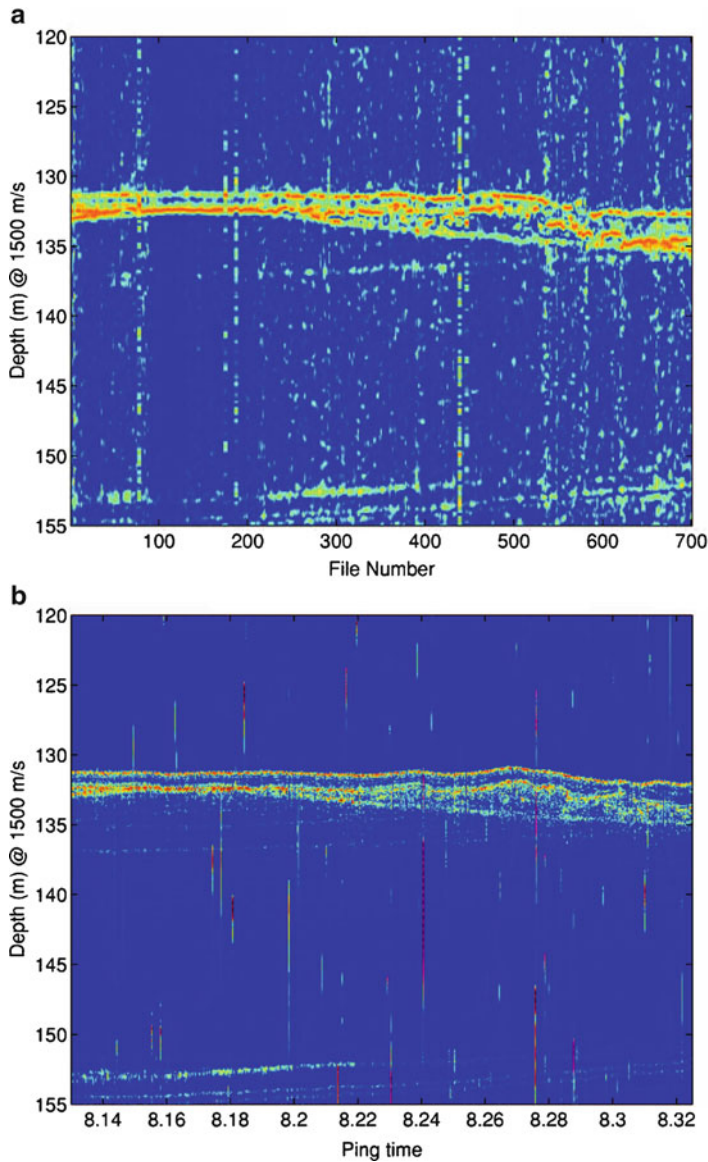


**Fig. 10.8** Comparison of results from active and passive fathometers from Siderius et al. [13]. (a) Passive fathometer even shows sublayers; (b) A conventional fathometer output over the same bottom

## 10.5 Performance Prediction: Modeling, Beamforming and the Sonar Equation

The performance of a sonar over a wide area can be estimated by combining some of the techniques we have already discussed in detail. Here, we present an example of this methodology for a towed array (from the modeling point of view it is simply a movable horizontal array) employing plane-wave beamforming for the purpose of detecting a radiating object embedded in a directional noise field.

There are many metrics one can use for performance prediction. We will use a quantity referred to as the minimum detectable level (MDL) of an array, seeking to acoustically monitor a specified area in which propagation may be dependent on range and azimuth and the noise may be directional. The MDL is the source level of a target such that it has a greater than 50% probability of being detected (with a specified false alarm rate) and would be typically contoured over a geographical region about the array. Returning to the definition of signal excess SE as given by (10.14), MDL is then given by the source level for SE= 0,

$$\text{MDL}(r, \varphi) = \text{TL}(r, \varphi) + \text{DT} + [\text{NL}(\varphi, \phi) - \text{AG}], \quad (10.56)$$

where  $r, \varphi$  is the range and azimuthal angle of a potential target position relative to the array;  $\phi$  is the angular orientation of the array (e.g., its heading with respect to north). We use AG here rather than DI because the noise is directional as per the discussion below (10.4). Further, the noise in any beam must include the fact that for a horizontal line array, the bearing line is a symmetry axis such that noise from either side of the axis at the same angle adds into that beam since these symmetric beams are indistinguishable. This is contained in the NL term which we define as

$$\text{NL} = 10 \log \{180 [N_B(\varphi + \phi) + N_B(\varphi - \phi)] / \sin \phi\}, \quad (10.57)$$

which has units dB/deg (the  $\sin \phi$  in the denominator comes from normalizing to these units in polar coordinates). The quantity  $N_B$  is the unambiguous noise in a beam which can be modeled directly from shipping distributions or measured by a procedure that uses accumulated noise data at multiple array headings to unravel the ambiguity (see for example [18] and references contained therein). Further, we have grouped the terms  $\text{NL}(\varphi, \phi) - \text{AG}$  to emphasize that one interpretation of beamforming is that AG manifests itself as reduced noise in a beam as opposed to an omni-directional sensor which registers the total noise coming from all directions.

A simple example is shown in Fig. 10.9 for an ambient noise scenario containing a discrete noise source. The pattern plotted in Fig. 10.9a corresponds to  $N_B$  whereas that plotted in Fig. 10.9b corresponds to the terms in the square brackets on the right-hand side of (10.56). Note two features in this latter plot: the ambiguous

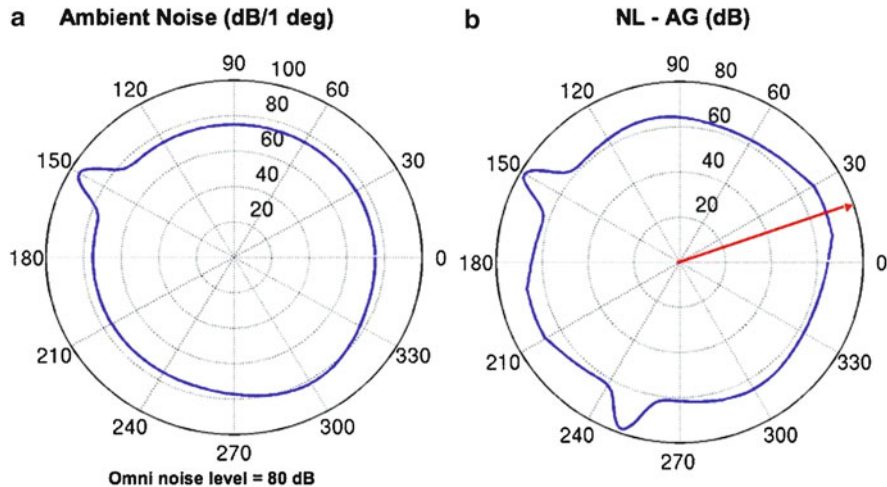


**Fig. 10.9** Ambient noise with discrete source. (a) Noise “rose” showing a discrete source at absolute bearing  $150^\circ$ ; (b) Beamformed result for an array with heading direction indicated by red arrow

beams about the array heading and the reduced level over the actual ambient noise as discussed above in which the AG acts to reduce beam noise and hence enhance MDL. Figure 10.10 shows a series of MDL plots using Fig. 10.9b together with parabolic-equation-modeled transmission loss that is azimuth dependent and computed along the various azimuths indicated by the red numbers in the plot. Such a transmission loss procedure is often referred to as  $N \times 2$ -D and does not include azimuthal coupling that would be contained in a full three-dimensional (massive) computation. Because we included the discrete source, it is very easy to see that the change in array bearing changes the structure of the MDL plots by shifting the ambiguities about the changing symmetry line of the array.

The MDL plots show that different orientations of the array provide different coverage. The color scale is to be interpreted to mean that a source radiating above the MDL would be detected according to the detection criterion used in the particular sonar equation as built into the assumptions of the detection threshold, see Sect. 10.2.2. For example, for an array heading of  $120^\circ$ , we predict that sources louder than about 130 dB at ranges of 20 km or less in the first quadrant ( $0 - 90^\circ$ ) would have a 50% probability of detection and a probability of false alarm of  $10^{-4}$ , whereas for an array heading of  $40^\circ$  the source would need to be 10 dB higher for the same detection.

Finally, we mention that the waveguide invariant, discussed in Chaps. 2, 3 and 5 can be applied to various sonar processing problems. Examples are given in [19, 20] for passive sonar and [21, 22] for active sonar.

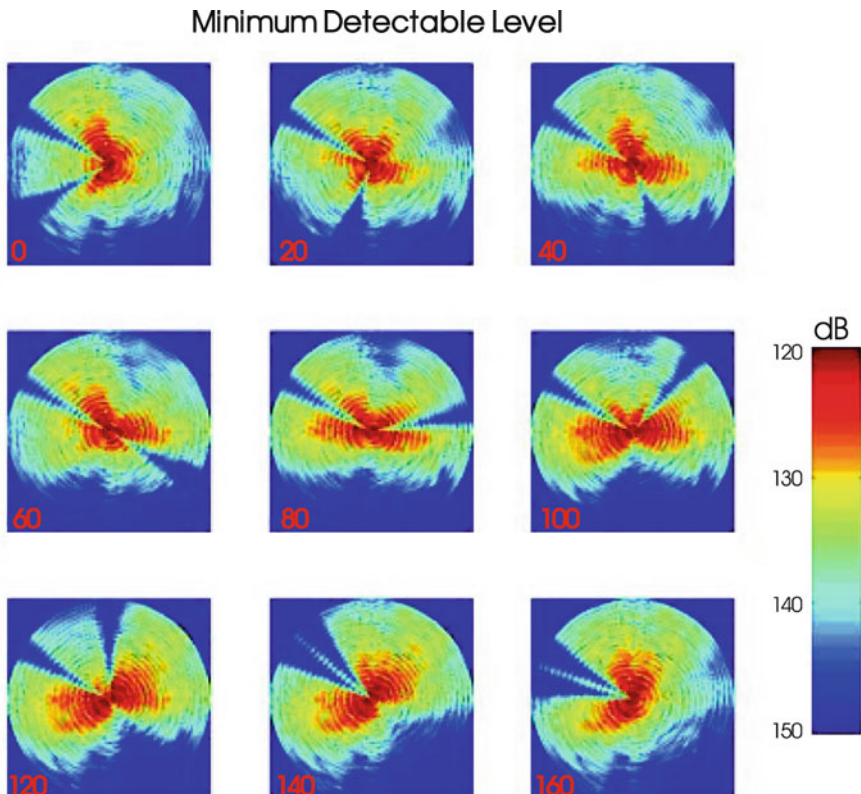


**Fig. 10.10** Minimum detectable level associate with the array scenario of Fig. 10.9 together with an azimuthal-dependent transmission loss calculated for a downward refracting Atlantic environment. Each plot is for a different array heading as indicated by the *red numbers*. The maximum range in these plots is 30 km

## 10.6 Matched-Field Processing

Matched-Field Processing (MFP), as introduced by Bucker [23] and Hinich [24] and further discussed by Fizell [25] and Baggeroer et al. [26], is the three-dimensional generalization of the conventional lower-dimensional, plane-wave beamformer. The one or two dimensions in the latter case are angles, and the matching is done to plane waves. Localization in this case refers to determining a direction. The generalized matched-field beamformer matches the measured field at the array with replicas of the expected field for all source locations. These replicas are derived by the propagation models discussed in earlier chapters. The unique spatial structure of the field permits localization in range, depth, and azimuth depending on the array geometry and the complexity of the ocean environment. The interference pattern of the acoustic field is a function of the source location, and this pattern can be

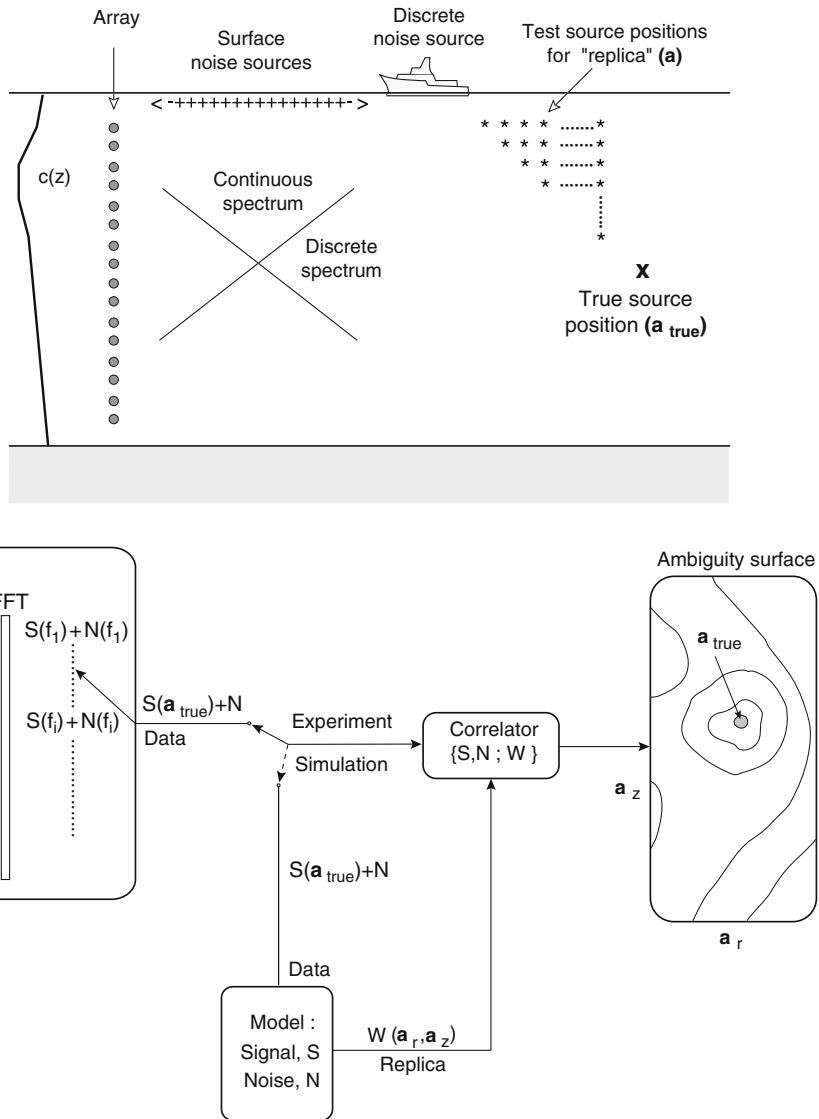


**Fig. 10.11** Matched-field processing: Schematic of the procedure and block diagram of the processor

matched. In terms of rays, we can say that the refractive properties of the waveguide generate a pattern of arrival angles that can also be matched. The process is shown schematically in Fig. 10.11. The process consists of systematically placing a test point source at each point of a search grid, computing the acoustic field (replicas) at all the elements of the array and then correlating this modeled field with the data from the real point source whose location is unknown. When the test point source is

co-located with the true point source, the correlation will be a maximum. A review of MFP algorithms with an extensive reference list is given both by Baggeroer and Kuperman [27], and by Tolstoy [28].

We now construct  $\mathbf{w}$  from one of the numerical solutions to the acoustic wave equation as discussed in the earlier chapters (see Sect. 10.7 for normalization details). It then represents a replica field at each element of the array for a specific ocean environment and for an arbitrary source location  $\mathbf{a}$ . Rather than just finding the direction of the source from the array, we can search for its actual location by matching the received data  $\mathbf{K}(\mathbf{a}_{\text{true}})$  from the true source location against solutions of the wave equation. The output of this matched-field processor, denoted  $B_{\text{Bart}}(\mathbf{a})$  to indicate the generalization beyond plane-wave beamforming, at each point in space  $\mathbf{a}$  is, in analogy to (10.21),

$$B_{\text{Bart}}(\mathbf{a}) = \mathbf{w}^\dagger(\mathbf{a}) \mathbf{K}(\mathbf{a}_{\text{true}}) \mathbf{w}(\mathbf{a}), \quad (10.58)$$

where the peak of the output of the beamformer  $B_{\text{Bart}}(\mathbf{a})$  is at  $\mathbf{a}_{\text{true}}$ .  $B_{\text{Bart}}(\mathbf{a})$  is also referred to as the *ambiguity function* (or surface) of the matched-field processor because it also contains ambiguous peaks which are analogous to the sidelobes of a conventional plane-wave beamformer. Sidelobe suppression can often be accomplished by using a nonlinear beamformer such as the Minimum Variance (MV) beamformer,

$$B_{\text{MV}}(\mathbf{a}) = [\mathbf{w}^\dagger(\mathbf{a}) \mathbf{K}^{-1}(\mathbf{a}_{\text{true}}) \mathbf{w}(\mathbf{a})]^{-1}. \quad (10.59)$$

The above beamformer was first derived for the plane-wave beamformer as discussed in Sect. 10.3.2, but now  $\mathbf{a}$  refers to angles or spatial coordinates (or any other unknown parameter of the problem to be estimated, e.g., bottom type). This beamformer gives the same peak-level output at the true source location as the Bartlett beamformer.

The final example we use here is the MCM beamformer [10]; the generalization of (10.40) is

$$B_{\text{MCM}}(\mathbf{a}) = \mathbf{c}^\dagger [\mathbf{W}^\dagger(\mathbf{a}) \mathbf{K}^{-1}(\mathbf{a}_{\text{true}}) \mathbf{W}(\mathbf{a})]^{-1} \mathbf{c}. \quad (10.60)$$

The usefulness of a tolerant beamformer becomes more evident in the matched-field case, since the unknown parameters are not restricted to the coordinates of the source. They can include any parameter in the problem, such as sound speed or bottom descriptors. Furthermore, we note that high-resolution procedures such as MV are high resolution in all of the parameters of the problem. Hence, extremely accurate knowledge of the environment is required to localize a source with a high-resolution processor. The analogy to broadening the beam in the plane-wave beamformer is opening up the spot size in the matched field processor. Opening up the spot size, in effect, averages the environment over that spot, lowering the high-resolution requirements for knowledge of the environment. The trade-off is reduced resolution for localization, but, as demonstrated in the plane-wave example, sidelobe suppression is still achieved. We will give an MCM matched-field example in the next section.

The above array processing methods are examples of a wide class of processors. This section is far from all-inclusive and the theory is far more advanced than the simple ideas presented here. For example, direct modal matching has been investigated by Yang [29], Wilson et al. [30], Shang [31], and Jesus [32]; extensive work has also been done by Porter et al. [33], Hamson and Heitmeyer [34], Gingras [35], Tolstoy [36], and Feuillade et al. [37] investigating the effect of mismatch on performance and resolution. Other investigations into tolerant beamforming is being carried out by Richardson and Nolte [38] and Krolik and Hodgkiss [39]; techniques are even under development to search for the location of a point source in an unknown environment by Collins and Kuperman [40], which bypasses the mismatch problem. Moreover, applications of new computational methods and concepts such as neural networks are beginning to appear, e.g., see Ozard et al. [41]. Though the details are different, the concept of matching array data to solutions or partial solutions of the wave equation still remains the central precept. Furthermore, it is important to note that the procedures discussed throughout this book take on the additional value of providing techniques for effecting actual signal processing through the generation of accurate replica fields obtained from the solution of the wave equation. For this reason, a specific example of a tolerant processor was presented to emphasize the new trend of integrating the physics of wave propagation with both the uncertainty of measurements and signal processing algorithms.

## 10.7 Simulating Matched-Field Processing

Simulating the replica fields is straightforward. However, we require appropriately normalized point-source solutions to the wave equation. In plane-wave beamforming, one normalization convention is to have unity as the beamformer response when the look direction corresponds to the true bearing. We adopt an MFP normalization that the weight vectors all have unit length, i.e.,

$$\mathbf{w}(\mathbf{a}) = \frac{\Phi(\mathbf{a})}{|\Phi(\mathbf{a})|}, \quad (10.61)$$

where  $\Phi(\mathbf{a})$  is the vector whose  $i$ th element is the solution to the ocean wave-guide wave equation, e.g., (2.60), at the field (hydrophone) position  $(\mathbf{r}, z) = (\mathbf{r}_i, z_i)$  for a source at  $\mathbf{a}$ . In this section we will present a series of examples to illustrate MFP and its relationship to environmental acoustic modeling. The examples will be for range-independent shallow and deep water, and we will consider both searches in depth–range space (vertical slices), range–range space (horizontal slices), and a fully three-dimensional case. We will also demonstrate environmentally tolerant MFP where we use the normalization

$$B_{MCM}(\mathbf{a}) = \frac{\mathbf{c}^\dagger [\mathbf{W}^\dagger(\mathbf{a}) \mathbf{K}^{-1}(\mathbf{a}_{true}) \mathbf{W}(\mathbf{a})]^{-1} \mathbf{c}}{\mathbf{c}^\dagger [\mathbf{W}^\dagger(\mathbf{a}) \mathbf{W}(\mathbf{a})]^{-1} \mathbf{c}}. \quad (10.62)$$

### 10.7.1 Depth–Range Matched Field Processing

In this section we present results of MFP which simulates depth–range localization. We use a range-independent environment for an illustrative example in this section, leaving the more complex environment for the next section which illustrates the procedure in complex 3-D geometries.

#### 10.7.1.1 Shallow-Water Simulation

We here use the spectral method (Chap. 4) to generate the replicas. The 100-m deep range-independent environment depicted in Fig. 10.12 shows a downward-refracting water column over a viscoelastic homogeneous bottom. We study the localization of a 100-Hz source with strengths of either 110 or 130 dB located at mid-depth and 10 km downrange from a 15-element vertical array. For the same environment, we construct a noise field of spectrum level 50 dB, corresponding to  $q$  in (9.40).

It is instructive to examine plane-wave beamforming first for just the noise as computed from (9.16) and then for the signal plus noise. Equations (10.21) and (10.31) are used to obtain the vertical directionality (negative angle is in the upward direction) which is shown in Fig. 10.13a. For the noise alone, we see a 10 dB notch in the horizontal which arises from a trade-off between the lossless direct paths from the overhead surface (continuous spectrum) with the slightly lossy long-distance contributions from a large surface area (discrete modes, none of which can correspond to  $0^\circ$  angle – see Fig. 2.20). Furthermore, we note the higher levels coming from the upward direction, caused by direct surface noise. Figure 10.13a also shows a 2–5 dB lower level of output of the noise for the MV processor compared to the Bartlett processor because of the coherence of the noise as explained in the MV derivation of Sect. 10.3.2.

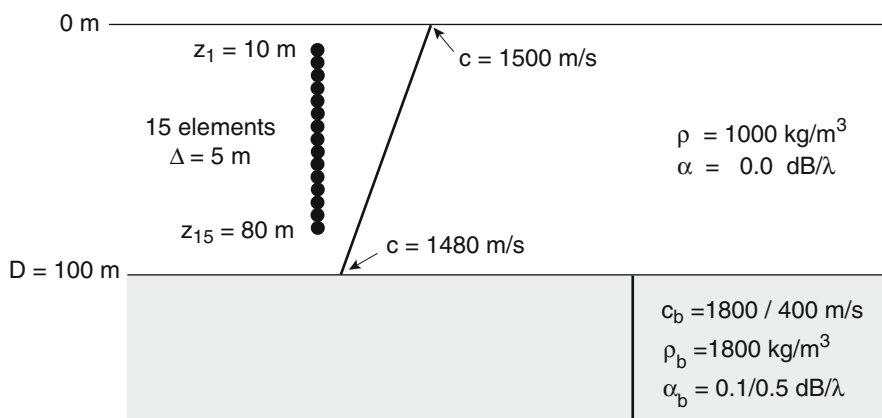


**Fig. 10.12** Environment and geometry for shallow-water example

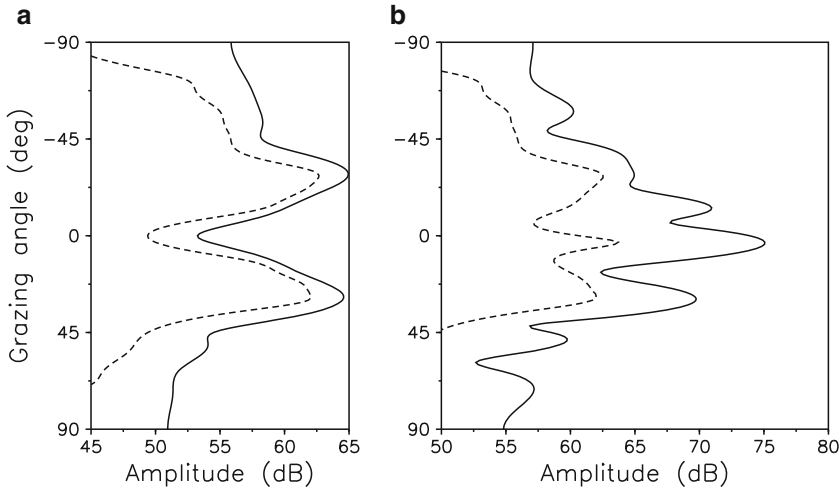


**Fig. 10.13** Vertical directionality from plane-wave beamforming. **(a)** Noise only, **(b)** Signal plus noise. *Solid line: Bartlett. Dashed line: MV*

On the other hand, the signal-plus-noise example in Fig. 10.13b shows poor MV performance relative to Bartlett. This occurs because the MV processor is matching with a plane-wave-type replica over the entire aperture of the vertical array, while the signal in the inhomogeneous waveguide is not composed of plane waves with constant amplitude over this aperture. Furthermore, for either plane-wave beamformer, it is evident that position localization cannot be obtained by plane-wave beamforming alone, in the vertical or otherwise. Hence, we see the motivation for MFP using replicas which are waveguide fields.

We now consider two cases separately, 110 and 130-dB sources in the Fig. 10.12 geometry, but now we use the waveguide solutions obtained from the wavenumber integration method (Chap. 4) for the replicas subject to the normalization of (10.61). The noise field is constructed such that there is a  $-10$  and  $+10$  dB SNR at an omni-directional hydrophone at the middle of the array for the 110 and 130-dB sources, respectively. Figures 10.14 and 10.15 show the Bartlett, MV, and MCM matched-field ambiguity-function results for these two sources. Figure 10.14 shows the 110-dB Bartlett case where the signal is buried in the noise; for this low source level, the MV shows a little more structure than the Bartlett because there is about a 2-dB rejection of correlated noise. In Fig. 10.15, the 130-dB source-level Bartlett result displays strong ambiguities competing with the true source position, whereas the MV processor suppresses the sidelobes and the source is unambiguously localized. We note here that the MV has a signal-to-noise threshold [26] above which its sidelobe suppression capabilities are activated, and below which it performs similarly to a Bartlett processor. The two source levels bracket this threshold. Though an ideal example, the basic features of MFP are apparent.

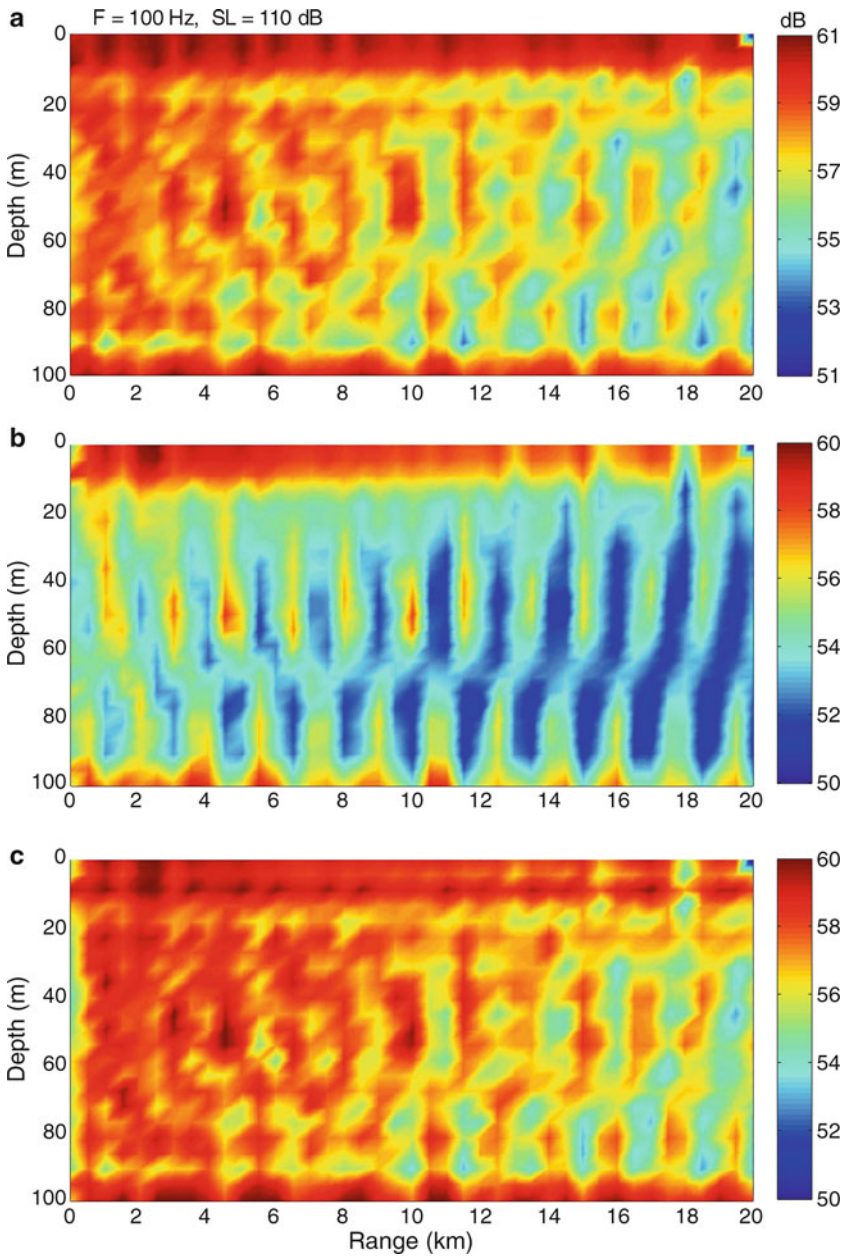


**Fig. 10.14** Shallow-water matched-field ambiguity surfaces for a 110-dB source placed at range 10 km and depth 50 m. (a) Bartlett, (b) MV, (c) MCM

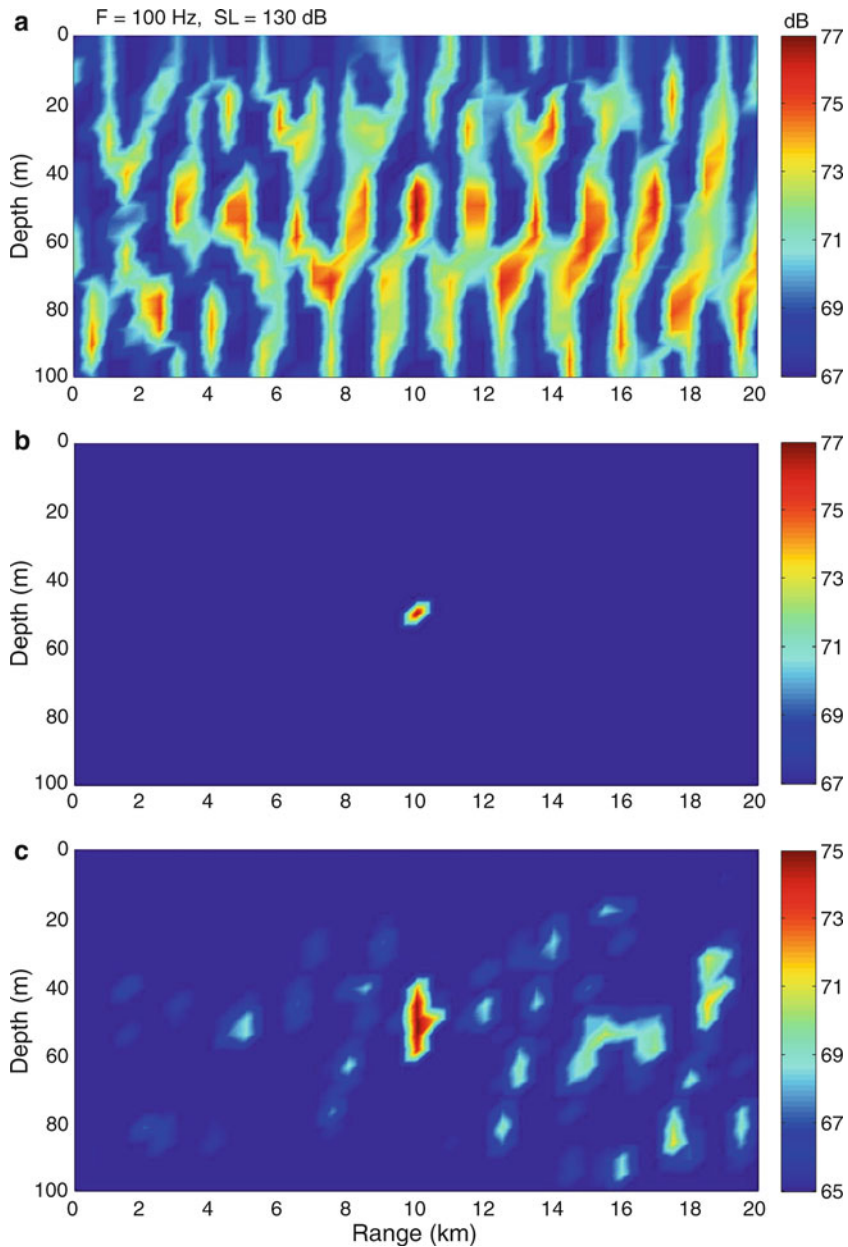


**Fig. 10.15** Shallow-water matched-field ambiguity surfaces for a 130-dB source ( $r_s = 10 \text{ km}$ ,  $z_s = 50 \text{ m}$ ). (a) Bartlett, (b) MV, (c) MCM

We also use this shallow-water example to illustrate the tolerant matched-field processor (MCM). Figures 10.14c and 10.15c show the results of applying the MCM processor to the above environment, with exact knowledge of the environment parameters. For the low SNR, Fig. 10.14c, the performance is similar to the Bartlett. This is because the SNR is below the threshold for the MV sidelobe suppression to function. On the other hand, Fig. 10.15c shows the sidelobe suppression with the associated increased spot size (decreased resolution).

Figure 10.16 shows a mismatch example for the high SNR case for all three processors. The mismatch is accomplished by changing the environment used for simulating the data; specifically we change the bottom sound speed value in the water column from 1480 to 1482 m/s. The low-resolution (robust) Bartlett beamformer shows some change, but is essentially as ambiguous as the perfect match case. However, the high resolution MV completely degrades. This indicates that the high resolution of the MV beamformer requires accurate data and is intolerant to even a slight environmental mismatch. The MCM, however, maintains its correct localization result. Opening up the spot window and lowering the local resolution also increases its tolerance for environmental mismatch but still maintains its sidelobe suppression capability. This property is particularly desirable because accurate information about the ocean environment is difficult to obtain.

It is also worthwhile illustrating some of the high-resolution aspects of MFP by examining a multiple source case. Figure 10.17 has two 130-dB sources, the second one being at a range of 10.1 km. Whereas the Bartlett processor shows a complex ambiguity structure with the sources not distinguishable, the MV processor easily resolves the two sources. For this separation, the tolerant MCM processor is barely adequate, but Fig. 10.18 shows that increasing the source separation to 1 km degrades its performance to an unacceptable level. This points immediately to a problem which is likely to occur when designing such an environmentally robust processor. In effect, the enlarged spot size makes field positions less distinct from each other and hence the increased ambiguity. This ambiguity is likely to show up a distance away from one of the sources and very often at a cycle distance (in the context of the ray-mode analogy).

### 10.7.1.2 Deep-Water Arctic Simulation

The problem discussed in this section adds complexity for the matched-field procedure. The general features of the Arctic environment have already been discussed in Chap. 1. The specific environment to be considered is shown in Fig. 10.19; the contour plot of propagation loss shows the partitioning of the acoustic field for a shallow 20-Hz source at 100-m depth into two dominant long-distant modes of propagation: surface duct and convergence zone propagation. This gives rise to significant acoustic spatial variability in both depth and range.

We use an equally-spaced, 18-element array spanning the water column from 30 to 960 m depth. Although the array spacing is approximately the  $\lambda/2$  standard

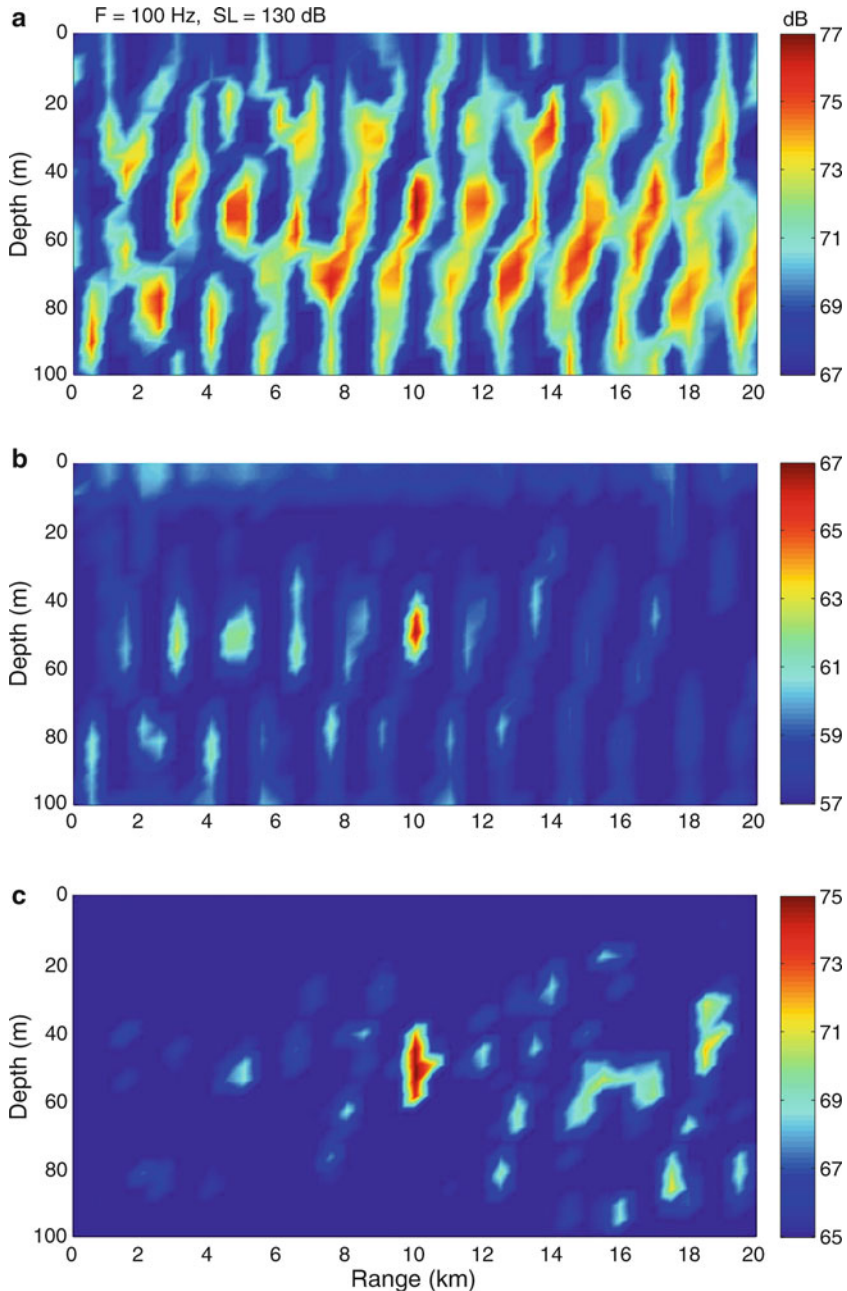


**Fig. 10.16** Shallow-water matched-field ambiguity surfaces for a 130-dB source ( $r_s = 10 \text{ km}$ ,  $z_s = 50 \text{ m}$ ) with a sound-speed mismatch of only 2 m/s at the bottom of the water column. (a) Bartlett, (b) MV, (c) MCM

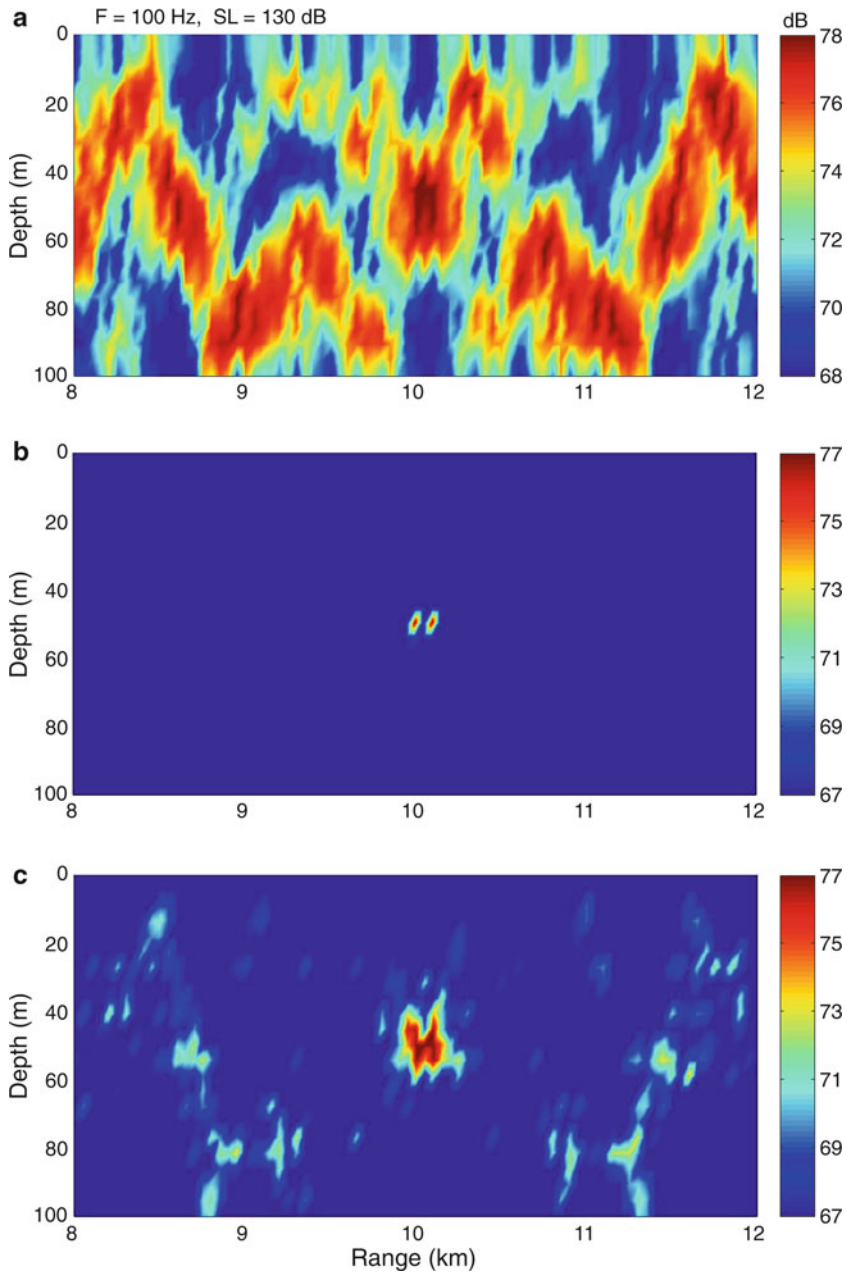


**Fig. 10.17** Matched-field ambiguity surfaces for two 130-dB sources placed 100 m apart ( $r_{s1} = 10.0 \text{ km}$ ,  $r_{s2} = 10.1 \text{ km}$ ,  $z_s = 50 \text{ m}$ ) and with no mismatch. (a) Bartlett, (b) MV, (c) MCM

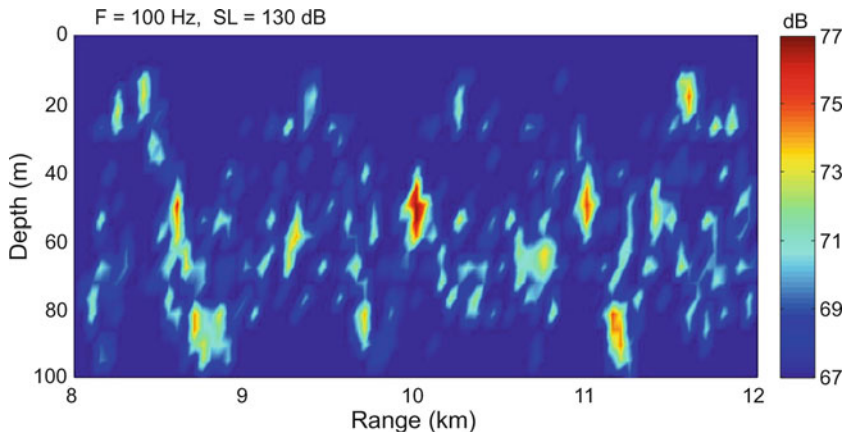


**Fig. 10.18** MCM matched-field ambiguity surface for two 130-dB sources separated by 1 km in range ( $r_{s1} = 10$  km,  $r_{s2} = 11$  km,  $z_s = 50$  m)

used for plane-wave beamforming, it is the vertical wavelength that is more relevant for a vertical array. Because the propagation channel strips high-angle energy, the sampling can be less dense, typically by a factor of four as compared to plane-wave beamforming.

The noise simulation is done with a surface-noise-source level of  $50 \text{ dB} - q$  in (9.40) – and therefore the signal-to-noise level varies with depth. The 180-dB source is located 250 km downrange and we can vary the effective SNR at the array by choosing two source depths. With Fig. 10.19 as a guide we use depths of 100 and 900 m, which result in average signal-to-noise levels at the array of +6 dB and –5 dB in and below the surface duct, respectively.

Figures 10.20 and 10.21 show the MV and MCM results for the shallow source with perfect match and a mismatch of 1 m/s at the sea surface. Figures 10.22 and 10.23 show the same sequence for the deep source but for a deep-gradient mismatch of 4%. For both the shallow and deep-source cases, the MV processors unambiguously locate the sources when the environment is perfectly known. However, their performance deteriorates significantly with a small realistic mismatch. Just as in the shallow-water example, the MCM (with larger spot size than MV) retains its localization and sidelobe suppression ability for the mismatch cases.

### 10.7.2 Three-Dimensional Matched Field Processing

As we increase the number of dimensions, visualization becomes an issue. Here we will present two cases. The first will be for a complex 3-D environment where we present the ambiguity function in a range/cross-range plane (2-D) at the depth of

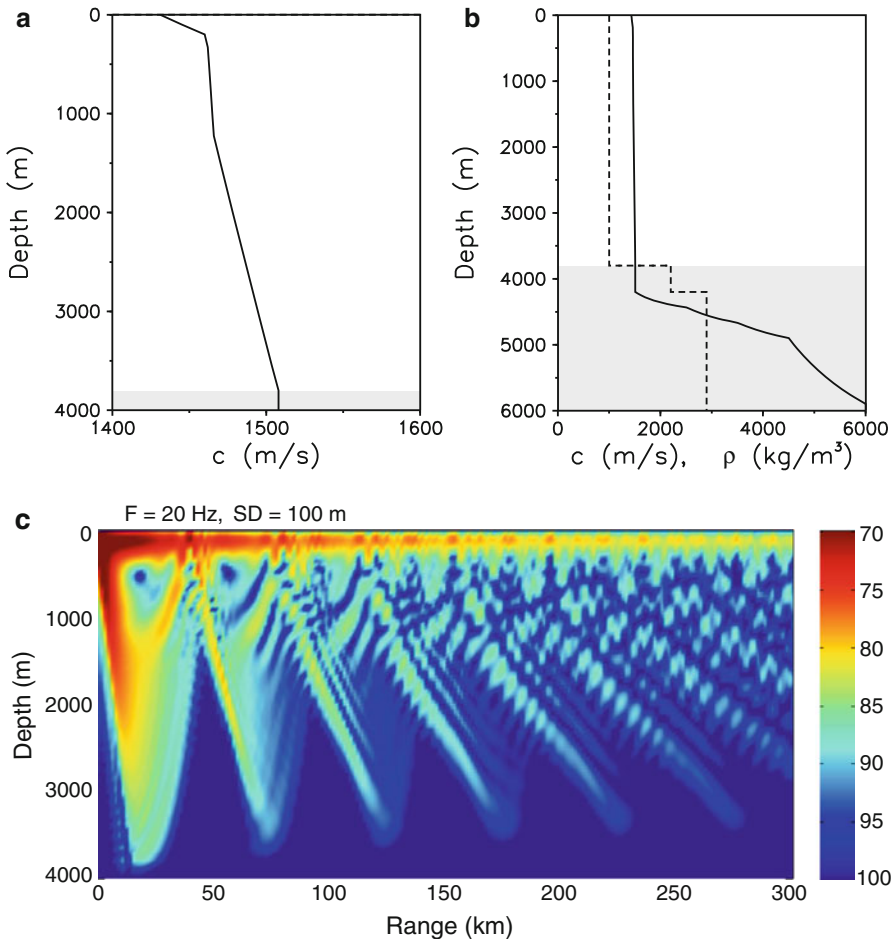


**Fig. 10.19** Arctic environment. (a) Sound-speed profile in the water column. (b) Sound speed (*solid line*) and density (*dashed line*) in the water column and bottom. (c) Depth–range contours of propagation loss for a 20-Hz source at 100-m depth

the localized source. The second example will be the more complex 3-D structure of the ambiguity function, but for a simpler horizontally stratified ocean.

#### 10.7.2.1 2-D Ambiguity Surface for 3-D Problem

Perkins and Kuperman [42] and Zala and Ozard [43] have shown that in three dimensions, the connection between environment and acoustics becomes more apparent. Here, we return to the Gulf-Stream environment discussed in Sects. 5.13.1 and 9.4.2, where simulations of propagation and noise were performed, respectively.

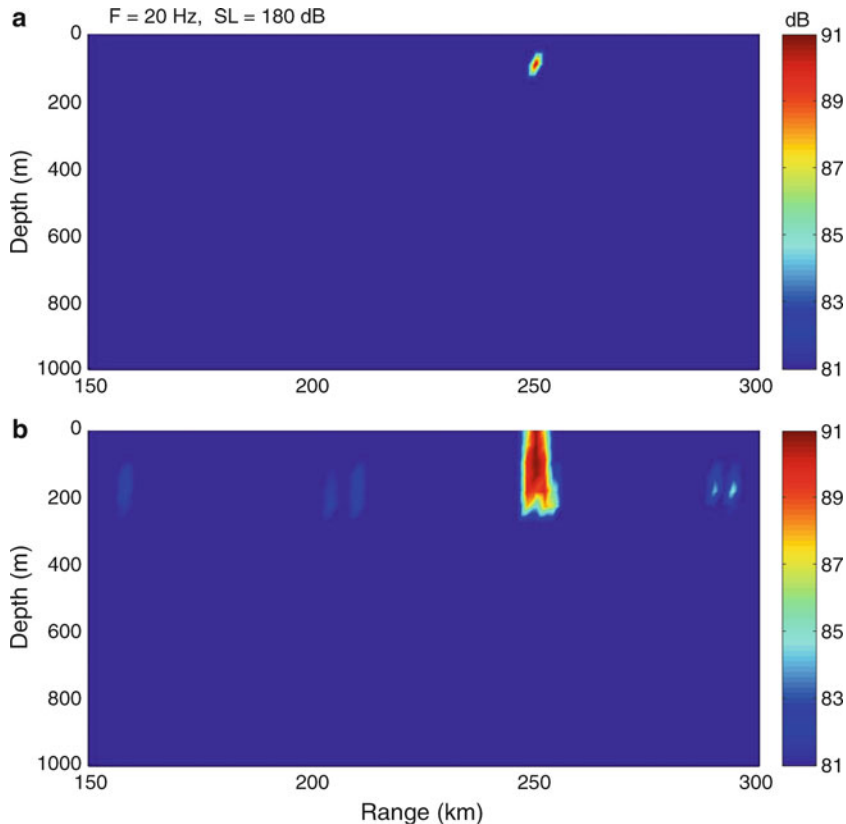


**Fig. 10.20** Arctic matched-field ambiguity surfaces for a 180-dB source placed at range 250 km and depth 100 m. (a) MV with perfect match, (b) MCM with perfect match

For this case, a vertical array at the position  $\mathbf{X}$  covering a depth extent of 100–1500 m is located in the center of an environment where both oceanography and bathymetry vary with position as shown in Fig. 10.24a. For the 10-Hz noise field on the 21-element array with 75-m element spacing, we use the simulated results in Sect. 9.4.2 constructed for an average SNR of 0 dB at each hydrophone. For the signal field, we use adiabatic mode theory as computed from the method of Sect. 5.13.1. The sound-speed profiles and the bathymetry along the line in Fig. 10.24a is given in Fig. 10.24b. We will perform the simulations [42] for source locations A and B in Fig. 10.24a, both at a depth of 100 m.

Figure 10.25 shows the Bartlett and MV ambiguity functions in the source plane for location A, which is to the southeast of the array in a benign environment. Both ambiguity functions identify the correct source location, however, with more ambiguities in the Bartlett result. These ring ambiguities result from the non-uniqueness of the environment in which the source is located. For example, in a totally range-independent environment, a source at any azimuth, but at the same range and depth

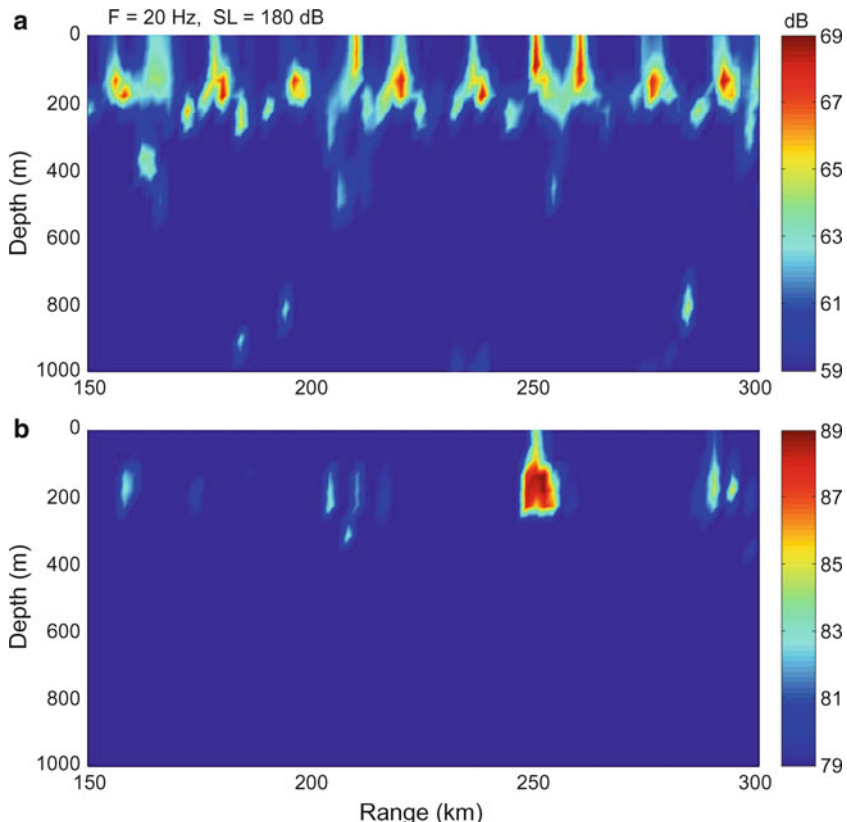


**Fig. 10.21** Arctic matched-field ambiguity surfaces for a 180-dB source ( $r_s = 250$  km,  $z_s = 100$  m). (a) MV with mismatch of 1 m/s at the sea surface, (b) MCM with same mismatch

as the true source, would propagate to the array exactly like the true source, and the ambiguities would be complete rings. The range ambiguities, as discussed earlier in Sect. 10.7.1, result from the similarity in structure of successive convergence zones.

The second location B is in a rather unique environment – a kink in the Gulf Stream. Figure 10.26 shows the Bartlett and MV results for this case. Here, the Bartlett processor shows an absolute minimum at the true source location with some weaker, though significant, ambiguities. The MV processor suppresses these side-lobes (ambiguities) for an unambiguous localization of the source.

This latter example shows that a complex 3-D environment, if known, can enhance MFP by providing more diversity in the acoustic structure across an array. Thus, we have shown that a vertical array can localize in azimuth as well as in range and depth. In effect, the environment provides horizontal aperture for a vertical array, a non-intuitive result when considering only plane-wave beamforming.

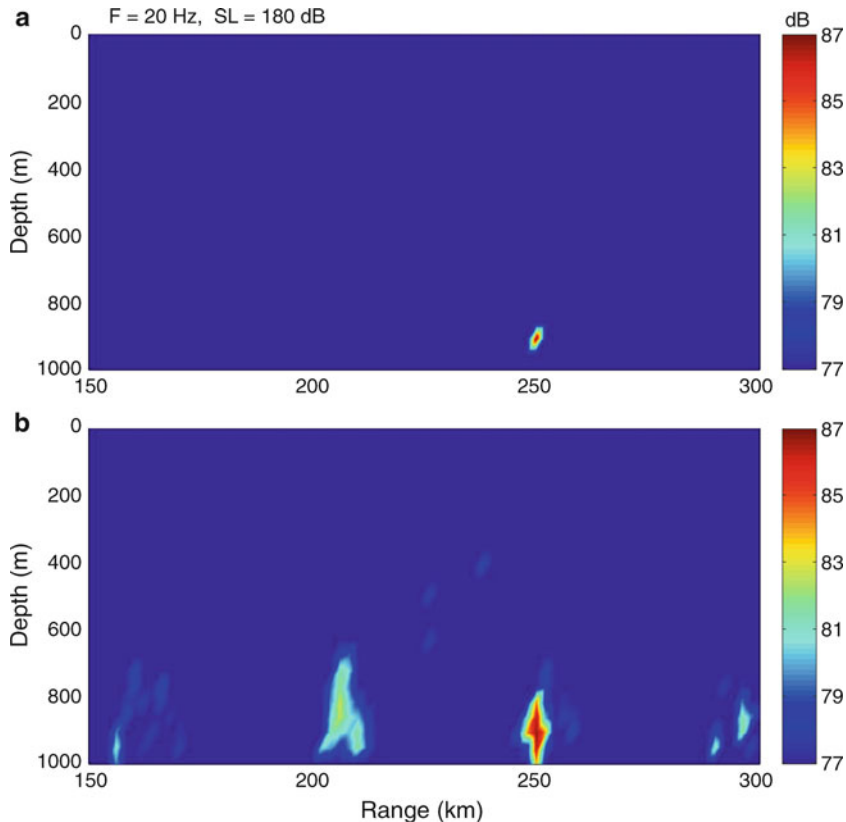


**Fig. 10.22** Arctic matched-field ambiguity surfaces for a 180-dB source placed at range 250 km and depth 900 m. (a) MV with perfect match, (b) MCM with perfect match

### 10.7.2.2 3-D Ambiguity Function

More complicated 3-D environments not only present a computational challenge, but also require more sophisticated search and display techniques. To illustrate this, we present a 3-D Bartlett ambiguity function which is now, in actuality an ambiguity volume. The internal structure of the volume is a function of the ocean-acoustic environment and the geometry of the array. The computations are performed using adiabatic mode theory for signal and noise for a 5000-m deep-water environment. For this example, we use a tripod array located at the center of the region with 48 elements on each leg; the apex of the tripod is 100 m below the ocean surface and the base of the tripod is at a depth of 2000 m (with a slant distance of about 6000 m).

The projection of the array onto the ocean surface is shown in Fig. 10.27a. For this simulation, archived position-dependent sound-speed profiles are used over a 5° square of the Atlantic Ocean. Figure 10.27 displays a set of four cubic ambiguity

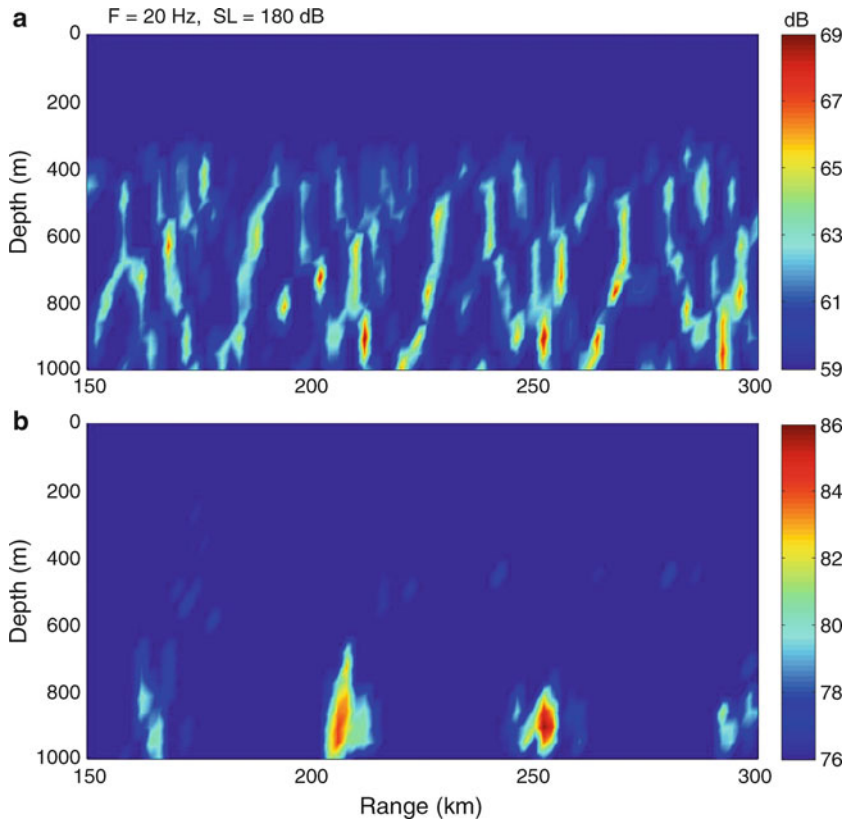


**Fig. 10.23** Arctic matched-field ambiguity surfaces for a 180-dB source ( $r_s = 250$  km,  $z_s = 900$  m). (a) MV with mismatch of 4% in the deep sound-speed gradient, (b) MCM with same mismatch

volumes. The circular rings are the ambiguities associated with the convergence zones. Since this graphic display is not transparent, we have to slice the various sides of the cube in an appropriate manner to search for the peak. The source, which is the absolute peak, is located at about 220 km from the center at a depth of 300 m as indicated by the arrow in the three sliced cubes, Figs. 10.27b, c, d. Figure 10.27a shows the outer sides of the ambiguity volume. In Fig. 10.27b, the upper face is the ambiguity surface at a depth of 300 m. Figures 10.27c, d show the ambiguity structure in the  $xz$  and  $yz$ -planes for  $y$  and  $x$  at the source range coordinates, respectively. The combination of the 3-D environment and 3-D aperture breaks most of the azimuthal symmetry, but we do see some residual tripod array ambiguities (or sidelobes) at about  $\pm 120^\circ$  about the radial to the localized source.

Clearly, full 3-D signal processing poses major challenges for future developments. Furthermore, the process redefines the meaning of environmental information. Earlier in the chapter, we discussed the concept of tolerant beamformers.

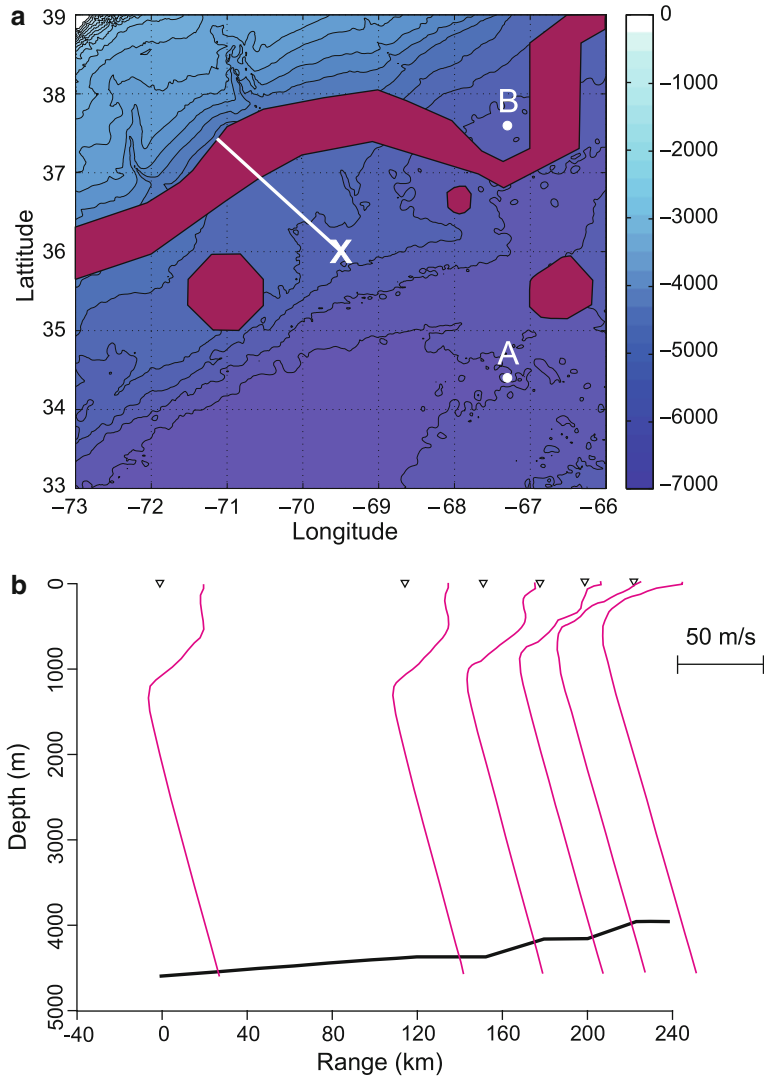


**Fig. 10.24** Gulf-Stream environment for matched-field simulations. (a) Bathymetry and position of the Gulf Stream; (b) Sound-speed profiles along line

The real 3-D ocean environment provides much more uncertainty than the 2-D examples given. Completely new approaches will be necessary to treat the problem of environmental uncertainty in a practical manner.

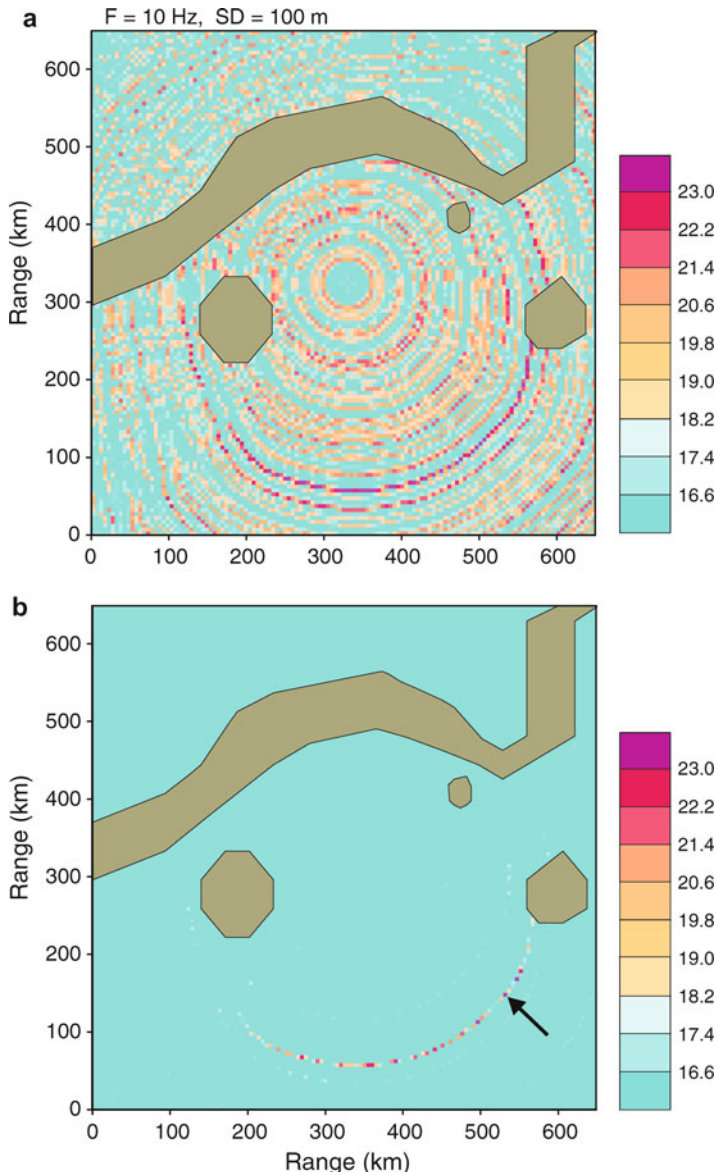


**Fig. 10.25** Ambiguity surfaces for source location A as indicated by the *arrow*. (a) Bartlett, (b) MV

### 10.7.2.3 Broadband Matched-Field Processing

Here, we have two choices: (a) Frequency-incoherent MFP [26]: Sum the MFP beamformer outputs at each frequency. This is incoherent frequency processing since the inter-frequency phases are not included in the processing.

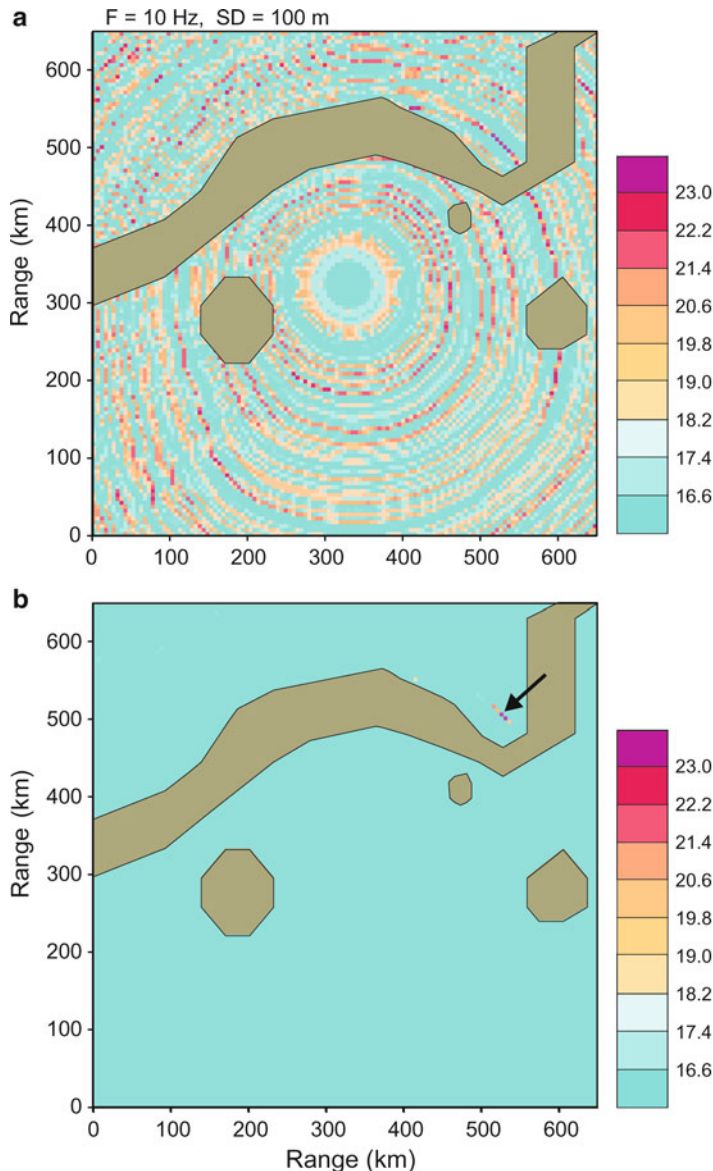


**Fig. 10.26** Ambiguity surfaces for source location B as indicated by the *arrow*. (a) Bartlett, (b) MV

(b) Frequency-coherent MFP: The source's phases between frequencies is typically random and certainly unknown. Therefore, one needs a processor that includes the different propagation phases but does not require the source phases as input. The literature includes a number of papers dealing with this issue [44–54].

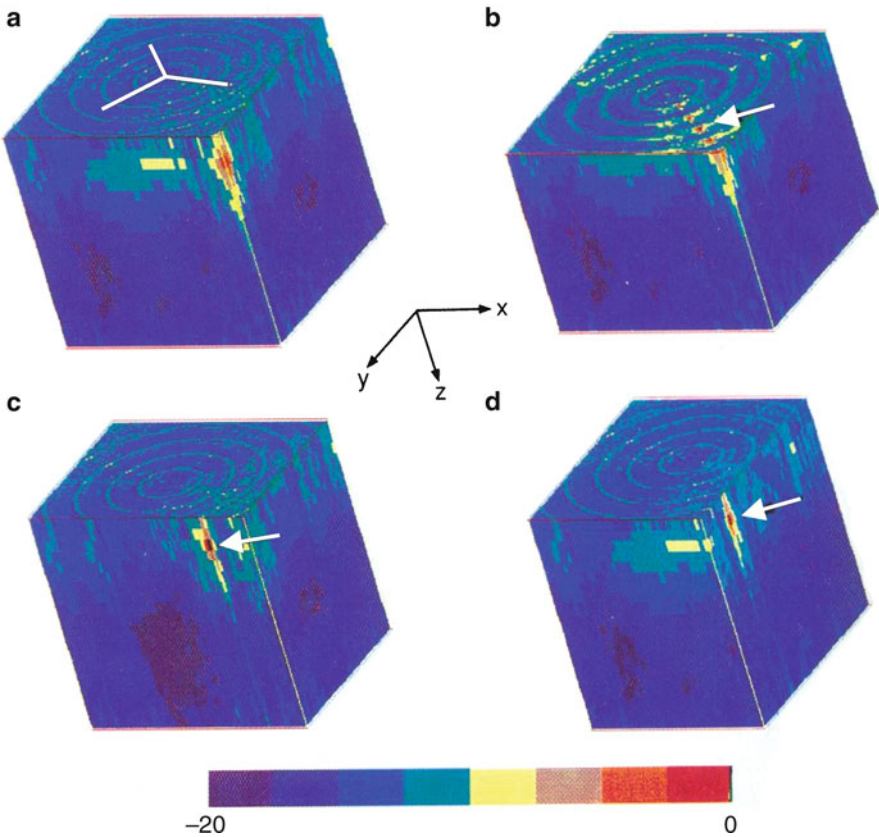


**Fig. 10.27** Bartlett ambiguity volume of dimensions  $300 \times 300 \times 2$  km. (a) Outer sides of volume; (b) Upper face sliced at source depth  $z_s$ ; (c) Front face sliced at source range  $y_s$ ; (d) Right-side face sliced at source range  $x_s$

## 10.8 Vector-Sensor Beamforming

A vector sensor, as mentioned in Sect. 1.3.1, typically refers to a combination of sensors that measure both vector properties of an acoustic field, such as particle velocity or acceleration, and the scalar pressure [55, 56]. These sensors can be applied to either plane-wave or matched-field scenarios. Without loss of generality, we will work in the frequency domain and only consider velocity and pressure in this section. There is extensive literature on vector-sensor signal processing, see for example [57–62] and the references therein.

Returning to (2.11) and writing it in its one-dimensional discrete form, we have, for example,

$$i\omega v_z(x, y, z) = \frac{1}{\rho_0} \frac{p(x, y, z + \Delta z) - p(x, y, z)}{\Delta z}. \quad (10.63)$$

Measuring the pressure gradient between two closely separated (with respect to wavelength) points is equivalent to a velocity measurement. Therefore, already we have that a velocity sensor can be considered as a very small two-element array with shading factors of 1 and  $-1$ , or in other words, a dipole receiver. In free space, we can take the velocity sensor to be located at the origin with no loss in generality; inserting a plane wave  $p$  with amplitude  $P$  for the pressures in (10.63) we have,

$$i\omega v_z = P \frac{e^{ik_z \Delta z} - 1}{\rho_0 \Delta z} e^{ik \cdot R} \approx \frac{ik_z}{\rho_0} P e^{ik \cdot R} \rightarrow v_z = \frac{\cos \phi}{\rho_0 c} P e^{ik \cdot R}, \quad (10.64)$$

where  $\phi$  is the angle between the propagation direction and the alignment of the velocity sensor. (In three dimensions, we would have  $\cos \phi_x, \cos \phi_y, \cos \phi_z$  be the direction cosines for the three velocity components.) Therefore, a velocity sensor has, in principle, a *frequency-independent* directivity as opposed to a pressure sensor which is omni-directional or a pair of pressure sensors spaced at larger distances, say  $\lambda/2$ , whose directivity is frequency dependent. A velocity sensor then has the advantage that as a small receiver, it can have significant angle discrimination, even at very low frequencies. Below, we examine the response of a vector sensor consisting of three orthogonal velocity sensors and a pressure sensor.

First we consider the signal. We can construct the beamformed output of this device in a similar vector/matrix notation as that in (10.20) and (10.21). In these equations, the pressure or modeled pressure (replica) at each array element vector are the elements of the vectors  $\mathbf{d}$  and  $\mathbf{w}$ , respectively. By analogy, each vector sensor output should be represented by a four-component vector. For a vector sensor, we can represent the modeled data given by (10.64) by the 4-element vector using polar coordinates,

$$\mathbf{d}_v = \begin{bmatrix} p \\ (\rho_0 c) v_x \\ (\rho_0 c) v_y \\ (\rho_0 c) v_z \end{bmatrix} = \begin{bmatrix} 1 \\ \sin \theta \cos \varphi \\ \sin \theta \sin \varphi \\ \cos \theta \end{bmatrix} P e^{ik \cdot R}, \quad (10.65)$$

where the  $\rho_0 c$  factors are (pre-weights) included to equalize the units of the vector entries, in this case to pressure. Therefore a simple choice for the normalized replica vector  $\mathbf{w}_v$  could be,

$$\mathbf{w}_v = \frac{1}{\sqrt{2}} \begin{bmatrix} 1 \\ \sin \theta \cos \varphi \\ \sin \theta \sin \varphi \\ \cos \theta \end{bmatrix} e^{ik \cdot R} \quad (10.66)$$

though there can be additional weighting factors for each of the vector entries to further specify additional beamforming options. The beamformed output of this vector sensor is then of the form

$$B_v(\theta, \varphi) = \mathbf{w}_v^\dagger (\mathbf{d}_v \mathbf{d}_v^\dagger) \mathbf{w}_v \equiv \mathbf{w}_v^\dagger \mathbf{K}_v \mathbf{w}_v. \quad (10.67)$$

We can, therefore, write out the sample covariance matrix of the signal which includes the snapshot averaging process as per (10.23),

$$\hat{\mathbf{K}}_{vs} = \rho_0 c \begin{bmatrix} \overline{|p|^2} & \overline{pv_x^*} & \overline{pv_y^*} & \overline{pv_z^*} \\ \overline{p^*v_x} & \rho_0 c \overline{|v_x|^2} & \overline{v_x v_y^*} & \overline{v_x v_z^*} \\ \overline{p^*v_y} & \overline{v_x^* v_y} & \rho_0 c \overline{|v_y|^2} & \overline{v_y v_z^*} \\ \overline{p^*v_z} & \overline{v_x^* v_z} & \overline{v_y^* v_z} & \rho_0 c \overline{|v_z|^2} \end{bmatrix}. \quad (10.68)$$

The first element of the diagonal is proportional to the potential energy (PE) density of the acoustic field while the other three entries are related to the kinetic energy (KE) density for motion in the  $x$ ,  $y$ , and  $z$ -directions (see Sect. 1.3.2). The sum of these last three entries is the total KE density so that the trace of the matrix is proportional to the total energy density and hence also to the total intensity of the plane wave. Therefore, when the array is steered in the direction of the plane-wave signal it will pick up twice its amplitude (we can rotate the coordinate system so the signal is along the  $z$ -axis so that the CSDM is a  $2 \times 2$  matrix with only  $x,z$ -entries and the replica is a 2-component vector) corresponding to a signal gain of 6 dB by direct calculation using (10.67).

The AG in isotropic noise is the DI. We must therefore determine the noise counterpart to (10.68),  $\hat{\mathbf{K}}_{vn}$ . This is straightforward for an isotropic noise field because all of the off-diagonal terms vanish (the mean velocity direction is zero as is the correlation between velocity components). This is equivalent to saying that the scalar and vector components add incoherently, i.e., intensities add rather than amplitudes. Since the  $x$ ,  $y$  and  $z$ -parts of the KE are separately equal to 1/3 of the KE in an isotropic noise field when the vector sensor is pointed in the signal direction, the summed output of the pressure and velocity sensors will be 4/3 the intensity. Then the DI as per (10.4) of a vector sensor in an isotropic noise field with Bartlett-like beamforming is

$$DI_{vs} = 6.0 - 10 \log(4/3) = 4.77 \text{ dB}. \quad (10.69)$$

However, there is also significant self noise [61] because ocean currents or flow noise couples into the vector fields. In this case, not only is noise added, but it is partially coherent with the velocity field producing motion-induced self noise that shows up as off-diagonal terms (that were assumed to vanish) in  $\hat{\mathbf{K}}_{vn}$ . Hence, the DI of a vector sensor is typically less than 4.77 dB. In particular, it is found that a self-noise to ocean-noise ratio of about 4.30 dB reduces the DI to zero, the same as an omni-directional pressure sensor. Since the flow noise tends to be greater at lower frequencies, an important part of vector sensor calibration is to determine some transitional frequency above which the vector sensor provides some decent gain.

For non-isotropic noise, one can build up a plane-wave representation using a density distribution function  $F(\theta, \varphi, \omega)$  of the scalar and vector fields [62]. Alternatively, one can model the correlation in the same way as presented in Chap. 9. In the latter case, we can then model the most general case of a signal and noise field in a waveguide; again, the noise field at one point would be of the form

$\Phi = [p \ v_x \ v_y \ v_z]^T$  where  $T$  is the transpose operation. The 4-vector noise field at the vector sensor, using (2.11) and (9.4) is,

$$\begin{aligned} \Phi(\mathbf{r}, z) &= [p \ v_x \ v_y \ v_z]^T \\ &= \int S(\mathbf{r}') \left[ g(\mathbf{r}, \mathbf{r}'; z, z') \ \frac{g_x(\mathbf{r}, \mathbf{r}'; z, z')}{i\omega\rho_0} \ \frac{g_y(\mathbf{r}, \mathbf{r}'; z, z')}{i\omega\rho_0} \ \frac{g_z(\mathbf{r}, \mathbf{r}'; z, z')}{i\omega\rho_0} \right]^T d^2\mathbf{r}', \end{aligned} \quad (10.70)$$

where we note that the surface source distribution  $S(\mathbf{r}')$  is not a function of the field coordinates  $(\mathbf{r}, z)$ ; the bracket denotes a vector and the subscripts on the waveguide Green's function  $g$  denote partial derivatives. The CSDM of the vector sensor is then a  $4 \times 4$  matrix,

$$\mathbf{C}_\omega(\mathbf{r}, z) = \Phi(\mathbf{r}, z) \Phi^\dagger(\mathbf{r}, z), \quad (10.71)$$

where we note this CSDM is at *one point* specifying all the correlations between four field quantities. One then follows the analogous mathematics of Sect. 9.2.

An array of  $N$  vector sensors would then be represented by a concatenation of the data and replica vectors resulting in vectors of length  $4N$  and a  $4N \times 4N$  dimensional CSDM,  $\mathbf{K}_{va}$ . Thus, for example, the data (the replica has the same form) for a two-element vector sensor array is an eight component vector,

$$\mathbf{d}(\mathbf{R}_1, \mathbf{R}_2) = [p(\mathbf{R}_1) \ v_x(\mathbf{R}_1) \ v_y(\mathbf{R}_1) \ v_z(\mathbf{R}_1) \ p(\mathbf{R}_2) \ v_x(\mathbf{R}_2) \ v_y(\mathbf{R}_2) \ v_z(\mathbf{R}_2)]^T, \quad (10.72)$$

where  $\mathbf{R}_i = (\mathbf{r}_i, z_i)$  are the locations of the two vector sensors. The CSDM for the two-element vector sensor array is just the usual  $\mathbf{K} = \mathbf{d}\mathbf{d}^\dagger$  as per (10.20). For modeling, where we assume signal-independent noise, we have from the discussion below (10.33) that the CSDM is the sum of signal and noise CSDM's,  $\mathbf{K}_{va} = \mathbf{K}_s + \mathbf{K}_n$ . The signal-only CSDM is  $\mathbf{K}_s = \mathbf{d}_s \mathbf{d}_s^\dagger$ , where  $\mathbf{d}_s$  is simply the signal-only form of (10.72). Similarly, the two-element vector sensor noise CSDM is, from (10.71), the outer product of the concatenation of the noise vectors at the two positions. Therefore, the total modeled CSDM of the two-element vector sensor array is given by,

$$\mathbf{K}_{va}(\mathbf{R}_1, \mathbf{R}_2) = \mathbf{d}(\mathbf{R}_1, \mathbf{R}_2) \mathbf{d}^\dagger(\mathbf{R}_1, \mathbf{R}_2) + [\Phi(\mathbf{R}_1) \ \Phi(\mathbf{R}_2)][\Phi(\mathbf{R}_1) \ \Phi(\mathbf{R}_2)]^\dagger, \quad (10.73)$$

where the individual entries of the noise matrix (second term) are again easily specified from Sect. 9.2. Clearly, (10.73) generalizes to an  $N$ -element vector sensor array. Therefore, using the vector sensor representation in this section, the various array processing methods presented earlier in this chapter, as well as in the literature [59, 61, 63], can be directly implemented. For simulating signal-plus-noise data, the methods of Sect. 10.9 are directly applicable.

The vector sensor also provides an opportunity to do directional intensity processing since intensity is related to the product of pressure and velocity [61, 64]. In this multiplicative, rather than additive processing, the first-order signal

processing quantities are contained in the vector intensity, which itself is a second-order acoustic quantity. Hence the correlations are fourth-order acoustic quantities. Of interest here is that the average vector intensity of an isotropic noise field is theoretically zero. However, one must also note, from Sect. 10.2.2.2, that system performance is ultimately measured through the probability of detection, which in turn is related to the *variance* of the noise and the signal plus noise–fourth-order quantities in this case. Optimal processors for weak signal detection are additive rather than multiplicative, but for localization with high SNR, intensity processing can be advantageous [61].

## 10.9 Synthetic Signals and Sensor Stimulation

Matched-field work based on field simulation generally uses covariance matrices directly computed from the physics-based models described earlier. Thus, at each angular frequency  $\omega$  the signal covariance matrix is derived from the complex field vector  $\mathbf{G}(\omega, \mathbf{r}, \mathbf{r}_s)$  over the array at receivers at coordinates  $\mathbf{r}$  for a source at position  $\mathbf{r}_s$ , by creating the outer product,

$$\mathbf{K}_S(\omega) = \mathbf{G}(\omega, \mathbf{r}, \mathbf{r}_s) \mathbf{G}^\dagger(\omega, \mathbf{r}, \mathbf{r}_s). \quad (10.74)$$

The contributions from the discrete noise sources  $\mathbf{K}_D$  are simulated using the same expressions, while a stochastic model for surface-generated noise, such as that of Kuperman and Ingénito [65], is used to directly compute the covariance matrix for the correlated surface-noise contribution. This approach is useful for addressing many of the issues associated with MFP, such as investigating parameter sensitivities, and comparing beamformer performance. However, it totally bypasses all the issues a real-world implementation has in terms of estimating the covariance matrix by ensemble averaging in an unsteady ocean. Thus, to properly investigate the performance of an end-to-end sonar processing system in simulation, it is necessary to create synthetic, element-level time series which as closely as possible represent what the array would be exposed to in the real ocean, including finite spatial and temporal correlation associated with the natural ocean variability. Such element-level simulation is often referred to as *Simulation and Stimulation*, SIM-STIM.

The central enabling methodology for data simulation is to generate a  $q$ -element random vector  $\mathbf{d}$  according to a probability-density function (PDF)

$$P_{\mathbf{d}} = \frac{e^{-\frac{1}{2} \mathbf{d}^\dagger \mathbf{K}^{-1} \mathbf{d}}}{\sqrt{(2\pi)^q \det \mathbf{K}}} , \quad (10.75)$$

where  $\mathbf{K}$  is a  $q \times q$  covariance matrix. The procedure is to transform to a space in which the covariance matrix is the identity matrix. The PDF then is a simple multi-dimensional Gaussian from which one can easily draw random number vectors. The inverse transformation on these vectors then produces a data vector according to the above PDF. Two such transformations corresponding to eigenvector and Cholesky decompositions are demonstrated below for simulating signal and noise data.

### 10.9.1 Stochastic Signal and Noise Model

The spatial and temporal variability results in finite correlation properties for noise as well as signal components. Further, due to the multi-scale nature of the variability, there is very limited cross-frequency correlation. In deep water, the early convergence-zone arrivals dominated by the stable, deep ocean have high cross-spectral coherence and appear as close replicas of the source signal in the time domain. In contrast, the later, ducted arrivals are controlled by the upper, variable parts of the ocean volume and therefore have very limited cross-spectral coherence properties. In shallow water, the entire field is exposed to spatial and temporal variability, and it is well-established that under such conditions, a robust signal model for MFP has to assume no cross-spectral correlation, which require phase and amplitude randomness across frequency. In addition, simulating the time-domain field over time periods which are comparable to or longer than the correlation times of the signal, finite phase stability has to be represented by a random process in time.

Thus, let  $b_\omega(\tau)$  be a time series of complex numbers drawn from a random process with temporal correlation function  $C(\omega, \tau_1, \tau_2)$ , then two effects are combined using the following model for the signal component at angular frequency  $\omega$  and “slow” time  $\tau$ ,

$$\mathbf{R}_\omega(\tau) = b_\omega(\tau) S_\omega \mathbf{G}_\omega(\mathbf{r}, \mathbf{r}_s) + \mathbf{n}_\omega(\mathbf{r}), \quad (10.76)$$

where

$S_\omega$  is the Fourier transform of a coherent source signal;

$\mathbf{G}_\omega(\mathbf{r}(\tau), \mathbf{r}_s(\tau))$  is a vector of Green’s functions at angular frequency  $\omega$  for the propagation to the receiver array, incorporating Doppler effects associated with the source and receiver dynamics, as described in Sect. 8.4;

$\mathbf{n}_\omega(\mathbf{r})$  is a stationary noise vector with spectral covariance matrix  $\mathbf{K}_N$ .

### 10.9.2 Snapshot Synthesis

The synthesis of the time series requires the Fourier synthesis of the frequency components in (10.76). Since the components in the signal model are dependent on “slow” time  $\tau$ , the synthesis must be performed in “windows” or *snapshots* of a duration short enough to ensure stationarity of (10.76). This, in general, requires the motion to be along straight lines within the snapshot. In addition, it is required that the snapshots be short compared to the correlation time for the acoustic environment, but also that the Doppler effects are adequately represented by the Green’s function.

To ensure a smooth transition between snapshots, it is recommended to use a consistent *overlap-and-add* procedure, for example overlapping  $2N$  Hanning-windowed snapshots of length  $T$  by 50%, as illustrated in Fig. 10.28, to create a resulting time series of length  $NT$ ,

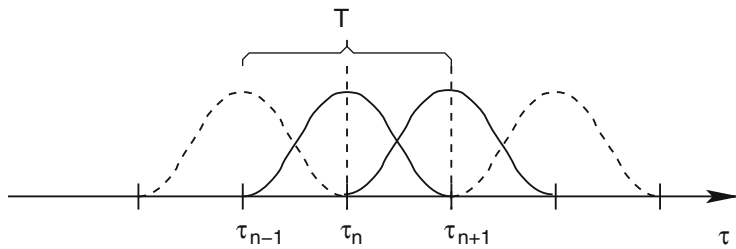


**Fig. 10.28** Snapshot time series generation using 50% overlapped Hanning-weighted snapshots of length  $T$

$$\mathbf{R}(t \in [\tau_n, \tau_{n+1}]) = w(t - \tau_n) \mathbf{R}_n(t - \tau_n) + w(t - \tau_{n+1}) \mathbf{R}_{n+1}(t - \tau_{n+1}), \quad n = 1, \dots, 2N, \quad (10.77)$$

where  $w(\tau)$  is a standard Hanning window of length  $T$ ,

$$w(\tau) = 0.5 [1 + \cos(2\pi\tau/T)] \quad (10.78)$$

and  $\mathbf{R}_n(\tau)$  is the time series snapshot of length  $T$ , centered at  $\tau_n = nT/2$ ,

$$\mathbf{R}_n(\tau) = \frac{1}{2\pi} \int_{-\infty}^{\infty} [e^{-i\omega\tau_n} \mathbf{R}_\omega(\tau_n)] e^{-i\omega\tau} d\omega. \quad (10.79)$$

The process now proceeds by the generation of the individual snapshot realizations associated with the stochastic signal model in (10.76), and the associated noise, which are then added and inserted into (10.77). It is here assumed that the window size  $T$  is chosen short enough for both the signal and the noise to be perfectly correlated temporally within each snapshot. We will for simplicity assume that the signal is perfectly correlated across the array, but with a finite temporal correlation function, while the noise is spatially correlated over the array, but uncorrelated temporally. Obviously, spatial decorrelation of the signal within a snapshot can be incorporated similarly to the generation of the noise signal.

### 10.9.3 Signal Variability

Assume we have to generate the random process  $b_\omega(\tau)$  representing the *slow* variability between the time snapshots, which is assumed to be a Gaussian random process with exponential temporal correlation,

$$C(\omega, \tau_1, \tau_2) = e^{-|\tau_1 - \tau_2|/T_C(\omega)}, \quad (10.80)$$

where  $T_C(\omega)$  is the coherence time for the field at frequency  $\omega$ .

This correlation function is next translated into a correlation matrix for the center times of the snapshots,  $\tau_m = mT/2, m = 1, \dots, 2N$ ,

$$\mathbf{C}_\omega = C_{mn}(\omega) = e^{-|\tau_m - \tau_n|/T_C(\omega)}. \quad (10.81)$$

Note that the correlation matrix  $\mathbf{C}_\omega$  is an  $M \times M$  matrix, with  $M$  being the number of snapshots, not to be confused with the spatial correlation matrix for the noise and signal, which are of dimension  $N$ , the number of elements in the array.

To generate realizations with this correlation, the Hermitian correlation matrix is factorized using Cholesky factorization as

$$\mathbf{C}_\omega = \mathbf{L}_\omega \mathbf{L}_\omega^\dagger, \quad (10.82)$$

where  $\mathbf{L}$  is a lower-triangular matrix. Now assume  $\mathbf{d}_\omega$  is a vector of independent, random complex numbers with Gaussian statistics and unit *rms*, then a realization of the random process is

$$b_\omega(\tau_m) = \sum_n L_{mn}(\omega) d_n(\omega). \quad (10.83)$$

A large number of these realizations satisfy the correct temporal correlation function,

$$\begin{aligned} \langle b_\omega(\tau_m) b_\omega^\dagger(\tau_n) \rangle &= \langle \mathbf{L}_\omega \mathbf{d}_\omega \mathbf{d}_\omega^\dagger \mathbf{L}_\omega^\dagger \rangle \\ &= \mathbf{L}_\omega \langle \mathbf{d}_\omega \mathbf{d}_\omega^\dagger \rangle \mathbf{L}_\omega^\dagger = \mathbf{L}_\omega \mathbf{L}_\omega^\dagger = \mathbf{C}_\omega. \end{aligned} \quad (10.84)$$

### 10.9.4 Noise Realizations

The generation of the noise snapshots takes as its starting point the noise covariance matrix composed of its white noise and correlated components,  $\mathbf{K}_N = \mathbf{K}_W + \mathbf{K}_C$ . One proceeds similarly to the generation of the signal phase described above. Thus, realizations of  $\mathbf{N}(\omega, \mathbf{a})$  consistent with the covariance matrix  $\mathbf{K}_N$  can again be obtained by taking the matrix “square root” through Cholesky factorization in (10.82) and multiplying a random-number vector to the lower-triangular matrix as in (10.83).

Alternatively, one can use *singular-value decomposition* (SVD) to generate the realizations. Thus SVD decomposes the full-rank, Hermitian covariance matrix into its eigenfunction basis,

$$\mathbf{K}_N(\omega) = \mathbf{V}_\omega \Lambda_\omega \mathbf{V}_\omega^\dagger, \quad (10.85)$$

where  $\Lambda_\omega$  is a diagonal matrix containing the positive eigenvalues at angular frequency  $\omega$  and  $\mathbf{V}_\omega$  is a matrix composed of the associated eigenvectors. Again, let  $\mathbf{d}_\omega$  be a vector of random complex numbers with *rms* unity, i.e.  $\langle \mathbf{d} \mathbf{d}_\omega^\dagger \rangle = \mathbf{I}$ , then the matrix product

$$\mathbf{N}_\omega = \mathbf{V}_\omega \Lambda_\omega^{\frac{1}{2}} \mathbf{d}_\omega, \quad (10.86)$$

where  $\Lambda_{\omega}^{\frac{1}{2}}$  is the diagonal matrix of the square root of the eigenvalues, represents a noise realization consistent with the covariance  $\mathbf{K}_N$ , because

$$\langle \mathbf{N}_{\omega} \mathbf{N}_{\omega}^{\dagger} \rangle = \mathbf{V}_{\omega} \Lambda_{\omega}^{\frac{1}{2}} \langle \mathbf{d}_{\omega} \mathbf{d}_{\omega}^{\dagger} \rangle \Lambda_{\omega}^{\frac{1}{2}\dagger} \mathbf{V}_{\omega}^{\dagger} = \mathbf{V}_{\omega} \Lambda_{\omega} \mathbf{V}_{\omega}^{\dagger} = \mathbf{K}_N . \quad (10.87)$$

## 10.10 Phase Conjugation and Time Reversal

Phase conjugation (PC) [66] and its time-domain analog referred to as a time-reversal mirror (TRM) is a process that was first demonstrated in nonlinear optics. In ultrasonics, the time reversal mirror was implemented first by Fink and co-workers [67, 68]. The mirror refers to an array of sources rather than point-to-point time reversal. In underwater acoustics aspects of PC have been explored theoretically in the 1990s by Jackson and Dowling [69–72]. Actually, the first ocean time reversal process demonstrating temporal focusing was performed earlier by Parvulescu and Clay [73, 74]. The full space–time focusing of a time reversal mirror in the ocean was subsequently demonstrated by Kuperman and co-workers [75–78] in various frequency regimes from 400 Hz to 15 kHz. PC and the TRM process are related to MFP in that a TRM, rather than using a replica, uses actual acoustic propagation from a source located at each element of the receiving array.

PC takes advantage of reciprocity which is a property of wave propagation in a static medium and is a consequence of the invariance of the linear, lossless wave equation to time reversal. In the frequency domain, time reversal corresponds to conjugation invariance of the Helmholtz equation. The property of reciprocity allows one to retransmit a time-reversed version of a multipath-dispersed probe pulse back to its origin, arriving there time-reversed, with the multipath structure having been undone [73, 74]. This process is equivalent to using the ocean as a matched filter since the probe pulse arrival has embedded in it the transfer function of the medium. This process can be extended further by receiving and retransmitting the probe signal with a source–receive array, i.e., a TRM. Depending on the spatial extent of the array, the above process results in significant spatial focusing of the signal at the originating position of the probe signal.

A time reversal mirror (TRM) can therefore be realized with a source–receiver array. Figure 10.29 illustrates the time-reversal process in a shallow-water environment. The incident signal from the probe source (PS) is received, time reversed and transmitted from sources contiguous with the receiving hydrophones. The time reversal can be accomplished in a straightforward way, e.g., by using the rewind output of an analog tape recorder or by a simple program that reverses a digitized segment of a received signal. Since the TRM transmits the last arrivals first and the first, last, etc., the arrival structure compresses to the time reverse of the original signal emitted by the probe source. This final focus has a larger extent than the original source for two reasons. First, a small source has a nearfield that cannot be sensed at distances greater than a few wavelengths. Second, attenuation as discussed in

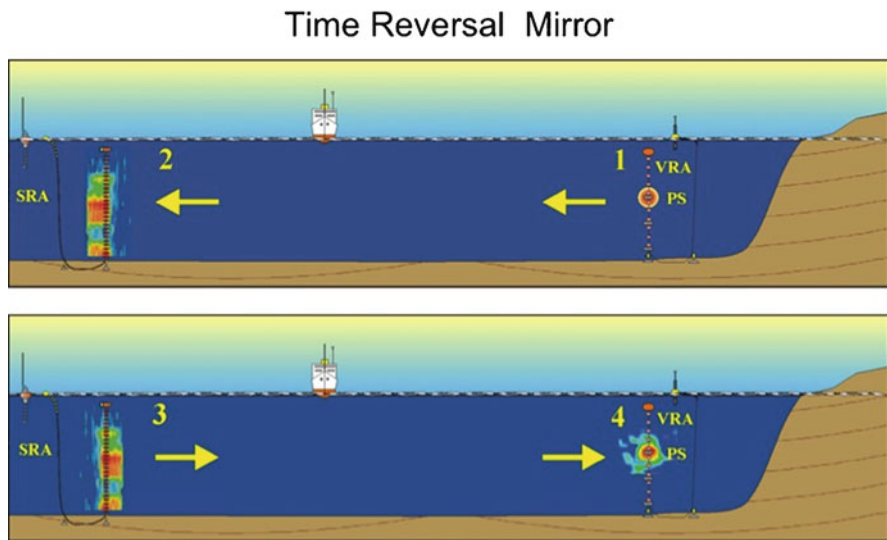


**Fig. 10.29** The time-reversal-mirror process. (1) A probe source (PS) at the same location of a vertical receive array (VRA) emits a pulse. (2) A source–receive array (SRA) receives the dispersed field. (3) The SRA time-reverses the field and retransmits the resultant time series at each element. (4) The time-reversed transmission focuses at PS and VRA, which was co-located with PS, and receives the same pulse, though time-reversed, that was originally transmitted

Chap. 5 typically eliminates the higher-order modes and it is, by simple arguments of Fourier synthesis, the vertical wavelength of the highest mode that determines the size of the focus back at the probe source.

PC, or the implementation of a TRM in the ocean, will be shown to be related to MFP [79], the latter requiring detailed knowledge of the environment. PC is an environmentally self-adaptive process which may therefore have significant applications to localization and communications in complicated ocean environments. Though the “effective” ocean environment must remain static over the turn-around time of the PC process, ocean variability on time scales shorter than this turn-around time might be compensated for with feedback algorithms. However, an understanding of relevant ocean time scales vis-à-vis the stability of the PC process will be required. In any event, the PC process can be thought of as one that demonstrates the capacity of an ocean channel to propagate multiple signals coherently; whether the analogous coherent gain can be achieved through signal processing alone is one of the challenges of passive-sonar signal-processing research.

### 10.10.1 Theory and Simulation for Phase Conjugation/TRM in the Ocean

The theory of PC vis-à-vis ocean acoustics is well-established. Here, we briefly review salient issues using the basic geometry of an ocean TRM experiment in the

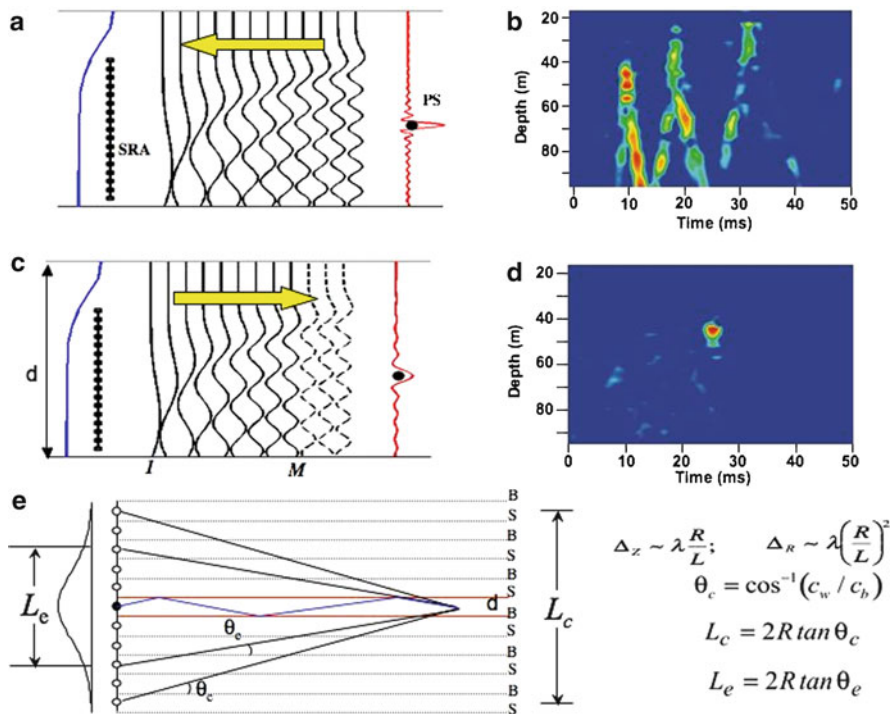


**Fig. 10.30** Modal and image interpretation of a time-reversal-mirror (TRM) process. (a) The harmonic (3.5 kHz) modal acoustic field from a probe source (PS) is received on a SRA. (b) The broadband (3–4 kHz) pulse arrival structure at the SRA. (c) The signal is time-reversed (equivalent to PC of each frequency component) at the SRA and retransmitted. Some of the higher modes are attenuated significantly. (d) The focused field at the range of the PS. (e) Image interpretation of the TRM

context of mode and image theory, see Fig. 10.30. In Fig. 10.30a, we show that a harmonic point source at PS emits an acoustic modal field that is received at the SRA, time-reversed and retransmitted back as in Fig. 10.30c. Figure 10.30b is the broadband case for the reception at the SRA showing the time-spread wavefronts. The time reversal process sends out the last arrivals first and the first arrivals last and Fig. 10.30d shows the recompressed signal at the probe source position. This focused signal is larger than the extent of the original source because of losses as indicated by the dashed lines in Fig. 10.30c. That is, since the focused field can be thought of as a synthesis of modes, the focus cannot be sharper than the smallest vertical modal wavelength which corresponds to the highest mode number. As discussed in Chap. 5, the higher modes tend to have higher attenuation.

Figure 10.30e shows the image interpretation of the TRM process. The real waveguide is contained within the red lines. An array on the left has a virtual aperture from image theory determined by the critical angle of the bottom reflection coefficient. The effective aperture will be slightly less because bottom attenuation tapers

the reflection coefficient with additional loss at higher grazing angles, which is consistent with the above-mentioned higher modal attenuation. The formulas given on the right are for range and depth Rayleigh resolution of an aperture of size  $L$ . This corresponds to the effective focal region.

### 10.10.1.1 Harmonic Point Source

For a unit harmonic source of angular frequency  $\omega$  located at  $(\mathbf{r}_{\text{PS}}, z_{\text{PS}})$ , the pressure field  $G_\omega(R; z_j, z_{\text{PS}})$  at the  $j$ th receiver element of the SRA from the point source (PS) in Fig. 10.29 is determined from (5.14),

$$G_\omega(r; z, z_{\text{PS}}) = \frac{i}{\rho(z_{\text{PS}})\sqrt{8\pi r}} e^{-i\pi/4} \sum_n \frac{\Psi_n(z_{\text{PS}})\Psi_n(z)}{\sqrt{k_n}} e^{ik_n r}. \quad (10.88)$$

The received field at the SRA at range  $R$  from PS with source–receive elements at depths  $z_j$ , is  $G_\omega(R; z_j, z_{\text{PS}})$ . The PC process consists of exciting the SRA sources by the complex conjugate of the received field  $G_\omega^*(R; z_j)$ . The resulting acoustic field transmitted from the  $J$  sources satisfies the wave equation,

$$\nabla^2 P_{\text{PC}}(r, z) + k^2(z) P_{\text{PC}}(r, z) = \sum_{j=1}^J \delta(z - z_j) G_\omega^*(R; z_j, z_{\text{PS}}), \quad (10.89)$$

where the range  $r$  is with respect to the SRA. Using Green’s function theory, the solution of (10.89) is the volume integral of the product of the Green’s function as specified by (10.88) and the source term of (10.89). For a vertical line of discrete sources, the integral reduces to a sum over the source positions,

$$P_{\text{PC}}(r, z; \omega) = \sum_{j=1}^J G_\omega(r; z, z_j) G_\omega^*(R; z_j, z_{\text{PS}}), \quad (10.90)$$

where  $R$  is the horizontal distance of the SRA from PS and  $r$  is the horizontal distance from the SRA to a field point. We can implement (10.90) with propagation models other than the normal-mode example we are using. For mildly range-dependent environments, we can use the adiabatic mode theory for  $G_\omega(r; z, z_j)$ . For more highly range-dependent environments the parabolic equation model is not only more appropriate, it is intuitively suitable in the sense that it uses a range-marching algorithm. Hence, it is a direct implementation of back propagation; the PC or TRM process is also referred to as retro-focusing.

Note that the magnitude squared of the *rhs* of (10.90) is the unnormalized (see (10.61)) ambiguity function of the matched-field processor of (10.58), where the data (see (10.20))  $d$  is given by  $G_\omega(R; z_j, z_{\text{PS}})$  and the unnormalized replica field by  $G_\omega(r; z, z_j)$ . In effect, the process of PC is an implementation of MFP where the

ocean itself is used to construct the replica field. Or, alternatively, MFP simulates the experimental implementation of PC in which a source–receive array is used.

To demonstrate that  $P_{\text{PC}}(r, z)$  focuses at the position of the probe source  $(R, z_{\text{PS}})$ , we simply substitute (10.88) into (10.90) which specifies that we sum over all modes and array sources,

$$P_{\text{PC}}(r, z; \omega) \approx \sum_m \sum_n \sum_j \frac{\Psi_m(z)\Psi_m(z_j)\Psi_n(z_j)\Psi_n(z_{\text{PS}})}{\rho(z_j)\rho(z_{\text{PS}})\sqrt{k_m k_n r R}} e^{i(k_m r - k_n R)}. \quad (10.91)$$

For an array which substantially spans the water column and adequately samples most of the modes, we may approximate the sum of sources as an integral and invoke orthonormality as specified by (5.5) and (5.6). Then, the sum over  $j$  selects out modes  $m = n$  and (10.91) becomes

$$P_{\text{PC}}(r, z; \omega) \approx \sum_m \frac{\Psi_m(z)\Psi_m(z_{\text{PS}})}{\rho(z_{\text{PS}})k_m\sqrt{rR}} e^{ik_m(r-R)}. \quad (10.92)$$

The individual terms change sign rapidly with mode number. However, for the field at PS, where  $r = R$ , the closure relation of (5.33) and (5.35), which together give  $\delta(z - z_{\text{PS}}) \approx \sum_m \rho^{-1}(z_{\text{PS}}) \Psi_m(z) \Psi_m(z_{\text{PS}})$ , can be applied assuming that the  $k_m$ 's are nearly constant over the interval of the contributing modes. We, here, use the symbol “ $\approx$ ” because we are neglecting the continuous mode spectrum. The result is that  $P_{\text{PC}}(R, z) \approx \delta(z - z_{\text{PS}})$ , which is totally consistent with Fig. 10.29. Notice that the focusing in the vertical is indicative of the closure property of the modes. As a matter of fact, for an SRA with substantially fewer elements, we see that the focusing still is relatively good.

### 10.10.1.2 Pulse Excitation

In the actual TRM experiments, pulses were used for the probe-source transmission. We therefore need to Fourier synthesize the above results. The  $j$ th element of the SRA receives the following time-domain signal given by Fourier synthesis,

$$P(R, z_j; t) = \int G_\omega(R; z_j, z_{\text{PS}}) S(\omega) e^{-i\omega t} d\omega, \quad (10.93)$$

where  $S(\omega)$  is the Fourier transform of the probe source pulse. This expression incorporates all waveguide effects, including time elongation due to multipath propagation. For convenience, take the time origin such that  $P(R, z_j; t) = 0$  outside the time interval  $(0, \tau)$ . Then, the time-reversed signal that will be used to excite the  $j$ th transmitting element of the SRA is  $P(R, z_j; T - t)$  such that  $T > 2\tau$ . This condition is imposed by causality; the signal has to be completely received before it can be time-reversed. Then,

$$\begin{aligned} P(R, z_j; T - t) &= \int G_\omega(R; z_j, z_{\text{PS}}) S(\omega) e^{-i\omega(T-t)} d\omega \\ &= \int [G_\omega^*(R; z_j, z_{\text{PS}}) e^{i\omega T} S^*(\omega)] e^{-i\omega t} d\omega, \end{aligned} \quad (10.94)$$

where the sign of the integration variable  $\omega$  has been reversed and the conjugate symmetry of the frequency-domain Green's function and probe pulse has been used. The quantity in brackets in (10.94) is the Fourier transform of the signal received by the  $j$ th SRA receiver element after time reversal and time delay. Hence we again notice the equivalence of time reversal and PC in their respective time and frequency domains.

Noting that the bracketed quantity in (10.94) is the frequency-domain representation of the signal retransmitted by the  $j$ th element of the SRA, Fourier synthesis can be used to obtain the time-domain representation of the field produced by the TRM. Using (10.90), we get

$$P_{\text{PC}}(r, z; t) = \sum_{j=1}^J \int G_\omega(r, z, z_j) G_\omega^*(R, z_j; z_{\text{PS}}) e^{i\omega T} S^*(\omega) e^{-i\omega t} d\omega. \quad (10.95)$$

This expression can be used to show that the TRM produces focusing in time as well as in space. Focusing in time occurs because a form of matched filtering occurs. To understand this, examine the TRM field at the focus point, i.e., take  $r = R$ ,  $z = z_{\text{PS}}$  in (10.95). Neglecting density gradients, reciprocity allows the interchange  $G_\omega(R, z_{\text{PS}}, z_j) = G_\omega(R, z_j, z_{\text{PS}})$ . Then the time-domain equivalent of (10.95) is

$$\begin{aligned} P_{\text{PC}}(r, z; t) &= \frac{1}{(2\pi)^2} \int \sum_{j=1}^J \left[ \int G_{t'+t''}(R, z_j, z_{\text{PS}}) G_{t'}(R, z_j, z_{\text{PS}}) dt' \right] \\ &\quad \times S(t'' - t + T) dt'', \end{aligned} \quad (10.96)$$

where the time-domain representations of the Green's function and probe pulse are used. Note that the Green's function is correlated with itself. This operation is matched filtering, with the filter matched to the impulse response for propagation from the probe source to the  $j$ th SRA element and results in focusing in the time domain; that is, it reduces the time elongation due to multipath propagation [73]. The sum over array elements is a form of spatial matched filtering, analogous to that employed in the matched-field processor. In addition, this sum further improves temporal focusing as the temporal sidelobes of the matched filters for each channel tend to average down which also is analogous to broadband MFP results [46]. Finally, note that the integral over  $t''$  in (10.96) is a convolution of each matched-filtered channel impulse response with the time-reversed and delayed probe pulse. As a consequence, this pulse is *not* matched-filtered, for example, a linear FM up-sweep will appear as a down-sweep at the focus and will not be compressed. Figure 10.30d illustrates the spatial focusing and the recompression to the original 2-ms, 3.5-kHz tone pulse from the 50-ms dispersed signal at the SRA.

### 10.10.1.3 Properties of the Focal Region: Modes and Images

The TRM focus is robust, provided the SRA adequately samples the field in the water column. First, the focus tends to depend primarily on the properties of the ocean near the focus and tends to be independent of (the possibly range-dependent) properties of the medium between the SRA and the focus. Temporal changes in the medium due to, for example, surface waves and internal waves degrade the focus, but this degradation will be tolerable if the average (or coherent) Green's function is not severely reduced by these time variations. Generally, the shape of the focus is approximated by the field that a point source placed at the focus generates after non-propagating modes are subtracted. Thus, if absorption or scattering tends to eliminate high-order modes, the focus will be comprised of the remaining lower-order modes and will be relatively broader. Very roughly, the vertical width of the focus will be equal to the water depth (or depth of the duct) divided by the number of contributing modes, if the sound speed (in the duct) is not strongly dependent upon depth.

One can also use image theory to very physically argue why there is such a high degree of spatial focusing in a waveguide vs. free space. These arguments are equally applicable to MFP. Thus, as shown in Fig. 10.30e, the Rayleigh focus for an array (or lens) in free space, say, transverse to propagation is  $\Delta_z \sim (R/L)\lambda$ ; that is, the focus is proportional to the size of the lens relative to wavelength and distance from the lens. In an ideal waveguide, using the image theory of Sect. 2.4.4, one immediately sees that the “virtual” aperture in a waveguide caused by images of the lens (could be sources and/or receivers) is infinite. After careful calculation, one obtains the diffraction limit of resolution in a waveguide to be proportional to the wavelength.

A more realistic image resolution discussion would be for a Pekeris waveguide which has a fluid bottom and attenuation. In that case, there is not just a critical angle limiting the size of the virtual aperture, the attenuating higher modes act as a kind of lens darkener for its outer rim creating a tapered effective aperture, as also depicted in Fig. 10.30e.

### 10.10.1.4 Non-Reciprocal Time Reversal and Passive Time Reversal

As discussed below (10.96), time reversal involves a spatial matched filter between forward and back-propagating fields. A consequence of this is that any non-reciprocal effect such as currents would degrade the TR process. However, it also suggests that once these Green's functions are obtained, a time reversal focus can be constructed by processing them as per (10.96). We can obtain all these in a procedure in which all Green's functions from one-way propagation between a source and receive array are measured and then invoke reciprocity in the processing thereby constructing a focus from one-way fields. Hence the term non-reciprocal time reversal [78] refers to the aspect of the procedure that does not, for example, involve traversing non-reciprocal currents in both directions. The main purpose of the

## Nonreciprocal Time Reversal

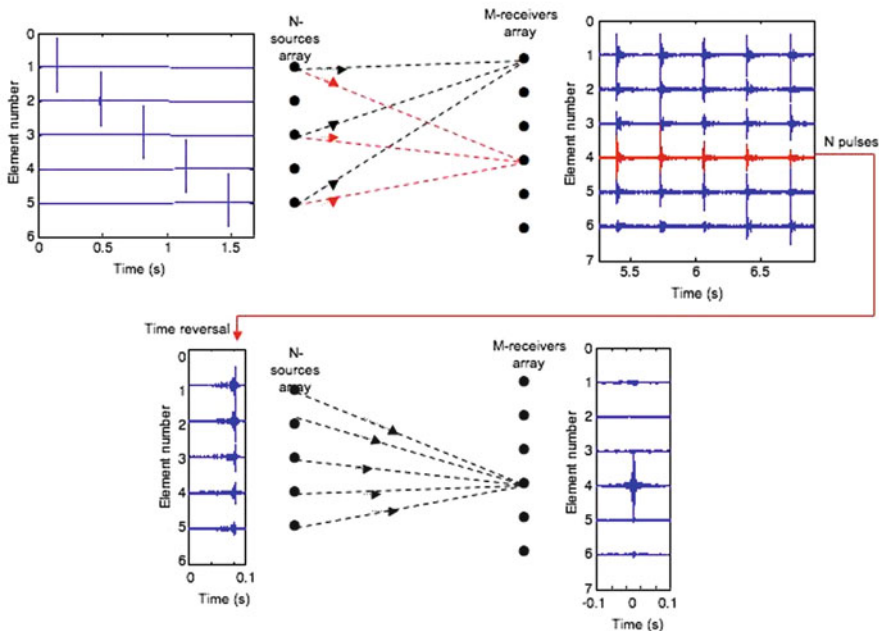


**Fig. 10.31** The non-reciprocal time reversal procedure starts by sequentially sending a pulse from each of the  $N$  sources in the transmit array shown in the upper left of the schematic

process described below is to simply and rapidly obtain data to study time reversal phenomena in the ocean, though it is also related to the more practical application referred to as passive time reversal.

A schematic of the non-reciprocal time reversal procedure is shown in Fig. 10.31. The transmitting array on the left sequentially sends out pulses, each of which are received at all the elements of the receive array on the right. The matrix of received pulses are transferred back to the transmitter. Then, for example, a set of time reversed pulses from one of the receive elements (the red sequence on the upper right) is transmitted from the left array thereby focusing at that particular receive element. Further, since the pulse to all the receive elements are measured, one does not even have to perform the above refocusing transmission; matched filtering the red sequence with each of the other receiver responses is equivalent to obtaining the field at these receiver positions, as shown in the lower right-hand corner of Fig. 10.31. This latter result can be obtained by either physically performing the transmission or implementing the above processing. The reason why the latter is a very helpful research procedure is that the stability of the focus can be measured by matched filtering a baseline red sequence with data received at a later time.

The “passive” version of PC or time reversal [80] is related to the latter non-reciprocal procedure. Even though it is described as passive, it does use a source,

though not as a probe source. The process is particularly useful to undersea communication. A single source sends a signal to a receive array. The signal consists of two separable components. The first is a short channel probe which, when received, approximates the impulse response of the medium. The second part can be another more complicated signal (e.g., a communications sequence) within the same bandwidth. Upon reception, the second component on each receive array element is matched-filtered with the first component. The output of each channel is then summed. The output is the same as the time reversal as if the second component was transmitted by the probe source and time reversed back to its location. Hence, in the passive, one-way case, the second signal is eventually received undistorted by the waveguide. For the purpose of communications, these procedures can be combined with other communication processing methods [81–84].

#### 10.10.1.5 Variable Range Focusing

A signal processing algorithm [76] has been developed to shift the focus of the TRM by as much as 10%. The focal shift is based on invariant theory (see Sects. 2.4.6 and 5.14). First consider that a time-reversal focus is simply a constructive interference maximum and then recall that the invariant formulation arises from determining the trajectory of interference maxima of intensity in the frequency–range plane. Setting  $r = R$  in (10.90) results in an intensity-like quantity in which the invariant formula of (2.215) is directly applicable; we can therefore rewrite it as

$$\frac{f_{\text{shift}}}{f_c} \approx \beta \frac{R_{\text{shift}}}{R_{\text{focus}}}. \quad (10.97)$$

This formula states that one can shift the focus from its original range of  $R_{\text{focus}}$  a distance  $R_{\text{shift}}$  by frequency shifting the pulse from the SRA whose original central frequency was  $f_c$  by an amount  $f_{\text{shift}}$ . Up or down frequency shifts cause range shifts in the opposite directions, accordingly. Depth shifting is more complicated because it appears to require specific knowledge of the environment and a subsequent modal calculation to redistribute the modes. Such a process is unattractive in the context of the self-adaptive nature of PC.

#### 10.10.1.6 Adaptive Phase Conjugation

We can combine some of the adaptive processing discussed earlier in this chapter with phase conjugation – particularly for the purpose of nulling. For the latter, we need to know the impulse response to the nulling locations. In practice this can be accomplished by having probe sources at these desired positions and nulling this particular data from the total data at the SRA [85].

### 10.10.1.7 Sourceless Time Reversal

In astronomy, there is a field known as adaptive optics. One of the processes used in adaptive optics is to shine a laser beam into the atmosphere creating a guide star or surrogate source caused by backscatter from sodium atoms. The light from the guide star is received on a mirror which is mechanically adjusted so as to bring the guide star into focus. At that point, the mirror is now focused such that it is correcting for distortion from atmospheric conditions between itself and the sodium source. By aiming the mirror in the direction of the guide stars, it essentially sees through the distorting medium. The concept of the guide star in underwater acoustics has been discussed in the literature somewhat in the context of MFP where a source is deliberately placed at a location in order to localize in the vicinity eliminating the requirement for computing replica fields along the total path between the receiver and source to be localized [86, 87]. More analogous to astronomical adaptive optics is to use a window of a boundary reverberation field to refocus at the boundary [88]. An alternative is to null the reverberation at a particular range cell since it is unwanted interference [89].

## 10.11 Summary

Signal and array processing can be simulated at different levels of complexity. The simplest level is to treat signals as plane waves in an unbounded homogeneous medium either without noise or in white noise. The next levels of complexity still involve simple plane-wave processors, with the acoustic signal levels arrived at by using more sophisticated propagation models and the complexity of the noise increased to isotropic. Adaptive beamforming in many cases enhances the performance of such processors. The highest level of complexity in processing discussed in this chapter involves utilizing the ocean acoustic environment in the processing. The performance of such matched-field processors, particularly the adaptive beamformers, is very much a function of signal-to-noise level and the relative structure of the signal and noise fields, the latter contributing to ambiguities in marginal cases (which are always the most challenging). Hence, the importance of accurate modeling for simulation as well as the choice of signal processing scheme is clear. However, we have also shown that there are limits to the processors' ability to localize when there is a realistic uncertainty in our knowledge of the environment. Addressing this latter important issue is a task best suited for researchers well-versed in both computational ocean acoustics and signal processing.

## Problems

- 10.1.** Assume you are using a long horizontal array for passively detecting a sound source in the ocean. The array characteristics are as follows: To estimate the source

Length:	4050 m
Element spacing:	75 m
Number of elements:	55

bearing in deep water it is often a good approximation to perform the beamforming assuming the source and the array are at equal depth in an infinite, homogeneous medium with the sound speed equal to the one existing at the array depth (assume 1500 m/s).

- a. Under such conditions write a linear beamformer algorithm for estimating source bearing, and use it to compute the beamformer response to a 10-Hz point source at bearing  $45^\circ$  off broadside, at a range of 80 km from the center of the array.
- b. Discuss the features of the beamformer response.
- c. Compute the corresponding beamformer response at 30 Hz, and discuss the result.

**10.2.** Assume you have to use the array from the previous problem in an isovelocity (1500 m/s), shallow water environment with water depth 120 m, and with an infinitely rigid bottom. Assume you are towing the array at 60-m depth, and that the source is at 60-m depth as well.

- a. For a 10-Hz source at  $45^\circ$  bearing, and 80-km range, write an algorithm for computing the field on the elements of the array in terms of a modal expansion.
- b. Use the linear beamformer developed for problem 10.1 to compute the response.
- c. Discuss the features of the beamformer response and provide a physical explanation for the performance.
- d. How do you suggest to modify the beamformer to yield a correct bearing estimate?
- e. Implement the modification and discuss the performance.

**10.3.** From problem 9.3 we learned that directionality is related to the Fourier transform of the cross-spectral density. In this chapter, we note that plane-wave beamforming is a finite spatial Fourier transform of the acoustic field with sensor spacing being one of the conjugate Fourier variable. Using a vertical array, beamform on a range-independent shallow water noise field with sufficient resolution to show that there is a “horizontal notch.” Physically, why must such a notch exist?

**10.4.** For an acoustic field in a waveguide, how would you take advantage of the orthogonality of normal modes to construct a modal, rather than plane-wave beamformer? Use a vertical array.

**10.5.** Write down an expression in terms of discrete normal modes for the field of a point source received on a vertical array. Take the complex conjugate of this result and use the result to represent a distribution of point sources. With this source distribution and the known Green’s function of this problem, propagate the resulting field outward. (With this range-independent geometry, outward is the same as “backward.”)

- a. What happens at the position of the original point source?
- b. How does the vertical array geometry affect the results?
- c. This method is called backpropagation. Is there a difference between this method and Bartlett matched field processing?

## References

1. R.J. Urick, *Principles of Underwater Sound*, 3rd edn. (McGraw-Hill, New York, 1983)
2. H.G. Urban, *Handbook of Underwater Acoustic Engineering* (STN ATLAS Elektronik GmbH, Bremen, 2002)
3. X. Lurton, *An Introduction to Underwater Acoustics*, 2nd edn. (Springer-Praxis, Chichester, 2010)
4. M.A. Ainslie, *Principles of Sonar Performance Modelling* (Springer-Praxis, Chichester, 2010)
5. A.B. Baggeroer, Sonar signal processing. in *Applications of Digital Signal Processing*, ed. by A.V. Oppenheim (Prentice-Hall, Englewood Cliffs, NJ, 1978)
6. D.H. Johnson, The application of spectral estimation methods to bearing estimation problems. Proc. IEEE **70**, 1018–1028 (1982)
7. B. Widrow, S.D. Stearns, *Adaptive Signal Processing* (Prentice-Hall, Englewood Cliffs, NJ, 1985)
8. L. Marple, *Digital Spectral Analysis* (Prentice-Hall, Englewood Cliffs, NJ, 1987)
9. R.O. Schmidt, Multiple emitter location and signal parameter estimation. IEEE Trans. Antennas Propagat. **34**, 276–280 (1986)
10. H. Schmidt, A.B. Baggeroer, W.A. Kuperman, E.K. Sheer, Environmentally tolerant beamforming for high-resolution matched field processing: Deterministic mismatch. J. Acoust. Soc. Am. **88**, 1851–1862 (1990)
11. H. Cox, R.M. Zeskind, M.M. Owen, Robust adaptive beamforming. IEEE Trans. Acoust. Speech Signal Process. **35**, 1365–1376 (1987)
12. M.A. Dzieciuch, P.F. Worcester, W. Munk, Turning point filters: Analysis of sound propagation on a gyre-scale. J. Acoust. Soc. Am. **110**, 135–149 (2001)
13. M. Siderius, C.H. Harrison, M.B. Porter, A passive fathometer technique for imaging seabed layering using ambient noise. J. Acoust. Soc. Am. **120**, 1315–1323 (2006)
14. C.H. Harrison, M. Siderius, Bottom profiling by correlating beamsteered noise sequences. J. Acoust. Soc. Am. **123**, 1282–1296 (2008)
15. P. Gerstoft, W.S. Hodgkiss, M. Siderius, C.-F. Huang, C.H. Harrison, Passive fathometer processing. J. Acoust. Soc. Am. **123**, 1297–1305 (2008)
16. C.H. Harrison, Anomalous signed passive fathometer impulse response when using adaptive beam forming. J. Acoust. Soc. Am. **125**, 3511–3513 (2009)
17. J. Traer, P. Gerstoft, H.C. Song, W.S. Hodgkiss, On the sign of the adaptive passive fathometer impulse response. J. Acoust. Soc. Am. **126**, 1657–1658 (2009)
18. W.M. Carey, R.A. Wagstaff, Low-frequency noise fields. J. Acoust. Soc. Am. **80**, 1523–1526 (1986)
19. S. Lee, N.C. Makris, The array invariant. J. Acoust. Soc. Am. **119**, 336–351 (2006)
20. K.L. Cockrell, H. Schmidt, Robust passive range estimation using the waveguide invariant. J. Acoust. Soc. Am. **127**, 2780–2789 (2010)
21. R. Goldhahn, G. Hickman, J.L. Krolik, Waveguide invariant broadband target detection and reverberation estimation. J. Acoust. Soc. Am. **124**, 2841–2851 (2008)
22. J.E. Quijano, L.M. Zurk, D. Rouseff, Demonstration of the invariance principle for active sonar. J. Acoust. Soc. Am. **123**, 1329–1337 (2008)
23. H.P. Bucker, Use of calculated sound fields and matched field detection to locate sound sources in shallow water. J. Acoust. Soc. Am. **59**, 368–373 (1976)

24. M.J. Hinich, Maximum likelihood estimation of the position of a radiating source in a waveguide. *J. Acoust. Soc. Am.* **66**, 480–483 (1979)
25. R.G. Fizell, Application of high-resolution processing to range and depth estimation using ambiguity function methods. *J. Acoust. Soc. Am.* **82**, 606–613 (1987)
26. A.B. Baggeroer, W.A. Kuperman, H. Schmidt, Matched field processing: Source localization in correlated noise as an optimum parameter estimation problem. *J. Acoust. Soc. Am.* **83**, 571–587 (1988)
27. A.B. Baggeroer, W.A. Kuperman, Matched field processing in ocean acoustics. in *Acoustic Signal Processing for Ocean Exploration*, ed. by J.M.F. Moura, I.M.G. Lourtie (Kluwer, Dordrecht, The Netherlands, 1993), pp. 79–114
28. A. Tolstoy, *Matched Field Processing for Underwater Acoustics* (World Scientific, Singapore, 1993)
29. T.C. Yang, A method of range and depth estimation by modal decomposition. *J. Acoust. Soc. Am.* **82**, 1736–1745 (1987)
30. G.A. Wilson, R.A. Koch, P.J. Vidmar, Matched mode localization. *J. Acoust. Soc. Am.* **84**, 310–320 (1988)
31. E.C. Shang, An efficient high-resolution method of source localization processing in mode space. *J. Acoust. Soc. Am.* **86**, 1960–1967 (1989)
32. S.M. Jesus, Normal mode matching localization in shallow water: Environmental and system effects. *J. Acoust. Soc. Am.* **90**, 2034–2041 (1990)
33. M.B. Porter, R.L. Dicus, R.G. Fizell, Simulation of matched field processing in a deep-water Pacific environment. *IEEE J. Oceanic Eng.* **12**, 173–181 (1987)
34. R.M. Hamson, R.M. Heitmeyer, Environmental and system effects on source localization in shallow water by the matched-field processing of a vertical array. *J. Acoust. Soc. Am.* **86**, 1950–1959 (1989)
35. D.F. Gingras, Methods of predicting sensitivity of matched-field processors to mismatch. *J. Acoust. Soc. Am.* **86**, 1940–1949 (1989)
36. A. Tolstoy, Sensitivity of matched-field processing to sound-speed profile mismatch for vertical arrays in a deep water Pacific environment. *J. Acoust. Soc. Am.* **85**, 2394–2404 (1989)
37. C. Feuillade, W.A. Kinney, D.R. DelBalzo, Shallow-water matched-field localization off Panama City, Florida. *J. Acoust. Soc. Am.* **88**, 423–433 (1990)
38. A.M. Richardson, L.W. Nolte, *A posteriori* probability source localization in an uncertain sound speed, deep ocean environment. *J. Acoust. Soc. Am.* **89**, 2280–2284 (1991)
39. J.L. Krolik, W.S. Hodgkiss, Matched field source localization in an uncertain environment using constraints based upon sound speed perturbations. in *Proceedings of the IEEE Oceans'91 Conference*, 1991
40. M.D. Collins, W.A. Kuperman, Focalization: Environmental focusing and source localization. *J. Acoust. Soc. Am.* **90**, 1410–1422 (1991)
41. J.M. Ozard, P. Zakarauskas, P. Ko, An artificial neural network for range and depth discrimination in matched field processing. *J. Acoust. Soc. Am.* **90**, 2658–2663 (1991)
42. J.S. Perkins, W.A. Kuperman, Environmental signal processing: Three-dimensional matched-field processing with a vertical array. *J. Acoust. Soc. Am.* **87**, 1553–1556 (1990)
43. C.A. Zala, J.M. Ozard, Matched-field processing in a range-dependent environment. *J. Acoust. Soc. Am.* **88**, 1011–1019 (1990)
44. L.N. Frazer, P.I. Pecholcs, Single-hydrophone localization. *J. Acoust. Soc. Am.* **88**, 995–1002 (1990)
45. E.K. Westwood, Broadband matched-field source localization. *J. Acoust. Soc. Am.* **91**, 2777–2789 (1992)
46. R.K. Brienzo, W.S. Hodgkiss, Broadband matched field processing. *J. Acoust. Soc. Am.* **94**, 2821–2831 (1993)
47. D.P. Knobles, S.K. Mitchell, Broadband localization by matched fields in range and bearing in shallow water. *J. Acoust. Soc. Am.* **96**, 181–1820 (1994)
48. S.P. Czyszak, J.L. Krolik, Robust wideband matched-field processing with a short vertical array. *J. Acoust. Soc. Am.* **101**, 749–759 (1997)

49. Z.-H. Michalopoulou, M.B. Porter, Matched-field processing for broad-band source localization. *IEEE J. Oceanic Eng.* **21**, 384–392 (1996)
50. Z.-H. Michalopoulou, Robust multi-tonal matched-field inversion: A coherent approach. *J. Acoust. Soc. Am.* **104**, 163–170 (1998)
51. G.J. Orris, M. Nicholas, J.S. Perkins, The matched-phase coherent multi-frequency matched-field processor. *J. Acoust. Soc. Am.* **107**, 2563–2575 (2000)
52. P. Hursky, M.B. Porter, M. Siderius, High-frequency 8–16 kHz model-based source localization. *J. Acoust. Soc. Am.* **115**, 3021–3032 (2004)
53. Z.-H. Michalopoulou, The effect of source amplitude and phase in matched field source localization. *J. Acoust. Soc. Am.* **119**, EL:21–26 (2006)
54. C. Debever, W.A. Kuperman, Robust matched-field processing using a coherent broadband white noise constraint processor. *J. Acoust. Soc. Am.* **122**, 1979–1986 (2007)
55. G.L. D'Spain, W.S. Hodgkiss, G.L. Edmonds, Energetics of the deep ocean's infrasonic sound field. *J. Acoust. Soc. Am.* **99**, 1134–1158 (1991)
56. G.L. D'Spain, W.S. Hodgkiss, G.L. Edmonds, The simultaneous measurement of infrasonic acoustic particle velocity and acoustic pressure in the ocean by freely drifting swallow floats. *IEEE J. Oceanic Eng.* **16**, 195–207 (1991)
57. A. Nehorai, E. Paldi, Acoustic vector-sensor array processing. *IEEE Trans. Signal Process.* **42**, 2481–2491 (1994)
58. M. Hawkes, A. Nehorai, Acoustic vector-sensor correlation in ambient noise. *IEEE J. Oceanic Eng.* **26**, 337–347 (2001)
59. B.A. Cray, A.H. Nuttall, Directivity factors for linear arrays of velocity sensors. *J. Acoust. Soc. Am.* **110**, 324–331 (2001)
60. B.A. Cray, V.M. Evora, A.H. Nuttall, Highly directional acoustic receivers. *J. Acoust. Soc. Am.* **113**, 1526–1532 (2003)
61. G.L. D'Spain, J.C. Luby, G.R. Wilson, R.A. Gramann, Vector sensors and vector sensor line arrays: Comments on optimal array gain and detection. *J. Acoust. Soc. Am.* **120**, 171–185 (2006)
62. H. Cox, H. Lai, K. Bell, Spatial correlation for directional sensors in arbitrary noise fields. in *Proceeding of the 43rd Asilomar Conference on Signals, Systems and Computers*. Pacific Grove, CA, 2009
63. H. Cox, H. Lai, Performance of line arrays of vector and higher order sensors. in *Proceedings of the 41st Asilomar Conference on Signals, Systems and Computers*. Pacific Grove, CA, 2007
64. V.A. Gordienko, B.I. Goncharenko, Ya.A. Ilyushin, Basic rules of vector-phase structure formation of the ocean noise field. *Acoust. Phys.* **39**, 237–242 (1993)
65. W.A. Kuperman, F. Ingenito, Spatial correlation of surface generated noise in a stratified ocean. *J. Acoust. Soc. Am.* **67**, 1988–1996 (1980)
66. B.Y. Zel'dovich, N.F. Pilipetsky, V.V. Shkunov, *Principles of Phase Conjugation* (Springer, Berlin, 1985)
67. M. Fink, C. Prada, F. Wu, D. Cassereau, Self focusing with time reversal mirror in inhomogeneous media. *Proc. IEEE Ultrason. Symp.* **2**, 681–686 (1989)
68. M. Fink, Time reversal mirrors. in *Acoustical Imaging*, vol. 21, ed. by J.P. Jones (Plenum, New York, 1995), pp. 1–15
69. D.R. Jackson, D.R. Dowling, Phase conjugation in underwater acoustics. *J. Acoust. Soc. Am.* **89**, 171–171 (1991)
70. D.R. Dowling, D.R. Jackson, Narrow-band performance of phase-conjugate arrays in dynamic random media. *J. Acoust. Soc. Am.* **91**, 3257–3277 (1992)
71. D.R. Dowling, Phase-conjugate array focusing in a moving medium. *J. Acoust. Soc. Am.* **94**, 1716–1718 (1993)
72. D.R. Dowling, Acoustic pulse compression using passive phase-conjugate processing. *J. Acoust. Soc. Am.* **95**, 1450–1458 (1994)
73. A. Parvulescu, C.S. Clay, Reproducibility of signal transmissions in the ocean. *Radio Electr. Eng.* **29**, 223–228 (1965)
74. A. Parvulescu, Matched-signal ('Mess') processing by the ocean. *J. Acoust. Soc. Am.* **98**, 943–960 (1995)

75. W.A. Kuperman, W.S. Hodgkiss, H.C. Song, T. Akal, C.M. Ferla, D.R. Jackson, Phase conjugation in the ocean: Experimental demonstration of a time reversal mirror. *J. Acoust. Soc. Am.* **103**, 25–40 (1998)
76. H.C. Song, W.A. Kuperman, W.S. Hodgkiss, A time-reversal mirror with variable range focusing. *J. Acoust. Soc. Am.* **103**, 3234–3240 (1998)
77. W.S. Hodgkiss, H.C. Song, W.A. Kuperman, T. Akal, C.M. Ferla, D.R. Jackson, A long range and variable focus phase conjugation experiment in shallow water. *J. Acoust. Soc. Am.* **105**, 1597–1604 (1999)
78. P. Roux, W.A. Kuperman, W.S. Hodgkiss, H.C. Song, T. Akal, M. Stevenson, A nonreciprocal implementation of time reversal in the ocean. *J. Acoust. Soc. Am.* **116**, 1009–1015 (2004)
79. W.A. Kuperman, D.R. Jackson, Ocean acoustics, matched-field processing and phase conjugation. in *Imaging of Complex Media with Acoustic and Seismic Waves*, ed. by M. Fink, W.A. Kuperman, J.-P. Montagner, A. Tourin (Springer, Berlin, 2002), pp. 43–97
80. D. Rouseff, D.R. Jackson, W.L.J. Fox, C. Jones, J.A. Ritcey, D.R. Dowling, Underwater acoustic communications by passive-phase conjugation: Theory and experimental results. *IEEE J. Oceanic Eng.* **26**, 821–831 (2001)
81. J. Flynn, J.A. Ritcey, D. Rouseff, W.L.J. Fox, Multichannel equalization by decision-directed passive phase conjugation: Experimental results. *IEEE J. Oceanic Eng.* **29**, 824–836 (2004)
82. H.C. Song, W.S. Hodgkiss, W.A. Kuperman, T. Akal, M. Stevenson, Multiuser communications using passive time reversal. *IEEE J. Oceanic Eng.* **32**, 915–926 (2007)
83. H.C. Song, W.A. Kuperman, W.S. Hodgkiss, Basin-scale time reversal communications. *J. Acoust. Soc. Am.* **125**, 212–217 (2009)
84. H.C. Song, W.S. Hodgkiss, W.A. Kuperman, T. Akal, M. Stevenson, High-rate synthetic aperture communications in shallow water. *J. Acoust. Soc. Am.* **126**, 3057–3061 (2009)
85. J. Kim, W.S. Hodgkiss, W.A. Kuperman, H.C. Song, Null broadening in a waveguide. *J. Acoust. Soc. Am.* **112**, 189–197 (2002)
86. M. Siderius, D.R. Jackson, D. Rouseff, R.P. Porter, Multipath compensation in range dependent shallow water environments using a virtual receiver. *J. Acoust. Soc. Am.* **102**, 3439–3449 (1997)
87. A.M. Thode, Source ranging with minimal environmental information using a virtual receiver and waveguide invariant theory. *J. Acoust. Soc. Am.* **108**, 1582–1594 (2000)
88. J.F. Lingevitch, H.C. Song, W.A. Kuperman, Time reversed reverberation focusing in a waveguide. *J. Acoust. Soc. Am.* **111**, 2609–2614 (2002)
89. H.C. Song, W.S. Hodgkiss, W.A. Kuperman, K.G. Sabra, T. Akal, M. Stevenson, Passive reverberation nulling for target enhancement. *J. Acoust. Soc. Am.* **122**, 3296–3303 (2007)

## About the Authors



**Finn B. Jensen** received the MSc and PhD degrees from the Technical University of Denmark (TUD) in 1968 and 1971, respectively. From 1969 to 1973, he was an Assistant Professor in the Department of Fluid Mechanics at TUD. Since 1973, he has been employed at the NATO Undersea Research Centre, La Spezia, Italy. He started as a research scientist developing numerical models of sound propagation in the ocean, then served for 17 years as Head of the Environmental Modelling Group at NURC, and since 1999 as a Senior Scientist and Project Leader for research related to propagation, reverberation, and target strength modeling.



**William A. Kuperman** received his PhD in Physics from the University of Maryland and presently is a Professor at the Scripps Institution of Oceanography, University of California, San Diego and the director of its Marine Physical Laboratory. Before coming to UCSD in 1993, he was at the Naval Research Laboratory and the NATO Undersea Research Centre in La Spezia, Italy. He has done experimental and theoretical research in an assortment of underwater acoustics and signal processing areas and has spent about 3 years at sea doing experiments.



**Michael B. Porter** graduated from Caltech in 1979 and received his PhD from the Northwestern University in 1984. He held civil service positions at the Naval Ocean Systems Center, the Naval Research Laboratory, and the NATO Undersea Research Centre in Italy. In academia, he was a Professor at the New Jersey Institute of Technology, and held visiting positions at the Scripps Institution of Oceanography, and the University of Algarve (Portugal). In the commercial sector, he was an Assistant Vice President and Chief Scientist at SAIC before joining HLS Research as its President and CEO. His research interests include propagation modeling, target scattering, communications, bioacoustics, and environmental inversion.



**Henrik Schmidt** is Professor of Mechanical & Ocean Engineering at the Massachusetts Institute of Technology. He received his MS degree from the Technical University of Denmark in 1974, and his PhD from the same institution in 1978. Following a postdoctoral fellowship at the Risoe National Laboratory in Denmark, he joined the NATO Undersea Research Centre in Italy in 1982, where he worked on computational ocean acoustics until he joined the MIT faculty in 1987. Professor Schmidt's research has focused on underwater acoustic propagation and signal processing, in particular on the interaction of sound in the ocean with seismic waves in the ocean bottom and the Arctic ice cover.

# Name Index

## A

- Abawi, A.T., 582, 609  
Abramowitz, M., 141, 142, 153, 260, 273, 333  
Achenbach, J.D., 598, 599, 610  
Ainslie, M.A., 709, 769  
Akal, T., 9, 333, 335, 678, 679, 703, 758, 766, 767, 772  
Aki, K., 216, 231, 391, 452, 634, 659  
Alford, R.M., 541, 608  
Alippi, A., 454  
Alterman, Z., 541, 608  
Anderson, K.D., 454  
Anderson, W.L., 272, 333  
Andreevoi, I.B., 152, 455  
Andrew, R.K., 57, 64  
Athanasoulis, G.A., 430, 455

## B

- Babuska, I., 566, 608  
Backus, G.E., 254, 333  
Baer, R.N., 426, 454, 465, 509, 528, 529  
Baggeroer, A.B., 374, 453, 714, 722, 730, 732, 769, 770  
Bamberger, A., 464, 471, 528  
Barbagelata, A., 675, 678, 679, 703  
Bartberger, C.L., 372, 378, 453  
Baumgartner, G.B., 454  
Beisner, H.M., 374, 453  
Belibassis, K.A., 430, 455  
Bell, K., 750, 771  
Bender, C.M., 216, 232  
Beran, M.J., 666, 703  
Bérenger, J.P., 566, 568, 608, 609  
Bergman, P.G., 71, 152, 495, 528  
Berkhous, B.V., 678, 703  
Berkson, J.M., 333, 335, 703  
Berliner, M.J., 11, 63  
Berman, D.H., 465, 528

## B

- Biondi, B., 179, 231  
Björk, Å., 533, 542, 608  
Bleistein, N., 189, 230  
Block, S., 645, 660  
Blottman, J.B., 566, 590, 595, 598, 608  
Bold, G.E.J., 189, 231  
Botseas, G., 499, 511, 528, 529, 694, 696, 698, 704  
Bovio, E., 315, 335  
Bowlin, J.B., 206, 231  
Bowman, J.J., 416, 420, 454  
Boyles, C.A., 372, 453  
Brekhovskikh, L.M., 41, 43, 50, 51, 64, 67, 115, 133, 138, 152, 153, 221, 232, 410, 454, 455  
Brent, R.P., 376, 453  
Brienz, R.K., 749, 763, 770  
Brock, H.K., 476, 493, 495, 528  
Brooke, G.H., 470, 471, 528  
Brown, M.G., 218, 232  
Brown, R., 272, 333  
Browning, D.G., 664, 694, 703  
Bucker, H.P., 174, 175, 183, 184, 193, 200, 208, 210, 226, 230, 231, 300, 301, 354, 453, 730, 769  
Buckingham, M.J., 426, 429, 454, 678, 703, 704  
Burenkov, S.V., 443, 455  
Burnett, D.S., 547, 566, 599, 600, 608, 610  
Burridge, R., 408, 426, 454

## C

- Cakmak, A., 454  
Campbell, J., 192, 231  
Canepa, G., 584, 595, 610  
Cannelli, G.B., 454  
Carbó-Fitέ, C., 63  
Carbone, N.M., 678, 703

Carey, W.M., 664, 694, 696, 698, 703, 704, 728, 769  
 Cassereau, D., 758, 771  
 Cavanagh, R.C., 457, 460, 468, 481, 490, 527  
 Červený, V., 155, 168, 183, 191, 194, 200, 230, 231  
 Chapman, C.H., 219, 232  
 Chapman, N.R., 34, 63, 372, 379, 453, 454, 465, 528  
 Chapman, R.P., 52, 56, 64  
 Chen, C.F., 511, 529  
 Chew, W.C., 272, 333  
 Chin-Bing, S.A., 511, 528, 529, 546, 608  
 Chuprova, S.D., 133, 152, 444, 455  
 Claerbout, J.F., 463, 464, 511, 527  
 Clark, C.A., 372, 453  
 Clay, C.S., 3, 23, 62, 63, 71, 152, 758, 771  
 Cockrell, K.L., 729, 769  
 Colborn, J.G., 5, 63  
 Colladen, J.-D., 2  
 Collino, F., 566, 608  
 Collins, M.D., 464, 470–472, 474, 487, 498, 508, 511, 517, 528, 529, 532, 607, 621, 659, 733, 770  
 Cook, R., 160, 230  
 Cornuelle, B.D., 3, 63  
 Cornyn, J.J., 206, 231  
 Cox, C.S., 671, 703  
 Cox, H., 662, 703, 723, 750, 752, 754, 769, 771  
 Cray, B.A., 750, 753, 771  
 Cristini, P., 379, 454  
 Cron, B.F., 669, 671, 703  
 Czenszak, S.P., 749, 770

**D**

D'Alembert, J., 1  
 D'Spain, G.L., 11, 63, 133, 153, 220, 232, 443, 455, 681, 686, 704, 750, 752–754, 771  
 Dahlquist, G., 533, 538, 542, 608  
 Dashen, R., 694, 704  
 Davies, B., 379, 454  
 Davis, J.A., 189, 192, 231, 457, 460, 468, 472, 481, 490, 527, 528, 694, 696, 698, 704  
 Dawson, T.W., 277, 281, 334, 571, 609  
 Deane, G.B., 219, 232, 678, 703, 704  
 Deavenport, R.L., 141, 153, 233, 234, 260, 265, 332  
 Debever, C., 749, 771  
 Del Grosso, V.A., 3, 63  
 DelBalzo, D.R., 733, 770  
 Delves, L.M., 378, 453  
 Deschamps, G.A., 180, 231

Diachok, O.I., 694, 696, 704  
 Dicus, R.L., 733, 770  
 DiNapoli, F.R., 141, 153, 233, 234, 260, 265, 307, 332, 335  
 Doolittle, R., 426, 454  
 Doombos, D.J., 453  
 Dougherty, M.E., 633, 659  
 Dowling, D.R., 758, 765, 771, 772  
 Dozier, L.B., 369, 375, 453  
 Drummond, R., 219  
 Dubbelday, P.S., 379, 454  
 Dubra, A., 272, 333  
 Duda, T.F., 206, 231  
 Dushaw, B.D., 3, 63  
 Dzieciuch, M.A., 57, 64, 725, 769  
 Dziewonski, A., 645, 660

**E**

Ebbeson, G.R., 33, 34, 63  
 Edmonds, G.L., 750, 771  
 Engquist, B., 463, 464, 471, 528  
 Epifanio, C.L., 678, 704  
 Etter, P.C., 61, 64  
 Evans, R.B., 353, 403, 407, 429, 452, 454, 472, 528, 531, 532, 555, 607, 664, 694, 696, 698, 703, 704  
 Everstine, G.C., 600, 610  
 Evora, V.M., 750, 771  
 Ewing, W.M., 24, 63, 71, 122, 152, 233, 234, 242, 243, 245, 333, 352, 452, 644, 659

**F**

Fan, H., 292, 334  
 Fawcett, J.A., 277, 281, 334, 420, 429, 454, 571, 582, 609, 629, 659  
 Feit, D., 568, 609  
 Feit, M.D., 465, 528  
 Felsen, L.B., 281, 334  
 Ferla, C.M., 369, 407, 453, 454, 506–508, 529, 758, 772  
 Ferrari, J.A., 272, 333  
 Ferris, R.H., 640, 659  
 Feshbach, H., 116, 152, 621, 659  
 Feuillade, C., 733, 770  
 Fialkowski, J.M., 52, 54, 64  
 Fialkowski, L.T., 687, 704  
 Fink, M., 758, 771, 772  
 Fisher, F.H., 36, 63  
 Fisher, G.A., 233, 333, 546, 608  
 Fitzgerald, R.M., 624, 630, 659  
 Fizell, R.G., 730, 733, 770  
 Flatté, S.M., 7, 63  
 Fleck, J.A., 465, 528

- Fletcher, C.A.J., 547, 608  
 Flynn, J., 766, 772  
 Fock, V.A., 457, 527  
 Foreman, T.L., 193, 206, 231  
 Forsythe, G.E., 533, 540, 543, 607  
 Fox, W.L.J., 315, 335, 765, 766, 772  
 Francois, R.E., 37, 38, 63  
 Franssens, G.R., 254, 333  
 Frazer, L.N., 277–279, 334, 617, 659, 749, 770  
 Freitag, L.F., 206, 231  
 Fricke, J.R., 534, 541, 543, 545, 608  
 Fried, S., 683, 704  
 Frisk, G.V., 71, 152  
 Fry, W.J., 337, 452  
 Fuchs, K., 233, 234, 256, 332
- G**  
 Galerkin, B.G., 548, 608  
 Gamow, G., 1, 62  
 Garrison, G.R., 37, 38, 63  
 Gaul, R.D., 664, 703  
 Gauss, R.C., 52, 54, 64  
 Geissler, P., 704  
 Georges, T.M., 226, 232  
 Gerstoft, P., 220, 232, 279, 281, 334, 571, 574,  
     587–589, 609, 727, 769  
 Gettrust, J.F., 278, 334  
 Giddings, T.E., 568, 609  
 Gilbert, F., 254, 333  
 Gilbert, K.E., 499, 503, 528  
 Gingras, D.F., 733, 770  
 Glattetre, J., 282, 283, 286, 334, 431, 455, 582,  
     609, 687, 704  
 Glegg, S.A.L., 678, 703  
 Godin, O.A., 43, 50, 64, 67, 71, 115, 133, 152,  
     410, 454, 584, 610  
 Goh, J.T., 287, 334  
 Goldhahn, R., 729, 769  
 Goncharenko, B.I., 753, 771  
 Gordienko, V.A., 753, 771  
 Gordon, D.F., 175, 231, 372, 451  
 Gottlieb, D., 544, 608  
 Gruber, H.C., 664, 703  
 Grachev, G.A., 133, 136, 153  
 Gragg, R.F., 52, 54, 64  
 Gramann, R.A., 11, 63, 752–754, 771  
 Greene, R.R., 463, 471, 479, 480, 482, 527,  
     528  
 Gubbins, D., 215, 231  
 Guidi, G., 675, 678, 679, 703  
 Gunzberger, M., 544, 608  
 Guthrie, A.N., 630, 659  
 Guthrie, K.M., 359
- H**  
 Hale, F.E., 20, 21, 63  
 Halpern, L., 463, 464, 471, 528  
 Hamilton, E.L., 39, 63, 647, 660  
 Hamming, R.W., 379, 454  
 Hamson, R.M., 733, 770  
 Hardin, R.H., 457, 459, 463, 486, 488, 510,  
     527  
 Harkrider, D.G., 241, 333  
 Harris, J.H., 52, 64  
 Harrison, C.H., 678, 686, 703, 704, 726, 727,  
     769  
 Haskell, N.A., 234, 252, 333  
 Haussecker, H., 678, 704  
 Hawker, K.E., 624, 630, 659  
 Hawkes, M., 750, 771  
 Heaney, K.D., 426–429, 443, 454, 455  
 Heitmeyer, R.M., 733, 770  
 Hickman, G., 729, 769  
 Hildebrand, F.B., 196, 231  
 Hill, R.J., 468, 528  
 Hines, P.C., 315, 335  
 Hinich, M.J., 730, 769  
 Hitney, H.V., 379, 454  
 Hoback, H., 474, 528  
 Hodgkiss, W.S., 220, 232, 681, 686, 704, 727,  
     733, 749, 750, 758, 763, 764, 766, 767,  
     769–772  
 Holland, C.W., 314, 315, 317, 335  
 Hollett, R., 315, 317, 335  
 Horrigan, A.A., 133, 137, 153  
 Hovem, J.M., 63, 546, 608  
 Howe, B.M., 3, 57, 63, 64  
 Huang, C.-F., 727, 769  
 Huang, D., 497, 508, 528, 546, 608  
 Hursky, P., 749, 771
- I**  
 Ide, J.M., 337, 452  
 Ihlenburg, F., 566, 599, 600, 608  
 Ilyushin, Ya.A., 753, 771  
 Ingard, K.U., 71, 152, 415, 416, 454, 605, 610,  
     628, 659  
 Ingenito, F., 285, 334, 374, 388, 413, 417, 421,  
     453, 454, 580, 609, 663, 678, 687, 688,  
     702–704, 754, 771
- J**  
 Jackson, D.R., 39, 64, 756, 758, 759, 765, 767,  
     771, 772  
 Jacobson, M.J., 666, 703  
 Jahne, B., 678, 704

- Jardetzky, W.S., 122, 152, 233, 234, 242, 243, 245, 333, 352, 452, 659
- Jeong, W.-K., 160, 230
- Jerzak, W., 472, 528
- Jesus, S.M., 733, 770
- Johnson, D.H., 716, 720, 769
- Joly, P., 463, 464, 471, 528
- Jones, C., 765, 772
- Jones, D.S., 175, 231
- Jones, J.P., 771
- Jones, R.M., 226, 232
- Joshi, S.M., 664, 703
- Julian, B.R., 215, 231
- Junger, M.C., 568, 609
- K**
- Kaplunov, J.D., 592, 610
- Karal, F.C., 541, 608
- Kargl, S.G., 592, 610
- Kawase, H., 281, 334, 571, 609
- Keenan, R.E., 174, 230
- Keller, H.B., 216, 231, 375, 453
- Keller, J.B., 155, 178, 216, 230, 527
- Kelly, K.R., 541, 608
- Kennett, B.L.N., 233, 234, 255, 333
- Kerman, B.R., 57, 64, 703
- Kerry, N.J., 233, 234, 255, 333
- Kessel, R.T., 580, 609
- Kewley, D.J., 664, 694, 703
- Kibblewhite, A.C., 671, 703
- Kim, J., 766, 772
- Kim, S., 160, 230
- King, D.B., 192, 231, 472, 528
- Kinney, W.A., 733, 770
- Knightly, G.H., 463, 527
- Knobles, D.P., 664, 703, 749, 770
- Ko, P., 733, 770
- Koch, R.A., 372, 453, 733, 770
- Kolsky, H., 243, 333, 528
- Kong, J.A., 272, 333
- Kosloff, D., 545, 608
- Kosloff, R., 545, 608
- Kossovich, L.Y., 592, 610
- Kravtsov, Yu.A., 178, 231
- Krenk, S., 279, 284, 334, 429, 576, 609
- Kriegsmann, G.A., 509, 529
- Krolik, J.L., 729, 733, 749, 769, 770
- Kutschale, H.W., 233, 234, 251, 254, 306, 332
- L**
- Lai, H., 750, 752, 753, 771
- Landau, L.D., 224, 232
- Landisman, M., 645, 660
- Lara-Sáenz, A., 63
- Lasky, M., 2, 62
- Lee, D., 216, 230, 231, 300, 334, 453, 454, 457, 463, 486, 497, 499, 500, 503, 505, 508, 509, 511, 527–529
- Lee, J., 285, 309, 311–314, 334, 592, 595, 610
- Lee, S., 729, 769
- Lehmer, D.H., 378, 453
- Leighton, T.G., 7, 63
- Leonardo da Vinci., 2
- Leontovich, M.A., 457, 527
- LePage, K.D., 272, 288, 292, 295, 314, 325, 328, 333–335
- Levinson, S.J., 372, 453
- Li, F.-H., 453
- Lichte, H., 155, 230
- Lifshitz, I.D., 224, 232
- Liggett, W.S., 666, 703
- Lin, Y.-T., 511, 529
- Lindberg, J.F., 11, 63
- Lindsay, R.B., 1, 62
- Lingevitch, J.F., 767, 772
- Liu, Q.H., 272, 333, 334, 567, 568, 608, 609
- Liu, Y.-C., 173, 230
- Livingston, E.S., 453
- Lobkis, O.I., 680, 704
- Lourtie, I.M.G., 770
- Lu, I.T., 281, 334
- Luby, J.C., 11, 63, 750, 752–754, 771
- Lucifredi, I., 286, 334, 581, 592, 609
- Ludwig, D., 178, 231
- Luo, W., 408, 429, 431, 433, 435, 454
- Lurton, X., 709, 769
- Lyness, J.N., 378, 453
- Lyons, A., 310, 312, 335
- Lysanov, Yu., 41, 43, 51, 64, 133, 138, 153, 221, 232
- M**
- Maguer, A., 315, 335
- Makris, N.C., 285, 334, 420, 454, 664, 678, 692, 703, 704, 729, 769
- Mallick, S., 277, 279, 334, 617, 659
- Malm, N., 566, 590, 595, 598, 608
- Maranda, B.H., 629, 659
- Marburg, S., 703
- Marple, L., 720, 769
- Marshall, J.R., 56, 64
- Marston, P.L., 592, 610
- Matar, O.B., 568, 609
- May, J., 372, 453

McDaniel, S.T., 300, 334, 457, 466, 486, 497, 500, 505, 508, 527–529  
 McDonald, B.E., 426–429, 454, 622, 659  
 McGirr, R.W., 192, 200, 210, 231  
 Medwin, H., 3, 62, 71, 152  
 Mellen, R.H., 307, 335  
 Mercer, J.A., 57, 64  
 Mersenne, M., 1  
 Metzger, K., 3, 63  
 Michalopoulou, Z.-H., 749, 770, 771  
 Miklowitz, J., 129, 152, 240, 333, 471, 528  
 Miller, B.E., 307, 335, 655, 660  
 Mindlin, R.D., 655, 660  
 Mitchell, S.K., 372, 453, 749, 770  
 Moler, C.B., 211, 231  
 Monk, P., 566, 567, 608  
 Montagner, J.-P., 772  
 Morse, P.M., 71, 116, 152, 415, 416, 454, 605, 610, 621, 628, 659  
 Moura, J.M.F., 770  
 Mueller, G., 233, 234, 256, 332  
 Muir, T.G., 474, 528  
 Muller, G., 191, 194, 231  
 Munk, W., 71, 152, 356, 453, 694, 704, 725, 769  
 Murphy, E.L., 189, 231  
 Murphy, J.E., 546, 608, 611, 659

**N**

Naugolnykh, K., 10, 63  
 Nehorai, A., 11, 63, 750, 771  
 Nero, R.W., 52, 54, 64  
 Neumann, P., 317, 335  
 Newman, A.V., 374, 453  
 Newmark, N.M., 541, 569, 608  
 Newton, I., 1  
 Nghiem-Phu, L., 465, 528, 611, 659  
 Nicholas, M., 749, 771  
 Nielsen, P.L., 517, 529  
 Nolde, E.V., 592, 610  
 Nolet, G., 230  
 Nolte, L.W., 733, 770  
 Northrup, J., 4, 5, 63  
 Novikov, B.K., 10, 63  
 Nutile, D.A., 624, 630, 659  
 Nuttall, A.H., 750, 753, 771

**O**

Oberhettinger, F., 666, 670, 703  
 Officer, C.B., 71, 152  
 Ogilvy, J.A., 51, 64  
 Olson, A.H., 233, 333, 546, 608

Oppenheim, A.V., 262, 266, 309, 333, 613, 614, 659, 769  
 Orcutt, J.A., 233, 333, 546, 608, 671, 703  
 Orlov, Yu.I., 178, 231  
 Orris, G.J., 749, 771  
 Orszag, S.A., 216, 232  
 Osler, J., 317, 335  
 Ostrovsky, L., 10, 63  
 Outing, D.A., 472, 517, 528  
 Owen, M.M., 723, 769  
 Ozard, J.M., 733, 742, 770

**P**

Pace, N.G., 310, 312, 335  
 Paldi, E., 11, 63, 750, 771  
 Papadakis, J.S., 527  
 Papadakis, P., 529  
 Pappert, R.A., 379, 454  
 Parent, G.B., 666, 703  
 Parvulescu, A., 758, 763, 771  
 Pecholcs, P.I., 749, 770  
 Pedersen, M.A., 175, 211, 231, 372  
 Pekeris, C.L., 70, 118, 125, 152, 233, 234, 245, 251, 333, 337, 452  
 Perciante, D., 272, 333  
 Perkins, J.S., 509, 529, 687, 704, 742, 743, 749, 770, 771  
 Pernod, P., 568, 609  
 Perozzi, P.J., 216, 231  
 Pierce, A.D., 2, 62, 408, 454, 568, 599, 600, 604, 609, 610, 623, 624, 659  
 Pilipetsky, N.F., 758, 771  
 Popov, M.M., 183, 231  
 Porter, R.P., 767, 772  
 Post, R.F., 337, 452  
 Potter, J.R., 678, 704  
 Pouliquen, E., 310, 312, 315, 335  
 Prada, C., 758, 771  
 Preobrazhensky, V., 568, 609  
 Press, F., 71, 122, 152, 233, 234, 242, 243, 245, 333, 352, 452, 644, 659  
 Pryce, J.D., 384, 454  
 Pšencík, I., 183, 191, 194, 231  
 Pythagoras, 1

**Q**

Quijano, J.E., 729, 769

**R**

Ranz-Guerra, C., 63  
 Rauch, D., 645, 646, 660

- Rayleigh, J.W.S., 129, 152  
 Readhead, M.L., 678, 704  
 Reiss, E.L., 367, 369, 375–377, 392, 395, 452,  
     453  
 Rekdal, T., 179, 231  
 Revie, R., 133, 137, 153  
 Richards, P.G., 216, 231, 391, 393, 452, 634,  
     659  
 Richardson, A.M., 733, 770  
 Richardson, M.D., 39, 63, 64, 608  
 Richter, J.H., 379, 454  
 Riley, J.P., 226, 232  
 Ritcey, J.A., 765, 766, 772  
 Roberts, B.G., 208, 231  
 Rogers, A., 314, 335  
 Rosenberg, A.P., 458, 527  
 Ross, D., 57, 64, 665, 703  
 Rouseff, D., 673, 703, 729, 765–767, 769, 772  
 Roux, P., 680–684, 686, 704, 758, 764, 772  
 Rudenko, O.V., 10, 63
- Smith, L.C., 281, 334, 571, 609  
 Snoek, M., 675, 678, 679, 703  
 Solomon, L.P., 211, 231  
 Song, H.C., 443, 445, 455, 727, 758, 764, 766,  
     767, 769, 772  
 Spiesberger, J.L., 3, 63, 206, 231  
 St. Mary, D.F., 463, 527  
 Stakgold, I., 338, 351, 386, 452  
 Stearns, S.D., 717, 769  
 Stegun, I.A., 141, 142, 153, 260, 273, 333  
 Stepanishen, P., 580, 609  
 Stephen, R.A., 257, 333, 534, 541, 590, 608,  
     633, 659  
 Stephens, R.W.B., 452  
 Sternberg, R.L., 453  
 Stevenson, M., 764, 766, 767, 772  
 Stickler, D.C., 354, 372, 453  
 Stoll, R.D., 63, 608  
 Sturm, F., 509–511, 519–524, 529, 641–644,  
     659  
 Sturm, J., 2

**S**

- Sabra, K.G., 680, 681, 683, 686, 704, 767, 772  
 Sarkissian, A., 580, 609  
 Schafer, R.W., 262, 266, 309, 333, 613, 614,  
     659  
 Schmalfeldt, B., 645, 646, 660  
 Schmidt, R.O., 721, 769  
 Schneider, H.G., 216, 232  
 Schultz, M.H., 230, 453  
 Schuster, G.T., 281, 334, 571, 609 (PM: Spelt  
     as "Shuster" in page 281. Please check  
     and change.)  
 Sellschopp, J., 6, 63  
 Senior, T.B.A., 416, 420, 454  
 Seong, W., 281, 334, 546, 608  
 Sethian, J.A., 160, 230  
 Shaffer, J.D., 624, 630, 659  
 Shang, E.C., 733, 770  
 Sheer, E.K., 722, 732, 769  
 Sheppard, C.V., 372, 453  
 Sherman, C.H., 669, 671, 703  
 Shirron, J.J., 566, 568, 608, 609  
 Shkunov, V.V., 758, 771  
 Siderius, M., 609, 686, 704, 726, 727, 749,  
     767, 769, 771, 772  
 Siegmann, W.L., 472, 509, 511, 517, 528, 529  
 Simmen, J., 453  
 Simmons, G., 272, 333  
 Simmons, V.P., 36, 63  
 Simons, D.G., 609, 678, 703  
 Smith, G.D., 533, 538, 540, 543, 607  
 Smith, K.B., 372, 453

**T**

- Tang, D.J., 673, 703  
 Tango, G., 234, 245, 257, 333, 616, 633, 645,  
     659  
 Tao, J., 568, 609  
 Tappert, F.D., 156, 216, 230, 231, 369, 375,  
     453, 457–459, 463, 465, 476, 486, 488,  
     490, 495, 496, 510, 527, 528, 611, 659  
 Taroudakis, M.I., 429, 431, 454, 529  
 Tesei, A., 566, 584, 590, 595, 598, 608, 610  
 Thode, A.M., 443, 445, 455, 681, 686, 704,  
     767, 772  
 Thomas, S.J.L., 133, 137, 153  
 Thomson, D.J., 465, 479, 528  
 Thomson, W.T., 234, 252, 333  
 Thorp, W.H., 36, 63  
 Thurston, R.N., 610  
 Timoshenko, V.I., 10, 63  
 Tindle, C.T., 189, 219, 231, 232, 359, 372,  
     379, 453, 454, 474, 516, 528, 529, 678,  
     703  
 Tolstoy, A., 426, 454, 509, 529, 732, 733, 770  
 Tolstoy, I., 22, 23, 63, 71, 143, 146, 152, 372,  
     453, 619, 659  
 Tourin, A., 772  
 Tracey, B., 291, 334  
 Traer, J., 727, 769  
 Trefethen, L.N., 463, 528  
 Treitel, S., 541, 608  
 Troiano, L., 315, 317, 335

Tsang, L., 272, 333  
Turkel, E., 544, 608

**U**

Urban, H.G, 10, 63, 709, 769  
Urick, R.J., 2, 3, 10, 22, 25–27, 29, 30, 36, 37,  
    54, 57, 62–64, 709, 710, 713, 769  
Uslenghi, P.L.E., 416, 420, 454

**V**

Veksler, N.D., 602, 610  
Veljkovic, I., 580, 584, 609  
Vichnevetsky, R., 454  
Vidale, J., 160, 230  
Vidmar, P.J., 189, 231, 733, 770  
Vilmann, O., 279, 334  
Virovlyansky, A.L., 224, 225, 232

**W**

Wagstaff, R.A., 694, 696, 704, 728, 769  
Wales, S.C., 694, 696, 704  
Ward, R.W., 541, 608  
Wasow, W.R., 533, 540, 543, 607  
Watson, W.H., 200, 210, 231  
Weaver, R.L., 680, 704  
Weinberg, H., 174, 216, 230, 408, 426, 454  
Wenz, G.M., 58, 59, 64  
Westervelt, P.J., 10, 63  
Weston, D.E., 133, 137, 153  
Westwood, E.K., 189, 231, 372, 379, 453, 472,  
    508, 517, 528, 529, 749, 770  
Wetton, B.T.R., 470, 471, 528  
Whitaker, R.T., 160, 230  
White, D., 457, 460, 468, 481, 490, 527  
Whitham, G.B., 619, 659

Widrow, B., 717, 769  
Wilkinson, J.H., 453  
Williams, A.O., 337, 452  
Williams, N.J., 664, 703  
Wilson, G.A., 733, 770  
Wilson, G.R., 11, 63, 752–754, 771  
Wilson, J.D., 664, 692, 703  
Wilson, J.H., 694, 704  
Wilson, O.B., 10, 63  
Woodhouse, J.H., 377, 453  
Worcester, P.F., 3, 63, 71, 152, 725, 769  
Worzel, J.L., 24, 63  
Wright, E.B., 465, 528  
Wu, F., 758, 771  
Wunsch, C., 71, 152  
Wurmser, D., 52, 54, 64

**Y**

Yang, T.C., 733, 770  
Yefet, A., 566, 567, 608

**Z**

Zakarauskas, P., 733, 770  
Zala, C.A., 742, 770  
Zampolli, M., 517, 529, 566, 580, 584, 590,  
    595, 598–600, 608–610  
Zel'dovich, B.Y., 758, 771  
Zeng, Y.Q., 568, 609  
Zeskind, R.M., 723, 769  
Zhang, X., 39, 64  
Zhang, Z.Q., 272, 334  
Zhou, J.-X., 39, 64, 374, 453  
Zienkiewicz, O.C., 547, 548, 552, 557, 558,  
    563, 569, 570, 608  
Zurk, L.M., 729, 769



# Subject Index

## A

- Acoustic lens, 512, 513, 515
- Adaptive beamforming
  - eigenvector decomposition, 721
  - minimum variance (MV), 716, 719–720
- Adaptive integration, 259, 260, 279–280, 332
- Adiabatic approximation, 403, 407–410, 412–413, 426, 441–443, 445
- Afternoon effect, 3
- Airy phase, 125, 150, 637, 639
- Aliasing, 259, 262–268, 275, 277, 323, 612–617
- Ambient noise, 57–60, 429, 661–703, 726, 728–729
  - See also* Noise
- Ambient noise spectra, 57, 58
- Ambiguity
  - function, 732, 735, 741–743, 745–748, 761, 767
  - surface, 735–746, 748, 749
  - volume, 745–747, 750
- Angular limitation
  - of PEs, 466, 473, 476, 483
- Arctic propagation, 7, 25, 27–28, 305–309, 571, 585, 654, 655
- Array gain, 705–708, 712, 714–715, 723, 728–729, 752
- Array processing, 705, 718, 722, 725, 733, 753, 767
- Artificial bottom
  - in PEs, 472, 533
- Attenuation, 130–132, 243–244, 496–497
  - conversion of units, 37
  - in mode solutions, 687
  - in PE solutions, 515, 519, 524
  - in ray solutions, 178–179
  - in seawater, 36–38
  - in sediments, 43, 131, 317, 494, 644
  - in WI solutions, 243–244

loss tangent, 35, 131, 151, 243, 244

perfectly matched layer, 566–568

quality factor, 151, 244

## B

- Backscattering
  - at rough seafloor, 281
  - at rough sea surface, 51, 571
  - from volume inhomogeneities, 54–57, 292–296, 316, 319
- Bartlett beamformer, 716, 720, 732, 738
- Beam
  - focusing, 512, 515
  - propagation, 180, 512–516
  - splitting, 512–514
- Beamforming
  - adaptive, 716–721, 767
  - for vector sensor, 750–754
  - linear (Bartlett), 715
  - time delay, 681–683, 724–726, 763
    - with multiple constraints, 722
    - with white-noise constraints, 723–724
- BEM: Boundary Element Method
- Bottom loss, 27, 29, 38–50, 102, 132, 305, 428, 429, 642, 672
- Bottom scattering, 54
- Boundary conditions
  - acoustic halfspace, 191, 382, 398–399, 606
  - Dirichlet, 148, 397–398, 580, 599, 600
  - elastic halfspace, 281, 330, 354, 367, 377, 382, 385, 399–400, 571, 587
  - natural, 148, 542, 552, 561, 565, 566, 573, 575–577
  - Neumann, 148, 283, 286, 398, 431, 557, 580, 599, 600
- Boundary Element Method (BEM)
  - boundary-element equations, 573–576, 578, 579

- B**
- Boundary Element Method (BEM) (*cont.*)  
     boundary-integral equation, 571–573  
     coupled domains, 576–579
- Branch cut  
     EJP, 122, 123, 125, 127, 150, 352  
     Pekeris, 125, 127, 148, 234, 352, 354, 355
- Branch line integral, 123, 125–127, 353, 354, 628, 667
- Branch point, 123, 132, 270, 309, 355
- Broadband modeling, 611–659
- Bulk modulus, 7, 8, 69, 151, 237, 244
- C**
- Cauchy's theorem, 106, 268, 352
- Caustic  
     cusped, 648  
     false, 179, 211–213
- Cell methods  
      $c$ -linear, 206, 208–212, 226  
      $n^2$ -linear, 206–208, 211, 226
- Chapman–Harris formula, 52
- Characteristic equation, 121, 124, 125, 132, 150, 151, 331, 353, 361, 375–377
- Coherent transmission loss  
     for modes, 22, 340  
     for rays, 169–173
- Completeness relation, 343, 419
- Complex source point method, 180–182
- Continuous spectrum, 43, 116, 125, 127, 259, 279, 287, 297, 300, 301, 343, 349, 403, 616, 662, 667, 672, 673, 676–678, 731, 734
- Continuous Wave (CW), 13, 114, 312, 570, 611, 612, 624, 645, 650, 651, 658, 716
- Contour integration  
     for Pekeris waveguide, 118–133, 138, 352, 355  
     for pressure-release waveguide, 106
- Convergence gain, 22
- Convergence zone (CZ), 16, 20–24, 32, 62, 306, 379, 411, 413, 433, 440, 516, 526, 652, 654, 738, 744, 746, 755
- Convergence zone spacing  
     in the Atlantic, 22  
     in the Mediterranean, 21, 22
- Correlation function  
     of noise field (NCF), 664–666, 671, 678–686, 726
- Coupled modes, 139, 281, 403–409, 411, 429–435, 437, 506, 507, 531, 532, 555
- Crank–Nicolson integration, 472
- Critical angle, 25, 41, 42, 45, 50, 62, 96, 98, 100, 136, 170, 230, 313–316, 355, 359, 498, 512, 516, 590, 634, 672, 677, 678, 760, 764
- Critical depth, 16
- Cross-spectral density  
     of noise field, 664, 667, 668, 671
- Cross-Spectral Density Matrix (CSDM), 715, 718–721, 723, 724, 752, 753
- CSDM: Cross-Spectral Density Matrix
- Cutoff frequency  
     in Pekeris waveguide, 125, 350, 636  
     in pressure-release waveguide, 111  
     in rigid-bottom waveguide, 337  
     in shallow-water duct, 29, 30, 130  
     in surface duct, 26
- CW: Continuous Wave
- Cycle distance, 16, 221–223, 359, 451, 738
- Cylindrical spreading, 14, 15, 61, 75, 113, 181, 263, 268, 355, 634, 668
- CZ: Convergence Zone
- D**
- Damping matrix, 562, 563, 570
- Decibel (dB), 13, 43, 52, 707–709, 711–713
- Deep scattering layer, 56
- Deep sound channel, 4, 5, 15, 16, 24–25, 36, 61, 440
- Depth-dependent Green's function, 87–92, 296–301, 320–323, 625–628, 667–668, 672  
     for fluid halfspace, 80, 87, 92, 93, 320  
     for  $n^2$ -linear profile layer, 177  
     for pressure-release waveguide, 111  
     for unbounded medium, 77
- Depth excess, 16, 22
- Depth-separated wave equation, 85, 86, 105, 140, 143, 144, 258, 526  
     WKB approximation, 143–145
- Detection threshold, 709–713, 729
- DGM: Direct Global Matrix method
- Differential equations  
     classification of, 532–533
- Diffracted arrival, 648–649, 654
- Direct Global Matrix method (DGM), 121, 245, 251–255, 257, 258, 321, 331
- Direct global matrix solution, 245–251, 546
- Directivity index, 707–708, 711–714
- Dirichlet boundary condition, 148, 599
- Discrete methods  
     boundary elements, 532, 570

- finite differences, 531, 532, 545, 550, 562, 564, 570, 571, 580–581, 585, 590, 600–601  
 finite elements, 531, 532, 545, 550, 562, 564, 570, 571, 585, 590
- Discrete spectrum, 42, 43, 125, 127, 128, 132, 259, 279, 297, 300, 301, 349, 662, 672, 673, 676, 677, 731
- Discretization error, 284, 537, 538, 542
- Dispersion  
 geometrical, 636  
 intrinsic, 636
- Dispersion curves  
 for Pekeris waveguide, 636  
 for pressure-release waveguide, 112–113  
 for seismic interface wave, 643–647
- Dispersion relation, 150, 345, 400, 452, 461
- Displacement potential  
 definition, 68–69
- Doppler shift  
 in waveguide, 623–633  
 normal mode representation, 628–630  
 numerical example for propagating ice fractures, 654–657  
 wavenumber integral representation, 625–628
- Double-duct profile, 21
- Dynamic ray tracing, 168–169, 183
- E**
- Eigenfunction, 110, 338, 341, 345, 351, 357, 359, 364, 367, 374, 376, 382–384, 387, 410, 428, 432, 442, 445, 446, 473–474, 526, 554–556, 629, 668, 757
- Eigenray, 107, 169, 170, 172, 177, 179, 187, 199, 200, 213–216, 218, 220, 226, 229, 617  
 complex, 176
- Eigenray finding, 187, 200, 213–216, 226  
 interpolation, 214–215  
 iteration, 215  
 the bending method, 215–216  
 the continuation method, 216
- Eigenvalue, 137, 147, 338–339, 346, 351–352, 355, 360–361, 364–369, 371–379, 383–387, 389, 392–394, 396, 410, 428, 445, 446, 449–451, 471, 473–476, 520–521, 526, 527, 544, 628, 629, 669, 720, 721, 724, 757–758
- Eigenvector-decomposition beamformer, 720–721
- Eikonal equation, 159–163, 187
- EJP: Ewing, Jardetzky and Press
- Elasticity  
 in mode solution, 391–402  
 in PE solution, 470–472
- Energy conservation  
 in PEs, 506–508
- Energy density  
 of plane wave, 12, 752
- Energy leakage, 654
- Euler's method, 201, 227
- Evanescence modes, 108, 109, 346, 349, 471, 475
- Evanescence spectrum, 89–91, 100, 108, 109, 127, 128, 322–323, 568, 621, 671, 676, 677
- Ewing, Jardetzky and Press (EJP), 122, 123, 125, 127, 150, 234, 352
- F**
- Fast field approximation, 260–261
- Fast Field Program (FFPs), 60, 216, 233, 234, 260, 265–267, 272–277, 279, 320–323, 332, 469, 470, 612, 620, 621, 635
- Fast Fourier Transform (FFT), 260, 265, 266, 269, 272–274, 276, 277, 279, 323, 332, 490, 525, 612–616, 621, 731
- Fathometer  
 passive, 686, 726–727
- FDM: Finite Difference Method
- FDTD: Finite-Difference Time-Domain
- FEM: Finite Element Method
- Fermat's principle, 195–196, 223–225
- FFP: Fast Field Program
- FFP integration  
 along real axis, 266, 267, 279  
 with contour offset, 332
- FFT: Fast Fourier Transform
- Figure of Merit (FOM), 712, 714
- Filon integration, 278–279, 332
- Finite Difference Method (FDM)  
 convergence and stability, 537–538  
 difference approximations, 165, 363, 534–538, 606  
 sol'n of acoustic wave equation, 538–545
- Finite-difference solution  
 of modal equation, 362  
 of parabolic equation, 501, 541  
 of wave equation, 532  
*See also* IFD solution
- Finite-Difference Time-Domain (FDTD), 568
- Finite Element Method (FEM)  
 coupled fluid-elastic domains, 565–566  
 mathematical derivation, 547–551  
 perfectly matched layer, 566–568

- F**
- Finite Element Method (FEM) (*cont.*)  
 sol'n of acoustic wave equation, 551–561  
 sol'n of elastic wave equation, 562–564  
 steady-state solution, 566  
 time recurrence, 569–570
- Flexural wave, 309, 589, 590, 657
- FOM: Figure of Merit
- Fourier synthesis, 66, 72, 432, 458, 566, 569, 611–618, 621, 627, 628, 633, 638, 645, 649, 652, 657, 658, 663, 680, 755, 759, 762, 763
- Fourier transform, 71, 75, 77, 85, 90, 91, 93, 111, 116–118, 233, 258, 262, 265, 270, 273, 280, 289, 290, 292, 457, 476, 479, 487–489, 494, 506, 525, 541, 612–615, 618–620, 624–627, 630, 666, 680, 702, 705, 715, 725, 755, 762, 763, 768
- Fredholm integral equation, 572
- Frequency integration, 244, 280–281, 627  
 complex, 616–617
- G**
- Galerkin's method, 548, 549, 553–556, 558, 569
- Gaussian beams  
 in free space, 180–181  
 tracing, 174, 181–185, 194, 212, 216, 218, 618
- Gauss's theorem, 164
- Geoacoustic model, 38, 39, 189
- Geoacoustic properties, 39
- Geometric beams, 173–175, 184
- Global propagation (Perth–Bermuda), 426–429
- Green's function  
 depth-dependent form, 85, 87–92, 105, 106, 110, 115, 125, 126, 128, 148, 244, 296–301, 320–323, 329, 330, 332, 554, 625–628, 665, 667, 668, 672  
 for source in fluid halfspace, 80–81  
 for source in unbounded medium, 77  
 general form, 78–80, 85  
 modal expansion, 343–344  
 reciprocity principle, 77, 129, 130
- Green's identity, 147, 553
- Green's theorem, 78–81, 85, 87, 147, 149, 413, 415, 417, 532, 544, 566, 571, 573, 582
- Group slowness, 135, 220, 221, 441, 442, 444
- Group velocity, 111–113, 125, 135, 136, 150, 345, 390–391, 438, 443, 452, 616, 629, 636, 637, 639, 658
- H**
- Hamiltonian  
 Fermat's principle, 223–225
- Hankel function  
 asymptotic form, 74–75, 87, 99, 108, 260, 273, 342, 418, 436, 459, 695–696, 701–702
- Hankel transform, 86–88, 90, 98–99, 110, 119, 122, 123, 127, 217, 219, 234, 236, 239, 243, 257–258, 260, 264, 272–277, 283, 285, 286, 292, 296, 323, 619–620, 625, 628
- Head wave, 100, 316–319, 616, 633–635, 658
- Helmholtz equation, 74–78, 240, 341, 425, 533, 625  
 depth-separated form, 216  
 derivation of, 75, 217, 458, 459, 465, 467, 469, 663–664  
 for point source, 89, 282  
 in Cartesian coordinates, 73, 84, 86, 158–159, 624  
 in cylindrical coordinates, 74, 86, 235–236, 283, 408, 458, 541, 619–620  
 in spherical coordinates, 74–75, 84  
 integral transform solution, 86–87, 131, 235–236  
 sol'n for deep-ocean waveguide, 140  
 sol'n for fluid halfspace, 86  
 sol'n for homogeneous medium, 71–83, 89, 181, 476, 482, 500, 541, 606  
 sol'n for Pekeris waveguide, 102–103  
 sol'n for pressure-release waveguide, 527  
 sol'n for rigid-bottom waveguide, 102–103  
 sol'n for two fluid halfspaces, 94
- Helmholtz–Kirchhoff integral theorem, 592, 595, 604
- Hooke's law, 69, 237, 241–242, 564, 599
- Horizontal refraction, 423–427, 510, 512, 519–520, 522, 641, 643, 644
- I**
- IFD: Implicit Finite Difference  
 IFD solution of parabolic equation, 505  
 error analysis, 503–505  
 numerical implementation, 505
- Image method, 81, 103–105, 107, 109
- Impedance  
 acoustic, 13, 14, 81–82, 544
- Implicit Finite Difference (IFD), 497, 498, 500–503, 505, 506
- Incoherent transmission loss  
 for modes, 340–341  
 for rays, 172

- Index of refraction, 3, 141, 162, 175, 223  
 complex, 493, 497, 505  
 effective, 426, 495
- Integral representations  
 for homogeneous elastic layer, 239–242  
 for homogeneous fluid layer, 235, 237–238  
 for  $n^2$ -linear fluid layer, 238–239
- Integral transforms  
 for axisymmetric problems, 291  
 for plane problems, 84–85
- Intensity  
 of plane wave, 12–15, 52
- Intensity striation, 134, 136
- Interface wave, 43, 91, 127, 248, 255, 287,  
 297, 474, 633, 643–647, 674–675, 677,  
 678
- Interference  
 constructive, 19, 43, 81, 82, 171, 450, 451,  
 482, 629, 766  
 destructive, 19, 81, 171, 175, 482  
 modal, 113–114, 127, 132, 137, 297, 522,  
 641
- Intromission angle, 42, 62, 98
- Invariant  
 of waveguide propagation, 133
- Invariant embedding solution, 255
- Inverse iteration, 365, 367–368, 379–380, 446
- J**
- Jacobian, 166–167  
 relation to phase, 227–228
- K**
- KMAH index, 178, 205–206
- L**
- Lagrange extrapolation, 542
- Lambert’s law, 54
- Lamé constants, 240, 243, 326, 329, 392, 471,  
 562, 599
- Lateral wave, 100, 309, 316
- Leaky precursor, 654
- Limiting ray, 175, 176, 178
- Linear beamforming, 714–716
- Lloyd mirror pattern, 17–20, 81, 91, 93, 171,  
 172, 359, 479, 483
- Loss tangent, 35, 131, 151, 243–244
- M**
- Mass matrix, 562, 563, 570
- Matched Field Processing (MFP), 260, 276,  
 329, 705, 730–750, 761, 763, 767,  
 769  
 numerical examples, 329, 732
- MCM: Multiple Constraints Matching
- MDL: Minimum Detectable Level
- Method of canonical problems, 72, 167
- Method of characteristics, 160
- MFP: Matched Field Processing
- Minimum Detectable Level (MDL), 728–730
- Minimum-variance beamformer, 716, 717,  
 720, 722, 732, 735, 738
- Minimum Variance Distortionless Response  
 (MVDR), 716, 719, 723, 724
- Minimum Variance processor (MV), 716, 717,  
 719–724, 732, 734–741, 743–746, 748,  
 749
- Mixed layer, 3–4, 25, 26, 375
- Modal dispersion  
 in Pekeris waveguide, 125–126  
 in pressure-release waveguide, 111, 114
- Modal equation  
 in cylindrical geometry, 338, 339  
 in plane geometry, 341
- Modal excitation, 108, 123, 127, 150, 631
- Modal interference, 113–114, 127, 132, 137,  
 267, 297, 522, 641
- Modal losses  
 as a perturbation, 385–389
- Mode coupling, 408, 413, 429–438, 531–532  
 adiabatic approximation, 409–410  
 around seamount (3-D), 429–438  
 single-scatter approximation, 408, 531–532
- Mode cycle distance, 359, 451, 738
- Mode expansion  
 for Pekeris waveguide, 118–121  
 for pressure-release waveguide, 111, 124  
 for rigid-bottom waveguide, 337  
 of the Green’s function, 291–292, 343–344
- Mode solution for 3-D environment, 423–438  
 horizontal refraction equations, 423–426
- Mode solution for elastic medium, 241,  
 243–244, 282, 306, 308, 325–326, 329,  
 391–402, 458, 470, 474, 541, 543, 544,  
 561, 565, 598–599, 671
- Mode solution for range-dependent  
 environment  
 adiabatic modes, 407–412  
 coupled modes, 403–409, 411, 412  
 one-way coupled modes, 407–408, 411
- Mode theory  
 for 3-D environment, 662, 745

- Mode theory (*cont.*)**
- for range-dependent environment, 402–413
  - mathematical derivation, 158–175, 688
- Modes**
- bottom-bounce, 359, 360
  - evanescent, 108–109, 346, 349, 471, 475
  - for Munk profile, 213, 358, 360, 375, 437, 449
  - in Pekeris waveguide, 124–126, 151, 297, 355, 356, 527
  - in pressure-release waveguide, 527
  - in rigid-bottom waveguide, 337
  - leaky, 127, 309, 354, 355, 359, 360, 376, 378, 399, 404
  - normalization of, 371–373
  - orthogonality of, 110, 768
  - propagating, 108, 110–111, 113, 114, 127, 266, 346, 347, 367, 382, 419, 445, 468, 516, 519, 522, 527, 641, 650
  - virtual, 122, 125, 297, 300, 652
  - waterborne, 300, 359, 360, 677
- Multiple-constraints beamforming, 722
- Multiple Constraints Matching (MCM), 716, 717, 722, 732, 733, 735–741, 743–746
- Munk profile, 212, 213, 356–360, 374, 437, 439, 449, 450
- MV: Minimum Variance processor
- MVDR: Minimum Variance Distortionless Response
- N**
- NCF: Noise Correlation Function
- Neumann boundary condition, 148, 557, 580, 599, 600
- Neumann stability analysis, 540
- Newmark's method, 541, 569, 570
- Noise
- in continental-slope environment, 691, 693, 698
  - in elastic waveguide, 674–678
  - in fluid waveguide, 671–674
  - in Gulf Stream environment, 742–743
  - in homogeneous halfspace, 669–671
  - in seamount environment, 691–692
- Noise Correlation Function (NCF), 665, 678–686, 726
- Noise fields
- extracting time-domain Green's functions, 678–686
  - intensity distribution, 691, 692
  - spatial correlation, 661, 662, 673, 674, 757
  - vertical directivity, 672, 681, 693, 694, 696, 698, 734, 735
- Noise modeling in 3-D oceans
- adiabatic-mode representation, 687–690
  - parabolic equation representation, 694
- Noise modeling in stratified oceans
- mathematical derivation, 663–665
  - normal-mode representation, 667–669
  - wavenumber-integral representation, 666–667
- Noise notch, 673, 694, 696
- Noise sources
- correlation function, 664–666, 671, 680, 682, 683
  - normalized strength, 663, 667, 668, 670, 733
- Noise spectra
- in elastic waveguide, 674–678
- Normal modes
- See* Modes
- Normalization
- of modes, 371–373
- Numerical discretization
- Euler's method, 201
  - Runge–Kutta method, 200–202
- Numerical evaluation of frequency integral, 259, 280, 287, 612
- Numerical evaluation of wavenumber integral, 106, 262–263, 268, 284, 320
- wavenumber discretization, 262–265
- Numerical examples of FD/FE solutions
- scattering by Arctic ice features, 584–590
- Numerical examples of MFP solutions
- Arctic environment, 738, 742
  - 3-D environment, 741–750
  - shallow-water environment, 734–738
- Numerical examples of mode solutions
- global propagation (3-D), 226, 426–429
  - Gulf Stream problem (3-D), 423–425
  - ideal, rigid-bottom waveguide, 337
  - Munk profile, 358, 360, 375, 437, 450
  - propagation around seamount (3-D), 429–438
  - warm-core eddy, 411–413
- Numerical examples of noise modeling
- continental-slope environment, 691
  - 3-D Gulf Stream environment, 423, 424, 691, 747
  - 3-D seamount environment, 431, 691
  - elastic waveguide, 674–678
  - fluid waveguide, 671–674
- Numerical examples of PE solutions, 458, 471, 474, 483, 484, 487, 506, 524
- beam propagation, 512–515
  - propagation in 2-D wedge, 515–516

- propagation in 3-D wedge, 517–523  
 propagation over elastic bottom, 472, 517,  
 518  
 propagation over seamount, 514, 516  
 propagation through ocean front, 32–33
- Numerical examples of pulse solutions  
 acoustic emission from ice fractures,  
 654–657  
 Arctic propagation, 305–309  
 deep-water propagation, 647–651  
 mode dispersion in waveguide, 636–640  
 propagation in 3-D wedge, 640–643  
 seismic interface waves, 643–647  
 surface-duct propagation with leakage,  
 652–654  
 the head-wave problem, 633–635
- Numerical examples of ray solutions  
 Balearic Sea, 162, 171  
 Dickins seamount, 192  
 global propagation (3-D), 226, 426–429  
 parabolic bathymetry profile, 195  
*See also* Ray diagram
- Numerical examples of WI solutions  
 Arctic propagation, 305–309  
 beam propagation, 317  
 bottom reverberation, 571  
 Bucker waveguide, 300–301  
 elastic-bottom waveguide, 297–300  
 scattering from volume inhomogeneities,  
 292–296  
 target scattering, 260, 285–287, 313–314
- Numerical Hankel transform, 243, 258, 272
- Numerical solution of depth-separated wave  
 equation, 85–88, 105, 140, 141, 143,  
 144, 233, 236, 238, 526, 546, 554, 606,  
 625  
 direct global matrix approach, 245–251  
 invariant embedding approach, 255–257  
 propagator matrix approach, 251–255
- Numerical solution of frequency integral, 244,  
 280–281, 612–613
- Numerical solution of modal equation  
 finite-difference methods (FDMs),  
 361–372, 376, 534–545  
 inverse iteration, 367–368  
 layer methods, 372–373  
 root finders, 375–379  
 shooting methods, 373–375  
 Sturm sequences, 446
- Numerical solution of PEs  
 FD/FE methods, 60, 487, 497  
 split-step Fourier method, 465, 487–490,  
 523
- Numerical solution of ray equations, 156, 202,  
 214, 227  
*c*-linear cell method, 200, 206, 208–212,  
 226, 318  
 direct integration, 200–206, 211, 226  
*n*<sup>2</sup>-linear cell method, 146, 176, 177,  
 206–208, 211, 213, 226
- Numerical solution of wavenumber integral  
 adaptive integration, 259, 279–280, 332  
 Fast Hankel transform, 264, 272–277  
 FFP integration, 234, 261, 266, 267, 269,  
 279, 332  
 Filon integration, 278–279, 332  
 trapezoidal rule integration, 269, 276–279,  
 332
- Numerical stability  
 of direct global matrix (DGM) solution,  
 121, 234, 248–251  
 of invariant embedding solution, 234, 256  
 of propagator matrix solution, 234,  
 253–254
- Numerov’s method, 369, 450
- Nyquist sampling criterion, 266, 615, 616
- O**
- Optimum frequency  
 in the Arctic, 27  
 in shallow water, 30–32, 388, 389
- Orthogonality of modes, 110, 339, 386, 432,  
 768
- P**
- Parabolic equation (PE), 457–527  
 angular limitation of, 466–470  
 energy conservation in, 506–508, 527  
 for 3-D environment, 510, 691, 741,  
 744–748  
 for elastic medium, 7, 470–472, 474–476,  
 517, 518  
 for horizontal interface, 498–500  
 for variable density, 495–496  
 generalized form, 460–462  
 generalized high-angle form, 464  
 in the time domain, 621–623  
 mathematical derivation, 458–470  
 nonlinear, 622, 623  
 phase error in, 466–470  
 standard form, 458–459  
 starting fields, 472–486  
 wide-angle form, 463–466, 468, 470, 479,  
 482, 483, 486, 498, 503, 506, 511

- Paraxial approximation, 66, 459, 462, 623
- Partial discretization  
in finite-element method, 551
- PC: Phase Conjugation
- PE: Parabolic Equation
- PE forms  
Claerbout, 463, 464, 466–469, 481–483, 486, 498, 501, 506, 507, 511, 512  
elastic, 470–472  
Greene, 463, 468, 469, 471, 479–483, 485, 486, 494, 498, 501, 516  
LOGPE, 465  
Padé, 464  
Tappert, 459, 462  
Thomson–Chapman, 482, 483, 485, 506, 507, 516
- PE starting fields  
Gaussian source, 476–486, 494, 523  
generalized Gaussian source, 480–482  
Greene’s source, 479, 481, 483, 485, 486  
modal starter, 469, 473–474  
self starter, 474–476, 486  
spectral properties of, 479, 482–486  
Thomson’s source, 479, 480, 483, 486
- Pekeris waveguide, 103, 110, 118–133, 137, 138, 148, 150, 151, 222, 261, 263, 264, 266, 267, 270, 271, 275, 297, 331, 332, 349, 350, 352, 354–356, 372, 379, 420–422, 438, 439, 445, 449, 468, 527, 606, 607, 636, 637, 639–641, 764  
modal solution, 124
- Perfectly Matched Layer (PML), 566–568, 579, 591–597
- Phase Conjugation (PC), 758–767
- Phase error  
in PEs, 463, 465–470, 483, 486, 506
- Phase shift  
at caustic, 177–178  
upon reflection, 41, 42, 96–98
- Phase slowness, 136, 221, 442, 444
- Phase velocity, 111, 135, 303, 345, 438, 443, 444, 467, 520, 629, 636, 657
- Plane wave  
energy density, 11–12  
intensity, 12
- Plane-wave beamforming  
adaptive, 716–721  
linear (Bartlett), 714–716  
with multiple constraints, 722  
with white-noise constraints, 723–724
- PML: Perfectly Matched Layer
- Poisson sum, 116–118
- Pressure-release waveguide, 111, 124, 127, 527, 682
- mode solution, 107–110  
ray solution, 103
- Probability of detection, 709, 710, 712, 713, 729, 754
- Propagation  
characteristic paths, 15–17  
convergence zone, 20–24, 306, 359–360, 411, 516, 652–654  
in 2-D wedge, 515–516  
in 3-D wedge, 517–523, 640–643  
in deep sound channel, 15, 16, 24–25, 36  
in deep water, 17–28, 495, 647–651  
in the Arctic, 25, 27–28, 305–309, 571  
in shallow water, 9, 28–32, 42, 45, 341, 388, 486  
in surface duct, 15, 25–26, 306, 379, 652–654  
over elastic bottom, 472, 512, 517, 518  
over seamount, 32–35, 192, 516  
through ocean front, 32–33
- Propagator matrix solution, 234, 251–256, 321
- Prüfer transforms, 380–385
- Pulse modeling in time domain  
parabolic equations, 621–623  
ray methods, 617–619  
spectral integral techniques, 619–621
- Pulse modeling via frequency domain  
Fourier synthesis, 612–617
- Q**
- QR algorithm, 365
- Quality factor, 151, 244
- R**
- Radiation condition, 70, 76, 78, 79, 88, 91, 94, 106, 107, 119, 122, 142, 148, 243, 253, 340, 342, 343, 406, 432, 472, 493, 505, 533, 537, 539, 542–545, 561, 566, 570–572, 579, 581, 599
- Range dependence, 32, 60, 149, 208, 379, 411, 412, 460, 461, 467, 494
- Ray  
displacement, 99, 100, 189  
loop length, 22, 23, 359  
trajectory, 158, 160, 161, 214, 215, 220, 223, 316  
travel time, 160, 168, 173, 195, 199, 428  
turning point, 100, 145, 146, 315, 358, 359, 648, 651, 652, 725  
*See also* Eigenray

- Ray anomaly  
 caustic, 175–178  
 false caustic, 211–213  
 shadow zone, 175–178
- Ray caustic, 522, 641
- Ray coordinates, 160, 163, 218
- Ray diagram  
 for Arctic profile, 27  
 for convergence-zone propagation, 21  
 for Dickins seamount, 192, 193  
 for leaky surface duct, 652, 653  
 for Mediterranean profile, 162  
 for Munk profile, 212, 651  
 for  $n^2$ -linear profile, 176, 177, 179, 184  
 for parabolic bathymetry profile, 195  
 for propagation over seamount, 34  
 for propagation through ocean front, 33  
 for shallow-water propagation, 29  
 for SOFAR-channel propagation, 24  
 for surface-duct propagation, 26
- Ray equations  
 numerical solution, 200–216  
 $r(z)$ -form, 186–187  
 $s$ -form, 160–161  
 $\sigma$ -form, 185–186  
 for stratified media, 196–198  
 $z(r)$ -form, 186–187
- Ray expansion  
 for pressure-release waveguide, 103, 104
- Ray family, 648, 651
- Ray invariant, 220–224
- Ray series, 159, 619
- Ray theory  
 in 3-D, 225–226  
 in the time domain, 617–619  
 mathematical derivation, 158–175  
 region of validity, 178–179  
 sol'n of eikonal equation, 160–163  
 sol'n of transport equation, 163–165  
 via the WKB approximation, 232, 219–220
- Ray tube, 164–166, 168, 174, 175, 226, 617, 618
- Ray types  
 refracted bottom-reflected (RBR), 17, 28, 162  
 refracted refracted (RR), 17, 162  
 refracted surface-reflected (RSR), 18, 173, 17, 162  
 surface-reflected bottom-reflected (SRBR), 17, 162
- Rayleigh reflection coefficient, 41, 43
- Rayleigh roughness parameter, 51
- Rayleigh wave, 392, 400, 644
- Ray-mode analogy, 118, 359, 450, 520, 738
- Real Fast Fourier Transform (RFFT), 615, 617
- Receiver Operating Characteristic (ROC),  
 709–711, 713
- Recipe  
 for mode code, 445–446  
 for PE code, 523–525  
 for ray code, 226–227  
 for WI/FFP code, 320–323
- Reciprocity  
 of displacement potentials, 128–130  
 of Green's function, 77–78, 147–149, 321, 626, 763, 764  
 in layered media, 128–130  
 of parabolic equations, 465  
 in Pekeris waveguide, 128–129, 148  
 of ray solution, 147, 199–200
- Reciprocity principle, 77, 129–130, 147–148, 465  
 for Green's function, 77, 129, 147–148
- Recognition differential, 712
- Reflection  
 at fluid–fluid interface, 40–43, 96, 157, 189, 515  
 at fluid–solid interface, 43–45  
 at half-wavelength layer, 48–50  
 at layered fluid halfspace, 39, 45–50  
 at layered solid halfspace, 39, 97, 98, 102  
 at quarter-wavelength layer, 48  
 at rough interface, 51
- Reflection examples  
 different bottom types, 39, 46, 101  
 hard bottom, 95–97, 100, 101  
 soft bottom, 95, 97–98
- Reflectivity method, 233, 256, 257
- Reflectivity zone, 256, 257
- Refraction index, 141, 162, 175, 185, 187, 206, 207, 223, 238, 373, 426, 458, 462, 465, 466, 487, 490, 491, 493–495, 497, 505, 510, 524–526
- Reverberation  
 from rough interfaces, 139, 281, 287–292, 531
- RFFT: Real Fast Fourier Transform
- Richardson extrapolation, 365, 368–369, 446, 450
- Riemann sheet, 122
- Rigid-bottom waveguide, 124, 337  
 modal solution, 385, 449
- Robin boundary condition, 398–399
- ROC curves, 709–711, 713
- ROC: Receiver Operating Characteristic
- Root-finding  
 analytic estimates, 378  
 bisection, 367, 375–377

- Root-finding (*cont.*)  
 brute-force search, 377  
 complex plane, 378–379  
 continuation methods, 378  
 deflation, 377
- Roughness perturbation operators, 324–328
- Rounding error, 538
- Runge–Kutta method, 200–202, 226, 374
- S**
- Scattering, 51–55, 413–422, 590–597  
 at the seafloor, 16–17, 28, 51, 281  
 at the sea surface, 51–53, 57  
 by Arctic ice features, 584–590  
 Chapman–Harris formula, 52  
 column strength, 55  
 farfield computations, 604–605  
 from buried spherical shell, 594–595  
 from half-buried spherical shell, 595, 597  
 from object buried in the seabed, 309  
 from object in waveguide, 413–422  
 from rippled seabed, 310–313  
 from rough interfaces, 290  
 from spherical shell on the seabed, 590–594  
 from volume inhomogeneities, 292–296  
 Lambert’s law, 54  
 virtual source concept (VSC), 579–584
- Scattering cross section, 51–52, 315, 316
- Scattering strength, 52–56, 296
- Scholte wave, 297, 299, 300, 330, 400, 402, 644, 645
- Secular equation, 353, 396
- Sediment stratification, 8
- Seismic interface wave, 91, 127, 248, 287, 297, 643–647, 674
- Seismic profile, 9
- Seismogram, 219, 257, 309, 310, 648, 649
- Semicoherent transmission loss  
 for rays, 172–173
- Separation of variables, 1, 84, 138–140, 281, 338, 349, 466
- Shadow zone, 25, 175–178, 183, 184, 359, 413, 433–434, 520, 522, 641
- Shallow water propagation, 9, 28, 42, 45, 388  
 variability of, 29
- Shape function  
 in finite-element method, 547, 550, 551
- Shear speed  
 in sediments, 38, 39, 45, 298, 401, 645
- Signal excess, 712, 728
- Signal processing, 11, 57, 139, 260, 678, 694, 711, 712, 716, 722, 725, 727, 733, 746, 750, 759, 766, 767
- Simulation and stimulation, 754
- Slowness, 135, 136, 220–224, 440–442, 444
- Snapshot, 379, 586, 612, 633–635, 640, 718, 752, 755–757
- Snell’s law, 15, 16, 22, 25, 40–43, 47–48, 144, 154, 157, 158, 198–199, 210, 220–221, 223, 224, 283, 440, 441, 462, 515, 725, 726
- SOFAR channel, 24, 61, 155
- Sommerfeld–Weyl integral, 88–89, 286, 669
- Sonar equation  
 active, 705, 713–714  
 passive, 705, 711–713
- Sonar performance prediction, 172, 486–487, 711
- Sound propagation models, 50, 60–61
- Sound speed  
 generic profiles, 4, 672  
 in seawater, 13, 15, 37  
 in seawater w. bubbles, 7, 8  
 in sediments, 39, 42, 391  
 microstructure variability, 6–7  
 Munk profile, 357, 375, 433, 434, 437, 438  
 $n^2$ -linear profile, 176, 177  
 profile interpolation, 140–141, 190, 202  
 pseudo-linear profile, 141, 302
- Source strength  
 of point source, 76, 82, 238  
 of surface noise source, 663
- Spectral domains  
 continuous, 127  
 discrete, 127  
 evanescent, 96, 97, 110, 127  
 for elastic waveguide, 127  
 for Pekeris waveguide, 127  
 radiating, 96, 127
- Spectrum level, 13, 734
- Spherical spreading, 14, 15, 19, 22, 29, 75, 276, 639, 648
- Split-step Fourier algorithm, 465, 487–490, 523  
 error analysis, 488, 502–505  
 numerical implementation, 505
- Spreading loss, 130, 512  
 cylindrical, 14, 15, 75, 113  
 spherical, 14, 75
- Square-root operator, 461–465, 467–468, 501  
 Feit–Fleck splitting, 465  
 Padé expansion, 464, 471, 487, 510  
 rational-linear expansion, 463  
 Taylor expansion, 461, 510, 511

- Stability error, 538  
 Starting fields  
*See* PE starting fields  
 Stationary phase method, 99, 107, 112, 219, 220  
 Stiffness matrix, 562–564, 580–582, 595, 607  
 Stoneley wave, 297, 644  
 Striation, 134, 136  
 Sturm–Liouville problem, 137, 338, 339, 349, 353, 360–361, 365, 380, 445, 554, 667–668  
 Sturm sequence, 365–367, 371, 375–376, 446  
 Sturm’s method, 365–367  
 Surface duct, 3, 4, 15, 25–26, 32, 33, 179, 306, 379, 411, 652–654, 671, 674, 738, 741  
 Surface scattering, 25, 27, 52–53, 57, 388–389, 458, 531
- T**  
 Target scattering  
     in waveguide, 285, 416–417  
 Target strength, 285, 592, 593, 596, 597, 713  
 Taylor series, 201, 362, 363, 461, 462, 490–491, 499, 504, 510, 511, 535, 537  
 TDGF: Time Domain Green’s Function  
 Time-delay beamforming, 724–726  
 Time Domain Green’s Function (TDGF), 104–105, 613, 678–686  
 Time recurrence  
     in finite-element method, 569–570  
 Time reversal, 758–767  
 Time Reversal Mirror (TRM), 758–764, 766  
 Topology matrix, 248, 559–560, 607  
 Transducers, 10–11, 441, 444  
 Transmission loss, 14–15, 30, 81–83  
     coherent, 169–171, 341  
     incoherent, 171–172, 340–341, 388, 389  
     semicoherent, 172–173  
 Transport equation, 159, 163–167, 218, 227  
 Trapezoidal rule integration, 269, 276–279, 332  
 Trial function, 575–577, 606  
     in finite-element method, 546, 548, 550, 551, 553–556, 558, 562, 569  
 TRM: Time Reversal Mirror  
 Tunneling  
*See* Energy leakage  
 Turning point, 100, 145–147, 210, 218, 220–221, 315, 358, 359, 374, 375, 441, 648, 651, 652, 725–726
- U**  
 Units, 11, 13, 35, 37, 39, 56, 496, 728, 751
- V**  
 Variational formulation  
     for fluid-elastic domains, 598–604  
 Variational principle, 532, 545, 547, 549  
 Vector sensor, 10, 11, 402  
     beamforming, 750–754  
 Velocity potential  
     definition, 68, 413  
 Virtual Source Concept (VSC), 579–584  
 Volume scattering, 15, 51–57, 315, 713  
 VSC: Virtual Source Concept
- W**  
 Wave equation  
     depth-separated form, 85–88, 105, 140, 141, 143, 144, 233, 236, 238, 245, 251, 252, 258–259, 318, 324, 546, 554, 625  
     derivation, 83, 623  
     for displacement potential, 68–69  
     for particle velocity, 67–68  
     for pressure, 67–69  
     for velocity potential, 68  
     in frequency domain, 71, 86  
     in time domain, 77, 458, 536, 537, 551, 621–623  
     linear, 67–71, 83, 569  
     nonlinear, 66  
     one-way form, 460, 462, 465, 466, 472, 479, 483, 500, 508, 621  
     solution of, 60, 69–72, 75, 83, 86, 175, 233, 245, 251–252, 258, 259, 458, 546, 547, 551, 612, 732, 733  
*See also* Helmholtz equation  
 Wavefront, 90, 109, 156, 158, 160, 166, 189, 191, 358, 450, 561, 634, 681–682, 716, 760  
     extracted from noise data, 682–686  
 Waveguide  
     deep ocean, 139–147  
     ideal, pressure release, 527  
     ideal, rigid bottom, 337  
 Pekeris, 103, 110, 118–133, 137, 138, 148, 150, 261, 271, 275, 297, 331, 332, 349, 350, 352, 354–356, 372, 379, 420–422, 438, 439, 445, 468, 636, 637, 639–641, 764  
 Waveguide invariant, 133–139, 438–445, 440–441  
     for isovelocity waveguide, 118, 222, 674

- Waveguide invariant (*cont.*)  
 for  $n^2$ -linear refracting waveguide, 223  
 for range-dependent environments,  
 443–445  
 ray representation, 220–223
- Waveguide propagation, 118, 133, 140,  
 416–417, 579, 590, 600, 613  
 continuous spectrum, 42–43, 662  
 discrete spectrum, 42–43, 662  
 evanescent spectrum, 89–91, 108, 109, 662  
 radiating spectrum, 89–91, 93
- Wavenumber Integration (WI), 107, 110, 122,  
 126, 233–332, 407, 420, 473, 531, 571,  
 580, 582, 584, 588, 590, 619–620, 624,  
 628, 633, 661, 665, 735  
 aliasing in, 262–265  
 along real axis, 266–268, 270, 277  
 in 3-D, 282–284  
 integral representations for homogeneous  
 elastic layer, 240–242
- integral representations for homogeneous  
 fluid layer, 237–238  
 integral representations for  $n^2$ -linear fluid  
 layer, 238–239  
 in the time domain, 619–620  
 mathematical derivation, 235–244  
 with contour offset, 270
- Weak interfaces, 194–195
- Weighted residuals method, 547–548  
 Galerkin’s approach, 548
- White-Noise constraint (WN) processor,  
 723–724
- WI: Wavenumber Integration
- WKB approximation  
 to depth-separated wave equation, 144  
 to modal eigenfunctions, 357–358
- WKB: Wenzel, Kramers and Brillouin
- Wrap-around, 244, 259, 262, 265, 266, 268,  
 270–271, 275, 276, 614, 617
- Wronskian, 199–200, 351–353, 447, 449